

RTCME'16

25th September ~ 27th September; 2016

NATIONAL CONFERENCE
ON

Recent Trends in Civil and Mechanical Engineering



AIET Bhubaneswar

Aryan Institute of Engineering and Technology Bhubaneswar



Organised By:

Department of Civil and Mechanical Engineering,
AIET, Bhubaneswar - 752050

Recent Trends in Civil and Mechanical Engineering

25th Sep. – 27th Sep. 2016

CONFERENCE PROCEEDING



Organized by

**Department of Civil & Mechanical Engineering
Aryan Institute of Engineering and Technology
Bhubaneswar – 752050**



List of Sponsors

OLTRON Technology

Citicon Engineers Pvt. Ltd

Oritech Computers

Index Consulting and Research Pvt Ltd



ABOUT THE CONFERENCE

Science and materials has continuously evolved through decades. RTCME-2016 was organized in Sep-2016 and was successful in capturing the development of materials and processing. Department of Mechanical and Civil Engineering, AIET, Bhubaneswar is organizing RTCME-2016 to showcase recent advances in materials processing and applications. In keeping up with the research interest of the materials community, RTCME-2016 will provide an update on scientific and technical aspects covering broad areas of interests in engineering materials, processing and applications.

ABOUT THE DEPARTMENT

The Department of Mechanical and Civil Engineering has been in existence since 2009 with the inception of the college with an initial intake capacity of 60 and is producing high quality technical manpower needed by industry, R&D organizations, and academic institutions. The intake capacity was enhanced to 120 in the year 2011. The Department has full fledged faculty members who are specialized in the fields of design, thermal, production and CAD/CAM. Laboratories are fully equipped to enhance the knowledge of the student, periodic industry trips and visits to various project sites are arranged. Special lectures and seminars are held on a frequent basis to assist them tailor in their particular areas of interest and trying hard to transform students of even mild talent to professionals in the mechanical and mechatronics field. Already more than 750 nos of alumni have been produced so far, placed in different Government, private, Public & other sectors and some of them have pursued higher studies. However, with the progress of time, many more frontier areas of mechanical engineering have been taken up for active research.

ABOUT THE INSTITUTE

Established in the year 2009, Aryan Institute of Engineering and Technology (AIET) is one of the premier engineering colleges in the self-financing category of Engineering education in eastern India. It is situated at temple city Bhubaneswar, Odisha and is a constituent member of Aryan Educational Trust. This reputed engineering college is accredited by NAAC, UGC and is affiliated to BPUT, Odisha. AIET aims to create disciplined and trained young citizens in the field of engineering and technology for holistic and national growth.

The college is committed towards enabling secure employment for its students at the end of their four year engineering degree course. (The NAAC accreditation in the year 2018 vouches for the college's determination and dedication for a sustainable learning environment). The academic fraternity of AIET is a unique blend of faculty with industry and academic experience. This group of facilitators work with a purpose of importing quality education in the field of technical education to the aspiring students. Affordable fee structure along with approachable location in the smart city of Bhubaneswar, makes it a preferred destination for aspiring students and parents.

The Institute works with a mission to expand human knowledge beneficial to society through inclusive education, integrated with application and research. It strives to investigate on the challenging basic problems faced by Science and Technology in an Inter disciplinary atmosphere and urges to educate its students to reach their destination, making them come up qualitatively and creatively and to contribute fruitfully. This is not only its objective but also the ultimate path to move on with truth and brilliance towards success.



Organizing Committee Members

PATRON:

Dr. Madhumita Parida

Chairperson

Aryan Institute of Engineering and Technology

Director

Prof. Sasmita Parida

Jt. Organizing Secy.

Asst. Prof. Mr. Shaik Mozammil

Convener

Asst. Prof. Mr. P. K. Swain

Treasurer

Asst. Prof. Sthitiprajanya Satpathy

Organizing Secy.

Prof. P. Paulpandian

Jt. Treasurer

Prof. Sourav Debasish



NATIONAL ADVISORY COMMITTEE

Dr. P. K. Jha

Professor
Department of Mechanical and Industrial
Engineering
Indian Institute of Technology
Roorkee

Dr. Arvind Bharti

DRDO Headquarters
New Delhi

Dr. Dipak Mazumdar

Professor
Department of Materials and Metallurgical
Engineering
National Institute of Technology, Patna

Dr. B. S. Banerjee

Professor and Head
Department of Civil Engineering
Indian Institute of Technology, Bombay

Dr. S. L. Mukherjee

Professor
Department of Civil Engineering
National Institute of Technology,
Trichy

Dr. Indradeep Singh

Professor
Department of Mechanical Engineering
Indian Institute of Technology, Roorkee

Dr. B.S.S Daniel

Professor
Department of Metallurgy Engineering
Indian Institute of Technology, Roorkee

Dr. B. Ravi

Institute Chair Professor
Department of Mechanical Engineering
Indian Institute of Technology,
Bombay

Dr. S. K. Ray

Distinguished Visiting Professor
Indian Institute of Technology, Mandi

Dr. Vikas Kumar

Director
Defense Metallurgical Research Laboratory
Hyderabad

LOCAL COMMITTEE MEMBERS

Prof. Dr. Amiya Kumar Sahoo

Department of Computer Science
Engineering

Prof. Sagarika Pasayat

Department of Civil Engineering

Asst. Prof. Jagdish Pradhan

Department of Mechanical Engineering

Asst. Prof. Sarchidananda Mohanty

Department of Mechanical Engineering



Asst. Prof. Akashprava Panda
Department of Civil Engineering

Asst. Prof. Chandrabhanu Malla
Department of Mechanical Engineering

Asst. Prof. Dr. Smita Sahoo
Department of Civil Engineering

Asso. Prof. J. N. Biswal
Department of Mechanical Engineering


Asst. Prof. Ajit Kumar Panda
Department of Electrical Engineering

Asso. Prof. Priyadarshana Mahana
Department of Mechanical Engineering

Asst. Prof. Archana Mandal
Department of Electrical Engineering

Asst. Prof. Jhalaka Hota
Department of Computer Science Engineering

Asst. Prof. Nilgrib Mohanty
Department of Civil Engineering



Conference Committee Management

Seminar Hall Management

- Pratap Kumar Swain
- Bharat Baliarsingh
- Dhananjaya Sahoo
- Rajesh Khatei
- Abhaya Kumar Behera

Printing/Stationary Management

- Fatimun Nisha
- Charan Behera
- Hemanta Kumar Barik
- Sandeep Kumar Dash

Design Team Management

- Sridhar Jena
- Samarendra Nayak
- Bhabanisankar Das

Anchoring In Inauguration Ceremony

- Rudra Prasad Nanda
- Nilimashree Niharika

Sub-Committee Management

- Deepak Kumar Mishra
- Soumya Ranjan Swain
- Punarbasu Mall
- Jyoti Prakash Debata
- Siraj Khan
- Khulana Sethi
- Bidyadhar Mohanty

CHAIRPERSON'S MESSAGE



On behalf of the Organizing Committee, it is my great pleasure to welcome you to National Conference on “National Conference on Recent Trends in Civil and Mechanical Engineering” (RTCME-2016). In our endeavour to raise the standards of discourse, we continue to remain aware in order to meet with the changing needs of our stakeholders. The idea to host the RTCME-2016 is to bring together Researchers, Scientists, Engineers, Scholars and Students in the areas of Civil and Mechanical Engineering. The RTCME-2016 Conference will foster discussions and hopes to inspire participants from a wide array of themes to initiate Research and Development and collaborations within and across disciplines for the advancement of Technology. The conference aims to bring together innovative academic experts, researchers and Faculty in Engineering and Management to provide a platform to acquaint and share new ideas. The various thematic sessions will showcase important technological advances and highlight their significance and challenges in a world of fast changes. I welcome all of you to attend the plenary sessions and invite you to interact with the conference participants. The Conference Committees will make any possible effort to make sure that your participation will be technically rewarding and a pleasurable experience.

I am looking forward to meeting you in during RTCME-2016 and to sharing a most pleasant, interesting and fruitful conference.

Dr. Madhumita Parida

**With regards,
Dr. Madhumita Parida**

Chairperson
Aryan Institute of Engineering & Technology
Arya Vihar, Bhubaneswar, Odisha

DIRECTORS'S MESSAGE



It is a great pleasure and an honour to extend to you a warm invitation to attend the National Conference on 'National Conference on Recent Trends in Civil and Mechanical Engineering (RTCME-2016)' to be held on 25th – 27th September 2016, at Aryan Institute of Engineering and Technology, Bhubaneswar. The theme of Emerging Trends in Civil and Mechanical Engineering will underpin the need for participation in forums for collaborative Research and cooperation of individuals from a wide range of professional backgrounds. The Conference will provide a wonderful forum for you to refresh your knowledge in the technical field in Civil and Mechanical Engineering. The Conference will strive to offer plenty of networking opportunities, providing you with the opportunity to meet and interact with the scientists and researchers, friends as well as sponsors and exhibitors.

I hope you will join us for a symphony of the outstanding conference, and spare a little time to enjoy the spectacular and unique beauty of Bhubaneswar city.

Sasmita Parida

**With regards,
Prof. Sasmita Parida**

Director
Aryan Institute of Engineering & Technology
Arya Vihar, Bhubaneswar, Odisha

PRINCIPAL'S MESSAGE



I am pleased to welcome you to the National Conference on “Recent Trends in Civil and Mechanical Engineering” (RTCME-2016) to be held on 25th - 27th September, 2016.

The intent of this conference is not only to discuss lively and emerging issues of a particular domain but also dissemination of the awareness among other learned people. Over the years, dramatic improvements have been made in the field of Engineering, and Technology. I hope RTCME-2016 will become the most useful National Conference dedicated to bring out latest trends in Engineering, and Technology.

In order to provide an outstanding technical level for the presentations at the conference, we have invited distinguished experts to participate in the Technical Programmes. We will have technical sessions, plenary sessions by keynote speakers during three days of conference including the awards presentation during the valedictory session on the last day of the conference.

I hope RTCME-2016 will make you aware of state-of-the art systems and provide a platform to discuss various emerging technologies in Civil and Mechanical Engineering.

With regards,
Prof. (Dr.) S. S. Khuntia

Principal
Aryan Institute of Engineering & Technology
Arya Vihar, Bhubaneswar, Odisha

CONVENER'S MESSAGE



National Conference on “Recent Trends in Civil and Mechanical Engineering” (RTCME-2016) is a prestigious event jointly organized by Mechanical and Civil Engineering Department with a motivation to share a progress in recent technologies. The objective of RTCME-2016 is to present the latest research and results of scientists (preferred under graduate and post graduate students, research scholars, post-doc scientists, academicians and working professionals) related to the subjects of Mechanical and Civil Engineering. The conference will provide with paper presentations and research paper presentation by prominent speakers who will focus on related state-of-the-art technologies in the areas of the conference.

I wish all the success to the conference RTCME-2016.

A handwritten signature in blue ink, appearing to read 'P.K. Swain'.

**With regards,
P.K. Swain**

HOD of Mechanical Engineering
Aryan Institute of Engineering & Technology
Arya Vihar, Bhubaneswar, India

ORAL		Session 1	Break	Session 2	Break	Session 3
25-Sep	Virtual Room 1	Surveying Engineering		Surveying Engineering		Surveying Engineering
	Virtual Room 2	Water Science and Engineering		Water Science and Engineering		Water Science and Engineering
	Virtual Room 3	Corrosion and Coating Science		Corrosion and Coating Science		Rock Mechanics and Geotechnical Engineering
	Virtual Room 4	Advanced Structural Steels		Advanced Structural Steels		Construction and Building Materials
26-Sep	Virtual Room 1	Rock Mechanics and Geotechnical Engineering		Rock Mechanics and Geotechnical Engineering		Rock Mechanics and Geotechnical Engineering
	Virtual Room 2	Construction and Building Materials		Construction and Building Materials		Construction and Building Materials
	Virtual Room 3	Heat Treated Alloys and Compounds		Heat Treated Alloys and Compounds		Heat & Mass Transfer
	Virtual Room 4	Materials Joining		Materials Joining		Composite Material
27-Sep	Virtual Room 1	Heat & Mass Transfer				
	Virtual Room 2	Composite Material				
	Virtual Room 3	Heat Treated Alloys and Compounds				

INDEX

PAPER 01	Negative Stiffness Absorbers Study of Vibration Mitigation for Wind Turbine Towers	Raghupatruni Bhima Rao Sikendar Sharma Biswa Ranjan Pradhan Deepikarani Swain Nalinikanta Swain	01-17
PAPER 02	Genetic Algorithm Designed for Stability of Slope Analysis	Saleema Panda, Nilgrib Mohanty, Barsa Priyadarshini Sahoo, Debi Prasad Singh	18-27
PAPER 03	Seismic Design of Integral Abutment Bridges	Murari Prasad Panda Bipash Mohanty S. C. Mishra Ranjan Kumar	28-41
PAPER 04	Production of Topology-optimized Structural Nodes	Mdaras Aras Ansari Sourav Debasish Pili Kumari Sahoo Jagruti Swain	42-48
PAPER 05	Evaluation of the Influencing Factors in Target Value Design Process	Akashprava Panda Jyotikusum Acharya Binapani Mohapatra Saswati Nayak	49-57
PAPER 06	Determination of Dynamic Impact Factor of an Existing Pre-stressed Concrete I-Girder Bridge	Sagarika Pasayat Sharadhananda Ghadei Shradha Jena Deepika Priyadarshini Palai	58-71
PAPER 07	Optimization of the Heavy Cable Suspending a Deck	Harish Chand Giri Saruk Mallick Chinmay Swain Satyaprakash Mishra	72-80
PAPER 08	Seismic Design of Integral Abutment Bridges	Sampad Kumar Pradhan Tapan Kumar Mohanty Suryaleen Rout Anand Mandal	81-94
PAPER 09	Determination of the Geotechnical Parameters of Stabilized Soils by Stone Column Method based on SPT Results	Alivasakhi Mishra, Suchismita Satpathy, Subrat Kumar Panda, Sudeepta Kishor Dash	95-101
PAPER 10	Development and validation of a TRNSYS type for simulating heat pipe heat exchangers in waste heat recovery transient applications	Pradyut Kumar Swain Deepikarani Swain Nalinikanta Swain Debi Prasad Singh	102-124

PAPER 11	Vibration Control of Transmission Line Tower	Flora Das Pradipta Kumar Das Sidharth Pradhan Bijayalaxmi Behera	125-137
PAPER 12	Study of Impulsive Force of Debris Flow and Flexible Retaining Structure Based on SPH-DEM-FEM Coupling	Raghupatruni Bhima RaoSikendar Sharma Biswa Ranjan Pradhan Deepikarani Swain	138-148
PAPER 13	Personality Traits on the Evacuation Choice Behavior Pattern in Urban Road Network During Natural Disaster	Nilgrib Mohanty Saleema Panda Barsa Priyadarshini Sahoo Bipash Mohanty	149-164
PAPER 14	Under Circular Dynamic Stress Paths Analysis on the Dynamic Modulus and Damping Ratio of Compacted Loses	Mdaras Aras Ansari S. C. Mishra Sourav Debasish Jagruti Swain	165-179
PAPER 15	Unified Failure Strength Analysis for Terrace Slope Reinforcement Materials	Akashprava Panda Nalinikanta Swain Tapan Kumar Mohanty Jyotikusum Acharya	180-188
PAPER 16	Effect of load on Stress Relaxation of Rock Joints	Sagarika Pasayat Jitendra Narayan Biswal Binapani Mohapatra Shradha Jena	189-199
PAPER 17	Design of RC-Braced Long Columns Based on New Moment Magnifiers	Deepika Priyadarshini Palai Saruk Mallick Sagarika Pasayat Satyaprakash Mishra	200-219
PAPER 18	Dynamic Response of the Bridge-Vehicle System of Random Road Roughness by Moment Method	Sharadhananda Ghadei Suryaleen Rout Debi Prasad Singh Ranjan Kumar	220-231
PAPER 19	Characteristic of Specimens of Circular Concrete-Filled CFRP-Steel Tubular Beam-Column	Anand Mandal Alivasakhi Mishra Harish Chand Giri P. Paulpandian	232-250
PAPER 20	Random Shape Rockfalls in Steeply Dipping Coal Seams	Sampad Kumar Pradhan Sudeepta Kishor Dash Sidhanta Behera Bijayalaxmi Behera	251-264
PAPER 21	Synthesis of heat exchanger networks and it's design and parameters for capital cost estimation	Chinmay Swain Saswati Nayak Ranjan Kumar Shaik Mozammil	265-280

PAPER 22	Analysis on Plane and Radial Wall Jets to Validate the 2D for an Idealized Downburst Outflow	Suchismita Satpathy Rakesh Kumar Panda Suchampa Bagchi Swarup Sahoo	281-297
PAPER 23	Analysis on NSM CFRP Strengthened RC Concrete Beams	Flora Das Anjan Kumar M. U. Monalika Mohanty Kankan Mandal	298-313
PAPER 24	Hydraulic Fracturing Pressure Relief Technology in the Deep High-Stress Roadway for Rock Control	Harish Chand Giri Sikendar Sharma Biswa Ranjan Pradhan Deepikarani Swain	314-326
PAPER 25	Evaluation of heating performance of the PVC earthair tubular heat exchanger applied to a greenhouse in the coastal area of west Syria: An experimental study	Niranjan Behera Abinash Sahoo Shakyasingha Sahoo Himanshu Sekhar Moharana	327-343
PAPER 26	“Relief-Retaining” Control Technology of Floor Heave in Mining Roadway with Soft Rock	Bipash Mohanty S. C. Mishra Sourav Debasish Mdaras Aras Ansari	344-356
PAPER 27	Gas Drainage Based on Multifield Coupling Model of Gas-Bearing Coal	Ram Narayan Mishra Jagruiti Swain Jyotikusum Acharya Binapani Mohapatra	357-371
PAPER 28	Determination of Shear Strength in RC Beams Using ANN Trained with Tabu Search Training Algorithm	Atul Ajaya Kumar Beura Shradha Jena Deepika Priyadarshini Palai	372-385
PAPER 29	Design of Backfill Highway Subgrade on the Lower Bearing Capacity Foundation By Finite Element Method	Nilgrib Mohanty Saruk Mallick Satyaprakash Mishra Suryaleen Rout	386-394
PAPER 30	Measurements of Heart Rate and Facial Expression to Assess Human Reactions in Glass Structures	Anand Mandal Alivasakhi Mishra Sudeepta Kishor Dash Murari Prasad Panda	395-409
PAPER 31	Designing a Large MarineTwo-Stroke Diesel Engine with Cylinder Bypass Valve and EGR System	Shaik Mozammil Deepikarani Swain Nalinikanta Swain	410-415
PAPER 32	Experimental Investigation of an RC Slab Culvert Rehabilitated with Grouted CSPs	Shradhanjali Moharana Akashprava Panda Raushan Gupta Debi Prasad Singh	416-425

PAPER 33	Experimental Analysis on Axial Compression of Reinforced Concrete Short Circular Columns Strengthened with Prestressed Semicircular Steel Plates	Ranjan Kumar Sagarika Pasayat Satchidananda Mohanty Suchampa Bagchi	426-437
PAPER 34	Alternative Load Path Analysis for Assessing the Geometric Agreement of a Cable-Stayed Bridge with Steel Truss Girders	Sharadhananda Ghadei Swarup Sahoo Ajaya Kumar Beura Saswati Nayak	438-450
PAPER 35	Use of nanofluids to improve heat exchanger performance	Ranjan Kumar Saswati Nayak Chinmay Swain Subhasis Sarkar	451-467
PAPER 36	Strength Analysis of Flat and Folded Fly Ash-Based Geopolymer Ferrocement Panels under Flexure and Impact	Sikendar Sharma Biswa Ranjan Pradhan Saleema Panda Sampad Kumar Pradhan	468-479
PAPER 37	Modeling of a Ballastless Track System Resulting from Early-Aged Relative Humidity for the Construction Process	Subrat Kumar Panda Barsa Priyadarshini Sahoo Bipash Mohanty S. C. Mishra	480-495
PAPER 38	Machine Learning Algorithms to Predict Uniaxial Compressive Strength for Soft Sedimentary Rocks	P. Paulpandian Suchismita Satpathy Chinmay Swain Subhasis Sarkar Mdaras Aras Ansari Jagruti Swain	496-512
PAPER 39	Numerical Analysis and Simulation of Maximum Turbidity Zone Formation at Inlet to River	Jyotikusum Acharya Binapani Mohapatra Shradha Jena Rakesh Kumar Panda	513-522
PAPER 40	Analysis of Resilient Modulus Inversion and Evaluation of Different Asphalt Pavement Structures	Flora Das Priyadarshan Mahana Deepika Priyadarshini Palai Saruk Mallick Satyaprakash Mishra	523-531
PAPER 41	Method for Construction of an Extra-Long Underwater Tunnel in Soft Soils.	Sourav Debasish Sidhanta Behera Bijayalaxmi Behera Binoda Bihari Sahoo	532-548
PAPER 42	Effect of various factors influencing thermal conductivity of building insulation materials	Sarat Kumar Mishra Debi Prasad Singh Ranjan Kumar Saswati Nayak	549-562

PAPER 43	Designing a energy-efficient HVAC sysstem by utilization of U-shaped finned heat pipe heat exchanger	Pradyut Kumar Swain Kalpana Mallick Priyabrata Jena Hemant Ku Nayak	563-574
PAPER 44	Steady-State Response Analysis of the Incompressible Nonlocal Saturated Poroelastic Beam under a Vertical Harmonic Load	Nalinikanta Swain, Sthitiprajangya Satpathy Saleema Panda Barsa Priyadarshini Sahoo	575-585
PAPER 45	Using response surface methods (RSM), the effect of alumina nanoparticles as additive with diesel–biodiesel blends has been studied on performance and emission characteristic of a six-cylinder diesel engine	Pili Kumari Sahoo Rajaram Sahu Sidharth Pradhan Subhasis Sarkar	586-594
PAPER 46	Use of Steel Slag-Superfine Blast Furnace Slag Composite Mineral Admixture on Mortar and Concrete	Binoda Bihari Sahoo Shradhanjali Moharana Raushan Gupta Subrat Kumar Panda	595-603
PAPER 47	Thermodynamic analysis and optimization of a water-cooled multi-spilit heat pipe system in finite time (MSHPS)	Himanshu Sekhar Moharana Debi Prasad Singh Nalinikanta Swain Sikendar Sharma Biswa Ranjan Pradhan	604-614
PAPER 48	Numerical Investigation of Double Corrugated Steel Plate Shear Walls	Rakesh Kumar Panda Jitendra Narayan Biswal Sidhanta Behera Subhasis Sarkar	615-629
PAPER 49	Analysis for Sustainable Concrete Structure Reinforced by Embedded Parts	Harish Chand Giri Anjan Kumar M. U. Monalika Mohanty Kankan Mandal	630-639
PAPER 50	A thorough examination of the impact of biodiesel's physical and chemical qualities on combustion parameters, engine performance, and emissions.	Sarat Kumar Mishra Sidharth Pradhan Rajaram Sahu Shakyasingha Sahoo	640-659

Negative Stiffness Absorbers Study of Vibration Mitigation for Wind Turbine Towers

Raghupatruni Bhima Rao, *Department of Civil Engineering, Aryan Institute of Engineering & Technology, Bhubaneswar, raghupatruni_r@outlook.com*

Sikendar Sharma, *Department of Civil Engineering, Raajdhani Engineering College, Bhubaneswar, sikendarsharma92@gmail.com*

Biswa Ranjan Pradhan, *Department of Civil Engineering, Capital Engineering College, Bhubaneswar, biswaranjanpradhan78@gmail.com*

Deepikarani Swain, *Department of Mechanical Engineering, NM Institute of Engineering & Technology, Bhubaneswar, depika_r19@yahoo.co.in*

Nalinikanta Swain, *Department of Mechanical Engineering, Capital Engineering College, Bhubaneswar, nalini_526@yahoo.co.in*

Abstract: The use of dynamic vibration absorbers (DVA) on wind turbine (WT) towers has the potential to increase the dampening of the tower and nacelle dynamic responses, hence boosting WT reliability. The Tuned Mass Damper (TMD) is limited by the need for huge masses, as well as the site of its installation. Two different concepts are addressed in this study. The nacelle is first detached from the WT tower via a low-strength connection. This solution is based on the concept of seismic isolation. In addition, based on the KDamper concept, a novel passive vibration absorption arrangement is built. The KDamper is essentially a TMD extension with negative stiffness (NS) parts added. The vibration absorption capability of the KDamper can be enhanced by raising the value of the NS element rather than adding more mass. As a result, a KDamper with the same added mass always implies stronger isolation qualities than a TMD. A built-in home programme is being created for the WT's nonlinear dynamic response. The proposed vibration reduction concepts' dynamic performance is quantitatively evaluated. All solutions outperform the uncontrolled structure in terms of dynamic behaviour, but only the KDamper-based designs considerably increase the effective damping of the WT tower while keeping the additional masses within practical limits.

Keywords: Wind turbines; Vibration control; Negative stiffness; KDamper; Effective damping.

1. Introduction

As wind power continues its rapid growth worldwide, wind farms are likely to comprise a significant portion of the total production of wind energy, and may even become a sizable contributor to the total electricity production in some countries. The high-quality wind resource and the proximity to load centres make wind energy a compelling proposition. The installed Wind Turbines (WT) energy potential is currently estimated at 539GW, according to the WWEA [1]. An important part of the WT network is the offshore wind turbines (OWT). OWT are expected to increase significantly as European coasts and seas offer a large wind energy potential. The WWEA predicts that offshore wind farms of 150GW will operate in the EU by 2030, contributing 14% of the EU's total electricity consumption.

However, the above prediction is very ambitious. It is noted, that in 2018 the annual rate of WT installation reached the lowest rate (10.8%) since the start of their industrial growth. Moreover, in recent years, several failures have been recorded in existing WT. It is estimated that the structural failure (tower, foundation) of the installed WT amounts up to 10% [2], significantly reducing their contribution to the energy network. These failures stem mainly from: i) WT collapse due to earthquake excitations, that cause structural failures due to high dynamic stress loading exceeding structural strength, and ii) WT collapse due to wind loading, because of its continuous and cyclic nature, that causes failure due to structural fatigue. In addition, the structural and foundation costs are excessively high, reaching up to 17% for land based (onshore) and fixed bottom offshore WT, while when considering floating offshore WT the cost rises up to 40% [3–5].

From the above comments, and according to the International Energy Agency [6], it emerges as top priority to enhance research to avoid WT structural failures. A way to extend the feasibility of Wind Turbine towers is by means of structural control. The application of a vibration control system in a WT will result in a structural system with enhanced dynamic behavior under vibrating loading. It is classified as passive, active, hybrid, or semi-active control. Several researchers have been studying the use of structural control to help suppress the wind-induced

vibrations experienced by WT towers [7–10]. The passive control methods are simple and reliable, as they do not require an external force, are easy to implement to reduce the structural vibration, and are widely used in WT technology for enhancing their effective damping. The purpose of the installation of such devices, for the control of WT, is to mitigate their dynamic responses, due to the fact that the vibrations caused by aerodynamic loads are lasting and cause fatigue problems to the body of the tower, and to their foundation.

The concept of a resonant damper, like a Tuned Mass Damper (TMD) is among the approaches that have received the most attention in the literature. The principal of the TMD system [11] is the degradation of the dynamic response of the system through energy transfer to a system of an additional mass, designed with optimum characteristics and adapted in a suitable position in the structure [12,13]. The TMD system consist of an additional small mass and a positive stiffness element in combination with an artificial damper. The parameters that concern the design of such devices, are determined with the resonance of the frequency of the device with the fundamental eigenfrequency of the initial system. As a result, a great portion of the vibration energy of the structure, due to a vibratory excitation, is consumed by the additional mass of the device and then dissipated through the damper.

The Active Tuned Mass Damper (ATMD) is a hybrid devise consisting of a passive TMD supplemented by an actuator parallel to the spring and damper. It is a well-known concept in structural control and has been proved to yield enhanced damping performance compared to the passive TMD [14,15]. Semi-active TMDs are examined thoroughly recently, that introduce negative stiffness elements and negative stiffness tension adjusting mechanisms [16–20]. The downside of such designs is that their performance is directly (or obliquely) depended by the accuracy of the actuators output, which over time can have an alternation in its performance by false estimation of the desirable function of the vibration absorption concept and eventually burden the structure.

In addition, various forms of Dynamic Vibration Absorbers (DVA) have been used, such as Tuned Liquid Column Dampers (TCLDs) and multiple TMDs. Some of the pioneering work concerning applications in WTs include the work by [21] in which the damping effect of a TLCD installed in an offshore WT has been investigated by assuming correlated wind and wave load conditions, whereas the potential of using a pair of TMDs simultaneously targeting the dominant fore-aft and side-side modes has been demonstrated by [10]. More recently, attention has focused on how to address the absence of aerodynamic damping in the side-side direction, when significant wind-wave misalignment is present, e.g. in the work by [9] where the beneficial of a TMD in reducing the tower base moment is demonstrated through numerical simulation, and in particular, a significant reduction in the side-side moment has been reported.

The essential limitations of all the aforementioned TMD-related concepts, are related with the location and the selected mass of these devices. In order to be effective, a resonant damper like the TMD should be installed where the absolute motion of the targeted vibration mode is largest, which is at the top of the tower or inside the nacelle. Effective damping by a TMD is furthermore associated with large additional masses, which constitutes a major limitation, since additional mass is highly undesirable at the top of the WT. In addition, a slight alteration in the control system parameters can alter the TMD tuning and consequently the system's performance is significantly reduced [22].

In this paper, two alternative vibration absorption approaches for mitigation of the WT dynamic responses are considered. First, the nacelle is released from the WT tower (nacelle isolation concept), using a low stiffness connection. This option is based on the seismic isolation concept of structures. This way, the nacelle is no longer rigidly connected to the WT tower, but is connected with a low stiffness element (elastomeric bearings). In order to retain the relative displacements of the nacelle-WT tower, an energy dissipation mechanism is implemented to reduce and control the displacements. In the second option, the KDamper (or an extension of it) is intervened between the nacelle and the WT tower. The KDamper, introduced in [23], is essentially an extension of the classical TMD, by incorporating appropriate negative stiffness elements. Instead of increasing the additional mass, the vibration isolation capability of the KDamper can be increased by increasing the value of the negative stiffness element, overcoming the sensitivity problems of TMDs as the tuning is mainly controlled by the negative stiffness element's parameters. Thus, the KDamper always indicates better isolation properties than a TMD with the same additional mass, finding numerous applications for vibration absorption of structural systems [24–30]. Although the KDamper incorporates a negative stiffness element, it is designed to be both statically and dynamically stable.

This paper is structured as follows. In Section 2 the vibration control approaches under consideration are presented, along with the dynamic model of the WT tower. The developed model is an assemblage of prismatic beam elements with sway degrees of freedom considered to be the dynamic degrees of freedom. In order to verify the validity and the efficiency of the developed formulation, a set of simplified analyses were conducted and the obtained results were compared with those obtained from the commercial software package SOFiSTiK (FEM Software for Structural Engineers | SOFiSTiK AG, n.d.) based on FEM. The aerodynamic load is taken into account by generating artificial basic wind velocities following the corresponding regulations of EC1, Part1,4 (EN 1991 - Wind actions, 2010) and applying it at the WT following the procedure described in [33]. Section 3, presents the optimization procedure from which the optimal parameters of the KDamper, and the extended versions of it, are obtained. The free design variables are presented, and proper limitations and constraints are imposed on the

free design variables and the system main dynamic responses, respectively, based on the proposed engineering-criteria driven optimization procedure. The NS element is realistically designed with a displacement-dependent configuration using pre-compressed positive stiffness elements (spiral springs), that generates 'linear' two-dimensional negative stiffness. Furthermore, the optimum design approach for the selection of the controlled WT with a TMD and the nacelle-isolation concept is presented. In section 4, a numerical example is presented, where the effectiveness of the proposed KDamper-based vibration mitigation approaches is verified. Based on a comparison with a conventional TMD (5% additional mass), and the proposed nacelle-isolation concept, the KDamper designs (0.1% additional mass) manage to significantly increase the effective damping of the WT tower, and thus mitigate the WT dynamic responses, with small additional masses and a realistically designed configuration. In section 5, the conclusive remarks are presented, and finally, in Appendix A, the formation of the submatrices of the controlled WT tower is presented considering all the vibration control approaches.

2. Methodology and modeling

This section presents the vibration mitigation approaches considered in this paper. The developed dynamic model of the wind turbine tower is an assemblage of prismatic beam elements with sway degrees of freedom considered to be the dynamic degrees of freedom. The validity and the efficiency of the developed formulation is verified with simplifies analyses, based on a comparison with a commercial software package, based on FEM [31]. Finally, the aerodynamic load is taken into account based on artificial wind basic velocities.

2.1 Vibration control approaches

Figure 1 presents the dynamic vibration absorber design options considered in this paper. The first vibration mitigation approach is the classical Tuned Mass Damped (TMD). The schematic representation of the TMD concept implemented in WT is depicted in the same figure, where the additional mass (m_D) of the TMD is attached at the top of the WT tower or inside the nacelle, using a positive stiffness element and a linear damper (k_D, c_D). This concept is employed as a benchmark because it has received the most attention in the literature due to the simplicity of its implementation. The main drawback of this option is the need for large additional masses, in order for the TMD to achieve significant effective damping, as will be observed in the numerical results.

The second vibration absorption option is based on the TMD concept combined with the seismic isolation principle, where the superstructure is isolated from its base/foundation with a low stiffness connection. Figure 1 presents the schematic representation of the proposed vibration absorption concept, where the mass that corresponds to the mechanical parts (nacelle, rotor and blades) is used as the additional mass of a TMD. Thus, the additional mass concentrated mass at the top of the tower is no longer connected rigidly to the steel tower, but is realized with a stiffness connection and a linear damper (k_D, c_D), as in the case of the classical TMD concept. This system will be referred to hereafter as nacelle-isolation concept. The main drawback that is to be expected, is that in order to isolate the steel tower from the vibrations of the nacelle, large relative displacements between the nacelle and the steel tower are required, which may prohibit the good function of the wind turbine.

In an effort to combine the aforementioned vibration control options, exploiting their advantages without their respective drawbacks, the KDamper is employed. As in the case of the nacelle isolation concept, the additional mass of the nacelle, rotor and blades is no longer rigidly attached to the WT tower but is mounted on a KDamper device. In this concept, the additional oscillating mass of the KDamper (m_D) is connected with the nacelle with a positive stiffness element and a linear damper (k_{PS}, c_{PS}), and with the steel tower with a negative stiffness (NS) element (k_{NS}), and the steel tower is connected with the nacelle with a positive stiffness connection (k_R). This way, the KDamper aims to isolate the vibrations of the nacelle from the steel tower, as in the case of the nacelle-isolation concept, retaining the relative displacements nacelle-tower within reasonable ranges. In addition, the KDamper aims to increase the effective damping of the WT tower compared to the TMD with the same additional mass, as it has been proven that the KDamper always presents an improved dynamic behavior as compared to the TMD. Finally, two extended version of the KDamper are also presented in Figure 1. In the proposed extensions, the additional mass, m_D is connected with the nacelle with a NS element and an artificial damper (k_{NS}, c_{NS}), and with the steel tower with a positive stiffness element (k_{PS}). The extended version of KDamper will be referred to hereafter as EKD. Finally, the EKD is equipped with an inerter (EKDI) that connects the top of the tower directly with the nacelle, and thus is parallel to the stiffness element k_R . The addition of the inerter aims to further reduce the vibrations of the WT tower retaining the relative displacement nacelle-WT tower within reasonable ranges.

2.2 Dynamic model of the wind turbine

In this section, the NREL baseline 5-MW nacelle and rotor, supported by a steel tower of 120 m height is examined. This choice is made due to the fact that is widely used in the literature as a benchmark option for vibration control of WT towers. The WT tower of variable tubular cross section supporting the NREL baseline 5-MW nacelle and rotor [34] is examined. The base diameter is 8.43m with steel thickness 4.8cm, the top diameter

is $3.87m$ with thickness $2.5cm$, the Young's modulus is taken as $210GPa$, while the steel density is assumed $8.5tn/m^3$ and damping ratio (all modes) of 1% . In order to take into account, the inertial forces applied by the mechanical parts (nacelle, rotor and blades), an additional concentrated mass $m_{top} = 403.22 m$ [34] is added at the top of the WT tower. The WT tower is modeled as an assemblage of beam elements with sway degrees of freedom considered to be the dynamic degrees of freedom. The theoretical development is based on the assumption that the cross-sectional dimension within the element remains the same, i.e. prismatic beam element. Additional assumptions made for the analytical formulation are: (i) the WT tower is considered to remain within the elastic limit under the aerodynamic loads, (ii) the effects of soil-structure-interaction (SSI) are not taken into consideration, and (iii) the axial DoFs are not considered in this formulation, as the purpose of this work is to mitigate the dynamic responses of the WT tower due to horizontal aerodynamic loads, and thus is reasonable to neglect them. Figure 1 presents the lumped mass model of the WT tower.

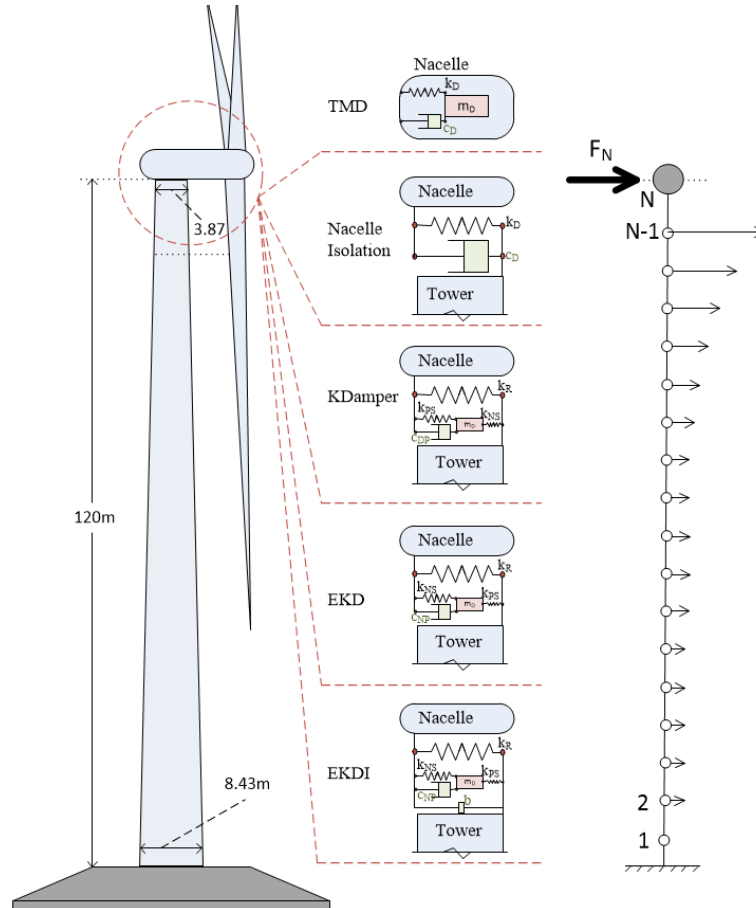


Figure 1. Vibration absorption concepts of the uncontrolled WT, TMD, nacelle-isolation, KDamper, EKD, and EKDI. The lumped mass model is used, with the sway as dynamic DoFs.

This model is serviceable due to the fact that it can incorporate easily each of the considered vibration absorption concepts, presented in section 2.1, and therefore evaluate their optimized parameters for vibration absorption, via optimization. The equations of motion of the uncontrolled WT, considering the equilibrium of forces at the location of each degree of freedom is expressed as follows:

$$[M_S]\{\ddot{u}_S\} + [C_S]\{\dot{u}_S\} + [K_S]\{u_S\} = [P_S] \quad (1)$$

where $[M_S]$, $[C_S]$ and $[K_S]$ are the mass, damping and stiffness matrices of the original WT tower, respectively of order $(N \times N)$, N indicating the number of prismatic beam elements selected to model the WT tower. The initial stiffness matrix is of order $(2N \times 2N)$, as each beam element has two rotational and two sway DoFs, respectively. The condensed stiffness matrix of the uncontrolled WT tower is corresponding to the sway degrees of freedom, taken as the dynamic DoF, and thus is $[K_S]_{N \times N}$. The damping matrix $[C_N]_{N \times N}$ is not explicitly known but is obtained with the help of the Rayleigh's approach using the same damping ratio in all modes, 1% [34]. The unknown nodal displacements, relative to the base, are expressed as u_i , and are collected in the array $\{u_S\} = \{u_1, u_2, u_3, \dots, u_N\}^T$.

In order to verify the validity and the efficiency of the developed formulation, a set of simplified analyses were conducted and the obtained results were compared with those obtained from the commercial software package SOFiSTiK [31] based on FEM. More specifically, in Table 1, the first five eigenperiods of vibration, are presented using SOFiSTiK, and are compared with those obtained from a FEM solution employing 24 prismatic beam elements for the tower, the corresponding flexural modal shapes of the tower are illustrated. In Figure 2, the respective first five fundamental eigenshapes of the wind turbine are presented. It is observed that the largest amplitude at the top of the tower is presented at the first eigenshape followed by the second eigenshape. Thus, the tower response will be mainly determined by the first two vibration modes.

The response of the tower is examined performing a simplified linear static analysis, applying a concentrated force $\bar{F}_N = 1353.2 \text{ kN}$ (starting value of the generated aerodynamic load presented in section 2.3) at the top of the tower. Table 1 presents the static deflections u_{top} at the top of the WT tower obtained from the developed model as compared with the aforementioned FEM solution, using SOFiSTiK software. It can be observed that the validity of the developed model of the WT tower is verified, as both the values of the WT eigenperiods and the static deflection of the top of the WT tower are in a very good agreement.

Table 1. Eigenperiods of the WT tower, and static deflection at the top of the tower under static analysis.

	Natural Periods T (sec)					Static deflection at the top of the tower u_{top} (m)
	T1	T2	T3	T4	T5	
Present study	3.156	0.467	0.164	0.081	0.048	0.7063
SOFiSTiK	3.164	0.474	0.172	0.089	0.056	0.711

The governing equations of motion for the WT including the respective vibration mitigation concept to be considered are obtained by considering the equilibrium of forces at the location of each degree of freedom as follows:

$$[M]\{\ddot{u}\} + [C]\{\dot{u}\} + [K]\{u\} = [P] \quad (2)$$

where $[M]$, $[C]$ and $[K]$ are the mass, damping and stiffness matrices of the controlled wind turbine tower, respectively of order $(N+n) \times (N+n)$. As stated previously, N indicates the wind turbine's DoFs and n the extra DoFs of each of the vibration isolation option to be considered. Furthermore, $\{u\} = \{\{u_N\}, \{u_n\}\}^T$ are the unknown, relative to the base, nodal displacements. The matrices of mass $[M]$, damping $[C]$, and stiffness $[K]$ are of order $(N+n) \times (N+n)$, and are expressed as follows:

$$[M] = \begin{bmatrix} [M_S]_{N \times N} & [0]_{N \times n} \\ [0]_{n \times N} & [0]_{n \times n} \end{bmatrix} + \begin{bmatrix} [M_{n,a}]_{N \times N} & [0]_{N \times n} \\ [0]_{n \times N} & [M_{n,d}]_{n \times n} \end{bmatrix}_{(N+n) \times (N+n)} \quad (3.a)$$

$$[K] = \begin{bmatrix} [K_S]_{N \times N} & [0]_{N \times n} \\ [0]_{n \times N} & [0]_{n \times n} \end{bmatrix} + \begin{bmatrix} [K_{n,a}]_{N \times N} & -[K_{n,b}]_{N \times n} \\ -[K_{n,c}]_{n \times N} & [K_{n,d}]_{n \times n} \end{bmatrix}_{(N+n) \times (N+n)} \quad (3.b)$$

$$[C] = \begin{bmatrix} [C_S]_{N \times N} & [0]_{N \times n} \\ [0]_{n \times N} & [0]_{n \times n} \end{bmatrix} + \begin{bmatrix} [C_{n,a}]_{N \times N} & -[C_{n,b}]_{N \times n} \\ -[C_{n,c}]_{n \times N} & [C_{n,d}]_{n \times n} \end{bmatrix}_{(N+n) \times (N+n)} \quad (3.c)$$

where the submatrices $[M_{n,i}]$, $[C_{n,i}]$, and $[K_{n,i}]$ ($i=a, b, c, d$) are expressed corresponding to the DoF associated with the respective control system to be considered. For the numerical modelling of the proposed formulation a build-in house software is developed in MATLAB code. The expressions of the additional matrices in Equations (3), that correspond to the employed vibration absorption concepts, are given in Appendix A.

2.3 Aerodynamic loads

The wind load varies along the height of the WT tower. The total horizontal wind force $\bar{F}_N(t)$ action on the blades can be calculated as three times the force $\hat{F}_N(r, t)$ acting at any position r along the single wind turbine blade. The $\hat{F}_N(r, t)$ accounts for the air density and the lift and drag coefficients as presented in [35]. The values of the latter coefficients depend on the airfoil characteristics of the blades and their distribution with respect to the angle of attack of the wind velocity $\bar{V}(t)$ passing through the blade profile. It is noted that $\bar{V}(t)$ is assumed to have a uniform spatial distribution over the actuator disc. In order to evaluate the horizontal wind force the blade element momentum theory incorporating Prandtl's tip loss factor and Glauert's correction [33] is employed with an

assumption of constant angular velocity of the blades. Subsequently, breaking $\bar{V}(t)$ down into a mean component V_m and a fluctuating component $V(t)$, the corresponding mean and fluctuating components of $\bar{F}_N(r, t)$ can be obtained as a mean force (steady state) and the dynamic part.

In this work, the mean velocity is obtained by employing a basic velocity at the altitude of 10m, V_b and applying the corresponding regulations of EC1, Part1,4 [32]. Moreover, in order to take into account, the wind velocity fluctuation at the altitude an artificial velocity time history is generated applying the procedures presented in [36–39] assuming a value of standard deviation σ . Apart from the concentrated force applied on the top of the steel tower due to operation of the turbine, an additional distributed loading along the tower height is taken into account due to the fact that a portion of wind forced is exerted directly on the tower. The spatial and time distribution of this loading is obtained by employing the procedures of (EN 1991 - Wind actions, 2010) and of the studies [36–38]. The basic wind velocity that is employed has corresponding standard deviation $V_b=27.0\text{m/s}$ with $\sigma=3.3\text{m/s}$ ($V_m(120\text{m})=39.93\text{m/s}$). The rotor is assumed to develop a constant angular velocity 12.1rpm, while all the necessary blade profile characteristics are retrieved from [34,39]. Figure 3.a presents the wind velocity, and Figure 3.b the time history of the evaluated total forces.

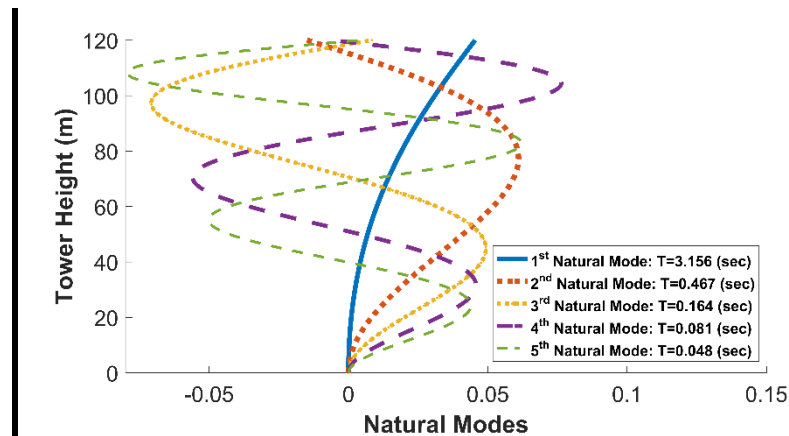


Figure 2. First five natural modes and eigenperiods of the uncontrolled WT.

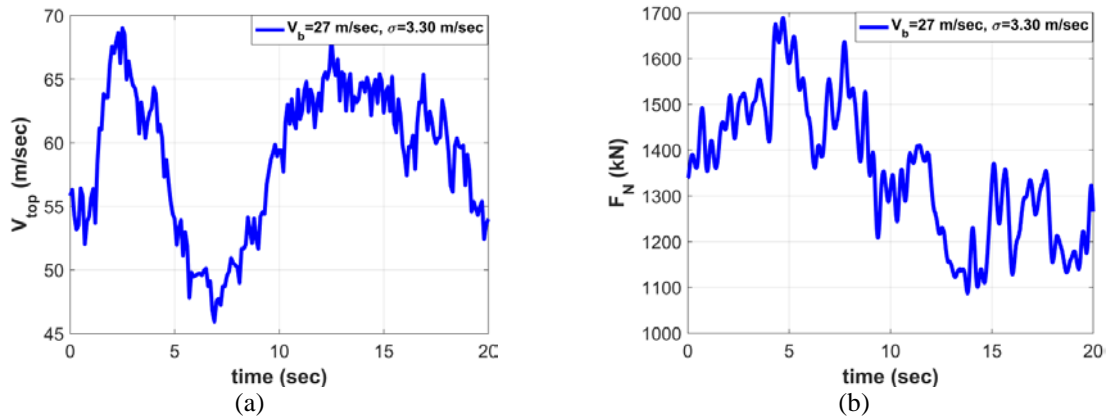


Figure 3. Basic wind speed V_b at the altitude of 10 m (a) and (b) time history of the total Force $\bar{F}_N(t)$ applied at the top of the wind turbine tower.

3. Optimal design of KDamper-based designs

In this section, an engineering-criteria driven optimization approach is followed for the selection of the proposed KDamper-based configuration parameters. The excitation input is generated according to section 2.3 of this paper. The free design variables of the devices implemented in between the nacelle and the WT tower are presented, and proper limitations and constraints are imposed on the free design variables and the system main dynamic responses, respectively. The NS element is realistically designed with a displacement-dependent configuration using pre-compressed positive stiffness elements, that generates 'linear' two-dimensional negative stiffness. The effectiveness of the proposed devices is evaluated by comparing its performance to a controlled system with a conventional TMD, and an alternative approach proposed in this paper, namely the nacelle-isolation concept presented in section 2.1 of this paper.

3.1 Free design variables

The Configurations of KDamper, extended KDamper (EKD), and EKD equipped with inerter (EKDI) are presented in section 2.1. The following positions concerning the KDamper concept, presented in Figure 1 are presented:

$$\mu_D = m_D/m_{top} \quad (4.a)$$

$$k_D = k_{NS} + k_{PS} \quad (4.b)$$

$$\omega_D = 2\pi f_D = \sqrt{k_D/m_D} = \sqrt{\frac{k_{NS}+k_{PS}}{m_D}} \quad (4.c)$$

$$k_0 = k_R + \frac{k_{NS}k_{PS}}{k_{NS}+k_{PS}} \quad (4.d)$$

$$\omega_0 = 2\pi f_0 = \sqrt{k_0/(m_D + m_{top})} = \sqrt{\left(k_R + \frac{k_{NS}k_{PS}}{k_{NS}+k_{PS}}\right)/(m_D + m_{top})} \quad (4.e)$$

$$\zeta_{PS} = c_{PS}/(2m_D\omega_D) = c_{PS}/(2\sqrt{k_D m_D}) \quad (4.f)$$

where μ_D is the mass ratio of the KDamper additional mass. The positions regarding the extended version of KDamper (EKD), and the EKD equipped with an inerter are exactly the same as with the KDamper. The EKDI is presented in Figure 1 where an inerter is implemented, connecting the nacelle directly with the WT tower. The inertance coefficient is expressed as follows:

$$\mu_b = m_b/m_{top} \quad (5)$$

where μ_b is the inertance mass ratio. In order for the proposed configuration to be realistic, the design of the KDamper-based designs foresees variation in all the stiffness elements to ensure that the system remain statically and dynamically stable:

$$(1 - \varepsilon_R)k_R + \frac{(1-\varepsilon_{PS})k_{PS}(1+\varepsilon_{NS})k_{NS}}{(1-\varepsilon_{PS})k_{PS}+(1+\varepsilon_{NS})k_{NS}} = 0 \quad (6)$$

As a result, the stiffness elements k_{PS} and k_R , result from Equations (4.e, 6) as a function of f_0 , and k_{NS} . Therefore, assuming that the m_D , and the values of the stability factors ε_{NS} , ε_{PS} , and ε_R are supposed known, the free design variables sought in the optimization are:

- 1) the nominal frequency f_0 ;
- 2) the value of the negative stiffness (NS) element k_{NS} ;
- 3) the value of the damping coefficient c_{NS} ;
- 4) the value of the inerter b ;

For the optimization process, the Harmony Search (HS) algorithm, a novel metaheuristic algorithm is used [40].

3.2 Realization of the negative stiffness element

Based on the proposed configuration for the realization of the negative stiffness element in [23] and [41], with pre-compressed springs, an alternative mechanism is hereby described, as depicted in Figure 4. The negative stiffness spring k_N is realized by a linear vertical spring with constant k_H , which connects the additional mass m_D and the structure by an articulated mechanism. Further information regarding the geometrical parameters of the proposed configuration presented in Figure 4.b, can be found in [23], the selection of which follows the procedure described also in [23]. The negative stiffness produced by the linear pre-compressed vertical spring, k_H , is given by:

$$k_{NS} = \frac{\partial f_N}{\partial u_{NS}} = -k_H \left[1 + c_I \frac{1}{(1-u_{NS}^2/a^2)^{3/2}} \right] \quad (7)$$

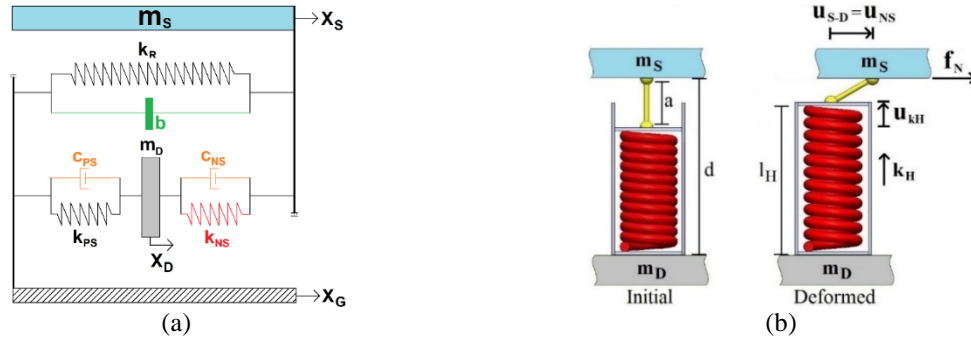


Figure 4. Schematic representation of the EKDI concept (a), and realization of the negative stiffness element (b).

3.3 Statement of the optimization problem

The purpose of the proposed vibration absorption configurations, based on the KDamper concept (KDamper, EKD and EKDI) is to enhance the dynamic performance of WT towers, by increasing the effective damping, and thus mitigate their dynamic responses. For the design to be realistic and efficient, at the same time, proper engineering criteria constraints and limitation must be applied in the system dynamic responses and free design variables, respectively. In particular:

- 1) The top displacement of the WT tower u_{TOP} is set as the objective function.
- 2) A geometric limitation is imposed, regarding the relative displacement between the additional oscillating mass of the KDamper-based designs (m_D) and the top of the WT tower, $u_{D,REL} = u_D - u_{TOP}$. The upper limit of $u_{D,REL}$ is set equal to $1.5m$, lower than half of the top diameter of the steel tower ($3.84/2 = 1.92m$).
- 3) Another geometrical limitation is the nacelle's relative displacement with respect to the top of the wind turbine tower, $u_{NAC,REL} = u_{NAC} - u_{TOP}$. In order to ensure the effective operation of the WT, an upper limit of $0.5m$ is placed in the $u_{NAC,REL}$.
- 4) The additional mass of the KDamper-based designs should be within reasonable ranges, since large masses constitute a major limitation, and are highly undesirable at the top of the wind turbine. For this reason, various sets of optimized EKDI parameters are selected for different values of the mass ratio μ_D , in the range $[0.1 \ 0.5] \%$, more than one order of magnitude smaller as compared to the TMD concept.
- 5) The nominal frequency f_0 varies in the range $[0.1 \ 2.0] \text{ (Hz)}$.
- 6) The upper limit of the inertance mass ratio μ_b is set equal to 0.5 .
- 7) The damping coefficients maximum value c_{PS} for the KDamper, and c_{NS} for the extended KDamper designs, is set equal to 1000 kNs/m , which based on previous work of KDamper is a realistic value for a superstructure mass 403.22 m , which in this case is the concentrated mass at the top, m_{top} .
- 8) The NS element is realized with the proposed displacement-dependent configuration presented in section 3.2. The maximum (absolute) value is set equal to -50 kN/m per m of structure mass, 50% lower as compared to the study of [23];

Finally, the limits of the free design variables are: a) the nominal frequency $f_0 \text{ (Hz)}$ $[0.1 \ 2.0]$, b) the negative stiffness element $k_{NS} \text{ (kN/m)}$ $[-20000 \ -1]$, c) the damping coefficient c_{NS} and $c_{PS} \text{ (kNs/m)}$ $[1 \ 1000]$, and the inertance mass ratio μ_b $[0 \ 0.5]$.

3.4 Comparison approaches

The considered comparison approaches selected to verify the effectiveness of the KDamper-based design concepts are the conventional TMD and the nacelle-isolation concept, presented thoroughly in section 2.1. The TMD system, consists of 3 elements, an additional mass, m_D , a positive stiffness element, k_D , and a linear damper, c_D . The following positions concerning the TMD design are introduced, considering implementation at the top of the WT tower or inside the nacelle, as presented in Figure 1.

$$\mu_D = m_D / m_{top} \quad (8.a)$$

$$\omega_D = 2\pi f_D = \sqrt{k_D / m_D} \quad (8.b)$$

$$\zeta_D = c_D / (2\omega_D m_D) = c_D / (2\sqrt{k_D m_D}) \quad (8.c)$$

where μ_D is the mass ratio of the TMD. The WT tower is a MDoF structural system, therefore the TMD design is not straightforward. The TMD tuning frequency is usually selected to be equal to the fundamental frequency, f_1 , of the primary structure. In order to verify that this approach is indeed optimum for the implementation of the TMD to a WT tower, the maximum top displacement over the TMD tuning frequency is illustrated in Figure 5,

for various values of the TMD damping ratio, and the aerodynamic load presented previously.

The optimum value of the TMD frequency is indeed near the fundamental frequency of the uncontrolled WT, and more specifically in the range $[0.9 \ 1.3]f_l$. The optimum value observed from Figure 5a of the f_D is $1.25 f_l$, and this value is adopted in this study for the optimum tuning of the TMD. It is observed that the damping ratio ζ_D of the TMD does not significantly affects u_{TOP} of the controlled system. However, from Figure 5.b, it is clear that the TMD stroke is directly affected by the ζ_D . The μ_D of TMD is selected for the considered analysis as 5%.

In order to optimally select the TMD damping ratio, ζ_D , the u_{TOP} and the TMD stroke are plotted in Figure 6, over ζ_D , for various values of the TMD mass ratio μ_D . In this case, as stated previously, the TMD tuning frequency is selected to be equal to $1.25 f_l$, and is 0.396 Hz . It is observed that in the range of ζ_D [5 15] %, the maximum u_{TOP} are minimized. However, for greater values of ζ_D over 15%, u_{TOP} is not much affected. At the same time, from Figure 6.b it is observed that as ζ_D increased, the TMD stroke decreases, as expected. Therefore, ζ_D is selected equal to 30%, to mitigate the response of the WT tower, and at the same time retain the TMD stroke as small as possible. This value of $\zeta_D=30\%$ is usually high for a large mass of $\mu_D=5\%$, but for the purpose of the comparison it can be adopted, as we are not interested in a realistic design, but a comparison basis.

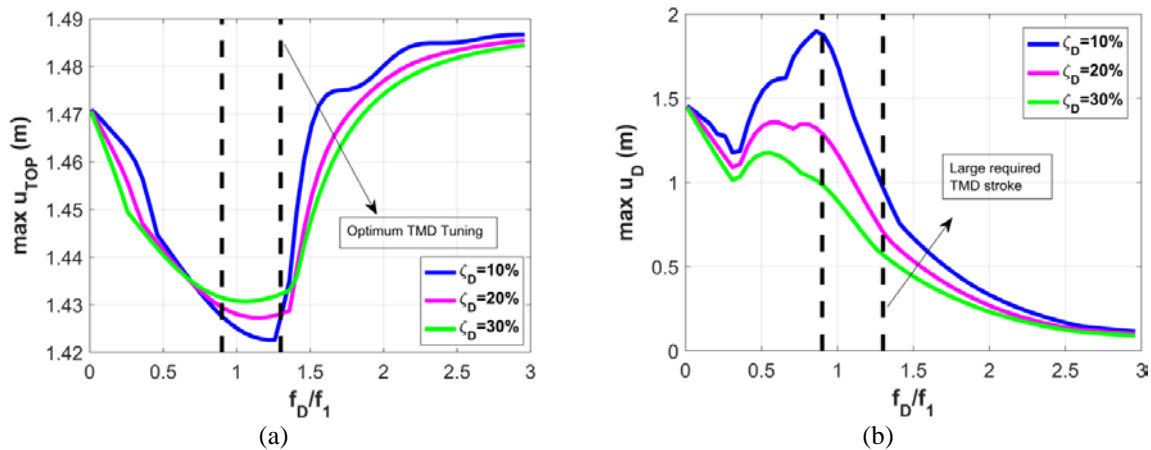


Figure 5. Maximum top tower displacement (a), and TMD stroke (b) over nominal frequency ratio f_D/f_1 , for various values of ζ_D .

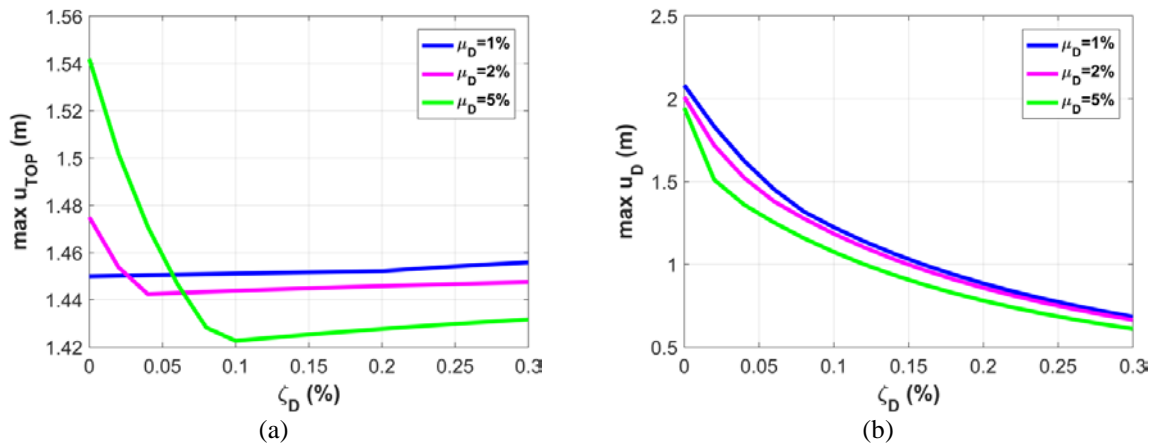


Figure 6. Maximum top tower displacement (a) and TMD stroke (b) over ζ_D , for various values of the μ_D .

Figures 7.a, b present the effect of μ_D , to the system main dynamic responses, i.e. u_{TOP} , and the TMD stroke. In addition, the effect of the implementation of the TMD to the ζ_{eff} of the WT tower is examined. In order to calculate the exact value of ζ_{eff} , the system is subjected to a free vibration with initial conditions, according to the first modal eigenform of the uncontrolled WT. The initial condition of the TMD's DoF is selected to be equal to the one at the top of the WT. The ζ_{eff} is calculated according to the logarithmic rule, Equation (9) where T is the time between two consecutive peaks of u_{TOP} . Figure 7.c presents the effect of μ_D to the ζ_{eff} .

$$\ln \left[\frac{u_{TOP}(t)}{u_{TOP}(t+T)} \right] = \frac{2\pi\zeta_{eff}}{\sqrt{1-\zeta_{eff}^2}} \quad (9)$$

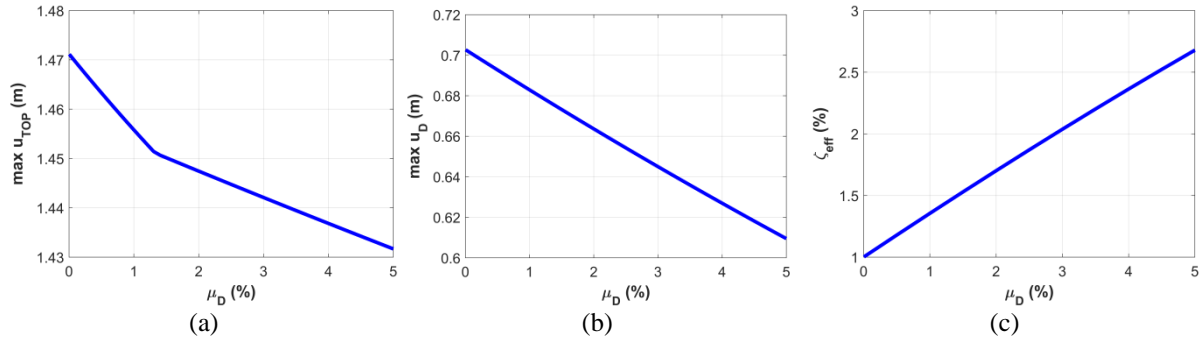


Figure 7. Effect of the TMD mass ratio μ_D to the top tower displacement(a), the TMD stroke (b), and the effective damping of the controlled system (c).

The increase of the additional mass ratio, μ_D , greatly affects the top tower dynamic response, as expected. It is observed that as the μ_D increases the effect to the top displacement decreases. Furthermore, the mass ratio affects linearly the improvement of the TMD stroke, and the increase of the effective damping of the controlled system. Regarding the nacelle-isolation concept, the design parameters are the positive stiffness element k_D , and the artificial damper c_D . Based on the geometrical limitation presented for the KDamper-based designs, that the nacelle relative to the top of the tower displacement to be lower than 0.5 m, in order to have an equal comparison basis, the same constraint applies for the nacelle isolation concept. Furthermore, the maximum value of the c_D is set to be equal to 1000 kNs/m, as in the KDamper-based designs. Parametric analyses are conducted and plotted in Figure 8, in order to select the optimum system parameters, reported in Equations (10).

$$\omega_D = 2\pi f_D = \sqrt{k_D/m_{tot}} \quad (10.a)$$

$$\zeta_D = c_D/(2\omega_D m_D) = c_D/(2\sqrt{k_D m_{tot}}) \quad (10.b)$$

In Figure 8.a, the nacelle, relative to the top tower, displacement, $u_{NAC,REL}$ is plotted over the tuning frequency f_D . It is observed that the tuning frequency of the nacelle-isolation concept is around 0.6 Hz, applying the constraint that the upper limit of the $u_{NAC,REL}$ is set to be equal to 0.5 m.

The damping ratio ζ_D does not affect the $u_{NAC,REL}$, as observed in Figure 8.a, but significantly affects u_{TOP} , which is the minimization goal of all the proposed vibration control strategies. For this reason, the damping ratio is selected to be equal to the upper limit ($c_{D,max}=1000$ kNs/m). The optimal system parameters of the nacelle-isolation concept therefore are $f_D=0.556$ Hz (limit case where $u_{NAC,REL}=0.5$ m), and $\zeta_D=35.5$ %.

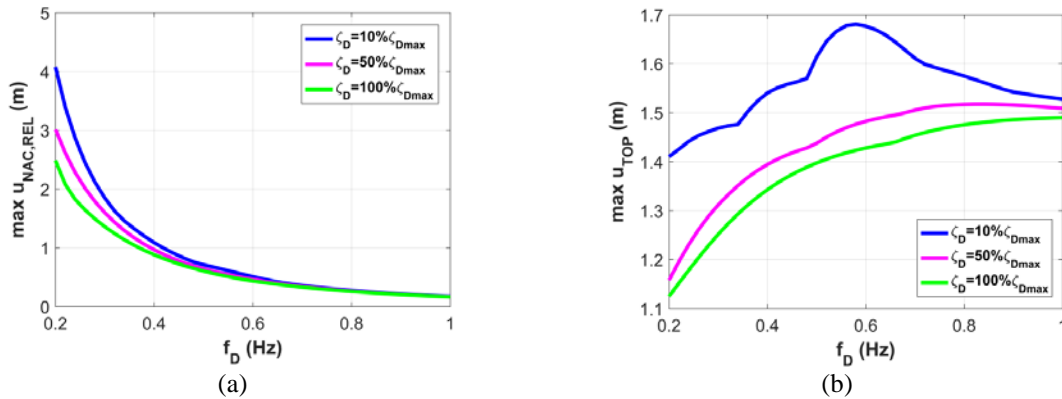


Figure 8. Nacelle-isolation design. Tuning frequency (a) and damping ratio (b).

4. Numerical application – optimization results

In this section, the KDamper-based designs are implemented for vibration control in the considered WT. The optimal system parameters are selected following the optimization procedure described previously in section 3.3 of this paper. The parameters of the KDamper, EKD, and EKDI system are presented in Tables 2-4, respectively.

The WT tower dynamic responses and ζ_{eff} are illustrated in Figure 9, over the KDamper-based designs μ_D , considering the optimized KDamper, EKD and EKDI vibration control configurations. In addition, the dynamic behavior of the nacelle is of great importance to the performance of the WT, and is greatly influenced by the

nacelle's angle of deflection, angular velocity, and relative (to the base) velocity. The aforementioned response variables of the nacelle, of the controlled system with KDamper, EKD, and EKDI are illustrated in Figure 10, over the μ_D of the respective system. Finally, the relative displacement of the additional mass, m_D , and the NS element stroke of all the KDamper-based designs are plotted in Figure 11, over the additional mass ratio, μ_D .

Table 2. KDamper components.

μ_D (%)	f_0 (Hz)	k_{NS} (kN/m)	c_{PS} (kNs/m)	k_{PS} (kN/m)	k_R (kN/m)
0.1	0.547	-3558.16	993.13	6714.58	12343.34
0.2	0.557	-3492.81	966.73	6472.92	12538.02
0.3	0.547	-3674.95	931.00	7006.28	12514.36
0.4	0.550	-3371.66	831.60	6227.71	12181.48
0.5	0.548	-3504.47	989.40	6564.08	12326.82

Table 3. Extended KDamper (EKD) components

μ_D (%)	f_0 (Hz)	k_{NS} (kN/m)	c_{NS} (kNs/m)	k_{PS} (kN/m)	k_R (kN/m)
0.1	0.541	-9501.00	986.08	32385.78	18103.61
0.2	0.532	-9335.64	968.12	32313.48	17638.61
0.3	0.532	-8822.59	996.64	28789.43	17240.72
0.4	0.532	-8758.40	963.99	28341.94	17201.80
0.5	0.523	-8668.35	993.72	28732.58	16783.15

Table 4. Extended KDamper equipped with inerter (EKDI) components.

μ_D (%)	f_0 (Hz)	k_{NS} (kN/m)	c_{NS} (kNs/m)	μ_b (%)	k_{PS} (kN/m)	k_R (kN/m)
0.1	0.551	-12543.61	997.34	0.498	58079.07	20829.40
0.2	0.545	-10395.09	986.69	0.496	38285.04	19015.52
0.3	0.544	-10380.34	960.28	0.497	38435.78	18938.34
0.4	0.538	-8995.40	939.73	0.493	29242.48	17618.43
0.5	0.540	-9086.47	996.11	0.497	29604.58	17772.91

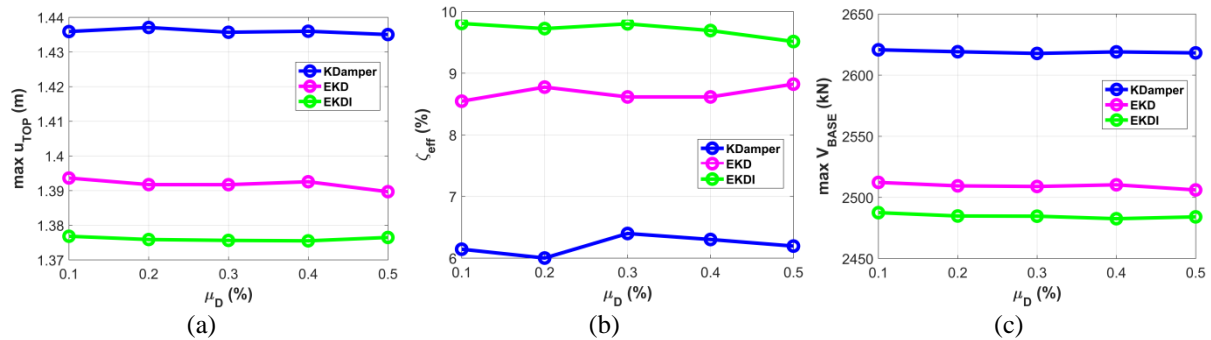


Figure 9. Optimization results for KDamper, EKD and EKDI. u_{TOP} (a), ζ_{eff} (b), and V_{BASE} (c).

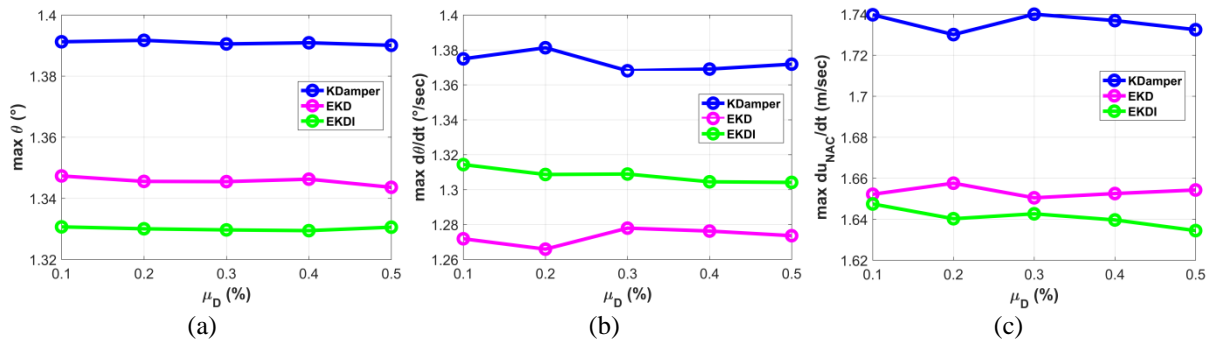


Figure 10. Optimization results for the KDamper, EKD and EKDI. Nacelle's angle of deflection (a), angular velocity (b), and relative (to the base) velocity (c).

In order to assess the effectiveness of the proposed absorbers, their performance is compared to a TMD and the nacelle-isolation concept, presented in section 2.1, and optimized for the specific implementation as presented in section 3. More specifically, the TMD has an μ_D of 5%, its nominal frequency is tuned to $1.25f_1$, and ζ_D is selected as 30%. The nacelle isolation concept is tuned to $f_D=0.556$ Hz, and the value of its c_D is equal to 1000 kNs/m. The

maximum values of the dynamic responses and the ζ_{eff} of all the considered vibration control systems are collected in Table 5. Regarding the KDamper-based designs, the presented results concern the optimized sets of parameters with an μ_D of 0.1%. The KDamper-based designs manage to greatly improve the dynamic behavior of the WT tower. The ζ_{eff} of the WT tower increases up to 10% with the EKDI system. The nacelle's dynamic response variables are also improved, with the exception of the nacelle's relative velocity, where a slight increase is observed. In addition, EKD and EKDI, greatly reduce the u_{NS} and u_D , making the configuration design more realistic. The dynamic responses of the WT tower and the nacelle's response variables, considering the TMD, the nacelle-isolation, and EKDI are illustrated in Figures 12, 13, respectively. Finally, the time history of the u_{NS} and u_D are illustrated in Figure 14 for all the KDamper-based designs.

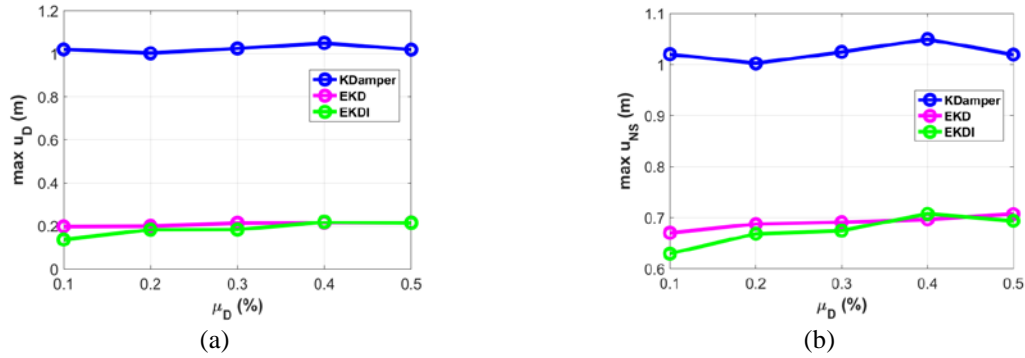


Figure 11. Optimization results for the KDamper, EKD and EKDI. u_D (a), and u_{NS} (b).

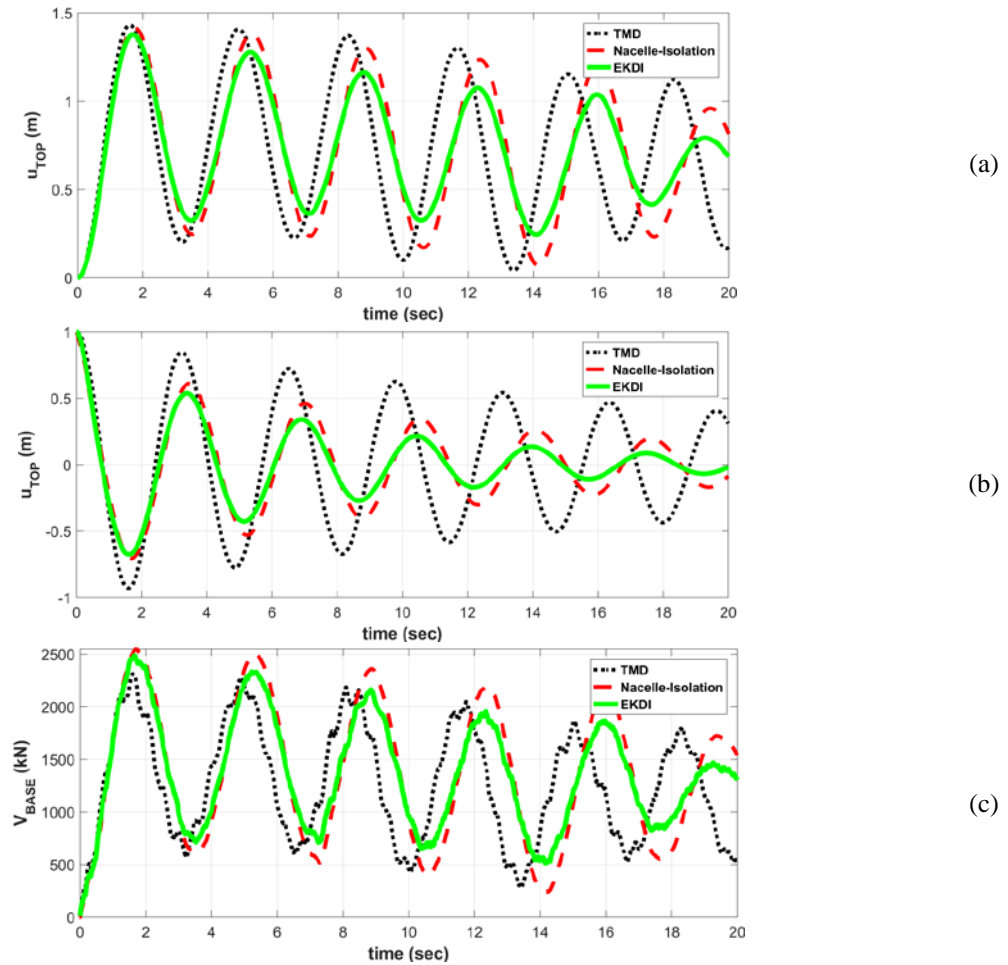


Figure 12. Dynamic responses of the controlled WT: top tower displacement due to the aerodynamic load (a), top tower displacement considering a free vibration with initial conditions (b), and base shear due to the aerodynamic load (c).

Table 5. Maximum values of the WT tower's effective damping ratio, ζ_{eff} , dynamic responses of the WT tower and the respective control system, and the nacelle's response variables.

	Dynamic Control system					
	Uncontrolled	TMD	Nacelle-isolation	KDamper	EKD	EKDI
u_{TOP} (m)	1.471	1.429	1.4167	1.436	1.394	1.377
ζ_{eff} (%)	1	2.68	7.82	6.14	8.55	9.81
V_{BASE} (kN)	2677.6	2308.6	2547.1	2620.7	2512.3	2487.5
θ (°)	1.424	1.391	1.368	1.391	1.347	1.331
$d\theta/dt$ (°/sec)	1.484	1.451	1.238	1.375	1.272	1.314
du_{NAC}/dt (m/sec)	1.448	1.406	1.703	1.740	1.652	1.647
u_D (m)	-	0.701	0.500	1.020	0.198	0.136
u_{NS} (m)	-	-	-	1.020	0.670	0.629

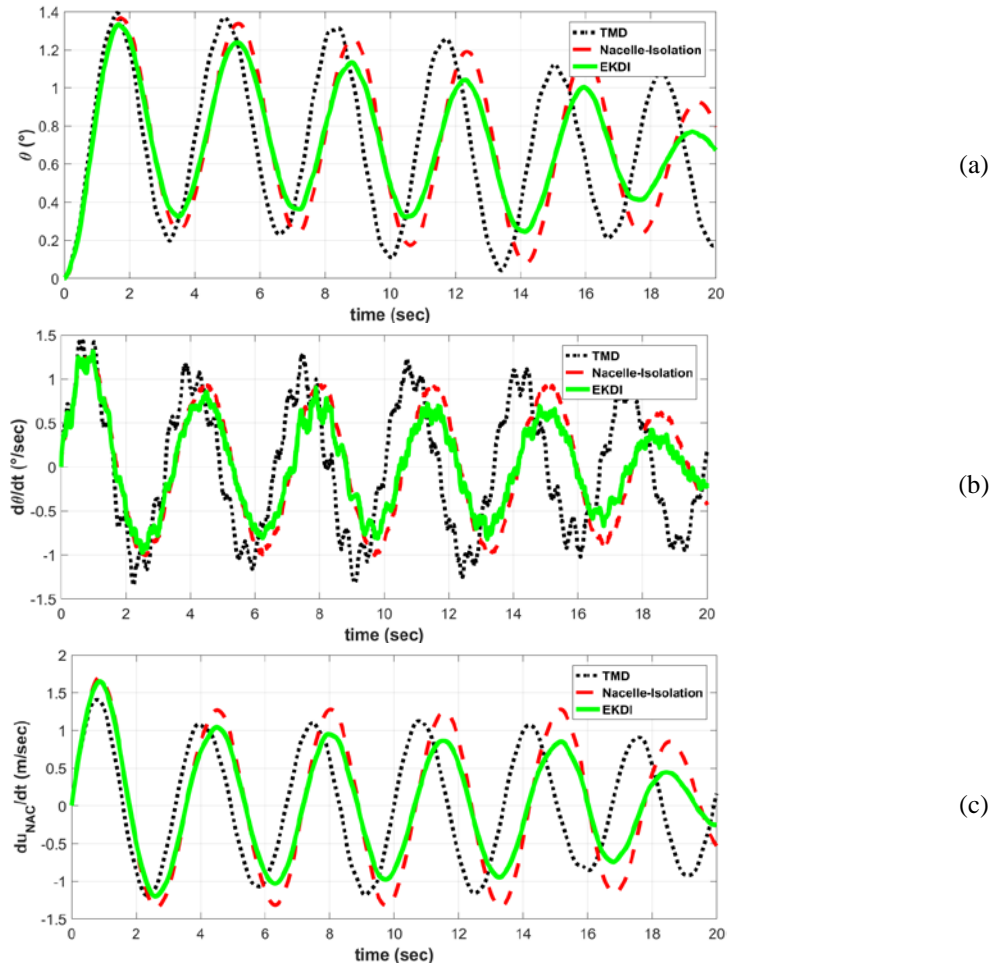


Figure 13. Nacelle's response variables of the controlled WT angle of deflection (a), angular velocity (b), and relative (to the base) velocity (c), due to the aerodynamic load.

5. Concluding remarks

In this paper, three dynamic vibration absorber options are examined for improving the WT tower dynamic behavior and increasing the effective damping, i.e. the conventional TMD, the nacelle-isolation concept, and three KDamper-based designs. A wind turbine of 5MW supported by a steel tower of 120 m was analyzed under a horizontal aerodynamic load due to the wind. The vibration mitigation approaches are presented, along with the dynamic model of the WT tower. The developed model is an assemblage of prismatic beam elements, the validity of which is verified based on a comparison with a commercial software package on FEM. The aerodynamic load is taken into account by generating artificial basic wind velocities applying the corresponding regulations of EC1, Part1.4. The TMD and the nacelle-isolation concepts, are optimally design for the specific implementation for the protection of the WT tower. An engineering-criteria optimization procedure is followed for the design of the

KDdamper-based configurations. The NS element is realistically designed with a displacement-dependent configuration. Based on a comparison with a conventional TMD, and the proposed nacelle-isolation concept, the KDdamper designs manage to significantly increase the effective damping, and thus mitigate the WT dynamic responses, with small additional masses and a realistically designed configuration. Finally, the following conclusive comments can be made:

1) The dynamic model of the WT tower developed here is serviceable due to the fact that it can incorporate easily each of the considered vibration absorption concepts, and the validity of the proposed formulation is verified as compared with a commercial software package based on FEM.

2) The increase of the effective damping of the WT tower is much greater with the implementation of the KDdamper-based designs (6.14%, 8.55%, 9.81%), compared to that with a TMD (2.68%) with an additional mass of 5%, and the nacelle-isolation concept (7.82%).

3) The KDdamper-based configurations are much more effective than the conventional TMD approach, employing a small additional mass of only 0.1%, 50 times lower compared to the TMD's.

4) Regarding the dynamic behavior of the WT tower, the KDdamper-based concepts provided the best results followed by the TMD concept and the nacelle-isolation concept. More specifically, the tower's top displacement is reduced 2.38%, 5.23% and 6.39% with the KDdamper-based concepts (0.1% mass ratio), 2.86% with the TMD concept (5% mass ratio) and 3.69% with the nacelle-isolation concept and the shear force of the tower is reduced 2.12%, 6.17% and 7.10% with the KDdamper-based concepts, 13.78% with the TMD concept and 4.87% with the nacelle-isolation concept.

5) The use of a TMD has a small influence on the nacelle's response variables. The KDdamper-based concepts, and the nacelle-isolation concept improve all the response variables of the nacelle, except for the maximum value of the nacelle's velocity which in the first peak of the dynamic response present a slight increase.

6) The proposed extensions of KDdamper manage to significantly decrease the NS element stroke, making the device's design more realistic.

7) The addition of the inerter in the EKD configuration has a beneficial impact in the overall dynamic behavior of the WT.

According to the comments made above, the KDdamper-based designs can provide a realistic alternative to the existing vibration absorption design options in WT towers, providing a great increase to the tower's damping as well as improving the dynamic performance both of the nacelle and the WT tower. The reliability and simplicity of the system are also advantages that render the device suitable for various technological implementations and competitive against other vibration absorption designs.

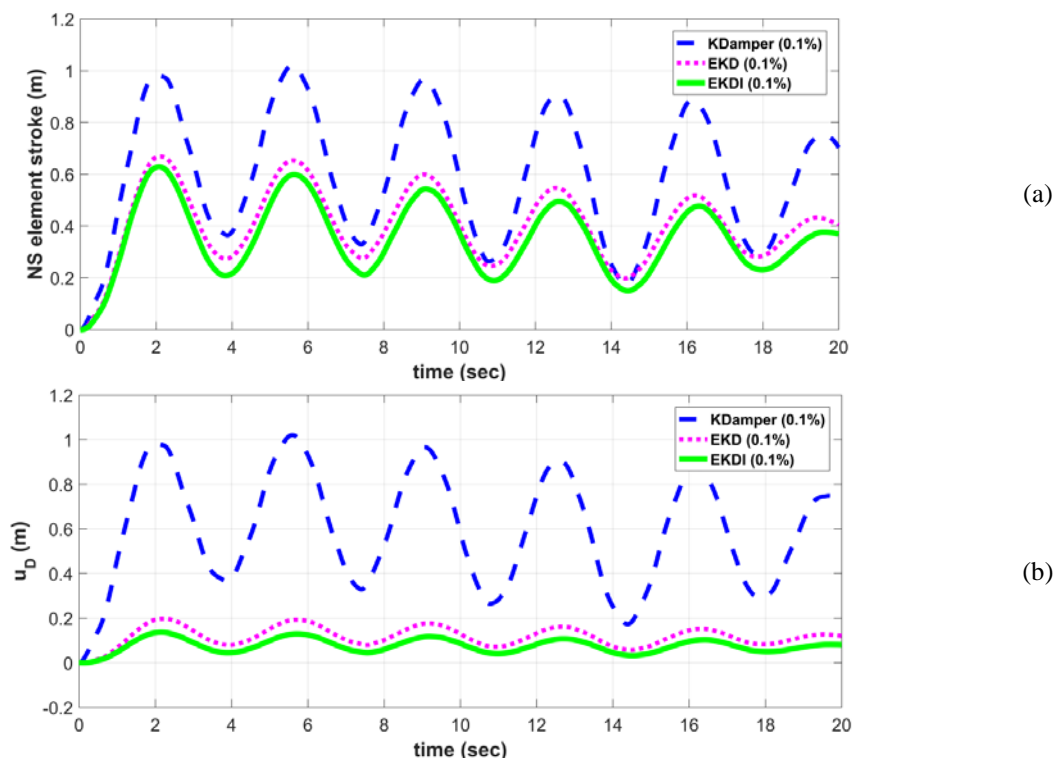


Figure 14. KDdamper-based designs responses NS element stroke(a) and relative displacement of the oscillating mass with the top of the WT tower (b), due to the aerodynamic load.

6. References

- [1] Wind Power Capacity Reaches 546 GW, 60 GW Added in 2017 – World Wind Energy Association [Online]. Available from: <https://wwindea.org/blog/2018/02/12/2017-statistics/>. [Accessed: 22-Apr-2020].
- [2] Li Y. Research and development of the wind turbine reliability. *International Journal of Mechanical Engineering and Applications*. 2018;6(2):35.
- [3] Renewable Energy Agency. Renewable energy technologies: cost analysis series Volume 1: Power sector acknowledgement. 2012.
- [4] Mone C, Hand M, Bolinger M, Rand J, Heimiller D, Ho J. 2015 Cost of Wind Energy Review. 2015.
- [5] Morais M et al. Dynamic behavior analysis of wind turbine towers. 2009.
- [6] Sustainable Development Scenario – World Energy Model – Analysis - IEA [Online]. Available from: <https://www.iea.org/reports/world-energy-model/sustainable-development-scenario>. [Accessed: 24-Apr-2020].
- [7] Nigdeli SM, Bekdaş G..Optimum tuned mass damper design in frequency domain for structures. *KSCE Journal of Civil Engineering*. 2017;21(3):912–922.
- [8] Avila S, Shzu M, Morais M, Prado Z. Numerical modeling of the dynamic behavior of a wind turbine tower. *Advances in Vibration Engineering*. 2016;4.
- [9] Stewart G, Lackner M. The impact of passive tuned mass dampers and wind–wave misalignment on offshore wind turbine loads. *Engineering Structures*. 2014;73.
- [10] Lackner MA, Rotea MA. Passive structural control of offshore wind turbines. *Wind Energy*. 2011;14(3):373–388.
- [11] Frahm H. Device for damping of bodies. U.S. Pat., (989). 1911.
- [12] Soong TT, Dargush GF. Passive energy dissipation systems in structural engineering. Wiley. 1997.
- [13] Casciati F, Giuliano F. Performance of multi-TMD in the towers of suspension bridges. *Journal of Vibration and Control*. 2009;15(6):821–847.
- [14] Ricciardelli F, Pizzimenti AD, Mattei M. Passive and active mass damper control of the response of tall buildings to wind gustiness. *Engineering Structures*. 2003;25(9):1199–1209.
- [15] Ankireddi S, Yang HTY. Simple ATMD control methodology for tall buildings subject to wind loads. *Journal of Structural Engineering* 1996;122(1):83–91.
- [16] Liao GJ, Gong XL, Kang CJ, Xuan SH. The design of an active–adaptive tuned vibration absorber based on magnetorheological elastomer and its vibration attenuation performance. *Smart Materials and Structures*. 2011;20(7):075015.
- [17] Weber F, Boston C, Maślanka M. An adaptive tuned mass damper based on the emulation of positive and negative stiffness with an MR damper. *Smart Materials and Structures*. 2011;20(1):015012.
- [18] Casciati F, Rodellar J, Yildirim U. Active and semi-active control of structures – theory and applications: a review of recent advances. *Journal of Intelligent Materials Systems and Structures*. 2012;23(11):1181–1195.
- [19] Acar MA, Yilmaz C. Design of an adaptive-passive dynamic vibration absorber composed of a string-mass system equipped with negative stiffness tension adjusting mechanism. *Journal of Sound and Vibration*. 2013;332(2):231–245.
- [20] Weber F. Optimal semi-active vibration absorber for harmonic excitation based on controlled semi-active damper. *Smart Materials and Structures*. 2014;23(9):095033.
- [21] Colwell S, Basu B. Tuned liquid column dampers in offshore wind turbines for structural control. *Engineering Structures*. 2009;31(2):358–368.
- [22] Weber B, Feltrin G. Assessment of long-term behavior of tuned mass dampers by system identification. *Engineering Structures*. 2010;32(11):3670–3682.
- [23] Antoniadis IA, Kanarachos SA, Gryllias K, Sapountzakis IE. KDamping: A stiffness based vibration absorption concept. *Journal of Vibration and Control*. 2018;24(3):588–606.
- [24] Kapasakalis K, Sapountzakis E, Antoniadis I. Implementation of the KDamper concept to wind turbine towers. In: 6th International Conference on Computational Methods in Structural Dynamics and Earthquake Engineering (COMPDYN 2017). 2017.
- [25] Kapasakalis K, Antoniadis I, Sapountzakis E. Control of multi storey building structures with a new passive vibration control system combining base Isolation with KDamper. In: 7th International Conference on Computational Methods in Structural Dynamics and Earthquake Engineering (COMPDYN 2019). 2019.

- [26] Antoniadis I, Kapasakalis K, Sapountzakis E. Advanced negative stiffness absorbers for the seismic protection of structures. In: International Conference on Key Enabling Technologies 2019 (KEYTECH2019). 2019.
- [27] Kapasakalis K, Antoniadis I, Sapountzakis E. Performance assessment of the KDamper as a seismic absorption base. structural control and health monitoring. <https://onlinelibrary.wiley.com/doi/10.1002/stc.2482>. 2019
- [28] Kapasakalis K, Antoniadis I, Sapountzakis E. KDamper concept for base isolation and damping of high-rise building structures. In: 14th International Conference on Vibration Problems (ICOVP 2019). 2019.
- [29] Kapasakalis K, Sapountzakis E, Antoniadis I. Optimal design of the KDamper concept for structures on compliant supports. In: 16th European Conference on Earthquake Engineering (16ECEE 2018). 2018.
- [30] Kapasakalis KA, Antoniadis IA, Sapountzakis EJ. Constrained optimal design of seismic base absorbers based on an extended KDamper concept. Engineering Structures. <https://www.sciencedirect.com/science/article/pii/S0141029620339134?via%3Dihub>. 2021.
- [31] FEM, BIM and CAD software for structural engineers | SOFiStiK AG [Online]. Available from: https://www.sofistik.com/?__hstc=136929903.778d8a8e3515c0a0f7da049d7f27258a.1587748377743.1587748377743.1587748377743.1&__hssc=136929903.2.1587748377744&__hsfp=4014916924. [Accessed: 24-Apr-2020].
- [32] EN 1991-1-4: Eurocode 1: Actions on structures - Part 1-4: General actions - Wind actions. 2010.
- [33] Hansen ML. Aerodynamics of wind turbines, Earthscan. 2008.
- [34] Quilligan A, O'Connor A, Pakrashi V. Fragility analysis of steel and concrete wind turbine towers. Engineering Structures. 2012;36:270–282.
- [35] Sapountzakis EJ, Dikaros IC, Kampitsis AE, Koroneou AD. Nonlinear response of wind turbines under wind and seismic excitations with soil-structure interaction. Journal of Computational and Nonlinear Dynamics. 2015;10(4).
- [36] Koulatsou K, Petrini F, Vernardos S, Gantes CJ. Artificial time histories of wind actions for structural analysis of wind turbines. 2013.
- [37] Paola DM. Digital simulation of wind field velocity. Journal of Wind Engineering and Industrial Aerodynamics. 1998;(74–76):91–109.
- [38] Norske Veritas (Organization), Forskningscenter Risø. Guidelines for design of wind turbines., Det Norske Veritas, Copenhagen ;[Roskilde Denmark]. 2002.
- [39] Jonkman JM. Dynamics modeling and loads analysis of an offshore floating wind turbine. Technical Report No. NREL/TP-500-41958. 2007.
- [40] Zong WG, Joong HK, Loganathan GV. A new heuristic optimization algorithm: Harmony search. Simulation. 2001;76(2):60–68.
- [41] Carrella A, Brennan MJ, Waters TP. Static analysis of a passive vibration isolator with Quasi-Zero-Stiffness characteristic. Journal of Sound and Vibration. 2007;301(3–5):678–689.

Appendix A: Formation of the DVA submatrices

A.1 TMD

The controlled system has $(N+1)$ dynamic DoFs, where N indicates the number of prismatic beam elements simulating the WT. The submatrices Equations (3) are expressed as follows:

$$[M_{n,a}] = [0]_{N \times N} \quad [M_{n,b}] = [M_{n,c}]^T = \{0\}_{N \times 1} \quad M_{n,d} = +m_D = +\mu_D m_{tot} \quad (A.1.1)$$

$$[K_{n,a}] = \begin{bmatrix} 0 & \cdots & 0 \\ \vdots & \ddots & \vdots \\ 0 & \cdots & +k_D \end{bmatrix}_{N \times N} \quad [K_{n,b}]^T = [K_{n,c}] = [0 \quad \cdots \quad -k_D]_{1 \times N} \quad K_{n,d} = +k_D \quad (A.1.2)$$

$$[C_{n,a}] = \begin{bmatrix} 0 & \cdots & 0 \\ \vdots & \ddots & \vdots \\ 0 & \cdots & +c_D \end{bmatrix}_{N \times N} \quad [C_{n,b}]^T = [C_{n,c}] = [0 \quad \cdots \quad -c_D]_{1 \times N} \quad C_{n,d} = +c_D \quad (A.1.3)$$

A.2 Nacelle-isolation

The controlled system has $(N+1)$ dynamic DoFs. The submatrices Equations (3) are expressed as follows:

$$[M_{n,a}] = \begin{bmatrix} 0 & \cdots & 0 \\ \vdots & \ddots & \vdots \\ 0 & \cdots & -m_{top} \end{bmatrix}_{N \times N} \quad [M_{n,b}] = [M_{n,c}]^T = \{0\}_{N \times 1} \quad M_{n,d} = +m_{top} \quad (A.2.1)$$

$$[K_{n,a}] = \begin{bmatrix} 0 & \cdots & 0 \\ \vdots & \ddots & \vdots \\ 0 & \cdots & +k_D \end{bmatrix}_{N \times N} \quad [K_{n,b}]^T = [K_{n,c}]_{1 \times N} = [0 \quad \cdots \quad -k_D]_{1 \times N} \quad K_{n,d} = +k_D \quad (\text{A.2.2})$$

$$[C_{n,a}] = \begin{bmatrix} 0 & \cdots & 0 \\ \vdots & \ddots & \vdots \\ 0 & \cdots & +c_D \end{bmatrix}_{N \times N} \quad [C_{n,b}]^T = [C_{n,c}] = [0 \quad \cdots \quad -c_D]_{1 \times N} \quad C_{n,d} = +c_D \quad (\text{A.2.3})$$

A.3 KDamper

The controlled system has $(N+2)$ dynamic DoFs. The submatrices Equations (3) are expressed as follows:

$$[M_{n,a}] = \begin{bmatrix} 0 & \cdots & 0 \\ \vdots & \ddots & \vdots \\ 0 & \cdots & -m_{top} \end{bmatrix}_{N \times N} \quad [M_{n,b}]^T = [M_{n,c}] = \{0\}_{2 \times N} \quad [M_{n,d}] = \begin{bmatrix} +m_D & 0 \\ 0 & +m_{top} \end{bmatrix}_{2 \times 2} \quad (\text{A.3.1})$$

$$[K_{n,a}] = \begin{bmatrix} 0 & \cdots & 0 \\ \vdots & \ddots & \vdots \\ 0 & \cdots & +k_R + k_{NS} \end{bmatrix}_{N \times N} \quad [K_{n,b}]^T = [K_{n,c}] = \begin{bmatrix} 0 & \cdots & -k_{NS} \\ 0 & \cdots & -k_R \end{bmatrix}_{2 \times N} \quad [K_{n,d}] = \begin{bmatrix} +(k_{PS} + k_{NS}) & -k_{PS} \\ -k_{PS} & k_R + k_{PS} \end{bmatrix}_{2 \times 2} \quad (\text{A.3.2})$$

$$[C_{n,a}] = [0]_{N \times N} \quad [C_{n,b}]^T = [C_{n,c}] = [0]_{2 \times N} \quad [C_{n,d}] = \begin{bmatrix} +c_{PS} & -c_{PS} \\ -c_{PS} & +c_{PS} \end{bmatrix}_{2 \times 2} \quad (\text{A.3.3})$$

A.4 EKD

The controlled system has $(N+2)$ dynamic DoFs. The mass terms as the same as the Kdamper (A.3.1). The stiffness and damping submatrices Equations (3) are expressed as follows:

$$[K_{n,a}] = \begin{bmatrix} 0 & \cdots & 0 \\ \vdots & \ddots & \vdots \\ 0 & \cdots & +(k_R + k_{PS}) \end{bmatrix}_{N \times N} \quad [K_{n,b}]^T = [K_{n,c}] = \begin{bmatrix} 0 & \cdots & -k_{PS} \\ 0 & \cdots & -k_R \end{bmatrix}_{2 \times N} \quad [K_{n,d}] = \begin{bmatrix} +(k_{NS} + k_{PS}) & -k_{NS} \\ -k_{NS} & k_R + k_{NS} \end{bmatrix}_{2 \times 2} \quad (\text{A.4.1})$$

$$[C_{n,a}] = [0]_{N \times N} \quad [C_{n,b}]^T = [C_{n,c}] = [0]_{2 \times N} \quad [C_{n,d}] = \begin{bmatrix} +c_{NS} & -c_{NS} \\ -c_{NS} & +c_{NS} \end{bmatrix}_{2 \times 2} \quad (\text{A.4.2})$$

A.5 EKDI

The only difference with the EKD is the addition of the inerter. The submatrices that differ from A4 are:

$$[M_{n,a}] = \begin{bmatrix} 0 & \cdots & 0 \\ \vdots & \ddots & \vdots \\ 0 & \cdots & -m_{top} + m_b \end{bmatrix}_{N \times N} \quad [M_{n,b}]^T = [M_{n,c}] = \{0\}_{2 \times N} \quad [M_{n,d}] = \begin{bmatrix} +m_D & -m_b \\ -m_b & +(m_{top} + m_b) \end{bmatrix}_{2 \times 2} \quad (\text{A.5.1})$$

Genetic Algorithm Designed for Stability of Slope Analysis

Saleema Panda, *Department of Civil Engineering, NM Institute of Engineering & Technology, Bhubaneswar, saleemapanda25@gmail.com*

Nilgrib Mohanty, *Department of Civil Engineering, Aryan Institute of Engineering & Technology, Bhubaneswar, nilgribmohanty25@outlook.com*

Barsa Priyadarshini Sahoo, *Department of Civil Engineering, Raajdhani Engineering College, Bhubaneswar, barsap_sahoo@gmail.com*

Debi Prasad Singh, *Department of Mechanical Engineering, Raajdhani Engineering College, Bhubaneswar, deboprasad_1159@gmail.com*

ABSTRACT

In this study, a real-coded genetic algorithm (GA) is used to calculate the factor of safety for soil slopes using the wedge method. The purpose of the problem is to solve the nonlinear equilibrium equation and determine the safety factor as a restricted optimization problem. The findings are compared to those previously published in the literature. The sensitivity analysis of the GA optimization technique is shown in terms of the evolution of the failure surface. In a single run, the GA discovers a number of failure surfaces as well as the suitable factor of safety. The shape of the failure wedge was discovered to be dictated by the slope angles when all other factors were held constant.

Keywords: Slope stability, analysis, genetic algorithm

INTRODUCTION

The stability of slope is one of the most important problems in stability analysis of geomechanics. Out of various methods (finite element analysis, limit analysis), limit equilibrium method is widely used for its simplicity form and the results found to be close to that rigorous methods. The limit equilibrium method is taken as 2-D plane strain problem with no variation in geometry, material and surcharge in direction parallel to the crest of the slope. The problem lies in finding out the critical failure surface and its corresponding factor of safety (FOS). The above concept has given rise to consider it as an optimization problem (Basudhar, 1976; Baker, 1980).

The development of limit equilibrium as optimization is straight forward, consisting of (i) development of objective function and (ii) selection of optimization technique. Development of objective function is based on different stability analysis method for the sliding mass of the slope. The different methods in use for this are Bishop, Janbu, Spencer, Morgenstern & Price, Chen & Morgenstern, Sharma etc. (Abramson et al., 2002). The stability analysis methods basically differ from one another in the hypothesis assumed in order to satisfy the equilibrium conditions of the potential sliding mass. It has been proved that all these methods, if used respecting the basic hypothesis, gives satisfactory results.

Different sophisticated optimization techniques have been used to search for the critical slip surface, are calculus of variation, linear programming, nonlinear programming and dynamic programming. The variational technique cannot be applied to heterogeneous soil, and as the stability analysis equation is nonlinear, linear programming has not been widely accepted. Dynamic programming has the difficulty in dimensionality, so the nonlinear

unconstraint optimizations like Nelder Meade, Hookes & Jeeve & Powells Conjugate direction method, steepest descent, Fletcher-Reeve (FR), Davidon,- Fletcher – Powel(DFP), Broydon-Fletcher-Goldfarb-Shanno (BFGS) have been widely used. Many practical slope problems are not convex (De Natale, 1991), there by having multiple optima. All the above optimization techniques are initial point dependant and there is a need to analyze with wide separated points. It is usually not possible to find global minimum except in special cases (De Natale, 1991).

To avoid the difficulty in finding out the global minima, evolutionary methods such as genetic algorithm is being used, which is more robust in finding out the optimal solution in many complex problems (Goldberg, 1989). Goh (1999) has used GA to find out the critical surface and the factor of safety using method of wedges. McCombie and Wilkinson (2002) used Bishop's simplified method and Sabhahit et al. (2002) have used Janbu's method to search for the critical surface using GA. In the above studies GA could find better solution compared to other traditional optimization tools.

With the above in view, in this study a real-coded GA has been used to find out the critical failure surface and the corresponding factor of safety for three wedge method. The real-coded GA has several advantages over binary coded GA (Deb, 2001) and three-wedge method is widely used for stability analysis of mine spoils (Huang, 1983).

METHODOLOGY

The analysis of the problem can be considered in two stages: (i) development of objective function and (ii) the application of GA in solving the objective function.

Development of objective function

In the present study, the three-wedge method for stability analysis of slopes (Huang, 1983) is used for the development of objective function. This is a force equilibrium method and development of the equations used for the analysis is described in details in Huang (1983).

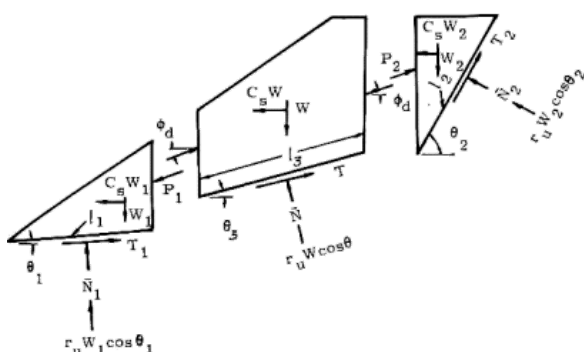


Figure 1. The free-body diagram for three-wedge method

Figure 1 shows the free-body diagram showing the forces on each block. There are total six (6) unknowns (P_1 ,

P_2 , N_1 , N_2 , N_3 and factor of safety, F) which can be solved by six equilibrium equations, two for each block. The F can be found out by solving the nonlinear equation as shown in Eq. 1 (Huang, 1983). There are different iterative methods to solve Eq. 1. However, there are some problems in solving such equation using the iterative methods (Bhattacharya and Basudhar, 2001), which is inherent in all numerical techniques. So in the present study the Eq. 1 is solved using optimization method.

$$(P_1 - P_2) \cos \phi_d - N_3 \sin \theta - r_u W_3 \cos \theta \sin \theta + T_3 \cos \theta_3 - C_s W_3 = 0 \quad (1)$$

Where

$$\phi_d = \tan^{-1} \left(\frac{\tan \phi}{F} \right)$$

r_u = pore pressure parameter, W_3 = weight of the 3rd wedge, C_s is horizontal seismic acceleration coefficient and

P_1, P_2, N_1, N_2, N_3 are as shown in Fig. 1.

The optimization method may be described as finding out the minimum factor safety which satisfies the Eq. 1 and in mathematical programming form it can be written as:

Min F :
Subjected to

$$(P_1 - P_2) \cos \phi_d - N_3 \sin \theta - r_u W_3 \cos \theta \sin \theta + T_3 \cos \theta_3 - C_s W_3 = 0. \quad (2)$$

The variables (design vectors) are $l_1, l_2, l_3, N_1, N_2, N_3$ and F and the application dependent input parameters are

slope angle (b), cohesion (c_i), height of slope (H), angle of internal friction (f) pore pressure parameter (r_u) and

seismic acceleration coefficient C_s

In order to ascertain that the shape and location of the slip surface are physically reasonable and kinematically compatible, the following constraints need to be imposed on the choice of design variable. As per physically condition it is found that the direction of the T_i should be positive (Huang, 1983), and the kinematical conditions are applied for the geometry of the failure surface.

$$l_1 \times \cos \theta_1 + l_2 \cos \theta_2 + l_3 \cos \theta_3 = H / \tan \beta \quad (3)$$

$$l_1 \times \sin \theta_1 + l_2 \sin \theta_2 + l_3 \sin \theta_3 = H \quad (4)$$

$$b^3 q_1 \quad (5)$$

$$T_i^3 0.0; i = 1, 2, 3 \quad (6)$$

Genetic algorithm

The GA is a random search algorithm based on the concept of natural selection inherent in natural genetics, presents a robust method for search for the optimum solution to the complex problems. The algorithms are mathematically simple yet powerful in their search for improvement after each generation (Goldberg, 1989). The artificial survival of better solution in GA search technique is achieved with genetic operators: selection, crossover and mutation, borrowed from natural genetics. The major difference between GA and the other classical optimization search techniques is that the GA works with a population of possible solutions; whereas the classical optimization techniques work with a single solution. Another difference is that the GA uses probabilistic transition rules instead of deterministic rules. The GA that employs binary strings to represent the variables (chromosomes) is called binary-coded GA. The binary-coded GA consists of three basic operators, selection, crossover or mating, and mutation, which are discussed as follow. In the selection procedure, the chromosomes compete for survival in a tournament selection, where the chromosomes with high fitness values enter the mating population and the remaining ones die off. The selection probability (P_s) determines the number of chromosomes to take part in tournament selection process. The selected chromosomes form an intermediate population known as the mating population, on which crossover and mutation operator is applied. The selected

chromosomes are randomly assigned a mating partner from within the mating population. Then, a random crossover location is selected in any two parent chromosomes and the genetic information is exchanged between the two mating parent chromosomes with a certain mating probability (P_c), giving birth to a child (new variable) or the next generation. In binary-coded GA, mutation is achieved by replacing 0 with 1 or vice versa in the binary strings, with a probability of P_m . This process of selection, crossover, and mutation is repeated for many generations (iterations) with the objective of reaching the global optimal solution. The flow chart of the general solution procedure of GA is depicted in Figure 2.

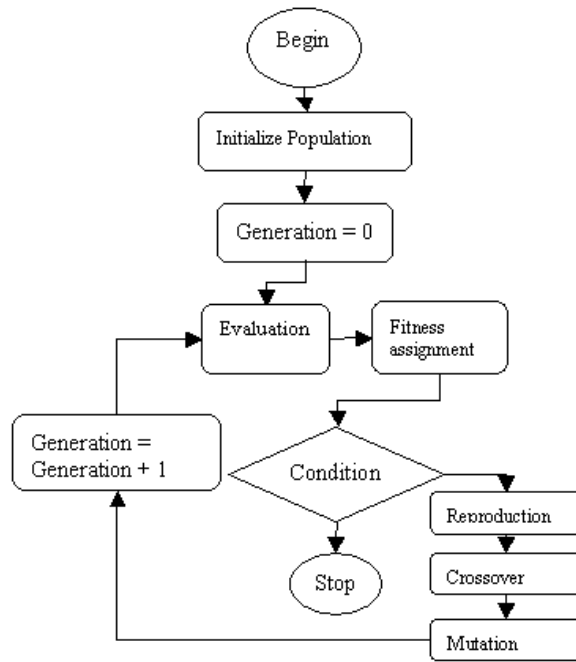


Figure 2. Flow chart for working principles of genetic algorithm

In the present analysis, a real- coded GA has been used, in which there is no need of coding and decoding the design variables. The real- coded GA with simulated binary crossovers (SBX), polynomial mutations and a tournament selection type of selection procedure have been used, details of which are available in Deb (2001). The GA was implemented using pseudo code available as freeware at

http://www.iitk.ac.in/mech/research_labs.htm.

The GA has an inherent limitation of not being able to handle the equality constraints. The equality constraints need to be converted to inequality constraint using a dummy variable ϵ (0.001 is considered for the present study) in the GA formulation and the revised constraint is written as in Eq.7-11. So the total objective function and the corresponding constraints can be written as

$$F^2 + \{(P_1 - P_2) \cos \phi_d - N_3 \sin \theta - r_u W_3 \cos \theta \sin \theta + T_3 \cos \theta_3 - C_s W_3\}^2 \quad (7)$$

Subject to:

$$\epsilon - \{l_1 \times \cos \theta_1 + l_2 \cos \theta_2 + l_3 \cos \theta_3 - H / \tan \beta\}^2 \geq 0.0 \quad (8)$$

$$\varepsilon - \{l_1 \times \sin \theta_1 + l_2 \sin \theta_2 + l_3 \sin \theta_3 - H\}^2 \geq 0.0 \quad (9)$$

$$b^3 q_1 \quad (10)$$

$$T_i^3 0.0; i = 1, 2, 3 \quad (11)$$

The common method of handling the constraints is by penalty function method. However, in the present study the following method (Deb, 2001) is used for constraint handling.

- The method uses tournament selection as the selection operator and two solutions are compared at a
- time. Any feasible solution is preferred to any infeasible solution;
- Among two feasible solutions the one having better objective function is preferred and among two infeasible solutions, the one having smaller constraint violation is preferred.

Thus, at any iteration, the infeasible solutions are not computed for objective function if some feasible solutions are present, which helps in reducing the computational effort.

For the present study the GA parameters of the crossover probability (P_c) varied from 0.58 to 0.78 and the

mutation probability (P_m) 0.21 to 0.41.

RESULTS & DISCUSSION

Three field problems (Problem I, Problem II and Problem III) as discussed in Jade and Shankar (1995) were considered for the present study. The three dry slopes with its geometry, soil parameter and the corresponding critical factor safety using Bishops simplified method is shown in Table 1. Unlike previous GA studies, in this study the fitness is considered as the objective function itself. As tournament selection is used, so the minimum value is the winner. The variation of the fitness function (objective function) with generation number is shown in Figure 3. It can be seen that the best fitness (minimum objective function) is almost constant after 100 generation. However, there is sufficient diversity in the results as observed from average fitness and worst fitness. The results of the present study are compared with the results of Jade and Shankar (1995). As it can be seen from Table 1 that for all the three cases the factor of safety obtained by the present study is less than that obtained by Bishop's simplified method. Though, it can be pointed out that the Bishop's simplified method assumes circular slips surface, where as the present study assumes the wedge failure. So it was observed that though the factor of safety is similar the slip surface was different and the above observations have been observed by other studies in slope stability analysis.

Figure 4, 5 and 6 shows the different failure surface along with the critical surface for the Problem I, II and III respectively. Unlike traditional optimization problem, working with GA has the advantages of storing a number of solutions close to the optimum value, along with the optimum one. This will help in finding the variability of the FOS over the slope (Baker and Leshchinsky, 2001). It can be observed that for the Problem I and II, the critical failure surface is almost single wedge. This may be due to the fact that both the problems may be

considered as steep slope $b = 78^\circ$ and 65° respectively). The critical surface in Problem III ($b = 45^\circ$) shows a two wedge failure surface. To study the effect of slope angle on the type of failure wedge, Problem II was solved

for different slope angle and the results are shown in Figure 7. It can be seen that when $b = 65^\circ$ the critical failure surface is single wedge and as the slope angle reduces the failure wedge changes to two wedges and subsequently to three wedges. This may help in choosing the type of wedge analysis depending upon the slope angle.

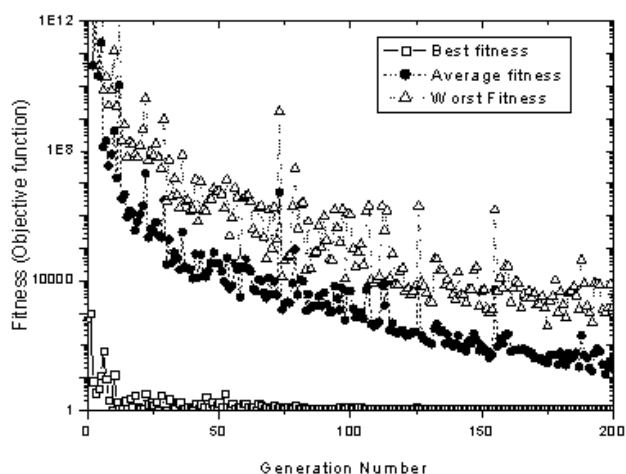


Figure 3. Variation of the fitness of the objective function with generation number

Table 1. Comparisons of results of present study with Jade and Shankar (1995)

	H (m)	b	c (kN/m ²)	f	g (kN/m ³)	r_u	C_s	F^1	F^2
Problem I	8.3	78 ⁰	7.5	28 ⁰	19.04	0.0	0.0	0.92	0.663
Problem II	3.8	65 ⁰	7.5	28 ⁰	19.04	0.0	0.0	1.30	1.178
Problem III	11.6	45 ⁰	15.0	22 ⁰	19.10	0.0	0.0	1.15	1.13

¹ Jade and Shankar (1995); ² Present study

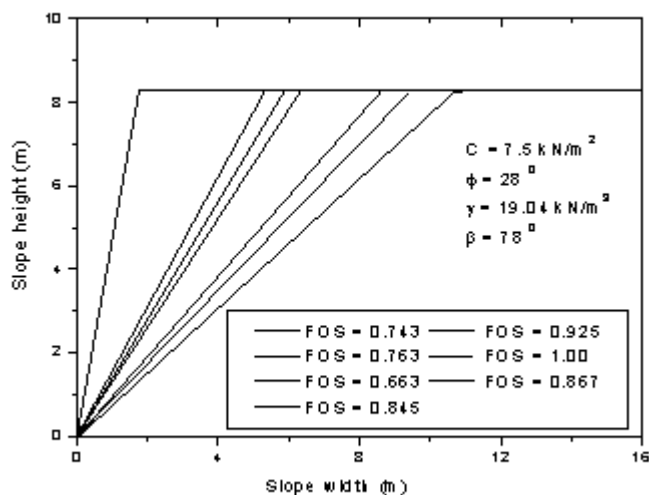


Figure 4. Different failure surfaces along with the critical failure surface for Problem I

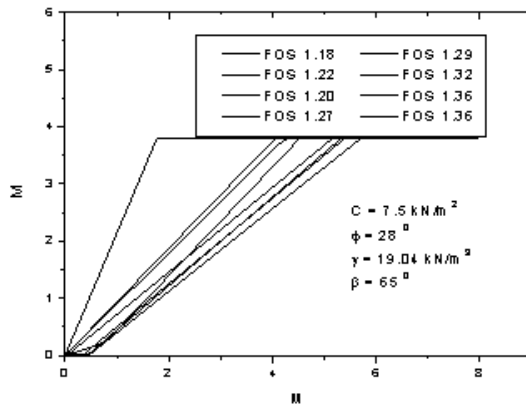


Figure 5. Different failure surfaces along with the critical failure surface for Problem II

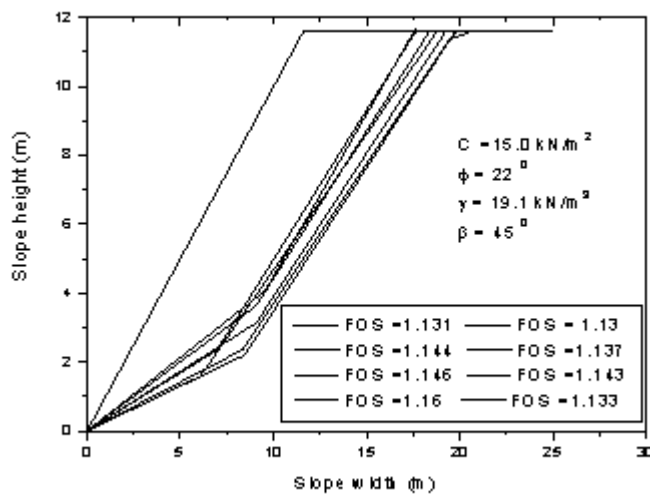


Figure 6. Different failure surfaces along with the critical failure surface for Problem III

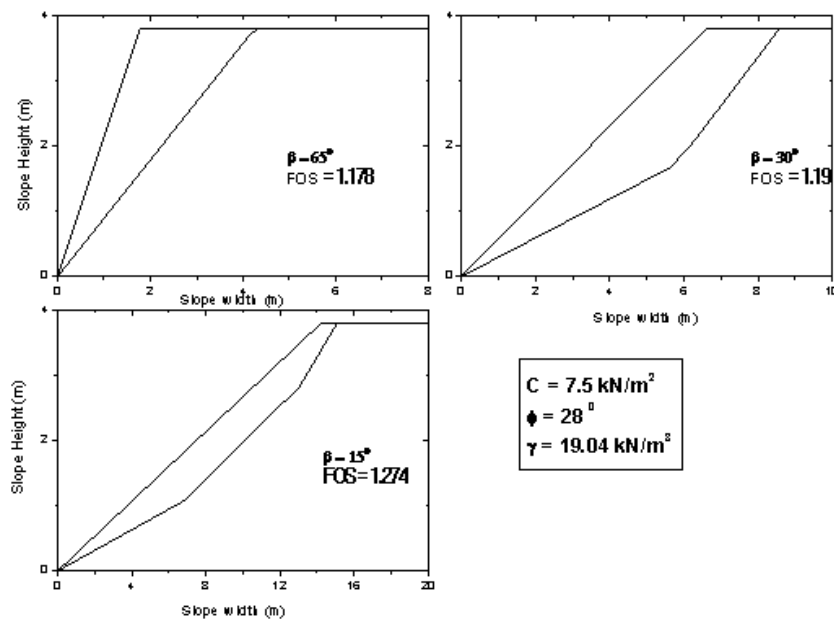


Figure 7. Variation of type of critical failure surface with different slope angle for Problem II

Sensitivity Analysis

Like NLP optimization methods, population based algorithms first optimizes the parameter which is the most sensitive to the objective function (Marseguerra et al. 2003). Marseguerra et al. (2003) have shown that for GA, the sensitivity of the parameter can be correlated with square of coefficient of variation. The coefficient of variation is defined as the ratio of the standard deviation to the mean of the population. The parameter which is the most sensitive should quickly converge to low value of square of coefficient of variation with generation. The behavior of square of coefficient of variation with generation is shown in Figure 8. It can be seen that the

GA first optimize the material parameter FOS. The sensitivities of the geometric terms are in the order as, q_3 , l_3 ,

q_2 , l_2 , q_1 , and l_1 . It can be seen that GA tries to first minimize the angle and then the corresponding length of wedge. Malkawi et al. (2001) through Monte Carlo simulation observed that the minimization of factor of safety is achieved by gradual fixing of failure segments.

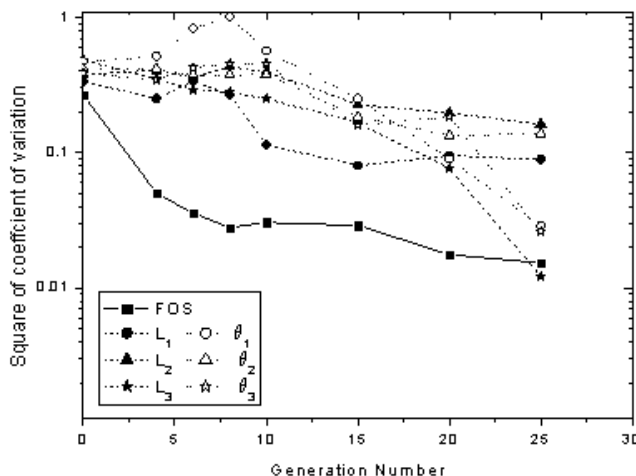


Figure 8. Variation of type of square of coefficient variation with generation number
CONCLUSIONS

In this paper, application of genetic algorithm in analyzing soil slopes using three-wedge method was discussed. The factor of safety obtained by the present study for three cases was less than that obtained by Bishop's simplified method. Unlike traditional optimization problem, working with GA has the advantages of storing a number of solutions close to the optimum value, along with the optimum one. This will help in finding the variability of the FOS over the slope. The number of failure wedge at critical condition found to depend upon

the slope angle. The sensitivities of the geometric terms in terms of minimizing the FOS are in the order as, l_3 ,

q_3 , q_1 , l_1 , q_2 , and l_2 .

REFERENCES

1. Abramson, L.W., T.S. Lee, S. Sharma, and G.M. Boyce (2002) "Slope stability and stabilization methods," John Wiley & Sons, Inc. New York, USA.
2. Baker, R. (1980) "Determination of the critical slip surface in slope stability computation," International J. of Numerical and Analytical methods in Geomechanics, Vol.14, pp.333-359.
3. Baker, R., and D. Leshchinsky (2001) "Spatial Distribution of Safety Factors," Journal of Geotechnical Engineering, Vol. 127, pp.135-145.
4. Basudhar, P.K. (1976) "Some applications of mathematical programming technique to stability problems in geotechnical engineering," Ph.D. Thesis, Indian Institute of Technology, Kanpur, India.
5. Bhattacharya, G. and P.K. Basudhar (2001) "A New Procedure for Finding Critical Slip Surfaces in Slope Stability Analysis," Indian Geotechnical Journal, Vol. 31, No. 1, pp.149-172.
6. Deb, K. (2001) "Multi-objective optimization using evolutionary algorithms," Wiley, Chichester, UK.
7. DeNatale, J.S. (1991) "Rapid Identification of Critical Slip Surfaces: Structure," Journal of Geotechnical Engineering, Vol. 117, No.10, pp.1568-1589.
8. Goh, A.T.C. (1999) "Genetic algorithm search for critical slip surface in multiple-wedge stability analysis," Canadian Geotechnical Journal, Vol. 36, pp. 382-391.

9. Goldberg, D.E. (1989) "Genetic algorithm in search, optimization, and machine learning," Addison-Wesley, Massachusetts, USA.
10. Huang, Y.H. (1983) "Stability analysis of slopes," Van Nostrand Reinhold Company, USA.
11. Jade, S. and K.D. Shanker (1995) "Modelling of slope failure using a global optimization technique," Engineering Optimization, Vol. 23, No.2, pp. 255-266.
12. Malkawi, A.I.H., W.F. Hassan, and S.K. Sharma (2001) "Global search method for locating global slip surface using Monte Carlo technique," Journal of Geotechnical Engineering, Vol 127, No. 8, pp. 688-698.
13. Marseguerra, M., E. Zio, and L. Podofillini (2003) "Model parameters estimation and sensitivity by genetic algorithms," Annals of Nuclear Energy, Vol. 30, No.14, pp. 1437-1456.
14. McCombie, P. and P. Wilkinson (2002) "The use of the simple genetic algorithm in finding the critical factor of safety in slope stability analysis," Computer and Geotechnics, Vol. 29, pp. 699-714.
15. Sabhahit, N., J. Sreeja, and M.R. Madhav (2002) "Genetic algorithm for searching critical slip surface," Indian Geotechnical Journal, Vol. 32, No.2, pp.86-101.

Seismic Design of Integral Abutment Bridges

Murari Prasad Panda, *Department of Civil Engineering, Aryan Institute of Engineering & Technology, Bhubaneswar, muraripanda25@outlook.com*

Bipash Mohanty, *Department of Civil Engineering, Capital Engineering College, Bhubaneswar, bipashmohanty784@gmail.com*

S. C. Mishra, *Department of Civil Engineering, NM Institute of Engineering & Technology, Bhubaneswar, scmishra11@yahoo.co.in*

Ranjan Kumar, *Department of Mechanical Engineering, NM Institute of Engineering & Technology, Bhubaneswar, kumarranjan75@gmail.com*

Abstract: For estimating the design seismic forces applied to a bridge structure, the response modification factor (R factor) is a critical quantity. This component takes into account the nonlinear behaviour of bridges when severe ground vibrations occur. To withstand earthquake forces, traditional bridge systems rely on substructure components. As a result, depending on the kind of bridge substructure system, R factors are accessible in the design codes. In the longitudinal direction, the lateral load resisting system of Integral Abutment Bridges (IABs) is more sophisticated than that of standard bridges. In addition to the current stiff link between the superstructure and abutments, it includes contributions from soils behind the abutments and soil/structure interaction (SSI). There is no R factor for IABs in the longitudinal direction that takes into account all of these characteristics in any design code anywhere in the globe. In this study, the R factor for IABs was calculated using the FEMA P695 technique published by the Federal Emergency Management Agency. In the longitudinal direction, it was discovered that 3.5 might be a safe and valid R factor for seismic design of such bridges. **Keywords:** Response modification factor; Integral abutment bridge; Seismic design; FEMA P695; Soil/Structure interaction.

1. Introduction

For many years, long span bridges were mainly designed and constructed as multiple simply supported spans until the moment distribution method was published in 1930 and facilitated the analysis of continuous spans and rigid frame bridges [1]. The integral abutment bridge (IAB) also benefits from continuity in a different way, namely between the superstructure and substructure, very similar to an arch bridge. This continuity eliminates the need for expansion joints at the abutments and due to extensive and costly problems associated with these joints, IABs are becoming a bridge system of choice throughout the world. The integration of abutment and deck speeds up the construction process of IABs and especially the accuracy required to install bearing devices. The maintenance costs of expansion joint devices are no longer of concern for IABs and less damage is expected to the structure as cars pass over the bridge. Also, in an earthquake, the unseating of the deck, which is a major problem in conventional bridges, is eliminated for IABs. Despite many advantages, secondary stresses due to thermal, shrinkage and creep are more of a concern for IABs. In general, the analysis of IABs is very complex and involves an indeterminate structure with soil/structure interaction (SSI) in its fullest form. The SSI should encompass soil/pile and soil/abutment and near/far field soil effects. Many researchers have worked on this complex SSI problem and suggested simplified analysis techniques for IABs under gravity, thermal and seismic actions [2-8].

The response modification factor (R factor) is a crucial parameter for calculating the design earthquake forces of a bridge structure in the code specified linear seismic analysis procedures such as equivalent static load and response spectrum analyses [9]. This factor considers the nonlinear performance of bridges during strong ground motions. Conventional bridge structures rely on the substructure components to resist earthquake forces. Accordingly, there are R factors available in the design codes like AASHTO [9] based on the type of substructure system. The lateral force resisting system (LFRS) of IABs in the longitudinal direction is more complex than ordinary bridges. This is because of the lateral stiffness contribution from many components like the deck, abutments, piles, near field soils in the active and passive states, and soil inertia in the farfield and the interaction between them. There is no R factor available in any design code throughout the world for seismic design of IABs in the longitudinal direction that considers all the above parameters. This is mainly because an accurate analytical nonlinear analysis of these bridges under seismic actions is a hard task. In addition, the actual measured seismic responses of these bridges are only available in limited cases.

Note that the transverse seismic response of IABs is very similar to conventional bridges with abutment walls resisting the seismic forces. Hence, in the transverse direction the available bridge design code prescribed R factors can be used with confidence.

This paper uses a nonlinear finite element (FE) analysis model that can capture the interaction between soils and all the structural components to analyze the IABs under gravity and seismic loading. In addition, the new FEMA P695 [10] methodology has been used to estimate the R factor for seismic design of IABs in the longitudinal direction.

2. Literature review

Seismic behavior of integral abutment bridges by considering soil-pile-abutment interaction has been the focus of research for the past two decades. Erhan and Dicleli [2] have shown that using loose sand around piles that are oriented to bend about their weak axes and abutment height less than 4 m without compaction of backfill results limited forces on abutment. In a parametric study of integral abutment bridges, Civjan et al. [3] have shown that IABs behavior is greatly affected by soil parameters and analysis procedure of structure. It was found that soil characteristics might change over time and after several cycles of loading and unloading of the bridge. Another study by Spyarakos et al. [4] have shown the importance of SSI and soil properties on the seismic behavior of IABs. Itani and Pekcan [5] have investigated the behavior of IABs with steel plate girders which led to the development of design recommendations. One of their most important findings was that the pile axis orientation is insignificant in the longitudinal behavior of IABs, because it is controlled by soil-abutment interaction. Another important finding was that the seismic performance of integral abutment bridges is better than the conventional seat type abutment bridges in terms of overall displacement. Also, a formulation for damping of IABs resulting to about 6% damping ratio for steel girder IABs in the longitudinal was recommended.

More recently, Mahjoubi and Maleki [6,7] have developed a new approach for considering embankment static and dynamic active and passive pressures on retaining walls and bridge abutments including IABs. As a result, an appropriate length of embankment finite element model length that minimizes the radiation damping effects has been found. In their study, about 4 times the abutment height for extension length of soil behind abutments was suggested. In their new approach in finite element modeling of IABs, soil pile structure interaction involving both near field and far field soil responses was considered. This method is practical for design purposes, resulting that nonlinearity of piles and soil are significant in analyzing of this system.

Experimental studies on collapse assessment of H-piles under abutment of IABs are very rare, however, Burdette et al. [8] have studied several steel piles driven into clay and noted that that H-piles have high levels of ductility while proposing 0.1 radians as the collapse margin for steel H-piles. Itani and Peckan [5] also have reported 0.1 radians as an appropriate collapse margin rotation for H-piles in their report.

3. FEMA methodology in brief

According to FEMA P695 [10], finding the right R factor for a structural system is a trial-and-error process. A trial R factor of 3.5 was initially selected for the IABs of this research. This value is justified because the longitudinal behavior of IABs is very similar to bents with vertical piles and AASHTO [9] recommends the use of 3.5 for these systems. In the next step, several so-called archetype structures should be developed and designed, such that they can cover all possible geometries and properties that IAB systems in practice might have (e.g., variety of abutment heights, embankment soil properties, etc.). In addition, the potential nonlinearities in the structural system under earthquake loading should be identified and considered in structural modeling and analysis of archetypes. After performing an incremental dynamic analysis (IDA) on each archetype using 22 prescribed far-field ground motions the values of collapse margin ratios (CMRs) are obtained. The ratio of the median collapse intensity to the maximum considered earthquake (MCE) intensity defines the CMR. Pushover analyses are also performed to determine the overstrength and ductility factor for each archetype. These are needed to calculate the spectral shape factors (SSFs). Then the adjusted collapse margin ratios (ACMRs) are calculated by multiplying CMRs and SSFs. The initial R factor is acceptable only if the individual and average ACMRs meet the safety criteria set in the standard, otherwise R factor is adjusted and the procedure is repeated.

The archetypes considered in this study are among the most used IABs in practice. They consist of single span and two span continuous bridges with varying span lengths, soil properties and abutment wall heights. In two-span continuous IABs, the superstructure was considered to be roller supported on the piers. The abutment wall heights were of two types: a 7 m wall type and a 3 m stub type. Two types of embankment soil types were considered: dense and loose, with properties as shown in Table 1. Three span lengths of 10, 20 and 30 meters were also considered. The slab-beam type superstructure of all archetypes was the same and is shown in Fig. 1-2. The abutment pile cap and piles are also depicted in Fig. 3.

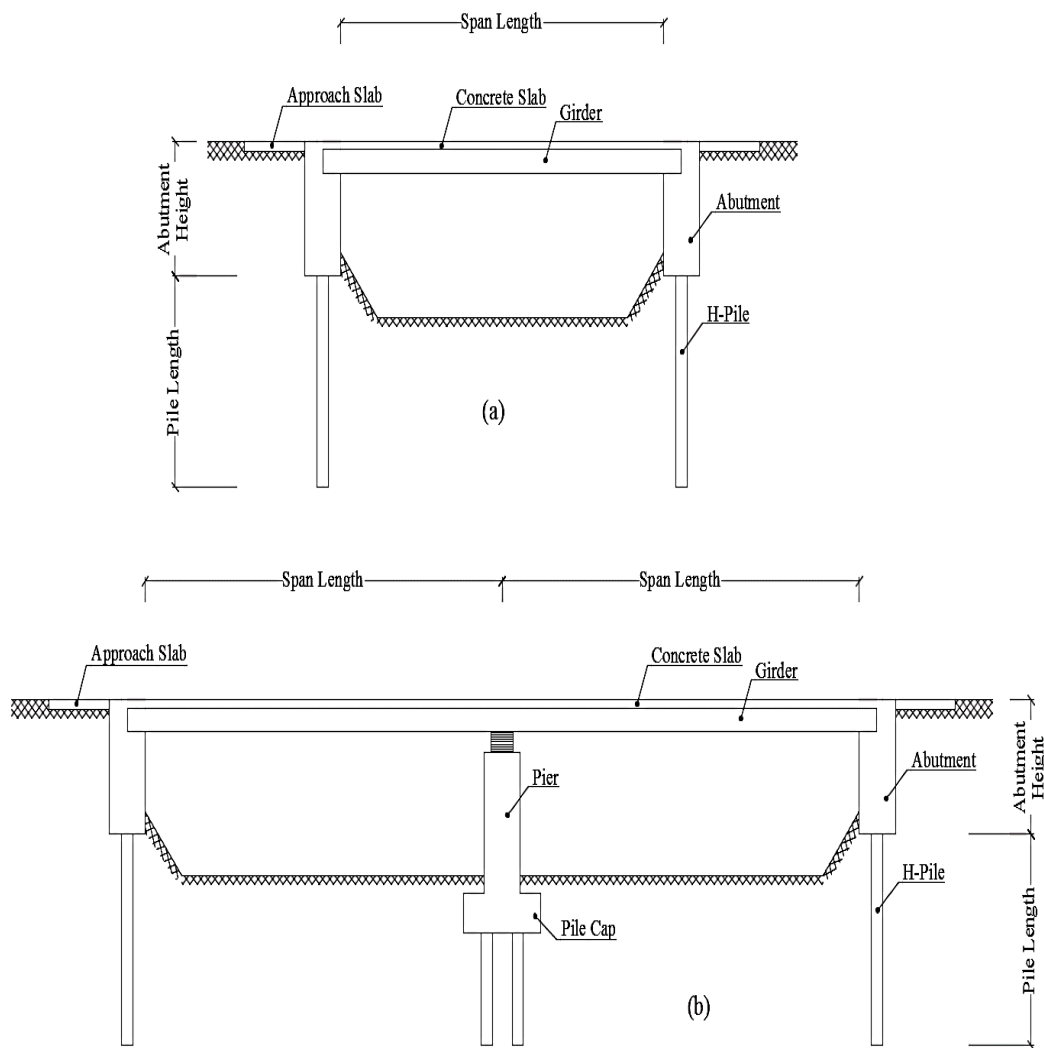


Fig. 1. Archetypes layout (a) Single span bridge (b) Multi-span bridge

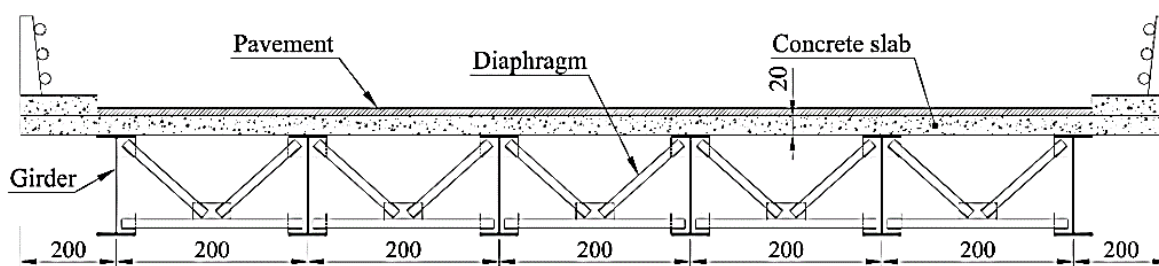


Fig. 2. Superstructure of all archetypes (dimensions in cm)

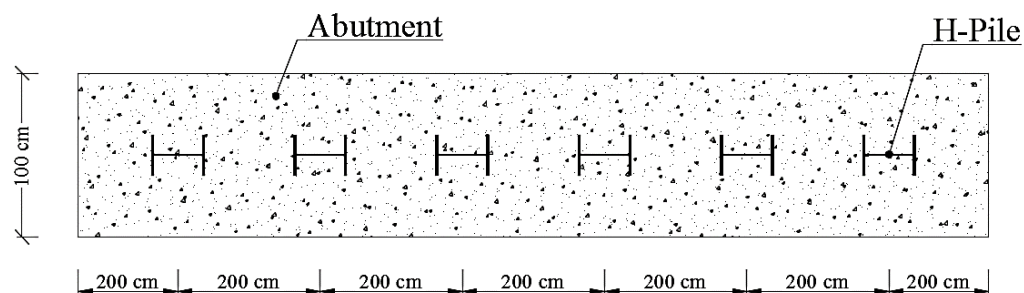


Fig. 3. Abutment and H-pile cross sections

Table 1. Properties of dense and loose soil

Soil Properties	Dense Soil (D)	Loose Soil (L)
Elasticity Modulus E (MPa)	80	15
Poisson Ratio	0.35	0.25
Internal Friction Angle ϕ (Degree)	38	30
Minimum Unit Weight (kN/m ³)	17	14
Maximum Unit Weight (kN/m ³)	22	18

4. Finite element modeling

4.1 Software and modeling

Because of its special features and strong graphical user interface, SAP2000 [11] is used for modeling and analysis of archetypes. A single 2 m wide 2D FE model of each IAB containing one girder and one pile was considered for all analyses to account for the longitudinal behavior of structures. Since every 2 m slice of the bridge width is similar, this 2D modeling assumption would be a great time saving idea. Previous studies have shown that the longitudinal behavior of IABs using 3D and 2D modeling can yield similar results and 2D modeling is more efficient (Faraji et al. [12]).

4.2 Deck modeling

Deck consists of a 20 cm thick concrete slab made of normal weight concrete with $f'_c=28$ MPa. Steel girders and concrete slab were modeled using frame and shell elements, respectively. Both frame and shell elements were meshed such that they were constrained together at their junction to simulate the composite behavior of the girders. The steel girders used were American W sections of ST-37 grade with yield strength of 240 MPa. All girders were embedded inside the abutments for 50 cm in order to make rigid connections.

4.3 Abutment and embankment modeling

Abutments were modeled using shell elements made of normal weight concrete with $f'_c=28$ MPa. A fine grid mesh was used in modeling the abutments to increase accuracy and avoid unreasonable results. The modeling of the embankment soil behind the abutments followed the procedure described in Mahjoubi and Maleki [7] with some minor changes. Embankment modeling consisted of 2 parts: a multilinear elastic near-field soil springs capturing the static active/passive behavior of the soil and a far-field soil which is assumed to remain elastic in an earthquake but contributes to mass inertia (see Figs. 4-5). Membrane elastic shell elements were used for modeling the far-field soil to an extent (length) equal to 4 times the abutment height to eliminate radiation damping occurrence in the system due to earthquake wave propagation [7]. Note that, far-field soil can become nonlinear only in very severe earthquakes and in most cases remains elastic (Richards, et al. [13]).

In order to account for shear modulus variation of far-field-soil with depth, the soil was divided into sublayers of different mechanical properties. There are two assumptions for shear modulus variation of cohesionless soils with depth: linear and parabolic. Following Richards et al. [13] and assuming parabolic variation, the shear modulus for each sublayer is calculated as:

$$G_i = G_b \sqrt{z_i/H} \quad (1)$$

where, G_i = average shear modulus of sublayer i , G_b = shear modulus at the bottom of embankment, z_i = mean depth of sublayer i , H = total depth of embankment.

The far-field-soil elements were restrained against horizontal and vertical translation at the bottom, where the earthquake time-history accelerations were also applied. The far end of far-field soil was restrained only against vertical translation. Far-field soil mass and stiffness will contribute to the inertia and stiffness of the total bridge structure when the gap elements are closed and the soil and structure are in contact.

The near-field soil behavior is modeled by a massless multilinear spring. The behavior is nonlinear but it is elastic. This means that the element loads and un-loads along the same curve, and no energy is dissipated. The elastic stiffness was calculated as follows:

$$k_i = k_s^z \times A_i \quad (2)$$

where, k_s^z = subgrade modulus at depth z calculated by Eq. (3)

$$k_s^z = CG_z/H \quad (3)$$

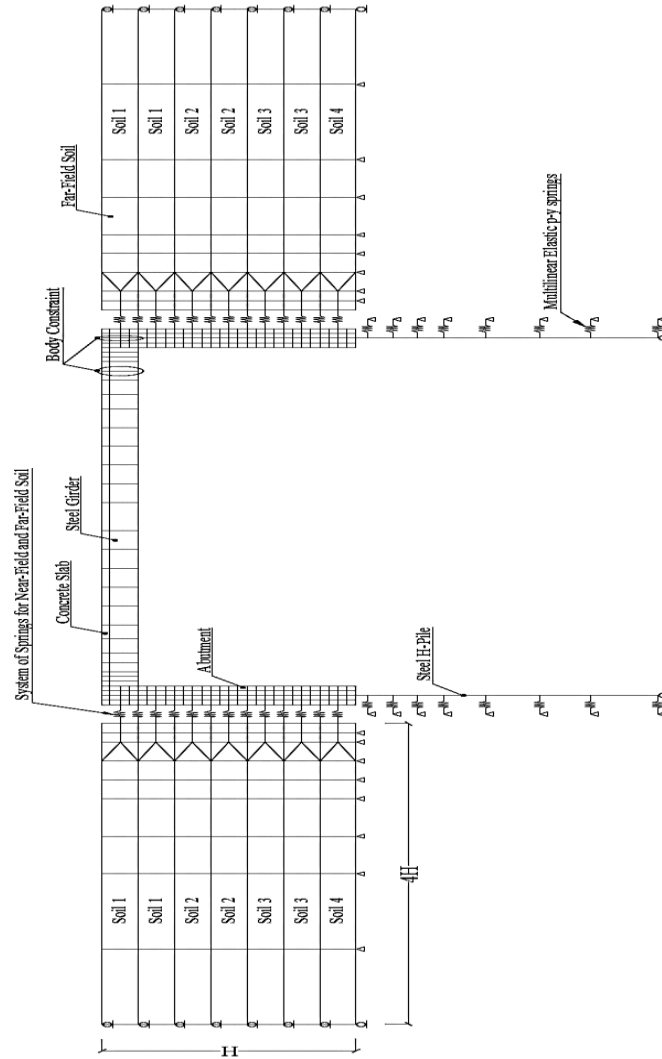


Fig. 4. Modeling layout of archetypes in the software

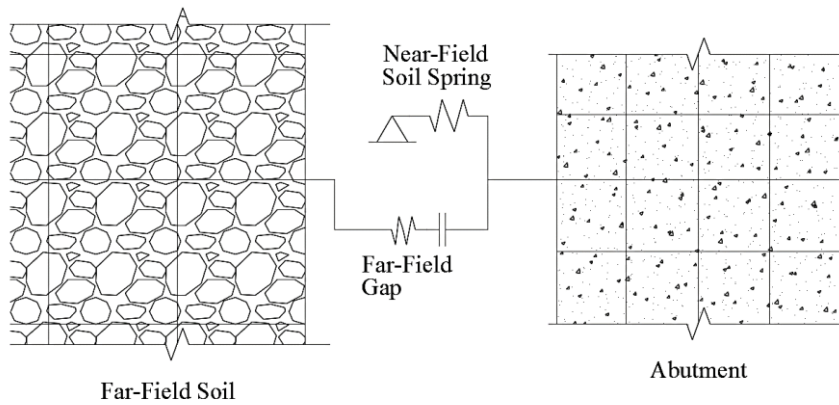


Fig. 5. System of springs for near-field and far-field soils

In Eq. (3), G_z = shear modulus at depth of z , C = a shape factor of 1.35 based on Richards et al. [13]. A_i = tributary area of spring calculated as:

$$A_i = B \times d \quad (4)$$

where, B = model width, d = tributary height of spring, which is equal to distance between springs.

There are upper (passive) and lower (active) limits for these springs as mathematically shown in Eq. (5). The exerted soil forces on the wall is always within these limits:

$$P_a = k_a \cdot \gamma_i \cdot z_i \cdot A_i \leq F_i = k_i \cdot \delta_i \leq P_p = k_p \cdot \gamma_i \cdot z_i \cdot A \quad (5)$$

in which, γ_i is soil unit weight at depth, z_i which is calculated by assuming linear variation of unit weight in depth. δ_i is abutment displacement or spring deformation at depth z_i . k_a is active and k_p as passive earth pressure coefficients computed based on Rankine formulation for simplicity:

$$k_a = \frac{1 - \sin \phi}{1 + \sin \phi}; k_p = \frac{1 + \sin \phi}{1 - \sin \phi} \quad (6)$$

where ϕ is the soil internal friction angle.

General force-displacement relationship for near-field soil spring model is shown in Fig. 6.

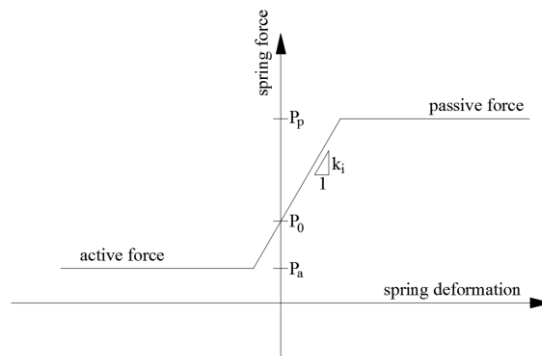


Fig. 6. Near field soil behavior

4.4 Pile and adjacent soil modeling

The 7 m length piles were modeled using frame elements of steel H sections. Multilinear elastic springs with force-deformation relationship based on API p-y curves [14] were developed and modeled along pile length for accounting the actual soil pressure acting on piles. An example of p-y curve assigned to a multilinear elastic link element in SAP2000 is shown in Fig. 7. The pile bottom was restrained against vertical displacement in all models. In this research, the source of potential nonlinearity is considered to be in piles. Thus, fiber P-M-M hinges was defined continuously along the upper 3 m of piles where the occurrence of plastic hinges was expected.

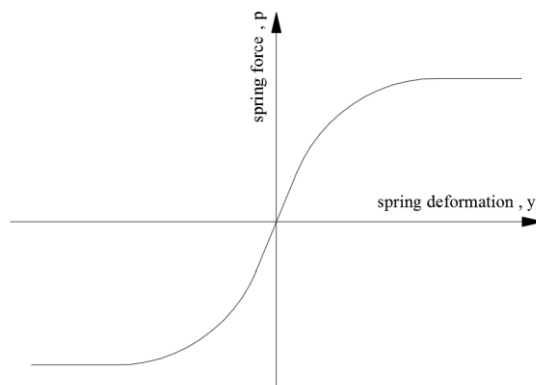


Fig. 7. p-y curve concept used in multilinear elastic springs along pile length

4.5 Analysis

The piles in IABs experience large displacements. Therefore, P-Delta effects must be considered in the analyses of all archetypes. Damping ratio of 5% is a common value for analysis of bridge structures and is considered to be conservative to use in this study.

5. Design of Archetypes

Archetypes were first designed based on AASHTO LRFD [9] specifications for gravity, thermal and seismic loading. SAP2000 was used for analysis and calculation of demands in structural elements. The details of structural modeling were discussed in the previous sections. Seismic demands were calculated based on the assumption that the bridges were located in China Town, Los Angeles, California. Thus, site class D was assigned and S_s and S_l values of 1.664 and 0.5576 were used, respectively. The PGA for the site was 0.7064. The design basis earthquake (DBE) and MCE spectra are shown in Fig. 8. Temperature loading was considered in calculating demands according to moderate climate conditions. The designed girder sections were chosen from American wide flange sections and piles were selected from HP sections. The designed IAB archetypes properties are shown in Table 2.

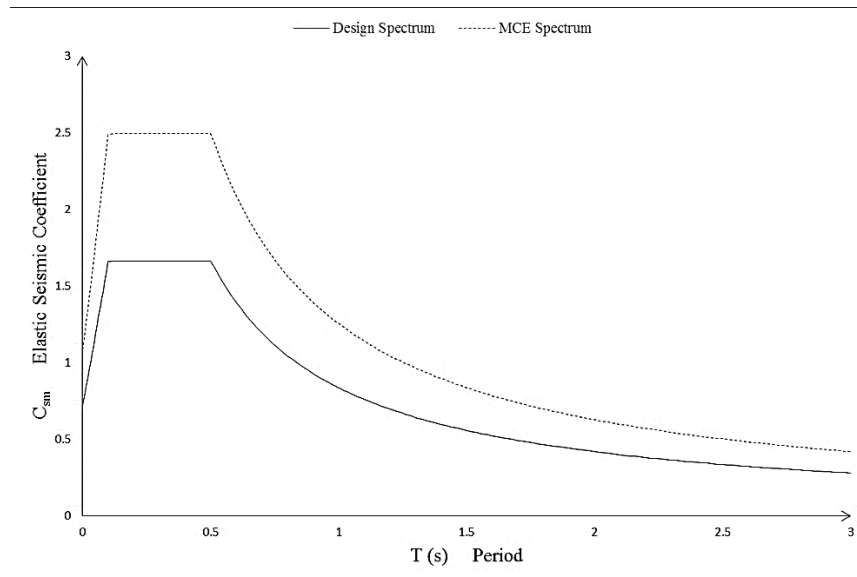


Fig. 8. DBE and MCE earthquake spectra

Table 2. Designed archetypes properties

Model ID	Abutment Type	Soil Type	Span Length (m)	No. of Spans	Pile Section	Girder Section
W10D1	Wall type	Dense	10	1	HP12X63	W24X68
W10D2			10	2	HP13X60	W24X68
W20D1			20	1	HP12X53	W40X167
W20D2			20	2	HP12X63	W44X262
W30D1			30	1	HP12X63	W44X262
W30D2			30	2	HP13X87	W44X262
W10L1		Loose	10	1	HP12X63	W24X76
W10L2			10	2	HP13X73	W24X76
W20L1			20	1	HP13X60	W40X183
W20L2			20	2	HP13X73	W40X183
W30L1			30	1	HP13X73	W44X262
W30L2			30	2	HP13X73	W44X262
S10D1	Stub type	Dense	10	1	HP12X53	W24X84
S10D2			10	2	HP12X53	W24X84
S20D1			20	1	HP13X73	W40X167
S20D2			20	2	HP13X73	W40X167
S30D1			30	1	HP14X117	W40X262
S30D2			30	2	HP16X121	W44X262
S10L1		Loose	10	1	HP12X53	W24X76
S10L2			10	2	HP13X60	W24X76
S20L1			20	1	HP14X89	W40X149
S20L2			20	2	HP13X73	W40X149
S30L1			30	1	HP16X141	W44X262
S30L2			30	2	HP16X121	W44X262

5.1 Input ground motions

Ground motions are selected according to FEMA-P695 specifications [10]. The methodology provides 22 pairs of preselected far-field record set from sites farther than 10 km from fault rupture (see Table 3). The record set does not include the vertical component of ground motions. In addition, since the analysis models were 2D, only the horizontal component with higher PGA was used in nonlinear analyses. There are two steps of scaling in this methodology. First, the set of ground motions are normalized with respect to the median PGV of record set. Thus, each ground motion record should be multiplied by the factor NM_i calculated as:

$$NM_i = \frac{\text{Median}(PGV_i)}{PGV_i} \quad (7)$$

Table 3. Far-Field ground motions [10]

ID	Name Station	Year	Magnitude	Component (°)
1	Northridge	1994	6.7	MUL279
2	Beverly Hills – Mulhol	1994	6.7	LOS270
3	Canyon Country – WLC	1999	7.1	BOL090
4	Duzce, Turkey	1999	7.1	HEC090
5	Bolu	1979	6.5	DLT352
6	Hector Mine	1979	6.5	E11230
7	Hector	1995	6.9	NIS090
8	Imperial Valley	1995	6.9	SHI090
9	Delta	1999	7.5	DZC270
10	Imperial Valley	1999	7.5	ARE000
11	El Centro Array #11	1992	7.3	YER270
12	Kobe, Japan	1992	7.3	CLW-TR
13	Nishi-Akashi	1989	6.9	CAP000
14	Kobe, Japan	1989	6.9	G03000
15	Shin-Osaka	1990	7.4	ABBAR--L
16	Kocaeli, Turkey	1987	6.5	ICC000
17	Duzce	1987	6.5	POE270
18	Kocaeli, Turkey	1992	7.0	*
19	Arcelik	1999	7.6	N
20	Landers	1999	7.6	N
21	Yermo Fire Station	1971	6.6	PEL090
22	Landers	1976	6.5	TMZ000
	Coolwater			
	Loma Prieta			
	Capitola			
	Loma Prieta			
	Gilroy Array #3			
	Manjil, Iran			
	Abbar			
	Superstition Hills			
	El Centro Imp. Co.			
	Superstition Hills			
	Poe Road (temp)			
	Cape Mendocino			
	Rio Dell Overpass			
	Chi-Chi, Taiwan			
	CHY101			
	Chi-Chi, Taiwan			
	TCU045			
	San Fernando			
	LA – Hollywood Stor			
	Friuli, Italy			
	Tolmezo			

*This record has been removed from PEER database.

where, $Median(PGV_i)$ is the median of peak ground velocities of all ground motions and PGV_i is the peak ground velocity of each ground motion record. This phase is to eliminate unwarranted variability among the records because of the inherent variances in distance to source, source type, event magnitude and site conditions without removing the entire record-to-record variability. In the second scaling phase, normalized ground motions should be collectively scaled to a specified ground motion intensity in a way that the median spectral acceleration of record set matches the spectral acceleration at the fundamental period of T of analyzed archetype [10]. Fig. 9 shows a sample of the scaled spectrum.

5.2 Calculation of median collapse intensity and CMR

While incremental dynamic analysis (IDA) is used to show the collapse assessment process, methodology needs the median collapse intensity (\hat{S}_{CT}) calculated with fewer nonlinear analyses than is necessary to develop the full IDA curve. \hat{S}_{CT} could be obtained by scaling all the records to MCE intensity (S_{MT}) by raising the intensity of scaled records until over one half of ground motion records cause collapse. The least intensity at which one half of records cause collapse is the median collapse intensity. MCE intensity is gained from the response spectrum of MCE ground motions at T (fundamental period). The ratio between MCE intensity and median collapse intensity is the collapse margin ratio (CMR) [10].

$$CMR = \frac{\hat{S}_{CT}}{S_{MT}} \quad (8)$$

5.3 Pile collapse criteria

As mentioned before, very few experimental studies covering the collapse of steel H-pile sections about their weak axes have been performed and can not be generalized for all types of steel H-pile sections. As a safe and reasonable assumption, it is considered in this research that piles behavior and performance levels can be measured using ASCE 41-13 [15] criteria for steel columns in moment frames. This is not far from reality, because the piles under cyclic loading in their upper portions where plastic hinges develop tend to loosen the adjacent soil support. Thus, it is conservative to assume a behavior like steel columns.

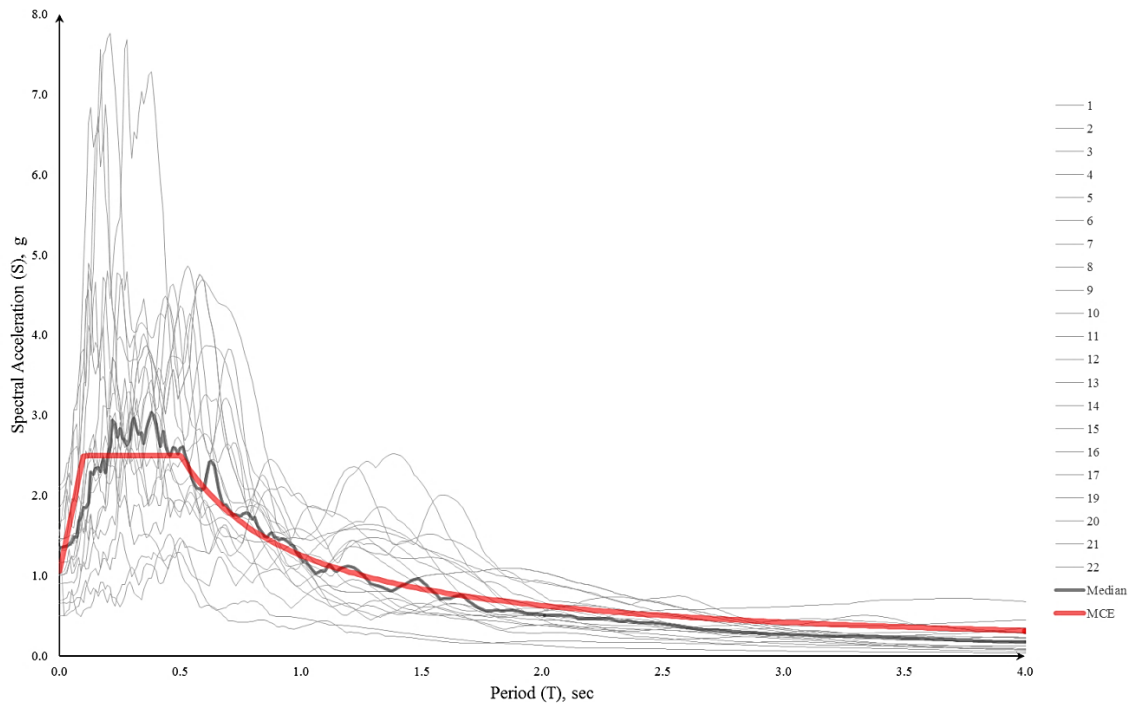


Fig. 9. Ground motions spectra scaled to MCE for W20D1 with $T=0.20$ s

5.4 Calculation of spectral shape factor, SSF, and ACMR

According to Baker and Cornell [16], the rare ground motions in the western United States corresponded to MCE have a distinct spectral shape which are different from the spectral shape of design spectrum applied for the structural design in ASCE/SEI 7.

To remove this conservative bias, a simplified spectral shape factor, SSF, which depends on the fundamental period (T) and period based ductility (μ_T), are used to adjust collapse margin ratios as [10]:

$$ACMR = SSF \times CMR \quad (9)$$

SSF is the spectral shape factor and is calculated by Eq. (12).

5.5 Fundamental period of archetypes

To obtain the fundamental period of archetypes, modal analyses were performed and the period of predominant longitudinal mode of vibration (with the highest mass contribution) was selected as the fundamental period and is reported in Table 4.

Table 4. Ground motion and structural behavior parameters

ID	T (s)	μ	$\bar{\varepsilon}(T)_{records}$	$\bar{\varepsilon}_0$	β_1	SSF	CMR	ACMR
W10D1	0.19	1.60	0.60	1.50	0.11	1.11	2.15	2.38
W10D2	0.24	2.20	0.60	1.50	0.15	1.15	2.03	2.33
W20D1	0.20	1.50	0.60	1.50	0.10	1.10	1.80	1.98
W20D2	0.29	1.50	0.60	1.50	0.10	1.10	1.73	1.90
W30D1	0.23	1.60	0.60	1.50	0.11	1.11	2.11	2.34
W30D2	0.38	3.20	0.60	1.50	0.19	1.19	1.90	2.26
W10L1	0.30	1.90	0.60	1.50	0.13	1.13	1.64	1.85
W10L2	0.38	2.90	0.60	1.50	0.18	1.18	1.61	1.90
W20L1	0.30	2.00	0.60	1.50	0.14	1.13	1.57	1.78
W20L2	0.43	1.20	0.60	1.50	0.07	1.07	2.10	2.24
W30L1	0.33	1.60	0.60	1.50	0.11	1.11	1.70	1.88
W30L2	0.54	1.40	0.58	1.50	0.10	1.09	1.50	1.64
S10D1	0.11	1.70	0.60	1.50	0.12	1.11	2.95	3.29
S10D2	0.16	1.50	0.60	1.50	0.10	1.10	3.08	3.38
S20D1	0.12	2.10	0.60	1.50	0.15	1.14	3.29	3.75
S20D2	0.22	1.60	0.60	1.50	0.11	1.11	3.36	3.72
S30D1	0.14	2.00	0.60	1.50	0.14	1.13	3.39	3.85
S30D2	0.35	1.70	0.60	1.50	0.12	1.11	3.11	3.47
S10L1	0.17	2.30	0.60	1.50	0.16	1.15	2.51	2.89
S10L2	0.23	2.10	0.60	1.50	0.15	1.14	2.62	2.99
S20L1	0.18	2.60	0.60	1.50	0.17	1.17	2.82	3.29
S20L2	0.29	2.10	0.60	1.50	0.15	1.14	1.90	2.17
S30L1	0.20	3.60	0.60	1.50	0.21	1.21	2.48	2.99
S30L2	0.39	2.50	0.60	1.50	0.17	1.16	1.99	2.31

5.6 Ductility, μ

Nonlinear static analyses were conducted on archetypes in order to calculate their ductility. Control node for pushover analyses was chosen at the middle of the deck. Since the source of nonlinearity is located at the top part of piles and there is no other source of nonlinearity in the models, then the structure would not face instability or large loss of stiffness after formation of plastic hinges. In this case, ductility was calculated based on piles pushover diagram as:

$$\mu = \frac{\Delta_u^{Collapse}}{\Delta_y^{eff.yield}} \quad (10)$$

in which, $\Delta_u^{Collapse}$ is the control node displacement corresponding to the first collapse plastic rotation occurrence in piles and $\Delta_y^{eff.yield}$ is displacement of control node corresponding to first yield rotation in piles. Calculated ductility values are listed in Table 4.

5.7 Epsilon parameter

The epsilon (ε) ground motion parameter is defined as an indicator of spectral shape. This parameter is a difference measurement between the spectral acceleration of a record and the mean of a ground motion prediction equation at a given period [16]. With regards to the equation proposed for Far-Field ground motions set:

$$\bar{\varepsilon}(T)_{records} = (0.6)(1.5 - T) \leq 0.6 \quad (11)$$

where T is the fundamental free vibration period of structure. Value of $\bar{\varepsilon}(T)_{records}$ is calculated for each archetype and reported in Table 4.

5.8 β_1 and SSF parameters

SSF factor is calculated as:

$$SSF = \exp[\beta_1(\bar{\varepsilon}_0(T) - \bar{\varepsilon}(T)_{records})] \quad (12)$$

where, β_1 is based on the building inelastic deformation capacity and $\bar{\varepsilon}_0$ is based on SDC equivalent to 1.0 for SDC B/C, 1.5 for SDC D, and 1.2 for SDC E. In this research, $\bar{\varepsilon}_0$ is considered to be 1.50, and β_1 is applied to quantify how drastically the spectral shape (ε) impacts the collapse capacity as below:

$$\beta_1 = (0.14)(\mu - 1)^{0.42} \leq 0.32 \quad (13)$$

5.9 Acceptable values of $ACMR$

Acceptable values of $ACMR$ are based on total system collapse uncertainty (β_{TOT}) and on the established variables of acceptable collapse probabilities assumed that the distribution of collapse level spectral intensities is lognormal with a median value (\hat{S}_{CT}) and a lognormal standard deviation that is equivalent to total system collapse uncertainty (β_{TOT}).

$$ACMR_{acceptable} = \frac{1}{e^{(\phi^{-1}(P_{Collapse}) \times \beta_{TOT})}} \quad (14)$$

Acceptable performance is achieved when [10]:

Average $ACMR$ value for all archetypes in a performance group exceeds $ACMR_{10\%}$:

$$\overline{ACMR}_i \geq ACMR_{10\%} = 2.30 \quad (15)$$

the individual variable of $ACMR$ for every index archetype exceeds $ACMR_{20\%}$:

$$ACMR_i \geq ACMR_{20\%} = 1.73 \quad (16)$$

It means that the collapse probability for MCE ground motions is about 10%, or lower averagely during the archetypes group and the collapse probability for MCE ground motions is about 20% or lower for all index archetype into the group.

5.10 Total system collapse uncertainty

Majority of uncertainty sources are contributed to variability. Larger variability in the overall collapse prediction necessitates larger collapse margins to confined the collapse probability to a confirmed level at MCE intensity. Evaluating all the significant uncertainty sources in collapse response and for incorporating their impact in the collapse assessment procedure is important. The following uncertainty sources are taken in the collapse assessment procedure:

1) Record-to-Record Uncertainty (RTR) is because of the variability of index archetypes response to altered ground motion records as below [10]:

$$\beta_{RTR} = 0.1 + 0.1\mu_T \leq 0.4 \quad (17)$$

That will be $\beta_{RTR} = 0.30$ on average of all archetypes.

2) Design Requirements Uncertainty (DR) is associated to the robustness and completeness of design requirements, and to the extent provided for safeguards against unanticipated failure mode(s). This ranking has been defined by a range from “(A) Superior” to “(D) Poor” that is shown in Ref. [10] tables. Regarding the use of AASHTO LRFD for design of archetypes, there is a level of confidence in design specifications, but because of few experimental studies related to IAB’s seismic behavior, $\beta_{DR} = 0.2$ equivalent to (B) good quality has been chosen.

3) Test Data Uncertainty (TD) is associated to the robustness and completeness of the data applied to identify the system and it can be quantitatively chosen from Ref. [10] tables. Considering the low experimental researches on connections, soil-pile-structure interaction and seismic loadings of IABs, $\beta_{TD} = 0.5$ equivalent to (D) poor quality has been selected for this parameter.

4) Modeling Uncertainty (MDL) is associated to how properly index archetype models show the full range of structural response features and to the associated design parameters of archetype design space and how properly the analysis model(s) captures the structural collapse behavior by non-simulated or direct simulation of component checks. Bridges have been modeled in one or two spans (wall and stub type abutment) 10, 20 and 30 meter spans and two types of loose and dense soil. Thus, soil-pile-structure interaction has been taken into account beside non-linear modeling of piles using fiber elements, however, with regarding 2D modeling and ignoring material deterioration. $\beta_{MDL} = 0.2$ equivalent to (B) good quality has been chosen for this parameter.

Total system collapse uncertainty is calculated as:

$$\beta_{TOT} = \sqrt{\beta_{RTR}^2 + \beta_{DR}^2 + \beta_{TD}^2 + \beta_{MDL}^2} = 0.65 \quad (18)$$

6. Results and discussions

In this chapter, results are evaluated and discussed. As mentioned in section 5.9, *ACMR* average values for every performance group and *ACMR* values for individual index archetype should be above the acceptable limit. Here, the results in terms of all archetypes as one performance group are discussed, then breaking up the archetypes based on some specific characters into some new performance groups are examined.

If all archetypes are put into one performance group, then $\overline{ACMR}_i = 2.61$ which is above $ACMR_{10\%} = 2.30$. \overline{ACMR}_i for all archetypes is above $ACMR_{20\%} = 1.73$, except W30L2 that has an *ACMR* value of 1.64 that is below the acceptable value. This means that R factor of 3.5 is suitable for IABs in the longitudinal direction with a marginal error.

Another approach in evaluation of *ACMR* is making performance groups as shown in Fig. 10. Accordingly, all performance groups have average *ACMR* above the allowable *ACMR* based on 20% collapse probability, except the performance group of IABs with wall type abutment (7 m height). This observation shows that the *ACMR* of all performance groups are only slightly higher than the acceptable *ACMR*, except for wall type abutment bridges, then it could be concluded that 3.5 could be a good and optimized response modification factor for IABs in the longitudinal direction.

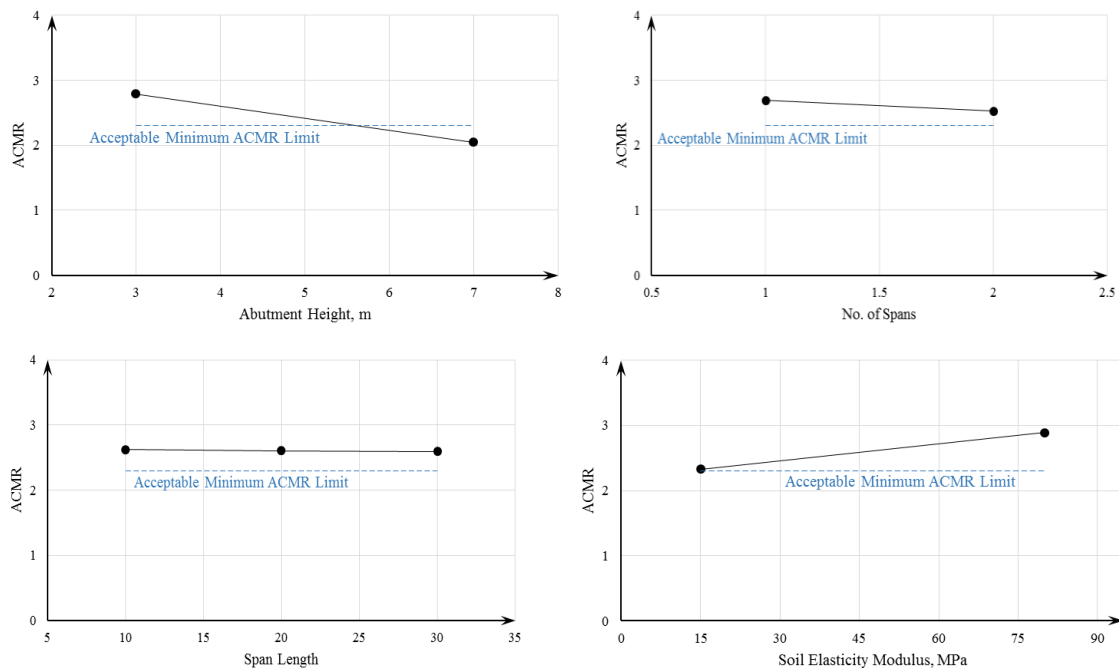


Fig. 10. The *ACMR* of performance groups compared to the acceptable minimum *ACMR* limit. (a) performance groups separated based on abutment height (b) performance groups separated based on number of spans (c) performance groups separated based on span length (d) performance groups separated based on soil elasticity modulus

Another approach in evaluation of *ACMR* is making performance groups as shown in Fig. 11. Thus, all performance groups have an average *ACMR* above the allowable *ACMR* based on 20% collapse probability, except the performance group of IABs with wall type abutment with height of 7 meters with either loose or dense soil type and any number of spans.

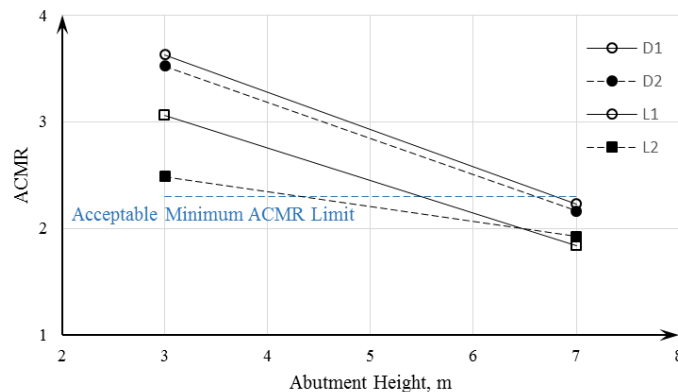


Fig. 11. values of *ACMR* vs. Abutment height considering performance groups separated based on soil type, no. of spans and abutment height

As a result, the response modification factor 3.5 is acceptable for IABs in the longitudinal direction for all archetypes considered with the following reservations:

- 1) IABs with an abutment height more than 6.5 meters with dense soil behind abutment.
- 2) IABs with an abutment height more than 5 meters with loose soil behind abutment.

From the results, it is observed that:

- 1) The collapse capacity of IABs with stub type abutment is 55% more than the IABs with wall type abutments.
- 2) The collapse capacity of IABs with dense soil behind abutment is 24% more than those with loose soil behind abutment.
- 3) The collapse capacity of single span IABs is more than multiple span IABs.
- 4) The collapse capacity of IABs with 10 meters span is 0.8% more than the IABs with 20 meters span, and the collapse capacity of IABs with 20 meters span is 0.4% more than the IABs with 30 meters span.

From the observations mentioned above, it is seen that the height of abutment is the most important factor in the collapse capacity of IABs. The second most important parameter is the type of soil behind abutments. The least effective parameter in the collapse capacity of IABs is the number of spans and span length.

7. Conclusions

Based on the extensive analyses prescribed in FEMA P695 [10] the *R* factor in the longitudinal direction of common non-skewed IABs were determined. It was concluded that the response modification factor $R = 3.5$ is appropriate for design purposes. However, for IABs with abutment height above 6.5 m with dense backfill this value can be unsafe.

It is recommended by the authors that for IABs in seismic regions designers should avoid using loose soils behind abutments. Loose soils cause the collapse capacity of IABs to decline, especially those having abutment wall heights above 5 meters. Otherwise, in such cases, a lower response modification factor should be utilized.

It was also observed that stub type abutments had a better seismic performance than wall type abutments.

It was shown that the seismic performance of IABs were less sensitive to the number and length of spans within the range considered.

8. References

- [1] Burke Jr MP. Integral and semi-integral bridges. 1st ed. John Wiley & Sons; 2009.
- [2] Erhan S, Dicleli M. Effect of dynamic soil-bridge interaction modeling assumptions on the calculated seismic response of integral bridges. *Soil Dyn Earthq Eng*. 2014;66:42–55. doi:10.1016/j.soildyn.2014.06.033.
- [3] Civjan S, Bonczar C, Brena S. Integral abutment bridge behavior: Parametric analysis of a Massachusetts bridge. *Journal of Bridge Engineering*. 2007;12:64–71. doi:10.1061/(ASCE)1084-0702(2007)12:1(64).
- [4] Spyarakos C, Loannidis G. Seismic behavior of a post-tensioned integral bridge including soil-structure interaction (SSI). *Soil Dyn Earthq Eng*. 2003;23:53–63. doi:10.1016/S0267-7261(02)00150-1.

- [5] Itani AM, Pekcan G. Seismic performance of steel plate girder bridges with integral abutments. 2011.
- [6] Maleki S, Mahjoubi S. A new approach for estimating the seismic soil pressure on retaining walls. *Sci. Iran. Trans. Civ. Eng.* 2010;17(4): 273-284.
- [7] Mahjoubi S, Maleki S. Finite element modelling and seismic behaviour of integral abutment bridges considering soil-structure interaction. *Eur J Environ Civ Eng.* 2020;24(6):767-786.
- [8] Burdette EG, Ingram EE, Tidwell, JB, Goodpasture DW, Deatherage JH, Howard SC. Behavior of integral abutments supported by steel H-piles. *Transportation Research Record.* 2004. <https://doi.org/10.3141/1892-03>.
- [9] AASHTO (American Association of State Highway and Transportation Officials). LRFD bridge design specifications. 8th Edition. Washington DC, U.S.A. 2017.
- [10] FEMA P695, Quantification of building seismic performance factors. Federal Emergency Management Agency, Washington DC, U.S.A. June 2009.
- [11] Computers and Structures, Inc. SAP2000, Version 20, Integrated Structural Analysis and Design Software. Berkeley, CA, 2018.
- [12] Faraji S, Ting JM, Crovo DS, Ernst H. Nonlinear analysis of integral bridges: Finite-element model. *J Geotech Geoenvironmental Eng.* 2001;127:454–461.
- [13] Richards R. Huang C, Fishman KL. Seismic earth pressure on retaining structures. *J Geotech Geoenviron Eng.* 1999;125:771–778.
- [14] American Petroleum Institute (API). Recommended practice for planning, designing and constructing fixed offshore platforms-working stress design. 1st edition. API Recommended Practice 2A-WSD(RP2A-WSD). Dallas. 1993.
- [15] Seismic evaluation and retrofit of existing buildings(ASCE/SEI 41-13). American Society of Civil Engineers(ASCE). 2013.
- [16] Baker JW, Cornell CA. A vector-valued ground motion intensity measure consisting of spectral acceleration and epsilon. *Earthq Eng Struct Dyn.* 2005;1193–1217. doi:10.1002/eqe.474.

Production of Topology-optimized Structural Nodes

Mdaras Aras Ansari, *Department of Civil Engineering, Raajdhani Engineering College, Bhubaneswar, mdarasansari2578@gmail.com*

Sourav Debasish, *Department of Civil Engineering, Aryan Institute of Engineering & Technology, Bhubaneswar, souravdebasish1@gmail.com*

Pili Kumari Sahoo, *Department of Mechanical Engineering, Aryan Institute of Engineering & Technology, Bhubaneswar, p.kumari4@gmail.com*

Jagruti Swain, *Department of Civil Engineering, Capital Engineering College, Bhubaneswar, jagrutiswain26@yahoo.co.in*

Abstract: The need to create a stress-optimized structural node with optimum stability is frequently combined with the drive to reduce production costs and use material efficiently. Topology-optimized structures that are complicated, three-dimensional free-form structures are only partially suitable for conventional manufacture. By using arc welding procedures, wire arc additive manufacturing (WAAM) provides a cost-effective and flexible option for the individual creation of complicated metallic components. Due to build-up rates of up to 5 kg/h, gas metal arc welding (GMAW) is particularly well suited to producing large-volume, load-bearing structures. In order to develop topology-optimized structural nodes, this work studied the generation of strength and stiffness suited support structures using the numerical simulation method of topology-optimisation. The generated node is then converted into a robot route using CAD/CAM software and fabricated using WAAM and the GMAW process from the filler material G4Si1. The path planning and therefore the manufacturability of the topology-optimised supporting structure nodes is tested and confirmed using a sample structure built of the welding filler material G4Si1 based on the WAAM process boundary conditions. Due to variations in t8/5 timings, an improvement in mechanical properties could be realised depending on path planning.

Keywords: WAAM; Wire arc; GMAW; Gas metal arc welding; Wire-based; Arc; Additive manufacturing; Topology-optimisation.

1. Introduction

Stress-optimised structures, which have been designed based on nature (bionics), are becoming increasingly important. Strength and stiffness-adapted supporting structures as well as iconic architecture and individual aesthetics can be realised. The motivation of a lightweight node structure with maximum stability is often coupled with the desire for minimal and adapted material use and low manufacturing costs.

Over the last decades, topology-optimisation has established itself in various engineering disciplines as a robust tool for optimising material distribution within a given design space [1-5]. Topology-optimisation typically results in complex and abstract structures with undercuts and cavities. These structures cannot be produced with conventional manufacturing methods, or only to a limited extent. Therefore, a manufacturing technology for load-bearing structures made of metals is required with which these topology-optimised structures can be produced. Additive manufacturing (AM) processes offer the necessary freedom of design to produce highly complex components. This paper presents a production and process strategy view regarding a topology-optimised structural node, which was previously published in [6].

Additive manufacturing describes the layered construction of three-dimensional objects by the targeted application or joining of wire, powder or foil materials made of metal or plastic [7]. Which allows to produce complex geometries from a batch size of 1 with a resource-efficient material application.

Up to now, the production of complex metallic 3D components has mainly been realised by laser-based processes. The processes used for this purpose are Direct Energy Deposition (DED) and powder bed fusion by laser (PBF). The powder bed process in particular is severely limited in productivity for larger components due to the achievable layer thicknesses of a few tenths of a millimetre and a low build-up rate of approx. 1-10 cm³/h. This results in long production times and limited component dimensions [8-10]. The laser-based DED process offers build-up rates of approx. 300 cm³/h-700 cm³/h and layer thicknesses of up to 1.5 mm, which results in a significantly higher productivity than PBF processes [11].

Galjaard et. al. carried out the topology-optimisation of a structural node for a tensegrity structure, which is only stressed in tension. After the optimisation, the node was produced additively in a Laser PBF process. For

reasons of production time and costs, the component was manufactured in 40% of its original size. The authors estimate that the production in original size would have taken about 15 days with today's means, which in combination with the high powder costs renders the component uneconomical to produce [12].

Wire arc additive manufacturing (WAAM) can achieve significantly higher build-up rates, which has made it the focus of attention in recent years [13]. Figure 1 shows an example of the WAAM process chain, taking topology-optimisation into account. WAAM can utilise gas metal arc welding (GMAW), the tungsten inert gas welding (TIG), as well as plasma processes during additive manufacturing. In these processes, a layer-by-layer structure is realised by feeding and melting a wire-shaped filler material. This process enables the generation of undercuts, cavities for lightweight construction applications or any cooling channels running in the component which cannot be produced or can only be produced to a limited extent using conventional methods (e.g. [14, 15]). The GMAW process is particularly characterised by its cost-effective and robust process technology for additive manufacturing. Due to the local inert gas cover, there are no restrictions for the workspace size. In addition, the coaxial supply of filler material makes it possible to work independent of direction. Depending on the material and component geometry, the WAAM process using GMAW welding technology allows deposition rates of approx. 5 kg/h [16, 17].

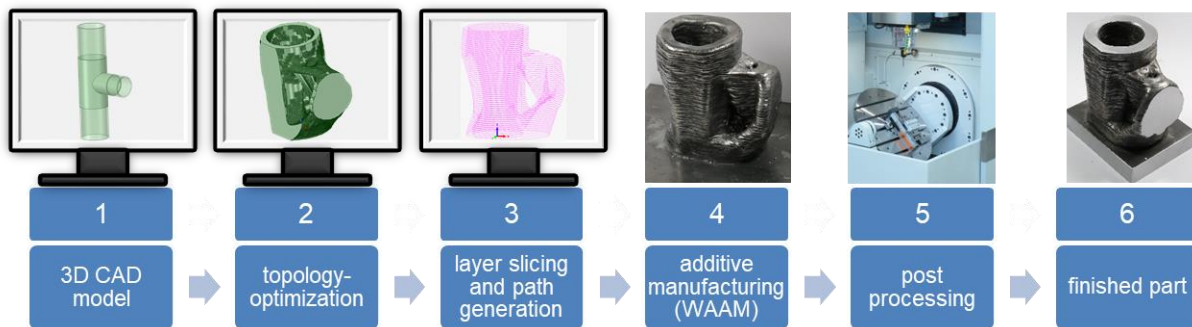


Figure 1. Process chain of additive manufacturing using WAAM according to [12].

2. Experimental methods of additive manufacturing

The welding tests and additive manufacturing of the topology-optimised structural nodes were carried out using an GMAW welding power source "EWM alpha Q 552 Expert 2.0 puls MM". The welding tests were carried out with the energy-reduced short arc technology "coldArc". A 6-axis industrial articulated arm robot "Kuka KR150-2" was used to ensure reproducible torch movement.

As base material (substrate) S355J2+N with a thickness of 20 mm was used. The additive structure (Figure 2) was realised with the low-alloyed solid wire electrode DIN EN ISO 14341-A-G4Si1. To determine suitable welding parameters, preliminary tests were carried out on wall structures, which were 300 mm long and 160 mm in height, with different energy inputs, with widths of one, two or three weld beads (Figure 2 right) and varying overlaps. In addition, a parameter set with a meandering path planning was tested. Tensile samples were taken from additive manufactured wall structures along and across the build-up direction. In addition, the $t_{8/5}$ time was measured using a thermocouple type C. The approach of using parallel weld beads to increase the structure width comes from the field of filling strategies for volume bodies. Usually, a meander path or an increase in the material discharge is used to widen the weld bead. For surface filling in solids, meander paths are sometimes used, but also contour-parallel and line filling. In analogy to this, a meandering path, parallel welding beads and an increase in material output are now to be used to create wide wall structures. The knowledge gained can in turn be transferred to more complex bodies. The underlying idea for using the welding beads is to reduce the heat input at each point in time in order to reduce the heat build-up.

Un- and low alloyed steel is commonly characterized during welding by its $t_{8/5}$ time according to DIN EN 1011-2:2001-05 [18]. It describes the cooling time of the weld bead and the heat effected zone (HAZ) in a temperature interval between 800°C and 500°C. This temperature range is decisive for the mechanical properties due to the phase transformation from γ - to α -phase.

The CAD/CAM program DCAM 2018 from SKM was used to slice the 3D component, i.e., to break it down into layers, which makes sequential 2D contour generation possible. The path planning was created from this. Finally, an integrated post-processor is used to convert the data into the Kuka programming language.

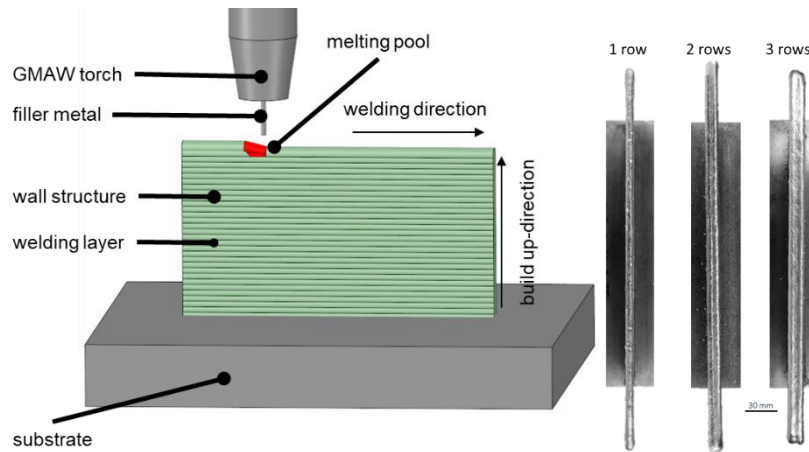


Figure 2. additive manufacturing of a wall structure (left: schematic of WAAM process; right: wall structures with one, two and three adjacent rows)

3. Results and discussion

In preliminary parameter studies three parameter sets found to be suitable for additive manufacturing of G4Si1 in general and were investigated further to ensure the mechanical properties of thick structures are suitable to generate loadbearing parts. Thereby $t_{8/5}$ time and energy input were related to each other.

Different wall thicknesses were tested throughout the course of this investigation with varying energy inputs per unit length at 4 kJ/cm, 6 kJ/cm and 8 kJ/cm. The thickness was varied between 6 mm for one row, to up to 12 mm for three rows and the meandering wall structure.

The mechanical properties of the weld metal are primarily determined by its chemical composition and the rate at which it cools from the liquid phase. Welding temperature cycles are generally characterised by the time required to pass through a certain temperature interval. The cooling time from 800°C to 500°C ($t_{8/5}$ time) has proven itself in welding technology to characterise the mechanical-technological properties of the weld metal [19].

The $t_{8/5}$ times were measured in the middle of the wall structure at the 150 mm length mark and at a height of 80 mm (40th layer). This position was chosen because a quasi-static condition for the cooling time occurs after 20 deposited layers according to Henckell et. al. [20], and the chosen position is well above this boundary condition. The aim was to achieve the highest possible significance of the values. Due to the periodic heating, there are several $t_{8/5}$ times for each welding layer. In these tests, the last $t_{8/5}$ cycle was used for evaluation, as this is the last complete cycle of the γ - to α - transformation.

It can be seen from the plots that the $t_{8/5}$ times for G4Si1 (Figure 3) increase with increasing energy input per unit length. Furthermore, the $t_{8/5}$ times decrease with increasing number of rows. In order to be able to evaluate additive manufacturing using the GMAW process for samples generated in multiple rows, the cooling time ($t_{8/5}$ time) is considered for the different numbers of rows. Figure 3 shows that the $t_{8/5}$ time decreases with increasing number of rows and is halved in the comparison of single-row generated samples to three-row generated samples at a line energy of 4 kJ/cm. The reduction in $t_{8/5}$ time is evident for both materials and all line energies used.

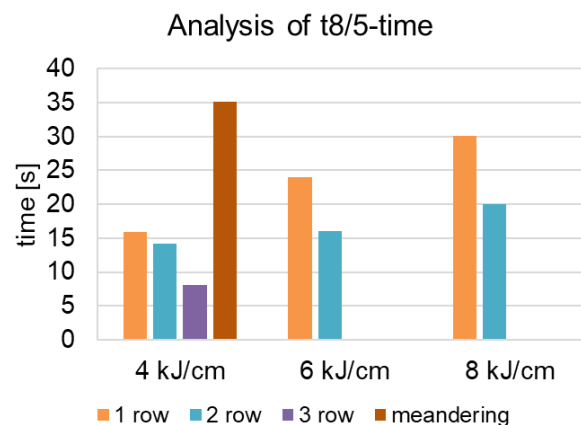


Figure 3. left: $t_{8/5}$ time compared to energy input and number of rows

The fastest cooling time ($t_{8/5}$ time) was measured at 4 kJ/cm line energy and three-row build-up with 8 s. The slowest cooling time ($t_{8/5}$ time) was recorded with 4 kJ/cm line energy and meandering generation of the wall structure.

To evaluate the tensile tests, the first step was to examine the mechanical properties of the specimens generated in welding direction and in build-up direction from the point of view of possible dependencies.

The following Figure 4 shows the tensile strength and the yield strength for G4Si1 as a function of the specimen orientation with a number of specimens of $n=3$. Only very small deviations of the tensile strength and yield strength for different specimen orientations are shown there. The examination of the respective test results for the tensile strength do not reveal any significant deviations with regard to the specimens generated in welding direction and in build-up direction. In this respect, the present test results do not allow any conclusions to be drawn about different mechanical properties in the different directions considered for this material.

Figure 4 illustrates the resulting tensile and yield strength with their corresponding energies. The tensile strength in build-up direction and in welding direction are within margin of error of each other, which leads to the conclusion that the mechanical properties are nearly homogeneous on both directions. It is evident that the mechanical strength increases with decreasing energy input and increasing number of rows (Figure 4). Moreover, the meandering welding path achieved the lowest overall strength of all tested parameter sets. To achieve at least a yield strength as high as the value in the datasheet of G4Si1 (460MPa), it is necessary to use a low energy parameter set and use a building strategy with at least two rows of thickness.

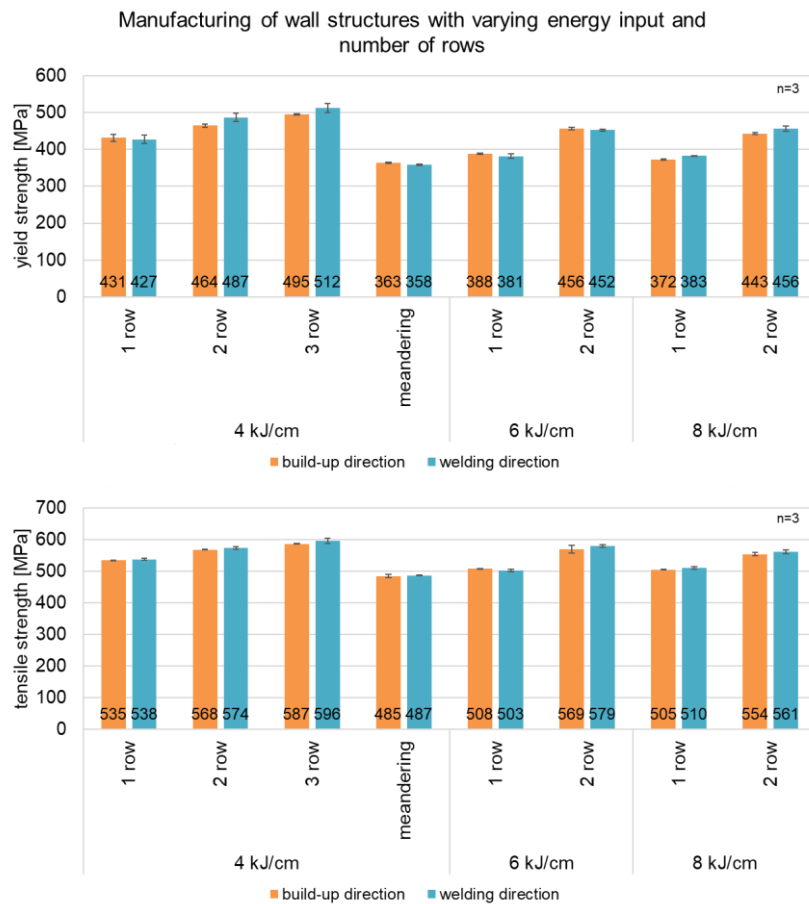


Figure 4. tensile and yield strength in build-up and welding direction compared to energy input and path planning strategy

Furthermore, a lower line energy and a higher number of rows lead to better mechanical properties, i.e., higher strength. This is due to the lower $t_{8/5}$ times for lower line energies and a higher number of rows. This can be clearly seen in Figure 5 using a wall thickness of 9 mm and 12 mm as a reference for G4Si1. The results show that the use of a parallel with two rows build up approach for a thickness of 9 mm will increase the tensile strength by more than 12% and the yield strength by nearly 25% in comparison to a generation via one weld bead. The results for a structure width of 12 mm are comparable to the smaller structure width. Therefore, a parallel build up of three welding beads with lower energy input is more suitable to achieve better mechanical properties than the

datasheet states. The tensile strength for a build up with three parallel rows could be increased by nearly 6% compared to two parallel rows and nearly by 22% with meandering. Moreover, the yield strength for three rows is 12% higher than for two rows and nearly 40% higher than a meandering path planning.

A structural design shows better mechanical-technological properties for the same wall thicknesses when a low line energy is used in a multi-row design.

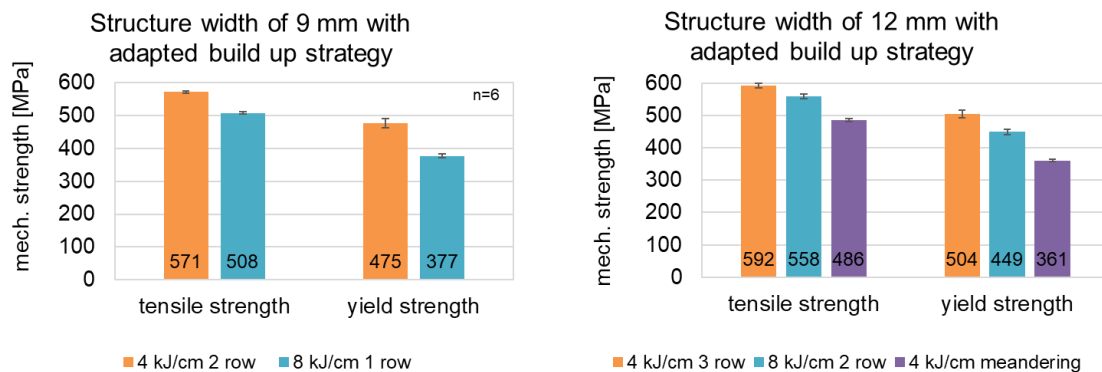


Figure 5. Comparison of mechanical strength for varying energy inputs and path planning strategies for two different widths

4. Production of topology-optimised node geometry

After finishing the evaluation of the mechanical properties of G4Si1 in additive manufacturing it could be ensured, that the minimal needed yield strength of approx. 420 MPa to generate a structural node as calculated by Reimann et. al. could be achieved [6]. The production of a complex structure using WAAM often requires reworking in CAD, as it is only possible to a limited extent to produce horizontal overhangs or structures with a deviation of more than 40° from the vertical in a layer-by-layer, 3-axis design. The reason for this is that, unlike other additive manufacturing processes, the WAAM process does not use supporting structures. Therefore, the geometry was reworked in the ANSYS SpaceClaim Design Modeler to ensure manufacturability. Figure 6 shows the original geometry. The red marked areas had to be adjusted to ensure manufacturability. The horizontal overhangs of the structure were removed, and the overhang angle of the connection area was slightly adjusted to achieve an angle of 40° to the vertical.

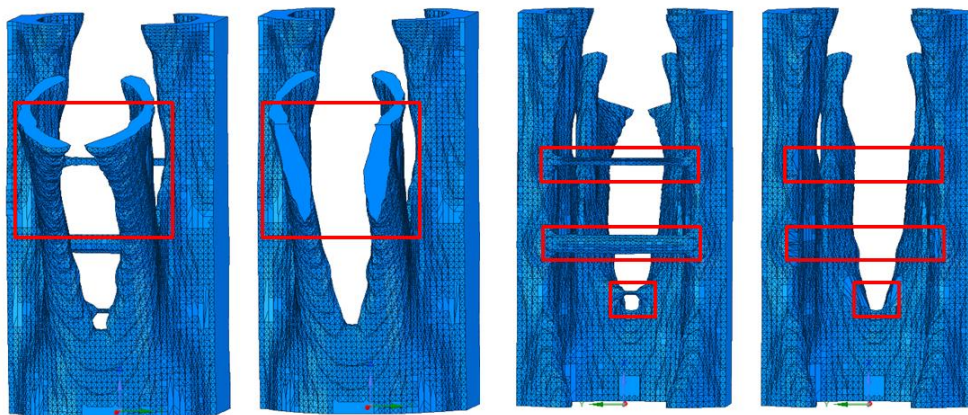


Figure 6. Improving the manufacturability of the 30° oblique joint.

As stated, before it was possible to achieve the needed mechanical properties to be able to manufacture a structural node with the needed properties. Considering the approached 420 MPa three different parameter sets could be used (Figure 5). The parameter with 4 kJ/cm and at least 3 adjacent rows was used for the production of the structural node in order to have a sufficient reserve between the resulting mechanical properties and the needed properties to ensure the stability and longevity of the structural node. Using this parameter set 208 layers of 1.8 mm each were needed to achieve a resulting overall height of approx. 375 mm. Figure 7 shows the path planning for the component and the top welding layer. It can be seen that the top layer has three welding paths with contour-parallel filling strategy, which results in six adjacent welding beads. The component was produced with a contour-

parallel filling strategy to improve the connection between the welding beads inside the component. This should result in slightly better mechanical properties than presented in the tensile tests, because of a higher wall thickness, which might add up to an even better safety factor.

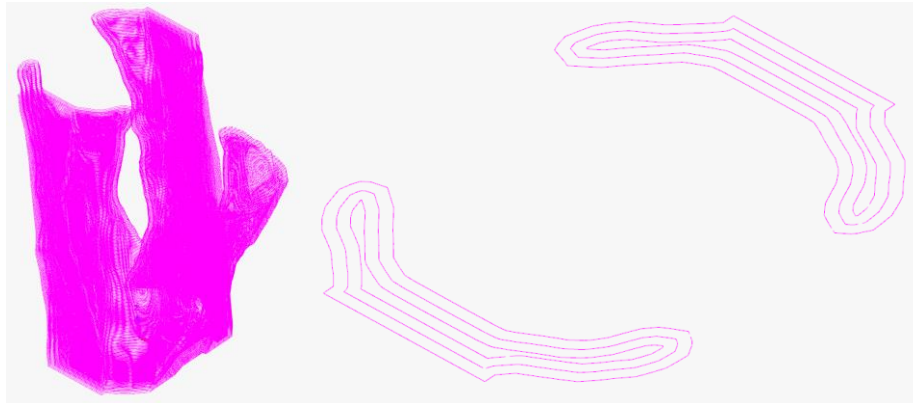


Figure 7. Path planning (left: entire component; right: top welding layer)

The component was produced on a substrate plate using the GMAW welding process. The assembly was carried out in a layer by layer process and an interpass temperature of 100°C was maintained. Figure 8 shows the additively manufactured, topology-optimised component which was cleaned and not yet removed from the substrate.



Figure 8. Additively manufactured, topology-optimized 30° oblique joint.

5. Conclusion and outlook

This study has shown that the build-up strategy is as important as the overall welding parameter set to achieve the desired mechanical properties for additively manufactured structures. Therefore, a parameter set with low energy input and a build-up strategy with adjacent rows of welding beads rather than meandering should be used for the additive manufacturing, if possible, due to the increasing tensile and yield strength. The increase in mechanical strength can be traced back to a decreasing $t_{8/5}$ time for wider structures, due to a better capability to transfer heat away from the last welded layer.

Despite the high degree of design freedom in additive manufacturing, it became apparent during the production of the node that reworking of the design is absolutely necessary, since today's boundary conditions of topology-optimisation do not offer the possibility of defining limiting angles in advance or avoiding horizontal overhangs. One way of counteracting this is to use a 5-axis machining strategy in which the welding torch can be moved in x, y and z directions and the component can be positioned under the welding torch using a turn-tilt table. This allows to avoid constrained positions and to create arbitrary angular positions and even overhangs, as the welding torch itself is always in a neutral position.

The use of additive manufacturing makes it possible to create geometries which cannot be produced or can only be produced to a limited extent using conventional methods, which can result in a significant added value in production. However, when calculating and using additive manufacturing processes, it must be considered that reworking is necessary for components, especially for connecting and functional surfaces.

6. References

- [1] Abdelwahab M, Tsavdaridis K. Optimised 3D-printed metallic node-connections for reticulated structures. In: The 9th International Conference on Steel and Aluminium Structures, 03-05 Jul 2019. Bradford, UK.
- [2] Bikas H, Stavridis J, Stavropoulos P, Chyssolouris G. A design framework to replace conventional manufacturing processes with additive manufacturing for structural components: A formula student case study. In: Procedia CIRP (Volume 57). 2016. p.710-715.
- [3] Hintereder J, Sattler S, Gunzert U. Development of a disruptive lightweight semitrailer truck. ATZ - Automotive Magazine Special Issue 3. 2018. p.104-111. (in German)
- [4] Suksuwan A, Spence S. Performance-based multi-hazard topology optimization of wind and seismically excited structural systems. Engineering Structures. 2018;172:573-588..
- [5] Tsavdaridis K, Efthymiou E, Aduguc A, Hughes J, Grekavicius L. Application of structural topology optimisation in aluminium cross-sectional design. Thin-Walled Structures. 2019;139:372-388.
- [6] Reimann J, Hammer S, Henckell P, Ali Y, Hildebrand J, Bergmann JP. Topology optimized structural nodes. Industrie 4.0 Management 4. 2020. p.15-19. (in German)
- [7] VDI- Department of Production Engineering and Manufacturing Processes. Additive manufacturing processes, rapid manufacturing - Basics, definitions, processes. VDI-Gesellschaft Produktion und Logistik. 2014. (in German)
- [8] Bundesverband der Deutschen Industrie. Implications of 3D printing for securing raw materials in German industry. Position Paper Security and Raw Materials. 2016. (in German)
- [9] Berger R. Additive manufacturing – next generation Amnx. Roland Berger. 2016. (in German)
- [10] Peters S. Additive manufacturing - the path to individual production. Hessen-Nanotech 25. 2015. (in German)
- [11] Brockmann R, Candel-Ruiz A, Kaufmann S, Müllerschön O. Strategies for high deposition rate additive manufacturing by laser metal deposition. ICALEO 2015. p.680.
- [12] Galjaard S, Hofman S, Ren S. New opportunities to optimize structural designs in metal by using additive manufacturing. Advances in Architectural Geometry. 2014. p.79-93.
- [13] Bergmann JP, Henckell P, Ali Y, Hildebrand J, Reimann J. Basic scientific conceptualization of existing challenges and perspectives for additive manufacturing with electric arc. DVS-Berichte Band 345. 2018. (in German)
- [14] Hildebrand J, Ali Y, Ullrich J, Dahms S, Eilenberger D, Bergmann JP, Seul T, Jahn S. Use of arc and diffusion welding technology for additive manufacturing of large temperature-controlled tools. Tagungsband Werkstoffe und Additive Fertigung. 2018. p.121-126. (in German)
- [15] Jahn S, Gemse F, Broich U, Sändig S. Efficient diffusion bonding of large scale parts. Materials Science Forum (Vol. 838). 2015. p.838–839.
- [16] Martina F. Recent developments in large-scale wire+arc additive manufacturing. Additive Manufacturing in Aerospace, ILA Berlin. 2016.
- [17] Ding D, Pan Z, Cuiuri D, Li H. Wire-feed additive manufacturing of metal components: technologies, developments and future interests. International Journal of Advanced Manufacturing Technology. 2015;81:1-4.
- [18] DIN EN 1011-2:2001-05. Welding—Recommendation for welding of metallic materials—Part 2: Arc welding of ferritic steels. Beuth Verlag. 2001.
- [19] Stahlinstitut VDEh. Weldable non-alloy and low-alloy steels - recommendations for processing, especially for fusion welding. Beuth Verlag. 2017.
- [20] Henckell P, Gierth M, Ali Y, Reimann J, Bergmann JP. Reduction of energy input in wire arc additive manufacturing (WAAM) with gas metal arc welding (GMAW). Materials. 2020;13(11):2491.

Evaluation of the Influencing Factors in Target Value Design Process

Akashprava Panda, *Department of Civil Engineering, Aryan Institute of Engineering & Technology, Bhubaneswar, a_panda12@gmail.com*

Jyotikusum Acharya, *Department of Civil Engineering, NM Institute of Engineering & Technology, Bhubaneswar, jyotikusumacharya@yahoo.co.in*

Binapani Mohapatra, *Department of Civil Engineering, Raajdhani Engineering College, Bhubaneswar, binapanimohapatra@yahoo.co.in*

Saswati Nayak, *Department of Mechanical Engineering, Capital Engineering College, Bhubaneswar, saswatinayak2574@gmail.com*

Abstract: In the construction sector, target value design is a novel method that promotes concurrent engineering and collaborative design. This paper presents the findings of a literature review that was conducted to determine the contributing elements in the target value design. The article also includes the results of a questionnaire survey that looked into the perceptions of industry practitioners on the relative importance of the contributing elements. Integration of multiple project stakeholders in the design process is considered crucial by project stakeholders who participated in the survey. The project definition is also important for putting the goal value design into action. Market conditions and project features, on the other hand, are regarded as the least important factors in the target value design process.

Keywords: Target costing; Target value design; Influencing factors; Survey; Integration; Project definition.

1. Introduction

The construction industry globally has been viewed as highly inefficient. Most construction projects suffer from low productivity compared to production systems in other sectors. Industry experts have proposed innovation in various areas of industry's traditional practices in cost reduction [1]. A central concern of any organization is how to reduce project costs while improving productivity. However, cost reduction must be accomplished without impacting the ability of the organization to achieve its long-term goals. The real issue is how to manage the cost and reduce unnecessary cost [2].

Decisions made in a design phase influence project cost more than those in a production phase. In this regard, there are many cost reduction efforts in a design phase. Chief among them is the use of target costing (TC) techniques to ensure that the product is initially designed to have a sufficient profit [3]. In Japan, about 15% of the construction projects have adopted target costing for their cost planning and management. In the construction industry, target costing research has been carried out within the framework of lean construction as target value design (TVD) method [4]. Many research reports show that projects can achieve an average cost reduction of 15% if target value design is being applied systematically to the projects [5].

In the construction industry, target value design considers that the final cost is a design parameter driving product and process design while it is regarded as an outcome of the design process in the traditional design process [6]. In target value design, associated stakeholders including specialty contractors are involved in early design to develop target cost and determine design variables from the beginning of design phase. A target value design team could estimate costs for design alternatives while ensuring not to exceed the target cost. The team should be able to use different skills to maintain the target cost without impacting on the quality and the function of the project [7].

The review of the literature on target value design reveals that no formal study on the influencing factors is available to guide the process of target value design. In this regard, the goal of this study is to investigate the influencing factors in a target value design process.

2. Literature review

2.1 Target Costing (TC)

Target costing (TC) was initially developed in Japan after the first oil crisis in 1972. Since then the process of target costing has been improved and adapted [8]. Target costing aims to reduce the overall cost of products over the entire life-cycle making sure that product quality and reliability are guaranteed. Therefore, target costing controls the product attributes and respective production processes. Target costing can be efficiently implemented by controlling the design process through defining and analyzing different production-based on engineering-driven

alternatives. This analysis is denoted as Value Engineering (VE) and considered as a crucial part of the target costing process [9].

A study from Langfield-Smith asserted that target costing is prevalent in the manufacturing industry, not in other sectors [10]. Langfield-Smith [10] reviewed the diffusion of strategic target costing techniques over the past twenty-five years. The study [10] suggested that it would be useful to understand how target costing techniques are diffused into organizational processes.

Kato et al. [11] found that many corporations estimated costs in the product design phase. Since the initial successful application of target costing to a building project [6], the interest of using target costing methods in design phase has grown in the construction industry. Target costing has been renamed as target value design (TVD) when target costing was applied to the construction industry.

2.2 Target Value Design (TVD)

Traditional design and cost estimating process in the construction industry are sequential. A designer initially designs a facility and estimates it later. The sequential process results in non-value adding activities through negative iterations [4]. All too often, the project scope has to be altered to meet the project's budget. These iterations keep designers from delivering value to a customer while meeting the owner's requirements. Furthermore, the negative iterations create significant delay and waste.

In contrast, the application of target costing, which refers to 'design to target cost,' to design process enables a project team to develop the design outcomes that meet the project's budget (i.e., 'allowable cost'). Therefore, target value design helps a team avoid going over budget while delivering the features of a building that provides value to the owner. Since its inception, target value design has allowed multiple institutional projects to be completed on or below budget while adding value delivery to the customer [6, 12, 13]. As for their cost performance, a number of projects where target value design was explicitly applied have reported two persistent outcomes [14]: (1) The projects were completed below market cost, and (2) the estimated costs tend to decline as designs are developed.

2.3 Benefits and barriers

The use of target value design in the construction industry imposes many advantages that project stakeholders can benefit. Target value design is a management system focusing on cost reduction [11]. It also promotes the team spirit and collaborative attitude among competitors (owners and contractors) in construction projects. To efficiently implement target value design, companies should be able to overcome silo-minds and internal boundaries that each stakeholder set. Target value design is also a managerial practice which helps increase the speed of knowledge transfer and propel organizational changes by creating a culture of continuous improvement as well as enhancing employee awareness and empowerment.

Although the adoption of target value design promotes numerous benefits in the industry, there are still barriers and challenges. The main problem for target value design is that the construction industry is a limited competitive market. In other words, an exclusive market is not willing to use target costing that leverages market competitiveness [15]. According to Costa and Formoso [16], the construction industry has barriers that prevent the industry from adopting target value design as follows:

- (1) construction is a project-oriented industry, and each project is unique in terms of project team and design;
- (2) there are no clear guidelines in how project teams execute the process of target value design;
- (3) every construction project is run by a different management team.

3. Literature survey on factors influencing the successful implementation of TVD

The study aims to analyze the target value design influencing factors through in-depth literature review. A comprehensive review of literature in the field was conducted with a view to identifying the factors affecting on the target value design process. The literature review found that there are thirty-two factors in five categories that impact on the target value design process.

3.1 Category 1. Market competition

Market condition is characterized by politics, law, economics, sociology, and technology [17]. Contractors have to maintain a long-term coordinated interaction with the local market and their competitors. The category of market competition includes five factors: the competitiveness of the construction market (V1) [17], social demand of the project type (V2) [18], the availability of reference project cost data (V3) [6], the availability of a reliable cost data (V4), and the availability of A/E and contractors capable of target value design process (V5).

These factors help determine the attributes of information on the competitors in the market analysis. These factors constitute a set of external determinants for contractors to consider in determining target costs on target pricing practices [17].

3.2 Category 2. Customer's attributes

This category of factors addresses the involvement of project owners in the target value design process. There are seven factors that represent the attributes of a customer influencing on the target value design process: plan on the customers of future projects (V6), experiences of similar target value design projects (V7), robustness of project requirements (V8), ability to define project requirements clearly in early design stage (V9), reasonable project requirement (V10) [24], and timely responsiveness to requests from project stakeholders (V11).

3.3 Category 3. Means

This category of factors represents the project management tools that project stakeholders use to manage the target value design process. This category has six factors: BIM and simulations' tools (V12), process management tools such as the Last Planner System (V13), value engineering (V14), the use of decision-making tool such as Choose-by-Advantage (V15), risk management process (V16), and contractual arrangement for profit and risk sharing (V17).

3.4 Category 4. Project characteristics

This category of factors represents the characteristics of the project that is influencing the target costing process. The attributes of projects determine the level of uncertainty and the role of stakeholders which eventually play essential roles in the practices of a target value design project [18, 19]. There are five factors in this category: project complexity (V18), project size (V19), the level of uncertainty and degrees of risk (V20), project delivery method (V21), and project contract method (V22).

Table 1. Factors and their Variables Influencing on TVD Process

Category 1. Market Competition	
V1	Competitiveness of the construction market
V2	Social demand of the project types
V3	Availability of benchmark data for target price
V4	Availability of reliable project cost data.
V5	Availability of qualified A/E and contractors
Category 2. Attributes of Customer	
V6	Prospect of future projects
V7	Experiences of similar TVD projects
V8	Robustness of project requirements
V9	Ability of define project requirements in early design
V10	Reasonable project requirement
V11	Timely Response to requests from A/E or contractors
Category 3. Means	
V12	Technology tools such as BIM and simulations
V13	Process management tools such as LPS (Last Planner)
V14	Value engineering (VE)
V15	Decision making tools such as CBA (Choose-by-Advantages)
V16	Risk management process
V17	Contractual arrangement for profit/risk sharing
Category 4. Project Characteristics	
V18	Project complexity
V19	Project size
V20	The level of uncertainty
V21	Project delivery method (DB, GCCM, DBB, and IPD)
V22	Project contract method (Lumpsum, GMP, and Unit Price)
Category 5. Process and Culture	
V23	Degree of innovation
V24	Degree of early involvement of project stakeholders
V25	Level of stakeholders' commitments
V26	Cultural alignment of team organization
V27	Mutual respect
V28	Trust
V29	Stakeholder's relation and degree of cooperation
V30	Timely communication among stakeholders
V31	Develop parametric estimate
V32	Allowing time for feedback before commitment

3.5 Category 5. Process and culture

Literature suggests that the process and organizational culture influence the successful implementation of target value design [14, 20]. The category of process and culture has 14 factors: the degree of innovation (V23), the early involvement of project parties (V24), the level of stakeholders' commitments to target value design (V25), cultural alignment of team organization (V26), mutual respect (V27), trust (V28), stakeholder's relation and degree of cooperation (V29), timely communication among stakeholders (V30), accurate and conceptual estimate (V31), and allowing time for feedback before commitment (V32).

The full list and its source of each factor in five categories influencing the successful implementation of the target value design process are shown in Tables 1 and 2.

Table 2. The source of each Factor

	Cooper and Slagmulder 1997	Azari and Kim 2016	Lai et al. 2008	Drew and Skitmore 1992	Ballard and Reiser 2004	Tommelein et al 2011
Category 1. Market Competition						
V1	x					
V2				x		
V3					x	
V4	x					
V5					x	
Category 2. Attributes of Customer						
V6		x				
V7		x				
V8		x				
V9					x	
V10			x			
V11		x				
Category 3. Means						
V12					x	
V13					x	
V14						x
V15						x
V16						x
V17					x	
Category 4. Project Characteristics						
V18				x		
V19				x		
V20						x
V21		x				
V22						x
Category 5. Process and Culture						
V23		x				
V24		x				
V25	x					
V26		x				
V27						x
V28		x				
V29		x				
V30		x				
V31						x
V32			x			

4. Identifying Critical Factors through Survey

4.1 Questionnaire design and data collection

Survey research, particularly a questionnaire survey, collects data from a sample through a cross-sectional or longitudinal study with the objective of generalizing the results of the analysis to a larger population [21]. This type of research provides a quantitative portrayal of the trends or opinions of a community through studying a sample of that population [22].

To identify critical influencing factors on the successful implementation of target value design, we used the survey as a data collection method. The questionnaires for the survey were developed based on the factors identified through literature review. Those factors have potential impacts on the target value design process as well as the outcome of target value design. The questionnaires were piloted with two senior professionals to review the list for the accuracy.

The 32 factors were addressed in a questionnaire format for the survey. The questionnaire requests that a respondent judge the importance level of each variable on a predefined five-point Likert scale (5 = extremely important, 4 = important, 3 = neutral, 2 = unimportant, 1 = extremely unimportant). The survey request was distributed to 78 professionals who have experienced target value design process through an online survey tool. 26 responses were collected over a two-month period. The response rate is 33.33%.

Table 3 presents the role breakdown of each of the 26 respondents. Contractors made up the majority of the respondents, followed by designers and owners' representatives.

Table 3. Distribution of Questionnaire Response by Respondent Role

Respondent Role	# of Participants	Percentage
General Contractor	11	42%
MEP Contractor	2	8%
Owner's Rep	6	23%
Architect/Engineers	7	27%
Total	26	100%

4.2 Descriptive statistics

The questionnaire collected information on the level of influence of each factor on the target value design process. Descriptive statistics for the variables in the questionnaire survey (including sample size, mean, standard deviation, minimum, and maximum) are presented in Table 4.

4.3 Reliability of the influencing factors

The validity of survey data involves the consistency and repeatability of results using the same observations [21]. Although there are various measures of reliability assessment, internal consistency using Cronbach's Alpha is the most widely accepted measure [22].

Cronbach's coefficient alpha was employed to assess internal consistency of the scales under the headings of the influencing factors. In other words, the reliability of any given measurement refers to the extent to which it is a consistent measure of a concept, and Cronbach's alpha is one way of measuring the strength of that consistency [22, 23].

Table 5 shows the overall Cronbach's coefficient alpha on the data while Table 6 shows the Cronbach's alpha if each factor is deleted. Tables 5 and 6 provide evidence that all the factors had high internal consistency and considered reliable.

4.4 Rankings of the influencing factors

This section focuses on the ranking of the influencing factors. The ranking of the influencing factors was carried out based on their mean values. Table 7 shows the ranking of the influencing factors with the category information; Table 8 shows the ranking of the categories.

As shown in Table 7, all the mean values except two factors (V2 and V19) are more than 3.0, which suggest that most influencing factors identified through literature are regarded as essential in implementing the target value design process by all groups. Due to lack of responses or the sample size, the analysis by each stakeholder group has not been done.

From Table 8, an apparent finding is that the categories of customer attributes and process and culture were usually regarded critical among five categories. On the other hand, the categories of market condition and project characteristics are considered less critical in implementing the target value design process. The reasons why market competition and project characteristics are ranked low in this survey may include two issues. The first issue is that customer's demands are reflected in customers' attributes. The second issue is that most target value design process

begins in schematic design phase rather than in business planning. Therefore, most procurement processes of selecting major stakeholders are completed before the target value design process launches.

Table 4. Descriptive Statistics

	N	Minimum	Maximum	Mean	Std. Deviation
V1	26	2	5	3.5769	0.70274
V2	26	1	3	2.5385	0.58177
V3	26	2	4	3.2308	0.51441
V4	26	2	4	3.1154	0.43146
V5	26	3	4	3.4615	0.50839
V6	26	3	4	3.5769	0.50383
V7	26	3	4	3.6923	0.47068
V8	26	4	5	4.4231	0.50383
V9	26	3	5	4.0769	0.56022
V10	26	3	4	3.5	0.5099
V11	26	4	5	4.3462	0.48516
V12	26	3	4	3.7692	0.42967
V13	26	3	4	3.3077	0.47068
V14	26	3	4	3.6923	0.47068
V15	26	3	4	3.4231	0.50383
V16	26	2	4	3	0.4
V17	26	3	4	3.3846	0.49614
V18	26	3	4	3.3077	0.47068
V19	26	1	3	2.0769	0.48358
V20	26	3	4	3.3462	0.48516
V21	26	3	4	3.5769	0.50383
V22	26	3	5	3.6923	0.61769
V23	26	3	5	3.8077	0.49147
V24	26	3	5	4.2692	0.66679
V25	26	3	4	3.8846	0.32581
V26	26	3	5	3.9615	0.66216
V27	26	3	5	3.7308	0.60383
V28	26	3	5	3.9231	0.56022
V29	26	4	5	4.6538	0.48516
V30	26	3	4	3.5769	0.50383
V31	26	3	5	4.1154	0.5159
V32	26	3	4	3.4231	0.50383

Table 5. Cronbach's Alpha on all factors

Cronbach's Alpha	Cronbach's Alpha Based on Standardized Items	No. of Items
0.707	0.699	32

Table 6. Cronbach's Alpha if each factor is deleted

	V1	V2	V3	V4	V5	V6	V7	V8	V9	V10	V11	V12
Cronbach's Alpha if each factor is deleted	0.72	0.7	0.7	0.71	0.73	0.68	0.73	0.7	0.69	0.69	0.71	0.68
	V13	V14	V15	V16	V17	V18	V19	V20	V21	V22	V23	V24
Cronbach's Alpha if each factor is deleted	0.7	0.69	0.7	0.71	0.7	0.69	0.7	0.71	0.71	0.7	0.7	0.67
	V25	V26	V27	V28	V29	V30	V31	V32				
Cronbach's Alpha if each factor is deleted	0.7	0.67	0.68	0.72	0.71	0.7	0.68	0.71				

Table 7. The ranking, the Influencing Factors

Ranking		Factor	Category	Mean
1	V29	Stakeholder's relation and degree of cooperation	Process and Culture	4.654
2	V8	Robustness of project requirements	Customer Attributes	4.423
3	V11	Timely response (owner)	Customer Attributes	4.346
4	V24	Degree of early involvement of project stakeholders	Process and Culture	4.269
5	V31	Developing parametric estimate	Process and Culture	4.115
6	V9	Ability to define project requirements in early design	Customer Attributes	4.077
7	V26	Cultural alignment of team organization	Process and Culture	3.962
8	V28	Trust	Process and Culture	3.923
9	V25	Level of stakeholders' commitments	Process and Culture	3.885
10	V23	Degree of innovation	Process and Culture	3.808
11	V12	Technology tools such as BIM and simulations	Means	3.769
12	V27	Mutual respect	Process and Culture	3.731
13	V7	Experiences of similar TVD projects	Process and Culture	3.692
14	V14	Value engineering (VE)	Means	3.692
15	V22	Project contract method (L/S, Unit Price, GMP)	Project Characteristics	3.692
16	V1	Competitiveness of the construction market	Market Conditions	3.577
17	V6	Prospect of future projects	Market Conditions	3.577
18	V21	Project delivery method (DB, GCCM, DBB, and IPD)	Project Characteristics	3.577
19	V30	Timely communication among stakeholders	Process and Culture	3.577
20	V10	Reasonable project requirement	Customer Attributes	3.500
21	V5	Availability of qualified A/E and contractors	Market Conditions	3.462
22	V15	Decision making tools such as CBA (Choose-by-Advantages)	Means	3.423
23	V32	Allowing time for feedback before commitment	Process and Culture	3.423
24	V17	Contractual arrangement for profit/risk sharing	Means	3.385
25	V20	The level of uncertainty	Project Characteristics	3.346
26	V13	Process management tools such as LPS (Last Planner)	Means	3.308
27	V18	Project complexity	Project Characteristics	3.308
28	V3	Availability of benchmark data for target price	Market Conditions	3.231
29	V4	Availability of reliable project cost data	Market Conditions	3.115
30	V16	Risk management process	Means	3.000
31	V2	Social demand of the project types	Market Conditions	2.539
32	V19	Project size	Project Characteristics	2.077

Table 8. Category Ranking

Category	Mean Value	Stand. Dev.	Ranking
1. Market Competition	3.185	0.405	4
2. Customer Attributes	3.935	0.411	1
3. Means	3.436	0.263	3
4. Project Characteristics	3.179	0.642	5
5. Process and Culture	3.900	0.365	2

From Table 7, factor 29 of "Stakeholder's relation and the degree of cooperation among stakeholders" was ranked the highest among all factors. This means that most survey participants who carried out the target value design process consider this factor as the most critical factor for the successful target value design process. In addition to factor 29, factors 24 (Degree of early involvement of project stakeholders, ranked 4th), 26 (Cultural alignment of team organization, ranked 7th), and 28 (Trust, ranked 8th) are the components required for project integration. The result is in line with the research outcomes on integrated project delivery process [20]. Azari and Kim [20] carried out their survey on integrated design process in which the cooperation and mutual trust are critical to the success of integrated design process.

It is also notable that the respondents have highly ranked factors 8 (Robustness of project requirements, ranked 2nd), 11 (Owner's timely response, ranked 3rd), and 9 (Ability to define project requirements in early design, ranked 6th). These factors are related to the owner's project definition, which is in line with the findings in the literature on design-build. Schaufelberger et al. [25] claim that the project definition by a project owner is one of the most critical success factors in design-build projects, which also promote concurrent engineering where the process design is carried out concurrently with the product design.

However, factors 19 (Project size, ranked 32th), 2 (Social demands of the project type, ranked 31st), and other factors in the category of market conditions or project characteristics are considered not significant compared to other factors. Most respondents rated them low. This reflects the view that market conditions or project attributes do not make a substantial impact on the target value design process.

5. Conclusions

Target value design is a new practice in the construction industry promoting concurrent engineering and collaborative design. The method is new and contradicts against the traditional way of design development in which each stakeholder (e.g., designers and contractors) work in a sequential and fragmented way as opposed to collaborative and integrated approach. As a result, many owners and service providers (i.e., designers and contractors) are concerned over the process and possible challenges.

Few studies appear to have undertaken the task of investigating the influencing factors in the target value design process. This paper shows the results of literature survey to identify the influencing factors in the target value design. The paper also presents the results of a questionnaire survey to explore the industry practitioners' perception of the relative importance of the influencing factors.

A total of 32 influencing factors were identified and synthesized in the survey, which was shown to be reliable based on Cronbach's coefficient alpha values. Data were collected from various stakeholders who went through the target value design process in their past projects. Since the target value design is not prevalent in the construction market, the number of respondents participating in the survey was only 26, which restricts the scope of statistical analysis.

Findings from the analysis suggest that most influencing factors identified in the literature survey are regarded as important in carrying out the target value design. Project stakeholders participating in the survey consider the integration of different project stakeholders in the design phase as critical. The project definition is also regarded as critical in implementing the target value design. The results suggest that the customer's demands are clearly defined and fully communicated with a team of target value design including designers and contractors from the beginning of the target value design process. However, the market conditions and project attributes are considered as least significant in the target value design process.

Overall, the results reflect that the organizational integration, as well as project owners' early project definition, are most important while market conditions and project characteristics are not considered critical. These findings should be useful to construction practitioners and project owners when they undertake the target value design in their projects.

6. References

- [1] De Melo RS, Kaushik AD, Koskela L, Tzortzopoulos P, Granja A, Keraminiyage K. Target costing in construction: A comparative study. 22nd Annual Conference of the International Group for Lean Construction: Understanding and Improving Project Based Production. 2014. p.183-194.
- [2] Steven M. Cost reduction analysis: tools and strategies. John Wiley & Sons, New York, NY. 2010.
- [3] Yazdifar H, Askarany D. A comparative study of the adoption and implementation of target costing in the UK, Australia and New Zealand. International Journal of Production Economics. 2012;135(1):382-392.
- [4] Ballard G. Lean Project Delivery System. White Paper 8, Lean Construction Institute. 2000. <http://www.leanconstruction.org/pdf/WP8-LPDS.pdf>.
- [5] Zimina D, Ballard G, Pasquire C. Target value design: using collaboration and a lean approach to reduce construction cost. Construction Management and Economics. 2012;30(5):383-398.
- [6] Ballard G, Reiser P. The St. Olaf College fieldhouse project: A case study in designing to target cost. Proceedings of the 12th Annual Conference of the International Group for Lean Construction (IGLC 12). Elsinore, Denmark. 2004. p.234-249.
- [7] Macomber H, Howell G, Barberio J. Target-value design: nine foundational practices for delivering surprising client value. Practice Management Digest, the American Institute of Architects (AIA). Washington, DC. 2007.
- [8] Sakurai M. Target costing and how to use it. Journal Cost Management. 1989; 3(2): 39-50.
- [9] Agndal H, Nilsson U. Inter-organizational cost management in the exchange process. Management Accounting Research. 2009; 20(2): 85-101.

- [10] Langfield-Smith K. Strategic MA: how far have we come in 25 years? *Accounting, Auditing, and Accountability Journal*. 2008; 21(2): 204–228.
- [11] Kato Y, Boer G, Chow C. Target costing: An integrative management process. *Journal of Cost Management*. 1995; 9(1): 39.
- [12] Ballard G, Rybkowski ZK. Overcoming the hurdle of first cost: action research in target costing. *Proceedings of 2009 Construction Research Congress*. ASCE, Seattle, WA. 2009. p.1038-1047.
- [13] Ahmed S, Pasquire C, Manu E. Exploratory study of ‘costing collaboratively’ in the UK construction industry. In: *Proc. 27th Annual Conference of the International Group for Lean Construction (IGLC)*. Dublin, Ireland. 2019.p.1163-1174.
- [14] Tommelein I, Ballard G, Lee H. Task 4 progress report: develop target value design and delivery process to incorporate energy efficiency metrics. Report for the United States Department of Energy. University of California, Berkeley. 2011.
- [15] Sharafoddin S. The utilization of target costing and its implementation method in Iran. *Procedia Economics and Finance*. 2012; 36: 123-127.
- [16] Costa DB, Formoso CT. A set of evaluation criteria for performance measurement systems in the construction industry. *Journal of Management Property Construction*. 2004; 9(2): 91-102.
- [17] Cooper R, Slagmulder R. Target costing and value engineering. Productivity Press, Portland.1997.
- [18] Ballard G. Current benchmark for target value design. Project production systems laboratory white paper (P2SL). University of California, Berkeley, CA. 2009.
- [19] Ballard G, Morris P. Maximizing owner value through target value design. *AACE International Transactions*. 2010; 1: 347-361.
- [20] Azari R, Kim YW. Integration evaluation framework for integrated design teams of green buildings: Development and validation. *Journal of Management in Engineering*. 2016;32(3):04015053.
- [21] Babbie E. *The practice of social research* (12th ed.). Belmont, CA: Wadsworth Cengage Learning. 2010.
- [22] Creswell JW. *Qualitative inquiry and research design: choosing among five approaches*. Thousand Oaks, CA: SAGE Publications, Inc. 2012.
- [23] Hinkin TR. A review of scale development practices in the study of organizations. *Journal of Management*. 1995; 21(5): 967-988.
- [24] Lai X, Xie M, Tan KC, Yang B. Ranking of customer requirements in a competitive environment. *Computers & Industrial Engineering*. 2008;54(2):202-214.
- [25] Schaufelberger J, Kim Y, Han S, Jin K. *The Truth of Design-Build, Bounding*. Seoul, Korea.

Determination of Dynamic Impact Factor of an Existing Pre-stressed Concrete I-Girder Bridge

Sagarika Pasayat, *Department of Civil Engineering, Aryan Institute of Engineering & Technology, Bhubaneswar, s.pasayat@gmail.com*

Sharadhananda Ghadei, *Department of Civil Engineering, Aryan Institute of Engineering & Technology, Bhubaneswar, sharadhananda@outlook.com*

Shradha Jena, *Department of Civil Engineering, Capital Engineering College, Bhubaneswar, shradhajena98@gmail.com*

Deepika Priyadarshini Palai, *Department of Civil Engineering, NM Institute of Engineering & Technology, Bhubaneswar, deepikadalai2561@gmail.com*

Abstract: Many elements influence a bridge's dynamic Impact Factor (IM), including Vehicle-Bridge Interaction (VBI), vehicle speed, and road roughness. Using VBI modelling, this article depicts the dynamic effects of moving vehicles and the determination of IM for an existing pre-stressed concrete I-girder bridge. The evaluation of the IM is expected to give useful information for assessing and managing the existing bridge's condition. A dynamic model for the bridge structure subsystem, a dynamic model for the vehicle subsystem, interaction restrictions, road roughness modelling, and numerical solution techniques for the dynamic systems are all part of the vehicle-bridge interaction problem. The vehicle dynamics are modelled using the Half-car model, while the bridge dynamics are idealised using the Finite Element Method (FEM). The Equation of Motion (EOM) for the bridge subsystem is then determined using FEM and the mode superposition method. The EOM for the vehicle subsystem is developed using D'Alembert's approach. The interaction between vehicle vibration and bridge vibration is established by using the compatibility relationship between the contact points and applying the static equilibrium condition to the contact forces between the wheels and the bridge. Finally, to determine the reactions of the two sub-systems, Newmark's technique is utilised to solve the coupled mathematical model of the vehicle and bridge interaction problem. The technique is then repeated for various vehicle speeds and bridge deck surface roughness conditions in order to estimate the dynamic impact on the existing I-girder bridge in India, the Teesta Bridge.

Keywords: Dynamic impact factor; Vehicle bridge interaction; Half-car vehicle model; Bridge dynamic response; Finite element method; Newmark's- β method.

1. Introduction

In the last years, the ever-growing span length of bridges and the increase of vehicle loads and vehicle speeds have led to the consequent increase in dynamic influence on bridge structures [1]. The dynamic effects produced by vehicles passing over the bridge structures and viaducts result in the increase of dynamic forces and displacements over that of the static responses [2]. This phenomenon is known as Dynamic Impact on bridges which is generally considered as Impact Factor (IM) or Dynamic load allowance (DLA) in the bridge design standards. It is calculated as the percent difference between the maximum dynamic responses to the maximum static response. The dynamic impact on bridges depends on various factors such as the dynamic characteristics of bridges, the dynamic characteristics of vehicles, vehicle speeds, the road roughness conditions and, finally the Vehicle-Bridge Interactions (VBI). In earlier research for developing bridge design code, field or experimental test results were used to develop the empirical formulas of IM. However, consideration of all those influencing factors were not possible in the field test. Moreover, due to the limitation of theoretical and computational technologies, those effects were difficult to investigate in the past. Therefore, the dynamic impact due to traffic loads on the existing bridges which were designed with earlier bridge design standards are required to be investigated considering the vibration mechanism between the bridge and vehicles by incorporating all those complex factors.

To assess the dynamic effect of traffic loads, the research on vehicle-bridge interaction phenomena has been performed for decades [3, 4]. Moreover, the research considering the dynamic responses of bridges are performed to assess the fatigue life of the bridges [5], environmental issues [6], safety and comfort of the passengers [7] and also for damage identification of bridges [8]. A lot of research has been performed for the study of vehicle-bridge interaction problems. Ayre et al. [9] and Ayre and Jacobsen [10] first studied the dynamic responses of two-span beam models under moving load. Vellozzi [11] presented the vibration of suspension bridges under the moving load. Frýba [12-13] considered the vehicle and the bridge as a coupled system and derived the analytic solutions when the beam subjected to moving loads. Henchi et al. [14] studied the dynamic response of a bridge-vehicle

interaction system and proposed an algorithm for the dynamic analysis of the coupled system. Yang [15] simplified the effect of the vehicle as two sets of concentrated forces and studied the dynamic responses of the bridge. Chen et al. [16] studied the effect of varying speed when the sprung-mass model is moving on a simply supported beam. Blejwas et al. [17] proposed a solution to solve the interaction problem using Lagrange's equation with multipliers and constraint equation. Various methods of solving the vehicle bridge interaction problems have also been reported (Galdos et al. [18], Yang and Lin [19], Chu et al. [20], Yang and Duan [21]).

Using the vehicle bridge interaction theory, the dynamic impact on bridges has also been studied as presented in the review paper by Deng et al. [22]. Deng and Cai [2, 23] studied dynamic impact factor for evaluating the performance of the bridges. Chen and Wu [24] researched the effect of wind and bridge length on bridge vehicle interaction. Cai et al. [25] studied the influence of approach span condition on slab-on-girder bridges. Li et al. [26] studied the dynamic response of a highway bridge subjected to moving vehicles and observed that the dynamic impact increases with vehicle speed and depends on road roughness conditions. Huang et al. [27] analyzed the impact of vehicles on multi-girder steel bridges with different span lengths. Deng et al. [3] found that the impact on continuous bridges is larger than those of simply supported bridges. Zhu and Law [28] also studied the continuous bridge and vehicle interaction to investigate the dynamic load effects. Mohseni et al. [29] conducted an extensive numerical study to evaluate the influence of some key parameters on the dynamic impact factors for skew composite concrete-steel slab-on-girder bridges and proposed that apart from AASHTO [30] bridge design specification, all the current design specifications for considering IM are un-conservative. Pieraccini et al. [31] performed an experimental study to assess the IM of a railway bridge using the interferometric radar sensor. Gao et al. [32] investigated numerically the dynamic load allowance characteristics of a concrete-filled steel tube (CFST) arch bridge and some conclusions are drawn for evaluating the condition of CFST arch bridges.

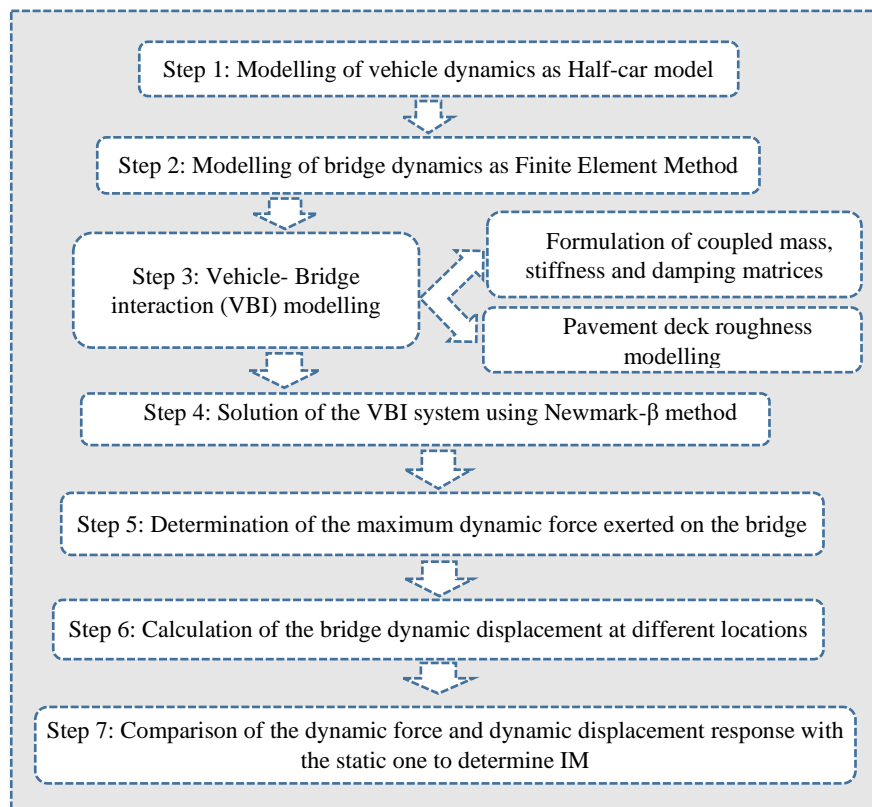


Figure 1. Flow chart of the methodology

As mentioned earlier, estimation of dynamic impact factor is a complicated task because of vehicle-bridge interaction mechanism associated with a large number of influencing parameters, including the dynamic characteristics of both the bridge and the vehicle, road surface condition, vehicle speed etc. Accurate evaluation of the impact factor utilizing the recent theoretical and computational development may lead to valuable information for condition evaluation and management of existing bridges which were designed following the earlier bridge design codes. In this paper, the dynamic behavior of an existing Pre-stressed concrete (PC) I-girder bridge structures under moving vehicle is investigated numerically considering all the complex factors mentioned above and finally the dynamic impact factor is determined. A medium span PC I-girder bridge which is a very common bridge type in Bangladesh is considered as a case study bridge which was designed with earlier bridge

design standard without considering VBI. The bridge is named as Teesta Bridge which is situated in Rangpur district of Bangladesh. The paper is organized by the following main sections. Firstly, the dynamic behavior of vehicle and bridge, modelling and solution of the interaction between the bridge and the vehicle moving over it are presented considering the influence of different vehicle speeds and various extents of pavement roughness. Later, the dynamic impact factor is analyzed following the numerical investigation of the dynamic behavior of the bridge. The methodology of this study is shortly described with a flow chart as in Fig. 1.

2. Vehicle modelling

Modelling of a real vehicle is a very complex task. As a result, in literature, the Half-car model are frequently used for modelling vehicle dynamics as the model is much capable of representing various real vehicle experiences like effect of suspension, energy dissipation, pitching effect [33-36]. For this reason, in this study, a Half-car model is considered as the design vehicle as in Fig. 2. The vehicle model has four Degrees of Freedoms (DOFs). Among them, the body of the vehicle has two DOFs, vertical vehicle body displacement, y_s and pitching rotation, θ_s . The front and rear wheel have also a set of DOFs for vertical displacement, y_{t1} and y_{t2} respectively. Then, a set of kinetic equilibrium functions are formulated for each DOF according to Alembert's principle. The formulation is based on the existing literature [34-36] as shown in Eqns. (1) to (4) respectively.

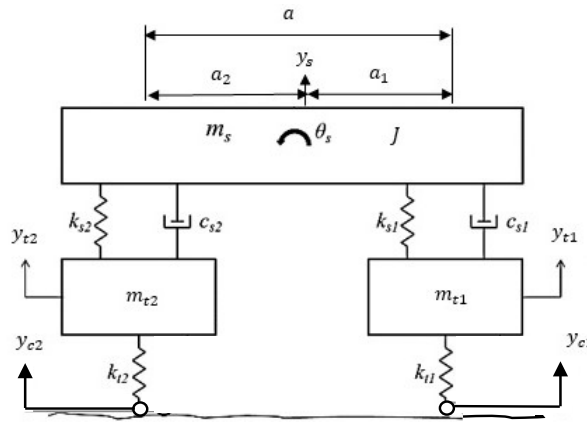


Figure 2. Half-car vehicle model

For vehicle body vibrations up and down:

$$m_s \ddot{y}_s + c_{s1}(\dot{y}_s - \dot{y}_{t1} + \dot{\theta} a_1) + c_{s2}(\dot{y}_s - \dot{y}_{t2} - \dot{\theta} a_2) + k_{s1}(y_s - y_{t1} + \theta a_1) + k_{s1}(y_s - y_{t2} - \theta a_2) = 0 \quad (1)$$

For vehicle body nodes vibration:

$$J \ddot{\theta} + k_{s1} a_1 (y_s - y_{t1} + \theta a_1) - k_{s2} a_2 (y_s - y_{t2} - \theta a_2) + c_{s1} a_1 (\dot{y}_s - \dot{y}_{t1} + \dot{\theta} a_1) - c_{s2} a_2 (\dot{y}_s - \dot{y}_{t2} - \dot{\theta} a_2) = 0 \quad (2)$$

For front axle vertical vibration:

$$m_{t1} \ddot{y}_{t1} - k_{s1}(y_s - y_{t1} + \theta a_1) - c_{s1}(\dot{y}_s - \dot{y}_{t1} + \dot{\theta} a_1) + k_{t1}(y_{t1} - y_{c1}) = 0 \quad (3)$$

For rear axle vertical vibration:

$$m_{t2} \ddot{y}_{t2} - k_{s2}(y_s - y_{t1} + \theta a_2) - c_{s2}(\dot{y}_s - \dot{y}_{t2} + \dot{\theta} a_2) + k_{t2}(y_{t2} - y_{c2}) = 0 \quad (4)$$

where, m_s is the mass of the body and the frame of the vehicle; m_{t1} and m_{t2} are the mass of the axle between the front and rear wheel set and tires; k_{s1} , k_{s2} , c_{s1} , c_{s2} are the suspension stiffness and suspension damping between wheel set and the body of the vehicle; k_{t1} , k_{t2} , are the stiffness of the front and rear tires respectively; a_1 , a_2 are the distances from the center of gravity to the front wheel and rear wheel. y_{c1} , y_{c2} are the vertical contact point displacements of the wheels on the bridge. Eqns. (1-4) are represented as matrix form as in Eq. (5).

$$[M_v]\{\ddot{y}_v(t)\} + [C_v]\{\dot{y}_v(t)\} + [K_v]\{y_v(t)\} = \{F_v\} \quad (5)$$

where, $[M_v]$ is the mass matrix, $[C_v]$ is damping matrix, $[K_v]$ is the stiffness matrix, $\{y_v(t)\}$ is the DOF vector, $\{F_v\}$ is the exciting force of the vehicle vibration. Here,

$$[M_v] = \begin{bmatrix} m_s & 0 & 0 & 0 \\ 0 & J & 0 & 0 \\ 0 & 0 & m_{t1} & 0 \\ 0 & 0 & 0 & m_{t2} \end{bmatrix} \quad (6)$$

$$\{y_v\} = \begin{Bmatrix} y_s \\ \theta \\ y_{t1} \\ y_{t2} \end{Bmatrix} \quad (7)$$

$$[K_v] = \begin{bmatrix} k_{s1} + k_{s2} & k_{s1}a_1 - k_{s2}a_2 & -k_{s1} & -k_{s2} \\ k_{s1}a_1 - k_{s2}a_2 & k_{s1}a_1^2 + k_{s2}a_2^2 & -k_{s1}a_1 & k_{s2}a_2 \\ -k_{s1} & -k_{s1}a_1 & k_{s1} + k_{t1} & 0 \\ -k_{s2} & k_{s2}a_2 & 0 & k_{s2} + k_{t2} \end{bmatrix} \quad (8)$$

$$[C_v] = \begin{bmatrix} c_{s1} + c_{s2} & c_{s1}a_1 - c_{s2}a_2 & -c_{s1} & -c_{s2} \\ c_{s1}a_1 - c_{s2}a_2 & c_{s1}a_1^2 + c_{s2}a_2^2 & -c_{s1}a_1 & c_{s2}a_2 \\ -c_{s1} & -c_{s1}a_1 & c_{s1} & 0 \\ -c_{s2} & c_{s2}a_2 & 0 & c_{s2} \end{bmatrix} \quad (9)$$

3. Modelling of bridge

The Teesta Bridge is located in the northern part of Bangladesh. It is situated in Rangpur District of Bangladesh on Rangpur-Kurigram Highway. The length and width of the bridge are 750 m and 12.11 m respectively. It is a two lane bridge and the bridge system consists of precast girders made composite with cast-in situ 200 mm thick reinforced concrete deck slab [37]. It consists of 15 nos. of medium span (50 m) simply supported PC I-girder bridges. The bridge is modelled according to FEM as shown in Fig. 3 which consists of constant flexural rigidity, EI along the span, where, E is Young's modulus, I is the moment of inertia of the bridge cross section, m is the mass per unit length of span. The equation of motion (EOM) of the bridge is expressed in Eq. (10).

$$[M_b]\{\ddot{y}_b(t)\} + [C_b]\{\dot{y}_b(t)\} + [K_b]\{y_b(t)\} = \{F_b(x, t)\}\delta(x - vt) \quad (10)$$

Where, $[M_b]$ is the mass matrix, $[C_b]$ is damping matrix, $[K_b]$ is the stiffness matrix of the bridge, $F_b(x, t)$ is the coupled forces on the bridge and $\{y_b(t)\}$ is the vertical bridge displacement at nodal points at time t and δ is the function of Dirac.

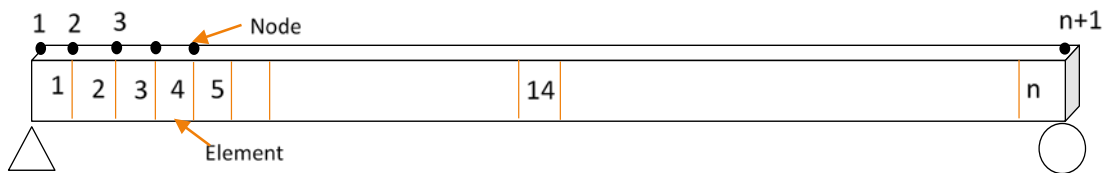


Figure 3. FE model of the bridge

Nevertheless, the dynamic response of a structure is in fact, controlled mainly by some low order modes of vibration. Therefore, generally, a few lowest modes are often enough to obtain a satisfied result when the superposition method is used. Hence, the computational efficiency can be considerably increased. By taking N number of vibration modes, the DOF of the bridge will decrease to N , and the bridge displacement can be calculated as in Eq. (11) using N -order motion equations using method of mode superposition.

$$y_b(x, t) = \{y_b(t)\} = \sum_{i=1}^N \{\varphi_i\} \eta_i(t) = [\varphi]\{\eta(t)\} \quad (11)$$

where, $\{\varphi_i\}$ is the vibration mode shape of the bridge and $\eta_i(t)$ is modal co-ordinates. Replacing Eq. (11) into Eq. (10), the EOM of the bridge in modal co-ordinate is obtained as in Eq. (12). Multiplying both side of Eq. (12)

by $\{\varphi_n\}^T$, Eq. (13) is obtained and after applying modal orthogonality principal ($\{\varphi_n\}^T[M]\{\varphi_i\} = 0$, $\{\varphi_n\}^T[M]\{\varphi_n\} = M_n$; $\{\varphi_n\}^T[K]\{\varphi_i\} = 0$, $\{\varphi_n\}^T[K]\{\varphi_n\} = K_n$) [38], the N uncoupled second order differential equations in modal co-ordinates are obtained as in Eq. (14).

$$[M_b][\varphi]\{\ddot{\eta}(t)\} + [C_b][\varphi]\{\dot{\eta}(t)\} + [K_b][\varphi]\{\eta(t)\} = -\{F_b(x, t)\}\delta(x - vt) \quad (12)$$

$$\{\varphi_n\}^T[M_b][\varphi]\{\ddot{\eta}(t)\} + \{\varphi_n\}^T[C_b][\varphi]\{\dot{\eta}(t)\} + \{\varphi_n\}^T[K_b][\varphi]\{\eta(t)\} = -\{\varphi_n\}^T\{F_b(x, t)\}\delta(x - vt) \quad (13)$$

$$\ddot{\eta}_n(t) + 2\zeta_n\omega_n\dot{\eta}_n(t) + \omega_n^2\eta_n(t) = -\frac{1}{M_n}\{\varphi_n\}^T\{F_b(x, t)\}\delta(x - vt) \quad n = 1, 2, 3, \dots, N \quad (14)$$

where, ω_n = natural frequency of vibration mode; M_n, ζ_n = modal mass, and modal damping ratio of n^{th} mode respectively; if $x = vt$, $\delta(x - vt) = 1$ else 0.

The natural frequencies and vibration mode shapes of the bridge are determined by solving the Eigen-value problem of the bridge. Static condensation is applied for having reduced mass and stiffness matrix related to only translational DOF. The stiffness and mass matrices of the bridge are partitioned as in Eq. (15). Then, the reduced matrices are calculated as in Eq. (16). Where, \hat{k}_{tt} = reduced stiffness matrix and \hat{m}_{tt} = reduced mass matrix corresponding only to the translational DOFs. The Eigen-value problem is formulated in Eq. (17) and the Eigen parameters (i.e., natural frequencies and mode shapes) of the bridge are calculated by using Eigen solution.

$$[K_b] = \begin{bmatrix} k_{tt} & k_{ot} \\ k_{to} & k_{oo} \end{bmatrix}, [M_b] = \begin{bmatrix} m_{tt} & m_{ot} \\ m_{to} & m_{oo} \end{bmatrix} \quad (15)$$

$$\hat{k}_{tt} = k_{tt} - k_{ot}^T k_{oo}^{-1} k_{ot}, \hat{m}_{tt} = m_{tt} \quad (16)$$

$$[\hat{k}_{tt} - \omega_r^2 \hat{m}_{tt}]\{\phi_r\} = \{0\} \quad (17)$$

4. Vehicle bridge interaction

Now, two sets of differential equations have been developed as in Eq. (5) and (14). One of which is for the vehicle as in Eq. (5) and another set is for the bridge as in Eq. (14). For developing interaction between the vehicle and the bridge sub-systems, the compatibility conditions are applied at the contact points and the coupled equation of motions are formulated. The effect of pavement roughness is incorporated here as wheel displacement are the resultant of both pavement roughness and bridge displacement as in Eqns. (18-19) where the wheel vertical displacement, y_{c1} and y_{c2} are calculated. The forces on the bridge consist of the weight of vehicle and wheel body and the elastic forces as calculated in Eqns. (20-21). These forces result in the coupling between the bridge and vehicle vibration. The coupled vehicle bridge model is shown in Fig. 4.

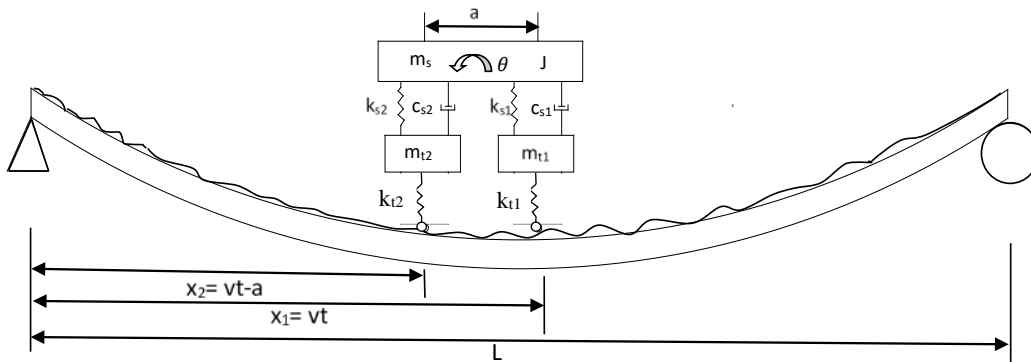


Figure 4. The model of coupled vehicle bridge vibration

$$y_{c1} = y_b(x_1, t) + r(x_1) = \sum_{i=1}^N \varphi_i(x_1)\eta_i(t) + r_1 \quad (18)$$

$$y_{c2} = y_b(x_2, t) + r(x_2) = \sum_{i=1}^N \varphi_i(x_2)\eta_i(t) + r_2 \quad (x_2 = x_1 - a) \quad (19)$$

$$F_1(x_1, t) = W_1 - K_{t1}(y_{t1} - y_{c1}) \quad (20)$$

$$F_2(x_2, t) = W_2 - K_{t2}(y_{t2} - y_{c2}) \quad (21)$$

where, y_{c1} and y_{c2} are the displacements of the front and rear wheels respectively; r_1 and r_2 are the roughness at the front and rear wheel contact points respectively. $F_1(x_1, t)$ and $F_2(x_2, t)$ are the point forces at the wheel contact points; W is the static load which comprises of sprung weight and un-sprung weight.

Now according to compatibility conditions, the coupling is done within matrix format using equations (1), (2), (3), (4) and (12). Replacing $F_i(x, t)$ from Eqns. (20-21) in Eq. (14), Eq. (26) is obtained. Eqns. (22-26) are converted to a matrix representation as in Eq. (27) which is the coupled matrix formulation of both the vehicle and the bridge subsystems interacting together.

$$m_s \ddot{y}_s + c_{s1}(\dot{y}_s - \dot{y}_{t1} + \dot{\theta}a_1) + c_{s2}(\dot{y}_s - \dot{y}_{t2} - \dot{\theta}a_2) + k_{s1}(y_s - y_{t1} + \theta a_1) + k_{s1}(y_s - y_{t2} - \theta a_2) = 0 \quad (22)$$

$$J\ddot{\theta} + k_{s1}a_1(y_s - y_{t1} + \theta a_1) - k_{s2}a_2(y_s - y_{t2} - \theta a_2) + c_{s1}a_1(\dot{y}_s - \dot{y}_{t1} + \dot{\theta}a_1) - c_{s2}a_2(\dot{y}_s - \dot{y}_{t2} - \dot{\theta}a_2) = 0 \quad (23)$$

$$m_{t1}\ddot{y}_{t1} - k_{s1}(y_s - y_{t1} + \theta a_1) - c_{s1}(\dot{y}_s - \dot{y}_{t1} + \dot{\theta}a_1) + k_{t1}(y_{t1} - y_{c1}\delta_1) = 0 \quad (24)$$

$$m_{t2}\ddot{y}_{t2} - k_{s2}(y_s - y_{t1} + \theta a_2) - c_{s2}(\dot{y}_s - \dot{y}_{t2} + \dot{\theta}a_2) + k_{t2}(y_{t2} - y_{c2}\delta_2) = 0 \quad (25)$$

$$\frac{a_2\varphi_{1n}\delta_1 + a_1\varphi_{2n}\delta_2}{a}m_s\ddot{y}_s + \frac{\varphi_{1n}\delta_1 - \varphi_{2n}\delta_2}{a}J\ddot{\theta} + \varphi_{1n}\delta_1m_{t1}\ddot{y}_{t1} + \varphi_{2n}\delta_2m_{t2}\ddot{y}_{t2} + \ddot{\eta}_n + 2\zeta_n\omega_n\dot{\eta}_n + \omega_n^2\eta_n = -(\varphi_{1n}W_1\delta_1 + \varphi_{2n}W_2\delta_2) \quad (26)$$

$$[M(t)]\{\ddot{Y}\} + [C(t)]\{\dot{Y}\} + [K(t)]\{Y\} = \{Q(t)\} \quad (27)$$

Here, $[M(t)]$, $[C(t)]$ and $[K(t)]$ are (n+4) orders coupled time dependent mass, damping and stiffness matrices; $\{Q(t)\}$ is (n+4) order force vector as shown in Eq. (28) and $\{Y\}$ is (n+4) order displacement vector consisting of modal response of bridge combined with vehicle response as shown in Eq. (29). By solving Eq. (27), vehicle responses can be obtained directly from the solution and bridge responses are calculated using Eq. (11).

$$\{Q(t)\} = \begin{Bmatrix} 0 \\ 0 \\ k_{t1}r_1\delta_1 \\ k_{t2}r_2\delta_2 \\ -(\varphi_{11}W_1\delta_1 + \varphi_{21}W_2\delta_2) \\ -(\varphi_{12}W_1\delta_1 + \varphi_{22}W_2\delta_2) \\ \vdots \\ -(\varphi_{1n}W_1\delta_1 + \varphi_{2n}W_2\delta_2) \end{Bmatrix} \quad (28)$$

$$\{Y(t)\} = \begin{Bmatrix} y_s(t) \\ \theta \\ y_{t1}(t) \\ y_{t2}(t) \\ \eta_1(t) \\ \eta_2(t) \\ \vdots \\ \eta_n(t) \end{Bmatrix} \quad (29)$$

5. Bridge deck surface roughness modelling

The wheels of the vehicle are presumed to remain in contact with the bridge deck. Therefore, the displacement of the wheels remain equal to that of the bridge deck at the contact points. The deck surface roughness plays a vital role in stimulating vehicle vibrations which is simulated theoretically. Artificial surface roughness of Class A-B profile according to ISO 8608 classification [39-40] is generated using Eq. (30).

$$r(x) = \sum_{i=0}^N \sqrt{\Delta n} \cdot 2^k \cdot 10^{-3} \cdot \left(\frac{n_0}{i \cdot \Delta n} \right) \cdot \cos(2\pi \cdot i \cdot \Delta n \cdot x + \varphi_i) \quad (30)$$

Where, L is the length of the road profile and B is the sampling interval; x is the abscissa variable from 0 to L ; $\Delta n = 1/L$; $n_{max} = 1/B$; $N = n_{max}/\Delta n = L/B$; k is a constant value which depends on ISO road roughness classification and varies from 3 to 9, corresponding to the road roughness profiles from class A to class H. Also, $n_0 = 0.1$ cycles/m; φ_i is the random phase angle following a uniform probabilistic distribution within 0 to 2π .

6. Determination of dynamic impact factor of the bridge

The equations representing the VBI system are the differential equation set with time-varying coefficients. Numerical analysis is performed here to solve the coupled system. Newmark's β method is used for solving numerically the coupled formulation as in Eq. (27) resulting from the differential equations of bridge and vehicle subsystems. This numerical method breaks the time into different number of steps with an increment of Δt . Δt represents the time required for the vehicle to traverse one bridge element (ΔL) with a vehicle speed (v), where, $\Delta t = \Delta L/v$. In this section, the vehicle induced bridge dynamic responses are analyzed and the dynamic impact factor of the existing I-girder bridge (Teesta Bridge) is determined. The influence of vehicle speed and bridge deck surface roughness are also investigated. The vehicle wheel and the vehicle body will be studied in terms of acceleration and displacement.

6.1 Vehicle and bridge dynamic parameters

The dynamic parameters of the Half-car vehicle model are provided in Table 1 following the references [8, 41]. The vehicle model is based on the H20-44 truck design loadings included in the American Association of State Highway and Transportation Officials (AASHTO) specifications [42].

Table 1. Vehicle dynamic parameters

Element	Notation	Value
Stiffnesses (N/m)		
Front wheel	k_{t1}	1570000
Rear wheel	k_{t2}	3140000
Front suspension	k_{s1}	232000
Rear suspension	k_{s2}	746000
Damping (N-s/m)		
Front suspension	c_{s1}	50000
Rear suspension	c_{s2}	70000
Masses (kg)		
Front axle	m_{t1}	600
Rear axle	m_{t2}	1000
Body	m_s	17000
Rotary Inertia (kg-m^2)	J	90000
Vehicle speed (km/h)	V	40, 60, 80, 100
Distances from C.G.(m)		
From front wheel	a_1	3.8
From rear wheel	a_2	1.5

Teesta Bridge is a simply supported PC I-girder bridge and consists of five girders with 200 mm thick deck slab. Each span of the bridge is 50 m. A single lane of the bridge subjected to one vehicle is considered for the finite element modelling. The flexural rigidity (EI) and mass of the bridge girder is calculated as $6.96 \times 10^{10} \text{ Nm}^2$ and 6818.5 kg/m respectively. 5% modal damping is assumed for the bridge for all the modes. It is to be mentioned that the allowable maximum vehicle speed is 60 km/hr for this bridge.

6.2 Dynamic impact on bridge for front wheel

Using the parameters of vehicle and bridge, the coupled vehicle-bridge interaction problem as in Eq. (27) is solved and the contact point forces are calculated using Eqns. (20-21). Four vehicle speeds are considered such as 40 km/hr, 60 km/hr, 80 km/hr and 100 km/hr.

In this section, a detail description of IM for the first contact point is provided. This study also describes the amplification of the contact point forces on the bridge due to VBI with respect to static vehicle loading. The front wheel contact point force of the vehicle passing the bridge at different speeds are typically shown in Fig. 5. It gives the insight of actual point force on the bridge in a vehicle bridge interaction system. The static point force of front wheel at the first contact point on the bridge is $(\frac{m_s}{a} \times a_2 + m_{t1}) \times g$ or $5.30 \times 10^4 \text{ N}$. Fig. 5 shows that the dynamic contact point force varies on the bridge profile due to VBI which is significantly higher than static contact point

force. The difference between the static point force and the maximum dynamic point force is calculated in Table 2 which varies from 22.5% to 47.2% for different vehicle speeds. It also shows that maximum dynamic force increases rapidly with the increase of vehicle speed.

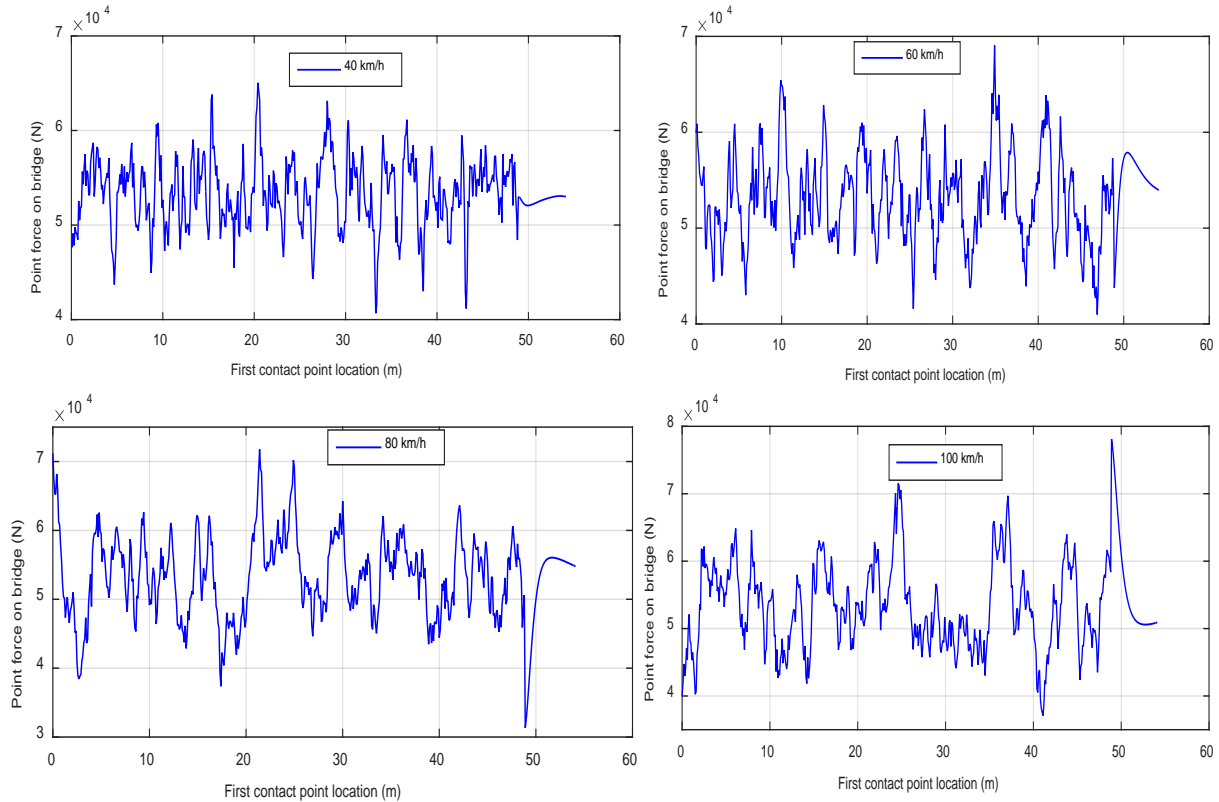


Figure 5. Front wheel contact point forces at different vehicle speeds along the bridge span

Table 2. Front wheel contact point forces

Vehicle speed (kmh-1)	Static Point Force (N)	Maximum Dynamic Point Force (N)	Percent Increase (%)
40	5.30×10^4	6.51×10^4	22.5
60	5.30×10^4	6.91×10^4	30.1
80	5.30×10^4	7.18×10^4	35.2
100	5.30×10^4	7.81×10^4	47.2

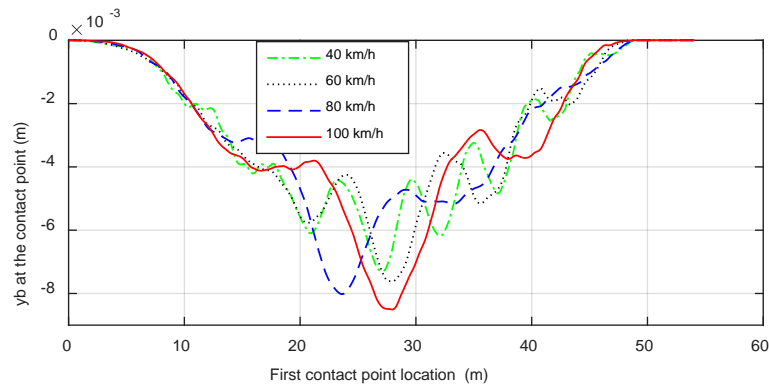


Figure 6. Bridge dynamic displacement at front wheel contact point considering VBI

Now, the vehicle induced dynamic displacement of the bridge is calculated for different vehicular velocities. Fig. 6 displays the vertical displacement (y_b) of bridge at different contact point of the wheel on the bridge considering vehicle bridge interaction obtained from Eq. (27). It also shows the vertical displacement responses of the bridge with the change of vehicle speeds. At lower vehicle speed, due to comparatively lower dynamic

influence, the bridge vertical displacement is less while with the increase of speed, the displacement increases. A finite element software package, SAP2000 [43] is used to obtain the bridge static displacement response at wheel contact points using the built-in moving load analysis program of the software to compare with the dynamic displacement as calculated following the VBI formulation considered in this study. Fig. 7(a) shows the moving static wheel loads on the bridge and Fig. 7(b) represents the maximum vertical displacement envelope of the bridge due to moving static vehicle loads. From Fig. 7(b), the maximum static displacement is calculated which is tabulated in Table 3.

At this point, the dynamic displacement considering VBI and maximum static displacement of the bridge for the given vehicle are available, the dynamic impact factor (IM) for front wheel contact point of the Teesta Bridge is calculated in Table 3. The bridge was built according to AASHTO 2005 [44] bridge standard, where dynamic impact factor was calculated as per Eq. (31), where, L is the length of the bridge in feet, which result in the IM value of 0.176 or 17.6%. However, from Table 3, it is evident that the considerations of bridge deck roughness and also the VBI have result in higher IM than the design IM value used in the bridge.

$$IM = \frac{50}{L+125} \quad (31)$$

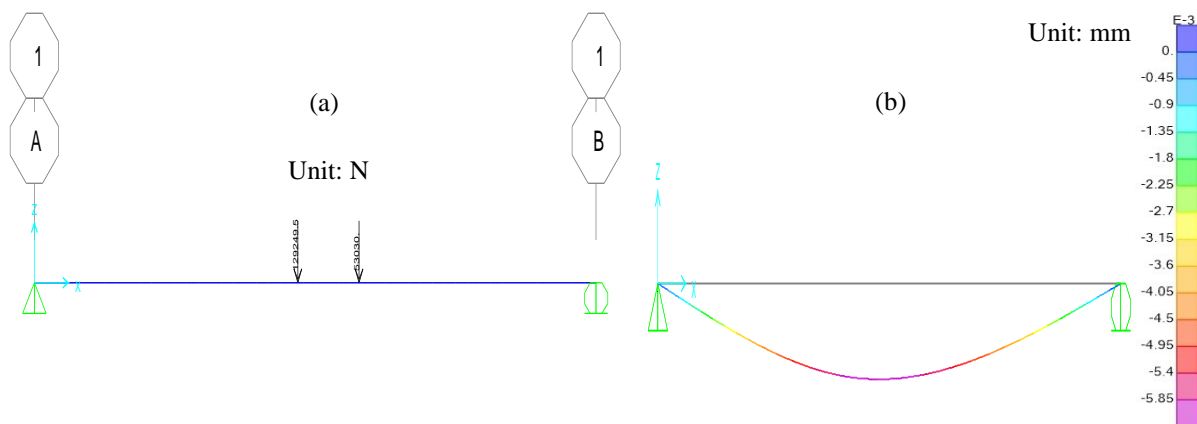


Figure 7. Bridge static displacement due to moving vehicle load

Table 3. Dynamic impact factor (IM) for front wheel contact point

Vehicle speed (kmh-1)	Static Displacement (mm)	Maximum Dynamic Displacement (mm)	IM (%)
40	6.1	7.3	19.7
60	6.1	7.7	26.2
80	6.1	8.0	31.2
100	6.1	8.5	39.3

6.3 Dynamic impact with and without considering VBI

Usually, most of the common finite element software do not consider Vehicle-Bridge Interaction while calculating the dynamic vertical displacement of bridge subjected to moving vehicle load calculated using dynamic time history analysis procedure. In this section, the dynamic impact is compared with and without considering VBI. To determine the dynamic impact without considering VBI, the bridge is modeled using SAP2000 FE software as in Fig. 7(a) and the dynamic time history analysis is performed under moving vehicle load. Fig. 8 displays the comparison between the dynamic displacement response of the bridge with and without considering the VBI for a particular vehicle speed of 80 Kmh⁻¹, where vertical displacement of the bridge is plotted against the first wheel contact point location of vehicle on the bridge. It is evident from Fig. 8 that, there is significant rise in bridge displacement if VBI is considered. Table 4 shows the difference in IM between the two cases.

Table 4. Bridge dynamic deflection with and without consideration of VBI

Type of Analysis	Maximum Dynamic Displacement (mm)	IM (%)
Without VBI	6.5	6.6
With VBI	8.1	32.8

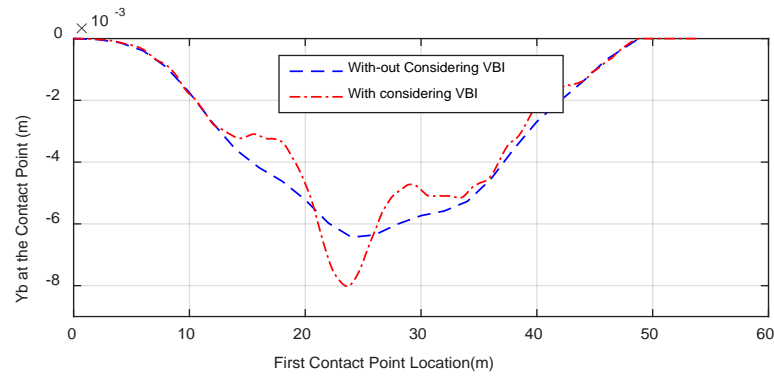


Figure 8. Vertical dynamic displacement of bridge with and without considering VBI

6.4 Dynamic impact on bridge for rear wheel

Similar to the front wheel, the contact point force for the rear wheel also varies throughout the bridge length due to VBI. The static point force for rear wheel at the second contact point on the bridge is $(\frac{m_s}{a} \times a_1 + m_{t2}) \times g$ or 1.29×10^5 N. Fig. 9 shows that the contact point force on the bridge for different vehicle speeds while the rear wheel passes the bridge is neither constant nor equal to the static force. The maximum dynamic force is determined and percent increase as compared to the static force is calculated in the Table 5.

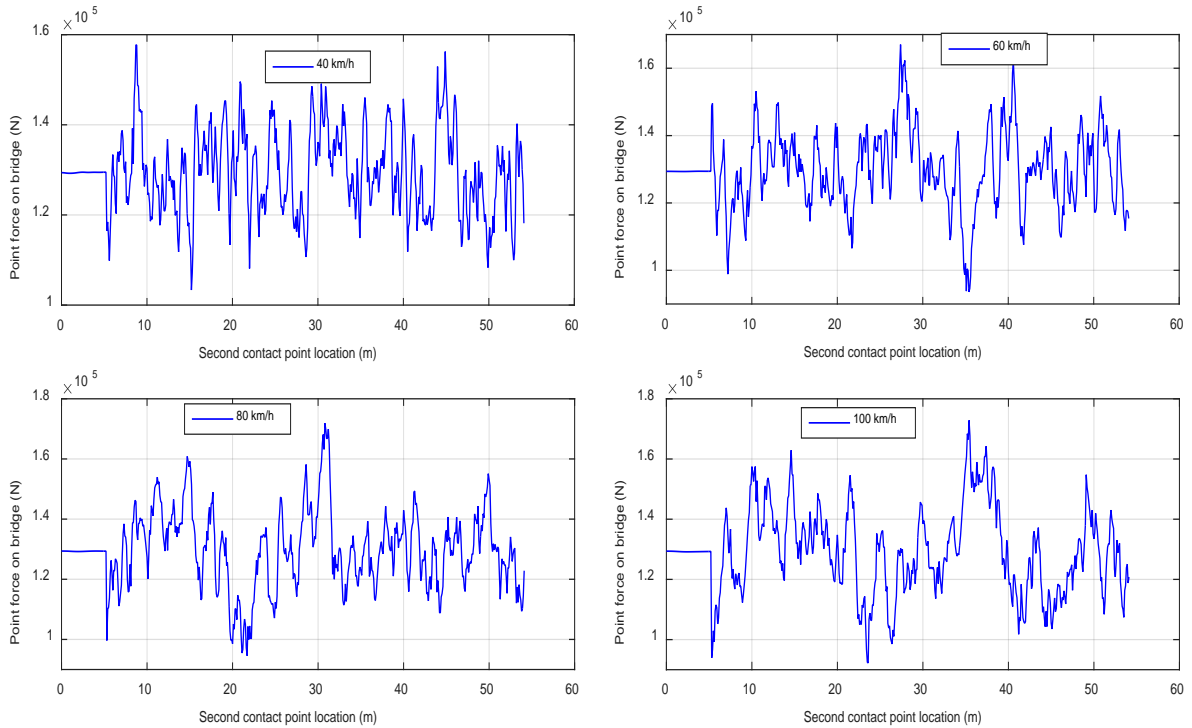


Figure 9. Contact point force of rear wheel along the bridge span

Table 5. Rear wheel contact point forces

Vehicle Speed (kmh-1)	Static Point Force (N)	Maximum Dynamic Point Force (N)	Percent Increase (%)
40	1.29×10^5	1.58×10^5	21.8
60	1.29×10^5	1.67×10^5	29.1
80	1.29×10^5	1.71×10^5	32.2
100	1.29×10^5	1.73×10^5	33.7

The dynamic displacement of the bridge at rear wheel contact point is shown in Fig. 10 for the different vehicle speeds considered in this study. The displacement is much more than the front wheel contact point as higher value of dynamic force is observed on the rear wheel contact point. The displacement curve is not smooth as well due to

variation of dynamic forces over the bridge. Dynamic impact with respect to the static displacement of bridge, is also determined for this case in Table 6. It is understood that dynamic impact of the rear wheel contact point follows the same trend as front wheel contact location with the higher magnitude than previous one as the static force on rear wheel contact point is higher than that of the front wheel.

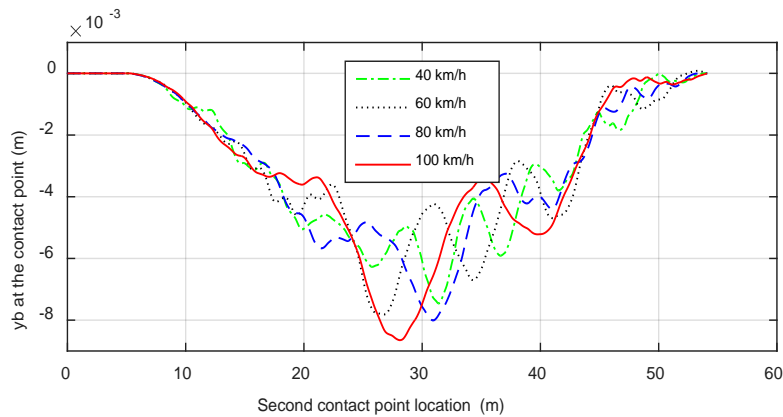


Figure 10. Bridge dynamic displacement at rear wheel contact point

Table 6. Dynamic impact (IM) for rear wheel contact point

Vehicle Velocity (kmh-1)	Static Displacement (mm)	Maximum Dynamic Displacement (mm)	IM (%)
40	6.1	7.4	21.3
60	6.1	7.8	27.9
80	6.1	8.1	32.8
100	6.1	8.7	42.6

6.5 Dynamic impact for different pavement deck surface roughness

For calculation of the dynamic magnification of a bridge, deck surface roughness plays a vital role. Surface characteristics of the deck pavement has influence on the VBI system by increasing the force on the bridge and thereby influencing the dynamic displacement of the bridge. Higher pavement surface roughness will eventually result in increasing the contact force on the bridge which will result in large vertical displacement of the bridge. Four surface roughness conditions are considered as Class A-B, Class B-C, Class C-D and Class D-E. Next, all the calculations are performed similarly as described in the previous sections and finally the dynamic contact point forces and vertical dynamic displacements of the bridge for each roughness cases are determined. Table 7 shows the percent increase in wheel contact forces over static one for various deck surface roughness conditions for a typical vehicle speed of 80 km/h. Fig. 11 shows the bridge contact point dynamic displacement for different roughness conditions. It is observed that the bridge vertical dynamic displacement is comparatively higher for the higher surface roughness condition. The dynamic impact for different roughness conditions are also calculated in Table 8.

Table 7. Dynamic contact point force for different surface roughness

Surface Roughness	Maximum Dynamic Point Force (N)	Percent Increase (%)
Class A-B	7.18×10^4	35.2
Class B-C	8.60×10^4	62.0
Class C-D	1.11×10^5	109.1
Class D-E	1.76×10^5	231.5

Table 8. Dynamic impact for different bridge deck surface roughness

Surface Roughness	Maximum Dynamic Displacement (m)	IM (%)
Class A-B	0.0080	31.2
Class B-C	0.0088	44.3
Class C-D	0.0102	67.2
Class D-E	0.0129	111.8

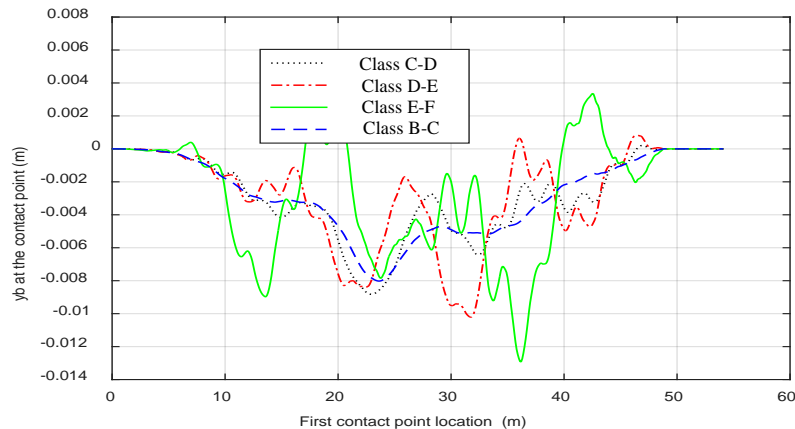


Figure 11. Bridge dynamic displacement under wheel contact point for different surface roughness

7. Conclusions

Pre-stressed Concrete (PC) I-girder bridges are widely used for highways; the dynamic impact factors (IM) of these bridges vary within a wide range. This paper examines the dynamic impact factor of a 50 m span existing PC I-girder Bridge named as Teesta Bridge situated in Bangladesh considering the effect of vehicle bridge interaction phenomenon. The influences of the vehicle travelling speed and bridge deck surface roughness on the impact factor are also investigated. For vehicle bridge interaction modelling, the Half-car vehicle dynamic model is utilized and for the bridge, a discretized finite element model is developed. The coupling between the two subsystems is performed based on compatibility condition at the contact point of the wheel and the bridge which results in a time dependent complex mathematical formulation of the combined system. Newmark- β method, is utilized to solve the coupled formulation to obtain the bridge and the vehicle responses. The conclusions of this study can be drawn as follows:

- The contact point forces of wheels on the bridge increase significantly due to dynamic effect than that of static wheel loads.
- The dynamic displacement and IM of the bridge increase with the increase of vehicle speed.
- The bridge was designed for an impact factor of 17.6%. However, in this study, it is observed that with due consideration of vehicle bridge interaction and pavement surface roughness, the dynamic impact exceeds the designed value for all the vehicle speeds considered.
- For the allowable speed limit of 60 km/hr for the bridge, the IM is found in the range of 26% to 28% for front and rear wheel contact points. For higher value of vehicle speed, the impact factor keeps rising and for a speed of 100 kmh^{-1} , it becomes more than 40%.
- The IM for the rear wheel contact is higher than that of front wheel, which infers that with increment in loading the IM also increases.
- Deck surface roughness also affects the dynamic behavior of the bridge significantly. The impact factor increases with the increase of roughness. Therefore, the deck surface roughness should be kept in good condition to avoid the increase in IM value.

A future work is required to be performed on the implementation of this method in the field experiment to investigate the impact factor of the bridge experimentally.

8. Reference

- [1] Xia H, De Roeck G, Goicolea JM. Bridge vibration and controls: new research. Nova Science Publisher, Inc., New York. 2012.
- [2] Deng L, Cai CS. Development of dynamic impact factor for performance evaluation of existing multi-girder concrete bridges. *Engineering Structures*. 2010; 32(1):21-31.
- [3] Deng L, He W, Shao Y. Dynamic impact factors for shear and bending moment of simply supported and continuous concrete girder bridges. *Journal of Bridge Engineering*. 2015; 20(11):04015005.
- [4] Huang D. Dynamic analysis of steel curved box girder bridges. *Journal of Bridge Engineering*. 2001; 6(6):506-513.
- [5] Battista RC, Pfeil MS, Carvalho EML. Vehicle-structure interaction effect on the fatigue life of steel orthotropic decks. *Proceedings of the 8th International Conference on Structural Dynamics, EUROLYN 2011, Leuven, Belgium*. 2011 July 4-6. p.1-7.

- [6] Akiyama H, Fukada S, Kajikawa Y. Numerical study on the vibrational serviceability of flexible single span bridges with different structural systems under traffic load. *Structural Engineering International*. 2007; 17(3):256-263.
- [7] Chen SR, Cai CS, Levitan M. Understand and improve dynamic performance of transportation system—a case study of Luling Bridge. *Engineering structures*. 2007; 29(6):1043-1051.
- [8] Law SS, Li J. Updating the reliability of a concrete bridge structure based on condition assessment with uncertainties. *Engineering Structures*. 2010; 32(1):286-296.
- [9] Ayre RS, Ford G, Jacobsen LS. Transverse vibration of a two-span beam under action of a moving constant force. *J. Appl. Mech*. 1950; 17(1):1-12.
- [10] Ayre RS, Jacobsen LS. Transverse vibration of a two-span beam under the action of a moving alternating force. *J. Appl. Mech*. 1950; 17(3):283-290.
- [11] Vellozzi J. Vibration of suspension bridges under moving loads. *J. Struct. Eng., ASCE*. 1967; 93(4):123-138.
- [12] Frýba L. *Dynamics of railway bridges*, 2nd ed. Thomas Telford Publishing, London. 1996.
- [13] Fryba, L. *Vibrations of solids and structure under moving loads*, 3rd ed. Thomas Telford, London. 1999.
- [14] Henchi K, Fafard M, Talbot M, Dhett G. An efficient algorithm for dynamic analysis of bridges under moving vehicles using a coupled modal and physical components approach. *Journal of Sound and Vibration*. 1998; 212(4):663-683.
- [15] Yang YB, Yau JD. Vehicle-bridge interaction element for dynamic analysis. *Journal of Structural Engineering*. 1997; 123(11):1512-1518.
- [16] Chen Y, Tan CA, Bergman LA. Effects of boundary flexibility on the vibration of a continuum with a moving oscillator. *J. Vib. Acoust*. 2002; 124(4):552-560.
- [17] Blejwas TE, Feng CC, Ayre RS. Dynamic interaction of moving vehicles and structures. *Journal of Sound and Vibration*. 1979; 67(4):513-521.
- [18] Galdos NH, Schelling DR, Sahin MA. Methodology for impact factor of horizontally curved box bridges. *Journal of Structural Engineering*. 1993; 119(6):1917-1934.
- [19] Yang YB, Lin BH. Vehicle-bridge interaction analysis by dynamic condensation method. *Journal of Structural Engineering*. 1995; 121(11):1636-1643.
- [20] Chu KH, Garg VK, Wang TL. Impact in railway prestressed concrete bridges. *Journal of Structural Engineering*. 1986; 112(5):1036-1051.
- [21] Yang J, Duan R. Modelling and simulation of a bridge interacting with a moving vehicle system. [M.Sc. Eng. Thesis]. Blekinge Institute of Technology, Sweden, 2013.
- [22] Deng L, Yu Y, Zou Q, Cai CS. State-of-the-art review of dynamic impact factors of highway bridges. *Journal of Bridge Engineering*. 2015; 20(5):04014080.
- [23] Deng L, Cai CS. Identification of parameters of vehicles moving on bridges. *Engineering Structures*. 2009; 31(10):2474-2485.
- [24] Chen SR, Wu J. Dynamic performance simulation of long-span bridge under combined loads of stochastic traffic and wind. *Journal of Bridge Engineering*. 2010; 15(3):219-230.
- [25] Cai CS, Shi XM, Araujo M, Chen SR. Effect of approach span condition on vehicle-induced dynamic response of slab-on-girder road bridges. *Engineering Structures*. 2007; 29(12):3210-3226.
- [26] Li H, Wekezer J, Kwasniewski L. Dynamic response of a highway bridge subjected to moving vehicles. *Journal of Bridge Engineering*. 2008; 13(5):439-448.
- [27] Huang D, Wang TL, Shahawy M. Impact analysis of continuous multigirder bridges due to moving vehicles. *Journal of Structural Engineering*. 1992; 118(12):3427-3443.
- [28] Zhu XQ, Law SS. Dynamic load on continuous multi-lane bridge deck from moving vehicles. *Journal of Sound and Vibration*. 2002; 251(4):697-716.
- [29] Mohseni I, Ashin A, Choi W, Kang J. Development of dynamic impact factor expressions for skewed composite concrete-steel slab-on-girder bridges. *Advances in Materials Science and Engineering*. 2018; ID: 4313671.
- [30] AASHTO. AASHTO LRFD bridge design specifications: Customary US units. American Association of State Highway and Transportation Officials, Washington, DC, USA, 7th edition. 2014.
- [31] Pieraccini M, Miccinesi L, Nejad AA, Fard ANN. Experimental dynamic impact factor assessment of railway bridges through a radar interferometer. *Remote Sensing*. 2019; 11(19):2207.
- [32] Gao Q, Ma Q, Cui K, Li J, Xu C. Numerical investigation of the characteristics of the dynamic load allowance in a concrete-filled steel tube arch bridge subjected to moving vehicles. *Shock and Vibration*. 2020, Article ID 8819137.
- [33] Yang YB, Yau JD, Yao Z, Wu YS. *Vehicle-bridge interaction dynamics: with applications to high-speed railways*. World Scientific Publishing Co. Pte. Ltd, Singapore. 2004.
- [34] Yang YB, Lin CW, Yau JD. Extracting bridge frequencies from the dynamic response of a passing vehicle. *Journal of Sound and Vibration*. 2004; 272(3-5):471-493.

- [35] Yang YB, Yau JD. Vehicle-bridge interaction element for dynamic analysis. *Journal of Structural Engineering*. 1997; 123(11):1512-1518.
- [36] Feng D, Sun H, Feng MQ. Simultaneous identification of bridge structural parameters and vehicle loads. *Computers & Structures*. 2015; 157:76-88.
- [37] Bureau of Research Testing & Consultation (BRTC). Teesta bridge project report. File No. 1247, Dept. of Civil Engineering Library, Bangladesh Univ. of Engineering and Technology, Dhaka, Bangladesh. 2007.
- [38] Chopra, AK. *Dynamics of structures*, 4th ed. Prentice Hall, New Jersey. 2012.
- [39] Múčka P. Simulated road profiles according to ISO 8608 in vibration analysis. *Journal of Testing and Evaluation*. 2017; 46(1):405-418.
- [40] Agostinacchio M, Ciampa D, Olita S. The vibrations induced by surface irregularities in road pavements—a Matlab® approach. *European Transport Research Review*. 2014; 6(3):267-275.
- [41] OBrien EJ, Cantero D, Enright B, González A. Characteristic dynamic increment for extreme traffic loading events on short and medium span highway bridges. *Engineering Structures*. 2010; 32(12):3827-3835.
- [42] AASHTO. AASHTO-LRFD Bridge design specifications. American Association of State Highway and Transportation Officials, Washington DC, 6th edition. 2012.
- [43] SAP2000. *Structural Analysis Program*, Computers and Structures Inc., Berkeley, California. 2020.
- [44] AASHTO 2005. AASHTO LRFD Bridge Design Specifications. American Association of State Highway and Transportation Officials, Washington DC. 2005.

Optimization of the Heavy Cable Suspending a Deck

Harish Chand Giri, *Department of Mechanical Engineering, Aryan Institute of Engineering & Technology, Bhubaneswar, harishchand4@gmail.com*

Saruk Mallick, *Department of Civil Engineering, Raajdhani Engineering College, Bhubaneswar, sarukmallik57@yahoo.co.in*

Chinmay Swain, *Department of Mechanical Engineering, Raajdhani Engineering College, Bhubaneswar, chinmayswain1972@gmail.com*

Satyaprakash Mishra, *Department of Civil Engineering, Capital Engineering College, Bhubaneswar, satyaprakash_m25@gmail.com*

Abstract: For estimating the design seismic forces applied to a bridge structure, the response modification factor (R factor) is a critical quantity. This component takes into account the nonlinear behaviour of bridges when severe ground vibrations occur. To withstand earthquake forces, traditional bridge systems rely on substructure components. As a result, depending on the kind of bridge substructure system, R factors are accessible in the design codes. In the longitudinal direction, the lateral load resisting system of Integral Abutment Bridges (IABs) is more sophisticated than that of standard bridges. In addition to the current stiff link between the superstructure and abutments, it includes contributions from soils behind the abutments and soil/structure interaction (SSI). There is no R factor for IABs in the longitudinal direction that takes into account all of these characteristics in any design code anywhere in the globe. In this study, the R factor for IABs was calculated using the FEMA P695 technique published by the Federal Emergency Management Agency. In the longitudinal direction, it was discovered that 3.5 might be a safe and valid R factor for seismic design of such bridges.

Keywords: Cable; Deck; Optimization; Discrete loads.

1. Introduction

The heavy spanning cable, or cable with self-weight, is a classic example in physics, mathematics and engineering. It was studied since Galileo, but its exact shape, the catenary, awaits the Bernoulli brothers [1]. Recent discussions can be found in [2,3]. The catenary supporting a single concentrated load was first discussed by Routh [4]. Multiple loads were studied by Irvine and Sinclair [5], and by Kim and Lee [6] using finite elements. The catenary cable was extended to include non-uniform self-weight [7], and to three dimensions [8,9]. When inverted, the catenary represents a funicular (moment-less) arch [10].

For a suspension bridge, the main cable (which has self-weight) may also support a horizontal load such as a deck. The cable shape is no longer a catenary. In these cases, numerical means (finite elements, iteration etc) are used. See e.g. [11,12].

Recently the closed-form solution for the heavy cable loaded with a uniform deck was found independently by Wang and Wang [13] and Lewis [14]. This analytic solution greatly simplifies the computation for the cable shape, or the form-finding process. Being exact, it also serves as a benchmark for numerical and other approximate methods. Optimization was not considered in these sources.

A cable can be optimized differently, depending on the object of optimization. Aside from cost optimization (e.g. [15]), there are three basic shape optimizations. The first class of optimization considers the cable of variable cross-sectional area such that the stress everywhere is constant (fully-stressed) [16-19]. The second class of optimization considers the loaded, uniform cable which has a minimum total weight [20-22]. The third class of optimization considers the uniform cable with minimal maximum tension. Such an optimum was found by Wang [23] but only for the uniform catenary (without a load) and Wang [24] for the catenary with a single concentrated load. Minimizing total weight is different from minimizing tension. For example, the cable can be very taut, with minimal weight but very large tension.

The main purpose of the present work is to optimize the heavy uniform cable with a uniform load (deck) with respect to the least cable tension. Such an endeavor is fundamental in the design of suspension bridges. We shall consider the cable spanning different heights, which is important for side spans of suspension bridges.

We assume the weight of the suspenders is negligible in comparison to that of the cable or the deck, and the load due to the deck is spanwise continuously distributed. The assumption of continuous distribution versus the actual situation of discrete distribution will be discussed.

2. Formulation

Fig. 1(a) shows a cable of weight per length ρ suspending a horizontal deck of weight per length $\bar{\rho}$ through discrete suspenders of negligible weight (for twin cables, divided appropriately by two). The deck has span length

L , the cable length is lL , and the cable ends have a height difference of hL . Note that the main span of a suspension bridge usually has cables of equal heights while the end spans must have different heights. Our question is, given the afore-mentioned parameters, what are the maximum tension and the sag of the cable?

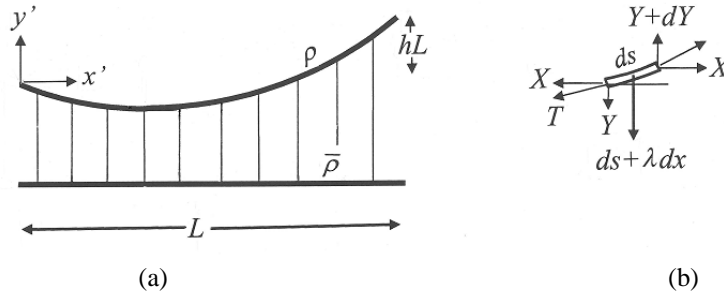


Fig. 1 (a) Spanning cable supporting a deck. (b) Force balance on an elemental segment

Normalize all lengths by L , and all forces by ρL . Let (x,y) be Cartesian coordinates place at the lower (left) end of the cable. Let θ be the local angle of inclination and T be the tension of the cable. The normalized horizontal force X is constant but the vertical force Y varies with the arc length s from the origin.

$$X = T(s) \cos \theta = \text{constant}, \quad Y = T(s) \sin \theta \quad (1)$$

A vertical force balance on an elemental segment ds (Fig. 1b) gives

$$dY = ds + \lambda dx \quad (2)$$

where the density ratio is $\lambda = \bar{\rho}/\rho$.

Geometry dictates

$$\frac{dx}{ds} = \cos \theta, \quad \frac{dy}{ds} = \sin \theta \quad (3)$$

Eqs.(1-3) yield

$$\frac{d}{ds} (T \sin \theta) = 1 + \lambda \cos \theta \quad (4)$$

or

$$X \frac{d\theta}{ds} = \cos^2 \theta [1 + \lambda \cos \theta] \quad (5)$$

The boundary conditions are

$$x|_{s=0} = 0, y|_{s=0} = 0 \quad (6)$$

$$x|_{s=l} = 1, y|_{s=l} = h \quad (7)$$

Integrating Eqs.(3,5) gives

$$x = X \int \frac{d\theta}{\cos \theta (1 + \lambda \cos \theta)} = X [\ln(\tan \theta + \sec \theta) - F(\theta, \lambda) + A] \quad (8)$$

where

$$F(\theta, \lambda) = \begin{cases} \frac{2\lambda}{\sqrt{1-\lambda^2}} \tan^{-1} \left(\frac{\sqrt{1-\lambda}}{\sqrt{1+\lambda}} \tan \frac{\theta}{2} \right), & \lambda < 1 \\ \tan \frac{\theta}{2}, & \lambda = 1 \\ \frac{\lambda}{\sqrt{\lambda^2-1}} \ln \left(\frac{\lambda + \cos \theta + \sqrt{\lambda^2-1} \sin \theta}{1 + \lambda \cos \theta} \right), & \lambda > 1 \end{cases} \quad (9)$$

$$y = X \left[\sec \theta - \lambda \ln \left(\frac{\sec \theta + \lambda}{1 + \lambda} \right) + B \right] \quad (10)$$

Except for the constants A and B , Eqs.(8-10) essentially have the same form as the analytic solution for equal heights [13,14]. However, the form-finding method is different.

Our method is as follows. In order to relate θ and s we further integrate Eq.(5) to obtain

$$s = X[\tan \theta - \lambda \ln(\tan \theta + \sec \theta) + \lambda^2 F(\theta, \lambda) + C] \quad (11)$$

For the present problem, it is still not trivial to find the unknowns A, B, C, X from the boundary conditions Eqs.(6.7).

Let θ_0 be the angle at $s=0$, and θ_l be the angle at the end $s=l$. Evaluating Eqs.(11, 8, 10) at the origin gives

$$C = -\tan \theta_0 + \lambda \ln(\tan \theta_0 + \sec \theta_0) - \lambda^2 F(\theta_0, \lambda) \quad (12)$$

$$A = -\ln(\tan \theta_0 + \sec \theta_0) + F(\theta_0, \lambda) \quad (13)$$

$$B = -\sec \theta_0 + \lambda \ln\left(\frac{\sec \theta_0 + \lambda}{1 + \lambda}\right) \quad (14)$$

Eq.(11) at $s=l$ is then

$$l = X[\tan \theta_l - \lambda \ln(\tan \theta_l + \sec \theta_l) + \lambda^2 F(\theta_l, \lambda) + C] \quad (15)$$

Then eliminate X from Eqs.(7, 8, 10, 15) to yield

$$l[\ln(\tan \theta_l + \sec \theta_l) - F(\theta_l, \lambda) + A] = \tan \theta_l - \lambda \ln(\tan \theta_l + \sec \theta_l) + \lambda^2 F(\theta_l, \lambda) + C \quad (16)$$

$$h[\ln(\tan \theta_l + \sec \theta_l) - F(\theta_l, \lambda) + A] = \sec \theta_l - \lambda \ln\left(\frac{\sec \theta_l + \lambda}{1 + \lambda}\right) + B \quad (17)$$

From Eqs.(16,17) we solve for θ_0, θ_l using a 2D root search algorithm. The horizontal force X can then be obtained from Eq.(15), and the shape of the cable from the parametric Eqs.(8,10). The maximum tension is at the higher end. Eq.(1) gives

$$T = \frac{X}{\cos \theta_l} \quad (18)$$

The sag (if any) is located at $\theta = 0$ or at $s=XC$, provided $0 < s < l$. Table 1 shows the results. For $\lambda = 0$, the deck is absent and the cable is a free catenary. An increase in λ increases the tension and decreases the sag. For shorter cable lengths, the sag disappears since the cable always have positive slope. If $l < \sqrt{1 + h^2}$ the cable cannot span the two end points. Sag always increases with the cable length l . The maximum tension T first decreases then increases with increased l . Given the end points, the cable length and the densities of the cable and deck, one can obtain the tension and sag from Table 1. These tables, presented here for the first time, can be interpolated for practical purposes.

Table 1a. Maximum tension T and sag S (with asterisk) for given height h and length of cable l (density ratio $\lambda = 0$). Empty cells denote the end points cannot be spanned.

l/h	0	0.25	0.5	0.75	1	1.5
1.1	0.8572 0.199*	1.0940 0.067*	--	--	--	--
1.2	0.7621 0.292*	0.9151 0.162*	1.217 0.027*	--	--	--
1.4	0.7782 0.437*	0.9098 0.310*	1.062 0.177*	1.286 0.043*	--	--
1.6	0.8488 0.564*	0.9763 0.437*	1.111 0.308*	1.260 0.174*	1.467 0.043*	--
1.8	0.9342 0.682*	1.060 0.556*	1.190 0.428*	1.325 0.297*	1.474 0.164*	--
2	1.027 0.796*	1.151 0.670*	1.279 0.543*	1.409 0.414*	1.544 0.283*	1.900 0.024*
2.2	1.120 1.015*	1.246 0.781*	1.372 0.654*	1.500 0.526*	1.630 0.397*	1.916 0.133*
2.4	1.216 1.015*	1.342 0.890*	1.468 0.763*	1.594 0.636*	1.723 0.508*	1.989 0.246*

Table 1a. (Continued).

2.6	1.314	1.439	1.564	1.691	1.818	2.077
	1.122*	0.997*	0.871*	0.744*	0.617*	0.358*
2.8	1.411	1.537	1.662	1.788	1.914	2.170
	1.228*	1.103*	0.977*	0.851*	0.724*	0.467*
3	1.510	1.635	1.760	1.886	2.012	2.266
	1.334*	1.209*	1.083*	0.957*	0.830*	0.574*

Table 1b. Maximum tension T and sag S (with asterisk) for given height h and length of cable l (density ratio $\lambda = 2.5$).

l/h	0	0.25	0.5	0.75	1	1.5
1.1	2.849	3.590	--	--	--	--
	0.201*	0.069*				
1.2	2.399	2.814	3.724	--	--	--
	0.295*	0.165*	0.031*			
1.4	2.212	2.506	2.873	3.489	--	--
	0.444*	0.317*	0.185*	0.052*		
1.6	2.212	2.463	2.742	3.083	3.622	--
	0.573*	0.447*	0.318*	0.186*	0.054*	
1.8	2.263	2.490	2.730	2.999	3.326	--
	0.694*	0.568*	0.440*	0.311*	0.180*	
2	2.334	2.545	2.764	2.998	3.259	4.095
	0.810*	0.684*	0.557*	0.429*	0.299*	0.039*
2.2	2.416	2.615	2.819	3.033	3.262	3.842
	0.922*	0.797*	0.671*	0.543*	0.414*	0.154*
2.4	2.503	2.693	2.887	3.087	3.297	3.782
	1.033*	0.907*	0.781*	0.654*	0.527*	0.268*
2.6	2.594	2.777	2.963	3.153	3.350	3.784
	1.141*	1.016*	0.890*	0.763*	0.636*	0.380*
2.8	2.687	2.864	3.044	3.226	3.414	3.816
	1.248*	1.123*	0.997*	0.871*	0.745*	0.489*
3	2.782	2.954	3.128	3.305	3.485	3.865
	1.355*	1.230*	1.104*	0.978*	0.852*	0.597*

Table 1c. Maximum tension T and sag S (with asterisk) for given height h and length of cable l (density ratio $\lambda = 5$).

l/h	0	0.25	0.5	0.75	1	1.5
1.1	4.849	6.088	--	--	--	--
	0.201*	0.069*				
1.2	4.031	4.709	6.208	--	--	--
	0.296*	0.167*	0.033*			
1.4	3.644	4.102	4.687	5.681	--	--
	0.446*	0.319*	0.188*	0.054*		
1.6	3.574	3.953	4.379	4.912	5.772	--
	0.575*	0.449*	0.321*	0.190*	0.058*	
1.8	3.591	3.924	4.280	4.684	5.189	--
	0.697*	0.571*	0.444*	0.315*	0.183*	
2	3.642	3.944	4.259	4.601	4.991	6.294
	0.813*	0.687*	0.561*	0.433*	0.304*	0.043*
2.2	3.711	3.990	4.277	4.582	4.914	5.786
	0.926*	0.801*	0.675*	0.547*	0.419*	0.158*
2.4	3.789	4.050	4.318	4.597	4.893	5.599
	1.037*	0.911*	0.785*	0.659*	0.531*	0.273*
2.6	3.874	4.121	4.373	4.632	4.904	5.519
	1.146*	1.020*	0.895*	0.768*	0.641*	0.385*
2.8	3.962	4.198	4.437	4.682	4.936	5.492
	1.254*	1.128*	1.002*	0.876*	0.750*	0.494*
3	4.053	4.280	4.508	4.742	4.982	5.497
	1.360*	1.235*	1.109*	0.983*	0.857*	0.603*

3. Optimization

Since the maximum tension is large when the cable is taut (large horizontal force X), and again large when the cable is slack (large self-weight), there exists an optimum length for given end points and relative deck weight such that maximum tension is minimized. Using our method described in the previous section and varying the cable length, this optimum is determined. Table 2 shows the optimum cable length for various deck relative weights λ and height ratios h . The optimum length (for minimum tension) increases with both deck weight and height difference.

Table 2. The optimum length l , the maximum tension T (in parentheses), and the sag S (in brackets).

$h \backslash \lambda$	0	0.5	1	2	5
0	1.258	1.319	1.370	1.453	1.637
	(0.7544)	(1.057)	(1.351)	(1.922)	(3.573)
	[0.338]	[0.383]	[0.421]	[0.479]	[0.598]
0.5	1.377	1.461	1.537	1.670	1.987
	(1.061)	(1.417)	(1.757)	(2.410)	(4.259)
	[0.161]	[0.223]	[0.275]	[0.361]	[0.553]
1	1.673	1.762	1.846	2.007	2.414
	(1.453)	(1.839)	(2.208)	(2.914)	(4.893)
	[0.0859]	[0.148]	[0.203]	[0.302]	[0.539]
2	2.491	2.571	2.656	2.828	3.320
	(2.351)	(2.764)	(3.161)	(3.925)	(6.066)
	[0.0387]	[0.0896]	[0.142]	[0.244]	[0.519]
5	5.335	5.395	5.464	5.620	6.143
	(5.258)	(5.691)	(6.116)	(6.944)	(9.302)
	[0.0138]	[0.0492]	[0.0910]	[0.181]	[0.466]

The $\lambda = 0$ (cable without a deck) values agree, to 1%, with the results of the free catenary studied by Wang [23]. Fig.2 shows typical shapes of the optimum cable.

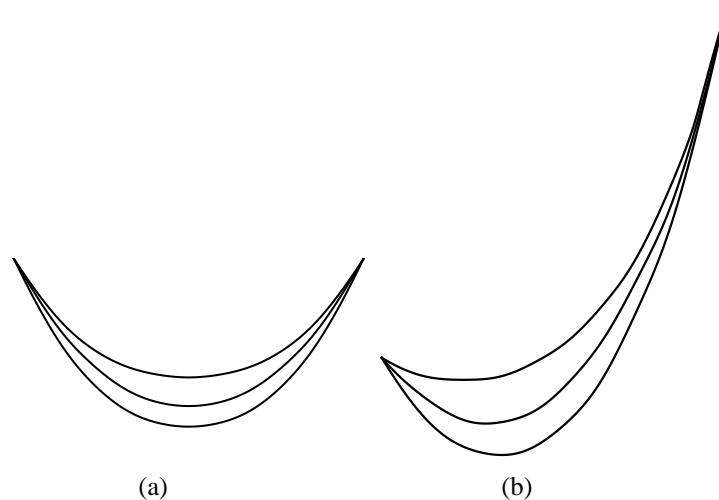


Fig. 2. Optimum cable shapes. The cable is supported at two ends with a deck (not shown). The horizontal distance between the supports is L while the vertical height difference is hL . The ratio of the deck density to the cable density is λ . (a) $h=0$, from top: $\lambda=0,1,2$ (b) $h=1$, from top: $\lambda=0,1,2$

4. Discrete loads

In the previous formulation we assumed the deck weight is continuously distributed on the cable. However, for a suspension bridge the deck is usually hung from the cable at equally-spaced discrete points. In this section we investigate the condition such that the continuous load would be a good approximation to the discrete load. We shall illustrate using a cable which spans equal heights ($h=0$).

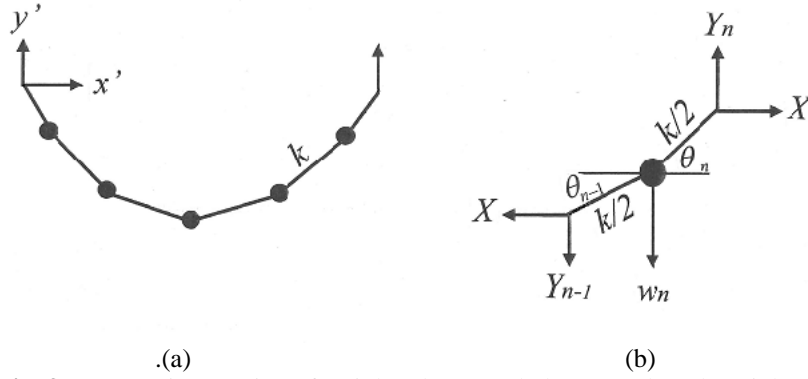


Fig. 3. (a) Hanging a string of weights (b) Force balance on the n^{th} weight.

Fig. 3(a) shows a heavy cable discretized into N concentrated weights connected by cable segments of negligible mass. The lengths and forces are normalized as before. The total length of the cable is $l=Nk$, where k is the distance between the weights, except the distance to the ends is $k/2$. Fig. 3(b) shows the force balance on the n^{th} weight from the left end. Let the location of this weight be (x_n, y_n) and the inclination angles of the cable segments be θ_{n-1} and θ_n as shown. The discrete weight includes the normalized self-weight of the cable k and the weight of the deck, proportional to the vertical projection

$$w_n = k + k\lambda(\cos \theta_{n-1}/2 + \cos \theta_n/2) \quad (19)$$

The vertical force balance is

$$Y_n = w_n + Y_{n-1} \quad (20)$$

The constant horizontal force X is related by

$$X \tan \theta_n = Y_n \quad (21)$$

Eqs.(19-21) yield

$$X(\tan \theta_n - \tan \theta_{n-1}) = k + k\lambda(\cos \theta_n + \cos \theta_{n-1})/2 \quad (22)$$

From geometry, the coordinates are

$$x_n = x_{n-1} + \frac{k}{2}(\cos \theta_n + \cos \theta_{n-1}) \quad (23)$$

$$y_n = y_{n-1} + \frac{k}{2}(\sin \theta_n + \sin \theta_{n-1}) \quad (24)$$

Due to symmetry

$$\theta_n = -\theta_{N-n} \quad (25)$$

the vertical forces at the ends are equal to half the total weight

$$-Y_0 = Y_N = \frac{kN+\lambda}{2} \quad (26)$$

From Eqs.(21,26)

$$\theta_0 = -\tan^{-1} \left(\frac{kN+\lambda}{2X} \right) \quad (27)$$

Our method of solution is as follows. Given the deck density ratio λ , the number of concentrated weights N , the length of cable l , then segment length is $k=l/N$. Now guess X and use Eq.(27) as an initial condition for the nonlinear first order difference equation Eq.(22). When the sequence of θ_n is obtained, Eq.(23) yields

$$x_n = \frac{k}{2} (\cos \theta_0 + 2 \sum_{j=1}^{n-1} \cos \theta_j) \quad (28)$$

Thus if

$$x_N + \frac{k}{2} \cos \theta_N = 1 \quad (29)$$

a solution is obtained. Otherwise the guess X is adjusted. Then the maximum tension is

$$T = \sqrt{Y_0^2 + X^2} \quad (30)$$

Eq.(24) gives the vertical displacement. For the n^{th} weight

$$y_n = \frac{k}{2} (\sin \theta_0 + 2 \sum_{j=1}^{n-1} \sin \theta_j) \quad (31)$$

If N is even, $\theta_{N/2} = 0$ and the cable segment at the mid point is horizontal. The sag is

$$S = -y_{N/2} = -y_{1+N/2} \quad (32)$$

If N is odd, the mid point is at the weight at $n=(N+1)/2$. Thus the sag is

$$S = -y_{(N+1)/2} \quad (33)$$

Our question is, for the same length and weight of the cable and the weight of the deck, when would the discrete solution of this section be equivalent to the continuous solution of the previous section? Since l is also the normalized total weight of the cable, we fix $l=Nk$ and increase N (decrease k), starting from a single concentrated weight $N=1$.

Table 3 shows the results when the deck is absent ($\lambda = 0$) and $l=2$. Notice when odd N increases, the horizontal force X , the maximum tension T and the sag S decrease to the continuous values indicated by $N = \infty$. When even N increases, X , T , S increase to the continuous values. The table shows that when $N>10$, the maximum tension is within 0.1% and the sag is within 1% of the continuous values. We conclude that a continuous catenary cable is statically equivalent to a string of equally-spaced discrete weights if the number of weights is more than 10.

Table 4 shows the case when the cable is supporting a deck. Here we used a density ratio of $\lambda = 5$ and the optimum length of $l=1.637$ from Table 2. Although the tension is larger and the sag smaller, the general trend with increased N is similar to that of Table 3, i.e., for $N>10$ the cable with discrete loads is equivalent to the cable with continuous loads.

Table 3. Results for the horizontal force X , the maximum tension T and the sag S for equal heights and $\lambda = 0$, $l = 2$. The cable is approximated by N discrete weights.

N	X	T	S
1	0.577	1.155	0.866
2	0.000	1.000	0.500
3	0.265	1.035	0.844
4	0.215	1.023	0.704
5	0.238	1.028	0.824
6	0.228	1.026	0.753
7	0.232	1.027	0.812
8	0.230	1.026	0.772
9	0.231	1.026	0.806
10	0.230		0.781
11	0.230		0.803
12			0.786
13			0.801
14			0.789
∞	0.230	1.026	0.796

Table 4. Results for the horizontal force X , the maximum tension T and the sag S for equal heights and $\lambda = 5, l = 1.637$. The cable is approximated by N discrete weights.

N	X	T	S
1	2.561	4.192	0.648
2	0.755	3.403	0.399
3	1.346	3.581	0.627
4	1.281	3.557	0.535
5	1.321	3.572	0.613
6	1.314	3.569	0.568
7	1.321	3.572	0.606
8	1.320	3.572	0.581
9	1.322	3.572	0.603
10	1.322	3.572	0.587
11	1.323	3.573	0.602
12	1.323	3.573	0.591
13	1.324		0.601
14			0.593
∞	1.326	3.573	0.598

5. Conclusions

The form-finding method is as follows. Given the horizontal span L , the weight per length of the cable ρ the weight per length of the deck $\bar{\rho}$, the height between the cable ends hL , and the cable length lL , one can find the maximum tension $T' = T\rho L$ and sag SL from Table 1. However, if one seeks optimum length such that the maximum tension is minimized, then one uses Table 2. Notice that Tables 1,2 are applicable to systems with more than 10 discrete suspenders. If there are fewer suspenders, the discrete load method of Section 4 should be used.

The spanning cable with non-negligible weight and suspending a uniform deck is now solved semi-analytically. The problem is determined by three non-dimensional parameters: the cable length ratio l , the height ratio h , and the density ratio λ . Useful tables for maximum tension and sag are constructed. In addition, optimum cables lengths for minimum tension are found. These new results are useful for the preliminary design of deck-carrying cables, such as suspension bridges.

Notation

A, B, C constants

h ratio of support height difference to span

k distance between discrete weights

l ratio of cable length to deck span

L deck span

N number of weights

s normalized arc length of cable

S normalized sag

T normalized tension of cable

w discrete weight

x, y normalized coordinates

X normalized horizontal force

Y normalized vertical force

λ $\bar{\rho}/\rho$

ρ cable density (weight/length)

$\bar{\rho}$ deck density (weight/length)

θ local inclination of cable

Subscripts

0 evaluated at $s=0$

1 evaluated at $s=1$

n n th weight

6. References

- [1] Salmon G. Higher plane curves. Chelsea, New York. 1960; p.289.
- [2] Griva IA. Case studies in optimization: Catenary problem. *Opt. Eng.* 2009; 6: 463-482.
- [3] Behrooz F. A fresh look at the catenary. *Eur. J. Phys.* 2014; 35: 055007.
- [4] Routh EJ. A treatise on analytical statics. Vol.1 2nd Ed. 1909; Chap. 10.
- [5] Irvine HM, Sinclair GB. The suspended elastic cable under the action of concentrated vertical loads. *Int. J. Solids Struct.* 1976; 12: 309-317.
- [6] Kim KS, Lee HS. Analysis of target configurations under dead loads for cable-supported bridges. *Comp. Struct.* 2001; 79: 2681-2692.
- [7] Fallis MC. Hanging shapes of nonuniform cables. *Am. J. Phys.* 1997; 65: 117-122.
- [8] Impollonia N, Ricciardi G, Saitta F. Statics of elastic cables under 3D point forces. *Int. J. Solids Struct.* 2011; 48: 1268-1276.
- [9] Greco L, Impollonia N, Cuomo M. A procedure for the static analysis of cable structures following elastic catenary theory. *Int. J. Solids Struct.* 2014; 51: 1521-1533.
- [10] Heyman J. The masonry arch. Horwood, Chichester, England 1982.
- [11] Li C, He J, Zhang Z, Liu Y, Ke H, Dong C, Li H. An improved analytical algorithm on main cable system of suspension bridge. *Appl. Sci.* 2018; 8:1358.
- [12] Zhou Y, Chen S. Iterative nonlinear cable shape and force finding technique of suspension bridges using elastic catenary configuration. *J. Eng. Mech.* 2019;145(5): 04019031.
- [13] Wang CY, Wang CM. Closed-form solutions for funicular cables and arches. *Acta Mech.* 2015; 226:1641-1645.
- [14] Lewis WJ. Mathematical model of a moment-less arch. *Proc. Roy. Soc. A.* 2016; 472: 20160019.
- [15] Lewis WJ. A mathematical model for assessment of material requirements for cable supported bridges: Implications for conceptual design. *Eng. Struct.* 2012; 42: 266-277.
- [16] Hill RD, Rozvany GIN, Wang CM, Leong KH. Optimization, spanning capacity, and cost sensitivity of fully-stressed arches. *J. Struct. Mech.* 1979; 7: 375-410.
- [17] Tadjbakhsh IG. Stability and optimum design of arch-type structures. *Int. J. Solids Struct.* 1981; 17: 565-574.
- [18] Serra M. Optimal arch: Approximate analytical and numerical solutions. *Comp. Struct.* 1994; 52: 1213-1220.
- [19] Marano GC, Trentadue F, Petrone F. Optimal arch shape solution under static vertical loads. *Acta Mech.* 2014; 225: 679-686.
- [20] Wang CM. Optimum shape of cables. *J. Eng. Mech.* 1984; 110: 1649-1653.
- [21] Teo KL, Ang BW, Wang CM. Least weight cables: Optimal parameter selection approach. *Eng. Opt.* 1986; 9: 249-264.
- [22] Wang CM, Pulmano VA, Lee SL. Cable optimization under self-weight and concentrated loads. *J. Struct. Mech.* 1986; 14: 191-207.
- [23] Wang CY. The optimum spanning catenary. *Eur. J. Phys.* 2015; 36: 028001.
- [24] Wang CY. Optimum length of a heavy cable with a concentrated load. *J. Eng. Mech.* 2017; 143(12): 06017017.

Seismic Design of Integral Abutment Bridges

Sampad Kumar Pradhan, *Department of Civil Engineering, Aryan Institute of Engineering & Technology, Bhubaneswar, s_kumar6@gmail.com*

Tapan Kumar Mohanty, *Department of Mechanical Engineering, Aryan Institute of Engineering & Technology, Bhubaneswar, tapankmohanty789@yahoo.co.in*

Suryaleen Rout, *Department of Civil Engineering, NM Institute of Engineering & Technology, Bhubaneswar, suryaleenrout@yahoo.co.in*

Anand Mandal, *Department of Civil Engineering, Raajdhani Engineering College, Bhubaneswar, anandmandal1@gmail.com*

Abstract: For estimating the design seismic forces applied to a bridge structure, the response modification factor (R factor) is a critical quantity. This component takes into account the nonlinear behaviour of bridges when severe ground vibrations occur. To withstand earthquake forces, traditional bridge systems rely on substructure components. As a result, depending on the kind of bridge substructure system, R factors are accessible in the design codes. In the longitudinal direction, the lateral load resisting system of Integral Abutment Bridges (IABs) is more sophisticated than that of standard bridges. In addition to the current stiff link between the superstructure and abutments, it includes contributions from soils behind the abutments and soil/structure interaction (SSI). There is no R factor for IABs in the longitudinal direction that takes into account all of these characteristics in any design code anywhere in the globe. In this study, the R factor for IABs was calculated using the FEMA P695 technique published by the Federal Emergency Management Agency. In the longitudinal direction, it was discovered that 3.5 might be a safe and valid R factor for seismic design of such bridges.

Keywords: Response modification factor; Integral abutment bridge; Seismic design; FEMA P695; Soil/Structure interaction.

1. Introduction

For many years, long span bridges were mainly designed and constructed as multiple simply supported spans until the moment distribution method was published in 1930 and facilitated the analysis of continuous spans and rigid frame bridges [1]. The integral abutment bridge (IAB) also benefits from continuity in a different way, namely between the superstructure and substructure, very similar to an arch bridge. This continuity eliminates the need for expansion joints at the abutments and due to extensive and costly problems associated with these joints, IABs are becoming a bridge system of choice throughout the world. The integration of abutment and deck speeds up the construction process of IABs and especially the accuracy required to install bearing devices. The maintenance costs of expansion joint devices are no longer of concern for IABs and less damage is expected to the structure as cars pass over the bridge. Also, in an earthquake, the unseating of the deck, which is a major problem in conventional bridges, is eliminated for IABs. Despite many advantages, secondary stresses due to thermal, shrinkage and creep are more of a concern for IABs. In general, the analysis of IABs is very complex and involves an indeterminate structure with soil/structure interaction (SSI) in its fullest form. The SSI should encompass soil/pile and soil/abutment and near/far field soil effects. Many researchers have worked on this complex SSI problem and suggested simplified analysis techniques for IABs under gravity, thermal and seismic actions [2-8].

The response modification factor (R factor) is a crucial parameter for calculating the design earthquake forces of a bridge structure in the code specified linear seismic analysis procedures such as equivalent static load and response spectrum analyses [9]. This factor considers the nonlinear performance of bridges during strong ground motions. Conventional bridge structures rely on the substructure components to resist earthquake forces. Accordingly, there are R factors available in the design codes like AASHTO [9] based on the type of substructure system. The lateral force resisting system (LFRS) of IABs in the longitudinal direction is more complex than ordinary bridges. This is because of the lateral stiffness contribution from many components like the deck, abutments, piles, near field soils in the active and passive states, and soil inertia in the farfield and the interaction between them. There is no R factor available in any design code throughout the world for seismic design of IABs in the longitudinal direction that considers all the above parameters. This is mainly because an accurate analytical nonlinear analysis of these bridges under seismic actions is a hard task. In addition, the actual measured seismic responses of these bridges are only available in limited cases.

Note that the transverse seismic response of IABs is very similar to conventional bridges with abutment walls resisting the seismic forces. Hence, in the transverse direction the available bridge design code prescribed R factors can be used with confidence.

This paper uses a nonlinear finite element (FE) analysis model that can capture the interaction between soils and all the structural components to analyze the IABs under gravity and seismic loading. In addition, the new FEMA P695 [10] methodology has been used to estimate the R factor for seismic design of IABs in the longitudinal direction.

2. Literature review

Seismic behavior of integral abutment bridges by considering soil-pile-abutment interaction has been the focus of research for the past two decades. Erhan and Dicleli [2] have shown that using loose sand around piles that are oriented to bend about their weak axes and abutment height less than 4 m without compaction of backfill results limited forces on abutment. In a parametric study of integral abutment bridges, Civjan et al. [3] have shown that IABs behavior is greatly affected by soil parameters and analysis procedure of structure. It was found that soil characteristics might change over time and after several cycles of loading and unloading of the bridge. Another study by Spyarakos et al. [4] have shown the importance of SSI and soil properties on the seismic behavior of IABs. Itani and Pekcan [5] have investigated the behavior of IABs with steel plate girders which led to the development of design recommendations. One of their most important findings was that the pile axis orientation is insignificant in the longitudinal behavior of IABs, because it is controlled by soil-abutment interaction. Another important finding was that the seismic performance of integral abutment bridges is better than the conventional seat type abutment bridges in terms of overall displacement. Also, a formulation for damping of IABs resulting to about 6% damping ratio for steel girder IABs in the longitudinal was recommended.

More recently, Mahjoubi and Maleki [6,7] have developed a new approach for considering embankment static and dynamic active and passive pressures on retaining walls and bridge abutments including IABs. As a result, an appropriate length of embankment finite element model length that minimizes the radiation damping effects has been found. In their study, about 4 times the abutment height for extension length of soil behind abutments was suggested. In their new approach in finite element modeling of IABs, soil pile structure interaction involving both near field and far field soil responses was considered. This method is practical for design purposes, resulting that nonlinearity of piles and soil are significant in analyzing of this system.

Experimental studies on collapse assessment of H-piles under abutment of IABs are very rare, however, Burdette et al. [8] have studied several steel piles driven into clay and noted that that H-piles have high levels of ductility while proposing 0.1 radians as the collapse margin for steel H-piles. Itani and Peckan [5] also have reported 0.1 radians as an appropriate collapse margin rotation for H-piles in their report.

3. FEMA methodology in brief

According to FEMA P695 [10], finding the right R factor for a structural system is a trial-and-error process. A trial R factor of 3.5 was initially selected for the IABs of this research. This value is justified because the longitudinal behavior of IABs is very similar to bents with vertical piles and AASHTO [9] recommends the use of 3.5 for these systems. In the next step, several so-called archetype structures should be developed and designed, such that they can cover all possible geometries and properties that IAB systems in practice might have (e.g., variety of abutment heights, embankment soil properties, etc.). In addition, the potential nonlinearities in the structural system under earthquake loading should be identified and considered in structural modeling and analysis of archetypes. After performing an incremental dynamic analysis (IDA) on each archetype using 22 prescribed far-field ground motions the values of collapse margin ratios (CMRs) are obtained. The ratio of the median collapse intensity to the maximum considered earthquake (MCE) intensity defines the CMR. Pushover analyses are also performed to determine the overstrength and ductility factor for each archetype. These are needed to calculate the spectral shape factors (SSFs). Then the adjusted collapse margin ratios (ACMRs) are calculated by multiplying CMRs and SSFs. The initial R factor is acceptable only if the individual and average ACMRs meet the safety criteria set in the standard, otherwise R factor is adjusted and the procedure is repeated.

The archetypes considered in this study are among the most used IABs in practice. They consist of single span and two span continuous bridges with varying span lengths, soil properties and abutment wall heights. In two-span continuous IABs, the superstructure was considered to be roller supported on the piers. The abutment wall heights were of two types: a 7 m wall type and a 3 m stub type. Two types of embankment soil types were considered: dense and loose, with properties as shown in Table 1. Three span lengths of 10, 20 and 30 meters were also considered. The slab-beam type superstructure of all archetypes was the same and is shown in Fig. 1-2. The abutment pile cap and piles are also depicted in Fig. 3.

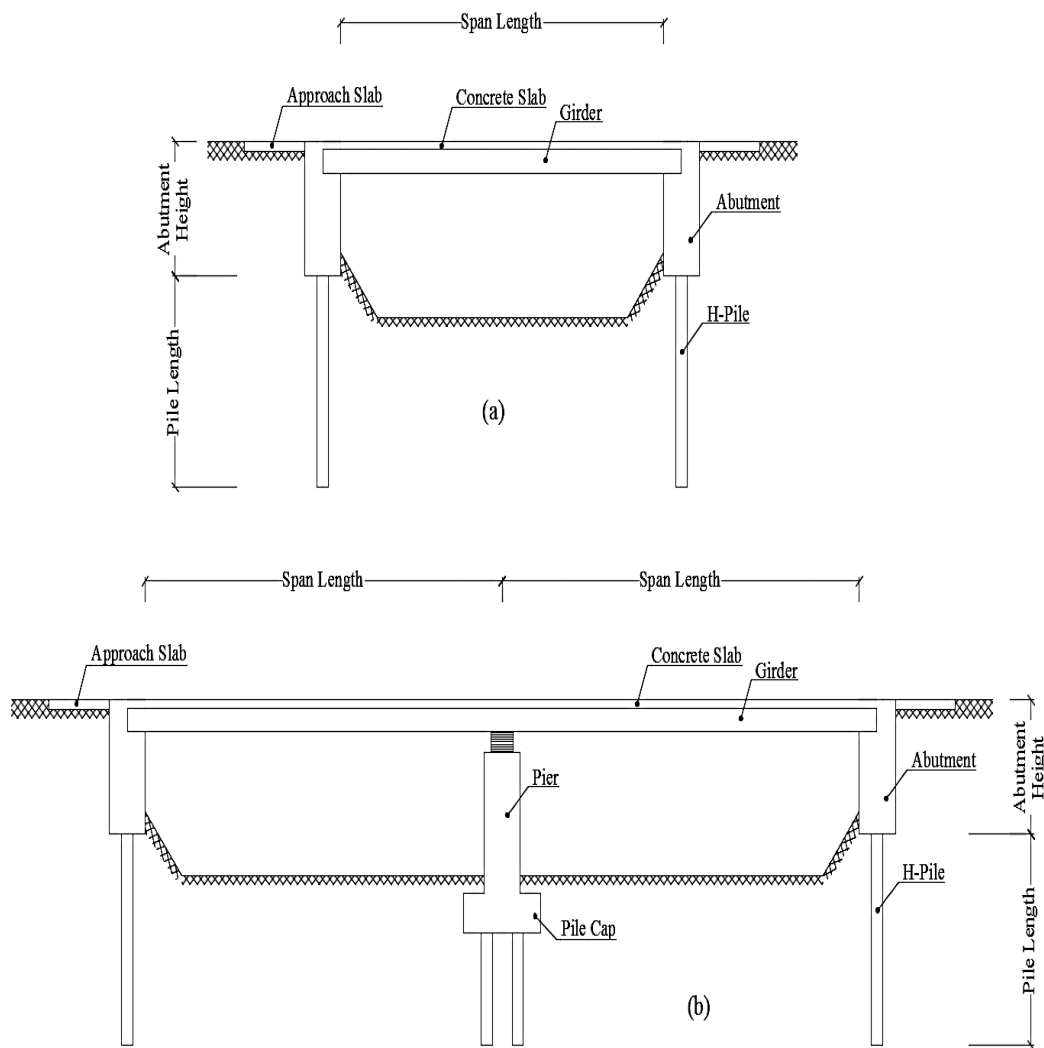


Fig. 1. Archetypes layout (a) Single span bridge (b) Multi-span bridge

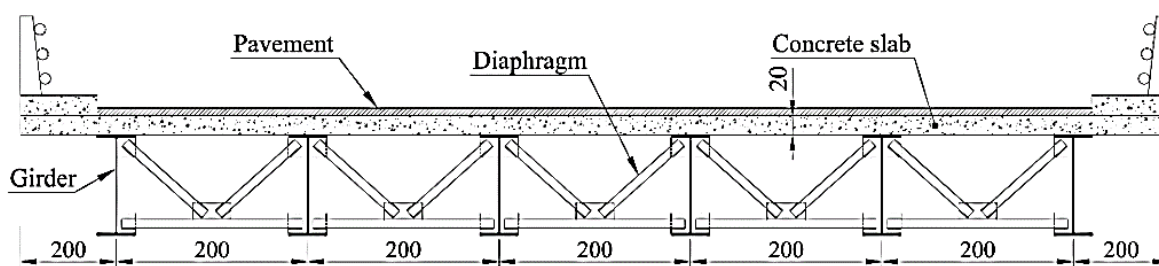


Fig. 2. Superstructure of all archetypes (dimensions in cm)

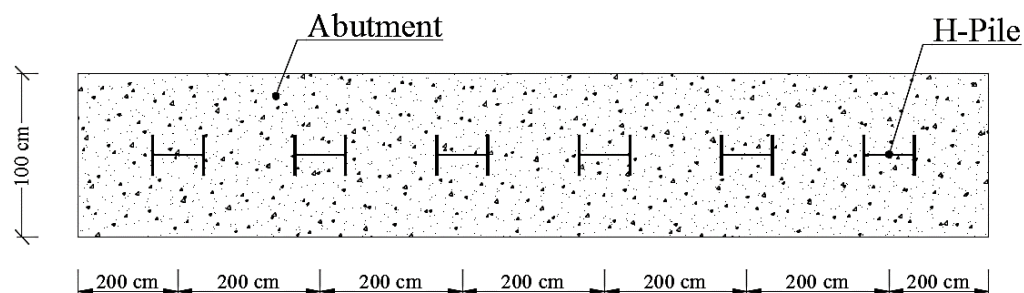


Fig. 3. Abutment and H-pile cross sections

Table 1. Properties of dense and loose soil

Soil Properties	Dense Soil (D)	Loose Soil (L)
Elasticity Modulus E (MPa)	80	15
Poisson Ratio	0.35	0.25
Internal Friction Angle ϕ (Degree)	38	30
Minimum Unit Weight (kN/m ³)	17	14
Maximum Unit Weight (kN/m ³)	22	18

4. Finite element modeling

4.1 Software and modeling

Because of its special features and strong graphical user interface, SAP2000 [11] is used for modeling and analysis of archetypes. A single 2 m wide 2D FE model of each IAB containing one girder and one pile was considered for all analyses to account for the longitudinal behavior of structures. Since every 2 m slice of the bridge width is similar, this 2D modeling assumption would be a great time saving idea. Previous studies have shown that the longitudinal behavior of IABs using 3D and 2D modeling can yield similar results and 2D modeling is more efficient (Faraji et al. [12]).

4.2 Deck modeling

Deck consists of a 20 cm thick concrete slab made of normal weight concrete with $f'_c=28$ MPa. Steel girders and concrete slab were modeled using frame and shell elements, respectively. Both frame and shell elements were meshed such that they were constrained together at their junction to simulate the composite behavior of the girders. The steel girders used were American W sections of ST-37 grade with yield strength of 240 MPa. All girders were embedded inside the abutments for 50 cm in order to make rigid connections.

4.3 Abutment and embankment modeling

Abutments were modeled using shell elements made of normal weight concrete with $f'_c=28$ MPa. A fine grid mesh was used in modeling the abutments to increase accuracy and avoid unreasonable results. The modeling of the embankment soil behind the abutments followed the procedure described in Mahjoubi and Maleki [7] with some minor changes. Embankment modeling consisted of 2 parts: a multilinear elastic near-field soil springs capturing the static active/passive behavior of the soil and a far-field soil which is assumed to remain elastic in an earthquake but contributes to mass inertia (see Figs. 4-5). Membrane elastic shell elements were used for modeling the far-field soil to an extent (length) equal to 4 times the abutment height to eliminate radiation damping occurrence in the system due to earthquake wave propagation [7]. Note that, far-field soil can become nonlinear only in very severe earthquakes and in most cases remains elastic (Richards, et al. [13]).

In order to account for shear modulus variation of far-field-soil with depth, the soil was divided into sublayers of different mechanical properties. There are two assumptions for shear modulus variation of cohesionless soils with depth: linear and parabolic. Following Richards et al. [13] and assuming parabolic variation, the shear modulus for each sublayer is calculated as:

$$G_i = G_b \sqrt{z_i/H} \quad (1)$$

where, G_i = average shear modulus of sublayer i , G_b = shear modulus at the bottom of embankment, z_i = mean depth of sublayer i , H = total depth of embankment.

The far-field-soil elements were restrained against horizontal and vertical translation at the bottom, where the earthquake time-history accelerations were also applied. The far end of far-field soil was restrained only against vertical translation. Far-field soil mass and stiffness will contribute to the inertia and stiffness of the total bridge structure when the gap elements are closed and the soil and structure are in contact.

The near-field soil behavior is modeled by a massless multilinear spring. The behavior is nonlinear but it is elastic. This means that the element loads and un-loads along the same curve, and no energy is dissipated. The elastic stiffness was calculated as follows:

$$k_i = k_s^z \times A_i \quad (2)$$

where, k_s^z = subgrade modulus at depth z calculated by Eq. (3)

$$k_s^z = CG_z/H \quad (3)$$

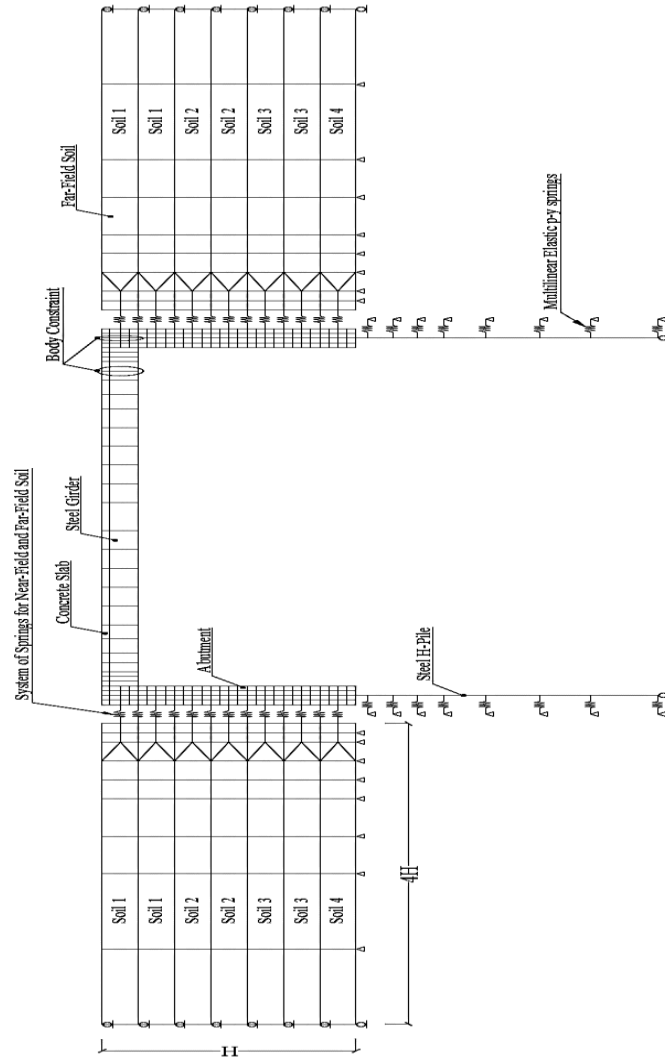


Fig. 4. Modeling layout of archetypes in the software

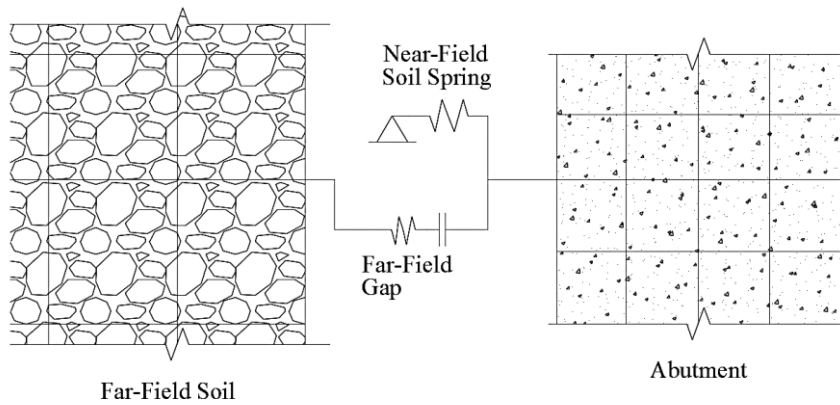


Fig. 5. System of springs for near-field and far-field soils

In Eq. (3), G_z = shear modulus at depth of z , C = a shape factor of 1.35 based on Richards et al. [13]. A_i = tributary area of spring calculated as:

$$A_i = B \times d \quad (4)$$

where, B = model width, d = tributary height of spring, which is equal to distance between springs.

There are upper (passive) and lower (active) limits for these springs as mathematically shown in Eq. (5). The exerted soil forces on the wall is always within these limits:

$$P_a = k_a \cdot \gamma_i \cdot z_i \cdot A_i \leq F_i = k_i \cdot \delta_i \leq P_p = k_p \cdot \gamma_i \cdot z_i \cdot A \quad (5)$$

in which, γ_i is soil unit weight at depth, z_i which is calculated by assuming linear variation of unit weight in depth. δ_i is abutment displacement or spring deformation at depth z_i . k_a is active and k_p as passive earth pressure coefficients computed based on Rankine formulation for simplicity:

$$k_a = \frac{1 - \sin \phi}{1 + \sin \phi}; k_p = \frac{1 + \sin \phi}{1 - \sin \phi} \quad (6)$$

where ϕ is the soil internal friction angle.

General force-displacement relationship for near-field soil spring model is shown in Fig. 6.

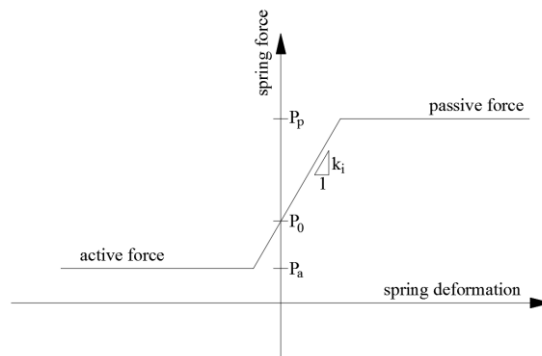


Fig. 6. Near field soil behavior

4.4 Pile and adjacent soil modeling

The 7 m length piles were modeled using frame elements of steel H sections. Multilinear elastic springs with force-deformation relationship based on API p-y curves [14] were developed and modeled along pile length for accounting the actual soil pressure acting on piles. An example of p-y curve assigned to a multilinear elastic link element in SAP2000 is shown in Fig. 7. The pile bottom was restrained against vertical displacement in all models. In this research, the source of potential nonlinearity is considered to be in piles. Thus, fiber P-M-M hinges was defined continuously along the upper 3 m of piles where the occurrence of plastic hinges was expected.

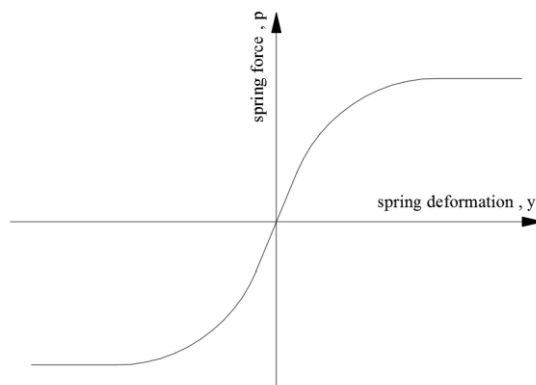


Fig. 7. p-y curve concept used in multilinear elastic springs along pile length

4.5 Analysis

The piles in IABs experience large displacements. Therefore, P-Delta effects must be considered in the analyses of all archetypes. Damping ratio of 5% is a common value for analysis of bridge structures and is considered to be conservative to use in this study.

5. Design of Archetypes

Archetypes were first designed based on AASHTO LRFD [9] specifications for gravity, thermal and seismic loading. SAP2000 was used for analysis and calculation of demands in structural elements. The details of structural modeling were discussed in the previous sections. Seismic demands were calculated based on the assumption that the bridges were located in China Town, Los Angeles, California. Thus, site class D was assigned and S_s and S_I values of 1.664 and 0.5576 were used, respectively. The PGA for the site was 0.7064. The design basis earthquake (DBE) and MCE spectra are shown in Fig. 8. Temperature loading was considered in calculating demands according to moderate climate conditions. The designed girder sections were chosen from American wide flange sections and piles were selected from HP sections. The designed IAB archetypes properties are shown in Table 2.

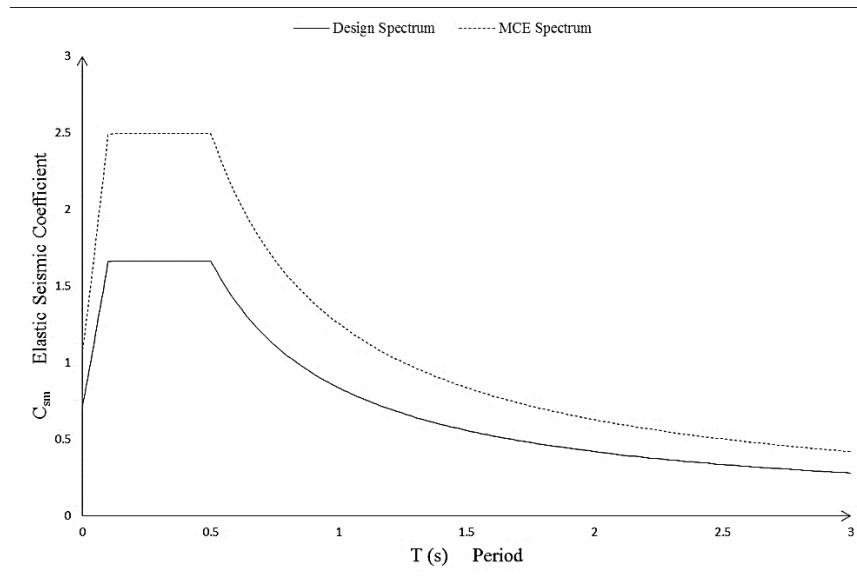


Fig. 8. DBE and MCE earthquake spectra

Table 2. Designed archetypes properties

Model ID	Abutment Type	Soil Type	Span Length (m)	No. of Spans	Pile Section	Girder Section
W10D1	Wall type	Dense	10	1	HP12X63	W24X68
W10D2			10	2	HP13X60	W24X68
W20D1			20	1	HP12X53	W40X167
W20D2			20	2	HP12X63	W44X262
W30D1			30	1	HP12X63	W44X262
W30D2			30	2	HP13X87	W44X262
W10L1		Loose	10	1	HP12X63	W24X76
W10L2			10	2	HP13X73	W24X76
W20L1			20	1	HP13X60	W40X183
W20L2			20	2	HP13X73	W40X183
W30L1			30	1	HP13X73	W44X262
W30L2			30	2	HP13X73	W44X262
S10D1	Stub type	Dense	10	1	HP12X53	W24X84
S10D2			10	2	HP12X53	W24X84
S20D1			20	1	HP13X73	W40X167
S20D2			20	2	HP13X73	W40X167
S30D1			30	1	HP14X117	W40X262
S30D2			30	2	HP16X121	W44X262
S10L1		Loose	10	1	HP12X53	W24X76
S10L2			10	2	HP13X60	W24X76
S20L1			20	1	HP14X89	W40X149
S20L2			20	2	HP13X73	W40X149
S30L1			30	1	HP16X141	W44X262
S30L2			30	2	HP16X121	W44X262

5.1 Input ground motions

Ground motions are selected according to FEMA-P695 specifications [10]. The methodology provides 22 pairs of preselected far-field record set from sites farther than 10 km from fault rupture (see Table 3). The record set does not include the vertical component of ground motions. In addition, since the analysis models were 2D, only the horizontal component with higher PGA was used in nonlinear analyses. There are two steps of scaling in this methodology. First, the set of ground motions are normalized with respect to the median PGV of record set. Thus, each ground motion record should be multiplied by the factor NM_i calculated as:

$$NM_i = \frac{\text{Median}(PGV_i)}{PGV_i} \quad (7)$$

Table 3. Far-Field ground motions [10]

ID	Name Station	Year	Magnitude	Component (°)
1	Northridge	1994	6.7	MUL279
2	Beverly Hills – Mulhol	1994	6.7	LOS270
3	Canyon Country – WLC	1999	7.1	BOL090
4	Duzce, Turkey	1999	7.1	HEC090
5	Bolu	1999	7.1	HEC090
6	Hector Mine	1979	6.5	DLT352
7	Hector	1979	6.5	DLT352
8	Imperial Valley	1979	6.5	DLT352
9	Delta	1979	6.5	DLT352
10	Imperial Valley	1979	6.5	E11230
11	El Centro Array #11	1995	6.9	NIS090
12	Kobe, Japan	1995	6.9	NIS090
13	Nishi-Akashi	1995	6.9	SHI090
14	Kobe, Japan	1995	6.9	SHI090
15	Shin-Osaka	1999	7.5	DZC270
16	Kocaeli, Turkey	1999	7.5	DZC270
17	Duzce	1999	7.5	ARE000
18	Kocaeli, Turkey	1999	7.5	ARE000
19	Arcelik	1992	7.3	YER270
20	Landers	1992	7.3	YER270
21	Yermo Fire Station	1992	7.3	CLW-TR
22	Landers	1992	7.3	CLW-TR
23	Coolwater	1989	6.9	CAP000
24	Loma Prieta	1989	6.9	CAP000
25	Capitola	1989	6.9	G03000
26	Loma Prieta	1989	6.9	G03000
27	Gilroy Array #3	1990	7.4	ABBAR--L
28	Manjil, Iran	1990	7.4	ABBAR--L
29	Abbar	1987	6.5	ICC000
30	Superstition Hills	1987	6.5	ICC000
31	El Centro Imp. Co.	1987	6.5	POE270
32	Superstition Hills	1987	6.5	POE270
33	Poe Road (temp)	1992	7.0	*
34	Cape Mendocino	1992	7.0	*
35	Rio Dell Overpass	1999	7.6	N
36	Chi-Chi, Taiwan	1999	7.6	N
37	CHY101	1999	7.6	N
38	Chi-Chi, Taiwan	1999	7.6	N
39	TCU045	1999	7.6	N
40	San Fernando	1971	6.6	PEL090
41	LA – Hollywood Stor	1971	6.6	PEL090
42	Friuli, Italy	1976	6.5	TMZ000
43	Tolmezo	1976	6.5	TMZ000

where, $Median(PGV_i)$ is the median of peak ground velocities of all ground motions and PGV_i is the peak ground velocity of each ground motion record. This phase is to eliminate unwarranted variability among the records because of the inherent variances in distance to source, source type, event magnitude and site conditions without removing the entire record-to-record variability. In the second scaling phase, normalized ground motions should be collectively scaled to a specified ground motion intensity in a way that the median spectral acceleration of record set matches the spectral acceleration at the fundamental period of T of analyzed archetype [10]. Fig. 9 shows a sample of the scaled spectrum.

5.2 Calculation of median collapse intensity and CMR

While incremental dynamic analysis (IDA) is used to show the collapse assessment process, methodology needs the median collapse intensity (\hat{S}_{CT}) calculated with fewer nonlinear analyses than is necessary to develop the full IDA curve. \hat{S}_{CT} could be obtained by scaling all the records to MCE intensity (S_{MT}) by raising the intensity of scaled records until over one half of ground motion records cause collapse. The least intensity at which one half of records cause collapse is the median collapse intensity. MCE intensity is gained from the response spectrum of MCE ground motions at T (fundamental period). The ratio between MCE intensity and median collapse intensity is the collapse margin ratio (CMR) [10].

$$CMR = \frac{\hat{S}_{CT}}{S_{MT}} \quad (8)$$

5.3 Pile collapse criteria

As mentioned before, very few experimental studies covering the collapse of steel H-pile sections about their weak axes have been performed and can not be generalized for all types of steel H-pile sections. As a safe and reasonable assumption, it is considered in this research that piles behavior and performance levels can be measured using ASCE 41-13 [15] criteria for steel columns in moment frames. This is not far from reality, because the piles under cyclic loading in their upper portions where plastic hinges develop tend to loosen the adjacent soil support. Thus, it is conservative to assume a behavior like steel columns.

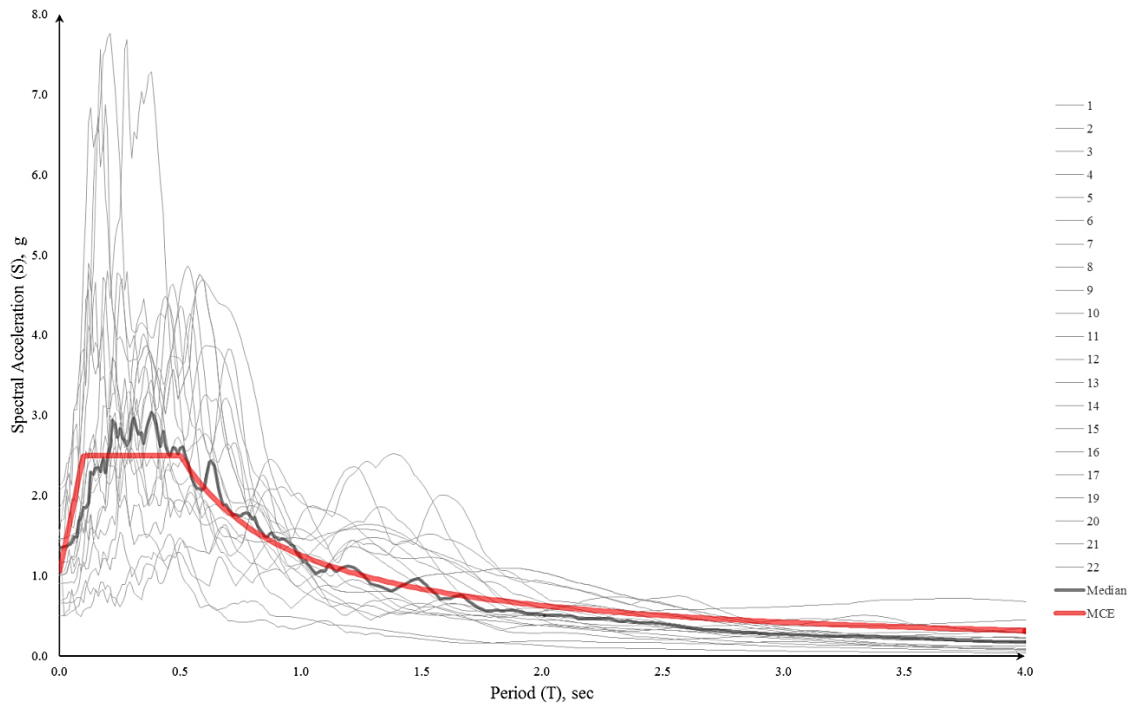


Fig. 9. Ground motions spectra scaled to MCE for W20D1 with $T=0.20$ s

5.4 Calculation of spectral shape factor, SSF, and ACMR

According to Baker and Cornell [16], the rare ground motions in the western United States corresponded to MCE have a distinct spectral shape which are different from the spectral shape of design spectrum applied for the structural design in ASCE/SEI 7.

To remove this conservative bias, a simplified spectral shape factor, SSF, which depends on the fundamental period (T) and period based ductility (μ_T), are used to adjust collapse margin ratios as [10]:

$$ACMR = SSF \times CMR \quad (9)$$

SSF is the spectral shape factor and is calculated by Eq. (12).

5.5 Fundamental period of archetypes

To obtain the fundamental period of archetypes, modal analyses were performed and the period of predominant longitudinal mode of vibration (with the highest mass contribution) was selected as the fundamental period and is reported in Table 4.

Table 4. Ground motion and structural behavior parameters

ID	T (s)	μ	$\bar{\varepsilon}(T)_{records}$	$\bar{\varepsilon}_0$	β_1	SSF	CMR	ACMR
W10D1	0.19	1.60	0.60	1.50	0.11	1.11	2.15	2.38
W10D2	0.24	2.20	0.60	1.50	0.15	1.15	2.03	2.33
W20D1	0.20	1.50	0.60	1.50	0.10	1.10	1.80	1.98
W20D2	0.29	1.50	0.60	1.50	0.10	1.10	1.73	1.90
W30D1	0.23	1.60	0.60	1.50	0.11	1.11	2.11	2.34
W30D2	0.38	3.20	0.60	1.50	0.19	1.19	1.90	2.26
W10L1	0.30	1.90	0.60	1.50	0.13	1.13	1.64	1.85
W10L2	0.38	2.90	0.60	1.50	0.18	1.18	1.61	1.90
W20L1	0.30	2.00	0.60	1.50	0.14	1.13	1.57	1.78
W20L2	0.43	1.20	0.60	1.50	0.07	1.07	2.10	2.24
W30L1	0.33	1.60	0.60	1.50	0.11	1.11	1.70	1.88
W30L2	0.54	1.40	0.58	1.50	0.10	1.09	1.50	1.64
S10D1	0.11	1.70	0.60	1.50	0.12	1.11	2.95	3.29
S10D2	0.16	1.50	0.60	1.50	0.10	1.10	3.08	3.38
S20D1	0.12	2.10	0.60	1.50	0.15	1.14	3.29	3.75
S20D2	0.22	1.60	0.60	1.50	0.11	1.11	3.36	3.72
S30D1	0.14	2.00	0.60	1.50	0.14	1.13	3.39	3.85
S30D2	0.35	1.70	0.60	1.50	0.12	1.11	3.11	3.47
S10L1	0.17	2.30	0.60	1.50	0.16	1.15	2.51	2.89
S10L2	0.23	2.10	0.60	1.50	0.15	1.14	2.62	2.99
S20L1	0.18	2.60	0.60	1.50	0.17	1.17	2.82	3.29
S20L2	0.29	2.10	0.60	1.50	0.15	1.14	1.90	2.17
S30L1	0.20	3.60	0.60	1.50	0.21	1.21	2.48	2.99
S30L2	0.39	2.50	0.60	1.50	0.17	1.16	1.99	2.31

5.6 Ductility, μ

Nonlinear static analyses were conducted on archetypes in order to calculate their ductility. Control node for pushover analyses was chosen at the middle of the deck. Since the source of nonlinearity is located at the top part of piles and there is no other source of nonlinearity in the models, then the structure would not face instability or large loss of stiffness after formation of plastic hinges. In this case, ductility was calculated based on piles pushover diagram as:

$$\mu = \frac{\Delta_u^{Collapse}}{\Delta_y^{eff.yield}} \quad (10)$$

in which, $\Delta_u^{Collapse}$ is the control node displacement corresponding to the first collapse plastic rotation occurrence in piles and $\Delta_y^{eff.yield}$ is displacement of control node corresponding to first yield rotation in piles. Calculated ductility values are listed in Table 4.

5.7 Epsilon parameter

The epsilon (ε) ground motion parameter is defined as an indicator of spectral shape. This parameter is a difference measurement between the spectral acceleration of a record and the mean of a ground motion prediction equation at a given period [16]. With regards to the equation proposed for Far-Field ground motions set:

$$\bar{\varepsilon}(T)_{records} = (0.6)(1.5 - T) \leq 0.6 \quad (11)$$

where T is the fundamental free vibration period of structure. Value of $\bar{\varepsilon}(T)_{records}$ is calculated for each archetype and reported in Table 4.

5.8 β_1 and SSF parameters

SSF factor is calculated as:

$$SSF = \exp[\beta_1(\bar{\varepsilon}_0(T) - \bar{\varepsilon}(T)_{records})] \quad (12)$$

where, β_1 is based on the building inelastic deformation capacity and $\bar{\varepsilon}_0$ is based on SDC equivalent to 1.0 for SDC B/C, 1.5 for SDC D, and 1.2 for SDC E. In this research, $\bar{\varepsilon}_0$ is considered to be 1.50, and β_1 is applied to quantify how drastically the spectral shape (ε) impacts the collapse capacity as below:

$$\beta_1 = (0.14)(\mu - 1)^{0.42} \leq 0.32 \quad (13)$$

5.9 Acceptable values of $ACMR$

Acceptable values of $ACMR$ are based on total system collapse uncertainty (β_{TOT}) and on the established variables of acceptable collapse probabilities assumed that the distribution of collapse level spectral intensities is lognormal with a median value (\hat{S}_{CT}) and a lognormal standard deviation that is equivalent to total system collapse uncertainty (β_{TOT}).

$$ACMR_{acceptable} = \frac{1}{e^{(\phi^{-1}(P_{Collapse}) \times \beta_{TOT})}} \quad (14)$$

Acceptable performance is achieved when [10]:

Average $ACMR$ value for all archetypes in a performance group exceeds $ACMR_{10\%}$:

$$\overline{ACMR}_i \geq ACMR_{10\%} = 2.30 \quad (15)$$

the individual variable of $ACMR$ for every index archetype exceeds $ACMR_{20\%}$:

$$ACMR_i \geq ACMR_{20\%} = 1.73 \quad (16)$$

It means that the collapse probability for MCE ground motions is about 10%, or lower averagely during the archetypes group and the collapse probability for MCE ground motions is about 20% or lower for all index archetype into the group.

5.10 Total system collapse uncertainty

Majority of uncertainty sources are contributed to variability. Larger variability in the overall collapse prediction necessitates larger collapse margins to confined the collapse probability to a confirmed level at MCE intensity. Evaluating all the significant uncertainty sources in collapse response and for incorporating their impact in the collapse assessment procedure is important. The following uncertainty sources are taken in the collapse assessment procedure:

1) Record-to-Record Uncertainty (RTR) is because of the variability of index archetypes response to altered ground motion records as below [10]:

$$\beta_{RTR} = 0.1 + 0.1\mu_T \leq 0.4 \quad (17)$$

That will be $\beta_{RTR} = 0.30$ on average of all archetypes.

2) Design Requirements Uncertainty (DR) is associated to the robustness and completeness of design requirements, and to the extent provided for safeguards against unanticipated failure mode(s). This ranking has been defined by a range from “(A) Superior” to “(D) Poor” that is shown in Ref. [10] tables. Regarding the use of AASHTO LRFD for design of archetypes, there is a level of confidence in design specifications, but because of few experimental studies related to IAB’s seismic behavior, $\beta_{DR} = 0.2$ equivalent to (B) good quality has been chosen.

3) Test Data Uncertainty (TD) is associated to the robustness and completeness of the data applied to identify the system and it can be quantitatively chosen from Ref. [10] tables. Considering the low experimental researches on connections, soil-pile-structure interaction and seismic loadings of IABs, $\beta_{TD} = 0.5$ equivalent to (D) poor quality has been selected for this parameter.

4) Modeling Uncertainty (MDL) is associated to how properly index archetype models show the full range of structural response features and to the associated design parameters of archetype design space and how properly the analysis model(s) captures the structural collapse behavior by non-simulated or direct simulation of component checks. Bridges have been modeled in one or two spans (wall and stub type abutment) 10, 20 and 30 meter spans and two types of loose and dense soil. Thus, soil-pile-structure interaction has been taken into account beside non-linear modeling of piles using fiber elements, however, with regarding 2D modeling and ignoring material deterioration. $\beta_{MDL} = 0.2$ equivalent to (B) good quality has been chosen for this parameter.

Total system collapse uncertainty is calculated as:

$$\beta_{TOT} = \sqrt{\beta_{RTR}^2 + \beta_{DR}^2 + \beta_{TD}^2 + \beta_{MDL}^2} = 0.65 \quad (18)$$

6. Results and discussions

In this chapter, results are evaluated and discussed. As mentioned in section 5.9, *ACMR* average values for every performance group and *ACMR* values for individual index archetype should be above the acceptable limit. Here, the results in terms of all archetypes as one performance group are discussed, then breaking up the archetypes based on some specific characters into some new performance groups are examined.

If all archetypes are put into one performance group, then $\overline{ACMR}_i = 2.61$ which is above $ACMR_{10\%} = 2.30$. \overline{ACMR}_i for all archetypes is above $ACMR_{20\%} = 1.73$, except W30L2 that has an *ACMR* value of 1.64 that is below the acceptable value. This means that R factor of 3.5 is suitable for IABs in the longitudinal direction with a marginal error.

Another approach in evaluation of *ACMR* is making performance groups as shown in Fig. 10. Accordingly, all performance groups have average *ACMR* above the allowable *ACMR* based on 20% collapse probability, except the performance group of IABs with wall type abutment (7 m height). This observation shows that the *ACMR* of all performance groups are only slightly higher than the acceptable *ACMR*, except for wall type abutment bridges, then it could be concluded that 3.5 could be a good and optimized response modification factor for IABs in the longitudinal direction.

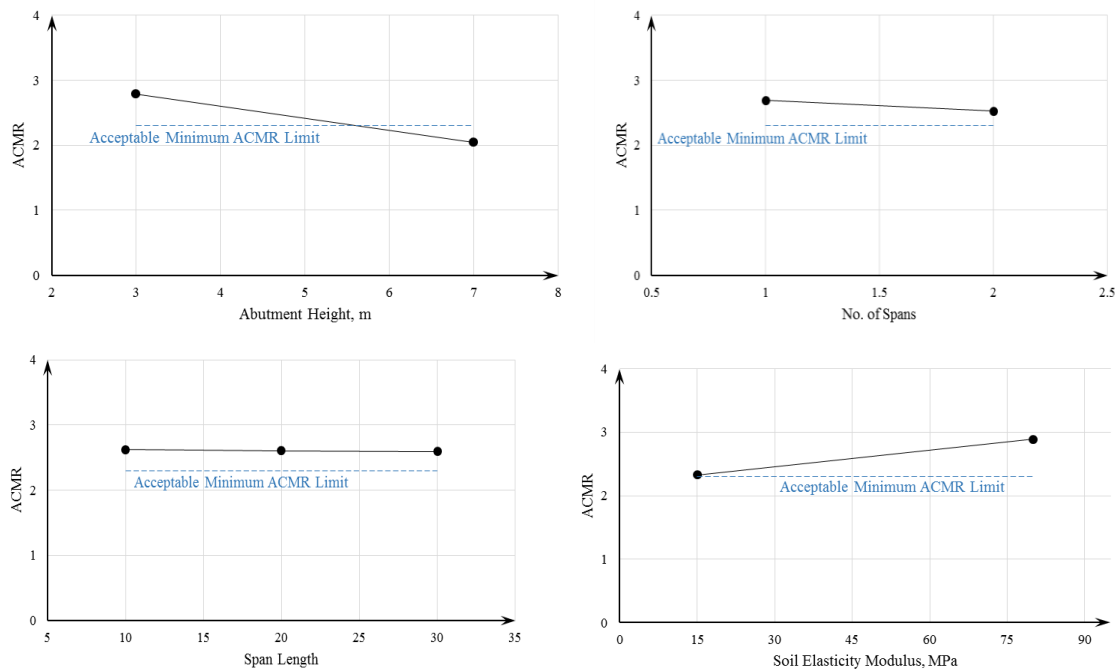


Fig. 10. The *ACMR* of performance groups compared to the acceptable minimum *ACMR* limit. (a) performance groups separated based on abutment height (b) performance groups separated based on number of spans (c) performance groups separated based on span length (d) performance groups separated based on soil elasticity modulus

Another approach in evaluation of *ACMR* is making performance groups as shown in Fig. 11. Thus, all performance groups have an average *ACMR* above the allowable *ACMR* based on 20% collapse probability, except the performance group of IABs with wall type abutment with height of 7 meters with either loose or dense soil type and any number of spans.

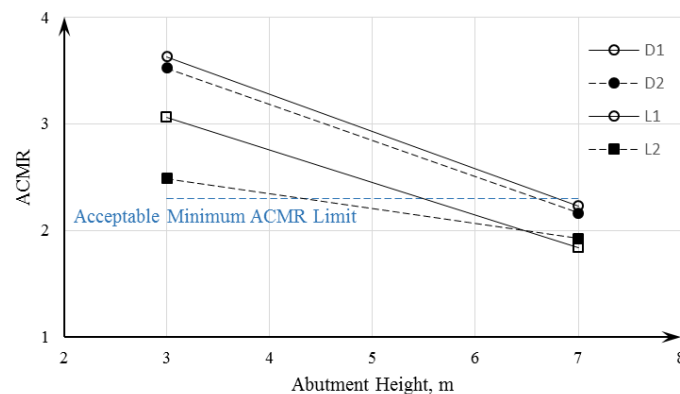


Fig. 11. values of *ACMR* vs. Abutment height considering performance groups separated based on soil type, no. of spans and abutment height

As a result, the response modification factor 3.5 is acceptable for IABs in the longitudinal direction for all archetypes considered with the following reservations:

- 1) IABs with an abutment height more than 6.5 meters with dense soil behind abutment.
- 2) IABs with an abutment height more than 5 meters with loose soil behind abutment.

From the results, it is observed that:

- 1) The collapse capacity of IABs with stub type abutment is 55% more than the IABs with wall type abutments.
- 2) The collapse capacity of IABs with dense soil behind abutment is 24% more than those with loose soil behind abutment.
- 3) The collapse capacity of single span IABs is more than multiple span IABs.
- 4) The collapse capacity of IABs with 10 meters span is 0.8% more than the IABs with 20 meters span, and the collapse capacity of IABs with 20 meters span is 0.4% more than the IABs with 30 meters span.

From the observations mentioned above, it is seen that the height of abutment is the most important factor in the collapse capacity of IABs. The second most important parameter is the type of soil behind abutments. The least effective parameter in the collapse capacity of IABs is the number of spans and span length.

7. Conclusions

Based on the extensive analyses prescribed in FEMA P695 [10] the *R* factor in the longitudinal direction of common non-skewed IABs were determined. It was concluded that the response modification factor $R = 3.5$ is appropriate for design purposes. However, for IABs with abutment height above 6.5 m with dense backfill this value can be unsafe.

It is recommended by the authors that for IABs in seismic regions designers should avoid using loose soils behind abutments. Loose soils cause the collapse capacity of IABs to decline, especially those having abutment wall heights above 5 meters. Otherwise, in such cases, a lower response modification factor should be utilized.

It was also observed that stub type abutments had a better seismic performance than wall type abutments.

It was shown that the seismic performance of IABs were less sensitive to the number and length of spans within the range considered.

8. References

- [1] Burke Jr MP. Integral and semi-integral bridges. 1st ed. John Wiley & Sons; 2009.
- [2] Erhan S, Dicleli M. Effect of dynamic soil-bridge interaction modeling assumptions on the calculated seismic response of integral bridges. *Soil Dyn Earthq Eng*. 2014;66:42–55. doi:10.1016/j.soildyn.2014.06.033.
- [3] Civjan S, Bonczar C, Brena S. Integral abutment bridge behavior: Parametric analysis of a Massachusetts bridge. *Journal of Bridge Engineering*. 2007;12:64–71. doi:10.1061/(ASCE)1084-0702(2007)12:1(64).
- [4] Spyarakos C, Loannidis G., Seismic behavior of a post-tensioned integral bridge including soil-structure interaction (SSI). *Soil Dyn Earthq Eng*. 2003;23:53–63. doi:10.1016/S0267-7261(02)00150-1.

- [5] Itani AM, Pekcan G. Seismic performance of steel plate girder bridges with integral abutments. 2011.
- [6] Maleki S, Mahjoubi S. A new approach for estimating the seismic soil pressure on retaining walls. *Sci. Iran. Trans. Civ. Eng.* 2010;17(4): 273-284.
- [7] Mahjoubi S, Maleki S. Finite element modelling and seismic behaviour of integral abutment bridges considering soil-structure interaction. *Eur J Environ Civ Eng.* 2020;24(6):767-786.
- [8] Burdette EG, Ingram EE, Tidwell, JB, Goodpasture DW, Deatherage JH, Howard SC. Behavior of integral abutments supported by steel H-piles. *Transportation Research Record.* 2004. <https://doi.org/10.3141/1892-03>.
- [9] AASHTO (American Association of State Highway and Transportation Officials). LRFD bridge design specifications. 8th Edition. Washington DC, U.S.A. 2017.
- [10] FEMA P695, Quantification of building seismic performance factors. Federal Emergency Management Agency, Washington DC, U.S.A. June 2009.
- [11] Computers and Structures, Inc. SAP2000, Version 20, Integrated Structural Analysis and Design Software. Berkeley, CA, 2018.
- [12] Faraji S, Ting JM, Crovo DS, Ernst H. Nonlinear analysis of integral bridges: Finite-element model. *J Geotech Geoenvironmental Eng.* 2001;127:454–461.
- [13] Richards R. Huang C, Fishman KL. Seismic earth pressure on retaining structures. *J Geotech Geoenviron Eng.* 1999;125:771–778.
- [14] American Petroleum Institute (API). Recommended practice for planning, designing and constructing fixed offshore platforms-working stress design. 1st edition. API Recommended Practice 2A-WSD(RP2A-WSD). Dallas. 1993.
- [15] Seismic evaluation and retrofit of existing buildings(ASCE/SEI 41-13). American Society of Civil Engineers(ASCE). 2013.
- [16] Baker JW, Cornell CA. A vector-valued ground motion intensity measure consisting of spectral acceleration and epsilon. *Earthq Eng Struct Dyn.* 2005;1193–1217. doi:10.1002/eqe.474.

Determination of the Geotechnical Parameters of Stabilized Soils by Stone Column Method based on SPT Results

Alivasakhi Mishra, *Department of Civil Engineering, Capital Engineering College, Bhubaneswar, alivasakhimishra258@gmail.com*

Suchismita Satpathy, *Department of Civil Engineering, Aryan Institute of Engineering & Technology, Bhubaneswar, suchismita@outlook.com*

Subrat Kumar Panda, *Department of Civil Engineering, Aryan Institute of Engineering & Technology, Bhubaneswar, spanda226@gmail.com*

Sudeepta Kishor Dash, *Department of Civil Engineering, NM Institute of Engineering & Technology, Bhubaneswar, sudeeptakishordash1@gmail.com*

ABSTRACT

One of the soil stabilisation solutions is to employ a stone column to improve the strength and minimise the compressibility of soft and loose fine-grained soils. The bearing capacity and loading-settlement behaviour of stone columns have been determined using a variety of methods, all of which are based on finite element analysis and experimental data. The purpose of this study is to present a new, simple method for estimating the characteristics of treated soil as a function of the standard soil and stone column penetration test number.

INTRODUCTION

Since the availability of suitable construction sites decreases, and the need to utilize poor soils for foundation support and earthwork construction increases, it is necessary to strength the ground under existing structures to insure stability against adjacent excavation or tunneling, or to improve resistance to seismic or other special loadings. Therefore, soil improvement techniques have been rapidly developed in the past several years. Several methods are used to stabilize soils such as: compaction, consolidation, grouting, admixtures, thermal, reinforcement, and stone column. The ability of any of these methods to improve soil properties depends on several factors, including: soil type, degree of saturation and water table, initial relative density, initial in-situ stresses, initial soil structure, and special characteristics of the method used. In most cases the goal of treating soil is increasing shear strength and loading capacity, increasing stability and settlement control. Stone column is one of the methods used for treating fine and loose aggregates soils. Installation of stone column in loose and fine graded soils causes increasing strength and load capacity of these soils. Stone columns in saturated clay soils work as drainage system and results in decreasing consolidation time. Also stone column in loose and saturated non-cohesive fine graded soils act like a drainage system and reduce the drainage path and lessens liquefaction probability in case of earthquake occurring. Stone column systems in soft, compressible soils are somewhat like pile foundations, except that pile caps, structural connections, and deep penetration into underlying firm strata are not required, and the stone columns are, of course, more compressible. The strength of stabilized soil by stone column is consisting of soil strength and stone column strength. It is not possible to provide a sample that contains soil and stone column. In order to determine the supporting capacity and load settlement behavior of stone column foundation, finite element analyses, have been proposed. This analyses need to perform test and to determine strength parameters of stone column and soil material, modeling and performing complex analysis. In order to overcome difficulties, a new method based on standard penetration test

number is introduced in this paper. Unlike finite element methods, the new method easily determine load-settlement behavior and shear strength of soils treated by stone column, with standard penetration number test.

CHARACTERISTICS OF STONE COLUMN

Most stone column installations are made using the vibro-replacement method in a manner similar to vibroflotation. A cylindrical vertical hole is made by a vibrating probe penetrating by jetting under its own weight. In some cases a dry process without water jets is used. Gravel backfill is dumped into hole in increments of 0.4 to 0.8 m and compacted by the probe which simultaneously displaces the material radially into the soft soil. The diameter of resulting stone column can be estimated from the consumption material. It will usually be in the range of 0.6 to 1.0 m. larger columns diameter can be formed by coupling two or three vibrators simultaneously. Gravel particle sizes in the range of 20 to 75 mm are typical. After installing stone columns a blanket of sand or gravel 0.3 m or more in thickness is usually placed over the top. This blanket works both as drainage layer and also to distribute uniform stresses from above structure. Stone columns may be used in clusters and rows to support walls and footings or as groups in square or triangular grid patterns with center-to-center columns spacing of 1.5 to 3.5 m. When stone columns are used in foundation construction the supporting capacity and settlement are of primary concern. When stone column used for stability purposes under embankments or in slopes, the shear strength of the columns is of primary interest. In fact stone columns transfer applied loads to extend layers of soil and cause stress distribution and reduce settlement. Design values of 20 to 30 tons per column are typical for columns in soft to medium stiff clays. The required minimum column length in soft soil can be estimated based on shearing strength along sides and end bearing capacity. The settlement of a stone column foundation depends on the cross sectional area of the column and their spacing. A load test on single columns within a group will ordinarily give a settlement in the range of 5 to 10 mm under design load. But experience and analyses indicated that the settlement of large loaded area supported by stone columns will be about 5 to 10 times greater than this.

The effectiveness of stone column installation is increasing load capacity of soil, increasing stability of slopes, decreasing foundations settlement and decreasing liquefaction potential. Some designers assume conservatively that all the applied foundation loads are carried by columns and for analysis purposes the friction angle of compacted stone columns can be taken about 35° to 40° and elastic modulus of it in the range of 40 to 70 (Mpa) are appropriate. In proposed method it's assumed that the applied foundation loads are divided between stone column and soil by relative stiffness ratio. And standard penetration test results are used to determine all necessary parameters for stone column analyses.

PROPOSED METHOD

In spite of the complexity of the load transfer mechanism in a stone column foundation and need for simplifying assumptions in analysis, the following assumptions are needed:

_ stone columns settlement is equal to the settlement of surrounding soil and applied loads to foundation are divided between soil and stone column proportional to stiffness ratio.

_under applied loads; lateral strain is formed in soil and stone column. The strength of stabilized soil by stone column is provided from interaction between soil and stone column that comes from radial strain of column and surrounding soil that is controlled by the passive resistance of the soil which can be mobilized to withstand radial bulging and by the friction angle of compacted material in the column. The settlement of unstabilized soft soils can be computed as

$$S = \frac{qH}{M_c} \quad (1)$$

Where S is the settlement, q is the average applied stress to soil and M_c is the confined (constrained modulus) of the soil. M_c depends on elastic constant and Poisson's ratio and expressed by

$$M_c = \frac{E_c(1-\nu_c)}{(1+\nu_c)(1-2\nu_c)} \quad (2)$$

Where E_c is the Young's modulus and ν_c is Poisson's ratio assigned to the soil.

Assuming the average Poisson's ratio of clay is 0.3. Therefore, Eq. 2 would be

$$M_c = 1.346E_c \quad (3)$$

The elasticity modulus of fine graded soils using SPT test, can be computed as suggested by Shultz and Horn (1967)

$$E_c = 0.517N_c + 7.64 \quad (4)$$

By substituting Eq. (4) in Eq. (3) it's possible to express elastic constant of surrounded soil's as a function of the standard penetration test number

$$M_c = 0.696N_c + 10.28 \text{ (Mpa)} \quad (5)$$

Confined elastic constant of stone column material would be

$$M_s = \frac{E_s(1-\nu_s)}{(1+\nu_s)(1-2\nu_s)} \quad (6)$$

where E_s is elastic constant of stone column material and ν_s is its Poisson's ratio.

Elastic constant of coarse aggregate soils based on standard penetration number, can be computed by

$$E_c = 0.756N_s + 18.7 \quad (7)$$

(D'Appolonia et al. 1969) where N_s is number of blows obtained from SPT test on stone column.

Poisson's ratio for coarse aggregate soils defined as a function of angle of internal friction (Kulhawy, 1984), that angle of internal friction of coarse aggregate soils can also be obtained from standard penetration test (Robertson and Campanella, 1983).

$$\nu_s = 0.1 + 0.3 \frac{\phi_s - 25}{20} \quad (8)$$

$$\phi_s = \frac{1}{3} N_s + 26.67 \quad (9)$$

substituting Eqs.(7), (8) and (9) in Eq. (6) confined elastic constant of stone column material also can be obtained as a function of N_s .

$$M_s = (0.756N_s + 18.75) \frac{(0.875 - 0.005N_s)}{(1.125 + 0.005N_s)(0.75 - 0.001N_s)} \quad (10)$$

If ratio of N_c is assumed, the quantity n can be obtained from Eqs. (5) and (10). Also, from Figure (1) the quantity n which can be obtained with different values of N_c and N_s .

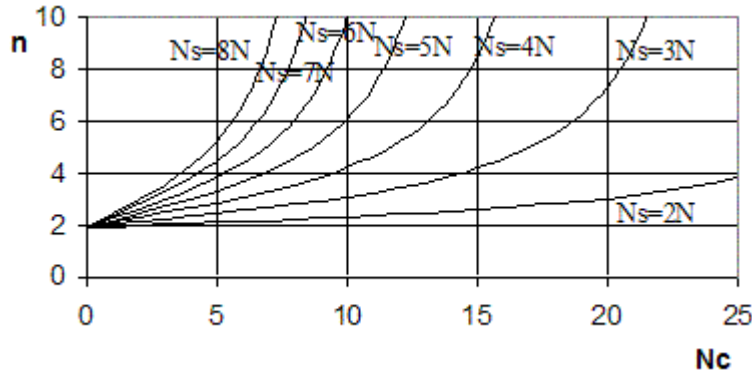


Figure 1. Stress distribution ratio (n) for different value of N_c and N_s .

Assuming that stone column settlement is equals to surrounding soft soil, stress distribution in soil and stone column is proportional to their relative stiffness ratio.

$$q = \frac{Q}{A} = \frac{A_s \sigma_s + A_c \sigma_c}{A_s + A_c} = \frac{n \alpha A_c \sigma_c + A_c \sigma_c}{\alpha A_c + A_c} = \sigma_c \frac{1 + n \alpha}{1 + \alpha} \quad (11)$$

Where A is total cross section, A_s is stone column's area, A_c is soil's area and Q is total applied load to foundation, and ratio of stone column's area to soil's area is defined as $\alpha = \frac{A_s}{A_c}$.

Therefore, it concluded that the applied stress to soil after installation of stone column will be equal to

$$\sigma_c = q \frac{1 + \alpha}{1 + n \alpha} \quad (12)$$

And the settlement of stabilized soil can be computed by equation (1).

Since the settlement is assumed to be directly proportional to the applied stress, decreasing settlement due to stone column installation is equal to stress decreasing in soft soil. If one considers the settlement ratio of stabilized soil to that of primary loose soil, defined as k

$$k = \frac{S'}{S} = \frac{\sigma_c}{q} = \frac{1 + \alpha}{1 + n \alpha} \quad (13)$$

settlement of untreated soil (S) is computed from equation (1). Knowing the allowable foundation settlement S' , the required area for stone column can be obtained as

$$A_s = \frac{\alpha}{1 + \alpha} A \quad (14)$$

$$\alpha = \frac{1 - k}{n k - 1} \quad (15)$$

Maximum allowable stress for stone column is defined as

$$\sigma_{s\max} = \frac{25C_u}{FS} \quad (16)$$

where C_u is undrained shear strength of untreated soil and is computed as [Sowers (1968)].

$$C_u = 7.26N_c \text{ (kPa)} \quad (17)$$

In stone column computations a safety factor of 3 is considered. So allowable stress in stone columns in term of number of blows of SPT test can be computed by equation (18).

$$\sigma_{s\max} = 60.5N_c \text{ (kPa)} \quad (18)$$

The shear strength of treated soil can be expressed as a combination of shear strength of stone column and soil as

$$\tau = \frac{\alpha}{1+\alpha} \tau_s + \frac{1}{1+\alpha} \tau_c \quad (19)$$

where τ_s is shear strength of column and τ_c is shear strength of untreated soil. τ_s and τ_c are computed from Mohr-coulomb's failure criteria. Since the cohesion of stone column's coarse aggregate material is zero, the shear strength of stone column material is equal to

where ϕ_s is angle of internal friction of stone column's material and σ_{ns} is effective vertical stress in stone column. ϕ_s is computed from equation (9) considering number of blows in standard penetration test, in this case τ_s equals:

$$\tau_s = \sigma_{ns} \tan\left(\frac{1}{3}N_s + 26.67\right) \quad (20)$$

The shear strength of untreated soil is obtained by

$$\tau_c = C_u + \sigma_{nc} \tan(\phi_c) \quad (21)$$

can be obtained from equation (17) considering number of τ . And also τ can be computed as [Olsen and Farr (1986)].

$$\phi_c = 0.67N_c + 6.9 \quad (22)$$

Considering Eqs. (17), (21) and (22) shear strength of untreated soil based on is defined as

$$\tau_c = 7.26N_c + \sigma_{nc} \tan(0.67N_c + 6.9) \quad (23)$$

substituting Eqs. (20) and (23) in Eq. (19) the shear strength of stabilized soil with stone column based on number of blows of SPT test is obtained (N_c) in soil and (N_s) in stone column.

$$\tau = \frac{\alpha}{1+\alpha} \sigma_{ns} \tan\left(\frac{1}{3}N_s + 26.67\right) + \frac{1}{1+\alpha} [7.26N_c + \sigma_{nc} \tan(0.67N_c + 6.9)] \quad (24)$$

where s_{ns} and s_{nc} are vertical effective stress in stone column and soil at failure surface, which results from transferred stress to desired depth and its magnitude can be computed from different stress distribution theories.

COMPARING RESULTS OF PROPOSED METHOD WITH FINITE ELEMENTS METHOD

Assuming $N_c = 5-15$ for soil and $N_s = 25-50$ for stone column and regarding to Eqs. 5 and 10 and Figure 1, stress distribution ratio between stone column and soil is obtained about 2-9. Also maximum allowable load for a stone column with 0.8m diameter due to Eq. 17 computed and equal to 15-45 tons. The results from finite element analysis maximum allowable load is between 20-30 tons [Mitchell and Huber(1985)].

Comparing result shows a satisfactory agreement between proposed method and finite element method.

CONCLUSION

The stress distribution ratio between stone column and soil calculated by the proposed method about 2-9 which depends on soil type and stone column material, whereas finite element analysis results shows this ratio is about 2-6.

Maximum allowable force for a stone column which is computed by the proposed method is about 15-45 tons, and its accurate analysis results shows that this value between 20-30 tons that results from both methods are satisfactory with each other.

In loose noncohesive fine graded soils in case of earthquake, there is a probability of liquefaction occurring. Stone column installation in these soils cause shortening in drainage path and pore water pressure is rapidly dissipated. If loose soil liquefies, it will lose its shear strength and will work as a fluid with high density and water pressure will be hydrostatic. In case of stone column existence in this condition, hydrostatic pressure difference which results from liquefied soil with pressure from applied over load on ground surface, work as lateral limiting load for stone column, and will result in forming passive strength in stone column. In this case,

vertical stress which column can carry will be $\tan^2(45 + \frac{\phi}{2})$ times more.

REFERENCES

1. D'Appolonia, D.J., R.V. Whitman, and E. D'Appolonia (1969) "Sand compaction with vibratory rollers," Journal of the Soil Mechanics and Foundations Division, American Society of Civil Engineers, Vol. 95, No. SMI, pp263-284.
2. Engelhardt, K., and H . C. Golding (1975) "Field testing to evaluate stone column performance in a seismic area, Geotechnique No.25, pp61-69.
3. Goughnour, R.R., and A.A. Bayuk (1979) "Analysis of stone column soil matrix interaction under vertical load," Proc. ENPC-LCPC CR coil. Int. Reinforcement des sols, 271 TYV- Paris.
4. Goughnour, R.R., and A.A. Bayuk (1979) "A field study of long term settlement of loads supported by stone columns in soft grounds," Proc. ENPC-LCPC CR coil, Int. Renforcement des sols, pp279 -285 Paris.
5. Hughes, J.M.O. and N.J. Withers (1974) "Reinforcing soft cohesive soil with stone columns," Ground Engineering, may, pp.42-49
6. Kulhawy, F. H. (1984) "Limiting tip or side resistance: fact or fallacy," Proceedings of ASCE Symposium on Analysis and Design of Pile Foundations, San Francisco, California, pp.80-98.
7. Mitchell, J.K. (1976) *Fundamentals of Soil Behavior*, John Wiley & Sons, Inc., New York, 422 pp.

8. Mitchell, J.K., and T.R. Huber (1985) "Performance of a Stone Column Foundation," *Journal of Geotechnical Engineering*, American Society of Civil Engineers, Vol. 111, No. GT2, pp.205-223.
9. Olsen, R. S., and V. Farr (1986) "Site Characterization using the cone penetration test," *Proceedings of In-Situ 86*, ASCE Specialty Conference, Blacksburg, Virginia, pp.854-868.
10. Peck, R.B., W.E. Hansen, and T.H. Thornburn (1974) *Foundation Engineering* 2nd. ed. Wiley, New York.
11. Robertson, P.K., and R. G. Campanella (1983a) "Interpretation of cone penetration tests" part I, sand. *Canadian Geotechnical Journal*, Vol. 20, No. 4, pp.718-733.
12. Robertson, P.K., and R. G. Campanella (1983b) "Interpretation of cone penetration tests," part II, clay. *Canadian Geotechnical Journal*, Vol. 20, No. 4, pp.734-745.
13. Schultze, E., and A. Horn (1967) "Base Friction for Horizontally Loaded Footings in Sand and Gravel," *Geotechnique*, Vol. 17 no. 4, December, pp. 329-347.
14. Sowers, G. F., (1968) "Foundation Problems in Sanitary Land Fills," *Journal of Sanitary Engineering ASCE*, Vol. 94, SA I, pp.103-116.

Development and validation of a TRNSYS type for simulating heat pipe heat exchangers in waste heat recovery transient applications.

Pradyut Kumar Swain, *Department of Mechanical Engineering, Aryan Institute of Engineering & Technology, Bhubaneswar, pkswain25@gmail.com*

Deepikarani Swain, *Department of Mechanical Engineering, NM Institute of Engineering & Technology, Bhubaneswar, depika_r19@yahoo.co.in*

Nalinikanta Swain, *Department of Mechanical Engineering, Capital Engineering College, Bhubaneswar, nalini_526@yahoo.co.in*

Debi Prasad Singh, *Department of Mechanical Engineering, Raajdhani Engineering College, Bhubaneswar, deboprasad_1159@gmail.com*

ARTICLE INFO

Keywords:

Heat pipe heat exchanger
Waste heat recovery
Transient modelling
System simulation
TRNSYS

ABSTRACT

Heat pipe heat exchangers (HPHEs) are becoming more popular as a low-grade waste heat recovery solution in energy-intensive businesses. The effect of the heat exchanger within the system requires modelling prior to installation of an HPHE to simulate the entire impact. This allows for the calculation of possible savings and emission reductions, as well as the optimization of waste heat utilisation. TRNSYS is one such simulation programme. In TRNSYS, the currently available heat exchanger simulation components employ averaged values for the inputs, such as constant effectiveness, constant heat transfer coefficient, or conductance, which are fixed throughout the simulation. These forecasts are effective in a steady-state regulated temperature setting, such as a heat treatment plant, but they are not ideal for the bulk of energy recovery systems that operate in variable conditions. The Effectiveness-Number of Transfer Units (-NTU) technique was used to construct a transient TRNSYS HPHE component, which was then validated against experimental data. When compared to existing experimental results, the model predicts outlet temperatures and energy recovery with an accuracy of 15% and an average error of 4.4 percent, which is suitable for engineering purposes.

1. Introduction

Energy is a central topic of conversation of many developed nations, particularly the overreliance on fossil fuels for energy production. Global energy consumption keeps increasing as the world population and the needs of its people increase, but its source may be shifting. So far, petroleum consumption around the world has been steadily increasing ever since its inception, and consequently, mounting greenhouse gas emissions [1]. Simultaneously, the current zeitgeist is that of a green, carbon-neutral planet which pushes for more sustainable sources of energy, either from harnessing renewable energies but additionally by improving the heat recovery of existing systems. At the 2019 United Nations Climate Change Summit, it was announced that countries around the world should reduce emissions by 45% by 2030 on the way to net zero carbon emissions by 2050 [2]. This is a follow up to the 2016 Paris Agreement [3], and has been reinforced by European Union (EU) 2030 energy targets [4], which aim to reduce greenhouse gas emissions to 80–95% below 1990 levels by 2050. Further information on European and UK regulatory frameworks and policies on energy efficiency, in industry, are provided within Ref. [5].

The industrial sector contributes 30.5% of the total worldwide GDP [6] whilst also being accountable for 33% of the total greenhouse

gas emissions [7]. One way to reduce this contribution is by upgrading or retrofitting inefficient plants with modern technology. One of the methods used is Waste Heat Recovery (WHR) by way of heat exchangers, as it has been reported that 70% of global energy demand in the industrial sector is for heat or thermal processes [8], 72% in the United Kingdom [7].

A heat exchanger is a device whose purpose is to transfer heat energy between two or more fluids. As previously mentioned, a growing area of interest for heat exchangers is the recovery of waste heat [9]. Waste heat is defined as any heat produced by a machine or as a by-product of an industrial process that is lost to atmosphere and has the potential to be captured or reused. A subset of heat exchangers used as WHR devices are heat exchangers equipped with heat pipes (a Heat Pipe Heat Exchanger or HPHE).

Wickless heat pipes, also known as thermosyphons or gravity-assisted heat pipes, are passive heat recovery devices [10]. They consist of hollow tubes partially filled with a working fluid in both liquid and vapour phase. As heat is applied to the pool of fluid at the bottom half of the pipe, termed evaporator, the fluid evaporates and, in gaseous form, travels to the top of the pipe. By having a colder stream make contact with the top section of the pipe, the cooler walls at the top of the heat pipe cause the fluid to condense and, due to the action of gravity, travel back to the bottom of the heat pipe in liquid form (Fig. 1). This is a continuous process that takes place as long as there is a temperature difference between the evaporator and the

Nomenclature

Acronyms

ϵ -NTU	Effectiveness - Number of Transfer Units
DLL	Dynamic Link Library
EU	European Union
Fortran	FORmula TRANslation
GDP	Gross Domestic Product
HPHE	Heat Pipe Heat Exchanger
LMTD	Log Mean Temperature Difference
TRNSYS	TRaNsient SYStems Simulation
WHR	Waste Heat Recovery

Symbols and Units

A	Overall heat transfer area (m^2)
C	Heat capacity (J.K^{-1})
c_p	Specific heat capacity ($\text{J.kg}^{-1}.\text{K}^{-1}$)
D_o	Outer diameter (of tube) (m)
e	Thickness (m)
F_a	Correction factor associated with arrangement (Dimensionless)
H	Width (m)
h	Heat transfer coefficient ($\text{W.m}^{-2}.\text{K}^{-1}$)
h_{fg}	Latent heat (J.kg^{-1})
k	Thermal conductivity ($\text{W.m}^{-1}.\text{K}^{-1}$)
K	Constant (Dimensionless)
L_{ch}	Characteristic length (m)
\dot{m}	Mass flow rate (kg.s^{-1})
P	Pitch (m)
Pr	Prandtl number (Dimensionless)
Nu	Nusselt number (Dimensionless)
N_r	Number of longitudinal rows of heat pipes (Dimensionless)
N_t	Number of heat pipes in a transverse row (Dimensionless)
R	Thermal resistance (K.W^{-1})
Re	Reynolds number (Dimensionless)
T	Temperature ($^{\circ}\text{C}$)
u	Flow velocity (m.s^{-1})
V_{max}	Maximum velocity across tube bundle (m.s^{-1})
U	Overall heat transfer coefficient ($\text{W.m}^{-2}.\text{K}^{-1}$)
v_f	Free stream velocity (m.s^{-1})
A_{min}	Location of minimum free flow area (m^2)
S_L	Longitudinal row pitch (m)
S'_L	Diagonal row pitch (m)
S_T	Transverse row pitch (m)
\dot{Q}	Heat transfer rate (kW)

Greek symbols

α	Thermal diffusivity ($\text{m}^2.\text{s}^{-1}$)
Δ	Difference (Dimensionless)
ϵ	Effectiveness (Dimensionless)
η	Efficiency (Dimensionless)
μ	Dynamic viscosity (N.s.m^{-2})
ν	Kinematic viscosity (momentum diffusivity) ($\text{m}^2.\text{s}^{-1}$)
ρ	Density (kg.m^{-3})
σ	Surface tension (N.m^{-2})
Φ	Figure of merit (W.m^{-2})

Subscripts and superscripts

act	Actual
b	Boiling

c	Condenser
cd	Condensation
D	Associated with diameter of pipe
e	Evaporator
f	Fin
fc	Forced convection
h	Convection
hl	Helical
hp	Heat pipe
in	Inlet
k	Conduction
l	Liquid
LM	Logarithmic mean
max	Maximum
min	Minimum
n	Associated with a row
o	Outer
out	Outlet
s	Associated with external wall
t	Thermosyphon
tot	Total

condenser of the heat pipe. When working at full capacity, if there are no non-condensable gases present inside the heat pipe, it operates nearly isothermally, with little difference in temperature between the top and bottom of the heat pipe. This is also the reason the heat pipe is often referred to as a superconductor.

Some heat pipes are equipped with an inner wick structure which allows them to function against the force of gravity. Historically, this was when heat pipes first started gaining popularity as useful heat sinks for space applications or small electronic devices [11]. Throughout this paper, the heat pipes referred to are wickless heat pipes. A HPHE uses bundles of these heat pipes with the evaporator section in contact with a hot stream and the condenser section in contact with the cooler stream, isolated by a separation plate.

This paper provides a literature review, outlines previous simulations conducted, and shows how an improved simulation methodology has been developed using TRNSYS software to simulate a HPHE's performance transiently by creating a dedicated HPHE component, which provides accurate predictions on outlet temperatures and energy recovery. A full-scale working HPHE unit installed to recover waste heat from a continuous roller kiln that fires ceramic tiles has been used to empirically validate the model.

2. Literature review

2.1. Industrial applications

When looking at heat recovery applications, the main advantage of a HPHE over traditional heat exchangers is their superior flow separation and increased redundancy as each pipe functions as an individual heat exchanger. This means that if one pipe fails, it will not put the integrity or overall performance of the heat exchanger at risk and, importantly, prevents any cross-contamination between heat streams. This is crucial when contamination between streams is undesirable. Heat pipes also have a high effective thermal conductivity compared with traditional heat exchangers due to the two-phase boiling and condensation heat transfer, which allows its heat transfer coefficient to be directly correlated with the specific heat of the working fluid being used. Heat transfer coefficients in the magnitude of 10^3 – $10^5 \text{ W.m}^{-2}.\text{K}^{-1}$ have been reported [12].

In heat exchangers, counter-flow is usually preferable to parallel-flow. Heat transfer is a function of temperature difference, and counter-

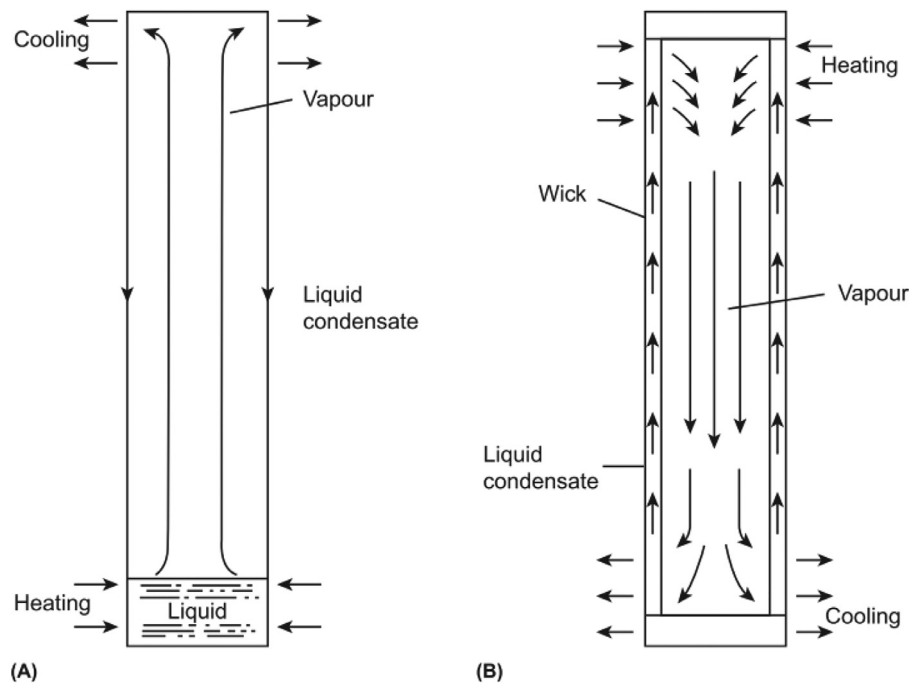


Fig. 1. Thermosyphon (A) and Heat pipe (B) operating principle [10].

flow allows for a continuous difference in temperature between the two streams. The difference in temperature between the evaporator and the condenser is also an operating requirement in a heat pipe. Therefore, in a HPHE, the designer must ensure that each heat pipe is located between two flows at different temperatures, thus consistently having a difference in temperature (ΔT) between its ends. Furthermore, in counter-flow, the temperature of the hot outlet stream can be lower than the cold sink outlet stream. A counter-flow HPHE and a comparison between parallel and counter-flow is shown in Fig. 2. The component created in this paper was to replicate a counter-flow HPHE.

In most applications, a HPHE is defined as a counter-flow heat exchanger as a whole, but in essence it is a combination of two cross-flow heat exchangers if divided between evaporator and condenser: counter-flow due to the direction of the incoming streams and cross-flow as there is a 90° angle between the incoming flow direction and the flow inside the heat pipes. Both crossflow heat exchangers and counter-flow heat exchangers have a higher effectiveness than other heat exchanger geometries [14].

Faghri [11] and Jouhara [15, 16] provide a review on current applications for heat pipes and some examples include solar water heating [17, 18, 19, 20], desalination [21, 22] and domestic space heating applications [23, 24]. However, one of the most promising applications is in WHR. Existing WHR applications of HPHEs include: an EU project, ETE-KINA [25], with installations of HPHE technology within steel, aluminium and ceramic industries [26]; the DREAM Project (Design for Resource and Energy efficiency in cerAMic kilns) with specific focus on the application of HPHEs to a kiln cooling section [27]; and i-ThERM, an EU funded project which looked at the development of an array of technology related to heat pipes and in particular to heat recovery focusing on energy transfer by the radiation mechanism [28]. An example of a 12.6 MW HPHE installed to recover energy contained within exhaust gas from a steel mill blast furnace is shown in Fig. 3.

2.2. Working fluid

When choosing the working fluid inside the heat pipe, the main limits are the liquid boiling and vapour condensation temperatures of each fluid. Ref. [29] provides examples of available and tested working fluids with their applicable temperature ranges. Since the heat pipe is

effectively working at a constant temperature, one must be aware of the range of boiling temperatures of different fluids as it is possible to boil all the working fluid in the heat pipe and reach the 'dry out' limit. Heat pipe design is outside the scope of this paper, but the choice of working fluid usually comes down to the working temperatures, and its effectiveness is measured by the specific heat of the fluid. For low grade heat recovery, distilled water is ideal due to its high specific heat [29].

For most applications the working fluid inside the heat pipe itself is assumed to be isothermal throughout the heat pipe's length. However, there is a small temperature difference which determines the figure of merit of the heat pipe. A figure of merit is a measure of the heat pipe's thermal resistance; a high figure of merit for the fluid in a thermosyphon means that the heat pipe will have a low temperature difference between its two ends. Consequently, a heat pipe with a high figure of merit can achieve a good performance due to its low thermal resistance and high heat transfer capability [30]. The figure of merit also depends on the operating temperature of the heat pipe. Eq. (2.1) calculates figure of merit values for typical working fluids in thermosyphons:

$$\Phi = \left(\frac{h_{fg} k_l^3 \rho_l^2}{\mu_l} \right)^{1/4} \quad (2.1)$$

where Φ is the figure of merit ($\text{kg.K}^{-3/4}.\text{s}^{-5/2}$), h_{fg} is the latent heat of vaporisation (J.kg^{-1}), k_l is the thermal conductivity of the working fluid ($\text{W.m}^{-1}.\text{K}^{-1}$), ρ_l is the density of the working fluid (kg.m^{-3}) and μ_l is the liquid viscosity (Pa.s^{-1}) [31]. A visualisation of the application of this equation is shown in Fig. 4.

2.3. Transient conditions and previous modelling

HPHEs tend to be installed in challenging streams and as such, each unit is bespoke for a specific plant's needs. In order to predict its size, numerous papers in literature have referenced using the Effectiveness-Number of Transfer Units (ϵ -NTU) method [33, 34, 35]. A limitation so far of this method is that it has only been applied to HPHEs operating under steady-state conditions or with averaged values, which are often the exception in real life heat recovery systems unless significant control measures are undertaken.

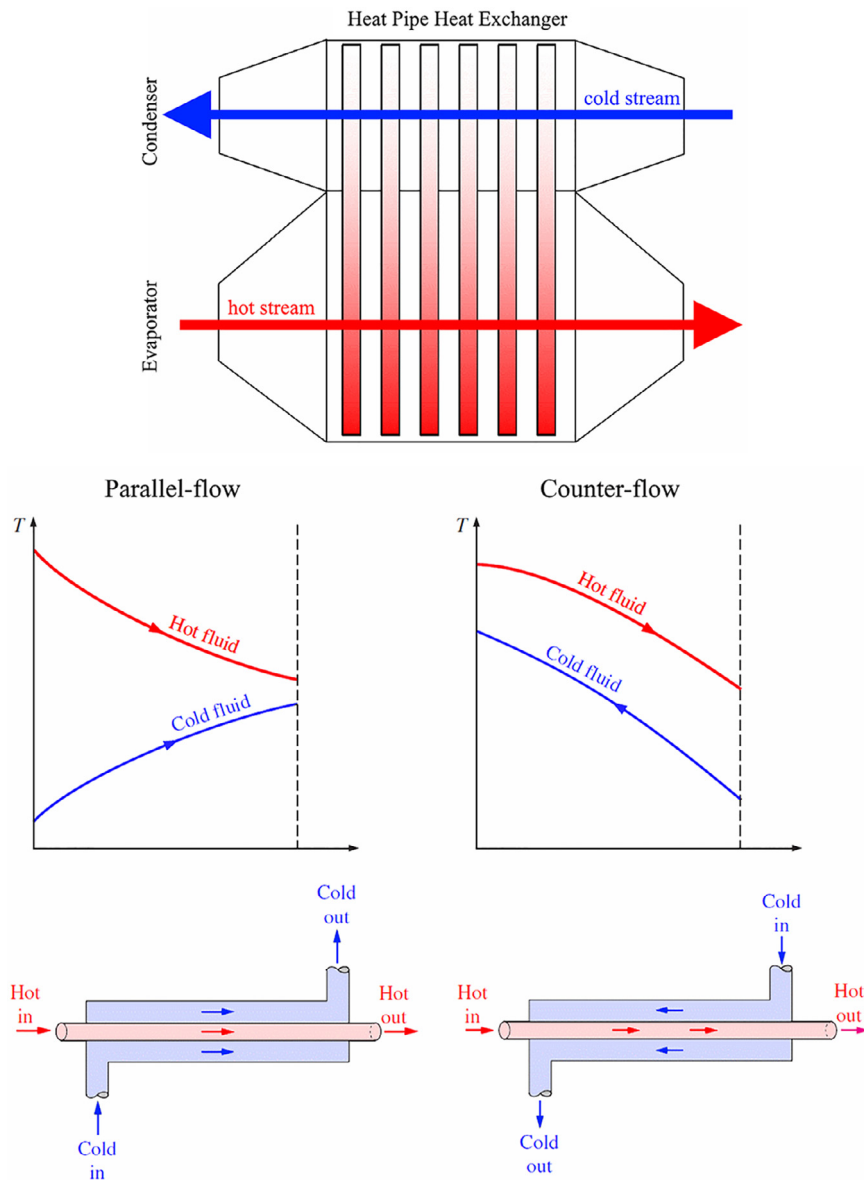


Fig. 2. Counter-flow heat pipe heat exchanger with flow comparison. Adapted from [13].

Regarding literature on modelling transient heat pipe behaviour, the first few mentions of models are the works by Chang and Colwell [36] who compared numerical predictions to experimental data and achieved a moderate level of success. Due to limited technology at the time, the computational model assumed that the dominant heat transfer modes were two-dimensional conduction in the heat pipe shell and wick. Other variables were neglected such as the thermal resistance along the vapour space and along the liquid-vapour interface. Performance was predicted using a finite-difference method.

Many of the first transient heat pipe models dealt with start-up problems, particularly the change of solid working fluids into liquid and eventually gas. For example, Deverall et al. [37] described the transient behaviour of water and metallic heat pipes. They concluded that start-up was possible from a solid-state working fluid, however, it was highly dependant on the amount of heat provided.

Colwell [38] is one of the first published pieces of work that attempts to model the complete transient behaviour of a heat pipe. In his work he models a heat pipe with a metallic working fluid for high temperature applications, during start-up from a frozen state.

Another example of start-up from frozen state is from Yang et al. [39] who developed a transient analysis code for a flat heat pipe receiver

in a solar power tower plant. The model was able to predict the temperature distributions reasonably well, and the experimental results showed promise for the application of flat heat pipes to solar towers.

Tournier and El-Genk developed their own two-dimensional heat pipe transient model [40], and the results achieved were in reasonable agreement with the experiments, albeit the transient response was found to be faster than in the experiment, due to the time taken for the heat to travel through the insulation. Brocheny [41] listed the state-of-the-art efforts on transient heat pipes and modelled the transient operation of low-temperature heat pipes from room-temperature conditions. He contributed to previous work by including dry-out and recovery in the thermal predictions. In terms of limitations, the effect of wick saturation was not considered in this work.

The earliest literature found regarding the use of TRNSYS and heat pipes was in 2003 by Budihardjo, Morrison and Behnia [42]. This work developed TRNSYS models for predicting the performance of water-in-glass evacuated tube solar water heaters (Fig. 5). Though not WHR or a HPHE, this work highlighted the use of TRNSYS to simulate 21 inclined open thermosyphons. TRNSYS was used to simulate the collector efficiency and natural circulation flow rate.



Fig. 3. A functioning heat pipe heat exchanger unit.

Yau and Tucker [43] in the same year calculated the overall effectiveness of a wet six-row wickless HPHE for a HVAC system. The main aim was to determine whether moisture content and film condensation on fins reduced the total effectiveness value of the HPHE. This was a very small lab scale unit consisting of six copper heat pipes with an outer diameter of 9.55 mm and finned with 315 0.33 mm aluminium fins per metre. The TRNSYS model for the HPHE is the closest work related to this presented work. The model simulates a lab scale HPHE for only copper heat pipes and fins to determine the overall effectiveness of this heat exchanger and specially requires an inclination angle and humidity of the air. This is an example of WHR but the focus of the work was on HVAC systems and removing humidity from air, particularly for hospitals, and predicting the onset of film condensation. This model used hour-by-hour climatic data from Kuala Lumpur and dealt with low temperature ranges i.e. $<35^{\circ}\text{C}$.

The HPHE component presented here can simulate multiple heat sink fluids, any design configuration and number of heat pipes and is configured for WHR rather than dehumidification.

In 2005, Shah [44] provided a report on TRNSYS models of four types of evacuated tubular collectors, two of importance including heat pipes, namely:

- Type 238- Heat pipe evacuated tubular collectors with curved fins.
- Type 239- Heat pipe evacuated tubular collectors with flat fins.

Previous work by [45] saw the use of TRNSYS to model a multi-pass HPHE applied to a lab scale ceramic kiln using exhaust gases to preheat water. The authors noted the necessity for a dedicated HPHE component to simulate the performance more accurately rather than a counter-flow heat exchanger component. Energy recovery rates were within $\pm 15\%$ with an uncertainty of $<5.8\%$, though temperature prediction differences of up to around 35% were seen. The model could not be confidently used for simulation predictions and used averaged values of conductance taken from the experimental work. This paper presents work that builds upon the conclusions previously published, whilst demonstrating validity on a full-scale installation using a component that can be used to predict performance in the future.

To date there has been no publications for a dedicated transient simulation component of a HPHE configured for WHR on an industrial scale. The aim of this paper is to fill this gap in knowledge using TRNSYS.

3. Theoretical background

The aim of this chapter is to describe current methods of characterising HPHE performance and the principles behind how the TRNSYS component was created.

3.1. Methods of calculating and characterising hphe performance

There are currently three predominant methods available for predicting or characterising the performance of a heat exchanger. These are the Log Mean Temperature Difference (LMTD) method, the ε -NTU method and, more specifically for HPHEs, the thermal network analysis method.

3.1.1. The logarithmic mean temperature difference method

The LMTD method can be used to quantify HPHE performance when inlet and outlet temperatures are known. This method can be used for steady-state but cannot be applied to the TRNSYS model requiring a transient simulation. The LMTD method oversimplifies the model as averaged values need to be used, which does not reflect the real nature of energy intensive processes. Furthermore, this is not

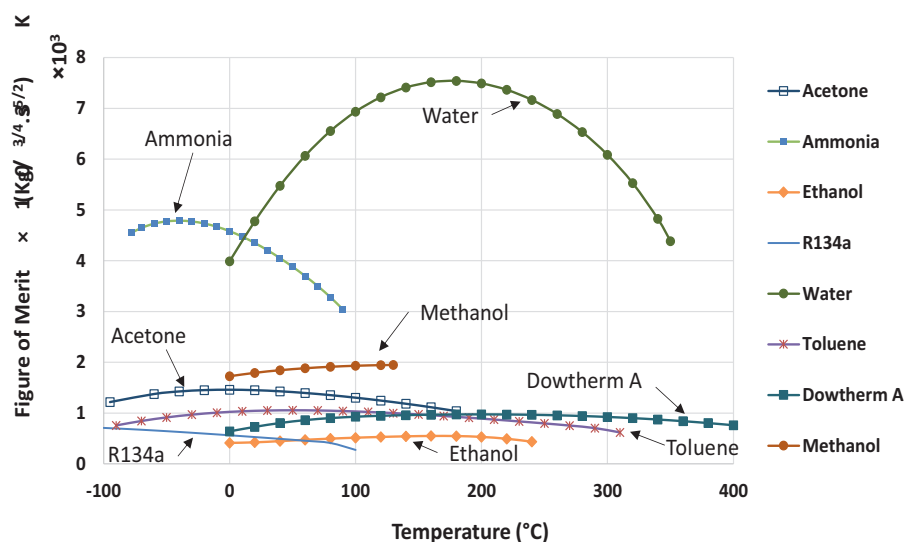


Fig. 4. Figure of merit values for typical working fluids at a range of temperatures in a thermosyphon [32].

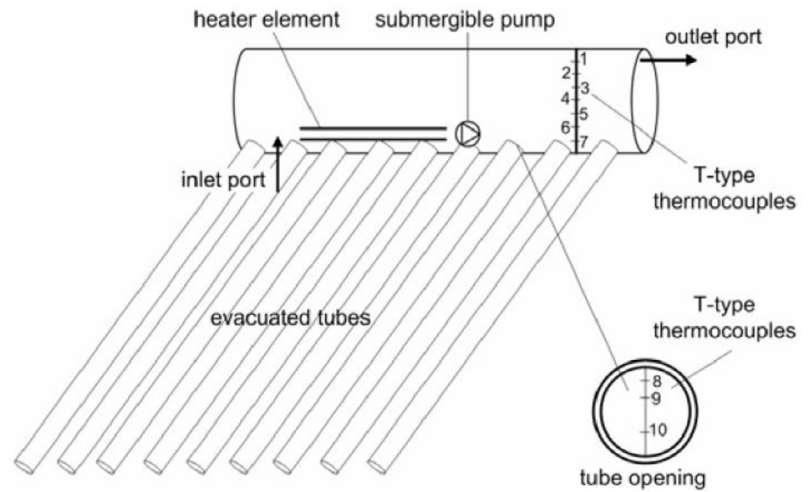


Fig. 5. Schematic and photo of water-in-glass evacuated tube solar water heater [43].

a predictive method as outlet temperatures must be known. This method can be used for HPHEs but relies on previously determined data for inlets and outlets of an existing unit and so it is less useful for predicting performance. For a crossflow heat exchanger, the equation is [13]:

$$\Delta T_{LM} = \frac{(T_{e,in} - T_{c,out}) - (T_{h,out} - T_{c,in})}{\ln \left(\frac{T_{h,in} - T_{c,out}}{T_{h,out} - T_{c,in}} \right)} \quad (3.1)$$

3.1.2. Thermal network analysis

The thermal network analysis is a proven way of viewing the thermal resistances in a heat exchanger [35]. As each heat pipe is an individual miniature heat exchanger, they are all assumed to be heat transfer devices working in parallel with one another within a larger heat exchanger assembly. In an electrical circuit, resistance blocks the transfer of current, in a thermal energy analogy, current is heat flow and resistance is thermal resistance (R), defined as the difference in temperature (ΔT) divided by the heat transfer rate (\dot{Q}), as shown in Eq. (3.2). This is better visualised as a thermal circuit, as shown in Fig. 6.

$$R = \Delta T \dot{Q} \quad (K.W^{-1}) \quad (3.2)$$

This method is often used in tandem with the following ϵ -NTU method as the thermal resistances of the heat pipes are a requirement. Boiling [46], evaporation and condensation correlations can

also be used to calculate the resistances and heat transfer performance of thermosyphons [47].

3.1.3. The effectiveness-NTU method

The ϵ -NTU method is used to predict outlet temperatures by calculating the effectiveness, a dimensionless parameter related to the heat transfer performance of the heat exchanger. It is a measure between 0 and 1 and it is the measure of the actual heat transfer rate compared to the maximum theoretical heat transfer rate for the heat exchanger. This method was determined to be the most useful for transient predictions and was used to create the TRNSYS component. The general equation is shown below and has been developed for the evaporator and condenser sections of a HPHE [35]:

$$\epsilon_e = \frac{q_{act}}{q_{max}} = \frac{C_e(T_{e,in} - T_{e,out})}{C_{min}(T_{e,in} - T_{c,in})} \quad \text{and} \quad \epsilon_c = \frac{C_c(T_{c,out} - T_{c,in})}{C_{min}(T_{e,in} - T_{c,in})} \quad (3.3)$$

3.2. Using the effectiveness-NTU and thermal network analysis methods to predict hphe performance

To determine the equations requiring coding for the TRNSYS HPHE component, the ϵ -NTU equations needed to be expanded to their base components so that the relevant TRNSYS inputs, parameters and calculations could be fed into the equations. Eqs. (3.4) and (3.5) are developed from Eq. (3.3), with ϵ_e and ϵ_c being the

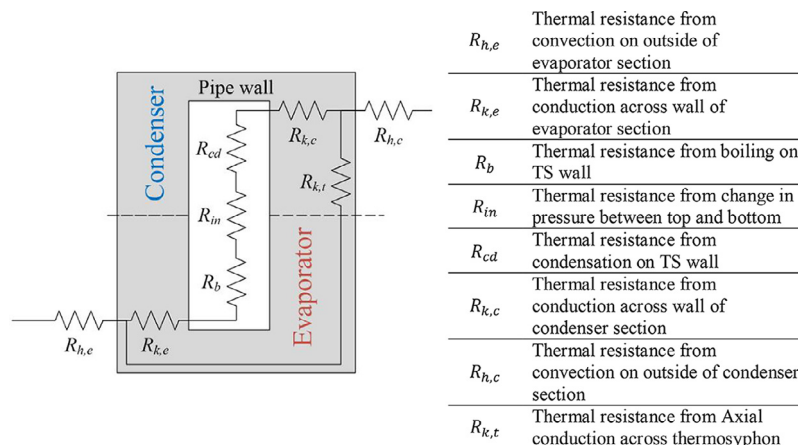


Fig. 6. Schematic of the thermal resistances within a heat pipe [35].

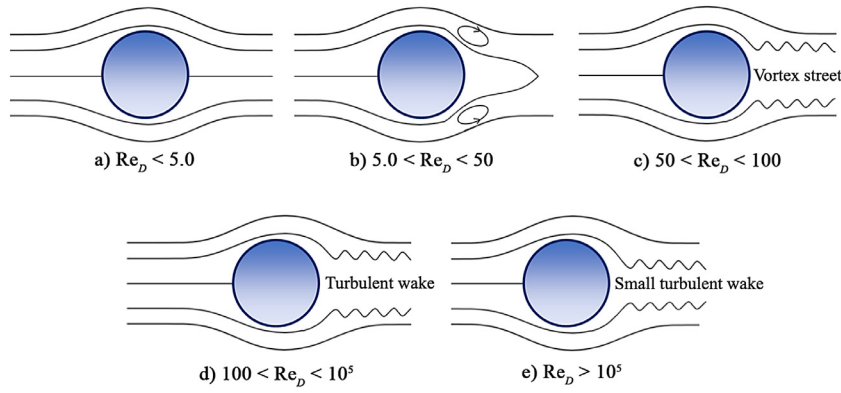


Fig. 7. Crossflow flow patterns for fluids passing across a cylinder with increasing Reynolds number. Adapted from [53].

effectiveness of the evaporator and condenser sections. They show how the outlet temperatures for the evaporator and condenser section can be found from the effectiveness of that section.

$$T_{e,out} = T_{e,in} - \varepsilon_t \frac{C_{min}}{C_e} (T_{e,in} - T_{c,in}) \quad (3.4)$$

$$T_{c,out} = T_{c,in} + \varepsilon_t \frac{C_{min}}{C_c} (T_{e,in} - T_{c,in}) \quad (3.5)$$

where $T_{e,in}$, $T_{e,out}$, $T_{c,in}$ and $T_{c,out}$ are the inlet and outlet temperatures of the evaporator (e) and condenser (c) fluids, C_{min} is the minimum value of C_e and C_c , the heat capacities of the evaporator and condenser fluids, a measure of the mass flow rate (\dot{m} in kg.s^{-1}) multiplied by the specific heat capacity (c_p in $\text{J.kg}^{-1}.\text{K}^{-1}$) of each stream. ε_t is the total effectiveness of the heat exchanger, traditionally calculated using the equations below. Depending on which heat capacity is the larger of the condenser and evaporator fluids, the total effectiveness (ε_t) equation varies:

$$\text{If } C_e > C_c \quad \varepsilon_t = \left(\frac{1}{\varepsilon_{c,n}} + \frac{C_c/C_e}{\varepsilon_{e,n}} \right)^{-1} \quad (3.6)$$

$$\text{If } C_c > C_e \quad \varepsilon_t = \left(\frac{1}{\varepsilon_{e,n}} + \frac{C_e/C_c}{\varepsilon_{c,n}} \right)^{-1} \quad (3.7)$$

where $\varepsilon_{c,n}$ and $\varepsilon_{e,n}$ are the effectiveness associated with a transverse row of thermosyphons. For this reason, different equations are coded into the component depending on whether C_e or C_c is larger. The effectiveness of a row of evaporator ($\varepsilon_{e,n}$) or condenser ($\varepsilon_{c,n}$) thermosyphons can be written by Eqs. (3.8) and (3.9), respectively.

$$\varepsilon_{e,n} = 1 - (1 - \varepsilon_e)^{N_t} \quad (3.8)$$

$$\varepsilon_{c,n} = 1 - (1 - \varepsilon_c)^{N_t} \quad (3.9)$$

where ε_e and ε_c are the effectiveness of a single thermosyphon's evaporator or condenser section and N_t is the number of thermosyphons in a row. The effectiveness of the evaporator and condenser sections of a thermosyphon can be written by Eqs. (3.10) and (3.11).

$$\varepsilon_e = 1 - e^{(-NTU_e)} \quad (3.10)$$

$$\varepsilon_c = 1 - e^{(-NTU_c)} \quad (3.11)$$

where NTU_e and NTU_c are the number of transfer units for the evaporator and condenser. The number of transfer units of the evaporator and condenser sections (NTU_e and NTU_c) are equivalent to Eqs. (3.12) and (3.13).

$$NTU_e \equiv \frac{U_e A_e}{C_e} \quad (3.12)$$

$$NTU_c \equiv \frac{U_c A_c}{C_c} \quad (3.13)$$

where U_e and U_c are the overall heat transfer coefficients of the evaporator and condenser section of the thermosyphon and A_e and A_c are the overall heat transfer areas.

With a HPHE, the UA values are equivalent to the inverse of the thermal resistance of that section and U is equal to h_{fc} , the forced convection heat transfer coefficient. This is shown in Eqs. (3.14) and (3.15):

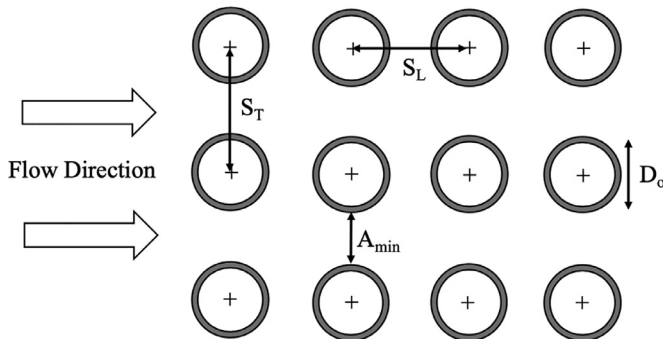


Fig. 8. In-line tube bundle arrangement.
 S_T - Transverse row pitch
 S_L - Longitudinal row pitch
 D_o - Outer diameter
 A_{min} - Location of minimum free area

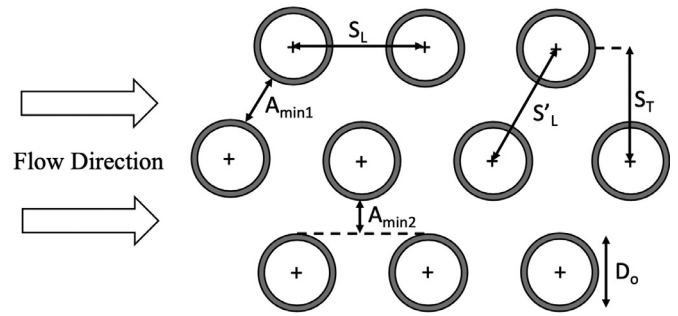


Fig. 9. Staggered tube bundle arrangement.
 S_T - Transverse row pitch
 S_L - Longitudinal row pitch
 S'_L - Diagonal distance between longitudinal centres
 D_o - Outer diameter
 $A_{min1/2}$ - Potential locations of minimum cross flow area



Fig. 10. A selection of available fin configurations.

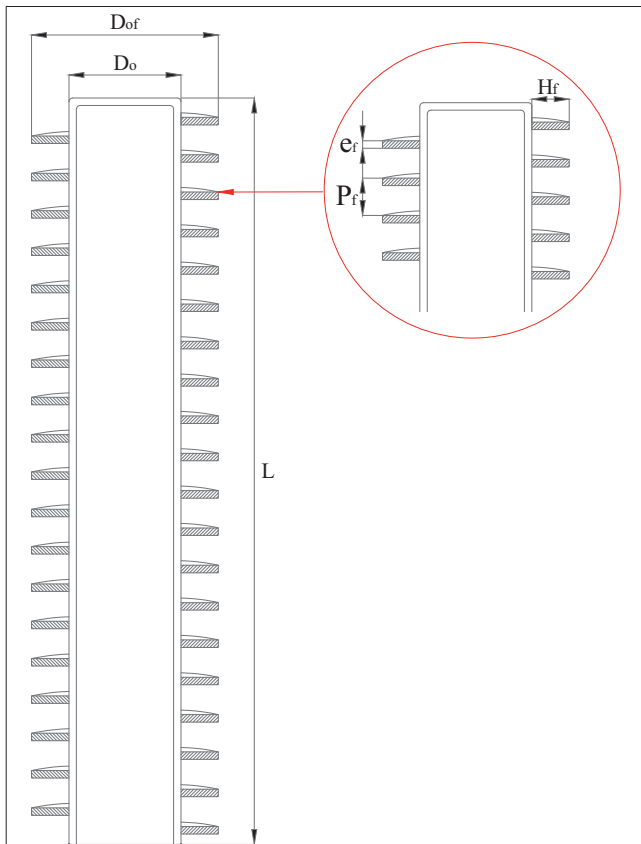


Fig. 11. Diagram of helical finning with symbols.

$$U_e A_e = \frac{1}{R_{e,out}} = h_{fc,e} A_e \quad (3.14)$$

$$U_c A_c = \frac{1}{R_{c,out}} = h_{fc,c} A_c \quad (3.15)$$

where $R_{e,out}$ and $R_{c,out}$ are the thermal resistances of the evaporator section and the condenser section. The thermal resistance decreases as the number of pipes increases, due to the increased surface area. Section 3.3 deals with how h_{fc} is calculated.

Heat capacitance is found by Eqs. (3.16) and (3.17).

$$C_e = \dot{m}_e c_{p,e} \quad (3.16)$$

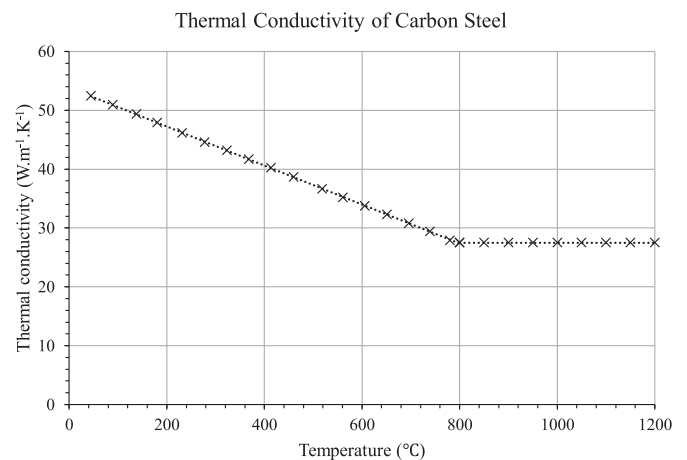


Fig. 12. Thermal conductivity of carbon steel [61].

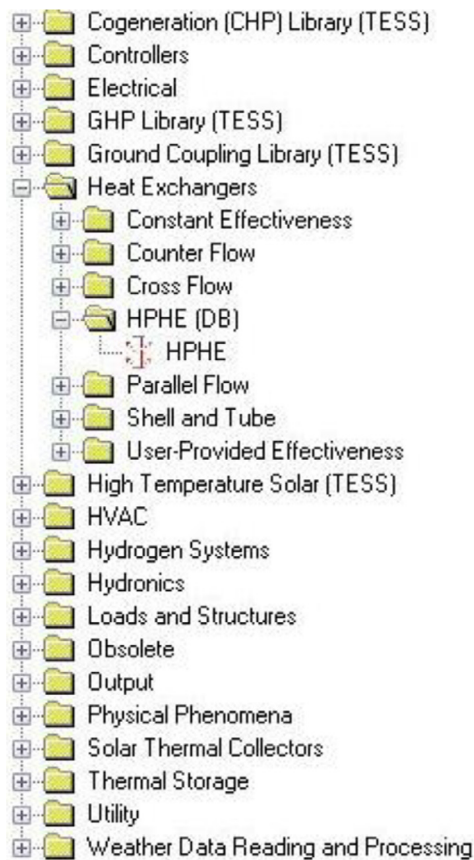


Fig. 13. A view of the standard TRNSYS component library and the location of the newly developed HPHE component.

$$C_c = \dot{m}_c c_{p,c} \quad (3.17)$$

where \dot{m}_e and \dot{m}_c are the mass flow rates of the evaporator and condenser streams and $c_{p,e}$ and $c_{p,c}$ are the specific heat capacities of the fluids.

The equations in this section, along were coded using Fortran language for the HPHE component in the TRNSYS model to determine the outlet temperatures depending on the variables in the model.

3.3. Calculating the heat transfer coefficient of forced convection

The heat transfer coefficient of forced convection, h_{fc} , is the most challenging variable to determine and it depends on a variety of flow properties. The calculations predominantly depend upon the design of the HPHE. h_{fc} must be calculated for both the evaporator and condenser sections, as below:

$$h_{fc} = \frac{Nu_D k}{D_o} \quad (3.18)$$

Nu_D is the Nusselt number (dimensionless) in respect to the diameter of the heat pipe and the calculations are shown in Section 3.3.1, k is the thermal conductivity of the fluid ($W.m^{-1}.K^{-1}$) and D_o is the outer diameter of the heat pipe (m).

3.3.1. Nusselt, Prandtl and Reynolds dimensionless numbers

Each of the numbers below are calculated for the inlet, outlet and heat pipe outer wall temperatures of both the evaporator and condenser sections. Tables for natural gas, flue gas, air, water and thermal oil (specifically Therminol-66) are used to calculate the thermophysical properties from [48, 49, 50, 51]. The significant

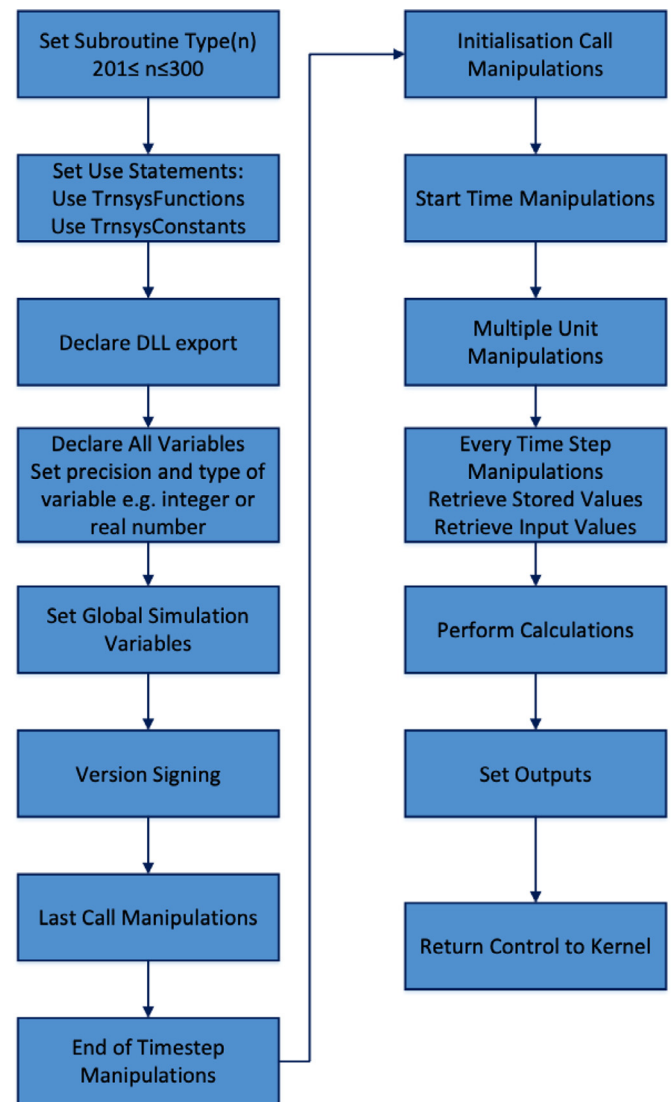


Fig. 14. A flowchart of the TRNSYS component coding process.

properties are density, kinematic viscosity, thermal conductivity and specific heat capacity.

The Nusselt number is traditionally calculated from Eq. (3.19), a rearrangement of Eq. (3.18), in order create a non-dimensional number from many contributing variables. In essence, the Nusselt number represents a ratio of heat transfer by convection to conduction across a fluid layer to quantify which mechanism contributes the most to heat transfer [13].

$$Nu = \frac{h L_{ch}}{k} \quad (3.19)$$

L_{ch} is the characteristic length, in this case substituted with D_o .

The Prandtl number (Pr) of a fluid is the ratio between momentum diffusivity and thermal diffusivity. The number describes the thickness of the thermal boundary layer relative to the thermal boundary layer. Gases have Prandtl numbers around 0.7–1.0 and water is 1.7–13.7. [13]. The Prandtl number can be calculated from Eq. (3.20) [52].

$$Pr = \frac{\text{Momentum diffusivity of momentum}}{\text{Thermal diffusivity of heat}} = \frac{\nu}{\alpha} = \frac{\mu/\rho}{k/c_p \rho} = \frac{c_p \mu}{k} \quad (3.20)$$

ν is the momentum or kinematic viscosity ($m^2.s^{-1}$), α is the thermal diffusivity ($m^2.s^{-1}$), μ is the dynamic viscosity (Pa.s), ρ is the density ($kg.m^{-3}$), k is the thermal conductivity ($W.m^{-1}.K^{-1}$), c_p is the specific heat ($J.kg^{-1}.K^{-1}$).

```
!Inputs
Double precision Thi !Temperature of source inlet fluid [deg C]
Double precision Tci !Temperature of sink inlet fluid [deg C]
Double precision FLWe !Mass flow rate evaporator (source) fluid [kg/s]
Double precision FLWc !Mass flow rate condenser (sink) fluid [kg/s]

!Parameters
Integer Nr !Number of rows in heat exchanger (longitudinal)
Double precision Dout !Outer diameter of heat pipes [m]
Double precision Le !Length evaporator [m]
Double precision Lc !Length of condenser [m]
Integer Nt !Number of tubes in row (transverse)
Double precision ST !Distance between row centres [m]
Double precision SL !Distance between heat pipe centres [m]
Double precision Ae !Flow area of evaporator [m2]
Double precision Ac !Flow area of condenser [m2]
Integer FinningMode !(1=none, 2=con finned, 3=evap finned, 4=both)
Integer FluidMode !Sink: 1=air 2=water 3=thermal oil
Double precision Dofin !Outer diameter of fins [m]
Double precision efin !Thickness of fins [m]
Double precision Pfin !Pitch of fins [m]
Double precision Hfin !Width of fins [m]
```

Fig. 15. Code to declare all the variables that Type202 uses throughout the subroutine.

The Reynolds number (Re) provides an indication of the flow regime and also when laminar flow will transition to turbulent flow. Large Reynolds number indicate turbulent flow and a quick transition and vice versa for a small Reynolds number. [13]. Fig. 7 shows typical Reynolds numbers associated with crossflow flow patterns and Eq. (3.21) the general equation used to determine the Reynolds number.

$$Re = \frac{\text{Inertial forces}}{\text{Viscous forces}} = \frac{\rho u L_{ch}}{\mu} = \frac{u L_{ch}}{\nu} \quad (3.21)$$

where ρ is the fluid density, u is the velocity, μ is the dynamic viscosity, L_{ch} is the characteristic length and ν is the momentum or kinematic viscosity. The Reynolds number associated with the outer diameter of a tube (D_o) can be determined using:

$$Re_D = \frac{V_{max} D_o}{\nu} \quad (3.22)$$

The calculation of V_{max} , the maximum velocity occurring in the minimum flow area between tubes (in this case the heat pipes), depends on whether the tubes are in a staggered or in-line arrangement. Fig. 8 shows an in-line tube bundle arrangement with the varying parameters and Eq. (3.24) provides the calculation. Fig. 9 shows a staggered arrangement with the V_{max} calculations provided by Eqs. (3.25) to (3.27).

$$A_{min} = S_T - D_o \quad (3.23)$$

$$V_{max} = \frac{S_T}{S_T - D_o} \times v_f \quad (3.24)$$

where v_f is the free-flow velocity at the inlet face area without tubes.

The minimum free-flow area, A_{min} , can potentially occur in two places in staggered arrangements. It can be, as in Eq. (3.23), transversely between the tube rows. However, if S_T is much larger than S_L such that:

$$\sqrt{\left(\frac{S_T}{2}\right)^2 + S_L^2} < \frac{S_T + D_o}{2} \quad (3.25)$$

according to [53]:

$$V_{max} = \frac{S_T/2}{\sqrt{\left(\frac{S_T}{2}\right)^2 + S_L^2} - D_o} \times v_f \quad (3.26)$$

The authors have rearranged this to:

$$V_{max} = \frac{v_f}{\sqrt{1 + \left(2 \frac{S_L}{S_T}\right)^2} - 2 \frac{D_o}{S_T}} \quad (3.27)$$

Table 1 provides the available correlations, based on empirical data, for calculating the Nusselt number from literature using Reynolds and Prandtl numbers with the varying applications and conditions where they can be applied; adapted from [54].

Pr_s is the Prandtl number evaluated at the external wall temperature of the heat pipe.

For the correlations provided by Ref. [59], if the number of rows (Nr) is <16 and $Re_D > 1000$, a correction factor can be used as seen in Table 2, adapted from [13].

3.3.2. Effect of finning heat pipes

The final factor that needs to be considered is whether the heat pipes are finned. External pipe finning is used to increase the heat transfer surface and increase turbulence and is primarily for gaseous applications but can also be used for liquids. The HPHE tested had helical fins on both the evaporator and condenser sections. Helical fins are currently the favoured configuration for heat exchangers for WHR units. Ponsoi, Pikulkajorn and Wongwises [60] provide a thorough review on spiral finning, the available configurations and available correlations for Colburn and friction factors. Fig. 10 provides a schematic of a selection of available tube finning configurations. The model can be adapted to incorporate other finning configurations and used equations for their area and correlations determining efficiency.

The total heat transfer area (A_{tot}) of a heat pipe section with fins is found by adding the heat transfer area of the heat pipe (A_{hp}) to the heat transfer area of the fins (A_f) taking into account the efficiency of the fins. Heat transfer is reduced the farther the fin section is from the pipe as the energy is passed by conduction. Therefore, a coefficient of efficiency for the fin is introduced (η_f). Fig. 11 shows a diagram of a finned heat pipe and symbols used in the following equations. These equations are calculated for both the evaporator and condenser section separately for helical fins.


```

!Internal Variables
Double precision HTFe !Heat transfer coefficient evaporator [W/m2.K]
Double precision HTFeo !Heat transfer coefficient evaporator outlet [W/m2.K]
Double precision HTFc !Heat transfer coefficient condenser [W/m2.K]
Double precision HTFco !Heat transfer coefficient condenser outlet [W/m2.K]
Double precision HTAe !Heat transfer area of one evaporator row [m2]
Double precision HTAe_smooth !Heat transfer area of one evaporator row smooth [m2]
Double precision HTAc !Heat transfer area of one condenser row [m2]
Double precision HTAc_smooth !Heat transfer area of one condenser row smooth [m2]
Double precision Ce !Heat capacity rate of evaporator [j/K.s]
Double precision Ceo !Heat capacity rate of evaporator outlet [j/K.s]
Double precision Cc !Heat capacity rate of condenser [j/K.s]
Double precision Cco !Heat capacity rate of condenser outlet [j/K.s]
Double precision Cmin !Smaller or Ce and Cc [j/K.s]
Double precision Cmino !Smaller or Ce and Cc outlet [j/K.s]
Double precision Et !Overall effectiveness
Double precision Eto !Overall effectiveness outlet
Double precision een !Effectiveness of evaporator row
Double precision eeno !Effectiveness of evaporator row outlet
Double precision ecn !Effectiveness of condenser row
Double precision ecno !Effectiveness of condenser row outlet
Double precision ee !Effectiveness of evaporator
Double precision eeo !Effectiveness of evaporator outlet
Double precision ec !Effectiveness of condenser
Double precision eco !Effectiveness of condenser outlet
Double precision NTUe !Number of effectiveness units evaporator
Double precision NTUeo !Number of effectiveness units evaporator outlet
Double precision NTUc !Number of effectiveness units condenser
Double precision NTUco !Number of effectiveness units condenser outlet
Double precision Pre !Prandtl number evaporator
Double precision Preo !Prandtl number evaporator outlet
Double precision Prc !Prandtl number condenser
Double precision Prco !Prandtl number condenser outlet
Double precision Vmaxe !Maximum velocity evaporator [m/s]
Double precision Vmaxeo !Maximum velocity evaporator outlet [m/s]
Double precision Vmaxc !Maximum velocity condenser [m/s]
Double precision Vmaxco !Maximum velocity condenser outlet [m/s]
Double precision ReDe !Reynolds number evaporator
Double precision ReDeo !Reynolds number evaporator outlet
Double precision ReDc !Reynolds number condenser
Double precision ReDco !Reynolds number condenser outlet
Double precision Nuse !Nusselt number evaporator
Double precision Nuseo !Nusselt number evaporator outlet
Double precision Nusc !Nusselt number condenser
Double precision Nusco !Nusselt number condenser outlet
Double precision ve !Free flow velocity evaporator [m/s]
Double precision veo !Free flow velocity evaporator outlet [m/s]
Double precision vc !Free flow velocity condenser [m/s]
Double precision vco !Free flow velocity condenser outlet [m/s]
Double precision RHOe !Density evaporator fluid [kg/m3]
Double precision RHOeo !Density evaporator fluid outlet [kg/m3]
Double precision RHOC !Density condenser fluid [kg/m3]
Double precision RHOCO !Density condenser fluid outlet [kg/m3]
Double precision Nue !Kinematic viscosity evaporator [m2/s]
Double precision Nueo !Kinematic viscosity evaporator outlet [m2/s]
Double precision Nuc !Kinematic viscosity condenser [m2/s]
Double precision NUco !Kinematic viscosity condenser outlet [m2/s]
Double precision LAMDAe !Thermal conductivity evaporator fluid [W/m.K]
Double precision LAMDAeo !Thermal conductivity evaporator fluid outlet [W/m.K]
Double precision LAMDAc !Thermal conductivity condenser fluid [W/m.K]
Double precision LAMDAco !Thermal conductivity condenser fluid outlet [W/m.K]
Double precision SHCe !Specific heat capacity evaporator fluid [J/kg.K]
Double precision SHCeo !Specific heat capacity evaporator fluid outlet [J/kg.K]
Double precision SHCc !Specific heat capacity condenser fluid [J/kg.K]
Double precision SHCco !Specific heat capacity condenser fluid outlet [J/kg.K]
Double precision Timestep,Time !Simulation timestep and time [s]
Double precision PI !Pi, 3.1415927
Integer CurrentUnit, CurrentType

```

Fig. 15 Continued.

```
!Evaluation Of Pr At Wall Temperature
Double precision Pres !Pr evaluated at evaporator wall temperature
Double precision Prcs !Pr evaluated at condenser wall temperature
Double precision NUew !Kinematic viscosity at evaporator wall [m2/s]
Double precision NUcw !Kinematic viscosity at condenser wall [m2/s]
Double precision LAMDAew !Thermal conductivity at evaporator wall [W/m.K]
Double precision LAMDAcw !Thermal conductivity at condenser wall [W/m.K]
Double precision Twe !Iterating evap wall temperature to determine Pres [deg C]
Double precision Twc !Iterating cond wall temperature to determine Prcs [deg C]
Double precision SHCew !Specific heat capacity at evaporator wall temperature [J/kg.K]
Double precision SHCcw !Specific heat capacity at condenser wall temperature [J/kg.K]

!Goalseeking
Double precision Twe_up !Goalseek up function for Twe [deg C]
Double precision Twe_down !Goalseek down function for Twe [deg C]
Double precision Twc_up !Goalseek up function for Twc [deg C]
Double precision Twc_down !Goalseek down function for Twc [deg C]
Double precision Q1e !m.cp.dT
Double precision Q2e !((Thi-Tho)/log(Thi-Twe)/Tho-Twe))
Double precision Q4e !((Thi-Tho)/log(Thi-Twe(up/down))/Tho-Twe(up/down)))
Integer numiterations
Double precision dQ1e !Q1e - Q2e
Double precision dQ2e !Q1e - Q4e
Double precision Q1c !m.cp.dT
Double precision Q2c !((Tco-Tci)/log(Tci-Tw)/Tco-Tw))
Double precision Q4c !((Tco-Tci)/log(Tci-Tw(up/down))/Tco-Tw(up/down)))
Double precision dQ1c !Q1c - Q2c
Double precision dQ2c !Q1c - Q4c
Double precision Thog !Source outlet temperature initial guess [deg C]
Double precision Tcog !Sink outlet temperature initial guess [deg C]

!Finning influence
Double precision CF !Correction factor for Nusselt equations
Double precision efffe !Efficiency of the fin evaporator
Double precision efffc !Efficiency of the fin condenser
Double precision Afe !Heat transfer area of the evaporator fins [m2]
Double precision Afc !Heat transfer area of the condenser fins [m2]
Double precision xe !sqrt(2hfc/kfe*efffe)
Double precision xc !sqrt(2hfc/kfe*efffc)
Double precision kfe !Thermal conductivity of evaporator fin [W/m.K]
Double precision kfc !Thermal conductivity of condenser fin [W/m.K]
Double precision Lhle !Length of helical evaporator [m]
Double precision Lhlc !Length of helical condenser [m]

!Outputs
Double precision Tho !Temperature of source outlet fluid [deg C]
Double precision Tco !Temperature of sink outlet fluid [deg C]
```

Fig. 15 Continued.

$$A_{tot} = A_{hp} + \eta_f A_f \quad (3.51)$$

$$\eta_f = \frac{\tanh(xH_f)}{xH_f} \quad (3.52)$$

H_f is the width of the fins and x is:

$$x = \sqrt{\frac{2h_{fc}}{k_f e_f}} \quad (3.53)$$

h_{fc} is the heat transfer coefficient of forced convection, k_f is the thermal conductivity of the fin material, e_f is the thickness of the fin.

The heat transfer area of the fins is:

$$A_f = 2\pi H_f L_{hl} N_t \quad (3.54)$$

L_{hl} is the length of the helical found by:

$$L_{hl} = \frac{L}{P_f} \sqrt{\left(\pi \frac{D_{of} + D_o}{2}\right)^2 + P_f^2} \quad (3.55)$$

L is the length of the finned heat pipe section, whether it is the evaporator or condenser. D_{of} is the outer diameter of the heat pipe including the fins, D_o is the outer diameter of the heat pipe and P_f is the pitch of the fins.

The heat transfer area of just the heat pipe (A_{hp}) without fins is found by:

$$A_{hp} = \pi D_o L \quad (3.56)$$

A HPHE consists of many individual heat pipes. The heat transfer area in the entire exchanger condenser A_c and evaporator A_e section is determined by:

$$A_c = N_t N_t A_{tot,c} \quad (3.57)$$

$$A_e = N_t N_t A_{tot,e} \quad (3.58)$$

3.3.2.1. Thermal conductivity of carbon steel fins. As well as the fin configuration, the thermal conductivity of the material type of fins used in heat exchangers is vital to the overall fin efficiency. The fin material in the HPHE unit used to validate the model was carbon steel. The thermal conductivity of the fins, k_f , was determined using


```
!Check Parameters for Problems
If (Nr <= 1) Call FoundBadParameter(1, 'Fatal', 'The number of rows must be positive.')
If (Dout > 1.d0) Call FoundBadParameter(2, 'Fatal', 'Ensure diameter is in metres')
If (Le <= 0.d0) Call FoundBadParameter(3, 'Fatal', 'The length evaporator must be positive.')
If (Lc <= 0.d0) Call FoundBadParameter(4, 'Fatal', 'The length condenser must be positive.')
If (Nt <= 0.d0) Call FoundBadParameter(5, 'Fatal', 'Number of heat pipes in row must be positive.')
If (ST >= 1.d0) Call FoundBadParameter(6, 'Fatal', 'Ensure distance between rows is in metres')
If (SL >= 1.d0) Call FoundBadParameter(7, 'Fatal', 'Ensure distance between heat pipes is in metres')
If (Ae <= 0.d0) Call FoundBadParameter(8, 'Fatal', 'Ae must be positive')
If (Ac <= 0.d0) Call FoundBadParameter(9, 'Fatal', 'Ac must be positive')
If ((FinningMode <= 0) .or. (FinningMode > 4)) Call FoundBadParameter(10, 'Fatal', 'Finning mode must be between 1 and 4')
If ((FluidMode <= 0) .or. (FluidMode > 3)) Call FoundBadParameter(11, 'Fatal', 'Fluid mode must be between 1 and 3')
If (Dofin >= 1) Call FoundBadParameter(12, 'Fatal', 'Ensure fin diameter is in metres')
If (efin >= 1) Call FoundBadParameter(13, 'Fatal', 'Ensure outer fin diameter is in metres')
If (Pfin >= 1) Call FoundBadParameter(14, 'Fatal', 'Ensure pitch is in metres')
If (Hfin >= 1) Call FoundBadParameter(15, 'Fatal', 'Ensure fin height is in metres')
If (ErrorFound()) Return
```

Fig. 16. Code to provide error notification if parameters are outside correct ranges for calculations to function.

```
If (Thi < 0.) Call foundBadInput(1, 'Fatal', 'The source inlet temperature must be positive')
If (Tci < 0.) Call foundBadInput(2, 'Fatal', 'The sink inlet temperature must be positive')
If (FLWe < 0.) Call foundBadInput(3, 'Fatal', 'The source inlet flow rate must be positive')
If (FLWc < 0.) Call foundBadInput(4, 'Fatal', 'The sink inlet flow rate must be positive')
If (ErrorFound()) Return
```

Fig. 17. Code to provide an error notification if out of range inputs are entered.

data from [61]. This was extracted to create Fig. 12. Carbon steel is predominantly used for finning but the use of aluminium or forms of stainless steel is also seen. The model can be altered to use other material thermal conductivity characteristics, if required.

4. Methodology

A desktop simulation has been conducted with a personally developed transient HPHE model and results compared with experimental data. The software TRNSYS (TRAnsient System Simulation) 17 was used to create a transient simulation with varying inputs and parameters. This simulation engine was developed by members of the Solar Energy Laboratory at the College of Engineering within the University of Wisconsin. The software is used to study thermal systems and has latterly been employed to study waste heat recovery. It is installed with a library of over 150 components. These components are used to model a transient system, which allows the user to evaluate and analyse chosen inputs and parameters and view results. An interface called 'Simulation Studio' is used where the system is graphically modelled using the library of components, which are known as 'Types'. These Types are internally composed of a series of mathematical equations where inputs and parameters are converted to output values. The values and units of the inputs and parameters can be altered to provide a graphical view of the system's functionality over a set period of time. A parameter is fixed throughout the entire simulation, but an input can be fixed or changed in each iteration step over the simulation. A transient nature can be achieved by linking an external file (.txt.csv) as the input or linking the output of another component as the input for another, for example, data logged real temperature profiles from a furnace or weather temperature data from cities around the world can be used.

A HPHE component is not available in the TRNSYS library and so the authors coded a new component. The standard TRNSYS library with the location of the newly created HPHE Type is shown in Fig. 13. The component needs a 'skeleton' where the user can change inputs and parameters, which is also the icon that can be visualised in

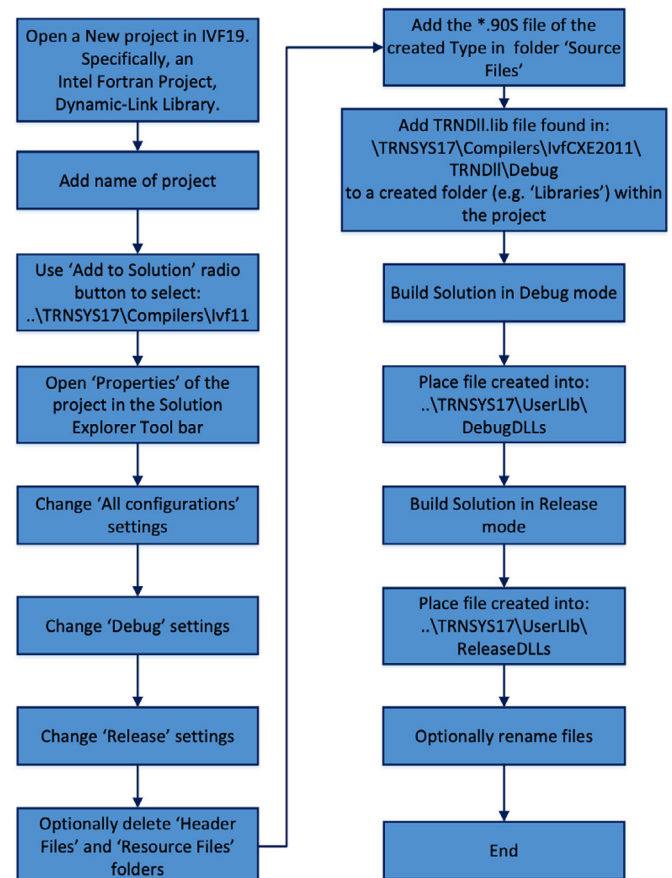


Fig. 18. Flowchart for the process of compiling a component into a *.dll file to be used in TRNSYS.

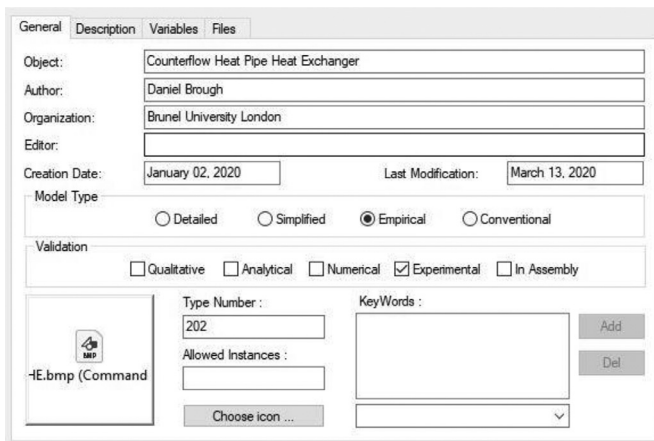


Fig. 19. View of 'General' tab for HPHE component in Simulation Studio.

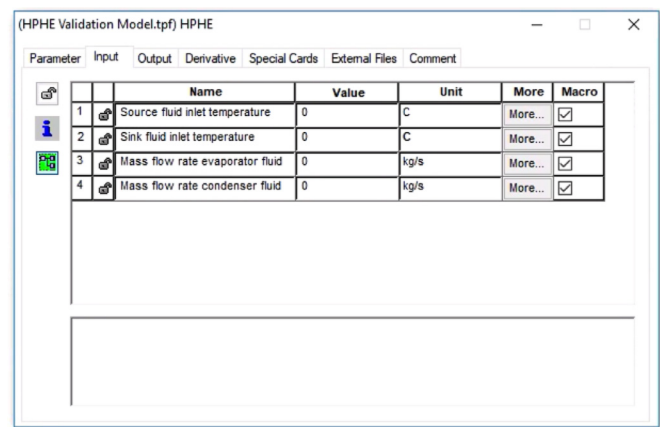


Fig. 21. View of Type202 component 'Input' tab in Simulation Studio.

simulation studio. It then has the internal mathematical operation which takes the inputs and creates the outputs.

4.1. Process for coding the HPHE component

The process for coding and including a new component in the TRNSYS library is not straightforward; it requires the use of multiple software and is coded in Fortran. Fortran (FORmula TRANslation) is a compiled imperative programming language. TRNSYS was written in this language and as such, it is required to code a Type in this language and then compile it. The Fortran language was developed by the International Business Machines (IBM) Corporation in the 1950s for the purpose of numerical computation and scientific computing specifically for engineering and scientific purposes. The first manual was released in 1956 and the first compiler was released in 1957. The idea was to ease the process of inputting equations into computers. Fortran has many iterations and releases, specifically the Fortran 90 language was used to code the Type, developed in 1991. The process for creating a new component is described in the Programmer's guide (Volume 7) [62] provided within the software. However, not all sections or code is required so the process for building the novel HPHE Type is described in this section. Fig. 14 provides a flowchart diagram to explain the coding process.

To build a new model, TRNSYS 17 must be installed and a Fortran compiler capable of generating a 32-bit dynamic link library (DLL). Many compilers are available, but in this case Intel Parallel Studio XE 2019 with the additional Intel Visual Fortran package was used. Intel Visual Fortran is an add-on for Microsoft Visual Basic.

The TRNSYS code is split into the kernel and the Types. The kernel provides all the background and functionality inputs to the Types. Types have the mathematical coding to perform calculations of the components used in the simulation as well as how to communicate with the kernel and call various other codes at given steps, in essence, converting inputs to outputs. Types distinguish between inputs that change with time and inputs that do not change with time. These are known as inputs and parameters, respectively. For the HPHE component, the following inputs were required, shown in Table 3.

For the HPHE component, the following parameters were required, shown in Table 4.

Within the Type, further internal calculations were carried out. These are summarised in the theoretical section of the paper.

4.1.1. HPHE coding in intel visual Fortran

This section explains how the HPHE component (Type202) code was written. The first line of the code calls the particular subroutine to which the component in simulation studio is linked, in this case the Type number. Type numbers 201–300 are reserved for user written components and Type1–200 are reserved for the standard TRNSYS library. For this reason, Type202 was arbitrarily chosen.

A TRNSYS 17 simulation requires the access global constants and functions provided in the source code. To choose which are called into the simulation is done by 'Use' statements. Type202 requires *TrnsysConstants* and *TrnsysFunctions*. *TrnsysConstants* is a module containing fixed values that do not change throughout a simulation, for example, declaring the maximum amount of equations or outputs that can be used in a simulation. A table of these constants can be found in Section 7.4.1.1 of the Programmers manual [62].

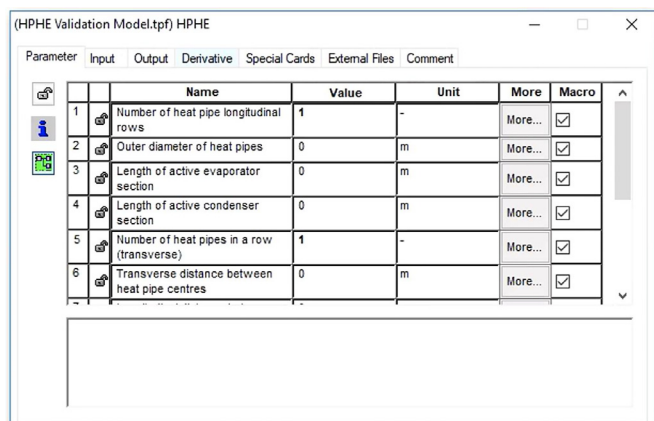


Fig. 20. View of Type202 component 'Parameter' tab in Simulation Studio.

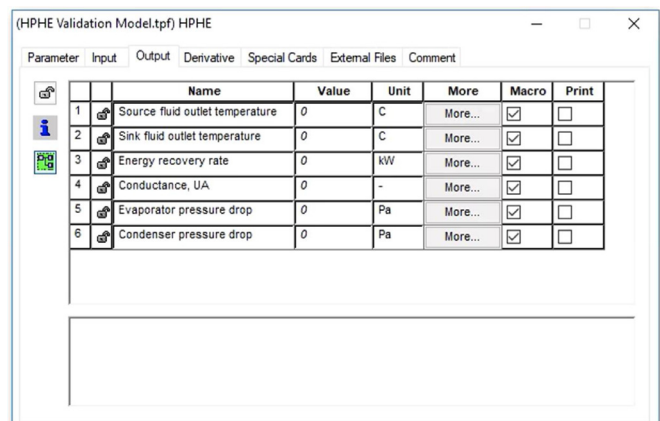


Fig. 22. View of Type202 component 'Output' tab in Simulation Studio.

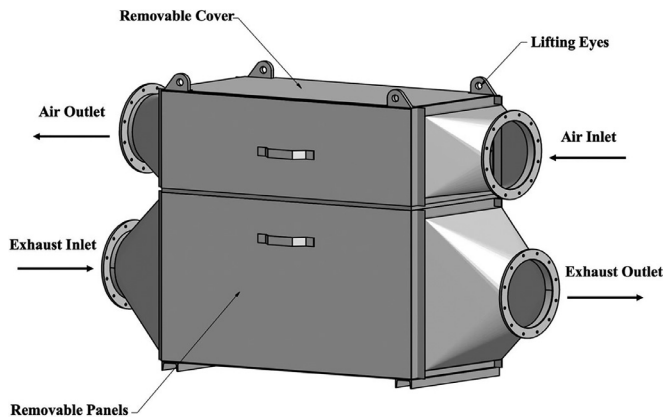


Fig. 23. 3D schematic of the HPHE.

TrnsysFunctions are all the functions that the subroutines can use to handle the stored data. A full description of each function is found in Section 7.4.2 of the Programmers manual [62].

In previous versions of TRNSYS, Types could not exist in an external *.dll file, it required altering the standard TRNDLL.dll. In TRNSYS 17, the Types can exist in an external *.dll. The kernel examines the contents of a user library directory to determine if any external *.dll files need to be loaded into the simulation. In this case, the Type202.dll file is an external *.dll file placed in the user library and is loaded into the memory for the duration of the simulation. The code below tells the kernel to search for Type202 in the user library and load it into the memory.

Declaring the variables is a section of code that comes after initially defining the subroutine, giving access to global variables and exporting the component. This is a larger section of code where all the local variables used through the simulation are given. *Implicit None* is used to instruct that all variables need to be explicitly declared. If the variable is a real number, *Double precision* is used to set the variable to be a real number with twice the amount of significant decimal digits and a magnitude range of 10^{-308} to 10^{308} . This accuracy is not necessary but modern computing power allows the use of it. *Integer* is used to set the variable to be an integer number.

Data can be used before the variable to set a parameter to a fixed value; however, this command was not used for Type202. Fig. 15 shows all the local variables used within the Type.

After declaring the variables, the entirety of the code underneath is the executable section. Each line is read and executed sequentially. The variables *Time*, *Timestep*, *CurrentUnit*, *CurrentType* are global variables that are required to be read during each iteration to provide the transient nature output of the simulation.

The code needs to be 'version signed'. This is done to inform the kernel which version of TRNSYS and therefore the convention in which the component was written. This alters how the kernel handles the component. This allows backward compatibility with components of TRNSYS written in earlier versions and will allow future compatibility with the next versions of TRNSYS. This step is vital as the simulation will call an error if the Type is not signed to a particular version.

On the last run through of the code, at the end of the simulation, it may be required to perform certain actions such as closing external files before returning control to the kernel. This is known as last call manipulation. No last call functions were required for Type202 so it was only necessary to return control to the kernel.

When a particular timestep finishes, every Type in the simulation is recalled. End of timestep manipulations allows functions to occur before the Type is recalled into the simulation. No end of timestep manipulations were required for Type202 so the *Return* function allows the Type to be recalled.

To operate correctly, the kernel needs to be told what Type202 is composed of. The code required informs the kernel that there are fifteen parameters, four inputs, zero derivatives and two outputs. The iteration mode tells the kernel how often the type should be called. A value of one indicates that Type202 should be called at every timestep regardless of whether the input values have altered to the previous iteration. The number of stored variables sets the required number of static and dynamic storage spots. Type202 completes a calculation every timestep with the inputs and so no stored variables are required. No discrete controls are required.

The code assigns units to the input and output values. This is an extremely important step to avoid inadvertently performing calculations or connecting components with different units. A good example of this is whether the component calculates using Kelvin or degrees

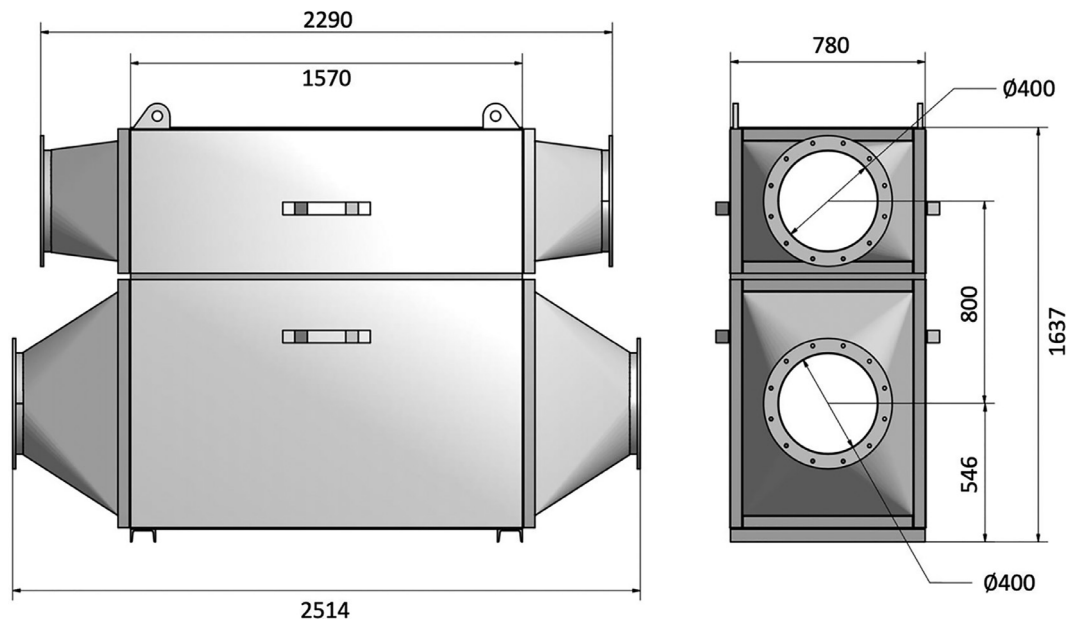


Fig. 24. Dimensions of the HPHE.

NO OF ROWS: 18
HOLES PER ROW 9
TOTAL NO. OF HOLES: 162

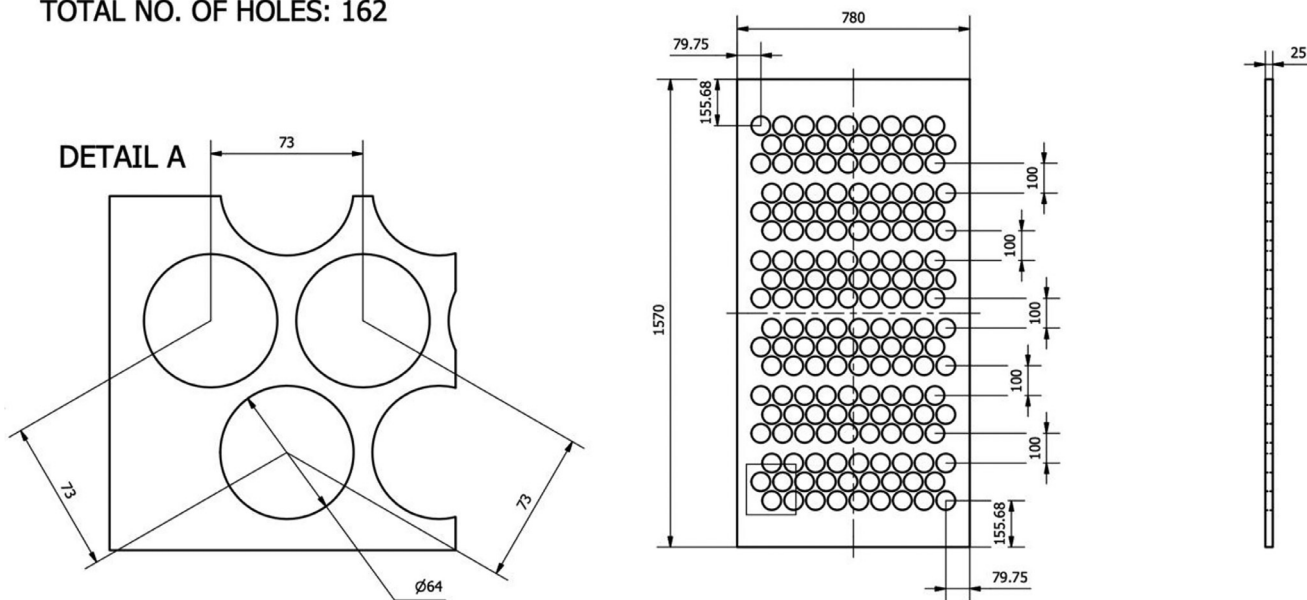


Fig. 25. Separation plate and heat pipe arrangement detail.

Celsius. If an output value of one parameter is in a different unit to another, as long as the measurement type is the same (e.g. temperature), TRNSYS will convert the value to the correct unit. The programmer's manual provides a breakdown of the available measurement types, the units, the TRNSYS code and the mathematical conversion used.

On the first run of the code there are no iterations, but the initial input and output values of the parameters are read. The initial parameter values are read from external data files or component input values. The order within the component determines the number assigned to it. The *JFIX* function is used to ensure the number read is an integer.

If an out of range parameter is found, to prevent erroneous and incorrect calculations, error messages were built into the code. If a parameter is out of range and the simulation is run, an error message pops up. This is essential to ensure all the parameters are correctly input and results are obtained incorrectly. Fig. 16 shows the coded ranges with the error messages that are shown in a pop-up box and the results file if out of range parameters are input.

In this case:

- The number of rows (Nr) in the HPHE had to be greater than one. The input defaults to zero. This was to ensure that an input was in place.

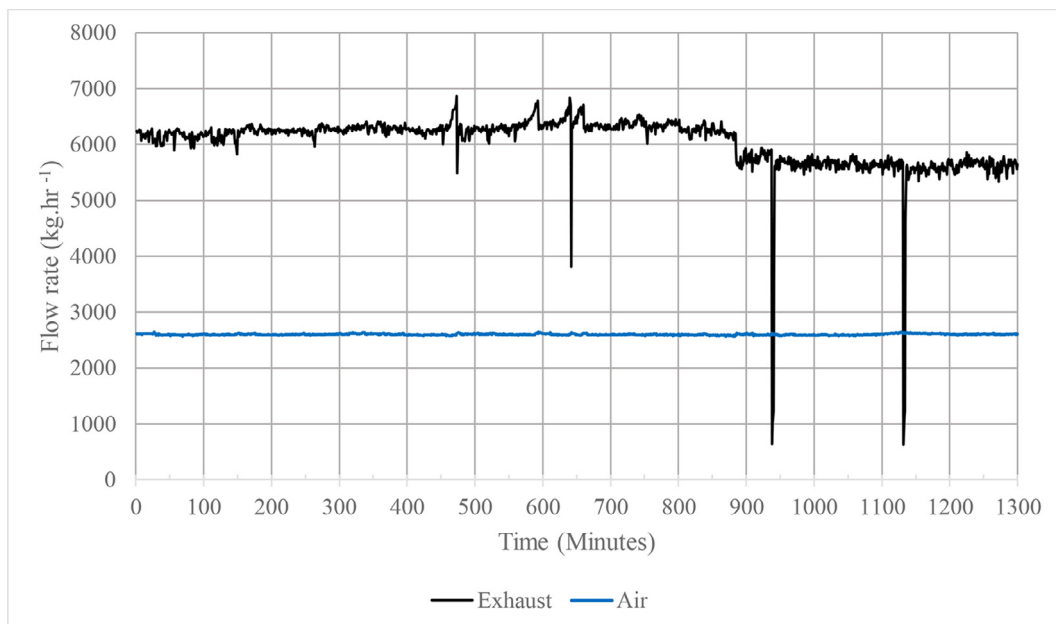


Fig. 26. Graph showing the inlet flow rate of the exhaust and air streams.

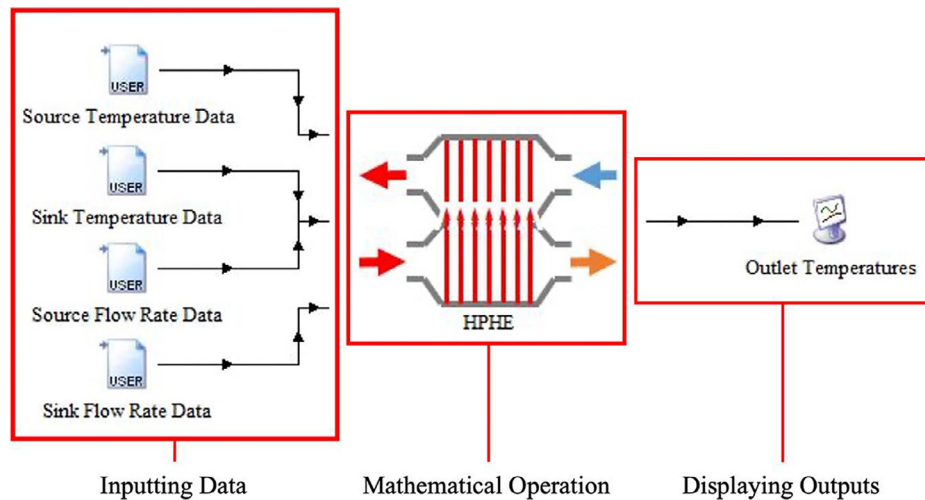


Fig. 27. Labelled model in Simulation Studio.

- It is easy to input the outer diameter of the pipe in millimetres or centimetres rather than metres. If Dout was over one, it was obvious that the incorrect unit and therefore input was used.
- As the initial default value of the length of the evaporator (Le) and length of the condenser (Lc) was zero, ensuring that Le and Lc were greater than zero ensured that a value was input in the initial parameters.
- To ensure the number of heat pipes in a row (Nt) was input, an error occurred if the value was less than or equal to zero.
- To ensure the distance between the heat pipes rows and the heat pipe centres in a row (ST and SL) was input in metres, a value greater than or equal to one gave an error.
- To ensure an input was given for the flow area of the evaporator and condenser (Ae and Ac), a value less than or equal to zero gave an error.
- The finning mode depends on whether the evaporator or condenser sections were finned. 1= no finning, 2= condenser finned, 3= evaporator finned, 4= both finned. Inputs outside of 1–4 are not allowed.
- The fluid mode told the component which heat sink was being used. 1= air, 2= water 3= thermal oil. Inputs outside of 1–3 are not allowed.
- Errors for the finning parameters ensured measurements were in input in metres.

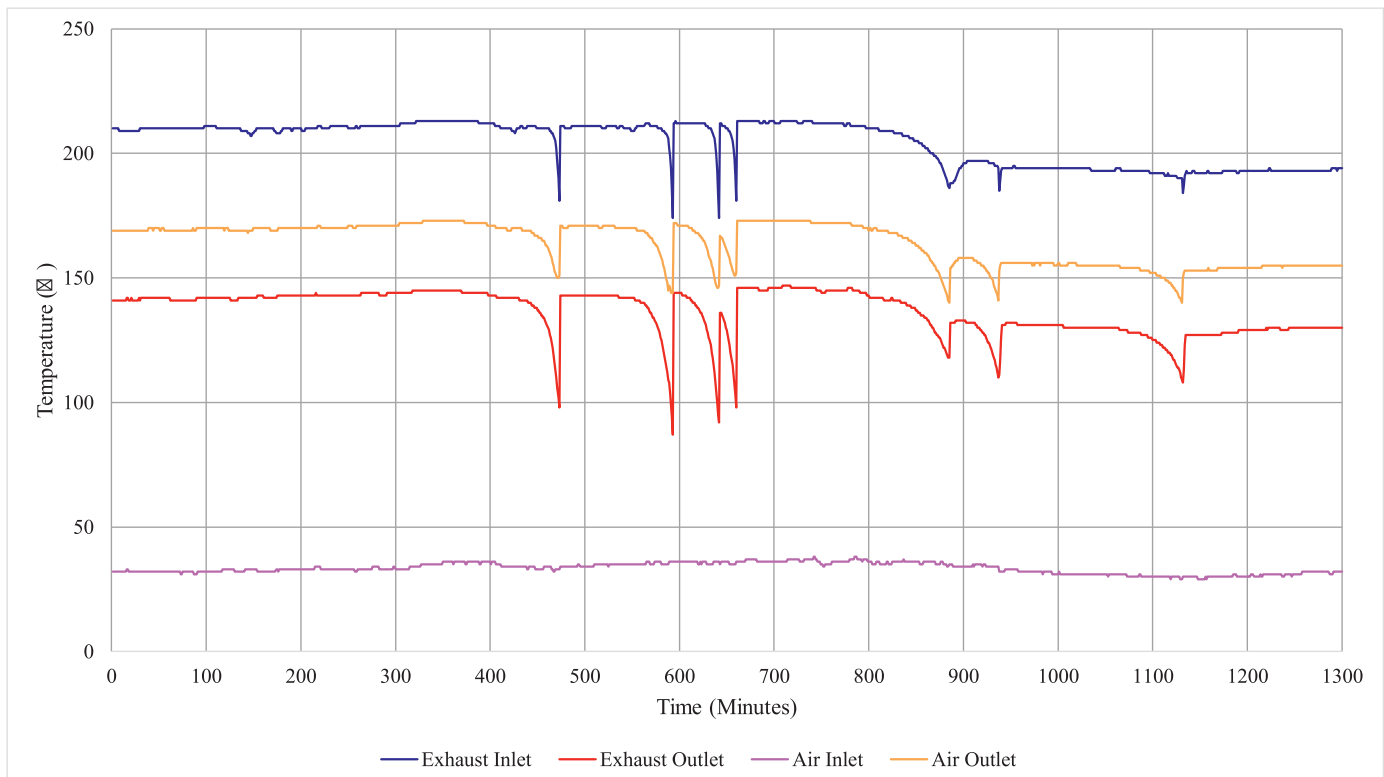


Fig. 28. A graph showing the experimental inlet and outlet temperatures of the source and sink fluids.

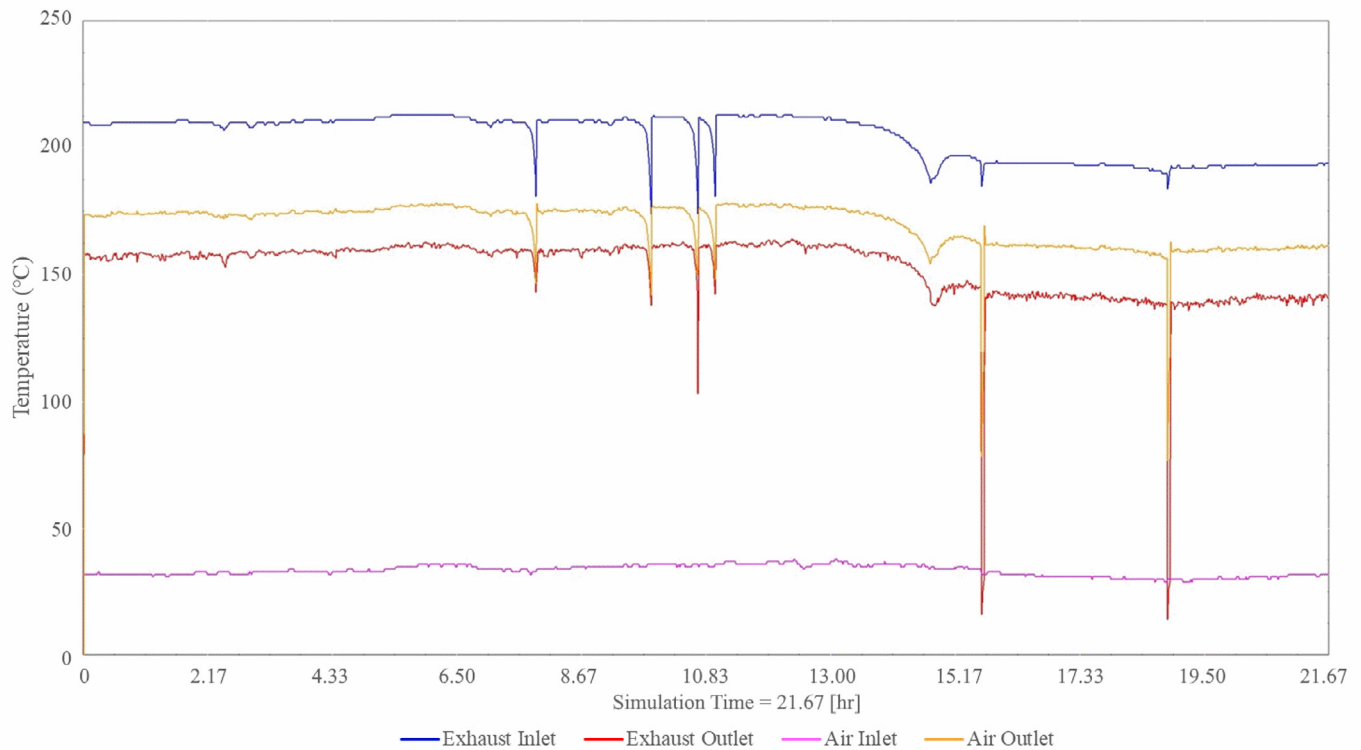


Fig. 29. A graph showing the simulation inlet and outlet temperatures of the source and sink fluids.

At the first timestep the outputs of the simulation need an initial value. In this case the output values were set to the values of T_{ho} and T_{co} ; temperature of the hot and cold stream outlets.

In a simulation, it is possible to run multiples of the same Type. For example, if multiple HPHEs are in a simulation, multiple Type202 components will be put into the simulation. The simulation needs to treat these Types separately. For this reason, there is a dedicated

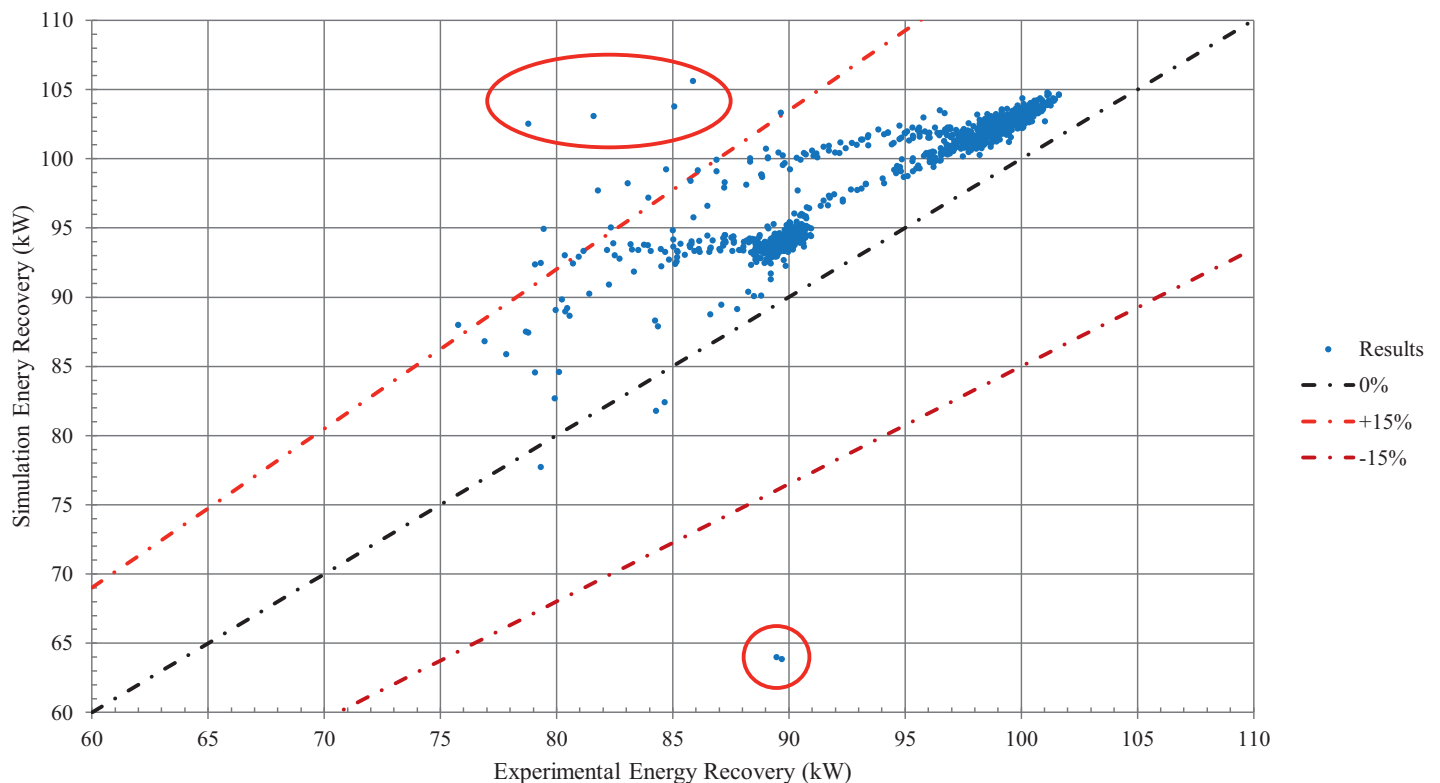


Fig. 30. A comparison of energy recovery between experimental and simulation results.

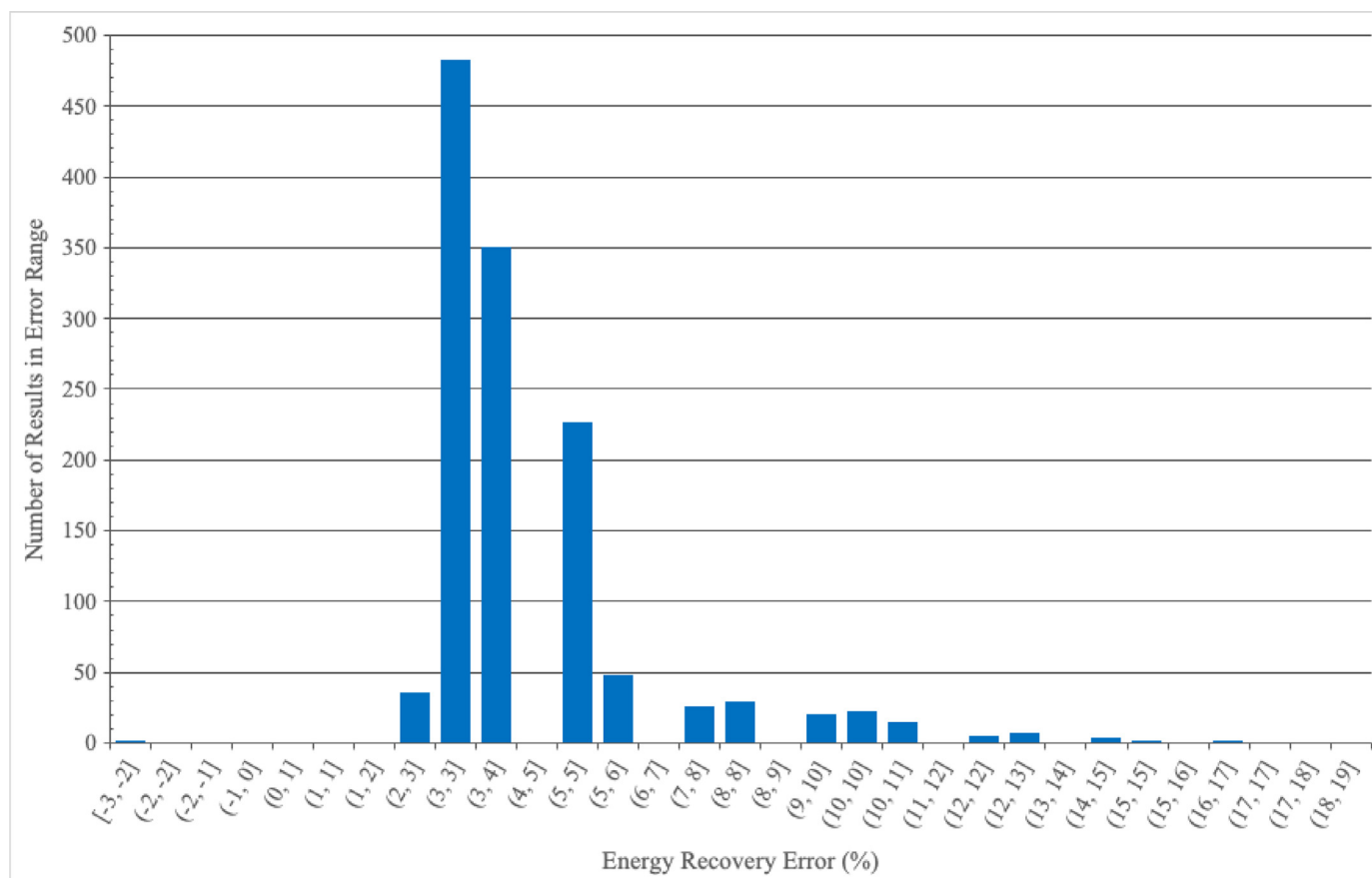


Fig. 31. A histogram plot of percentage error.6. Conclusion.

code for multiple unit manipulation. If (*getIsReReadParameters()*) is the function used that causes the parameters list to be reread if there is more than one Type in a simulation.

There are four inputs for Type202, namely: temperatures and mass flow rates of the source and sink inlet streams. As with the parameters, the inputs need to be in range for a successful calculation and to check that they have been entered. For this reason, error messages were coded (Fig. 17) to ensure the simulation was not run if this was the case.

All the internal calculations then occur. After all the internal calculations, the final values for T_{ho} and T_{co} are calculated. At each iteration, T_{ho} and T_{co} are set as visualisable output values. These values are stored in the memory and can be used at the next timestep. *End Subroutine* is then used to return control to the kernel after all the calculations are completed and the values are stored. The subroutine for Type202 is then ended.

4.1.2. Creating a *.dll file using intel visual Fortran 19

The TRNSYS Programmer's Guide [62] is slightly outdated as the manual only provides instructions on how to add a Type to the TRNDLL.dll using Intel Visual Fortran 11. This process was done using Intel Visual Fortran 19 and so it varied from the instructions given in the manual. The instructions to add a new project to the Ivf11.x solution is provided in this section by a flowchart for the process, Fig. 18.

4.1.3. HPHE TYPE202 component skeleton

A Type that is used for a simulation consists of two parts, the internal code that tells the component how to work, as detailed in Section 4.1.1 HPHE Coding, as well as the 'skeleton', which is used to enter the component into the simulation, link the component with other components in the simulation, house the code and provide parameter and input values.

The empty skeleton for Type 202 (HPHE) was created in Simulation Studio by pressing File>New>New Component (TRNSYS TYPE). A view of the final skeleton with all inputted data for the General, Parameter, Input and Output tab pages are provided in Fig. 19 to Fig. 22, respectively.

4.1.4. Model limitations

There are several limitations to this model. Firstly, it does not take into account start-up of the heat pipes. It assumes start-up is achieved and the heat pipes are operational. In saying this, the model is used to determine recovered heat energy in a process system that would be operational, so start-up is not essential.

Secondly, HPHEs have thermal inertia. For example, there is residual heat in the casing of the HPHE and the heat pipes themselves that will be transferred to the sink fluid if the source stream is cooling down. Axial conduction through the heat pipe and conduction through the separation plate is also present. These factors are not taken into account. This means the model adapts more quickly than what would occur in reality, as witnessed in the results.

The model assumes perfect insulation whereas the HPHE loses heat through the casing. As such, the model slightly overpredicts the performance, as seen in the results. It is possible to predict temperature loss from the HPHE casing based on the design parameters. However, it was deemed unnecessary as many additional parameters would have to be input and would make the model much more cumbersome for little return.

The Type, currently, only provides outlet data about the temperature. Additional work is being undertaken to provide, for example, pressure drop, energy recovery rate and conductance values.

Currently, only helical finning is available as an option, whereas, in reality, other configurations are possible. Future work can be undertaken to validate other configurations, and the code can be updated accordingly.

Table 1
Available correlations for calculation Nusselt numbers over tube bundles.

Ref.	Equation	Condition	Equation
[55]	$Nu_D = 0.33 Re_D^{0.6} Pr^{1/3}$	Staggered > 10 rows $10 < Re_D < 40,000$	(3.28)
[56]	$Nu_D = K Re_D^n$ K and n values are tabulated in [57, 53]	Air only > 10 rows	(3.29)
[14]	$Nu_D = K_1 Re_D^n$ K ₁ and n values are tabulated in [57, 53]	Air only < 10 rows	(3.30)
[56]	$Nu_D = 0.32 F_a Re_D^{0.61} Pr^{0.31}$ F _a is an arrangement correction factor provided in [56]		(3.31)
[58]	$Nu_D = 0.34 F_a Re_D^{0.61} Pr^{0.31}$ $F_a = 1 + \left(\frac{S_L}{S_T} + \frac{7.12}{S_T} - 6.52 \right) \times \left[\frac{0.266}{(S_T - 0.8)^2} - 0.12 \right] \times \sqrt{\frac{1000}{Re_D}}$	In-line	(3.32)
	$Nu_D = 0.35 F_a Re_D^{0.57} Pr^{0.31}$ $F_a = 1 + \frac{S_L}{10} + \frac{0.34}{S_T^{0.4}}$	Staggered	(3.33)
[59]	$Nu_D = 0.9 Re_D^{0.4} Pr^{0.36} (Pr/Pr_s)^{0.25}$	> 16 rows 0–100 Re _D In-line	(3.34)
	$Nu_D = 0.52 Re_D^{0.5} Pr^{0.36} (Pr/Pr_s)^{0.25}$	> 16 rows 100–1000 Re _D In-line	(3.35)
	$Nu_D = 0.27 Re_D^{0.63} Pr^{0.36} (Pr/Pr_s)^{0.25}$	> 16 rows 1000–20,000 Re _D In-line	(3.36)
	$Nu_D = 0.033 Re_D^{0.8} Pr^{0.4} (Pr/Pr_s)^{0.25}$	> 16 rows 20,000–200,000 Re _D In-line	(3.37)
	$Nu_D = 1.04 Re_D^{0.4} Pr^{0.36} (Pr/Pr_s)^{0.25}$	> 16 rows 0–500 Re _D Staggered	(3.38)
	$Nu_D = 0.71 Re_D^{0.5} Pr^{0.36} (Pr/Pr_s)^{0.25}$	> 16 rows 500–1000 Re _D Staggered	(3.39)
	$Nu_D = 0.35 (S_T/S_L)^{0.2} Re_D^{0.6} Pr^{0.36} (Pr/Pr_s)^{0.25}$	> 16 rows 1000–20,000 Re _D Staggered	(3.40)
	$Nu_D = 0.031 (S_T/S_L)^{0.2} Re_D^{0.8} Pr^{0.36} (Pr/Pr_s)^{0.25}$	> 16 rows 20,000–200,000 Re _D Staggered	(3.41)
[53]	$Nu_D = 0.8 Re_D^{0.4} Pr^{0.36} (Pr/Pr_s)^{0.25}$	> 10 rows 0.7 < Pr < 500 10 < Re _D < 100 In-line	(3.42)
	$Nu_D = 0.9 Re_D^{0.4} Pr^{0.36} (Pr/Pr_s)^{0.25}$	> 10 rows 0.7 < Pr < 500 10 < Re _D < 100 Staggered	(3.43)
	$Nu_D = 0.27 Re_D^{0.63} Pr^{0.36} (Pr/Pr_s)^{0.25}$	0.7 < Pr < 500 1000 < Re _D < 10,000 In line	(3.44)
	$Nu_D = 0.35 \left(\frac{S_T}{S_L} \right)^{0.2} Re_D^{0.6} Pr^{0.36} (Pr/Pr_s)^{0.25}$	S _T /S _L ≥ 0.7 0.7 < Pr < 500 1000 < Re _D < 10,000 Staggered	(3.45)
	$Nu_D = 0.4 Re_D^{0.6} Pr^{0.36} (Pr/Pr_s)^{0.25}$	S _T /S _L < 2 0.7 < Pr < 500 1000 < Re _D < 10,000 Staggered	(3.46)
	$Nu_D = 0.021 Re_D^{0.84} Pr^{0.36} (Pr/Pr_s)^{0.25}$	S _T /S _L ≥ 2 0.7 < Pr < 500 Re _D > 10,000 In-line	(3.47)
	$Nu_D = 0.022 Re_D^{0.84} Pr^{0.36} (Pr/Pr_s)^{0.25}$	0.7 < Pr < 500 Re _D > 10,000 Staggered	(3.48)
	$Nu_D = 0.019 Re_D^{0.84}$	Pr = 0.7 Re _D > 10,000 Staggered	(3.49)
	$Nu_D = 0.0131 Re_D^{0.883} Pr^{0.36}$	450,000 < Re _D < 700,000 Staggered S _T /D = 2 S _L /D = 1.4	(3.50)

Table 2

Correction Factor for Zukauskas Correlations with <16 Rows of Heat Pipes [13].

Nr	1	2	3	4	5	7	10	13
In-line	0.70	0.80	0.86	0.90	0.93	0.96	0.98	0.99
Staggered	0.64	0.76	0.84	0.89				

Table 3

Inputs for HPHE TRNSYS component.

Input	Designated Symbol	Units
Source fluid inlet temperature	Thi	°C
Sink fluid inlet temperature	Tci	°C
Mass flow rate of evaporator fluid	FLWe	kg.s ⁻¹
Mass flow rate of condenser fluid	FLWc	kg.s ⁻¹

4.2. Experimental unit

The HPHE unit that was used to validate the model was installed to recover energy from the cooling section of a ceramic continuous roller kiln used to fire tiles. Further information on this exhaust-air HPHE can be found in Ref. [63]. Fig. 23 and Fig. 24 provide the 3D drawing of the HPHE unit and the dimensions. Fig. 25 provides the detail of the separation plate between the two streams and the heat pipe arrangement.

Fig. 26 shows the inlet flow rate data from the experimental HPHE. There was the inlet of the exhaust to the evaporator section and the inlet of the air to the condenser. A data point was taken every minute. 1300 min of data were used. Data for flow rate were measured in Nm³.hr⁻¹, which had to be converted to kg.hr⁻¹ for the TRNSYS simulation. This was achieved using the ideal gas law equation as done by [45]. There were fluctuations in the data mainly in the exhaust flow rate. A maximum error of mass flow rate of 2.78% was reported. The average values for the exhaust and air inlet flow rate were 6047 and 2600 kg.hr⁻¹, respectively. The maximum and minimum flow rates for the exhaust were 6869 and 632 kg.hr⁻¹ and for the air were 2644 and 2560 kg.hr⁻¹. These fluctuations assisted in showing that the model would adapt to fluctuating conditions.

4.3. Model for validation

Fig. 27 shows the model built to validate the component. The left highlighted box shows the real-world experimental data input into the model. These are connected to the HPHE Type that does the mathematical operation. The outputs of the Type are sent to a plotter


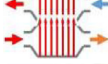

Table 4

Parameters for HPHE TRNSYS component.

Parameter	Designated Symbol	Units
Number of heat exchanger rows	Nr	N/A
Outer diameter of heat pipes	Dout	m
Length of active evaporator section	Le	m
Length of active condenser section	Lc	m
Number of heat pipes in row	Nt	N/A
Distance between heat centres in row	ST	m
Distance between heat pipe centres between rows	SL	m
Flow area of evaporator	Ae	m ²
Flow area of condenser	Ac	m ²
Finning Mode	FinningMode	–
Fluid Mode	FluidMode	–
Outer diameter of fins	Dofin	m
Thickness of fins	efin	m
Pitch of fins	Pfin	m
Width of fins	Hfin	m

Table 5

Components used in the TRNSYS model, their Type and description.

Component	Type	Description
	Type 9a	Data reader for generic data files
	Type 202	HPHE component developed.
	Type 65	Online Graphical Plotter

to graphically display the results. Table 5 gives further information on each Type used in the simulation.

5. Results and discussion

5.1. Comparison of results

Fig. 28 shows the experimental inlet and outlet temperature data of the installed HPHE. The inlet temperatures were fed into the model and the outlet temperatures were used for comparison against the simulation to validate the component. Fig. 29 shows the graph produced in TRNSYS of the simulation inlet and outlet temperatures of the source and sink fluids for comparison.

In the experiments, the air inlet is roughly 35 °C and rises to between 150 and 175 °C depending on the flow rate. The exhaust drops from between 190 and 210 °C to 130–145 °C.

In the simulation, the air and exhaust inlets directly relate to the experimental set up as these were used as the inputs. The air outlet rose to between 160 and 175 °C and the exhaust dropped to between 140 and 160 °C. It can be seen by comparing the graphs that the simulation follows the experimental results very similarly.

5.2. Energy recovery comparison

The energy recovered was calculated from the secondary stream, air, using:

$$\dot{Q} = \dot{m}_p c_p \Delta T \quad (5.1)$$

The energy recovery of the experiment was plotted against the simulation for comparison, shown in Fig. 30. It is seen that most results fall well within a $\pm 15\%$ difference with a few outliers predominantly caused by the faster response of the simulation compared to the experiment and lack of thermal inertia. The simulation slightly overpredicted the performance of the HPHE, this is as expected as the model assumes perfect insulation, with no energy losses. Also, with the large number of variables and extensive calculations that need to be conducted, this performance is more than acceptable. The errors between simulation and experiment were rounded and a histogram plot (Fig. 31) shows the spread of error with the majority falling between 3 and 4%. Six major outliers, circled in red, in Fig. 30 were removed and the average error was 4.4%.

A TRNSYS Type has been built to simulate a counter-flow HPHE component that provides accurate predictions on outlet temperatures of both the source and sink fluid. This was done using the ϵ -NTU method and real-world installation data. The results of the simulation were well

within $\pm 15\%$, with an average of 4.4% error, compared to the experimental results. This component can now be used confidently in larger waste heat recovery system simulations that encompass a HPHE of this configuration. Furthermore, transient HPHE calculations are now possible whereas previously averaged fixed values would have to be used as inputs. Future work will be required to ensure the method of calculating ε_t is applicable to further applications. Now the component has been validated, the TRNSYS performance of an entire system including a HPHE can be simulated to determine the system performance over time and aid the design and installation of HPHEs for the purpose of WHR. In this paper, an exhaust gas to air unit was validated using an available full-scale unit. Further full-scale units that are currently being installed will be used to validate thermal oil and water as heat sinks, once sufficient data has been collected, in a future article. Methods will be included for determining pressure drop as well as conductance values and energy recovery rate as outputs of the model.

Declaration of Competing Interest

None

References

- [1] H. Ritchie and M. Roser, "CO₂ and greenhouse gas emissions," our world in data, December 2019. [Online]. Available: <https://ourworldindata.org/CO2-and-other-greenhouse-gas-emissions>. [Accessed 26 April 2020].
- [2] United Nations Secretary-General, Report of the Secretary-General on the 2019 Climate Action Summit, United Nations, 2019.
- [3] United Nations Treaty Collection, Paris Agreement Chapter XXVII Environment, United Nations, New York, 2015.
- [4] European Commission, "2030 climate & energy framework," [Online]. Available: https://ec.europa.eu/clima/policies/strategies/2030_en. [Accessed 24 April 2020].
- [5] J. Malinauskaitė, H. Jouhara, L. Ahmad, M. Milani, L. Montorsi, M. Venturelli, Energy efficiency in industry: EU and national policies in Italy and the UK, Energy 172 (April 2019) 255–269 <https://doi.org/10.1016/j.energy.2019.01.130>.
- [6] Central Intelligence Agency, The World Factbook 2016/17, 2016 New Zealand.
- [7] A. Simeone, Y. Luo, E. Woolley, S. Rahimifard, C. Boër, A decision support system for waste heat recovery in manufacturing, CIRP Ann. 65 (1) (2016) 21–24 <https://doi.org/10.1016/j.cirp.2016.04.034>.
- [8] H. Jouhara, A.G. Olabi, Editorial: industrial waste heat recovery, Energy 160 (2018) 1–2 <https://doi.org/10.1016/j.energy.2018.07.013>.
- [9] D. Brough, H. Jouhara, The aluminium industry: a review on state-of-the-art technologies, environmental impacts and possibilities for waste heat recovery, Int. J. Thermofluids 1–2 (2020) 100007 Vols. <https://doi.org/10.1016/j.ijft.2019.100007>.
- [10] D. Reay, P. Kew, Heat pipes: Theory, Design and Applications, Elsevier Limited, 2006.
- [11] A. Ghaghi, Heat pipes: review, opportunities and challenges, Front. Heat Pipes 5 (1) (2014) 1–48 <https://doi.org/10.5098/fhp.5.1>.
- [12] L. Vasiliev, Heat pipes in modern heat exchangers, Appl. Therm. Eng. 25 (2005) 1–19 <https://doi.org/10.1016/j.applthermaleng.2003.12.004>.
- [13] Y. Çengel, Heat Transfer: a Practical Approach, 2nd edition, McGraw-Hill, 2002.
- [14] W.M. Kays, A.L. London, Compact Heat Exchangers, 3rd ed., McGraw-Hill, New York, 1984.
- [15] H. Jouhara, 4.3 Heat Pipes, Compr. Energy Syst. 4 (2018) 70–97 <https://doi.org/10.1016/b978-0-12-809597-3.00403-x>.
- [16] H. Jouhara, A. Chauhan, T. Nannou, S. Almahmoud, B. Delpch, L. Wrobel, Heat pipe based systems - advances and applications, Energy 128 (2017) 729–754 <http://dx.doi.org/10.1016/j.energy.2017.04.028>.
- [17] A. Mehmood, A. Waqas, Z. Said, S.M.A. Rahman, M. Akram, Performance evaluation of solar water heating system with heat pipe evacuated tubes provided with natural gas backup, Energy Reports 5 (1) (2019) 1432–1444 <https://doi.org/10.1016/j.egyr.2019.10.002>.
- [18] H. Hussein, Theoretical and experimental investigation of wickless heat pipes flat plate solar collector with cross flow heat exchanger, Energy Convers. Manag. 48 (4) (2007) 1266–1272 <https://doi.org/10.1016/j.enconman.2006.09.021>.
- [19] H. Jouhara, J. Milko, J. Danielewicz, M. Sayegh, M. Szulgowska-Zgrzywa, J. Ramos, S. Lester, The performance of a novel flat heat pipe based thermal and PV/T (photovoltaic and thermal systems) solar collector that can be used as an energy-active building envelope material, Energy 108 (1) (2016) 148–154 <http://dx.doi.org/10.1016/j.energy.2015.07.063>.
- [20] G. Morrison, I. Budiardjo, Performance of water-in-glass evacuated tube solar water heaters, Sol. Energy 83 (1) (2009) 49–56 <http://dx.doi.org/10.1016/j.solener.2008.06.010>.
- [21] H. Jouhara, V. Anastasov, I. Khamis, Potential of heat pipe technology in nuclear seawater desalination, Desalination 249 (3) (2009) 1055–1061 <http://dx.doi.org/10.1016/j.desal.2009.05.019>.
- [22] X. Zhang, Y. Liu, X. Wen, C. Li, X. Hu, Low-grade waste heat driven desalination with an open loop heat pipe, Energy 163 (2018) 221–228 <https://doi.org/10.1016/j.energy.2018.08.121>.
- [23] K. Kerrigan, H. Jouhara, G. O'Donnell, A. Robinson, Heat pipe-based radiator for low grade geothermal energy conversion in domestic space heating, Simul. Model. Pract. Theory 19 (4) (2011) 1154–1163 <http://dx.doi.org/10.1016/j.simpat.2010.05.020>.
- [24] L. Ayompe, A. Duffy, M. Mc Keever, M. Conlon, S. McCormack, Comparative field performance study of flat plate and heat pipe evacuated tube collectors (ETCs) for domestic water heating systems in a temperate climate, Energy 36 (5) (2011) 3370–3378 <http://dx.doi.org/10.1016/j.energy.2011.03.034>.
- [25] Etekina - Thermal Energy Recovery, 22 April 2020. [Online]. Available: <https://www.etekina.eu/>. [Accessed 26 April 2020].
- [26] B. Egilegor, H. Jouhara, J. Zuazua, F. Al-Mansour, K. Plesnik, L. Montorsi, L. Manzini, ETEKINA: analysis of the potential for waste heat recovery in three sectors: aluminium low pressure die casting, steel sector, and ceramic tiles manufacturing sector, Int. J. Thermofluids 1–2 (February 2020) Vols. <https://doi.org/10.1016/j.ijft.2019.100002>.
- [27] B. Delpch, B. Axcell, H. Jouhara, Experimental investigation of a radiative heat pipe for waste heat recovery in a ceramics kiln, Energy 170 (2019) 636–651 <https://doi.org/10.1016/j.energy.2018.12.133>.
- [28] I-THERM, 21 May 2019. [Online]. Available: <http://www.itherm-project.eu/>. [Accessed 26 April 2020].
- [29] P. Dunn, D.A. Reay, Heat Pipes, 3rd edition, Pergamon Press, 1982.
- [30] J. Kim, S.J. Kim, Experimental investigation on working fluid selection in a micro pulsating heat pipe, Energy Convers. Manag. 205 (2020) 112462 <https://doi.org/10.1016/j.enconman.2019.112462>.
- [31] Heat Transfer Committee, "Convective heat transfer during forced crossflow of fluids over a circular cylinder, including free convection effects," ESDU 69004a, 1970.
- [32] S. Almahmoud, Experimental and Theoretical Investigation of a Radiative Flat Heat Pipe Based Heat Exchanger for Waste Recovery in the Steel Industry, Mechanical, Aerospace and Civil Engineering: Brunel University London, 2019.
- [33] E. Azad, Theoretical and experimental investigation of heat pipe solar collector, Exp. Therm. Fluid Sci. 32 (8) (2008) 1666–1672 <https://doi.org/10.1016/j.expthermflusci.2008.05.011>.
- [34] H. Mroue, J. Ramos, L. Wrobel, H. Jouhara, Experimental and numerical investigation of an air-to-water heat pipe-based heat exchanger, Appl. Therm. Eng. 78 (2015) 339–350 <http://dx.doi.org/10.1016/j.applthermaleng.2015.01.005>.
- [35] J. Ramos, A. Chong, H. Jouhara, Experimental and numerical investigation of a cross flow air-to-water heat pipe-based heat exchanger used in waste heat recovery, Int. J. Heat Mass Transfer 102 (2016) 1267–1281 <https://doi.org/10.1016/j.ijheatmasstransfer.2016.06.100>.
- [36] W.S. Chang, G.T. Colwell, Mathematical modeling of the transient operating characteristics of low-temperature heat pipe, Numer. Heat Transf. 8 (1985) 169–186 <https://doi.org/10.1080/01495728508961848>.
- [37] J.E. Deverall, J.E. Kemme, L.W. Florschuetz, Sonic Limitations and Startup Problems of Heat Pipes, NASA, Los Alamos, 1970.
- [38] G.T. Colwell, Modeling of Transient Heat Pipe Operation, 23665, Langley Research Centre, NASA, Hampton, Virginia, 1989 <https://ntrs.nasa.gov/archive/nasa/casi.ntrs.nasa.gov/19890010131.pdf>.
- [39] L. Yang, X. Ling, H. Peng, L. Duan, X. Chen, Starting characteristics of a novel high temperature flat heat pipe receiver in solar power tower plant based of "Flat-front" Startup model, Energy 183 (2019) 936–945 <https://doi.org/10.1016/j.energy.2019.07.007>.
- [40] J.-M. Tournier, M.S. El-Genk, A heat pipe transient analysis model, Int. J. Heat Mass Transf. 37 (5) (1994) 753–762 [https://doi.org/10.1016/0017-9310\(94\)90113-9](https://doi.org/10.1016/0017-9310(94)90113-9).
- [41] P. Brocheny, Modeling of the Transient Behavior of Heat Pipes With Room-Temperature Working Fluids, 10, Tigerprints, 2006.
- [42] I. Budiardjo, G. Morrison, M. Behnia, Development of TRNSYS models for predicting the performance of water-in-glass evacuated tube solar water heaters in Australia, Destination Renewables - ANZSES, 2003.
- [43] Y. Yau, A. Tucker, The performance study of a wet six-row heat-pipe heat exchanger operating in tropical buildings, Int. J. Energy Res. 27 (3) (2003) 187–202 <https://doi.org/10.1002/er.867>.
- [44] L.J. Shah, TRNSYS Models of Evacuated Tubular Collectors, Danmarks Tekniske Universitet, 2005.
- [45] D. Brough, A. Mezquita, S. Ferrer, C. Segarra, A. Chauhan, S. Almahmoud, N. Khordeghah, L. Ahmad, D. Middleton, H.I. Sewell, H. Jouhara, An experimental study and computational validation of waste heat recovery from a lab scale ceramic kiln using a vertical multi-pass heat pipe heat exchanger, Energy 208 (2020) <https://doi.org/10.1016/j.energy.2020.118325>.
- [46] V. Guichet, H. Jouhara, Condensation, evaporation and boiling of falling films in wickless heat pipes (two-phase closed thermosyphons): a critical review of correlations, Intern. J. Thermofluids 1–2 (February 2020) Vols. <https://doi.org/10.1016/j.ijft.2019.100001>.

- [47] V. Guichet, S. Almahmoud, H. Jouhara, Nucleate pool boiling heat transfer in wickless heat pipes (two-phase closed thermosyphons): a critical review of correlations, *Therm. Sci. Eng. Process.* 13 (October 2019) <https://doi.org/10.1016/j.tsep.2019.100384>.
- [48] Engineers Field, "Flue gas properties," [Online]. Available: <https://engineersfield.com/flue-gases-properties-table-density-viscosity/>. [Accessed 16 July 2020].
- [49] The Engineering Toolbox, "Dry air properties," [Online]. Available: https://www.engineeringtoolbox.com/dry-air-properties-d_973.html. [Accessed 21 July 2020].
- [50] P. Evans, "Properties of water at atmospheric pressure," [Online]. Available: <https://theengineeringmindset.com/properties-of-water-atmospheric-pressure-saturated-liquid/>. [Accessed 21 July 2020].
- [51] Solutia, "Therminol 66," [Online]. Available: <http://twf.mpei.ac.ru/TTHB/HEDH/HTF-66.PDF>. [Accessed 16 July 2020].
- [52] J. Backhurst, J. Harker, R. J.F., J. Coulson, *Chemical Engineering, 1*, Butterworth-Heinemann, 1999 Volume.
- [53] F. Kreith, R. Manglik, M. Bohn, *Principles of Heat Transfer*, 7th ed., Stamford: Cengage Learning, Inc, 2011.
- [54] W. Khan, J. Culham, M. Yovanovich, Convection heat transfer from tube banks in crossflow: analytical approach, *Int. J. Mass Transf.* (2006) 4831–4838 <https://doi.org/10.1016/j.ijheatmasstransfer.2006.05.042>.
- [55] A. Colburn, A method of correlating forced convection heat transfer data and a comparison with fluid friction, *Trans. Am. Inst. Chem. Eng.* (1933) 174–210.
- [56] E. Grimson, Correlation and utilization of new data on flow resistance and heat transfer for cross flow of gases over tube banks, *Trans. Am. Soc. Mech. Eng.* (1937) 583–594.
- [57] J. Holman, *Heat Transfer*, 7th edition, McGraw-Hill, New York, 1992.
- [58] H. Hausen, *Heat Transfer in Counter Flow, Parallel Flow and Cross Flow*, McGraw-Hill, New York, 1983.
- [59] A. Zukauskas, Heat transfer from tubes in crossflow, *Adv. Heat Transf.* (1972) 93–160.
- [60] P. Pongsoi, S. Pikulkajorn, S. Wongwises, Heat transfer and flow characteristics of spiral fin-and-tube heat exchangers: a review, *Int. J. Heat Mass Transf.* 79 (2014) 417–431 <https://doi.org/10.1016/j.ijheatmasstransfer.2014.07.072>.
- [61] T. Domański, K. Kmiecik, Load-bearing capacity of the steel-to-timber connections in fire temperature, *MATEC Web Conf.* 262 (2019) <https://doi.org/10.1051/mateconf/201926209005>.
- [62] University of Wisconsin-Madison. Solar Energy Laboratory, TRNSYS 17, Volume 7, Programmer's Guide, n.d.
- [63] B. Delpach, M. Milani, L. Montorsi, D. Boscardin, A. Chauhan, S. Almahmoud, B. Axcell, H. Jouhara, Energy efficiency enhancement and waste heat recovery in industrial processes by means of the heat pipe technology: case of the ceramic industry, *Energy* 158 (2018) 656–665 <https://doi.org/10.1016/j.energy.2018.06.041>.

Vibration Control of Transmission Line Tower

Flora Das, *Department of Civil Engineering, Aryan Institute of Engineering & Technology, Bhubaneswar, floradas22@yahoo.co.in*

Pradipta Kumar Das, *Department of Mechanical Engineering, Aryan Institute of Engineering & Technology, Bhubaneswar, pkdas751@gmail.com*

Sidharth Pradhan, *Department of Mechanical Engineering, Capital Engineering College, Bhubaneswar, sidharthpradhan265@gmail.com*

Bijayalaxmi Behera, *Department of Civil Engineering, Capital Engineering College, Bhubaneswar, bijayalaxmi759@gmail.com*

ABSTRACT

The optimization of viscoelastic dampers (VEDs) for transmission line tower vibration control is investigated in this work. The mechanical model of the VED-brace system was developed using the stiffness of the steel brace coupled to a VED. The increased modal damping ratio of the transmission line tower with VEDs was then calculated analytically. In addition, using ANSYS software, a finite element model of a two-circuit transmission line tower with VEDs was created, and the effects of VED installation positions and parameters on the additional modal damping ratio were investigated. The control performance of VEDs on a transmission line tower subjected to wind excitations was also demonstrated emphatically. The findings reveal that the stiffness of the steel brace attached to a VED has a considerable impact on the maximum additional modal damping ratio of the VED-brace system provided for the transmission line tower, as well as the ideal parameters of the VED-brace system.

1. Introduction

Transmission line tower is one of the typical high-rise structures, which is widely used throughout the world for energy supplying [1, 2]. The transmission line tower is vulnerable to suffering from wind-induced vibrations owing to its high flexibility and low inherent damping characteristics [3–5]. Frequent and excessive vibration could potentially induce damage and even collapse of the transmission line tower and have adverse effects on the serviceability of the whole transmission tower-line system [6–8]. Considerable investigations focused on theoretical [9–11], experimental [12–14], and field measurement [15] have been carried out in recent decades, which is devoted to mitigating the dynamic responses of the line transmission

tower. To guarantee the normal operation of the transmission line tower, several measures have been proposed for the vibration control of the transmission line tower, which mainly include increasing the stiffness of the transmission line tower [16, 17] and attaching energy dissipation devices on the transmission line tower.

Attaching energy dissipation devices is a commonly used method for mitigating vibrations of the transmission line tower [18–20]. The tuned mass damper (TMD) is a typical energy dissipation device, which has been commonly utilized for mitigating vibrations of high-rise structures [21, 22]. It has been found that the application of TMDs helps reduce the dynamic responses of the transmission line tower [23–25]. However, the disadvantage is that several additional masses should be installed on top of a

transmission tower, which requires the occupancy of the structural space. To overcome the shortcomings of the TMD, several energy-dissipating dampers were further proposed to enhance the vibration control performance of the transmission line tower. The magnetorheological (MR) damper has been successfully used on suppressing the wind-induced response of a real transmission line tower [26]. It has shown that the MR damper with optimally designed parameters has some advantages in controlling the wind-induced response of the transmission line tower. Nevertheless, the MR damper is quite complicated, and the requirement in the additional energy supply during the vibration control process is unrealistic while accepting strong excitations. Besides that, the passive friction dampers have been used in a finite element tower model with lumped mass, which is further applied in a real transmission line tower for verifying its superior control performance [27]. In addition, the use of viscoelastic dampers (VEDs) for the wind-resistant design of the transmission line tower has also been proposed [28]. Note that the optimal design of VEDs for vibration control of the transmission line tower has not been investigated.

This paper investigates the optimal design of VEDs for vibration control of a transmission line tower subjected to wind excitations. The paper is organized as follows. Firstly, the mechanical model of the VED-brace system was established. Subsequently, the maximum additional modal damping ratio of the transmission line tower attached with VEDs was calculated. Next, based on the finite element model of a two-circuit transmission line tower with VEDs, the influences of installation positions and parameters of VEDs on the additional modal damping ratio were clarified. Finally, the control performance of VEDs on the transmission line tower subjected to wind excitations was numerically demonstrated.

2. Model of VED-Brace System and Optimal Design of VED

2.1. Mechanical Model of the VED-Brace System. A coupled system combined with a viscoelastic damper and a supported steel brace, also denoted as VED-brace system, is shown in Figure 1. The VED is represented by a parallel spring (with stiffness K_d) and damper (with damping coefficient C_d), while the supported steel brace, connected to the VED and primary structure, is modeled by a spring with stiffness K_b and in series with the VED. Assuming that a sinusoidal displacement $u(t) = u_0 \sin \omega t$ with amplitude u_0 and natural frequency ω is applied on the VED, its output force is given as

$$F_d(t) = K_d u(t) + C_d \dot{u}(t), \quad (1)$$

where $\dot{u}(t)$ denotes the first-order derivative of $u(t)$ with time t .

Introducing the energy dissipation stiffness of VED as $K'_d = C_d \omega$, the output force of the VED can be rewritten as

$$F_d(t) = K_d u_0 \sin(\omega t) + K'_d u_0 \cos(\omega t). \quad (2)$$

Supposing that the displacement of the VED-brace system is represented by $u_A = u_a \sin \omega t$, the displacement of the VED and the brace can be expressed as

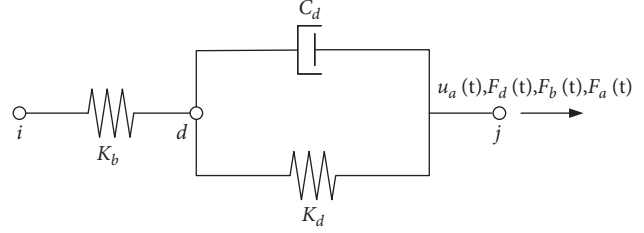


FIGURE 1: Mechanical Model of the VED-brace system.

$$\begin{aligned} u_D &= u_d \sin(\omega t - \varphi), \\ u_B &= u_A - u_D, \end{aligned} \quad (3)$$

where φ is the displacement phase difference between the VED and the brace.

Based on the equality of internal force for the series system, we obtain

$$\begin{aligned} F_b(t) &= F_d(t) \\ &= F_a(t) \\ &= K_d u_a \sin \omega t + K'_d u_a \cos \omega t, \end{aligned} \quad (4)$$

where

$$K_a = \frac{(K_b + K_d)K_b K_d + K_b (K'_d)^2}{(K_b + K_d)^2 + (K'_d)^2}, \quad (5)$$

$$K'_a = \frac{K_b^2 K'_d}{(K_b + K_d)^2 + (K'_d)^2}. \quad (6)$$

The ratio of the relative displacement amplitude at both ends of the VED to the relative displacement amplitude at both ends of the VED-brace system is expressed as

$$\begin{aligned} \beta &= \frac{u_d}{u_a} \\ &= \frac{K_b}{\sqrt{(K_b + K_d)^2 + (K'_d)^2}}. \end{aligned} \quad (7)$$

According to equation (7), it is straightforward to see that the ratio β approaches 1 if the brace stiffness K_b is sufficiently large. Otherwise, the effect of the limited stiffness of the steel brace must be included during vibration control analysis. For the convenience of analysis, the nondimensional parameters are introduced here:

$$\begin{aligned} \eta &= \frac{K'}{K_d}, \\ \alpha &= \frac{K_b}{K_d}, \\ \alpha_1 &= \frac{K_a}{K_d}, \\ \alpha_2 &= \frac{K'_a}{K_d}, \end{aligned} \quad (8)$$

where α denotes the ratio of the brace stiffness to the damper stiffness; α_1 is the ratio of the energy storage stiffness of the VED-brace system to the energy storage stiffness of the VED; α_2 denotes the ratio of the energy dissipation stiffness of the VED-brace system to the energy storage stiffness of the VED; η denotes the loss factor of the VED, and its typical value ranges from 0.2 to 5.0.

Figure 2 shows the variations of β , α_1 , and α_2 with respect to the stiffness ratio α . It can be seen from Figure 2(a) that β increases with α and will eventually converge to 1, which means that increasing the brace stiffness is beneficial to improve the energy dissipation efficiency of the VED. As shown in Figure 2(b), when α is greater than 2, α_1 will be greater than 1, and K_a finally converges to K_d as K_b continues to increase. In this case, the brace can be regarded as a rigid rod, indicating that the energy storage stiffness of the VED-brace system is equal to the energy dissipation stiffness of the VED. It can be found in Figure 2(c) that α_2 increases with α . Moreover, K'_a finally converges to K_d as α grows, which can be considered that the energy dissipation stiffness of the VED-brace system is also equal to that of the VED.

2.2. Optimal Design of VED. The simplified model of the tower segment with the VED-brace system is depicted in Figure 3. Note that the VED-brace system is connected in parallel to the main member of the transmission line tower.

Assume the relative displacement of both the i end and j end of the tower segment as

$$u(t) = u_{\max} \sin \omega t. \quad (9)$$

For the tower segment coupled with the VED-brace system, the output force becomes

$$\begin{aligned} F(t) &= F_f(t) + F_a(t) \\ &= (K_f + K_a)u_{\max} \sin \omega t + K'_a u_{\max} \cos \omega t. \end{aligned} \quad (10)$$

The equivalent damping ratio for the tower segment may be obtained as

$$\begin{aligned} \xi_a &= \frac{E_d}{4\pi E_s} \\ &= \frac{K'_a}{2(K_f + K_a)}. \end{aligned} \quad (11)$$

By defining the additional stiffness ratio $\alpha_a = K_a/K_f$, equation (10) can be rewritten as

$$F(t) = u_{\max} K_f (1 + \alpha_a) \sin(\sin \omega t + 2\xi_a \cos \omega t), \quad (12a)$$

where

$$\alpha_a = \alpha_b \alpha_d \frac{\alpha_b \eta + (1 + \eta^2) \alpha_d}{(\alpha_b \eta + \alpha_d)^2 + \eta^2 \alpha_d^2}, \quad (12b)$$

$$\xi_a = \frac{1}{2} \frac{\alpha_b^2 \eta^2 \alpha_d}{(\alpha_b \eta + \alpha_d)(\alpha_b \eta + \alpha_b \alpha_d + \alpha_d) + (1 + \alpha_b) \alpha_d^2 \eta^2}, \quad (12c)$$

where $\alpha_b = K_b/K_f$ represents the ratio of the brace stiffness to the tower segment stiffness; $\alpha_d = K'_d/K_f$ represents the energy dissipation stiffness ratio of the VED.

From equations (12a) to (12c), it is shown that α_a and ξ_a are dependent on α_b , α_d , and η . Again, η is taken as 1.4. Figure 4 shows the variations of the stiffness ratio α_a with respect to α_d under various α_b . It is apparent that the stiffness ratio α_a increases with the increase of α_d and approaches α_b for a large α_d . This is because extremely large damper stiffness will lock the damper, which causes the damper to fail to dissipate the vibration energy. The variations of the equivalent damping ratio ξ_a with respect to α_d under various α_b are further illustrated in Figure 5. Note that the equivalent damping ratio ξ_a firstly increases with the increase with α_d , reaching the maximum value when the α_d reaches a certain value, and then decreases with the increase of α_d .

By taking the derivatives of the damping ratio ξ_a with respect to α_d , there is

$$\xi_a = \frac{1}{2} \frac{\alpha_b^2 \eta^2}{(1 + \eta^2)(1 + \alpha_b) \alpha_d + \alpha_b^2 \eta^2 / \alpha_d + \alpha_b^2 \eta + 2\alpha_b \eta}. \quad (13)$$

By defining $f(\alpha_d) = (1 + \eta^2)(1 + \alpha_b) \alpha_d + \alpha_b^2 \eta^2 / \alpha_d$ and letting $\partial f(\alpha_d) / \alpha_d = 0$, we obtain

$$\alpha_d = \frac{\alpha_b \eta}{\sqrt{(1 + \eta^2)(1 + \alpha_b)}}. \quad (14)$$

Substituting equations (14) into equation (12c), the peak damping ratio is derived as

$$\xi_{a,\text{peak}} = \frac{1}{4} \frac{\alpha_b \eta}{\sqrt{(1 + \alpha_b)(1 + \eta^2)} + 1 + \alpha_b/2}. \quad (15)$$

The variations of the peak damping ratio $\xi_{a,\text{peak}}$ with respect to the stiffness ratio α_b for $\eta = 1.4$ and loss factor η for $\alpha_b = 0.2$ are illustrated in Figure 6. As shown in Figure 6, the peak damping ratio $\xi_{a,\text{peak}}$ increases with the increase of stiffness ratio α_b and loss factor η . In summary, equation (15) describes peak damping ratio for the tower segment when equation (14) is fulfilled. These two equations constitute the optimal parameter design for VEDs in the transmission line tower.

After the brace stiffness K_b and the loss factor η of the VED are determined, the damping ratio of the energy dissipation system reaches the maximum value. The ratio of the equivalent

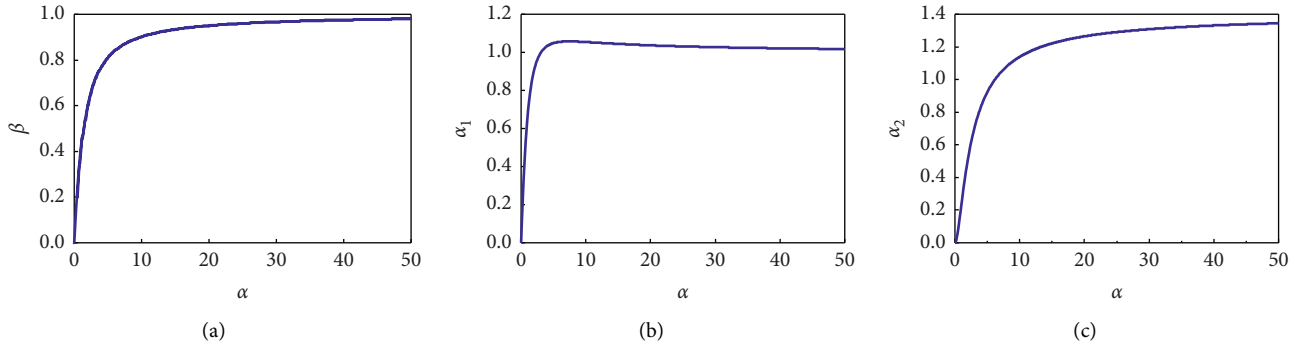


FIGURE 2: Variations of β , α_1 , α_2 with the stiffness ratio α for $\eta = 1.4$.

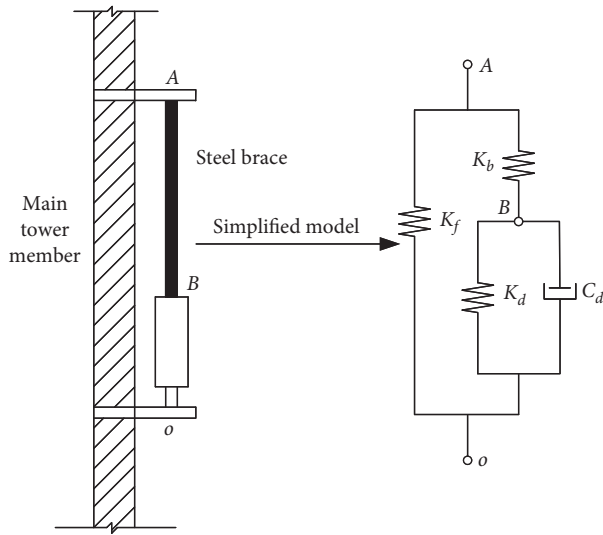


FIGURE 3: Simplified model of the tower segment with the VED-brace system.

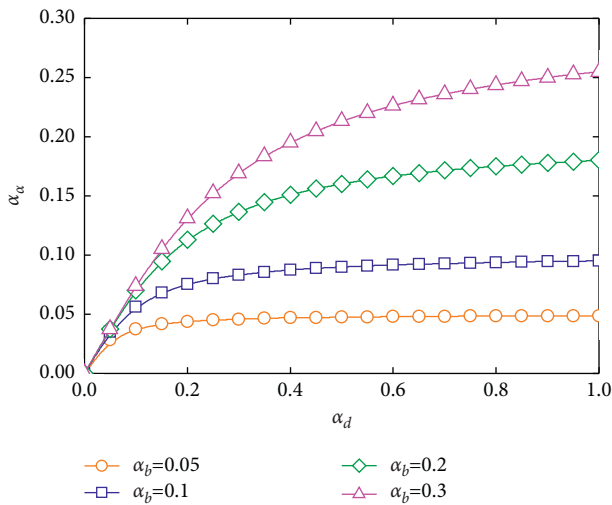


FIGURE 4: Variations of the stiffness ratio α_a with respect to α_d under various α_b .

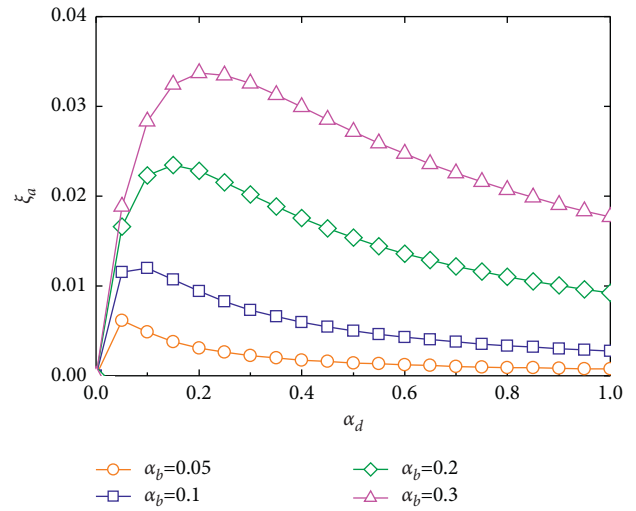


FIGURE 5: Variations of the equivalent damping ratio ξ_a with respect to α_d under various α_b .

energy storage stiffness K_d of the VED to the brace stiffness K_b can be calculated by the following formula as

$$\lambda = \sqrt{\frac{1}{(1 + \eta^2)(1 + \alpha_b)}} \quad (16)$$

It should be noted that when the additional modal damping ratio of the VED-brace system reteaches maximum, its energy dissipation efficiency is also the largest. Thus, the optimal parameters of the VED-brace system can be determined by equations (14) and (16), and the maximum additional modal damping ratio of the tower section can be calculated by equation (15).

3. Numerical Simulation of a Transmission Line Tower with VEDs

3.1. Finite Element Model of Transmission Line Tower. To investigate the vibration control performance of VEDs for a transmission line tower, a three-dimensional finite element

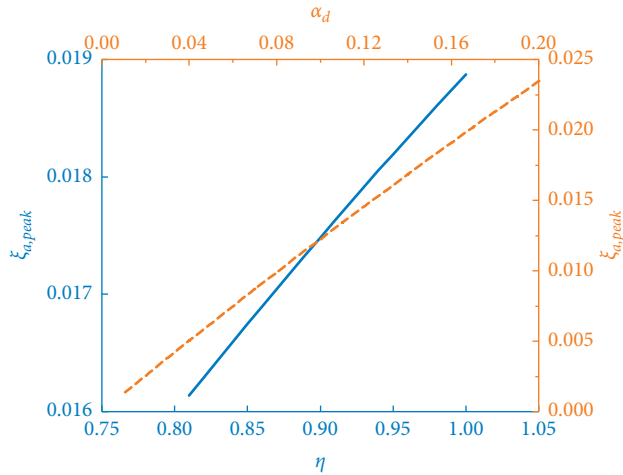


FIGURE 6: Variations of the peak damping ratio $\xi_{a,peak}$ with respect to α_b and η .

model of a two-circuit transmission line tower shown in Figure 7 is built in ANSYS software. The transmission line tower height is 103.6 m, and two cross arms are symmetrically arranged at the heights of 57 m, 78.2 m, and 99.6 m above the ground. The end of the cross arm is 16.6 m, 17.6 m, and 20.22 m away from the center of the transmission tower, respectively. The main structure of the transmission line tower is composed of steel pipes and connected with high-strength bolts. The cross section of the steel pipe is varied with height of the transmission line tower. The most important stressed components are the four tower columns, and their cross-sectional area decreases from bottom to top. The main material parameters of members are as follows: elastic modulus 206 GPa, density 7850 kg/m³, and Poisson's ratio 0.3.

The spatial beam element BEAM188 is used for each member, without considering the coupling vibration of the conductor, ground wire, and transmission tower. The transmission line tower without control consists of 527 nodes and 1406 elements in total. The overall coordinate system is divided into the horizontal X axis, the forward Y axis, and the Z axis along with the tower height. The origin of coordinates is at the midpoint of the bottom of the tower. The first three mode shapes of the transmission tower are obtained by modal analysis, as illustrated in Figure 8. The first mode shape is the bending vibration mode perpendicular to the conductor direction, the second mode shape is the bending vibration mode along the conductor direction, and the third mode shape is the torsional vibration mode rotating around the centerline of the tower. Based on the finite element model of the transmission tower, the modal analysis of the transmission tower is carried out, and the properties of the transmission line tower shown in Table 1 are further obtained.

3.2. The Installation Position of VED. Figure 9 presents the strain energy distribution in the transmission tower for the first second mode. It can be seen from Figure 9(a) that the first modal strain energy of the primary members is much

greater than that of the inclined bars and the cross arms, and the first modal strain energy of the lower part of the tower legs is also greater than that of the upper parts. As shown in Figure 9(b), the distribution law of the second modal strain energy in the transmission tower is consistent with that of the first modal strain energy. Thus, the VEDs should be installed on the lower primary members with the largest possible modal strain energy, which helps to efficiently control the vibration of the transmission line tower for the first two modes.

The main tower columns with the same function are recorded as a unit, and there are 72 main tower column units numbered from bottom to top of the transmission line tower. The axial deformation of each main tower column for the first mode is shown in Table 2. The variations of the axial deformation with the unit number are further illustrated in Figure 10. Note that the large deformation occurs at the 1, 2, 3, 4, 21, 22, 23, 25, and 49 units of the transmission line tower. To effectively control the bending and the axial deformation of the transmission line tower, the installation positions of VEDs need to be taken into account in combination with the data in Table 2 and Figure 10. There are mainly two installation schemes: scheme 1 is to install VEDs on the tower column unit with large axial deformation, and scheme 2 is to install the same number VEDs with the same parameters as scheme 1 on the tower column unit from the bottom to top of the transmission line tower. 44 VEDs used in installation scheme 1 are installed in parallel on the four main tower columns of the transmission tower, and 44 VEDs used in installation scheme 2 are installed on the tower column unit from bottom to top of the transmission line tower. Note that the unit numbers of VEDs corresponding to installation scheme 1 and installation scheme 2 are shown in Table 3.

3.3. The Optimal Parameters of VED. The outer diameters of the circular steel pipes of the main tower columns of the transmission tower vary from 109.5 mm to 213 mm, and the wall thickness of the steel pipes varies from 6 mm to 10 mm. $K = EA/L$ is the axial stiffness of the tower column unit, A is the area of steel pipe, and L is the unit length. The stiffness of the tower column unit installed with VEDs is shown in Table 4.

For the convenience of calculation and analysis, the ratio of the stiffness between each brace and each tower column is taken as 0.2, and the loss factor of the VED is taken as 1.4. Then, the ratio of the equivalent energy storage stiffness of the VED to brace stiffness λ can be calculated by equation (16), and the additional modal damping ratio ξ_a of the transmission line tower installed with VEDs can be further gained. The stiffness of the i th tower segment, the energy storage stiffness of the i VED, and the energy dissipation stiffness of the i VED are defined as

$$K_{bi} = \alpha_{bi} K_{fi}, \quad (17)$$

$$K_{di} = \lambda_i K_{bi}, \quad (18)$$

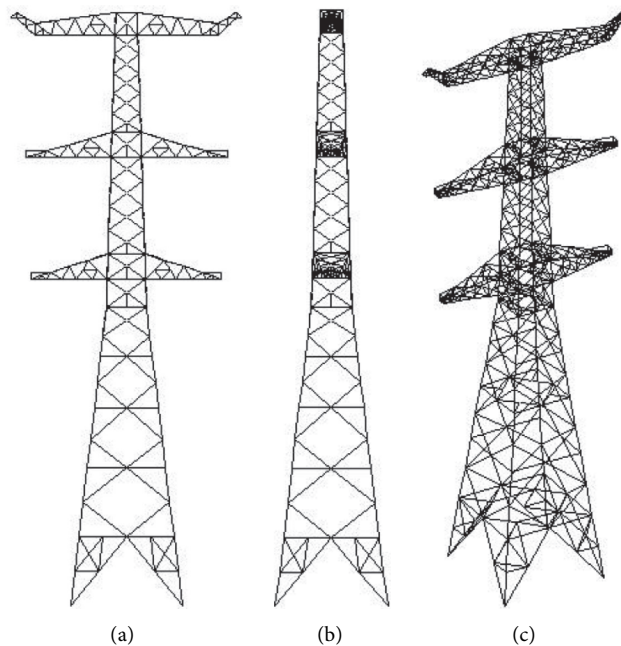


FIGURE 7: Finite element model of the transmission line tower: (a) X-Z plane; (b) Y-Z plane; (c) X-Y-Z space.

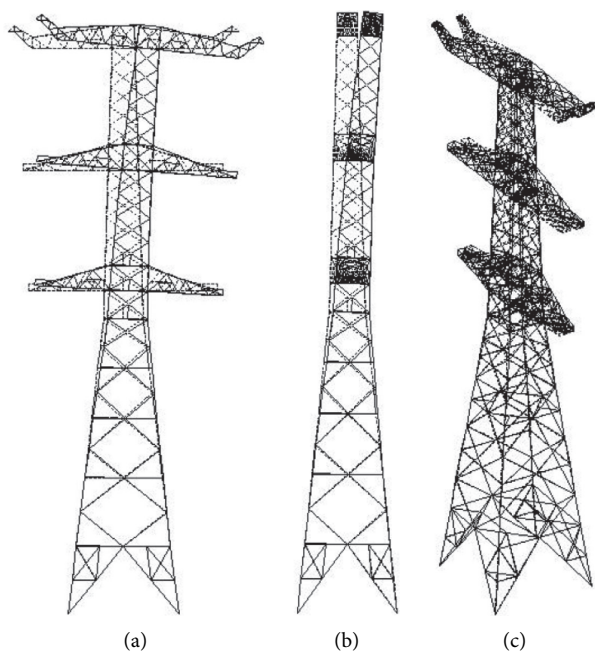


FIGURE 8: The first three mode shapes of the transmission line tower: (a) the first mode; (b) the second mode; (c) the third mode.

TABLE 1: Properties of the transmission line tower.

Modal order	Frequency f (Hz)	Modal strain energy W_s (N·m)	Generalized mass m (ton)	Characteristics of vibration mode
1	0.832	341896	25.00	Transverse bending
2	0.849	337865	23.74	Vertical bending
3	1.411	193149	4.91	Torsion

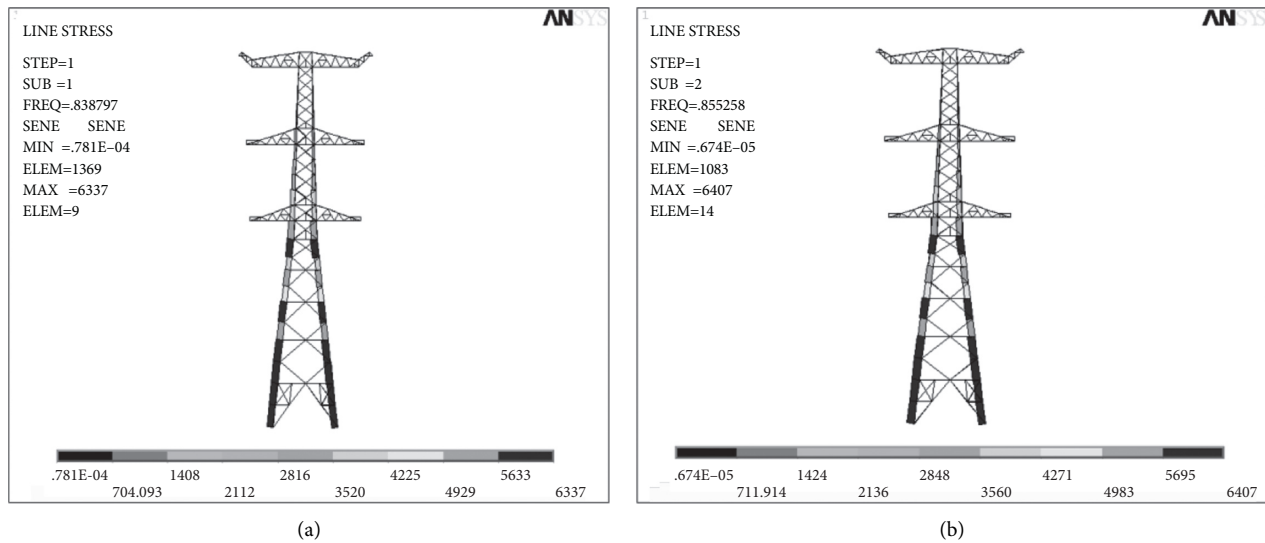


FIGURE 9: Strain energy distribution: (a) the first mode; (b) the second mode.

TABLE 2: Axial deformation of each main tower column for the first mode.

Unit number	Unit length (m)	Axial strain	Axial deformation (mm)
1	6.08	0.000616955	3.75
2	6.08	0.000619991	3.77
3	6.08	0.000636258	3.87
4	6.11	0.000646764	3.95
5	5.04	0.000648939	3.27
21	5.61	0.000667406	3.75
22	4.53	0.000670219	3.04
23	4.48	0.000685088	3.07
24	3.63	0.000688744	2.50
25	5.07	0.000693175	3.52
41	5.00	0.000678386	3.40
42	4.40	0.000627275	2.76
49	4.20	0.000754969	3.17
50	4.20	0.000667704	2.81
57	4.20	0.000623425	2.62
58	4.20	0.000503736	2.12
65	4.40	0.000589224	2.60
66	3.40	0.000540314	1.84
73	3.40	0.000544409	1.85
74	3.40	0.000397533	1.35
75	3.40	0.000261701	0.89
76	3.40	0.000105639	0.36
77	4.00	5.09371E-06	0.02

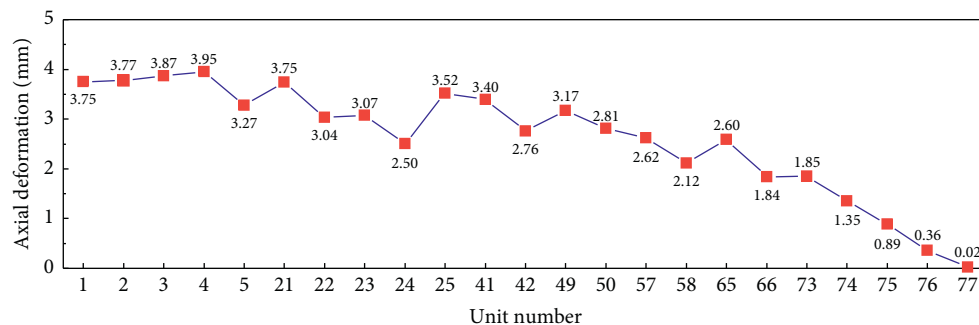


FIGURE 10: Variations of the axial deformation with the unit number for the first mode.

TABLE 3: Installation scheme of VEDs.

Unit number of the main tower column				Axial deformation of the tower column (mm)	Installation scheme 1	Installation scheme 2
1# tower column	2# tower column	3# tower column	4# tower column			
1	6	11	16	3.75	w/installed	w/installed
2	7	12	17	3.77	w/installed	w/installed
3	8	13	18	3.87	w/installed	w/installed
4	9	14	19	3.95	w/installed	w/installed
5	10	15	20	3.27	w/installed	w/installed
21	26	31	36	3.75	w/installed	w/installed
22	27	32	37	3.04	w/installed	w/installed
23	28	33	38	3.07	w/installed	w/installed
24	29	34	39	2.50	w/o installed	w/installed
25	30	35	40	3.51	w/installed	w/installed
41	43	45	47	3.40	w/installed	w/installed
42	44	46	48	2.76	w/o installed	w/o installed
49	51	53	55	3.18	w/installed	w/o installed
50	52	54	56	2.81	w/o installed	w/o installed
57	59	61	63	2.62	w/o installed	w/o installed
58	60	62	64	2.12	w/o installed	w/o installed
65	67	69	71	2.60	w/o installed	w/o installed
66	68	70	72	1.84	w/o installed	w/o installed
73	78	83	88	1.85	w/o installed	w/o installed
74	79	84	89	1.36	w/o installed	w/o installed
75	80	85	90	0.90	w/o installed	w/o installed
76	81	86	91	0.40	w/o installed	w/o installed
77	82	87	92	0.02	w/o installed	w/o installed

TABLE 4: Stiffness of the main tower column unit installed with VEDs.

Unit number of the main tower column				Unit stiffness (N/m)
1# tower column	2# tower column	3# tower column	4# tower column	
1	6	11	16	442038825
2	7	12	17	442038825
3	8	13	18	442038825
4	9	14	19	440236029
5	10	15	20	533066110
21	26	31	36	456295733
22	27	32	37	565187787
23	28	33	38	571298462
24	29	34	39	705064904
25	30	35	40	504937712
41	43	45	47	474209703
42	44	46	48	538877694
49	51	53	55	428210759

$$K'_{di} = \eta \lambda_i K_{bi}, \quad (19)$$

$$C_a = \frac{K'}{\omega}. \quad (20)$$

where a_{bi} denotes the ratio of the brace stiffness to the tower column unit stiffness; K_{fi} denotes the axial stiffness of the tower column; λ_i denotes the ratio of the energy storage stiffness of the VED to the corresponding brace stiffness.

Equations (17)–(19) require that the parameters of VEDs in each tower section be different, which increases the difficulty of manufacturing dampers. Thus, the VEDs with the same parameters are used in this paper. Furthermore, the equivalent damping coefficient of the VED-brace system can be defined as

3.4. Calculation Method of Supplemental Modal Damping Ratio. There are mainly two methods used in calculating the additional modal damping ratio of the transmission line tower installed with VEDs: the modal strain energy method and the complex mode calculation method. The modal strain energy method is regarded as a simple method, which assumes that the tower frequency and vibration mode show less variation before and after installing VEDs. When the modal strain energy method is adopted, the additional

modal damping ratio of the transmission line tower provided by VEDs can be expressed as

$$\xi_a = \frac{E_d}{4\pi E_s} \quad (21)$$

$$= \frac{\pi\omega \sum_{i=1}^{n_d} C_{di} u_i}{4\pi E_s},$$

where E_d denotes the consumed energy by all VEDs in one cycle; n_d is the number of VEDs; u_i is the elongation at both ends of the VED; E_s is the modal strain energy of the tower in one vibration cycle. It can be seen from equation (21) that the modal damping ratio can be calculated by the parameters of the VED and modal parameters such as the vibration mode and frequency of the transmission line tower.

When using the complex modal analysis method, it is necessary to establish the finite element model of the tower-VED-brace system. The VED-brace system is regarded as a mechanical model with equivalent stiffness and equivalent damping, which is simulated with COMBIN14 element in ANSYS software. A total of 44 COMBIN14 elements are attached to both ends of the main tower column units of the transmission line tower. In the establishment of the COMBIN14 element, only one COMBIN14 element is needed to be added to the transmission tower node with VEDs, and the program automatically defaults that the two elements are in parallel mode. Accordingly, it is very convenient for establishing the finite element model of the tower-VED-brace system. In addition, the modal damping ratio can be further obtained by the complex modal analysis method. And the r th vibration circular frequency and modal damping ratio of the transmission tower are computed as

$$\omega_r = \text{Im}(\lambda_r), \quad (22)$$

$$\xi_r = \frac{-\text{Re}(\lambda_r)}{\text{Im}(\lambda_r)}.$$

3.5. Influence of Installation Position and Parameters of VEDs on the Additional Modal Damping Ratio. The brace stiffness is taken as 0.1 to 0.2 times the tower column unit stiffness, and the loss factor η of the VED is taken as 1.4. The ratio of the equivalent energy storage stiffness of the VED to brace stiffness λ is calculated as 0.531 by equation (16). Based on the modal strain energy method and the complex modal analysis method, the variations of the first additional modal damping ratio ξ_1 with α_b provided by VEDs under two installation schemes are presented in Figure 11. It can be seen from Figure 11 that the first additional modal damping ratio ξ_1 of provided by VEDs installed in accordance with installation scheme 1 is greater than that provided by VEDs installed in accordance with installation scheme 2. Hence, since installation scheme 1 is superior to installation scheme 2, installation scheme 1 will be used in the following research.

The brace stiffness K_b is taken as 0.2 times of the axial stiffness of the tower column unit, and the loss factor η of the

VED is taken as 1.4. The ratio of the equivalent energy storage stiffness of the VED to brace stiffness λ is calculated as 0.531 by equation (16), and the value of λ is further varied from 0.491 to 0.631. Based on the modal strain energy method and the complex modal analysis method, the variations of the first additional modal damping ratio ξ_1 with λ are illustrated in Figure 12. It can be found in Figure 12 that when the brace stiffness K_b is a setting value, and the ratio of the equivalent storage of the VED to the brace stiffness is taken as the calculated value of equation (16), the first additional modal damping ratio ξ_1 of the transmission line tower obtained by the complex modal analysis method reaches the maximum value. Note that the first additional modal damping ratio ξ_1 predicted by the complex modal analysis method is greater than that of the modal strain energy method, and the value of the λ corresponding to the first maximum additional modal damping ratio ξ_1 calculated by the complex modal analysis method is less than that of the first maximum additional modal damping ratio ξ_1 calculated by the modal strain energy method. In addition, the first additional modal damping ratio of the transmission line tower can be improved by increasing the bracing stiffness K_b .

The variations of the second additional modal damping ratio ξ_2 with λ are further depicted in Figure 13. It is noteworthy that the variation of the second additional modal damping ratio ξ_2 with λ is consistent with that of the first additional modal damping ratio ξ_1 with λ . It means that lower-order vibration control of the transmission line tower can be realized by controlling the first-order modal vibration of the transmission tower. Hence, the influences of the ratio of brace stiffness to tower column unit stiffness α_b and the loss factor η on the first additional modal damping ratio ξ_2 of the transmission line tower are emphatically investigated in the following research.

The loss factor η of the VED is taken as 1.4, and the ratio of the equivalent energy storage stiffness of the VED to brace stiffness λ is calculated by equation (16). Based on the modal strain energy method and the complex modal analysis method, the variations of the first additional modal damping ratio ξ_1 with the ratio of brace stiffness to tower column unit stiffness α_b are shown in Figure 14. As shown in Figure 14, the first additional modal damping ratio ξ_1 increases linearly with the increase of the α_b . In addition, the first additional modal damping ratio ξ_1 predicted by the complex modal analysis method is also greater than that of the modal strain energy method.

The ratio of brace stiffness to tower column unit stiffness α_b is taken as 0.2, and the ratio of the equivalent energy storage stiffness of the VED to brace stiffness λ is calculated by equation (16). Based on the modal strain energy method and the complex modal analysis method, the variations of the first additional modal damping ratio ξ_1 with the loss factor η of the VED are shown in Figure 15. Note that the first additional modal damping ratio ξ_1 increases linearly with the increase of the η . Consistent with the result of Figure 14, the first additional modal damping ratio ξ_1 predicted by the complex modal

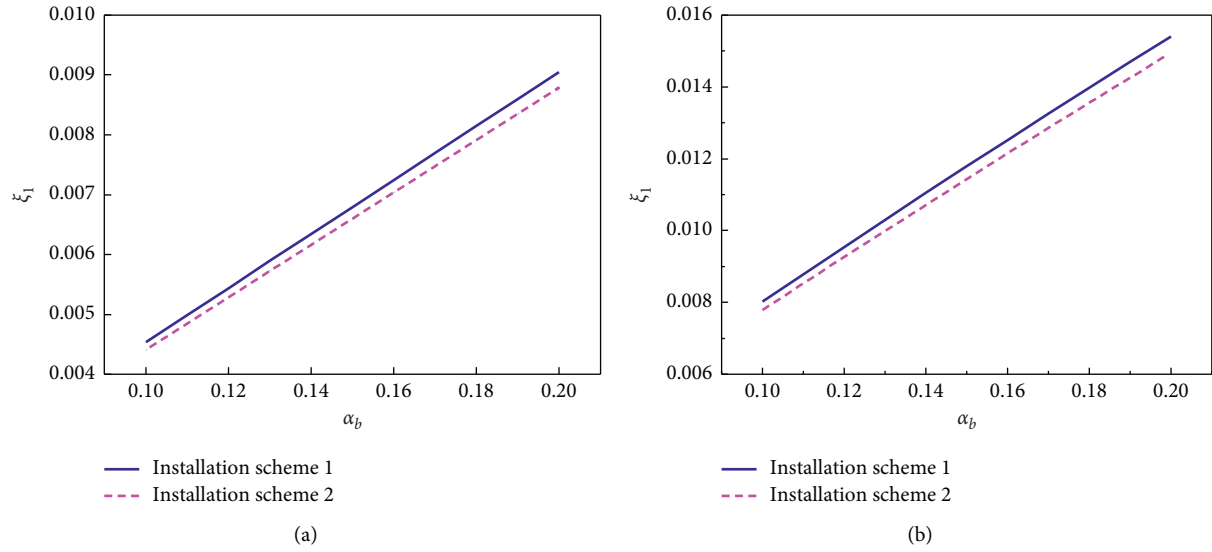


FIGURE 11: Variations of the first additional modal damping ratio ξ_1 with α_b under two installation schemes: (a) the modal strain energy method; (b) the complex modal analysis method.

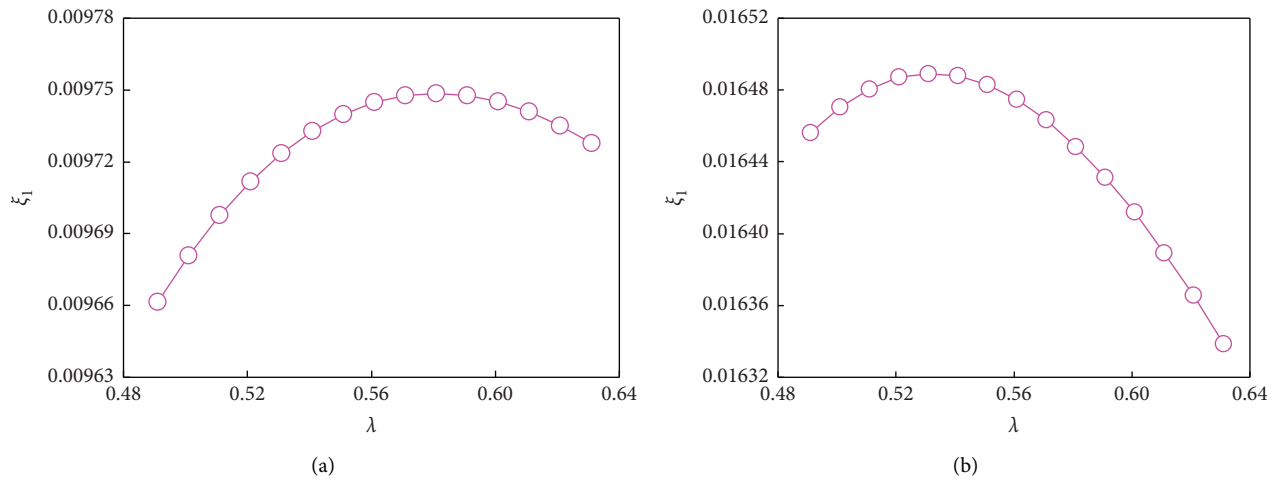


FIGURE 12: Variations of the first additional modal damping ratio ξ_1 with λ : (a) the modal strain energy method; (b) the complex modal analysis method.

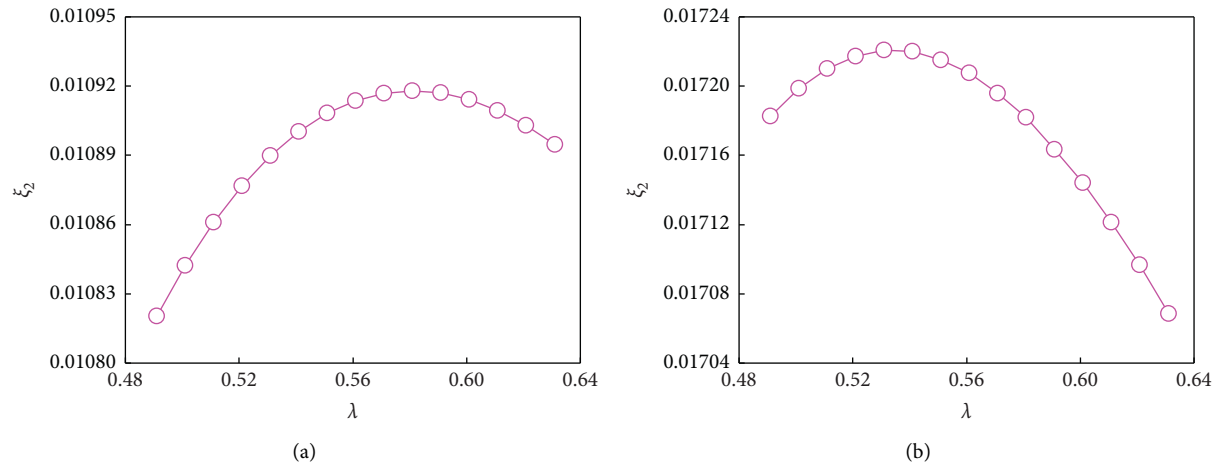


FIGURE 13: Variations of the second additional modal damping ratio ξ_2 with λ : (a) the modal strain energy method; (b) the complex modal analysis method.

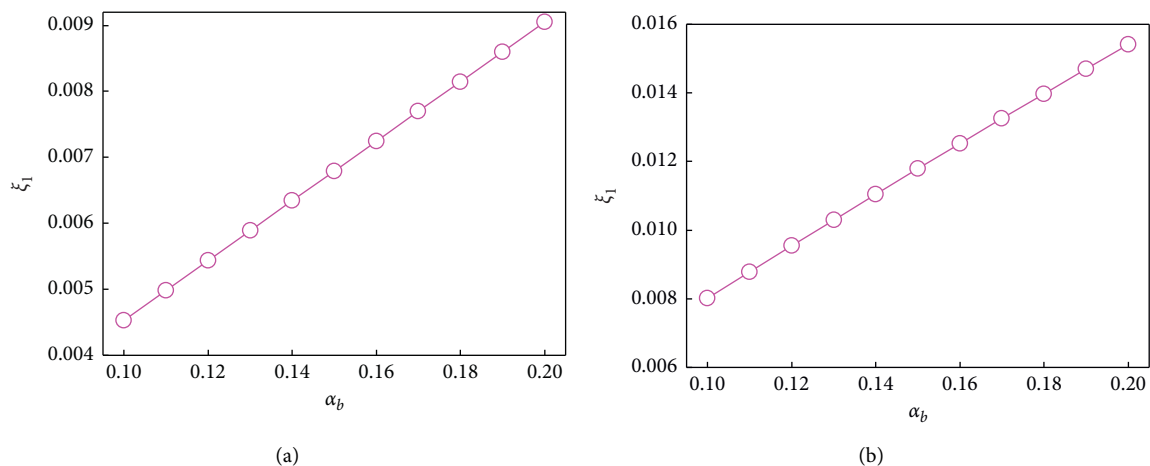


FIGURE 14: Variations of the first additional modal damping ratio ξ_1 with α_b : (a) the modal strain energy method; (b) the complex modal analysis method.

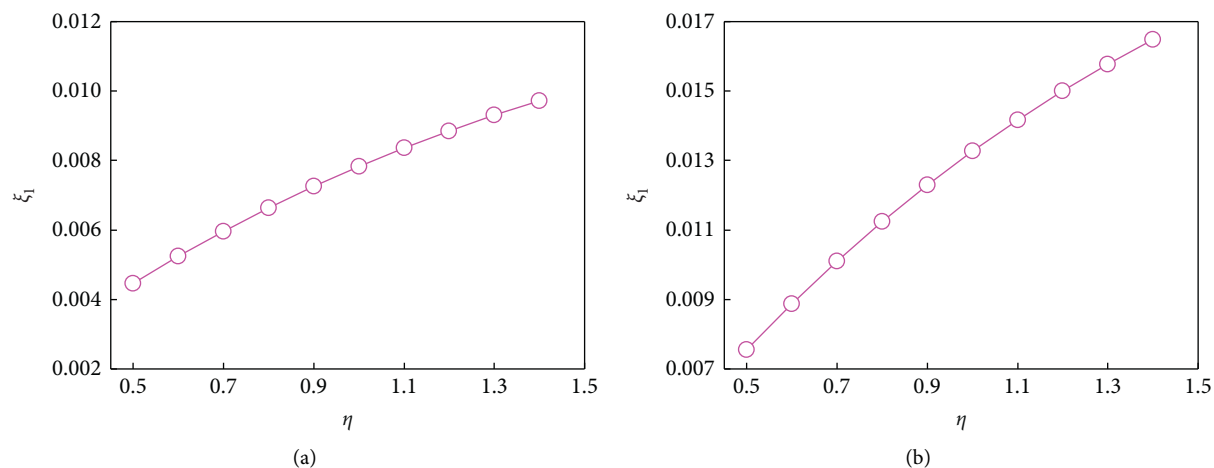


FIGURE 15: Variations of the first additional modal damping ratio ξ_1 with η : (a) the modal strain energy method; (b) the complex modal analysis method.

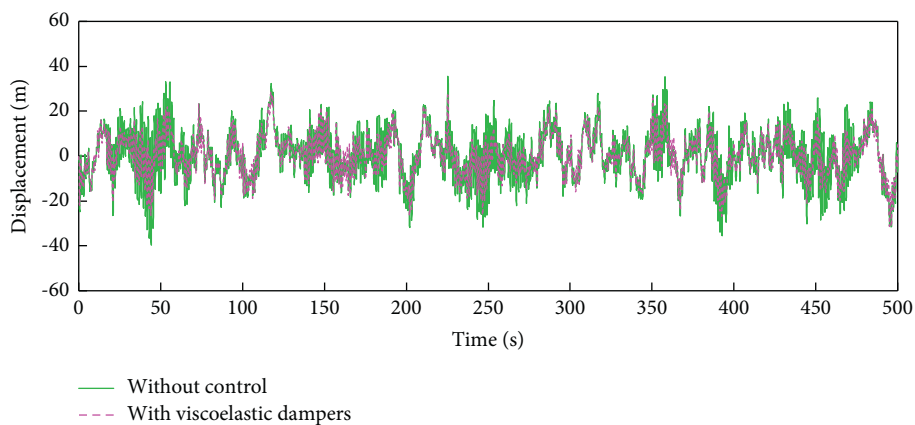


FIGURE 16: Time history response of the top displacement of the transmission line tower.

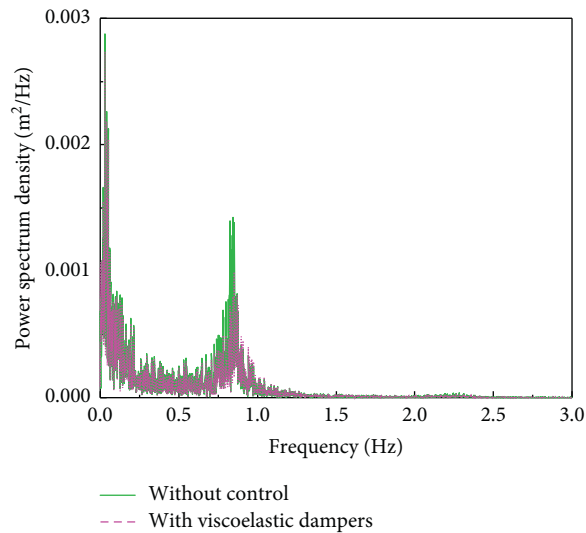


FIGURE 17: Power spectrum density of the displacement response.

analysis method is also greater than that of the modal strain energy method.

4. Control Performance of VEDs for Wind-Induced Excitations

The wind load in the vertical direction is applied to the transmission line tower without control and controlled by VEDs, respectively. The basic wind speed at 10 mm elevation is 30 m/s, and the site type is class B. The wind speed corresponding to each elevation is different, and the fluctuating wind speed time history at each height of the transmission line tower is simulated according to the harmonic synthesis method. In ANSYS, the buffeting force-time history is input along the main tower column of the transmission line tower, and the time domain response of the buffeting displacement is calculated by the time history integration method. The first two natural modal damping ratios of the transmission line tower are 0.02. The transmission line tower is subjected to random vibration under fluctuating wind load in the range of 0 s to 500 s.

Figure 16 illustrates the time history response of the displacement of the 481 nodes on the top of the transmission line tower along the wind direction without control and controlled by VEDs. The mean square value of the displacement on the top of the transmission line tower control by VEDs is 0.0091 m, which is 18.9% lower than that of the transmission line tower without control 0.1124 m. The power spectrum density of the displacement response of the transmission line tower without control and controlled by VEDs is shown in Figure 17. Compared with the transmission line tower without control, the transverse bending vibration energy of the transmission line tower control by VEDs presents a significant decrease.

5. Conclusions

This paper investigates the optimization of VEDs for vibration control of a transmission line tower subjected to wind excitations. The mechanical model of the VED-brace

system was first established, and the maximum additional modal damping ratio of the transmission line tower attached with VEDs was calculated. Based on the finite element model of a two-circuit transmission line tower with VEDs, the influences of installation positions and parameters of VEDs on the additional modal damping ratio were clarified. In the end, the control performance of VEDs on the transmission line tower subjected to wind excitations was numerically demonstrated. The main conclusions are summarized as follows:

- (1) The stiffness of the steel brace connected to a VED has a significant effect on the maximum additional modal damping ratio of the VED-brace system provided for the transmission line tower and the optimal parameters of the VED, which indicates that the stiffness of the steel brace cannot be ignored for the refined theoretical analysis and numerical simulation.
- (2) The installation positions of VEDs dramatically influence the additional modal damping ratio of the transmission line tower. Studies indicate that the first additional modal damping ratio provided by VEDs installed in accordance with installation scheme 1 is greater than that provided by the VED installed in accordance with installation scheme 2. Hence, installation scheme 1 is superior to installation scheme 2. Besides that, the first additional modal damping ratio predicted by the complex modal analysis method is greater than that of the modal strain energy method.
- (3) The increase of the brace stiffness and the loss factor helps to improve the vibration control performance of the transmission line tower with VEDs. The equivalent additional modal damping ratio provided by VEDs is increased with the brace stiffness and the loss factor, which presents a significant advantage in carrying out the optimal design of VEDs for mitigating tower vibrations.
- (4) The VEDs present superior control performance on the top displacement of the transmission line tower as well as the transverse bending vibration energy. The mean square value of the displacement on the top of the transmission line tower control by VEDs is 0.0091 m, which is 18.9% lower than that of the transmission line tower without control 0.1124 m.

References

- [1] T. Okamura, T. Ohkuma, E. Hongo, and H. Okada, "Wind response analysis of a transmission tower in a mountainous area," *Journal of Wind Engineering and Industrial Aerodynamics*, vol. 91, no. 1-2, pp. 53-63, 2003.
- [2] E. P. U. S. Salunkhe and Y. M. Ghugal, "Analysis and design of three legged 400kV double circuit steel transmission line towers," *International Journal of Civil Engineering & Technology*, vol. 4, no. 3, pp. 197-209, 2013.
- [3] R. C. Battista, R. S. Rodrigues, and M. S. Pfeil, "Dynamic behavior and stability of transmission line towers under wind forces," *Journal of Wind Engineering and Industrial Aerodynamics*, vol. 91, no. 8, pp. 1051-1067, 2003.
- [4] Y. Ming, Z. H. He, Y. C. Zhang, Y. C. Liu, J. Yang, and Z. Y. Zhang, "Dynamic response of transmission lines crossing high-speed railway," *IEEE Transactions on Power Delivery*, vol. 2021, Article ID 3104902, 2021.
- [5] M. Zhang, G. F. Zhao, L. Wang, and J. Li, "Wind induced coupling vibration effects of high voltage transmission tower line systems," *Shock And Vibration*, vol. 2017, Article ID 1205976, 34 pages, 2017.
- [6] B. Asgarian, S. Dadras Eslamlou, A. Mehr, and M. Mehr M, "Progressive collapse analysis of power transmission towers," *Journal of Constructional Steel Research*, vol. 123, pp. 31-40, 2016.
- [7] X. Fu and H.-N. Li, "Uncertainty analysis of the strength capacity and failure path for a transmission tower under a wind load," *Journal of Wind Engineering and Industrial Aerodynamics*, vol. 173, pp. 147-155, 2018.
- [8] H. Patil, G. Doshi, N. P. Rao, D. Lakhpati, and V. Subramanian, "Failure analysis of transmission line tower: a case study," *The IUP Journal of Structural Engineering*, vol. 3, no. 1, pp. 20-27, 2010.
- [9] F. G. A. Albermani and S. Kitipornchai, "Numerical simulation of structural behaviour of transmission towers," *Thin-Walled Structures*, vol. 41, no. 2-3, pp. 167-177, 2003.
- [10] B. Eltaly, A. Saka, and K. Kandil, "FE simulation of transmission tower," *Advances in Civil Engineering*, vol. 2014, pp. 343-355, Article ID 258148, 2014.
- [11] E. Veg, M. Regodic, A. Joksimovic, and N. Gubeljak, "Development of the transmission tower virtual 3D model for structural analysis in ANSYS," *FME Transaction*, vol. 45, no. 2, pp. 232-235, 2017.
- [12] H.-N. Li, S.-Y. Tang, and T.-H. Yi, "Wind-rain-induced vibration test and analytical method of high-voltage transmission tower," *Structural Engineering & Mechanics*, vol. 48, no. 4, pp. 435-453, 2013.
- [13] J. H. Park, B. W. Moon, K. W. Min, S. K. Lee, and C. K. Kim, "Cyclic loading test of friction-type reinforcing members upgrading wind-resistant performance of transmission towers," *Engineering Structures*, vol. 29, no. 11, pp. 435-453, Article ID 31853196, 2007.
- [14] H. Z. Deng, S. Y. Zhu, Y. Chen, and Z. M. Wang, "Study on wind-induced vibration control of long span transmission line system," *Journal of Building Structures*, vol. 24, no. 4, pp. 60-64+75, 2003, in Chinese.
- [15] H. Z. Deng, R. J. Si, X. Y. Hu, and C. Y. Duan, "Wind tunnel study on wind-induced vibration responses of a UHV transmission tower-line system," *Advances in Structural Engineering*, vol. 16, no. 7, pp. 1175-1185, 2013.
- [16] L. Tian, Q. Wang, Q. Yu, and N. Xu, "Wind-induced vibration optimal control for long span transmission tower-line system," *The Open Civil Engineering Journal*, vol. 7, no. 1, pp. 159-163, 2013.
- [17] Q. Xie and L. Sun, "Failure mechanism and retrofitting strategy of transmission tower structures under ice load," *Journal of Constructional Steel Research*, vol. 74, pp. 26-36, 2012.
- [18] B. Chen, W. H. Guo, P. Y. Li, and W. P. Xie, "Dynamic responses and vibration control of the transmission tower-line system: a state-of-the-art review," *Science World Journal*, vol. 2014, Article ID 538457, 20 pages, 2014.
- [19] D. M. Lima, P. A. L. Yanez, and M. A. Pareira Ma, "Vibration control device for steel tubular towers of horizontal axis wind turbines," *Latin American Journal of Solids and Structures*, vol. 16, no. 6, pp. 1-21, 2019.
- [20] S. Roy and C. K. Kundu, "State of the art review of wind induced vibration and its control on transmission towers," *Structure*, vol. 29, pp. 254-264, 2021.
- [21] L. Suresh and K. M. Mini, "Effect of multiple tuned mass dampers for vibration control in high-rise buildings," *Practice Periodical on Structural Design and Construction*, vol. 24, no. 4, Article ID 04019031, 2019.
- [22] F. Rahimi, R. Aghayari, and B. Samali, "Application of tuned mass dampers for structural vibration control: a state-of-the-art review," *Civil Engineering Journal*, vol. 6, no. 8, pp. 1622-1651, 2020.
- [23] L. Tian and Y. Zeng, "Parametric study of tuned mass dampers for long span transmission tower line system under wind loads," *Shock and Vibration*, vol. 2016, Article ID 4965056, 11 pages, 2016.
- [24] X. Lei, W. P. Xie, M. Nie, H. W. Niu, J. L. Chen, and Y. X. Wang, "Development and application of a new type of TMD in transmission tower vibration reduction," *Journal of Vibration and Shock*, vol. 38, no. 13, pp. 73-80, 2019, in Chinese.
- [25] B. Zhao, D. Wu, and Z. Lu, "Shaking table test and numerical simulation of the vibration control performance of a tuned mass damper on a transmission tower," *Structure and Infrastructure Engineering*, vol. 17, no. 8, pp. 1110-1124, 2021.
- [26] B. Chen, J. Zheng, and W. Qu, "Control of wind induced response of transmission tower line system by using magnetorheological dampers," *International Journal of Structural Stability and Dynamics*, vol. 9, no. 4, pp. 661-865, 2009.
- [27] B. Chen, X. Xiao, P. Li, and W. Zhong, "Performance evaluation on transmission tower-line system with passive friction dampers subjected to wind excitations," *Shock And Vibration*, vol. 2015, Article ID 310458, 13 pages, 2015.
- [28] C. Zeng, D. X. Hao, and L. Q. Hou, "Research on calculation of equivalent damping ratio of electrical transmission tower-line system with viscoelastic dampers," *Advanced Materials Research*, vol. 1064, pp. 115-119, 2014.

Study of Impulsive Force of Debris Flow and Flexible Retaining Structure Based on SPH-DEM-FEM Coupling

Raghupatruni Bhima Rao, *Department of Civil Engineering, Aryan Institute of Engineering & Technology, Bhubaneswar, raghupatruni_r@outlook.com*

Sikendar Sharma, *Department of Civil Engineering, Raajdhani Engineering College, Bhubaneswar, sikendarsharma92@gmail.com*

Biswa Ranjan Pradhan, *Department of Civil Engineering, Capital Engineering College, Bhubaneswar, biswaranjanpradhan78@gmail.com*

Deepikarani Swain, *Department of Mechanical Engineering, NM Institute of Engineering & Technology, Bhubaneswar, depika_r19@yahoo.co.in*

ABSTRACT

The use of a flexible retaining structure to divide water and stone, reduce particle mass, and disperse kinetic energy has been shown to be an effective strategy for debris flow avoidance in hilly environments. A sophisticated dynamic interaction model of particle-fluid-structure has been created using the SPH-DEM-FEM coupling numerical analysis approach to investigate the impulsive force and dynamic response of flexible retaining structure hit by solid-liquid two-phase debris flow. The mechanism, impulse force, and dynamic reaction of a flexible retaining structure subjected to debris flow under various slopes were all explored in this work. The numerical results are compared to the peak impulsive force of the semi empirical debris flow calculation formula. Meanwhile, the coupling numerical simulation's efficacy is confirmed. The simulation results show that the combined SPH-DEM-FEM numerical analysis method can visualize the impact of a solid-liquid two-phase debris flow on a flexible retaining structure, reproducing the impact, retaining, water-stone separation, climbing, silting, and deposition processes of debris flow. The coupling numerical analysis method's dynamic time-history curve for the flexible retaining structure is consistent with current literature results. The empirical formula results match the debris flow evaluation results of a flexible retaining structure hit by solid-liquid two-phase debris flow by an order of magnitude. Furthermore, the outcomes are trustworthy. For the study of the impulsive force and dynamic response of the flexible retaining structure influenced by solid-liquid two-phase debris flow, as well as the engineering design of the flexible retaining structure, the obtained results have a specified reference value.

1. Introduction

Debris flow is a solid-liquid two-phase mixed fluid containing a large number of rubbles and sediments, showing the movement characteristics of viscous laminar flow or dilute turbulent flow. It is the result of the combined action of topography, meteorology, hydrology, soil, and vegetation in the basin [1]. Debris flows are characterized by rapid flow velocity, large flow velocity, sudden eruption, and amazing destructive power. It is a special fluid-solid coupling material formed by rainfall confluence. Limited by a certain slope groove, it pours down to the accumulation area at a significantly fast speed, which can cause great damage to a variety of buildings along the way [2].

Debris flow disasters are extensively distributed around the world, while China is a mountainous country and the mountainous area accounts for approximately 69% of the total land area. The Tianshan Mountains, Kunlun Mountains, Himalayas, Qinling Mountains, Hengduan Mountains, and Changbai Mountains in China are all high-risk areas of debris flow. The total area of debris flow distribution is 4.3 million km², of which 1.3 million km² is an intense active area [3]. In China, there have been many major debris flow disasters, among which, the most notable one is the August 8 Zhouqu debris flow disaster in Gansu Province, with the severe consequences of 1,481 deaths, 1,824 injuries, 284 missing persons, and nearly 20,000 people affected [3]. The data show that debris flow

composed of particles and fluids has great kinetic energy and impulsive force and can cause devastating damage to the structure [4].

Debris flow study is relatively complex, and previous studies are generally simplified into pure particle matter and fluid. For example, Ashwood and Hungr [5] used quartz sand and rubble for performing the physical simulation test to study the impact of debris flow. Ng [6] et al. studied the impact performance of dry sand and viscous fluid by the conducting centrifugal test. However, some scholars have studied the mixture of solid-liquid debris flow. Haas [7] et al. studied the solid-liquid mixture composed of rubble, sand, clay, and water. The results proved that the performance of solid-liquid mixture was significantly different from that of single-phase flow. The interaction between solid particles and fluid of debris flow would significantly change the movement characteristics and impulsive force of debris flow. It is challenging to describe and quantify the formation, movement, impact, and deposition process of solid-liquid two-phase debris flow due to solid-liquid interaction, which has always been the difficulty of study.

In addition to the formation, movement, impact, and deposition process of debris flow, the prevention and control measures of debris flow have also dominated a vital role in the protection of life and property [8–10]. As for the design of debris flow retaining structure, the impact of debris flow should be considered; otherwise, structural damage will be caused and the safety of life and property downstream will be seriously threatened [11–13]. The retaining structure can generally be divided into rigid retaining structure and flexible retaining structure [14], and the peak impulsive force of debris flow plays a key role in the design of retaining dam. At present, it is generally based on the fluid statics model, fluid dynamics model, or hybrid model [15]. In particular, the fluid dynamics model has been widely applied in engineering design due to the reliability of data. However, because of the different conditions, the value of empirical coefficient varies greatly among different scholars, seriously affecting the accurate prediction of the peak impulsive force of debris flow [16].

In recent years, the flexible retaining dam becomes increasingly popular because of its simple installation, high construction efficiency, good economy, and small impact on the environment [17]. Compared with the rigid retaining structure, the flexible retaining structure can generate large deformation under the impact, resulting in a better energy dissipation mechanism, thereby lowering the peak impulsive force [18]. However, the dynamic coupling among the particle-fluid flexible retaining structure is significantly complex, which depends on the hydrodynamic mechanism, the particle movement characteristics, and the deformation and mechanical characteristics of the flexible retaining structure, as well as the energy conversion and dissipation between them. It remains a highly challenging topic. At present, there is no reasonable theoretical basis for the design of flexible retaining structure. Therefore, a limited test and numerical simulation are carried out and the engineering is only designed and constructed by experience. Although the failure analysis of flexible retaining dam under debris flow impact is rarely discussed, this is the key issue of engineering design [19].

One of the main aspects of the study of the coupling effects of debris flow and flexible support structure is the numerical simulation method, which is mainly divided into continuous environment calculation method, discrete environment method, and mixed environment method [17, 20, 21]. The continuous environment calculation method relies on the continuous distribution of mass and deformation of the object under study. The equations describing the dynamic characteristics are established. These equations are discretized on the computational domain based on grids or particles and solved by combining the initial and boundary conditions [18, 22]. The main continuous medium calculation methods are the finite element method and the smooth particle kinematics method, or in other words, both debris flow and flexible retaining structures are simulated by the finite element method or the SPH method. This method is more mature and has been verified in theory and experiment. The discrete medium method in the analysis of debris flow and flexible retaining structure is mainly the discrete element method [19, 23]. Leonardi et al. [24] employed the DEM method to study the coupling effect of debris flow and flexible retaining structure and compared with the experimental results. The results showed that the DEM method could better reflect the interaction between debris flow and flexible retaining structure and was close to the experimental results, thus verifying the effectiveness of numerical analysis method.

In order to make full use of the advantages of different methods, the coupling numerical analysis method of debris flow and retaining structure has become a research hotspot in recent years. Leonardi et al. [25–27] used the LBM-DEM method to address the effect of the debris flow on the structure and adopted the coupling numerical analysis method to conduct a series of analysis and numerical verification, proving the robustness of the method in various cases. The debris flow impact of different flexible retaining structures was carried out, and the failure mode of the flexible retaining structure was explored. Li and Zhao [28, 29] adopted the coupled CFD-FEM method to simulate the debris flow, as well as the impact on rigid and flexible retaining dams. The model revealed that the actual simulation of the debris flow needs to consider the solid-liquid interaction. In addition, the effect of erosion on the impulsive force of debris flow was taken into account. The results showed that the debris flow impulsive force was significantly influenced by the slope and the solid-liquid ratio. The impact law and failure mode of flexible retaining dam are studied by employing the coupling numerical analysis method. Liu et al. [30, 31], respectively, used SPH-FEM and DEM-FEM to investigate the impact characteristics of debris flow, large stone, and retaining dam as well as the coupling effect of debris flow and flexible retaining structure. The results showed that the coupling numerical method could well reproduce the impact-climbing-silting process of debris flow and the impact issue of flexible retaining structure. Li et al. [32] used the SPH-DEM method to study the dynamic performance and impact force of debris flow on a rigid retaining structure. Although the coupling numerical analysis method provides the basis and

reference for the theory and method of this paper, there is no research and discussion on the mechanical properties and impulsive force of flexible retaining structure. The flow process of debris flow is shown in Figure 1 [3].

In summary, there is no reasonable theoretical basis for the design of flexible retaining structure. Instead, the design and construction of the project only depend on experience, and no corresponding specification for the prevention and control of debris flow by flexible retaining dams has been formulated in various countries. There are very few research studies on dynamic response analysis of flexible retaining structure impacted by debris flow. Currently, the research only concentrates on the retaining structure affected by large rock, debris flow fluid, or debris flow fluid along with large rock. Only few numerical analysis methods are used to analyze the coupling effect of debris flow and flexible retaining structure. The SPH-DEM-FEM numerical analysis method is applied to investigate the dynamic response of a retaining structure impacted by debris flow here, providing a certain reference for debris flow prevention engineering practice.

2. Numerical Calculation Theory

LS-DYNA code is adopted for SPH-DEM-FEM numerical simulation, in which SPH is used to simulate liquid debris flow, DEM is used to simulate solid particles, and FEM is used to simulate flexible retaining structure and debris flow channel. The SPH-DEM-FEM coupling analysis method is adopted to establish a complex dynamic interaction model of particle-fluid-structure, which can truly simulate the dynamic interaction between actual debris flow and flexible retaining structure. The realization principle and control equations of numerical simulation are introduced in this chapter.

2.1. DEM Control Equation. Debris flow particles in the solid phase are modelled by DEM. An elastic model is adopted for the contact between solid-phase debris flow particles [33–36].

The expression of force on particles is shown as follows:

$$\left. \begin{aligned} f_n &= -(k_n \lambda + c_n \gamma_{ij} \cdot n_n) n_n \\ f_t &= -(k_t \delta + c_t s_{ij} \cdot n_t) n_t \end{aligned} \right\} \quad (1)$$

Among which, λ and δ represent the overlapping distances of normal direction and tangential direction, respectively, and k_n and k_t denote normal stiffness and tangential stiffness, respectively.

The resulting external force and the resulting external moment on the particles are expressed as follows:

$$\left. \begin{aligned} F_i &= \sum_{j=1}^k (f_{nij} + f_{tij}) \\ T_i &= \sum_{j=1}^k r_i (f_{sij} \cdot n_t) \end{aligned} \right\} \quad (2)$$

Among which, f_s represents the friction between particles.



FIGURE 1: Dynamic process of debris flow [3].

An elastic material model is adopted for the interaction force between particles, and the constitutive model of the material is shown as follows:

$$\sigma_e = E_e \varepsilon_e. \quad (3)$$

Among which, E_e represents the particle elastic model and ε_e is the particle elastic strain.

2.2. SPH Control Equation. In this paper, SPH is used to simulate the flow of debris in the liquid phase. The basic concept of this method is to regard the fluid (or solid) as continuous one and describe it by interacting particle groups. Each particle point carries various physical parameters, including mass and velocity [37–40].

The approximate function of particles is shown in the following formula:

$$\Pi^h f(x) = \int W(x-y) dy, \quad (4)$$

where W is the kernel function.

Kernel function W can be obtained by function θ , and their relation is shown in the following formula:

$$W(x, h) = \frac{1}{h(x)^d} \theta(x), \quad (5)$$

where d is the spatial dimension and h is the smooth length that varies with time and space.

In this paper, the smooth kernel function is shown as follows:

$$\theta(u) = C \times \begin{cases} 1 - \frac{3}{2}u^2 + \frac{3}{4}u^3; & |u| \leq 1, \\ \frac{1}{4}(2-u)^3; & 1 \leq |u| \leq 2, \\ 0; & 2 < |u|, \end{cases} \quad (6)$$

where C is a generalized constant depending on the spatial dimension.

The SPH method bases on the integral formula of moving particles $((x_i(t)))$, $i \in \{1, 2, \dots, N\}$, among which $x_i(t)$ is the spatial position vector of particle i , which moves along the velocity field v .

At this time, the approximation function of particle can be expressed by the following formula:

$$\Pi^h f(x_i) = \sum_{j=1}^N w_j f(x_j) W(x_i - x_j, h), \quad (7)$$

where $w_j = (m_j/\rho_j)$, and the gravity of the particle w_j changes in proportion to the divergence of the fluid.

2.3. SPH-DEM-FEM Coupling Control Equation. The DEM-FEM coupling equation is used to describe the complex dynamic interaction between solid-phase particles and a flexible containment structure, which can be found in the following equation [18, 41–43]:

$$\left. \begin{aligned} m_i \ddot{u}_i &= m_i g + \sum_{k=1}^m (f_{n,ik} + f_{t,ik}) + \sum_{j=1}^l (f_{n,ij} + f_{t,ij}) \\ I_i \ddot{\theta}_i &= \sum_{k=1}^m T_{ik} + \sum_{j=1}^l T_{ij} \\ M \ddot{X} + C \dot{X} + K X &= f_a + f_b \end{aligned} \right\}, \quad (8)$$

where $f_{n,ij}$ and $f_{t,ij}$ represent the normal and the tangential contact force.

The DEM-FEM coupling equation is shown as follows:

$$M \ddot{U} + CU + K d = F + F_C. \quad (9)$$

The SPH-DEM coupling control equation is used to describe the complex dynamic interaction between the particles in the solid phase of the debris flow and the fluid in the liquid phase of the debris flow [18], as presented in the following equation:

$$\left. \begin{aligned} m_i^s \frac{du_i^s}{dt} &= F_i^c + F_i^{bs} + m_i^f f_i^{fs} \\ I_i^s \frac{d\omega_i^s}{dt} &= M_i^c + M_i^{fs} + M_i^{bs} \\ \frac{du_i^f}{dt} &= - \sum_{j=1}^N m_j \left(\frac{p_i}{\rho_i} + \frac{p_j}{\rho_j} + \Pi_{ij} + R_{ij} f_{ij}^4 \right) \nabla_i W_{ij} + f_i^{sf} + f_i^{bf} \end{aligned} \right\}, \quad (10)$$

where F_i^{bs} and F_i^{bs} are the force on each other and M_i^{fs} , M_i^{bs} , and M_i^c denote the torque.

3. Calculation Model

This paper selects Nanjiaogou as the prototype. The rugged topography in the ditch is sharp, the gullies can be found anywhere, and the slope of the main ditch formation area is $19^\circ \sim 47^\circ$, which belong to a vast debris flow ditch. The detailed geological information of Nanjiaogou can be found in [32].

In order to study the impulsive force and dynamic response of flexible retaining structure impacted by debris flow, a complex dynamic interaction model of particle-fluid-

structure is established in the present study. Considering that the debris flow impulse force and the dynamic response of the flexible retaining structure are mainly studied in this paper and the actual gully is basically in trapezoidal distribution, to facilitate the study, the debris flow gully is simplified into trapezoidal one, and retaining and governance measures are performed on the main gully formation area with the steep slope. Considering that the slope of the main ditch formation area is $19^\circ \sim 47^\circ$, the average slope of the main gully formation area is confirmed at 30° . In this paper, the impulsive force and dynamic response of flexible retaining structure are analyzed, when the slope of gully is 15° , 20° , 30° , 40° , and 50° .

3.1. Geometric Model. The geometric model of the debris flow is shown in Figure 2, and the geometric model of the flexible retaining structure is presented in Figure 3. The specific parameters of the geometric model are displayed in Table 1. The parameters such as debris flow channel and DEM particle density, elastic modulus, and Poisson's ratio are shown in the literature [32], and the specific mechanical parameters of the flexible retaining net and support cable are shown in the literature [24, 28, 29].

The research object of this paper is mainly the impact force and dynamic response of the flexible retaining structure. Then, according to the field survey, the channel is roughly trapezoidal distribution and the bottom and the side of the gully are then simplified into the trapezoidal section according to the on-site situation. Furthermore, in view of the fact that the slope of the main ditch formation area is $19^\circ \sim 47^\circ$, the average value 30° is selected; debris flow is composed of solid particles and fluids, which impacts the flexible retaining structure under the action of gravity, reproducing scenery of the impact, blocking by the flexible retaining structure, climbing along the flexible retaining structure, and water-rock separating in the process of impacting by debris flow. And this paper studies the impulsive force and dynamic response of flexible retaining structure impacted by solid-liquid two-phase debris flow.

The flexible retaining structure consists of flexible retaining nets and support cables. The four support cables are numbered as NO.1, NO.2, NO.3, and NO.4 from the bottom to top. The distance between the support cables is 0.5 m. The geometric model of the flexible retaining structure is shown in Figure 3. With a diameter of 20 mm, the flexible retaining net is formed by steel wires winding. The hexagonal side length of the retaining net is 0.1 m, which can smoothly discharge debris flow and effectively prevent debris flow particles from flowing out. The support cable is formed by a steel wire winding with a diameter of 20 mm, having an equivalent diameter of 0.1 m. The flexible retaining net and the supports cable are fixedly connected to bear the force in a better way. The specific mechanical parameters of the flexible retaining net and support cable are shown in the literature [24, 28, 29].

3.2. Constitutive Model of Materials. Because the channel rock mass in this paper relatively remains stable, the debris flow channel is simulated by rigid shell material. In this

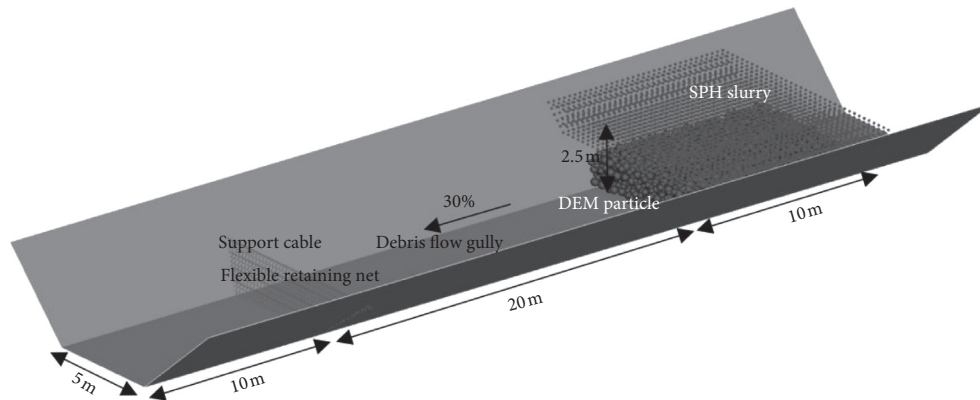


FIGURE 2: Geometric model of debris flow.

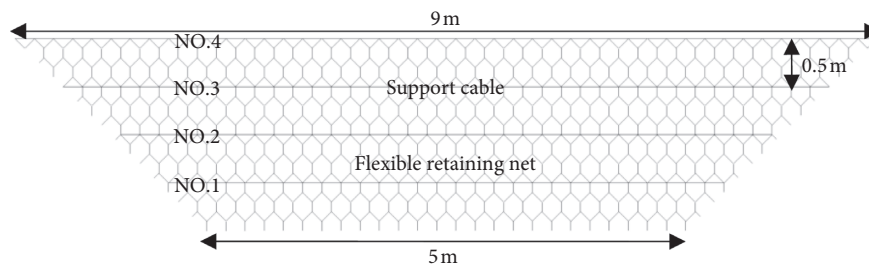


FIGURE 3: Geometric model of flexible retaining structure.

TABLE 1: Basic setting parameters of simulation.

	Density (kg/m^3)	Elastic modulus (GPa)	Poisson's ratio	Yield strength (MPa)	Ultimate strain	Constitutive model
Channel	3000	30.0	0.24	—	—	RIGID
DEM particles	2650	30.0	0.30	—	—	ELASTIC
Flexible retaining net	7850	177	0.30	1770	0.05	PLASTIC_KINEMATIC
Support cable	7850	177	0.30	1770	0.05	PLASTIC_KINEMATIC

paper, the RIGID material model is adopted, with 6056 shell elements in total. The parameters of debris flow channel adopt the numerical simulation parameters in the literature [19].

According to the field sampling test, the measured average density of solid particles in debris flow source is 2650 kg/m^3 . Based on the field survey and laboratory test, we measured that the particle size range of provenance is 0.2~0.4m. The size range of DEM particles set by us is consistent with the field test results. The solid-liquid ratio of debris flow exerts a great influence on the characteristics of debris flow. In this paper, the ratio of solid to liquid is 1:1. This paper uses discrete element particle simulation. The LS-DYNA ELASTIC model is adopted for the material constitutive, the LS-DYNA DE_BY_PART contact model is adopted for the interaction between the particles, and the LS-DYNA DE_SURFACE_COUPLING model is used for the contact between the particles and the channel. In addition, the LS-DYNA DE_TO_BEAM_COUPLING model is used for the contact between particles and flexible retaining

structure, with a total of 2236 particles in the above-mentioned models.

The object of this paper is the low-speed moving dilute debris flow, without considering the effect of viscous force for the time being. The density of water is 1000 kg/m^3 , and the friction force between fluids is 0.12. The value of friction coefficient will be described in detail in Section 3.3. The SPH model is used for analysis, and the constitutive model employs the NULL material model, with the viscosity coefficient of 0.001. The constitutive model of water is involved in this paper, while the constitutive model uses the EOS_MURNAGHAN model, and the constant of state equation GAMMA is 7.0, with K_0 of 150,000. To sum up, there are totally 4351 particles in the model. The SPH_DE_COUPLING contact model is adopted for the interaction between SPH particles and DEM particles, and the AUTOMATIC_NODES_TO_SURFACE model is adopted for the contact between SPH particles and channels. The parameters of fluids adopt the numerical simulation parameters in the literature [19].

The support cable of flexible retaining structure is modelled by cable element, with the density of 7850 kg/m^3 and yield strength of 1770 MPa . Because the flexible retaining structure bears the dynamic impact, the material constitutive model adopts the PLASTIC_KINEMATIC model, with the ultimate strain of 0.05 . The flexible retaining net is simulated by BEAM element, with the density of 7850 kg/m^3 and yield strength of 1380 MPa . Because the flexible retaining structure bears the dynamic impact, the constitutive model of the material adopts the PLASTIC_KINEMATIC model. The specific mechanical parameters of flexible retaining nets and support cables can be found in the literature [24, 28, 29].

3.3. Boundary Conditions. The channel and the flexible retaining structure are firmly connected with the ground. The bottom and both sides of the debris channel are completely fixed and capped. The flexible retaining net and the supporting cable are connected with the ground through the anchor cable. Therefore, the flexible retaining net and support cables are fully fixed in this paper.

The coefficient of friction between debris flow solids is typically $0.1\text{--}0.5$ [16–18] by analyzing and comparing the experimental and simulation results in a large amount of relevant literature. According to similar studies, the trial-and-error method is generally used to explore and compare the numerical simulation results with actual cases. When the peak velocity data of debris flow numerical simulation are close to the experimental or actual data, the parameters are regarded to be more accurate. After adopting the trial-and-error method and reviewing similar literature, it can be found that the simulated results are close to the actual results, when the coefficient of friction between the debris flow solids and the channel and the retaining wall is 0.3 and the coefficient of friction between the debris flow fluid and the channel and the flexible retaining structure is 0.12 .

We use the dynamic explicit method of LS-DYNA code for performing the analysis. The analysis step time is 10 s . The debris flow begins to slide with an initial velocity of 0 m/s^2 . The gravitational acceleration of both the debris flow fluid and the debris flow solid particles is 9.8 m/s^2 . Totally, the calculation gets 1974743 incremental steps. The CPU time is 22 h 3 min 43 s.

4. Establishment of Calculation Model

4.1. Impacting Process. The impact, retaining, water-rock separation, and deposition process of flexible retaining structure impacted by debris flow are shown in Figure 4. When $t = 0.9 \text{ s}$, the debris flow starts to move, and at this time, “dragon head, dragon body, and dragon tail” have basically taken shape. Debris flow fluid and solid particles yield complex dynamic coupling interaction. When $t = 2.3 \text{ s}$, the solid-liquid two-phase debris flow reaches the bottom of the flexible retaining structure. At this moment, the maximum velocity of debris flow reaches 10.52 m/s , and the particle-fluid-structure joint is forced to produce complex dynamic interaction and impact the flexible retaining

structure. Meanwhile, the “dragon head” of debris flow impacts the flexible retaining structure, climbing high and separating water-rock, and the solid particles remain at the bottom of the retaining structure under the action of retaining structure. At the same time, most of the fluid is discharged from the retaining structure. When $t = 3.5 \text{ s}$, the “dragon body” impacts the flexible retaining structure. Most of the debris flow solid particles are retained at the bottom, and the fluid is discharged. The debris flow will continue to impact the flexible retaining structure. At this time, because of the climbing effect, the bottom of the flexible retaining structure produces a dead load due to particle deposition, while the top part is still impacted by the dynamic impact of the debris flow. The SPH method can greatly deal with the splash and diffusion of fluid particles and participate in complex dynamic interaction with flexible retaining structure and debris flow particles. The numerical simulation well reflects the complex dynamic interaction of particle-fluid-structure. When $t = 5.2 \text{ s}$, the debris flow silts back and the particles finally deposit at the bottom of the retaining dam to produce a dead load. The fluid is slowly discharged.

4.2. Climbing and Silting Process. The climbing and silting process of the flexible retaining structure impacted by debris flow is illustrated in Figure 5. When $t = 2.5 \text{ s}$, debris flow particles reach the bottom of the flexible retaining structure and start to impact the debris flow retaining dam and climb high. At this time, the water-rock separation has already taken shape and the fluid is discharged through the retaining structure. The flexible retaining structure is deformed. Besides, the most deformed parts are the middle and bottom of the flexible retaining structure. When $t = 3.0 \text{ s}$, debris flow particles continue to climb high and some even silt back in certain part. At this time, it can be observed that particle-fluid-structure shapes complex dynamic interaction, and the current climbing height is 1.3 m . When $t = 3.5 \text{ s}$, the “dragon body” impacts the retaining dam, and the debris flow particles climb to the highest level, with obvious back silting and particle splashing. The climbing height is as high as 2.1 m . When $t = 5.2 \text{ s}$, the debris flow silts back, finally producing a dead load at the bottom of the retaining dam. At this moment, the height of silting is the height of the retaining structure.

4.3. Analysis of Displacement Change of Flexible Retaining Structure over Time. The displacement change over time in the middle position of four support cables (NO.1, NO.2, NO.3, and NO.4) of flexible retaining structure under different slopes is monitored in Figure 6. The results reveal that when the slope is 50 degrees and $t = 3 \text{ s}$, the displacement of the middle position of NO.4 support cable of flexible retaining structure reaches the maximum, and the maximum value is 0.265 m . Then, it decreases rapidly to 0.160 m after reaching the peak value. When the slope is 15 degrees, 20 degrees, 30 degrees, and 40 degrees, the peak displacement value of the middle position of the support cable of the flexible retaining structure is 0.0283 m , 0.071 m , 0.164 m , and 0.221 m , respectively. Subsequently, all decrease to dead

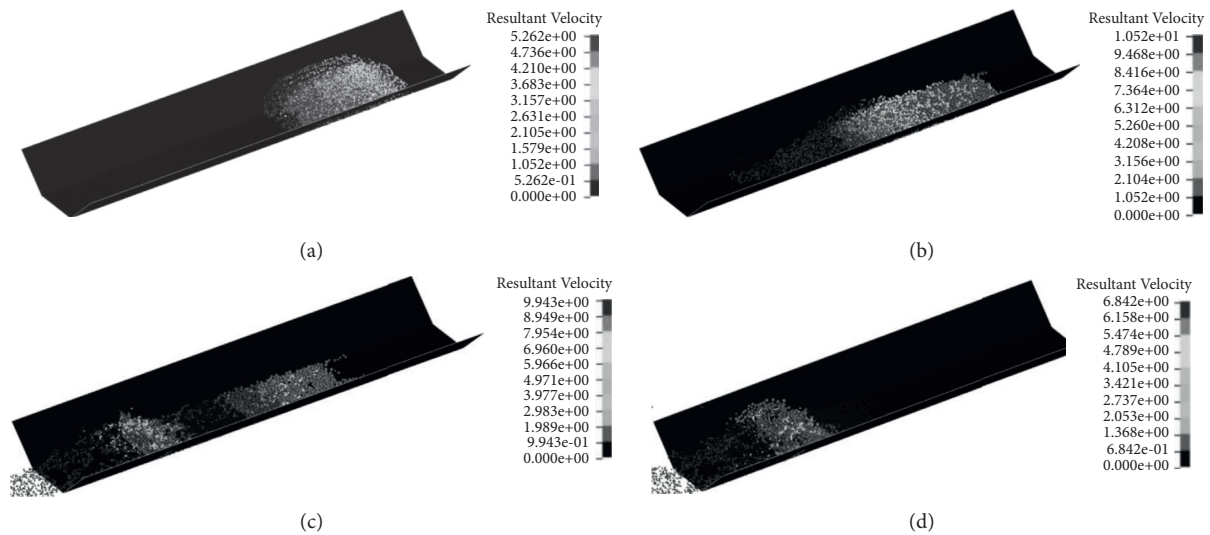


FIGURE 4: Process of flexible retaining structure impacted by debris flow. (a) $t = 0.9$ s. (b) $t = 2.3$ s. (c) $t = 3.5$ s. (d) $t = 5.2$ s.

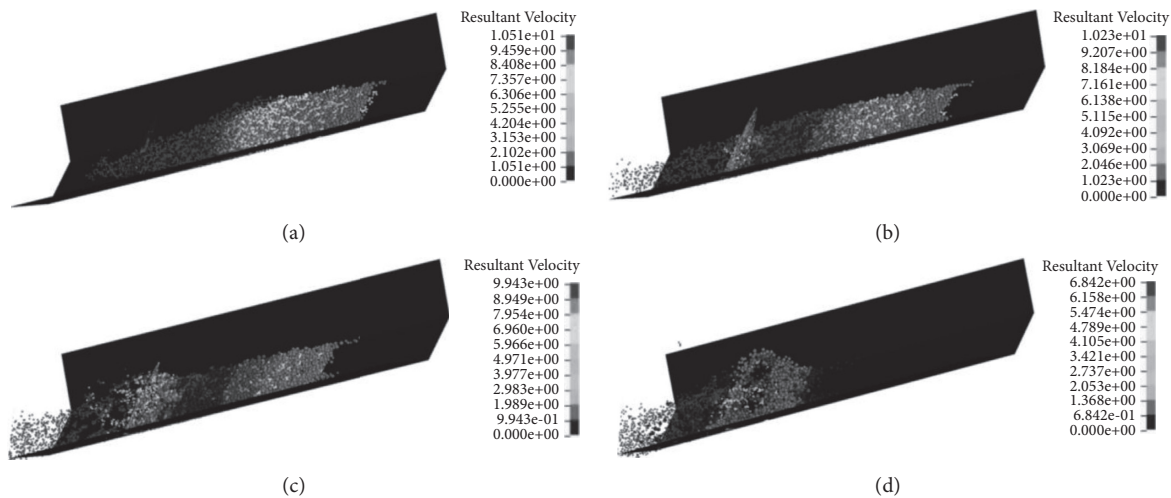


FIGURE 5: Climbing and silting process of debris flow. (a) $t = 2.5$ s. (b) $t = 3.0$ s. (c) $t = 3.5$ s. (d) $t = 5.2$ s.

displacement, which are 0.0146 m, 0.055 m, 0.122 m, and 0.170 m, respectively. When the slope is 15°, 20°, 30°, 40°, and 50°, the difference between the maximum peak displacement and static displacement of the flexible barrier structure is 0.0137 m, 0.016 m, 0.042 m, 0.051 m, and 0.105 m, respectively. Moreover, the simulation results are identical to the numerical simulation and test results performed by Leonardi et al. [24–27], showing that the above method is suitable for simulating the flexible retaining structure impacted by debris flow.

4.4. Analysis of Impulsive Force Change over Time. The impulsive force change of flexible retaining structures with different slopes (15°, 20°, 30°, 40°, and 50°) over time is displayed in Figure 7. It can be observed from the figure that when the slope is 50 degrees and $t = 2.9$ s, the impulsive force of the debris flow on the retaining dam reaches its peak value,

which is 6089 kN, and then decreases rapidly to 3832 kN. When the slope is 15°, 20°, 30°, and 40°, the peak values of impulsive force of the retaining dam are 987 kN, 1983 kN, 3690 kN, and 4625 kN, respectively, and subsequently all decrease to dead loads. With the increase of the slope, the start time of the debris flow impact force is 3.4 s, 3.2 s, 3 s, 2.5 s, and 2 s, respectively. In addition, the peak time of the debris flow impact force is 4.9 s, 4.7 s, 3.9 s, 3.2 s, and 2.9 s, respectively.

We compare the numerical calculation results according to the semiempirical formula of impulsive force peak value of the debris flow based on hydrodynamic theory proposed by Kwan [44]:

$$F_{\max} = \kappa \rho v^2 h_0 w \sin \beta, \quad (11)$$

where $\kappa = aFr^b$ is the dynamic pressure coefficient, ρ represents the density, v is the impulsive velocity, w is the width, and h_0 is the height of debris flow.

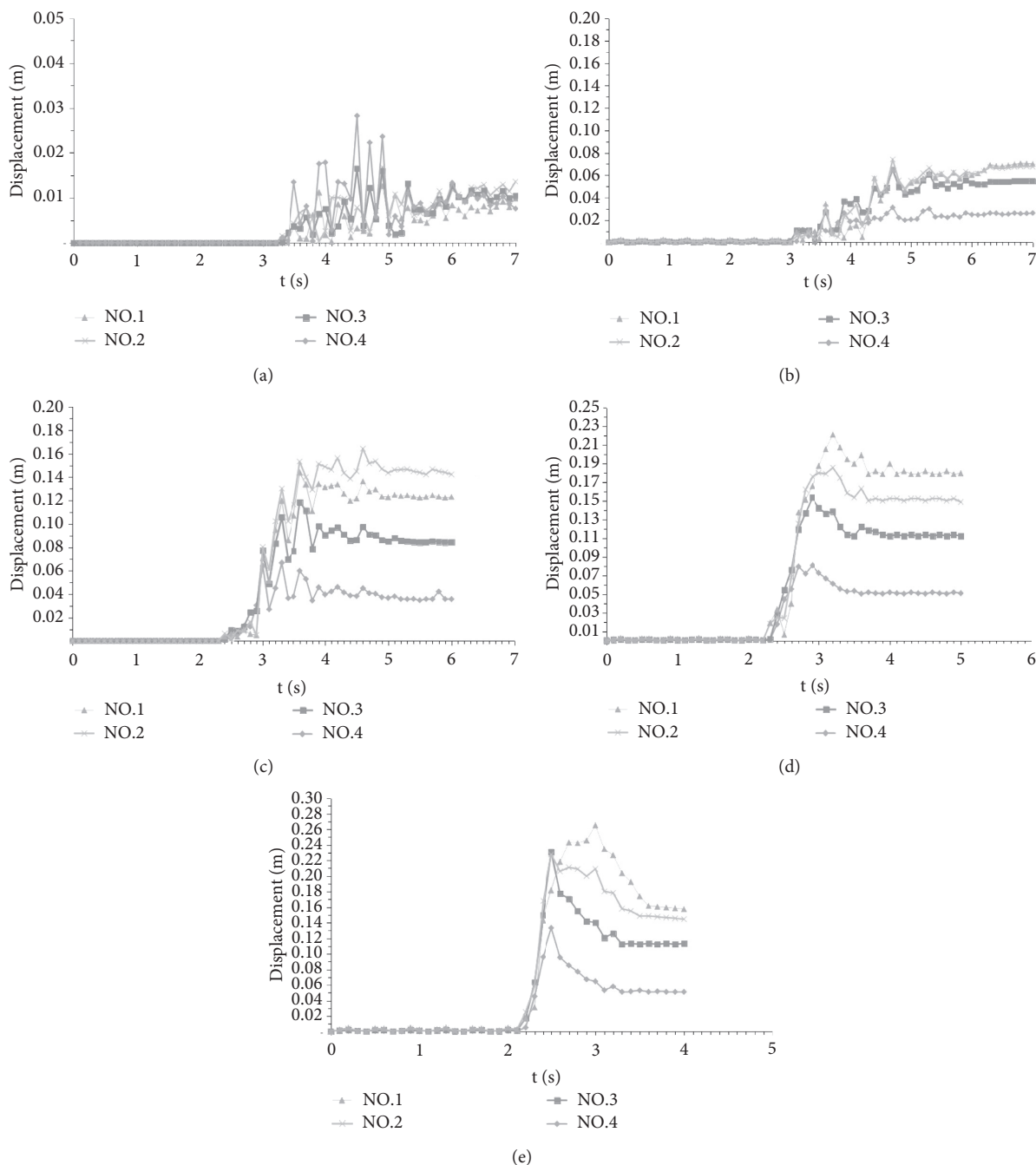


FIGURE 6: Analysis of the displacement change on the monitoring point of the flexible barrier structure over time. (a) 15 degrees. (b) 20 degrees. (c) 30 degrees. (d) 40 degrees. (e) 50 degrees.

The calculation results are obtained from the numerical calculation method in this paper, and the existing empirical formulas are shown in Table 2. The calculation error ranges from 12.1% to 27.4%. Comparing the numerical calculation method adopted in the present study with the empirical values, the impulsive force results of the two methods are relatively close. However, the empirical methods do not consider the water-rock separation and the complex dynamic interaction of particle-fluid-structure. Therefore, the numerical analysis method is more reasonable than the empirical methods.

4.5. Maximum Deformation of Flexible Retaining Structure.

The maximum deformation of flexible retaining structure with different slopes (15°, 20°, 30°, 40°, and 50°) can be found in Figure 8. The maximum deformation of flexible retaining structure is positively associated with the channel slope, and the maximum deformation position is located in the middle of flexible retaining structure, which is consistent with the observed results in practice. When the slope is 15°, 20°, 30°, 40°, and 50°, the maximum peak displacement values in the middle of the flexible retaining structure are 0.0283 m,

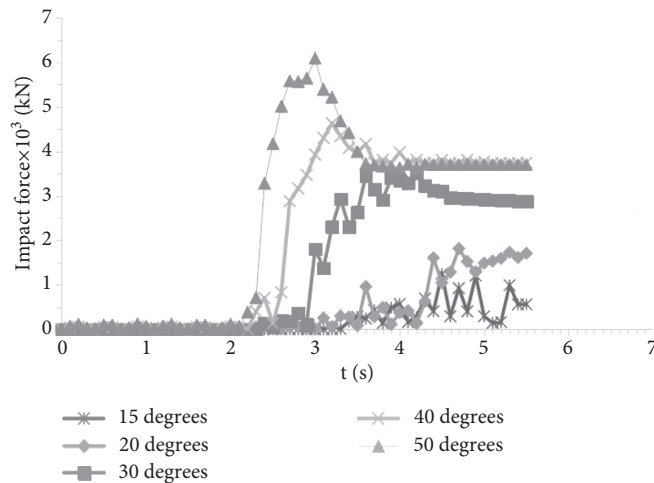


FIGURE 7: Analysis of impulsive force change of flexible retaining structure over time.

TABLE 2: Comparison of maximum impact force.

	15°	20°	30°	40°	50°
Kwan empirical value (kN)	1359	2532	4516	5409	6927
Method adopted in this paper (kN)	987	1983	3690	4625	6089
Error (%)	27.4	21.7	18.3	14.5	12.1

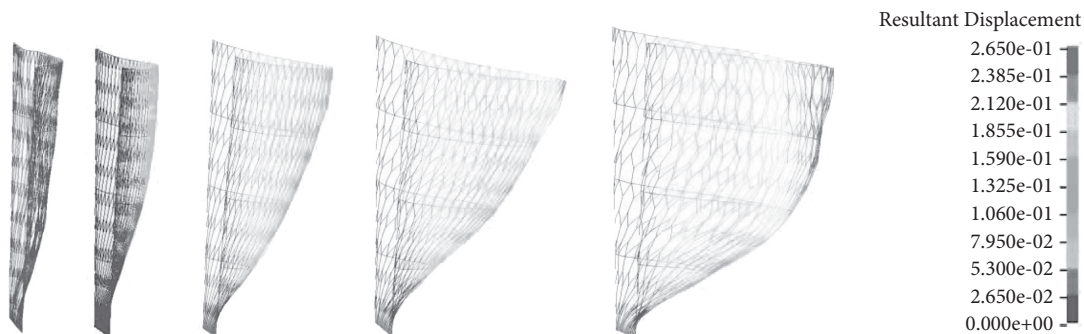


FIGURE 8: Maximum deformation of flexible retaining structure.

0.071 m, 0.164 m, 0.221 m, and 0.265 m, respectively. Clearly, it can be seen that the support cable can restrain the flexible retaining net from deformation. Because the flexible retaining net and the supporting cables are fixed to each other, the deformation of the two is consistent with each other. In addition, the deformation of the flexible retaining net between the supporting cables is bigger than the deformation of the supporting cable, showing a convex shape.

5. Discussion

According to the results, the SPH-DEM-FEM coupling numerical analysis method vividly simulates the complex dynamic interaction of particle-fluid-structure, reproducing the impact, retaining, water-stone separation, climbing, silting, and deposition process of debris flow. The SPH method can greatly handle the splashing and diffusion of fluid particles and participate in complex dynamic interaction with flexible retaining structure and debris flow

particles. The water-stone separation phenomenon can well reproduce the real debris flow blocking process, which is difficult to be reflected by other numerical analysis methods, which can also build up a good foundation for better evaluating the accuracy of debris flow impact assessment of flexible retaining structure. The displacement change of flexible retaining structure over time is analyzed here. Moreover, the simulation results and laws are consistent with the existing research results.

The analysis of impulsive force change over time is carried out. Although the analysis results are similar to the existing empirical formula, the empirical formula does not consider the water-rock separation and the complex dynamic interaction between particle-fluid-structure, and the error between the numerical simulation results and the empirical formula ranges from 12.1% to 27.4%. Therefore, the numerical analysis method is more reasonable than the empirical method. The peak impulsive force of debris flow is positively correlated with the slope of the channel, and the

larger the slope is, the greater the peak impulsive force of debris flow is. Then, the impulsive force of debris flow is decreased to a dead load, with enormous decrease in amplitude. When the slope is small, the peak impulsive forces of debris flow are close to a dead load. The impulsive force of debris flow will decrease slowly in the later stage, which is caused by the fluid removal from the flexible retaining structure due to the water-rock separation. It cannot be presented by employing the empirical formula method and traditional numerical analysis method. The results of the coupled numerical analysis method are more convincing than the empirical formula method.

The maximum deformation of flexible retaining structure is analyzed, and the deformation is positively associated with the slope of the channel. This is because when the slope of the channel is sharp, the gravitational potential energy of debris flow is relatively large, and once the debris flow takes shape, the kinetic energy and impulsive force produced by debris flow will be far greater than when the slope is small. Li et al. [32] explore the impulsive force and dynamic performance of rigid retaining structure impacted by debris flow by adopting the SPH-DEM-FEM method. By comparing impulsive force and dynamic performance of flexible retaining structure impacted by solid-liquid two-phase debris flow discussed in this paper, the dynamic performance and impact characteristics of flexible retaining structure and rigid retaining structure are quite different. Because of the water-rock separation and the remarkable ability to absorb energy, the impulsive force of the flexible retaining structure is much smaller than that of the rigid retaining structure. This also indicates that the traditional impulsive force formula of debris flow is not applicable to the flexible retaining structure, which is also the research significance of the present study. The results show that the mechanical performance of flexible retaining structure is more reasonable than that of rigid retaining structure.

Since the rigidity of the flexible retaining structure is much smaller than that of the rigid retaining structure, the dynamic characteristics between them are significantly different. The displacement change over time between the flexible retaining structure and rigid retaining structure is different by two orders of magnitude. The recovery ability after deformation of the flexible retaining structure is far less than that of the rigid retaining structure, requiring us to accordingly monitor the deformation of the flexible retaining structure in order to prevent dam collapse from bringing devastation to the downstream. The maximum deformation position is located in the middle of the flexible retaining structure, which gradually decreases to both sides. The support cable plays an obvious role in restraining the flexible retaining net and acts as a major carrier in bearing and transmitting force. The results of numerical simulation are compared with the deformation of real flexible retaining structure, showing good consistence.

In this article, the terrain conditions are simplified, considering neither the impact of the unevenness of the movement path on the motion characteristics of the debris flow and the dynamic characteristics of the flexible retaining structure nor the impact of the loose accumulation layer on

the movement path on the impulsive force of the debris flow and the dynamic characteristics of the flexible retaining structure. All the abovementioned problems are the research difficulties and can be further studied in future research.

6. Conclusion

- (1) Based on the coupling numerical method, this article considers the complex dynamic interaction of particle-fluid-structure, reproducing the whole process of flexible retaining structure impacted by debris flow, such as impact, retaining, water-rock separation, climbing, siltation, and deposition.
- (2) We compare the dynamic response analysis of flexible retaining structure impacted by debris flow under different slopes, monitoring the displacement change of the middle position of four support cables (NO.1, NO.2, NO.3, and NO.4) of flexible retaining structure over time. It can be found that the simulation results and laws are consistent with the existing research results.
- (3) We compare the change law of the impulsive force of debris flow under different slopes. However, the empirical formula does not consider the water-rock separation and the complex dynamic interaction of particle-fluid-structure, and thus, the error of empirical formula results and the numerical simulation results ranges from 12.1% to 27.4%. As a result, the numerical analysis method is more reasonable than the empirical method.
- (4) We analyze the maximum deformation of the flexible retaining structure, concluding that the deformation is positively associated with the slope of the channel. The maximum deformation is located in the middle of the flexible retaining structure, and the support cable can obviously restrain the flexible retaining net.

References

- [1] J. L. Miao, W. Z. Zhang, and J. Y. Zhou, "Numerical simulation of the accumulation state of viscous debris flow by smooth particle hydrodynamics method," *Journal of Natural Disasters*, vol. 22, no. 6, pp. 125–130, 2013.

- [2] M. Jakob, O. Hungr, and D. M. Jakob, "Debris-flow hazards and related phenomena," *Environmental and Engineering Geoscience*, vol. 8, no. 1, pp. 165–171, 2007.
- [3] C. A. Dowling and P. M. Santi, "Debris flows and their toll on human life: a global analysis of debris-flow fatalities from 1950 to 2011," *Natural Hazards*, vol. 71, no. 1, pp. 203–227, 2014.
- [4] C. Tang, N. Rengers, T. W. J. van Asch, Y. H. Yang, and G. F. Wang, "Triggering conditions and depositional characteristics of a disastrous debris flow event in Zhouqu city, Gansu province, northwestern China," *Natural Hazards and Earth System Sciences*, vol. 11, no. 11, pp. 2903–2912, 2011.
- [5] W. Ashwood and O. Hungr, "Estimating total resisting force in flexible barrier impacted by a granular avalanche using physical and numerical modeling," *Canadian Geotechnical Journal*, vol. 53, no. 10, pp. 1700–1717, 2016.
- [6] C. W. W. Ng, D. Song, C. E. Choi, L. H. D. Liu, and J. S. H. Kwan, "Impact mechanisms of granular and viscous flows on rigid and flexible barriers," *Canadian Geotechnical Journal*, vol. 54, no. 2, pp. 188–206, 2016.
- [7] T. Haas, L. Braat, J. R. Leuven, I. R. Lokhorst, and M. G. Kleinhans, "Effects of debris flow composition on runout, depositional mechanisms, and deposit morphology in laboratory experiments," *Journal of Geophysical Research: Earth Surface*, vol. 120, no. 9, pp. 19493–1972, 2015.
- [8] X. B. Zhou, *Debris Flow's Harm to Bridge Engineering and its Prevention*, Tongji University, Shanghai, China, 2006.
- [9] Z. Tao, M. Li, C. Zhu, M. He, X. Zheng, and S. Yu, "Analysis of the critical safety thickness for pretreatment of mined-out areas underlying the final slopes of open-pit mines and the effects of treatment," *Shock and Vibration*, vol. 2018, no. 2, pp. 1–8, 2018.
- [10] X. J. Yang, J. M. Wang, C. Zhu, M. C. He, and Y. Gao, "Effect of wetting and drying cycles on microstructure of rock based on SEM," *Environmental Earth Sciences*, vol. 78, no. 6, pp. 1866–1880, 2019.
- [11] Z. Liang, C. Wang, D. Ma, and K. U. J. Khan, "Exploring the potential relationship between the occurrence of debris flow and landslides," *Natural Hazards and Earth System Sciences*, vol. 21, no. 4, pp. 1247–1262, 2021.
- [12] L. Ban, C. Zhu, C. Qi, and Z. Tao, "New roughness parameters for 3D roughness of rock joints," *Bulletin of Engineering Geology and the Environment*, vol. 78, no. 6, pp. 4505–4517, 2019.
- [13] C. Zhu, K. Zhang, H. Cai et al., "Combined application of optical fibers and CRLD bolts to monitor deformation of a pit-in-pit foundation," *Advances in Civil Engineering*, vol. 2019, no. 1, 16 pages, Article ID 2572034, 2019.
- [14] A. Leonardi, F. K. Wittel, M. Mendoza, and J. Herrmann, "Multiphase debris flow simulations with the discrete element method coupled with a lattice-Boltzmann fluid," in *Proceedings of the III International Conference on Particle-based Methods Fundamentals and Applications*, pp. 276–287, Stuttgart (Germany), 2013.
- [15] A. Armanini, "On the dynamic of debris flows," *Recent Development on Debris Flows*, pp. 208–226, Springer, Heidelberg, Germany, 1997.
- [16] C. Lichtenhan, *Die berechnung von sperren in beton und eisenbeton, kolloquium on torrent dams odc 384.3*, pp. 91–127, Mitteilungen der Forstlichen Bundes-Versuchsanstalt, Wien, 1973.
- [17] A. Albaba, S. Lambert, F. Kneib, B. Chareyre, and F. Nicot, "DEM modeling of a flexible barrier impacted by a dry granular flow," *Rock Mechanics and Rock Engineering*, vol. 50, no. 11, pp. 3029–3048, 2017.
- [18] W. Anthony, G. Laurence, and V. Guillaume, "Grains3D, a flexible DEM approach for particles of arbitrary convex shape part I: numerical model and validations," *Powder Technology*, vol. 224, pp. 374–389, 2012.
- [19] C. Scheidl, M. Chiari, R. Kaitna et al., "Analysing debris-flow impact models, based on a small scale modelling approach," *Surveys in Geophysics*, vol. 34, no. 1, pp. 121–140, 2013.
- [20] Z. Tao, H. Zhang, C. Zhu, Z. Hao, X. Zhang, and X. Hu, "Design and operation of App-based intelligent landslide monitoring system: the case of Three Gorges Reservoir Region," *Geomatics, Natural Hazards and Risk*, vol. 10, no. 1, pp. 1209–1226, 2019.
- [21] Z. G. Tao, C. Zhu, M. C. He, and K. M. Liu, "Research on the safe mining depth of anti-dip bedding slope in Changshanhao Mine," *Geomechanics and Geophysics for Geo-Energy and Geo-Resources*, vol. 36, no. 6, pp. 1–20, 2020.
- [22] Z. Liang, C.-M. Wang, Z.-M. Zhang, and K.-U.-J. Khan, "A comparison of statistical and machine learning methods for debris flow susceptibility mapping," *Stochastic Environmental Research and Risk Assessment*, vol. 34, no. 11, pp. 1887–1907, 2020.
- [23] Z. Tao, Q. Geng, C. Zhu et al., "The mechanical mechanisms of large-scale toppling failure for counter-inclined rock slopes," *Journal of Geophysics and Engineering*, vol. 16, no. 3, pp. 541–558, 2019.
- [24] A. Leonardi, F. K. Wittel, M. Mendoza, R. Vetter, and H. J. Herrmann, "Particle-fluid-structure interaction for debris flow impact on flexible barriers," *Computer-Aided Civil and Infrastructure Engineering*, vol. 31, no. 5, pp. 323–333, 2016.
- [25] A. Leonardi, F. K. Wittel, M. Mendoza, and J. Hans, "Multiphase debris flow simulations with the discrete element method coupled with a lattice-Boltzmann fluid," in *Proceedings of the III International Conference on Particle-based Methods Fundamentals and Applications*, pp. 276–287, Stuttgart (Germany), 2013.
- [26] A. Leonardi, F. K. Wittel, M. Mendoza, and H. J. Herrmann, "Lattice-Boltzmann method for geophysical plastic flows," *Recent Advances In Modeling Landslides And Debris Flows*, pp. 131–140, Springer, Cham, Switzerland, 2015.
- [27] A. Leonardi, F. K. Wittel, M. Mendoza, and H. J. Herrmann, "Coupled DEM-LBM method for the free-surface simulation of heterogeneous suspensions," *Computational Particle Mechanics*, vol. 1, no. 1, pp. 3–13, 2014.
- [28] X. Li and J. Zhao, "A unified CFD-DEM approach for modeling of debris flow impacts on flexible barriers," *International Journal for Numerical and Analytical Methods in Geomechanics*, vol. 42, no. 14, pp. 1643–1670, 2018.
- [29] X. Li and J. Zhao, "Dam-break of mixtures consisting of non-Newtonian liquids and granular particles," *Powder Technology*, vol. 338, pp. 493–505, 2018.
- [30] C. Liu, Z. Yu, and S. Zhao, "Quantifying the impact of a debris avalanche against a flexible barrier by coupled DEM-FEM analyses," *Landslides*, vol. 17, no. 1, pp. 33–47, 2020.
- [31] C. Liu, Z. X. Yu, and L. R. Luo, "Dynamic behavior of a concrete dam impacted by debris flows with rock," *Journal of Vibration and Shock*, vol. 38, no. 14, pp. 161–168, 2019.
- [32] B. Li, C. Wang, Y. Li et al., "Dynamic response analysis of retaining dam under the impact of solid-liquid two-phase debris flow based on the coupled SPH-DEM-FEM method," *Geofluids*, vol. 2020, Article ID 6635378, 12 pages, 2020.
- [33] H.-k. Chen, H.-m. Tang, and Y.-i. Chen, "Research on method to calculate velocities of solid phase and liquid phase in debris

Personality Traits on the Evacuation Choice Behavior Pattern in Urban Road Network During Natural Disaster

Nilgrib Mohanty, *Department of Civil Engineering, Aryan Institute of Engineering & Technology, Bhubaneswar, nilgribmohanty25@outlook.com*

Saleema Panda, *Department of Civil Engineering, NM Institute of Engineering & Technology, Bhubaneswar, saleemapanda25@gmail.com*

Barsa Priyadarshini Sahoo, *Department of Civil Engineering, Raajdhani Engineering College, Bhubaneswar, barsap_sahoo@gmail.com*

Bipash Mohanty, *Department of Civil Engineering, Capital Engineering College, Bhubaneswar, bipashmohanty784@gmail.com*

ABSTRACT

Emergency traffic management necessitates a study of evacuation behavior in the event of a disaster. Because decision-making is not solely based on observable variables, this study attempts to examine the evacuation choice behavior pattern in the aftermath of an earthquake disaster by taking into account both physical and behavioral aspects. Confirmatory factor analysis (CFA) of the short form of the NEO-Five-Factor Inventory measures personality variables as behavioral latent factors (NEO-FFI). In Qazvin, Iran, a revealed preference survey with over 700 samples was conducted based on real-life earthquake experience, and the stated preference survey was undertaken for six selected scenarios with varying earthquake severities and times. Three types of discrete choice models (traditional binary logic model (TBLM), hybrid binary logic model (HBLM), and random parameters/mixed binary logic model (MBLM)) are used to study evacuation behavior. To begin, TBLM is expected to investigate the impact of observable variables on people's responses to seismic disasters. The model's correct prediction percentage increased after adding personality traits to the modeling structure and constructing HBLM. MBLM also takes into account heterogeneous population mixtures in terms of wealth, family size, and five personality traits in this study. The MBLM records the respondent's varied responses. The Log Likelihood function and pseudo square (2) of the model were improved by using these variables as random factors.

1. Introduction

An earthquake can be a catastrophic incident that kills thousands of people due to the lack of preparedness for confronting to it. Iran is always in danger of earthquake disasters due to its seismic belt. Iran's earthquake-related mortality rate is about 6% of the world compared to its population, which is only 1% of the world [1]. In countries such as Iran, the experiences of natural hazards indicate that management before an earthquake is very important. The importance of evacuation studies in the aftermath of a disaster is recognized by researchers of natural hazards [2, 3]. The prediction of the evacuation choice in the aftermath of an earthquake is challenging due to the uncertainties on the level of damage and decisions by individuals. Decisions are

influenced by the behavior of households and should be formulated probabilistically [4]. Modeling the evacuation choice behavior is challenging and the complexity of behavioral factors identification adds dimensionality to the problem of evacuation planning. Ignoring this component in evacuation planning may lead to inaccurate estimation of the demand for evacuation [2]. After the earthquake, abnormal traffic demand for unspecified purposes will lead to major traffic problems throughout the transportation network [5]. Post-earthquake travel demand could be substantially altered because of travellers' reaction to earthquake risk perception [6]. Human behavior is difficult to predict at all times and even more during emergencies, which are stressful and chaotic events. In this regard, it is necessary to study the behavior of people in the transport network in the event of an

earthquake disaster in order to predict the expected situation. The question of how people act during an earthquake is complex and the answers are inconclusive [7]. Currently, there is no unified recommendation regarding appropriate behavior when an earthquake occurred [8]. It has been noted that an individual's affective reaction to an environmental change can impact their behavioral intention. In order to predict the post-earthquake transport network situations, it is first necessary to examine how people behave in earthquake-prone situations. Therefore, it is important to understand what behavioral factors can influence people's decision to evacuate after an earthquake. Several researches have studied people's response to natural hazards [9–11] but few of them considered the effect of personality traits on responses to potential disasters. The main objective of this research is to study the effect of personality traits on evacuation choice in response to an earthquake disaster in different severities and times of earthquake. The required information in this study was collected through a revealed preference survey about earthquake that occurred on December 20, 2017 and a stated preference survey designed for earthquake scenarios at different times and severities. As the effect of personality traits on people's response to an earthquake is not considered in previous studies, in this research effects of personality traits as latent variables on evacuation behavior have been investigated. For this reason, first TBLM with observed variables is estimated. Then, to identify the effect of personality traits on evacuation choice behavior in response to earthquake disaster, HBLM with observed and latent variables are estimated. Finally, as income, family size, and five factors of personality traits are random variables and these random characteristics become more obvious during an earthquake because of an unexpected situation, the MBLM is estimated to capture the heterogeneous responses of respondents. The information obtained from this study can be used in post-crisis planning.

2. Literature Review

Many researchers surveyed the factors affecting decision-making of individuals on the occurrence of disasters and provided different behavioral models in this regard. In this section, in order to identify the factors that influence the action choice in response to disasters, a comprehensive review of previous studies is done.

Whitehead et al. investigated evacuation behavior in the occurrence of hurricanes. They indicate that socioeconomic characteristics affect how people respond to disaster by estimating logit model [9]. Horikiri and Odani investigated the behavior of the individuals after an earthquake. In their research, the number of family members was identified as influencing factors in evacuation behavior [10]. In the study of Bateman and Edwards, results show that women are more likely to evacuate than men because they feel more at risk or feel more responsible to protect children [11]. In a research by Walton and Lamb, travel behavior after the earthquake was studied using designated stated preference (SP) scenarios. The results of this research indicate that factors such as trip destination, estimated distance, and trip mode are factors affecting

trip choice behavior [12]. Solís et al. determined the individuals' choice behavior in the event of a Hurricane using probit modeling [13]. Eiser et al. proposed a general framework to assess the response to natural disasters. In their opinion, the perceived risk of disasters that affects the response of an individual depends on factors such as following previous experiences, values, individual feelings, cultural beliefs, and social variables [14]. Yun and Hamada investigated evacuation behavior during the 2011 Tohoku-Oki Earthquake. Results indicate evacuation starting time, age, and occupation had the greatest influence on evacuation [15]. In the study by Yang et al. the factors affecting evacuation behavior was investigated. In this research, structural equation models were used to estimate the choice behavior of individuals. It was found that age and education levels affect the evacuation decision [16]. Shapira et al. investigated the anticipated behavior patterns of residents in a high seismic risk area in Israel in the face of an earthquake scenario. Level of earthquake preparedness and dwelling type are significant predictors of behavioral strategy choice [7]. In the study of Sugiura et al., psychological processes and personality factors for an appropriate tsunami evacuation are investigated by logistic regression analyses. In this study, NEO-FFI inventory is used to analyse the effects of relevant personality traits on voluntary tsunami evacuation behavior. Results indicate that extraversion and openness factors had significant positive contributions, while neuroticism had a negative contribution to voluntary tsunami evacuation [17]. Mohajeri and Mirbaha studied decision-making in response to earthquake disaster including evacuation and destination choice behavior to analyse the pattern of choice behavior in transportation network in emergency situations. The results of their study indicate that religious belief decreases the likelihood of evacuation, while following previous experiences, trusting acquired trainings, and following decisions made by others increase the likelihood of evacuation [18]. Table 1 presents the summary of selected literature on choice behavior in disasters.

After reviewing previous researches, it can be concluded that the complexity of the individual's behavioral response to the disaster originates from the complexity of factors affecting hazard cognitions and motivates protective behavior. As behavioral choice is crucial in the study of responses to potential disasters, investigating the results of researches on factors affecting response to disaster indicates that the role of behavioral characteristics including personality traits in response to unpredictable disasters such as earthquake is neglected in previous studies. Therefore, in this study, the role of personality traits is investigated in response to earthquake disaster by HBLM. Finally, as the literature review shows that the effect of taste variation in evacuation choice with a focus on personality traits as latent variables is not taken into account in previous studies, this research identified the taste variation of latent variables by proposing a random coefficient model.

3. Methodology

Individuals' decision-making and response to disaster are considered in four stages [19] (as shown in Figure 1), including (a) the evacuation choice in response to earthquake

TABLE 1: Summary of selected literature on choice behavior in disasters.

Study (year)	Data collection method	Method of analysis	The most important factor affecting choice behavior in disasters
Whitehead (2000)	RP	Logit model	Socioeconomic characteristics including income, education, gender
Horikiri and Odani (2000)	RP	Descriptive analysis	The extent of house destruction, the distance to the earthquake location, number of family members
Bateman and Edwards (2002)	RP	Logit model	Gender, confronting the risk, perception of danger
Walton and Lamb (2009)	SP	Descriptive analysis	Trip destination, estimated distance, trip mode, and motivation
Solis et al. (2010)	RP	Probit model	Having children, having experience of hurricane, home ownership
Richard Eiser et al. (2012)	-	Review study	Following previous experiences, values, individual feelings, cultural beliefs, and social variables
Yi-Yun et al. (2015)	RP	Logit model	Evacuation starting time, evacuation location conditions, age, occupation
Yang et al. (2016)	RP	Structural equation model	Age, education levels, distance to the shore
Shapira et al. (2018)	SP	Multivariate logistic regression	Socioeconomic status, levels of earthquake preparedness, and dwelling type
Sugiura et al. (2019)	RP	Logistic regression analyses	Psychological processes and personality factors
Mohajeri and Mirbaha (2021)	SP	Binary logit Model, Multinomial Logit Model	Religious belief, following previous experiences, trust in acquired trainings, and following decisions made by others

RP refers to Revealed Preference method, SP refers to Stated Preference method.

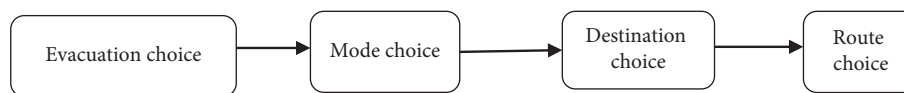


FIGURE 1: Decision-making stages in responding to earthquake disasters [19].

disaster, (b) mode choice (in case of evacuation), (c) destination choice, and (d) route choice. In this study, the issue to be analysed is decision-making in stage one: The evacuation choice in response to earthquake disaster.

In order to analyse and predict the condition of urban road network after earthquake, it is first necessary to examine how individuals behave during an earthquake disaster. For this purpose, the revealed preference survey was used for the earthquake that occurred on December 20, 2017. The earthquake occurred on December 20, 2017, with severity of 5.2 Richter's magnitude scale at 23:27' of Tehran. The focal of this earthquake is reported to be in Malard and its depth was 15 km. This earthquake was also felt in the Qazvin province. In addition, stated preference survey was used for the designated scenarios for the earthquake occurrence in the desired time and severity. Factors affecting the choice behavior under 6 earthquake scenarios (including earthquakes with minor, moderate, and severe severity, and in two time periods of day and night) are studied. In this study, the required data are collected using the designated questionnaire. The data consist of two parts: (1) Observed data including socioeconomic variables and daily trip characteristics, (2) 60-item NEO Five-Factor Inventory (NEO-FFI) data. First, the TBLM using observed variables is estimated and then using the data collected from NEO-FFI, the CFA is estimated in order to find the factor loading coefficients of the latent variables indicators. Then, in order to identify the effect of latent variables (personality traits) on

evacuation choice behavior in response to earthquake disaster, HBLM using observed variables and personality traits are estimated. Finally, to capture the taste variation of individuals, MBLM is estimated and the results of the fit model indices of these models are compared to identify better models. The research structure is presented in Figure 2.

3.1. Case Study. Qazvin is located in the west of Iran with a population of 400,000 and area around and 64.13 km². This city is important due to the presence of powerful seismic faults and active seismic history and the occurrence of earthquakes in the recent years [1]. Figure 3 shows the road network of Qazvin city and the grey area on the map is the worn-out texture of the city.

The data necessary for the seismic hazard analysis were obtained from surveying the type, location, and characteristics of seismic sources, especially faults [21]. Figure 4 indicates the area surveyed for assessing the seismicity comprised a circle with a radius of 150 Kilometers from the city.

In the research of Comijany et al., deterministic Seismic Hazard Analysis (DSHA) is performed to find the worst possible scenario among all the possible seismic sources related to the studied area. The Maximum Credible Design Level (MCL) Contour Map of Qazvin is shown in Figure 5. This level is defined as the strongest ground motion that can reasonably be expected at any structures from a nearby

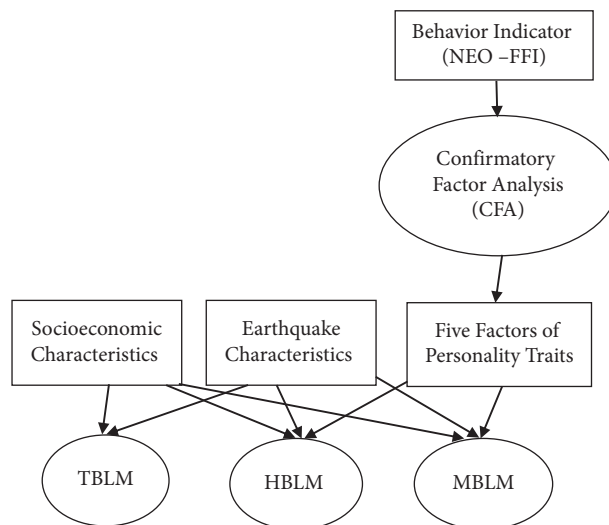


FIGURE 2: Proposed conceptual framework for evacuation choice modeling.

seismic source or on the basis of the seismic history and tectonics of the region [21]. Based on the population density map of Qazvin and data gathered through population census and Qazvin Comprehensive Plan (Figure 6), as the north section of Qazvin city with stronger ground motion has low density of population, devastating impact of earthquakes in all areas of the city is assumed to be the same.

3.2. Data Collection and Questionnaire Designation. A questionnaire is designed to study the factors affecting the choice behavior of the Qazvin city residents in response to earthquake disaster. The designated questionnaire consists of 4 sections:

In Section 1, the socioeconomic characteristics of individuals are surveyed.

In Section 2, the details of individuals' daily trips are surveyed.

In Section 3, the RP data are used as one of the scenarios of the questionnaire. In this research, RP data are used to increase the validity of the collected data, so we needed individuals that have experience about RP scenario. The RP and SP scenarios are presented in one questionnaire and asked simultaneously from the same people. As the majority of Qazvin residents have experience of the earthquake on December 20, 2017, sampling was performed randomly from residents in different regions of Qazvin city and if the person did not experience the earthquake at December 20, 2017 exceptionally, this person was omitted from data base. As having previous experience of earthquake can affect decision-making in response to earthquake disaster, both RP and SP data focused on persons having experience of earthquake on December 20, 2017. In this condition, all respondents are in the same situation for answering the questionnaire.

In Section 4, the designated scenarios are presented. In order to simplify the presentation of scenarios and according to the earthquake background in Qazvin city [21], three categories of minor, moderate, and severe earthquake severities are considered in designing the scenarios. Each individual stated

his/her evacuation choice in response to each severity of the earthquake and each time of earthquake occurrence. Table 2 shows the designated scenarios in the questionnaires in terms of time and the severity of the earthquake.

In Section 5, in order to investigate the psychological factors, personality traits of individuals are considered as qualitative and latent variables. These variables are measured with confirmatory factor analysis. To this end, the abbreviated form of the 60-item NEO-FFI personality questionnaire has been used. The NEO-FFI is a personality inventory that examines a person's Big Five personality traits (neuroticism, extraversion, openness to experience, agreeableness, and conscientiousness). The review of the literature focuses on behavioral factors that affect risk perception and evacuation decisions indicates that in the event of natural hazards, NEO-FFI inventory is a reliable tool for representing the psychological factors [17]. It is used to measure personality traits on a 5-point Likert-type scale where 1 means strongly disagree and 5 means strongly agree. Respondents answer 60 statements (12 items per domain). The higher the score on a particular scale, the stronger the intensification of the feature. Neo-FFI questionnaire has good internal consistency, with Cronbach's alpha ranging from 0.68 to 0.86 for five different personality traits which have been observed in previous studies. And, after decades of use, this personality questionnaire has been identified as having validity, reliability, and usability across different cultures [22]. The general structure of the indicators for estimating any latent psychology variable is given in Table 3.

Since it is not possible to investigate the whole society because of time and budget constraints, statistical sample should be analysed. Inadequate numbers of statistical samples cause unreliable results. The Cochran formula is one of the most common methods for calculating sample size [23]. For 381598 statistical population of the Qazvin, with 95% level of confidence, the minimum required sample size according to Cochran formula is 384. In order to increase the validity of the modeling, more than 700 questionnaires were prepared.



FIGURE 3: The road network of Qazvin [20].

For ensuring accurate and appropriate results of data collection, the interviewers were trained and evaluated for correct and uniform data gathering. The validity and reliability of questionnaire is checked by designing pilot questionnaire and conducting a pilot survey (60 people) in order to have a preliminary feedback and make the possible corrections for the main survey. The pilot survey is done by data collection from different regions of Qazvin city and the validity of questionnaire is evaluated by indicators such as α -Cronbach and correlation of collected data between pilot questionnaire and main questionnaire. The results of pilot survey indicate that the designated questionnaire has validity and reliability. α -Cronbach in each structure in the questionnaire is calculated separately and the value of more than

0.7 for this parameter presents acceptable internal consistency of the questionnaire. The abridged form of the questionnaire is presented in Table 4.

The main sampling was performed randomly among residents in different regions of Qazvin city. The respondents were chosen from employees, university students, clients of health centres, customers of gas stations, and businesses in different geographical areas of Qazvin. The required data for this research are provided through 546 questionnaires that were collected and completely answered by inhabitants of Qazvin based on their revealed experience and stated preference for six designated scenarios.

As earthquake is an unpredictable natural disaster, the decision-making in response to it is not only dependent on

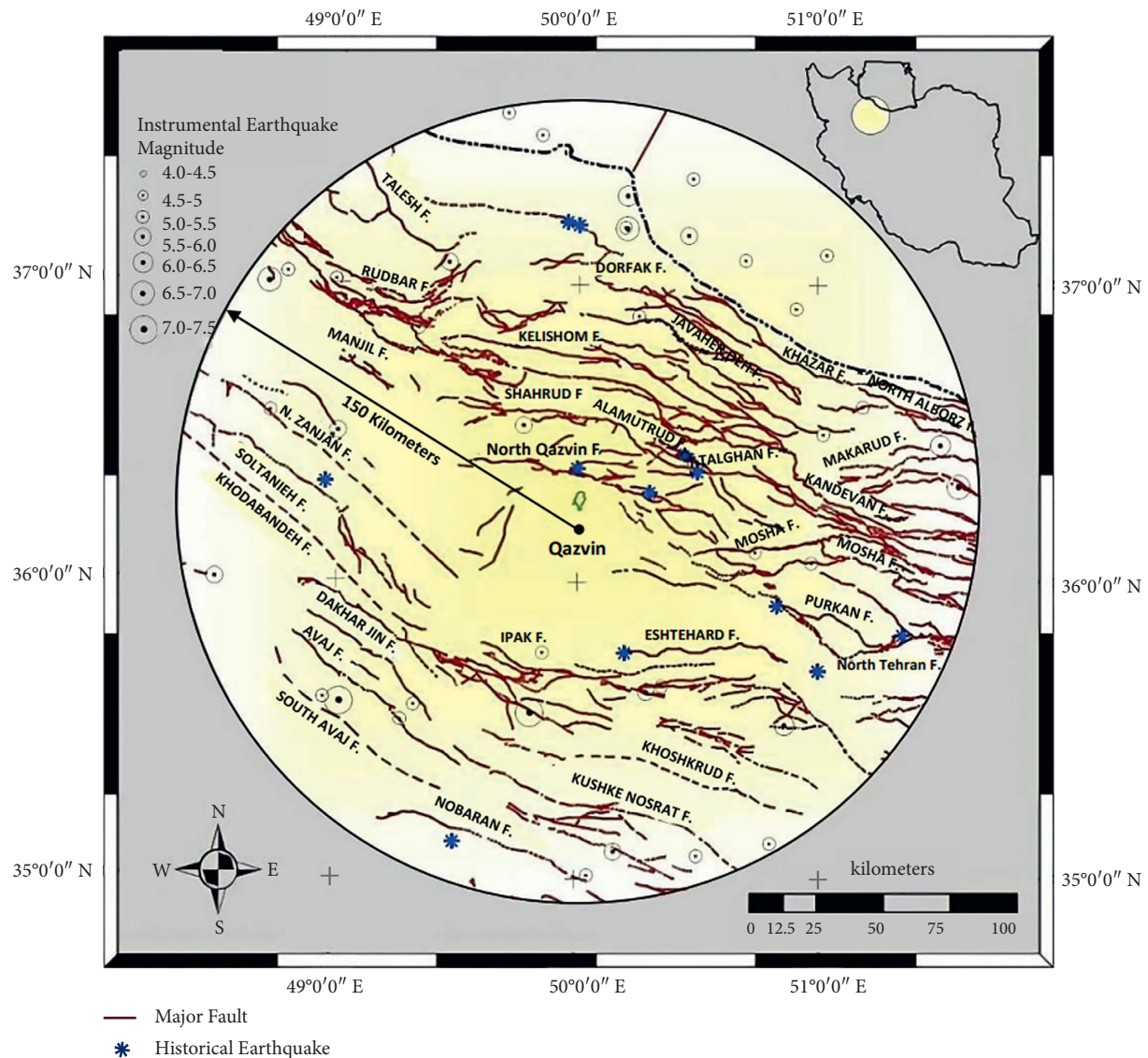


FIGURE 4: Seismotectonic map within a radius of 150 km around the city [21].

observed factors. So in this research, it is attempted to study the pattern of choice behavior in response to earthquake disaster in transportation network by considering physical and behavioral factors simultaneously by estimating hybrid models. The study of simultaneous effect of physical and behavioral characteristics and investigating the role of personality traits as latent variables in response to unpredictable natural disasters such as earthquakes is neglected in previous studies. Another innovation of this research is in terms of designing scenarios, expressing possible scenarios with three severities of earthquake disaster (minor, moderate, and severe) at two times (day, night). Also, simultaneous use of RP and SP data in the data collection method makes this research different from previous researches. Due to the stochastic nature of earthquake occurrence, since the choice behavior in response to the occurrence of earthquake crisis can be completely random, the analysis of data in this study has moved to models with random parameters in the field of personality traits, etc. In previous studies, random

parameters modeling approach for choice behavior in response to earthquake crisis has been neglected.

4. Modeling and Data Analysis

4.1. Modeling Approach. In this study, due to the discrete nature of the dependent variable under study (evacuation or not), discrete modeling was used for analysis. Understanding response to earthquake is used to forecast demand for transportation network and can also be used by emergency planners to improve the infrastructure. There are a number of techniques to understand the response of individuals to natural hazards. The most widely used technique is discrete choice model (DCM). DCM is applicable to evacuation choice modeling as the decision-makers select from a finite set of discrete alternatives. According to the assumption that the alternatives are mutually exclusive and collectively exhaustive, the choice of individuals can be explained by the principle of utility maximization. In this

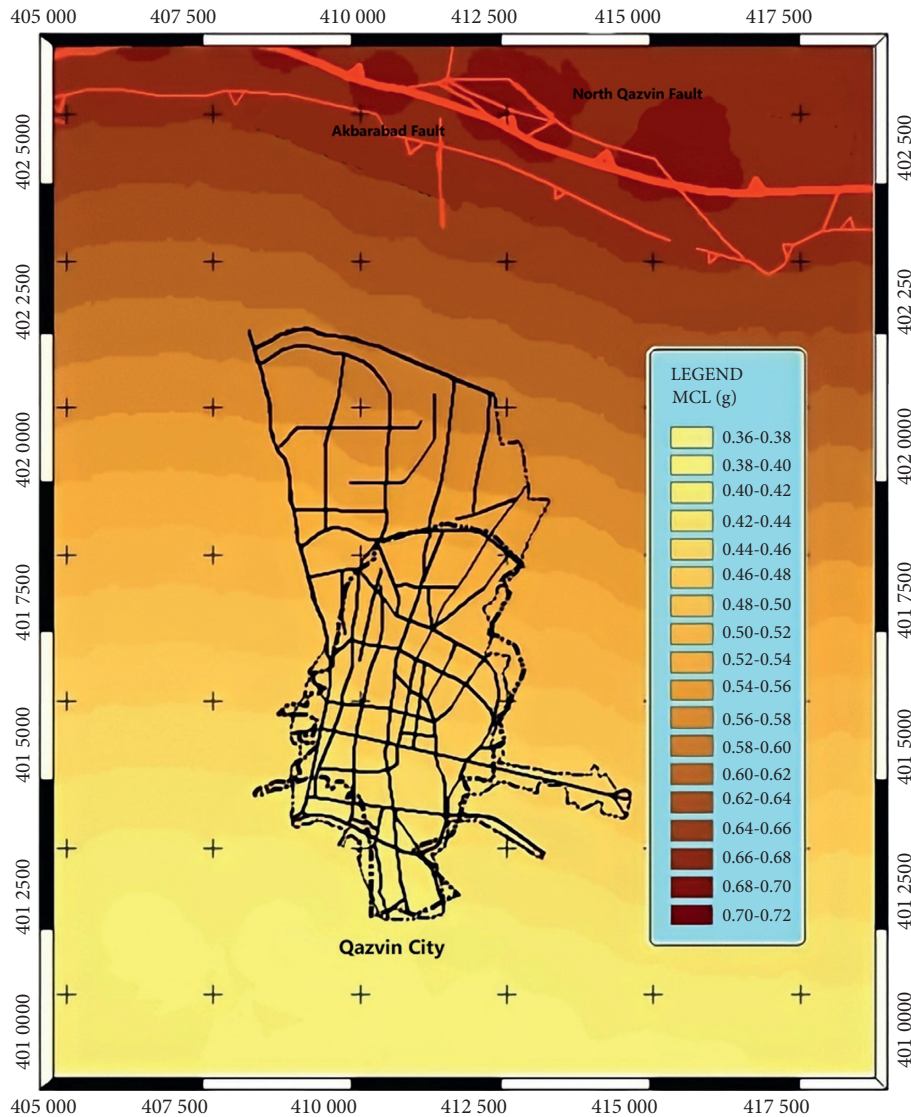


FIGURE 5: MCL Contour Map of Qazvin city [21].

study, first a utility function representing individual preferences for evacuation or not is calibrated to study evacuation choice in response to earthquake disaster.

In the context of discrete choice modeling, the utility function is defined as the sum of a representative component (V_{iq}) and an error term (ε_{iq}), which leads to the following equation [24]:

$$U_{iq} = V_{iq} + \varepsilon_{iq}. \quad (1)$$

V_{iq} , considering all attributes that can be quantified by an observer, is usually characterized through measurable properties of the alternatives and the individuals; the error term is considered to take into account all unknown elements affecting the decision. In this regard, if ε_{iq} follows Gumbel distribution, then the probability of occurrence of i for the individual q is $P(i, q)$ by using the traditional logit model which is represented by equation (2) [4].

$$P(i, n) = \frac{e^{T_{in}}}{\sum_{j \in C_n} e^{T_{jn}}}. \quad (2)$$

In the traditional logit model, if the dependent variable only has two possible values, such as evacuation/not which is represented by an indicator variable, this model will define as TBLM. Typically, TBLM only considers the measurable attributes of individuals. But over the past two decades, the influence of latent factors during individuals' decision-making process has been taken into account. Recent studies in DCM have emphasized the importance of the psychological factors affecting decision-making. It is also obvious that behavioral factors play a role in the decision-making process, and the usual approach to take these into account considers the estimation of a Multiple Indicator Multiple Cause (MIMIC) model, as suggested by Bollen [25]. In this research, as the evacuation choice is a binary variable, the

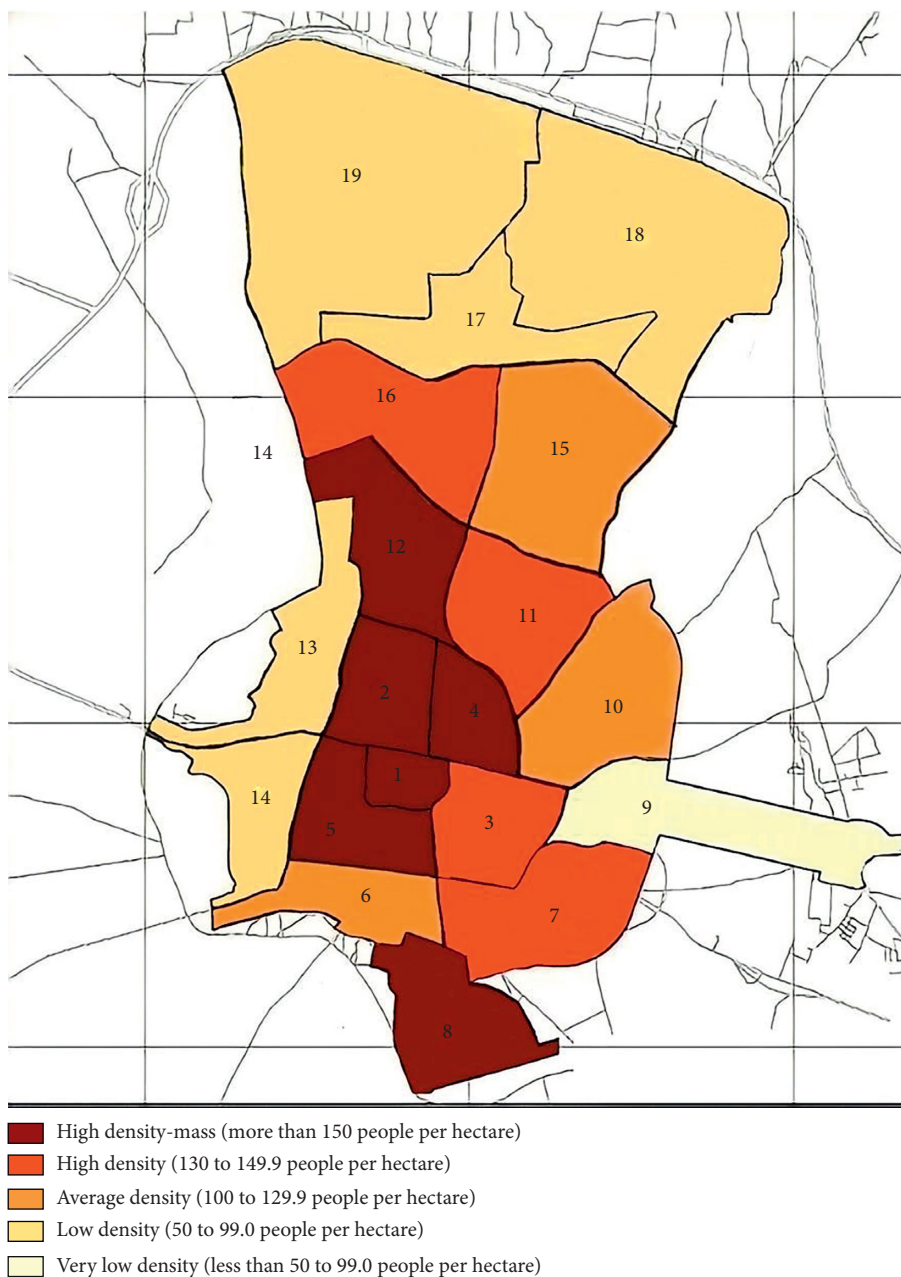


FIGURE 6: Population density map of Qazvin city [21].

joint use of MIMIC models and DCM leads to the hybrid binary choice model (HBLM). The role of the behavioral factors on choice behavior is evaluated by using the Integrated Choice and Latent Variable (ICLV) framework [26].

Hybrid modeling framework, also known as the integrated choice and latent variable (ICLV) model, incorporates psychometric data as indicators of latent variables in the estimation process. Indicators are obtained from responses to behavioral questions. The model consists of two components: a latent variable model and a choice model. Each component incorporates structural as well as measurement equations. The choice model consists of structural equations relating observable and latent variables to the

utility of each alternative, and measurement equations, which link the unobservable utility to choices [27].

Here, the latent variables are explained by a set of characteristics of the individuals and the alternatives (S_{iqr}), through the so-called structural equations, while explaining, at the same time, a set of attitudinal and/or perceptual indicators (y_{ziq}), previously gathered from the individuals, through the so-called measurement equations or CFA. This framework can be represented through the following equations:

$$\eta_{liq} = \sum_r \alpha_{lri} \cdot S_{riq} + v_{liq}, y_{ziq} = \sum_l \gamma_{lzi} \cdot \eta_{liq} + \zeta_{ziq}, \quad (3)$$

TABLE 2: Designated scenarios in the questionnaire.

Scenarios	Time of occurrence	Severity of earthquake
Scenario 1	Day: 8am–12am	Minor
Scenario 2	Night: 12am–8 am	Minor
Scenario 3	Day: 8am–12am	Moderate
Scenario 4	Night: 12am–8am	Moderate
Scenario 5	Day: 8am–12am	Severe
Scenario 6	Night: 12am–8am	Severe
<i>Earthquake Severity Guide</i>		
Minor (3–4.9 Richter)	These earthquakes, in addition to being recorded by seismic devices are also felt by humans, but do not result in significant losses and destructions.	
Moderate (5–6.9 Richter)	This class of earthquakes usually damages the buildings and other urban structures. All the people feel it.	
Severe (7–7.9 Richter)	This class of earthquakes cause mass casualties and damage the urban buildings and structures, especially in developing cities and countries.	

TABLE 3: The structure of latent variables and indicators.

Latent variable	Symbol	Indicator (the number of questions in NEO-FFI)
Neuroticism	N	M21,M26,M31,M36,M41,M46,M51,M56,M1,M6,M11,M16
Extroversion	E	M22,M27,M32,M37,M42,M47,M52,M57,M2,M7,M12,M17
Openness	O	M23,M28,M33,M38,M43,M48,M53,M58,M3,M8,M13,M18
Agreeableness	A	M24,M29,M34,M39,M44,M49,M54,M59,M4,M9,M14,M19
Conscientiousness	C	M25,M30,M35,M40,M45,M50,M55,M60,M5,M10,M15,M20

where the indices i , q , r , l , and z refer to alternatives, individuals, exogenous variables, latent variables, and indicators, respectively. The error terms ν_{liq} and ζ_{ziq} can follow any distribution but they are typically assumed to distribute normal with mean zero and a certain covariance matrix. Finally, α_{lri} and γ_{lzi} are parameters to be jointly estimated. Both equations must be continuously processed for their parameter estimation to use as a common variable in the HBLM. The latent variable is added to the fixed utility term so that the utility function includes not only observed variables such as trip characteristics and personal socioeconomic characteristics of passengers but also latent variables such as personality traits. The improved utility function can be expressed as Ref. [28].

$$U_{iq} = \sum_k \theta_{ki} \cdot X_{kqiq} + \sum_l \beta_{li} \cdot \eta_{liq} + \varepsilon_{iq}. \quad (4)$$

The parameters of these exogenous and endogenous variables are then estimated using the maximum likelihood method.

When the assumption of the standard logit model, that is, “parameters are fixed across observations” does not hold, inconsistent estimates of parameters will result [3]. To address the heterogeneity and flexible correlation structure, the random parameters or mixed binary logit model (MBLM) is usually considered. To allow for parameter variations across individuals (represented by variations in β), a mixed model is defined (i.e., a model with a mixing distribution). Mixed logit probabilities are the integrals of standard logit probabilities over a density of parameters that can be expressed in the form of equation (5) [2]:

$$P_i = \int P_{iq}(\beta) f\left(\frac{\beta}{\theta}\right) d(\beta), \quad (5)$$

where $f(\beta/\theta)$ is the density function of β , with θ referring to a vector of parameters of that density function (i.e., mean and variance). The mixed logit model for the probability of individual n for choosing evacuation in the aftermath of an earthquake is

$$P_{ni} = \int \frac{e^{U_{iq}}}{\sum_{A_j \in C_n} e^{U_{j_i}}} f\left(\frac{\beta}{\theta}\right) d(\beta). \quad (6)$$

The mixed logit probability is a weighted average of the logit formula evaluated at different values of β , with the weights given by the joint density $f(\beta)$. The values of β have some interpretable meaning as representing the decision criteria of individual decision-makers [4]. This density is a function of parameters θ that represent, for example, the mean and covariance of the β 's in the population. This specification is the same as for standard logit except that β varies over decision-makers rather than being fixed.

4.2. Variables. In order to investigate the choice behavior pattern of individuals after the earthquake disaster, the following variables were considered for modeling as mentioned in Table 5.

Before examining the results of modeling, in order to ensure proper distribution of the explanatory variables, their frequencies were statistically studied. In order to investigate the evacuation choice behavior in response to the earthquake disaster, the frequency percentage of bi-

TABLE 4: The abridged form of questionnaire.

Section 1: Socioeconomic characteristics				
Gender	Male	Female		
Marital status	Married	Single		
Age	18–24 years	25–32 years	33–45 years	
	46–55 years	56–69 years	+70 years	
Education	Diploma and below	Bachelor	Masters	Doctorate
Job	Employee	Manager	Self-employed	Doctor
	Faculty member	Student	Housewife	Retired
	Jobless	Other		
Family Income	Income.....			
Number of family members	No. of family members.....			
Geographical location of residence	Northern Parts	Central Parts	Southern Parts	
Access to vehicle at emergency situations	No access	Access to vehicle as a driver	Access to vehicle as an occupant	
Section 2: Daily trips' characteristics				
Purpose of daily trips	Education	Work	Entertainment	
	Shopping	Personal affairs	Other	
Traffic condition in daily trips	Very congested	Congested	Normal	
	Uncongested	Very uncongested		
Familiarity with alternative routes	Completely unfamiliar ($\leq 5\%$)	Unfamiliar ($5\% - 20\%$)	Normal ($20\% - 50\%$)	
	Familiar ($50\% - 80\%$)	Completely familiar ($\geq 80\%$)		
Section 3 (Revealed scenario1): Answer to this section according to your decision on the earthquake on December 20, 2017 , 23: 27.				
Did you choose evacuation in response to earthquake on December 20, 2017?	Yes	No		
Section 4 (Designated scenarios): In the questionnaire, the following question is repeated for each of the designated scenarios and people are asked to answer the question according to the severity and time of the earthquake in each of the scenarios.				
Do you choose evacuation in response to this scenario?	Yes	No		
Section 5: NEO-FFI				

nary dependent variable is analysed (Figure 7). The analysis of the results indicates that 46% of people tend to evacuate.

5. Results and Discussion

5.1. Confirmatory Factor Analysis (CFA). NEO-FFI instrument is used to measure the Big Five personality factors. The 60-item NEO-FFI provides a short measure of the Big Five personality factors. For each factor, 12 items are selected [22]. The CFA method is used to estimate all factor loadings and measure the 5 factor of NEO-FFI questionnaire. CFA is a statistical technique used to verify the factor structure of a set of observed variables. CFA allows the researcher to test the hypothesis that a relationship between observed variables and their underlying latent constructs exists [28]. Amos 24 software was used to estimate the CFA. The modeling structure is presented in Figure 8. Latent variables are represented by circles and observed variables by rectangles. Observed variables usually have a measurement error that is represented by circles and single-headed arrows correspond to linear effects. The model parameters were estimated using the maximum likelihood method based on the Amos software. The results show that the estimated models have good fit (Table 6).

5.2. Modeling Analysis. In order to investigate the evacuation choice pattern in response to the earthquake disaster, TBLM was first estimated with the use of observed variables. Then, to investigate the effect of latent variables on the modeling process, HBLM is estimated based on the maximum likelihood approach, which maximizes the probability of a chosen alternative. The modeling results indicate that several factors will affect future evacuation behavior in response to an earthquake disaster. The basic test for the adequacy of the models is the examination of the values and sign of the estimates. The results are achieved from the interpretation of estimated coefficients for the evacuation choice modeling in response to the earthquake disaster (Table 7). By comparing the TBLM and the HBLM, it is obviously seen that the HBLM provides greater explanatory power in evacuation choice behavior, indicating that incorporating the latent variables into the choice model improved the overall goodness of fit of the model. As shown in Table 7, by adding personality traits as latent variables to the modeling process and creating HBLM, the measures of correct prediction percentages, model fit, Pseudo R-squared, and Log likelihood function are increased, indicating that by adding individual personality traits better models are estimated. In both models, the negative sign of estimated coefficients for gender variable indicate that men are less likely to evacuate in response to an earthquake disaster. This

TABLE 5: Independent variables of modeling.

Variable	Variable name: explanation
Gender	GENDER (male = 1, female = 0)
Marital status	Marital status (married = 1, single = 0)
Age	AGE1: 18–24 years, AGE2: 25–32 years, AGE3: 33–45 years, AGE4: 46–55 years, AGE5: 56–69 years, AGE6: +70 years
Education	EDU1: Diploma and below, EDU2: Bachelor, EDU3: Master, EDU4: Doctorate
Job	JOB1: Employee, JOB2: Manager, JOB3: Self-employed, JOB4: Doctor, JOB5: Faculty member, JOB6: Student, JOB7: Housewife, JOB8: Retired, JOB9: Jobless, JOB10: Other
Family Income	Income (Numerical)
Number of family members	No. of family members (Numerical)
Access to vehicle at emergency situations	CARUSE1: No access, CARUSE2: Possible access to vehicle as a driver, CARUSE3: Possible access to vehicle as an occupant
Purpose of daily trips	Trip purpose1: Education, Trip purpose2: Work, Trip purpose3: Entertainment, Trip purpose4: Shopping, Trip purpose5: Personal affairs, Trip purpose6: Other
Geographical location of residence	North: Northern Parts, Central: Central Parts, South: Southern Parts
Traffic condition in daily trips	Traffic1: Very congested, Traffic2: Congested, Traffic3: Normal, Traffic4: Uncongested, Traffic5: Very uncongested
Familiarity with alternative routes	Familiar1: Completely unfamiliar ($\leq 5\%$), Familiar2: Unfamiliar (5%–20%), Familiar3: Normal (20%–50%), Familiar4: Familiar (50%–80%), Familiar5: Completely familiar ($\geq 80\%$)
Earthquake severity	Severity1: Minor, Severity2: Moderate, Severity3: Severe
Time of earthquake	Time (night = 1, day = 0)

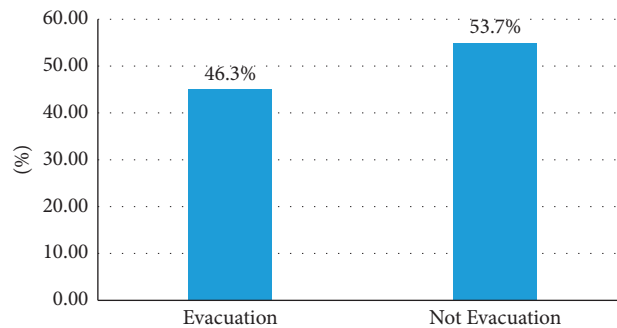


FIGURE 7: Frequency distribution of action choice in response to earthquake.

finding is consistent with the finding of previous research by Bateman and Edwards, which concluded that women are more likely to evacuate compared to men because of socially constructed gender differences in care-giving roles, access to evacuation incentives, exposure to risk, and perceived risk. Individuals in the age groups of 18–24 and 25–32 are more likely to evacuate in TBLM while the age group 33–45 is also significant in HBLM, and it indicates that people in the age group of 33–45 have a positive contribution to evacuation. The positive sign and bigger amount of estimated coefficient for AGE1 ($\beta = 3.611$) indicates that individuals in the age group of 18–24 tend more to evacuate. This finding is consistent with the results of studies by Yang et al. [16] which indicated that young persons are more likely to evacuate. Although marital status is not a significant factor in TBLM, the estimated coefficient of HBLM indicates that married individuals are more likely to evacuate (coefficient = 2.657). Protecting each other before protecting oneself is also a common explanation for the fact that married individuals were found to be more likely to evacuate in response to an earthquake. In both models, with the increase in the number

of family members, the tendency to evacuate also increases. In contrast, family size is not significantly correlated with evacuation in the study of solis et al. HBLM indicates that people who do not have accessibility to a car in emergency situations have less tendency to evacuate in response to an earthquake disaster (coefficient = -2.586). The coefficients indicate that people who have access to a car as a driver or occupant are more likely to evacuate in a convenient way in response to an earthquake disaster. The negative sign of estimated coefficient for NORTH variable indicates that people who stay in the northern parts of the city are less likely to evacuate. It can be because of new construction in this area and more confidence of people in the strength of the buildings. The positive sign of the estimated coefficient for TRAFFIC3 variable indicates that individuals facing normal traffic on their daily trips have more tendency to evacuate in the hybrid model. The negative sign of the estimated coefficient for FAMILIAR2 variable in both models indicates that people who are unfamiliar with alternative routes are less likely to evacuate. It can be because of the sense of being blocked in routine routes. While SEVERITY3

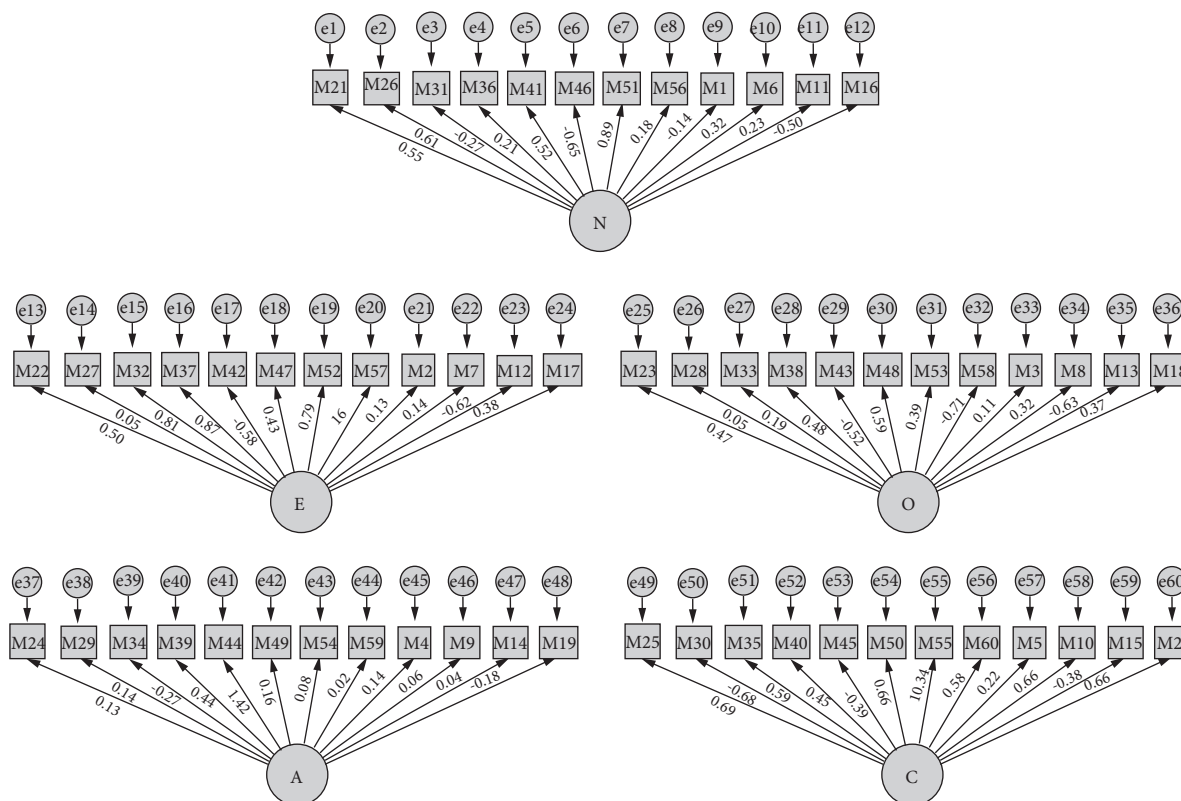


FIGURE 8: The confirmatory factor analysis structure.

TABLE 6: Modeling fit indices.

Fit index	Value	Criteria of good fit
Chi-square/degree of freedom (CMIN/DF)	4.791	<5
Root mean square error of approximation (RMSEA)	0.079	≤ 0.08
Goodness-of-fit index (GFI)	0.939	$0.9 \leq$
The parsimonious normal fit index (PNFI)	0.514	$0.5 <$
Comparative fit index (CFI)	0.918	$0.9 \leq$
Root mean square residual (RMR)	0.018	Good models have small RMR

variable is not significant in TBLM, the signs of the estimated coefficients for SEVERITY1, SEVERITY2, and SEVERITY3 variables in HBLM indicate that as the severity of the earthquake increases, the tendency to evacuate increases. The positive sign of the estimated coefficients for time in both models indicate that people are more likely to evacuate at night. The positive sign of estimated coefficients of HBLM indicate that people with more neuroticism, extraversion, openness, and conscientiousness factor are more likely to evacuate while people with more agreeableness factor are less likely to evacuate (coefficient = -0.522). As neuroticism refers to the propensity to experience negative emotions, anxiety, and psychological distress in response to threats; extraversion represents the tendency to enjoy social situations and interpersonal relationships; openness to experience reflects the tolerance of ambiguity; and conscientiousness implies both proactive and inhibitive aspects, such as competence, striving to achieve, and cautiousness, it is expected that people with these factors in their

personality are more likely to evacuate. However, agreeableness denotes the quality of interaction "along a continuum from compassion to antagonism," having facets of trust and altruism [22]. Therefore, it is reasonable that people with more agreeableness factor are less likely to evacuate.

Since the occurrence of an earthquake is one of the situations in which a person can decide based on his/her perception whether to evacuate or not, the MBLM was also calibrated to analyse the behavior of individuals comparing to TBLM and HBLM. This model is one of the most flexible structures of discrete choice models, which can be used to estimate almost any other structure in random utility models. A very good description of this model and its features was provided in 2000 by McFadden and Train [29]. This model allows for changes in random tastes, the use of a variety of substitution patterns, and correlations in the unobserved component over time for the model maker. The MBLM can be estimated and interpreted based on a wide

TABLE 7: The results of TBLM and HBLM.

Independent variable	TBLM		HBLM	
	Estimated coefficient	P value	Estimated coefficient	P value
Gender	-0.279**	0.0239	-0.417**	0.0144
Age1	1.324***	≤0.001	3.611***	≤0.001
Age2	1.244***	≤0.001	1.721***	0.0002
Age3	—	—	1.926***	0.0003
Edu2	-1.237***	≤0.001	-1.780***	≤0.001
Edu3	-2.418***	≤0.001	-0.922*	0.0689
Marital status	—	—	2.657***	≤0.001
Job7	1.240***	≤0.001	1.006***	0.0009
Car Use1	—	—	-2.586***	≤0.001
Car Use2	0.725**	0.0377	-1.094**	0.0338
Car Use3	0.761**	0.0127	-1.423***	0.0002
Trip Purpose2	0.962***	≤0.001	-0.895***	0.0001
North	—	—	-0.260*	0.0969
Traffic3	-0.360***	0.0084	—	—
Familiar2	-1.182***	≤0.001	-1.243***	0.0014
Severity1	-1.691***	0.0002	-1.281**	0.0120
Severity2	-1.691***	≤0.001	-1.199**	0.0218
Severity3	—	—	2.848***	0.0002
Time	0.261***	0.0057	0.249**	0.0109
Income	0.097**	0.0176	—	—
No. of family members	0.177*	0.0799	0.771***	≤0.001
N	—	—	0.229***	≤0.001
E	—	—	—	—
O	—	—	0.636***	≤0.001
A	—	—	-0.522***	≤0.001
C	—	—	0.104***	0.0028
Log likelihood function	-1406.783		-1308.464	
Chi-squared	215.986		412.62358	
McFadden pseudo R-squared	0.071		0.136	
Correct prediction (%)	54.881		58.485	
False prediction (%)	45.027		41.423	

range of behavioral characteristics, depending on the modeller. In the random coefficient model, random parameters are assumed to be randomly distributed over the population to capture the taste variation of the individual. As can be seen in Table 8, based on the model fit indices such as increasing in Log Likelihood function and pseudo square (ρ^2), MBLM is fitted better than the other models. The result of MBLM depicts that Age1, Marital status, Severity1, Severity2, and Severity3 are significant as nonrandom parameters in utility functions. The Age1, Marital status, and Severity3 variables have positive signs in $U(1)$ utility function. The results indicate that young (18–24 years old) and married individuals are more likely to get evacuated. Severity1 and Severity2 variables have positive signs in $U(0)$ utility function. These signs indicate that people are more likely not to evacuate in minor and moderate severity of earthquakes. These results are in accordance with the results of HBLM.

In addition, results show that income, number of family members, and five factors of personality traits are heterogeneous variables and these variables are significant as random parameters in MBLM. In other words, their effect is different. For instance, although the effect of income variable is positive for choosing evacuation, with the increase in income, the willingness of individuals to evacuate increases;

this effect is different for each of the respondents. This finding might be explained by the differences in the mindset of individuals. Increase in income can lead to having more required equipment for evacuation and more willingness to evacuate. On the other hand, increase in income can lead to having houses with more resistance and more confidence of people in the strength of their buildings and less willingness to evacuate. Besides, the number of family members is heterogeneous in the utility function of not choosing evacuation. Thus, it can be stated that the negative effect of the number of family members on not choosing evacuation is not the same for all the respondents. This finding might be explained by the differences of individuals in decision-making. As mentioned, five factors of personality traits are significant as random parameters in MBLM. Although the effect of openness and conscientiousness variables are positive in $U(1)$ utility function and as the openness and conscientiousness factors increase, the willingness of individuals to evacuate increases; this effect is different for each of the respondents according to the amount of self-control in their personality. Furthermore, although the effect of agreeableness factor is positive in $U(0)$ utility function and as the agreeableness factor increases, the willingness of individuals not to evacuate increases; this effect is different for each of the respondents according to the amount of

TABLE 8: The result of random parameters/mixed logit model.

Independent variable	Estimated coefficient	P value
<i>Nonrandom parameters in utility functions</i>		
Constant	-77.532***	0.0002
Age1	24.405***	0.0048
Marital Status	32.873***	0.0013
Familiar2	—	—
Severity1	36.321***	0.0055
Severity2	32.833***	0.0073
Severity3	28.209**	0.0313
<i>Random parameters in utility functions</i>		
Income	2.663**	0.0255
No. of family members	-13.216***	0.020
N	-0.533*	0.0488
E	-1.800**	0.0247
O	4.967***	0.0034
A	1.656*	0.0683
C	1.979**	0.0122
<i>The standard deviation of random parameters</i>		
Income	0.749*	0.0421
No. of family members	1.789*	0.0213
N	0.757*	0.0701
E	1.467***	0.0062
O	3.310*	0.0645
A	0.696*	0.0320
C	0.790**	0.0182
Log likelihood function	-328.410	
Chi-squared	97.32	
McFadden Pseudo R-squared	0.149	
Utility functions of mixed logit model: $U(1) = \text{Evacuation choice, } U(0) = \text{Not evacuation choice;}$ $U(1) = a_1 + a_2 * \text{Marital status} + a_3 * \text{Familiar2} + a_4 * \text{Age1} + a_5 * \text{O} + a_6 * \text{C} + a_7 * \text{Severity3} + a_8 * \text{Income,}$ $U(0) = a_9 * \text{A} + a_{10} * \text{Severity1} + a_{11} * \text{No of family members} + a_{12} * \text{Severity2} + a_{13} * \text{N} + a_{14} * \text{E.}$		

cooperativity in their personality. Besides, neuroticism and extroversion factors are heterogeneous in the utility function of not choosing evacuation. Thus, it can be stated that the negative effect of neuroticism and extroversion factors on not choosing evacuation is not the same for all the respondents. This finding might be explained by emotional instability and self-consciousness of individuals. The standard deviations of random parameters are significantly different from zero, which implies that different individuals in the same income, number of family members, and same personality traits perceive the alternatives' utilities differently.

6. Conclusion

Many researchers have examined the factors affecting evacuation decision in response to natural hazards but most of the previous studies have investigated the effect of socioeconomic factors on trip choice behavior and study about the role of personality traits on evacuation choice behavior is neglected. Hence, this paper focuses on examining the effect of personality traits on evacuation choice behavior in response to an earthquake disaster. The study was conducted in the city of Qazvin and the RP and SP methods were used for data collection. RP data were based on the real

earthquake experience of December 20, 2017 and SP data were collected from field survey assuming six hypothetical earthquake scenarios with three different severities in two times (day-night) of the day. Personality traits as latent variables were obtained from the CFA of NEO-FFI.

First, TBLM was used for identifying effective socio-economic characteristics and earthquake characteristics on the evacuation choice of individuals. Then, by applying the HBLM, the role of the personality traits as latent variables on evacuation choice behavior is obtained. The results from the HBLM are more comprehensive than those from the TBLM since it accounts for factors that impact decisions on evacuation choice. The results of HBLM show that personality traits make a significant contribution to people's evacuation decision in response to an earthquake disaster. Results also indicate that gender, marital status, and family size have a positive impact on evacuation choice, while no possible access to vehicle, residence in north parts of the city, and unfamiliarity with alternative routes have a negative impact on evacuation choice. As the severity of the earthquake increases, the tendency of people to evacuate also increases. In earthquakes occurring at night, the tendency of people to evacuate is more. People with high neuroticism, openness, and conscientiousness personality factors are more likely to evacuate, while people who have a high

agreeableness personality factor are less likely to evacuate.

Also, the effect of taste variation of personality traits on evacuation choice behavior was investigated using MBLM. The model concludes that different individuals with the same family income, the same number of family members, and the same neuroticism, extroversion, openness, agreeableness, and conscientiousness factors of personality traits can perceive the alternatives' utilities differently.

This study is expected to provide a better understanding for urban planners on the influential factors of evacuation choice behavior in emergency situations like an earthquake. Results of this study can be used for pre-disaster planning. The results of this study can be related to identifying the general behavior of users and estimating their reactions in times of crisis, providing the needed training for users in times of crisis, strengthening network components according to possible destinations, forecasting transportation network demand in the event of a crisis based on the reaction of users, forecasting the conditions of the transportation network after the crisis in order to make the necessary plans, including routing and managing ambulances, designing city escape routes, and locating shelters needed to accommodate people in the situation of an earthquake crisis.

There are some recommendations for future researches. In order to provide future directions and way forward to the study, the following suggestions are presented:

- (i) Future research could include gathering more information about other decision-making variables about choice behavior in response to an earthquake crisis such as cultural beliefs, following others, etc.
- (ii) Explaining hypothetical scenarios for the two seasons of summer and winter can be another suggestion for future research.
- (iii) Studying the mode, destination, and route choice behavior to predict the status of transport network links after the earthquake crisis helps to complete the research.

References

- [1] M. Najafi, S. Eshghi, and K. Eshghi, "A framework for earthquake emergency response in Iran," *Scientia Iranica*, vol. 27, no. 5, pp. 2604–2620, 2019.
- [2] U. Tamima and L. Chouinard, "Decision making behavior of earthquake evacuees: an application of discrete choice models," in *Numerical Methods for Reliability and Safety Assessment*, pp. 721–735, Springer, Cham, 2015.
- [3] S. Hasan, S. Ukkusuri, H. Gladwin, and P. T. Murray, "Behavioral model to understand household-level hurricane evacuation decision making," *Journal of Transportation Engineering*, vol. 137, no. 5, pp. 341–348, 2011.
- [4] K. E. Train, *Discrete Choice Methods with Simulation*, Cambridge University Press, Cambridge, United Kingdom, 2009.
- [5] Y. Chen and R. T. Eguchi, "Post-earthquake road unblocked reliability estimation based on an analysis of randomness of traffic demands and road capacities," in *Proceedings of the Sixth U.S. Conference and Workshop on Lifeline Earthquake Engineering (TCLEE) 2003*, pp. 916–925, CA, USA, August 2003.
- [6] S. D. Werner, C. E. Taylor, S. Cho et al., "Redars 2 methodology and software for seismic risk analysis of highway systems (no. mceer-06-sp08)," Special Report (No. MCEER-06-SP08), 2006.
- [7] S. Shapira, L. D. Aharonson, and Y. B. Dayan, "Anticipated behavioral response patterns to an earthquake: the role of personal and household characteristics, risk perception, previous experience and preparedness," *International journal of disaster risk reduction*, vol. 31, pp. 1–8, 2018.
- [8] F. Mohajeri and B. Mirbaha, "Studying the trip choice behavior of individuals in urban road network after the earthquake disaster (case study of Qazvin city) (No. TRBAM-21-02744)," in *Proceedings of the Transportation Research Board 100th Annual Meeting*, Washington D. C., USA, January 2021.
- [9] J. C. Whitehead, B. Edwards, M. V. Willigen, J. R. Maiolo, K. Wilson, and K. T. Smith, "Heading for higher ground: factors affecting real and hypothetical hurricane evacuation behavior," *Global Environmental Change Part B: Environmental Hazards*, vol. 2, no. 4, pp. 133–142, 2000.
- [10] M. Horikiri and M. Odani, "Analysis of residents' evacuation behavior after the great hanshin-awaji earthquake," *Infrastructure Planning Review*, vol. 17, pp. 819–826, 2000.
- [11] J. M. Bateman and B. Edwards, "Gender and evacuation: a closer look at why women are more likely to evacuate for hurricanes," *Natural Hazards Review*, vol. 3, no. 3, pp. 107–117, 2002.
- [12] D. Walton and S. Lamb, "An experimental investigation of post-earthquake travel behaviors: the effects of severity and initial location," *International Journal of Emergency Management*, vol. 6, no. 1, pp. 14–32, 2009.
- [13] D. Solís, M. Thomas, and D. Letson, "An empirical evaluation of the determinants of household hurricane evacuation choice," *Journal of Development and Agricultural Economics*, vol. 2, no. 3, pp. 188–196, 2010.
- [14] J. R. Eiser, A. Bostrom, I. Burton et al., "Risk interpretation and action: a conceptual framework for responses to natural hazards," *International Journal of Disaster Risk Reduction*, vol. 1, pp. 5–16, 2012.
- [15] N. Y. Yun and M. Hamada, "Evacuation behavior and fatality rate during the 2011 Tohoku-Oki earthquake and tsunami," *Earthquake Spectra*, vol. 31, no. 3, pp. 1237–1265, 2015.
- [16] H. Yang, E. F. Morgul, K. Ozbay, and K. Xie, "Modeling evacuation behavior under hurricane conditions," *Transportation Research Record*, vol. 2599, no. 1, pp. 63–69, 2016.
- [17] S. Tanaka, M. Kuwahara, T. Yoshii, R. Horiguchi, and H. Akahane, "Estimation of travel demand and network simulators to evaluate traffic management schemes in disaster," in *Proceedings of the INCEDE-NCEER Center-to-Center Project Workshop in Earthquake Engineering—Frontiers in Transport Systems*, pp. 1–16, Tokyo, Japan, 2001.
- [18] F. Mohajeri and B. Mirbaha, "Studying the role of behavioral characteristics in individuals travel choice behavior in

response to earthquake disaster using discrete choice models,” *Mathematical Problems in Engineering*, vol. 2021, Article ID 6917548, 17 pages, 2021.

- [19] S. Tanaka, M. Kuwahara, T. Yoshii, R. Horiguchi, and H. Akahane, “Estimation of travel demand and network simulators to evaluate traffic management schemes in disaster,” *Avenue*, pp. 1–16, 2001.
- [20] Noandishaan Consulting Engineers, *Comprehensive Plan of Qazvin City*, Housing and Urban Development organization, Qazvin province, Iran, 2014.
- [21] N. A. Comijany, A. A. Fard, and M. Pourkermani, *An Overview of Seismic Hazard of Qazvin City and Comparison with Iranian Code of Practice for Resistant Design of Buildings*, Springer, Berlin, Germany, 2013.
- [22] P. T. Costa and R. R. McCrae, *The Revised NEO Personality Inventory (NEO-PI-R)*, Sage Publications, Inc, CA, USA, 2008.
- [23] W. G. Cochran, *Sampling Techniques*, John Wiley & Sons, NJ, USA, 2nd edition, 1963.
- [24] J. D. D. Ortúzar and L. G. Willumsen, *Modeling Transport*, John Wiley & Sons, NJ, USA, 2011.
- [25] K. A. Bollen, “A new incremental fit index for general structural equation models,” *Sociological Methods & Research*, vol. 17, no. 3, pp. 303–316, 1989.
- [26] J. L. Walker, “Extended discrete choice models: integrated framework, flexible error structures, and latent variables,” Doctoral dissertation, Massachusetts Institute of Technology, MA, USA, 2001.
- [27] C. G. Prato, S. Bekhor, and C. Pronello, “Latent variables and route choice behavior,” *Transportation*, vol. 39, no. 2, pp. 299–319, 2012.
- [28] F. J. B. Bahamonde, U. Kunert, H. Link, and J. D. D. Ortúzar, “About attitudes and perceptions: finding the proper way to consider latent variables in discrete choice models,” *Transportation*, vol. 44, no. 3, pp. 475–493, 2017.
- [29] D. McFadden and K. Train, “Mixed MNL models for discrete response,” *Journal of Applied Econometrics*, vol. 15, no. 5, pp. 447–470, 2000.

Under Circular Dynamic Stress Paths Analysis on the Dynamic Modulus and Damping Ratio of Compacted Loses

Mdaras Aras Ansari, *Department of Civil Engineering, Raajdhani Engineering College, Bhubaneswar, mdarasansari2578@gmail.com*

S. C. Mishra, *Department of Civil Engineering, NM Institute of Engineering & Technology, Bhubaneswar, scmishra11@yahoo.co.in*

Sourav Debasish, *Department of Civil Engineering, Aryan Institute of Engineering & Technology, Bhubaneswar, souravdebasish1@gmail.com*

Jagriti Swain, *Department of Civil Engineering, Capital Engineering College, Bhubaneswar, jagritiswain26@yahoo.co.in*

ABSTRACT

Dynamic stresses, such as earthquakes and traffic, cause vertical dynamic stress and horizontal shear stress in the foundation soil at the same time. A series of experiments of compacted loess under the operation of a circular dynamic stress path were carried out using a hollow cylindrical torsion shear apparatus to replicate the stress state of soil in the area of the circular dynamic stress path generated by bidirectional dynamic stress coupling. The dynamic modulus and damping ratio of compacted loess were primarily investigated in relation to mean principal stress, dry density, and deviatoric stress ratio (the ratio of deviator stress to average principal stress). The test findings reveal that the bigger the mean primary stress is, the larger the dynamic compression modulus and dynamic shear modulus are under the influence of the circular dynamic stress path. With increasing dry density, the dynamic compression modulus increases noticeably, while the dynamic shear modulus just little. The dynamic compression modulus and dynamic shear modulus increase to some amount as the deviator stress ratio increases from 0 to 0.4. Furthermore, the first dynamic compression modulus and initial dynamic shear modulus of compacted loess increase with increasing dry density and deviatoric stress ratio. The dynamic compression damping ratio of compacted loess rises as mean principal stress rises, but the dynamic shear damping ratio falls as mean principal stress rises. The dynamic compression damping ratio and dynamic shear damping ratio of compacted loess are mostly unaffected by dry density. The bigger the deviatoric stress ratio, the smaller the dynamic compression damping ratio and the dynamic shear damping ratio are when the dynamic strain surpasses 1%. The findings can be used as a starting point for further research into the dynamic modulus and damping ratio of loess under various stress pathways.

1. Introduction

The dynamic modulus and damping ratio are the basis of foundation engineering seismic design, seismic stability evaluation, settlement prediction, and other works. Researchers also attach great importance to this research work and carry out a series of studies on various types of soil through field tests, indoor resonant column tests, dynamic triaxial tests, and dynamic torsional shear tests [1–4]. In actual engineering, dynamic loads such as earthquakes, traffic, waves, and other dynamic loads produce vertical dynamic stress and horizontal dynamic stress in foundation

soil. The amplitude and direction of the dynamic stress are constantly changing, resulting in continuous rotation of the principal stress axis in foundation soil. Inevitably, there will be areas acting on elliptical and circular dynamic stress paths [5, 6]. There are many factors that affect the dynamic characteristics of soil [7, 8]. The dynamic stress path is one of the important factors that affect the dynamic deformation characteristics of soil. Therefore, research on the dynamic modulus and damping ratio of soil under special dynamic stress paths is more consistent with the actual situation and can obtain more accurate variation rules of the dynamic modulus and damping ratio.

Research on special dynamic stress paths of soil dynamics begins with the rotation of the principal stress axis. With the continuous development and improvement of hollow cylindrical torsion shear apparatuses, many scholars have carried out research on the principal stress axis rotation of different soils, and research on the influence of complex dynamic stress paths on the dynamic characteristics of soils has been deepening. Ishihara et al. [9] analyzed the situation in which the principal stress axis rotation of seabed soil caused by wave loading might appear as a "circular dynamic stress path," and the test simulation showed that the strength of sand under such a stress path was lower than that under ordinary unidirectional cyclic loading. Towhata et al. [5] found that the continuous rotation of the principal stress axis can produce greater excess pore water pressure than that without rotation, which greatly reduces the liquefaction resistance of saturated sand. Miura et al. [10] and Lashkari et al. [11] established a new constitutive model considering principal stress axis rotation to describe the deformation and liquefaction behavior of anisotropic sand. Zhou et al. [12] and Zhang et al. [13] used a hollow cylindrical torsion shear apparatus to carry out saturated silt experiments with different cyclic loading amplitude ratios in axial and torsional and simulated circular dynamic stress paths and elliptical dynamic stress paths, respectively, indicating that the dynamic stress path has a significant influence on the liquefaction of saturated silt. Gu et al. [14, 15] simulated the shear stress and normal stress caused by earthquakes in saturated clay by cyclic triaxial tests with variable confining pressures. The dynamic stress path formed by bidirectional dynamic load coupling is more suitable for simulating the stress field formed by earthquakes in foundations and has a great influence on the strength and pore water pressure of saturated soft clay. Hu et al. [16] also simulated the figure-eight-shaped shear stress path that may be formed by earthquake action and analyzed the influence of the cyclic dynamic stress ratio and frequency on the cumulative cyclic strain and strength. Inam et al. [17], Gallage et al. [18], and Dareeju et al. [19] simulated the rotation of the principal stress axis caused by traffic loads through experiments and proved that the rotation of the principal stress axis has significant effects on the cumulative cyclic plastic deformation of different subgrade soil materials. Qian et al. [20] studied the influence of principal stress rotation caused by traffic loads on the stress-strain behavior of saturated soft clay. Wang et al. [21] compared and analyzed the influence of a nonstandard elliptical stress path and circular stress path on the cyclic strength of seabed sand. Wang et al. [22] tested the circular dynamic stress path formed by the rotation of the principal stress axis of marine soft clay caused by a simulated wave load and studied the changes in pore water pressure and the stress-strain hysteresis curve of soft clay under a long-term cyclic circular dynamic stress path.

The above research simulates the complex dynamic stress path caused by the rotation of the principal stress axis of the soil due to the bidirectional dynamic load coupling caused by earthquakes, traffic, waves, and other dynamic loads, which has a great influence on the dynamic characteristics of saturated sand, silt, and soft clay. However, there

are relatively few studies on the dynamic modulus and damping ratio of compacted loess. Cheng et al. [23] carried out experiments on the dynamic modulus and damping ratio of compacted loess under a complex initial stress state and studied the effects of principal stress axis deflection and average principal stress on the dynamic modulus and damping ratio of compacted loess. Wang et al. [24] studied the dynamic modulus and damping ratio of compacted loess under long-term cyclic dynamic loads and evaluated the influence of the number of cycles, confining pressure and dynamic stress on the dynamic modulus and damping ratio of compacted loess. Among them, there is no literature on the dynamic modulus and damping ratio of compacted loess under bidirectional dynamic load.

Loess is widely distributed in China and the world. Compacted loess is widely used in construction engineering foundations, road subgrades, and embankment engineering in these areas. Therefore, this study will use a hollow cylindrical torsion shear instrument to simultaneously apply axial dynamic stress and torsional dynamic shear stress, coupling them to form a circular dynamic stress path, and truly simulate the special dynamic stress path formed by bidirectional dynamic loads. The effects of the mean principal stress, dry density, and deviatoric stress ratio of compacted loess on the dynamic elastic modulus, dynamic shear modulus, dynamic compression damping ratio, and dynamic shear damping ratio under a circular dynamic stress path are mainly studied. The research results of this article can provide references and new ideas for subsequent research.

2. Materials and Methods

2.1. Test Equipment. The instrument used in the test is the DTC-199HVS hollow cylindrical torsion shear system produced by SEIKEN Inc. in Japan, which uses a hollow cylindrical sample. The instrument can independently control the axial force W , torque M_T , internal confining pressure P_i , and external confining pressure P , which can not only simulate various complex initial stress states and static stress paths but also independently control the dynamic load applied in four directions. The phase difference of each direction can be controlled to simulate various complex dynamic stress paths. The maximum axial loading force is 20 kN, the maximum torque loading is 100 N·m, and the maximum loading coupling frequency is 5 Hz. The instrument consists of a pressure chamber, hydraulic pump, loading unit, electrical control cabinet, water and air control system, and data collection system, as shown in Figure 1. The data acquisition software was used to automatically record test data points.

2.2. Test Material and Sample Preparation. All the loess materials used in the test were taken from the construction site of a project in Xi'an, China, with a depth of 3-4 m and belonging to Q3 loess. According to ASTM standards, the measured basic physical properties of the loess are shown in Table 1. The grain size distribution curve of loess is shown in

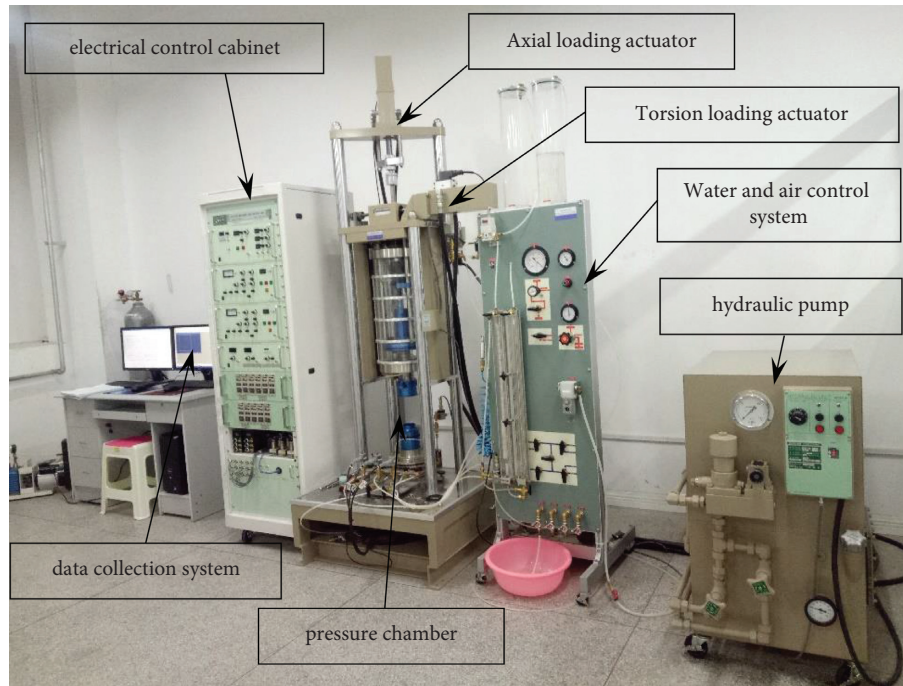


FIGURE 1: Hollow cylindrical torsion shear apparatus.

TABLE 1: Physical properties of loess.

Index properties	Value	Specification
Specific gravity	2.70	ASTM D 854
Liquid limit (%)	32	ASTM D 4318
Plastic limit (%)	21	ASTM D 4318
Plasticity index	11	ASTM D 4318
Soil classification	CL	USCS
Maximum dry density, ρ_{dmax} (g/cm ³)	1.69	ASTM D 698
Optimum moisture content, ω_{op} (%)	20.1	ASTM D 698

Figure 2. Through the light compaction test, the maximum dry density ρ_{dmax} of loess is 1.69 g/cm³, and the optimal moisture content ω_{op} is 20.1%. The construction of building foundations and road subgrades often takes compactness as the standard of design and evaluation of engineering quality, so this test selects $0.96\rho_{dmax}$, $0.90\rho_{dmax}$, and $0.85\rho_{dmax}$ for comparison of three dry densities, namely, 1.62 g/cm³, 1.52 g/cm³, and 1.44 g/cm³. Loess taken from the construction site was air-dried, crushed, and passed through a 2 mm sieve. The water needed to configure the target moisture content was calculated, and the water was evenly sprayed on the soil with a sprayer. Then, the fresh-keeping bag was sealed and placed in the moisturizing container for more than 3 days, and the moisture content was checked until it reached 20.1%. The sample then was prepared by the compaction method, the soil sample was evenly compacted in four layers to achieve the target dry density, the surface between each layer was fully shaved to facilitate the combination, and then the hollow core was cut out with a soil drill and a scraper. The prepared compacted hollow cylindrical loess sample is shown in Figure 3, with a height of 100 mm, an outer diameter of 70 mm, and an inner diameter of 30 mm.

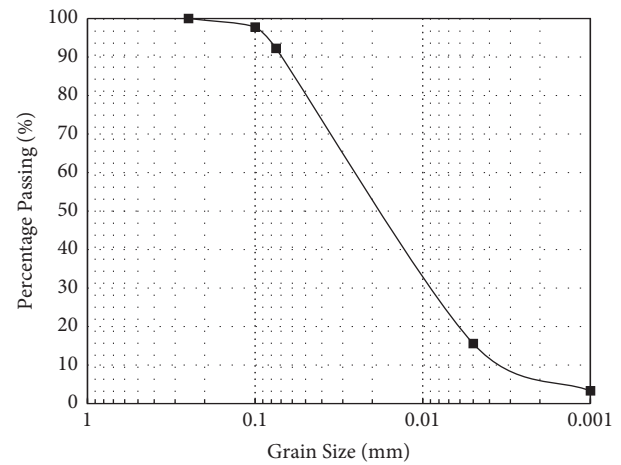


FIGURE 2: Grain size distribution curve of loess.

2.3. Test Loading Scheme. According to the results of test loading and stress analysis of hollow cylinders by Hight et al. [25, 26], the stresses on hollow cylinder specimens include axial stress σ_z , shear stress $\tau_{z\theta}$, radial stress σ_r , and hoop stress σ_θ . These stresses are caused by the axial load W , the torsion moment M_T around the axis, the outer chamber pressure P_o , and the inner chamber pressure P_i . These forces can be calculated by formulas (1) ~ (4). The application of these forces can be controlled by the stress parameters of the intermediate principal stress coefficient b , mean principal stress p , deviatoric stress ratio η , and principal stress direction angle α , which are defined in formulas (5) ~ (8). The stress state of the specimen and soil element is shown in Figure 4.



FIGURE 3: Compacted loess sample.

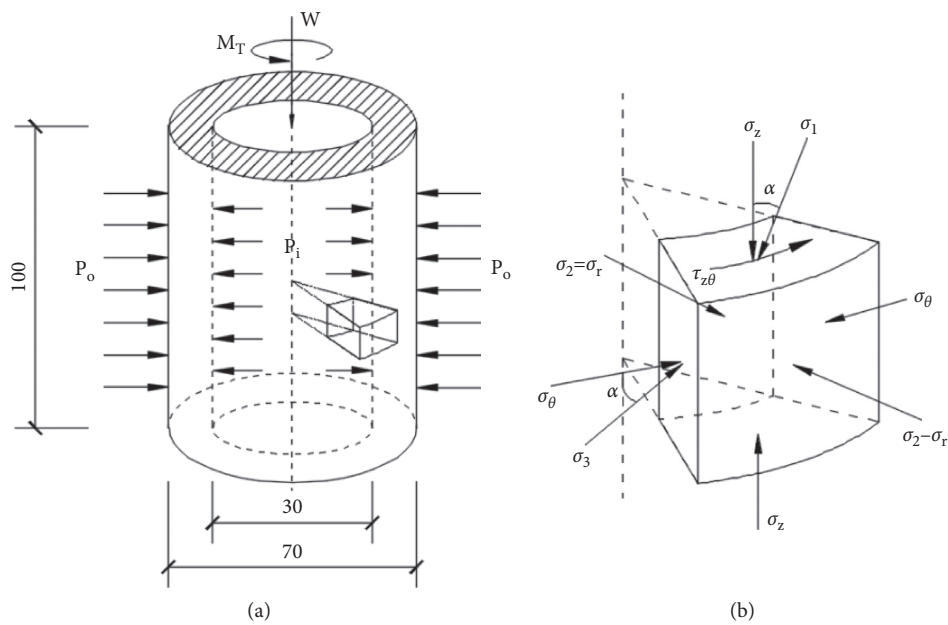


FIGURE 4: Schematic diagram of the stress on the sample. (a) Schematic diagram of sample size and force. (b) Soil element stress.

$$P_o = \frac{A\sigma_r + B\sigma_\theta}{2R_o}, \quad (1)$$

$$P_i = \frac{A\sigma_r - B\sigma_\theta}{2R_i}, \quad (2)$$

$$W = \pi \left[\sigma_z (R_o^2 - R_i^2) - (P_o R_o^2 - P_i R_i^2) \right], \quad (3)$$

$$M_T = \frac{2}{3} \pi \tau_{z\theta} (R_o^3 - R_i^3), \quad (4)$$

$$\alpha = \frac{1}{2} \arctan \frac{2\tau_{z\theta}}{\sigma_z - \sigma_\theta}, \quad (5)$$

$$b = \frac{\sigma_2 - \sigma_3}{\sigma_1 - \sigma_3}, \quad (6)$$

$$\eta = \frac{q}{p}, \quad (7)$$

$$p = \frac{1}{3} (\sigma_1 + \sigma_2 + \sigma_3), \quad (8)$$

where R_o is the outer radius of the sample; R_i is the inner radius of the sample; $A = R_o + R_i$; $B = R_o - R_i$; and σ_1 , σ_2 , and σ_3 are the major principal stress, the intermediate principal stress, and the minor principal stress, respectively. Deviator stress $q = 1/\sqrt{2}(\sqrt{(\sigma_1 - \sigma_2)^2 + (\sigma_2 - \sigma_3)^2 + (\sigma_3 - \sigma_1)^2})$, and p is the mean principal stress. The deviatoric stress ratio is mainly used to characterize the relative magnitude relationship between the deviator stress and the spherical stress. Existing studies have proven that the deviatoric stress ratio has a certain influence on the deformation characteristics of soil [27]. This test mainly studies the effects of the mean principal stress, dry density, and deviatoric stress ratio on the dynamic modulus and damping ratio of compacted loess under the action of a circular stress path.

2.4. Test Program and Scheme. Some scholars studied the dynamic modulus and damping ratio of frozen soil by applying dynamic loading step by step and obtained reliable test results [28, 29]. In this paper, referring to the above literature test method according to the principle of equivalent stress, and using a sine wave type, dynamic loads in the axial and torsional directions were applied step by step, at a load frequency of 1 Hz. Each level of bidirectional dynamic load was applied for 20 cycles. The time history curve of the load is shown in Figure 5. To simulate the circular dynamic stress path, the amplitude of the axial dynamic stress σ_m and the torsional shear stress τ_m is maintained at $\sigma_m = 2\tau_m$ at each stage of dynamic loading, and the phase difference between them is maintained at 90° . The ideal dynamic stress path in the $\tau_{z\theta d} \sim (\sigma_{zd} - \sigma_{\theta d})/2$ stress coordinate system and an actual dynamic stress path in the test are shown in Figure 6(a) and 6(b), respectively, indicating that the test can better simulate the circular dynamic stress path. To ensure the stability of the data, a complete hysteresis loop of the 10th cycle was selected as the research object for each stage of loading, and all stresses and strains were taken as the average value of a cycle. In this paper, the influence of the average effective principal stress, dry density, and deviatoric stress ratio on the dynamic modulus and damping ratio of compacted loess under a circular dynamic stress path is considered. Under the action of additional stress and gravity stress of the soil under the building foundation, as the depth increases, the mean principal stress and deviator stress are constantly changing, so the deviator stress ratio is also different. There will be both isotropic stress state and anisotropic stress state in the foundation. In order to compare the test results with each other and reflect the influence of spherical stress and deviator stress on the dynamic modulus and damping ratio, three average principal stresses of 50 kPa, 100 kPa, and 200 kPa and three deviatoric stress ratios of 0, 0.2, and 0.4 were selected. The specific test plan is shown in Table 2. The initial principal stress direction angle of all samples is $\alpha = 0^\circ$, and the intermediate principal stress coefficient $b = 0$. After the sample is installed, the consolidation stress is applied according to the test plan, and all the samples are consolidated by drainage. According to the specification [30], when the axial deformation of the sample

within 5 minutes is less than 0.005 mm, it is considered that its consolidation has reached stability. The two-way dynamic load is applied to the sample at the same time according to the test requirements.

3. Results and Discussion

In soil dynamics, the Hardin–Drnevich model is a widely used dynamic viscoelastic-plastic model that can describe the dynamic stress-strain relationship of soil by a hyperbolic curve. The model regards soil as a viscoelastic body. It assumes that the skeleton curve of the dynamic stress-dynamic strain relationship is a hyperbola and uses the equivalent dynamic shear modulus G_{eq} and equivalent damping ratio λ_{eq} reflect the nonlinearity and hysteresis of the soil dynamic stress-strain relationship, and both the shear modulus and damping ratio are expressed as functions of dynamic strain amplitude, namely, $G_{eq} = G(\gamma_d)$ and $\lambda_{eq} = \lambda(\gamma_d)$. When the dynamic shear strain $\gamma_d = \infty$, the curve takes the maximum dynamic shear stress τ_{dmax} as the asymptote. When $\gamma_d = 0$, the tangent slope of the curve is the maximum shear modulus G_0 . The expression of the torsional dynamic shear stress-strain relationship is as follows:

$$\tau_d = \frac{\gamma_d}{1/G_0 + \gamma_d/\tau_{dmax}} = \frac{\gamma_d}{a + b\gamma_d}, \quad (9)$$

$$\frac{1}{G_d} = \frac{\gamma_d}{\tau_d} = \frac{1}{G_0} + \frac{\gamma_d}{\tau_{dmax}} = a + b\gamma_d, \quad (10)$$

where τ_{dmax} is the maximum dynamic shear stress; G_0 is the initial dynamic shear modulus; G_d is the dynamic shear modulus; and a and b are the intercept and slope corresponding to the straight line in the relationship curve $1/G_d \sim \gamma_d$, respectively. The axial dynamic stress-strain relationship curve is similar.

3.1. The Effect of the Mean Principal Stress on the Dynamic Shear Modulus and Dynamic Compression Modulus.

Figure 7 shows the dynamic compression modulus curve and dynamic shear modulus curve of different mean principal stresses of compacted loess with a dry density of 1.62 g/cm^3 at the same deviatoric stress ratio. Figures 7(a), 7(c), and 7(e) shows the variation curve of the dynamic compression modulus with axial dynamic strain, and Figures 7(b), 7(d), and 7(f) shows the variation curve of the dynamic shear modulus with shear strain. The figure shows that the mean principal stress has an obvious influence on the dynamic compression modulus and dynamic shear modulus. When the same shear strain is reached under the same conditions, the larger the mean principal stress is, the greater the dynamic compression modulus and dynamic shear modulus are. The spherical stress represented by the mean principal stress can produce a larger “binding force” on the soil unit, and the dynamic deformation requires greater dynamic stress, so the dynamic compression modulus and dynamic shear modulus are both greater. Both the dynamic compression modulus and the dynamic shear modulus decrease continuously with the development of strain and finally tend

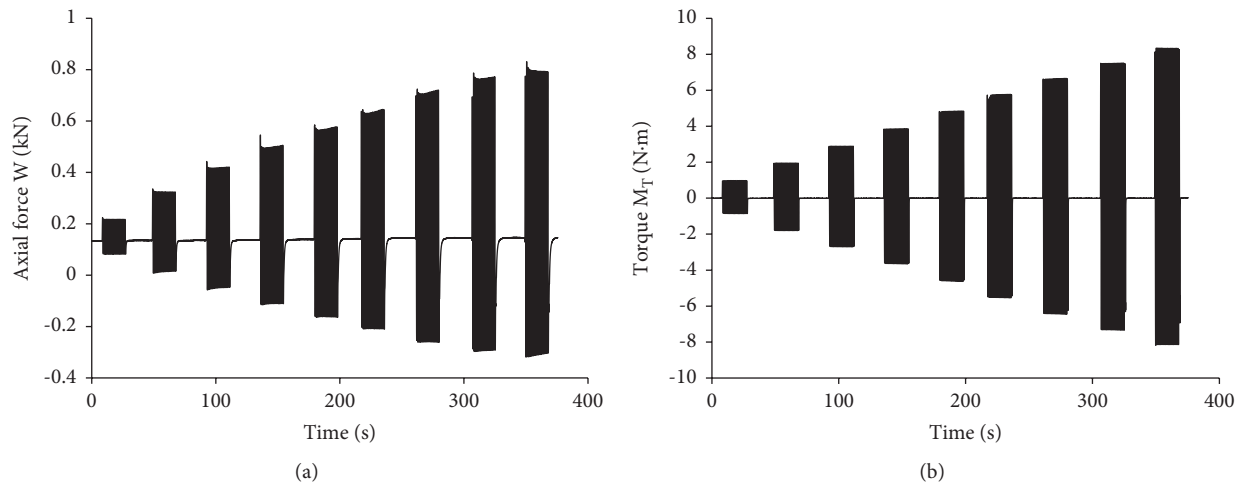


FIGURE 5: The actual time history curve of a certain test with two-way and step-by-step loading. (a) Time history curve of axial force loading step by step. (b) Time history curve of torque loading step by step.

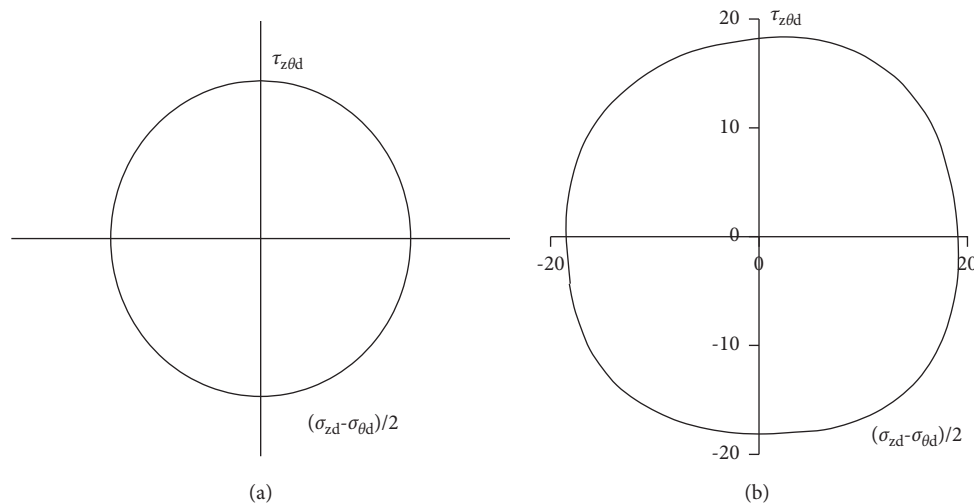


FIGURE 6: Ideal dynamic stress path and the certain dynamic stress path actually loaded. (a) Ideal circular dynamic stress path. (b) A cyclic dynamic stress path of measured loading.

TABLE 2: Test plan.

Dry density, ρ_d (g/cm ³)	Deviatoric stress ratio (η)	Mean principal stress, p (kPa)	Consolidation state
1.62	0	50, 100, 200	Isotropic consolidation
1.62	0.2	50, 100, 200	Anisotropic consolidation
1.62	0.4	50, 100, 200	Anisotropic consolidation
1.52	0	50	Isotropic consolidation
1.52	0.2	50	Anisotropic consolidation
1.52	0.4	50	Anisotropic consolidation
1.44	0	50	Isotropic consolidation
1.44	0.2	50	Anisotropic consolidation
1.44	0.4	50	Anisotropic consolidation

Note. Deviatoric stress ratio, $\eta = q/p$, where p is the mean principal stress, $q = 1/\sqrt{2}(\sqrt{(\sigma_1 - \sigma_2)^2 + (\sigma_2 - \sigma_3)^2 + (\sigma_3 - \sigma_1)^2})$.

to be close and stable, but the degradation rate of the dynamic shear modulus is faster than that of the dynamic compression modulus in the early stage of strain

development. This is due to the horizontal reciprocating torsional shear action that destroys the soil structure; microcracks appear inside, the deformation develops

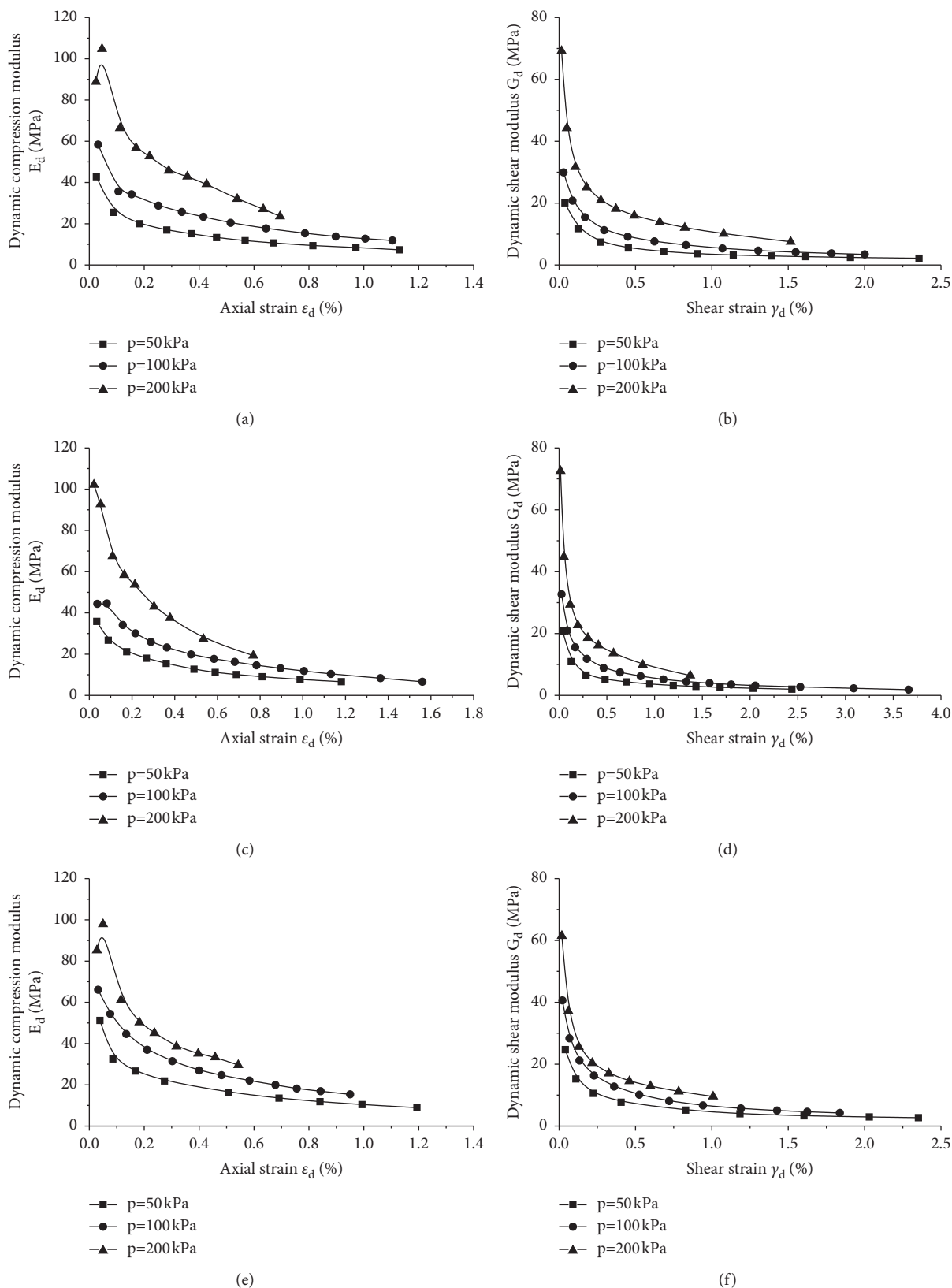


FIGURE 7: Curves of the dynamic compression modulus and dynamic shear modulus of compacted loess with different mean principal stresses under a circular dynamic stress path ($\rho_d = 1.62 \text{ g/cm}^3$). (a) Dynamic compression modulus curve ($\eta = 0$). (b) Dynamic shear modulus curve ($\eta = 0$). (c) Dynamic compression modulus curve ($\eta = 0.2$). (d) Dynamic shear modulus curve ($\eta = 0.2$). (e) Dynamic compression modulus curve ($\eta = 0.4$). (f) Dynamic shear modulus curve ($\eta = 0.4$).

rapidly, and the dynamic modulus drops sharply. The small vertical dynamic stress will further compact the soil sample at the initial stage, so part of the dynamic compression modulus slightly increases in the initial stage of strain. However, due to the combined action of shear stress, most specimens exhibit compressive deformation until they fail with increasing dynamic stress. Therefore, the rate of decrease of the dynamic compression modulus in the initial stage of strain development is slower than that of the dynamic shear modulus.

3.2. The Effect of Dry Density on Dynamic Shear Modulus and Dynamic Compression Modulus. Figure 8 shows the dynamic compression modulus curves and dynamic shear modulus curves of different dry densities under the same deviatoric stress ratio when the mean principal stress is 50 kPa. Figures 8(a), 8(c), and 8(e) show the variation curves of the dynamic compression modulus with axial dynamic strain when the deviatoric stress ratio is 0, 0.2, and 0.4, respectively. Figures 8(b), 8(d), and 8(f) shows the variation curves of the dynamic shear modulus with shear strain when the deviatoric stress is 0, 0.2, and 0.4, respectively. It can be seen from the figure that the dry density has a significant effect on the dynamic compression modulus of compacted loess and has a slight effect on the dynamic shear modulus. The dynamic modulus of compacted loess gradually decreases with the development of dynamic strain, but in the later stage of dynamic strain development, although the dynamic stress and dynamic strain increase significantly, the dynamic modulus eventually tends to a stable value, which is usually defined as the residual dynamic modulus. Under the same conditions, the dynamic compression modulus that reaches the same dynamic strain increases with increasing dry density, especially when the axial dynamic strain is less than 1%, and the residual dynamic compression modulus, which tends to be stable with the development of dynamic strain, is relatively large. Under the same conditions, the dynamic shear modulus reaching the same shear strain increases slightly with increasing dry density and finally tends to be basically the same as the residual dynamic shear modulus with the development of dynamic shear strain. It can be seen that that increasing the dry density of loess plays an important role in improving the dynamic compression modulus under axial strains below 1%, but the effect of resisting dynamic shear deformation is not obvious.

3.3. The Effect of the Deviatoric Stress Ratio on the Dynamic Shear Modulus and Dynamic Compression Modulus. Since the deviatoric stress ratio has roughly the same influence on the dynamic compression modulus curves and dynamic shear modulus curves of compacted loess with different dry densities, only the test result with a dry density of 1.62 g/cm³ is used as an example for illustration, as shown in Figure 9(a) and 9(b). It can be seen from the figure that the deviatoric stress ratio has a certain effect on the dynamic compression modulus curve and the dynamic shear modulus curve. When the deviatoric stress ratio is 0 and 0.2, the dynamic compression modulus curves almost coincide.

However, when the deviatoric stress ratio reaches 0.4, the dynamic compression modulus curve obviously improves. Although the dynamic shear modulus curve also shows the same rule, the increase in the dynamic shear modulus is relatively small. Existing studies have shown that the initial structural of undisturbed loess are easily destroyed by increased deviatoric stress, so the dynamic modulus of undisturbed loess decreases with the increase of the deviatoric stress ratio under cyclic torsional shear. The samples used in this test are all compacted loess, and the original structure has been destroyed during sample preparation, so the degree of compaction and the bite force between particles have become the main factors affecting the dynamic modulus [27]. Because the increase in the deviatoric stress ratio increases the axial force, the larger deviatoric stress ratio causes the soil sample to obtain a larger bite force in the consolidation stage; thus, the dynamic compression modulus and dynamic shear modulus of the soil sample are increased.

3.4. Initial Dynamic Shear Modulus and Initial Dynamic Compression Modulus under a Circular Dynamic Stress Path. The $1/G_d \sim \gamma_d$ relationship curve obtained by equation (10) is a straight line. When the dynamic shear strain γ_d or the dynamic strain ε_d approaches 0, the initial dynamic shear modulus and the initial dynamic elastic modulus can be obtained, that is, the reciprocal of intercept a , as shown in equations (11) and (12). When the dynamic shear strain γ_d or the dynamic strain ε_d approaches ∞ , the maximum dynamic shear stress and the maximum dynamic stress can be obtained, that is, the reciprocal of the straight line slope b , as shown in equations (13) and (14).

$$G_0 = G_d|_{\gamma_d \rightarrow 0} = \frac{1}{a_1}, \quad (11)$$

$$E_0 = E_d|_{\varepsilon_d \rightarrow 0} = \frac{1}{a_2}, \quad (12)$$

$$\tau_{d\max} = \tau_d|_{\gamma_d \rightarrow +\infty} = \frac{1}{b_1}, \quad (13)$$

$$\sigma_{d\max} = \sigma_d|_{\varepsilon_d \rightarrow +\infty} = \frac{1}{b_2}. \quad (14)$$

When the mean principal stress is 50 kPa, the initial dynamic modulus and maximum dynamic stress of compacted loess with different dry densities and deviatoric stress ratios under the action of the circular dynamic stress path are shown in Table 3. Except for individual data, the maximum axial dynamic stress and the maximum dynamic shear stress increase with increasing dry density and deviatoric stress ratio of the compacted loess under the same conditions. The initial dynamic compression modulus and initial dynamic shear modulus of compacted loess increase with increasing dry density. When the deviatoric stress ratio is 0, 0.2, and 0.4, the initial dynamic compression modulus and the initial dynamic shear modulus of compacted loess with a dry density of 1.62 g/cm³ compared to 1.44 g/cm³ increases percentage as shown in Table 4. The average

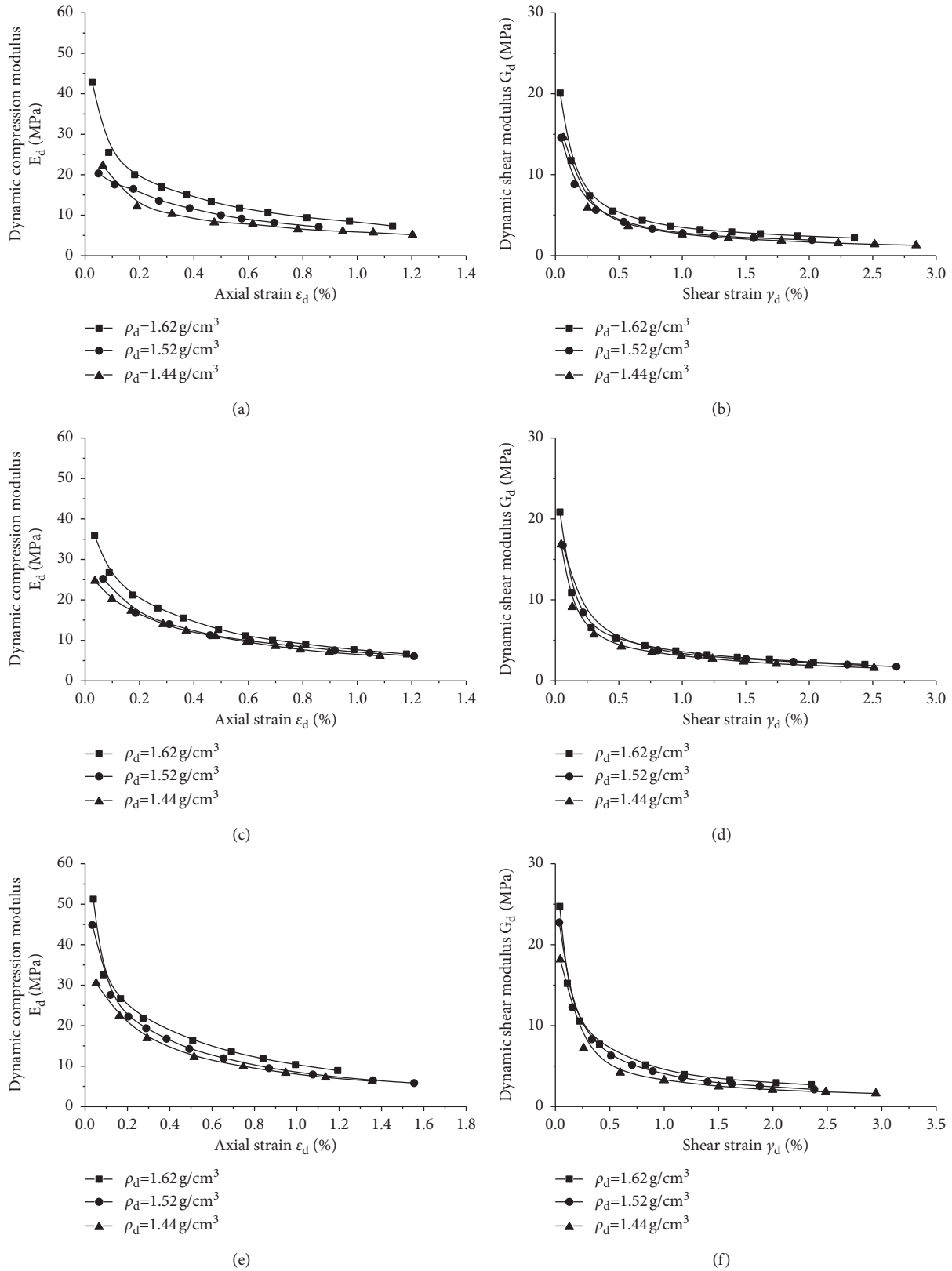


FIGURE 8: Curves of the dynamic compression modulus and dynamic shear modulus of compacted loess with different dry densities under a circular dynamic stress path ($p = 50 \text{ kPa}$). (a) Dynamic compression modulus curve ($\eta = 0$). (b) Dynamic shear modulus curve ($\eta = 0$). (c) Dynamic compression modulus curve ($\eta = 0.2$). (d) Dynamic shear modulus curve ($\eta = 0.2$). (e) Dynamic compression modulus curve ($\eta = 0.4$). (f) Dynamic shear modulus curve ($\eta = 0.4$).

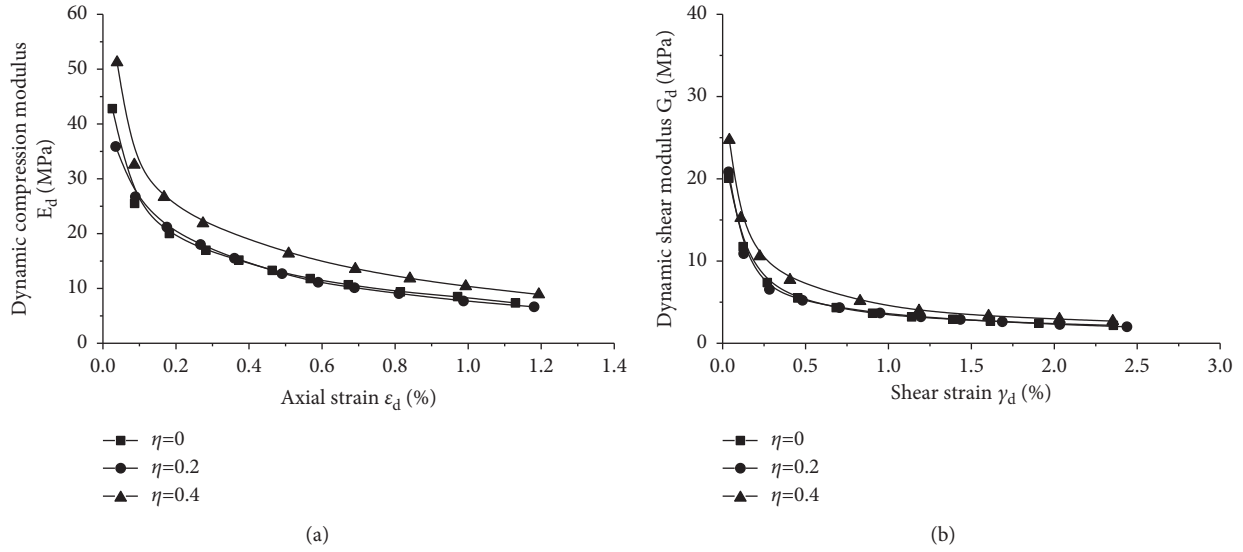


FIGURE 9: Curves of the dynamic compression modulus and dynamic shear modulus of compacted loess with different deviatoric stress ratios under a circular dynamic stress path ($\rho_d = 1.62 \text{ g/cm}^3$). (a) Dynamic compression modulus curve. (b) Dynamic shear modulus curve.

TABLE 3: Initial dynamic compression modulus and initial dynamic shear modulus of compacted loess with different dry densities and deviatoric stress ratios.

Dry density	$\rho_d = 1.62 \text{ g/cm}^3$				$\rho_d = 1.52 \text{ g/cm}^3$				$\rho_d = 1.44 \text{ g/cm}^3$			
Deviator stress ratio	σ_{dmax} (kPa)	E_0 (MPa)	τ_{dmax} (kPa)	G_0 (MPa)	σ_{dmax} (kPa)	E_0 (MPa)	τ_{dmax} (kPa)	G_0 (MPa)	σ_{dmax} (kPa)	E_0 (MPa)	τ_{dmax} (kPa)	G_0 (MPa)
$\eta = 0$	105.9	33.78	57.8	11.36	87.6	23.36	43.5	10.09	83.6	18.48	40.5	8.55
$\eta = 0.2$	95.9	36.76	56.8	11.47	96.1	26.46	54.0	11.40	86.6	26.74	45.4	10.62
$\eta = 0.4$	133.3	44.44	70.8	16.26	104.1	43.86	55.2	16.86	103.9	33.78	53.4	10.29

amplitude of the initial dynamic compressive modulus increase is higher than the dynamic shear modulus. With the increase in the deviatoric stress ratio, the initial dynamic compression modulus and initial dynamic shear modulus of compacted loess also increase. When the dry density is 1.62 g/cm^3 , 1.52 g/cm^3 , and 1.44 g/cm^3 , the initial dynamic compression modulus and the initial dynamic shear modulus of compacted loess with a deviatoric stress ratio of 0.4 compared to 0 increases percentage as shown in Table 5. This indicates that increasing the dry density and deviatoric stress ratio of compacted loess can greatly improve the bidirectional initial dynamic modulus, which is beneficial to the seismic resistance of soil under circular dynamic stress.

3.5. Dynamic Shear Damping Ratio and Dynamic Compression Damping Ratio under the Action of a Circular Dynamic Stress Path. According to the principle of the equivalent dynamic visco-elastoplastic model, the 10th cycle of dynamic load applied to each stage is selected, and the hysteresis curve of each cyclic stress-strain relationship can be drawn. Most of the hysteresis curves are approximately elliptical, and the shear stress-strain relationship is taken as an example for illustration, as shown in Figure 10. The torsional damping ratio λ_τ is defined as equation (15). The dynamic stress-strain relationship

in the axial direction is similar to that in the torsion-shear direction, so the axial damping ratio λ_z is similar.

$$\lambda_\tau = \frac{1}{4\pi} \frac{\Delta S}{S}. \quad (15)$$

In the formula, ΔS is the energy lost in a cycle, that is, the total area of the approximate ellipse. S is the elastic strain energy, that is, the area of ΔOAB .

The curves of the dynamic compression damping ratio and dynamic shear damping ratio of compacted loess with three mean principal stresses of 50 kPa, 100 kPa, and 200 kPa under a circular stress path are calculated and analyzed when the dry density is 1.62 g/cm^3 and the deviatoric stress ratio is 0, 0.2, and 0.4, respectively. Since the mean principal stress has roughly the same effect on the damping ratio under the same deviatoric stress ratio, the semilogarithmic curve of the damping ratio and strain with a deviatoric stress ratio of 0.2 is only taken as an example, as shown in Figure 11. It can be seen from the figure that the dynamic compression damping ratio and dynamic shear damping ratio can be fitted by equations (16) and (17), respectively:

$$\lambda_z = k_z \log(\varepsilon_d) + l_z, \quad (16)$$

$$\lambda_\tau = k_\tau \log(\gamma_d) + l_\tau, \quad (17)$$

TABLE 4: The percentage increase of the initial compressive modulus and initial shear modulus of compacted loess when the dry density is 1.62 g/cm^3 compared to 1.44 g/cm^3 at different deviator stress ratios.

Deviator stress ratio	Dynamic modulus	
	Relative increase percentage of E_0 (%)	Relative increase percentage of G_0 (%)
$\eta = 0$	82.8	32.9
$\eta = 0.2$	37.5	10.2
$\eta = 0.4$	31.6	58.0

TABLE 5: The percentage increase of initial compressive modulus and initial shear modulus of compacted loess with different dry density when deviator stress ratio $\eta = 0.4$ compared to $\eta = 0$.

Dry density	Dynamic modulus	
	Relative increase percentage of E_0 (%)	Relative increase percentage of G_0 (%)
$\rho_d = 1.62 \text{ g/cm}^3$	31.6	43.1
$\rho_d = 1.52 \text{ g/cm}^3$	87.8	67.1
$\rho_d = 1.44 \text{ g/cm}^3$	82.8	20.4

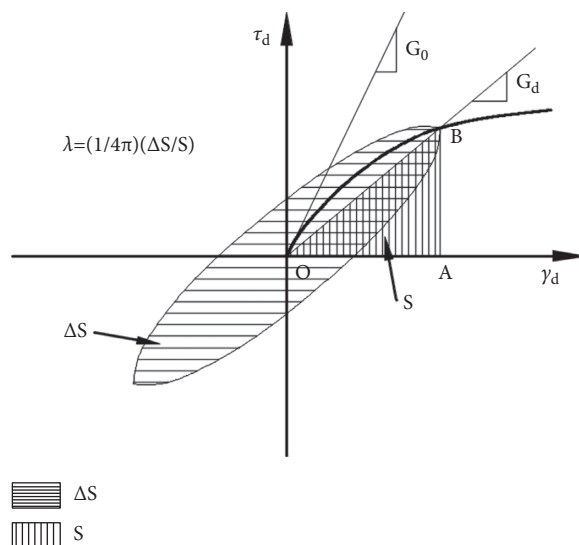


FIGURE 10: Schematic diagram of the hysteresis loop and damping ratio calculation.

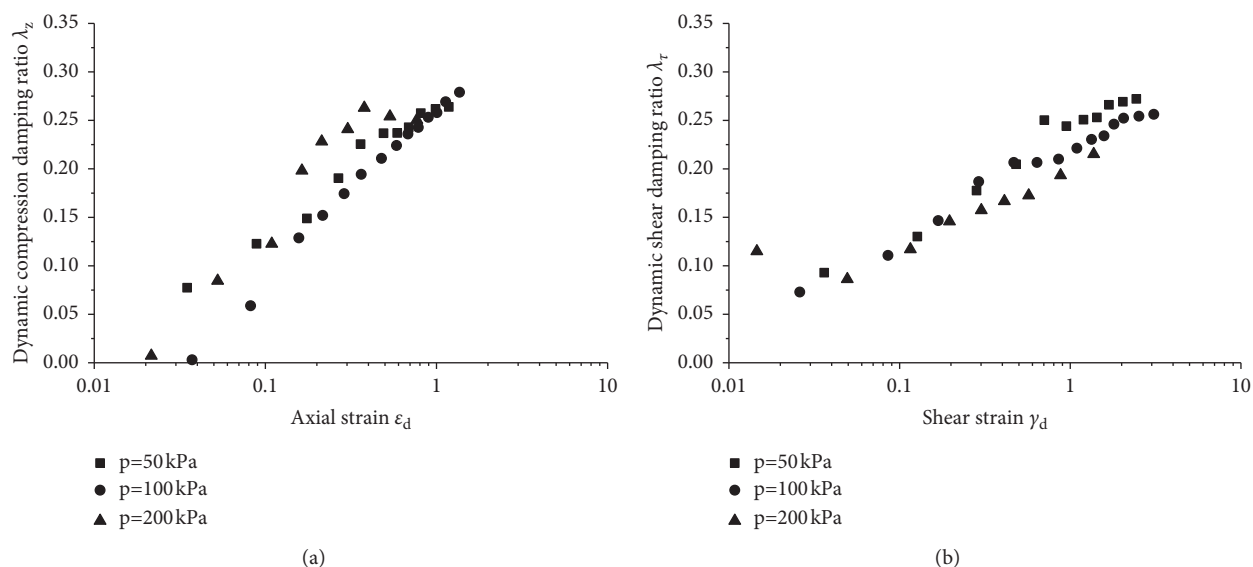


FIGURE 11: Scatter plot of the dynamic compression damping ratio and dynamic shear damping ratio of compacted loess with different mean principal stresses under the circular stress path ($\eta = 0.2$). (a) Dynamic compression damping ratio. (b) Dynamic shear damping ratio.

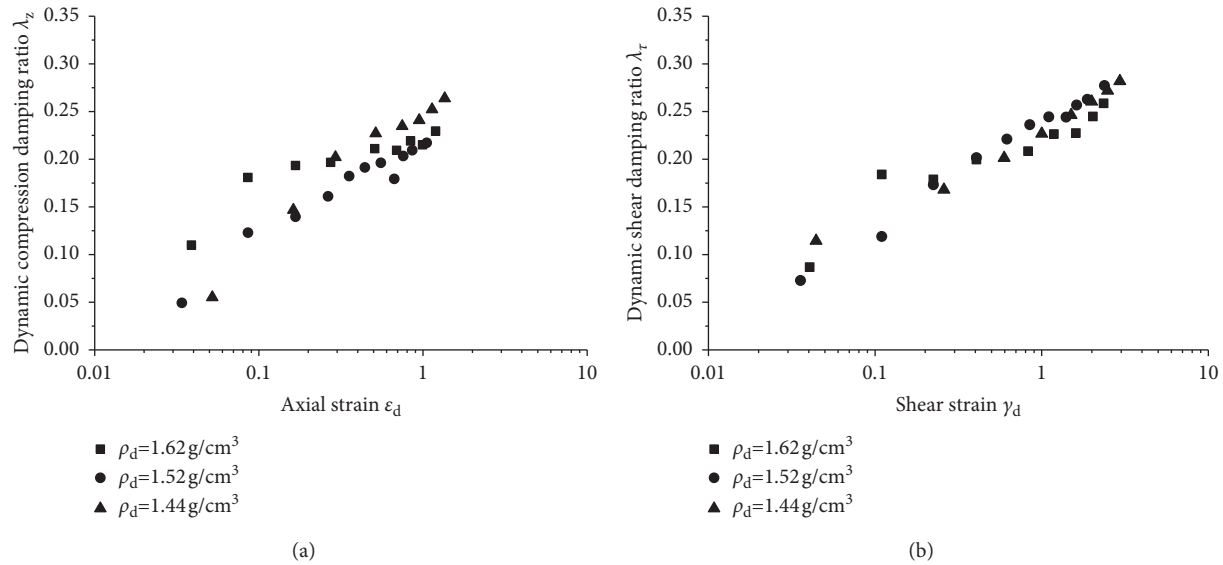


FIGURE 12: Scatter plot of the dynamic compression damping ratio and dynamic shear damping ratio of compacted loess with different dry densities under the circular stress path ($\eta = 0.4$). (a) Dynamic compression damping ratio. (b) Dynamic shear damping ratio.

where ε_d is the axial dynamic strain, γ_d is the dynamic shear strain, k_z is the slope of the fitted straight line in the $\lambda_z \sim \log(\varepsilon_d)$ graph, l_z is the intercept of the fitted straight line in the $\lambda_z \sim \log(\varepsilon_d)$ graph, k_τ is the slope of the fitted straight line in the $\lambda_\tau \sim \log(\gamma_d)$ graph, and l_τ is the intercept of the fitted straight line in the $\lambda_\tau \sim \log(\gamma_d)$ graph.

The dynamic compression damping ratio and dynamic shear damping ratio of compacted loess both increase with increasing dynamic strain. The slope of the straight line k_z is obviously larger than k_τ , indicating that the dynamic compression damping ratio increases faster than the dynamic shear damping ratio with the development of dynamic strain. However, the dynamic shear damping is larger than the dynamic compression damping ratio when it reaches the same dynamic strain at the beginning of the dynamic load. As the strain develops, the two eventually reach approximately 0.3 and become stable. It can be seen from the figure that the mean principal stress has a certain effect on the dynamic compression damping ratio and the dynamic shear damping ratio. Under the same conditions, the dynamic compression damping ratio reaching the same dynamic strain increases with increasing mean principal stress, and the dynamic shear damping ratio decreases with increasing mean principal stress.

In order to analyze the influence of dry density on damping ratio of compacted loess under circular dynamic stress path, the $\lambda_z \sim \log(\varepsilon_d)$ curve and $\lambda_\tau \sim \log(\gamma_d)$ curve of compacted loess with different dry density at the same deviatoric stress ratio are calculated when the mean principal stress is 50 kPa. Due to the influence of dry density on the damping ratio of compacted loess is almost the same at the same deviatoric stress ratio, only the semilogarithmic curve of the damping ratio and strain with a deviatoric stress ratio of 0.4 is taken as an example for illustration, as shown in Figure 12. It can be seen from the figure that the scatter points of the dynamic compression damping ratio and

dynamic shear damping ratio of different dry densities are concentrated in a band-shaped area, which can be fitted with the straight lines of equations (16) and (17), respectively, and the slopes and intercepts of the two are close, indicating that the dry density has no effect on the dynamic compression damping ratio and the dynamic shear damping ratio of compacted loess, which is similar to the conclusions obtained by Wang et al. on the effect of dry density on the damping ratio under unidirectional torsional shear [31].

In order to study the influence of deviatoric stress ratio on damping ratio of compacted loess under circular dynamic stress path, the $\lambda_z \sim \log(\varepsilon_d)$ curve and $\lambda_\tau \sim \log(\gamma_d)$ curve of compacted loess with different deviatoric stress ratios under the same dry density are calculated when the mean principal stress is 50 kPa. The semilogarithmic curves of the damping ratio and strain of the three deviator stress ratios when the dry density is 1.62 g/cm^3 are illustrated in Figure 13. It can be seen from the figure that when the dynamic strain and shear strain are less than 1%, the dynamic compression damping ratio and dynamic shear damping ratio of compacted loess slightly increase with the increase of deviator stress ratio. However, when the dynamic strain and the shear strain exceed 1%, the influence of the deviatoric stress ratio becomes more obvious. When the same strain is reached, the larger the deviatoric stress ratio is, the smaller the dynamic compression damping ratio and the dynamic shear damping ratio are. This is different from the research results of Wang Zhijie and others on the damping ratio of undisturbed loess under cyclic torsional shear [27]. The damping ratio of undisturbed loess increases obviously with the increase of partial stress ratio under simple torsional shear, which is consistent with the influence law of compacted loess in this test when the strain is less than 1%. However, when the dynamic strain is greater than 1%, the bidirectional dynamic stress makes the soil particles more prone to dislocation. The decrease of soil particle contact

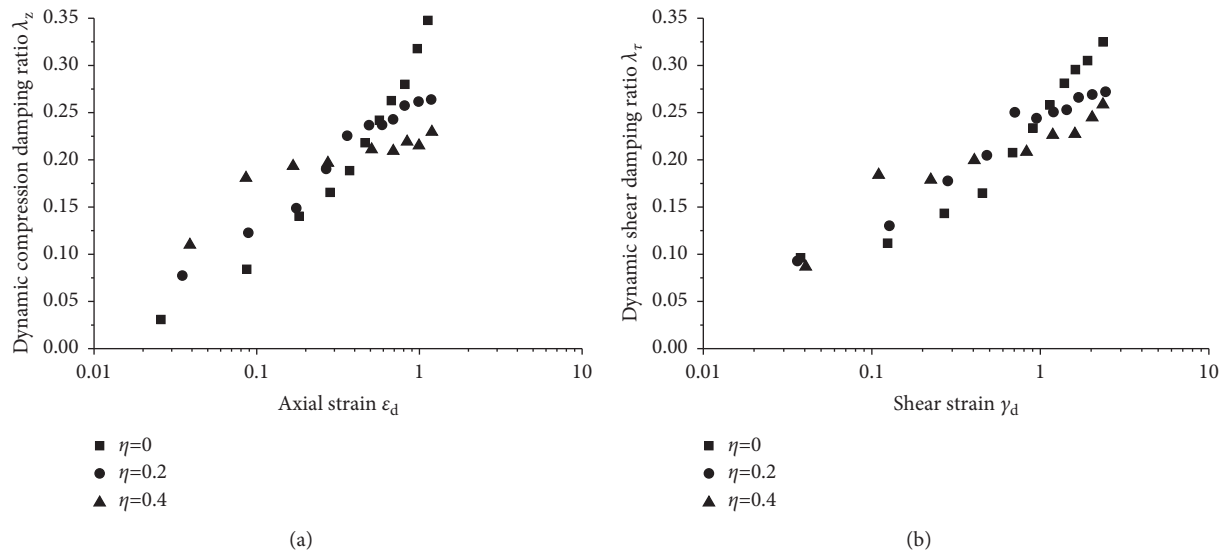


FIGURE 13: Scatter plot of the dynamic compression damping ratio and dynamic shear damping ratio of compacted loess with different deviatoric stress ratios under the circular stress path ($\rho_d=1.62 \text{ g/cm}^3$). (a) Dynamic compression damping ratio. (b) Dynamic shear damping ratio.

point increases the energy dissipation capacity of loess, but the increase in deviator stress can accelerate the development of dynamic strain and reduce the energy dissipation capacity of loess.

4. Conclusions

In light of the fact that compacted loess is widely used as a foundation and subgrade in engineering construction in Northwest China, a hollow cylindrical torsion shear system is used to apply dynamic stress in two directions step by step to simulate the circular dynamic stress path caused by earthquakes, traffic, waves, etc. The effects of the mean principal stress, dry density, and deviatoric stress ratio on the dynamic compression modulus, dynamic shear modulus, dynamic compression damping ratio, and dynamic shear damping ratio of compacted loess are studied experimentally, and the main conclusions are summarized as follows:

- (1) Under the action of the circular dynamic stress path, the mean principal stress has a significant effect on the dynamic compression modulus and dynamic shear modulus of compacted loess. When the same shear strain is reached under the same conditions, the greater the mean principal stress is, the larger the dynamic compression modulus and dynamic shear modulus are. The dry density of compacted loess has an obvious influence on the dynamic compression modulus. Under the same conditions, the dynamic compression modulus increases with increasing dry density. The effect of dry density on the dynamic shear modulus is relatively weak, and the dynamic shear modulus increases slightly with increasing dry density. The increase in the deviatoric stress ratio from 0 to 0.2 has little effect on the dynamic
- (2) The larger the dry density and deviatoric stress ratio of compacted loess under the action of the circular dynamic stress path, the larger its initial dynamic compression modulus and initial dynamic shear modulus, and the average amplitude of the increase in the initial dynamic compression modulus is greater than that of the increase in the initial dynamic shear modulus. The greater the dry density and deviatoric stress ratio, the greater the maximum dynamic stress and maximum dynamic shear stress of compacted loess, and the higher the dynamic stress required for failure.
- (3) Under the action of the circular dynamic stress path, the dynamic compression damping ratio and the dynamic shear damping ratio of the compacted loess can be well fitted by a straight line in semilogarithmic coordinates with the strain, and the damping ratio increases with increasing strain, finally stabilizing at approximately 0.3. The dynamic compression damping ratio increases with increasing mean principal stress, and the dynamic shear damping ratio decreases with increasing mean principal stress. Dry density has no effect on the dynamic compression damping ratio and dynamic shear damping ratio of compacted loess. The deviatoric stress ratio has little effect on the dynamic compression damping ratio and dynamic shear damping ratio under small values of strain. When the dynamic

strain exceeds 1%, the greater the deviator stress is, the smaller the dynamic compression damping ratio and the dynamic shear damping ratio.

References

- [1] P. Subramaniam and S. Banerjee, "Shear modulus degradation model for cohesive soils," *Soil Dynamics and Earthquake Engineering*, vol. 53, pp. 210–216, 2013.
- [2] P. Kalligiolou, T. Tika, and K. Pitilakis, "Shear modulus and damping ratio of cohesive soils," *Journal of Earthquake Engineering*, vol. 12, no. 6, pp. 879–913, 2008.
- [3] M. Y. Fattah, M. J. Al-Mosawi, and A. F. I. Al-Ameri, "Dynamic response of saturated soil - foundation system acted upon by vibration," *Journal of Earthquake Engineering*, vol. 21, no. 7, pp. 1158–1188, 2017.
- [4] T. Feng, Y. Tang, Q. Wang, J. Zhang, and J. Song, "Experimental investigation of dynamic characteristics of subsea sand-silt mixtures," *Advances in Civil Engineering*, vol. 2019, Article ID 5619039, 9 pages, 2019.
- [5] I. Towhata and K. Ishihara, "Undrained strength of sand undergoing cyclic rotation of principal stress axes," *Soils and Foundations*, vol. 25, no. 2, pp. 135–147, 1985.
- [6] D. Zhang, F. Luo, Z. Zhu et al., "Study on mechanical properties of gravelly sand under different stress paths," *Advances in Civil Engineering*, vol. 2021, Article ID 8898814, 21 pages, 2021.
- [7] K. W. Abdul Kareem, M. Y. Fattah, and Z. S. M. Khaled, "Response of circular machine foundation resting on sandy soil to harmonic excitation," *Journal of Engineering Science & Technology*, vol. 15, no. 2, pp. 831–845, 2020.
- [8] K. Abdul Kareem, M. Y. Fattah, and Z. Khaled, "Assessment of changes in shear strength parameters for soils below circular machine foundation," *International Journal of Engineering*, vol. 33, no. 8, pp. 1491–1498, 2020.
- [9] K. Ishihara and I. Towhata, "Sand response to cyclic rotation of principal stress directions as induced by wave loads," *Soils and Foundations*, vol. 23, no. 4, pp. 11–26, 1983.
- [10] K. Miura, S. Toki, and S. Miura, "Deformation prediction for anisotropic sand during the rotation of principal stress axes," *Soils and Foundations*, vol. 26, no. 3, pp. 42–56, 1986.
- [11] A. Lashkari and M. Latifi, "A constitutive model for sand liquefaction under continuous rotation of principal stress axes," *Mechanics Research Communications*, vol. 36, no. 2, pp. 215–223, 2009.
- [12] R. R. Zhou, F. Zhang, and K. Zhao, "Experimental study on excess pore pressure and deformation of saturated silt under complex stress paths," *Journal of Natural Disasters*, vol. 27, no. 6, pp. 173–179, 2018.
- [13] F. Zhang, G. X. Chen, Q. Wu, and Z. Zhou, "Experimental study on undrained behavior of saturated silt subject to wave loading," *Rock and Soil Mechanics*, vol. 40, no. 7, pp. 2695–2702, 2019.
- [14] C. Gu, J. Wang, Y. Cai, Z. Yang, and Y. Gao, "Undrained cyclic triaxial behavior of saturated clays under variable confining pressure," *Soil Dynamics and Earthquake Engineering*, vol. 40, pp. 118–128, 2012.
- [15] C. Gu, Y. Q. Cai, and J. Wang, "Coupling effects of P-waves and S-waves based on cyclic triaxial tests with cyclic confining pressure," *Chinese Journal of Geotechnical Engineering*, vol. 34, no. 10, pp. 1903–1909, 2012.
- [16] X. Hu, Y. Zhang, L. Guo et al., "Cyclic behavior of saturated soft clay under stress path with bidirectional shear stresses," *Soil Dynamics and Earthquake Engineering*, vol. 104, pp. 319–328, 2018.
- [17] A. Inam, T. Ishikawa, and S. Miura, "Effect of principal stress axis rotation on cyclic plastic deformation characteristics of unsaturated base course material," *Soils and Foundations*, vol. 52, no. 3, pp. 465–480, 2012.
- [18] C. Gallage, B. Dareeju, M. Dhanasekar, and T. Ishikawa, "Effects of principal stress axis rotation on unsaturated rail track foundation deterioration," *Procedia Engineering*, vol. 143, pp. 252–259, 2016.
- [19] B. Dareeju, C. Gallage, T. Ishikawa, and M. Dhanasekar, "Effects of principal stress axis rotation on cyclic deformation characteristics of rail track subgrade materials," *Soils and Foundations*, vol. 57, no. 3, pp. 423–438, 2017.
- [20] J. Qian, Z. Du, X. Lu, X. Gu, and M. Huang, "Effects of principal stress rotation on stress-strain behaviors of saturated clay under traffic-load-induced stress path," *Soils and Foundations*, vol. 59, no. 1, pp. 41–55, 2019.
- [21] Z. T. Wang, P. Liu, D. Jeng, and Q. Yang, "Cyclic strength of sand under a nonstandard elliptical rotation stress path induced by wave loading," *Journal of Hydrodynamics*, vol. 29, no. 1, pp. 89–95, 2017.
- [22] Y. Wang, Y. Gao, L. Guo et al., "Cyclic response of natural soft marine clay under principal stress rotation as induced by wave loads," *Ocean Engineering*, vol. 129, pp. 191–202, 2017.
- [23] D. W. Cheng, Y. S. Luo, L. G. Yang, and X. Chen, "Effect of complex initial stress conditions on dynamic deformation behaviors of compacted loess," *Applied Mechanics and Materials*, vol. 90–93, pp. 67–73, 2011.
- [24] R. Wang, Z. Hu, X. Ren, F. Li, and F. Zhang, "Dynamic modulus and damping ratio of compacted loess under long-term traffic loading," *Road Materials and Pavement Design*, vol. 2011, Article ID 1924232, 15 pages, 2021.
- [25] D. W. Hight, A. Gens, and M. J. Symes, "The development of a new hollow cylinder apparatus for investigating the effects of principal stress rotation in soils," *Géotechnique*, vol. 33, no. 4, pp. 355–383, 1983.
- [26] H. J. Wang, R. F. Shen, and Q. G. Ma, "Dynamic strength of soil under multi-direction loading," *Journal of Tsinghua University*, vol. 4, pp. 93–98, 1996.
- [27] Z. J. Wang, Y. S. Luo, H. Guo, and H. Tian, "Effects of initial deviatoric stress ratios on dynamic shear modulus and damping ratio of undisturbed loess in China," *Engineering Geology*, vol. 143–144, pp. 43–50, 2012.
- [28] F. Zhao, L. Chang, and W. Zhang, "Experimental investigation of dynamic shear modulus and damping ratio of Qinghai-Tibet frozen silt under multi-stage cyclic loading," *Cold Regions Science and Technology*, vol. 170, Article ID 102938, 2020.

- [29] X. Z. Ling, F. Zhang, Q. L. Li, L. S. An, and J. H. Wang, "Dynamic shear modulus and damping ratio of frozen compacted sand subjected to freeze-thaw cycle under multi-stage cyclic loading," *Soil Dynamics and Earthquake Engineering*, vol. 76, pp. 111–121, 2015.
- [30] National standards of People's Republic of China, *Standard for Geotechnical Testing Method: GB/T 50123-2019*, China Planning Press, Beijing, China, 2019.
- [31] Z. J. Wang, Y. S. Luo, and D. Y. Tan, "Experimental study on the effects of dry density on dynamic properties of remodeled loess under condition of pre-shearing stress," *Northwestern Seismological Journal*, vol. 33, no. 4, pp. 349–353, 2011.

Designing a energy-efficient HVAC sysstem by utilization of U-shaped finned heat pipe heat exchanger

Pradyut Kumar Swain, *Department of Mechanical Engineering, Aryan Institute of Engineering & Technology, Bhubaneswar, pkswain25@gmail.com*

Kalpana Mallick, *Department of Mechanical Engineering, Raajdhani Engineering College, Bhubaneswar, kalpanam11@outlook.com*

Priyabrata Jena, *Department of Mechanical Engineering, Capital Engineering College, Bhubaneswar, priyabratajena456@yahoo.co.in*

Hemant Ku Nayak, *Department of Mechanical Engineering, NM Institute of Engineering & Technology, Bhubaneswar, hemantnayak236@gmail.com*

ARTICLE INFO

Keywords:

U-shaped heat-pipe
Coefficient of performance
Energy recovery
Dehumidification

ABSTRACT

Given the shortage of energy sources and the environmental consequences of high energy consumption, the adoption of energy-efficient heating, ventilation, and air conditioning (HVAC) systems is essential to reduce energy consumption in buildings. The purpose of this study is to examine if a finned U-shaped heat pipe heat exchanger (HPHE) may be employed in a vertical design to reduce cooling and reheating in an HVAC system and save energy. The effectiveness of the U-shaped HPHE, the HVAC system's coefficient of performance (COP) when utilised in conjunction with the U-shaped HPHE, and dehumidification capability are all discussed in this study. The U-shaped HPHE was installed at the cooling coil's input fresh airstream ducts, with one- and two-row versions arranged in eight heat pipes per row being tested. In the evaporator section, the fresh air temperature and velocity were adjusted to 30 and 45 degrees Celsius and 1.5 and 2.5 metres per second, respectively. The results show that the two-row Ushaped HPHE has a significant impact on the precooling and reheating processes in the HVAC system when compared to the one-row design. When compared to HVAC without HPHE, the two-row U-shaped HPHE can improve the coefficient of performance (COP) by 39.9%. At 0.080 m³/s air volume, the maximum energy savings for precooling and reheating were 288.1 and 340.2 W, respectively, and can reduce relative humidity by 21.6 percent. According to the findings, the U-shaped heat pipe has succeeded in becoming a solution for an HVAC system that requires cooling to reheat.

Introduction

Increasing population and economic growth combined with global and local climate change conditions have encouraged the increasing demand for building cooling energy [1]. In a tropical climate with hot temperature and high relative humidity, heating, ventilating, and air-conditioning (HVAC) systems are required for maintaining a comfortable room in buildings [2]. Humidity control is essential for maintaining comfortable and healthy conditions for occupants in a building [3]. However, the energy consumed for cooling residential buildings is the most consumed in the world [1]. Further, in commercial buildings, the operating power cost of HVAC systems accounts for approximately 40–60% of the total energy consumption in the building [3–6]. According to the ASHRAE standard, the ideal air temperature for human occupancy in a building should be between 20 and 28 °C [7] with a relative humidity of less than 65% [8]. However, with the worldwide outbreak of COVID-19 in early 2020, controlling its spread has become a major challenge [9]. As the air circulating in the room is essential for

removing harmful particles from the environment [10], enhancing the ventilation system will be very useful. Similarly, demand for isolation rooms in hospitals has increased due to the COVID-19 pandemic, intensifying the need for a proper ventilation system in a hospital. According to ANSI/ASHRAE/ASHE Standard 170–2017 [11], the airborne infection isolation (AII) room in hospitals requires indoor air temperature in the range of 21–24 °C, a maximum relative humidity of 60%, and an air supply of approximately 12 air changes per hour (ACH), thus increasing the energy used to operate the HVAC system [9]. Therefore, efficient HVAC system utilization is necessary to reduce energy consumption in buildings amid the supply difficulties of energy sources and the environmental impacts of high energy use [4,9]. Recovery of waste heat from the HVAC system can obtain a more efficient system [12], significantly reducing the energy consumption of HVAC systems [9,13–15].

In a conventional HVAC system, fresh air is cooled to a dew-point temperature using a cooling coil. However, this decrease in air temperature increases the air relative humidity. Therefore, it is necessary to conduct a dehumidification process. The common solution to reduce air

Nomenclature

T	Temperature, [°C]
\dot{m}	Mass flow rate, [kg/s]
c_p	Specific heat, [kJ/kg.K]
$Q_{precooling}$	Cooling recovery energy, [W]
$Q_{reheating}$	Heating recovery energy, [W]
COP	Coefficient of performance, [-]
$CEF_{cooling}$	Combined Efficiency of cooling system or COP combine of HVAC with U-shaped HPHE, [-]
S	Associated error
v	Velocity, [m/s]
Δ	Difference

Special characters

ϵ	Effectiveness, [-]
------------	--------------------

Subscripts

e	Evaporator side of HPHE
c	Condenser side of HPHE
$e, U-in$	Fresh air inlet (evaporator inlet section)
$e, U-out$	Fresh air outlet (evaporator outlet section)
$c, U-in$	Exhaust air inlet (condenser inlet section)
$c, U-out$	Exhaust air outlet (condenser outlet section)

relative humidity is to increase the heat [16]. Therefore, additional energy is required to operate the electric heater and achieve the required relative humidity.

Heat pipes, fixed plates, rotary wheels, and run-around systems are some types of heat recovery equipment used to recover waste heat in buildings [9,17,18]. However, when viruses or harmful particles spread via airborne transmission, heat recovery devices can only be applied if there is no possibility of leakage between the fresh air and exhaust air side components [11]. Heat pipes have the advantage of no cross-contamination between the fresh air and exhaust air side of air ducting [9,17]. Many researchers have investigated the utilization of a straight heat pipe heat exchanger (HPHE) as a precooling device in HVAC systems [5,6,9,19–22], and the results show that its use can significantly reduce the energy consumption of HVAC systems. The working principle of room conditioning with the HVAC system is to cool fresh air below its dew point temperature and then reheating the cold air to meet the temperature and relative humidity suitable for the room. Therefore, using a straight HPHE for precooling the fresh air is insufficient to reduce energy consumption in the HVAC system.

Xiao-Ping et al. [23] conducted an experimental study using a straight thermosyphon HPHE by placing the evaporator side on the fresh air inlet before passing through the cooling coil, and the condenser side was placed on the cold air side after passing through the cooling coil. The air duct was designed in a U shape, allowing air to enter through the evaporator and condenser of the thermosyphon HPHE before entering the room. Thus, the straight thermosyphon HPHE can act as a precooling and reheating device to control the relative humidity. Thermosyphon HPHE consists of three rows with eight heat pipes per row and is equipped with fins. The working fluid used was R-22 with a filling ratio of 60%. The results showed that the cooling capacity increased by approximately 20–32.7%, and the condenser of the HPHE can be used as a reheater to control the relative humidity below 70%. The same configuration of ducting with thermosyphon HPHE as a precooler and reheater on HVAC systems was also used by Yau [24]. The results showed that the overall sensible heat ratio (SHR) decreased from 0.688 to 0.188 due to the increase in air inlet temperature. However, the use of a U-shaped duct configuration is complicated in its application.

A wrap-around or U-shaped heat pipe heat exchanger could be a

solution to HVAC systems requiring cooling and reheating [16,25,26]. The wrap-around or U-shaped configuration has many advantages over straight-type HPHE in applications for precooling and reheating fresh air, such as easy installation in a single air duct passage and compact size [27]. The evaporator side of the heat pipe was placed in the inlet duct before the cooling coil, the condenser side was placed in the inlet duct after the cooling coil, and the adiabatic side was wrapped around the cooling coil between the evaporator and condenser side of the heat pipe. Jouhara and Meskimmon [28] investigated the relationship between effectiveness and air flow velocity of an HPHE wrap-around loop heat pipe (WLHP) in the air handling unit. The WLHP consisted of seven individual loop heat pipes single row that contain refrigerant R134a as the working fluid. It was equipped with continuous aluminium fins in the condenser and evaporator section, and the adiabatic part was wrapped around the electric heater. The heat pipe design was typical as used in air conditioning systems for wrapping around the cooling coil, but in this test, an electric heater was used and located after the condenser section of the heat pipe instead of a cooling coil to reverse the temperature difference on the precool and reheat sides. Tests were carried out at six different volume air flow rates in the face velocity range of 1.65 m/s–2.5 m/s. The result showed that the effectiveness increased as the velocity was reduced, and the highest effectiveness of precooling and reheating was 27.2%. Jouhara and Ezzuddin [29] observed the performance of a single wraparound loop heat pipe (WLHP) charged with R134a. The heat pipe was made of copper which had two passes in the evaporator and condenser sections; each pass was 330 mm in length with an inner tube diameter of 11.2 mm. In this experiment, an electric heater was used to heat the evaporator side, while the condenser section was cooled by water using a 2-shell pass and tube heat exchanger. From the test results, the average value of the heat pipe effective thermal resistance was at 0.048 °C/W.

Kakkar [27] investigated the potential of U-shaped HPHE in HVAC systems. U-shaped heat pipes were arranged in two rows, with five heat pipes per row arranged inline, and the heat pipes were placed horizontally in the ducting. The heat pipe diameter was 15.9 mm, and the total length of the heat pipe was 920 mm and was equipped with fins. The results show that the U-shaped heat pipe's moderate effectiveness was in the range of 0.22–0.42 under varying operating conditions. Jouhara and Meskimmon [26] applied a WLHP to increase the energy efficiency in the dehumidification process. In this study, water was compared with R134 as the working fluid. According to the experimental results, using water can increase the efficiency by 18% compared to conventional refrigerant R134, and the maximum thermal effectiveness of R134a was 19.9%, while that of water was 23.6%. The results show that water can be used as a working fluid for the wrap-around heat pipe and enhance the heat transfer effectiveness. Kusumah et al. [17] evaluated the use of unfinned U-shaped HPHE in an HVAC system for precooling and reheating air to meet temperature and relative humidity room standards. The highest amount of heat recovery was 2190.43 kJ/hour, and the efficiency was 7.64%. Jouhara [30] also investigated the economic potential of utilizing wrap-around or U-shaped heat pipes in building HVAC systems. The result proved that wrap-around heat pipes had significant energy and cost savings in cooling and heating for ventilation.

Literature reviews have shown that a heat pipe heat exchanger in various configurations in a building can enhance performance and reduce energy consumption in cooling and reheating HVAC systems. However, new developments related to U-shaped heat pipe applications still need to be developed for a wide range of applications.

This study investigates the utilization of a finned U-shaped heat pipe heat exchanger in a vertical configuration to reduce cooling and reheating energy consumption in an HVAC system. The effectiveness of the U-shaped HPHE, coefficient of performance (COP) of the HVAC system coupled with U-shaped HPHE, and dehumidification capability are presented in this paper. The effect of fresh air temperature and velocity across the evaporator section was investigated for one- and two-

row configurations of the U-shaped HPHE to determine the best configuration.

Methodology

U-shaped heat pipe design

Conventional HVAC systems consist of a cooling coil and reheat coil used to overcool fresh air and reheat the overcooled air to bring to the required supply temperature and relative humidity [30]. The U-shape or the wrap-around heat pipe is ideal for an HVAC system that requires cooling with reheating. A U-shaped heat pipe heat exchanger (HPHE) consists of a group of individual closed U-shaped tubes containing a wick structure in the tube's inner surface and uses the phase change of the fluid to transfer heat from the evaporator flow through the adiabatic to the condenser side [14,17]. In a U-shaped HPHE mounted on the inlet duct, the evaporator side is placed on the airstream before passing through the cooling coil, while the

adiabatic side is placed on the upper side wrap around the cooling coil, as shown in Fig. 1. Fresh air with higher temperature flows through the evaporator side of the U-shaped HPHE, causing heat to be absorbed, and the fluid within the tube changes to vapor and moves to the adiabatic side and then to the condenser. This process causes the fresh air temperature that passes through the HPHE evaporator to decrease, decreasing the cooling energy.

The cold air from the cooling coil flows past the HPHE condenser side, causing the vapor in the tube to condense and release heat. This process causes the vapor to change back into the liquid state and flow to the HPHE evaporator side. This process continuously repeats as long as there is a temperature differential between the heat pipe evaporator and condenser [16]. The U-shaped heat pipe not only precool the fresh air by absorbing heat and dissipating it into the environment, but processes of the U-shaped heat pipe recovers the released heat for reheating. Precooling the air reduces the energy required for the cooling coil. Further, the reheating capability improves the dehumidification function of an HVAC system [16].

In this research, U-shaped heat pipes were installed in the ducting with a

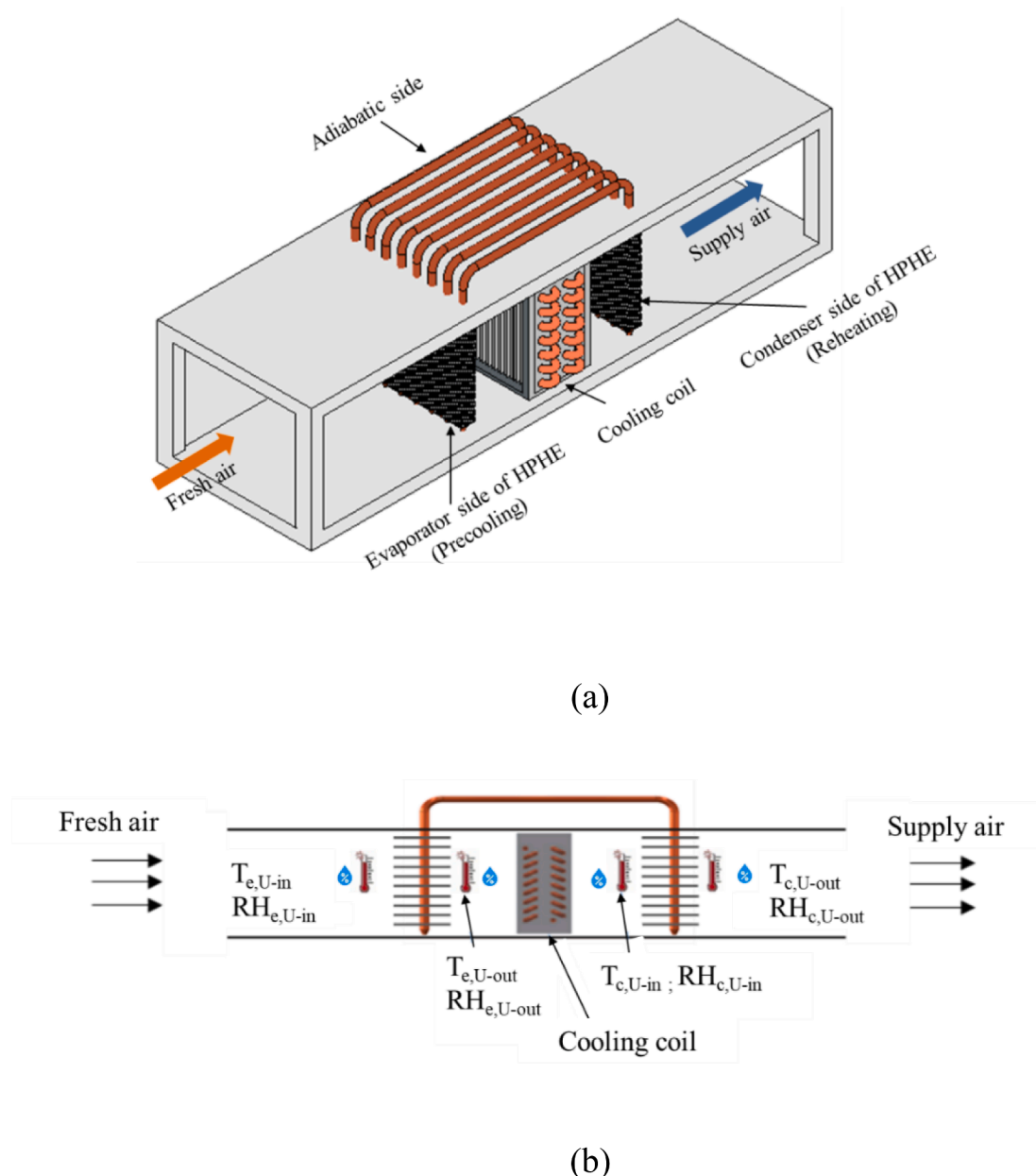


Fig. 1. Placement of U-shaped HPHE in the ducting (a); temperature and relative humidity measuring points (b).

configuration as shown in Fig. 2, to reduce cooling and reheating energy consumption in an HVAC system. The U-shaped heat pipe was equipped with sintered copper of wick structure on the tube's inner surface, aiming to produce a capillary-driven pump for returning the working fluid from the condenser to the evaporator [15,31], thus the U-shape heat pipe equipped with a wick structure can work properly even though against gravity. The U-shaped heat pipes used in the experiment were made of copper, with a total length of 710 mm and outer diameters of 10 mm. Internally, the pipes contained a wick structure of sintered copper, filled with water with a filling ratio of 50%. The length of the evaporator and condenser was 160 mm, while the adiabatic side was 390 mm. The U-shaped HPHE had eight heat pipes per row. The heat transfer area of the evaporator and condenser sides was enhanced with aluminum continuous wavy fins having a fin thickness of 0.105 mm and a spacing of 2 mm. The adiabatic side was isolated using glass wool to ensure no heat loss. Tests were carried out with one- and two-row configurations to evaluate the effectiveness of the U-shaped HPHE and its effect on HVAC system performance. The two rows of the U-shaped HPHE were arranged in a staggered configuration with a longitudinal spacing between the heat pipe of 22 mm and transverse spacing of 25 mm.

Experimental setup

The prototype test model equipped with measurement devices and a control system consists of a conditioned room, fresh airstream duct, exhaust airstream duct, inlet fan, outlet fan, cooling coil, and electric heater, as shown in Fig. 2. In the ducting, fresh air was cooled by passing it to a cooling coil device containing flowing chilled water. The chilled water supplied by a mini chiller was pumped into the cooling coil to absorb heat from the fresh air. After exiting the cooling coil device, the water was flown back into the water tank to be cooled again before flowing into the cooling coil to repeat the process. In this experiment, a mini chiller, consisting of a refrigerated coil submerged directly into the water tank, compressor, condenser, and expansion device, was used to cool the water [9].

The U-shaped HPHE was installed at inlet airstream ducts, with $0.2 \times 0.16 \text{ m}^2$ section areas, of the air handling unit. The fresh air

temperature across the evaporator section was varied in the range of $30\text{--}45^\circ\text{C}$ by a customized 6000-W heater, which was equipped with a proportional-integral temperature controller. In contrast, the heating load of the room was maintained at 200 W by two electric heaters. The air temperatures at each section were measured using type K thermocouples connected to the NI 9214 module and a data acquisition device (NI cDAQ-9174). The accuracy of the temperature sensor was $\pm 0.01^\circ\text{C}$. The fresh air duct was equipped with an axial fan to blow fresh air into the room. The fresh air velocity across the evaporator section of the U-shaped HPHE was varied between 1.5 and 2.5 m/s. The air velocities were measured at the center of the duct using a hotwire anemometer (Lutron AM-4204) with an accuracy of $\pm 0.1 \text{ m/s}$.

The compressor power was calculated by measuring the electric current using a panel meter Autonic MT4Y connected to the NI 9207 module. The voltage was adjusted by a voltage regulator. At each point, the air relative humidity was measured using the RH sensor Autonic THD-DD1-V with an accuracy of $\pm 2\%$ and recorded using the NI 9207 module, which was connected to a data acquisition device (NI cDAQ-9174). The experimental setup used in this study is shown in Fig. 3.

U-shaped HPHE performance

The measuring points for observing the performance of the U-shape of the HPHE are shown in Fig. 1(b). The U-shaped HPHE performance can be evaluated based on sensible effectiveness. Sensible effectiveness is the ratio of the actual temperature difference across the evaporator or condenser section of a U-shaped heat pipe divided by the maximum temperature difference between the fresh air entering the evaporator side and air entering the condenser side of the heat pipe, which is represented by Eq. (1) [23,24,26,32].

$$\varepsilon = \frac{(T_{e,U-in} - T_{e,U-out})}{(T_{e,U-in} - T_{c,U-in})} \text{ or } \varepsilon = \frac{(T_{c,U-in} - T_{c,U-out})}{(T_{e,U-in} - T_{c,U-in})} \quad (1)$$

Eq. (1) only applies to cases where there is no condensed water vapor in the evaporator side or condenser side of the heat pipe, where the

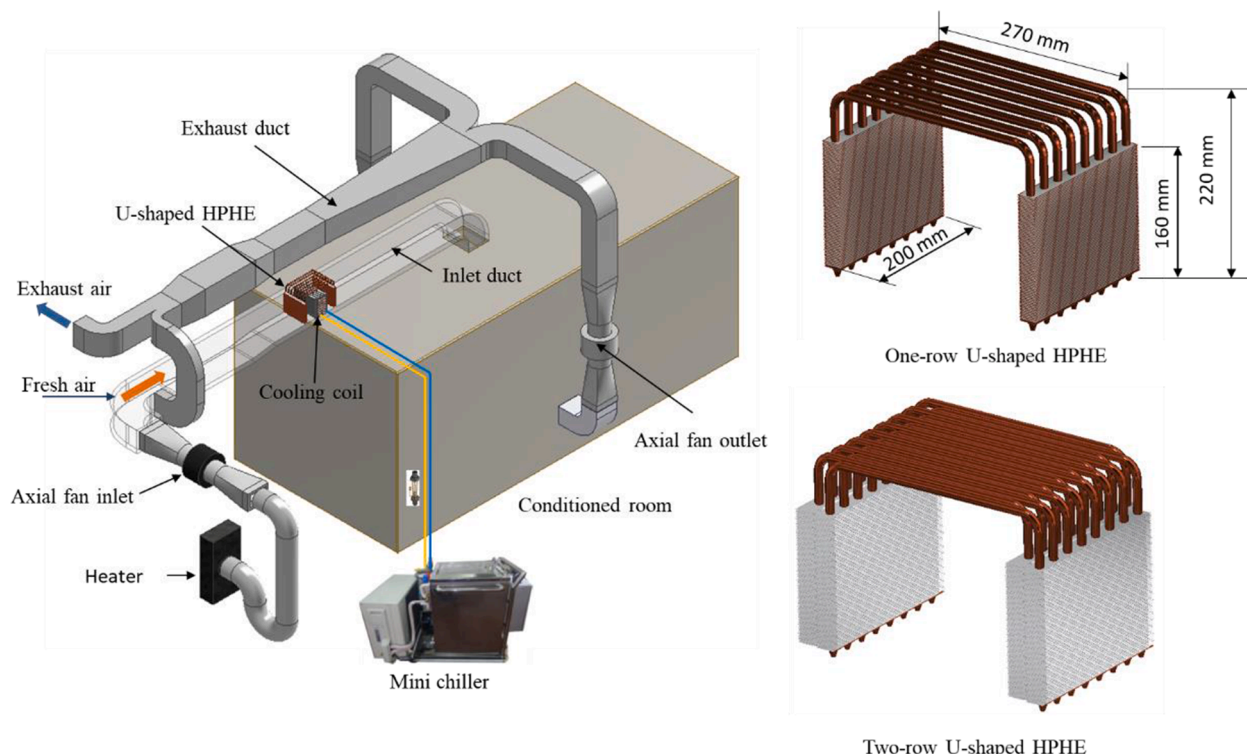


Fig. 2. Prototype test model and design of U-shaped HPHE [9].

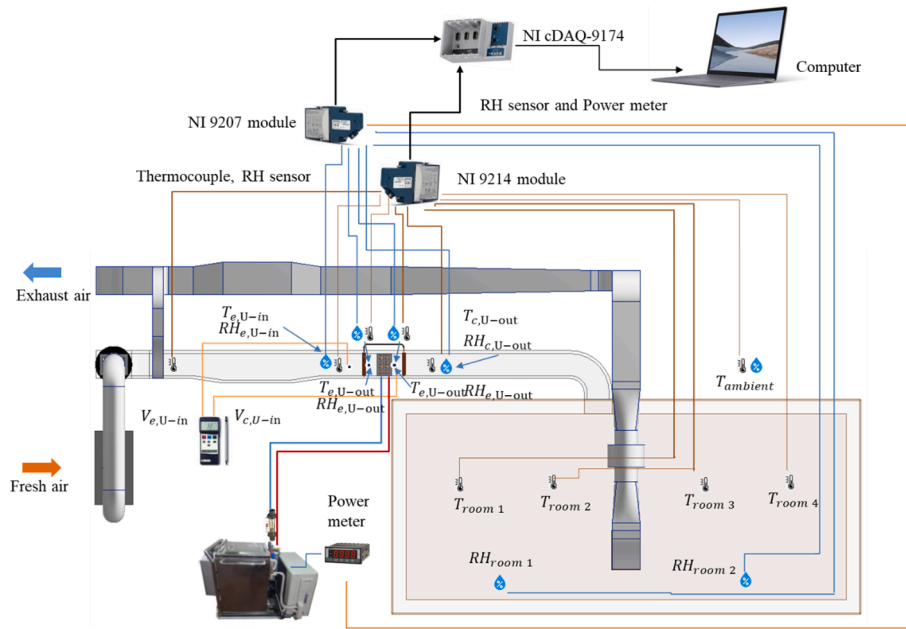


Fig. 3. Experimental setup [9].

temperature difference on the evaporator side ($T_{e,U-in} - T_{e,U-out}$) and the temperature difference on the condenser side ($T_{c,U-out} - T_{c,U-in}$) has the same value. If condensation occurs on the evaporator side and under extreme conditions, the energy balance ensures that the evaporator's heat transfer rate and the condenser side remain constant. However, the heat transfer on the evaporator side consists of sensible and latent, while the heat transfer on the condenser side is sensible only so that the temperature rise on the condenser side ($T_{c,U-out} - T_{c,U-in}$) is greater than in the evaporator side ($T_{e,U-in} - T_{e,U-out}$) [30]. In the use of the U-shaped HPHE, the precooling and reheating processes coincide. Therefore, energy savings could be obtained for both processes using Eqs. (2) and (3) [23,24,32].

$$q_{precooling} = \dot{m}c_p(T_{e,U-in} - T_{e,U-out}) \quad (2)$$

$$q_{reheating} = \dot{m}c_p(T_{c,U-out} - T_{c,U-in}) \quad (3)$$

The total energy savings achieved by the U-shaped HPHE in the HVAC system are due to the precooling effect in the evaporator section and the reheating effect in the condenser section U-shaped HPHE.

Effect of utilization U-shaped HPHE to HVAC performance

The effect of U-shaped HPHE on cooling performance can be evaluated by the coefficient of performance (COP), expressed as:

$$COP = \frac{\text{Net cooling capacity of the cooling coil}}{\text{Electric power consumption by the cooling coil}} \quad (4)$$

The HVAC system performance after adding a U-shaped HPHE can be evaluated using the combined efficiency of the cooling system (CEFCooling) [18,32,33].

$$CEFCooling = \frac{\text{Net cooling capacity of HPHE} + \text{Net cooling capacity of the cooling coil}}{\text{Electric power consumption by HPHE} + \text{Electric power consumption by cooling coil}} \quad (5)$$

The enhancement of COP can be described using Eq. (7) as follows [34]:

$$\text{Enhancement of COP} = \frac{COP_{\text{with U-shape HPHE}} - COP_{\text{without HPHE}}}{COP_{\text{without HPHE}}} \times 100\% \quad (6)$$

where: $COP_{\text{with U-shape HPHE}} = CEF_{\text{cooling}}$

Experimental results and discussion

U-shaped heat pipe heat exchanger performance

The effects of fresh air temperature, fresh air velocity, and the number of row combinations on the U-shaped HPHE and HVAC performance were evaluated experimentally. Each measurement combination was read at intervals of 30 min after steady-state conditions. Fig. 4 (a) shows the temperature profile for a two-row U-shaped HPHE at a fresh air velocity of 1.5 m/s. This figure shows that the U-shaped HPHE can reduce the temperature of fresh air (from $T_{e,U-in}$ to $T_{e,U-out}$) before passing through the cooling coil device and simultaneously raise the overcooled air temperature in the condenser section (from $T_{c,U-out}$ to $T_{c,U-in}$).

The highest temperature difference in the evaporator section or precooling of 4.0 °C and condenser section or reheating of 4.5 °C was obtained with the two-row U-shaped HPHE. The fresh air inlet temperature was 45 °C, and air velocity was 1.5 m/s. One-row U-shaped HPHE did not have a significant effect on precooling and reheating. The highest temperature decrease on the evaporator side was 0.9 °C, and the highest temperature rise on the condenser side was 1.1 °C. However, when the heat pipes were added in a two-row configuration, the U-shaped heat pipe provided a significant increase in the precooling and reheating effects. This improvement was caused by the increase in the

number of rows, which increased the heat transfer area and enhanced the heat transfer coefficient between the air and the heat pipes in forced

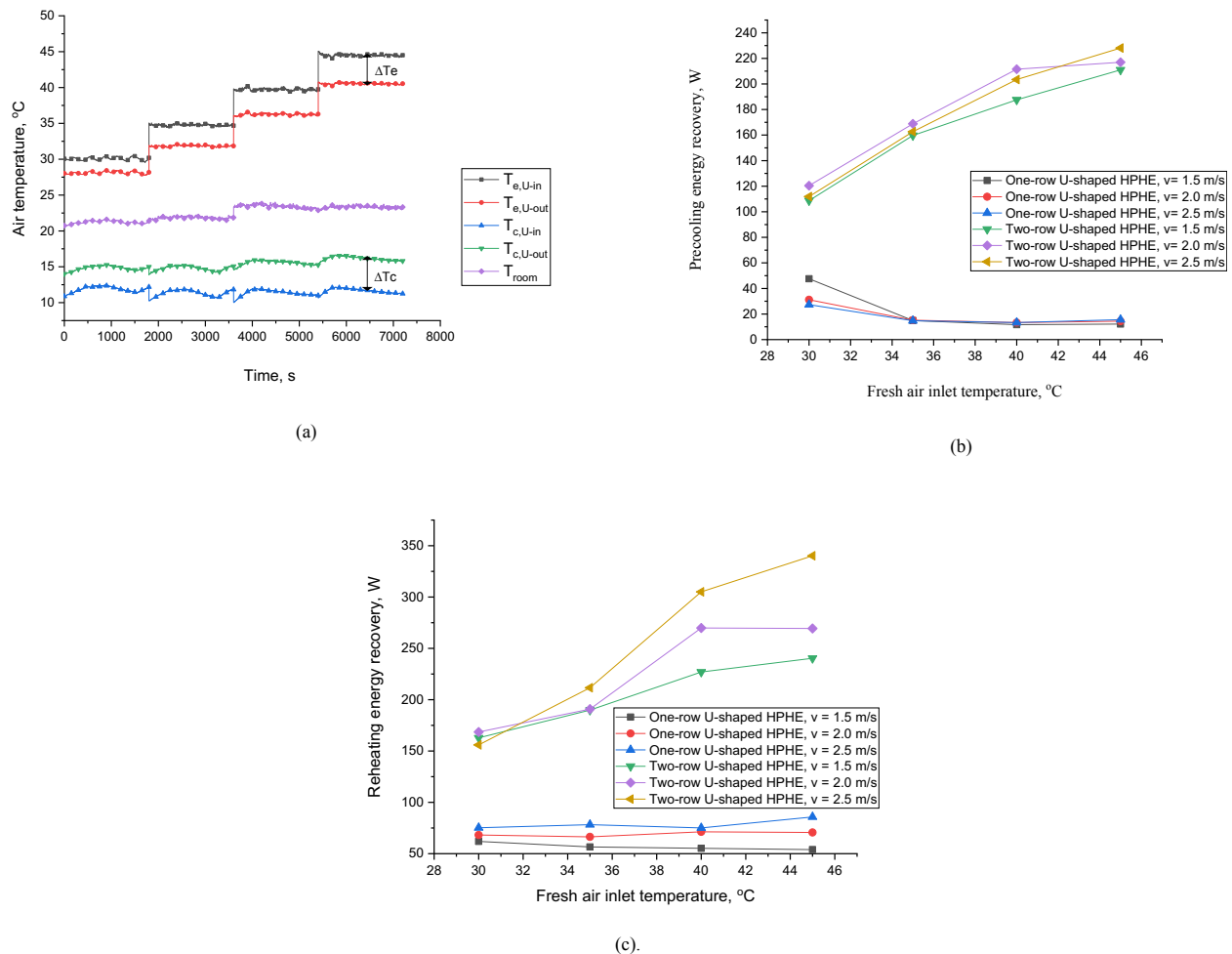


Fig. 4. Temperature profile for the two-row U-shaped HPHE at an air velocity of 1.5 m/s (a); Precooling energy recovery by evaporator of U-shaped HPHE (b); Reheating energy recovery by condenser of U-shaped HPHE (c).

convection, thereby increasing the effectiveness of the U-shaped HPHE. As a result, the heat transfer rate on the evaporator and the condenser side of the HPHE increases, enabling the temperature reduction on the evaporator side and the temperature rise on the condenser side [26]. Fig. 4(a) shows that at the same velocity, a higher inlet air temperature enhances the temperature decrease on the evaporator side (ΔT_e) and the temperature rise on the condenser side of the HPHE (ΔT_c), which shows that the heat absorbed by the heat pipe increases with the inlet air temperature on the evaporator side.

The precooling and reheating energy recoveries are shown in Fig. 4 (b) and Fig. 4(c), respectively. The highest precooling energy recovery was 228.1 W for the inlet air volume of 0.08 m³/s, fresh air velocity 2.5 m/s, and fresh air temperature of 45 °C. Meanwhile, the lowest precooling energy recovery of the two-row U-shaped heat pipe was 108.7 W for the inlet air volume of 0.048 m³/s, fresh air velocity 1.5 m/s, and fresh air temperature of 30 °C. The highest reheating energy recovery was 340.2 W for the inlet air volume of 0.08 m³/s, fresh air velocity 2.5 m/s, and fresh air temperature of 45 °C. The lowest energy recovery of using the two-row U-shaped heat pipe was 162.8 W at an inlet air volume of 0.064 m³/s, intake air velocity of 2.0 m/s, and intake air temperature of 30 °C.

Reheating of the overcooled air on the condenser side of the U-shaped HPHE indirectly affects the dehumidification process. The relative humidity after passing through the condenser side of the U-shaped HPHE can be reduced significantly. Fig. 5(a) shows that the relative humidity can be reduced from 91.9 to 70.3% at an inlet air temperature of 45 °C and air velocity of 1.5 m/s, and from 93.2 to 75.7% at an inlet

air temperature of 30 °C, using the two-row U-shaped HPHE. This result showed that no external energy was required to reheat the supply air stream for the given test conditions. The maximum air relative humidity decrease was 21.6%, and the lowest relative humidity decrease was 17.5%, which was obtained using the two-row U-shaped HPHE.

Fig. 5(a) shows the effect of fresh air inlet temperature variation on relative humidity at a constant fresh air inlet velocity of 1.5 m/s. Fig. 5 (b) shows the effect of fresh air inlet velocity on relative humidity at a constant fresh air inlet temperature of 45 °C. It can be concluded that the HVAC system's dehumidification capability, containing a U-shaped HPHE, increased as air inlet temperature across the evaporator side increased. Meanwhile, the variation of fresh air velocity on the evaporator side does not affect the decrease in the air's relative humidity.

The effect of the U-shaped HPHE on energy saving of the HVAC system can also be seen in the psychrometric diagram of Fig. 5(c) for the two-row U-shaped HPHE at a fresh air inlet temperature of 45 °C and inlet air velocity of 1.5 m/s. In the conventional HVAC system, the fresh air is cooled from points 1 to 3 by a cooling coil device and then reheated by the electric heater from points 3 to 4 [35]. In an HVAC system that uses U-shaped HPHE, the energy consumption of the conditioning room can be reduced. Processes 1–2 show the precooling process on the evaporator side ($T_{e,U-in}$ to $T_{e,U-out}$) resulting from the U-shaped HPHE installation. Processes 2–3 are the overcooling process by the cooling coil. Processes 3–4 show sensible reheating by the U-shaped HPHE, which indirectly decreases the relative humidity. In processes 1–2, there is a very small increase in the humidity ratio. Based on the condition that the increase in humidity ratio is small and not under extreme conditions,

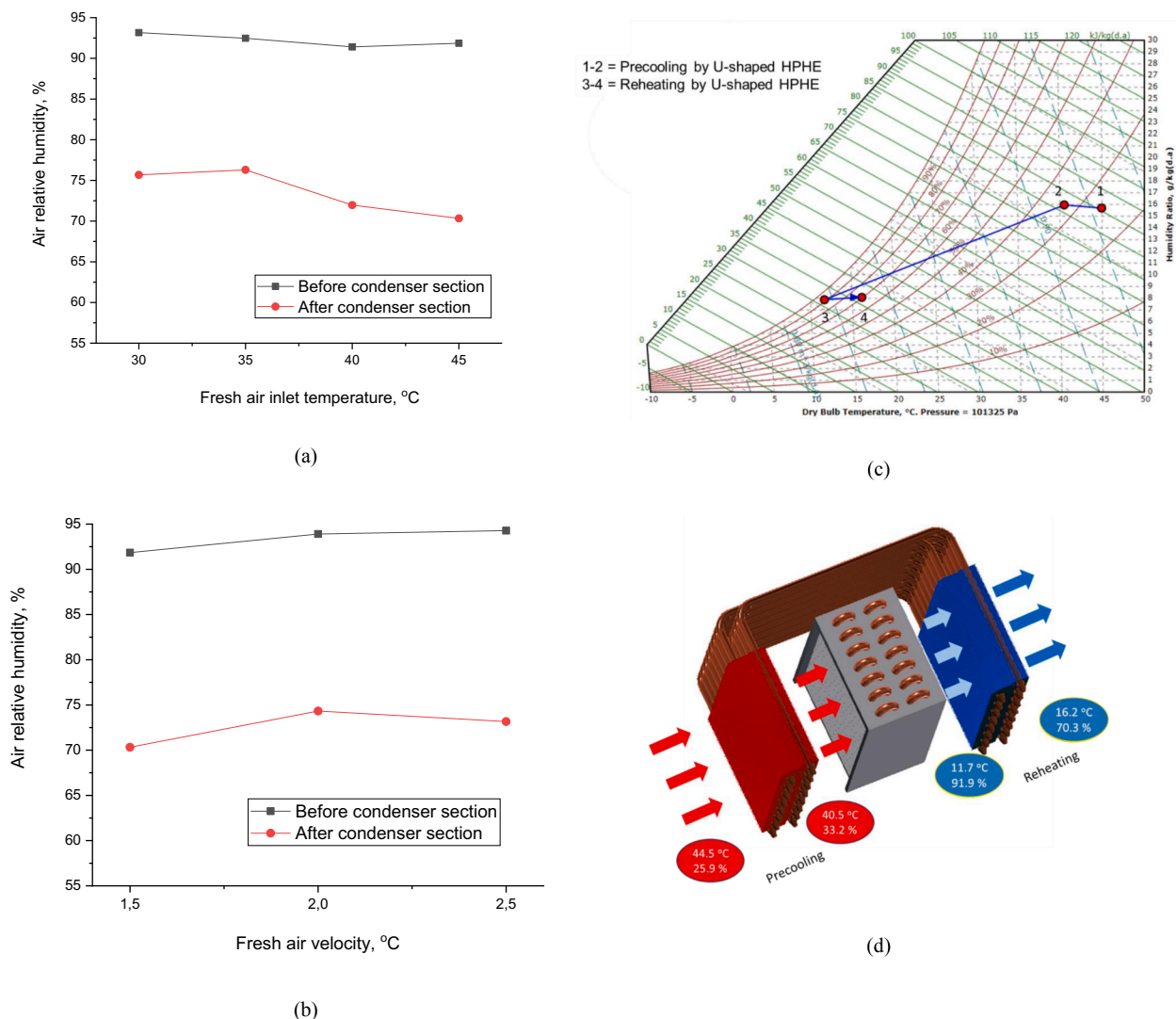


Fig. 5. Air relative humidity versus fresh air inlet temperature at an air velocity of 1.5 m/s (a); Air relative humidity versus fresh air inlet velocity at an air inlet temperature of 45 °C (b); Psychrometric diagram of two-row U-shaped HPHE at an inlet air temperature of 45 °C and an inlet air velocity of 1.5 m/s (c); Air conditioning process in the HVAC with two-row U-shaped HPHE at a fresh air inlet temperature of 45 °C and a fresh air velocity of 1.5 m/s (d).

sensible effectiveness is used to investigate the U-shaped HPHE performance [30]. The most effective precooling, reheating, and dehumidification process was achieved in the two-row U-shaped HPHE at a fresh air inlet temperature of 45 °C and fresh air velocity of 1.5 m/s, as shown in Fig. 5(d).

The U-shaped HPHE performance in terms of sensible effectiveness is shown in Fig. 6(a). The highest effectiveness of 12.4% was obtained in the two-row U-shaped HPHE at a fresh air inlet temperature of 35 °C and fresh air inlet velocity of 1.5 m/s. The lowest effectiveness of 0.6% was obtained in the one-row U-shaped at a fresh air inlet temperature of 45 °C and fresh air inlet velocity of 2.5 m/s. The effectiveness of the one-row U-shaped HPHE is relatively low, but the implementation of the two-row configuration has a significant effect on the precooling, reheating, and dehumidification processes. Increasing the number of rows increases the heat transfer area and the heat transfer coefficient between the air and the heat pipe. Thus, the heat transfer rate through the heat exchanger increases compared to the maximum heat available [26].

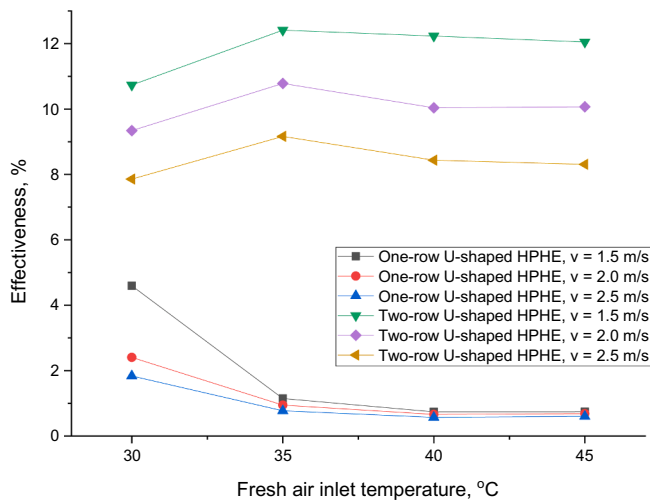
The effect of U-shaped HPHE on the HVAC performance

Fig. 6(b) shows the effect of adding U-shaped HPHE on HVAC system performance. The test was conducted for the two-row U-shaped

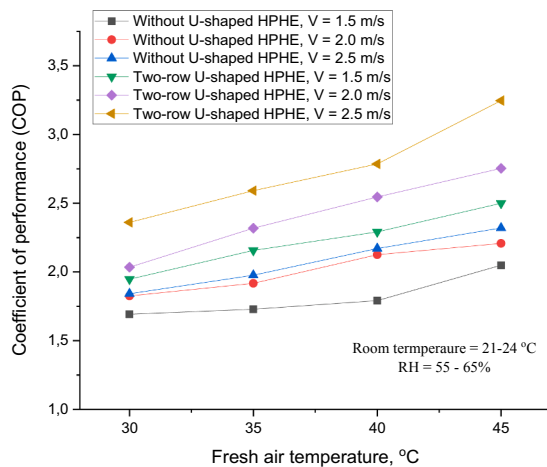
HPHE for various fresh air temperatures and velocities. The results showed that the addition of the U-shaped HPHE was able to increase the COP in the HVAC system significantly. In the room set, having the temperature in the range of 21–24 °C and the relative humidity of 55–65%, COP increased from 2.3 to 3.3 when the HVAC system operated in the fresh air inlet temperature of 45 °C and fresh air velocity of 2.5 m/s. These results confirmed that the COP increased from 2.1 to 2.5 at average operating condition, enhancing the COP by 39.9% compared to a conventional air conditioner without U-shaped HPHE, as shown in Fig. 6(c).

Uncertainty analysis

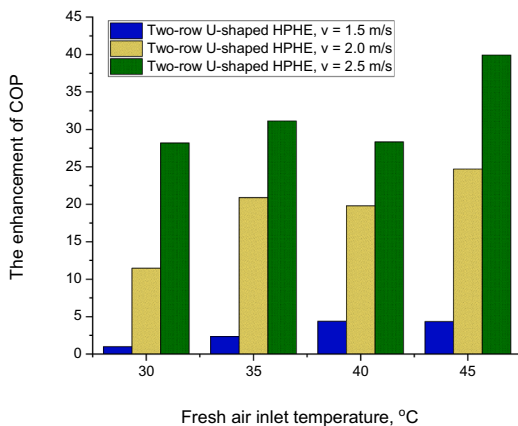
The use of two rows in the U-shaped HPHE significantly enhances energy savings during the precooling and reheating processes. An uncertainty analysis was conducted to determine the effectiveness and energy recovery obtained by the two-row U-shaped HPHE. From the calibration, the errors corresponding to $(T_{e, U-in} - T_{e, U-out})$ and $(T_{e, in} - T_{c, U-in})$ were found to be ± 0.1 and ± 0.2 °C, respectively. The uncertainties in the energy recovery ($Se/qrecovery$) calculation were evaluated assuming that specific heat (C_p) and air density (ρ) were constant, and there is no change in the ducting area (A). [9,36,37].



(a)



(b)



(c)

Fig. 6. Effectiveness of the two-row U-shaped HPHE for $T_{e,U-in}$ and $V_{e,U-in}$ (a); COP of an HVAC containing a two-row U-shaped HPHE (b); The enhancement of COP for an HVAC system with U-shaped HPHE and without U-shaped HPHE (c).

From the analysis, the maximum uncertainty of effectiveness (Se/ϵ) was $\pm 7.8\%$, and the maximum uncertainty of energy recovery ($Se/q_{recovery}$) was found to be $\pm 8.7\%$. The use of the two-row U-shaped HPHE could significantly reduce the relative humidity of the supply air.

After calibration, the maximum error associated with the relative humidity was $\pm 1.6\%$.

Conclusions

The potential energy savings in the cooling and reheating processes for dehumidification in an HVAC system combined with U-shaped heat pipe heat exchangers were investigated. The effectiveness of the one-row U-shaped HPHE was relatively low, but the application of two rows had a significant effect on the precooling, reheating, and dehumidification processes. The highest temperature difference in the evaporator section or precooling of 4.0°C and condenser section or precooling of 4.5°C was obtained with the two-row U-shaped HPHE at a fresh air inlet temperature of 45°C and an air velocity of 1.5 m/s . The results show that the U-shaped HPHE can enhance the COP by 39.9% compared to the HVAC without HPHE. The highest effectiveness of 12.4% was obtained for the two-row U-shaped HPHE. The highest energy saving for precooling and reheating was 288.1 and 340.2 W , respectively, at $0.080\text{ m}^3/\text{s}$ air volume, and the relative humidity was reduced by 21.6% . The two-row U-shaped HPHE significantly affects the precooling and reheating processes in the HVAC system compared to the one-row configuration. The investigation confirmed that the U-shaped HPHE succeeded in reducing the energy consumed by the precooling and reheating processes of the HVAC system, enhancing its dehumidification capability.

CRedit authorship contribution statement

Imansyah Ibnu Hakim: Supervision, Methodology, Writing - original draft, Writing - review & editing. **Ragil Sukarno:** Data curation, Investigation, Writing - review & editing, Visualization, Validation. **Nandy Putra:** Conceptualization, Methodology, Supervision, Writing - review & editing.

Declaration of Competing Interest

The authors declare that they have no known competing financial interests or personal relationships that could have appeared to influence the work reported in this paper.

Acknowledgment

The authors thank the Directorate of Research and Development Universitas Indonesia for funding this research through the PPI Q1 Program 2021.

References

- [1] M. Santamouris, Cooling the buildings – past, present and future, *Energy Build.* 128 (2016) 617–638, <https://doi.org/10.1016/j.enbuild.2016.07.034>.
- [2] Y.H. Yau, S.K. Lee, Feasibility study of an ice slurry-cooling coil for HVAC and R systems in a tropical building, *Appl. Energy* 87 (8) (2010) 2699–2711, <https://doi.org/10.1016/j.apenergy.2010.02.025>.
- [3] A.A. Eidan, S.E. Najim, J.M. Jalil, An experimental and a numerical investigation of HVAC system using thermosyphon heat exchangers for sub-tropical climates, *Appl. Therm. Eng.* 114 (2017) 693–703, <https://doi.org/10.1016/j.applthermaleng.2016.12.027>.
- [4] L. Pérez-Lombard, J. Ortiz, C. Pout, A review on buildings energy consumption information, *Energy Build.* 40 (3) (2008) 394–398, <https://doi.org/10.1016/j.enbuild.2007.03.007>.
- [5] N. Putra, T. Anggoro, A. Winarta, Experimental study of heat pipe heat exchanger in hospital HVAC system for energy conservation, *Int. J. Adv. Sci. Eng. Inf. Technol.* 7 (2017) 871, <https://doi.org/10.18517/ijaset.7.3.2135>.
- [6] R. Sukarno, N. Putra, I.I. Hakim, F.F. Rachman, T.M.I. Mahlia, Multi-stage heat-pipe heat exchanger for improving energy efficiency of the HVAC system in a hospital operating room, *Int. J. Low-Carbon Technol.* 16 (2) (2021) 259–267, <https://doi.org/10.1093/ijlct/ctaa048>.
- [7] A. Standard, “Standard 55–2017 Thermal Environmental Conditions for Human Occupancy,” American Society of Heating, Refrigerating and Air Conditioning Engineers: Atlanta, GA, USA, 2017.

- [8] A. Ashrae, "ASHRAE Standard 62.1-2016, Ventilation for Acceptable Indoor Air Quality," American Society of Heating, Refrigerating, and Air-Conditioning Engineers, Inc.: Atlanta, GA, 2016.
- [9] R. Sukarno, N. Putra, I.I. Hakim, F.F. Rachman, T.M. Indra Mahlia, Utilizing heat pipe heat exchanger to reduce the energy consumption of airborne infection isolation hospital room HVAC system, *J. Build. Eng.* 35 (2021), 102116, <https://doi.org/10.1016/j.jobe.2020.102116>.
- [10] REHVA, "REHVA COVID-19 guidance document, August 3, 2020," in How to operate and use building services in order to prevent the spread of the coronavirus disease (COVID-19) virus (SARS-CoV-2) in workplaces, August 3, 2020 ed: Federation of European Heating, Ventilation and Air Conditioning Associations (REHVA) 2020, pp. 1-17.
- [11] ANSI/ASHRAE/ASHE Standard 170-2017, Ventilation of Health Care Facilities, ANSI/ASHRAE/ASHE, Atlanta, 2017.
- [12] P.M. Cuce, S. Riffat, A comprehensive review of heat recovery systems for building applications, *Renew. Sustain. Energy Rev.* 47 (2015) 665–682.
- [13] V. Vakloraaya, B. Samali, A. Fakhar, K. Pishghadam, A review of different strategies for HVAC energy saving, *Energy Convers. Manage.* 77 (2014) 738–754.
- [14] W. Srimuang, P. Amatachaya, A review of the applications of heat pipe heat exchangers for heat recovery, *Renew. Sustain. Energy Rev.* 16 (6) (2012) 4303–4315, <https://doi.org/10.1016/j.rser.2012.03.030>.
- [15] D. Reay, R. McGlen, P. Kew, Heat pipes: theory, design and applications, Butterworth-Heinemann, 2013.
- [16] D.A. John, D. Elsberry, Wrap-around heat pipes in humid climates, *ASHRAE J.* 58 (2016) 28–38.
- [17] A. Mardiana-Idayu, S.B. Riffat, Review on heat recovery technologies for building applications, *Renew. Sustain. Energy Rev.* 16 (2) (2012) 1241–1255, <https://doi.org/10.1016/j.rser.2011.09.026>.
- [18] Guideline for Calculating the Efficiency of Energy Recovery Ventilation and its Effect on Efficiency and Sizing of Building HVAC Systems, AHRI, United States, 2011.
- [19] M.A. Abd El-Baky, M.M. Mohamed, Heat pipe heat exchanger for heat recovery in air conditioning, *Appl. Therm. Eng.* 27 (4) (2007) 795–801, <https://doi.org/10.1016/j.applthermaleng.2006.10.020>.
- [20] H. Jouhara, H. Merchant, Experimental investigation of a thermosyphon based heat exchanger used in energy efficient air handling units, *Energy* 39 (1) (2012) 82–89, <https://doi.org/10.1016/j.energy.2011.08.054>.
- [21] T.S. Jadhav, M.M. Lele, A case study on energy savings in air conditioning system by heat recovery using heat pipe heat exchanger, *Int. J. Eng. Res. Technol.* 3 (2) (2014) 12–16.
- [22] I.I. Hakim, N. Putra, R. Sukarno, M.R. Audi, F.F. Rachman, Experimental study on utilization of heat pipe heat exchanger for energy conservation of air conditioning system in a hospitals and its techno-economic feasibility, 1, in: AIP Conference Proceedings, AIP Publishing LLC, 2020, p. 030067.
- [23] W. Xiao Ping, P. Johnson, A. Akbarzadeh, Application of heat pipe heat exchangers to humidity control in air-conditioning systems, *Appl. Therm. Eng.* 17 (6) (1997) 561–568, [https://doi.org/10.1016/S1359-4311\(96\)00058-0](https://doi.org/10.1016/S1359-4311(96)00058-0).
- [24] Y.H. Yau, Application of a heat pipe heat exchanger to dehumidification enhancement in a HVAC system for tropical climates—a baseline performance characteristics study, *Int. J. Therm. Sci.* 46 (2) (2007) 164–171.
- [25] A. Kusumah, I. Hakim, R. Sukarno, F. Rachman, N. Putra, The Application of U-shape Heat Pipe Heat Exchanger to Reduce Relative Humidity for Energy Conservation in Heating, Ventilation, and Air Conditioning (HVAC) Systems, *Int. J. Technol.* 10 (2019) 1202, <https://doi.org/10.14716/ijtech.v10i6.3650>.
- [26] H. Jouhara, R. Meskimmon, An investigation into the use of water as a working fluid in wraparound loop heat pipe heat exchanger for applications in energy efficient HVAC systems, *Energy* 156 (2018) 597–605, <https://doi.org/10.1016/j.energy.2018.05.134>.
- [27] A. Kakkar, Potential of U-shaped heat pipe heat exchanger in tropical climates for low sensible heat ratio applications, *ASHRAE Trans.* 123 (2017) 263.
- [28] H. Jouhara, R. Meskimmon, Experimental investigation of wraparound loop heat pipe heat exchanger used in energy efficient air handling units, *Energy* 35 (12) (2010) 4592–4599, <https://doi.org/10.1016/j.energy.2010.03.056>.
- [29] H. Jouhara, H. Ezzuddin, Thermal performance characteristics of a wraparound loop heat pipe (WLHP) charged with R134A, *Energy* 61 (2013) 128–138, <https://doi.org/10.1016/j.energy.2012.10.016>.
- [30] H. Jouhara, Economic assessment of the benefits of wraparound heat pipes in ventilation processes for hot and humid climates, *Int. J. Low-Carbon Technol.* 4 (1) (2009) 52–60, <https://doi.org/10.1093/ijlct/ctp006> %J International Journal of Low-Carbon Technologies.
- [31] A. Faghri, Heat pipes: review, opportunities and challenges, *Front. Heat Pipes (FHP)* 5 (1) (2014).
- [32] ASHRAE, ASHRAE Handbook—HVAC Systems and Equipment, ASHRAE Inc., Atlanta, 2020, p. 2020.
- [33] AHRI GUIDELINE V: Guideline for Calculating the Efficiency of Energy Recovery Ventilation and its Effect on Efficiency and Sizing of Building HVAC Systems, 2011.
- [34] N. Nethaji, S.T. Mohideen, Energy conservation studies on a split airconditioner using loop heat pipes, *Energy Build.* 155 (2017) 215–224, <https://doi.org/10.1016/j.enbuild.2017.09.024>.
- [35] Y. Yau, M. Ahmadzadehtalatpeh, Heat pipe heat exchanger and its potential to energy recovery in the tropics, *Therm. Sci.* 19 (2015) 20, <https://doi.org/10.2298/TSCI100818020Y>.
- [36] X. Cui, Y. Zhu, Z. Li, S. Shun, Combination study of operation characteristics and heat transfer mechanism for pulsating heat pipe, *Appl. Therm. Eng.* 65 (1–2) (2014) 394–402, <https://doi.org/10.1016/j.applthermaleng.2014.01.030>.
- [37] V.K. Karthikeyan, K. Ramachandran, B.C. Pillai, A. Brusly Solomon, Effect of nanofluids on thermal performance of closed loop pulsating heat pipe, *Exp. Therm. Fluid Sci.* 54 (2014) 171–178, <https://doi.org/10.1016/j.expthermflusci.2014.02.007>.

Effect of load on Stress Relaxation of Rock Joints

Sagarika Pasayat, *Department of Civil Engineering, Aryan Institute of Engineering & Technology, Bhubaneswar, s.pasayat@gmail.com*

Jitendra Narayan Biswal, *Department of Mechanical Engineering, Aryan Institute of Engineering & Technology, Bhubaneswar, jnarayan679@gmail.com*

Binapani Mohapatra, *Department of Civil Engineering, Raajdhani Engineering College, Bhubaneswar, binapanimohapatra@yahoo.co.in*

Shradha Jena, *Department of Civil Engineering, Capital Engineering College, Bhubaneswar, shradhajena98@gmail.com*

ABSTRACT

A data analysis approach for the relaxation test under step loading was presented in this study by conducting creep and stress relaxation tests of discontinuities injected by cement mortar using a biaxial creep machine under step and single-stage loading. First, by evaluating the effect of loading history on the relaxation curve and analyzing the characteristic of relaxation, a superposition technique for the stress relaxation curve was determined based on the data processing method of the creep test. Second, data was tested under step and single-stage loading to confirm the superposition method. Finally, this work shows how to interpret relaxation test data accurately under step loading. The results reveal that the values of the relaxation curve after superposition differ from those obtained during the single-stage loading test at the same stress level. In addition, the relaxation curves in the step loading test at various stress levels are shown.

1. Introduction

Rock mass is a complex geological body, and the existence of structural planes such as fractures and joints is the source of discontinuities, anisotropy, and heterogeneity in rock engineering [1]. Consequently, mechanical properties of rocks not only include elasticity and plasticity but also time-dependent behavior. Several engineering studies have shown that the failure and instability of rock mass does not occur immediately after the excavation is completed. The deformation characteristic of rock mass is affected by the stress-strain state, and the deformation occurs and adjusts with time continuously for a long period of time [2]. The time-varying nature of the stress-strain state of a rock mass is defined as the rheology of the rock mass. The indoor rheological test is a vital method for studying the rheological mechanical properties of rocks, which includes two commonly used test methods. The first method is the single-stage loading method, where the sample is directly loaded to a certain stress level during the test, which avoids the impact

of loading history. However, it is rarely used because it is time consuming and requires many samples. The second method is the step loading method in which the load is divided into several levels during the test, and the rheological test is performed until the predetermined load is loaded. Although this method cannot avoid the impact of loading history, it is convenient and timesaving; besides, it avoids the effect of sample dispersion on the results of the rheological test.

The rheological properties of rocks comprise two aspects: creep and stress relaxation. Since the step loading method is convenient and timesaving, it is widely used in creep tests. For example, Liu et al. [3], Song et al. [4], Xiao et al. [5], Xie et al. [6], and Zhang et al. [7] used this method to perform the creep test on different types of rocks. The existence of structural planes significantly affects the mechanical properties of rock masses. Many researchers such as Xu et al. [8], Shen et al. [9], Zhang et al. [10], Wang et al. [11], and Lin et al. [12] used the step loading method to study the creep characteristics of structural planes. By analyzing the effect of

loading history on the deformation of rock specimens based on the data obtained from shale multi-stage cyclic single-pump compression creep tests, Xia et al. [13] proposed a method for collating the creep test data. The "Chen's loading method" proposed by Chen and Kang can be used to infer the creep curve of the load under one-step loading through a mapping method [14, 15]. This method can establish the superposition relationship of the true deformation process, and it has been widely accepted and used in geotechnical rheology research globally.

Stress relaxation is another important aspect of rheology. Roadways and underground engineering are often damaged by relaxation of surrounding rocks, which is commonly observed [16]. Stress relaxation uses a constant deformation while the stress on the specimen is monitored as a function of time, which is difficult to achieve in existing experimental machines, so there are fewer experimental studies on stress relaxation [17]. In addition, the current studies on stress relaxation of rocks are mostly based on the creep test method. For example, Yu et al. [18], Chen et al. [19], and Paraskevopoulou et al. [20] performed uniaxial and triaxial relaxation tests on cylindrical rock specimens using the step loading method. Moreover, the step loading method is also used to study the relaxation characteristics of structural surfaces [21–24]. With the continuous improvement of test equipment and technology along with the growing importance of stress relaxation in engineering, several researchers are focusing on the stress relaxation characteristics of rocks. They have implemented a test method that is similar to the creep test, which is based on the step loading method. However, the studies on the data processing methods for the relaxation test under step loading are relatively scarce, e.g., like the data processing method of creep test, whether there is a method to deduce the relaxation curve of one-time loading through step loading have not been explored yet.

In engineering applications, the mechanical properties of structural planes usually control the stability of the rock engineering. Numerous studies have been carried out to investigate the mechanical behaviors of structural planes of rock mass [25–30]. In consideration on the complexity of structural plane, literature usually simplifies the rough structural plane into regularly dentate discontinuity with different values of the slope angle. Patton [31] was the first researcher in rock mechanics to relate the shear behavior of joints to normal load and roughness. His work is based on an idealized model of a joint in which roughness is represented by a series of constant-angle triangles or saw-teeth. Barton [32] has studied the behavior of natural rock joints and proposed a criterion that is modified from Patton. Other scholars also studied the mechanical properties of regular toothed discontinuity with different values of the slope angle in the past decades [24, 33–37]. Meanwhile, regular toothed discontinuity can be found in practical engineering, such as the headscarp of the Aishihik River Landslide [38].

To address this issue, cement mortar is used to artificially cast the samples with regular toothed structural surfaces at different angles to reduce the dispersion of test results. In this study, first, the creep test and stress relaxation test under step loading are performed on samples with regular toothed

structural surface. Simultaneous, we have conducted the single-stage loading creep test and relaxation test under corresponding shear stress levels. Furthermore, a data processing method for the relaxation test under step loading is deduced from a theoretical perspective considering the influence of loading history, and the results are verified based on the test data. Then, the similarities and differences between the creep curve and relaxation curve according to the superposition principle are analyzed, and an appropriate method for the relaxation test under step loading is proposed. This knowledge resolves the outstanding issues of creep and relaxation equivalence, thereby enriching the theoretical understanding of rock mechanics.

2. Materials and Methods

2.1. Equipment. The test is performed on the CSS-1950 rock biaxial rheological testing machine manufactured by Changchun Testing Machine Research Institute at Tongji University (Figure 1). The maximum vertical and horizontal pressure applied by the testing machine are 500 and 300 kN, respectively, and these pressures can be applied simultaneously or separately. The vertical and horizontal biaxial deformation values of the sample can be measured simultaneously, where the measurement range is ± 3 mm and the measurement accuracy is 0.001 mm. The temperature and humidity of the room remained essentially constant during the test.

2.2. Sample Preparation. All samples were formed with the same material, mixing ratio, and curing time to avoid large dispersion of test results due to uneven sample materials. The dimensions of the complete cube sample and the regular sample with the saw-tooth structure were $10\text{ cm} \times 10\text{ cm} \times 10\text{ cm}$, where the length of single tooth in the latter sample was 10 mm and the number of tooth shapes was 10 with three climbing angles: 10° , 30° , and 45° . The schematics of the sample at 10° and 30° climbing angle are shown in Figure 2. The model materials were slag silicate 32.5 R cement, standard sand, and water, and they were mixed in water:cement:sand ratio of 1 : 2:4. This mixture was then stirred. Subsequently, it was placed into a steel mold and tapped to smoothen the surface for reducing the adverse effects during the sample preparation. Finally, the sample was disassembled after 24 h and cured for 28 days.

2.3. Testing and Loading Methods. Three complete cube samples were taken for the uniaxial compression test to obtain an average strength of 19.62 MPa. Subsequently, 10% and 20% of the average uniaxial compressive strength of the complete cube sample, i.e., 1.962 MPa and 3.924 MPa, were selected as the normal stress during the creep and relaxation tests under the step loading and single-stage loading.

Before the creep and relaxation tests, three specimens with climbing angles of 10° , 30° , and 45° were selected for direct shear tests, and the peak values of the shear stress and shear displacement curves were considered as the shear strength. The average shear strength of the structural surface

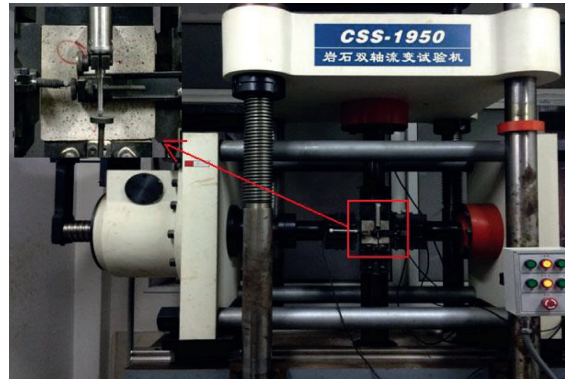


FIGURE 1: Snapshot of the test equipment.

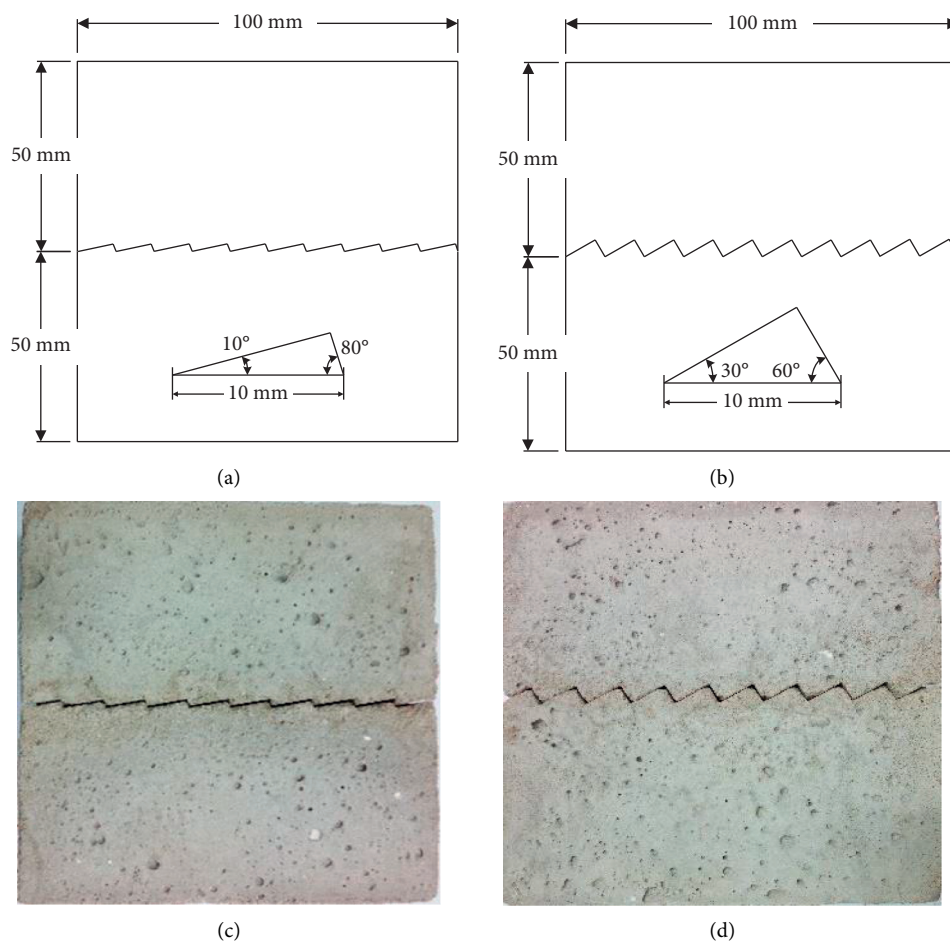


FIGURE 2: Ichnography of the dentate discontinuities and the sample preparation method: (a) section size of the 10° structural planes; (b) section size of the 30° structural planes; (c) sample with a slope angle of 10°; (d) sample with a slope angle of 30°.

samples at different angles under different normal stress is shown in Table 1. Step loading tests and single-stage loading tests were performed on the samples at different stress levels. The shear stress applied in the creep and relaxation tests under step loading were 40%, 60%, 80%, 90%, and 95% of the average shear strength τ_{\max} of the structural surface at the respective climbing angle. A schematic of the loading process is shown in Figure 3(a). While conducting the creep and

relaxation tests under single-stage loading, a shear stress was selected for the elastic phase and plastic phase of the stress-strain curve because of the creep and relaxation characteristics exhibited by the specimen in both these sections might be different in the past research [10, 13]. Here, the applied shear stress was 60% and 90% of τ_{\max} at the respective climbing angle, and a schematic of the loading process is shown in Figure 3(b). The details of the tests are as follows:

TABLE 1: Average shear strength of structural plane.

Normal stress (MPa)	Slope angle (°)	Shear strength τ_{max} (MPa)
1.962	10	1.69
1.962	30	2.60
1.962	45	3.57
3.924	10	3.40
3.924	30	4.40
3.924	45	5.59

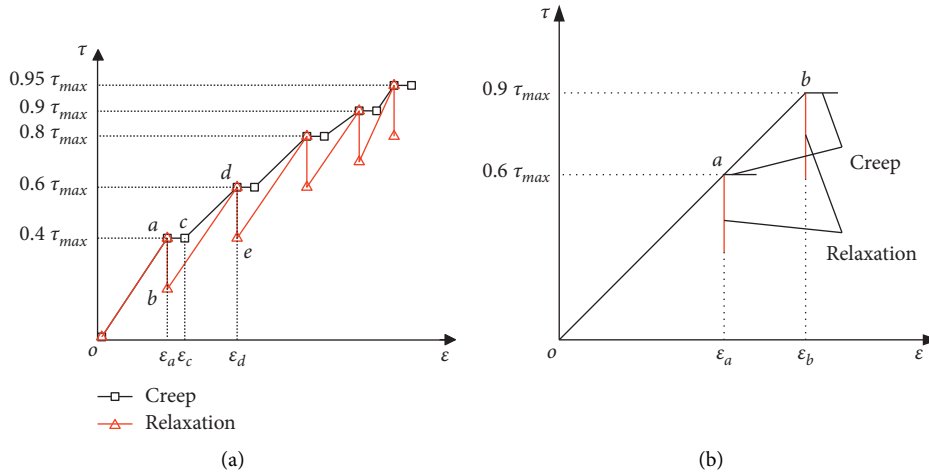


FIGURE 3: Schematic of the loading process: (a) step loading and (b) single loading.

- (1) Figure 3(a) shows the schematic of the creep (relaxation) test under step loading. First, a normal stress of 1.962 MPa or 3.924 MPa is applied and kept constant. After the normal deformation is stabilized, the shear stress is applied at a rate of 0.2 kN/s to 40% of the shear strength τ_{max} , i.e., point a. Subsequently, the shear stress (the strain ϵ_a generated at this time) is kept stable for 72 h, during which the strain (shear stress) is increased (reduced) from point a to point c (from a point to b point), following which the specified shear stress is applied step by step at the same rate, and the shear stress of each level (strain generated under each level of shear stress) is maintained for 72 h.
- (2) Figure 3(b) shows a schematic of the creep test and relaxation test under single loading. First, the normal stress of 1.962 MPa or 3.924 MPa is applied and kept constant. After the normal deformation is stabilized, the shear stress is applied at a rate of 0.2 kN/s to 60% (or 90%) of the shear strength τ_{max} , i.e., point a (or point b). The stress (or strain) generated at this time constant is maintained for 72 h.

factors at different times in a physical or mechanical system to a certain time in the future is considered. If this effect is linear, it can be processed using the Boltzmann superposition principle. If a certain stress $\sigma = \sigma(t)$ is acting on the object, it can be discretized into a series of single stress pulse acting on the object. According to the Boltzmann superposition principle, the deformation of an object is the comprehensive effect of these pulse stress effects and the general constitutive equation for creep is as follows:

$$\epsilon(t) = \frac{\sigma(t)}{E_0} + \int_{-\infty}^t \sigma(\tau) K(t - \tau) d\tau. \quad (1)$$

The general integral-type constitutive equation for relaxation can be derived as follows:

$$\sigma(t) = E_0 \epsilon(t) - \int_{-\infty}^t \epsilon(\tau) R(t - \tau) d\tau, \quad (2)$$

where E_0 is the instantaneous elastic modulus and $K(t - \tau)$ is the creep kernel function, which are determined by the creep properties of the material; $R(t - \tau)$ is the relaxation kernel function, which is determined by the relaxation properties of the material [15, 39].

3. Processing Method for the Rheological Curve

The Boltzmann principle is commonly used when test curves of single-stage loading are estimated based on that of step loading, i.e., the total effect due to the external

3.1. Finishing Method for the Creep Curve. The step loading is often used in creep tests [5, 10, 35, 40]. It is a cascade loading method with a step size of $\Delta\sigma$, which is a kind of step loading method. A schematic of this loading method

is shown in Figure 4(a). The mapping method is used to establish the superposition principle for the true deformation process by implementing appropriate experimental techniques. As shown in Figure 4(b), it can be applied regardless of whether the after effect is linear or nonlinear. However, this method requires that the deformation into the steady state creep during the lower stage loading is equal to that during the various stages. Yang et al. [39] found that this method is also applicable when the load increments $\Delta\sigma_i$ and loading times Δt_i are not equal at all levels, but the unsteady changes of rheological parameters are not considered.

The creep curves superposition can be expressed as follows:

$$\begin{aligned}\varepsilon(\Delta t) &= \frac{n\Delta\sigma}{E_0} + n\Delta\sigma \int_0^{\Delta t} K(t-\tau)d\tau \\ &= \frac{\sigma}{E_0} + \sigma \int_0^{\Delta t} K(t-\tau)d\tau.\end{aligned}\quad (3)$$

This equation is a creep-type integral equation for stress corresponding to one-time loading $\sigma = n \cdot \Delta\sigma$ in the time interval Δt , which proves that the effect of step loading is equal to that of the one-time loading [14, 15, 39].

3.2. Derivation of the Processing Method for the Relaxation Curve. Presently, the loading method of most relaxation tests is the same as that of the creep test [18–22], i.e., step loading method used to load the samples in steps of $\Delta\varepsilon$, and the loading method is shown in Figure 5. In this study, the superposition method for the relaxation curve is derived using a method similar to that for arranging the creep data.

The loading process in Figure 5 can be expressed by the following equation:

$$\begin{aligned}\varepsilon(t) &= \Delta\varepsilon\theta(t-t_0) + \Delta\varepsilon\theta(t-t_1) + \Delta\varepsilon\theta(t-t_2) + \dots \\ &\quad + \Delta\varepsilon\theta(t-t_i) + \dots + \Delta\varepsilon\theta(t-t_n),\end{aligned}\quad (4)$$

where $\theta(t)$ is the Heaviside step function.

The $\theta(t-t_i)$ function is defined as follows: if $(t-t_i) \geq 0$, $\theta(t-t_i) = 1$; if $(t-t_i) \leq 0$, $\theta(t-t_i) = 0$.

It can be simplified as $\theta(t-t_i) = \theta_i$.

Equation (4) is substituted into the relaxation-type integral equation based on the Boltzmann principle of linear superposition, i.e., equation (2) to obtain

$$\begin{aligned}\sigma(t) &= \Delta\varepsilon(\theta_0 + \theta_1 + \theta_2 + \dots + \theta_n)E_0 \\ &\quad - \int_0^t \Delta\varepsilon(\theta_0 + \theta_1 + \theta_2 + \dots + \theta_n)R(t-\tau)d\tau.\end{aligned}\quad (5)$$

If the test has been run until $t \geq t_n$, then equation (5) is equivalent to

$$\begin{aligned}\sigma(t) &= \Delta\varepsilon(\theta_0 + \theta_1 + \theta_2 + \dots + \theta_n)E_0 - \int_{t_0}^t \Delta\varepsilon\theta_0R(t-\tau)d\tau \\ &\quad - \int_{t_1}^t \Delta\varepsilon\theta_1R(t-\tau)d\tau - \dots - \int_{t_n}^t \Delta\varepsilon\theta_nR(t-\tau)d\tau \\ &= n \cdot \Delta\varepsilon E_0 - \Delta\varepsilon \int_{t_0}^t \theta_0R(t-\tau)d\tau \\ &\quad - \Delta\varepsilon \int_{t_1}^t \theta_1R(t-\tau)d\tau - \dots - \Delta\varepsilon \int_{t_n}^t \theta_nR(t-\tau)d\tau.\end{aligned}\quad (6)$$

It is evident from equation (6) that under the load function of strain shown in equation (4), the total relaxation of material at time t is the sum of the stress increase amount at each level minus the sum of the stress relaxation amounts under the individual strain effects.

The loading time is the same during the test, i.e.,

$$(t_1 - t_0) = (t_2 - t_1) = (t_3 - t_2) = \dots = (t_n - t_{n-1}) = \Delta t. \quad (7)$$

Define $n \cdot \Delta\varepsilon E_0 = \varepsilon \cdot E_0 = \sigma$, and equation (6) can be written as

$$\sigma(t) = n \cdot \Delta\varepsilon E_0 - n\Delta\varepsilon \int_0^{\Delta t} R(t-\tau)d\tau = \sigma - \varepsilon \int_0^{\Delta t} R(t-\tau)d\tau. \quad (8)$$

This equation is the relaxation-type integral equation for one-time loading $\varepsilon = n \cdot \Delta\varepsilon = n \cdot (\Delta\sigma/E_0) = \sigma/E_0$ in the time interval of Δt , which is similar to the integral equation for creep under one-time loading. The superposition method of the relaxation curve can be obtained by that of creep curve and the derived relaxation-type integral equation of one-time loading. It is evident from Figure 6 that material relaxation can be caused by the loading of the level-1 strain $\Delta\varepsilon$. From time $t = 0$ to $t = t_1$, material relaxation occurs under constant strain $\varepsilon = \Delta\varepsilon$, i.e., curve 1. If the next stage of strain $\Delta\varepsilon$ is not added when the test reaches time t_1 , the material stress continues along the dotted line of curve 1 because it has entered the regime of steady state relaxation. At time $t = t_1$, the material relaxes after the level-2 strain $\Delta\varepsilon$ is loaded, i.e., curve 2. Considering the effect of loading history and the derived integral equation (equation (8)) of one-time loading, the amount of relaxation generated by the level-2 strain $\Delta\varepsilon$ should be the area enclosed by the relaxation curve (curve (2) of the level-2 strain $\Delta\varepsilon$ and the relaxation curve (curve (1) of the level-1 strain $\Delta\varepsilon$, i.e., the hatched area A (which can be obtained by shifting the initial point of the relaxation curve of the level-2 strain $\Delta\varepsilon$ to the end point of the level-1 strain $\Delta\varepsilon$). Then, the relaxation curve of loading 2 $\Delta\varepsilon$ can be obtained by superimposing the hatched area A on the relaxation curve 1 of the level-1 strain (the superposition of the hatched area A and the area B), i.e., the curve 3. Based on the Boltzmann superposition principle, the superposition method for the relaxation curve derived according to the creep superposition method can reflect the loading process represented by equation (4).

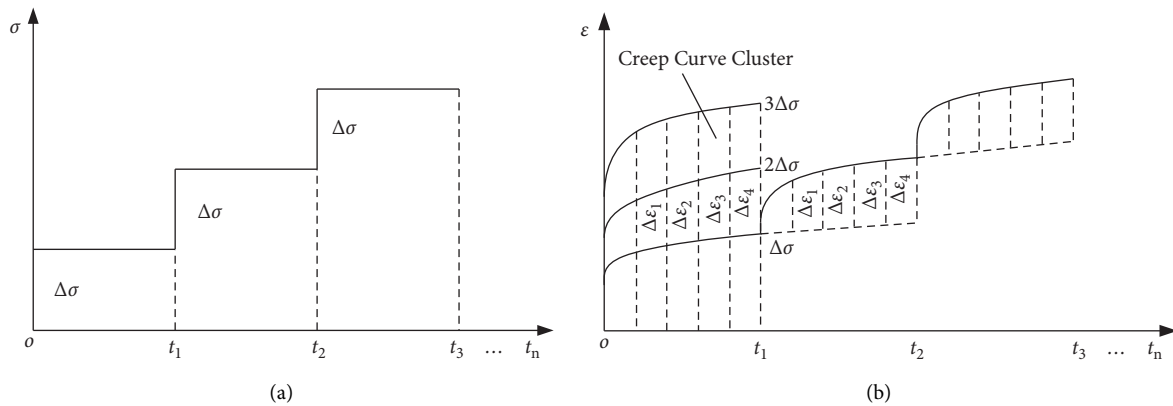


FIGURE 4: Processing methods for creep curves: (a) the diagram of loading process; (b) deformation diagram.

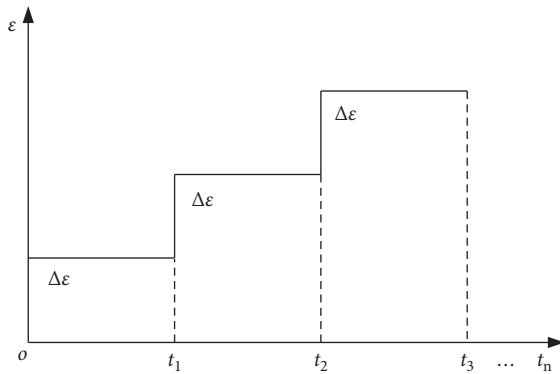


FIGURE 5: Loading process of relaxation test.

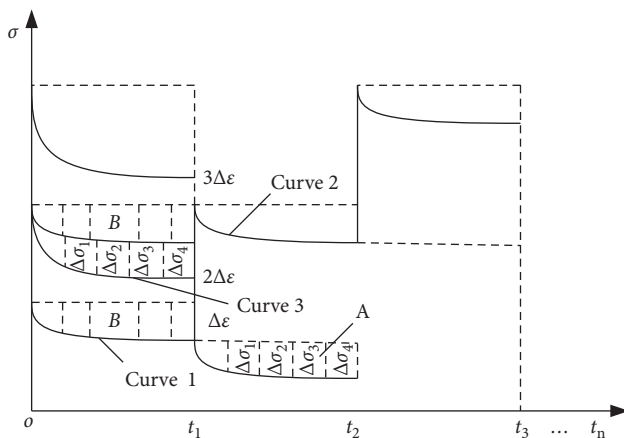


FIGURE 6: Processing methods of relaxation curves.

4. Analysis of Test Results

The stacking method for the step loading creep test has been widely studied [4, 6, 8, 10, 13, 35, 40], so it will not be repeated here. The step loading and single-stage loading relaxation experiment are carried out on the 10°, 30°, and 45° structural surfaces to verify the superposition method for relaxation curve derived in the previous section.

4.1. Basic Law of Relaxation. When the normal stress is 3.924 MPa, the entire process curve of step loading relaxation at each climbing angle on the structural surface is shown in Figure 7. When the initial shear stress is within the elastic range and plastic range of the stress-strain curve, respectively, the single-stage loading relaxation curve of 45° structural plane is shown in Figure 8. The following conclusions can be obtained from Figures 7 and 8:

- (1) Figure 7 shows that when step loading relaxation occurs, the initial shear stress level is the same, i.e., the value of τ_0/τ_{\max} remains the same. Therefore, under the same normal stress, the initial shear stress increases with the increase in the climbing angle, resulting in a stepwise change in the relaxation process curve.
- (2) The shape of the relaxation curve under step loading is similar to that under single-stage loading, and the stress significantly decreases with time, which is consistent with the general relaxation law of materials.
- (3) During the 72 h relaxation time, the stress of the step loading and single-stage loading relaxation curve did not relax to zero but approached a stable value. Therefore, the relaxation curve appears as a continuous and incomplete stress relaxation.
- (4) The stress relaxation curve can be roughly divided into two phases based on the speed of relaxation: attenuation relaxation and steady-state relaxation.

4.2. Comparison of the Test Results for Single-Stage Loading and Step Loading. Considering the step loading relaxation curve of 10° structural surface in Figure 7 as an example, the superposition is performed on it according to the superposition method derived in Section 2, i.e., equation (8). Thus, the relaxation curves before and after the superposition can be obtained. The relaxation curve clusters of 10° structural surface under different shear stress level are shown in Figure 9. Meanwhile, for verifying the superposition results of the relaxation curve and considering that the relaxation

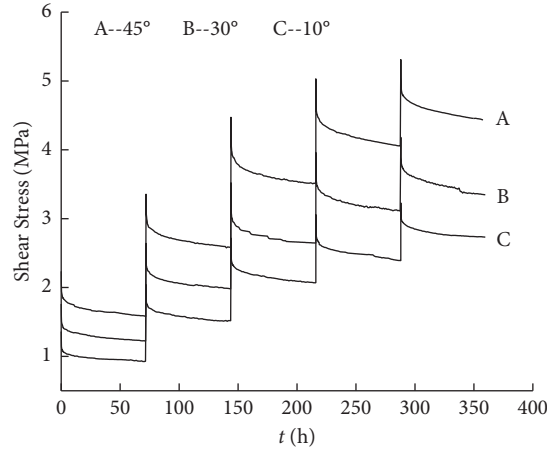


FIGURE 7: Relaxation curve of the entire process under step loading for $\sigma = 3.924$ MPa.

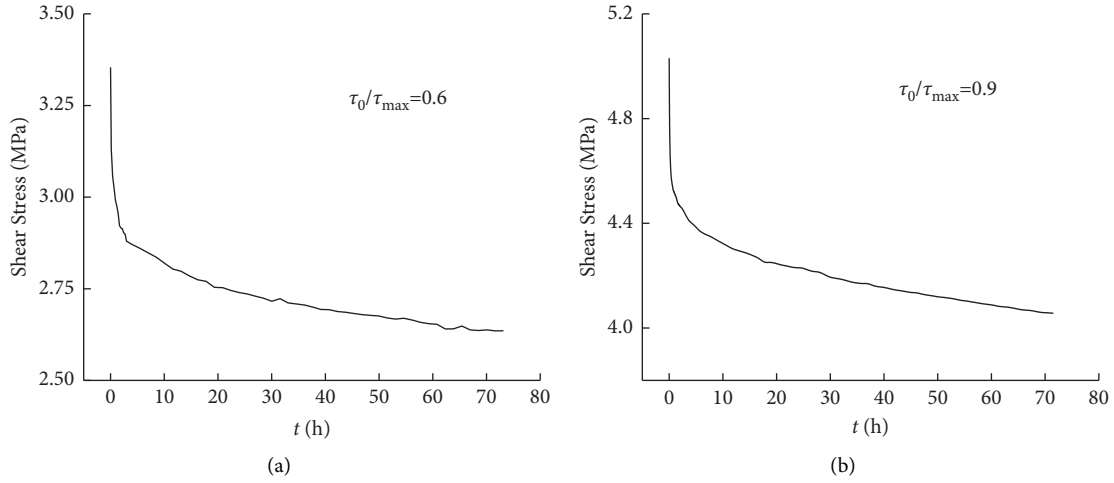


FIGURE 8: Relaxation curves of 45° discontinuities under single-stage loading: (a) $\tau_0/\tau_{\max} = 0.6$; (b) $\tau_0/\tau_{\max} = 0.9$.

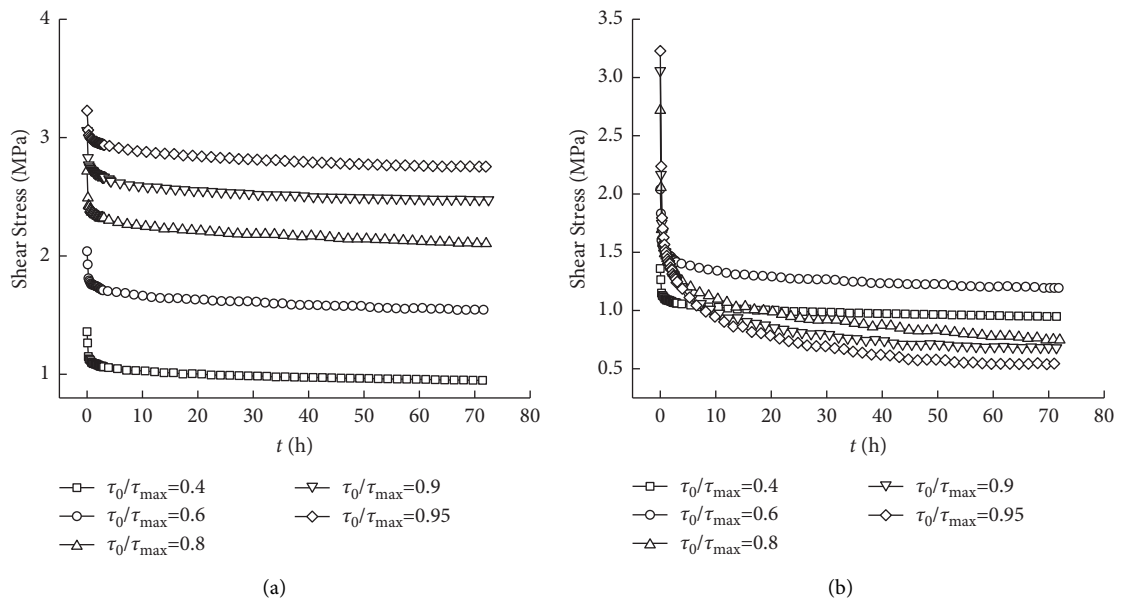


FIGURE 9: Relaxation curves of 10° discontinuities under different stress levels: (a) before superposition, $\tau_0 = 3.924$ MPa; (b) after superposition, $\tau_0 = 3.924$ MPa.

characteristics of the specimen in the elastic section and the plastic section might be different, the relaxation curve in elastic deformation sections and plastic deformation section of the 10° structural planes was taken as example. When the shear stress level of τ_0/τ_{\max} is 0.6 and 0.9, the relaxation curves with and without superposition treatment are shown in Figure 10. The relaxation curve loaded to the shear stress level of $\tau_0/\tau_{\max} = 0.6$ and 0.9 in a single stage is also shown in Figure 10.

At each shear stress level, the difference between initial shear stress τ_0 at the beginning of the relaxation test (i.e., at $t = 0$) and the residual stress $\Delta\tau(t) = \tau_0 - \tau(t)$ after time t is defined as relaxation stress $\Delta\tau(t) = \tau_0 - \tau(t)$, i.e. $\Delta\tau(t) = \tau_0 - \tau(t)$, where t is the relaxation time. The following inferences can be drawn from Figures 9 and 10:

- (1) Relaxation stress $\Delta\tau(72)$ after 72 h relaxation at each stress level can be calculated according to Figure 9(a). It is evident that the relaxation curve without superposition exhibits the maximum $\Delta\tau(72)$ at the stress level of $\tau_0/\tau_{\max} = 0.9$; the relaxation curve after superposition exhibits the maximum $\Delta\tau(72)$ at the stress level of $\tau_0/\tau_{\max} = 0.95$. This is attributed to the superposition process of relaxation curve considers the effect of the stress levels of the previous levels on the relaxation. Therefore, after the relaxation curve has undergone superposition treatment, the relaxation stress $\Delta\tau(72)$ reaches its maximum at the highest stress level $\tau_0/\tau_{\max} = 0.95$, which is different from the result without superposition.
- (2) Figure 10 shows that when the stress level is $\tau_0/\tau_{\max} = 0.6$, the maximum relaxation stress $\Delta\tau(72)$ after relaxation curve superposition is greater than that of the untreated curve because the relaxation stress generated under the previous stress level is considered. Besides, it is also greater than the relaxation stress generated by single-stage loading. The results of the relaxation curve with superposition and without superposition are quite different.
- (3) The shape of the relaxation curve without superposition is similar to that of the single-stage loading relaxation curve, and the amount of stress relaxation is close. For example, when the stress level is $\tau_0/\tau_{\max} = 0.6$, the relaxation stress $\Delta\tau(72)$ of the relaxation curve without superposition is about 0.495 MPa; the relaxation stress $\Delta\tau(72)$ of the single-stage relaxation curve is about 0.451 MPa, and the difference between the relaxation stress of the two curves is 0.044 MPa. When the stress level is $\tau_0/\tau_{\max} = 0.9$, the relaxation stress of the relaxation curve without superposition is about 0.584 MPa; the relaxation stress of the single-stage loading relaxation curve is about 0.669 MPa, and the difference between the relaxation stress of the two curves is 0.085 MPa.

It is evident from the above points that whether it is in the elastic phase (stress level is $\tau_0/\tau_{\max} = 0.6$) or plastic phase

(stress level is $\tau_0/\tau_{\max} = 0.9$), the shape of the relaxation curve without superposition is similar to that of the single-stage loading relaxation curve. Moreover, the difference in stress relaxation between the two curves is extremely small, which may be caused by the sample difference.

Although the materials, mixing ratio, and curing conditions used in the sample preparation are same, it is difficult to produce two identical samples. Therefore, it can be considered that the relaxation curve without superposition is equivalent to that with single loading. This implies that when the relaxation test is performed under step loading, the relaxation curve under each level of stress can reflect the relaxation curve when the sample is loaded to the same stress level at a single time without performing superposition on the relaxation curve unlike the step loading creep test.

5. Difference between Creep Superposition and Relaxation Superposition

For the creep test performed using the step loading method, the superposition method for creep derived based on the Boltzmann superposition principle has been widely used. Here, the same loading method was used for the creep test to perform the step loading relaxation test, and the superposition method for relaxation was derived based on the Boltzmann superposition principle. However, through experimental comparison, founding that the single-stage loading relaxation curve was very similar to the step loading relaxation curve without superposition, it was quite different from the relaxation curve with superposition treatment. Therefore, if the difference in the test results caused by sample variations is ignored, it can be considered that the step loading relaxation curve without superposition can reflect the relaxation curve of a single-stage load to the same stress level. The cause of this phenomenon was analyzed using the deformation-time curve of creep, the stress-time curve of relaxation, and the stress-strain curve during creep and relaxation processes, which is described as follows. Figures 11 and 12 show the typical creep curve and relaxation curve of step loading, respectively. Considering the 45° structural surface at normal stress of 1.962 MPa as an example, the shear stress-strain curve during the creep and relaxation tests are shown in Figures 13 and 14, respectively.

It is evident from Figure 11 that the creep deformation during step loading increases with time, and the deformation first increases from point *a* to point *b*, and then to point *c*, indicating a monotonically increasing trend. The typical relaxation curve shown in Figure 12 indicates that the stress decreases initially and then increases. For example, the first level of strain is applied at $t = 0$, and the stress is at point *a*. If the strain is kept constant, it increases with time, and the stress varies from point *a* to point *b*. At $t = t_1$, a second-level strain is applied, and the stress is restored from point *b* to the level of stress at $t = 0$, i.e., point *a'*, and then the stress increases to point *c*. Stress does not exhibit a monotonically decreasing or increasing trend. Furthermore, Figures 13 and 14 show that in the creep process, as the stress level increases, the creep deformation increases continuously, exhibiting a monotonically increasing trend. In the relaxation process,

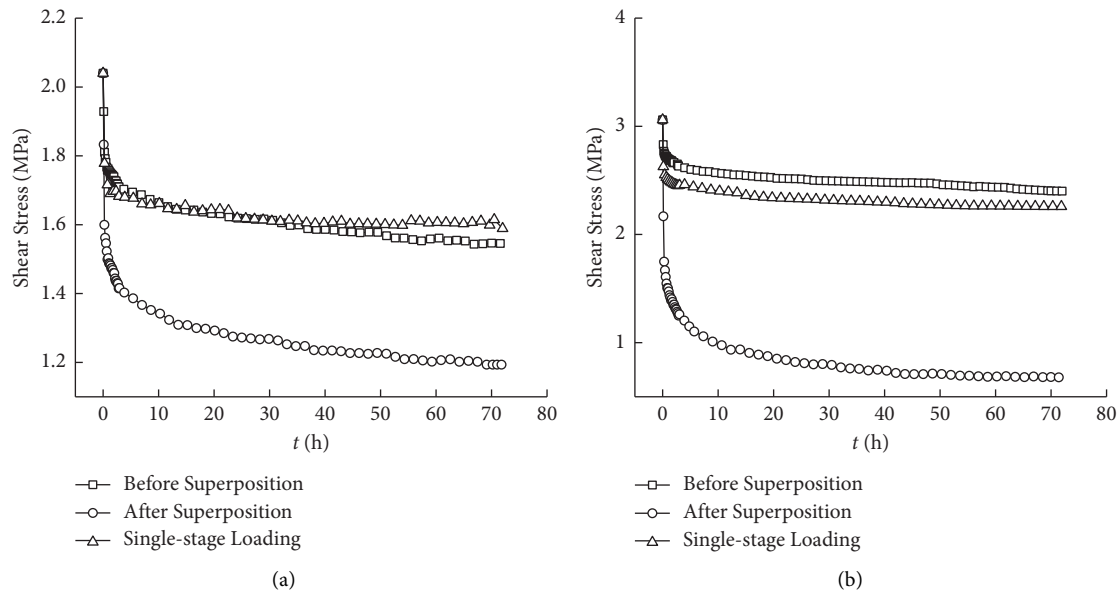


FIGURE 10: Relaxation curves of 10° discontinuities by different treatment processes: (a) $\tau_0/\tau_{\max} = 0.6$, $\sigma = 3.924$ MPa; (b) $\tau_0/\tau_{\max} = 0.9$, $\sigma = 3.924$ MPa.

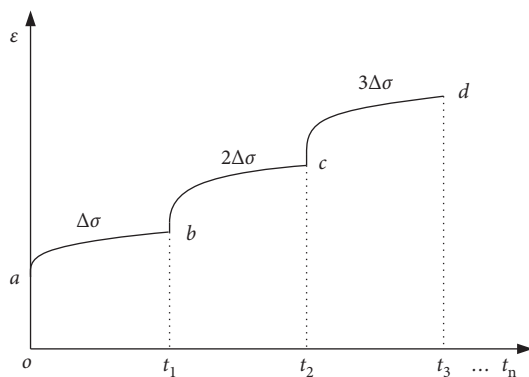


FIGURE 11: Typical creep curve for step loading.

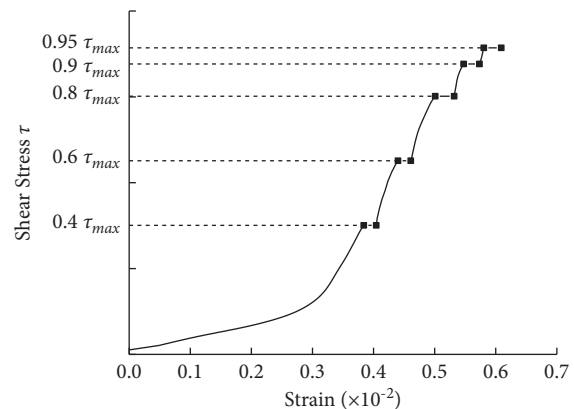


FIGURE 13: Stress-strain curve of 45° structural plane during creep.

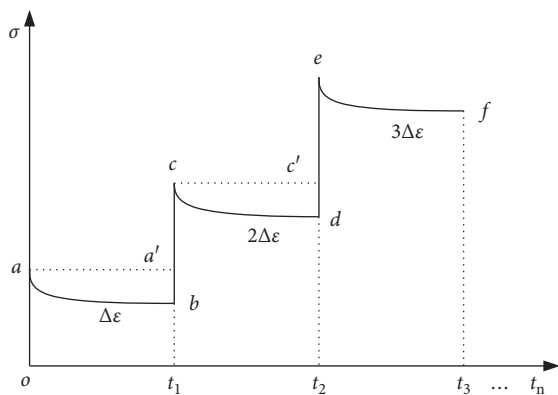


FIGURE 12: Typical relaxation curve for step loading.

the deformation increases monotonically, but the stress first increases, then decreases, and then increases, which is not a monotonic variation.

The Boltzmann superposition principle assumes that when the total external effects at different times τ continue to a certain time t in the future, the principle can be used for mathematical processing only when this effect is linear, i.e., when $\sigma_1(t)$, $\sigma_2(t)$, and $\sigma_1(t) + \sigma_2(t)$ are acting on the sample, the strains produced are $\varepsilon_1(t)$, $\varepsilon_2(t)$, and $\varepsilon_1(t) + \varepsilon_2(t)$, respectively [15].

The step loading method can be applied regardless of whether the after-effects are linear or nonlinear, but when superposition processing is performed, it is a prerequisite that the external effects on the material are monotonic. For example, in the creep test, the effect of stress on the deformation of the specimen is monotonic; thus, the creep curve can be processed by the superposition method.

In the previous section, based on the relaxation-type integral equation (equation (2)), the superposition method of the relaxation curve was derived according to principle of superposition for the creep method. However, the curve obtained by the relaxation superposition method did not

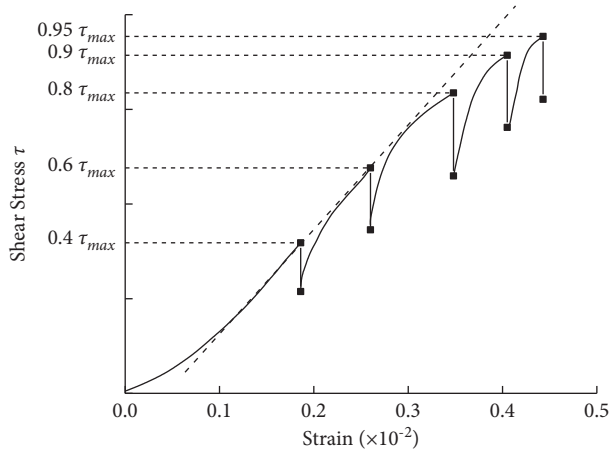


FIGURE 14: Stress-strain curve of the 45° structural surface during the relaxation process.

match with that of the single-stage loading test for the following reasons:

- (1) When the superposition method for the relaxation curve is derived based on the Boltzmann principle and the superposition principle of creep method, the relaxation process needs to satisfy the following conditions: when $\varepsilon_1(t)$, $\varepsilon_2(t)$, and $\varepsilon_1(t) + \varepsilon_2(t)$ are acting on the sample, the generated relaxation stress is $\Delta\sigma_1(t)$, $\Delta\sigma_2(t)$, and $\Delta\sigma_1(t) + \Delta\sigma_2(t)$, respectively. It can be seen from Figure 9 that the results of relaxation test do not satisfy this condition, so the superposition method for relaxation derived according to the creep superposition method is not applicable here.
- (2) In the relaxation process, the effect of strain on stress is not monotonic, but the stress first increases, then decreases, and then again increases, which is different from the monotonically increasing trend observed during the creep process.

6. Conclusions

- (1) The mathematical basis for the superposition of the relaxation curve under step loading is derived according to the Boltzmann principle. After processing the step loading relaxation curve according to the derived superposition method, it is found that the relaxation curve is significantly different from the single-stage loading relaxation curve at the same shear stress level.
- (2) In the step loading test, the relaxation curve of step loading test without superposition at each stress level is basically the same as the single loading stage relaxation curve at the corresponding stress level. It can be considered that when the step loading relaxation test is implemented, the relaxation curve at each level of stress can reflect the relaxation curve when the sample is loaded to the same stress level at a single time without performing superposition on the relaxation curve like the step loading creep test.

- (3) The typical creep curve shows that the creep deformation increases monotonically with time, and the curve can be processed by the superposition method, while the typical relaxation curve shows that the stress exhibits a nonmonotonic increasing trend with time during relaxation, which is inconsistent with the Boltzmann principle and cannot be processed by the superposition method.

References

- [1] M. R. Shen and J. F. Chen, *Rock Mechanics*, pp. 3-4, Tongji university press, Shanghai, China, 2006.
- [2] Q. Y. Zhang, *Rheological Test, Rheological Theory and Engineering Application of High Slope Rock Mass*, pp. 2-3, Science Press, Beijing, China, 2014.
- [3] H. Liu, H. Xie, J. He, M. Xiao, and J. Liu, "Experimental investigation on anisotropic creep characteristics of quartz mica schist," *Journal of Southwest Jiaotong University*, vol. 50, no. 4, pp. 656-661+697, 2015.
- [4] Y. M. Song, T. B. Zhao, and Y. D. Jiang, "Experimental study on the evolution of creep deformation field of rock based on DSCM," *Journal of China University of Mining & Technology*, vol. 42, no. 3, pp. 466-470, 2013.
- [5] W. J. Xiao, X. J. Wang, C. Chen, Y. L. Zhuo, and Y. X. Li, "Creep strain characteristics of deep limestone under step loading," *Journal of Yangtze River Scientific Research Institute*, vol. 34, no. 08, pp. 135-138+143, 2017.
- [6] W. J. Xie, C. Gong, Y. F. Liu, K. Zhao, and H. G. Li, "Experimental study on creep characteristics of red sandstone under step loading," *Journal of Safety Science and Technology*, vol. 13, no. 06, pp. 34-39, 2017.
- [7] Q. Zhang, Z. Song, J. Wang, Y. Zhang, and T. Wang, "Creep properties and constitutive model of salt rock," *Advances in Civil Engineering*, vol. 2021, no. 4, pp. 1-29, 2021.
- [8] W. Y. Xu, S. Q. Yang, S. L. Yang, S. Y. Xie, J. F. Shao, and Y. F. Wang, "Investigation on triaxial rheological mechanical properties of greenschist specimen(I): experimental results," *Rock and Soil Mechanics*, vol. 26, no. 4, pp. 531-537, 2005.
- [9] M. R. Shen and Q. Z. Zhang, "Study of shear creep characteristics of Greenschist discontinuities," *Chinese Journal of Rock Mechanics and Engineering*, vol. 29, no. 6, pp. 1149-1155, 2010.
- [10] Q. Z. Zhang, M. R. Shen, and W. Q. Ding, "Study on the shear creep characteristics and constitutive model of rock mass

- [11] Z. Wang, L. L. Gu, Q. Z. Zhang, Y. Songlin, and Z. Guokai, "Creep characteristics and prediction of creep failure of rock discontinuities under shearing conditions," *International journal of earth science*, vol. 109, pp. 945–958, 2020.
- [12] H. Lin, X. Zhang, Y. Wang, R. Yong, and X. Fan, "Improved nonlinear nishihara shear creep model with variable parameters for rock-like materials," *Advances in Civil Engineering*, vol. 2020, no. 3, pp. 1–15, 2020.
- [13] C. C. Xia and S. Y. Zhong, "Experimental data processing method in consideration of influence of loading history on rock specimen deformation," *Journal of Central-South Institute of Mining and Metallurgy*, vol. 20, no. 1, pp. 31–37, 1989.
- [14] Z. J. Chen and W. F. Kang, "On the locked in stress, creep and dilatation of rocks, and the constitutive equations," *Chinese Journal of Rock Mechanics and Engineering*, vol. 10, no. 4, pp. 299–312, 1991.
- [15] X. Liu, *Introduction to Rock Rheology*, pp. 139–143, Geology Publishing House, Beijing, China, 1994.
- [16] H. P. Xie and Z. H. Chen, *Rock Mechanics*, pp. 64–65, Science Press, Beijing, China, 2004.
- [17] B. Ladanyi and G. H. Johnston, "Behavior of circular footings and plate Anchors embedded in permafrost," *Canadian Geotechnical Journal*, vol. 11, no. 4, pp. 531–553, 1974.
- [18] H. Yu, M. Zhou, H. Liu, Z. Huang, and T. Jiang, "Experimental investigation on stress relaxation properties of silty mudstone under triaxial compression," *Chinese Journal of Rock Mechanics and Engineering*, vol. 30, no. 4, pp. 803–811, 2011.
- [19] F. M. Chen, Q. G. Hu, and G. Z. Ning, "Silt mudstone stress relaxation characteristics under tri-axial stress condition," *Journal of Shandong University*, vol. 47, no. 3, pp. 125–129, 2017.
- [20] C. Paraskevopoulou, M. Perras, M. Diederichs et al., "The three stages of stress relaxation - observations for the time-dependent behaviour of brittle rocks based on laboratory testing," *Engineering Geology*, vol. 216, pp. 56–75, 2017.
- [21] W. F. Zhou and M. R. Shen, "Experimental study of stress relaxation characteristics of regular rock mass discontinuities," *Soil Engineering and Foundation*, vol. 28, no. 2, pp. 138–141, 2014.
- [22] G. H. Tian, M. R. Shen, W. F. Zhou, Y. L. Li, and Z. K. Liu, "Shear relaxation characteristic of serrate structure surface under stepwise loading," *Journal of Harbin Institute of Technology*, vol. 48, no. 12, pp. 108–113, 2016.
- [23] Z. Wang, L. L. Gu, M. R. Sheng, F. Zhangd, G. Zhanga, and X. Wange, "Shear stress relaxation behavior of rock discontinuities with different joint roughness coefficient and stress histories," *Journal of Structural Geology*, vol. 126, pp. 272–285, 2019.
- [24] Q. Zhang, C. Wu, X. Fei, A. Bo, and D. Liu, "Time-dependent behavior of rock joints considering asperity degradation," *Journal of Structural Geology*, vol. 121, no. 2019, pp. 1–9, 2019.
- [25] B. Ladanyi and G. Archambault, "Simulation of shear behavior of a jointed rock mass," *Proceedings of the 11th US Symposium on Rock Mechanics*, USRMS, American Rock Mechanics Association, New York, NY, USA, 1969.
- [26] N. Barton and V. Choubey, "The shear strength of rock joints in theory and practice," *Rock Mechanics Felsmechanik Me*, vol. 10, no. 1–2, pp. 1–54, 1977.
- [27] P. H. S. W. Kulatilake, G. Shou, T. H. Huang, and R. M. Morgan, "New peak shear strength criteria for anisotropic rock joints," *International Journal of Rock Mechanics*
- [28] C. C. Xia, Z. C. Tang, W. M. Xiao, and Y. L. Song, "New peak shear strength criterion of rock joints based on quantified surface description," *Rock Mechanics and Rock Engineering*, vol. 47, no. 2, pp. 387–400, 2014.
- [29] L.-l. Gu, Z. Wang, F. Zhang, F. Gao, and X. Wang, "Dynamic evolution of shear rate-dependent behavior of rock discontinuity under shearing condition," *Journal of Central South University*, vol. 28, no. 6, pp. 1875–1887, 2021.
- [30] Z. Wang, L. L. Gu, Q. Z. Zhang, and B. A. Jang, "Influence of initial stress and deformation states on the shear creep behavior of rock discontinuities with different joint roughness coefficients," *Rock Mechanics and Rock Engineering*, 2021.
- [31] F. D. Patton, *Multiple Modes of Shear Failure in Rock*, Proceedings of the 1st Congress of International Society of Rock Mechanics, Lisbon PORTUGAL, 1966.
- [32] N. Barton, "Review of a new shear-strength criterion for rock joints," *Engineering Geology*, vol. 7, no. 4, pp. 287–332, 1973.
- [33] J. Seidel and C. Haberfeld, "The application of energy principles to the determination of the sliding resistance of rock joints," *Rock Mechanics and Rock Engineering*, vol. 28, no. 4, pp. 211–226, 1995.
- [34] H. B. Li, H. Feng, and B. Liu, "Study on strength behaviors of rock joints under different shear deformation velocities," *Chinese Journal of Rock Mechanics and Engineering*, vol. 25, pp. 2435–2440, 2006.
- [35] M. R. Shen and Q. Z. Zhang, "Experimental study of shear deformation characteristics of rock mass discontinuities with regular surface roughness," *Chinese Journal of Rock Mechanics and Engineering*, vol. 29, no. 4, pp. 713–719, 2010.
- [36] D. Huang, R. Q. Huang, and P. Lei, "Shear deformation and strength of through-going saw-tooth rock discontinuity," *Journal of China Coal Society*, vol. 39, no. 7, pp. 1229–1237, 2014.
- [37] H. Zhou, F. Z. Meng, C. Q. Zhang, J. J. Lu, and R. C. Xu, "Experimental study of acoustic emission characteristic of discontinuity under shearing condition," *Chinese Journal of Rock Mechanics and Engineering*, vol. 34, pp. 2827–2836, 2015.
- [38] M. A. Brideau, M. Yan, and D. Stead, "The role of tectonic damage and brittle rock fracture in the development of large rock slope failures," *Geomorphology*, vol. 103, no. 1, pp. 0–49, 2009.
- [39] W. D. Yang, Q. Y. Zhang, F. Chen et al., "Research on nonlinear rheological model of diabase and treatment for creep loading history," *Chinese Journal of Rock Mechanics and Engineering*, vol. 30, no. 7, pp. 1405–1413, 2011.
- [40] A. Liu, M. R. Shen, and J. C. Jiang, "Investigation of the shear stress relaxation characteristics of a structural plane using the isostress cyclic loading method," *Geotechnical Testing Journal*, vol. 38, no. 2, pp. 219–228, 2015.

Design of RC-Braced Long Columns Based on New Moment Magnifiers

Deepika Priyadarshini Palai, *Department of Civil Engineering, NM Institute of Engineering & Technology, Bhubaneswar, deepikadalai2561@gmail.com*

Saruk Mallick, *Department of Civil Engineering, Raajdhani Engineering College, Bhubaneswar, sarukmallik57@yahoo.co.in*

Sagarika Pasayat, *Department of Civil Engineering, Aryan Institute of Engineering & Technology, Bhubaneswar, s.pasayat@gmail.com*

Satyaprakash Mishra, *Department of Civil Engineering, Capital Engineering College, Bhubaneswar, satyaprakash_m25@gmail.com*

ABSTRACT

Different codes approximate the second-order effects by applying equations focused on the maximum extra moment through the column height, based on updated approaches for the results of first-order analysis of RC columns. The additional moments between the column and the connected beam are not taken into account in these equations; only the influence of the connected beams is taken into account by dealing with the effective length of the column, not the entire length. Furthermore, the second-order effect, which is induced by axial force and the inverse moments owing to beam restriction at the column ends, was not taken into consideration in these equations. As a simplified computation that may be employed in the design procedure, this work proposes a novel moment magnifiers matrix for the additional moments at the connection between braced columns and connected beams. That is, using a second-order analysis equation based on transforming the original long column.

1. Introduction

In braced long columns, a column is subjected to axial load and equal or unequal end moments, which are caused by the connected beam loads, and deformed laterally due to the existence of end moments. The axial load and occurred lateral deflection cause additional bending moments along the column height which is called second order. The additional bending moments cause additional lateral displacements and rotations of the column and additional rotation of the members connecting into the column.

This, in turn, leads to change to the first-order bending moments through the column height and at the connected ends of the column with the beams, which are computed from an elastic frame analysis. The equations of equilibrium in a first-order analysis are derived by assuming that the deflections have a negligible impact on the internal forces in the members. In a second-order analysis, the equations of equilibrium consider the deformed shape of the structure. Instability can be investigated only via a second-order analysis because it is the loss of equilibrium of the deformed structure that causes instability[1]. The elastic structural

analysis of the second-order effect can be performed in the finite element method by adding the geometric stiffness matrix to the elastic linear matrix “mechanical stiffness” for the beam column element. The geometric stiffness, as shown in (1), is not a function of the mechanical properties of the element and is only a function of the element’s length and the force in the element. Hence, the term “geometric” stiffness matrix is introduced so that the matrix has a different name from the “mechanical” stiffness matrix, which is based on the physical properties of the element. The geometric stiffness exists in all structures; however, it becomes important only if it is large compared to the mechanical stiffness of the structural system [2]. To use this stiffness, the element must be divided into small segments between the load points for more accuracy. Several trials must be done when using the geometric stiffness till achieving the equilibrium, as shown in equation (3).

$$\begin{bmatrix} F_i \\ M_i \\ F_j \\ M_j \end{bmatrix} = \frac{T}{30L} \begin{bmatrix} 36 & 3L & -36 & 3L \\ 3L & 4L^2 & -3L & -L^2 \\ -36 & -3L & 36 & -3L \\ 3L & -L^2 & -3L & 4L^2 \end{bmatrix} \begin{bmatrix} v_i \\ \theta_i \\ v_j \\ \theta_j \end{bmatrix} \quad (1)$$

$$\text{or } F_G = K_G v,$$

$$\begin{bmatrix} F_i \\ M_i \\ F_j \\ M_j \end{bmatrix} = \frac{EI}{L^3} \begin{bmatrix} 12 & 6L & -12 & 6L \\ 6L & 4L^2 & -6L & -2L^2 \\ -12 & -6L & 12 & -6L \\ -6L & -2L^2 & -6L & 4L^2 \end{bmatrix} \begin{bmatrix} v_i \\ \theta_i \\ v_j \\ \theta_j \end{bmatrix} \quad (2)$$

$$\text{or } F_E = K_E v,$$

$$\begin{aligned} F_T &= F_E + F_G \\ &= [K_E + K_G]v \\ &= K_T v. \end{aligned} \quad (3)$$

A nonlinear second-order frame analysis procedure can be performed to analyze reinforced concrete columns that are a part of frames. In order to account for second-order effects due to geometric and material nonlinearities, the theoretical model (computer software) uses classical stiffness analysis of linear elastic two-dimensional structural frames, the iterative technique combined with an incremental method for computing load-deflection behavior and failure load of the frame, frame discretization to account for column chord ($P-\Delta$) effects and axial load-bending moment-curvature ($P-M-\phi$) relationships to account for effects of nonlinear material behavior [3].

2. Computing of the Additional Moments in Different Codes

Design of RC long column must consider the induced additional moments in these columns due to the axial load and occurred lateral deflection. Computing the additional

moments for design requires simplified procedure and adequate accuracy. There are many methods that have been derived from modifying the results of a first-order analysis to approximate the second-order effects as which are recommended in a lot of codes such as American code ACI [4] and Canadian code CSA [5]. These codes permit the use of a moment magnifier approach to approximate the second-order moments due to the axial load acting through the lateral deflection caused by the end moments acting on a column. In the moment-magnifier analysis, unequal end moments are applied on the column shown in Figure 1(a). The column is replaced with a similar column subjected to equal moments at both ends, which is shown in Figure 1(b). The bending moments are chosen where the maximum magnified moment is the same in both columns. The expression for the factor C_m was originally derived for use in the steel beam-columns design and was adopted without change for concrete design.

M_2, M_1 are the larger and smaller end moments of the first-order analysis, respectively. If a single curvature bending occurred by the moments M_1 and M_2 , M_1/M_2 is positive. However, if the moments cause double curvature, M_1/M_2 is negative. The moment magnifier equation in the cases of no sway according to ACI,

$$\begin{aligned} M_c &= \delta_{ns} \cdot M_2 \\ &= C_m \delta_1 M_2 \geq M_2. \end{aligned} \quad (5)$$

$$C_m = 0.6 + 0.4 \frac{M_1}{M_2}, \quad (4)$$

Chen and Lui [6] explain that C_m and δ_1 for pin-ended columns subjected to end moments can be derived from the basic differential equation governing the elastic in-plane behavior of a column. ACI Code goes on to define δ_{ns} as follows:

$$\delta_{ns} = \frac{C_m}{1 - 0.75P/P_c}. \quad (6)$$

The 0.75 factor in equation (6) is the stiffness reduction factor ϕK , which is based on the probability of under strength of a single isolated slender column.

In Eurocode [7], three methods applied for second-order impacts analysis are pointed:

Simplified method: based on nominal stiffness (MNS), simplified method: based on nominal curvature (MNC), and overall method: based on nonlinear second-order analysis.

The method of nominal stiffness is based on the critical force due to the buckling computed for the nominal stiffness of the analyzed member. It is recommended that the material nonlinearity, creep, and cracking, which have an effect on the conduct of the structure members, are taken into consideration. The design moment in the members subjected to the bending moment and an axial force which includes the impact of the first and second-order effects can be illustrated as a bending moment boosted by the factor described below:

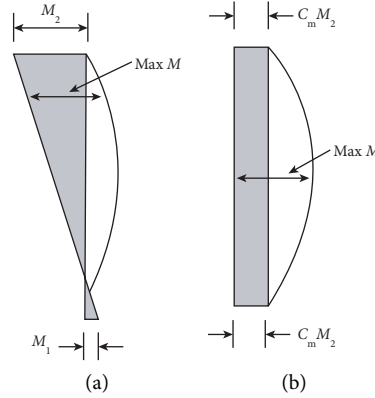


FIGURE 1: Equivalent moment factor C_m . (a) Actual moments at failure. (b) Equivalent moments at failure.

$$\begin{aligned}
 M_{E d} &= M_{0 E d} + M_2 \\
 &= M_{0 E d} + M_{0 E d} \cdot \frac{\beta}{(N_B/N_{E d}) - 1} \\
 &= M_{0 E d} \cdot \left[1 + \frac{\beta}{(N_B/N_{E d}) - 1} \right],
 \end{aligned} \quad (7)$$

where $M_{0 E d}$ is the 1st order moment, including the effect of imperfections, M_2 is the nominal 2nd order moment, N_B is the buckling load based on nominal stiffness, $N_{E d}$ is the design value of the axial load, β is the factor which depends on the distribution of the 1st and 2nd order moments.

The method of nominal curvature allows for the calculation of the second-order moment based on the assumed curvature distribution (which responds to the first-order moment increased by the second-order effects) on the length of the member. The distribution of the total curvature can be either parabolic or sinusoidal.

The value of the II order moment can be calculated as follows:

$$M_2 = N_{E d} \cdot e_2, \quad (8)$$

where $N_{E d}$ is the design value of the axial load, e_2 is the deflection calculated by taking into account such parameters as creep, the intensity of reinforced and also distribution of the reinforcement over the height of the cross-section

$$e_2 = \frac{1}{r} \cdot \frac{l_0^2}{c}, \quad (9)$$

where c is the factor depending on the curvature distribution, l_0 is the effective length, and $1/r$ is the curvature.

According to Egyptian Code [8], (M_{add}) is induced by the deflection (δ) given by the following:

$$M_{add} = P \cdot \delta. \quad (10)$$

If the column is long in t direction,

$$\delta_t = \frac{\lambda_t^2 t}{2000}, \quad (11)$$

$$M_{add} = P \cdot \delta_t.$$

However, if the column is long in b direction,

$$\delta_b = \frac{\lambda_b^2 b}{2000},$$

$$M_{add} = P \cdot \delta_b, \quad (12)$$

$$\lambda_b = \frac{H_e}{b},$$

$$H_e = k \cdot H_0,$$

where H_e is the effective height of the column, H_0 is clear height of the column, k is length factor which depends on the conditions of the end column and the bracing conditions.

The presented equations in the mentioned codes depend on their derivation on the isolated analysis for the long column and computed maximum bending moments induced through the height of the column. The additional moments analysis at the joints between the column and connected beams did not receive any interest in the different codes. Only the recommended equations in these codes take into account the effect of the connected beams on the additional moments through the column height by dealing with the effective length of the column, not the total length. In this research, a new moment magnifiers matrix will be presented in a derived equation for an equivalent column to compute the additional moments of the braced long column, including the moments at the joints between the column and the connected beams. In this model, the additional moment diagram of a braced long column and its deformations can be computed taking into consideration the second-order effect of the axial load and the inverse moments at the connection between the columns and the beams. Material nonlinearities will be considered by modifying the elastic flexural rigidity (EI) to effective flexural stiffness computed according to ACI (2019).

3. Lateral Displacements in a Long Column under End Moments

In the first-order analysis, the curvature equation for a long column under equal end moments as shown in Figure 2 can be expressed as follows:

$$\frac{d^2 y}{dx^2} = -\frac{M}{EI}, \quad (13)$$

where $M = M_0$

$$\frac{dy}{dx} = -\frac{M_0}{EI}x + C_1, \quad (14)$$

$$\delta_0 = -\frac{1}{EI} \left[\frac{M_0 x^2}{2} \right] + C_1 x + C_2. \quad (15)$$

By applying the boundary conditions, it is found that $C_2 = 0$ and $C_1 = M_0 L / 2EI$.

And equation (15) becomes as follows:

$$\delta_0 = \frac{1}{EI} \left[-\frac{M_0 x^2}{2} + \left(\frac{M_0 L}{2} \right) x \right]. \quad (16)$$

Maximum lateral displacement at the mid-span of the column can be expressed as follows:

$$(\delta_0)_{\max} = \frac{M_0 L^2}{8EI}. \quad (17)$$

Due to the second-order effect, the lateral displacement of the column increases and it can be expressed as $(\delta_0 + \delta_a)$, where δ_a is the lateral displacement which is caused by the additional moments. To compute the maximum additional lateral displacement at the middle span of the column, the virtual work method can be used. As observed that the deformation shape of the first-order analysis is 2nd curve as shown in equation (16). As a result, additional displacement and the additional moment diagram will be 2nd curve, where $M_{\text{add}} = P \cdot (\delta_0 + \delta_a)$.

The additional lateral displacement can be found as follows:

$$\delta_a = \int_0^L M_{\text{add}} M_{11} dx,$$

$$M_{\text{add}} = P \cdot (\delta_0 + \delta_a),$$

$$\delta_a = \frac{1}{EI} \left(2 * \frac{2}{3} P (\delta_0 + \delta_a) \cdot \frac{L}{2} \cdot \frac{5}{8} \cdot \frac{L}{4} \right), \quad (18)$$

$$\delta_a = \frac{\delta_0 5PL^2 / 48EI}{1 - 5PL^2 / 48EI},$$

$$\text{But } \frac{1}{P_e} = \frac{5L^2}{48EI} \text{ where } P_e \text{ is Euler load,}$$

$$\delta_a = \frac{\delta_0 P / P_e}{1 - P / P_e}.$$

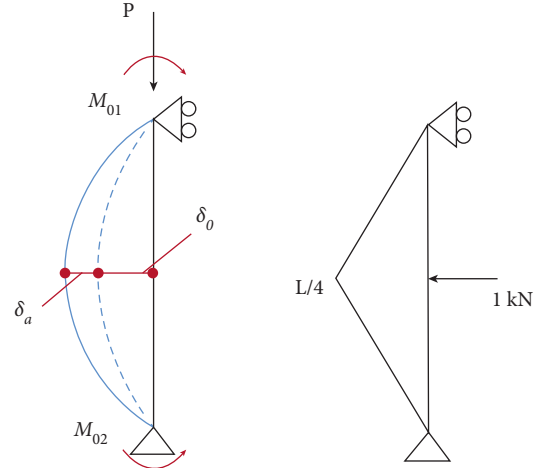


FIGURE 2: Deformed shape of a long column under end moments.

The final maximum displacement will be as follows:

$$\delta_f = \frac{\delta_0 P / P_e}{1 - P / P_e} + \delta_0,$$

$$\text{It can be put } \eta = \frac{1}{1 - P / P_e}, \quad (19)$$

$$\text{So } \delta_f = \delta_0 \eta.$$

The maximum additional moments can be formulated as follows:

$$M_{\text{add}} = P \delta_0 \eta. \quad (20)$$

When the column is deformed under unequal end moments, the bigger moment can be divided into two parts $M = M_0 + \Delta M$, and the column will be considered under equal end moments (M_0) which was illustrated previously and one end moment (ΔM).

In the first-order analysis, the curvature equation for a long column under one end moment can be expressed as follows:

$$\frac{d^2 y}{dx^2} = -\frac{M}{EI}, \quad (21)$$

$$M = Rx \text{ where } R \text{ is the reaction and equals } R = \frac{\Delta M}{L}, \quad (22)$$

$$\frac{dy}{dx} = -\frac{1}{EI} \left(\frac{Rx^2}{2EI} \right) + C_1, \quad (23)$$

$$\delta_{\Delta 0} = -\frac{1}{EI} \left[\frac{Rx^3}{6} \right] + C_1 x + C_2, \quad (24)$$

where $\delta_{\Delta 0}$: the lateral displacement due to ΔM .

By applying the boundary conditions, $C_2 = 0$, $C_1 = RL^2 / 6EI$ and put $R = \Delta M / L$

$$\delta_{\Delta 0} = \frac{1}{EI} \left[-\frac{\Delta M x^3}{6L} + \frac{\Delta M L x}{6} \right]. \quad (25)$$

As shown in equation (24), the deflection curve due to ΔM is 3rd-degree parabolic curve, and the maximum deflection occurs when $d\delta/dx = 0$

$$\text{Thus } \frac{dy}{dx} = \frac{1}{EI} \left(\frac{Mx^2}{2L} + \frac{\Delta M L}{6} \right) = 0. \quad (26)$$

By solving equation (26), max. lateral displacement due to ΔM will be at $x = L/\sqrt{3}$ and Max. lateral displacement due to ΔM is given by the following:

$$\delta_{\Delta 0} = \frac{\Delta M L^2}{9\sqrt{3}EI}. \quad (27)$$

Also, due to the second-order effect, the lateral displacement of the column increases, and it can be expressed as $(\delta_{\Delta 0} + \delta_{\Delta a})$, where $\delta_{\Delta a}$ is the lateral displacement which is caused by the additional moments. Considering that the deformation shape of the first-order analysis is 3rd curve as shown in equation (25), also additional displacement and the additional moment diagram will be 3rd curve. Similarly, the maximum lateral displacement due to ΔM in second-order analysis can be found as the same manner of the case of equal end moments as in the following equation:

$$\delta_{f\Delta} = \frac{\delta_{\Delta 0}}{1 - P/P_e} \quad (28)$$

$$= \delta_{\Delta 0} \eta.$$

The additional moments can be formulated as follows:

$$M_{\text{add}} = P\delta_{\Delta 0}\eta. \quad (29)$$

4. Equivalent Lateral Load for the Second-Order Effect in a Long Braced Column

As shown in section (2), when the column is loaded with an equal end moment, the deformed shape of the column in the second-order analysis was 2nd-degree curve. As a result, the expected additional bending moment diagram will be as the induced bending moment from the regular distributed load. Thus, the long column in the second-order effect can be replaced in a beam element subjected to an equivalent regular distributed load, and the equivalent load can be computed as follows:

$$\frac{w_{eqR} L^2}{8} = P\eta \left(\frac{M_0 L^2}{8EI} \right), \quad (30)$$

where $w_{eqR} L^2/8$: max. moment due to equivalent regular load, $P\eta(M_0 L^2/8EI)$: max. moment due to second-order analysis, w_{eqR} : equivalent regular distributed load.

$$w_{eqR} = P\eta \frac{M_0}{EI}. \quad (31)$$

In similar to the column under equally end moment, the deformed shape in the second-order analysis due to one end moment as shown in Figure 3 is 3rd-degree curve and the additional bending moment diagram in the second-order analysis will be as the induced bending moment from the triangular distributed load. Also, in this case, the long column in the second-order effect can be replaced in a beam that is subjected to equivalent triangular distributed load, and the equivalent load can be computed as follows:

$$\frac{w_{eq\Delta} L^2}{9\sqrt{3}} = P\eta \left(\frac{\Delta M L^2}{9\sqrt{3}EI} \right), \quad (32)$$

where $w_{eq\Delta} L^2/9\sqrt{3}$ is the max. moment due to equivalent triangular load, $P\eta(\Delta M L^2/9\sqrt{3}EI)$ is the max. moment due to second-order analysis, and $w_{eq\Delta}$ is the equivalent triangular distributed load

$$w_{eq\Delta} = P\eta \frac{\Delta M}{EI}. \quad (33)$$

5. New Moment Magnifiers Matrix of Braced Long Columns

5.1. Equivalent Column Modeling. Based on the equivalent column concept, Afefy and El-Tony [9] have shown equivalent pin-ended columns for columns bent in either single or double curvature modes where the impact of end eccentricity ratio was related to the equivalent column length. They deduced that the equivalent column concept can be generalized to simplify columns bent in single curvature modes with different end eccentricities combinations to pin-ended axially loaded columns. Furthermore, the equivalent column concept can be carried out for a specific state of a column bent in double curvature mode.

Here, in the suggested equivalent column model, the column at any structure will be analyzed as an isolated element. The equivalent column was represented as an element restricted by a rotational spring support at its ends and it is subjected to lateral distributed loads. The lateral distributed loads have the same influence of the second-order effect on the induced additional moments in the long column. Column (1), for example, in the shown closed frame in Figure 4 will be analyzed to illustrate the model. The column will be modeled as a pin-supported member restricted by the connected beams which are as rotational spring supports. Computing the rotational stiffness (K_θ) of these beams will be discussed later. The second-order analysis of the modeled column in Figure 5 can be divided into two parts.

The first part is concerned with the deformation due to the end moments of the first-order analysis without the existence of the reaction moments of the rotational spring. The induced moments of the second-order effect is equivalent to the induced moments of trapezoidal load. Thus, the column can be represented as a pin-supported column subjected to triangular distributed loads w_{eq1} and w_{eq2}

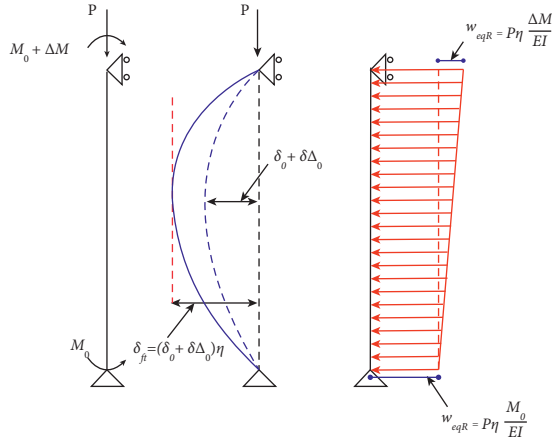


FIGURE 3: Equivalent lateral load for the second-order effect of a long column.

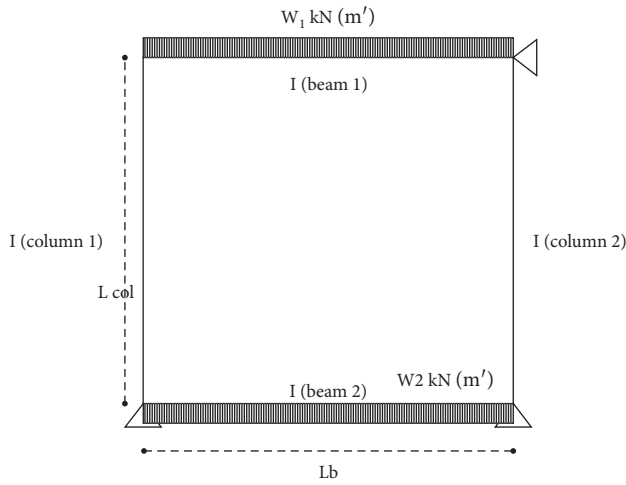


FIGURE 4: Closed frame as an example.

$$w_{eq1} = P\eta \frac{M_{01}}{EI}, \quad (34a)$$

where w_{eq1} is the triangular equivalent load for the second effect due to moment at the column end at the beam of higher stiffness and M_{01} is the the end moment at the beam of higher stiffness due to first order.

$$w_{eq2} = P\eta \frac{M_{02}}{EI}. \quad (34b)$$

w_{eq2} is the triangular equivalent load for the second effect due to the moment at the column end at the beam of lower stiffness.

M_{02} is the the end moment at the beam of lower stiffness due to first order.

The second part is concerned with the deformation due to the reaction moments of the spring rotational support only. Also, the column in the second effect will be represented as a pin-supported column subjected to triangular distributed loads w_{eq1}^* and w_{eq2}^*

w_{eq1}^* is the triangular equivalent load for the second effect due to the reaction moment of spring rotational support at the beam of higher stiffness, M_1 ; the additional moment of spring rotational support at the beam of higher stiffness.

$$w_{eq1}^* = P\eta \frac{M_1}{EI}, \quad (35)$$

w_{eq2}^* is the triangular equivalent load for the second effect due to the reaction moment of spring rotational support at the beam of lower stiffness, M_2 ; the additional moment of spring rotational support at the beam of lower stiffness.

$$w_{eq2}^* = P\eta \frac{M_2}{EI}. \quad (36)$$

By arranging the linear stiffness matrix of a beam element for computing the moments of the modeled column in Figure 5, the formula will be as follows:

$$\frac{EI}{L^3} \begin{bmatrix} 4L^2 & 2L^2 \\ 2L^2 & 4L^2 \end{bmatrix} \begin{bmatrix} \theta_1 \\ \theta_2 \end{bmatrix} + \begin{bmatrix} \frac{-w_{eq1}L^2}{20} - \frac{w_{eq2}L^2}{30} + \frac{P\eta M_2 L^2}{30EI} - \frac{P\eta M_1 L^2}{20EI} \\ \frac{w_{eq1}L^2}{30} + \frac{w_{eq2}L^2}{20} - \frac{P\eta M_2 L^2}{20EI} + \frac{P\eta M_1 L^2}{30EI} \end{bmatrix} = \begin{bmatrix} M_1 \\ M_2 \end{bmatrix}. \quad (37)$$

The terms in equation (37) are as shown below:

$$K_0 = \frac{EI}{L^3}, \quad (38a)$$

$$C = \frac{P\eta L^2}{EI}, \quad (38b)$$

$$\theta_1 = \frac{-M_1}{K_{\theta 1}}, \quad (38c)$$

$$\theta_2 = \frac{-M_2}{K_{\theta 2}}. \quad (38d)$$

The matrix in (37) can be divided into the following:

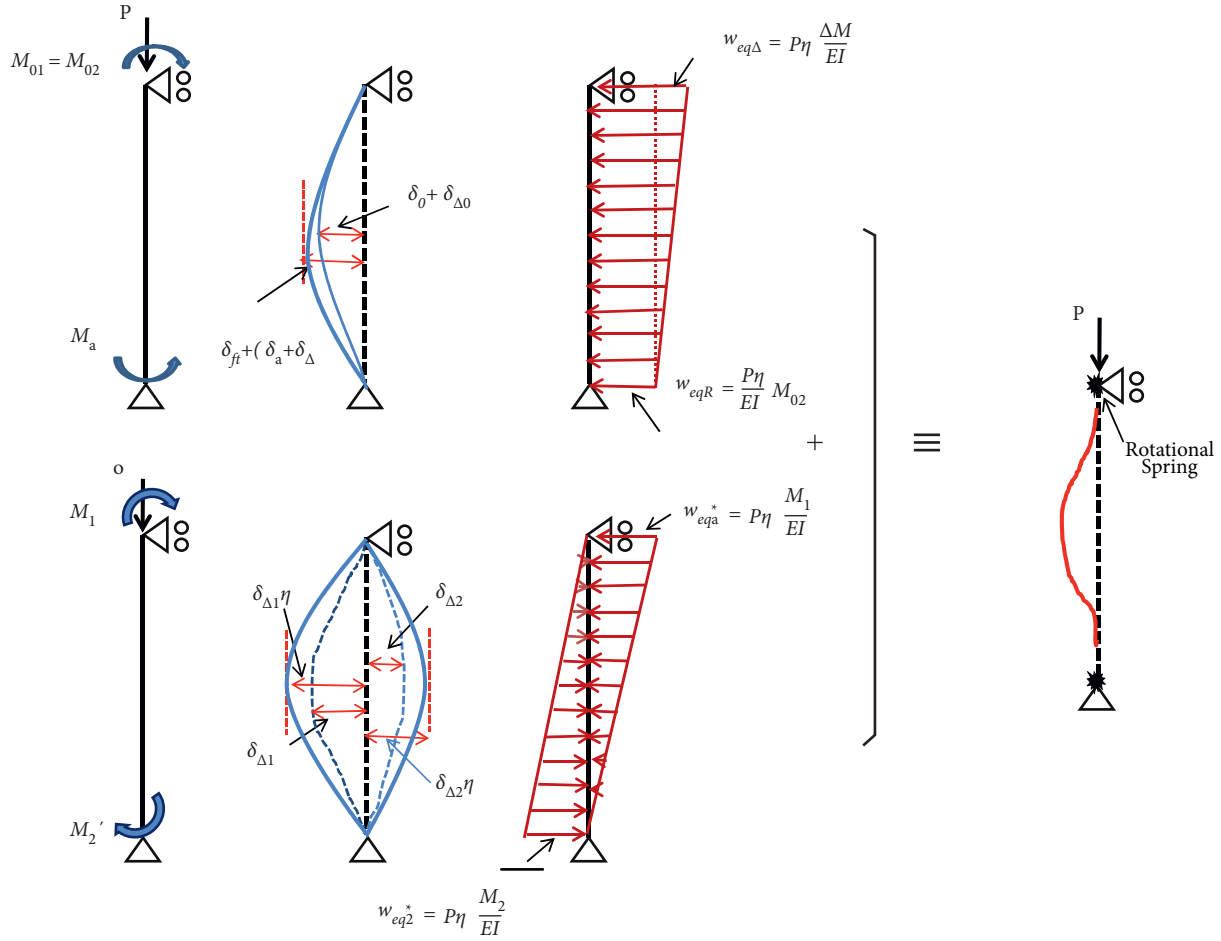


FIGURE 5: Equivalent column modeling for the restricted column (1) in the closed frame.

$$\begin{aligned} \left[-1 - \frac{4L^2K_0}{K_{\theta 1}} + \frac{C}{20} \right] M_1 + \left[-\frac{2L^2K_0}{K_{\theta 2}} + \frac{C}{30} \right] M_2 &= \frac{w_{eq1}L^2}{20} + \frac{w_{eq2}L^2}{30}, \\ \left[\frac{2L^2K_0}{K_{\theta 1}} + \frac{C}{30} \right] M_1 + \left[-1 - \frac{4L^2K_0}{K_{\theta 2}} - \frac{C}{20} \right] M_2 &= \frac{-w_{eq1}L^2}{30} - \frac{w_{eq2}L^2}{20}. \end{aligned} \quad (39)$$

The final formula to compute the additional moments at the column ends will be as follows:

$$\begin{bmatrix} M_1 \\ M_2 \end{bmatrix} = C \begin{bmatrix} -1 - \frac{4L^2K_0}{K_{\theta 1}} - \frac{C}{20} & -\frac{2L^2K_0}{K_{\theta 2}} + \frac{C}{30} \\ \frac{2L^2K_0}{K_{\theta 1}} + \frac{C}{30} & -1 - \frac{4L^2K_0}{K_{\theta 2}} - \frac{C}{20} \end{bmatrix}^{-1} \begin{bmatrix} \frac{M_{01}}{20} + \frac{M_{02}}{30} \\ -\frac{M_{01}}{30} - \frac{M_{02}}{20} \end{bmatrix}. \quad (40)$$

Equation (40) can be rewritten as follows:

$$\begin{bmatrix} M_1 \\ M_2 \end{bmatrix} = [A] \begin{bmatrix} \frac{M_{01}}{20} + \frac{M_{02}}{30} \\ -\frac{M_{01}}{30} - \frac{M_{02}}{20} \end{bmatrix}, \quad (41)$$

where $[A]$ is considered as moment magnifiers matrix for the end additional moments and it is equal to the following:

$$[A] = C \begin{bmatrix} -1 - \frac{4L^2K_0}{K_{\theta 1}} - \frac{C}{20} & -\frac{2L^2K_0}{K_{\theta 2}} + \frac{C}{30} \\ -\frac{2L^2K_0}{K_{\theta 1}} + \frac{C}{30} & -1 - \frac{4L^2K_0}{K_{\theta 2}} - \frac{C}{20} \end{bmatrix}^{-1}. \quad (42)$$

Just the additional moments at the column ends were computed, the final load of the equivalent column will be as shown in Figure 6.

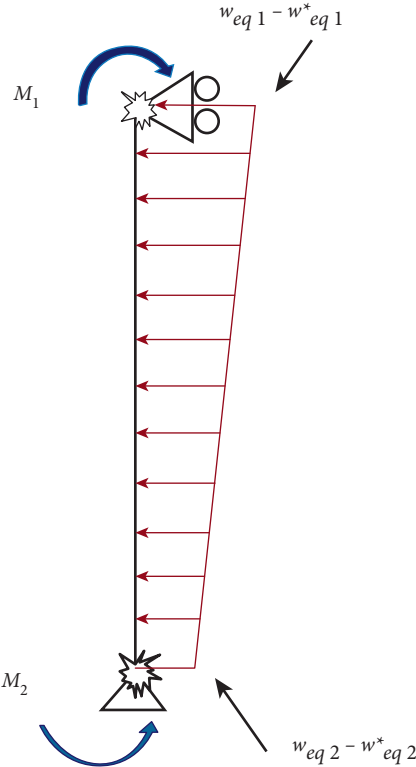


FIGURE 6: Final load of the equivalent column.

Through the model in Figure 6, the additional bending moment at any section can be computed and an additional bending moment diagram can be formed. Also, by using one of the methods of structural analysis, such as the virtual work method or area moment method, the additional lateral displacement and rotations at any point can be calculated. The total lateral displacement also can be computed easily, by dividing the additional bending moment at any section by the axial load ($\delta_{\text{final}} = M_{\text{add.}}/P$).

$$\theta_b = \frac{1}{EI_b} \left[\frac{1}{2} \cdot \frac{L_b}{3} \cdot 2 - \frac{L_b^2}{12} \cdot \frac{1}{3} \cdot \frac{1}{EI_b/K_{Acol} + L_b/3} + \frac{L_b^2}{36} \cdot \frac{1}{3} \left[\frac{1}{EI_b/K_{Acol} + L_b/3} \right]^2 \right] \quad (46)$$

The rotational rigidity of the connected beam end for the studied column can be expressed as follows:

$$K_b = \frac{EI_b}{L_b \left((1/3) - (L_b/36) \cdot (1/EI_b/K_{Acol} + L_b/3) + L_b^2/108 (1/EI_b/K_{Acol} + L_b/3)^2 \right)} \quad (47)$$

where L_b and EI_b are the length and moment of inertia of the connected beam.

In fact, most of the long columns are connected with beams that have stiffness bigger than or close to the column stiffness. Thus, the effect of the adjacent column, which as

6. Approximate Rotational Stiffnesses for the Column at Upper and Lower Joints

The connected beams which represent the rotational stiffness of the upper and lower joints of the column (K_b) can be approximately computed by applying one unit of the moment toward the end of the connected beams with the studied column as shown in Figure 7. The opposite end of the beam is considered as rotational restricted end by another pin column (adjust column to the studied column). Rotation of the beam end (θ_b) under the unit moment can be calculated. Then, the rotational stiffness will be computed as $K_b = 1/\theta_b$.

The rotation at the loaded end of the adjacent column is computed as follows:

$$\begin{aligned} \theta_{col} &= \frac{1}{EI_{col}} \int_0^L M_o \cdot M_1 \\ &= \frac{L_{Acol}}{3EI_{Acol}}, \end{aligned} \quad (43)$$

where L_{Acol} and I_{Acol} are the length and moment of inertia of the adjacent column.

The rotational stiffness of the adjacent column to the beam is as follows:

$$K_{Acol} = \frac{3EI_{col}}{L_{col}} \quad (44)$$

Due to the unit moment at the beam end, the reaction moment M^* at the opposite end of the beam can be found by the force method, as follows:

$$M^* = \left(\frac{L_b/6}{EI_b/K_{Acol} + L_b/3} \right) \quad (45)$$

By using the virtual work, the rotation at the loaded end of the beam can be determined as follows:

rotational spring for the beams, will be slight and (47) can be simplified as follows:

$$K_b = \frac{3EI_b}{L_b} \quad (48)$$

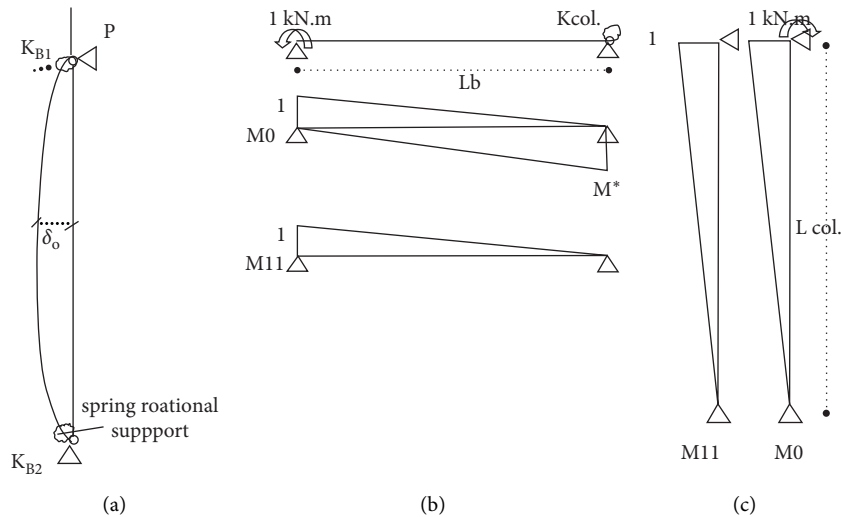


FIGURE 7: Rotational stiffness of the connected beam. (a) Studied column. (b) Connected beam. (c) Adjacent column.

7. Computing the Additional Moments by Using the Equivalent Column with More Accuracy

As mentioned before, the additional moments in a long column can be computed according to equation (41) as isolated column analysis. If there are other long columns adjacent to the studied columns, the additional moments of these columns will affect the additional moments of the studied column. For more accuracy, the effect of additional moments of adjacent columns must be considered, where a part of these moments will be transferred through the connected beams to the studied column. By one of the following two suggestions, the effect of the adjacent long columns can be taken into consideration.

7.1. Suggestion 1. Assume that the studied column is the left column in the shown closed frame in Figure 4. In this suggestion, the additional moments in each column will be computed according to equation (41) as a separate analysis of each of them. Then the transferring ratio of the additional moments between the columns will be found. Each column will be considered as a rotational spring for both the bottom and top beams. The rotational stiffness of the columns will be computed in the same manner in section 5, equation (44).

By using the force method, the transmitting moment from the right column to the left studied column at joint 1 as an example can be calculated as follows:

$$M_1^* = (M_{add})_2 \cdot \frac{(L_b/6EI_b)_{Top}}{(L_{col}/3EI_{col} + L_b/3EI_{bTop})}, \quad (49)$$

$$M_1^* = (M_{add})_2 \cdot \alpha_1,$$

where M_1^* is the transferred moment from the adjacent column (joint 2) to the studied column joint (1), $\alpha_1 = \alpha_2$: factor of transferring ratio by the top beam = $(L_b/6EI_b)_{Top}/(L_{col}/3EI_{col} + (L_b/3EI_b)_{Top})$, $(M_{add})_2$: the additional moment at joint 2 of the adjacent column.

$$M_3^* = (M_{add})_4 \cdot \frac{(L_b/6EI_b)_{bottom}}{(L_{col}/3EI_{col} + (L_b/3EI_b)_{bottom})}, \quad (50)$$

$$M_3^* = (M_{add})_4 \cdot \alpha_2.$$

where M_3^* is the the transferred moment from the adjacent column (joint 4) to the studied column joint (3), $\alpha_3 = \alpha_4$: factor of transferring ratio by the bottom beam = $(L_b/6EI_b)_{bottom}/(L_{col}/3EI_{col} + (L_b/3EI_b)_{bottom})$

After obtaining the transmitting moment between the two columns, (41) can be carried out one time for the second-order effect of the transmitting moments. Also, this can be considered by modifying equation (41) as follows:

$$\begin{bmatrix} M_1 \\ M_3 \end{bmatrix} = [A] \begin{bmatrix} \frac{(M_{01} + \alpha M_{add2})}{20} + \frac{(M_{03} + \alpha M_{add4})}{30} \\ -\frac{(M_{03} + \beta M_{add4})}{30} - \frac{(M_{01} + \beta M_{add2})}{20} \end{bmatrix} - \begin{bmatrix} \alpha_1 M_{add2} \\ \alpha_3 M_{add4} \end{bmatrix}. \quad (51)$$

Equation (51) takes into account the transmitting additional moments between two adjacent columns for one trial. The equation can be carried out for several trials till the ratio of transferred additional moment gets close to zero and it can be modified to include the effect of more adjacent columns. Whereas the deformations in reinforced concrete structures are small, thus the additional moments at the end of the long columns will not be large values. As a result, the expected transmitting moments will be small and it can be ignored, or one trial as maximum can be carried out. But for

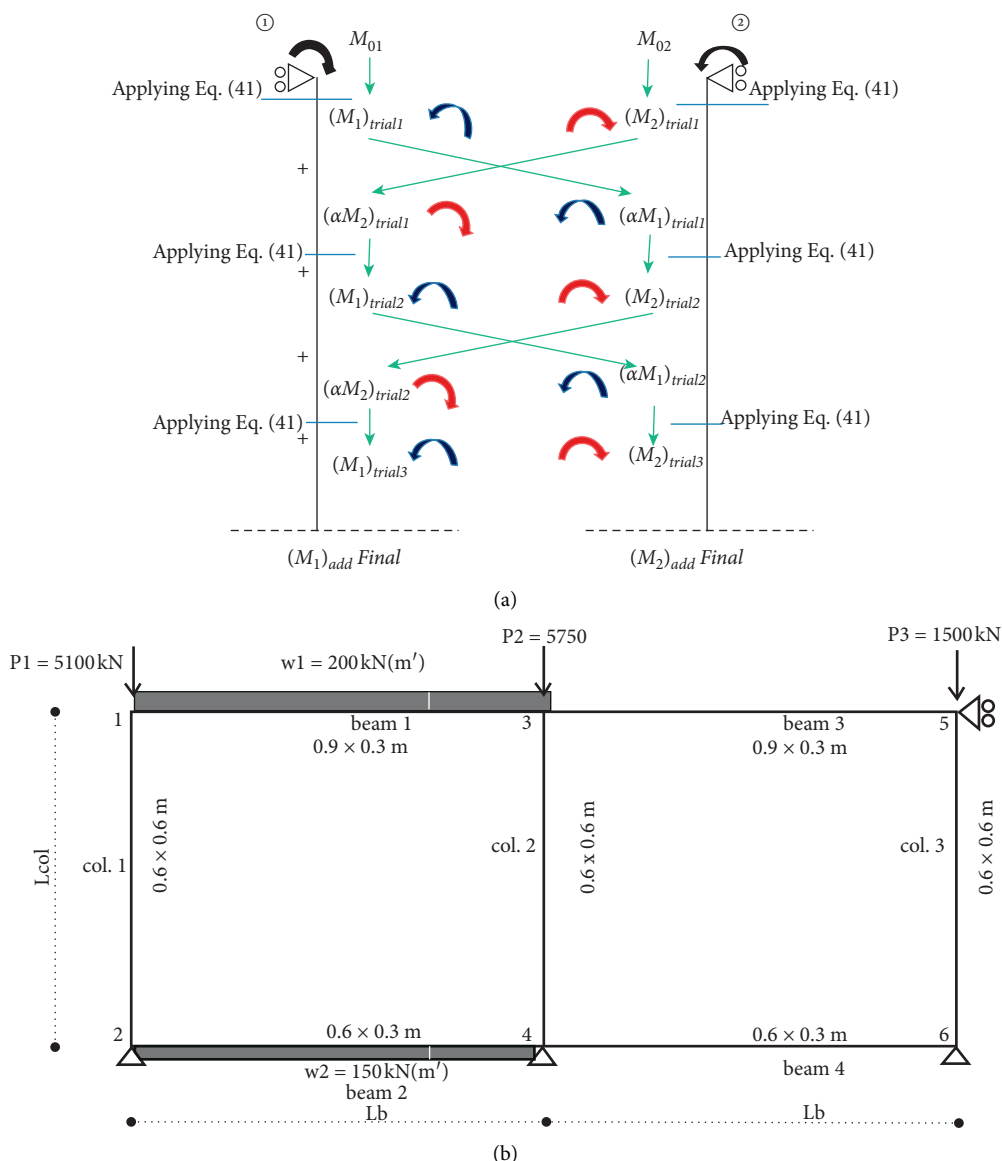


FIGURE 8: (a) Schematic method for the transmitting additional moments. (b) Multibays frame is an example of a structure that has more than two adjacent slender columns.

more accuracy, the effect of the additional moments of adjacent columns can be considered as in (51). The effect of adjacent additional moments can be considered schematic method as in Figures 8(a) and 9 presented the additional moments' transmission between the columns.

If a number of slender columns exist in the structure, as shown in Figure 8(b), equations (43) and (51) easily can be formulated as follows:

Equation (51) will become as follows:

$$M_{add} = \sum_{trial=1}^{trial=n} M_{trial1} + \alpha M_{trial1} + M_{trial2} + \alpha M_{trial2} + \dots + M_{trial(n)}, \quad (52a)$$

where n is the trial number which at it the condition of $(\alpha M_{trial(n)} \cong \text{zero})$ will be achieved

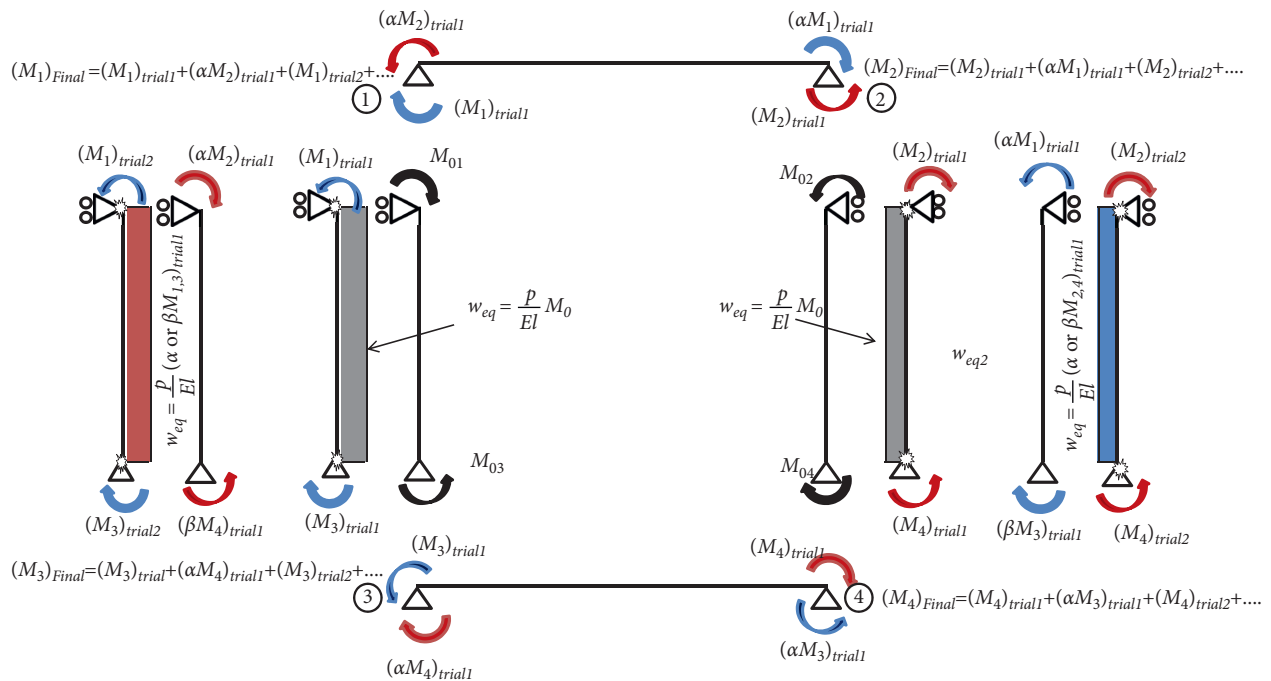


FIGURE 9: Additional moments transmission between the columns.

$$M_{\text{trail1}} = \begin{bmatrix} M_1 \\ M_2 \\ M_3 \\ M_4 \\ M_5 \\ M_6 \end{bmatrix}_{\text{trail1}}$$

$$= [A] \begin{bmatrix} \frac{1}{20} & \frac{1}{30} & 0 & 0 & 0 & 0 \\ -\frac{1}{30} & -\frac{1}{20} & 0 & 0 & 0 & 0 \\ 0 & 0 & \frac{1}{20} & \frac{1}{30} & 0 & 0 \\ 0 & 0 & -\frac{1}{30} & -\frac{1}{20} & 0 & 0 \\ 0 & 0 & 0 & 0 & \frac{1}{20} & \frac{1}{30} \\ 0 & 0 & 0 & 0 & -\frac{1}{30} & -\frac{1}{20} \end{bmatrix} \begin{bmatrix} M_{01} \\ M_{02} \\ M_{03} \\ M_{04} \\ M_{05} \\ M_{06} \end{bmatrix},$$

(52b)

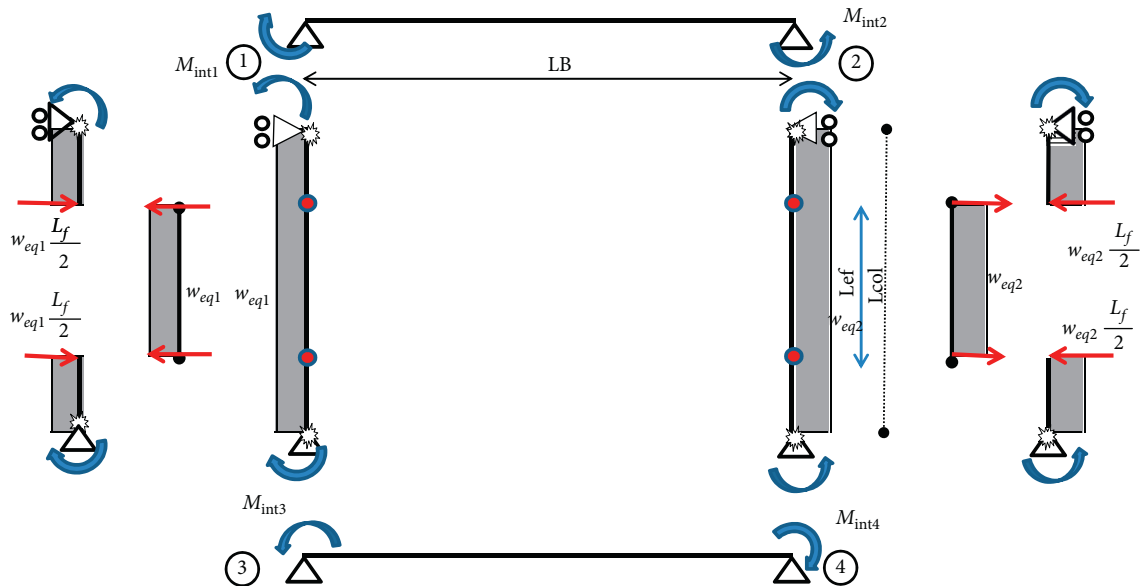


FIGURE 10: Approximate initial moments at the ends of the beam to calculate the relative rotational stiffness.

$$M_{\text{transferral}} = (\alpha) * [M]_{\text{trail1}}$$

$$= \begin{bmatrix} \alpha_1 M_3 \\ \alpha_2 M_4 \\ \alpha_{3L} M_1 + \alpha_{3R} M_5 \\ \alpha_{4L} M_1 + \alpha_{4R} M_6 \\ \alpha_5 M_3 \\ \alpha_6 M_4 \end{bmatrix}, \quad (52c)$$

$$M_{\text{trail2}} = \begin{bmatrix} M_1 \\ M_2 \\ M_3 \\ M_4 \\ M_5 \\ M_6 \end{bmatrix}_{\text{trail2}}$$

$$= [A] \begin{bmatrix} \frac{1}{20} & \frac{1}{30} & 0 & 0 & 0 & 0 \\ -\frac{1}{30} & -\frac{1}{20} & 0 & 0 & 0 & 0 \\ 0 & 0 & \frac{1}{20} & \frac{1}{30} & 0 & 0 \\ 0 & 0 & -\frac{1}{30} & -\frac{1}{20} & 0 & 0 \\ 0 & 0 & 0 & 0 & \frac{1}{20} & \frac{1}{30} \\ 0 & 0 & 0 & 0 & -\frac{1}{30} & -\frac{1}{20} \end{bmatrix} \begin{bmatrix} \alpha_1 M_3 \\ \alpha_2 M_4 \\ \alpha_{3L} M_1 + \alpha_{3R} M_5 \\ \alpha_{4L} M_1 + \alpha_{4R} M_6 \\ \alpha_5 M_3 \\ \alpha_6 M_4 \end{bmatrix}, \quad (52d)$$

$$(\alpha) = \frac{L_b / (6EI)_b}{\sum (L / (3EI)_{\text{elements}}} * \frac{(3EI/L)_{\text{columnn}}}{\sum (3EI/L)_{\text{elements}} - (3EI/L)_b}, \quad (52e)$$

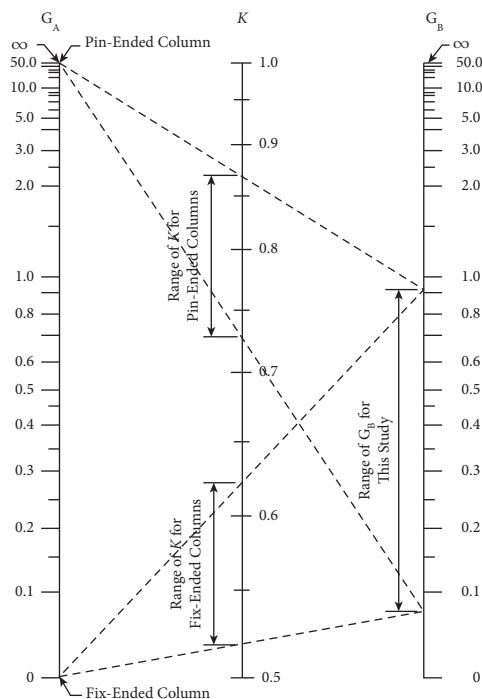


FIGURE 11: Jackson-Moreland Alignment Chart for braced frames [10].

$L_b/(6EI)_b$ is for the connected beam between the studied column and the other column sent the transferred moments, $(3EI/L)_{\text{column}}$ is for the studied column, and $(3EI/L)_{\text{elements}}$

is for the all connected elements with the studied column including it.

$$[A] = \begin{bmatrix} -C_1 - \frac{4C_1L_1^2K_{01}}{K_{\theta 1}} - \frac{C_1^2}{20} & -\frac{2C_1L_1^2K_{01}}{K_{\theta 2}} + \frac{C_1^2}{30} & 0 & 0 & 0 & 0 \\ -\frac{2C_1L_1^2K_{01}}{K_{\theta 1}} - \frac{C_1^2}{20} & -C_1 - \frac{4C_1L_1^2K_{01}}{K_{\theta 2}} - \frac{C_1^2}{20} & 0 & 0 & 0 & 0 \\ 0 & 0 & -C_2 - \frac{4C_2L_2^2K_{02}}{K_{\theta 3}} - \frac{C_2^2}{20} & -\frac{2C_2L_2^2K_{02}}{K_{\theta 4}} + \frac{C_2^2}{30} & 0 & 0 \\ 0 & 0 & -\frac{2C_2L_2^2K_{02}}{K_{\theta 3}} + \frac{C_2^2}{30} & -C_2 - \frac{4C_2L_2^2K_{02}}{K_{\theta 4}} - \frac{C_2^2}{20} & 0 & 0 \\ 0 & 0 & 0 & 0 & -C_3 - \frac{4C_3L_3^2K_{03}}{K_{\theta 5}} - \frac{C_3^2}{20} & -\frac{2C_3L_3^2K_{03}}{K_{\theta 6}} + \frac{C_3^2}{30} \\ 0 & 0 & 0 & 0 & -\frac{2C_3L_3^2K_{03}}{K_{\theta 5}} + \frac{C_3^2}{30} & -C_3 - \frac{4C_3L_3^2K_{03}}{K_{\theta 6}} - \frac{C_3^2}{20} \end{bmatrix} \quad (52f)$$

If a number of slender columns exist in the structure and the effect of additional moments of adjacent columns will be considered, the sequence of solving can be schematized as shown in Figure 8(a), or it can be programmed. The shown frame in Figure 8(b) was analyzed by MATLAB program.

M-file of programming and the results are shown in Appendix (I).

7.2. Suggestion 2. In this suggestion, the effect of the additional moments of the adjacent columns on the studied

column will be taken into the relative rotational stiffness of the connected beams. This will be considered by applying approximate values of additional moments at the ends of the connected beams to evaluate the relative rotational stiffness of these ends for the long columns.

As shown in Figure 10, the initial additional moments can be calculated as follows:

$$M_{int} = \frac{w_{eq(av)}}{4}(L - L_f)^2 + \frac{w_{eq(av)}}{4}(L - L_f), \quad (53)$$

where $w_{eq(av)}$ is the average equivalent regular load for the second effect due to the end moments of the column, L_f : effective length of the long column, and it can be calculated as in Figure 11.

The initial moments of the four joints of the shown frame in Figure 10 will be calculated as follows:

$$\begin{aligned} M_{int1} &= M_{int3} \\ &= \frac{p(M_{01} + M_{03})L_{col}}{8EI_{col}}(L_{col} - L_f), \end{aligned} \quad (54)$$

$$\begin{aligned} M_{int2} &= M_{int4} \\ &= \frac{p(M_{02} + M_{04})L_{col}}{8EI_{col}}(L_{col} - L_f). \end{aligned}$$

And by using the virtual work method, the rotation at the ends of the connected beams at joint 1 as an example can be calculated as follows:

$$\begin{aligned} \theta_1 &= \frac{1}{EI_B} \left(\frac{1}{2} M_{int1} L_b \cdot \frac{2}{3} + \frac{1}{2} M_{int2} \cdot L_b \cdot \frac{1}{3} \right), \\ \theta_1 &= \frac{L_B}{EI_B} \left(\frac{M_{int1}}{3} + \frac{M_{int2}}{6} \right). \end{aligned} \quad (55)$$

The rotational stiffness of the connected beams can be computed as follows:

$$\begin{aligned} K_{\theta1} &= \frac{M_{int1}(EI_b/L_b)_{Top}}{(M_{int1}/3 + M_{int2}/6)}, \\ K_{\theta2} &= \frac{M_{int2}(EI_b/L_b)_{Top}}{(M_{int2}/3 + M_{int1}/6)}, \\ K_{\theta3} &= \frac{M_{int3}(EI_b/L_b)_{Bottom}}{(M_{int3}/3 + M_{int4}/6)}, \\ K_{\theta4} &= \frac{M_{int4}(EI_b/L_b)_{Bottom}}{(M_{int4}/3 + M_{int3}/6)}. \end{aligned} \quad (56)$$

And by substituting the computed rotational stiffness in (41), additional moments in the long columns in the closed frame will be computed, taking into account the approximate effect of the additional moments of each column on each other.

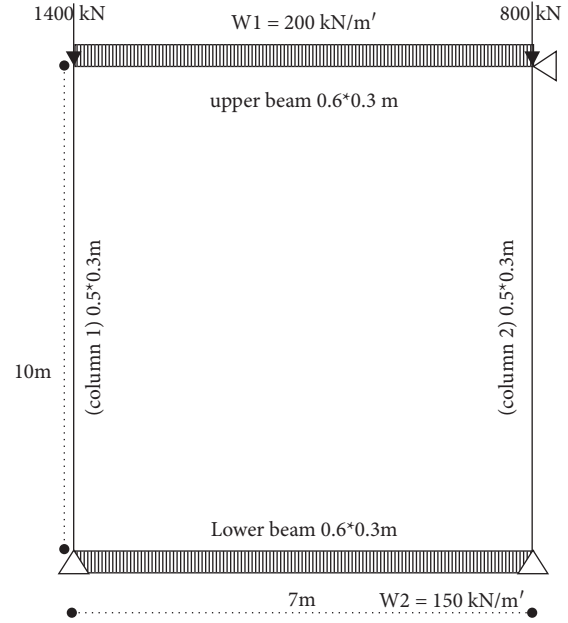


FIGURE 12: The analyzed frame.

8. Elastic Analysis for Checking the Structural Analysis Efficiency of the Equivalent Column

Numerous factors will be studied here through linear analysis of closed frames by utilizing the new moment magnifiers matrix and finite element method. The reason for this investigation is to check the structural analysis proficiency of the recommended model in a wide range without the restriction of materials failure. The factors were a variation of the stiffness of connected beams together, induced axial force to Euler load ratio, slenderness ratio, and the stiffness of upper beam to lower beam. The left column is the target column in this study. The results of the comparison are shown in Figures 12– 16.

Solving steps for the equivalent column model:

- (1) Calculating the terms K_0 , C , $K_{\theta1}$, and $K_{\theta2}$ according to equations (38-a), (38-b), (48) respectively, to satisfy the moment magnifiers matrix $[A]$.
- (2) Applying (41) for each column to compute the additional moments between the columns and the connected beams.
- (3) For more accuracy, the effect of the additional moments of each column on each other can be considered by using a schematic method in Figure 8, then find the final additional moments “suggestion 1.”
- (4) By using model of final loads in Figure 6, the additional moment diagram and additional deformations of the column (lateral displacements and rotations) can be computed.

From the results, it was observed that using (41) in the suggested equivalent column model gives values of additional moments close to their values calculated by the finite

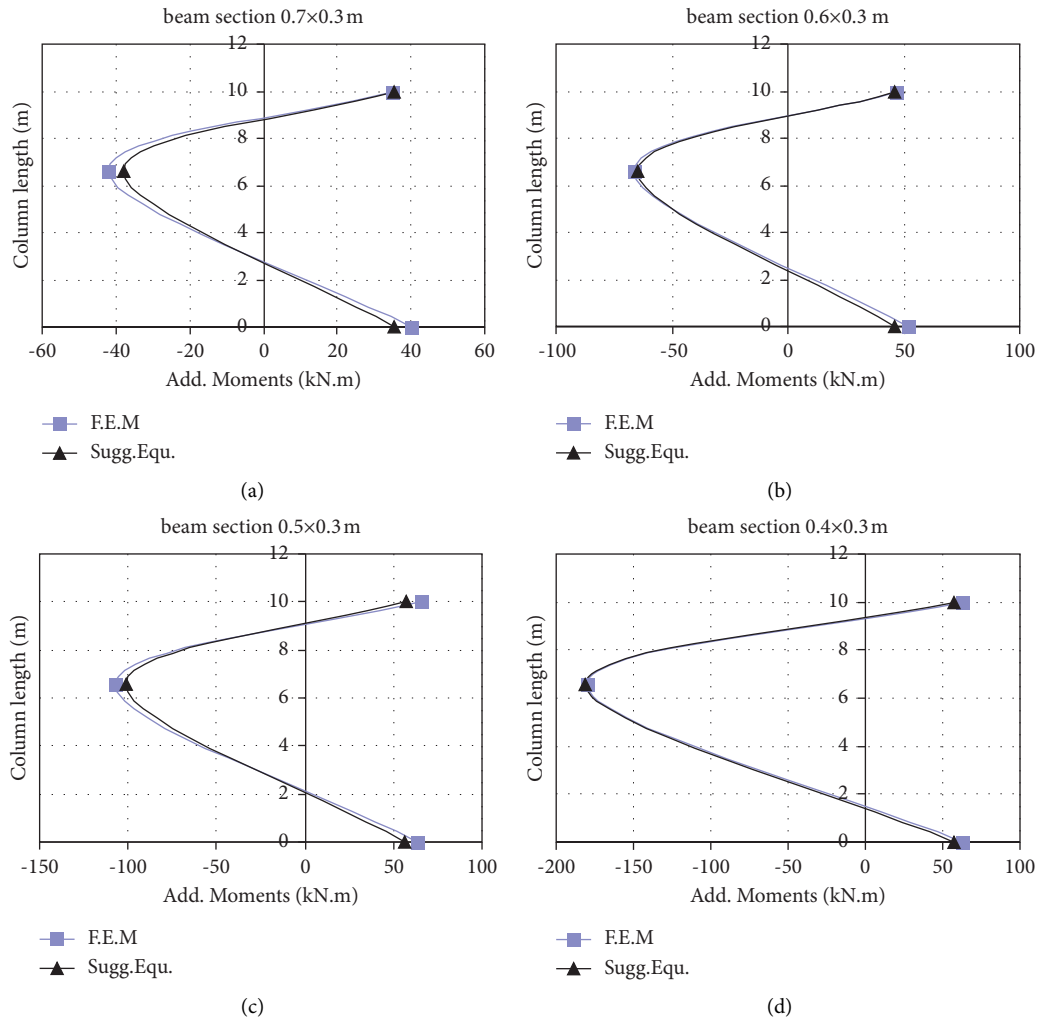


FIGURE 13: (a-d) Using equivalent column with varying of beam stiffnesses.

element method. The results proved the structural analysis efficiency of the proposed model for analyzing the long column as an isolated element. After the satisfaction to the efficiency of the model, the model can be developed by modifying the flexural rigidity (EI) to appropriate the materials case at the moment of computing the additional moments, as shown in the next section.

9. Design Procedures for Computing Additional Moments in Long Columns by Using New Moment Magnifiers Matrix

The calculation of terms (K_0 , C) and ($K_{\theta 1}$, $K_{\theta 2}$) in the moment magnifiers matrix of (41) involves the use of the flexural rigidity, EI , of the column and the connected beams, respectively. To use the suggested equation (41) in computing the additional moments in a long column, the flexural rigidity for a given column section must be considered at the time of failure, taking into account the effects of cracking and nonlinearity of the stress-strain curves. James G. MacGregor et al. [11, 12] describe empirical attempts to derive values for EI . ACI-318-19 includes two different sets

of stiffness values, EI , the first set is for the computation of EI in caudation the critical load of an individual column as follows:

$$EI = \frac{0.2E_c I_g + E_s I_{se}}{1 + \beta_{dn s}}, \quad (57)$$

$$EI = \frac{0.4E_c I_g}{1 + \beta_{dn s}}, \quad (58)$$

where E_c , E_s are the modules of elasticity of the concrete and the steel, respectively, I_g is the gross moment of inertia of the concrete section, I_{se} is the moment of inertia of the reinforcement about the centroidal axis of the concrete section, and $(1 + \beta_{dn s})$ term reflects the effect of creep on the column deflections.

It can be used in equation (57) or equation (58), but equation (57) is more accurate.

The second set is for values of the moment of inertia, I , for use in elastic frame analyses or in computing the effective length factor, k . In this set, the column and beam stiffnesses were computed as $0.7E_c I_c$ and $0.35E_c I_c$, respectively.

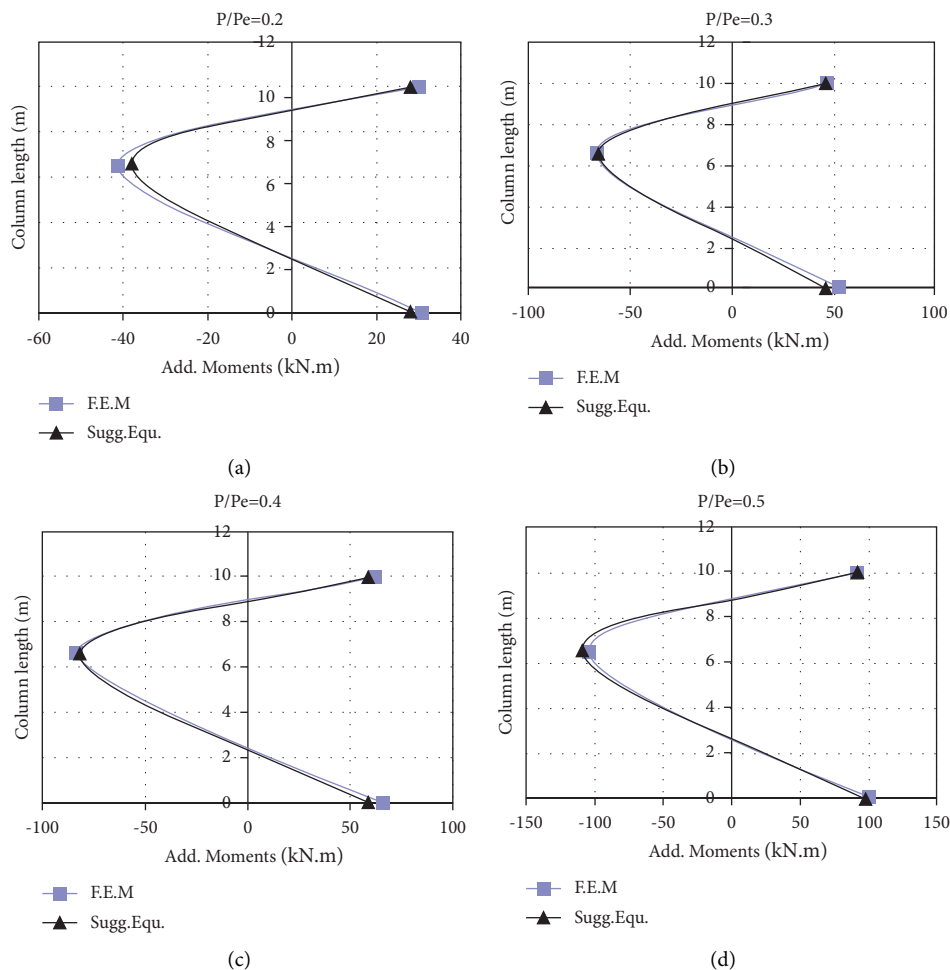


FIGURE 14: (a-d) Using equivalent column with varying axial force to Euler load.

According to the concepts of the previous recommendations in ACI-318-19 for using the approximate flexural rigidity in different cases, it is appropriate to use (EI) according to equation (57) or equation (58) when calculating the term (C) in equation (41). Either when calculating the terms (K_0) and (K_1 , K_2) in (41), the column and beam stiffnesses will be computed as $0.7E_cI_c$ and $0.35E_cI_b$, respectively.

A long column in closed frames as shown in Figure 10 will be analyzed by each of the equations of (ACI-318-19), (ECP 203-2018), the suggested equation (41) by using suggestions (1), (2) was considered the moment transmitting between the long columns and by using (41) with neglecting the moment transmitting. The frames were analyzed according to the design requirements and with changing two parameters, slenderness ratio, and P/P_e . The main cross section of the studied column is 50×30 cm with a reinforcement ratio in-between 0.01 to 0.035. The slenderness ratio will be varied from (9.8–21.5) and P/P_e will be varied from (0.23-0.95). The relationship between the maximum additional moment through the height of the column and the changed parameters are shown in Figures 18, 17.

The results of the analysis show that there is a large convergence of the additional moments calculated by (41) in

the equivalent column between each of suggestions (1) and (2), where the effect of transmitted additional moments was taken into account, and by using equation (41) directly where the transmitted additional moments were neglected. This is expected because of that the failure limitations of the material, which makes the additional moments induced in a long column are not the large values that strongly affect or get affected by the adjacent columns. Thus for easiness, (41) can only be used where a separate analysis of the long column is included without being affected by the additional moments of adjacent long columns.

Moreover, it is observed that (41) gives values of additional moments close to their values which are given by the equation of ACI. This means that using the suggested equation gives good efficiency. Also, it means the appropriate use of flexural rigidity (EI) according to Eqs. (57) or (58) for computing the term (C) in (41) while using the column and beam stiffnesses.

According to $0.7EI_c$ and $0.35EI_b$, respectively, for computing the terms (K_0) and (K_1 , K_2) in (41), the term (C) is the concern of the lateral deformations of the long column, and using (EI) according to Eqs. (57) or (58) in this term corresponds to using these equations for computing P_{cr} in the equation of ACI. While the terms (K_0)

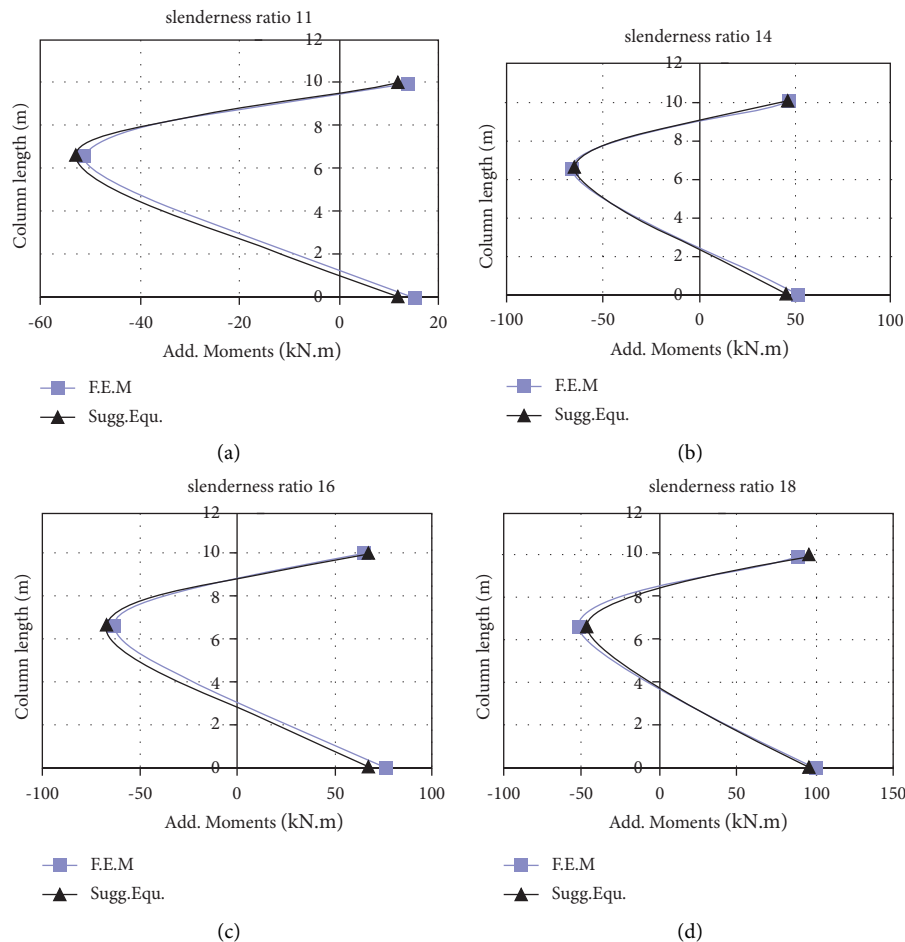


FIGURE 15: (a–d) Using equivalent column with varying slenderness ratio.

and (K_1, K_2) are the concern of the additional moments at the column ends, and the effects of these terms in (41) are similar to the effects of the effective length in the ACI equation.

The additional deformations of the long column (lateral displacement and rotations) at any point can be computed easily, as shown in Figures 19, 20 as an example.

It is clear that there is a big difference in the additional moments between each of ACI, the suggested equation in the equivalent column, and ECP. Prab Bhatt et al. [13] illustrated the basic and the assumptions of computing the additional moments in British code equation BS8110:1997 [14], which is the same as the ECP equation. He illustrates that the deformed column curvature will typically vary along the column as a sinusoidal value of $(1/\pi^2)$. Figure 21 shows the interaction diagram between the bending and the normal force and strain diagram in the ultimate stage (balanced failure). Thus, the central lateral deflection a_u will be assumed as follows.

$$a_u = \left(\frac{1}{\pi^2}\right) l_e^2 \left(\frac{1}{r}\right). \quad (59)$$

The column curvature $(1/r)$ is calculated based on the strain diagram at the balanced failure, as follows:

$$\frac{1}{r_b} = \frac{(0.003 + 0.002)}{d}. \quad (60)$$

The maximum deflection for the case set out above is given in the code by the following expression:

$$\begin{aligned} a_u &= \frac{0.0005 l_e^2}{h}, \\ a_u &= \frac{h}{2000} \cdot \left(\frac{l_e}{h}\right)^2 \\ &= \frac{\lambda^2}{2000} \cdot h. \end{aligned} \quad (61)$$

It was noted that the ECP equation was based on computing the additional moments in a specific case which is at the balanced failure, and this restriction is difficult to achieve when designing the columns. Thus if the failure mode of the column section is not compatible with the balanced failure, it is supposed that this equation is not valid and it will give far values of the additional acting moments, as shown in previous analyzing cases. So, it seems that the ECP equation cannot be used generally to compute the additional moments and it is for a specific case. Where it can

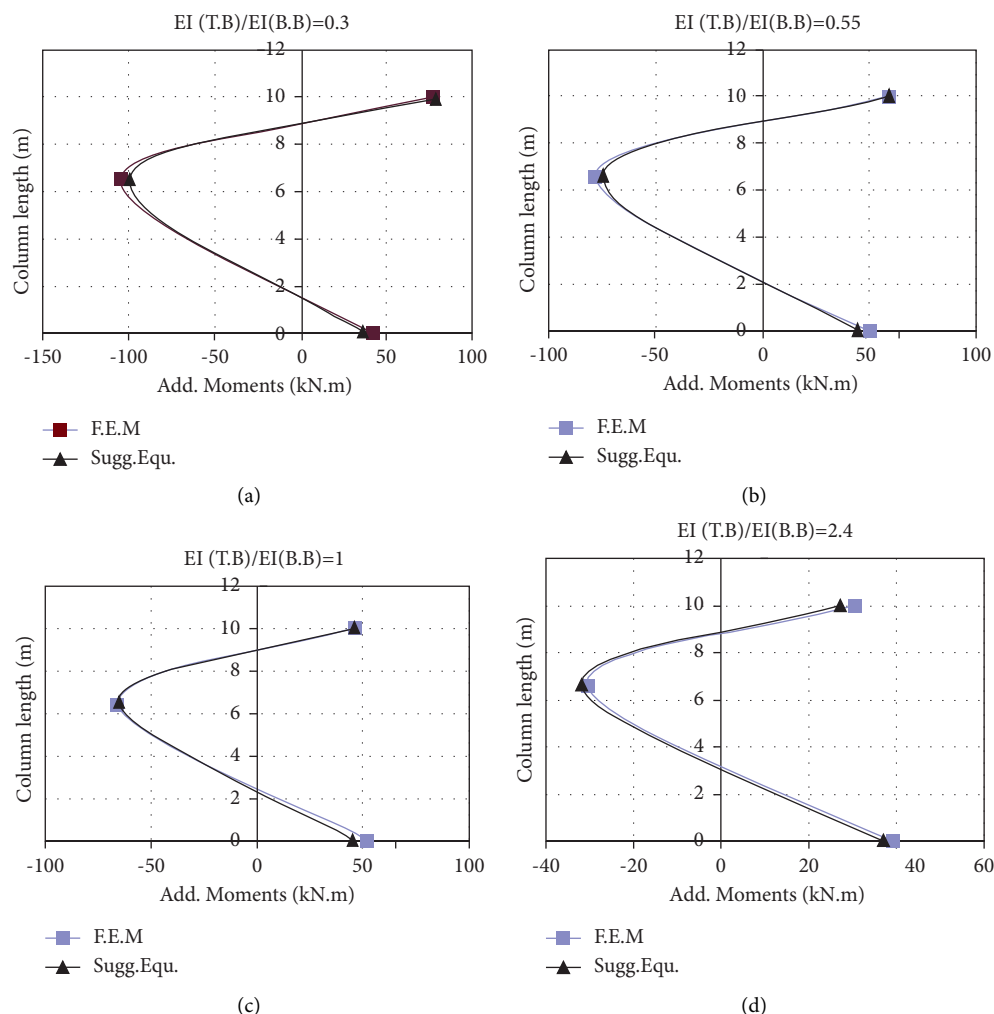


FIGURE 16: (a-d) Using equivalent column with varying upper beam to lower beam stiffness.

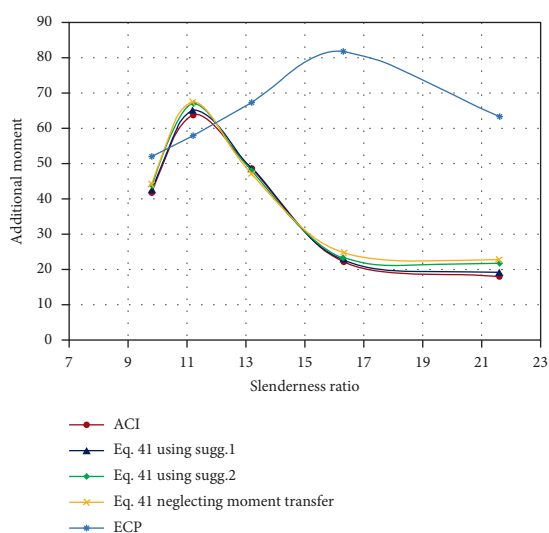


FIGURE 17: Additional moments vs. slenderness ratio.

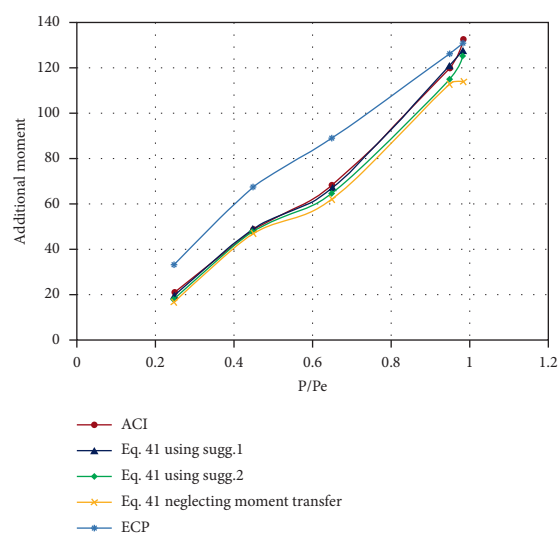


FIGURE 18: Additional moments Vs. P/P_e .

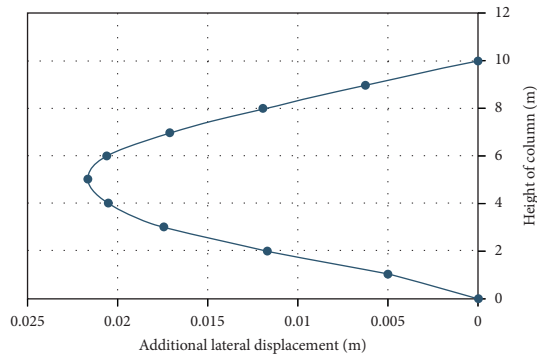


FIGURE 19: Computing additional lateral displacement by using equivalent column model for slenderness ratio 11.2 as an example.

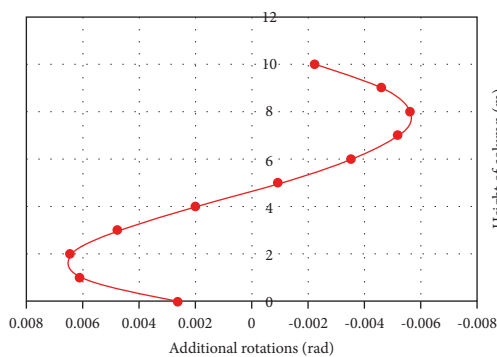


FIGURE 20: Computing the additional rotations by using an equivalent column model for slenderness ratio 11.2 as an example.

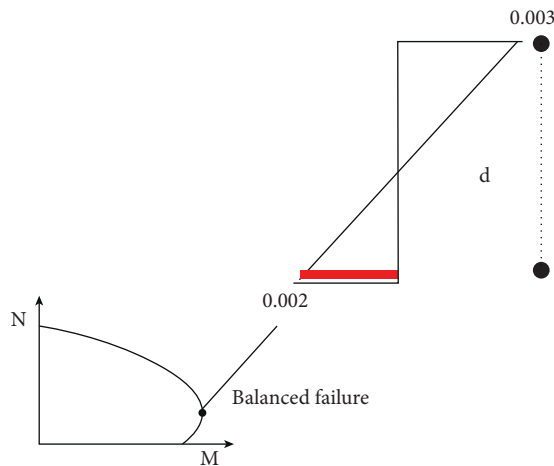


FIGURE 21: The interaction diagram between the bending and the normal force and strain diagram in the ultimate stage (balanced failure).

be used to evaluate the maximum allowable lateral displacement of the column at the balanced failure, then the moment capacity of the column section can be checked for restrained design (balanced failure). This is maybe one of the reasons for the big difference between the results of the ACI equation, the suggested equation in the equivalent column and the EPC equation.

Also, the ECP equation does not take into account the second-order effect which is caused by the axial force and the inverse moments due to beams restriction to the column ends. ECP equation considers only the connected beams effect by dealing with the effective length of the column, not the total length. ACI equation is similar to ECP equation at this point, but returning to the original equation of ACI (Eq. 62), a term $(1 + 0.23P/P_e)$ was found which was omitted from the final equation to generalize the use of the equation, where the factor 0.23 varies as a function of the moment diagram shape. This leads to a decrease in the additional moments among the inflected points, and that approaches the results between the ACI equation and the analysis, which takes into account the second-order effect, which is caused by the inverse moments as in the suggested equivalent column.

$$M_c = \frac{M_0(1 + 0.23P/P_e)}{1 - P/P_e} \quad (62)$$

On the other hand, the computed flexural rigidity (EI) according to ACI in Eq. (57) remains constant regardless of the magnitude of end moments and, therefore, P_c also remains constant. As a result, the moment magnifier remains constant for a given column. However, P_c is strongly influenced by the effective flexural stiffness (EI), which varies due to the nonlinearity of the concrete stress-strain curve and cracking along the height of the column among other factors [3].

10. Summary and Conclusions

Based on the equivalent column concept, a new moment magnifiers matrix was presented in this paper for computing the additional end moments in the braced long column. The equivalent column was an element restricted at its ends by two spring rotational supports and is subjected to lateral distributed loads, which have the same influence of the second-order effect in a long column. The additional moments' diagram and additional deformations (lateral displacements and rotations) can be computed by using the suggested equivalent column taking into consideration the second-order effect, which is caused by the axial load and the inverse moments due to beams restriction for the column ends, this effect is important although it is neglected in design codes. The long column in the suggested model was analyzed as an isolated element, but by two presented suggestions, the effect of the additional moments of other adjacent long columns, if any, can be considered. The first suggestion took into account the effect of adjacent additional moments by computing the transmitting additional moments among columns through transfer coefficients depended on the rigidity of the connected beams; then the equation of the moment magnifiers matrix was applied more than once for the transmitted moments. This suggestion can be carried out by schematic method as shown in the paper content. In the second suggestion, the adjacent additional moments' effect was considered in the relative rotational stiffness of the connected beams, which are as a rotational spring for the long columns. This will be

considered by applying approximate values of additional moments at the ends of the connected beams to evaluate the relative rotational stiffness of these beams. Development was carried out on the model by modifying the flexural rigidity (EI) in each of the connected beams and the long column as it is recommended in ACI to appropriate the time of failure. From the results presented in this paper, the following is concluded:

- (1) The suggested equivalent column proved a good efficiency for analyzed numerous factors linearly by finite element method, and the equivalent column was satisfying as a successful structural model.
- (2) For analyzing many designed long columns in closed frames, the results showed that there are small differences of computed additional moments by applying the suggested equation of moment magnifiers directly and by using the two suggestions of considering the adjacent additional moments, so the additional moments of the adjacent columns can be neglected for simplifying.
- (3) The developed model gave close values of the additional moments for many analyzed long columns with ACI equation, and it is appropriate to generalize this model for second-order analysis of long braced columns as an easy-to-use model that yields good results.
- (4) There was a gap between the values of the additional moments computed by the two methods, the suggested equivalent column and ECP equation. This may be because ECP equation was based on computing the additional moments in a specific case which is at the balanced failure. Moreover, the ECP equation did not take into account the second-order effect, which is caused by the axial force and the inverse moments due to beams' restriction for the column ends.

References

- [1] J. G. Wight and J. K. MacGregor, *Reinforced concrete: Mechanics and Design*, Prentice-Hall, Upper Saddle River, NJ, USA, 6th ed. edition, 2011.
- [2] R. D. Cook, D. S. Malkus, and M. E. Plesha, *Concepts and Applications of Finite Element Analysis*, John Wiley & Sons, Hoboken, NJ, USA, 3rd edition, Article ID 0-471-84788-7, 1989.
- [3] T. K. Tikka and S. A. Mirza, "Effective length of reinforced concrete columns in braced frames," *International Journal of Concrete Structures and Materials*, vol. 8, no. 2, pp. 99–116, 2014.
- [4] Aci Committee 318, *Building Code Requirements for Structural concrete (ACI 318-19) and Commentary*, American Concrete Institute, Farmington Hills, MI, USA, 2019.
- [5] Csa, *Design of concrete Structures*, Vol. A23.3-04, Canadian Standards Association, Mississauga, Canada, 2004.
- [6] W. F. Chen and E. M. Lui, *Structural Stability-Theory and Implementation*, Elsevier Science Publishing Company Inc, New York, NY, USA, 1987.
- [7] EN 1992-1-1, *Eurocode 2 (EC2): Design of concrete Structures-Part 1-1: General Rules and Rules for buildings*, European Committee for Standardization, Brussels, Belgium, 2004.
- [8] Ecp, *Egyptian Code for Design and Construction of Reinforced Concrete Structures*, ECP, Tamworth, UK, 2018.
- [9] H. M. Afefy and E.-T. M. El-Tony, "Simplified design procedure for reinforced concrete columns based on equivalent column concept," *International Journal of Concrete Structures and Materials*, vol. 10, no. 3, pp. 393–406, 2016.
- [10] L. Duan, W. S. King, and W. F. Chen, "K-factor equation to alignment charts for column design," *ACI Structural Journal*, vol. 90, no. 3, pp. 242–248, 1993.
- [11] J. G. MacGregor, U. H. Oelhafen, and S. E. Hage, "A Reexamination of the EI Value for Slender Columns" *Reinforced Concrete Columns*, pp. 1–40, American Concrete Institute, Farmington Hills, MI, USA, 1975.
- [12] J. G. MacGregor, J. E. Breen, and E. O. Pfrang, "Design of slender columns," *ACI Journal, Proceedings*, vol. 67, no. 1, pp. 6–28, 1970.
- [13] P. Bhatt, J. T. MacGinly, and B. S. Choo, *Reinforced Concrete, Design Theory and Examples*, CRC Press, Boca Raton, FL, USA, 3rd edition, 2006.
- [14] Bs8110, *Structural Use of Concrete Part 1: Code of Practice for Design and Construction*, BSI, London, UK, 1997.

Dynamic Response of the Bridge-Vehicle System of Random Road Roughness by Moment Method

Sharadhananda Ghadei, *Department of Civil Engineering, Aryan Institute of Engineering & Technology, Bhubaneswar, sharadhananda@outlook.com*

Suryaleen Rout, *Department of Civil Engineering, NM Institute of Engineering & Technology, Bhubaneswar, suryaleenrout@yahoo.co.in*

Debi Prasad Singh, *Department of Mechanical Engineering, Raajdhani Engineering College, Bhubaneswar, deboprasad_1159@gmail.com*

Ranjan Kumar, *Department of Mechanical Engineering, NM Institute of Engineering & Technology, Bhubaneswar, kumarranjan75@gmail.com*

ABSTRACT

Vehicles going through the bridge create vibration in the bridge-vehicle interaction (BVI) system. The vibration of the system is greatly influenced by road roughness. Poor road roughness is known to influence the comfort of vehicles crossing the bridge and exacerbate fatigue damage to the bridge in this regard. In numerical calculations, road roughness is frequently viewed as a random process. A random BVI model was created to properly consider the influence of road roughness randomization on the behavior of the BVI system. The random process of road roughness was then described using the (KLE), and the maximum probability value of the BVI system response was calculated using the moment approach. The proposed method outperforms the Monte Carlo simulation (MCS) computation method in terms of accuracy and economy. The effects of vehicle speed, roughness grade, and bridge span on the impact factor (IMF) were then investigated.

1. Introduction

The bridge-vehicle interaction (BVI) vibration caused by vehicles passing through the bridge will have a direct impact on the working state and service life of the bridge. It is an important design measure to evaluate the structural design parameters such as the stability and safety of vehicles running on the bridge [1, 2]. The main causes of the BVI vibration are vehicle dynamic characteristics, road roughness, vehicle braking, vehicle speed, dynamic characteristics of the bridge's structure, bridgehead overlap, bridge deck local potholes, vehicle driving position, etc.

Road roughness is an important factor affecting the BVI vibration. The influence of road roughness, which has strong randomness, cannot be ignored when calculating the BVI vibration. Road roughness is the main excitation source of the BVI vibration. Generally, road roughness is considered a stationary Gaussian random process with zero-mean value

wherein roughness can be characterized by power spectrum density (PSD). Oliva et al. [3] proposed an algorithm for generating road roughness samples with correlation based on Fourier transform. On the basis of this method, Zou et al. [4] studied the influence of the sample correlation coefficient of roughness on the vibration response of the BVI system, pointing out that there are obvious differences in the calculated responses of the BVI system under different road roughness.

At present, there are many achievements in the study of BVI vibration. Zou et al. [5] proposed a method for predicting the bounds of the BVI responses with uncertain bridge and vehicle parameters, whereas Wang et al. [6] estimated the road roughness based on the BVI system. Similarly, Zhong et al. [7] analyzed the BVI dynamic response considering the foundation settlement, while Liu et al. [8] analyzed the safety of vehicles running on the bridge during earthquakes. Xu et al. [9, 10] analyzed the vehicle-

track coupled system based on the multi-finite-element method. Xin et al. [11] analyzed the resonance of bridge considering the randomness of parameters, and Xin et al. [12] examined the uncertainty and sensitivity of parameters of the vehicle-bridge system. Meanwhile, Xiang et al. [13] analyzed the vehicle-bridge coupled dynamic system after considering the creep effect.

Generally, the response of the BVI system in consideration of road roughness can be calculated from the aspect of the random dynamic theory. In this context, Wu and Law [14] proposed a new method for dynamic analysis of the BVI considering uncertainty, in which the Karhunen–Loeve expansion (KLE) was applied to deal with the random field of road roughness. In addition, the statistical moment of system response was solved by the spectral method; the results showed that the method has high accuracy and efficiency. Then, Wu and Law [15] used a similar method to calculate the dynamic response of the BVI that considered the stochastic field of bridge structure parameters [15], vehicle axle load identification [16], and random system response calculation [17]. On the other hand, Chen et al. [18, 19] and Li et al. [20] proposed an efficient method to calculate the static and random response of the structural system. Xu et al. [21–25] carried out extensive research on the vehicle-bridge coupling vibration considering track irregularity. In the studies conducted by Liu et al. [26–28], KLE was also used to represent the stochastic process and combined with the point estimate method (PEM) [29, 30]. Thereafter, a new stochastic FEM approach and the dynamics response of vehicle and bridge were analyzed.

In order to study the dynamic response of vehicles crossing the bridge that fully considers the randomness of the road roughness, the moment method is applied to calculate the BVI system, in which KLE is used to mathematically express the random process of road roughness, whereas the PEM is used to calculate the statistical moment of the response. The system response can be evaluated quickly and easily by combining KLE and PEM methods (called KLE-PEM).

2. Dynamic Equation of the Bridge-Vehicle System

When a vehicle crosses a bridge, the two interact. Therefore, in the dynamic response analysis of the vehicle passing the bridge, the two are usually regarded as a system for analysis, which is referred to as the BVI system [31].

As shown in Figure 1, a car moves at a speed on a simply supported beam. The model of the vehicle is regarded as a mass-spring-dashpot system, which includes one car body, two wheel-axles, and two wheels. The car body has two degrees of freedom (DOFs), namely, vertical and nod displacement. Each wheel-axle has only one DOF. The wheel is supposedly in close contact with the road, which means that the wheel has no independent DOFs. Therefore, the whole vehicle system has four DOFs.

The FEM is used to model the bridge, in which the bridge damping matrix adopts Rayleigh damping. According to the energy law and considering the damping force of the system, the total potential energy of the BVI system can be obtained, which is expressed as follows:

$$\Pi_d = U_i + V_m + V_F + V_p + V_g + V_c, \quad (1)$$

where U_i is the strain energy of the BVI system; V_m refers to the negative work done by the inertia force of the system and $V_m = -\int_v (-u^T \rho \ddot{u}) dv$; V_c denotes the negative work done by damping force and $V_c = -\int_v (-u^T c \dot{u}) dv$; V_F is the negative work done by Coulomb friction of the system and $V_F = -u F \text{sign} \dot{u}$; V_p signifies the negative work done by external force of the system and $V_p = -u^T P$; and V_g is the system gravitational potential energy and $V_g = -u^T Q$.

The dynamic equation of the system can be obtained quickly by combining the first-order variation of the total potential energy Π_d and the principle of elastic potential energy invariance $\delta \Pi_d = 0$ [32]. The dynamic equation of the BVI can be written as follows:

$$\begin{bmatrix} M_{vv} & 0 \\ 0 & M_{bb} \end{bmatrix} \begin{Bmatrix} \ddot{X}_v \\ \ddot{X}_b \end{Bmatrix} + \begin{bmatrix} C_{vv} & C_{vb} \\ C_{bv} & C_{bb} \end{bmatrix} \begin{Bmatrix} \dot{X}_v \\ \dot{X}_b \end{Bmatrix} + \begin{bmatrix} K_{vv} & K_{vb} \\ K_{bv} & K_{bb} \end{bmatrix} \begin{Bmatrix} X_v \\ X_b \end{Bmatrix} = \begin{Bmatrix} F_v \\ F_b \end{Bmatrix}, \quad (2)$$

where M , C , and K represent mass matrix, damping matrix, and stiffness matrix, respectively; \ddot{X} , \dot{X} , and X denote acceleration vector, velocity vector, and displacement vector, respectively; the subscript vv or v denotes vehicle; bb or b signifies bridge; and vb or bv is the coupling part of bridge and vehicle. F denotes the force vector, whereas F_v signifies the force vector of the vehicle caused by the displacement and the first derivative of road roughness, which can be written as

$$F_v = [0 \ 0 \ F_{t1} \ F_{t2}]^T, \quad (3)$$

with $F_{t1} = k_{t1} r_{t1}(t) + c_{t1} \dot{r}_{t1}(t)$ and $F_{t2} = k_{t2} r_{t2}(t) + c_{t2} \dot{r}_{t2}(t)$, where $r_{t1}(t)$ and $r_{t2}(t)$ denote the roughness of front and rear axle positions at time t , and $\dot{r}_{t1}(t)$ and $\dot{r}_{t2}(t)$ denote the first derivative of the roughness of front and rear axle positions at time t . F_b denotes the force vector of the bridge caused by road roughness and axle load of the vehicle, which can be expressed as

$$F_b = F_t + F_g, \quad (4)$$

with

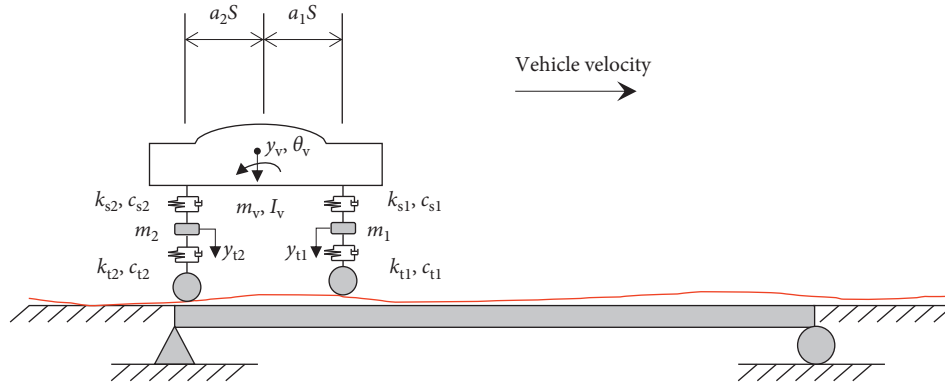


FIGURE 1: The BVI system.

$$\begin{aligned} F_{Bk} &= -(F_{t1}N_{t1} + F_{t2}N_{t2}), \\ F_g &= -[(m_1 + a_1m_v)gN_{t1} + (m_1 + a_2m_v)gN_{t2}], \\ N_{t1} &= [0 \ \dots \ 0 \ N_{t1}^1 \ N_{t1}^2 \ N_{t1}^3 \ N_{t1}^4 \ 0 \ \dots \ 0]^T, \\ \text{and } N_{t2} &= [0 \ \dots \ 0 \ N_{t2}^1 \ N_{t2}^2 \ N_{t2}^3 \ N_{t2}^4 \ 0 \ \dots \ 0]^T, \end{aligned} \quad (5)$$

where N_{ti}^m denotes the shape function of the bridge at the position of front or rear axle, which can be written as

$$\left\{ \begin{aligned} N_{t1}^m &= 1 - 3\left(\frac{\xi}{le}\right)^2 + 2\left(\frac{\xi}{le}\right)^3, \\ N_{t2}^m &= \xi \left[1 - 2\left(\frac{\xi}{le}\right) + \left(\frac{\xi}{le}\right)^2 \right], \\ N_{t3}^m &= 3\left(\frac{\xi}{le}\right)^2 - 2\left(\frac{\xi}{le}\right)^3, \\ N_{t4}^m &= \xi \left[\left(\frac{\xi}{le}\right)^2 - \left(\frac{\xi}{le}\right) \right], \end{aligned} \right. \quad (6)$$

where ξ is the distance between the axle and the left node of the element and le signifies the length of the element.

Equation (2) will be changed by the movement of the vehicle. Therefore, the system is a time-varying system, whereas the Newmark- β integral method can be used to calculate the BVI system response.

3. Dynamic Statistics Calculation Approach

The Karhunen–Loeve expansion (KLE) is applied as an expression method to simulate the random process of road roughness. The basic expression can be written as follows:

$$\begin{aligned} r(x, \theta) &= \bar{r}(x, \theta) + \tilde{r}(x, \theta) \\ &= \bar{r}(x, \theta) + \sum_{i=1}^M \sqrt{\lambda_i} \xi_i(\theta) \varphi_i(x), \end{aligned} \quad (7)$$

where $\bar{r}(x, \theta)$ denotes the mean value of road roughness process; λ_i and $\varphi_i(x)$ refer to the i^{th} eigenvalue and eigenfunction of the covariance kernel, respectively; and $\xi_i(\theta)$ denotes the i^{th} random variable, which is a set of uncorrelated random variables and can be expressed as follows:

$$\xi_i(\theta) = \frac{1}{\sqrt{\lambda_i}} \int_D \tilde{r}(x, \theta) \varphi_i(x) dx. \quad (8)$$

Because the road roughness is assumed to be a zero-mean Gaussian random process in this paper, $\xi_i(\theta)$ will be a set of uncorrelated random normal variables. Equation (7) can be transformed as

$$r(x, \theta) = \sum_{i=1}^M \sqrt{\lambda_i} \xi_i(\theta) \varphi_i(x). \quad (9)$$

After obtaining enough samples of road roughness, we can use the method introduced in [26] to solve λ_i and $\varphi_i(x)$ numerically.

According to the theory of statistical moment calculation, the first two central moments of the random system can be calculated by the following formula:

$$\left\{ \begin{aligned} \text{MEAN} &= \int_{-\infty}^{\infty} g(X) p(x) dx, \\ \text{VAR} &= \int_{-\infty}^{\infty} [g(x) - \text{MEAN}]^2 p(x) dx. \end{aligned} \right. \quad (10)$$

where MEAN and VAR denote mean value and variance value, respectively.

Because the integral in (10) is continuous, the result of MEAN and VAR can be obtained by the Gauss integral. By utilizing the dimension reduction technique, the problem of calculating the statistical moment of a system with multiple random variables can be transformed into the problem of calculating the statistical moment of a composite system with a single random variable [27]. Thereafter, the calculation of (10) can be converted to the calculation of the following formula:

$$\begin{aligned} \text{MEAN} &= \sum_{i=1}^n E[g_i(X_i)] - (n-1)g(c), \\ \text{VAR} &= \sum_{i=1}^n E\{[g_i(X_i) - \text{MEAN}]^2\} \\ &\quad - (n-1)[g(c) - \text{MEAN}]^2, \end{aligned} \quad (11)$$

with

$$\begin{aligned} E[g_i(X_i)] &= \sum_{l=1}^r \frac{w_{\text{GH},l}}{\sqrt{\pi}} g_i(\sqrt{2} x_{\text{GH},l}), \\ E[(g(X_i) - \text{MEAN})^2] &= \sum_{l=1}^r \frac{w_{\text{GH},l}}{\sqrt{\pi}} \\ &\quad \cdot [g_i(\sqrt{2} x_{\text{GH},l}) - \text{MEAN}]^2, \end{aligned} \quad (12)$$

where r denotes the number of quadrature points, whereas $x_{\text{GH},l}$ and $w_{\text{GH},l}$ represent the abscissa and weight of Gaussian-Hermite (G-H) quadrature, respectively. The detailed values of G-H are listed in Table 1. A more detailed derivation process can be found in [27, 34].

By combining the KLE and PEM (called KLE-PEM), the response of the BVI system can be easily and quickly obtained.

4. Simulation of Roughness

Road roughness spectrum recommended in Chinese code GB7031-2005 [35] was used as the roughness power spectral density (PSD) function to simulate the roughness samples, which can be written as follows:

$$G_q(n) = G_q(n_0) \left| \frac{n}{n_0} \right|^{-w}, \quad (13)$$

where n_0 is the spatial reference frequency and the value is 0.1 m^{-1} ; $G_q(n_0)$ denotes the road roughness PSD at the spatial frequency of n_0 , and its value is related to the road roughness class; w is the frequency index, which determines the frequency structure of road roughness spectrum, wherein generally $w = 2$; and n represents a spatial frequency in the effective frequency band of spatial frequency and signifies the number of cycles of waves contained in each meter of length, with its bandwidth being (n_1, n_2) . Meanwhile, n_1 and n_2 are the upper and lower limits of the effective frequency band, respectively. The bandwidth should ensure that the vehicle vibration kinetic energy caused by road roughness includes the main natural frequency of vehicle vibration when the vehicle is driving at the average speed. In the code GB7031-2005, according to the road PSD, the road surface is divided into eight classes in accordance with the roughness. In this paper, five roughness grades were taken for calculation, as shown in Table 2.

Using the trigonometric series method (TSM) [16], the PSD function can be transformed into spatial samples of road roughness. Notably, 20,000 road roughness samples

TABLE 1: G-H integration with $r = 3$ [33].

Point	1	2	3
Abscissa $x_{\text{GH},l}$	-1.22474	0	1.22474
Weight $w_{\text{GH},l}$	0.29541	1.18164	0.29541

corresponding to the PSD of class A, class B, class C, class D,

TABLE 2: Road roughness coefficient.

Road grade	Coefficient $G_q(n_0) \cdot 10^{-6} \text{ m}^2/\text{m}^{-1}$
A: very good	1
B: good	6
C: average	16
D: poor	64
E: very poor	256

and class E were simulated with the length of 120 m (which can meet the total length of vehicles before entering, during passing, and after leaving the bridge). The roughness samples of different road roughness classes are shown in Figure 2. It can be seen that the roughness range of class A was about -3 to 3 mm. Similarly, the roughness range of class B was about -7 to 7 mm, class C was about -10 to 10 mm, class D was about -20 to 20 mm, and class E was about -50 to 50 mm.

The eigenvalues and eigenfunctions of the road roughness samples under different road classes were calculated to obtain the KLE mathematical expression of the random process of road roughness. The first 160 items of the characteristic value of the roughness under each road class are illustrated in Figure 3. Through calculation, the first 115 items of KLE can meet the accuracy requirement of 98% under different road roughness conditions. Therefore, in the subsequent calculations, 115 was used as the number of truncation terms for each road roughness class; that is, the BVI system has 115 independent random variables.

5. Numerical Simulation

5.1. Verification of the BVI Model. In order to verify the accuracy of the BVI model, the results of the classical numerical case in [36] were used to verify the model. In this case, a moving mass-spring system passing through a simply supported beam was calculated. The parameters of the BVI model were set to be consistent with the parameters of the case, subsequent to which the results of the vertical displacement time history response of the midspan are compared with the results of the case, as shown in Figure 4. It can be seen that the results of the current BVI model were essentially consistent with the results of the classic case, thereby verifying the accuracy of the BVI model.

5.2. Comparison with MCS. To verify the applicability of KLE-PEM in the calculation of BVI model, an example was taken in which the bridge was a one-span simply supported beam. Its parameters are shown in Table 3, and the first four mode shapes are shown in Figure 5. The vehicle was a two-

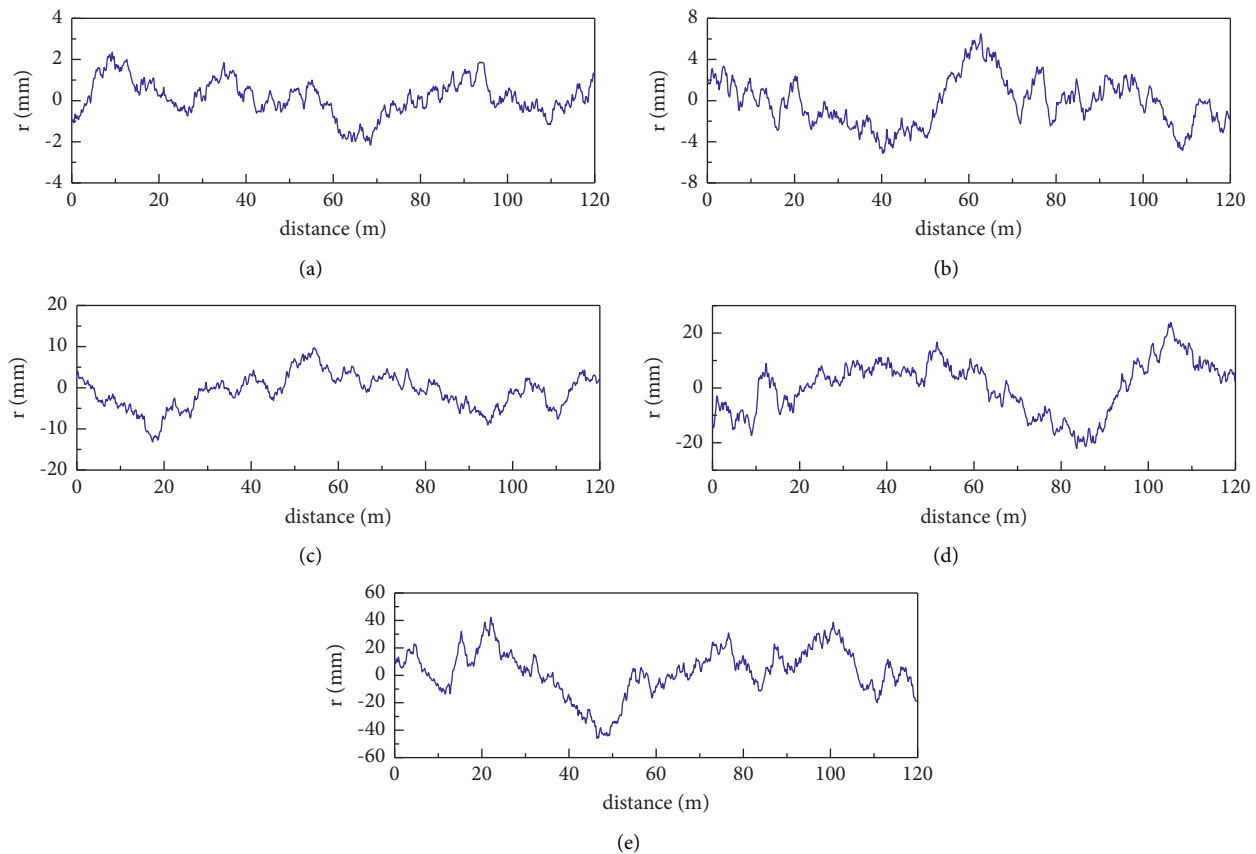


FIGURE 2: Road roughness of various roughness classes: (a) class A: very good; (b) class B: good; (c) class C: average; (d) class D: poor; (e) class E: very poor.

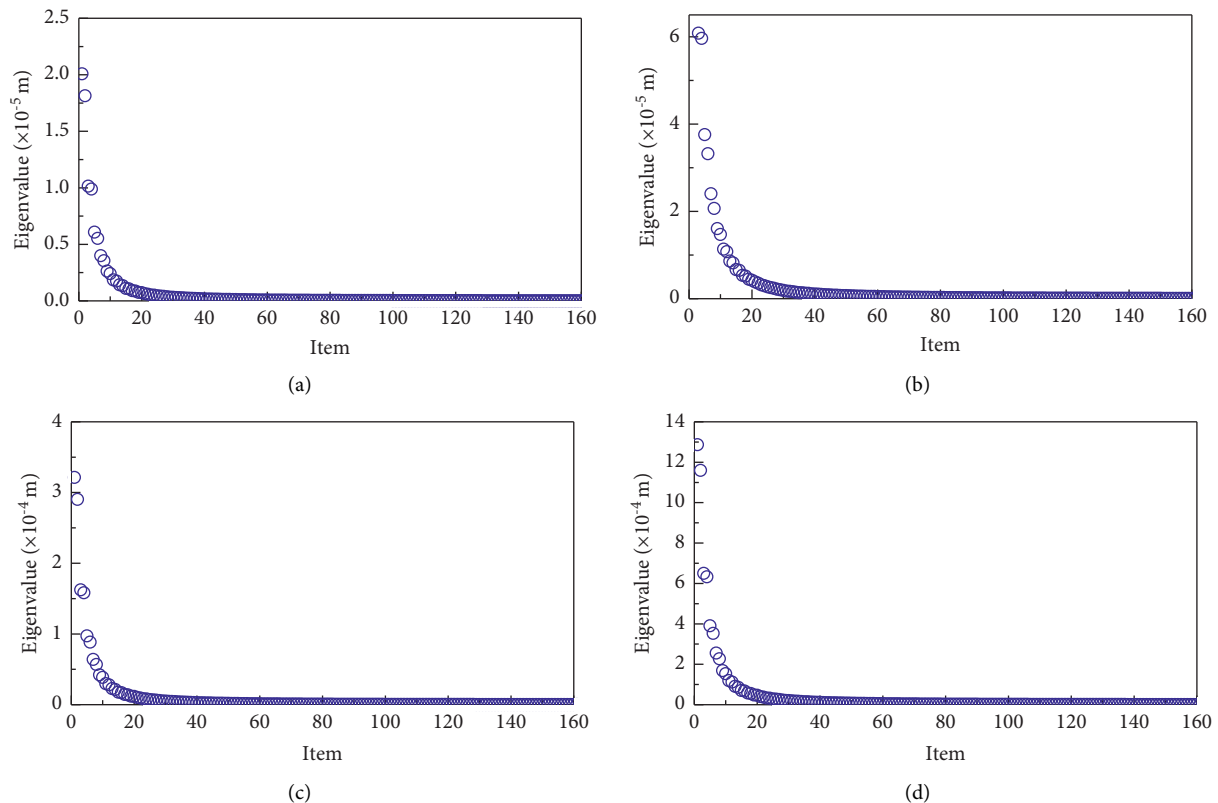


FIGURE 3: Continued.

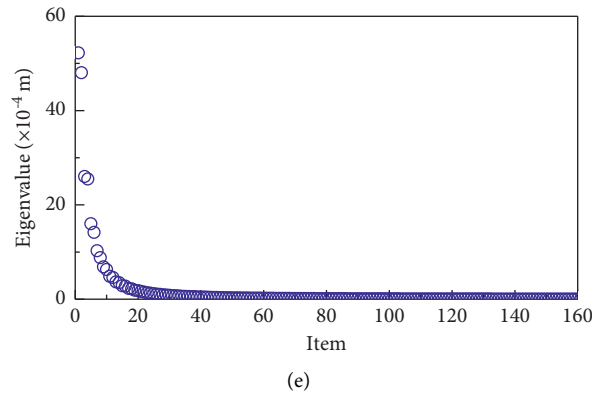


FIGURE 3: Eigenvalues of each grade of road roughness: (a) class A: very good; (b) class B: good; (c) class C: average; (d) class D: poor; (e) class E: very poor.

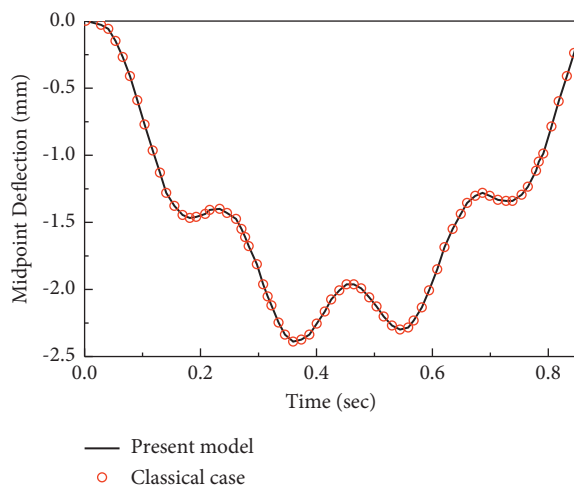


FIGURE 4: Verification of the BVI model.

TABLE 3: Parameters of the bridge [16].

Parameter	Unit	Value
Length	m	30
Area	m ²	8
EI	m ⁴	2.5×10^{10}
Density	kg/m ³	5000
Poisson's ratio	—	0.2
Damping ratio	—	2%
1 st vibration	Hz	3.905
2 nd vibration	Hz	15.623
3 rd vibration	Hz	35.187
4 th vibration	Hz	62.721

axle vehicle, and its parameters are displayed in Table 4. The speed of the vehicle was 20 m/s.

MCS can be used to calculate the response of a stochastic system as the exact solution to evaluate the accuracy of the new method in a stochastic system. Here, MCS and KLE-PEM were used to calculate the BVI system with class C road. The number of times BVI programs were called by MCS was 20,000. Since the number of KLE truncation terms of a random process of road irregularity was 115

times, the number of the BVI programs called by KLE-PEM with three estimation points was $115 \times 2 + 1 = 231$. The comparison of the mean and variance of the bridge mid-span displacement response obtained by calculation is shown in Figure 6. As evidenced by the figure, the results obtained by KLE-PEM coincide with the findings obtained by MCS in terms of mean or variance. In addition, the mean value of response of bridge displacement increased gradually with the passing of vehicles and then decreased gradually after the vehicles left the bridge, finally floating along zero. The variance of bridge displacement response increased when the vehicle moved forward and decreased when the vehicle moved forward. The time when the maximum value appears was essentially consistent with the time when the maximum absolute value of the mean displacement appeared.

The statistical moment results of the vertical acceleration time history response of the car body obtained by the two methods are demonstrated in Figure 7. The statistical moment obtained by KLE-PEM was essentially consistent with that obtained by the MCS method. In addition, for the mean value of response of the vehicle body, the mean value was zero before the vehicle entered the bridge. This is because the road roughness was assumed as a zero-mean random process.

5.3. Bridge Dynamic Response. The dynamic responses of the vehicle passing through the bridge at different vehicle speeds under different road grades were calculated, and the response's maximum probability value was determined by the triple standard deviation criterion [27]. The maximum probability value of vertical displacement response in the middle span of the bridge was obtained, as shown in Figure 8. It can be seen that the bridge displacement response did not change significantly with the vehicle speed and that the road roughness class had a greater impact on the bridge displacement response. The bridge displacement response increased with the increase of road roughness grade. For class A road, the bridge displacement response was less than 6 mm, while the bridge displacement response was 10 mm for class D.

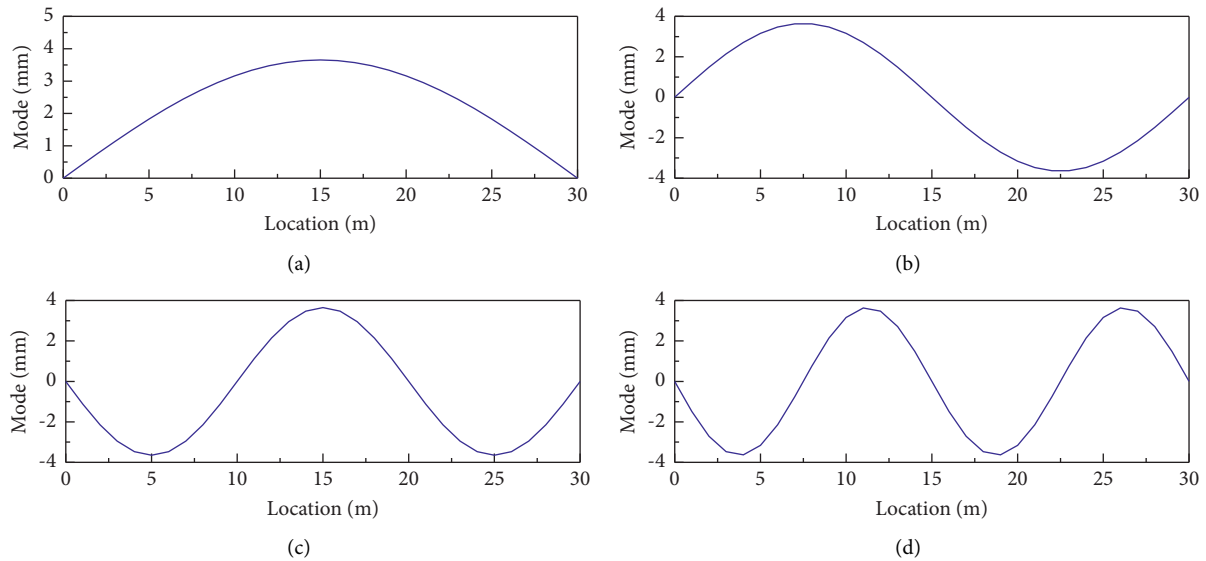


FIGURE 5: Mode shape of bridge: (a) mode shape 1; (b) mode shape 2; (c) mode shape 3; (d) mode shape 4.

TABLE 4: Parameters of the vehicle [16].

Symbol	Unit	Value
I_v	kgm^2	1.47×10^5
m_v	kg	177,35
a_1	—	0.519
a_2	—	0.481
m_1	kg	1500
m_2	kg	1000
k_{s1}/k_{s2}	N/m	$2.47 \times 10^6/4.23 \times 10^6$
k_{t1}/k_{t2}	N/m	$3.74 \times 10^6/4.6 \times 10^6$
c_{s1}/c_{s2}	N/m/s	$3.0 \times 10^4/4.0 \times 10^4$
c_{t1}/c_{t2}	N/m/s	$3.9 \times 10^3/4.3 \times 10^3$
S	m	4.27

The maximum probability value of vertical acceleration response in the middle of the bridge span is shown in Figure 9. Unlike the displacement response, the acceleration response in the middle of the bridge evidently changed with the change of the vehicle speed, whereas the acceleration response first increased and then decreased with the change of the vehicle speed. For bridges with different roughness grades, the maximum acceleration response appeared when the vehicle speed is 20 m/s. In addition, the acceleration response of the bridge increased with the increase of road roughness grade.

5.4. Vehicle Dynamic Response. The maximum value of the vertical acceleration of the car body calculated by KLE-PEM under different roughness classes without vehicle speed is shown in Figure 10. It can be seen that in the case of different roughness levels, the acceleration of the car changes with the speed. More specifically, it first shows a trend of a decline followed by an increase. When the speed was 20 m/s, the maximum acceleration of the car body was found to be the smallest. Similarly, the roughness grade of a road surface was found to have a great impact on the acceleration of the car body.

5.5. Impact Factor of the Bridge. Dynamic impact factor (IMF) is generally defined as the ratio of dynamic load effect and static load effect of the bridge under vehicle load; i.e.,

$$\mu = \frac{(S_d - S_s)}{S_s}, \quad (14)$$

where S_d is the maximum dynamic response of the bridge under moving vehicle load, S_s denotes the maximum static response of the bridge under corresponding vehicle load, and μ signifies the IMF.

IMF is not only an important index to characterize the impact effect of moving vehicle load on the bridge, but also a parameter affected by multiple factors. In traditional research studies, the dynamic IMF has been calculated by collecting the bridge response from the real bridge test, whereas the empirical calculation formula of IMF was obtained by regression analysis of the collected samples. However, on the one hand, the test method is expensive and difficult to implement; on the other hand, different bridges have different stress conditions, and the measured results of a limited number of bridges may not be widely representative. In contrast, IMF analysis based on numerical simulation has the characteristics of low cost and flexible simulation of different bridges and different working conditions, which is why it is eliciting widespread attention.

In Section 5.3, it can be inferred that road roughness has a great effect on the dynamic response of the bridge, thereby implying that road roughness influences the IMF of the bridge as well. To systematically discuss the IMF of the bridge, the IMFs with different vehicle speeds, different bridge spans, and different road grades were calculated from the random aspect. The range of vehicle speed was from 10 to 35 m/s; the bridge spans were 20 m, 22.5 m, 25 m, 27.5 m, and 30 m, whereas their first natural frequencies were 8.79, 6.94, 5.62, 4.65, and 3.90 Hz, respectively.

The calculated IMF under different cases is shown in Figure 11. For different bridge spans and road roughness

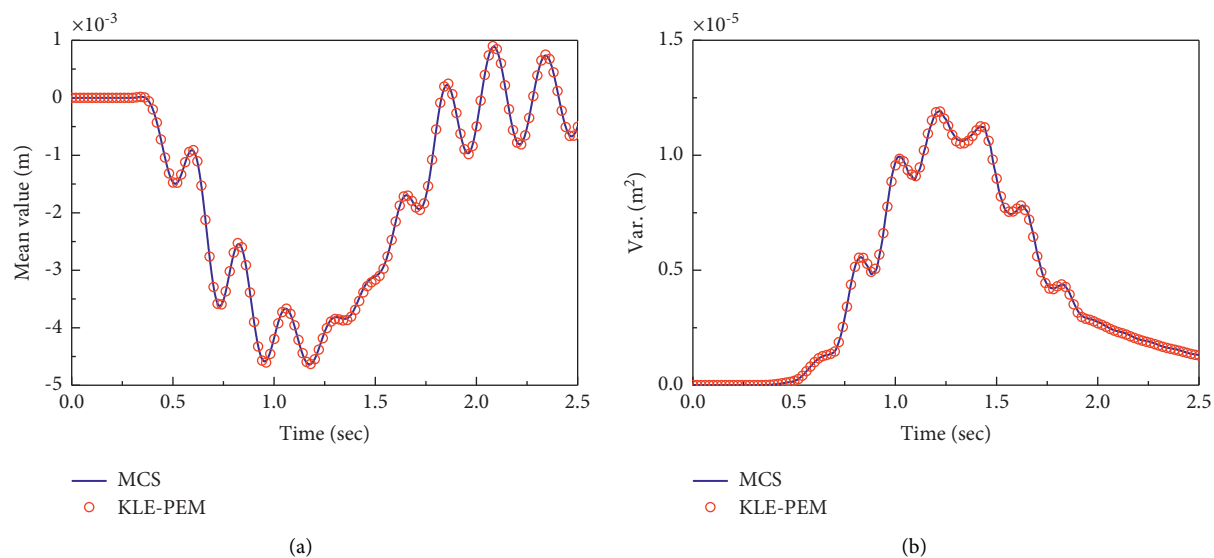


FIGURE 6: Comparison of the statistical moment of bridge midspan displacement of the two methods: (a) MEAN; (b) VAR.

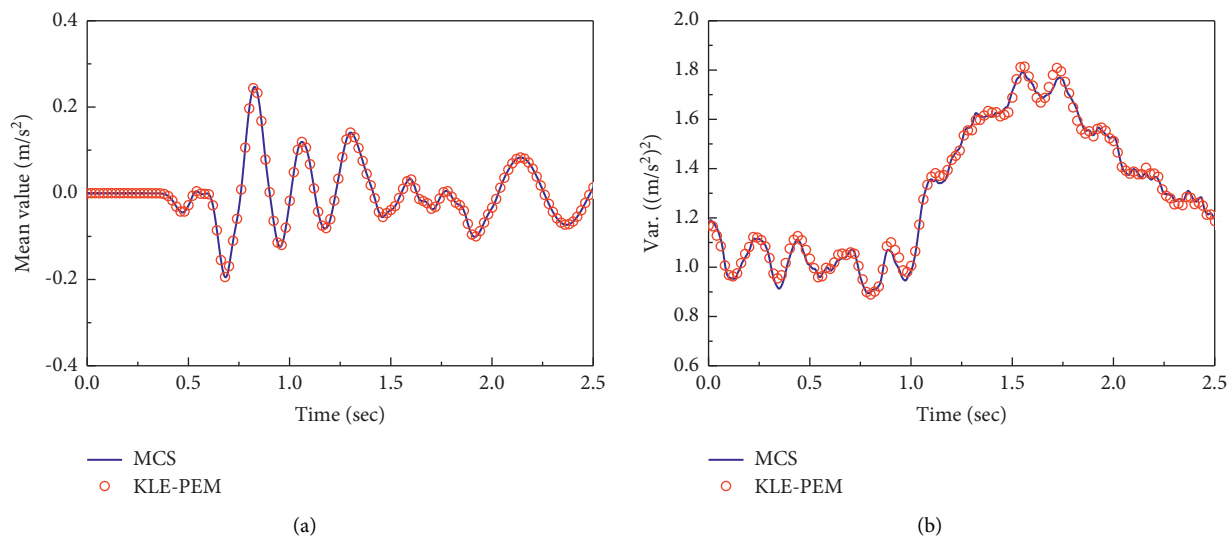


FIGURE 7: Comparison of the statistical moment of car body vertical acceleration of the two methods: (a) MEAN; (b) VAR.

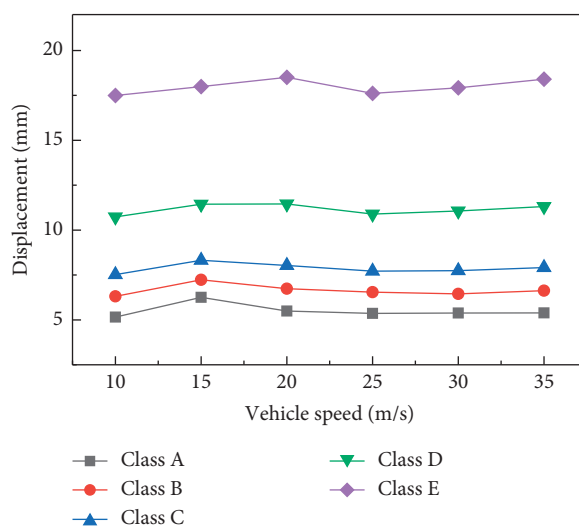


FIGURE 8: Maximum response of bridge displacement via various vehicle and roughness classes.
Dynamic Response of the Bridge-Vehicle...

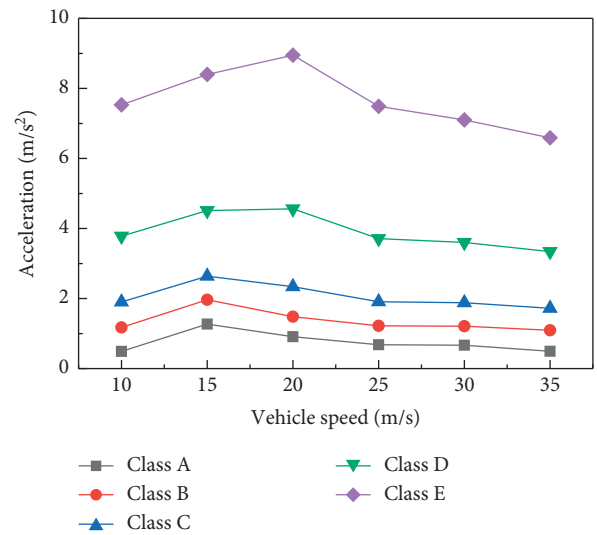


FIGURE 9: Maximum response of bridge acceleration via various vehicle and roughness classes.

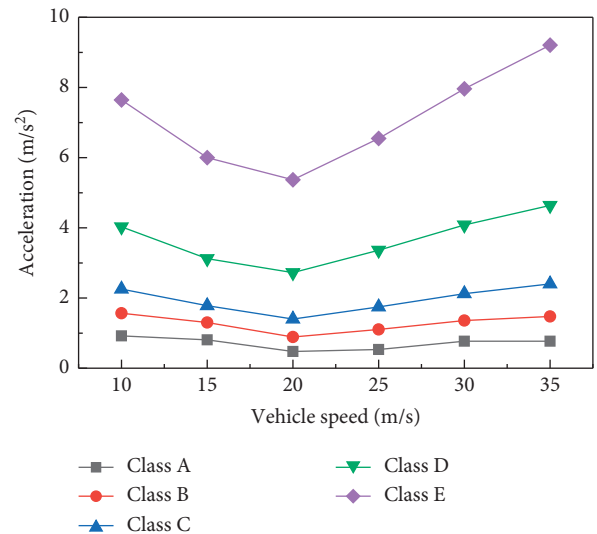
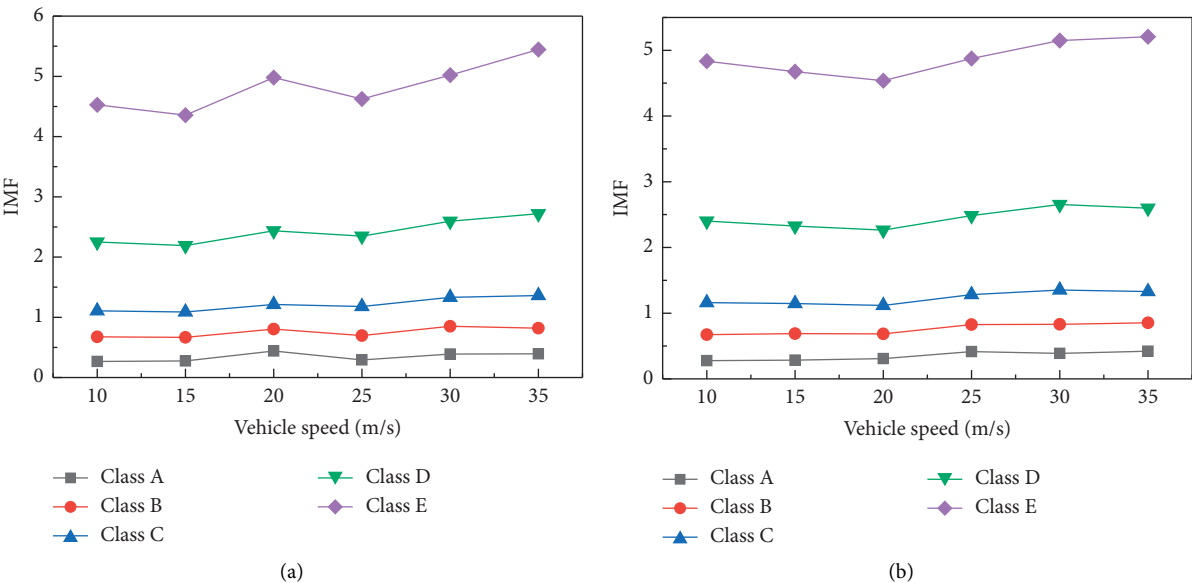


FIGURE 10: Maximum response of vehicle acceleration via various vehicle and roughness classes.



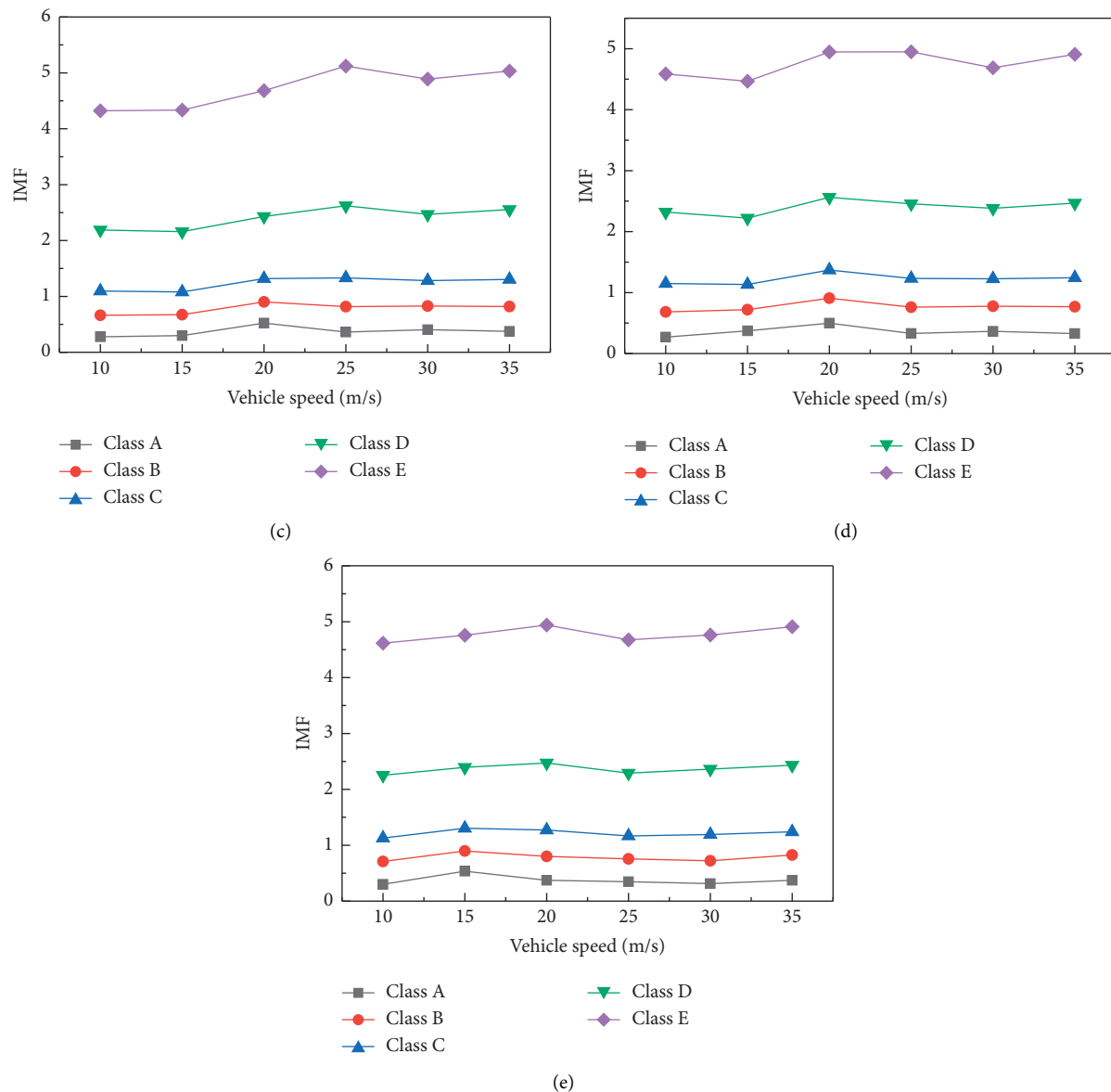


FIGURE 11: IMF under different cases: (a) 20 m span; (b) 22.5 m span; (c) 25 m span; (d) 27.5 m span; (e) 30 m span.

grades, the IMF of the bridge generally increased with the increase of vehicle speed. For different bridge spans, the change of IMF was not particularly obvious, while the influence of road roughness on IMF was strong. For class A and class B roughness, the IMF was smaller than 1, while the IMF value was larger than 5 for class E. With the growth of the bridge operation time, it was found that the pavement roughness gradually increases, which is why the IMF of the bridge will also gradually increase over time, thus jeopardizing the bridge's structural safety. Therefore, when maintaining the bridge, measurement and maintenance of the pavement roughness should be given due attention.

6. Conclusions

To comprehensively analyze the influence of road roughness on the response of the BVI system, a random BVI model

considering the randomness of road roughness was established. The vehicle model was simulated by a mass-spring-damping system, and the bridge was simulated by the FEM theory. The time-varying system equations of the two were obtained by the energy variational principle. Karhunen-Loeve expansion was used to express the road roughness, and the response's statistical moment was calculated by the PEM. Subsequently, the response of the BVI system with different speeds, different spans, and different roughness was analyzed. The results are as follows:

- (1) The KLE-PEM method can obtain the random response of the BVI quickly and precisely, and the computational efficiency is two orders of magnitude higher than that of MCS method.
- (2) The sensitivity of bridge displacement and acceleration response to the road roughness is higher than

the vehicle speed. In addition, the coarser the road surface, the more obvious the influence of vehicle speed change on the bridge response.

- (3) Vehicle speed has a great influence on vehicle acceleration, but it does not increase linearly with the increase of vehicle speed; on the other hand, road roughness has a great influence on vehicle acceleration.
- (4) Compared with different speeds, different bridge spans, and different pavement roughness, road roughness has a strong influence on the IMF of the bridge, which should elicit sufficient attention when carrying out bridge engineering maintenance.

References

- [1] Z. Lai, L. Jiang, and W. Zhou, "An analytical study on dynamic response of multiple simply supported beam system subjected to moving loads," *Shock and Vibration*, vol. 2018, Article ID 2149251, 14 pages, 2018.
- [2] Y. Feng, L. Jiang, and W. Zhou, "Dynamic response of a three-beam system with intermediate elastic connections under a moving load/mass-spring," *Earthquake Engineering and Engineering Vibration*, vol. 19, pp. 377–395, 2020.
- [3] J. Oliva, J. M. Goicolea, P. Antolin, and M. Á. Astiz, "Relevance of a complete road surface description in vehicle-bridge interaction dynamics," *Engineering Structures*, vol. 56, pp. 466–476, 2013.
- [4] Q. Zou, L. Deng, T. Guo, and X. Yin, "Comparative study of different numerical models for vehicle-bridge interaction analysis," *International Journal of Structural Stability and Dynamics*, vol. 16, Article ID 1550057, 2016.
- [5] Q. Zou, L. Deng, and C. Jiang, "Predicting the bounds of vehicle-induced bridge responses using the interval analysis method," *Journal of Bridge Engineering*, vol. 21, Article ID 04016046, 2016.
- [6] H. Wang, T. Nagayama, B. Zhao, and D. Su, "Identification of moving vehicle parameters using bridge responses and estimated bridge pavement roughness," *Engineering Structures*, vol. 153, pp. 57–70, 2017.
- [7] H. Zhong and M. Yang, "Dynamic effect of foundation settlement on bridge-vehicle interaction," *Engineering Structures*, vol. 135, pp. 149–160, 2017.
- [8] X. Liu, L. Jiang, P. Xiang, Z. Lai, Y. Feng, and S. Cao, "Dynamic response limit of high-speed railway bridge under earthquake considering running safety performance of train," *Journal of Central South University*, vol. 28, no. 3, pp. 968–980, 2021.
- [9] L. Xu, Z. Li, Y. Zhao, Z. Yu, and K. Wang, "Modelling of vehicle-track related dynamics: a development of multi-finite-element coupling method and multi-time-step solution method," *Vehicle System Dynamics*, pp. 1–28, 2020.
- [10] L. Xu and X. Liu, "Matrix coupled model for the vehicle-track interaction analysis featured to the railway crossing," *Mechanical Systems and Signal Processing*, vol. 152, Article ID 107485, 2021.
- [11] L. Xin, X. Li, J. Zhang, Y. Zhu, and L. Xiao, "Resonance analysis of train-track-bridge interaction systems with correlated uncertainties," *International Journal of Structural Stability and Dynamics*, vol. 20, Article ID 2050008, 2020.
- [12] L. Xin, X. Li, Y. Zhu, and M. Liu, "Uncertainty and sensitivity analysis for train-ballasted track-bridge system," *Vehicle System Dynamics*, vol. 58, no. 3, pp. 453–471, 2020.
- [13] P. Xiang, W. Huang, L. Jiang, D. Lu, X. Liu, and Q. Zhang, "Investigations on the influence of prestressed concrete creep on train-track-bridge system," *Construction and Building Materials*, vol. 293, Article ID 123504, 2021.
- [14] S. Q. Wu and S. S. Law, "Dynamic analysis of bridge-vehicle system with uncertainties based on the finite element model," *Probabilistic Engineering Mechanics*, vol. 25, no. 4, pp. 425–432, 2010.
- [15] S. Q. Wu and S. S. Law, "Dynamic analysis of bridge with non-Gaussian uncertainties under a moving vehicle," *Probabilistic Engineering Mechanics*, vol. 26, no. 2, pp. 281–293, 2011.
- [16] S. Q. Wu and S. S. Law, "Vehicle axle load identification on bridge deck with irregular road surface profile," *Engineering Structures*, vol. 33, no. 2, pp. 591–601, 2011.
- [17] S. Q. Wu and S. S. Law, "Evaluating the response statistics of an uncertain bridge-vehicle system," *Mechanical Systems and Signal Processing*, vol. 27, pp. 576–589, 2012.
- [18] G. Chen and D. Yang, "Direct probability integral method for stochastic response analysis of static and dynamic structural systems," *Computer Methods in Applied Mechanics and Engineering*, vol. 357, Article ID 112612, 2019.
- [19] G. Chen, Z. Meng, and D. Yang, "Exact nonstationary responses of rectangular thin plate on Pasternak foundation excited by stochastic moving loads," *Journal of Sound and Vibration*, vol. 412, pp. 166–183, 2018.
- [20] X. Li, G. Chen, H. Cui, and D. Yang, "Direct probability integral method for static and dynamic reliability analysis of structures with complicated performance functions," *Computer Methods in Applied Mechanics and Engineering*, vol. 374, Article ID 113583, 2021.
- [21] L. Xu, W. Zhai, and J. Gao, "A probabilistic model for track random irregularities in vehicle-track coupled dynamics," *Applied Mathematical Modelling*, vol. 51, pp. 145–158, 2017.
- [22] L. Xu, W. Zhai, and Z. Li, "A coupled model for train-track-bridge stochastic analysis with consideration of spatial variation and temporal evolution," *Applied Mathematical Modelling*, vol. 63, pp. 709–731, 2018.
- [23] L. Xu and W. Zhai, "A novel model for determining the amplitude-wavelength limits of track irregularities accompanied by a reliability assessment in railway vehicle-track dynamics," *Mechanical Systems and Signal Processing*, vol. 86, pp. 260–277, 2017.
- [24] L. Xu and W. Zhai, "Stochastic analysis model for vehicle-track coupled systems subject to earthquakes and track random irregularities," *Journal of Sound and Vibration*, vol. 407, pp. 209–225, 2017.
- [25] L. Xu, W. Zhai, J. Gao, M. Meacci, and X. Chen, "On effects of track random irregularities on random vibrations of

- vehicle-track interactions," *Probabilistic Engineering Mechanics*, vol. 50, pp. 25–35, 2017.
- [26] X. Liu, P. Xiang, L. Jiang, Z. Lai, T. Zhou, and Y. Chen, "Stochastic analysis of train-bridge system using the kl expansion and the point estimate method," *International Journal of Structural Stability and Dynamics*, vol. 20, no. 2, Article ID 2050025, 2020.
- [27] X. Liu, L. Jiang, Z. Lai, P. Xiang, and Y. Chen, "Sensitivity and dynamic analysis of train-bridge coupled system with multiple random factors," *Engineering Structures*, vol. 221, Article ID 111083, 2020.
- [28] X. Liu, L. Jiang, P. Xiang et al., "Probability analysis of train-bridge coupled system considering track irregularities and parameter uncertainty," *Mechanics Based Design of Structures and Machines*, pp. 1–18, 2021.
- [29] L. Jiang, X. Liu, P. Xiang, and W. Zhou, "Train-bridge system dynamics analysis with uncertain parameters based on new point estimate method," *Engineering Structures*, vol. 199, Article ID 109454, 2019.
- [30] X. Liu, L. Jiang, P. Xiang, W. Zhou, Z. Lai, and Y. Feng, "Stochastic finite element method based on point estimate and Karhunen–Loève expansion," *Archive of Applied Mechanics*, vol. 91, 2021.
- [31] C. Cui, Y. L. Xu, Q. H. Zhang, and F. Y. Wang, "Vehicle-induced dynamic stress analysis of orthotropic steel decks of cable-stayed bridges," *Structure and Infrastructure Engineering*, vol. 16, no. 8, pp. 1067–1081, 2020.
- [32] P. Lou and Q. Zeng, "Formulation of equations of motion of finite element form for vehicle-track-bridge interaction system with two types of vehicle model," *International Journal for Numerical Methods in Engineering*, vol. 62, no. 3, pp. 435–474, 2005.
- [33] Y. G. Zhao and T. Ono, "New point estimates for probability moments," *Journal of Engineering Mechanics*, vol. 126, no. 4, pp. 433–436, 2000.
- [34] L. Jiang, X. Liu, T. Zhou et al., "Application of KLE-PEM for random dynamic analysis of nonlinear train-track-bridge system," *Shock and Vibration*, vol. 2020, Article ID 8886737, 10 pages, 2020.
- [35] GB/T 7031-2005, "Mechanical vibration-road surface profiles-reporting of measured data," 2005, in Chinese.
- [36] Y. B. Yang and J. D. Yau, "Vehicle-bridge interaction element for dynamic analysis," *Journal of Structural Engineering*, vol. 123, no. 11, pp. 1512–1518, 1997.

Characteristic of Specimens of Circular Concrete-Filled CFRP-Steel Tubular Beam-Column

Anand Mandal, *Department of Civil Engineering, Raajdhani Engineering College, Bhubaneswar, anandmandal1@gmail.com*

Alivasakhi Mishra, *Department of Civil Engineering, Capital Engineering College, Bhubaneswar, alivasakhimishra258@gmail.com*

Harish Chand Giri, *Department of Mechanical Engineering, Aryan Institute of Engineering & Technology, Bhubaneswar, harishchand4@gmail.com*

P. Paulpandian, *Department of Mechanical Engineering, Aryan Institute of Engineering & Technology, Bhubaneswar, p_paulpandian@gmail.com*

ABSTRACT

Twelve specimens of circular concrete-filled CFRP-steel tubes were built, and their failure modes and P-curves were analysed, to investigate the differences in hysteretic behaviour under various influencing variables. The P-curves and deformation mode of the specimens were simulated using ABAQUS. The stress distribution of all of the specimens' component materials, as well as the interaction between the steel tube and concrete, were analysed throughout the loading process based on the simulation results, and the trilinear model, the restoring force model of circular concrete-filled CFRP-steel tube, was proposed. The P-curves of all of the specimens were full and showed outstanding hysteretic activity. The P-curves, skeleton curves, and deformation mode of the specimens were simulated using ABAQUS, and the simulation results were in good agreement with the experimental results. Furthermore, the results of the restoring force model based on the trilinear model were consistent with the results of the finite element simulation.

1. Introduction

In recent years, earthquakes are more and more widespread in the world. The distribution of seismic zones is not uniform, but they are widely distributed. Some scholars have carried out extensive and in-depth research on the seismic design of building structures, and the earthquakes have caused huge economic losses and casualties. To deal with the threat of earthquake disaster to buildings, the research on hysteretic behavior of building structures is more and more extensive. Nowadays, the most commonly used composite structure is steel-concrete composite structure. It is a composite structure composed of steel and concrete, which mainly uses the advantages of compressive performance of concrete and tensile performance of steel. Not only is this composite structure convenient for construction, but it also saves a lot of materials, so as to achieve the goals of reducing the cost, reducing the weight of components, and shortening the construction period. Therefore, the steel-concrete composite structure is widely used in practical engineering.

Liu and Dong [1] carried out the torsion tests of 16 circular CFRP concrete-filled steel tubes. The results show that the failure modes of the specimens bonded with longitudinal CFRP and circumferential CFRP are different. Romero et al. [2] carried out experimental research and finite element theoretical analysis on fire performance of concrete-filled steel tubular members. The results show that the steel tube and CFRP can work together, and the deformation of the component approximately conforms to the plane section assumption. Han and Zhong [3] deduced the axial force torque correlation equation of concrete-filled steel tubular members, described the moment torque correlation equation, and analyzed the whole process of such specimens. Nie et al. [4] conducted an experimental study on the torsional hysteretic behavior of concrete-filled steel tubes with circular section and rectangular section. The results show that the hysteretic curve is very full, and the unloading stiffness and the initial loading stiffness of the specimen are almost the same, and the specimen shows good energy dissipation performance; the torsion resistance of the

specimen with too large axial compression ratio is weakened due to too serious deformation. Zhou et al. [5] carried out the pure torsional hysteretic behavior test of hollow sandwich concrete-filled steel tubular specimens with section form and void ratio as the main parameters. The experimental results show that the initial elastic stiffness is close to the unloading stiffness, and the specimens show good energy dissipation capacity [6], and the hysteretic behavior of circular section hollow sandwich concrete-filled steel tube is better than that of square section [7, 8]. Sundarraja and Prabhu [9] found that the steel ratio and the number of CFRP layers have great influence on the bearing capacity of square CFRP-CFST specimens and proposed a finite element simulation method to reproduce the mechanical behavior of square CFRP-CFST effectively. Tao et al. [10, 11] indicated that the bearing capacity of CFRP-CFST specimens was significantly reduced after fire, but the fire resistance ability of concrete-filled CFRP-steel tube specimens was better than that of ordinary concrete-filled steel tube specimens. Peng et al. [12] studied the influence of various materials on the bearing capacity of square concrete-filled CFRP-steel tube under axial compression. Wang et al. [13] and Che et al. [14] studied the influence of slenderness ratio and eccentric ratio on the performance of square concrete-filled CFRP-steel tube. At present, most of the researches are focused on the static performance of components. Therefore, it is necessary to study the CFRP-CFST under hysteretic load and establish a more accurate restoring force model.

In view of this, 12 groups of circular CFRP concrete-filled steel tube specimens were designed in experiment. Referring to the hysteretic test of concrete-filled steel tube, the specimens' failure modes and the lateral force-deflection $P-\Delta$ curve were studied. The specimens' $P-\Delta$ curve and deformation mode were simulated with ABAQUS. On this basis, each component material's stress distribution and the interaction between the steel tube and concrete were analyzed. Based upon the trilinear model, the restoring force model of C-CF-CFRP-ST was proposed. Finally, the model's calculation results were compared with the results of finite element simulation to verify the model's accuracy.

2. Performance of Raw Materials and Test Design

2.1. Performance of Raw Material

2.1.1. Steel. Longitudinal welded steel tube was used. The material properties of the steel are shown in Table 1. f_y is the yield strength of steel tube. f_u is the ultimate strength of steel tube. E_s is the elastic modulus of steel tube. ϵ_{sy} is the yield strain of steel tube. ν_s is Poisson's ratio, and ϵ' is the elongation of steel.

2.1.2. Concrete. Portland cement with a strength grade of 42.5 was used in the experiment. Medium coarse sand was used as fine aggregate. The particle size of the coarse aggregate gravel was 5~15 mm, and a water reducer with 1% cement weight was added. The specific ratio of the concrete

TABLE 1: The material properties of steel tube used in experiment.

Section	f_y (MPa)	f_u (MPa)	E_s (GPa)	ϵ_{sy} ($\mu\epsilon$)	ν_s	ϵ' (%)
Circular	298	425	199	2502	0.28	27

is shown in Table 2. The concrete mix used in this experiment refers to the C50 concrete which is prepared according to the European concrete code and Chinese concrete code.

After 28 days of standard curing, the concrete cube's compressive strength (f_{cu}) was 47.8 MPa and the elastic modulus (E_c) was 34.6 GPa. The cube's compressive strength was 77.7 MPa during the hysteretic test.

2.1.3. CFRP and Viscose. Carbon fiber fabric is a unidirectional fabric woven with carbon fiber made in China. Its main properties are shown in Table 3.

The adhesive and base adhesive are building structural adhesives produced by China Institute of Construction Science and Technology in the test.

Firstly, concrete-filled steel tube was prepared according to Han et al. [15]. After that, acetone was used to clean the welding slag and oil on the steel tube surface. The viscose was evenly applied on the surface of steel tube, and part of the viscose was evenly applied on the surface of CFRP. The bubbles were removed by scraping to ensure that the adhesive completely penetrated into CFRP. The sequence of pasting CFRP is as follows: paste the longitudinal CFRP firstly. When its surface is dry, then paste the transverse CFRP, and lap length of transverse CFRP is 150 mm. Finally, apply a layer of adhesive on the outer layer to make it completely cured within one week.

2.2. Test Design. A total of 12 specimens were designed, and the hysteretic behavior of the specimens was tested. The main parameters include axial compression ratio (n) and longitudinal CFRP reinforcement coefficient (η):

$$n = N_0 / N_{u,CR} \quad (1)$$

where N_0 is the axial force applied to the specimen.

The calculated length (L) of each group is 2000 mm, the outer diameter (D_s) is 140 mm, the wall thickness (t_s) is 4 mm, and the number of transverse CFRP layers (m_t) is 1, where n is the axial compression ratio, η is the longitudinal CFRP reinforcement coefficient, m_l is the number of longitudinal CFRP layers, Δ_y is the yield displacement of the specimen, and the specific parameters of each specimen are shown in Table 4.

Before the test, the specimens are placed horizontally and hinged at both ends. The axial force is applied by the electrohydraulic servo system actuator set horizontally, and the hysteretic force is applied by the electrohydraulic servo system actuator set vertically in the middle section. The actuator is connected with the test piece through a rigid fixture. In order to avoid out-of-plane instability of the specimen during loading, a set of lateral support devices are designed, which are respectively set at two quarter points of the specimen. The loading panorama of specimens with

TABLE 2: Specific ratio of concrete kg/m³.

Cement	Water	Fine aggregate	Coarse aggregate
490	171.5	661.5	1078

TABLE 3: Basic performance parameters of CFRP.

Thickness of single layer (mm)	Weight (g/m ³)	Elongation at break (%)	Tensile strength of monofilament (GPa)	Elastic modulus (GPa)
0.111	200	2.1	4.9	230

TABLE 4: Parameters of C-CF-CFRP-ST specimens.

Order	Number	n	m_l (layers)	ηh	N_0 (kN)	D_y (mm)
1	A0	0	0	0	0	12.1
2	A1	0	1	0.157	0	13.1
3	A2	0	2	0.314	0	13.1
4	B0	0.2	0	0	228	13.1
5	B1	0.2	1	0.157	230	12.1
6	B2	0.2	2	0.314	233	12.1
7	C0	0.4	0	0	455	11.3
8	C1	0.4	1	0.157	460	9.3
9	C2	0.4	2	0.314	466	8.6
10	D0	0.6	0	0	681	11.1
11	D1	0.6	1	0.157	691	10.1
12	D2	0.6	2	0.314	698	6.6

compression bending hysteretic behavior is shown in Figure 1.

The load-displacement control method was used in the test. The actual load is constant, and lateral load is cyclic in this test. Both the lateral load and the axial load are loaded by actuators, and the direction has been shown in Figure 2. Section diagram of C-CF-CFRP-ST specimens is shown in Figure 3. At the initial stage of the test, the load was controlled and loaded in stages, respectively, according to $0.25P_{uc}$ (P_{uc} is the estimated lateral bearing capacity), $0.5P_{uc}$, and $0.7P_{uc}$, and each stage load cycle was 2 times; after that, the displacement was controlled and loaded in stages, according to $1.0\Delta_y$, $1.5\Delta_y$, $2.0\Delta_y$, $3.0\Delta_y$, $5.0\Delta_y$, $7.0\Delta_y$, and $8.0\Delta_y$, $\Delta_y = P_{uc}/K_{0.7}$, and the secant stiffness of $P-\Delta$ skeleton curve when $K_{0.7}$ is $0.7P_{uc}$. The load cycle of other stages is twice. Before the test, the axial force of $0.5N_0$ is used to load and unload once, so as to reduce the influence of the internal structure inhomogeneity [16–18].

During the test, the INV-306D intelligent signal acquisition and analysis system connected with the vertical actuator of the electrohydraulic servo system directly collects P and Δ . The INV-306D intelligent signal acquisition and analysis system connected with the horizontal actuator of the electrohydraulic servo system directly collects N_0 and Δ' . The deflection is measured with a displacement meter at two quarter points close to the two supports. One transverse strain gauge and one longitudinal strain gauge are, respectively, pasted on the steel tube and CFRP tube at the outermost edge of the middle section and the lower section to measure the strain. Loading system of C-CF-CFRP-ST specimens is shown in Figure 4.

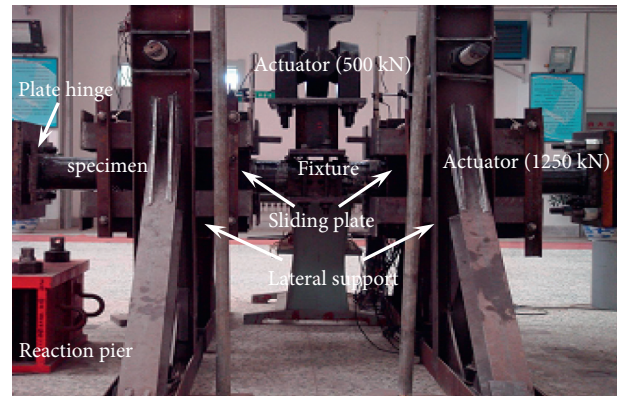


FIGURE 1: Loading equipment of hysteretic performance test of specimens.

3. Test Results and Analysis

3.1. Test Phenomenon. Before reaching the yield-loading, the $P-\Delta$ curve of the specimen is basically linear, and there is no obvious residual deformation. With the increase of the lateral displacement, there is a small bulge at the connection between the rigid fixture and the specimen. After that, the axial compression ratio has a significant effect on the experimental phenomena.

For the specimen with small axial compression ratio ($n \leq 0.2$), when loading to $3\Delta_y \sim 5\Delta_y$, the microbulge occurs on both sides of the fixture. With unloading and reverse loading, the bulge is flattened again, and causes the microbulge in the compression area on the other side. When loading to $5\Delta_y$, for the specimens with longitudinal CFRP, it can be found that the transverse CFRP fibers cracked, and the longitudinal CFRP began to break sporadically. When loading to $7\Delta_y$, the drumming began to develop significantly, and a continuous burst sound was emitted. At this time, the transverse CFRP is slightly fracture, and the longitudinal CFRP begins to fracture in large stage. As shown in Figure 5(a), A1 specimen has both transverse and longitudinal CFRP, naked leakage appears on the outer wall of the steel tube, which indicates that the longitudinal CFRP is fractured a lot. After that, the transverse CFRP begins to fracture in a large scale. For the specimens without longitudinal CFRP, as shown in Figure 5(b), only when the deflection is large at the later stage of loading, a large number of transverse CFRP fractures begin to appear.

As shown in Figure 6(a), for the specimen with large axial compression ratio ($n \geq 0.4$), the change of the specimen is basically consistent with that of the specimen with small

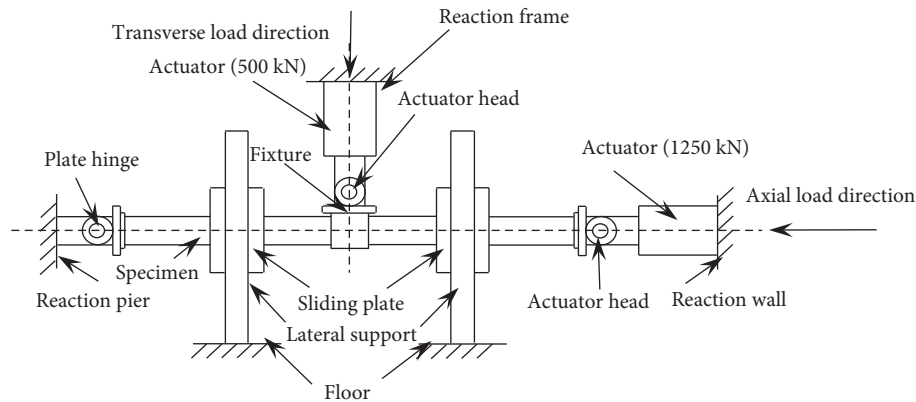


FIGURE 2: Loading diagram of C-CF-CFRP-ST specimens with compression bending hysteretic behavior.

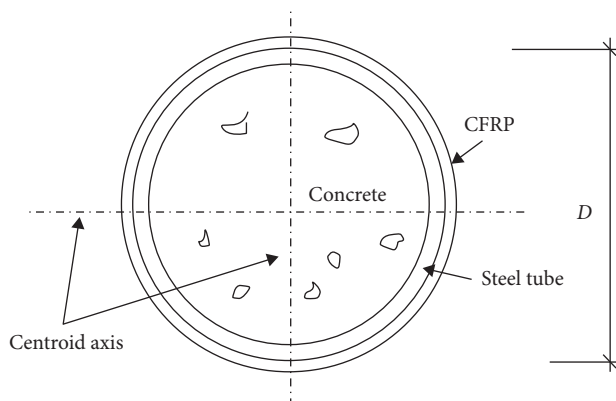


FIGURE 3: Section diagram of C-CF-CFRP-ST specimens.

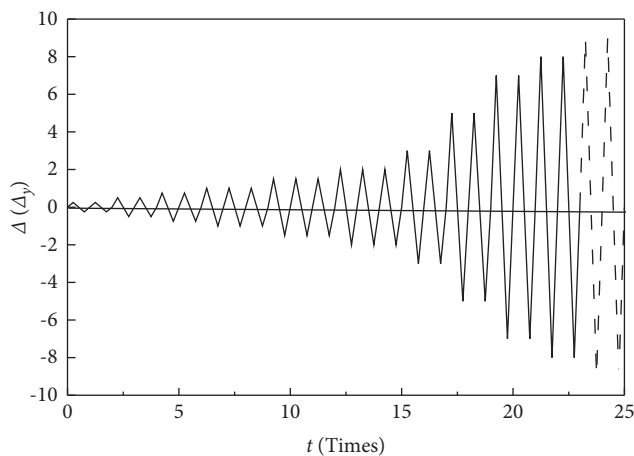


FIGURE 4: Loading system of C-CF-CFRP-ST specimens.

axial compression ratio ($n \leq 0.2$) when the load is $3\Delta_y \sim 5\Delta_y$. After loading to $7\Delta_y$, the transverse and longitudinal CFRP of specimens begin to fracture gradually. For specimens without longitudinal CFRP, the transverse CFRP begins to fracture gradually, as shown in Figure 6(b).

Based on this, it can be found that with the increase of η the damage degree of the specimen is reduced. Figure 7 shows all the specimens with circular section after loading.

After the loading specimen is broke, it can be seen that there are some tiny bulges in the interior of the specimen, as shown in Figure 8(a), and there are fewer cracks in the corresponding position of the concrete, as shown in Figure 8(b), which indicates that the concrete confined by CFRP and steel tube has good plastic filling performance, and the test performance is that the failure characteristics of the specimen are not obvious.

3.2. The Curve of $P-\Delta$

3.2.1. The Hysteresis Curve of $P-\Delta$. Figure 9 shows the $P-\Delta$ curve of the specimen. It can be seen that the hysteretic curve of the specimen is full and there is no pinch phenomenon. In the initial stage of loading, the specimen is basically in the elastic stage, and the hysteretic curve changes approximately linearly. After yielding, the residual deformation gradually increases, and the stiffness decreases. From unloading to reverse loading, the stiffness of the specimen changes little. For the specimen without axial compression ratio, the bearing capacity does not decrease in the later stage of loading. For the specimen with axial compression ratio, the bearing capacity decreases in the later stage of loading obviously. The specimen without axial compression ratio only bears the action of bending moment and consumes less energy. Compared with the specimen with axial compression ratio, its bearing capacity is not reduced. In addition, with the increase of axial compression ratio, the compression area of core concrete increases, which is more likely to lead to concrete cracking and reduce the later bearing capacity of specimens [3].

3.2.2. $P-\Delta$ Skeleton Curve. Figure 10 shows the $P-\Delta$ skeleton curves of specimens with different axial compression ratios. Figure 11 shows the local section $P-\Delta$ skeleton curves. It can be seen that, with the increase of axial compression ratio, the lateral bearing capacity and elastic stiffness of the specimen decrease. However, the curve of the circular specimen with $\eta = 0$ has no decreasing stage. When $\eta > 0$, the curve of the specimen has decreasing stage, and the descending range increases with the improvement of the axial compression ratio.



FIGURE 5: Fracture of CFRP of specimens with a small axial compression ratio. (a) Longitudinal CFRP of A1. (b) Transverse CFRP of A0.

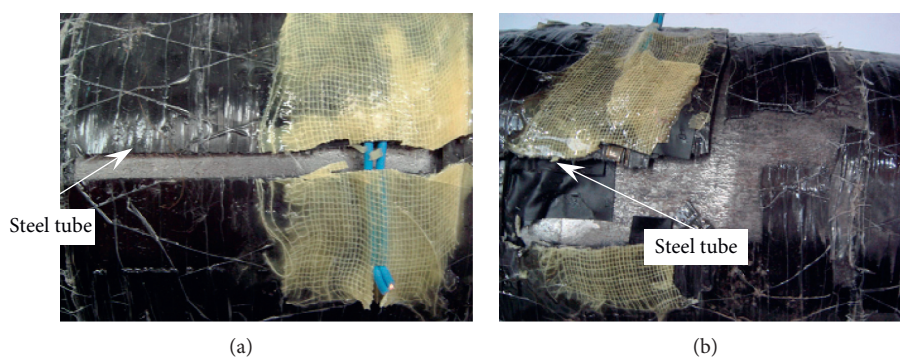


FIGURE 6: Fracture of CFRP of specimens with a large axial compression ratio. (a) Longitudinal CFRP of C1. (b) Transverse CFRP of C0.



FIGURE 7: The C-CF-CFRP-ST specimens after loading.

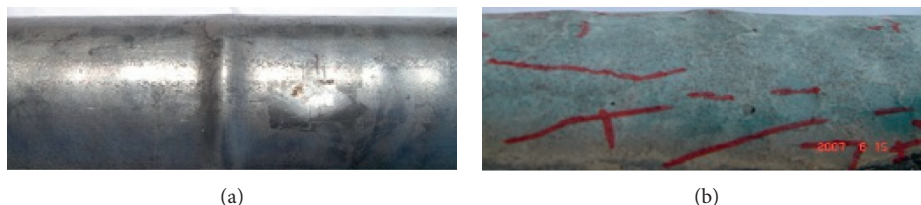


FIGURE 8: Internal and external damage of specimen failure. (a) Steel tube. (b) Concrete.

4. Finite Element Simulation

4.1. Element Type Selection and Mesh Discretization. The adopted element in the mesh of the steel tube is shell element S4 with full integration. Simpson integration

with 9 integrating points in the shell thickness direction is used. For the mesh of the concrete, 3D brick element C3D8R with reduced integration is used. Membrane element M3D4 with 4nodes is used for modelling CFRP [19, 20].

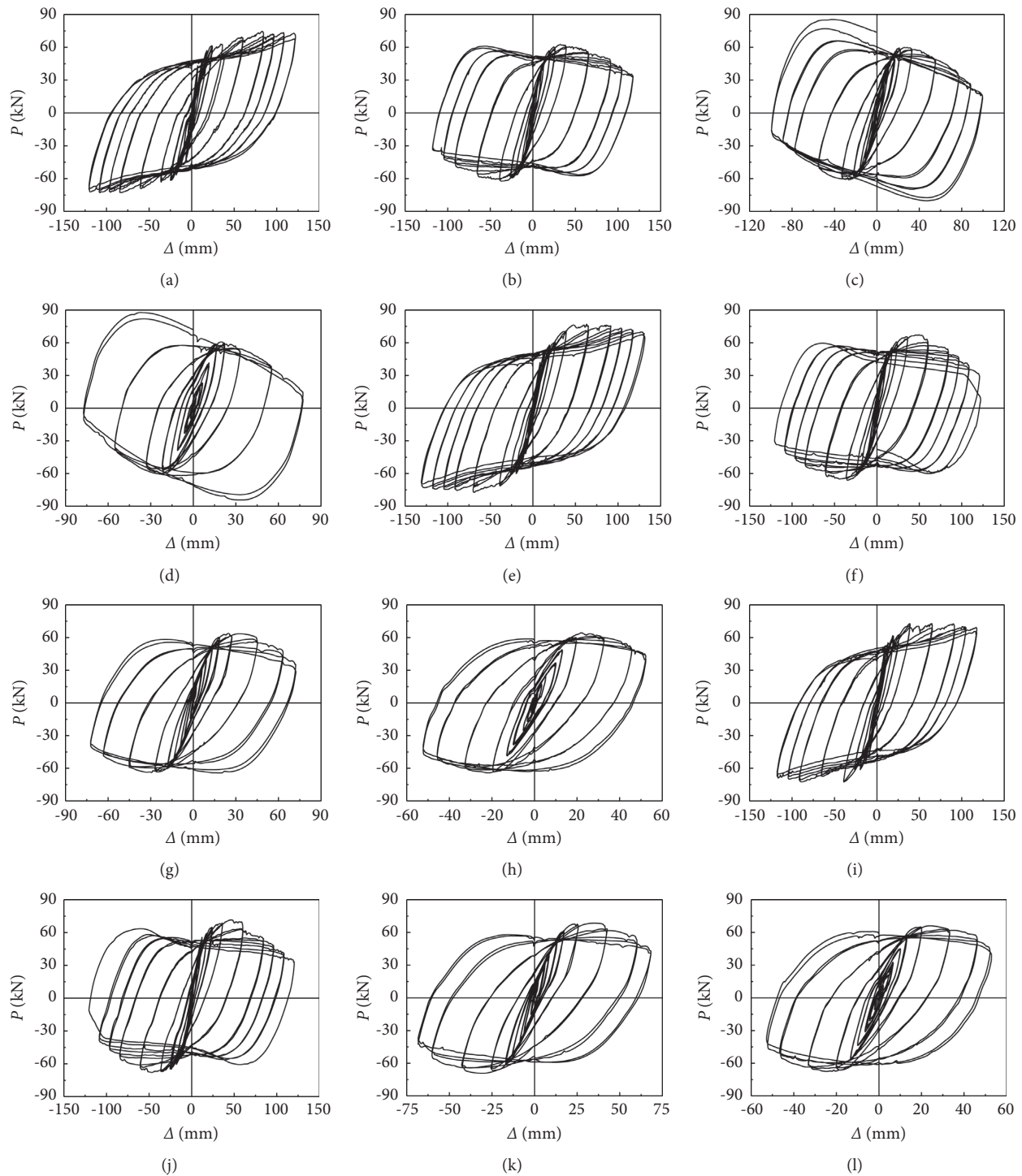


FIGURE 9: P - Δ curves of specimens. (a) A0 specimen. (b) B0 specimen. (c) C0 specimen. (d) D0 specimen. (e) A1 specimen. (f) B1 specimen. (g) C1 specimen. (h) D1 specimen. (i) A2 specimen. (j) B2 specimen. (k) C2 specimen. (l) D2 specimen.

4.2. Stress-Strain Relationship of Materials. The details of the stress-strain relationships of the steel are determined according to the constitutive model suggested by Han and

Zhong [3]. The Concrete Damage Plasticity is used in the finite element simulation of concrete, and stress-strain of concrete relationship is shown in the following equation:

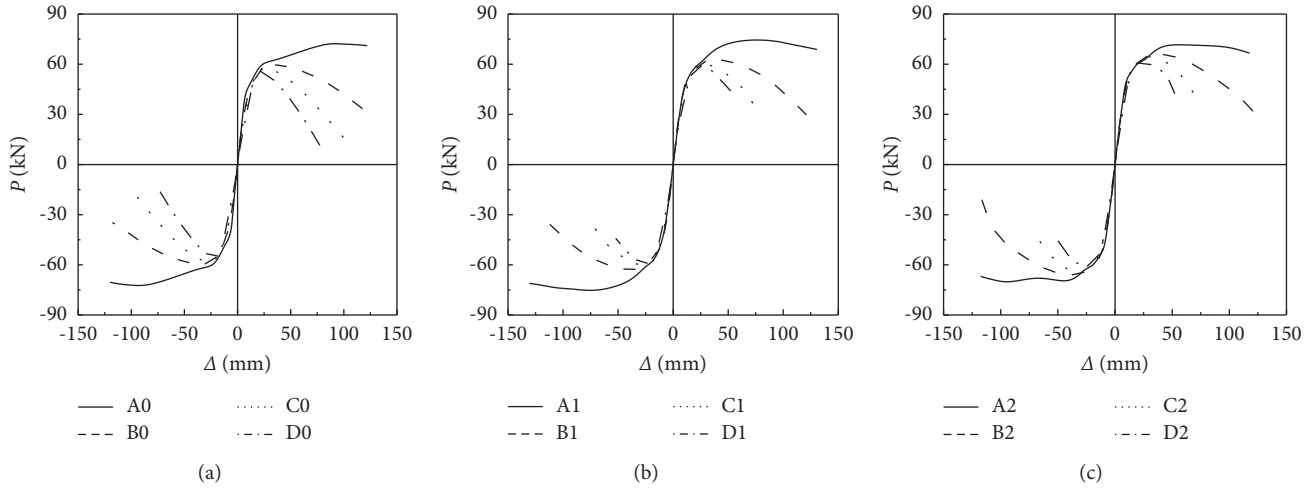


FIGURE 10: Effect of axial compression ratio on P - Δ skeleton curve of specimens. (a) $\eta = 0$ specimens. (b) $\eta = 0.157$ specimens. (c) $\eta = 0.314$ specimens.

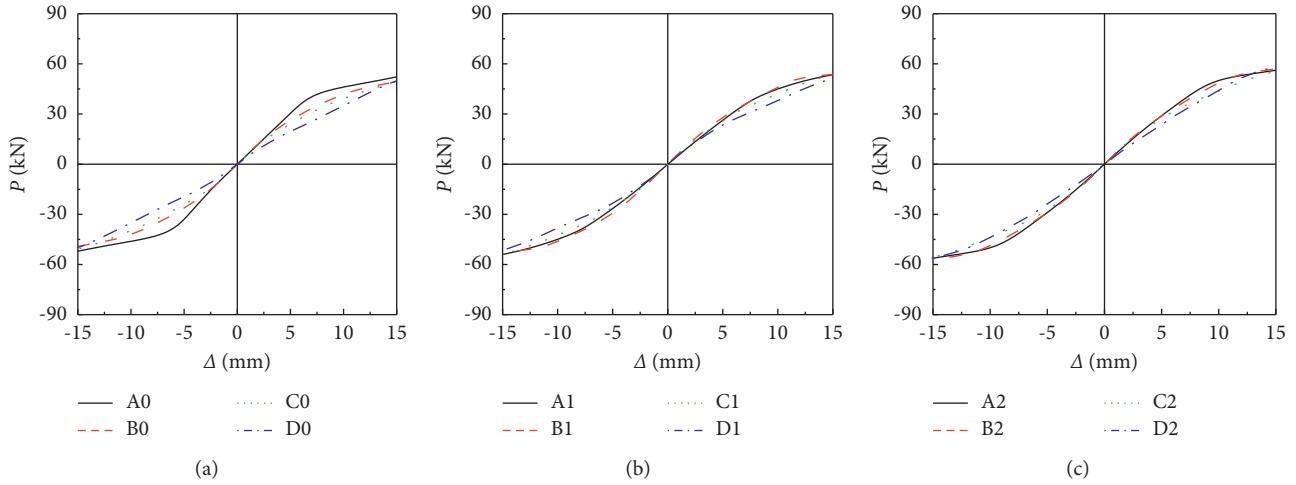


FIGURE 11: The local section on P - Δ skeleton curve of specimens. (a) $\eta = 0$ specimens. (b) $\eta = 0.157$ specimens. (c) $\eta = 0.314$ specimens.

$$\frac{\sigma_{cl}}{\sigma_0} = \begin{cases} 2\left(\frac{\varepsilon_{cl}}{\varepsilon_0}\right) - \left(\frac{\varepsilon_{cl}}{\varepsilon_0}\right)^2, & \varepsilon_{cl} \leq \varepsilon_0, \\ \left[\left[1 - q + q\left(\frac{\varepsilon_{cl}}{\varepsilon_0}\right)^{0.1\xi} \right] \left(\frac{\varepsilon_{cl}}{\varepsilon_0}\right)^C, & \xi_s \geq 1.12 \\ \frac{(\varepsilon_{cl}/\varepsilon_0)^{1+D}}{\beta((\varepsilon_{cl}/\varepsilon_0) - 1)^2 + (\varepsilon_{cl}/\varepsilon_0)}, & \xi_s < 1.12 \end{cases}, \quad \varepsilon_0 < \varepsilon_{cl} \leq \varepsilon_u, \quad (2)$$

$$\frac{\sigma_{cl}}{\sigma_0} = \frac{\varepsilon_{cl}/\varepsilon_0}{\beta_s((\varepsilon_{cl}/\varepsilon_0) - 1)^2 + (\varepsilon_{cl}/\varepsilon_0)}, \quad \varepsilon_{cl} > \varepsilon_u, \quad (3)$$

$$\varepsilon_0 = \varepsilon_{cc} + (600 + 32.4f'_c)\xi^{0.2} \times 10^{-6}, \quad (4)$$

$$\varepsilon_{cc} = (1300 + 12.09f'_c) \times 10^{-6}, \quad (5)$$

$$q = \frac{\xi^{0.745}}{(2 + \xi)}, \quad (6)$$

$$C = \zeta \iota (2.231 - 4.611\zeta \iota), \quad (7)$$

$$D = \zeta \iota (1.545 - 1.238\zeta \iota), \quad (8)$$

$$\beta = 3.28(2.36 \times 10^{-5})^{0.25+(\xi-0.5)^7} f_c'^2 \times 10^{-4}, \quad (9)$$

$$\beta_s = 0.5(2.36 \times 10^{-5})^{0.25+(\xi_s-0.5)^7} f_c'^2 \times 10^{-4}, \quad (10)$$

$$\varepsilon_u = \varepsilon_0 + 51659\xi_{cf} - 38904\xi_{cf}^2, \quad (11)$$

where compressive strength of the concrete is defined as f'_c . ξ' is confinement factor ratio. q , C , and D are related parameters about ξ . β and β_s are related parameters about ξ_s . ε_u is the longitudinal strain of the specimen. The failure energy criterion of concrete is used to simulate the tension of concrete.

$$\begin{aligned} G_f &= 40 + 4(f'_c - 20), \\ \sigma_{t0} &= 0.26(1.5f'_c)^{2/3}, \end{aligned} \quad (12)$$

where total energy consumed in concrete fracture process is defined as G_f and σ_{t0} is the ultimate tensile strength of concrete.

The shrinkage and the creep are not considered for concrete material in the finite element model.

The confinement of transverse CFRP is quantified by the confinement factor of transverse CFRP (ξ_{cf}) proposed. The reinforcement efficiency of longitudinal CFRP is defined as a strengthening coefficient (η). All influence factors are given from (15) to (17).

$$\begin{aligned} \eta &= \frac{A_{cfl}f_{cfl}}{(A_s f_y)}, \\ A_{cft} &= E_{cf}\varepsilon_{cft}, \\ f_{cfl} &= E_{cf}\varepsilon_{cfl}, \end{aligned} \quad (13)$$

where A_{cft} and f_{cft} are the cross-sectional area and the ultimate tensile strength of the transverse CFRP, respectively. A_{cfl} and f_{cfl} are the cross-sectional area and the ultimate tensile strength of the longitudinal CFRP, respectively. It has been verified by previous experiments that lateral restraint of CFRPs to the steel tube is lost once the fracture strain of transversal CFRP is reached ($\varepsilon_{cft} = 5500\mu\varepsilon$). When the rupture strain of longitudinal CFRPs is reached ($\varepsilon_{cfl} = 10000\mu\varepsilon$), the longitudinal strengthening effect to the members is lost [21, 22].

4.3. Division of Mesh, Interactions, and Boundary Condition.

The refined mesh method is used to analyze the mesh convergence before meshing. Because the pressure between steel tube and concrete can only be transferred on the surfaces of two materials, the hard contact mode is adopted between them. It is assumed that the steel tube and the end plate are integral part in the finite element model, so the element nodes of the steel tube and the end plate on the contact surface have the same nodal degree of freedom. In the finite element simulation, there is no slip in the tangential direction, and it is hard contact between the end plate and the concrete in the normal direction. CFRP and steel tube contact adopts bonding. Figure 12 shows the boundary conditions for the finite element simulation of specimens.

Firstly, half of the whole component was selected, and then quarter of the specimen was cut. According to the symmetry of the geometry and boundary conditions of the

component, the quarter model of the actual component is taken for analysis, and the symmetrical constraint conditions are imposed on the symmetry plane of the calculation model. The boundary condition is that the surface load is applied on the end plate and the lateral hysteretic force is applied on the middle section. In order to ensure that the loading mode is consistent with that in the test process, the loading-displacement control mode is adopted.

4.4. Comparison of Finite Element Simulation and Test Results.

Figures 13 and 14 show the comparison between the simulation results and the test results of P - Δ curve and P - Δ skeleton curve of partially C-CF-CFRP-ST specimens, respectively. Figures 15(a) and 15(b) show the actual failure modes and the finite element simulation failure modes of the steel tube in the specimens, respectively. Figures 16(a) and 16(b) show the failure modes of concrete in specimens and those of finite element simulation, respectively. It can be seen that the simulation results are in good agreement with the experimental results. The test results of each group are basically consistent with the finite element simulation results, which shows that the simulation results of the established model are in good agreement with the actual test results. Table 5 shows comparative error analysis of test and finite element skeleton curves. The elastic stiffness and ultimate bearing capacity of the test and finite element models are calculated, respectively. The calculation results show that the error between test and finite element is less than 20%. The mean square deviation of elastic stiffness and ultimate bearing capacity between test and finite element is calculated. The mean square deviation of elastic stiffness between test and finite element is 0.89, and the mean square deviation of the ultimate bearing capacity between test and finite element is 0.84. This shows that the finite element model is in good agreement with the experimental results.

5. Analysis of the Entire Load Process

Figure 17 shows the specimens' typical P - Δ curve. Six characteristic points were selected in the curve. Point O corresponds to the completed state of axial compression (N_0). A corresponds to the steel tube's yielding state. B corresponds to the fractured state of longitudinal CFRP, and C corresponds to the fractured state of transverse CFRP. Point D corresponds to the state of load reach bearing capacity, and E corresponds to the state of deflection (Δ) reached at $7\Delta_y$, when deflection is approximately $L/25$.

5.1. Distribution of the Interaction between Steel Tube and Concrete.

Figure 18 shows the distribution of the interaction between C-CF-CFRP-ST specimens' concrete and steel tubes during loading from point O to point E. It can be seen that the interaction between the tube and concrete was reflected primarily in the compression zone.

At point O, the interaction between steel tube and concrete is small because Poisson's ratio of steel tube is larger than that of concrete, and the transverse deformation of concrete is smaller than that of steel tube. With the yield

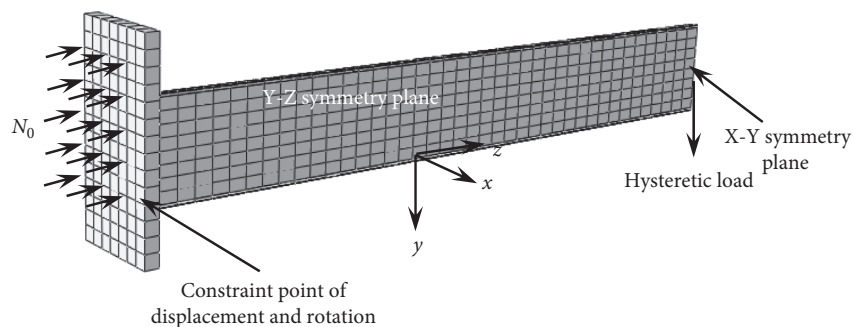


FIGURE 12: Boundary conditions for the specimens' finite element simulation.

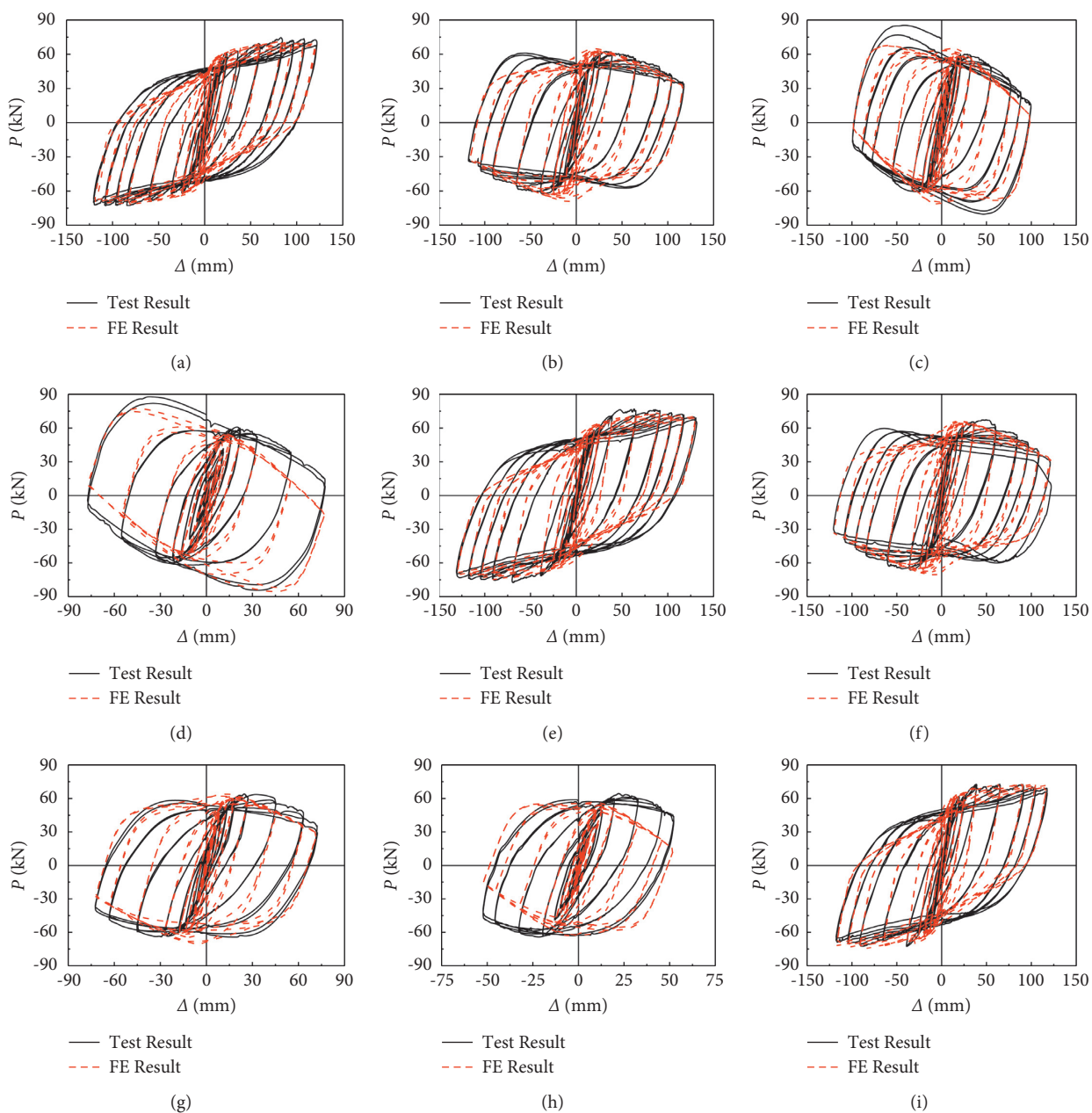


FIGURE 13: Continued.

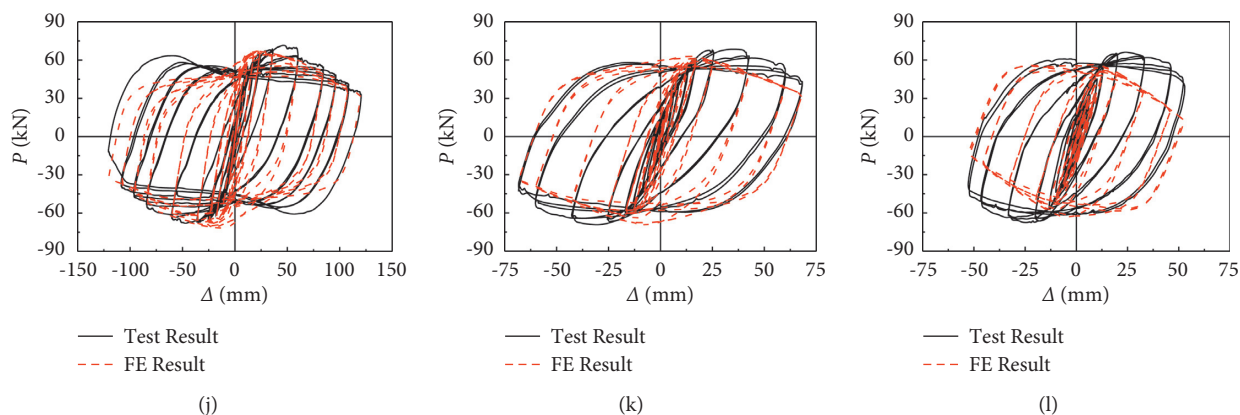


FIGURE 13: Comparison of simulation results and experimental results of P - Δ curves of specimens. (a) A0 specimen. (b) B0 specimen. (c) C0 specimen. (d) D0 specimen. (e) A1 specimen. (f) B1 specimen. (g) C1 specimen. (h) D1 specimen. (i) A2 specimen. (j) B2 specimen. (k) C2 specimen. (l) D2 specimen.

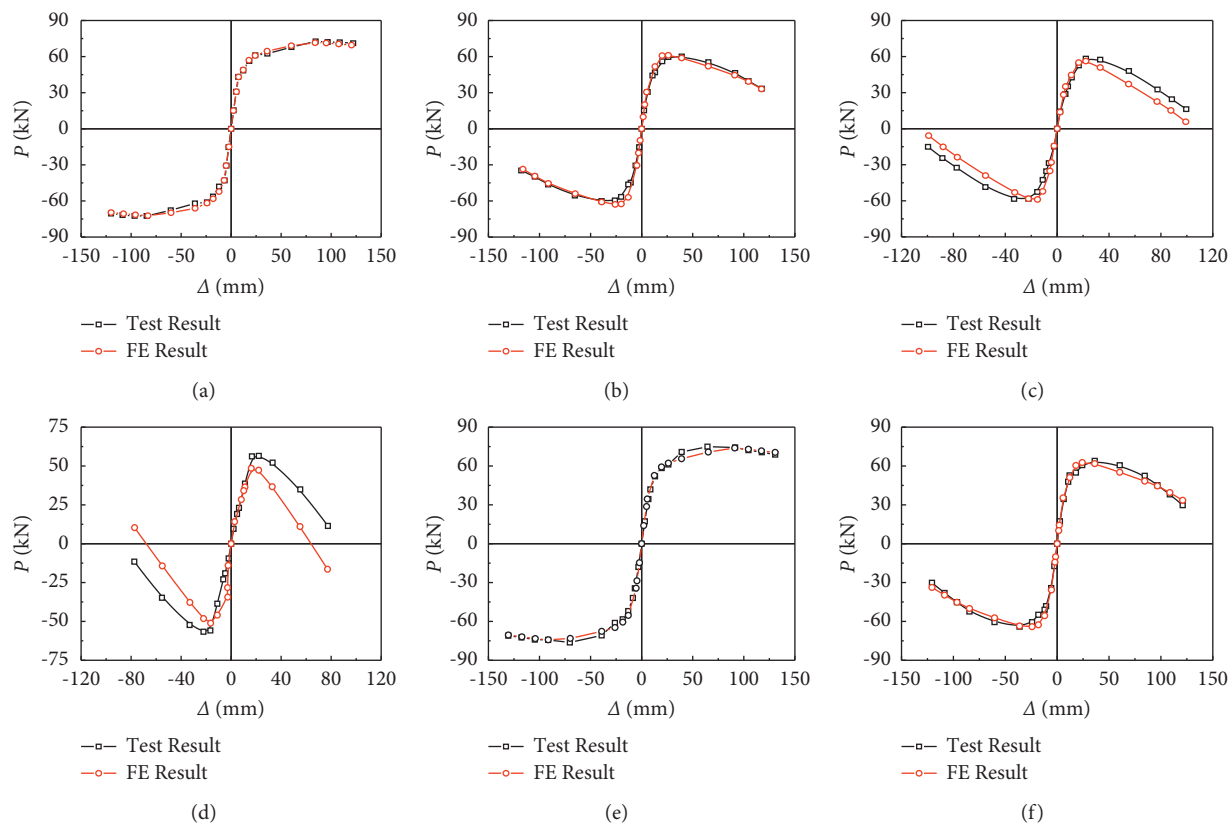


FIGURE 14: Continued.

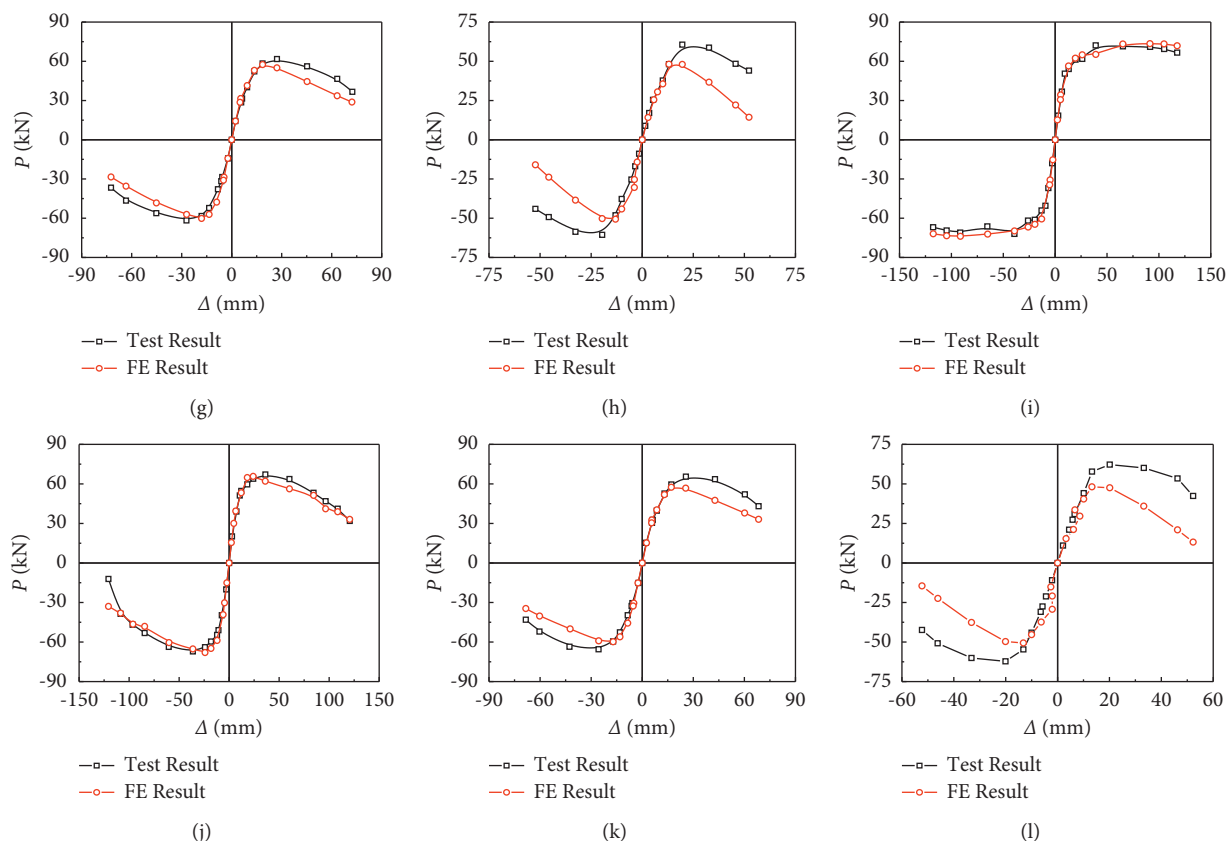


FIGURE 14: Comparison of simulation results and experimental results of P - Δ skeleton curves of specimens. (a) A0 specimen. (b) B0 specimen. (c) C0 specimen. (d) D0 specimen. (e) A1 specimen. (f) B1 specimen. (g) C1 specimen. (h) D1 specimen. (i) A2 specimen. (j) B2 specimen. (k) C2 specimen. (l) D2 specimen.

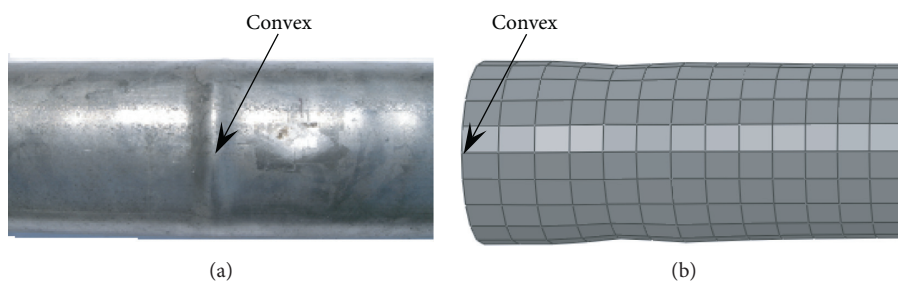


FIGURE 15: Failure modes of steel tube with middle section. (a) Test result. (b) FE result.

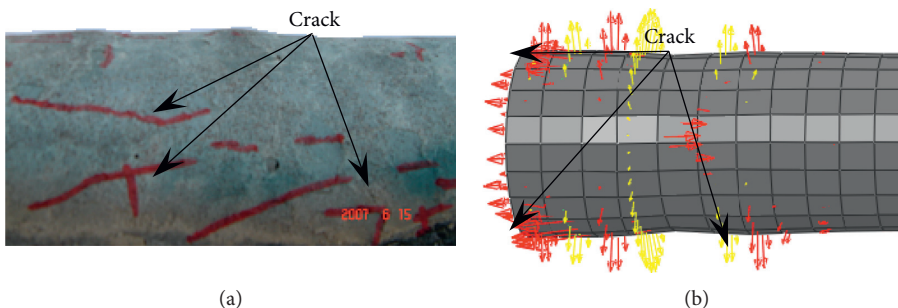


FIGURE 16: Failure modes of concrete with middle section. (a) Test result. (b) FE result.

TABLE 5: Comparative error analysis of test and finite element skeleton curves.

No.	Elastic stiffness of test (mm/kN)	Elastic stiffness of FE result (mm/kN)	The comparative error of elastic stiffness (%)	The ultimate bearing capacity of test (kN)	The ultimate bearing capacity of FE result (kN)	The comparative error of the ultimate bearing capacity (%)
A0	6.16	5.78	93.83	72.64	71.50	98.43
B0	5.18	4.85	93.62	60.08	61.09	98.34
C0	4.53	5.07	80.50	58.26	56.24	96.53
D0	3.67	3.48	94.82	56.47	48.52	85.92
A1	5.18	6.22	83.27	74.9	73.88	98.63
B1	5.41	6.12	88.39	63.92	62.60	97.93
C1	4.99	5.73	87.08	61.70	57.49	93.17
D1	4.79	4.45	92.90	60.61	48.72	80.39
A2	5.63	6.47	87.01	72.18	73.47	98.24
B2	5.31	5.94	89.39	67.13	65.7	97.86
C2	5.28	5.50	96.00	65.52	57.48	87.72
D2	4.73	3.95	83.50	62.21	50.14	79.38

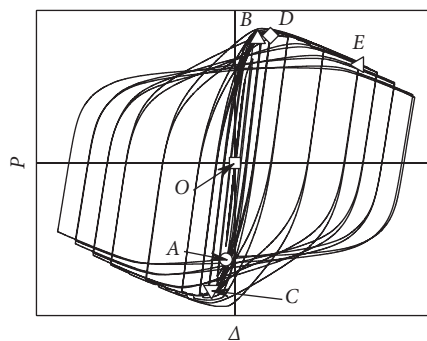


FIGURE 17: The typical $P-\Delta$ curve of specimens of S-CF-CFRP-ST.

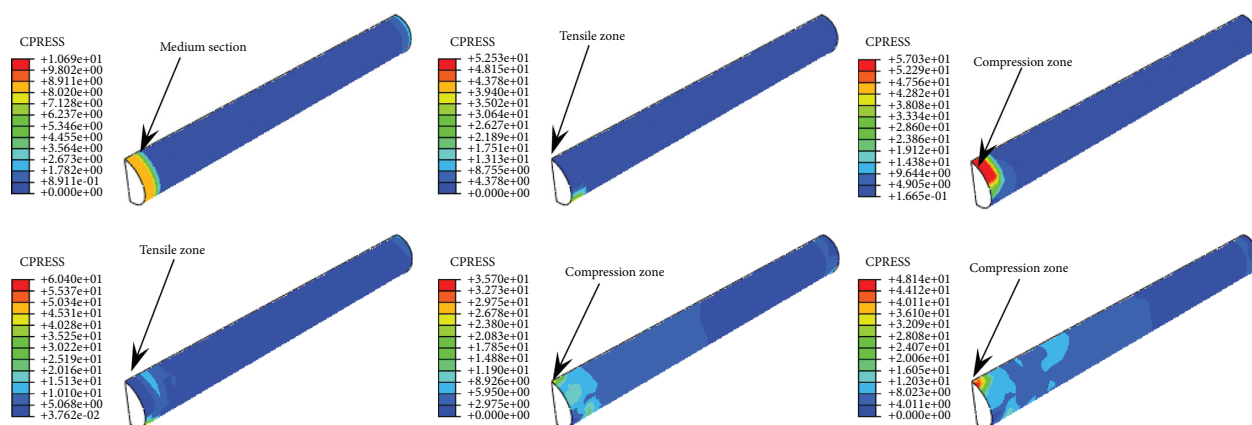


FIGURE 18: Distribution of interaction between steel tube and concrete in members.

range of steel tube reached (point A), the interaction increases sharply. After the CFRP fracture at points B and C, the interaction continues to increase. At point D, the load reaches the bearing capacity, and the interaction of member begins to decrease. At point E, the interaction of member has been increased again.

5.2. Longitudinal Stress Distribution of Concrete in Tube. Figure 19 shows the longitudinal stress distribution of concrete in the C-CF-CFRP-ST specimens during loading from point O to point E. It can be seen that, at point O, the concrete was under whole section compression, and the maximum compressive stress of the circular member is

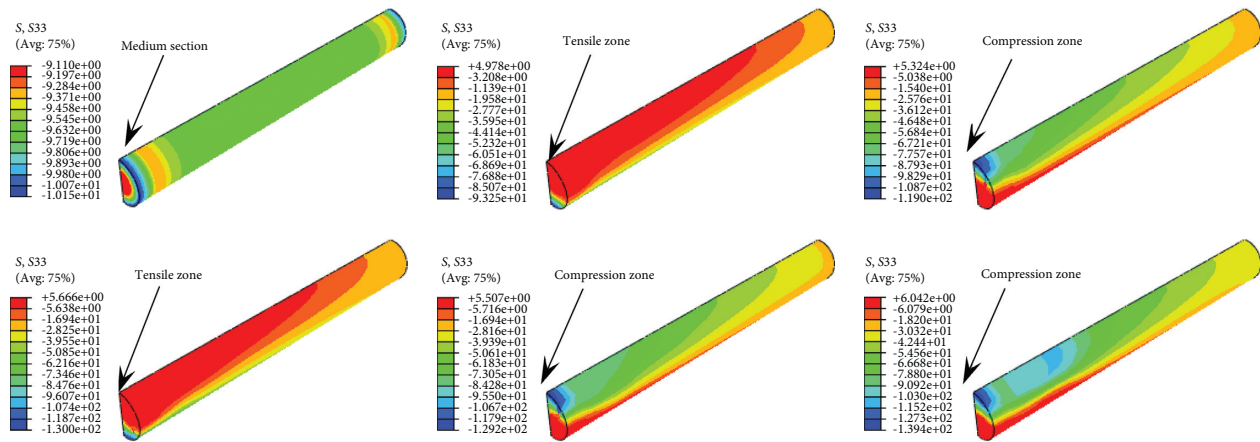


FIGURE 19: The longitudinal stress distribution of concrete in the specimens.

mainly concentrated in the outermost edge of the concrete. At point A, the stress of the concrete increases significantly due to the restraint effect of the steel tube, and the tensile zone begins to appear in the section. At points B and C, with the gradual increase of the deflection of the middle section, the maximum compressive stress of the concrete further increases. After that, the stress of the members almost does not increase. The longitudinal stress at point C is consistent with point D, and the specimen reaches the maximum compressive stress at point E.

5.3. Stress Distribution of Steel Tube. Figure 20 shows the longitudinal stress distribution of the steel tube in S-CF-CFRP-ST specimens during loading from point O to point E. It can be seen that the full section of the specimens was compressed at point O. The steel tube remained in the elastic stage with a light load at point O, and the stress distribution along the length of the specimens was relatively uniform. At point A, the steel tube in the tension zone of the middle section of the member enters the yield stage. When loading to points B and C, the stress of the steel tube gradually increases, and with the CFRP fracture, the yield region of the steel tube gradually develops to both ends of the member. At points C and D, the stress of the steel tube is basically unchanged. In addition, it can be seen that the distribution of longitudinal stress of steel tube is basically consistent with that of concrete.

5.4. Stress Distribution of Longitudinal CFRP. Longitudinal CFRP was taken as a variable in the test, so the longitudinal stress distribution was studied. Figure 21 shows the CFRP's longitudinal stress distribution in the C-CF-CFRP-ST specimens during loading from point O to point E. It can be seen that, at O point, the longitudinal CFRP is almost not stressed, because CFRP only produces tensile stress along the fiber direction. When the yield of steel tube is reached (A point), the stress in the section in the tensile zone is the largest, and the longitudinal CFRP is still in the elastic stage and does not fracture. With the gradual increase of the deflection of the section, the stress in the section of the

tensile zone gradually increases and reaches the fracture strength at point B. The results show that the longitudinal CFRP in tension zone delays the deformation. As the failure area of longitudinal CFRP increases, the stress decreases gradually. During the whole loading process, the longitudinal CFRP in the compression zone has no effect.

6. Restoring Force Model

The finite element simulation of C-CF-CFRP-ST specimens' $P-\Delta$ curve is complex to use in practice, so it is necessary to propose a simplified restoring force model. Through a large number of calculations on the C-CF-CFRP-ST specimens' $P-\Delta$ curves (the stage of each parameter: $n = 0 \sim 0.8$, $f_y = 235 \sim 420$ MPa, $f_{cu} = 30 \sim 90$ MPa, $\alpha = 0.03 \sim 0.2$, $\xi_{cf} = 0 \sim 0.6$, $\eta = 0 \sim 0.9$, and $\lambda = 10 \sim 80$), it was found that the specimens' restoring force model can be modified appropriately, and then a model suitable for C-CF-CFRP-ST beam-column was proposed [23, 24].

6.1. Trilinear Model. As shown in Figure 22, the restoring force model for S-CF-CFRP-ST specimens can be used to calculate from one circle at the end of the elastic stage to the end of loading. In Figure 18, point A is the end of the skeleton curve's linear elastic stage, and its lateral loading was taken as 0.6 times the skeleton curve's peak loading (P_y). The OA segment's stiffness was defined as K_a .

Point B is the skeleton line's peak point, and its lateral loading (P_y) corresponding to the displacement was Δ_p . The stiffness along the BC segment was defined as K_T . When unloading from point 1 or 4 in Figure 18, the unloading was performed according to the stiffness of the elastic stage (K_a) and was loaded to point 2 or 5. The loading value of point 2 was taken as $(0.2 + n)$ times the loading value of point 1 in the ordinate, and the loading value of point 4 in the ordinate was taken as $(0.2 + 1.2n)$ times the loading value of point 5 in the ordinate. As the reverse loading continued to increase, the model entered the softening segment of 23' or 5D'. Points 3' and D' were on the extension line of OA, and their ordinates were the same as points 1 (or 3) and 4 (or D), respectively. Finally, the loading path was carried out along

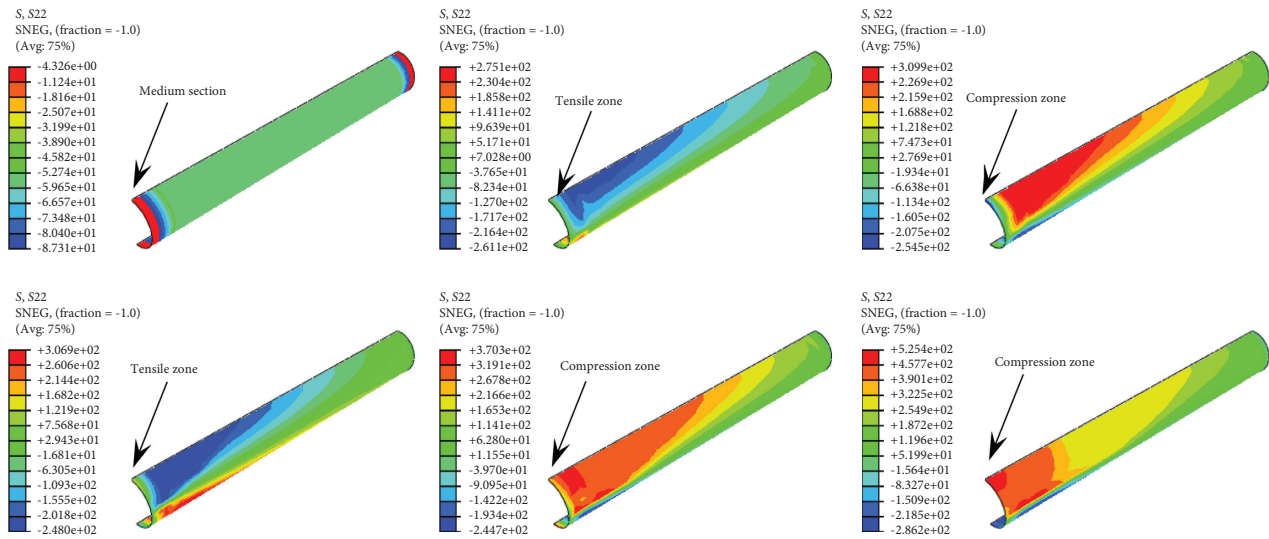


FIGURE 20: The longitudinal stress distribution of the steel tube in specimens.

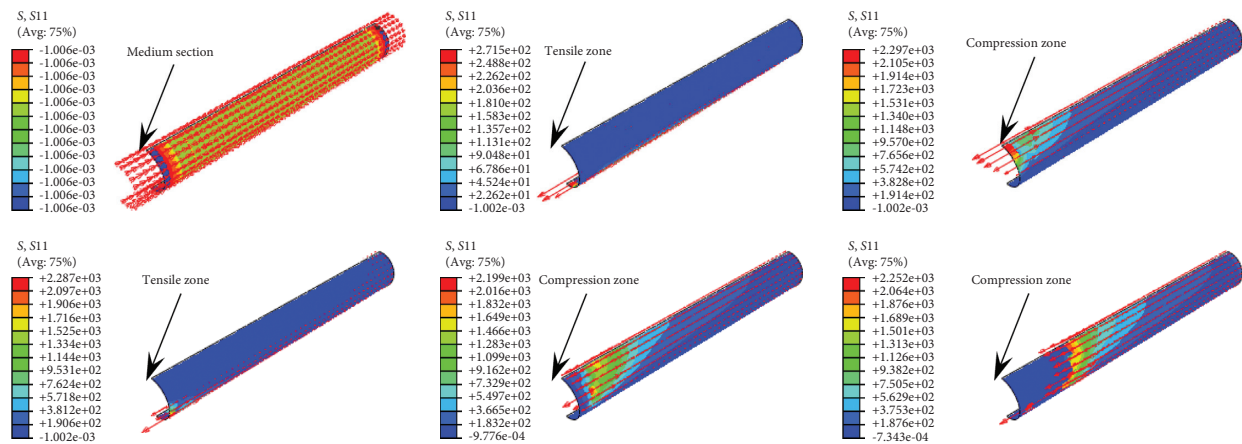


FIGURE 21: The CFRP's longitudinal stress distribution in the specimens.

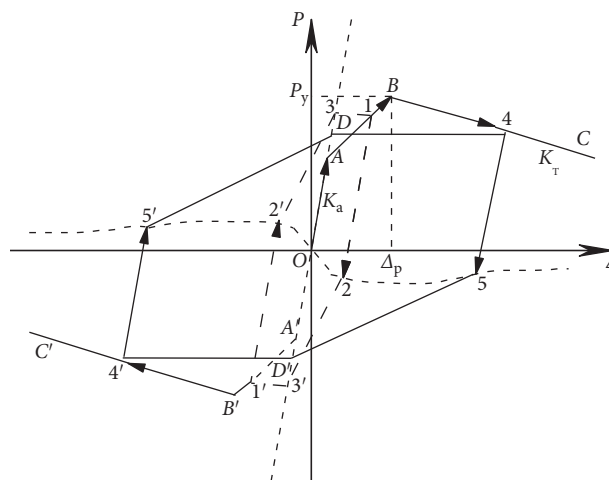


FIGURE 22: Restoring force model of S-CF-CFRP-ST specimens.

3'1'2'3 or D'4'5'D, and the method to determine the softening segment 2'3 and 5'D is similar to that of 23' and 5D', respectively.

It can be seen that if the displacement (Δ_p) and the lateral loading (P_y) at point B and the stiffness (K_a) in the elastic stage and the stiffness (K_T) of the third segment are determined, the restoring force model can be calculated according to the process above.

6.2. Determination of Trilinear Model

6.2.1. *Determination of K_a .* According to the results of the parametric analysis, the stiffness (K_a) of the S-CF-CFRP-ST specimens' restoring force model is shown as follows:

$$\Delta_p = \frac{6.74[(\ln r)^2 - 1.08 \ln r + 3.33](0.8 - n\xi_{cf})(0.8 - 0.7n\eta)f_1(n)}{8.7 - s} \frac{P_y}{K_a}, \quad (15)$$

$$f_1(n) = \begin{cases} 1.336n^2 - 0.044n + 0.804, & 0 \leq n \leq 0.5, \\ 1.126 - 0.02n, & 0.5 < n < 1. \end{cases} \quad (16)$$

where $r = \lambda/40$ and $s = f_y/345$.

The results show that the specific expression of component P_y is as follows:

$$P_y = \begin{cases} 1.05af_1(\xi_{cf}, \eta, n) \frac{M_y}{L_1}, & 1 < \xi \leq 4, \\ (0.2\xi + 0.85)af_1(\xi_{cf}, \eta, n) \frac{M_y}{L_1}, & 0.2 \leq \xi \leq 1, \end{cases} \quad (17)$$

$$a = \begin{cases} 0.96 - 0.002\xi, & 0 \leq n \leq 0.3, \\ (1.4 - 0.34\xi)n + 0.1\xi + 0.54, & 0.3 < n < 1. \end{cases} \quad (18)$$

The expression of $f_1(\xi_{cf}, \eta, n)$ is obtained by regression of a large number of calculation results.

$$f_1(\xi_{cf}, \eta, n) = \begin{cases} 1.4 - 5.7(0.35 - 20\xi_{cf}n)(n - 0.3) + 0.1(1 + \eta)^{2+n}, & \xi_{cf} \leq 0.1, \\ 1.34 - 2.37(1 - 3\xi_{cf})(n - 0.35) - 0.01\eta^{1+n}, & \xi_{cf} > 0.1. \end{cases} \quad (19)$$

The results show that the specific expression of component M_y of specimens is as follows:

$$M_y = \frac{A_1c + B_1}{(A_1 + B_1)(pn + q)} f_2(\xi_{cf}, \eta, n) M_{bc}, \quad (20)$$

$$A_1 = \begin{cases} -0.137, & b \leq 1, \\ 0.118b - 0.255, & b > 1, \end{cases} \quad (21)$$

$$B_1 = \begin{cases} -0.468b^2 + 0.8b + 0.874, & b \leq 1, \\ 1.306 - 0.1b, & b > 1, \end{cases} \quad (22)$$

$$K_a = \frac{3K_e}{L_1^3},$$

$$K_e = E_s I_s + 0.2E_c I_c + 5E_{cf} I_{cfl}, \quad (14)$$

$$L_1 = \frac{L}{2}.$$

which I_s , I_c , and I_{cfl} are the section inertia of the steel tube, concrete, and longitudinal CFRP, respectively.

6.2.2. *Determination of Δ_p and P_y .* The results show that the specific expression of component Δ_p is as follows:

$$p = \begin{cases} 0.566 - 0.789b, & b \leq 1, \\ -0.11b - 0.113, & b > 1, \end{cases} \quad (23)$$

$$q = \begin{cases} 1.195 - 0.34b, & b \leq 1, \\ 1.025, & b > 1, \end{cases} \quad (24)$$

$$b = \frac{\alpha}{0.1}. \quad (25)$$

The expression of $f_2(\xi_{cf}, \eta, n)$ is obtained by using formulas (1) and (20):

$$f_2(\xi_{cf}, \eta, n) = 1 - 1.5\xi_{cf}n - \eta^{0.1(1+n)}. \quad (26)$$

6.2.3. *Determination of K_T .* The stiffness (K_T) of the specimens' third segment is as follows:

$$K_T = \frac{[0.03f_2(n)f(r, \alpha)K_a]}{(c^2 - 3.39c + 5.41)},$$

$$f_2(n) = \begin{cases} 3.043n - 0.21, & 0 \leq n \leq 0.7, \\ 0.5n + 1.57, & 0.7 < n < 1, \end{cases}$$

$$f(r, \alpha) = \begin{cases} [8\alpha(1 + 5\xi_{cf})(1 + \eta) - 8.6]r + 6\alpha + 0.9, & r \leq 1, \\ [15\alpha(1 - 0.02\xi_{cf})(1 - 2\eta) - 13.8]r + 6.1 - \alpha, & r > 1, \end{cases} \quad (27)$$

where $c = f_{cu}/60$.

6.3. *Comparison of Restoring Force Model Results and Finite Element Simulation Results.* Figure 23 shows the comparison between the restoring force model's results and the finite element simulation results in the C-CF-CFRP-ST specimens' P-Δ curve. It can be seen that the restoring force model

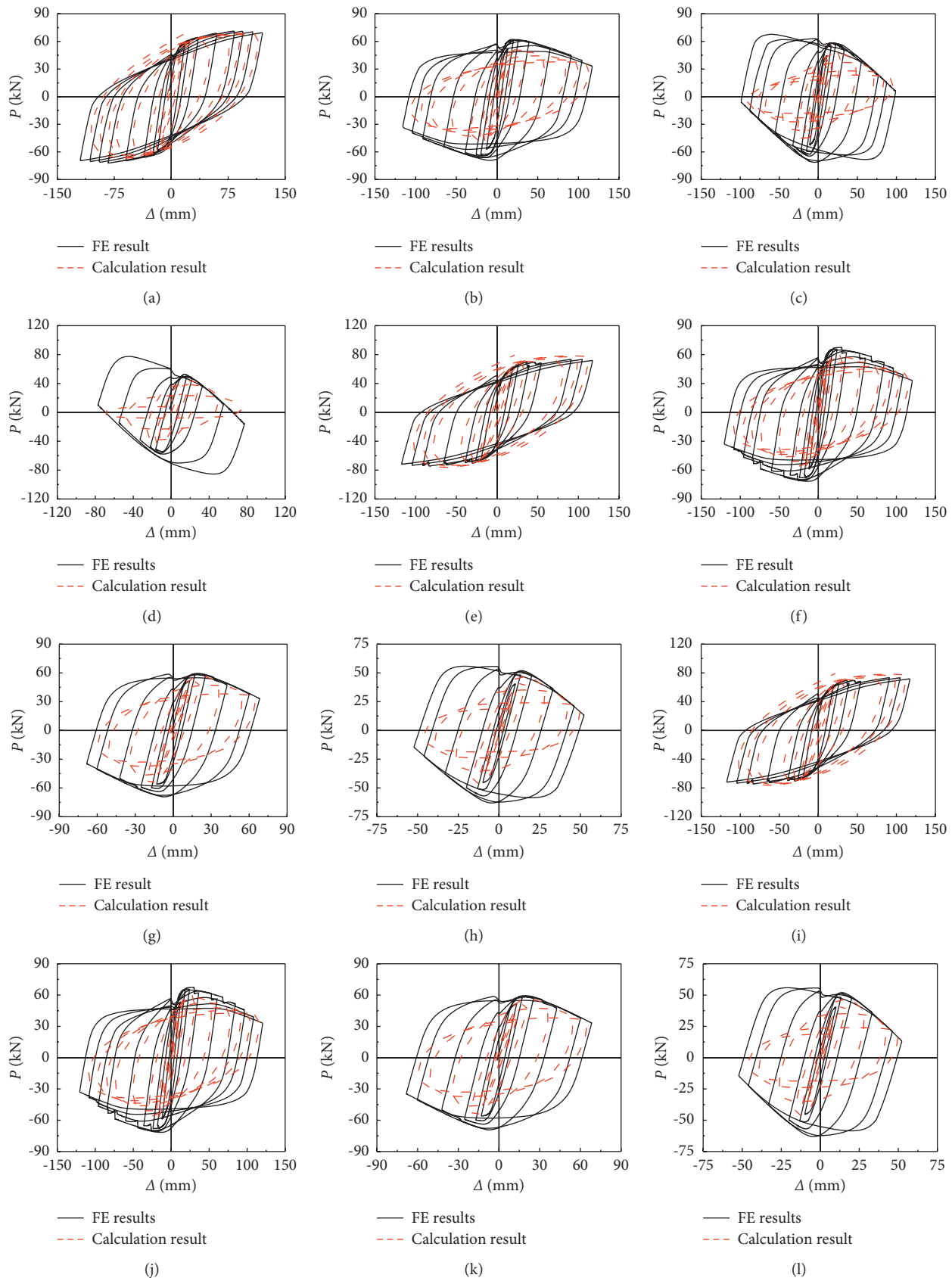


FIGURE 23: The comparison between the restoring force model's results and the finite element simulation results. (a) A0 specimen. (b) B0 specimen. (c) C0 specimen. (d) D0 specimen. (e) A1 specimen. (f) B1 specimen. (g) C1 specimen. (h) D1 specimen. (i) A2 specimen. (j) B2 specimen. (k) C2 specimen. (l) D2 specimen.

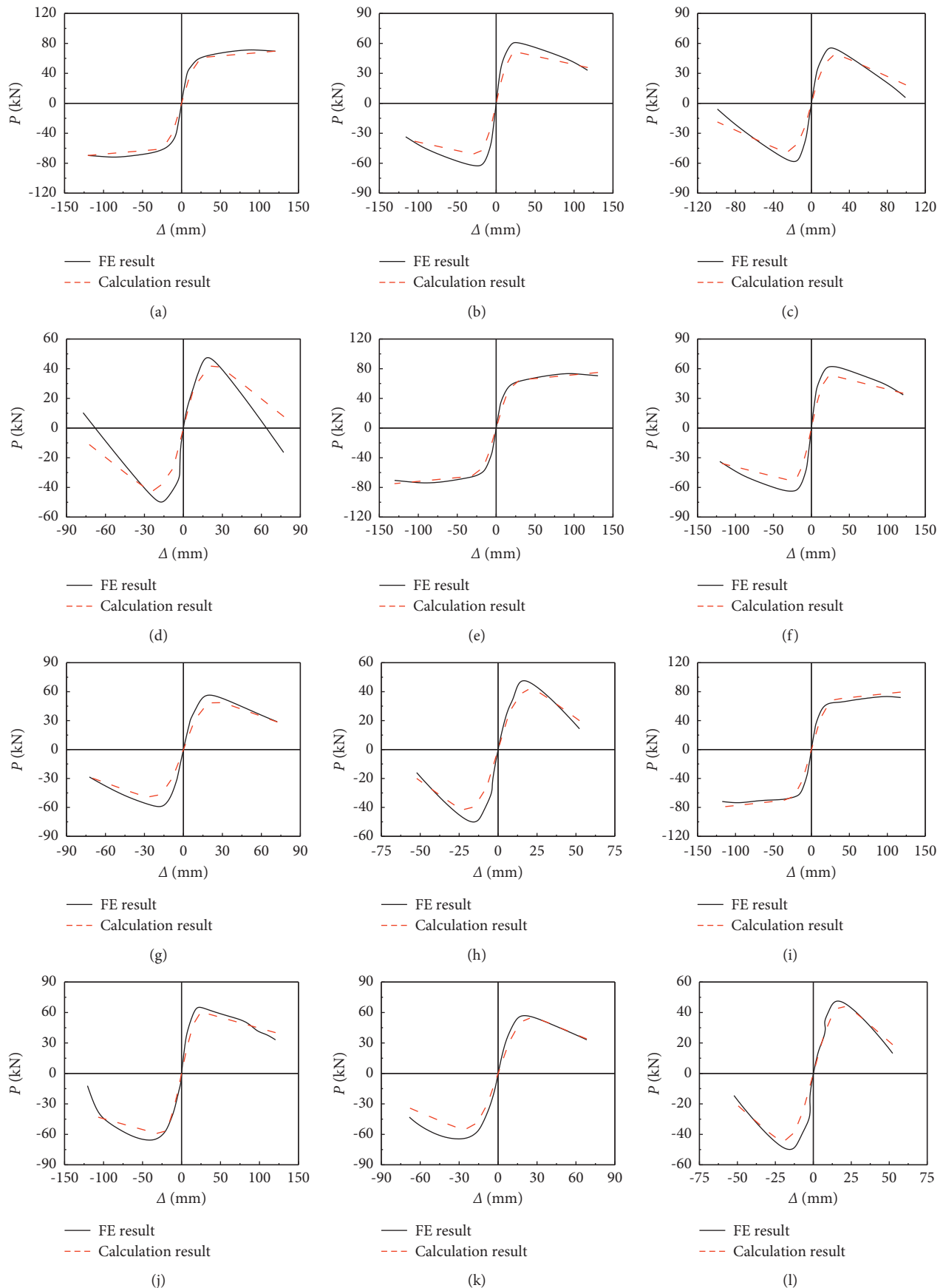


FIGURE 24: The comparison between the restoring force model's results and the finite element simulation results of skeleton curve. (a) A0 specimen. (b) B0 specimen. (c) C0 specimen. (d) D0 specimen. (e) A1 specimen. (f) B1 specimen. (g) C1 specimen. (h) D1 specimen. (i) A2 specimen. (j) B2 specimen. (k) C2 specimen. (l) D2 specimen.

TABLE 6: Comparative error analysis of calculation and finite element skeleton curves.

No.	Elastic stiffness of calculation result (mm/kN)	Elastic stiffness of FE result (mm/kN)	The comparative error of elastic stiffness (%)	The ultimate bearing capacity of calculation result (kN)	The ultimate bearing capacity of FE result (kN)	The comparative error of the ultimate bearing capacity (%)
A0	5.32	5.78	92.64	69.63	71.50	97.38
B0	3.97	4.85	78.16	51.4	61.09	84.13
C0	4.66	5.77	80.76	49.64	56.24	88.26
D0	3.47	3.48	99.28	44.48	48.52	91.67
A1	5.73	6.22	92.12	73.55	73.88	99.55
B1	4.67	6.12	76.20	53.74	62.60	85.84
C1	4.51	5.73	76.42	50.39	57.49	87.65
D1	3.77	4.45	82.03	44.56	48.72	91.45
A2	5.18	6.47	80.06	78.00	73.47	94.16
B2	4.39	5.94	73.90	60.7	965.7	92.38
C2	4.75	5.50	86.36	57.26	57.48	99.61
D2	3.64	3.95	92.51	46.73	48.14	97.07

results agreed well with those of the finite element simulation.

Figure 24 shows the comparison between the restoring force model's results and the finite element simulation results of skeleton curve. It can be seen that the restoring force model results agreed well with those of the finite element simulation. Table 6 shows comparative error analysis of calculation and finite element skeleton curves. The calculation results show that the error between test and finite element is less than 25%. The calculation results show that the error between test and finite element is less than 20%. The mean square deviation of elastic stiffness and ultimate bearing capacity between restoring force model and finite element is calculated. The mean square deviation of elastic stiffness between restoring force model and finite element is 0.81, and the mean square deviation of the ultimate bearing capacity between restoring force model and finite element is 0.93. This shows that the finite element model is in good agreement with the restoring force model results.

7. Conclusion

- (1) CFRP have a good transverse restraint and longitudinal reinforcement effect on CFST, and the steel tube's local buckling is delayed. The specimens' bearing capacity improved with the increase in the axial compression ratio and longitudinal CFRP reinforcement coefficient.
- (2) The typical $P-\Delta$ hysteretic curves of members are established by ABAQUS, and the simulation results are in good agreement with the experimental results. Combined with this model, the stress distribution of each component material is analyzed, which reflects that the longitudinal stress distribution of concrete and steel tube is consistent, and the stress increases gradually from both ends to the middle section. The maximum stress of each group of specimens appears at the outermost edge of the middle section of the specimens.
- (3) Based upon the trilinear model, the restoring force model of S-CF-CFRP-ST was built, and the results of

the model agreed well with those of the finite element simulation.

References

- [1] Y. Liu and Z. Dong, "Experimental study on torsional behavior of circular CFRP concrete filled steel tube," *Journal of Civil Engineering*, vol. 42, no. 11, pp. 91-101, 2009, in Chinese.
- [2] M. L. Romero and A. Espinos, F. Lapuebla, V. Albero, and A. Hospitaler, Recent developments and fire design provisions for CFST columns and slim-floor beams," *Journal of Constructional Steel Research*, vol. 172, no. 1-21, 2020.
- [3] L. H. Han and S. T. Zhong, "Bearing capacity correlation equations of concrete filled steel tubular members under compression torsion and bending torsion," *Journal of Harbin Institute of architectural engineering*, vol. 27, no. 2, pp. 32-37, 2004, in Chinese.
- [4] J. G. Nie, Y. H. Wang, and J. S. Fan, "Study on seismic behavior of concrete filled steel tube under pure torsion and compression torsion load," *Ocean Engineering*, vol. 47, no. 1, pp. 47-58, 2014.
- [5] X. H. Zhou, Y. H. Wang, and G. B. Lu, "Research on mechanical behavior of hollow sandwich concrete filled steel tubular columns under reciprocating pure torsion," *Journal of building structure*, vol. 38, no. S1, pp. 266-271, 2017.
- [6] J. G. Nie, Y. H. Wang, and J. S. Fan, "Study on seismic behavior of concrete filled steel tubular columns under pure

- torsion and compression torsion load," *Steel and Composite Structures*, vol. 47, no. 1, pp. 47–58, 2014.
- [7] J. Nie, C. S. Cai, and T. Wang, "Stiffness and capacity of steel-concrete composite beams with profiled sheeting," *Engineering Structures*, vol. 27, no. 7, pp. 1074–1085, 2005.
- [8] Y. K. Hong and S. M. Choi, "Behaviors of concrete filled square steel tubes confined by carbon fiber sheets (CFS) under compression and cyclic loads," *Steel and Composite Structures*, vol. 10, no. 2, pp. 187–205, 2010.
- [9] M. C. Sundarraja and G. G. Prabhu, "Investigation on strengthening of CFST members under compression using CFRP composites," *Journal of Reinforced Plastics and Composites*, vol. 30, no. 15, pp. 1251–1264, 2011.
- [10] Z. Tao, L.-H. Han, and J.-P. Zhuang, "Axial loading behavior of CFRP strengthened concrete-filled steel tubular stub columns," *Advances in Structural Engineering*, vol. 10, no. 1, pp. 37–46, 2007.
- [11] Z. Tao, L.-H. Han, and L.-L. Wang, "Compressive and flexural behaviour of CFRP-repaired concrete-filled steel tubes after exposure to fire," *Journal of Constructional Steel Research*, vol. 63, no. 8, pp. 1116–1126, 2007.
- [12] F. L. Peng, Z. Tao, and Z. W. Cheng, "Behavior of concrete-filled steel tube columns subjected to axial compression," *Advances in Materials Science and Engineering*, vol. 2018, Article ID 4059675, 153 pages, 2018.
- [13] Q.-L. Wang, J. Li, Y.-B. Shao, and W.-J. Zhao, "Flexural performances of square concrete filled CFRP-steel tubes (S-CF-CFRP-ST)," *Advances in Structural Engineering*, vol. 18, no. 8, pp. 1319–1344, 2015.
- [14] Y. Che, Q. L. Wang, and Y. B. Shao, "Compressive performances of the concrete filled circular CFRP-steel tube (C-CFRP-CFST)," *Advanced Steel Construction*, vol. 8, no. 4, pp. 311–338, 2012.
- [15] L.-H. Han, W. Li, and R. Bjorhovde, "Developments and advanced applications of concrete-filled steel tubular (CFST) structures: members," *Journal of Constructional Steel Research*, vol. 100, no. 3, pp. 211–228, 2014.
- [16] L. H. Han, Z. Tao, and W. Liu, "Concrete filled steel tubular structure-theory and practice," *Journal of Fuzhou University*, vol. 2001, no. 6, 34 pages, 2001, in Chinese.
- [17] Q. Y. Qiao, X. Y. Li, and W. L. Cao, "Study on seismic behavior of complex cross-section multi-cell CFST bifurcated-columns," *Earthquake Engineering & Engineering Dynamics*, vol. 1, no. 2, pp. 1–8, 2016.
- [18] Z. Tao, Z.-B. Wang, L.-H. Han, and B. Uy, "Fire performance of concrete-filled steel tubular columns strengthened by CFRP," *Steel and Composite Structures*, vol. 11, no. 4, pp. 307–324, 2011.
- [19] Q.-L. Wang, Z. Zhao, Y.-B. Shao, and Q.-L. Li, "Static behavior of axially compressed square concrete filled CFRP-steel tubular (S-CF-CFRP-ST) columns with moderate slenderness," *Thin-Walled Structures*, vol. 110, no. 1, pp. 106–122, 2017.
- [20] Z.-B. Wang, Z. Tao, and Q. Yu, "Axial compressive behaviour of concrete-filled double-tube stub columns with stiffeners," *Thin-Walled Structures*, vol. 120, no. 11, pp. 91–104, 2017.
- [21] J. Moon, C. W. Roeder, D. E. Lehman, and H.-E. Lee, "Analytical modeling of bending of circular concrete-filled steel tubes," *Engineering Structures*, vol. 42, pp. 349–361, 2012.
- [22] Z. Ou, B. Chen, K. H. Hsieh, M. W. Halling, and P. J. Barr, "Experimental and analytical investigation of concrete filled steel tubular columns," *Journal of Structural Engineering*, vol. 137, no. 6, pp. 635–645, 2011.
- [23] H. H. Yuan and Yu Tang, "Quasi-static research on seismic performance of steel bridge piers with thin-wall ribbed circular cross section," *Steel and Composite Structures*, vol. 44, no. 4, pp. 459–464, 2016.
- [24] W. Q. Zhu, "Fire Performance of steel reinforced concrete columns," *Journal of Structural Engineering*, vol. 141, no. 4, pp. 191–204, 2015.

Random Shape Rockfalls in Steeply Dipping Coal Seams

Sampad Kumar Pradhan, *Department of Civil Engineering, Aryan Institute of Engineering & Technology, Bhubaneswar, s_kumar6@gmail.com*

Sudeepta Kishor Dash, *Department of Civil Engineering, NM Institute of Engineering & Technology, Bhubaneswar, sudeeptakishordash1@gmail.com*

Sidhanta Behera, *Department of Civil Engineering, Raajdhani Engineering College, Bhubaneswar, sidhantabehera29@outlook.com*

Bijayalaxmi Behera, *Department of Civil Engineering, Capital Engineering College, Bhubaneswar, bijayalaxmi759@gmail.com*

ABSTRACT

It is difficult to precisely mimic rockfall movement in steeply dipping coal seams (SDCS) due to the randomness of rockfall shape and irregularity of the bottom floor of the working face. As a result, it is impossible to successfully defend against multirockfalls. As a result, a method for creating random shape rockfalls based on the ellipsoid equation is proposed, and a 3D grid model of the real bottom floor of the working face is built using GIS data. The trajectory simulated by Rockyfor3D programme is compared to the proposed method and 3D model in order to validate the accuracy and feasibility of the method and 3D model, and the proposed approach and 3D model prove to be effective in simulating rockfall movement more correctly. The proposed approach and 3D grid model are then used in numerical simulation to tackle the problem of multirockfalls protection, and the key elements impacting the structural stress response of protective nets are investigated.

1. Introduction

In recent years, with the development of SDCS mining and combining mining technology, the number of steep coal mines in China has increased year by year, and therefore the coal production, as well as the economic benefits, has increased [1–7]. At the same time, the rockfall hazard, a disaster that occurred in SDCS mining, has become increasingly prominent [8–19]. Rockfalls in the long walls of a SDCS also have a colloquial name, “flying gangue” hazards [20]. Because of the large difference in height between the lower end and the upper end of the mining working face, the kinetic energy of a coal/rock block falling off from the parent body would be significantly increased after acceleration; the collision of the coal/rock blocks with people or equipment would occur instantly, and thus it features complicated motion

and may lead to serious accidents. During mining, coal/rock blocks may be separated from coal walls or rest on the top beam of a support or stay still after the bottom plate is slipped and destroyed. The coal/rock blocks, once subjected to external disturbance such as coal swing or support moving, will start to move from static state. Since the natural-rest-angle of a coal/rock block is smaller than the coal seam inclination angle, it is difficult to stop after the first collision with the bottom plate and will slide downwards along the working face and may collide with people or equipment. The coal seam structural information and the main movement modes of rockfall are shown in Figure 1 [12]. As can be seen from Figure 1, the coal seam is on the left and goaf is on the right. In addition, Figure 1(a) shows the primary collision slip mode of rockfall, and Figure 1(b) shows the multiple intermittent collision and slip mode of rockfall.

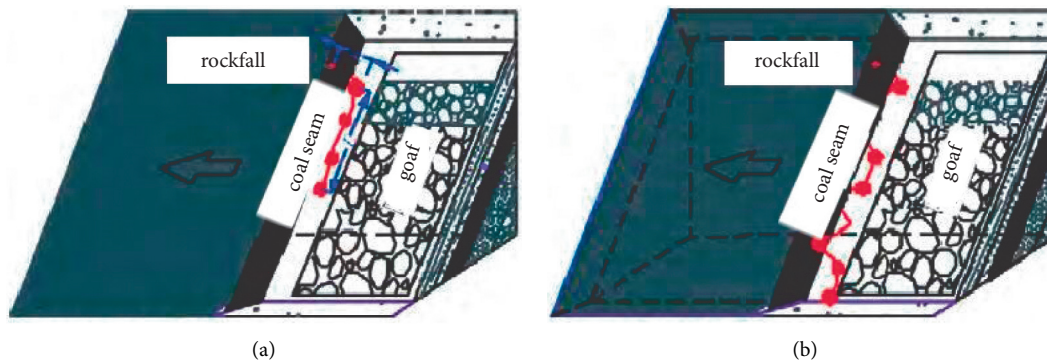


FIGURE 1: Movement mode of rockfall: (a) one-time collision slip of rockfall; (b) multiple intermittent collision and slip of rockfall.

Therefore, studies on the mechanism of rockfalls motion would fundamentally improve the protection against rockfalls that occurred in steep seam mining. While the research on steep seam mining mainly focuses on mining equipment, especially hydraulic supports and shearers [21–30], and technical management of longwall working faces, only few studies have been carried on the motion mechanism of rockfalls in steep seam mining [9, 10]. In 2015, Tu et al. comprehensively review the fully mechanized coal mining technology in steep coal seam in China. Reference [8] and different rockfalls prevention devices applied in practice are compared. In 2017, a rockfall control principle is proposed by Wu et al. [11]: depending on the occurrence locations of rockfalls, rockfalls can be dealt with through technical management. In 2018, based on the Kalman filter principle, the parameters of rockfall control are studied and the protective netting is proposed and applied in practice by Wu et al. [12, 13]. In 2019 and 2020, based on nonprobability interval analysis, the motion model of rockfalls is established under uncertain environment. With theoretical analysis and numerical simulation, the kinematic characteristics of rockfalls in steep seam mining on longwall mining working face are investigated, and the kinematic mechanism of rockfalls is demonstrated by Jing et al. [14]. Based on the grating to identify the dangerous source, automatic devices for preventing rockfalls are designed by Liu et al. [15–17]. The index scale method and analytic hierarchy method are used to calculate the weight, the expert scoring method is used to determine the membership function, and the safety evaluation of rockfall hazards is carried out by the fuzzy comprehensive evaluation method by Liu et al. [18]. And the dynamic Bayesian network model is used to evaluate the dynamic threat level for rockfalls along the working face by Liu et al. [19]. In 2021, a method for risk assessment and for determining the principles of protective systems is provided in underground steep coal seams by Wu et al. [20]. Hu and Luo do a case study about rockfall hazards and failure characteristics in steeply dipping coal seam [21, 22].

Although the above devices and technological managements have improved rockfalls prevention to a certain extent, they still cannot fundamentally enhance the protection against the rockfalls, without considering the

kinematic characteristics of rockfalls. Therefore, it is of great significance to explore the mechanism of rockfalls movement for establishing the safety protection system of longwall working face in SDCS mining area.

Most of the rockfall and working face floor models used in the above research are idealized models and in lack of research on three-dimensional movement of irregular random rockfall. The innovation of this research is: the previous two-dimensional space rockfall trajectory simulation is upgraded to three-dimensional stepping space rockfall trajectory simulation; the former regular shape rockfall modeling is converted into irregular random shape in model establishment; the idealized simple working face modeling is changed to the working face modeling based on geographic information system. The innovation of the current work contributes to the prediction of rockfall movement and therefore the protection against rockfall disasters. The research is given as follows: the modeling method of irregular rockfall and the modeling method based on geographic information system are put forward; according to the proposed principles, a group of simulation tests of rockfall movement are carried out to find out the most dangerous rockfall model; the protection simulation test is carried out for the most dangerous rockfall model.

2. Basic Principles

2.1. Energy Tracking Method. Energy tracking method (ETM) is based on the principle of energy iteration. The collision between irregular rockfalls and working face floor and the collision between rockfalls are mainly multipoint collisions, as shown in Figure 2 [31, 32].

There are a lot of blocks $b = \{b_0, b_1, b_2, \dots, b_m\}$ in the figure with multipoint collision. $c = \{c_0, c_1, c_2, \dots, c_n\}$ is the collision point, n is the number of all collision points, and m is the number of all collision bodies.

ETM uses the “Stronge assumption” [33], to express the energy dissipation in the normal direction. Let W_r be the work done by the normal component of the impact impulse in a collision. The relational expression can be as follows:

$$W_r = -e_n^2 W_{mc}, \quad (1)$$

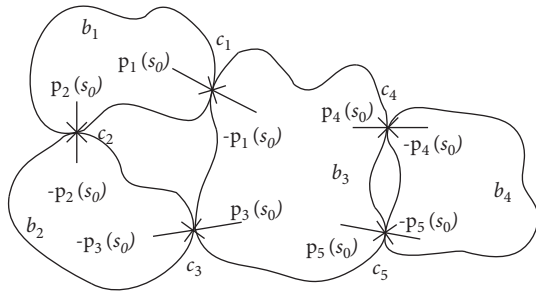


FIGURE 2: Multipoint collision model.

where e_n is normal impact recovery coefficient, and W_{mc} is work done by normal impulse at the maximum compression point where the relative normal velocity changes.

According to the normal component and tangential component of collision, the local orthogonal coordinates system is defined as $\{t_i, n_i, q_i\}$ at the contact, as shown in Figure 3.

The relational expression can be as follows:

$$t_i = \frac{\mathbf{n}_i \times \mathbf{p}_i(s_k)}{|\mathbf{u}_i(s_k)|}, \quad (2)$$

$$\mathbf{q}_i = t_i \times \mathbf{n}_i,$$

where \mathbf{n}_i is normal vector of contact point, and t_i and \mathbf{q}_i are tangent vectors of contact points, respectively.

Mirtich proposes that the work $\Delta W_i(s_k)$ of the contact force is a function of the relative velocity before and after the impulse is applied [31], which can be expressed as

$$\Delta W_i(s_k) = \frac{1}{2}(\mathbf{u}_i(s_{k+1}) + \mathbf{u}_i(s_k))^T \mathbf{K}_i^{-1} (\mathbf{u}_i(s_{k+1}) - \mathbf{u}_i(s_k)). \quad (3)$$

In ETM, the change of relative velocity along the normal direction is first calculated, and the change of relative normal velocity is

$$\tilde{\mathbf{u}}_i(s_{k+1}) = [0 \quad \tilde{\mathbf{u}}_{i,n}(s_k) + \Delta \tilde{\mathbf{u}}_{i,n}(s_k) \quad 0]^T. \quad (4)$$

The normal and tangential components decomposed by impulse $\mathbf{p}_i(s_k)$ can be expressed as

$$\begin{aligned} \mathbf{p}_{i,n}(s_k) &= n_i^T \mathbf{p}_i(s_k) \mathbf{n}_i, \\ \mathbf{p}_{i,q}(s_k) &= \mathbf{p}_i(s_k) - \mathbf{p}_{i,n}(s_k). \end{aligned} \quad (5)$$

Define the condition of static friction as

$$|\mathbf{p}_{i,q}(s_k)| \leq f |\mathbf{p}_{i,n}(s_k)|, \quad (6)$$

where f is friction factor.

To ensure that the relative change of normal velocity is $\Delta \tilde{\mathbf{u}}_{i,n}(s_k)$, the impulse must be calculated as follows:

$$\mathbf{p}_i(s_k) = \tilde{\mathbf{p}}_{i,n}(s_k) \mathbf{n}_i + f \tilde{\mathbf{p}}_{i,n}(s_k) \mathbf{q}_i, \quad (7)$$

where $\tilde{\mathbf{p}}_{i,n}(s_k) = \Delta \tilde{\mathbf{u}}_{i,n}(s_k) / n_i^T \mathbf{K}_i (\mathbf{n}_i + f \mathbf{q}_i)$.

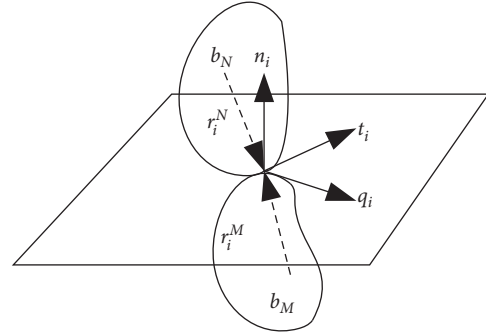


FIGURE 3: A local coordinate system defined at the contact point.

2.2. Modeling of Irregular Random Shape Rockfalls. Corresponding to the problem, randomness of rockfall shape, based on the model shown in Figure 3, an innovative model is established which can realize the randomness of rockfall shape.

The ellipsoid equation is used to transform into an irregular random rockfall model. Establishing a space coordinate system, the coordinates of any point in the space are represented by r , θ , and ϕ . Among them, r is the distance from the point to the center of the sphere, θ is the latitude of the point, and ϕ is the longitude of the point.

First determine the θ and ϕ of each vertex of the rockfall. Take two random variables x_i and x_j as intermediate variables, which can be determined by the following formula:

$$\begin{cases} x_i = \gamma(\delta_i - 0.5) + i, \\ x_j = \gamma(\delta_j - 0.5) + j, \end{cases} \quad (8)$$

where $x_i \in (i + \gamma(\delta_i - 0.5), i - \gamma(\delta_i - 0.5))$, $x_j \in (j + \gamma(\delta_j - 0.5), j - \gamma(\delta_j - 0.5))$, δ_i and δ_j are random variables on $(0, 1)$, $\gamma \in (0, 1)$, that is, to control variation amplitude of x_i and x_j , $i \in [1, n]$, $j \in [1, m]$, the number of vertices of the polyhedron is $m \cdot n + 2$, and among them $n \geq 1$, $m \geq 3$.

Then θ and ϕ can be expressed as

$$\begin{cases} \theta = \frac{\pi n}{x_i + 1}, \\ \phi = \frac{2\pi m}{x_j}. \end{cases} \quad (9)$$

Adding the two points $\theta = 0$ and $\theta = \pi$, any vertex on the polyhedron can be expressed as

$$\begin{cases} x = r(1 - \eta\delta_r)\cos\theta, \\ y = r(1 - \eta\delta_r)\sin\theta\cos\phi a, \\ z = r(1 - \eta\delta_r)\sin\theta\sin\phi b, \end{cases} \quad (10)$$

where $a \in (0, 1)$, $b \in (0, a)$, δ_r is a random variable on $(0, 1)$, $\eta \in (0, 1)$ is the value that controls the magnitude of change in r .

For a polyhedral rockfall, only the parameters n , m , a , b , γ , and η need to be given. Both δ_i , δ_j and δ_r are random numbers on $(0, 1)$, which control the randomness of the rockfall shape. Use the two parameters a and b to control the

overall shape of the rockfall and then control the sharpness of the rockfall. When a and b are close and small, the shape of the rockfall is relatively slender. When a is small and b is close to 1, the shape of the rockfall is relatively flat. When a and b are close, and both are close to 1, the rockfall shape is close to spherical. With this method, using the model established in this section, the rockfall with arbitrary sphericity and roundness of polyhedral random shapes can be simulated. The maximum diameter of the rockfall model is the longest diagonal length r of the polyhedron, and its value is usually a fixed value.

2.3. Modeling Base on Geographic Information System.

This article takes a test mine with SDCS in Gansu Province as an example. Contour lines and drilling information of the working face floor of the mine can be shown in Figure 4. Figure 4 is a horizontal projection drawing of contour lines of a super thick coal seam floor in Gansu province. The curve lines in the drawing are contour lines, and the points are drilling positions. The original drawing is CAD engineering information map, which has coded geographic information of coal seam working face and can be used to establish a three-dimensional model of the working face after extraction.

Extract contour and borehole information from Figure 4. Using CASS software, the drilling information is regarded as an elevation point, and a mesh model of the working face bottom plate is established, as shown in Figure 5.

The model is a 3D mesh model of $4500\text{ m} \times 2500\text{ m} \times 500\text{ m}$. It covers the geographic information of the entire coal seam floor, the inclination of the coal seam is about $25^\circ\text{--}35^\circ$, and the upper limit belongs to the SDCS. To select the location of the working face bottom plate that is most prone to rockfall hazards for numerical simulation experiments, Arcgis and Rockyfor3D software are used for model rasterization and face inclination analysis, and the results are shown in Figures 6 and 7, respectively.

It can be seen from Figures 6 and 7 that the purple area (marked in Figure 7) is the area that is most prone to rockfall hazards; the inclination angle of the working surface in this area is about 35° which belongs to the SDCS. The detailed bottom floor of working face of the area is presented in a 3D model, as shown in Figure 8.

2.4. Numerical Simulation Principle of Rockfalls Impact Protection Netting.

The problem of rockfalls collision protection structure belongs to the study of structural dynamics. This article adopts the explicit analysis algorithm in HyperMesh/LS-DYNA software. Numerical simulation of the process of rockfalls collision protection structure is analyzed. The structural dynamics equation is

$$\mathbf{m}\ddot{\mathbf{v}}(t) + \mathbf{c}\dot{\mathbf{v}}(t) + \mathbf{k}\mathbf{v}(t) = \mathbf{F}(t), \quad (11)$$

where \mathbf{m} , \mathbf{c} , and \mathbf{k} are the mass, damping, and stiffness matrices of the protective netting structure system, respectively, $\mathbf{v}(t)$ is the speed response of the falling rock

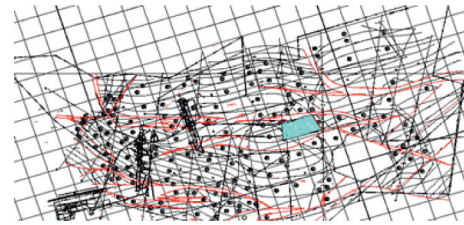


FIGURE 4: Contour lines and drilling information of bottom plate of working face.



FIGURE 5: The mesh model of bottom plate of working face.



FIGURE 6: The raster image of working face.



FIGURE 7: Analysis of inclination angle of working face.

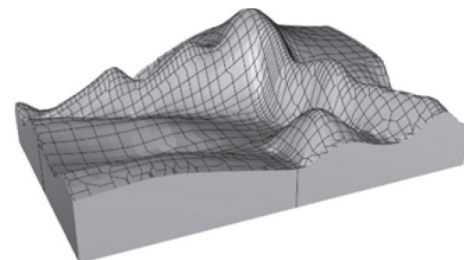


FIGURE 8: 3D model of bottom floor of working face.

collision protection netting, and $\mathbf{F}(t)$ is the load array of the protective netting.

The central difference method is an explicit algorithm commonly used in this field. During the operation, the time

can be divided into multiple steps. The acceleration at time t_n is

$$a_t = m^{-1}(F_{\text{extn}} - F_{\text{intn}}), \quad (12)$$

where F_{extn} is the external force of the protective netting at time t_n , and F_{intn} is the internal force of the protective netting.

Let $\Delta t_{(n+1/2)} = (\Delta t_n + \Delta t_{n+1})/2$; the velocity and displacement at time t_{n+1} can be obtained by the following formula:

$$\begin{aligned} v(t_{(n+1/2)}) &= v(t_{(n-1/2)}) + at_n, \\ x(t_{n+1}) &= x(t_n) + v(t_{(n+1/2)})\Delta t_{(n+1/2)}. \end{aligned} \quad (13)$$

To ensure the stability of this method, a small time step is required and needs to meet the following formula:

$$\Delta t \leq \Delta t_{cr} = \frac{2}{\omega_n}, \quad (14)$$

where ω_n is the maximum natural vibration frequency of the protective netting, and Δt_{cr} is the maximum time step that satisfies the stability condition.

3. Verification of ETM Model

This article takes a hexahedral rockfall as an example. Verify the multipoint collision between the rockfall of the polyhedron and the bottom of the working face. The bottom plate model of the working face is shown in Figure 8. The collision recovery coefficient of the working floor is 0.84, the friction coefficient is 0.4, the rockfall density is 2500 kg/m^3 , and the model size is $0.1 \text{ m} \times 0.2 \text{ m} \times 0.2 \text{ m}$. The coal/rock block falls from the roof to form rockfall. The rockfall moves from a height of 20 m above the end of the working face and collides with the bottom of the working face in free fall. Then bounce and roll motions occur along the bottom of the working face. The trajectories simulated by ETM and the Rockyfor3D software were compared. The motion trajectory and lateral offset trajectory of rockfall along the working face inclination are obtained as in Figures 9 and 10, respectively. It can be seen that the rockfall tendency trajectory and lateral movement trajectory simulated by ETM are consistent with Rockyfor3D simulation results.

4. Simulation Results

4.1. Movement of Irregular Random Shape Rockfall. The shape of the rockfall can be expressed by sphericity and roundness, as shown in Figure 11 [34].

The sphericity calculation formula is

$$S = \sqrt[3]{\frac{C^2}{AB}}, \quad (15)$$

where S is the sphericity of the rockfall, and A , B , C , respectively, represent the length of the three axes of the rockfall.

The roundness calculation formula is

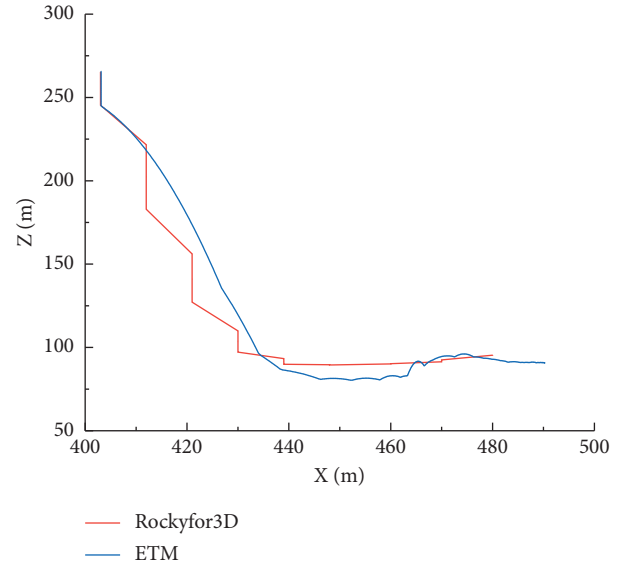


FIGURE 9: Contrastive diagram of inclination trajectory.

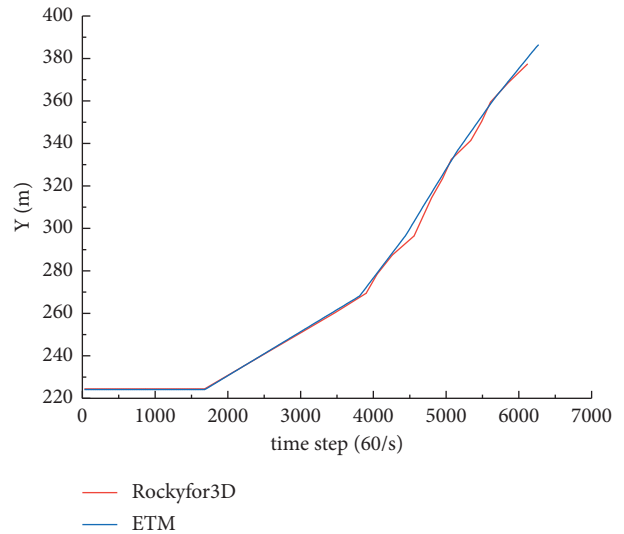


FIGURE 10: Lateral offset contrast diagram.

$$P = \frac{\sum r_n/N}{R}, \quad (16)$$

where P is the roundness of the rockfall, r_n represents the radius of the inscribed circle of the corner of the rockfall model, N represents the number of corners, and R represents the maximum inscribed circle radius of the rockfall model.

Field measurement found that most of the rockfalls present irregular random shapes, and the roundness of rockfalls is mainly concentrated in $[0.1, 0.7]$, and the sphericity is mainly concentrated in $[0.3, 0.7]$. Rockfall with extremely small roundness is not easy to move. After being formed, it mostly stays on the bottom of the working face and is not easy to slip off. And neither the sphericity nor the roundness will show extremely large values. Therefore, the irregular random shape rockfall production method in this

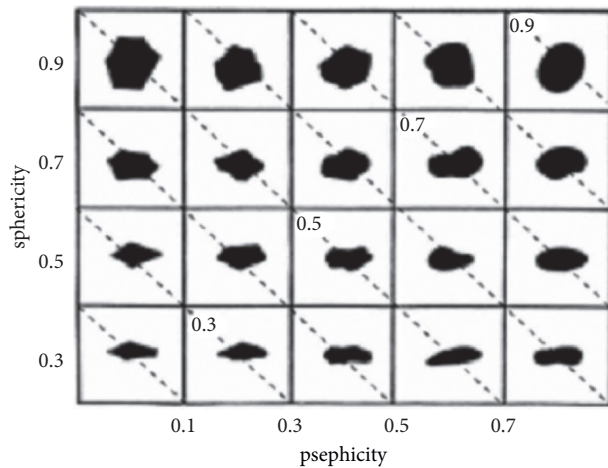


FIGURE 11: The comparison of sphericity and roundness.




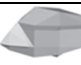
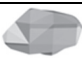




paper is used to generate the roundness in $[0.1, 0.7]$. Numerical simulation test is performed on nine rockfalls with sphericity in $[0.3, 0.7]$, as shown in Table 1, where $r = 0.2$ m.

The working face model in this paper is taken from an SDGS test mine in Gansu Province of China. The bottom plate model of the working face shown in Figure 9 is adopted. It is assumed that, during the mining process of the working face, the coal cutting trajectory is consistent with the contour line of the floor. The collision recovery coefficient of the working face bottom plate is 0.84, and the friction coefficient is 0.4. The density of rockfall is 2500 kg/m^3 , and the rockfall moves freely from 10 m above the working face. In order to study the movement law of rockfall, it is assumed that there are no equipment and other obstacles at the lower end of the working face.

ETM is used for numerical simulation experiments. All rockfall models fall in the same location. A comparison chart of rockfall trajectories as shown in Figure 12 is obtained. It can be seen from Figure 12 that the greater the sphericity of the rockfall, the stronger the bounce ability after a collision and the easier it is for a large-scale bounce motion to form a simpler parabolic motion trajectory. Rockfall with small sphericity will bounce many times on the working surface. Therefore, the uncertainty of the movement trajectory is increased. In engineering practice, rockfall with small sphericity is more unstable on the working face, and it is easy to slip with vibration. When the sphericity of rockfall is very small, the motion of rockfall will show sliding and rolling motion that fits the floor of working face, which leads to less intense movement. In the case of the same sphericity, the smaller the roundness, the higher the complexity of the rockfall motion trajectory, and the more difficult it is to protect.

The change of rockfall velocity is shown in Figure 13. It can be seen from Figure 13 that the larger the sphericity of the rockfall, the greater the initial velocity of the first bounce after the free fall, and the less the energy loss caused by collision. During the entire movement process, the peak velocity that can be reached is greater. In the case of the same sphericity, the smaller the roundness, the smaller the velocity change of rockfall after colliding with the working face floor.

TABLE 1: The irregular shape model of rockfalls.

	No.1	No.2	No.3
Group 1 ($S = 0.7$)	 $P = 0.154$	 $P = 0.412$	 $P = 0.647$
Group 2 ($S = 0.5$)	 $P = 0.113$	 $P = 0.352$	 $P = 0.523$
Group 3 ($S = 0.3$)	 $P = 0.133$	 $P = 0.471$	 $P = 0.680$

Its ability to convert kinetic energy into potential energy is lower, and the movement takes place longer on the working surface. Therefore, it should be focused on.

The energy changes of three groups of irregular rockfalls are shown in Figure 14. It can be seen from Figure 14 that the total kinetic energy of rockfall is composed of translational kinetic energy and rotational kinetic energy. The changing trend of the total kinetic energy of rockfall is similar to that of the center of mass velocity. It can be seen that the translational kinetic energy of rockfall accounts for a larger proportion of the total kinetic energy during the movement process. The roundness and sphericity of rockfall mainly affect the quality of rockfall by changing the shape of rockfall. And then it affects the total kinetic energy in the process of rockfall movement. The change law of total kinetic energy is affected by the shape of the bottom of the working face and the shape of the rockfall. The complexity of the field situation directly affects the occurrence of rockfall disaster. Therefore, as important technical means in the simulation process, the generation methods of irregular random shape rockfalls and working face can make the numerical simulation test effectively relate to the actual situation.

4.2. Process of Rockfall Collision Protection Netting. In the field practice, the setting of the protective netting in SDGS depends on the distribution of rockfall trajectory and the area that may be endangered. This article will adopt the principle of graded protection based on field experience. The protective netting is set at the position where the bounce height is small and the kinetic energy is small. Using HyperMesh combined with LS-DYNA software, the process of rockfalls collision protection netting is simulated numerically. Take the second set of No. 1 rockfall model as an example: set the protective netting between the second and third collisions between the rockfall and the working face floor, which is 40 m away from the lower end of the working surface. The direction is perpendicular to the floor of the working face. The rockfall enters the protective netting at a speed of 15.4 m/s and 47.33° with the horizontal plane of the protective netting. In order to explore the collision between many rockfalls and the protective netting, taking two falling rocks A and B as an example, the following three falling rocks incidence modes are used to simulate: parallel height, parallel steps, and the same trajectory. The shape and parameters of the protective netting refer to [13]. Under the

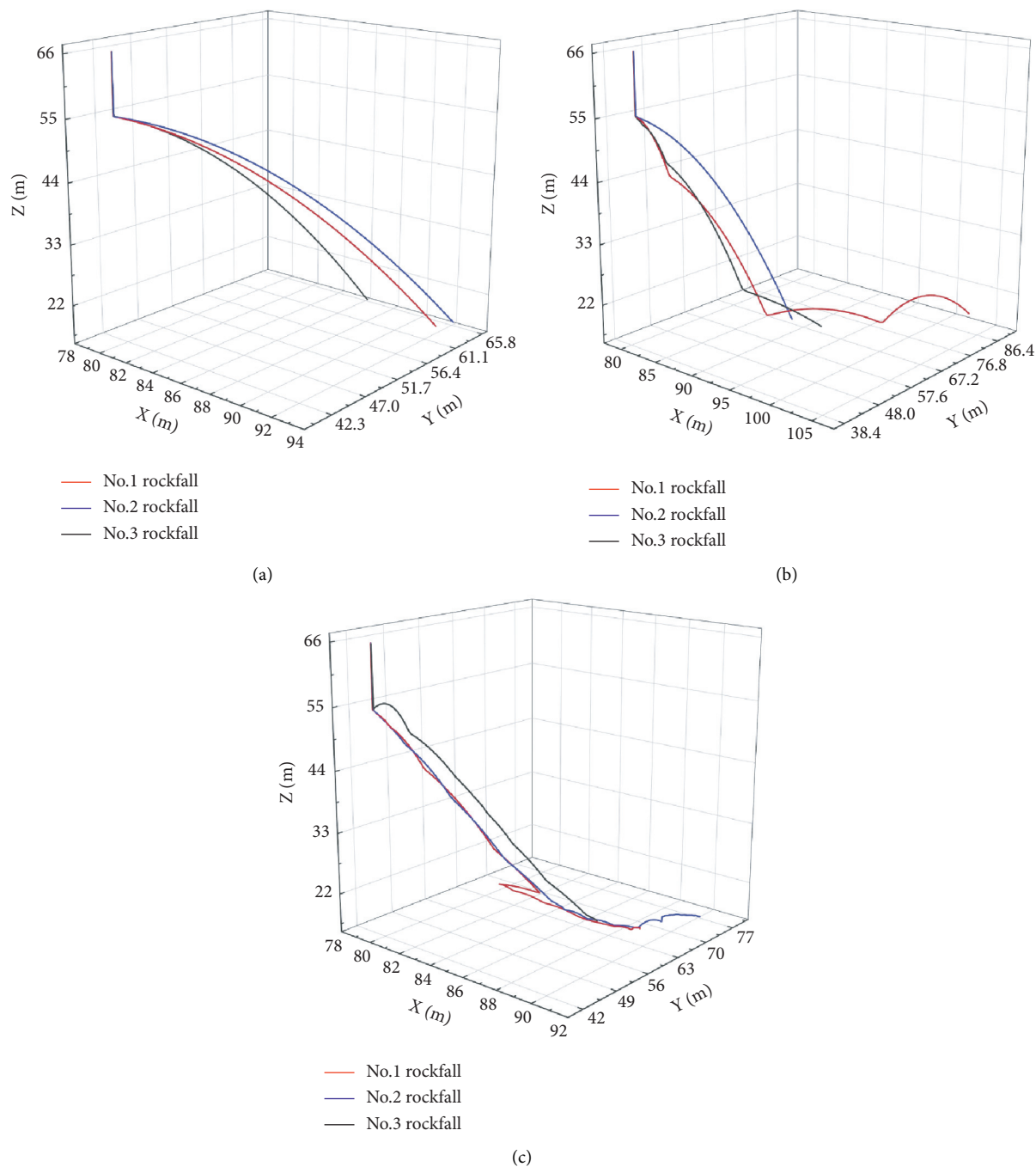


FIGURE 12: Comparison diagram of motion trajectory of rockfall. (a) Group 1. (b) Group 2. (c) Group 3.

three different incident modes, the rockfalls touch the netting, drop to the lowest point, and then contact and separate from the netting at three moments, as shown in Figure 15. It can be seen from Figure 15 that, with the change of time, the mesh of the middle protective netting is constantly stretched under tension. The mesh continues to slide, and the degree of tension becomes greater and greater, and

the middle part of the protective netting gradually begins to tighten. When the middle part of the protective netting is fully tightened, the rockfall starts to rebound. The motion of rockfall and protective netting depends on the posture and contact position of those and the incident speed of rockfall.

As shown in Figures 16 and 17, these are curve of stress distribution and limit stress changing with time of two

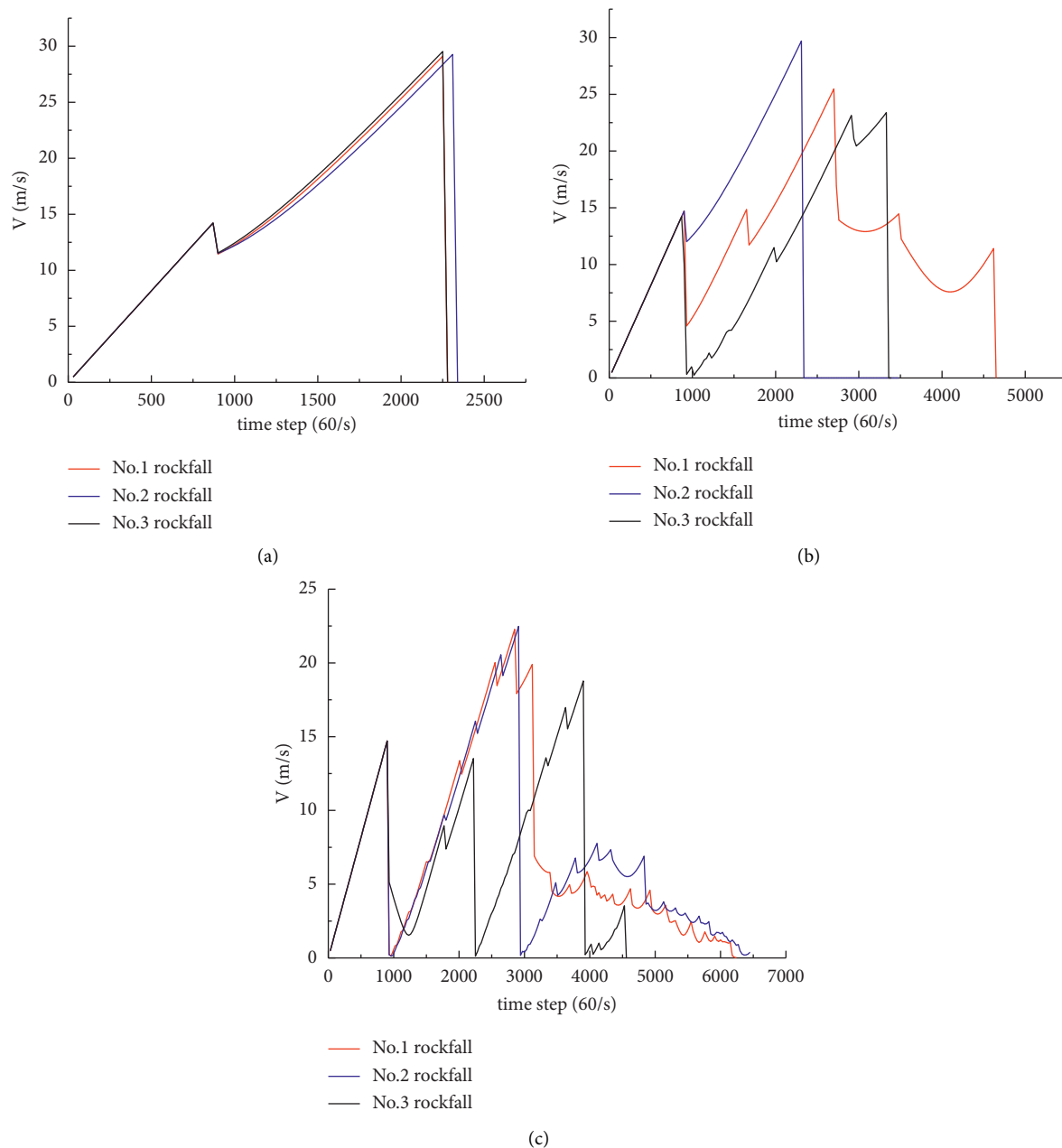


FIGURE 13: Comparison diagram of velocity of rockfall. (a) Group 1. (b) Group 2. (c) Group 3.

rockfalls A and B under three different incident modes. It can be seen from Figure 16 that, in the three modes, the connection between the mesh surface and the constraint and the mesh surface corners are the locations where the stress is the greatest. It can be seen from Figure 17 that the peak stress of the protective netting is related to the continuity of rockfall incidence. When the rockfall is parallel and incident at the same time, the stress peak value of the protective net is the largest. When two rockfalls are incident one after the other in a step parallel or in the same orbit and in the same direction, the peak stress of the protective netting will be

reduced, and it is inversely proportional to the time interval between two rockfalls. In the actual protection, we should pay more attention to the impact of multiple rockfalls on the protective netting.

Figure 18 shows the velocity curve of rockfalls during the collision. It can be seen from Figure 18 that the gangue blocking effect of the protective netting is affected by the incident position and interval time of the rockfalls. When two rockfalls enter the protective netting in a parallel step pattern, the touch screen points are far away and the touch screen has a certain interval time. The falling speeds of the

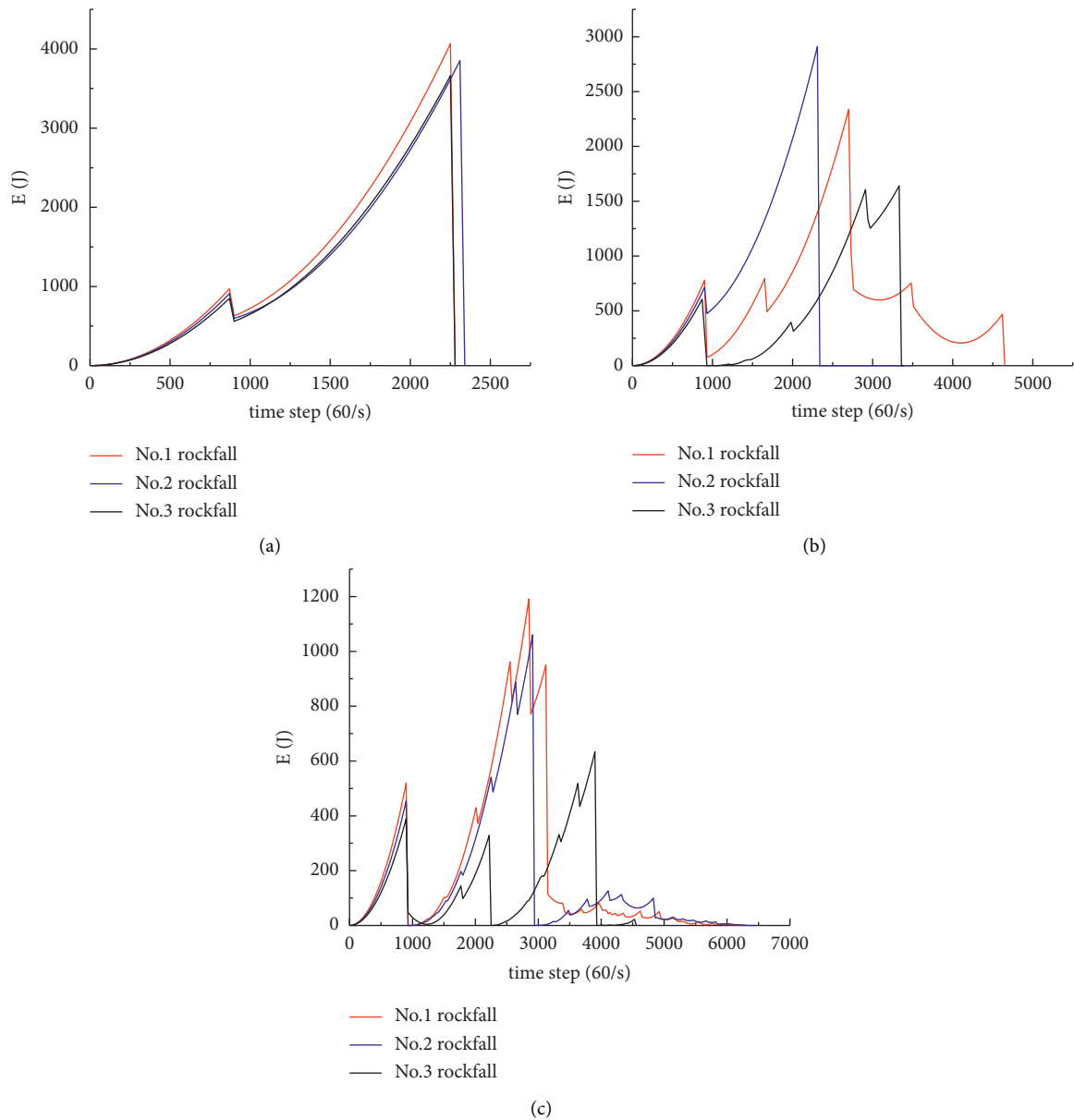


FIGURE 14: Comparison diagram of energy of rockfall. (a) Group 1. (b) Group 2. (c) Group 3.

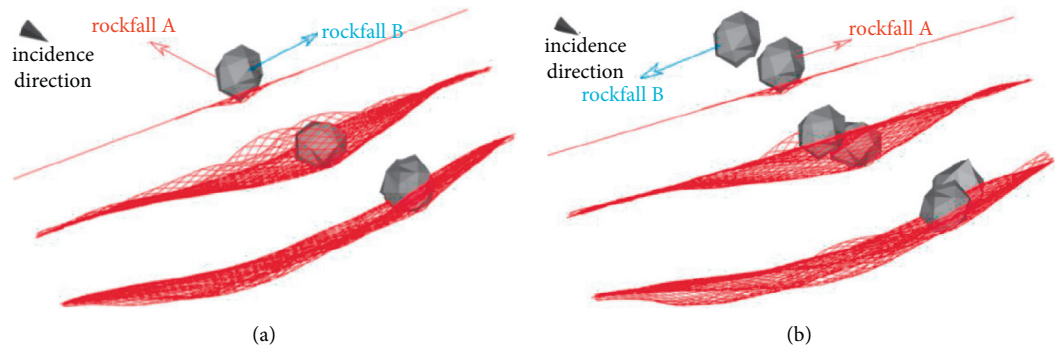


FIGURE 15: Continued.

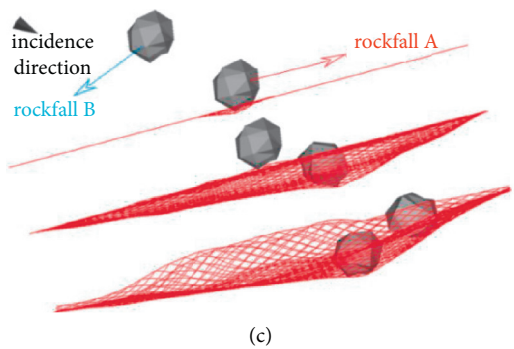


FIGURE 15: Process decomposition of rockfall collision retaining netting. (a) Parallel heights. (b) Parallel steps. (c) The same trajectory.

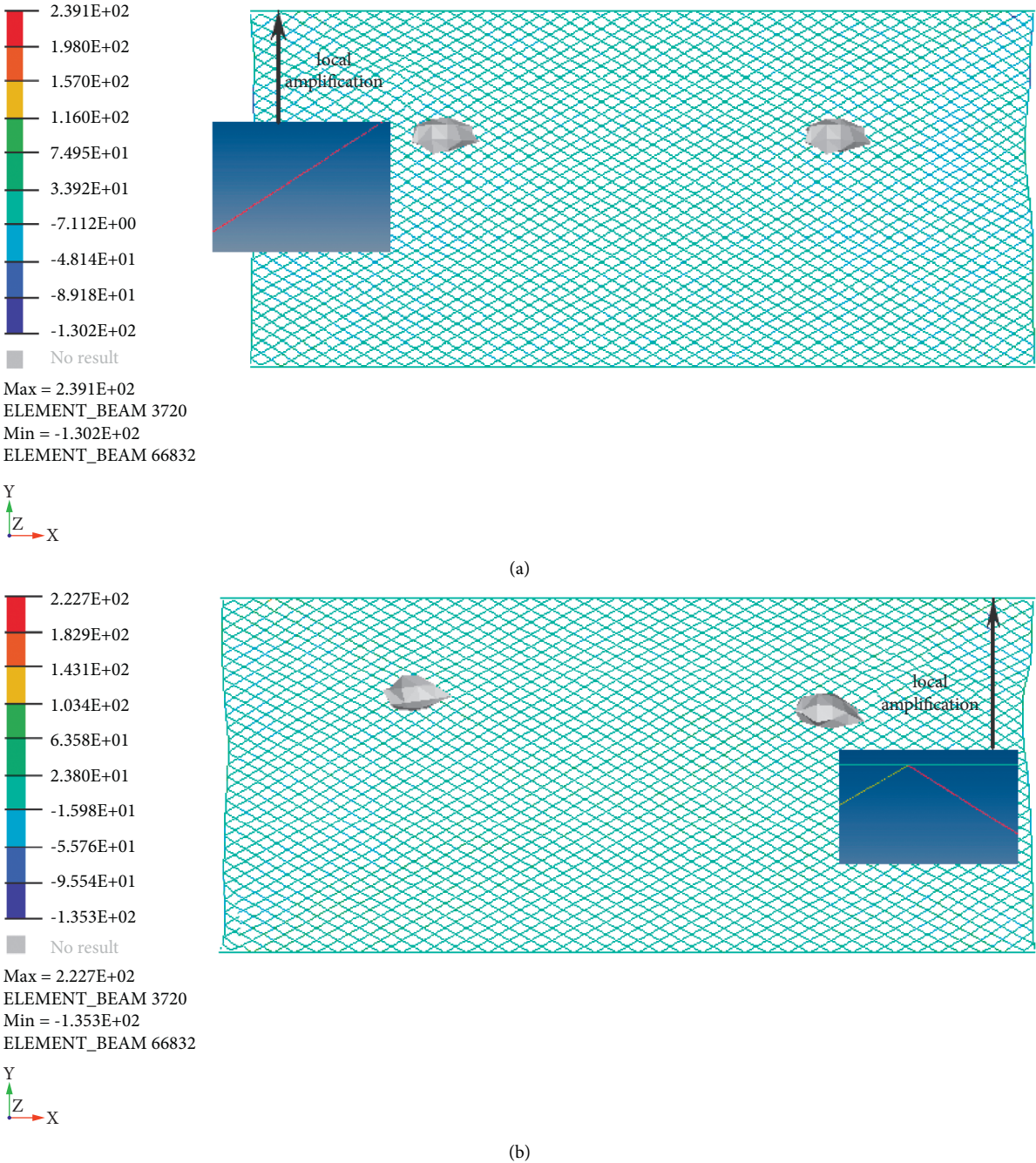
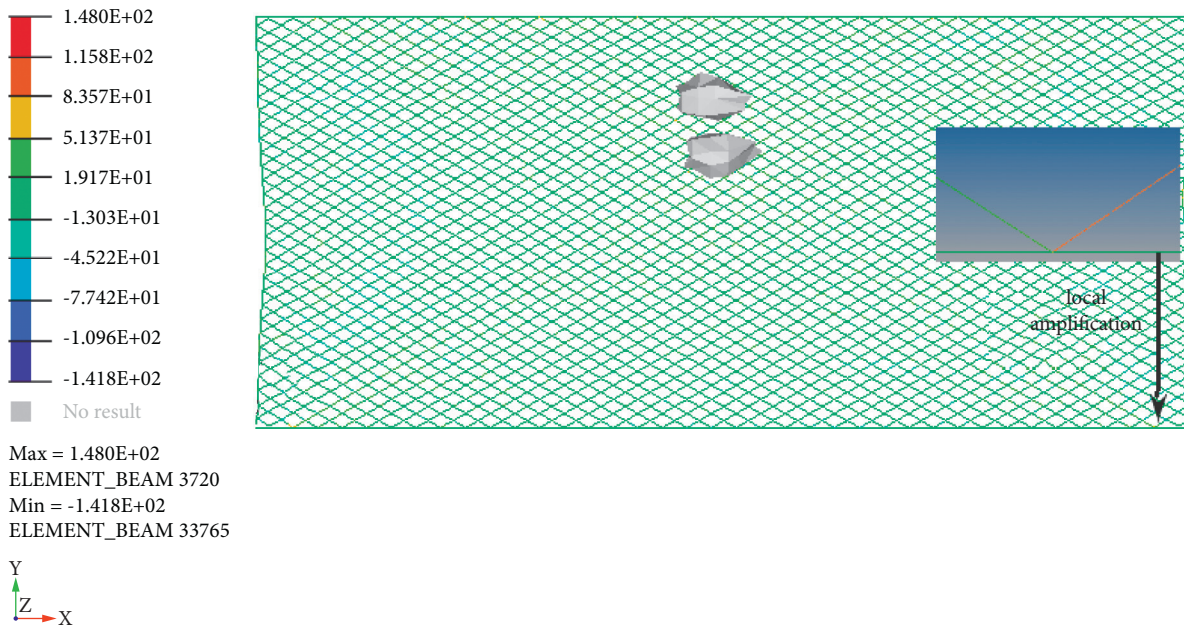


FIGURE 16: Continued.



(c)

FIGURE 16: Stress distribution diagram of rockfall retaining net. (a) Parallel height. (b) Parallel steps. (c) The same trajectory.

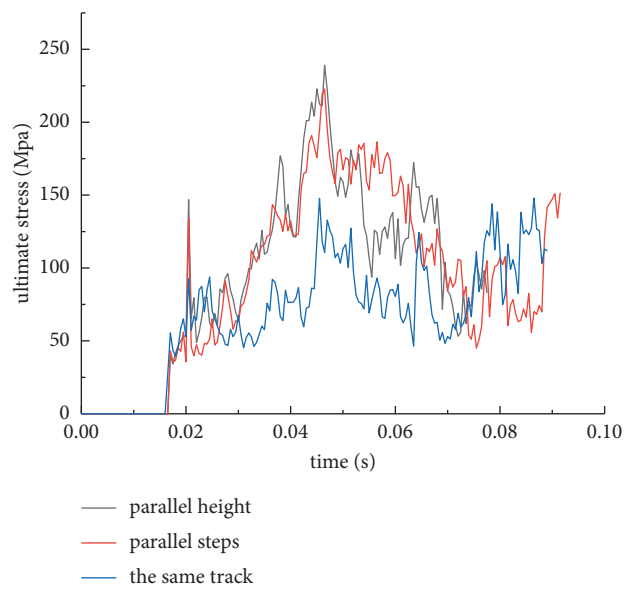


FIGURE 17: Limit pressure on rockfall retaining net.

two rockfalls when the rebound is separated are 3.17 m/s and 3.89 m/s, respectively; it is the minimum separation speed in the three modes. Therefore, the protective netting has the most obvious protective effect against rockfalls incident in

this mode. In addition, in the three modes, the protective netting has the best protective effect on the rockfall which first touches the netting, and the results are the same as the actual engineering results.

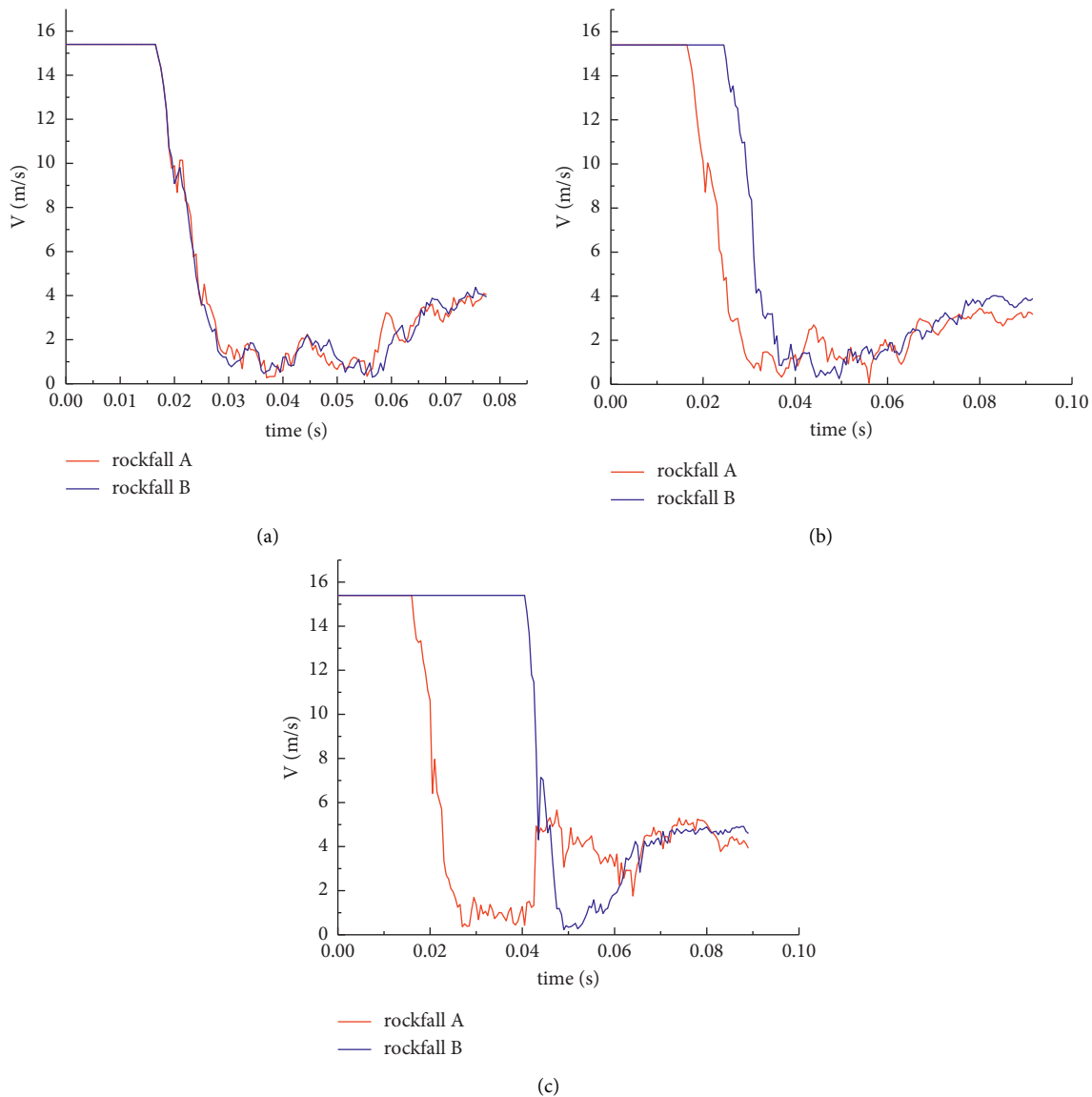


FIGURE 18: Speed change curve of rockfall. (a) Parallel height. (b) Parallel steps. (c) The same trajectory.

5. Conclusion

- (1) In the mining of SDCS, the movement of rockfalls is a complex dynamic process. This paper proposes a method for generating rockfalls with irregular random shapes. The rockfall models with arbitrary sphericity and roundness based on ellipsoid can be generated. Combining with ETM, the movement process of rockfalls with irregular random shape in three-dimensional space can be accurately simulated, including the speed and energy changes at any moment. The simulated trajectory is highly consistent with the trajectory simulated by Rockyfor3D software.
- (2) The trajectory of irregular rockfalls is greatly affected by the shape of rockfall and working face floor. The bigger the sphericity of rockfall is, the stronger the

jumping ability of rockfall is, and the smaller the change of velocity in the collision process is. In addition, the smaller the roundness is, the more complex the movement trajectory is. During the collision process between rockfall and protective netting, the joint between mesh and constraint and the corner of mesh are stressed the most, and fracture is most likely to occur. During the process of multiple rockfalls colliding with the protective netting, the peak stress on the protective netting is inversely proportional to the time interval between each rockfall and the distance to the netting.

- (3) This paper uses the contours of the working face bottom plate and drilling information for modeling, combines with ETM, simulates the three-dimensional movement process of random-shaped

rockfalls, and opens up the interface between the geographic information system data model and ETM self-programming. The perfect combination of three-dimensional visualization modeling of the real working face floor of the SDCS and the self-programming of ETM is realized. The matching degree between numerical simulation test and engineering practice is improved, which has an important theoretical and practical significance for predicting rockfall hazards in the working face.

References

- [1] Y. Wu, P. Xie, and H. Wang, "Theory and practices of fully mechanized longwall mining in steeply dipping coal seam," *Mining Engineering*, vol. 65, no. 1, pp. 35–41, 2013.
- [2] Y. P. Wu, D. F. Yun, P. S. Xie, H. W. Wang, D. Lang, and B. S. Hu, "Progress, practice and scientific issues in steeply dipping coal seams fully-mechanized mining," *Journal of China Coal Society*, vol. 45, no. 1, pp. 24–34, 2020, in Chinese.
- [3] Y. P. Wu, K. Z. Liu, D. F. Yun, P. S. Xie, and H. W. Wang, "Research progress on the safe and efficient mining technology of steeply dipping seam," *Journal of China Coal Society*, vol. 39, no. 8, pp. 1611–1618, 2014, in Chinese.
- [4] J. A. Wang and J. L. Jiao, "Criteria of support stability in mining of steeply inclined thick coal seam," *International Journal of Rock Mechanics and Mining Sciences*, vol. 82, no. 2, pp. 22–35, 2016.
- [5] D. Yun, Z. Liu, W. Cheng, Z. Fan, D. Wang, and Y. Zhang, "Monitoring strata behavior due to multi-slicing top coal caving longwall mining in steeply dipping extra thick coal seam," *International Journal of Mining Science and Technology*, vol. 27, no. 1, pp. 179–184, 2017.
- [6] X. P. Lai, P. F. Shan, J. T. Cao, F. Cui, and H. Sun, "Simulation of asymmetric destabilization of mine-void rock masses using a large 3D physical model," *Rock Mechanics and Rock Engineering*, vol. 49, no. 2, pp. 487–502, 2016.
- [7] Y. P. Wu, B. S. Hu, and P. S. Xie, "A new experimental system for quantifying the multidimensional loads on an on-site hydraulic support in steeply dipping seam mining," *Experimental Techniques*, vol. 43, pp. 571–585, 2019.
- [8] H. Tu, S. Tu, Y. Yuan, and F. Wang, "Present situation of fully mechanized mining technology for steeply inclined coal seams in China," *Arabian Journal of Geosciences*, vol. 8, no. 7, pp. 4485–4494, 2015.
- [9] M. Liu, Y. P. Wu, and G. Xu, "Research on rule of flying gangue in steeply dipping seam mining," *Coal Technology*, vol. 35, no. 7, pp. 17–18, 2016, in Chinese.
- [10] Y. P. Wu, B. S. Hu, H. W. Wang, P. S. Xie, M. Liu, and M. Y. Liu, "Mechanism of flying gangue-causing disasters in longwall mining of steeply dipping seam," *Journal of China Coal Society*, vol. 42, no. 9, pp. 2226–2234, 2017, in Chinese.
- [11] Y. P. Wu, B. S. Hu, P. S. Xie, and Y. F. Zeng, "Flying gangue regional control technology in longwall mining face of steeply dipping seam," *Coal Science and Technology*, vol. 45, no. 2, pp. 1–5, 2017, in Chinese.
- [12] Y. P. Wu, B. S. Hu, H. W. Wang, and K. Z. Liu, "Simulation and experiment research on the evolution characteristics of flying gangue energy in steeply dipping coal seam," *Journal of Xi'an University of Science and Technology*, vol. 38, no. 1, pp. 37–42, 2018, in Chinese.
- [13] Y. P. Wu, B. S. Hu, P. S. Xie, S. H. Li, and J. Y. Huangpu, "Impact damage of flying gangue in steeply dipping seams and its control," *Journal of China Coal Society*, vol. 43, no. 10, pp. 2694–2702, 2018, in Chinese.
- [14] L. L. Jing, J. L. Qu, M. Liu, and B. M. Qiao, "Non-probabilistic interval analysis method for estimation of flying gangue movement in steeply dipping seam," *Coal Technology*, vol. 38, no. 5, pp. 105–108, 2019, in Chinese.
- [15] M. Liu, K. Li, Y. P. Wu, S. Geng, and G. D. Zhang, "Design of flying gangue protection device for steeply dipping seam by grating recognition," *Coal Mine Machinery*, vol. 40, no. 8, pp. 29–30, 2019, in Chinese.
- [16] M. Liu, S. Geng, Y. P. Wu, and W. Y. Lv, "Design of flying gangue protection device driven by hydraulic system," *Coal Mine Machinery*, vol. 41, no. 1, pp. 102–103, 2020, in Chinese.
- [17] M. Liu, K. Li, Y. L. Duo, and Y. P. Wu, "Motion track analysis and protective device of flying gangue in roof leakage of steeply dipping working face," *Coal Science and Technology*, vol. 48, no. 8, pp. 139–144, 2020, in Chinese.
- [18] M. Liu, K. Li, Y. P. Wu, and W. Y. Lv, "Safety evaluation and application for flying gangue of steeply dipping coal seam based on fuzzy comprehensive evaluation method," *Safety In Coal Mines*, vol. 51, no. 2, pp. 244–247, 2020, in Chinese.
- [19] M. Liu, Y. P. Wu, S. Geng, Y. L. Duo, and W. Y. Lv, "Threat level assessment of flying gangue in steep seam mining," *Journal of China Coal Society*, vol. 45, no. 11, pp. 3688–3695, 2020, in Chinese.
- [20] Y. P. Wu, B. S. Hu, D. Lang, and Y. P. Tang, "Risk assessment approach for rockfall hazards in steeply dipping coal seams," *International Journal of Rock Mechanics and Mining Sciences*, vol. 138, pp. 1–17, 2021.
- [21] S. H. Luo, T. Wang, Y. P. Wu, J. Y. Huangfu, and H. T. Zhao, "Internal mechanism of asymmetric deformation and failure characteristics of the roof for longwall mining of a steeply dipping coal seam," *Archives of Mining Sciences*, vol. 66, no. 1, pp. 101–124, 2021.
- [22] B. Hu, Y. Wu, H. Wang, Y. Tang, and C. Wang, "Risk mitigation for rockfall hazards in steeply dipping coal seam: a case study in Xinjiang, northwestern China," *Geomatics, Natural Hazards and Risk*, vol. 12, no. 1, pp. 988–1014, 2021.
- [23] V. N. Kulakov, "Stress state in the face region of a steep coal bed," *Journal of Mining Science*, vol. 31, no. 3, pp. 161–168, 1995.
- [24] J. Bodi, "Safety and technological aspects of man less exploitation technology for steep coal seams," in *Proceedings of the 27th International Conference of Safety in Mines Research Institutes*, pp. 955–965, New Delhi, India, February 1997.

- [25] T. N. Singh and L. D. Gehi, "State behavior during mining of steeply dipping thick seams-A case study," in *Proceedings of the International Symposium on Thick Seam Mining*, pp. 311–315, Dhanbad, India, 1993.
- [26] S. S. Peng, *Longwall Mining*, Department of Mining Engineering West Virginia University, WV, USA, 2006.
- [27] V. K. Sehgal and A. Kumar, "Thick and steep seam mining in North Eastern Coalfields," in *Proceedings of the International Symposium on Thick Seam Mining: Problem and Issues*, pp. 457–469, Dhanbad, India, 1992.
- [28] V. V. Aksenov and G. E. Lukashev, "Design of universal equipment set for working steep seam," *Ugol*, vol. 4, pp. 5–9, 1993.
- [29] V. N. Kulakov, "Geomechanical conditions of mining steep coal beds," *Journal of Mining Science*, vol. 31, no. 2, pp. 136–143, 1995.
- [30] E. T. Proyavkin, "New nontraditional technology of working thin and steep coal seams," *Ugol Ukrainy*, vol. 3, pp. 2–4, 1993.
- [31] X. Tang, A. Paluszny, and R. W. Zimmerman, "An impulse-based energy tracking method for collision resolution," *Computer Methods in Applied Mechanics and Engineering*, vol. 278, no. 15, pp. 160–185, 2014.
- [32] X. Tang, A. Paluszny, and R. W. Zimmerman, "Energy conservative property of impulse-based methods for collision resolution," *International Journal for Numerical Methods in Engineering*, vol. 95, no. 6, pp. 529–540, 2013.
- [33] W. J. Stronge, *Impact Mechanics*, Cambridge University Press, Cambridge, UK, 2000.
- [34] W. C. Krumbein and L. L. Sloss, "Stratigraphy and s," *Soil Science*, vol. 71, no. 5, p. 401, 1951.

Synthesis of heat exchanger networks and it's design and parameters for capital cost estimation

Chinmay Swain, *Department of Mechanical Engineering, Raajdhani Engineering College, Bhubaneswar, chinmayswain1972@gmail.com*

Saswati Nayak, *Department of Mechanical Engineering, Capital Engineering College, Bhubaneswar, saswatinayak2574@gmail.com*

Ranjan Kumar, *Department of Mechanical Engineering, NM Institute of Engineering & Technology, Bhubaneswar, kumarranjan75@gmail.com*

Shaik Mozammil, *Department of Mechanical Engineering, Aryan Institute of Engineering & Technology, Bhubaneswar, smozammil157@gmail.com*

ARTICLE INFO

Keywords:

Heat exchanger networks
Energy conservation
MINLP Optimization
Shell and tube heat exchanger
MINLP
Cost estimation

ABSTRACT

A unique bi-level strategy for the optimum synthesis of HENs is provided in this research. In order for the heat exchangers in the HEN to have different capital cost parameters, a new capital cost parameter is iteratively updated in the capital cost function based on the detailed design of shell and tube heat exchangers, taking into account the shell diameter, tube length, area, and other parameters needed to calculate a total cost correction factor. The HEN synthesis is proposed at the outer level using a mixed-integer nonlinear programming (MINLP) model. While the HEN is being synthesised, another MINLP model is used to rigorously design the shell and tube heat exchangers using the Bell-Delaware approach. When comparing the final HEN to those generated using the identical settings in the capital cost function for all heat exchangers in the HEN, significant changes in the final HEN were discovered. The findings indicate that this technique can deliver more realistic costing solutions than those previously presented in the literature.

Introduction

One of the major concerns in industrial processes is the excessive consumption of hot and cold utilities and an optimal heat recovery system is essential in reducing costs and negative environmental effects. Since the 1970 s, due to the increased cost of energy, reduced fuel availability and, environmental constraints on pollutant emissions, different approaches have been proposed to synthesize optimal Heat Exchanger Networks (HENs). Many papers have addressed this theme and, usually, an optimization problem is proposed, whose objective function to be minimized is the Total Annualized Cost (TAC), which considers the energy costs and the fixed cost of purchasing and installing (capital cost) the heat transfer devices, subject to heat and mass balances and other heat exchanger constraints.

Traditional costing methods for HENs are based on correlations that are functions of the total heat transfer area. However, these correlations apply only to traditional equipment configurations and in limited size ranges to estimate the equipment purchase price. To achieve the TAC minimization, a superstructure can be used to derive an optimization model with a Mixed Integer Nonlinear Programming (MINLP) formulation.

The stagewise superstructure (SWS) of Yee and Grossmann [1] is, perhaps, the most common and widespread. This SWS is divided into

stages, and, in each stage, the hot process streams can be split into several branches equal to the number of cold streams and vice-versa, in such a way that all possible matches among the split process streams are possible. Coolers and heaters are allocated at the end of the process streams, if necessary. The assumption of isothermal mixing at the end of each split stream is used, to avoid non-convex heat balance equations, in such a way that the resulting equations are linear. These authors used a deterministic mathematical programming approach to solve the MINLP optimization problem.

Other approaches, based on this superstructure, were also used to find solutions to the HEN synthesis problem using hybrid *meta*-heuristics approaches, like Genetic Algorithms (GA) and Particle Swarm Optimization (PSO) [2], Simulated Annealing (SA) and Rocket Fireworks Optimization (RFO) [3], SA and PSO [4], SA and Differential Evolution (DE) [5].

Normally, short-cut methods are used to calculate the heat exchangers area during the HEN synthesis task. Some papers, however, have focused on considering the optimal design of the heat transfer devices. According to Caputo et al. [6], the literature presents approaches for the optimization of heat exchangers consisting of two main ideas: the optimal sizing, based on the cost minimization, and the maximization of thermal performance. Traditional design approaches are based on iterative procedures that gradually change design parameters until they reach a satisfactory solution that meets design

Nomenclature			
a	Capital cost function parameter	N_s	Number of shells
$Area$	Heat Exchange area	N_t	Number of tubes
A_{rr}	Tube arrangement	N_{tp}	Number of tube passes
B	Capital cost function parameter	T_{in}	Inlet temperature
b_{av}	The average weight for parameter b	T_{out}	Outlet temperature
c	Capital cost function parameter.	P	cost multiplier for tube o.d., pitch and layout angle
C_{CU}	Cost of cold utility	P_{cost}	Pumping cost
C_{HU}	Cost of hot utility	P_{ccost}	Pumping cost constant
C_L	Cost correction factor for tube length	Pt	Tube pitch
C_m	Cost correction factor for material	Q	Heat duty
C_P	Set of the cold process streams	$Q_{cu,i}$	Heat exchanged between stream i and cold utility.
C_p	Heat capacity	$Q_{hu,j}$	Heat exchanged between stream j and hot utility
C_T	Total cost correction factor	r_d	Fouling factor
C_s	Cost correction factor for shell type	R	Cost multiplier for TEMA-type rear head
C_x	Cost correction factor for expansion joint	T	Temperature
C_{Ntp}	Cost correction factor for tube passes	$t(i,k)$	Hot stream temperature i entering interval k
C_{ps}, C_{pt}	Cost correction factor for the pressure of design	$t(j,k)$	Cold stream temperature i entering interval k
d_{ex}	Tube external diameter	U	Overall heat transfer coefficient
d_{in}	Tube internal diameter	U_d, U_c	Dirty and clean overall heat transfer coefficient
D_{out}	Tube bundle diameter	$z(i,j,k)$	Binary variable indicating the existence of heat exchange (i,j) in the interval k
D_s	Shell external diameter	$z_{cu}(i)$	Binary variable indicating the existence of a cooler
$dt(i,j,k)$	Approximation temperature between streams i and j in the interval k	$z_{hu}(j)$	Binary variable indicating the existence of a heater
$dt_{cu}(i)$	Approximation temperature between stream i and cold utility	Greek letter	
$dt_{hu}(j)$	Approximation temperature between stream j and hot utility	β	Cost baseline
f	Cost multiplier for TEMA type front head	μ	Viscosity
G	Set of allowed matches	ρ	Density
h	Individual heat transfer coefficient	ΔP	Pressure drops
HP	Set of the hot process streams	Index	
k	Thermal conductivity	C	Cold stream
L	Tube length	CU	Cold Utility
l_c, l_s	Baffles cut and baffle spacing	H	Hot stream
$LMTD$	Log mean temperature difference	HU	Hot utility
m	Mass flow rate	i	Hot stream or hot utility
Nb	Baffles number	j	Cold stream or cold utility
$N_{cost_{mh}}$	Cost constant for hot utility in the Fcc function	k	Temperature interval
$N_{cost_{mc}}$	Cost constant for utility in the Fcc function	s	Shell side
		t	Tube side

specifications.

In the HEN synthesis in industrial processes, shell and tube heat exchangers (STHE) are the most widely used heat transfer devices, due to their flexibility for different operating conditions. The main components of STHE are tubes, shell, baffles, front and rear heads, tube bundles, and nozzles. Selection criteria for an appropriate combination of these components depend on the operating pressures, temperatures, fluid corrosion characteristics, fouling, cleanliness, and costs.

The detailed design of STHE involves several steps, including the selection of geometric and operational parameters. Considering that the desired heat transfer occurs on the tube surface, the choice of tube geometric variables is important for thermal performance. The outside diameter and the thickness of the wall specify the tube size. Smaller diameter tubes provide higher heat transfer coefficients, resulting in a compact heat exchanger. However, tubes with a larger diameter are easier to clean, stronger, and they are required when the permissible tube side pressure is small. For a given heat exchange area, a more economical heat exchanger can be designed with a small shell diameter and long tubing, consistent with the space and availability of handling facilities.

Works of cost estimation for heat exchanger design are well

discussed in the literature. Duran et al. [7] used Neural Networks for the cost estimation of STHE. In [8], GA was used in the optimal design of STHE from an economic point of view. Asadi et al. [9] used the Cuckoo-Search-Algorithm (CSA) for the same objective. Yang et al. [10] considered the Standards of TEMA to develop optimization models and used a GA to solve the problem. Ravagnani and Caballero [11], and Onishi et al. [12] used deterministic approaches for the STHE design considering the standards of TEMA and the method of Bell-Delaware for the shell-side. Mizutani et al. [13] included the detailed thermal-hydraulic design of STHE to the SWS model. Ravagnani and Caballero [14] used the same approach as Mizutani et al. [13], which considered STHE design under the TEMA standards, resulting in a more realistic area estimation. Xiao et al. [15] presented a simultaneous optimization approach including cases with phase changes using a hybrid *meta*-heuristic technique combining GA and SA in the synthesis of HENs considering the detailed STHE design.

Goncalves et al. [16] presented a rigorous reformulation of the Bell-Delaware method for the design optimization of STHE to obtain a mixed integer linear programming (MILP) formulation. This approach was able to identify feasible solutions for the design of heat exchangers at a lower cost. Lemos et al. [17], proposed the use of Set Trimming to

avoid using mathematical programming (MINLP or MILP) and reduces the computational time. In the work of Lemos et al. [17], the TAC problem formulation is similar to the minimization of the area, but the constraints related to the pressure drops can be omitted, once this alternative explores the tradeoff between the cost associated with the energy consumption for the streams' flow and the cost associated with the heat transfer area.

Rathjens and Fieg [18] proposed a flexible cost function framework for the cost-optimal design of HENs with different cost functions for heat exchangers, heaters, and coolers. These authors used match-based individual factors to allow different fluid properties and resulting in engineering costs. Piping and pumping costs were also included in the proposed model using an MINLP optimization and a GA to solve the problem.

All these works cited above bring somehow ways to minimize cost estimation in HENs, but they lack presenting changes in the parameters used for cost calculation, and the advantage of the approach used in the present paper is that it enables exploring other STHE characteristics to build cost parameters more precisely, not yet presented in the literature in a sequential way.

A bi-level approach is proposed for the optimal synthesis of HENs considering the detailed STHE design under the TEMA standards using the Bell-Delaware method. A new capital cost parameter is iteratively updated based on the detailed heat exchangers, incorporating the shell diameter, tube length, heat transfer area and other parameters needed to calculate a total cost correction factor, such as number of tube passes, design pressure, material, tube pitch, and tube external diameter. In each iteration the individual streams heat transfer coefficients and the pressure drop are also updated.

A capital cost function considering the specifications of each heat exchanger in the network is presented. As each heat exchanger in the HEN has different specifications, the cost parameters related to the area of these heat-transfer devices are also different. The capital cost function, considering the cost parameter varying according to the area and the internal shell diameter of each heat exchanger in the HEN synthesis stage, is the novelty in the present work. Thereafter, two case studies from the literature were used to compare the proposed approach with those commonly used to estimate capital costs and the results obtained show considerable differences.

Costs estimation

When the HEN synthesis task is formulated as an optimization problem considering only economic factors, the objective function to be minimized is the HEN Total Annualized Cost (TAC). It is given by the sum of the operational cost (OC) and the annualized capital cost (CC). The operational cost is given by the hot utility demand (Q_{hu}) multiplied by its cost (C_{hu}) plus the cold utility demand (Q_{cu}) multiplied by its cost (C_{cu}):

$$OC = (C_{hu}Q_{hu}) + (C_{cu}Q_{cu}) \quad (1)$$

Many works in the decade of 1990 used the capital cost equation proposed by Ahmad [19] concerning the synthesis and optimization of HENs in which the capital cost is given by:

$$CC = a + bA^c \quad (2)$$

In this equation A is the HEN total area, a is a constant cost coefficient, and b and c depend on the model and type of material used in the manufacture of the heat exchanger and on the operating pressures. In [24] the coefficients a , b and c are discussed in more detail. Those authors present several methods for the capital cost estimation, such as the Purohit [25], six-tenth method [26], and the methods of Guthrie [27], Pikulik and Diaz [28], Corripio et al. [29], Hall et al. [30], and Vatavuk [31].

Purohit [25] presented a cost-estimating method for STHE, considering different heat exchanger models, construction materials, and

Table 1

STHE parameters and range of utilization.

STHE Parameter	Range
D_s diameter	0.3 m to 3 m
Tube length	2.44 m to 11 m
Tube diameter	0.01905 m to 0.0508 m
Tube side passes	1 to 8 tube passes
Shell side pressure design	6.8 MPa to 19 MPa
Tube side pressure design	6.8 MPa to 17 MPa

Table 2

p , f and r multipliers proposed by Purohit [25].

Multiplier p		
Tube OD (m) × pitch (m)	Triangular pitch (30 or 60 degrees)	Square pitch (45 or 90 degrees)
0.0160 × 0.0198	0.62	Not common
0.0190 × 0.0238	0.80	Not common
0.0190 × 0.0254	0.85	1.00 (base)
0.0220 × 0.0278	0.87	Not common
0.0254 × 0.0318	0.98	1.16
0.0320 × 0.0397	1.23	1.45
0.0320 × 0.0401	1.29	1.49
0.0380 × 0.0476	1.47	1.73
0.0440 × 0.0306	1.72	2.03
0.0510 × 0.0630	1.81	2.13
0.0510 × 0.0640	1.97	2.32
0.0580 × 0.0640	2.08	2.45
TEMA front-end stationary-head type		
B A N	No front end (special case)	0.95
	Bonnet (integral cover) (base)	1.00
	Channel and removable cover	1.02–1.03
	Channel integral with tube sheet and removable cover	1.03–1.07
C	Channel integral with tube sheet and removable cover	1.06–1.07
D	Special high-pressure closure	1.50–1.70
TEMA rear-end head type		
		Multiplier, r
S	Floating head with the backing device (base)	1.00
M	Fixed tube sheet, type B stationary head	0.80
L	Fixed tube sheet, type A stationary head	0.83
N	Fixed tube sheet, type N stationary head	0.85
U	U-tube bundle	0.90
T	Pull-through floating head	1.05
P	Outside-packed floating head	1.04
W	Externally sealed floating tube sheet	1.02

operating pressure rates. The types of STHE considered by the author were fixed-tube-sheet, U-tube, split-ring floating-head, and pull-through floating-head. For each one of these types of heat exchangers, various configurations can be considered using the TEMA standards. Table 1 presents the range of utilization for some STHE parameters for carbon steel heat exchangers covered by the method proposed by Purohit [25].

The internal shell diameter (D_s) is used in the calculation of the base cost β , which is directly related to the characteristics of the heat exchanger type, given by:

$$\beta = \left[\frac{6.6}{1 - e^{[(7-D_s)/27]}} \right] p \cdot f \cdot r \quad (3)$$

In this equation, p is a cost multiplier for the tube outside diameter (OD), layout angle (arrangement), and pitch, f is a cost multiplier for the TEMA-type front head, and r is a cost multiplier for the TEMA-type rear head. Table 2 presents the p , f , and r multipliers proposed by Purohit

[25].

Some correction factors were highlighted, such as tube length correction (CL), the number of tube passes when greater than 2 (C_{NP}), the shell side (C_{PS}) and the tube side (C_{PT}) pressure drops when the internal pressure is greater than 10×10^5 Pa, and the pipe measure (CG) when the pipes are greater than 14 BWG. The heat exchanger total cost E_b is given by:

$$E_b = [\beta(1 + C_T)A_m]N, \quad (4)$$

where C_T is the sum of all base price corrections, A_m is the required material area and N is the number of heat exchangers.

During the 1990 s, several studies related to the costs of a HEN emerged due to economic factors, such as energy costs. Linnhoff and Ahmad [20] considered the optimal HEN cost using a linear model for the calculation of capital costs. The cost coefficient c present in Eq. (2) is considered equal to 1 and the area dependence in the capital cost equation is linear. The operational cost is calculated and in Eq. (1). The network capital cost considers that the total network area (A_{min}) is achieved with the maximum energy recovery ($U_{min,MER}$) given by:

$$NetworkCapitalCost = aU_{min,MER} + bA_{min}. \quad (5)$$

where a and b are installed capital cost law coefficients; $U_{min,MER}$ is the minimum number of units in a heat exchanger network with maximum energy recovery. The resulting total cost profile displays a minimum at some value of ΔT_{min} .

Colberg and Morari [21] assumed that the capital cost of each heat exchanger is given by an exponential function. These authors presented an objective function assuming that the capital cost could vary depending on the number of combinations in the HEN, even if the variables were independent of the heat transfer area. Each combination should compute different cost coefficients considering heat exchanger models and operating pressures.

Most of the published works on capital costs assume that all heat exchangers in the network obey a single cost law. This means, that construction materials, operating pressure ranges, and the type of heat exchangers are considered uniform. Hall [32] considered differences in the specification of the heat exchangers in the capital cost calculation. Cost factors were determined for each stream from the heat exchanger model considering the non-uniform construction materials, different pressure ranges, and different equipment types.

The conclusions were that changes in the heat exchanger specification alter the trade-off between energy and capital and this, in turn, may lead to changes in the network topology. Ahmad [19], Hall et al. [22], and Colberg and Morari [21] used a Nonlinear Programming (NLP) formulation to predict the trade-off between area and the number of thermal exchange units.

Hall et al. [22] pointed out that the area contribution of each heat exchanger contributes differently to the network capital cost. If a corrosive fluid is being used in the process and if it requires special building materials, it will have a greater contribution to the capital cost than a similar non-corrosive fluid. If only one cost law is used for a network that includes mixed building materials, the area contribution to different fluids requiring special materials should somehow increase. Therefore, the authors assigned weights to the heat transfer coefficient to reflect the cost of the material the fluid requires. Thus, taking the capital cost of a heat exchanger as a reference, Eq. (2) has the cost equation coefficients such as a_1 , b_1 , and c_1 . If another heat exchanger with different specifications were installed, then the coefficients of Eq. (2) would be represented as a_2 , b_2 , and c_2 . A specific fluid weighting factor φ was proposed to be applied to a value of the heat transfer coefficient (h^*) for a special fluid j .

Nonlinearities in the cost equation were considered by Linnhoff and Ahmad [20] and Ahmad et al. [23], to minimize the total area and the number of heat exchangers in the HEN. Caputo et al. [6] included pumping costs in the annual energy expenses in the total cost

calculation.

Considering the total annualized cost (TAC), from the earlier works (decades of 1990 to 2020), with emphasis on very few works, such as those by Short et al. [33], Kazi et al. [34], which brought very relevant contributions, only minor modifications to existing models were presented. It is very important not to use cost indices overtime periods of more than a few years. Some of these parameters have been in use for almost 40 years. Caputo et al. [6] presented a more accurate costing approach to be used during the design phase, considering the heat exchangers' cost in the optimization model. An analytical cost estimation procedure for STHE was developed, based on the detailed geometric characteristics and steps of the equipment manufacturing process. It was developed for TEMA (2007) standards, with one tube pass. The STHE configurations obtained according to the proposed costing procedure are cheaper than the optimal configurations obtained using traditional calculation methods. The manufacturing cost of the heat exchanger (C_E) is calculated by the sum of the materials and processing cost (C_M) of their main subassembly process, along with their main processing operations.

Short et al. [33] entails the use of correction factors to get networks that are based on shortcut models, such as the mixed integer non-linear programming (MINLP) stage-wise superstructure (SWS) of Yee and Grossmann [1]. The authors then, modify the objective function to include the correction factors that force its objective function towards the cost of a network whose individual heat exchangers are designed using methods such as Bell-Delaware, and heuristics. The correction factors account for pressure drops, Ft correction factors, number of shells, TEMA considerations, and changes to the overall heat transfer coefficient of each stream match.

In the work of Kazi et al. [34] the authors present a coupled differential algebraic equations (DAE) system, which is suitable for numerical optimization as replaces the nonsmooth log mean temperature difference (LMTD) term. For the costing approach, they used the resulting heat exchanger topology to discretize the detailed DAE model, which is solved as an NLP to obtain the detailed heat exchanger design by minimizing an economic objective function through varying the tube length. Then Kazi et al. [35] proposed a strategy to use a multistep approach by first obtaining a heat exchanger network topology through solving a modified version of the MINLP stage-wise superstructure of Yee and Grossmann [1], which includes a smoothed LMTD approximation and pressure drops. The NLPs are based on the detailed discretized optimization models of Kazi et al. [34]. These models solve a differential algebraic equation system and do not rely on usual assumptions associated with other heuristic-based exchanger design methods, such as, log mean temperature difference and FT correction factors.

Methodology

In the present paper, a modification in the capital cost used for the HEN synthesis given by Eq. (2) is proposed, considering that, in the majority part of the literature, the cost coefficient b is constant and multiplies the HEN total area. The cost coefficient b was considered depending on the internal shell diameter (D_s) of each heat exchanger. Eq. (3) is used to calculate the base cost β of each STHE presented in the HEN and is Eq. (4) adapted to Eq. (7) to calculate the cost coefficient b considering all cost correction factors of each heat exchanger. The escalation index is used to update the cost estimation values, like in the work of Vengateson [36].

Model formulation

According to the proposed approach, two optimization problems are solved in a bi-level approach: the HEN synthesis, in the outer level, and the detailed design of each one of the network heat exchangers, in the inner level. For the TAC calculation, the operating cost values found in the optimization problem proposed by Yee and Grossmann [1] (the

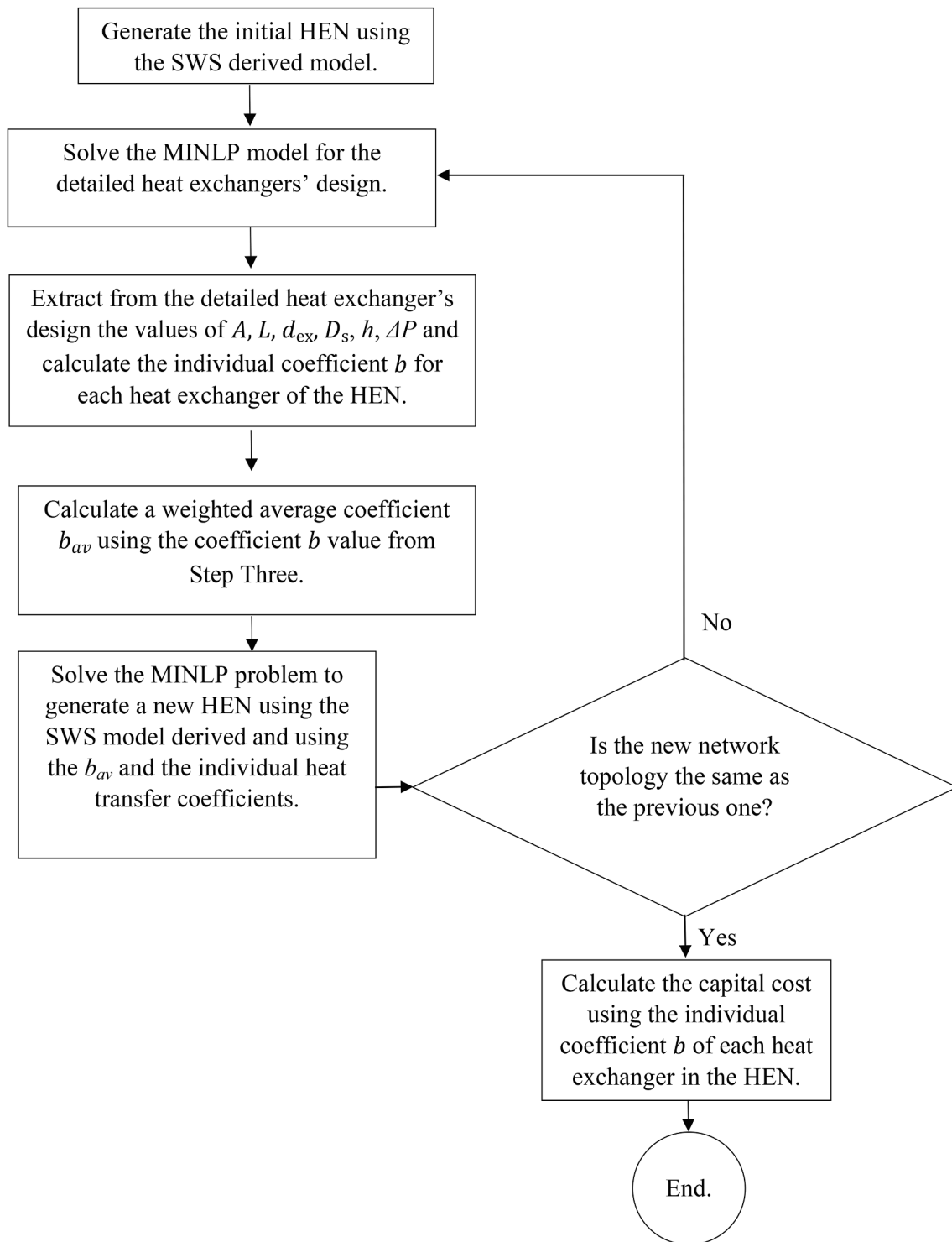


Fig. 1. Developed algorithm for the minimum global cost using variable coefficient b .

complete model formulation is presented in Appendix A) and the pumping costs used in the model of Ravagnani and Caballero [11] (the complete formulation is presented in Appendix B) are used. The capital cost (Fcc) is given by:

$$Fcc = a(n + m) + \left(\sum_{i=1}^n b_i A_i^c + N_{cost_{mh}} \sum_{j=1}^m A u h_j^c + N_{cost_{mc}} \sum_{j=1}^m A u c_j^c \right) \quad (6)$$

In this equation, a and c are constant cost coefficients, and b_i is calculated for each heat exchanger. Besides, n is the number of heat

exchangers; m is the number of hot and cold process utility heat exchangers; $N_{cost_{mh}}$ is the cost coefficient of hot utility heat exchange area, and $N_{cost_{mc}}$ is the cost coefficient for the cold utility heat exchange area; A_i is the heat exchanger area; $A u h_j$ is the heater area, and $A u c_j$ is the cooler area. The coefficient b_i is calculated using the Purohit [25] equation, given by:

$$b_i = \beta_i (1 + C T_i),$$

where β is the cost baseline from Purohit [25] given by Equation (3) and

CT represents the sum of all base price cost corrections for alternatives of different designs of heat exchangers in the HEN, given by:

$$CT_i = C_{s_i} + C_{x_i} + C_{L_i} + C_{Ntp_i} + C_{ps_i} + C_{pt_i} + C_{mt_i} + C_{ms_i} + C_{mc_i} + C_{mts_i} + C_{g_i}. \quad (8)$$

In Eq. (8), C_{s_i} is the cost correction for the shell type. The base price calculated by Eq. (3) must be adjusted using Table I from Purohit [25] (see Appendix C). C_{x_i} is the cost correction factor for the expansion joints. The cases considered are flanged-and-flued (FF), bellows (BL), and no expansion joints (NO). The cost correction for tube length (C_{L_i}) might be different for each heat exchanger in the HEN, as considered variable in the work of Kazi et al. [34], and it is given by:

$$C_{L_i} = \left[1 - \frac{L_i}{20} \right] \left[1.5 - \frac{0.002083(D_{s_i} - 12)}{1 - (L_i/20)} \right] \quad (9)$$

In which C_{Ntp_i} is the correction factor for the number of tube passes, given by:

$$C_{Ntp_i} = \frac{(N_{tp_i} - 1)}{100}, \quad (10)$$

where C_{ps_i} and C_{pt_i} are the correction factors for the design pressure in the shell side and the tube side, given by:

$$C_{ps_i} = [(P_{ds}/150) - 1][0.07 + 0.0016(D_{s_i} - 12)] + X. \quad (11)$$

In this equation, X is an adjustment factor for pressures over 2000 psi (1.379×10^7 Pa).

$$C_{pt_i} = [(P_{dt}/150) - 1][0.035 + 0.00056(D_{s_i} - 12)] \quad (12)$$

C_{mt_i} is the cost correction factor for the tube material, given by:

$$C_{mt_i} = y(M_1 - 1), \quad (13)$$

and y is calculated by:

$$y = 0.129 + 0.0016(D_{s_i} - 12) \left[\frac{d_{ex}(pt_i)^2 \alpha}{0.75} \right], \quad (14)$$

where d_{ex} is the tube external diameter, pt_i is the tube pitch, and α is the layout angle factor ($\alpha = 0.85$ for 30 or 60°, and $\alpha = 1.0$ for 45 or 90°). M_1 is the ratio of tubing cost (welded or seamless) relative to welded carbon steel tubes (i.e. for welded carbon steel tubes $C_{mt_i} = 0$). All ratios for different materials can be found in Purohit [25]. C_{ms_i} , C_{mc_i} , and C_{mts_i} are the cost correction factors for the shell, channel, and tube sheet material, respectively, and are given by:

$$C_{ms_i} = 0.1(M_2 - 1) \quad (15)$$

$$C_{mc_i} = 0.06(M_2 - 1) \quad (16)$$

$$C_{mts_i} = 0.04(M_2 - 1) \quad (17)$$

where M_2 is the relative cost of plate materials to the carbon steel plate, also found in Purohit [25].

The STHE type chosen for the evaluation of the approach in the case studies is the BFM, and only single STHEs are considered. The values for the configuration used in this work are $p = 1$, $f = 1$, and $r = 0.8$, extracted from Table 2. Besides, the definitions of the baseline are the same as the ones defined by Purohit [25]: Tube Welded 14 BWG, 1 tube pass, operating pressures lower than 10.34×10^5 Pa (150 psig), STHE built-in carbon steel, and tube length varying according to the detailed design of each heat exchanger in the HEN.

The objective function to be minimized is the TAC, given by the sum of the operating costs, the capital costs calculated using the average b_{av} , which is a weighted average coefficient, and the pumping costs:

$$TAC = \sum_{i,j \in HP, CP} Oper_{cost} + \sum_{i,j \in Gi,j} Fcc_{avcost} + Pump_{cost}. \quad (18)$$

where HP is the set of hot streams, CP is the set of cold streams and G is the set of allowed matches between streams i and j .

In this way, the optimization problem can be defined as the minimization of TAC, subject to the set of equations and inequalities (A.2 to A.6), and the set of equations and inequalities (B.1 to B.64).

Problem statement

The problem can be formulated as follows:

Given a particular group of hot and cold streams with their inlet and outlet temperatures, flow rates and physical properties, pressure drops, temperatures, and costs of hot and cold utilities, the goal is to find the HEN with the minimum TAC, including area, utilities, and pumping costs, considering the coefficient b for the capital cost depending on the detailed design of each one of the heat exchangers belonging to the network.

The HEN synthesis and the detailed design of the heat exchangers problems are solved simultaneously, in a bi-level approach. At the outer level, for the HEN synthesis, the stagewise superstructure (SWS) of Yee and Grossmann [1] is used to generate an MINLP formulation model. In the inner level, for the detailed design of the heat exchangers, the model proposed by Ravagnani and Caballero [11] is used and this optimization problem also has an MINLP formulation, using the Bell-Delaware method for the shell side calculations. After each heat exchanger is designed, the cost coefficients (b) are obtained, and the overall cost of the network is calculated. Fig. 1 presents the algorithm that proceeds to find the minimum TAC. The algorithm is formulated in four steps:

Step One: Solve the MINLP problem derived from the SWS of Yee and Grossmann [1] starting from a fixed coefficient (b) chosen for the entire network to generate the initial HEN configuration.

Step Two: Solve the MINLP problems proposed by Ravagnani and Caballero [11] for each one of the heat exchangers in the network generated in Step One.

Step Three: Extract from the detailed heat exchangers design, the heat exchanger area (A), the tube length (L), tube external diameter (d_{ex}), and the internal shell diameter (D_s), individual heat transfer coefficients (h), and pressure drop (ΔP) and calculate the coefficient b using Eq. (4).

Step Four: Calculate the streams' individual heat transfer coefficients as in Ravagnani and Caballero [11].

Step Five: Using the coefficient b values calculated in Step Three, a weighted average coefficient b_{av} must be calculated for the HEN, considering the different heat exchanger areas.

Step Six: With the coefficient b_{av} , from Step Five, and the individual heat transfer coefficients from Step Four, synthesize a new HEN as in Step One.

Step Seven: If the same network topology is found, the final TAC is calculated using the individual coefficient b of each heat exchanger in the HEN, and the algorithm stops. If the network topology is different, then run the algorithm again until the same topology is found. Fig. 1 illustrates the algorithm developed.

Case studies

To illustrate the potential applicability of the developed algorithm considering a different coefficient b for each one of the STHE, two case studies from the literature were used. Both examples were solved in GAMS 31.2 and CPLEX 12.10 and DICOPT 2 solvers were used. The SWS model has 45 continuous variables, 8 integer variables, and 45 constraints for Case 1. For case 2 the SWS model has 142 continuous variables, 33 integer variables, and 154 constraints. The absolute gap value of 0.00 was presented in the solver, with 224 iterations. The results obtained for the HENs Synthesis were at 0.204 s for Case 1, and 0.266 s for Case 2 for the last iteration. The detailed heat exchanger designs the model has 733 continuous variables, 619 integer variables, and 164

Table 3

Streams and utility data for case 1.

Stream	$T_{in}(K)$	$T_{out}(K)$	$m(kg/s)$	$\mu(kg/ms)$	$\rho(kg/m^3)$	$C_p(J/kgK)$	$k(W/mK)$	$\Delta P(kPa)$	$r_d(W/mK)$	Cost(\$/kWyear)
S1	368	348	8.15	2.4E-4	634	2454	0.114	68.95	1.7E-4	
S2	353	348	81.50	2.4E-4	634	2454	0.114	68.95	1.7E-4	
S3	303	363	16.30	2.4E-4	634	2454	0.114	68.95	1.7E-4	
S4	333	343	20.40	2.4E-4	634	2454	0.114	68.95	1.7E-4	
HU	500	500								60
CU	300	320								6

Area cost = $1000 + 60A^{0.6}$, A in m^2 . Pumping cost = $0.7(\Delta P^t m^t / \rho^t + \Delta P^s m^s / \rho^s)$, ΔP in Pa, m in kg/s and ρ in kg/m^3 . Overall heat transfer coefficients = $444 W/m^2K$.

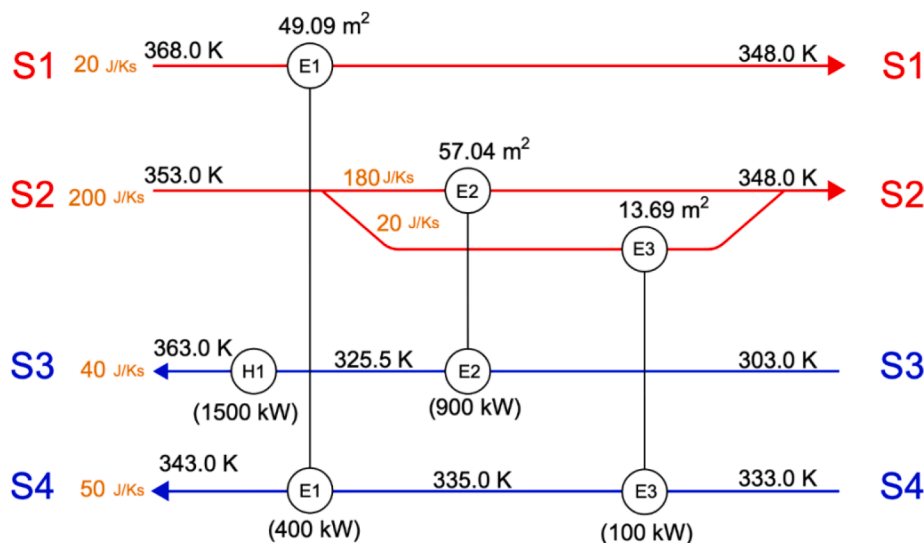


Fig. 2. Initial HEN topology for Case 1.

Table 4

Detailed design of heat exchangers for Case Study 1.

Parameters	E1	E2	E3
Area (m^2)	52.673	64.491	11.673
Q (kW)	400	900	100
LMTD (K)	18.35	35.74	14.23
D_s (m)	0.489	0.591	0.305
D_{out} (m)	0.457	0.546	0.260
d_{ex} (mm)	19.05	19.00	19.00
d_{in} (mm)	17.00	17.00	17.00
pt (mm)	24.00	24.00	25.00
L (m)	3.655	2.438	2.438
h_t (W/m^2C)	1602.279	1138.391	1299.421
h_s (W/m^2C)	1275.438	952.240	1058.382
ΔP_t (kPa)	8.70	2.89	1.76
ΔP_s (kPa)	2.12	0.48	1.15
b	30.19	24.24	65.61

constraints, and the results were at an average of 0.427 s for both cases in the last iteration on a Core i5 7200U computer.

The STHE type chosen for the evaluation of the approach in the case studies is the BFM, and only single STHEs are considered. Therefore, the design operating parameters from the detailed STHE design used to solve Case one and Case two problems are the inside shell diameter, the heat transfer area, the tube length, the individual heat transfer

coefficients, and the pressure drops.

Case Study 1

The first case study was extracted from Ravagnani and Caballero [14] and has two hot and two cold streams, a hot utility, and a cold utility. Table 3 presents streams and utility data.

Using the proposed algorithm, in the first step, a HEN topology is generated using the SWS [1] derived model and it is presented in Fig. 2, with three heat exchangers and one heater. The value used for the exchanger minimum approach temperature used was 10 K.

The Area values and pressure drops were used to calculate the HEN TAC considering the fixed b value of 60 for the HEN, the same as in the case study from Ravagnani and Caballero [14]. Also, as an initial estimate, overall heat transfer coefficients are assumed to be $444 W/m^2K$, for stream-stream and stream-utility matches. The value obtained was 95986.40 \$/year. In algorithm Step 2, for this HEN, each heat exchanger is detailed designed using the MINLP model proposed by Ravagnani and Caballero [11]. The results for the detailed equipment design and the values for coefficient b are presented in Table 4.

With the values for the area (Area) and the internal diameter of the shell (D_s), the cost coefficient b is calculated for each one of the heat exchangers, and these values are presented in Table 4. The weighted coefficient b_{av} is calculated using the coefficient b values of each

Table 5

Escalation index.

Cost parameter	Calculated weighted coefficient	1982 index	2003 index	Escalation index (E_i)	Escalated weighted coefficient
Indexes		314.0	401.7	1.27	
b_{av}	30.42				38.63

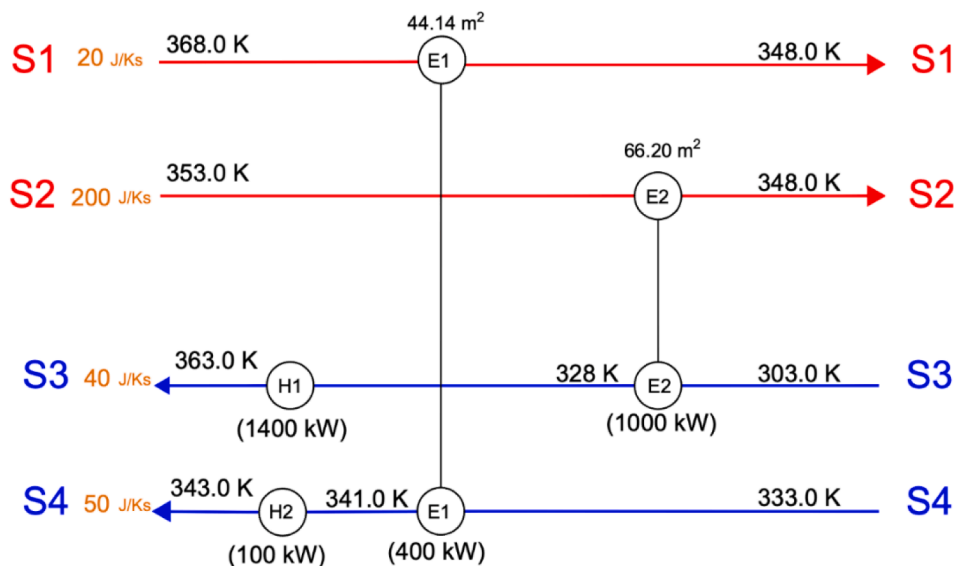


Fig. 3. New HEN generated for Case 1.

Table 6

Detailed design of heat exchangers for Case Study 1 HEN 2.

Parameters	E1	E2
Area (m ²)	35.89	57.05
Q (kW)	400	1000
LMTD (K)	20.41	33.43
D _s (m)	0.533	0.635
D _{out} (m)	0.489	0.594
d _{ex} (mm)	19.04	19.04
d _{in} (mm)	17.00	17.00
pt (mm)	25	25
L (m)	2.438	2.438
h _t (W/m ² ·C)	1465.281	1264.464
h _s (W/m ² ·C)	1251.183	1015.045
ΔP _t (kPa)	2.15	0.91
ΔP _s (kPa)	3.92	0.74
B	27.20	22.50
Hot end temperature difference (K)	27	25
Cold end temperature difference (K)	15	45

exchanger and their respective areas.

All parameters of cost coefficient b were calculated using the base price of 1982 extracted from Purohit [25]. The current base price of the cost coefficients can be updated using an escalation index (E_i) by multiplying the year of reference for the base price by the ratio of the values of the fabricated equipment components on both dates.

As the data used by Ravagnani and Caballero [14] were extracted from Mizutani et al. [13] the data need to be escalated to the year 2003 for comparison of results. The reason for choosing Ravagnani and Caballero [14] over Mizutani et al. [13], is because the first authors considered stream splitting, thus having more accurate results. Table 5 illustrates the escalation index for the weighted coefficient b_{av} .

A new HEN is synthesized, with different topology, and is presented in Fig. 3. This new topology has two heat exchangers and two heaters, and the minimum TAC found was \$ 94558.25. This new HEN configuration has a TAC lower than the previously reported in the literature and presents a more realistic result for the case studied. Besides, the new HEN has no streams splitting, which will influence less on piping, therefore, having a simpler operation.

As this HEN has a different topology, according to the proposed algorithm, a new HEN must be generated. The next step is to go back to the algorithm Step 2, for this HEN and each heat exchanger must be, again, detailed designed. The results for the new detailed equipment design and the values for coefficient b are presented in Table 6.

Table 7

Evolution of the algorithm.

Costs (\$/year)	Ravagnani and Caballero [14]	Iteration 1	Iteration 2	Final Solution
Operational cost	90000.00	90000.00	90000.00	90000.00
Capital cost	5844.09	4391.22	4391.58	4780.89
Pumping cost	169.56	177.23	166.67	166.67
TAC	96013.65	94568.45	94558.25	94947.56

With the values for the heat exchanger areas (Area) and the internal shell diameters (D_s), the cost coefficient b is calculated for each one of the heat exchangers. With the detailed design of the heat exchangers, it was possible to calculate a more accurate coefficient b_{av} using the area of the different heat exchangers. The calculated value was 24.32. Using the escalation index ($E_i = 1.27$) to update from 1982 to 2003 the escalated weighted coefficient b_{av} was 30.89. With the value of the escalated weighted coefficient b_{av} a new HEN is synthesized.

Now, it has the same topology as the previous one shown in Fig. 3. Therefore, the algorithm can stop, and the TAC can be calculated using the individual coefficient b of each STHE in the HEN to find the final solution.

The minimum TAC for iteration 2 was \$ 94558.25. Table 7 presents the evolution of the algorithm for this case study. TAC is 1.12 % lower than the reported solution in the literature.

Case Study 2

This case study was also extracted from Ravagnani and Caballero [14]. The problem has three hot streams and three cold streams, a hot utility and a cold utility are available. Table 8 presents streams and utility data. The value used for the exchangers minimum approach temperature used was 10 K.

According to the proposed algorithm, an initial HEN topology is generated and is presented in Fig. 4, with seven heat exchangers and one heater.

The TAC value calculated was 60804.44 \$/year. In the algorithm Step 2, for this network structure, each heat exchanger must be detailed designed. Results are presented in Table 9.

With the values for the area (Area) and the internal diameter of the shell (D_s), tube length, the cost coefficient b is calculated for each one of the heat exchangers, and these values are also presented in Table 9. The

Table 8

Streams and utility data for Case Study 2.

Stream	S1	S2	S3	S4	S5	S6	HU	CU
T_{in} (K)	423	363	454	293	293	283	700	300
T_{out} (K)	333	333	433	398	373	288	700	320
m (kg/s)	16.3	65.2	32.6	20.4	24.4	65.2		
μ (kg/ms)	2.4E-4	2.4E-4	2.4E-4	2.4E-4	2.4E-4	2.4E-4		
ρ (kg/m ³)	634	634	634	634	634	634		
cp (J/kgK)	2454	2454	2454	2454	2454	2454		
k (W/mK)	0.114	0.114	0.114	0.114	0.114	0.114		
ΔP (kPa)	68.95	68.95	68.95	68.95	68.95	68.95		
r_d (W/mK)	1.7E-4	1.7E-4	1.7E-4	1.7E-4	1.7E-4	1.7E-4		
cost (\$/kWyear)							60	6

Area cost = $1000 + 60A^{0.6}$, A in m². Pumping cost = $0.7(\Delta P^I m^I / \rho^I + \Delta P^S m^S / \rho^S)$, ΔP in Pa, m in kg/s and ρ in kg/m³. Initial overall heat transfer coefficients = 444 W/m²K.

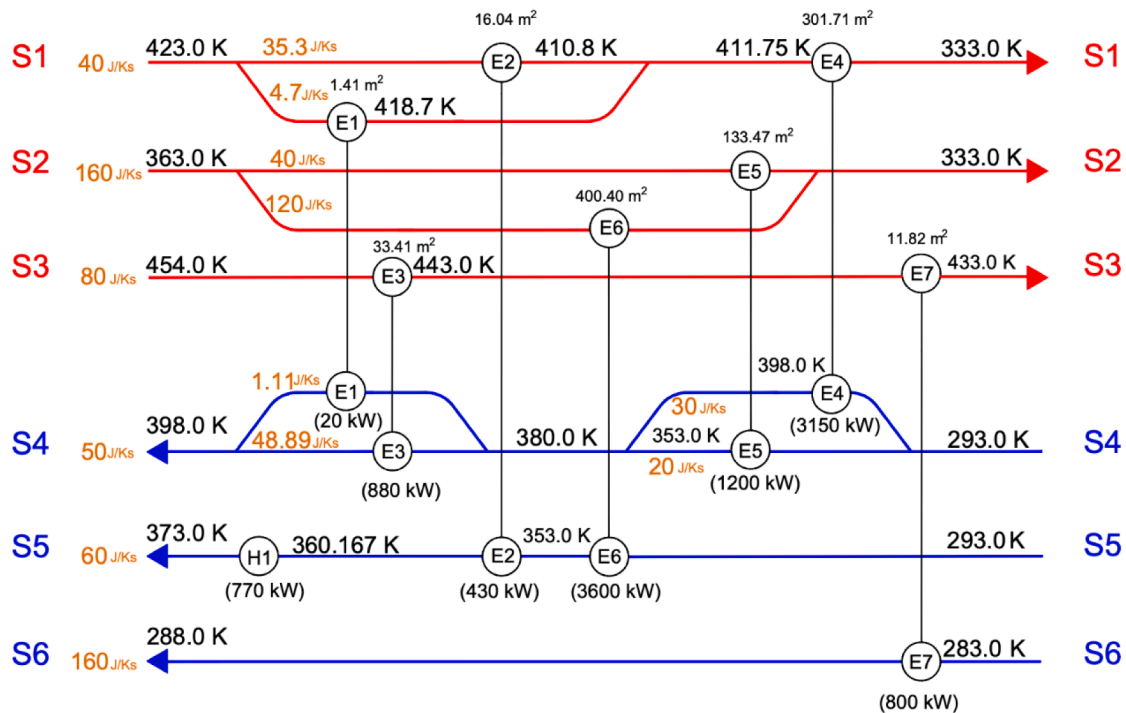


Fig. 4. Initial HEN for Case 2.

Table 9

Detailed design of exchangers for Case Study 2- round 1.

Parameters	E1	E2	E3	E4	E5	E6	E7
Area (m ²)	2.335	11.673	33.072	275.718	105.953	362.005	33.072
Q (kW)	20	430	880	3150	1200	3600	800
MLTD (K)	34.16	60.17	59.43	24.58	21.64	21.64	152.48
D_s (m)	0.205	0.337	0.533	0.838	0.533	0.940	0.533
D_{out} (m)	0.173	0.305	0.489	0.796	0.489	0.895	0.489
d_{ex} (mm)	19	25	25	19	19	19	25
d_{in} (mm)	17	23	23	17	17	17	23
pt (mm)	25	32	32	25	25	25	32
L (m)	2.438	2.438	2.438	6.706	6.706	3.658	2.438
h_t (W/m ² °C)	1945.26	1413.69	814.23	1227.48	1515.21	1365.27	1207.51
h_c (W/m ² °C)	301.48	965.23	1395.89	702.91	1210.86	143.97	1120.92
ΔP_t (kPa)	2.51	0.39	1.83	9.84	9.80	6.24	1.47
ΔP_s (kPa)	0.32	0.85	1.08	2.52	3.58	1.36	0.62
b	286.57	53.46	27.20	10.52	16.41	16.12	35.03

weighted coefficient b_{av} is calculated using the coefficient b values of each exchanger and their respective areas.

Just as in Case Study 1, in Case Study 2, the data used by Ravagnani and Caballero [14] were extracted from Mizutani [13], and the data was

also escalated to the year 2003 for comparison of the results with the literature. The calculated value of b_{av} is 16.78. Using the escalation index ($E_i = 1.27$) to update from 1982 to 2003, the escalated weighted coefficient b_{av} was 21.31 with the value of the weighted coefficient b_{av} .

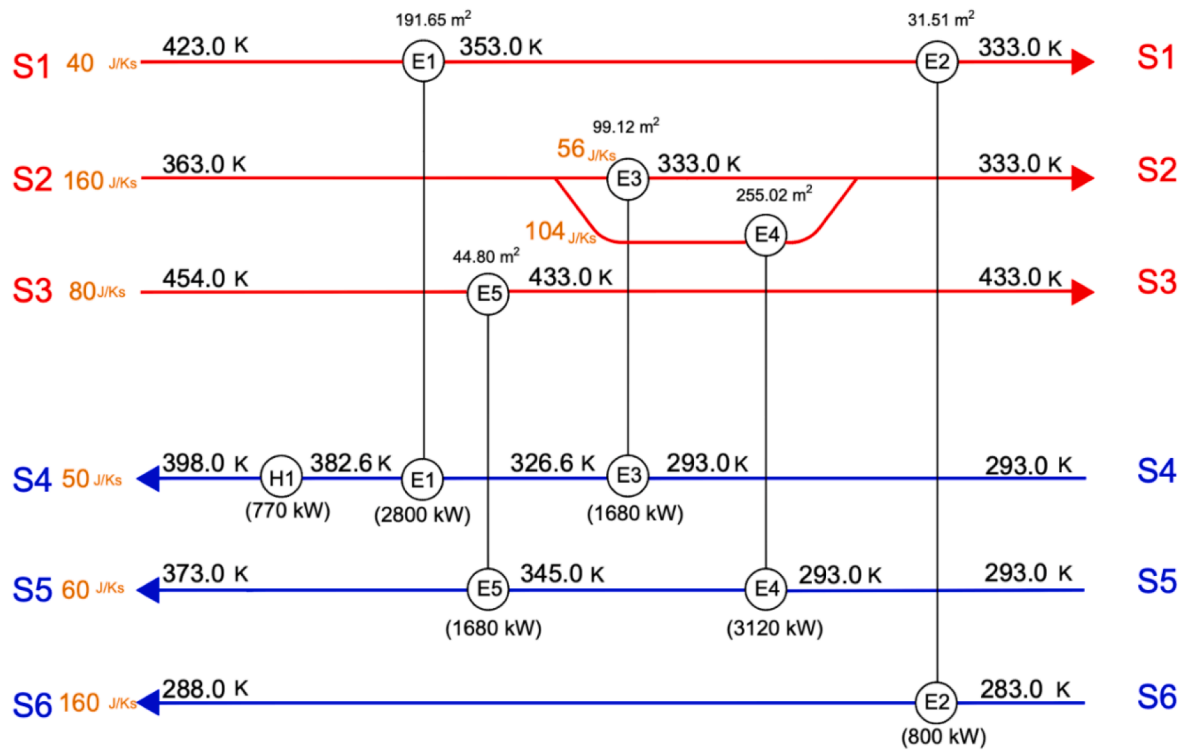


Fig. 5. New HEN with weighted mean b for Case 2.

Table 10

Detailed design of exchangers for Case Study 2- round 2.

Parameters	E1	E2	E3	E4	E5
Area (m ²)	168.561	40.271	80.833	242.407	40.271
Q (kW)	2800	800	1680	3120	1680
MLTD (K)	32.90	57.17	38.17	26.75	84.37
D _s (m)	0.591	0.533	0.737	0.737	0.533
D _{out} (m)	0.546	0.489	0.659	0.659	0.489
d _{ex} (mm)	19	19	19	19	19
d _{in} (mm)	17	17	17	17	17
pt (mm)	24	25	25	25	25
L (m)	6.076	2.438	2.438	6.706	2.438
h _t (W/m ² ·C)	1045.10	839.58	1458.05	1079.17	1462.29
h _s (W/m ² ·C)	928165.25	1172833.43	92397.96	728112.74	443135.29
ΔP _t (kPa)	2.57	0.38	1.36	2.76	1.36
ΔP _s (kPa)	0.19	1.16	0.02	0.16	0.26
B	14.60	27.20	19.56	11.74	27.20
Cold end temperature difference (K)	26.4	50	40	40	88
Hot end temperature difference (K)	40.4	65	36.4	18	81

A new HEN is synthesized with a weighted average coefficient b and is presented in Fig. 5, with a TAC of \$ 53633.11. This value is lower and better than the previous one, calculated with a fixed b coefficient.

The new HEN has a different topology, and according to the proposed algorithm, a new HEN must be generated. The next step is to go back to the algorithm Step 2, for this HEN and each heat exchanger must be detailed designed. The results for the new detailed equipment design and the values for coefficient b are presented in Table 10.

With the values for the area (Area) and the internal diameter of the shell (D_s), the cost coefficient b is calculated for each one of the heat exchangers, and these values are presented in Table 10. The weighted coefficient b_{av} is calculated using the coefficient b values of each exchanger and their respective areas.

The calculated value of b_{av} is 15.86. Using the escalation index (E_i = 1.27) to update from 1982 to 2003, the escalated weighted coefficient b_{av} was 20.14 with the value of the weighted coefficient b_{av}. A new HEN is synthesized with a weighted average coefficient b, with a TAC of \$

Table 12

Evolution of the algorithm for Case Study 2.

Costs (\$/year)	Ravagnani and Caballero [14] HENHHENHEN	Iteration 1	Iteration 2	Final Solution Solution
Operational cost	46200.00	46200.00	46200.00	46200.00
Capital cost	20887.57	6193.69	6183.78	6784.50
Pumping cost	2077.91	1239.42	300.430	300.43
TAC	69165.48	53633.11	52684.21	53284.93

52684.21. This value is lower and better than the previous one, calculated with a fixed b coefficient.

As the new HEN topology is the same as in the previous step, the algorithm stops, and the TAC is now calculated using the individual coefficient b of each STHE in the HEN to find the best solution. The final value obtained for Case 2 is 23% lower than the solution found in the

Table 13
Escalated TAC.

	Calculated TAC ((\$/year)	2003 index	2020 index	Escalation index (E _i)	Escalated TAC
Index data		401.7	593.6	1.48	
Case 1	94947.56				140522.38
Case 2	53284.93				78861.70

Table 14
Definition of baseline shell and tube exchanger.

Parameter	Base designation
Tubes	Welded c.s., 14 BWG, avg wall
Nominal tube length	20 ft
Number of tube passes	1 or 2
Shellside design pressure, psig	≤ 150
Tubeside design pressure, psig	≤ 150
Material of construction	All carbon steel

literature. The evolution of Capital Cost and TAC are presented in Table 12.

The TAC for the case studies 1 and 2 calculated and compared to the literature had used the base price of cost coefficients from the year 2003 as already discussed before in this paper. The TAC values found in this work can be updated to the year 2020 by using the escalation index (E_i). Table 13 shows the updated TAC values for cases 1 and 2. Table 14.

The use of the escalation index was important in this approach so that the values of parameter b could be updated, and the essence of the equation used as the basis Eq. (3) could show the most realistic values and the comparison with the literature works could be performed in a coherent way.

Conclusions

In the present work, a new approach is proposed for the synthesis of shell and tube heat exchanger networks including the detailed sizing of each one of the heat exchangers in which the capital cost function coefficient b depends on the specifications of each heat exchanger. Two

Appendix A

Problem Formulation

The optimization problem focuses on minimizing the objective function given by:

$$Min_{cost} = \sum_{i \in HP} C_{CU} Q_{CU,i} + \sum_{j \in CP} C_{HU} Q_{HU,j} + a \left(\sum_{(i,j) \in Gi_j} n_{i,j} + \sum_{(i,j) \in Gi_j} m_{i,j} \right) + \left(\sum_{i=1}^n b_{av} A_i^c + B \sum_{j=1}^m A_{uh_j}^c + C_{mc} \sum_{j=1}^m A_{uc_j}^c \right) + p_{cost} \sum_{i,j=1}^n \left(\Delta P_i \frac{m_{t_i}}{\rho_{t_i}} + \Delta P_{s_j} \frac{m_{s_j}}{\rho_{s_j}} \right) \quad (A.1)$$

Subject to:

Overall energy balance for each stream:

$$(TIN_i - TOUT_i) C_{p_i} = \sum_{k \in ST_j \in CP} q_{ijk} + q_{cu,i} \quad i \in HP$$

$$(TIN_j - TOUT_j) C_{p_j} = \sum_{k \in ST_i \in HP} q_{ijk} + q_{hu,j} \quad j \in CP. \quad (A.2)$$

Energy balance for each interval:

$$(t_{i,k} - t_{i,k+1}) F_i = \sum_{j \in CP} q_{ijk}, \quad k \in ST_i \in HP,$$

$$(t_{j,k} - t_{j,k+1}) F_j = \sum_{i \in HP} q_{ijk}, \quad k \in ST_j \in CP. \quad (A.3)$$

Logical constraints:

$$q_{ijk} - \Omega_{z_{ijk}} \leq 0, \quad i \in HP,$$

literature cases, one with four and the other with six process streams were used to test the applicability of the developed model. Results showed that considering the coefficient b different for each exchanger, different capital costs were obtained for the studied networks. More realistic values were obtained in comparison to the capital costs of HEN configurations considering the fixed-parameter b for all heat exchangers in the network.

The HEN costs were lower than those previously reported in the literature, because, with the detailed design of the individual heat exchangers, more accurate costing parameters were obtained.

The fixed value for all equipment in the capital cost function for parameter b, in the cases, studied, indicating an overestimation of the cost related to the area.

Since many methods in the literature have been used by other authors to correct the areas of the exchangers in the HEN, the major contribution in this work is that the costs were overestimated. So, the proposed approach showed that the use of a fixed parameter for all the heat exchangers in the network can change the trade-off between energy and capital and, in turn, can lead to changes in the network topology.

CRediT authorship contribution statement

Syntia L. Cotrim: Conceptualization, Methodology, Software, Writing - original draft. **Edwin V.C. Galdamez:** Visualization, Supervision, Writing - review & editing. **Kennedy B. Matos:** Software, Writing - review & editing. **Mauro A.S.S. Ravagnani:** Supervision, Methodology, Writing - review & editing.

Declaration of Competing Interest

The authors declare that they have no known competing financial interests or personal relationships that could have appeared to influence the work reported in this paper.

Acknowledgment

The authors acknowledge the National Council for Scientific and Technological Development – CNPq (Brazil), processes 311807/2018-6, 428650/2018-0, and 140127/2020-8.

$$qcu_i - \Omega zcu_i \leq 0, i \in HP,$$

$$qhu_j - \Omega zhu_j \leq 0, j \in CP,$$

$$z_{ijk}, zhu_j, zcu_i = 0, 1.$$

(A.4)

Where the upper limit correspondent Ω can be lowest energy exchange between two streams.

Heat exchangers design:

$$LMTD_{ij} = \frac{dT_{ij}^1 - dT_{ij}^2}{\ln \frac{dT_{ij}^1}{dT_{ij}^2}} \approx \text{Chen Approximation (A.5)}$$

$$Q_{ij} = U_{ij} A_{ij} LMTD_{ij}$$

(A.6)

Appendix B

Ravagnani and Caballero (2007) model for the detailed design of shell and tube heat exchangers.

Equations:

Definition of tube length (L):

$$L = 2.4385y_1^1 + 3.658y_2^1 + 4.877y_3^1 + 6.096y_4^1 + 6.706y_5^1 (B.1)$$

$$y_1^1 + y_2^1 + y_3^1 + y_4^1 + y_5^1 = 1 (B.2)$$

Definition of baffle spacing (l_s):

$$l_s \leq D_s (B.3)$$

$$l_s \geq \frac{D_s}{5} (B.4)$$

Definition of the flow regimen in the shell side:

$$Re_s = \frac{m_s d_{ex}}{\mu_s S_m} (B.5)$$

The shell side fluid velocity is given by:

$$v_s = \frac{m_s / \rho_s}{(D_s / \pi t)(\pi t - d_{ex}) l_s} (B.6)$$

The velocity limits must be:

$$0.5 \leq v_s \leq 2, v_s \text{ in m/s} (B.7)$$

Colburn factor (j_i) and Fanning factor (f_s) determination with a_1 - a_4 and b_1 - b_4 extracted from Ravagnani and Caballero¹¹

$$\sum_r \sum_s y_{r,s}^{\text{rearr}} A_{r,s}^{a_1} = a_1 (B.8)$$

$$\sum_r \sum_s y_{r,s}^{\text{rearr}} A_{r,s}^{a_2} = a_2 (B.9)$$

$$\sum_r y_r^{\text{arr}} A_r^{a_3} = a_3 (B.10)$$

$$\sum_r y_r^{\text{arr}} A_r^{a_4} = a_4 (B.11)$$

$$\sum_r \sum_s y_{r,s}^{\text{rearr}} A_{r,s}^{b_1} = b_1 (B.12)$$

$$\sum_r \sum_s y_{r,s}^{\text{rearr}} A_{r,s}^{b_2} = b_2 (B.13)$$

$$\sum_r y_r^{\text{arr}} A_r^{b_3} = b_3 (B.14)$$

$$\sum_r y_r^{\text{arr}} A_r^{b_4} = b_4 (B.15)$$

$$a = \frac{a_3}{1 + 0.14(Re_s)^{a_4}} (B.16)$$

$$ji = a_1 1.064^a (Re_s)^{a_2} (B.17)$$

$$b = \frac{b_3}{1 + 0.14(Re_s)^{b_4}} (B.18)$$

$$fl_s = b_1 1.064^b (Re_s)^{b_2} (B.19)$$

Number of baffles:

$$N_b = \frac{L}{l_s} - 1 (B.20)$$

$$N_c = \frac{D_s [1 - 2(l_c/D_s)]}{pp} (B.21)$$

$$l_c = 0.25D_s (B.22)$$

Fraction of total tubes in crossflow (F_c):

$$F_c = \frac{1}{\pi} [\pi + 2\lambda \sin(\arccos(\lambda)) - 2\arccos(\lambda)] (B.23)$$

where

$$\lambda = \frac{D_s - 2l_c}{D_{otl}} (B.24)$$

Number of effective cross-flow tube rows in each window (N_{cw}):

$$N_{cw} = \frac{0.8l_c}{pp} (B.25)$$

The fraction of cross-flow area available for bypass flow (F_{sbp}):

$$F_{sbp} = \frac{l_s [D_s - D_{otl}]}{S_m} (B.26)$$

Shell-to-baffle leakage area for one baffle (S_{sb}):

$$S_{sb} = \frac{D_s \delta_{sb}}{2} \left[\pi - \arccos \left(1 - \frac{2l_c}{D_s} \right) \right] (B.27)$$

where

$$\delta_{sb} = \left(\frac{3.1 + 0.004(D_s \times 1000)}{1000} \right) (B.28)$$

Tube-to-baffle leakage area for one baffle (S_{tb}):

$$S_{tb} (m^2) = 0.0006223 d_{ex} N_t (1 - F_c) (B.29)$$

Area for flow-through window (S_w):

$$S_w = S_{wg} - S_{wt} (B.30)$$

where

$$S_{wg} = \frac{(D_s)^2}{4} \left[\arccos \left(1 - 2 \frac{l_c}{D_s} \right) - \left(1 - 2 \frac{l_c}{D_s} \right) \sqrt{1 - \left(1 - 2 \frac{l_c}{D_s} \right)^2} \right] (B.31)$$

and

$$S_{wt} = \left(\frac{N_t}{8} \right) (1 - F_c) \pi (D_s)^2 (B.32)$$

Shell-side heat transfer coefficient for an ideal tube bank (h_{oi}):

$$h_{oi} = \frac{ji C_{p_s} m^s}{S_m} \left(\frac{k_s}{C_{p_s} \mu_s} \right)^{2/3} (B.33)$$

Correction factor for baffle configuration effects (J_c):

$$J_c = F_c + 0.54(1 - F_c)^{0.345} (B.34)$$

Correction factor for baffle-leakage effects (J_l):

$$J_l = \alpha + (1 - \alpha) \exp \left(-2.2 \frac{S_{sb} + S_{tb}}{S_m} \right) (B.35)$$

where

$$\alpha = 0.44 \left(1 - \frac{S_{sb}}{S_{sb} + S_{tb}} \right) (B.36)$$

Correction factor for bundle-bypassing effects (J_b):

$$J_b = \exp(-0.3833 F_{sbp}) (B.37)$$

Shell-side heat transfer coefficient (h_s):

$$h_s = h_{oi} J_c J_l J_b (B.38)$$

Pressure drops for an ideal cross-flow section (ΔP_{bi}):

$$\Delta P_{bi} = \frac{2 f l_s N_c (m_s)^2}{\rho_s S m^2} (B.39)$$

Pressure drop for an ideal window section (ΔP_{wi}):

$$\Delta P_{wi} = (2 + 0.6 N_{cw}) \frac{(m_s)^2}{2 S_w \rho_s S_m} (B.40)$$

Correction factor for the effect of baffle leakage on pressure drop (R_l):

$$R_l = \exp \left[-1.33 \left(1 + \frac{S_{sb}}{S_{sb} + S_{tb}} \right) \left(\frac{S_{sb} + S_{tb}}{S_m} \right)^k \right] (B.41)$$

where

$$k = -0.15 \left(1 + \frac{S_{sb}}{S_{sb} + S_{tb}} \right) + 0.8 (B.42)$$

Correction factor for bundle bypass (R_b):

$$R_b = \exp[-1.3456 F_{sbp}] (B.43)$$

The pressure drop across the shell-side (ΔP_s):

$$\Delta P_s = 2 \Delta P_{bi} \left(1 + \frac{N_{cw}}{N_c} \right) R_b + (N_b + 1) \Delta P_{bi} R_b R_l + N_b \Delta P_{wi} R_l (B.44)$$

Pressure drop limit, fixed before the design:

$$\Delta P_s \leq \Delta P_{s \text{ design}} (B.45)$$

Tube-side Reynolds number (Re_t):

$$Re_t = \frac{4 m_t N_p}{\pi d_{in} \mu_t N_t} (B.46)$$

Friction factor for the tube-side (f_l):

$$\frac{1}{\sqrt{f_l}} = -4 \log \left[\frac{0.27 \varepsilon}{d_{ex}} + \left(\frac{7}{Re_t} \right)^{0.9} \right] (B.47)$$

where ε is the roughness in mm.

Prandtl number for the tube-side (Pr_t):

$$Pr_t = \frac{\mu_t C_{p_t}}{k_t} (B.48)$$

Nusselt number for tube-side (Nu_t):

$$Nu_t = 0.027 (Re_t)^{0.8} (Pr_t)^{1/3} (B.49)$$

Tube-side heat transfer coefficient (h_t):

$$h_t = \frac{Nu_t k_t d_{in}}{d_{in} d_{ex}} (B.50)$$

Tube-side velocity (v_t):

$$v_t = \frac{\mu_t Re_t}{\rho_t d_{in}} (B.51)$$

The velocity limits are:

$$1 \leq v_t \leq 3, v_t \text{ in m/s} (B.52)$$

Tube-side pressure drop (including head pressure drop):

$$\Delta P_t = \rho_t \left(\frac{2f L_t N_{tp} L (v_t)^2}{d_{in}} + 1.25 N_{tp} (v_t)^2 \right) \quad (B.53)$$

Pressure drop limit, fixed before the design:

$$\Delta P_t \leq \Delta P_{t,design} \quad (B.54)$$

Heat exchanged:

$$Q = m_t C_{pt} (THIN - THOUT)_t \text{ or } Q = m_t C_{pt} (TCIN - TCOU)_t \quad (B.55)$$

$$Q = m_s C_{ps} (THIN - THOUT)_s \text{ or } Q = m_s C_{ps} (TCIN - TCOU)_s \quad (B.56)$$

Heat exchange area:

$$A = N_t \pi d_{ex} L \quad (B.57)$$

LMTD:

$$t_1 = THOUT - TCIN \quad (B.58)$$

$$t_2 = THIN - TCOU \quad (B.59)$$

LMTD Chen approximation:

$$LMTD = \left[\frac{t_1 t_2 (t_1 + t_2)}{2} \right]^{1/3} \quad (B.60)$$

Dirty overall heat transfer coefficient (U_d):

$$U_d = \frac{Q}{\text{Area}(LMTD)} \quad (B.61)$$

Clean overall heat transfer coefficient (U_c):

$$U_c = \frac{1}{\left(d_{ex}/d_{in} h_t + r_{in} d_{ex}/d_{in} + \frac{d_{ex} \log(d_{ex}/d_{in})}{2k_{tubc} + r_{out} + 1/h_s} \right)} \quad (B.62)$$

Fouling factor calculation (r_d):

$$r_d = \frac{U_c - U_d}{U_c U_d} \quad (B.63)$$

$$r_d \geq r_{d,design} \quad (B.64)$$

References

- [1] T.F. Yee I.E. Grossmann Simultaneous Optimization Models for Heat Integration-II. Heat Exchanger Network Synthesis. Comput Chem Eng 14 10 1990 1165 1184 Doi: [https://doi.org/10.1016/0098-1354\(90\)85010-8](https://doi.org/10.1016/0098-1354(90)85010-8).
- [2] Pávao LV, Costa CBB, Ravagnani MASS. Automated heat exchanger network synthesis by using hybrid natural algorithms and parallel processing. Comp Chem Eng 2016;94:370–86. <https://doi.org/10.1016/j.compchemeng.2016.08.009>.
- [3] Pávao LV, Costa CBB, Ravagnani MADSS, Jiménez L. Large-scale heat exchanger networks synthesis using simulated annealing and the novel rocket fireworks optimization. AIChE J. 2017;63(5):1582–601. <https://doi.org/10.1002/aic.15524>.
- [4] Pávao LV, Costa CBB, Ravagnani MASS. Heat Exchanger Network Synthesis without stream splits using parallelized and simplified Simulated Annealing and Particle Swarm Optimization. Chem Eng Sci 2017;158:96–107. <https://doi.org/10.1016/j.ces.2016.09.030>.
- [5] Aguitoni MA, Pávao LV, Ravagnani MASS. Heat exchanger network synthesis combining Simulated Annealing and Differential Evolution. Energy. 2019;181: 654–64. <https://doi.org/10.1016/j.energy.2019.05.211>.
- [6] Caputo AC, Pelagagge PM, Salini P. Heat Exchanger Design Based on Economic Optimisation. Appl Therm Eng 2008;28(10):1151–9. <https://doi.org/10.1016/j.applthermaleng.2007.08.010>.
- [7] Duran O, Rodriguez N, Consalter LA. Neural Networks for Cost Estimation of Shell and Tube Heat Exchangers. Exp Syst Applic 2009;36(4):7435–40. <https://doi.org/10.1016/j.eswa.2008.09.014>.
- [8] Selbaş R, Kizilkan Ö, Reppich M. A New Design Approach for Shell-and-Tube Heat Exchangers Using Genetic Algorithms from Economic Point of View. Chem Eng Proces 2006;45(4):268–75. <https://doi.org/10.1016/j.cep.2005.07.004>.
- [9] Asadi M, Song Y, Sunden B, Xie G. Economic Optimization Design of Shell-and-Tube Heat Exchangers by a Cuckoo-Search-Algorithm. Appl Therm Eng 2014;73 (1):1032–40. <https://doi.org/10.1016/j.applthermaleng.2014.08.061>.
- [10] Yang J, Fan A, Liu W, Jacobi AM. Optimization of Shell-and-Tube Heat Exchangers Conforming to TEMA Standards with Designs Motivated by Constructal Theory. Energy Convers Manage 2014;78:468–76. <https://doi.org/10.1016/j.enconman.2013.11.008>.
- [11] Ravagnani MASS, Caballero JA. A MINLP Model For The Rigorous Design Of Shell And Tube Heat Exchangers Using The Tema Standards. Chem. Eng. Res. Design 2007;85(A10):1423–35. [https://doi.org/10.1016/S0263-8762\(07\)73182-9](https://doi.org/10.1016/S0263-8762(07)73182-9).
- [12] Onishi V, Ravagnani MASS, Caballero J. Mathematical programming model for heat exchanger design through optimization of partial objectives. Energy Convers Manage 2013;74:60–9. <https://doi.org/10.1016/j.enconman.2013.05.011>.
- [13] Mizutani FT, Pessoa FLP, Queiroz EM, Grossmann HS, I. E.. Mathematical programming model for heat exchanger network synthesis including detailed heat exchanger designs. 1. Shell-and-tube heat exchanger design. Ind Eng Chem Res 2003;42:4009–18. <https://doi.org/10.1021/ie020964u>.
- [14] Ravagnani MASS, Caballero JA. Optimal Heat Exchanger Network Synthesis with the Detailed Heat Transfer Equipment Design. Comp Chem Eng 2007;31(11): 1432–48. <https://doi.org/10.1016/j.compchemeng.2006.12.005>.
- [15] Xiao Wu, Wang Kaifeng, Jiang Xiaobin, Li Xiangcun, Wu Xuemei, Hao Ze, et al. Simultaneous optimization strategies for heat exchanger network synthesis and detailed shell-and-tube heat-exchanger design involving phase changes using GA/SA. Energy. 2019;183:1166–77. <https://doi.org/10.1016/j.energy.2019.06.151>.
- [16] Gonçalves CO, Costa ALH, Bagajewicz MJ. Linear method for the design of shell and tube heat exchangers using the Bell-Delaware method. Process Systems Engineering. AIChE J 2019;65:1–16. <https://doi.org/10.1002/aic.16602>.
- [17] Lemos Julia C, Costa André LH, Bagajewicz Miguel J. Set Trimming Procedure for the Design Optimization of Shell and Tube Heat Exchangers. Ind Eng Chem Res

- 2020;59(31):14048–54. <https://doi.org/10.1021/acs.iecr.0c02129>. <https://doi.org/10.1021/acs.iecr.0c02129.s001>.
- [18] Rathjens M, Fieg G. Cost-Optimal Heat Exchanger Network Synthesis Based on a Flexible Cost Functions Framework. *Energies*. 2019;12:784. <https://doi.org/10.3390/en12050784>.
- [19] Ahmad S. Heat Exchanger Networks: Cost Tradeoffs in Energy and Capital. UK: University of Manchester Institute of Science and Technology; 1985.
- [20] Linnhoff B, Ahmad S. Cost Optimum Heat Exchanger Networks-1. Minimum Energy and Capital Using Simple Models for Capital Cost. *Comput Chem Eng* 1990; 14(7):729–50. [https://doi.org/10.1016/0098-1354\(90\)87083-2](https://doi.org/10.1016/0098-1354(90)87083-2).
- [21] Colberg RD, Morari M. Area and Capital Cost Targets for Heat Exchanger Network Synthesis with Constrained Matches and Unequal Heat Transfer Coefficients. *Comput Chem Eng* 1990;14(1):1–22. [https://doi.org/10.1016/0098-1354\(90\)87002-7](https://doi.org/10.1016/0098-1354(90)87002-7).
- [22] Hall SG, Ahmad S, Smith R. Capital Cost Targets For Heat Exchanger Networks Comprising Mixed Materials Of Construction, Pressure Ratings, And Exchanger Types. *Comput Chem Eng* 1990;14(3):319–35. [https://doi.org/10.1016/0098-1354\(90\)87069-2](https://doi.org/10.1016/0098-1354(90)87069-2).
- [23] Ahmad S, Linnhoff B, Smith R. Cost Optimum Heat Exchanger Networks-2. Targets and Design for Detailed Capital Cost Models. *Comput Chem Eng* 1990;14(7): 751–67. [https://doi.org/10.1016/0098-1354\(90\)87084-3](https://doi.org/10.1016/0098-1354(90)87084-3).
- [24] Taal M, Bulatov I, Klemes J, Stehlik P. Cost estimation and energy price forecasts for economic evaluation of retrofit projects. *Appl Therm Eng* 2003;23:1819–35. [https://doi.org/10.1016/S1359-4311\(03\)00136-4](https://doi.org/10.1016/S1359-4311(03)00136-4).
- [25] Purohit GP. Estimating costs of Shell-and-Tube Heat Exchangers. *Chem Eng* 1983; 90:56–67.
- [26] Remer DS, Chai LH. Design cost factors for scaling-up engineering equipment. *Chem Eng* 1990;86(8):77–82.
- [27] Guthrie KM. Capital cost estimating. *Chem Eng* 1969;114–42.
- [28] Pikulik A, Diaz HE. Cost estimating for process equipment. *Chem Eng* 1977;84(21): 106–22.
- [29] Corripio AB, Chrien KS, Evans LB. Estimate costs of heat exchangers and storage tanks via correlations. *Chem Eng* 1995;89(2):125–7.
- [30] Hall RS, Matley J, McNaughton KJ. Current costs of process equipment. *Chem Eng* 1982;89(7):80–116.
- [31] Vatauvuk WM. A potpourri of equipment prices. *Chem Eng* 1995;102(8):68–73.
- [32] Hall SG. Capital Cost Targets for Heat Exchanger Networks: Differing Materials of Construction and Different Heat Exchanger Types. Ph.D. Thesis. University of Manchester; 1986.
- [33] Short M, Isafiade AJ, Fraser DM, Kravanja Z. Two-step hybrid approach for the synthesis of multi-period heat exchanger networks with detailed exchanger design. *Appl Therm Eng* 2016;105:807–21. <https://doi.org/10.1016/j.applthermaleng.2016.05.065>.
- [34] Kazi SR, Short M, Biegler LT. Heat exchanger network synthesis with detailed exchanger designs: Part 1. A discretized differential algebraic equation model for shell and tube heat exchanger design. *Process Systems Engineering*. *AIChE J* 2020; e17056:1–17. <https://doi.org/10.1002/aic.17056>.
- [35] Kazi SR, Short M, Isafiade AJ, Biegler LT. Heat exchanger network synthesis with detailed exchanger designs—2. Hybrid optimization strategy for synthesis of heat exchanger networks. *Process Systems Engineering*. *AIChE J* 2021;67(e17057): 1–16. <https://doi.org/10.1002/aic.17057>.
- [36] Vengateson, U. (2010). Design of multiple shell and tube heat exchanger in series: E shell and F shell. *Chem. Eng. Rese. and Design, IchemE*. 2010, 88, 725-736. <https://doi.org/10.1016/j.cherd.2009.10.005>.

Analysis on Plane and Radial Wall Jets to Validate the 2D for an Idealized Downburst Outflow

Suchismita Satpathy, *Department of Civil Engineering, Aryan Institute of Engineering & Technology, Bhubaneswar, suchismita@outlook.com*

Rakesh Kumar Panda, *Department of Civil Engineering, Aryan Institute of Engineering & Technology, Bhubaneswar, rakeshpanda116@gmail.com*

Suchampa Bagchi, *Department of Civil Engineering, NM Institute of Engineering & Technology, Bhubaneswar, suchampabagchi@yahoo.co.in*

Swarup Sahoo, *Department of Civil Engineering, Capital Engineering College, Bhubaneswar, swarupsahoo26@outlook.com*

ABSTRACT

Over the last few decades, turbulent radial and plane wall jets have been studied extensively both experimentally and numerically. Previous research has mostly focused on the heat and mass transfer processes that occur in jet flows. In this study, a thorough investigation of turbulent radial and plane wall jets was carried out, taking into account both jet spread and velocity decay for various parameters. The numerical results were compared to previously collected experimental data. The Reynolds stress model (RSM) performed well in the simulation of both radial and plane wall jets, according to the comparison, which focused on the velocity profile, jet spread, and velocity decay. The results reveal that the effects of nozzle height and Reynolds number on the evolution of the radial wall jet are not substantial for most downburst occurrences with a typical ratio of cloud base height to diameter. The Reynolds number influences both the jet spread and the velocity decay.

1. Introduction

The occurrence of wall jet flows is common in many industrial applications. Traditional applications include ventilation, film cooling, and separation control over wings [1]. In some small-scale geometric engineering applications, turbulent jets are mainly used for heat transfer [2, 3]. In civil engineering, the wall jet flow can be used to design laboratory (or numerical) simulations of large-scale downburst outflow, which is a high-intensity wind that results in failures of transmission lines [4, 5]. There are two main methods for generating wall jet flows depending on the angle of injection of the high-momentum fluid. If the high-momentum fluid is injected normally to the wall, the resulting flow field is classified as a radial wall jet [6], which is a logical way to achieve flow similarity of downburst outflow [7]. A

plane wall jet is produced when the high-momentum fluid is parallel to the wall, and this can also be an idealized model for the outflow region of a downburst [8, 9].

Both radial and plane wall jets have been extensively studied over the past few decades. Owing to the extensive applications of wall jets, there are many studies on them. Launder and Rodi [10] provided a comprehensive review that reflects the state-of-the-art experimental research conducted until 1980. Reviews on more recent literature can be found in Naqavi et al. [11] and van Hout et al. [12] for plane and radial wall jets, respectively. These literature reviews suggest that the studies on wall jets usually focus on one type at a time. Radial [13–15] and plane [16–20] wall jets were investigated separately. Only a few studies have compared the basic characteristics, such as the evolution of the length and velocity scales, of the two types of wall jets.

Tanaka and Tanaka [21] compared the velocity and length scales of their experimental radial wall jet with those available in the literature on plane wall jets. It was revealed that the evolution of the half-maximum velocity location is very similar, while there is a difference between the evolutions of the maximum velocities. Banyassady and Piomelli [22] obtained similar conclusions through a large eddy simulation. Guo et al. [23] identified that the confinement of an impinging jet has no significant effect on the velocity decay rate, and the presence of the upper confinement plate accelerates the wall jet growth rates compared to those reported in the previous plane and radial wall jet experiments. However, the numerical study results of radial wall jet by Fillingham and Novosselov [24] exhibited an excellent agreement with those of plane wall jet reported by Naqavi et al. [11] in terms of the evolution of both length and velocity scales. Bagherzadeh et al. [2] reported that wall roughness influences the decay rate. They found that the decay of velocity increases with an increase in wall roughness.

Most previous studies on plane and radial wall jets focused on heat and mass transfers; they had relatively small Reynolds numbers [25, 26] and were not suitable for the study of downbursts. Due to the influence of the wall, the free jet region of the impinging jets is also different from the turbulent round jet [27]. In applications related to civil engineering, the majority of the previous investigations on radial and plane wall jets focused on the profiles and time series of velocity [28–30]. It is useful to characterize the length and velocity scales for high Reynolds numbers. In addition, an external stream exists in most practical situations of a plane wall jet. The external stream also provides fluid for jet entrainment [31]. In the case of downburst outflow simulation, an external stream may be applied to simulate a translating event [32]. In addition, the results from different wall jet studies have apparent discrepancies even in some basic characteristics. There is a fundamental geometric difference between plane and radial wall jets: radial wall jets have an additional direction of expansion. Although Lin et al. [33] verified that the frontal curvature has little effect on the resultant wind loading of a structure within a certain transverse width, which is a geometric analysis, the validity of the 2D assumption needs to be further investigated from the perspective of the difference between the longitudinal evolution of the 3D outflow and 2D wall jet.

The primary objectives of the present study were (1) to perform a systematic parametric study through the numerical simulation of radial and plane wall jets to determine the characteristics of evolution and (2) to further investigate the 2D assumption for the downburst outflow. Following Section 1, Section 2 introduces the numerical simulation details of the radial and plane wall jets; Section 3 presents the comparison of the results from existing literatures with those predicted in the current simulation. The Reynolds-number dependency was investigated for both types of wall jets. Subsequently, the influence of the nozzle height from the plate on the radial wall jet and the effect of co-flow on the plane wall jet are presented. Based on the simulation results,

the accuracy of approximating a downburst outflow with a plane wall jet was evaluated, as presented in Section 4. Section 5 summarizes the main findings of the present study.

2. Problem Formulation

2.1. Governing Equations. A commercially available computational fluid dynamics (CFD) package, FLUENT, was used to simulate the impinging jet and plane wall jet. The conservation equations of mass and momentum for an incompressible fluid flow can be expressed as follows:

$$\frac{\partial u_i}{\partial x_i} = 0, \quad (1)$$

$$\frac{\partial}{\partial t}(\rho u_i) + \frac{\partial}{\partial x_j}(\rho u_i u_j) = -\frac{\partial p}{\partial x_i} + \frac{\partial \tau_{ij}}{\partial x_j} + \frac{\partial}{\partial x_j} \left(\mu \frac{\partial u_i}{\partial x_j} \right),$$

where ρ is the fluid density; u_i and u_j are the mean velocity components corresponding to i and j , respectively; p is the pressure; μ is the fluid viscosity; and t is the time. The Reynolds stress tensor, $\tau_{ij} = -\rho u_i' u_j'$, needs to be numerically modeled to close the equations.

An exhaustive investigation on a plane wall jet was conducted by Yan et al. [34] using seven Reynolds-averaged Navier–Stokes (RANS) turbulence models and a large eddy simulation (LES). They found that the stress-omega Reynolds stress model (SWRSM) with adjusted turbulence model constants achieved the best results in simulating a steady wall jet without co-flow. In addition, Sengupta and Sarkar [35] indicated that the LES model, realizable k - ϵ model, and Reynolds stress model (RSM) perform better in simulating an impinging jet. In the current study, the Navier–Stokes equations were closed by employing RSM (stress-omega). The stress-omega model is a stress-transport model proposed by Wilcox [36], and a revised version was introduced subsequently [37]. The default constants from the original version [36] are used in FLUENT 16.0. The revised version was used in the current study. The parameters of the SWRSM are listed in Table 1.

2.2. Assumptions and Numerical Solution. The assumptions made for solving the pressure and flow fields inside the wind channel and their corresponding implications are as follows:

- (1) Constant and uniform properties, i.e., ρ and μ are constant.
- (2) Newtonian fluid.
- (3) Isotropic fluid.
- (4) Isothermal fluid.
- (5) Incompressible fluid.
- (6) Stokes' hypothesis holds true.

The differential equations governing the flow were integrated using the finite-volume method, which is a specific case of residual weighting methods [38, 39]. The least squares cell-based method was adopted for the numerical approximation of gradients, and bounded central

TABLE 1: Coefficients for SWRSM.

C_1	C_2	Alpha*_inf	Alpha_inf	Beta_i	Beta*_inf	zeta*	Mt0	TKE Prandtl number	SDR Prandtl number
1.8	10/19	1	0.52	0.0708	0.09	0.5	0.25	5/3	2

differencing was selected for the momentum discretization. The pressure was discretized using a second-order implicit scheme. The discretized governing equations were solved using the Semi-Implicit Method for Pressure-Linked Equations Consistent (SIMPLEC) algorithm, which is an improved version of the SIMPLE algorithm [40], for pressure-velocity coupling. The SIMPLEC algorithm adopted in this study is presented in Appendix A. The time step was selected to guarantee that the Courant number was less than one to maintain the stability of the computation. The absolute convergence criteria for the continuity equation and the other equations are 1×10^{-6} and 1×10^{-5} , respectively.

2.3. Flow Configuration and Computational Setup. The computational domains for the plane wall jet and impinging jet using the Cartesian coordinate system are shown in Figure 1, where b is the jet inlet height of the plane wall jet and D is the circular inlet diameter. For the plane wall jet domain, Yan et al. [41] indicated that the development of the wall jet is not affected up to the streamwise position $x/b = 80$ for $h/b = 20$, where h is the co-flow height. The domain height of the plane wall jet assumed in this study was $21b$. The bottom was set as a wall boundary with a no-slip condition. At the inflow plane, a velocity profile was set for the wall jet up to $y/b = 1.0$, and the rest of the plane had a uniform co-flow, U_E . Jet entrainment was provided by a uniform co-flow. The top boundary was specified as a free-slip boundary condition. The spanwise direction had periodic boundaries to attain two dimensionalities, and at the exit plane, a pressure outlet boundary condition was applied, as shown in Figure 1(a). Sengupta and Sarkar [35] showed that the geometric conditions of the domain have little influence on the flow profiles. For the current impinging jet simulation, a three-dimensional (3D) cylindrical domain was used, as illustrated in Figure 1(b). Pressure outlet boundary conditions were applied with a zero-normal gradient at the outflow boundaries. A no-slip condition was assumed at the bottom wall of the computational domain. The turbulence intensity of the inflow was set as 0.01 for both the impinging jet and plane wall jet.

A nonuniform hexahedral grid was used. The nearest node to the wall in the y -direction was located at $y^+ < 1$ for all grids, where $y^+ = \Delta y \rho u_\tau / \mu$ is the nondimensional wall distance, $u_\tau = (\tau_w / \rho)^{1/2}$ is the friction velocity, τ_w is the wall shear stress, μ is the dynamic viscosity of the fluid, and ρ is the density of the fluid. To ensure grid independency, two grids were employed for the radial wall jet simulation: coarse G1 (2.4 million) and fine G2 (4.1 million). Two grids were also employed for the plane wall jet simulation: coarse G3 (1.8 million) and fine G4 (3.2 million). As shown in Figure 2, the results for the two levels of grid resolution were very similar, and there was no noticeable difference between the mean velocities of the radial and plane wall jets. All the

results presented in this work are for the two fine grids shown in Figure 1.

The mean velocity is usually scaled with length and velocity variables, namely, the maximum velocity U_m and the distance $y_{1/2}$ from the wall to the position at which the mean velocity declines to half of its maximum value [7, 42], to obtain self-similar characteristics. Researchers often selected the height y_m of the maximum velocity location as the length scale [43–45] for the vertical mean velocity profile of the downburst.

Hjelmfelt [46] noted that approximately 50% of the observations from the Joint Airport Weather Studies (JAWS) Project were for traveling events. Storm translational velocities can be as high as 1/3 of the downdraft velocity. A downburst with “surface environmental wind” or a downburst embedded in a translating storm can be modeled through a plane wall jet approach with a co-flow [32, 33]. The velocity ratios are defined as $\beta = U_E / U_j$ for the plane wall jet. The Reynolds number is defined as $Re = U_{jet} D / \nu$ for impinging jet and $Re = U_{jet} b / \nu$ for plane wall jet, where ν is the kinematic viscosity. The simulation cases for investigating the influences of the Reynolds number and nozzle height on the impinging jet are listed in Table 2, while those for investigating the influences of the Reynolds number and co-flow on the plane wall jet are listed in Table 3.

2.4. Numerical Procedure Validation. To verify the reliability and accuracy of the current simulation, the results obtained from the current model were compared with the experimental results obtained by McIntyre [47] for a Reynolds number of $Re = 30,700$ and a velocity ratio of $\beta = 0.1$. Because the main objective of this study was to characterize the length and velocity scales, normalized mean velocities were used for validation. Figure 3 shows the velocity profiles at two downstream locations. As demonstrated in this figure, there is a good agreement between the current numerical results and experimental data from McIntyre [47]. It was concluded that the present numerical method is valid and can be used to predict the mean flow properties of wall jets.

3. Results and Discussions

3.1. Statistical Properties

3.1.1. Mean Axial Velocity of Impinging Jet. The axial velocity profile along the centerline of the jet at half of the nozzle height from the ground plane is shown in Figure 4. In order to obtain the nondimensional velocity profiles, the mean axial velocity of the impinging jet is normalized by the local maximum velocity V_m , and the radial distance is normalized by the local jet half-width $\delta_{1/2}$ (defined as the width at which the mean axial velocity has decreased to half of its maximum value). L is the downstream distance from the jet nozzle. It can be seen that the current results of

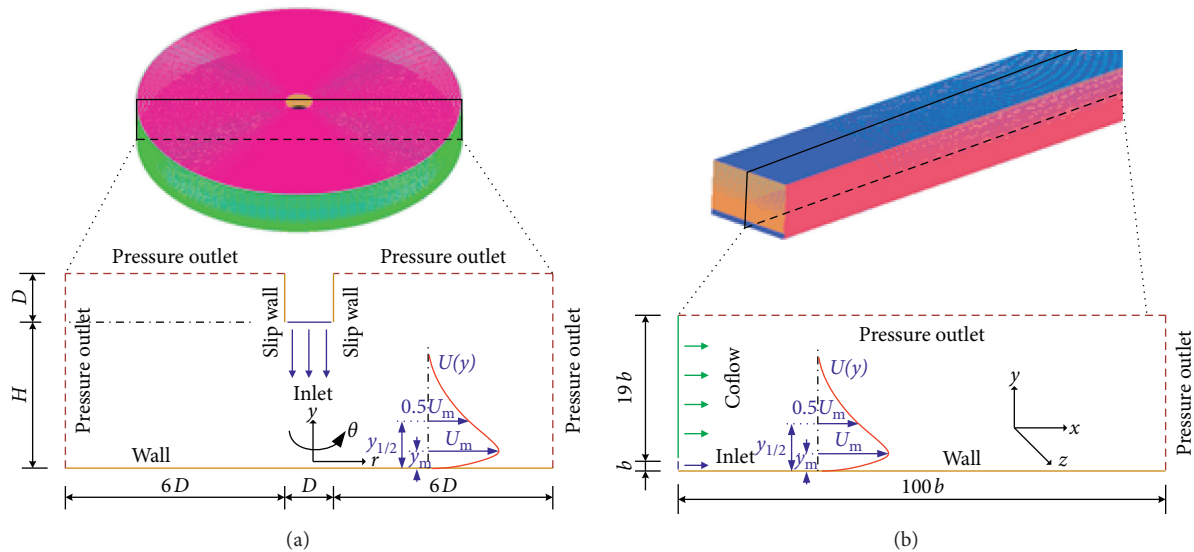


FIGURE 1: Computational domains and grids for radial and plane wall jets. (a) Radial wall jet. (b) Plane wall jet.

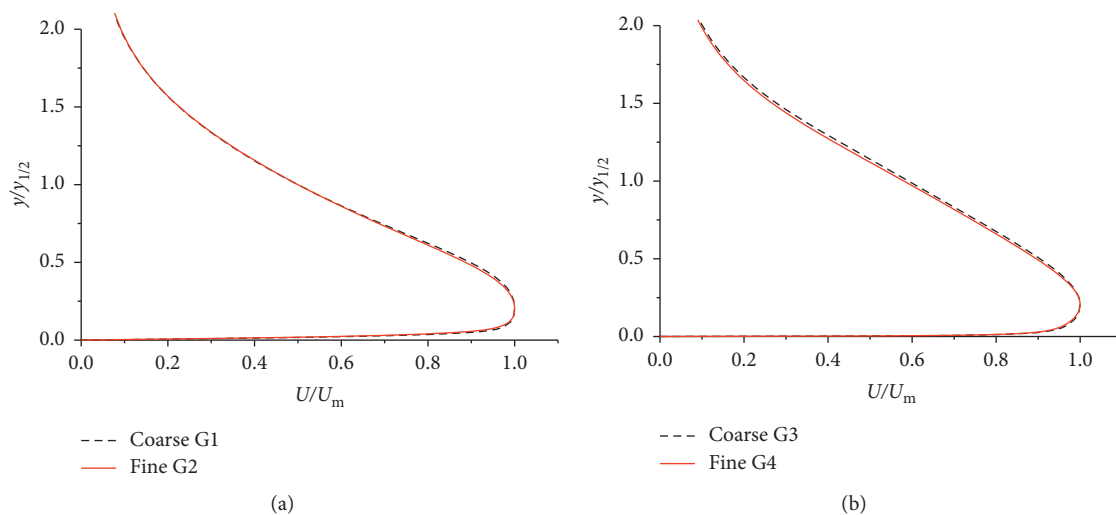


FIGURE 2: Grid independence study for: (a) radial wall jet, $r = 1.5D$ and (b) plane wall jet, $x = 30b$.

TABLE 2: Simulation cases for radial wall jet.

Cases	R1	R2	R3	R4	R5	R6	R7	R8	R9	R10
Re ($\times 10^4$)	5	10	15	20	25	5	5	5	5	5
H/D	2	2	2	2	2	1	3	4	5	6

TABLE 3: Simulation cases for plane wall jet.

Cases	P1	P2	P3	P4	P5	P6	P7	P8	P9	P10
Re ($\times 10^4$)	1	2	4	6	8	10	6	6	6	6
β	0.1	0.1	0.1	0.1	0.1	0.1	0.15	0.2	0.25	0.3

impinging jet match well with the experiment of Sengupta and Sarkar [35] on the right side and there are some differences on the left side. This discrepancy may be due to the concentration of seeding particles along the jet boundary,

which is a common problem in the use of PIV. Compared with the velocity profile near the nozzle of a round free jet [48], the profile of impinging jet has a top-hat shape due to the existence of the plate. After impacting the plate, the axial velocity of the impinging jet is transformed into the radial velocity, while the round free jet gradually develops and becomes self-similar [27].

3.1.2. Vertical Profile of Mean Streamwise Velocity in Wall Jet Region. Figure 5 shows the profiles of the mean velocity normalized using U_m and $y_{1/2}$ at $x = 1.5D$ for the radial wall jet with $Re = 50,000$ and $H = 2D$ and at $x = 30b$ for the plane wall jet with $Re = 60,000$ and $\beta = 0.1$. The current numerical results were compared with those of the plane wall jet experiment by Eriksson et al. [17]; the radial wall jet experiment by Cooper et al. [13]; and three empirical models for the vertical profile of the downburst [7, 44, 49]. The current

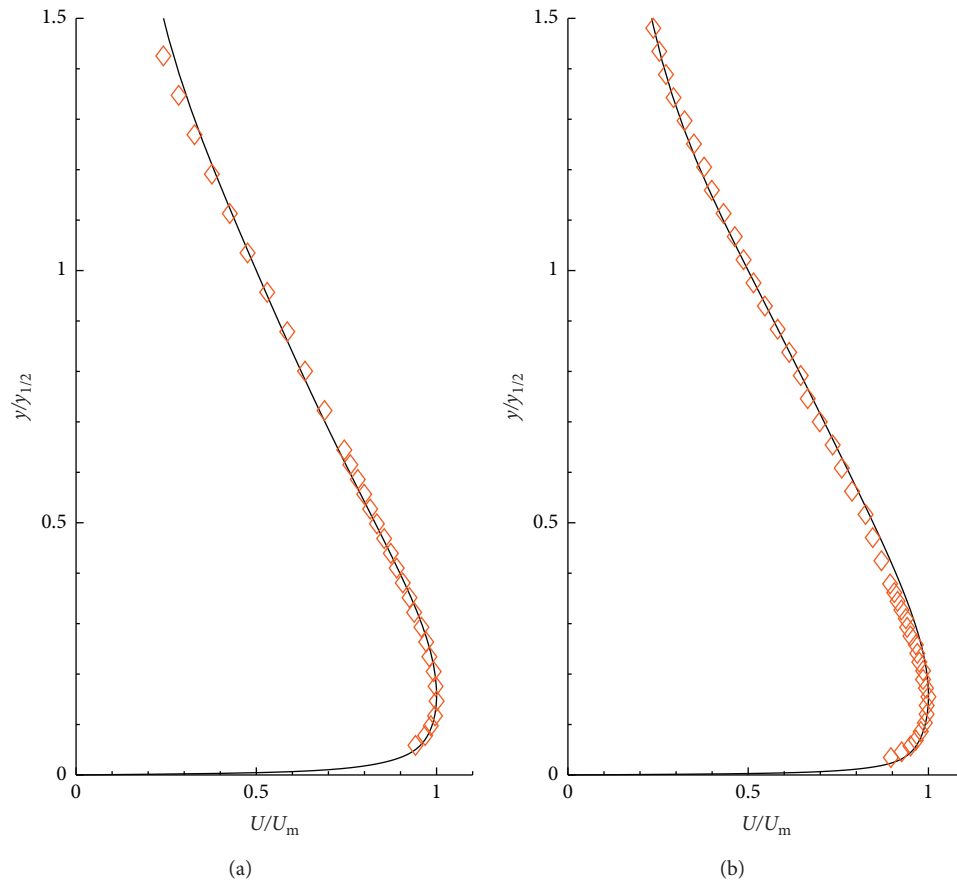


FIGURE 3: Comparison of mean streamwise velocity profiles, (a) $x = 20b$, (b) $x = 80b$: current simulation (—); McIntyre [47] (\diamond).

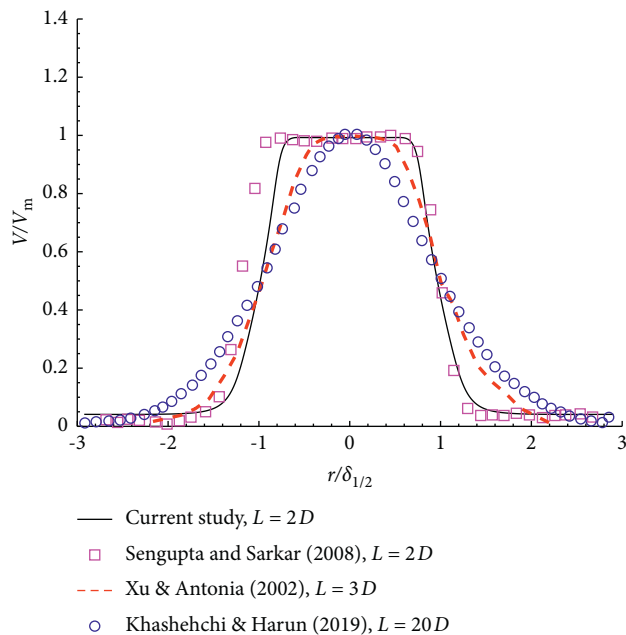


FIGURE 4: Comparison of normalized axial velocity profiles.

results of the plane wall jet are in good agreement with the vertical profile suggested by Wood et al. [7] and the results obtained by Eriksson et al. [17] for the outer region ($y > y_m$).

However, the current model underestimated the height of maximum velocity (y_m) by 7.8 and 4.9% and overestimated the velocity by 9.1 and 5.2% at the height of $y/y_{1/2} = 0.08$, compared with those obtained by Eriksson et al. [17] and Wood et al. [7], respectively. The current results of the radial wall jet exhibit a larger y_m and agree well with the vertical profile suggested by Oseguera and Bowles [49] for the region of $y/y_{1/2} > y_m$. In the inner region, the current model predicted a velocity lower by 10.1 and 11.8% compared to the experimental results of Cooper et al. [13] and Wood's profile at the height of $y/y_{1/2} = 0.08$, respectively. It can be concluded that both the approaches can generate a flow that is similar to a downburst outflow and are effective in investigating downburst outflows.

3.1.3. Turbulent Quantities. Figure 6 shows the distribution of RMS (root mean square) fluctuations in streamwise velocity profiles at different streamwise locations ($2 < x/b < 3.5$) and radial locations ($40 < r/D < 70$). It can be seen that the results from both wall jet and impinging jet are in good agreement with the literature data in the outer layer. The streamwise RMS velocity profiles of the wall jet show obvious twin-peak behavior and self-similarity, while there is no obvious peak near the wall in the simulation and experimental data of the impinging jet.

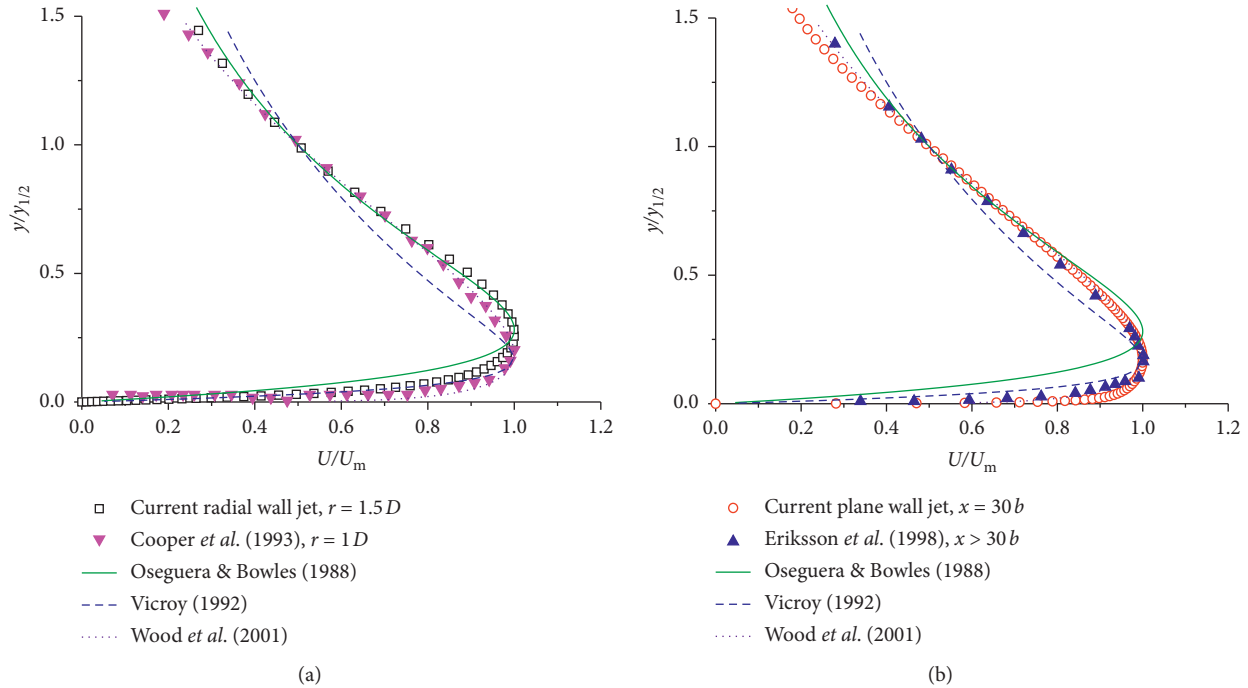


FIGURE 5: Vertical mean velocity profiles in outer scales. (a) Radial wall jet. (b) Plane wall jet.

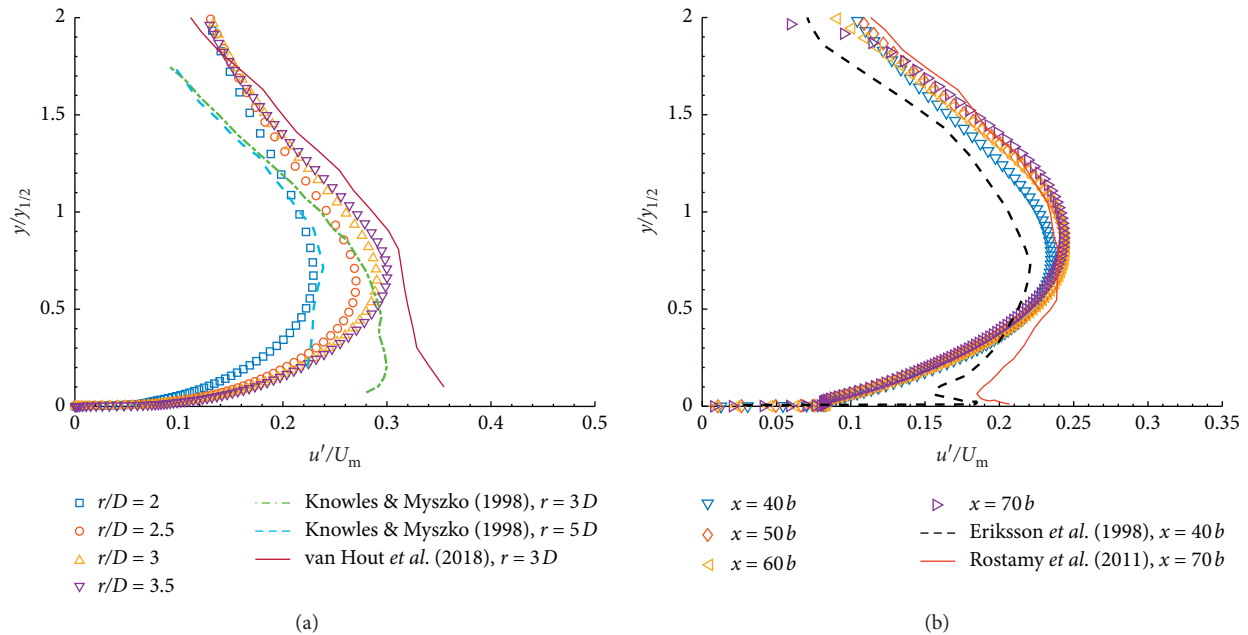


FIGURE 6: Profiles of streamwise RMS velocity. (a) Radial wall jet. (b) Plane wall jet.

Figure 7 presents the RMS profiles of vertical velocity at different streamwise locations (x/b) and radial locations (r/D). The numerical results of the plane wall jet are in good agreement with the experimental data and show obvious self-similarity, while the comparison for impinging jets with the hot-wire data sets is less good. The numerical results of the impinging jet are close to the experimental data of Knowles and Myszkowski [14] but smaller than the experimental results of van Hout *et al.* [12].

Figure 8 shows the profiles of Reynolds shear stress along the wall-normal direction at different streamwise locations (x/b) and radial locations (r/D). The profiles of Re shear stress of both plane wall jet and impinging jet also have two peak values. Different from streamwise RMS velocity, the peak values of Re shear stress near the wall are negative. The results of the plane wall jet match well with the experimental data of Rostamy *et al.* [18] while the result from Eriksson *et al.* [17] is smaller than the current simulation. The

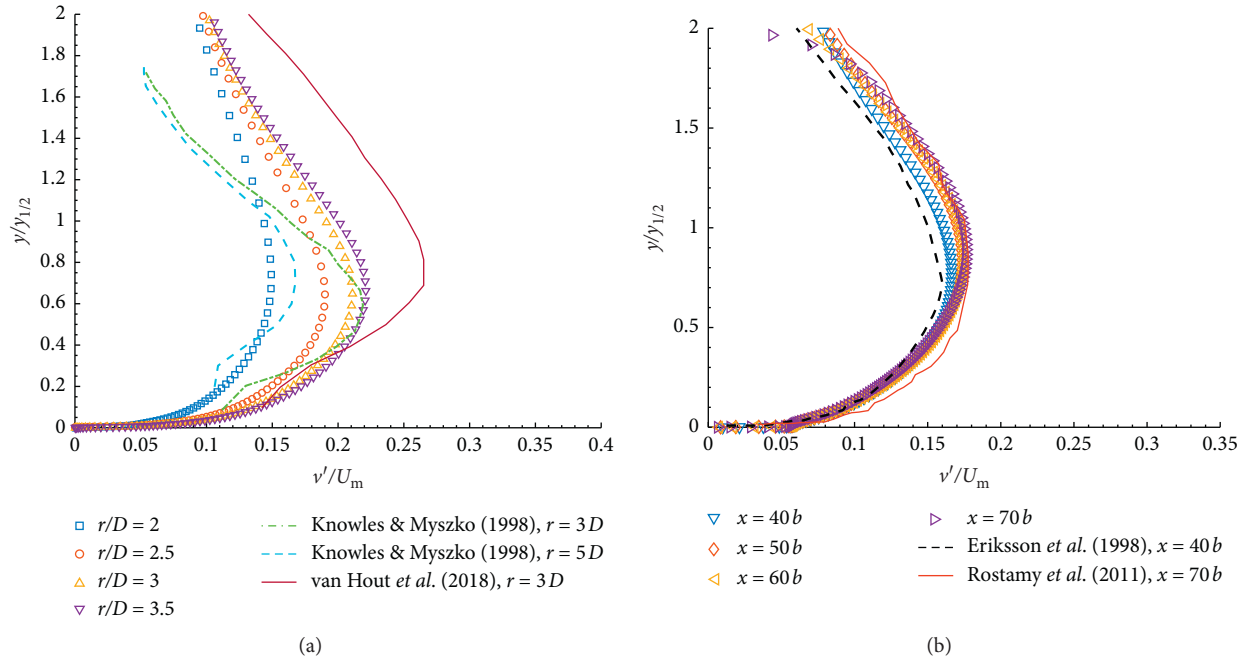


FIGURE 7: Profiles of vertical RMS velocity. (a) Radial wall jet. (b) Plane wall jet.

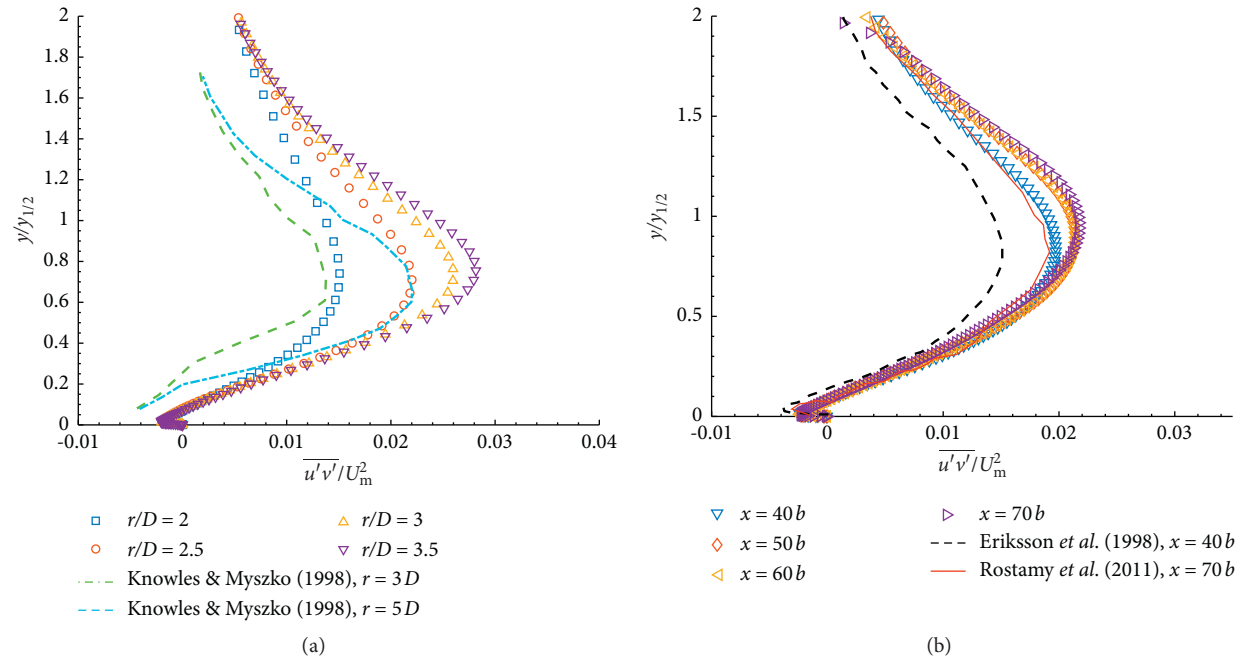


FIGURE 8: Profiles of Reynolds shear stress. (a) Radial wall jet. (b) Plane wall jet.

impinging jets values measured by Knowles and Myszko [14] are also considerably lower.

3.2. Jet Spread and Velocity Decay in Plane Wall Jet

3.2.1. Effect of Jet Reynolds Number. The dependence of the flow on the Reynolds number was studied for a fixed velocity ratio ($\beta = 0.1$). The decay of the spread of the jet flow and the

maximum velocity was investigated. The average spread rate of the plane wall jet was found to be linear and can be expressed as the half-height ($y_{1/2}$) with respect to the downstream distance [10]. The growth is represented by equation (2) as follows:

$$\frac{y_{(1/2)}}{b} = A_p \left(\frac{x}{b} \right) + C. \quad (2)$$

Many previous studies have reported the values of the slope A_p . Launder and Rodi [10] summarized a large number of experiments and found that most values of A_p fall within the range of 0.073 ± 0.002 , except those obtained in low-Reynolds-number tests. The experiments of Eriksson et al. [17], where measurements were performed using LDV, indicated that the spread rate should be 0.078 for $Re = 10,000$. The experimental data from Abrahamsson et al. [16] indicated a dependence of the slope on Re and reported that values of A_p varied from 0.075 to 0.081 with $Re = 10,000$ –20,000. Wygnanski et al. [19] also found a clear Reynolds-number dependence and a larger slope value of 0.088 for a Reynolds number ranging from 3,700 to 19,000. With an external stream, Zhou and Wygnanski [20] indicated that the influence of the Reynolds number is less significant when the velocity ratio is large.

Figure 9 shows the streamwise growth of the jet half-height for different Re values with a co-flow ratio of 0.1. The values of the slopes varied from 0.0781 to 0.0733 with $Re = 20,000$ –100,000. The obtained results and the experimental data from Abrahamsson et al. [16] are in good agreement for $Re = 20,000$. The Reynolds number does not seem to have a significant effect on the spread rates in the current study. The decrease in the spread rate tended to gradually decrease as the Reynolds number increased. A similar result was also observed by Abrahamsson et al. [16]. Schwarz and Cosart [50] reported that the variation in the spread rate was not apparent in their study for higher Re numbers ranging from 13,510 to 41,600. Therefore, there should exist a threshold, which was found to be 60,000 in the current study. When the Reynolds number is greater than this threshold, the dependence of the spread rate on the Reynolds number can be ignored. When the wall jet approach is used to simulate the downburst outflow in the boundary layer wind tunnel, the Reynolds number is usually greater than this threshold. The large-scale features of the simulated outflow were independent of the Reynolds number.

Few studies have been conducted on the maximum velocity height (y_m). Zhou and Wygnanski [20] reported that y_m exhibits an approximately linear relationship with the downstream distance, and the Reynolds number has no significant effect on y_m . However, Reynolds-number dependence is observed in the CFD results obtained by Ben et al. [51] who found that y_m decreases linearly with x at a higher rate for a lower Reynolds number. Figure 10 shows the longitudinal distributions of y_m for different Re numbers. The results from the current study are in agreement with the observations by Zhou and Wygnanski [20]. The growth rate of the maximum velocity height remained constant at $dy_m/dx = 0.0133$, whereas in the experiment by Zhou and Wygnanski [20], the value was $dy_m/dx = 0.0114$.

In previous studies [11, 19], the decay of the maximum velocity is represented by the following equation:

$$\frac{U_m}{U_j} = B_{p1} \left(\frac{x - x_0}{b} \right)^{N_p}, \quad (3)$$

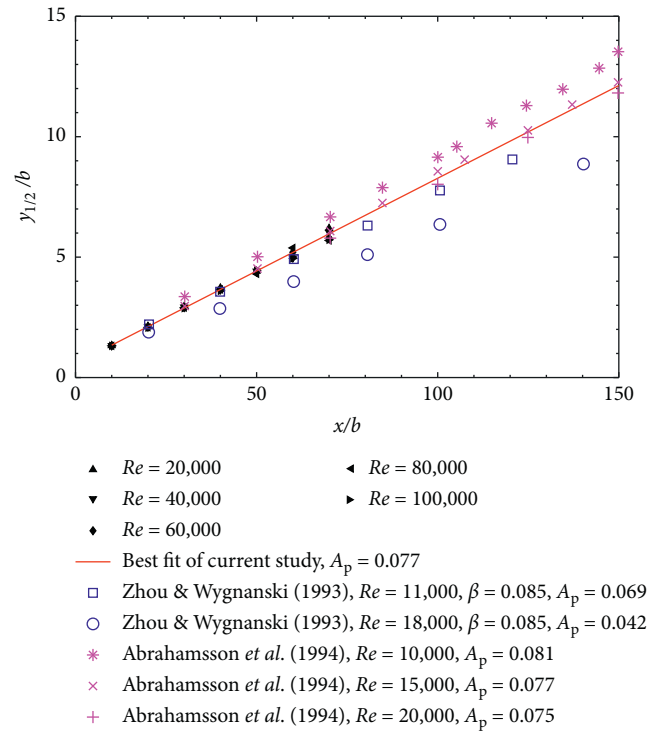


FIGURE 9: Plane wall jet growth rate for various Reynolds numbers.

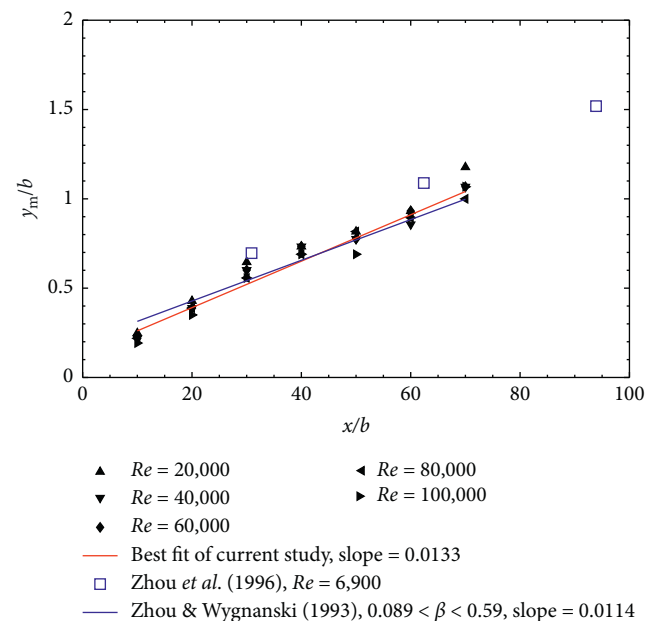


FIGURE 10: Rate of spread of y_m for various Reynolds numbers.

where x_0 is the virtual origin of the wall jet. The virtual origin is used to make the lines fit to converge the data to $U_m/U_j = 1$ at $x = x_0$ [19]. Velocity decay is well documented for the plane wall jet; however, the values of the coefficients B_p and N_p are different in different investigations. The exponents of the power law are reported to be $N_p = -0.47$, -0.56 , and -0.48 by Wygnanski et al. [19], Schneider and Goldstein

[52], and Tang et al. [26], respectively. However, Wygnanski et al. [19] also suggested that their results fit the power law fairly well, with $N_p = 0.5$. Lin [53] found that the arithmetic mean values of N_p and B_p in previous studies were -0.52 and 4.19 , respectively. Barenblatt et al. [54] indicated that $N_p = 0.5$ is necessary for achieving a completely similar flow. In the current study, the power law with $N_p = 0.5$ was used to fit the results. Thus, equation (4) can be rewritten as:

$$\left(\frac{U_j}{U_m}\right)^2 = B_p \left(\frac{x - x_0}{b}\right) + 1. \quad (4)$$

The effect of the Reynolds number on the decay of the maximum velocity $(U_j/U_m)^2$ is shown in Figure 11. The values of B_p decreased with increasing Reynolds number and varied from 0.081 to 0.072 with $Re = 10,000$ – $100,000$. The variation was approximately 13%. When the Reynolds number was higher ($Re > 20,000$), the variation in the coefficient B_p was insignificant. For example, the value of B_p varied from 0.074 to 0.072 with $Re = 60,000$ – $100,000$. The variation was only approximately 2%. This indicates that the effect of the Reynolds number is negligible for higher values ($Re > 60,000$). This is in complete agreement with the observations made by Schwarz and Cosart [50].

3.2.2. Effect of Velocity Ratio. The effect of the velocity ratio on the streamwise development of the half-width and maximum mean velocity for a fixed inlet Reynolds number was investigated. The Reynolds number has no significant effect on the rate of spread and the decay of the maximum velocity for $Re > 60,000$, as explained in Section 3.3.1. Thus, the simulations of the plane wall jet with various velocity ratios were conducted for $Re = 60,000$. The effect of the velocity ratio on the spread rate at half-height is shown in Figure 12. The value of A_p was between the measured values from Zhou and Wygnanski [20] and McIntyre et al. [55], at a velocity ratio of 0.1 . It can be observed that the velocity ratios have a significant effect on the half-height, which is in agreement with the findings by Zhou and Wygnanski [20]. The influence on the half-height, reported in Zhou and Wygnanski [20], is larger, which may be due to the low Reynolds number. The value of A_p decreased as the velocity ratio increased, and the intercepts from various co-flow ratios were nearly the same. However, the velocity ratios also had no significant effect on y_m , and dy_m/dx was still 0.0133 , as shown in Figure 13.

Few studies have reported the values of B_p for different velocity ratios. To compare the decay of the maximum velocity downstream, the studies of Wygnanski et al. [19] and McIntyre et al. [55] were considered. The effect of the velocity ratio on the streamwise decay of the maximum velocity is shown in Figure 14. The result from the current study at $\beta = 0.1$ is similar to that of Wygnanski et al. [19]. McIntyre et al. [55] reported the coefficient $B_p = 0.052$, which is 30% smaller than that in the current study. It was observed

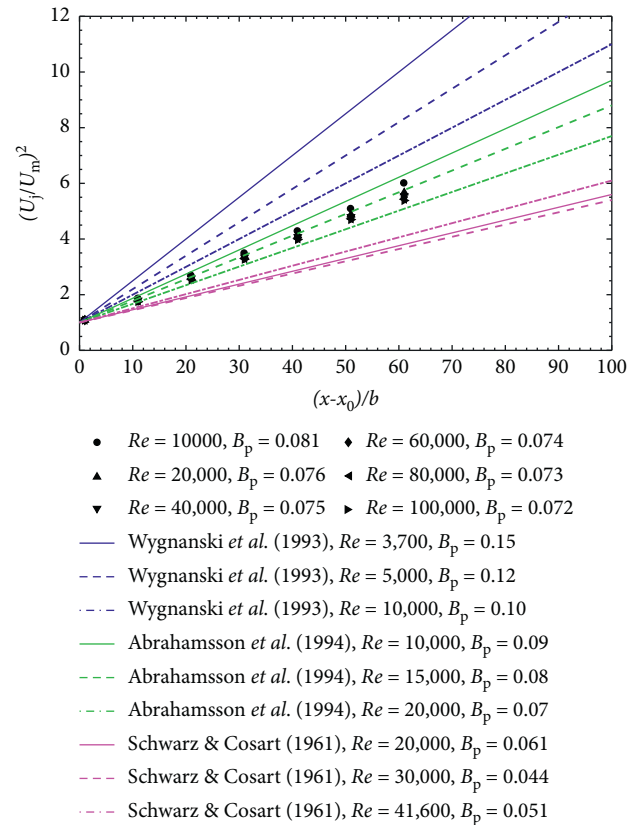


FIGURE 11: Decay of maximum velocity for various Reynolds numbers.

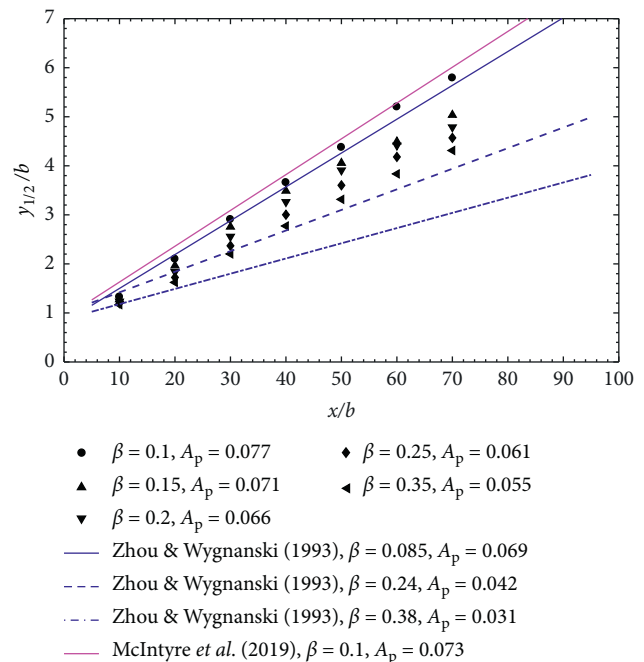


FIGURE 12: Streamwise development of $y_{1/2}$ for various velocity ratios.

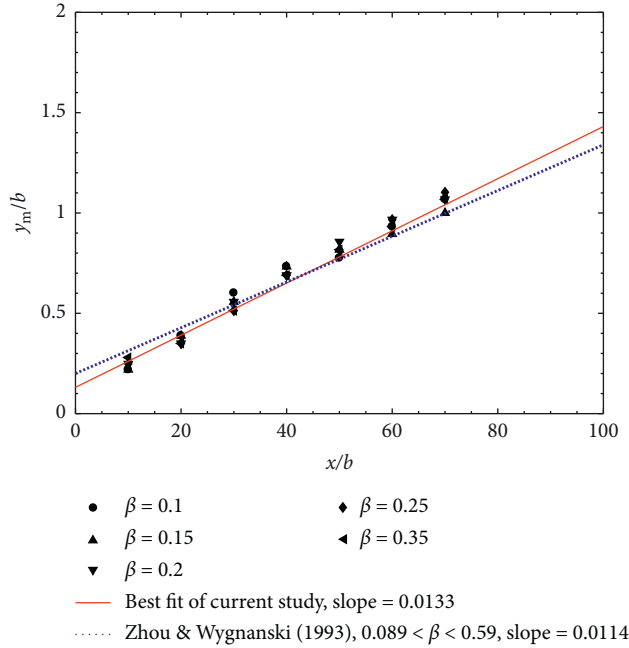


FIGURE 13: Rate of spread of y_m for various velocity ratios.

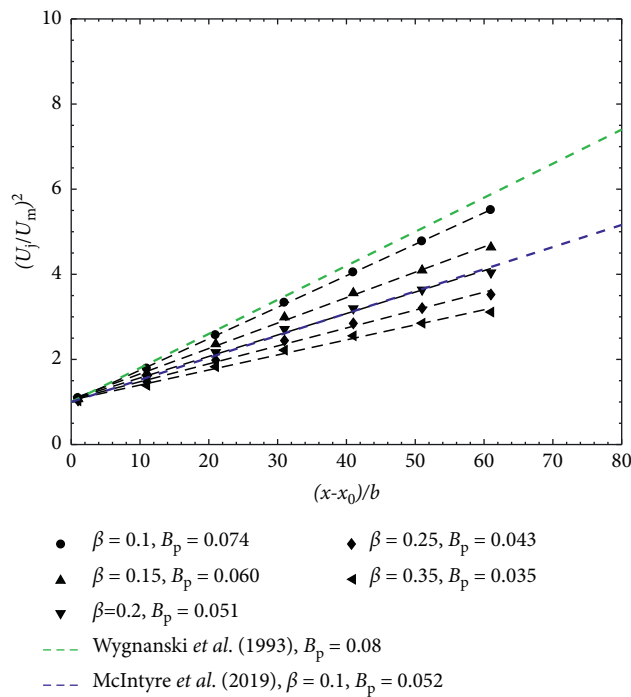


FIGURE 14: Decay of maximum velocity for various velocity ratios.

that the values of B_p decreased as the velocity ratio increased, that is, the decay of the maximum velocity slowed down.

The values of A_p and B_p obtained from the current data for different velocity ratios are shown in Figure 15. It can be observed that the velocity ratio had a significant influence on the evolution of the plane wall jet. The values of coefficient A_p increased linearly with the velocity ratio β , while the coefficient B_p decreased exponentially with an increase in the co-flow ratio β .

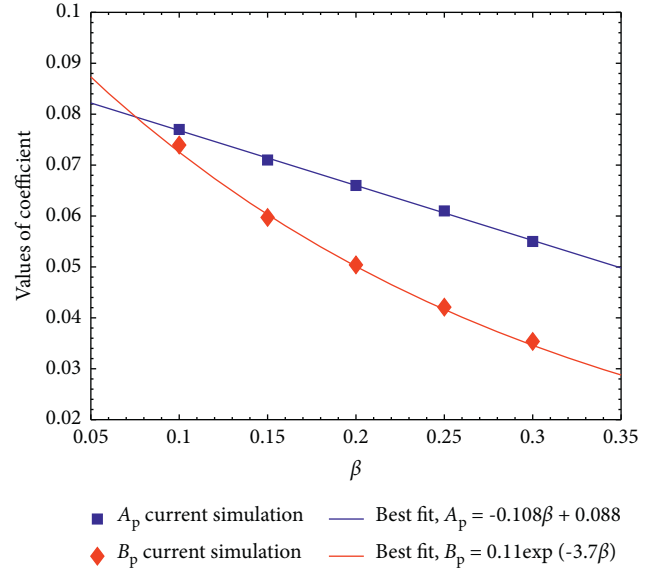


FIGURE 15: Values of A_p and B_p with respect to various velocity ratios.

According to the above analyses, the effect of a high Reynolds number can be neglected. Thus, only the effect of the velocity ratio needs to be considered when the plane wall jet method is used to simulate the downburst outflow. The spread of the plane wall jet with co-flow can be expressed as equation (5) and the decay of the maximum velocity with downstream distance for different velocity ratios can be expressed as equation (6).

$$\frac{y_{(1/2)}}{b} = (-0.108\beta + 0.0876) \times \left(\frac{x}{b}\right) + C_1, \quad (5)$$

$$\left(\frac{U_j}{U_m}\right)^2 = 0.11 \exp^{-3.7\beta} \left(\frac{x}{b}\right) + 1. \quad (6)$$

3.3. Jet Spread and Velocity Decay of Impinging Jet

3.3.1. Effect of Jet Reynolds Number. This section explains the effects of the Reynolds number on the jet spread and velocity decay for the wall jet region of the impinging jet. According to Hjelmfelt [46] summary of JAWS results, the average downburst diameter is approximately 1.8 km and the average distance from the cloud base to the ground surface is 2.7 km. On average, the ratio of the cloud base height to the downburst diameter is approximately 1.5. Thus, a widely used distance of $H = 2D$ from the jet nozzle to the bottom wall [56] was adopted in the current study.

For a fixed nozzle height above the plate board, $H = 2D$, the variation in the half-height with r positions for different Reynolds numbers is shown in Figure 16. It can be observed that the Reynolds number has no significant effect on the half-height, which can be considered independent of the Reynolds number. Sengupta and Sarkar [35] and Li *et al.* [56] proposed empirical expressions for the distribution of half-height based on experimental and CFD data, respectively.

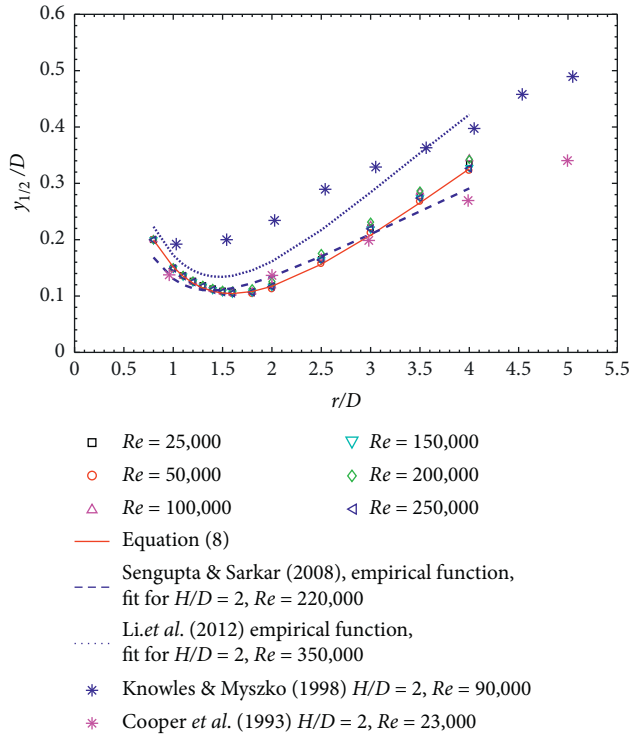


FIGURE 16: Radial growth of jet half-height for different Reynolds numbers.

The current CFD results are very similar to the empirical curve obtained by Sengupta and Sarkar as well as the hot-wire data from Cooper et al. [13] in the region of $r < 3.5D$. The empirical curve obtained by Li et al. [56] and the experimental data reported by Knowles and Myszko [14] exhibit larger values than those in this study. By fitting with the CFD results, the spread of the jet flow can be expressed as

$$\frac{y_{(1/2)}}{D} = -0.1771 + 0.1252 \frac{r}{D} + 0.9418 \exp\left(-1.532 \frac{r}{D}\right). \quad (7)$$

Because of the high convective heat transfer from the wall near the stagnation point, most of the studies on radial wall jets are limited to the stagnation region. The wall jet region of the impinging jet has been less emphasized. Xu and Hangan [45] suggested that the impingement region extended from the free jet axis to the location of $r/D = 1.4$. Tummers et al. [57] reported that the minimum value of half-height for an impinging jet is located at $r/D = 1.5$. Cooper et al. [13] indicated that the radial wall jet grows linearly with distance $r > 2D$, and the nozzle height has little effect on the slope of the jet growth. The results from Knowles and Myszko [14] exhibited a linear growth for $r > 2.5D$. Figure 17 shows the plot of the half-height with r for different Reynolds numbers and $r > 1.8D$. The slope obtained from the current study was 0.098, which is equal to the value reported by van Hout et al. [12].

The effect of the velocity ratio on the radial evolution of the maximum velocity decay, together with the available experimental results, is presented in Figure 18. The

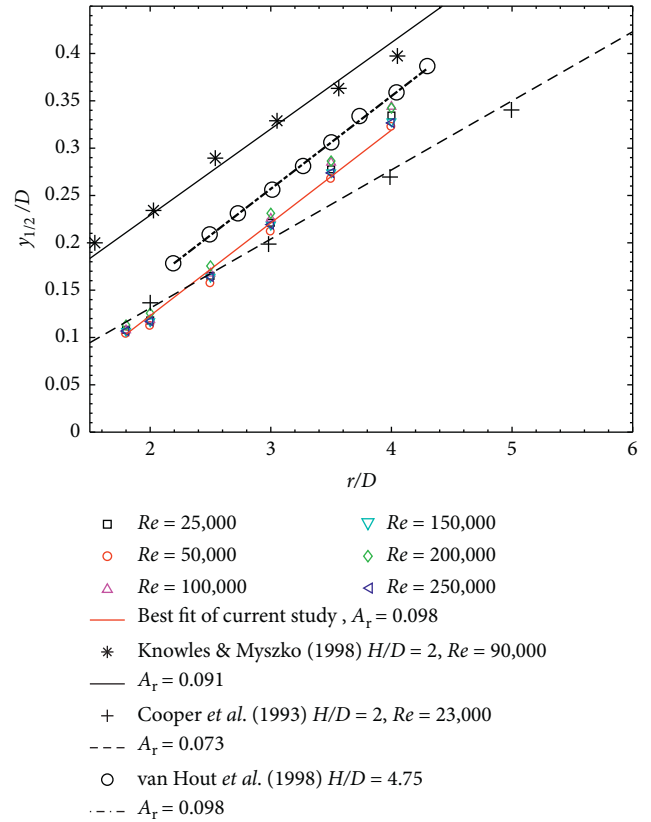


FIGURE 17: Variation of the growth rates for different Reynolds numbers.

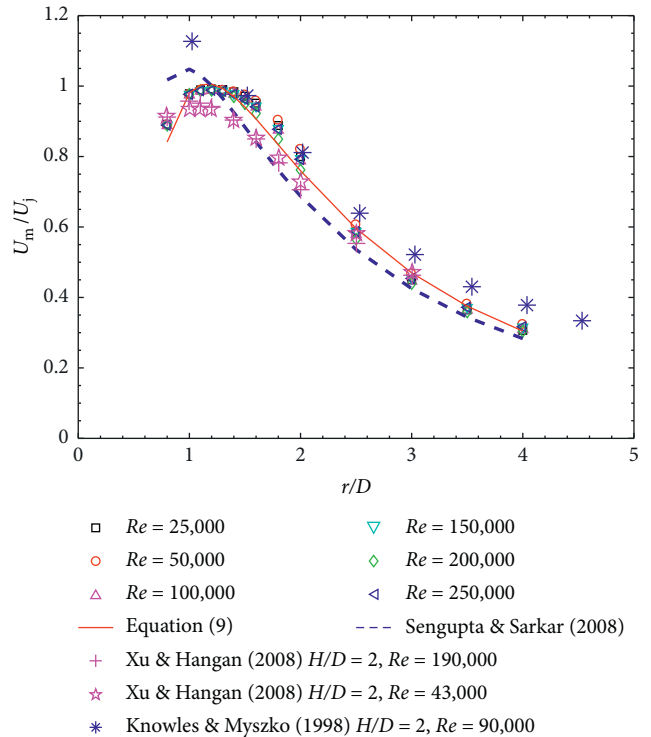


FIGURE 18: Decay of maximum mean radial velocity for different Reynolds numbers.

measured results from different studies do not agree well with each other. It can be observed that the values of U_m/U_j for different Reynolds numbers in the same radial position are the same. The maximum mean velocity scaled with the slot quantities is independent of the Reynolds number. This is in agreement with the observations made by Xu and Hangan [45]. Sengupta and Sarkar [35] proposed an empirical expression as follows:

$$\frac{U_m}{U_j} = \exp\left(a - \frac{b}{r/D} - c \ln\left(\frac{r}{D}\right)\right), \quad (8)$$

where $a = 1.905$, $b = 1.858$, and $c = 1.949$. However, to fit with the CFD results of the current simulation, the values of a , b , and c should be adjusted to 2.617, 2.637, and 2.27, respectively. For $1 < r/D < 2$, the current results agree well with those of Knowles and Myszko [14] for $Re = 90,000$. For $r/D > 2$, a good agreement can be observed between the current data and the results obtained by Xu and Hangan [45] for $Re = 43,000$. The maximum radial velocity (U_m) was almost equal to the jet velocity at the radial station for $r/D = 1.1$. This is in agreement with the findings by Tummers et al. [57].

3.3.2. Effect of Nozzle Height. To examine the effect of the nozzle height above the plate board on the evolution of the radial wall jet, the radial distributions of r location of the half-height for different nozzle height-to-plate distance ratios (H/D) are presented in Figure 19.

The impingement region gradually decreased with an increase in nozzle height H . In general, the half-height value increases with the increase in nozzle height H , which is in good agreement with the results obtained by Knowles and Myszko [14] and Cooper et al. [13]. The current results are similar to those of Copper et al. [13] in the impingement region and are in good agreement with the data obtained by Knowles and Myszko [14] in the radial wall jet region. However, when the outflow height $H/D < 2$ or $3 < H/D < 5$, the half-height did not change significantly. Therefore, for the range in which these nozzle heights are located, the outflow height has little effect on the half-height value.

The effect of the nozzle height on the radial evolution of the maximum velocity is shown in Figure 20. It can be observed that with an increase in the nozzle height, the closer the radial position of the maximum wind speed to the stagnation point, the lower the maximum wind speed. Compared with existing literature data, the current simulation results are similar to the data reported by Knowles and Myszko [14] in the impingement region, and they agree well with the results obtained by Cooper et al. [13] for $r > 1.5D$. The influence of the nozzle height on the maximum velocity decay also exhibited step characteristics, similar to the influence on the half-height.

Based on the data collected during the JAWS project, Hjelmfelt [46] found that the average ratio of the downburst outflow height to diameter is approximately 1.5. It can be observed from the above results that the nozzle height has no significant effect on the jet spread and velocity decay of the radial wall jet near this average ratio. Therefore, when the

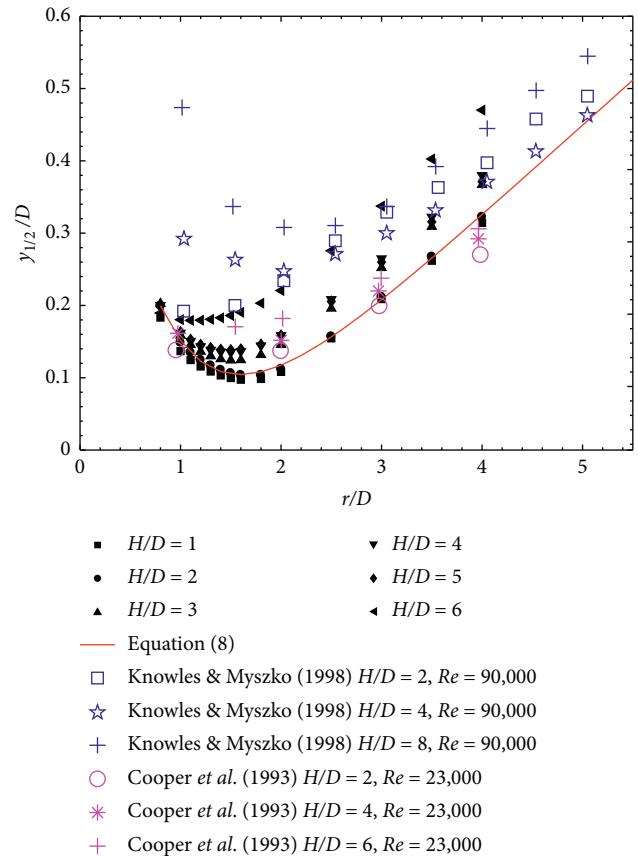


FIGURE 19: Radial growth of jet half-height for different nozzle heights.

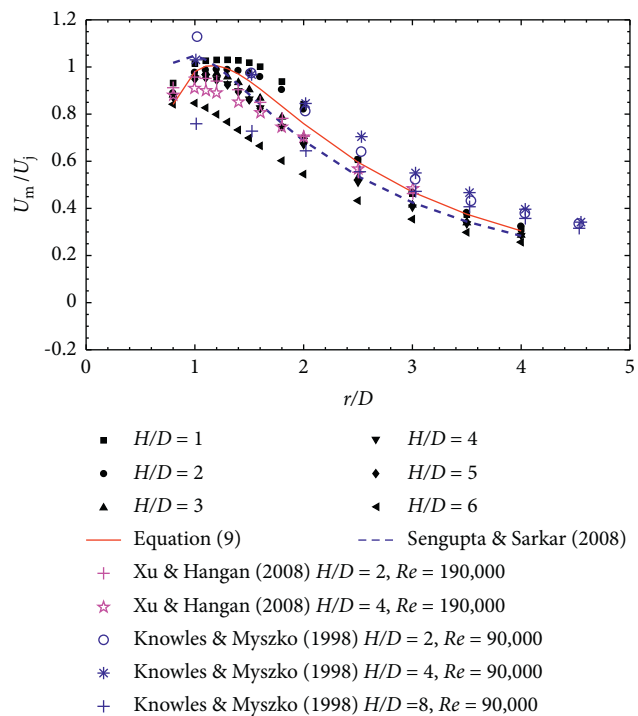


FIGURE 20: Decay of maximum mean radial velocity for different nozzle heights.

radial wall jet method is used to study the downburst, the influence of the outflow height can be ignored. The most widely used nozzle height is $2D$ [35, 56].

4. Validation of the 2D Assumption for the Downburst Outflow

The outflow of the stationary ideal downburst radially spreads outward from the stationary point. When the radial wall jet and plane wall jet are used to simulate the outflow of the downburst, although similar wind profiles can be generated, it can be seen from the above studies that there are differences between the jet spreads and velocity decays. In comparison, radial wall jets have faster decay rates. To evaluate the accuracy of approximating a 3D downburst outflow with a 2D wall jet, the configuration of the transmission tower and downburst, as presented in Figure 21, was examined. A single-span transmission tower-line system with a span length of S was used for the analysis. The distance r_A and angle θ were used to define the location of the center of the tower relative to the stagnation of the downburst.

The differences between the half-heights and maximum velocities of locations A and B are defined as $\Delta y_{1/2}$ and ΔU_m , respectively. The deviation of the half-height differences of the downburst outflow obtained using the two methods is

$$\gamma_1 = \Delta y_{(1/2)\text{-radial}} - \Delta y_{(1/2)\text{-plane}}, \quad (9)$$

and the deviation of the maximum velocity differences of the downburst outflow obtained using the two methods is

$$\gamma_2 = \Delta U_{m\text{-radial}} - \Delta U_{m\text{-plane}}. \quad (10)$$

A downburst case was assumed with $D = 1000$ m and $U_j = 80$ m/s to investigate the difference between the impinging jet and plane wall jet. Tower A is located at a distance of $1.8D$ from the stagnation point. Using simple trigonometry, the radial distance of tower B, which is the location of the stagnation point of the downburst relative to the center of the tower, can be evaluated. When the plane wall jet method is used, x_a is equal to r_a . Using simple trigonometry, the value of x_b can be calculated. In addition, the height of the jet nozzle (b) can be estimated according to the height of the maximum wind velocity (y_m) and the diameter of the downburst (D). The detailed algorithm is provided in Appendix B. Therefore, the length scale deviations between the radial and plane wall jet methods can be evaluated using equations (5), (7), and (9). The velocity scale deviations can be evaluated using equations (6), (8), and (10). For various combinations of angles (θ) and span lengths (S), the ratios of the length scale deviations to the half-height at location A for the radial wall jet are listed in Table 4, and the ratios of the velocity scale deviations to the maximum velocity at location A for the radial wall jet are listed in Table 5.

Assuming a ratio of less than 5% as an acceptable value, all the values in Table 4 and the upper left (unshaded) values in Table 5 indicate that the two-dimensional (2D) assumption is valid for wide structures. For example, for a 200 m transmission tower-line system, there are no clear

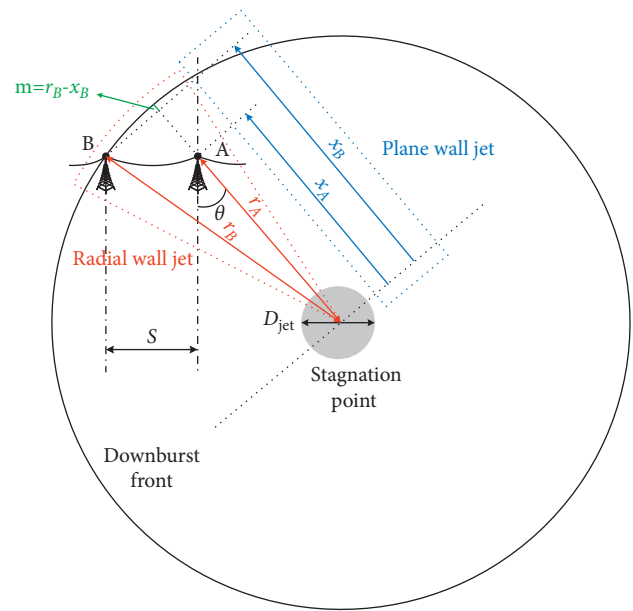


FIGURE 21: Horizontal projection of transmission tower and downburst.

TABLE 4: γ_1 as a percentage of half-height of radial wall jet at location A.

	S (m)				
θ	100	200	300	400	500
0°	0.0	0.2	0.5	0.8	1.3
15°	0.5	0.8	1.0	1.0	0.7
30°	1.0	1.7	2.1	2.2	2.1
45°	1.4	2.3	2.9	3.1	3.0
60°	1.7	2.8	3.5	3.7	3.6
75°	1.8	3.1	3.8	4.1	3.9
90°	1.9	3.2	3.9	4.2	4.0

TABLE 5: γ_2 as a percentage of the maximum velocity for the radial wall jet at location A.

	S (m)				
θ	100	200	300	400	500
0°	0.1	0.5	1.1	2.0	3.0
15°	0.8	1.9	3.1	4.5	6.1
30°	1.4	3.1	4.9	6.8	8.7
45°	2.0	4.1	6.3	8.5	10.8
60°	2.4	4.8	7.3	9.8	12.2
75°	2.6	5.3	8.0	10.5	13.0
90°	2.7	5.5	8.2	10.8	13.3

differences between the length and velocity scales of the radial and plane wall jets. The simplified 2D approach appears to be effective for simulating downbursts. Using the plane wall jet method, a large-scale wind tunnel test can be performed based on the traditional atmospheric boundary layer wind tunnel.

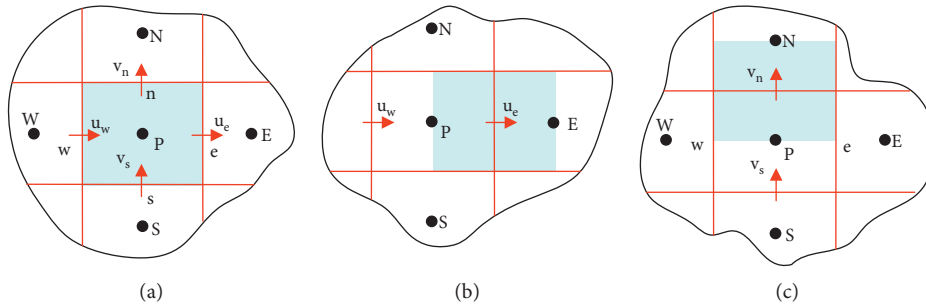


FIGURE 22: Control volume used to illustrate discretization of a scalar transport equation: (a) p-control volume, (b) u_e - control volume, (c) v_s -control volume.

5. Conclusions

In the present study, turbulent radial and plane wall jets were simulated numerically using RSM. The numerical results were compared with previous experimental measurements in the literature, and the effects of different parameters on the length and velocity scales were systematically evaluated. Based on the CFD results, it is valid to approximate a downburst outflow with a 2D assumption for a transmission line under specific conditions. The main findings of this study are summarized as follows:

- (1) The computed results show that the Reynolds stress model accurately predicts the behaviors of radial and plane wall jets. The predictions from the current simulation agree well with the experimental data available in the literature. Compared with the existing experimental results, the maximum difference was approximately 12%. Both radial and plane wall jet methods can effectively simulate the characteristics of the mean velocity profile of the downburst outflow.
- (2) The decay of the maximum velocity and rate of jet spread for the radial wall jet are independent of the Reynolds number for a fixed nozzle height. The nozzle height has a clear effect on the evolution of the radial wall jet. However, when the value of H/D is approximately less than 2, which includes the average ratio of cloud base height to the diameter of most downbursts, the influence of the nozzle can be ignored.
- (3) The decay of the maximum velocity and the half-height of the plane wall jet are dependent on the Reynolds number below a critical value, $Re_{cr} = 60,000$. Above Re_{cr} , the flow becomes asymptotically independent of the Reynolds number. The influence of the Reynolds number can thus be neglected when the plane wall jet is used to simulate the downburst outflow for $Re > Re_{cr}$. To improve the usability of the plane wall jet approach, the shape functions of scale parameters were proposed.
- (4) Co-flow has a significant influence on the plane wall jet. With an increase in the velocity ratio, the jet spread and decay of the maximum velocity gradually

slow down. When the velocity ratio increases from 0.1 to 0.35, the value of B_p decreases by 52.7%.

- (5) Within the span length of a conventional transmission tower-line system, the discrepancy between the downburst outflows simulated using the plane and radial wall jet approaches in the longitudinal direction can be neglected. It is valid to approximate the downburst outflow with a 2D assumption from the perspective of the longitudinal evolution of the flows. In large-scale facilities, the profile can be optimized by controlling the initial flow field conditions, and the plane wall jet method can produce a flow field several times larger than that of the radial wall jet method.

Appendix

A. The SIMPLEC algorithm

The SIMPLEC algorithm uses the relationship between the velocity and pressure corrections to enforce mass conservation and obtain the pressure field.

To provide a brief review of the SIMPLEC method, the staggered grid shown in Figure 22 is used. The discretized u -momentum equation can be written as follows:

$$a_e u_e = \sum \sum a_{nb} u_{nb} + b_e + A_e (p_P - p_E), \quad (A.1)$$

where p is the pressure, A_e is the area of the face of the P-control volume at e , and a_e is the coefficient of the finite-volume equations. A pressure field p^* is assumed to initiate the SIMPLE calculation process. The u^* velocity is obtained by solving the u -momentum equations and satisfy the following equation:

$$a_e u_e^* = \sum \sum a_{nb} u_{nb}^* + b_e + A_e (p_P^* - p_E^*). \quad (A.2)$$

However, the u^* velocities from equation (A.2) in general do not satisfy the continuity condition. To correct the u^* field, the estimated pressure is corrected by considering $p' = p - p^*$. Subtracting equation (A2) from equation (A1) gives

$$a_e u_e' = \sum \sum a_{nb} u_{nb}' + A_e (p_P' - p_E'), \quad (A.3)$$

where p' and u' are the pressure and velocity corrections, respectively. The correct pressure p and velocity u can be written as

$$\begin{aligned} u &= u^* + u', \\ p &= p^* + p'. \end{aligned} \quad (\text{A.4})$$

Subsequently, the u -velocity correction equation of SIMPLEC is given by

$$u_e = d_e (p'_P - p'_E), \quad (\text{A.5})$$

where

$$d_e = \frac{A_e}{a_e - \sum a_{nb}}. \quad (\text{A.6})$$

For the control volume shown in Figure 22, the continuity equation satisfies

$$(\rho u A)_{w^*} - (\rho u A)_e + (\rho v A)_s - (\rho u A)_n = 0. \quad (\text{A.7})$$

Substituting the correct u into the continuity equation gives the following result:

$$a_P p'_P = a_E p'_E + a_W p'_W + a_N p'_N + a_S p'_S + b, \quad (\text{A.8})$$

where

$$\begin{aligned} a_E &= (\rho A d)_e & a_W &= (\rho A d)_w, \\ a_N &= (\rho A d)_n & a_S &= (\rho A d)_s, \\ a_P &= a_E + a_W + a_N + a_S, \\ b &= (\rho u^* A)_w - (\rho u^* A)_e + (\rho v^* A)_s - (\rho u^* A)_n. \end{aligned} \quad (\text{A.9})$$

The pressure correction p' can be obtained using equation (A8). Subsequently, the correct velocity field can be obtained.

B. Evaluation of Effective Downdraft Diameter for the Plane Wall Jet

Previous studies have shown that the maximum mean velocity occurs at a height of less than $0.05D$ [28, 45, 58]. For the radial wall jet, the value of y_m obtained from the current RSM results at a distance of $1.5D$ from the stagnation point ($x = 1.5D$) is $0.03D$. The influences of Reynolds numbers on the maximum velocity and location are negligible when $Re > 60,000$. An effective plane wall jet downdraft diameter can be determined based on the height of the maximum velocity, as expressed in equation (B1):

$$\begin{aligned} D_{\text{equ}} &= \frac{y_m}{0.03} \\ &= \frac{(0.0133x + 0.131b)}{0.03}. \end{aligned} \quad (\text{B.1})$$

For example, the nozzle height of the plane wall jet is 0.03 m in the current simulation; thus, the effective plane wall jet downdraft diameter is evaluated as 0.53 m at the downstream distance of $x = 30b$.

Data Availability

The data used to support the findings of this study are included within the article.

References

- [1] B. E. Launder and W. Rodi, "The turbulent wall jet measurements and modeling," *Annual Review of Fluid Mechanics*, vol. 15, no. 1, pp. 429–459, 1983.
- [2] S. A. Bagherzadeh, E. Jalali, M. M. Sarafriz et al., "Effects of magnetic field on micro cross jet injection of dispersed nanoparticles in a microchannel," *International Journal of Numerical Methods for Heat and Fluid Flow*, vol. 30, no. 5, pp. 2683–2704, 2019.
- [3] E. Jalali, O. A. Akbari, M. M. Sarafriz, T. Abbas, and M. R. Safaei, "Heat transfer of oil/MWCNT nanofluid jet injection inside a rectangular microchannel," *Symmetry*, vol. 11, no. 6, p. 757, 2019.
- [4] E. Savory, G. A. R. Parke, M. Zeinoddini, N. Toy, and P. Disney, "Modelling of tornado and microburst-induced wind loading and failure of a lattice transmission tower," *Engineering Structures*, vol. 23, no. 4, pp. 365–375, 2001.
- [5] A. Y. Shehata, A. A. E. Damatty, and E. Savory, "Finite element modeling of transmission line under downburst wind loading," *Finite Elements in Analysis and Design*, vol. 42, no. 1, pp. 71–89, 2005.
- [6] P. Bradshaw, "The normal impingement of a circular air jet on a flat surface," *Wear*, vol. 5, no. 1, 1962.
- [7] G. S. Wood, K. C. S. Kwok, N. A. Motteram, and D. F. Fletcher, "Physical and numerical modelling of thunderstorm downbursts," *Journal of Wind Engineering and Industrial Aerodynamics*, vol. 89, no. 6, pp. 535–552, 2001.
- [8] W. E. Lin and E. Savory, "Large-scale quasi-steady modelling of a downburst outflow using a slot jet," *Wind and Structures*, vol. 9, no. 6, pp. 419–440, 2006.
- [9] W. E. Lin and E. Savory, "Physical modelling of a downdraft outflow with a slot jet," *Wind and Structures An International Journal*, vol. 13, no. 5, pp. 385–412, 2010.
- [10] B. E. Launder and W. Rodi, "The turbulent wall jet," *Progress in Aerospace Sciences*, vol. 19, pp. 81–128, 1981.
- [11] I. Z. Naqavi, J. C. Tyacke, and P. G. Tucker, "Direct numerical simulation of a wall jet: flow physics," *Journal of Fluid Mechanics*, vol. 852, pp. 507–542, 2018.
- [12] R. van Hout, V. Rinsky, and Y. G. Grobman, "Experimental study of a round jet impinging on a flat surface: flow field and vortex characteristics in the wall jet," *International Journal of Heat and Fluid Flow*, vol. 70, pp. 41–58, 2018.
- [13] D. Cooper, D. C. Jackson, B. E. Launder, and G. X. Liao, "Impinging jet studies for turbulence model assessment-I. Flow-field experiments," *International Journal of Heat and Mass Transfer*, vol. 36, no. 10, pp. 2675–2684, 1993.

- [14] K. Knowles and M. Myszkowski, "Turbulence measurements in radial wall-jets," *Experimental Thermal and Fluid Science*, vol. 17, no. 1-2, pp. 71-78, 1998.
- [15] S. Yao, Y. Guo, N. Jiang, and J. Liu, "An experimental study of a turbulent jet impinging on a flat surface," *International Journal of Heat and Mass Transfer*, vol. 83, pp. 820-832, 2015.
- [16] H. Abrahamsson, B. Johansson, and L. Löfdahl, "A turbulent plane 2-dimensional wall-jet in a quiescent surrounding," *European Journal of Mechanics - B: Fluids*, vol. 13, no. 5, pp. 533-556, 1994.
- [17] J. G. Eriksson, R. I. Karlsson, and J. Persson, "An experimental study of a two-dimensional plane turbulent wall jet," *Experiments in Fluids*, vol. 25, no. 1, pp. 50-60, 1998.
- [18] N. Rostamy, D. J. Bergstrom, D. Sumner, and J. D. Bugg, "The effect of surface roughness on the turbulence structure of a plane wall jet," *Physics of Fluids*, vol. 23, no. 8, Article ID 085103, 2011.
- [19] I. Wygnanski, Y. Katz, and E. Horev, "On the applicability of various scaling laws to the turbulent wall jet," *Journal of Fluid Mechanics*, vol. 234, no. 1, pp. 669-690, 1992.
- [20] M. D. Zhou and I. Wygnanski, "Parameters governing the turbulent wall jet in an external stream," *AIAA Journal*, vol. 31, no. 5, pp. 848-853, 1993.
- [21] T. Tanaka and E. Tanaka, "Experimental studies of a radial turbulent jet: 2nd report, wall jet on a flat smooth plate," *Bulletin of Jsme*, vol. 20, no. 140, pp. 209-215, 1977.
- [22] R. Banyassady and U. Piomelli, "Interaction of inner and outer layers in plane and radial wall jets," *Journal of Turbulence*, vol. 16, no. 5, pp. 460-483, 2015.
- [23] T. Guo, M. J. Rau, P. P. Vlachos, and S. V. Garimella, "Axisymmetric wall jet development in confined jet impingement," *Physics of Fluids*, vol. 29, no. 2, Article ID 025102, 2017.
- [24] P. Fillingham and I. V. Novoselov, "Wall jet similarity of impinging planar underexpanded jets," *International Journal of Heat and Fluid Flow*, vol. 81, Article ID 108516, 2020.
- [25] S. Pieris, X. Zhang, S. Yarusevych, and S. D. Peterson, "Vortex dynamics in a normally impinging planar jet," *Experiments in Fluids*, vol. 60, no. 5, 2019.
- [26] Z. Tang, N. Rostamy, D. J. Bergstrom, J. D. Bugg, and D. Sumner, "Incomplete similarity of a plane turbulent wall jet on smooth and transitionally rough surfaces," *Journal of Turbulence*, vol. 16, no. 11, pp. 1076-1090, 2015.
- [27] M. Khashehchi and Z. Harun, "Accuracy of tomographic particle image velocimetry data on a turbulent round jet," *International Journal of Heat and Fluid Flow*, vol. 77, pp. 61-72, 2019.
- [28] M. T. Chay and C. W. Letchford, "Pressure distributions on a cube in a simulated thunderstorm downburst-Part A: stationary downburst observations," *Journal of Wind Engineering and Industrial Aerodynamics*, vol. 90, no. 7, pp. 711-732, 2002.
- [29] C. Junayed, C. Jubayer, D. Parvu, D. Romanic, and H. Hangan, "Flow field dynamics of large-scale experimentally produced downburst flows," *Journal of Wind Engineering and Industrial Aerodynamics*, vol. 188, pp. 61-79, 2019.
- [30] A. C. McConville, M. Sterling, and C. J. Baker, "The physical simulation of thunderstorm downbursts using an impinging jet," *Wind and Structures An International Journal*, vol. 12, no. 2, pp. 133-149, 2009.
- [31] A. Dejoan and M. A. Leschziner, "Large eddy simulation of a plane turbulent wall jet," *Physics of Fluids*, vol. 17, no. 2, Article ID 025102, 2005.
- [32] W. E. Lin, E. Savory, R. P. McIntyre, C. S. Vandelaar, and J. P. C. King, "The response of an overhead electrical power transmission line to two types of wind forcing," *Journal of Wind Engineering and Industrial Aerodynamics*, vol. 100, no. 1, pp. 58-69, 2012.
- [33] W. E. Lin, L. G. Orf, E. Savory, and C. Novacco, "Proposed large-scale modelling of the transient features of a downburst outflow," *Wind and Structures*, vol. 10, no. 4, pp. 315-346, 2007.
- [34] Z. Yan, Y. Zhong, X. Cheng, R. P. McIntyre, and E. Savory, "A numerical study of a confined turbulent wall jet with an external stream," *Wind and Structures*, vol. 27, no. 2, pp. 101-109, 2018.
- [35] A. Sengupta and P. P. Sarkar, "Experimental measurement and numerical simulation of an impinging jet with application to thunderstorm microburst winds," *Journal of Wind Engineering and Industrial Aerodynamics*, vol. 96, no. 3, pp. 345-365, 2008.
- [36] D. C. Wilcox, *Turbulence Modeling for CFD*, Dcw Industries, Incorporated, CA, USA, Second edition, 1998.
- [37] D. C. Wilcox, *Turbulence Modeling for CFD*, Dcw Industries, CA, USA, Third edition, 2006.
- [38] H. Versteeg and W. Malalasekera, *An Introduction to Computational Fluid Dynamics*, Prentice-Hall, NJ, USA, 2007.
- [39] M. Safaei, M. Goodarzi, and M. Mohammadi, "Numerical modeling of turbulence mixed convection heat transfer in air filled enclosures by finite volume method," *The International Journal of Multiphysics*, vol. 5, no. 4, pp. 307-324, 2011.
- [40] J. P. Van Doormaal and G. D. Raithby, "Enhancements OF the simple method for PREDICTING incompressible fluid flows," *Numerical Heat Transfer*, vol. 7, no. 2, pp. 147-163, 1984.
- [41] Z. Yan, Y. Zhong, W. E. Lin, E. Savory, and Y. You, "Evaluation of RANS and LES turbulence models for simulating a steady 2-D plane wall jet," *Engineering Computations*, vol. 35, no. 1, pp. 211-234, 2018.
- [42] W. K. George, H. Abrahamsson, J. Eriksson, R. I. Karlsson, L. Löfdahl, and M. Wosnik, "A similarity theory for the turbulent plane wall jet without external stream," *Journal of Fluid Mechanics*, vol. 425, pp. 367-411, 2000.
- [43] M. T. Chay, F. Albermani, and R. Wilson, "Numerical and analytical simulation of downburst wind loads," *Engineering Structures*, vol. 28, no. 2, pp. 240-254, 2006.
- [44] D. D. Vicroy, "Assessment of microburst models for down-draft estimation," *Journal of Aircraft*, vol. 29, no. 6, pp. 1043-1048, 1992.
- [45] Z. Xu and H. Hangan, "Scale, boundary and inlet condition effects on impinging jets," *Journal of Wind Engineering and Industrial Aerodynamics*, vol. 96, no. 12, pp. 2383-2402, 2008.
- [46] M. R. Hjelmfelt, "Structure and life cycle of microburst outflows observed in Colorado," *Journal of Applied Meteorology*, vol. 27, no. 8, pp. 900-927, 1988.
- [47] R. P. McIntyre, *The Effect Of Inlet Geometry On the Development Of a Plane Wall Jet*, PhD Thesis, School of Graduate and Postdoctoral Studies, University of Western Ontario, London Canada, 2011.
- [48] G. Xu and R. Antonia, "Effect of different initial conditions on a turbulent round free jet," *Experiments in Fluids*, vol. 33, no. 5, pp. 677-683, 2002.
- [49] R. M. Oseguera and R. L. Bowles, *A Simple, Analytic 3-dimensional Downburst Model Based on Boundary Layer Stagnation Flow* (NASA Technical Memorandum 100632, National Aeronautics and Space Administration, Washington D. C., USA, 1988.
- [50] W. H. Schwarz and W. P. Cosart, "The two-dimensional turbulent wall-jet," *Journal of Fluid Mechanics*, vol. 10, no. 4, 1961.

- [51] S. H. A. Ben, S. Habli, N. S. Mahjoub, P. Bournot, and G. L. Palec, "A numerical study of a plane turbulent wall jet in a coflow stream," *Journal of Hydro-Environment Research*, vol. 12, pp. 16–30, 2016.
- [52] M. E. Schneider and R. J. Goldstein, "Laser Doppler measurement of turbulence parameters in a two-dimensional plane wall jet," *Physics of Fluids*, vol. 6, no. 9, pp. 3116–3129, 1994.
- [53] W. E. Lin, *Validation Of a Novel Downdraff Outflow Simulator: A Slot Jet Wind Tunnel [Doctor of Philosophy]*, The University of Western Ontario, Canada, USA, 2010.
- [54] G. I. Barenblatt, A. J. Chorin, and V. M. Prostokishin, "The turbulent wall jet: a triple-layered structure and incomplete similarity," *Proceedings of the National Academy of Sciences*, vol. 102, no. 25, pp. 8850–8853, 2005.
- [55] R. McIntyre, E. Savory, H. Wu, and D. S.-K. Ting, "The effect of the nozzle top lip thickness on a two-dimensional wall jet," *Journal of Fluids Engineering*, vol. 141, no. 5, Article ID 051106, 2019.
- [56] C. Li, Q. S. Li, Y. Q. Xiao, and J. P. Ou, "A revised empirical model and CFD simulations for 3D axisymmetric steady-state flows of downbursts and impinging jets," *Journal of Wind Engineering and Industrial Aerodynamics*, vol. 102, pp. 48–60, 2012.
- [57] M. J. Tummers, J. Jacobse, and S. G. J. Voorbrood, "Turbulent flow in the near field of a round impinging jet," *International Journal of Heat and Mass Transfer*, vol. 54, no. 23–24, pp. 4939–4948, 2011.
- [58] J. Kim and H. Hangan, "Numerical simulations of impinging jets with application to downbursts," *Journal of Wind Engineering and Industrial Aerodynamics*, vol. 95, no. 4, pp. 279–298, 2007.

Analysis on NSM CFRP Strengthened RC Concrete Beams

Flora Das, *Department of Civil Engineering, Aryan Institute of Engineering & Technology, Bhubaneswar, floradas22@yahoo.co.in*

Anjan Kumar M. U., *Department of Civil Engineering, NM Institute of Engineering & Technology, Bhubaneswar, anjankumar28@yahoo.co.in*

Monalika Mohanty, *Department of Civil Engineering, Raajdhani Engineering College, Bhubaneswar, monalika_m256@gmail.com*

Kankan Mandal, *Department of Civil Engineering, Capital Engineering College, Bhubaneswar, kankanmandal2@outlook.com*

ABSTRACT

The use of NSM FRP for concrete structure strengthening has become a popular choice for retrofitting existing structures against shear and flexure. In previous review articles, only the use of NSM for shear was discussed. To evaluate the existing design formulas for computing the NSM contribution in shear, a database of testing of NSM strengthened beams in shear is presented. These formulas corresponded to the database's experimental results. The shape of NSM FRP bars, the combined effects of existing steel stirrups, and NSM FRP reinforcement and analytical formulations are among the other study subjects mentioned.

1. Introduction

Sudden failure because of low resistance to shear is something required to be avoided. Thus, one of the priorities of researchers is to find an appropriate strengthening technique that can be employed to enhance RC beams when they are deficiently reinforced in shear, when they fall under higher loads, or when the shear capacity of beam is below the flexural capacity due to flexural strengthening for example. Employment of composite materials in strengthening/retrofitting concrete elements is one of these techniques. Externally bonded (EB) Carbon Fiber Reinforced Polymer (CFRP) is one of the earlier systems used in strengthening concrete elements in the case of using composite materials [1–7]. However, recently, using near surface mounted (NSM) with CFRP becomes one of the most investigated techniques in flexural [8–14] and shear strengthening [15–21] (see Figure 1) because of its advantages over externally bonded EB-CFRP reinforcement [18, 22]:

- (1) The previous experimental studies have demonstrated that the NSM strengthening technique can provide higher strengthening effectiveness compared to EBR due to higher bonded area-to-cross-sectional area of the CFRP element ratio. For this reason, the NSM technique is less prone to debonding failure.
- (2) The amount of site installation work needed in the case of the NSM technique is less than that required in EBR technique.
- (3) In the case of intending of use prestressed CFRP reinforcements, NSM bars can easily be used.
- (4) The NSM strengthening technique reduces the probability of harm resulting from accidental impact, mechanical damage, vandalism, and fire because the NSM bars are protected by the concrete cover.
- (5) The appearance of structural member is uninfluenced with using the NSM strengthening technique.

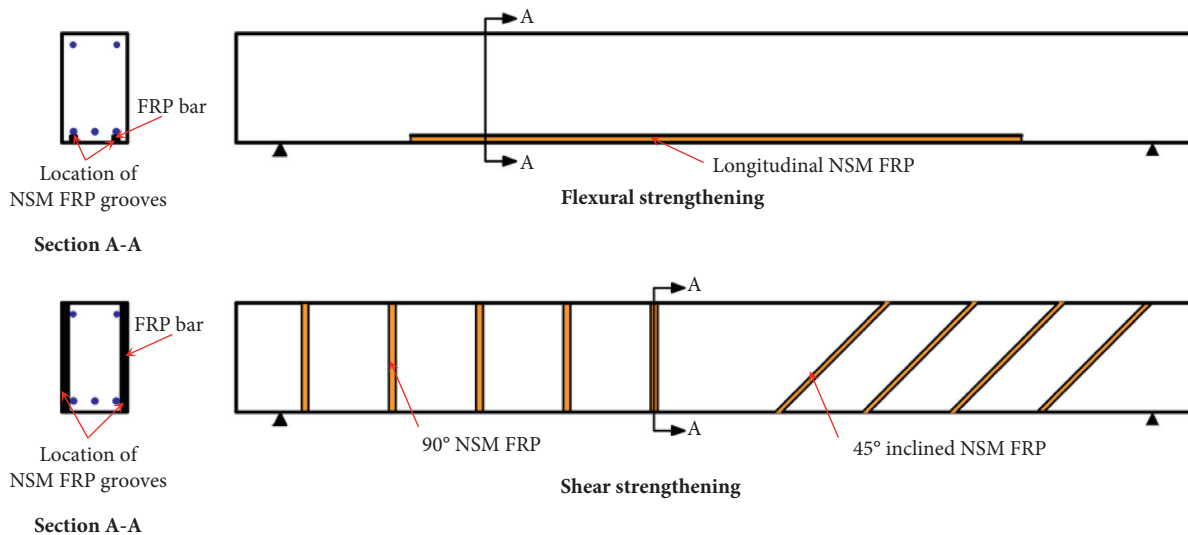


FIGURE 1: NSM FRP strengthening of beams in flexure and shear.

There is a growing body of literature that recognizes the importance of using the NSM strengthening technique because of the above listed advantages. Several review studies had been found in the literature [18,23–25]. However, to the best of the authors' knowledge, there is no one that has reviewed the research of shear contribution of NSM CFRP strengthening technique. This paper focuses on research studies that investigated the shear strengthening of RC beams with CFRP NSM technique. In addition, some aspects regarding the bond strength and the factors affecting the bond performance are also discussed. Finally, the design rules for prediction of the CFRP contribution of the NSM shear strengthening systems are evaluated.

2. NSM Strengthening Technique

In order to install the CFRP laminates using NSM system, grooves with a desired depth, width, inclination, and spacing were opened on the concrete cover by using saw-cutting [16, 26–28] or diamond cutter [29]. These grooves were then cleaned by compressed air [16, 26–29] and compressed water in some cases [30]. Then, the grooves were filled with the adhesive material. Finally, the CFRP laminates were inserted into the slits of the beam, and the excess adhesive material was removed.

2.1. FRP Reinforcement. FRP bars can be produced in a variety of shapes. Two different cross-sectional shapes were used in the previous research studies that conducted the strengthening of RC beam in shear, which are round bars and thin narrow strips (simply referred as “strips” hereafter). The selection of the cross-sectional shape depends on many factors such as the depth of the concrete cover, the cost of a particular type of bar, and the availability of this type. For instance, strips need a thicker concrete cover for a specific cross-sectional area, but they have better performance compared with round bars of equivalent cross-sectional area

due to maximizing bond surface and hence reduce the risk of debonding failures in beams strengthened with NSM FRP strips [11].

The surface texture of FRP bars reinforcement was also varied to improve bond properties. In some cases, these bars were coated with epoxy paste and then sprinkled with 0.2/0.3 mm of surface sanding materials [31]. In other cases, the surface of the round bars was spirally wound with a fiber tow and coated with sand [26].

2.2. Groove Geometry. It mainly depends on the FRP cross section and bars surface treatment. The choice of groove dimensions can influence the bond performance, and hence, it can cause premature debonding failure. The rectangular, square, or round bars are commonly used.

The square and rectangular bars have several merits over round bars, such that they provide a uniform adhesive thickness in their vertical and parallel sides. Moreover, the ratio of surface to cross section area of square and rectangular bars is higher than that of round bars. This can minimize the bond stresses for the same tensile force in the FRP, which may split the groove filling cover. Another advantage of using rectangular bars is related to the simplicity of opening the grooves. The main disadvantage of rectangular bars is the need for a deeper groove to provide the same reinforcement area [18, 32].

Several studies [33–36] showed that FRP rectangular bars, which have a large height-to-thickness ratio, are superior to NSM FRP bars of other shapes. This is due to a larger embedment depth and a higher perimeter/cross-sectional area ratio than those FRP bars of other shapes, which consequently leads to a higher utilization capacity of FRP. The deeper FRP in the web provided higher shear strengthening, and the inclined FRP gave a more ductile behavior after peak load for the beams that were shear strengthened with NSM [37–39].

2.3. Groove Filler. The role of groove filler adhesive is to transfer the stresses between the FRP reinforcement and concrete. Two types of adhesive can be epoxy or cement based. The most relevant mechanical properties of groove filler are tensile and shear strengths. The tensile strength is especially important in case of round bars, which induce high circumferential tensile stresses in the epoxy [40]. The shear strength is especially important when the bond is controlled by cohesive shear failure of the epoxy. The cement based adhesive has some advantages vs. epoxy as follows: it is cheaper, presents reduced hazard to workers and environment, allows bonding to wet surfaces, has a better behavior at elevated temperatures, and is compatible with the concrete substrate. The main disadvantage is the low tensile strength compared to epoxy, and during hardening of the mortar, adequate wetting should be assured. Bond and flexural tests identified some limitations of cement mortar as groove filler [41]. The performance of the specimens with epoxy-filled grooves was almost similar and provided higher pull-out loads compared to the specimens with cement mortar adhesives [42]. The cementitious matrix with NSM strengthening system has generally improved the deformational characteristics of the strengthened specimens [39]. The NSM CFRP bar repair resulted in only a slight increase in stiffness and a slight decrease in strength due to the debonding of the vertical FRP in the web at the epoxy/mortar interface [43].

3. Bond Behavior

A key issue of the structural performance of the NSM technique is the bond behavior as for the EBR one, since the debonding of the FRP reinforcement can be a very common failure mode. Failure modes of the beams strengthened by the NSM technique were not brittle as those observed in the beams strengthened by the EBR technique [29].

Direct pull-out tests (DPT) including single or double-lap shear tests and beam pull-out tests (BPT) are commonly used to investigate the bond between NSM CFRP and concrete [18], which are described in more details elsewhere [24]. The above test methods have been used to investigate a wide range of parameters affecting the bond mechanism including: FRP fiber type and external surface [32, 33, 44–50], FRP axial stiffness [44, 47–53], FRP cross section geometry [32, 33, 46, 49, 51, 54–58], groove surface [44, 47, 59, 60], groove's geometry [48, 50, 51, 54, 58, 61, 62], concrete strength [33, 45, 46, 50, 52], and adhesive material type and bonded length [32, 45, 46, 52, 53, 57, 63].

Different types of failure have been recorded in pull-out tests. However, in some cases, the authors of experimental works analysis tend to report more than one failure mode for the same specimen. Either this was a combination of several failure mechanisms or two failures may occur in sequence. It is thought by others [18] that any specimen should have one governing failure model and reporting more than one failure mode for a specific specimen may be caused by: (a) the occurrence of a sudden failure during the tests, hiding the possibility of observing the real failure mode, (b) in the case of BPT specimens, the test configuration itself could lead to erroneous identification of failure modes (the BPT are

performed with test region (face where the FRP is applied) downwards, being more difficult to observe the development of the failure mechanism).

In this section, the locations of main failure modes that occurred in bond between NSM FRP-concrete substrate are summarized, as follows (see Figure 2).

3.1. Failure in FRP Material (FRP Rupture). It is simpler than other failure modes to recognize, and it occurs in NSM specimens with adequate bond length [32, 45, 64].

3.2. Failure at Interface FRP/Adhesive. This failure occurred when a clean FRP bar/strip without adhesive attached detached from adhesive layer. In fact, mechanical interlock between FRP and the surrounding adhesive, in addition to chemical adhesion and friction between FRP and adhesive, is responsible to have an efficient bond. This kind of failure is observed in NSM specimens with inadequate bonded length or bad FRP surface cleaning, and some cases may occur as a result of low tensile strength of the used adhesive [25, 32, 65–67].

3.3. Cohesive Failure. This kind of failure occurs mainly as a result of the normal stresses developing together with longitudinal stresses during the test. When the normal stress reaches adhesive tensile strength, the cohesive failure then happens. The low tensile strength of adhesive material and the small NSM groove depth are of the common reasons that cause this failure [25, 40, 67, 68].

3.4. Failure at Interface Adhesive/Concrete. The failure between adhesive and concrete substrate is similar to that occurring between FRP bar and adhesive, and the reason of this failure may also be caused by the low tensile strength of adhesive material and inadequate bonded lengths [40, 41, 45, 50, 64, 69, 70].

3.5. Concrete Fracture. The failure in concrete substrate is mainly caused by the low strength of concrete, so the failure is shifted to the weakest material in joints. This type of failure is commonly observed when adequate bonded lengths and the grooves geometry are well designed [32, 58, 64].

In addition, when NSM FRP strengthening technique used in flexure a side-groove may be the choice to improve the bond strength, in this case, the system can be called (side NSM) SNSM FRP strengthening technique. Several studies showed that the SNSM FRP technique can prove the same contribution when compared to the one used in the bottom of beams [71]. It also showed that SNSM can overcome the issue of concrete fracture since a wider area of concrete can prevent such kind of failure.

It seems that the bond between NSM FRP reinforcement and concrete substrate is well covered. However, as an accurate method is needed to define and describe the failure modes observed, in addition, the prediction of pull-out strength of NSM FRP strips/rods, which are bonded to

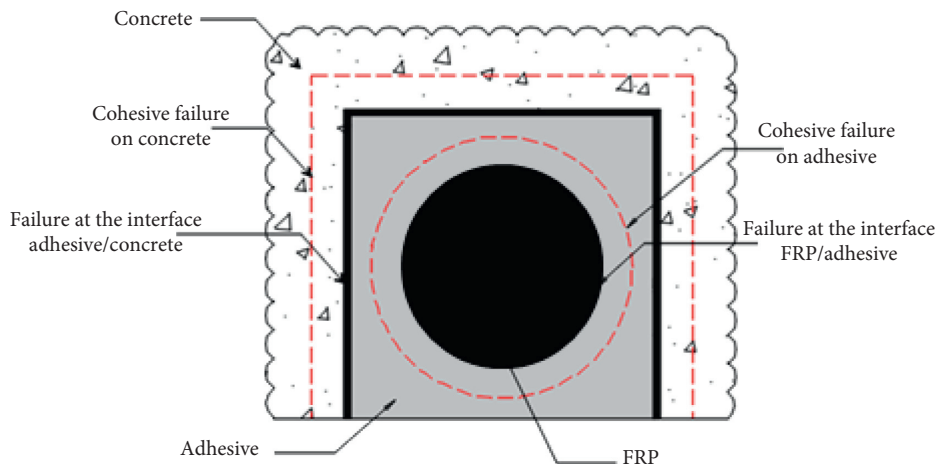


FIGURE 2: Possible failure modes associated with debonding mechanism [18].

concrete block, was investigated using fuzzy logic approach [72]. The results of the proposed model showed good accuracy against the experimental data and outperform the published models. For this reason, this kind of approach can also be utilized to propose methods of determining contribution of NSM FRP technique in flexure or shear as will be discussed later [72, 73].

4. Factors Affecting NSM Strengthening

The reported research studies that carried out the behavior of NSM CFRP strengthened RC beams in shear have investigated many parameters that can change the contribution of the NSM CFRP strengthening system in different levels. In the following sections, these parameters are listed and discussed.

4.1. Concrete Strength. The compressive strength of concrete was investigated in [16, 29, 74, 75] in three different series of experimental tests. The values of compressive strength were 18.6, 39.7, and 59.4 MPa at the age of beam tests. In each compressive strength of concrete, different NSM CFRP laminate inclinations (45° , 60° , and 90°), levels of CFRP percentage (0.06%, 0.09%–0.1%, and 0.13%–0.16%) and levels of steel stirrups percentage (0.1%, 0.16%, and 0.17%) were investigated. The experimental results demonstrated that the higher the concrete compressive strength, the higher the NSM CFRP effectiveness. This is related to the fact that the effective bond length is decreased with the higher concrete strength due to the decreasing of the fracture failure of concrete in the groove surface for the RC beams made by higher concrete strength class. Because of that, the contribution of the NSM CFRP laminates for shear resistance of beams is increased with the higher tensile strength of the concrete. It was also found that the NSM CFRP technique is still effective in beams produced by the lowest structural compressive strength of concrete.

4.2. Existing Steel Stirrups. The ratio of the presence tension steel reinforcement was found to be very effective when NSM FRP strengthening technique was applied in flexure

[76–78]. In a similar way, the presence of steel stirrups has also a clear effect on the contribution of NSM FRP strengthening technique when it is used in shear. Several studies have tried to investigate the effectiveness of NSM FRP strengthening technique with different percentages of steel shear reinforcements [29, 30, 74, 75, 79–81]. Lorenzis and Nanni [79] tested series of RC beams with absence and with steel stirrups. It is not possible to make a comparison between the tested beams because of the differences in the percentage of CFRP applied for the beams. However, it is only possible to conclude that the contribution of the NSM CFRP strengthening technique is still significant in the presence of steel stirrups. Another set of experimental studies [29, 74, 75, 80] revealed that the effectiveness of NSM CFRP rods is more pronounced in the beams with the lower internal steel stirrups ratio. This conclusion was made by investigating different percentages of steel stirrups (0.1, 0.16–0.17). In contrast, Mofidi et al. [30] claimed that the internal steel stirrups and strengthening NSM CFRP did not diminish each other's influence. Furthermore, a database of more than 69 RC beams strengthened with NSM CFRP laminates or rods was analyzed by the same authors [30]. It was found that the shear contribution of the NSM CFRP bars or laminates slightly increased with the increase in the internal shear steel reinforcement. Based on the aforementioned discussions, this discipline may need more research.

The effectiveness of NSM CFRP bars in improving the shear capacity of concrete beams with corroded steel stirrups was also studied [82]. Two corrosion levels were investigated comprising 8% and 15%. It was found that the contribution of the NSM CFRP strengthening technique was more pronounced with the lower stirrups corrosion of 8%. This is thought to be caused by the heavily corroded steel stirrups that minimized the friction resistance at the steel stirrups-concrete interface. This caused premature separation of the lateral concrete cover after onset of diagonal shear cracks. This process may reduce the effectiveness of NSM CFRP strengthening in shear.

The steel fibers would be used also to increase the shear resistance of concrete substrates. Therefore, NSM CFRP efficiency can be improved by using the steel fibers in

Concrete mix due to its ability to control the shear failure [83–86].

4.3. Shape of NSM CFRP Reinforcement. In the case of using NSM CFRP strengthening technique in enhancing RC beams in flexural capacity, it was found that using strips instead of round bars (having the same cross-sectional area) can improve the performance of NSM technique [11]. This was believed to be caused by maximizing the bond area and, therefore, reducing the debonding risk. Even with shear strengthening, the above conclusion can also be drawn [81]. However, this mechanism seems to be not identical with the test results reported by Rizzo and Lorenzis [26] who tested a series of RC concrete beams strengthened using NSM CFRP strengthening technique in shear. This finding cannot be normalized for many reasons, among which are the following:

- (i) The cross-sectional areas of the round bar and the strip are different (50 mm^2 for the round bars and 32 mm^2 for the strips).
- (ii) In the test reported in this section, all samples failed in concrete cover splitting in the region of the internal steel stirrups regardless of the strengthening configurations. Thus, the efficiency of CFRP strengthening cannot be obtained from this sample design.

More studies are needed to make the right selection of the NSM reinforcement shape.

4.4. Length of NSM Reinforcement. The length of FRP bars also plays an important role in controlling the contribution of this kind of strengthening technique [87]. Due to the limited depth of RC beams, the length of CFRP reinforcements was equal to the beam depth for the rectangular cross section beams in the most experimental tests [17, 31, 88]. However, using NSM strips with the length of $1/2D$ or $2/3D$ (D is the depth of beam) caused a noticeable improvement in the ultimate load of beam compared to using the length of NSM strips covering the full depth of beam [89]. The ultimate load of beams strengthened with full-length NSM strip was capable of sustaining a 144% higher load than that having length of NSM strips $1/2D$. The propagation crack passed directly into the end of the NSM strip in beams strengthened with NSM strips having the length of $1/2D$ or $2/3D$ causing a high stress concentration at the end, which accelerates the debonding. This did not occur in the case of using NSM CFRP strips with length equal to beam depth since the length contributes more of a bonding area than the other lengths.

In the case of T-beam strengthened with CFRP bars using NSM strengthening technique, extending the CFRP bars into the flange of the beam can increase the contribution of the CFRP bars [79, 90] as shown in Figure 3(a), whereas generally the CFRP bars or strips are installed on the side of the beam web as shown in Figure 3(b). This was partly caused by the extra CFRP material added to the beam. For

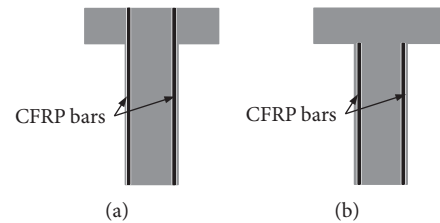


FIGURE 3: CFRP bars arrangements. (a) Anchorage in the flange. (b) On the side of the beam web.

example, 33% more material as reported by Lorenzis and Nanni [79] caused 45.5% increasing in the beam capacity. Another reason is the extra length of CFRP bars that caused an increase in the bonded length, and hence, it maximized the failure load.

These findings were also confirmed by other researchers [17, 28, 88] who investigated the influence of CFRP length on rectangular cross section beams. This was conducted by increasing the beam depth to examine its impact on the CFRP contribution.

4.5. Mechanical Properties of Groove Filling's Material. The influence of mechanical properties of groove filling material has widely been investigated [36, 47] to find its effect on the bond strength. It has been found that the change in the properties of groove filling material has a significant effect on the bond strength and lesser extends on the failure mode. In particular, when a stiffer adhesive material was used as a groove filling material, the bond strength was increased [36, 47]. However, these results are not in agreement with those obtained by Rizzo and Lorenzis [26] who studied the shear contribution of the NSM strengthening technique. They found that, by using an epoxy having lower elastic modulus as a groove filling material, the NSM CFRP contribution to the shear capacity was more than twice in comparison with that used an epoxy with higher elastic modulus. It was believed that the epoxy with lower modulus of elasticity leads to more ductile bond-slip response, which can then delay the onset of debonding. This contrast may be related to the points listed in Section 4.3. This factor needs more research to be clearer.

4.6. Percentage of NSM Reinforcement. Generally, the increase in the percentage of the CFRP leads to an increase in the shear resistance of the strengthened beams [16, 28, 29, 74, 75, 81, 88, 91]. It can be seen in Figure 4 that the increase of the beam's capacity as a result of increasing the percentage of the NSM CFRP reinforcement (ρ_f)—which can be calculated as in equation (1)—is sensitive to the value of concrete compressive strength [75]. In other words, the efficiency of NSM strengthening technique for the shear strengthening is maximized with the higher concrete strength. This is related to the fact that, in the case of lower concrete strength, the failure mode in the strengthened beams is concrete fracture, in which the concrete adhered to the detached laminates, while in the case of higher concrete

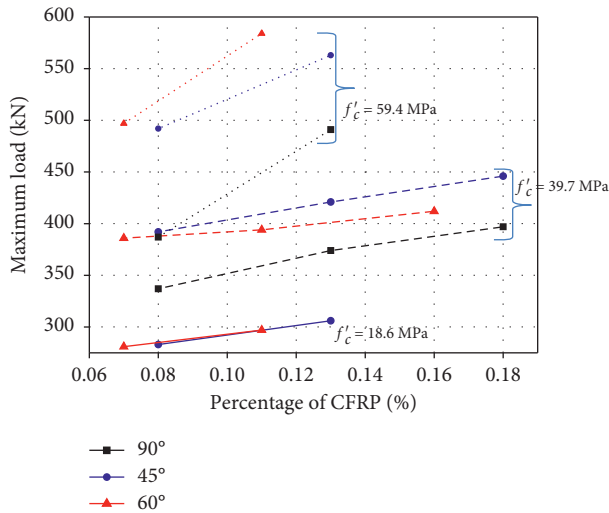


FIGURE 4: CFRP contribution against percentage of CFRP reinforcement with various concrete compressive strength and NSM CFRP inclination [75].

strength, the failure mode is either the sliding of CFRP laminate (between the CFRP and the epoxy) or the rupture of the CFRP [75]. Thus, it is expected for the lower concrete strength that the increase in the percentage of CFRP does not have a significant change in the efficacy of NSM technique for the shear resistance.

$$\rho_f = \frac{2 \times A_f}{b_w \times S_f \times \sin \theta_f} \times 100, \quad (1)$$

where A_f is the area of the CFRP reinforcement (strip or bar) cross section, b_w is the width of beam web, S_f is spacing of the CFRP reinforcement, and θ_f is the orientation angle of the CFRP reinforcement with respect to the beam axis.

These findings seem to be incompatible with those presented in Rizzo and Lorenzis [26], where the increase in the percentage of the CFRP caused a decrease in the shear capacity of the beam. It was thought that increasing the percentage of CFRP accelerated the formation of debonding between CFRP bar and adhered layer.

4.7. Inclination of NSM Reinforcement. It is well known that inclined steel stirrups are more effective in shear resistance than the vertical stirrups because of diagonal cracking pattern of shear failure in RC beams. This phenomenon is identical with that found in the case of NSM CFRP strengthening technique [27, 29, 74, 75, 79, 81, 88, 90, 92] (see Figure 4). This is partly caused by the orientation of the shear cracks that tend to be almost orthogonal to the inclined CFRP reinforcement [75]. In addition, the inclined CFRP reinforcement has better total resisting bond length than the vertical CFRP reinforcement because the inclined laminates are longer than vertical laminates. Thus, it is expected to delay the debonding failure and hence have higher shear resistance. It can be seen in Figure 4 that the orientation of CFRP reinforcement at 45° was the most effective in some cases, while the orientation of CFRP

laminate at 60° was the most effective than other orientations in the other cases [75]. Thus, more investigations about this point are needed.

4.8. Distance between Existing Steel Stirrups and NSM Reinforcement. The relative position between internal steel stirrups and applied CFRP reinforcement has a specific contribution on the effectiveness of CFRP shear strengthening configuration [27]. It was found that when the applied NSM reinforcement intercepted the existing steel stirrups, this may cause a debonding for the NSM bars/strips. This reflects the importance of applying the CFRP NSM reinforcement with a homogenous distance with the existing steel stirrups. Further studies are important here to find the minimum distance (between laminates and existing steel stirrups), in which the influence of this factor can be neglected.

4.9. End Conditions of FRP Bars. This kind of treatment is very important when the governing failure mode is the debonding of FRP bars or concrete cover separation. In these cases, this kind of treatment can play an important role to avoid these kinds of failures. One of the effective methods to improve end conditions of FRP bars is bending the ends of FRP bars with angles ranging between 45° and 90° as reported by others [93]. As a result, it was found that this kind of end condition can increase the load carrying capacity of RC beams in flexure by 201% and 185% compared to the reference beam. Based on that, bent ends can be also investigated in the case of shear strengthening to eliminate the problem of premature debonding in the case of shallow beams for instance.

4.10. Concrete Cover Depth. The effect of the side cover depth was investigated by [89]. Generally, it was found that, by increasing side concrete cover depth, the side concrete cover separation can be delayed or even prevented [89, 94, 95]. However, increasing the side cover could have a negative effect on the flexural response of beams since it may limit the space provided to position the longitudinal reinforcement. In addition, in many cases, NSM FRP strengthening technique is used for repairing or strengthening existing structures; thus, increasing the side concrete cover may not be an option to improve the entire contribution of this technique.

5. Failure Modes

In the cases of evaluating the shear strengthening contribution, the RC beams were designed to assure shear failure mode. The failure modes occurring in the case of using CFRP NSM in shear strengthening are as follows:

- The first failure mode happened when the normal or low strength concrete is used. In this failure mode, the laminates/bars failed by debonding (see Figure 5). However, along the bond length, a thin layer of concrete adhered to the laminate/bar;

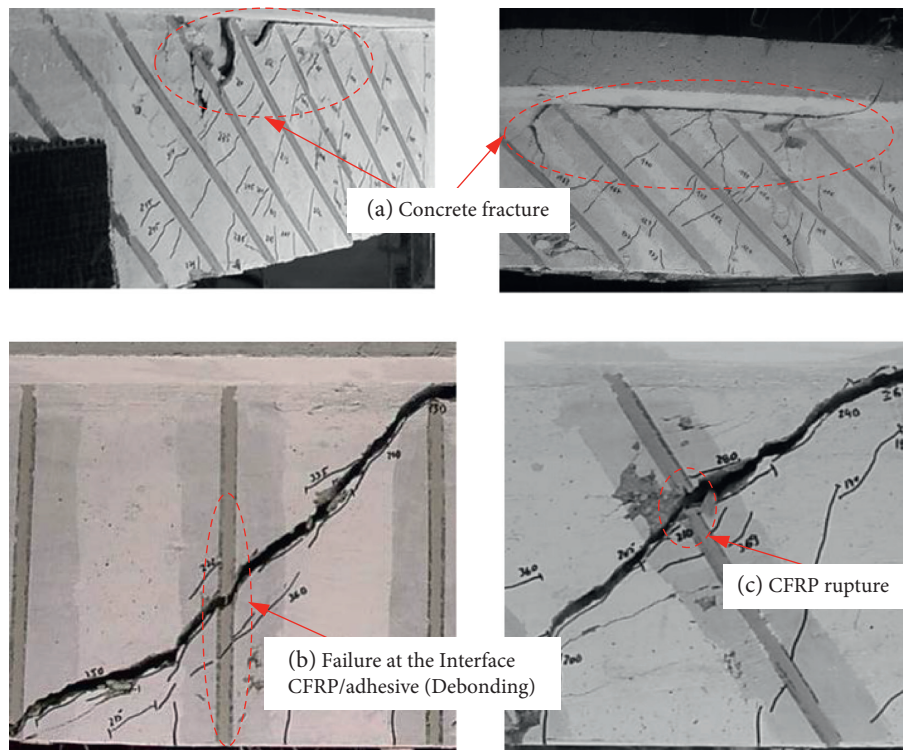


FIGURE 5: Failure modes (a, b, and c) of the RC beams shear strengthened with NSM CFRP laminates [75].

hence, this can be classified as a concrete fracture. In the case of high percentage of CFRP used, a concrete layer with a group of CFRP reinforcements detaches to create a “concrete lateral wall” that has separated from the overall volume of concrete [75, 88]. In this bullet-point, two failure modes are presented, which are failure at interface between adhesive and concrete (debonding) and cohesion failure on concrete (concrete fracture), because, in many cases, these failure modes are difficult to be experimentally separated.

- (b) The failure of interface between the NSM FRP reinforcement and the adhesive “debonding” shown in Figure 5 can be classified as the most common failure mode. This failure mode occurred when a normal to high concrete strength is used [75]. The interface CFRP/adhesive is the weakest point in the CFRP NSM strengthening technique. Thus, by using a high strength adhesive material, longer CFRP reinforcements, anchoring the CFRP in the flange of T-beam, etc., this weak point can be overcome.
- (c) The rupture of CFRP can occur when a normal to high concrete strength is used as shown in Figure 5.
- (d) In some cases, when the CFRP NSM reinforcement is applied to T-beams, shear splitting failure occurred along the web-flange interface region [90]. Extending CFRP NSM reinforcement can control this failure mode.

- (e) Regarding the beams tested without internal shear reinforcements, splitting of concrete cover of the flexural reinforcement occurred as a result of growing cracks along the flexural reinforcement. This was thought to be caused by designing the tested beams without steel stirrups, which are responsible for maintaining the dowel force and hence restraining the splitting cracks.

It should be noted that there is no cohesive failure on the adhesive observed in the experimental studies that conducted the shear contribution of CFRP NSM strengthening technique. This is because of the higher tensile strength of adhesive material compared to the concrete tensile strength in all tests.

6. Analytical Formulations

The prediction of the shear capacity of RC beams is a challenging task because shear mobilizes several complex resisting mechanisms such as (1) shear resistance assured by the uncracked concrete in the compression zone; (2) interface shear transfer by aggregate interlocking in the cracked concrete; and (3) the dowel action of the longitudinal reinforcement [96]. Several analytical formulations were proposed in order to predict the contribution of the NSM CFRP laminates for the shear capacity of RC beams [74, 75, 79, 97–108]. Some of these models were only set to predict a certain failure mode such as Rizzo and Lorenzis

TABLE 1: Different methods to calculate the shear stresses by NSM FRP.

Expression	Reference	Notation
$V_f = 2\pi d_b \tau_b L_{\text{tot min}} \sin \theta_f$	Nanni, et al. [98]	d_b and τ_b : diameter and average bond stress of the CFRP; θ_f : angle of CFRP bar to the beam longitudinal axis; and $L_{\text{tot min}}$: effective bond length.
$V_f = h_w \frac{A_{fv}}{s_f} \varepsilon_{fe} E_f (\cot \alpha + \cot \theta_f) \sin \theta_f$ $\varepsilon_{fe} = 3.76888 \times e^{(-0.116026\theta_f + 0.0010437\theta_f^2)} \times$ $[(E_f \times \rho_f + E_s \times \rho_{sw}) / (f_{cm})^{2/3}] - 0.460679 \times e^{(0.0351199\theta_f - 0.0003431\theta_f^2)}$	Dias and Barros [75]	h_w : web depth of the beam; A_{fv} : area of two CFRP bars; s_f : spacing of the bars; E_f : elastic modulus of the CFRP; α : orientation of the shear failure crack; and ε_{fe} : effective strain.

[107]. Two main analytical formulations are detailed in the later sections. From these analytical formulations, the FRP contribution can be calculated. However, the nominal shear strength of RC beams strengthened with NSM FRP technique can be computed as suggested by Lorenzis and Nanni [79] using the equation by adding a third term to the basic equation provided by ACI code [109], as in

$$V_u = \phi [(V_c + V_s) + \psi V_f], \quad (2)$$

where ϕ is the strength reduction factor for shear strengthening of RC elements, which has a value of 0.85 as reported by ACI [109]. ψ is an additional reduction factor for the case of externally bonded CFRP. The value of this reduction factor is 0.85 as recommended by ACI 440 committee [110]. The values of V_c and V_s are the contributions of concrete and steel stirrups, respectively, which may be computed according to standard concrete design codes. V_f represents the contribution of NSM FRP reinforcement to shear. The main output is the value of NSM FRP contribution (V_f) which can be calculated as per Table 1.

7. Evaluation of the Existing Formulations

In the previous section, a brief review is presented for the formations proposed in the literature that aimed at predicting the contribution of NSM FRP laminates in shear. In order to evaluate these formulations, the results obtained from them compared with the experimental results extracted from previous experimental research studies are listed in Tables 2 to 6. In these tables, f_f^1 and f_f^2 represent the values of shear contribution of the NSM FRP strengthening technique as predicted by Dias and Barros [75] and Nanni et al. [98] equations (equations 9 and 3), respectively.

The values of mean of f_f^1 / f_f^{exp} and f_f^2 / f_f^{exp} in Tables 2–6 have been calculated to evaluate these formations against the experiment's results. Since the mean values were 1.09 and 0.87 for the results using Dias and Barros [75] and Nanni et al. [98] formulations, respectively, the strength prediction using Dias and Barros [75] formula is closer than that obtained by using Nanni et al. [98] formula to the experimental strength. This may be attributed to the fact that the latter formula does not include the modulus of elasticity and effective strain of CFRP. However, these closed predictions do not mean that this formulation could capture the behavior in most cases. For instance, both formulations did not account for the effect of epoxy type into the contribution of NSM FRP technique as shown in Figure 6. It can be noticed

from this figure that the use of a stiffer and stronger groove filling epoxy resulted in a lower FRP contribution to the shear capacity. The reason for this is related to the fact that the stiffer bond-slip response of the joints induced larger peak bond stresses and then accelerated the initiation of debonding cracks in the concrete [26].

In addition, it can be seen from Figure 7 that the predictions of Dias and Barros [75] for the contribution of NSM FRP strengthening technique in shear (V_f^1) are less than the corresponding experimental values (V_f^{exp}) in most points. However, in others, the predictions of Dias and Barros [75] are not conservative since their predictions (V_f^1) are more than the corresponding experimental values. Furthermore, considering the formulation suggested by Nanni et al. [98], it seems that although this formulation provides quite conservative predictions, their conservatism is relatively high in some points.

Regarding the effect of existing steel stirrups shown in Figure 8, it seems that the later formulation did not account for the percentage of existing steel reinforcement in their formulations. Although the predictions of Dias and Barros [75] include the influence of steel stirrups, their predictions are still overestimated compared to the corresponding experimental values. Thus, further modifications regarding this point may be needed.

Generally, the accuracy of the predictions of the theoretical formulations discussed in this section is accepted in many cases. However, further improvement is required to include the effect of some parameters such as epoxy properties, while further modifications are required to improve the predictions for some parameters such as the percentage of existing steel stirrups.

8. Numerical Modelling

It is well known that the numerical modelling is a powerful tool that is widely used in order to provide a comprehensive understanding to many phenomena in structural engineering applications. However, the number of numerical studies conducting the response of NSM CFRP strengthened concrete beams in shear is still limited. Some of these studies were only presented a simple numerical model without a deep discussion about the materials modelling and other numerical model characteristics [19]. Others tried to use these models to investigate more parameters [113–115]. Some of these parameters were already experimentally covered such as concrete compressive strength [113–115],

TABLE 2: Comparison between experimental results [27] and analytical results.

Symbols	S_f (mm)	θ°	a_f (mm)	b_f (mm)	E_f (GPa)	V_f^1 (kN)	f_f^2 (kN)	f_f^{exp} (kN)	f_f^1/f_f^{exp}	f_f^2/f_f^{exp}
2S-3LV-I	267	90	1.4	10	166.6	21.6	20.4	22.2	0.97	0.91
2S-5LV-I	160	90	1.4	10	166.6	31.8	20.4	25.2	1.26	0.80
2S-8LV-I	100	90	1.4	10	166.6	41.7	40.8	48.9	0.85	0.83
2S-3LI45-I	367	45	1.4	10	166.6	43.4	14.4	29.4	1.47	0.48
2S-5LI45-I	220	45	1.4	10	166.6	47.3	28.8	41.4	1.14	0.69
2S-8LI45-I	138	45	1.4	10	166.6	63.5	28.8	40.2	1.57	0.71
2S-3LI60-I	325	60	1.4	10	166.6	28.0	17.6	35.4	0.79	0.50
2S-5LI60-I	195	60	1.4	10	166.6	37.4	22.3	46.2	0.80	0.48
2S-7LI60-I	139	60	1.4	10	166.6	50.8	35.3	54.6	0.93	0.64
2S-7LV-II	114	90	1.4	10	166.6	59.9	35.2	28.32	2.1	1.24
2S-4LI45-II	275	45	1.4	10	166.6	31.7	14.4	33.9	0.93	0.42
2S-7LI45-II	157	45	1.4	10	166.6	38.4	28.8	48.0	0.8	0.6
2S-4LI60-II	243	60	1.4	10	166.6	50.5	17.6	33.06	1.52	0.53
2S-6LI60-II	162	60	1.4	10	166.6	30.7	35.3	42.72	0.71	0.82
4S-7LV-II	114	90	1.4	10	166.6	38.2	35.2	6.9	5.53	5.10
4S-4LI45-II	275	45	1.4	10	166.6	31.7	14.4	26.04	1.21	0.55
4S-7LI45-II	157	45	1.4	10	166.6	38.4	28.8	31.56	1.21	0.91
4S-4LI60-II	243	60	1.4	10	166.6	50.5	17.6	25.08	2.013	0.70
4S-6LI60-II	162	60	1.4	10	166.6	30.7	35.3	35.1	0.87	1.00
3S-5LI45-III	275	45	1.4	10	174.3	38.2	39.9	66.1	0.57	0.60
3S-5LI45F1-III	275	45	1.4	10	174.3	93.6	39.9	85.75	1.09	0.46
3S-5LI45F2-III	275	45	1.4	10	174.3	93.6	39.9	65.35	1.43	0.61
5S-5LI45-III	275	45	1.4	10	174.3	93.6	39.9	74.9	1.24	0.53
5S-5LI45F-III	157	45	1.4	10	174.3	93.6	79.8	74.9	1.24	1.06
3S-9LI45-III	157	45	1.4	10	174.3	122.3	79.84	101.85	1.20	0.78
5S-9LI45-III	275	45	1.4	10	174.3	122.3	39.9	108.9	1.12	0.36
3S-5LI60-III	243	60	1.4	10	174.3	93.6	48.8	69	1.35	0.70
5S-5LI60-III	243	60	1.4	10	174.3	74.1	48.8	73.35	1.01	0.66
5S-5LI60F-III	243	60	1.4	10	174.3	74.1	48.8	72.55	1.02	0.67
3S-8LI60-III	162	60	1.4	10	174.3	74.1	75.7	112.3	0.65	0.67
5S-8LI60-III	162	60	1.4	10	174.3	91.8	75.7	122.45	0.74	0.61
3S-6LV-III	180	90	1.4	10	174.3	91.8	56.4	39.58	2.31	1.42
3S-10LV-III	114	90	1.4	10	174.3	40.3	71.3	83.25	0.48	0.85

TABLE 3: Comparison between experimental results [111] and analytical results.

Symbols	S_f (mm)	θ°	\varnothing_f (mm)	E_f (GPa)	f_f^1 (kN)	f_f^2 (kN)	f_f^{exp} (kN)	f_f^1/f_f^{exp}	f_f^2/f_f^{exp}
B2-FRP-V	152	90	9.0	124	47.8	67.2	44.5	1.07	1.51
B3-FRP-V	305	90	9.0	124	30.9	67.2	31	0.99	2.16
B4-FRP-V	191	90	9.0	124	44.6	67.2	35.5	1.25	1.89

TABLE 4: Comparison between experimental results [26] and analytical results.

Symbols	S_f (mm)	θ°	a_f (mm)	b_f (mm)	\varnothing_f (mm)	E_f (GPa)	f_f^1 (kN)	f_f^2 (kN)	f_f^{exp} (kN)	f_f^1/f_f^{exp}	f_f^2/f_f^{exp}
NB90-73-a-IV	73	90	—	—	8.0	145.7	58.2	80.2	54.2	1.07	1.47
NB90-73b-IV	73	90	—	—	8.0	145.7	58.2	80.2	26.4	2.20	3.03
NB90-45-b-IV	45	90	—	—	8.0	145.7	73.76	130.0	28.6	2.57	4.54
NB45-146-a-IV	146	45	—	—	8.0	145.7	43.0	61.9	39.1	1.09	1.58
NB45-73-a-IV	73	45	—	—	8.0	145.7	49.6	120.7	28	1.77	4.31
NS90-73-a-IV	73	90	2	16		121.5	48.9	49.8	50.5	0.96	0.98
NS45-146-a-IV	146	45	2	16		121.5	38.7	40.1	32.7	1.18	1.22

TABLE 5: Comparison between experimental results [112] and analytical results.

Symbols	S_f (mm)	θ°	a_f (mm)	b_f (mm)	E_f (GPa)	f_f^1 (kN)	f_f^2 (kN)	f_f^{exp} (kN)	f_f^1/f_f^{exp}	f_f^2/f_f^{exp}
VR-VII	160	90	3.46	3.46	235	26.2	23.9	33.41	0.78	0.71
IR-VII	240	45	3.46	3.46	235	30.8	16.9	53.94	0.57	0.31
VRA-VII	160	90	3.46	3.46	235	26.2	23.9	39.88	0.65	0.59
IRA-VII	240	45	3.46	3.46	235	30.8	16.9	63.82	0.48	0.26
VRA-VII	160	90	3.46	3.46	235	26.2	23.9	29.4	0.89	0.81

TABLE 6: Comparison between experimental results [90] and analytical results.

Symbols	S_f (mm)	θ°	\varnothing_f (mm)	E_f (GPa)	f_f^1 (kN)	f_f^2 (kN)	f_f^{exp} (kN)	f_f^1/f_f^{exp}	f_f^2/f_f^{exp}
B90-6a-VIII	115	90	8.0	210	70.6	92.8	58.3	1.21	1.59
B90-6b-VIII	115	90	8.0	124	67.4	92.8	55	1.22	1.68
B90-3a-VIII	230	90	8.0	210	43.0	70.6	11	3.90	6.41
B90-3b-VIII	230	90	8.0	124	45.6	70.6	6.3	7.23	11.20
B45-6a-VIII	115	45	8.0	210	56.3	171.2	74.2	0.75	2.30
B45-6b-VIII	115	45	8.0	124	66.1	171.2	98.2	0.67	1.74
B45-3a-VIII	230	45	8.0	210	55.8	72.1	40.2	1.38	1.79
B45-3b-VIII	230	45	8.0	124	48.1	72.1	81	0.59	0.89
S90-6a-VIII	115	90	8.0	210	59.6	73.9	75.8	0.78	0.97
S90-6b-VIII	115	90	8.0	124	56.9	73.9	38.9	1.46	1.89
S90-3a-VIII	230	90	8.0	210	35.1	52.7	10.5	3.34	5.01
S90-3b-VIII	230	90	8.0	124	37.2	52.7	20.4	1.82	2.58
S45-6a-VIII	115	45	8.0	210	52.8	133.1	77.1	0.68	1.72
S45-6b-VIII	115	45	8.0	124	62.0	133.1	106.4	0.58	1.25
S45-3a-VIII	230	45	8.0	210	49.6	58.4	58.1	0.85	1.00
S45-3b-VIII	230	45	8.0	124	42.8	58.4	98	0.43	0.59

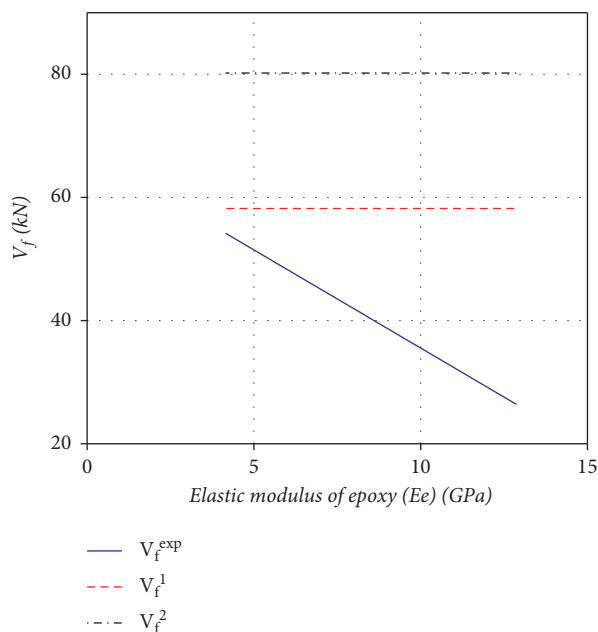


FIGURE 6: Effect of the elastic modulus of epoxy on the contribution of the NSM FRP shear strengthening technique (the experimental FRP contribution gained from [26]).

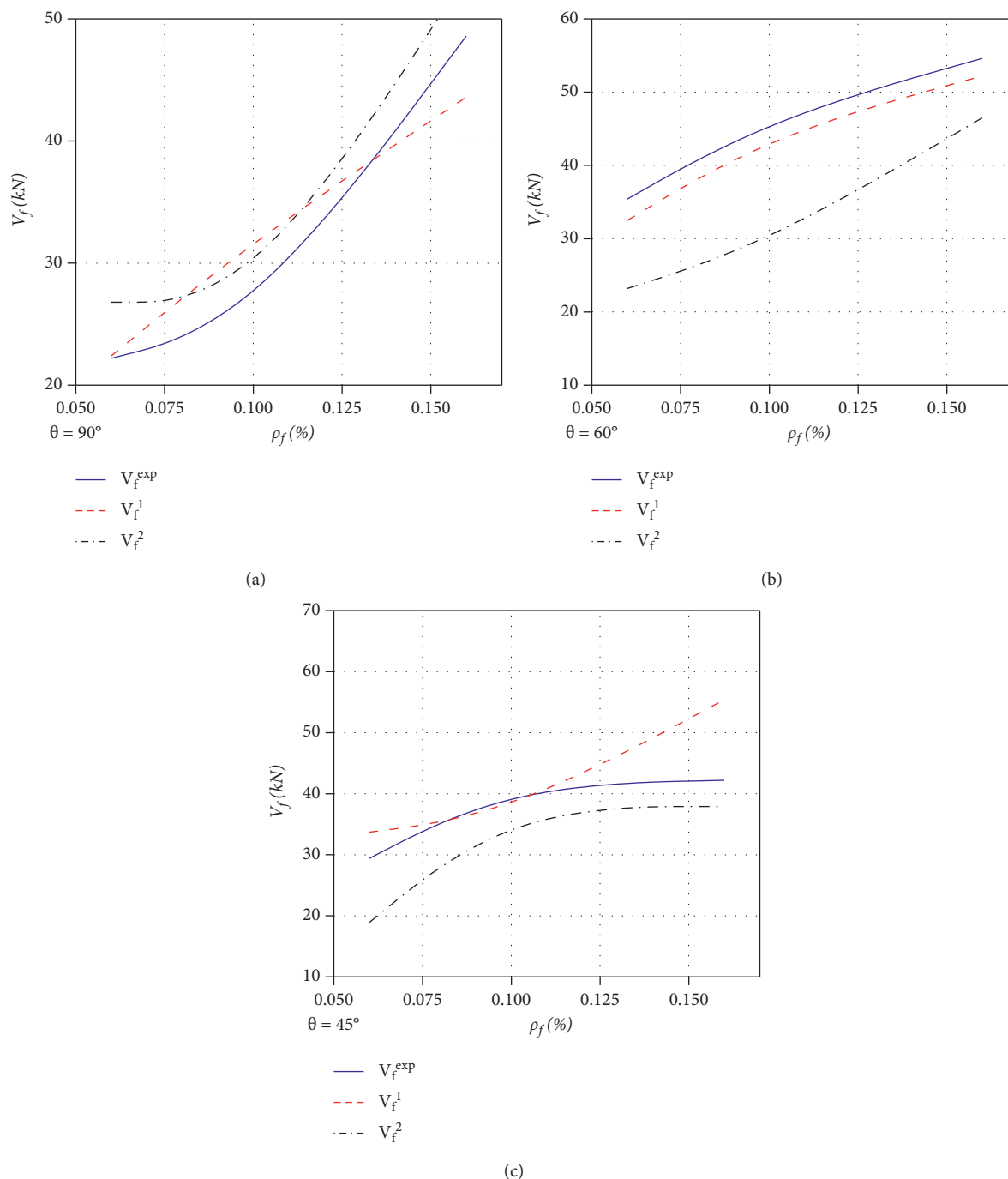


FIGURE 7: Effect of the percentage of the FRP for different reinforcement inclination angles on the contribution of the NSM FRP shear strengthening technique (the experimental FRP contribution gained from [27]).

while some of these were not investigated elsewhere such as the distance between existing shear reinforcement and SNM rods [113]. Generally, this powerful tool can more widely be used to investigate more parameters such as the percentage

of steel stirrups against the percentage of NSM FRP rods and optimum distribution of FRP reinforcement along the beam. Numerical simulation is also needed to extend the parameter ranges outside those used in the experimental works.

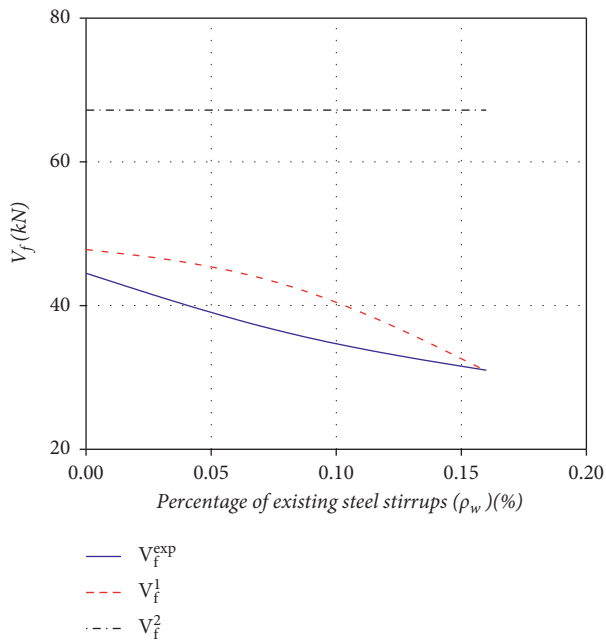


FIGURE 8: Effect of the percentage of existing steel stirrups on the contribution of the NSM FRP shear strengthening technique (the experimental FRP contribution gained from [27]).

9. Conclusions

This paper has provided a review of the current research on CFRP strengthened concrete beams with NSM technique in shear. Significant amounts of information and explanations of the existing researches on the NSM FRP strengthening of concrete beams have been provided. The important conclusions drawn from the reviewed studies can be summarized as follows:

- (i) Although the bond between NSM FRP reinforcement and concrete substrate is well investigated, some debate is still ongoing on the selection of the real failure mode. Some researchers tend to present several failure modes because they look essential to the final appearance of the specimens, while others preferred to indicate only the conditioning failure mode.
- (ii) Regarding the parameters that can influence the shear contribution of NSM FRP strengthening technique, it seems that most of these parameters are well covered. However, some of those still need deep investigation to remove the debate about that, such as the shape of NSM FRP reinforcement, inclination of NSM reinforcement, and percentage of the existing steel stirrups.
- (iii) The most common failure mode of NSM FRP strengthened RC beams is the failure at the interface between NSM FRP reinforcement and adhesive layer, whereas the fracture of the concrete substrate surrounding groove is also commonly observed when normal or low concrete is used.
- (iv) The study also considered a large number of experimental works to evaluate the contribution of

NSM strengthening in shear using formulations found in the literature. It appeared that the formula suggested by Dias and Barros [75] reasonably agrees with the experimental results with 9% of conservation.

References

- [1] J. F. Chen and J. G. Teng, "Shear capacity of FRP-strengthened RC beams: FRP debonding," *Construction and Building Materials*, vol. 17, no. 1, pp. 27–41, 2003.
- [2] C. P. Antonopoulos and T. C. Triantafillou, "Experimental investigation of FRP-strengthened RC beam-column joints," *Journal of Composites for Construction*, vol. 7, no. 1, pp. 39–49, 2003.
- [3] L. C. Hollaway and J. G. Teng, *Strengthening and Rehabilitation of Civil Infrastructures Using Fibre-Reinforced Polymer (FRP) Composites*, Elsevier, Amsterdam, Netherlands, 2008.
- [4] J. Bonacci and M. Maalej, "Behavioral trends of RC beams strengthened with externally bonded FRP," *Journal of Composites for Construction*, vol. 5, no. 2, pp. 102–113, 2001.
- [5] J. Teng, L. Lam, and J. Chen, "Shear strengthening of RC beams with FRP composites," *Progress in Structural Engineering and Materials*, vol. 6, no. 3, pp. 173–184, 2004.
- [6] M. M. A. Kadhim, "Effect of CFRP sheet length on the behavior of HSC continuous Beam," *Journal of Thermoplastic Composite Materials*, vol. 25, no. 1, pp. 33–44, 2012.
- [7] M. M. A. Kadhim, M. J. Mohammed, and A. J. Chabuk, "Effect of prestressed CFRP plate location on behavior of RC beam strengthened with prestressed CFRP plate," *Journal of the University of Bombay*, vol. 20, no. 1, pp. 105–113, 2012.
- [8] M. Badawi and K. Soudki, "Flexural strengthening of RC beams with prestressed NSM CFRP rods—experimental and analytical investigation," *Construction and Building Materials*, vol. 23, no. 10, pp. 3292–3300, 2009.
- [9] A. Hajihashemi, D. Mostofinejad, and M. Azhari, "Investigation of RC beams strengthened with prestressed NSM CFRP laminates," *Journal of Composites for Construction*, vol. 15, no. 6, pp. 887–895, 2011.
- [10] H. Y. Omran and R. E. Hacha, "Nonlinear 3D finite element modeling of RC beams strengthened with prestressed NSM-CFRP strips," *Construction and Building Materials*, vol. 31, pp. 74–85, 2012.
- [11] R. E. Hacha and S. H. Rizkalla, "Near-surface-mounted fiber-reinforced polymer reinforcements for flexural strengthening of concrete structures," *Structural Journal*, vol. 101, no. 5, pp. 717–726, 2004.
- [12] I. A. Sharaky, L. Torres, J. Comas, and C. Barris, "Flexural response of reinforced concrete (RC) beams strengthened with near surface mounted (NSM) fibre reinforced polymer (FRP) bars," *Composite Structures*, vol. 109, pp. 8–22, 2014.
- [13] G. Sas, T. Blanksvärd, O. Enochsson, B. Täljsten, A. Puurula, and L. Elfgren, "Flexural-shear failure of a full scale tested RC bridge strengthened with NSM CFRP. Shear capacity analysis," *Nordic Concrete Research*, vol. 44, no. 13, pp. 189–204, 2011.
- [14] B. Täljsten, J. Nilimaa, T. Blanksvärd, and G. Sas, "Flexural-shear failure of a full scale tested RC bridge strengthened with NSM CFRP," in *Proceedings of the International*

Conference on Structural Health Monitoring of Intelligent Infrastructure, (SHMI), Cancún, México, December 2011.

- [15] H. H. Kammona and A. S. H. A. Issawi, "Estimation of maximum shear capacity of RC deep beams strengthened by NSM steel bars," *Journal of the University of Bombay*, vol. 26, no. 3, pp. 13–22, 2018.
- [16] S. J. Dias and J. A. Barros, "Performance of reinforced concrete T beams strengthened in shear with NSM CFRP laminates," *Engineering Structures*, vol. 32, no. 2, pp. 373–384, 2010.
- [17] J. A. Barros, S. J. Dias, and J. L. Lima, "Efficacy of CFRP-based techniques for the flexural and shear strengthening of concrete beams," *Cement and Concrete Composites*, vol. 29, no. 3, pp. 203–217, 2007.
- [18] M. R. Coelho, J. M. C. Sena, and L. A. Neves, "A review on the bond behavior of FRP NSM systems in concrete," *Construction and Building Materials*, vol. 93, pp. 1157–1169, 2015.
- [19] P. Sabol and S. Priganc, "Shear strengthening of concrete members using NSM method," *Procedia Engineering*, vol. 65, pp. 364–369, 2013.
- [20] A. A. M. Ali and T. M. Mezher, "Shear strengthening of RC without stirrups for deep beams with near surface mounted CFRP rods," *International Journal of Engineering Research and Technology*, vol. 4, no. 6, pp. 545–547, 2015.
- [21] H. Tanarslan, "The effects of NSM CFRP reinforcements for improving the shear capacity of RC beams," *Construction and Building Materials*, vol. 25, no. 5, pp. 2663–2673, 2011.
- [22] M. M. Kadhim, A. Jawdhari, and A. Peiris, "Evaluation of lap-splices in NSM FRP rods for retrofitting RC members," in *Structures* Elsevier, Amsterdam, Netherlands, 2021.
- [23] S. S. Zhang, T. Yu, and G. Chen, "Reinforced concrete beams strengthened in flexure with near-surface mounted (NSM) CFRP strips: current status and research needs," *Composites Part B: Engineering*, vol. 131, pp. 30–42, 2017.
- [24] N. T. K. A. Saadi, A. Mohammed, R. A. Mahaidi, and J. Sanjayan, "Performance of NSM FRP embedded in concrete under monotonic and fatigue loads: state-of-the-art review," *Australian Journal of Structural Engineering*, vol. 20, no. 2, pp. 89–114, 2019.
- [25] L. D. Lorenzis and J. Teng, "Near-surface mounted FRP reinforcement: an emerging technique for strengthening structures," *Composites Part B: Engineering*, vol. 38, no. 2, pp. 119–143, 2007.
- [26] A. Rizzo and L. D. Lorenzis, "Behavior and capacity of RC beams strengthened in shear with NSM FRP reinforcement," *Construction and Building Materials*, vol. 23, no. 4, pp. 1555–1567, 2009.
- [27] S. J. Dias and J. A. Barros, "Shear strengthening of T cross section reinforced concrete beams by near-surface mounted technique," *Journal of Composites for Construction*, vol. 12, no. 3, pp. 300–311, 2008.
- [28] S. J. Dias and J. A. Barros, "NSM shear strengthening technique with CFRP laminates applied in high T cross section RC beams," *Composites Part B: Engineering*, vol. 114, pp. 256–267, 2017.
- [29] S. Dias and J. Barros, "NSM shear strengthening technique with CFRP laminates applied in high-strength concrete beams with or without pre-cracking," *Composites Part B: Engineering*, vol. 43, no. 2, pp. 290–301, 2012.
- [30] A. Mofidi, O. Chaallal, L. Cheng, and Y. Shao, "Investigation of near surface-mounted method for shear rehabilitation of reinforced concrete beams using fiber reinforced-polymer composites," *Journal of Composites for Construction*, vol. 20, no. 2, Article ID 04015048, 2015.
- [31] B. Almassri, A. Kreit, F. A. Mahmoud, and R. Francois, "Behaviour of corroded shear-critical reinforced concrete beams repaired with NSM CFRP rods," *Composite Structures*, vol. 123, pp. 204–215, 2015.
- [32] R. Seracino, N. M. Jones, M. Ali, M. W. Page, and D. J. Oehlers, "Bond strength of near-surface mounted FRP strip-to-concrete joints," *Journal of Composites for Construction*, vol. 11, no. 4, pp. 401–409, 2007.
- [33] D. Lee, L. Cheng, and J. Y. G. Hui, "Bond characteristics of various NSM FRP reinforcements in concrete," *Journal of Composites for Construction*, vol. 17, no. 1, pp. 117–129, 2012.
- [34] A. Bilotta, F. Ceroni, E. Nigro, and M. Pecce, "Strain assessment for the design of NSM FRP systems for the strengthening of RC members," *Construction and Building Materials*, vol. 69, pp. 143–158, 2014.
- [35] W. Perera, T. Ibell, and A. Darby, "Bond behaviour and effectiveness of various shapes of NSM CFRP bars," in *Proceedings of the 9th Int. Symp. on Fiber-Reinforced Polymers Reinforcement for Concrete Structures (FRPRCS-9)*, pp. 250–258, Edinburgh, Scotland, tember 2009.
- [36] W. Kalupahana, T. Ibell, and A. Darby, "Bond characteristics of near surface mounted CFRP bars," *Construction and Building Materials*, vol. 43, pp. 58–68, 2013.
- [37] J. A. Barros, S. J. Dias, H. Baghi, and A. V. Gouveia, "New shear strengthening configurations of near-surface-mounted CFRP laminates for RC beams," *Structural Journal*, vol. 113, no. 6, pp. 1275–1287, 2016.
- [38] S. J. Dias and J. A. Barros, "Experimental research of a new CFRP-based shear strengthening technique for reinforced concrete beams," *IBRACON Structural Journal*, 2005.
- [39] T. G. Wakjira and U. Ebead, "Hybrid NSE/EB technique for shear strengthening of reinforced concrete beams using FRCM: experimental study," *Construction and Building Materials*, vol. 164, pp. 164–177, 2018.
- [40] L. D. Lorenzis, A. Rizzo, and A. L. Tegola, "A modified pull-out test for bond of near-surface mounted FRP rods in concrete," *Composites Part B: Engineering*, vol. 33, no. 8, pp. 589–603, 2002.
- [41] J. Teng, L. D. Lorenzis, B. Wang, R. Li, T. Wong, and L. Lam, "Debonding failures of RC beams strengthened with near surface mounted CFRP strips," *Journal of Composites for Construction*, vol. 10, no. 2, pp. 92–105, 2006.
- [42] S. E. Gamal, Y. A. Salloum, S. Alsayed, and M. Aqel, "Performance of near surface mounted glass fiber reinforced polymer bars in concrete," *Journal of Reinforced Plastics and Composites*, vol. 31, no. 22, pp. 1501–1515, 2012.
- [43] F. A. Mahmoud, A. Castel, T. Q. Minh, and R. François, "Reinforced concrete beams strengthened with NSM CFRP rods in shear," *Advances in Structural Engineering*, vol. 18, no. 10, pp. 1563–1574, 2015.
- [44] T. Hassan and S. Rizkalla, "Bond mechanism of NSM FRP bars for flexural strengthening of concrete structures," *ACI Structural Journal*, vol. 101, no. 6, pp. 830–839, 2004.
- [45] A. Bilotta, F. Ceroni, M. D. Ludovico, E. Nigro, M. Pecce, and G. Manfredi, "Bond efficiency of EBR and NSM FRP systems for strengthening concrete members," *Journal of Composites for Construction*, vol. 15, no. 5, pp. 757–772, 2011.
- [46] F. Ceroni, M. Pecce, A. Bilotta, and E. Nigro, "Bond behavior of FRP NSM systems in concrete elements," *Composites Part B: Engineering*, vol. 43, no. 2, pp. 99–109, 2012.
- [47] I. A. Sharaky, L. Torres, M. Baena, and C. Miàs, "An experimental study of different factors affecting the bond of NSM FRP bars in concrete," *Composite Structures*, vol. 99, pp. 350–365, 2013.

- [48] I. A. Sharaky, L. Torres, M. Baena, and I. Vilanova, "Effect of different material and construction details on the bond behaviour of NSM FRP bars in concrete," *Construction and Building Materials*, vol. 38, pp. 890–902, 2013.
- [49] D. Oehlers, R. Rashid, and R. Seracino, "IC debonding resistance of groups of FRP NSM strips in reinforced concrete beams," *Construction and Building Materials*, vol. 22, no. 7, pp. 1574–1582, 2008.
- [50] D. Galati and L. De Lorenzis, "Effect of construction details on the bond performance of NSM FRP bars in concrete," *Advances in Structural Engineering*, vol. 12, no. 5, pp. 683–700, 2009.
- [51] P. M. Fernandes, P. M. Silva, and J. C. Sena, "Bond and flexural behavior of concrete elements strengthened with NSM CFRP laminate strips under fatigue loading," *Engineering Structures*, vol. 84, pp. 350–361, 2015.
- [52] N. Wahab, K. A. Soudki, and T. Topper, "Experimental investigation of bond fatigue behavior of concrete beams strengthened with NSM prestressed CFRP rods," *Journal of Composites for Construction*, vol. 16, no. 6, pp. 684–692, 2012.
- [53] A. S. Kalayci, B. Yalim, and A. Mirmiran, "Construction tolerances and design parameters for NSM FRP reinforcement in concrete beams," *Construction and Building Materials*, vol. 24, no. 10, pp. 1821–1829, 2010.
- [54] R. Rashid, D. Oehlers, and R. Seracino, "IC debonding of FRP NSM and EB retrofitted concrete: plate and cover interaction tests," *Journal of Composites for Construction*, vol. 12, no. 2, pp. 160–167, 2008.
- [55] C. Shield, C. French, and E. Milde, *The Effect of Adhesive Type on the Bond of NSM Tape to Concrete*, vol. 230, pp. 355–372, Special Publication, American Concrete Institute, Kansas, MO, USA, 2005.
- [56] N. Wahab, K. A. Soudki, and T. Topper, "Mechanics of bond fatigue behavior of concrete beams strengthened with NSM CFRP rods," *Journal of Composites for Construction*, vol. 15, no. 6, pp. 934–942, 2011.
- [57] M. M. Ali, D. Oehlers, M. Griffith, and R. Seracino, "Interfacial stress transfer of near surface-mounted FRP-to-concrete joints," *Engineering Structures*, vol. 30, no. 7, pp. 1861–1868, 2008.
- [58] A. Bilotta, F. Ceroni, J. A. Barros et al., "Bond of NSM FRP-strengthened concrete: round robin test initiative," *Journal of Composites for Construction*, vol. 20, no. 1, Article ID 04015026, 2015.
- [59] D. Lee and L. Cheng, "Bond of NSM systems in concrete strengthening—examining design issues of strength, groove detailing and bond-dependent coefficient," *Construction and Building Materials*, vol. 47, pp. 1512–1522, 2013.
- [60] J. R. Garzón, J. M. C. Sena, P. Fernandes, and J. Xavier, "Effect of wet-dry cycles on the bond behaviour of concrete elements strengthened with NSM CFRP laminate strips," *Composite Structures*, vol. 132, pp. 331–340, 2015.
- [61] K. Borchert and K. Zilch, "Bond behaviour of NSM FRP strips in service," *Structural Concrete*, vol. 9, no. 3, pp. 127–142, 2008.
- [62] I. Costa and J. A. Barros, "Assessment of the bond behaviour of NSM FRP materials by pullout tests," in *Proceedings of the 1st Middle East Conference on Smart Monitoring, Assessment and Rehabilitation of Civil Structures (SMAR 2011)*, 2011. International Society for Structural Health Monitoring of Intelligent, Dubai, UAE, February 2011.
- [63] L. Lorenzis and A. Nanni, "Bond between near-surface mounted fiber-reinforced polymer rods and concrete in structural strengthening," *Structural Journal*, vol. 99, no. 2, pp. 123–132, 2002.
- [64] S. M. Soliman, E. E. Salakawy, and B. Benmokrane, "Bond performance of near-surface-mounted FRP bars," *Journal of Composites for Construction*, vol. 15, no. 1, pp. 103–111, 2010.
- [65] J. M. C. Sena, J. A. Barros, R. Gettu, and A. F. Azevedo, "Bond behavior of near-surface mounted CFRP laminate strips under monotonic and cyclic loading," *Journal of Composites for Construction*, vol. 10, no. 4, pp. 295–303, 2006.
- [66] X. Yan, B. Miller, A. Nanni, and C. Bakis, "Characterization of CFRP rods used as near surface mounted reinforcement," in *Proceedings of the 8th International conference on structural faults and repair*, Edinburgh, Scotland, July 1999.
- [67] J. A. Barros and J. C. Sena, "Bond behavior of carbon laminate strips into concrete by pullout-bending tests," in *Proceedings of the third International Symposium on Bond in Concrete*, Budapest, Hungary, November 2002.
- [68] A. A. Abdwais and R. A. Mahaidi, "Modified cement-based adhesive for near-surface mounted CFRP strengthening system," *Construction and Building Materials*, vol. 124, pp. 794–800, 2016.
- [69] J. M. D. C. Sena and J. A. D. B. Oliveira, "Bond between near-surface mounted carbon-fiber-reinforced polymer laminate strips and concrete," *Journal of Composites for Construction*, vol. 8, no. 6, pp. 519–527, 2004.
- [70] D. Novidis, S. J. Pantazopoulou, and E. Tentolouris, "Experimental study of bond of NSM-FRP reinforcement," *Construction and Building Materials*, vol. 21, no. 8, pp. 1760–1770, 2007.
- [71] I. Sharaky, R. Reda, M. Ghanem, M. Seleem, and H. Sallam, "Experimental and numerical study of RC beams strengthened with bottom and side NSM GFRP bars having different end conditions," *Construction and Building Materials*, vol. 149, pp. 882–903, 2017.
- [72] K. Nasrollahzadeh and S. Afzali, "Fuzzy logic model for pullout capacity of near-surface-mounted FRP reinforcement bonded to concrete," *Neural Computing & Applications*, vol. 31, no. 11, pp. 7837–7865, 2019.
- [73] M. Mirrashid and H. Naderpour, "Recent trends in prediction of concrete elements behavior using soft computing (2010–2020)," *Archives of Computational Methods in Engineering*, vol. 28, no. 4, pp. 3307–3327, 2021.
- [74] S. Dias and J. Barros, "Shear strengthening of RC T-section beams with low strength concrete using NSM CFRP laminates," *Cement and Concrete Composites*, vol. 33, no. 2, pp. 334–345, 2011.
- [75] S. J. Dias and J. A. Barros, "Shear strengthening of RC beams with NSM CFRP laminates: experimental research and analytical formulation," *Composite Structures*, vol. 99, pp. 477–490, 2013.
- [76] H. E. Emam, A. E. Sisi, M. Bneni, S. S. Ahmad, and H. E. D. M. Sallam, "Effects of tensile reinforcing steel ratio and Near-Surface-Mounted bar development length on the structural behavior of strengthened RC beams," *Latin American Journal of Solids and Structures*, vol. 17, 2020.
- [77] I. Sharaky, M. Baena, C. Barris, H. Sallam, and L. Torres, "Effect of axial stiffness of NSM FRP reinforcement and concrete cover confinement on flexural behaviour of strengthened RC beams: experimental and numerical study," *Engineering Structures*, vol. 173, pp. 987–1001, 2018.
- [78] R. M. Reda, Z. Omar, H. Sallam, and S. S. Ahmad, "Effect of different parameters controlling the flexural behavior of RC beams strengthened with NSM using nonlinear finite

- element analysis," *Frattura Ed Integrità Strutturale*, vol. 14, no. 53, pp. 106–123, 2020.
- [79] L. D. Lorenzis and A. Nanni, "Shear strengthening of reinforced concrete beams with near-surface mounted fiber-reinforced polymer rods," *ACI Structural Journal*, vol. 98, no. 1, pp. 60–68, 2001.
- [80] S. J. Dias and J. A. Barros, "Experimental behaviour of RC beams shear strengthened with NSM CFRP laminates," *Strain*, vol. 48, no. 1, pp. 88–100, 2012.
- [81] D. Cisneros, A. Arteaga, A. D. Diego, A. Alzate, and R. Perera, "Experimental study on NSM FRP shear retrofitting of RC beams," in *Proceedings of the Sixth International Conference on FRP Composites in Civil Engineering (CICE-2012)*, Rome, Italy, June 2012.
- [82] T. E. Maaddawy and Y. Chekfeh, "Shear strengthening of t-beams with corroded stirrups using composites," *ACI Structural Journal*, vol. 110, no. 5, p. 779, 2013.
- [83] H. E. M. Abou, A. Sherbini, and H. Sallam, "Structural behavior of RC beams containing a pre-diagonal tension crack," *Latin American Journal of Solids and Structures*, vol. 15, 2018.
- [84] H. E. M. Abou, A. Sherbini, and H. Sallam, "Locating the site of diagonal tension crack initiation and path in reinforced concrete beams," *Ain Shams Engineering Journal*, vol. 6, no. 1, pp. 17–24, 2015.
- [85] H. E. M. Abou, A. Sherbini, and H. Sallam, "Mode II fracture toughness of hybrid FRCs," *International Journal of Concrete Structures and Materials*, vol. 9, no. 4, pp. 475–486, 2015.
- [86] H. E. Sallam and K. Fawzy, "Stirrups in RC beams: facts beyond assumptions," in *Proceedings of the 5th ICCAE Conf*, ICCAE, Cairo, Egypt, November 2004.
- [87] I. A. Sharaky, L. Torres, and H. Sallam, "Experimental and analytical investigation into the flexural performance of RC beams with partially and fully bonded NSM FRP bars/strips," *Composite Structures*, vol. 122, pp. 113–126, 2015.
- [88] J. A. Barros and S. J. Dias, "Near surface mounted CFRP laminates for shear strengthening of concrete beams," *Cement and Concrete Composites*, vol. 28, no. 3, pp. 276–292, 2006.
- [89] Y. S. A. Rjoub, A. M. Ashteyat, Y. T. Obaidat, and S. Y. Bani, "Shear strengthening of RC beams using near-surface mounted carbon fibre-reinforced polymers," *Australian Journal of Structural Engineering*, vol. 20, no. 1, pp. 54–62, 2019.
- [90] K. N. Rahal and H. A. Rumaih, "Tests on reinforced concrete beams strengthened in shear using near surface mounted CFRP and steel bars," *Engineering Structures*, vol. 33, no. 1, pp. 53–62, 2011.
- [91] D. Lim, "Shear behaviour of RC beams strengthened with NSM and EB CFRP strips," *Magazine of Concrete Research*, vol. 62, no. 3, pp. 211–220, 2010.
- [92] S. J. Dias and J. A. Barros, "NSM CFRP laminates for the shear strengthening of T section RC beams," *International FIB Congress*, vol. 2, 2006.
- [93] R. Reda, I. Sharaky, M. Ghanem, M. Seleem, and H. Sallam, "Flexural behavior of RC beams strengthened by NSM GFRP Bars having different end conditions," *Composite Structures*, vol. 147, pp. 131–142, 2016.
- [94] H. E.-D. M. Sallam, A.-A. M. Saba, H. H. Shahin, and H. R. Abdel, "Prevention of peeling failure in plated beams," *Journal of Advanced Concrete Technology*, vol. 2, no. 3, pp. 419–429, 2004.
- [95] K. Fawzy and H. Sallam, "Shear strengthening of rc beams by near surface mounted (nsm) steel strips," in *Proceedings of the 11th International Colloquium on Structural and Geotechnical Engineering*, Cairo, Egypt, May 2005.
- [96] S. A. Bellamkonda, *Modeling of Shear Strengthening of Reinforced concrete Beams Retrofitted with Externally Bonded Fiber Reinforced Polymers*, Master Thesis, Louisiana State University, LA, USA, 2013.
- [97] V. Bianco, G. Monti, and J. A. Barros, "Design formula to evaluate the NSM FRP strips shear strength contribution to a RC beam," *Composites Part B: Engineering*, vol. 56, pp. 960–971, 2014.
- [98] A. Nanni, M. D. Ludovico, and R. Parretti, "Shear strengthening of a PC bridge girder with NSM CFRP rectangular bars," *Advances in Structural Engineering*, vol. 7, no. 4, pp. 297–309, 2004.
- [99] H. Baghi and J. A. Barros, "Design approach to determine shear capacity of reinforced concrete beams shear strengthened with NSM systems," *Journal of Structural Engineering*, vol. 143, no. 8, Article ID 04017061, 2017.
- [100] V. Bianco, G. Monti, and J. A. Barros, "Theoretical model and computational procedure to evaluate the NSM FRP strips shear strength contribution to a RC beam," *Journal of Structural Engineering*, vol. 137, no. 11, pp. 1359–1372, 2010.
- [101] V. Bianco, J. A. Barros, and G. Monti, "Influence of the concrete mechanical properties on the efficacy of the shear strengthening intervention on rc beams by nsm technique," in *Proceedings of the Asia-Pacific Conference on FRP in Structures (APFIS 2007)*, Hong Kong, China, December 2007.
- [102] H. Baghi and J. A. Barros, "New approach to predict shear capacity of reinforced concrete beams strengthened with NSM technique," *Structural Journal*, vol. 1, no. 114, pp. 137–148, 2017.
- [103] J. A. Barros, V. Bianco, and G. Monti, "NSM CFRP laminates for shear strengthening of RC beams: tests and mechanical model," *The Open Construction & Building Technology Journal*, vol. 3, pp. 12–32, 2009.
- [104] D. M. Prado, I. D. G. Araujo, V. G. Haach, and R. Carrazedo, "Assessment of shear damaged and NSM CFRP retrofitted reinforced concrete beams based on modal analysis," *Engineering Structures*, vol. 129, pp. 54–66, 2016.
- [105] V. Bianco, J. A. Barros, and G. Monti, "New approach for modeling the contribution of NSM FRP strips for shear strengthening of RC beams," *Journal of Composites for Construction*, vol. 14, no. 1, pp. 36–48, 2010.
- [106] V. Bianco, J. A. Barros, and G. Monti, "Three dimensional mechanical model for simulating the NSM FRP strips shear strength contribution to RC beams," *Engineering Structures*, vol. 31, no. 4, pp. 815–826, 2009.
- [107] A. Rizzo and L. D. Lorenzis, "Modeling of debonding failure for RC beams strengthened in shear with NSM FRP reinforcement," *Construction and Building Materials*, vol. 23, no. 4, pp. 1568–1577, 2009.
- [108] V. Bianco, J. A. Barros, and G. Monti, "A new approach for modelling the nsm shear strengthening contribution in reinforced concrete beams," in *Proceedings of the Fiber Reinforced Polymer for Reinforced Concrete Structures*, Patras, Greece, July 2007.
- [109] ACI-318-14, "Building code requirements for reinforced concrete," 2014.
- [110] ACI-440-Committee, *Guide for the Design and Construction of Externally Bonded FRP Systems for Strengthening concrete Structures. ACI-440.2 R-08*, American Concrete Institute, Farmington Hills, MI, USA, 2008.

- [111] A. A. Islam, "Effective methods of using CFRP bars in shear strengthening of concrete girders," *Engineering Structures*, vol. 31, no. 3, pp. 709–714, 2009.
- [112] M. Jalali, M. K. Sharbatdar, J. F. Chen, and F. J. Alaei, "Shear strengthening of RC beams using innovative manually made NSM FRP bars," *Construction and Building Materials*, vol. 36, pp. 990–1000, 2012.
- [113] M. M. Kadhim, A. H. Adheem, and A. R. Jawdhari, "Nonlinear finite element modelling and parametric analysis of shear strengthening RC T-beams with NSM CFRP technique," *International Journal of Civil Engineering*, vol. 17, pp. 1–12, 2019.
- [114] V. Bianco, J. A. Barros, and G. Monti, "Three dimensional mechanical model to simulate the NSM FRP strips shear strength contribution to a RC beam: parametric studies," *Engineering Structures*, vol. 37, pp. 50–62, 2012.
- [115] J. A. Barros, H. Baghi, S. J. Dias, and A. G. Ventura, "A FEM-based model to predict the behaviour of RC beams shear strengthened according to the NSM technique," *Engineering Structures*, vol. 56, pp. 1192–1206, 2013.

Hydraulic Fracturing Pressure Relief Technology in the Deep High-Stress Roadway for Rock Control

Harish Chand Giri, *Department of Mechanical Engineering, Aryan Institute of Engineering & Technology, Bhubaneswar, harishchand4@gmail.com*

Sikendar Sharma, *Department of Civil Engineering, Raajdhani Engineering College, Bhubaneswar, sikendarsharma92@gmail.com*

Biswa Ranjan Pradhan, *Department of Civil Engineering, Capital Engineering College, Bhubaneswar, biswaranjanpradhan78@gmail.com*

Deepikarani Swain, *Department of Mechanical Engineering, NM Institute of Engineering & Technology, Bhubaneswar, depika_r19@yahoo.co.in*

ABSTRACT

Deep ground pressure has an exceedingly negative impact on safety production as mining depth increases in underground engineering, and the economic benefits of coal mines and the regulation of highway stability in deep mines are steadily highlighted. The engineering background for this study was the Zaoquan coal mine's working face 14203, and the surrounding rock deformation mechanism in the deep-buried high-stress roadway was analysed, and hydraulic fracturing pressure relief technology in the advanced roadway was proposed for surrounding rock control. Finally, numerical simulation and field experiments were utilised to verify the suggested technology's overall effect. Hydraulic fracturing pressure relief technique can maximise the stress environment and highway stability without compromising roadway stability in the working face by artificially controlling the roof fracture position. The numerical simulation reveals that when hydraulic pressure is applied.

1. Introduction

In recent years, the mining depth and mining scope have been continuously increased. Compared with the shallow mining, the geological process characteristics and mine pressure behavior law under the condition of deep mining have been changed greatly: for the deep mine, the vertical stress (caused by the gravity) and the in situ stress are higher, and the tectonic stress field is more complex. Deep ground pressure has an extremely unfavorable impact on safety production and economic benefits of coal mines [1–3]. In the deep mining, the

deformation characteristics of coal rock are changed from brittleness to plasticity, and the dilatancy and the impact risk of coal rock are increased. In the deep roadway, complex geological conditions and high ground stress fields often cause serious deformation and failure of surrounding rock [4, 5]. Therefore, the deformation and failure of surrounding rock should be effectively controlled under the strong mine pressure in deep mining to ensure safe mining.

Research on the deformation mechanism and stability of surrounding rock of deep high-stress roadway has been widely performed. Zhang [6] studied the loose blasting and

pressure release channel of surrounding rock through the FLAC numerical simulation software. To solve the problem of roadway deformation in short cantilever beam roof excavation theory, Yang et al. [7] proposed the roof excavation pressure relief method in the adjacent roadway and determined the presplit blasting technical parameters through theoretical analysis. Yang et al. [8] studied the stress process of bolt on the roof by three-dimensional numerical simulation, analyzed the time effect of bolt mechanical properties, and summarized the working mechanism of floor bolt. He et al. [9, 10] pointed out that in the deep coal mining, the rock mass medium is in the stage of large plastic deformation, leading to more significant nonlinear mechanical phenomena; as for the supporting technology, the coupling of the strength, stiffness, and structure between the support body and the surrounding rock should be considered. Zuo et al. [11] systematically analyzed the macro/meso failure mechanism of deep rock or coal rock combinations under different loading conditions. The stress gradient failure theory of surrounding rock, the hyperbolic movement model of uniform support in the deep roadway, and overburden simulation were established, and the combined grouting control technology of surface and underground was proposed. In addition, Xiao et al. [12–16] studied the failure mechanism and control measures of soft rock in the deep roadway.

In previous studies, hard roof collapse behind the working face has been mainly investigated, while the study on stability control of deep roadway has been rarely reported. The working face 14203 in the Zaoquan coal mine was a typical deep mining face with a large mining height. Under the joint influence of large buried depth, high stress, and advanced mining, large deformation occurred in the roadway. According to the stress environment of the roadway, on the premise of not affecting the production of the working face and the integrity of the presplit roadway roof, the hydraulic fracturing pressure relief technology for surrounding rock control was performed in the advanced roadway of the working face. Besides, theoretical analysis, numerical simulation, and field tests were employed to study the mechanism of the hydraulic fracturing pressure relief technology and its implementation effect. The research results can provide a reference for roadway stability control under similar conditions.

2. Engineering Background

2.1. Production and Geological Conditions. Zaoquan coal mine was located at the edge of Maowusu Desert, which was 62 km southeast of the Lingwu City, Ningxia Hui Autonomous Region. Its geographical coordinates were 106°30'–106°35' E and 37°52'–38°02' N. The coal seam 2 of the working face 14203 was the main fully mechanized working face with a large mining height. The thickness of coal seam 2 was 8.07–8.39 m, the dip angle was 2°–13°, the strike length was 2336 m, and the dip length was 182.82–235 m. The direct roof was composed of siltstone, mudstone, and carbonaceous mudstone, with an average thickness of 10.90 m; the main roof was composed of medium-grained sandstone and

fine-grained sandstone and siltstone, with an average thickness of 35.45 m. The floor was composed of mudstone, siltstone, and fine-grained sandstone, with an average thickness of 5.64 m. The east side of the working face was the excavated area, the south side was the F69 normal fault of No. 13 and No. 14 mining areas, the west side was the old goaf of the working face 14202. Between the working face 14203 and the goaf, there was a coal pillar of 14 m. The north side was the 2nd and 3rd middle yard of No. 14 mining area, and there was no goaf in the upper part of the working face. The buried depth of the rubber-tire haulage gateway in the fully mechanized working face 14203 was about 660 m, and the buried depth of the return airway was about 627 m. The cross section sizes of the rubber-tire haulage gateway and the return airway of the working face 14203 were 4500 mm × 3550 mm with the joint support of anchor, mesh, and cable, as shown in Figure 1.

2.2. Analysis of Deformation Characteristics of the Test Roadway

2.2.1. Deformation Characteristics of the Test Roadway. Due to the joint influence of the large buried depth, high ground stress, and advanced mining of the working face, the roof subsidence, floor heave, and serious shrinkage of two sides appeared in the rubber-tire haulage gateway and return airway. The roadway deformation within 30 meters ahead of the working face was still severe (serious roof subsidence, floor heave, and side shrinkage), the erected steel beam shed was compressed and fractured, and the single hydraulic prop was bent. As shown in Figure 2, the roof sank and pressed on the transfer machine section, and the transfer machine and end support were unable to move normally, which seriously affected the safety production of the working face.

2.2.2. Cause Analysis of Roadway Deformation. The complex structures such as large faults and collapse columns have not been exposed during the excavation process of the rubber-tire haulage gateway in the working face 14203. However, due to its large buried depth (660 m), the in situ stress environment had an important impact on the roadway deformation. In the field, the SY-56 Small Aperture Hydraulic Fracturing In Situ Stress Measurement System produced by Xi'an Zhongzhou Geotechnical Technology Co., Ltd., was used, and measurement stations at four typical positions of working faces 14203 and 14201 were set to measure the in situ stress near the roadway. As shown in Figure 1, the fracture pressure (P_b), fracture tension pressure (P_r), instantaneous closing pressure of hydraulic fracture surface (P_s), and in situ tensile strength (T) of rock in each measuring section were determined. According to the relevant formulas, the main stress value is shown in Table 1.

As shown in Table 1, there was large stress at the measuring points in the test area, and the value of vertical principal stress increases gradually with the increase of the buried depth. The underground in situ stress field type was $\sigma_v > \sigma_H > \sigma_h$ stress field, and the four measuring points were NNE direction. In a word, ground stress was an important

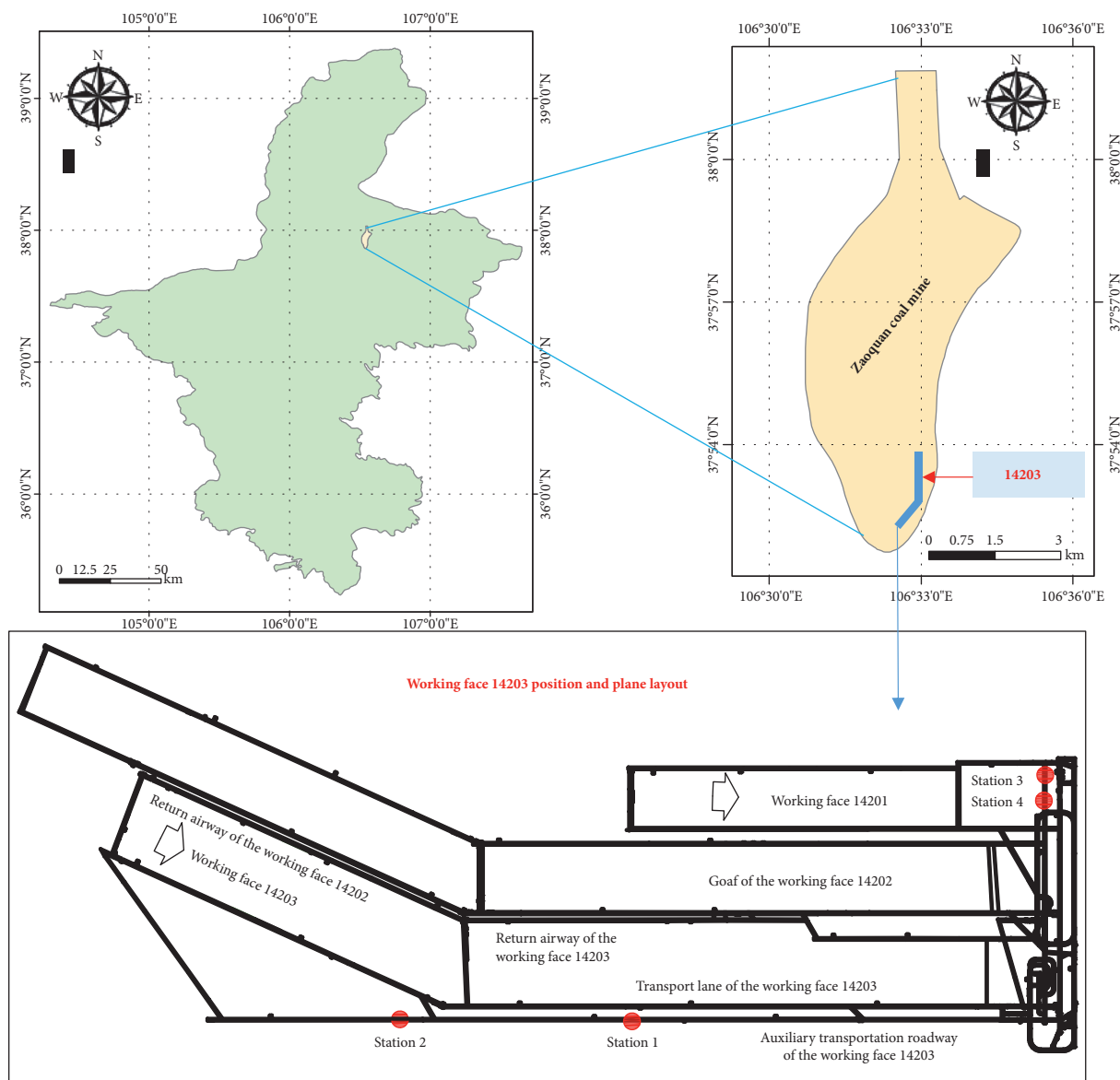


FIGURE 1: Position and plane layout of the working face 14203.

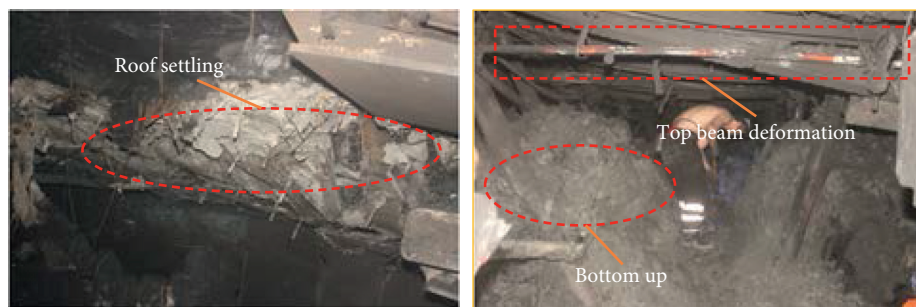


FIGURE 2: Deformation of two roadways in the working face 14203.

factor causing serious deformation of the roadway. At the same time, the average thickness of the main coal seam in the working face 14203 was 8.2 m, belonging to the large

mining-height working face. Compared with the thin coal seam mining, the overburden movement in the goaf of the working face with the large mining height was more intense

TABLE 1: In situ stress measurement results of hydraulic fracturing in Zaoquan coal mine.

Measuring point no.	Buried depth (m)	Fracturing parameters			Principal stress (MPa)			Fracture direction (°)	Saturated uniaxial compressive strength (MPa)
		P_b	P_r	P_s	σ_H	σ_h	σ_v		
1	608.8	5.44	5.03	3.99	6.52	3.78	15.22	N15.2°E	14.18
2	658.1	17.30	10.28	9.00	16.30	8.79	16.45	N23.2°E	12.93
3	525.4	11.74	7.47	6.13	10.49	5.91	13.14	N15.5°E	28.75
4	571	11.34	6.60	6.21	11.65	6.02	14.28	N8.2°E	29.64

after mining. As a result, the rubber-tire haulage gateway was disturbed, and the roadway deformation was inevitably caused.

3. Roof Hydraulic Fracturing Pressure Relief for Surrounding Rock Control

3.1. Mechanism of Roof Hydraulic Fracturing Pressure Relief and Roadway Protection. To ensure the normal connection of the working face, the roadway of the next working face is often excavated in advance. When the current working face is mined, the coal pillar between the adjacent working faces will become the stress concentration area, and the roadway serving the next working face will be in a stress concentration environment. As a result, serious roadway deformation is caused, especially in the condition of large buried depth. In this study, the roof hydraulic fracturing pressure relief technology was performed as follows: before the mining of the working face with a large mining height, a special slotting bit was used to prefabricate a transverse slot in the roof drilling; then, the transverse slot section was sealed. The high-pressure water was used to produce cracks at the end of the slot and expand along with the rock layer, and then a “quasifracture surface” was formed in the overburden strata of the roadway pillar. During the mining of the working face, under the action of periodic pressure of stope, the roof of goaf broke along the “quasifracture surface;” the span of cantilever beam was reduced, the action time of lateral abutment pressure was shortened, the stress transmitted by the lateral cantilever beam to the coal pillar of roadway protection was unloaded or transferred, and then the stress state of roadway retaining was improved [17–21]. Finally, the difficulty of roadway maintenance was reduced and the safe production of mine was ensured, as shown in Figure 3.

3.2. Numerical Simulation of Hydraulic Fracturing Pressure Relief in the Roof and Roadway Protection

3.2.1. Numerical Calculation Model and Schemes. Based on the geological data of the mine, a numerical calculation model was established by the FLAC6.0 software. The size of the model was 250 m in length, 100 m in width, and 80 m in height, with a total of 2,000,000 grids. The interface unit was used to establish 11 structural planes. A total of 12 strata were simulated from the fine sandstone of the basic floor to the topsoil, as shown in Figure 4. Table 2 shows the mechanical parameters of rock mass.

According to the Mohr–Coulomb criterion, the maximum unbalance force of the model was monitored during the calculation process. When the equilibrium state was obtained in the model, the simulated vertical stress level was 16 MPa, and the horizontal stress level was 12 MPa. The simulated calculation level was kept at the same level as the monitored in situ stress, as shown in Figure 5. To compare the influence of hydraulic fracturing on the stability of surrounding rock in the roadway, two models were designed for comparative analysis according to the design scheme of hydraulic fracturing drilling parameters .

Scheme 1: the influence of nonhydraulic fracturing in the roof on the stability of rubber-tire haulage gateway 14203 was simulated. According to the data provided by the mining enterprise, the goaf, the return airway, the working face 14203, the rubber-tire haulage gateway, and the auxiliary haulage gateway were excavated in coal seam 2. To meet the needs of numerical simulation calculation, the goaf was reserved for 15 m; the size of return airway, rubber haulage gateway, and auxiliary haulage gateway was 4.5 m × 3.55 m; the distance between the roadway and the coal pillar of 20 m was reserved in the goaf; and the maximum boundary limit of the working face was reserved for 130 m as shown in Figure 6(a).

Scheme 2: the influence of roof hydraulic fracturing on the stability of rubber-tire haulage gateway 14203 was simulated. According to the relevant theoretical analysis, the *Interface* command was used to generate a crack at 45° along the side face of the rubber-tire haulage gateway, and the length of the crack was 50 m. The other crack was distributed at 5° along the coal pillar, and the length of the crack was 50 m as shown in Figure 6(b). After the working face 14203 advanced 20 m in the working face 14203, the stress distribution and deformation characteristics of the surrounding rock of the roadway were analyzed and compared in the two schemes.

3.2.2. Simulation Results

(1) Influence of Hydraulic Fracturing Pressure Relief on the Stress of the Surrounding Rock. Figure 7 shows the vertical stress distribution nephogram of the two schemes. As shown in Figure 7(a), when roof hydraulic fracturing of rubber-tire haulage gateway is not performed, the low-stress (less than 6 MPa) areas are mainly concentrated in the position of 20 m above and below the goaf and 5–8 m above and below the excavated roadway. These areas are prone to tensile failure.

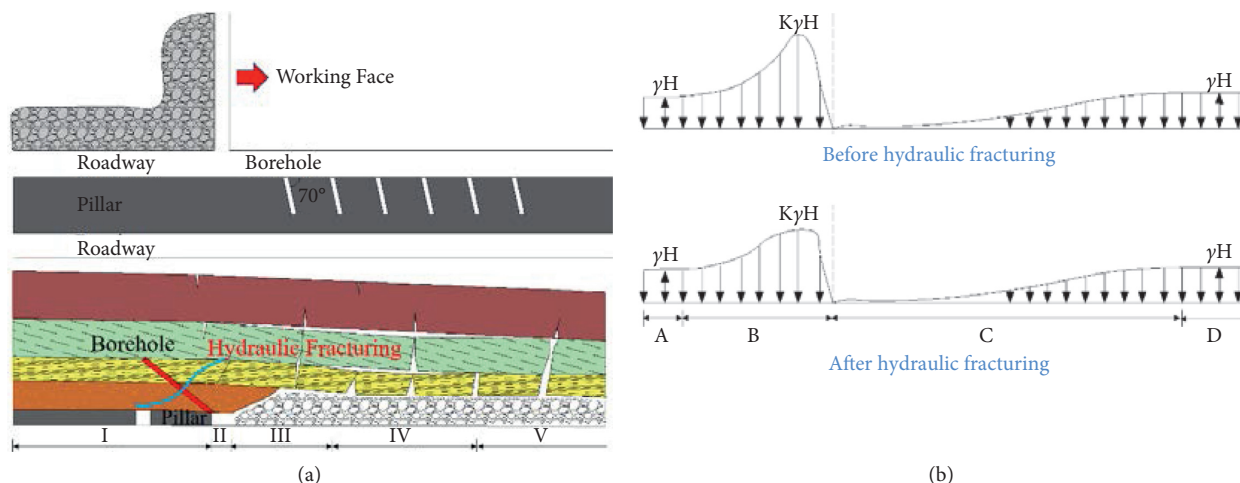


FIGURE 3: (a) Mechanism of roof hydraulic fracturing pressure relief technology. (b) Stress distribution before and after relief.

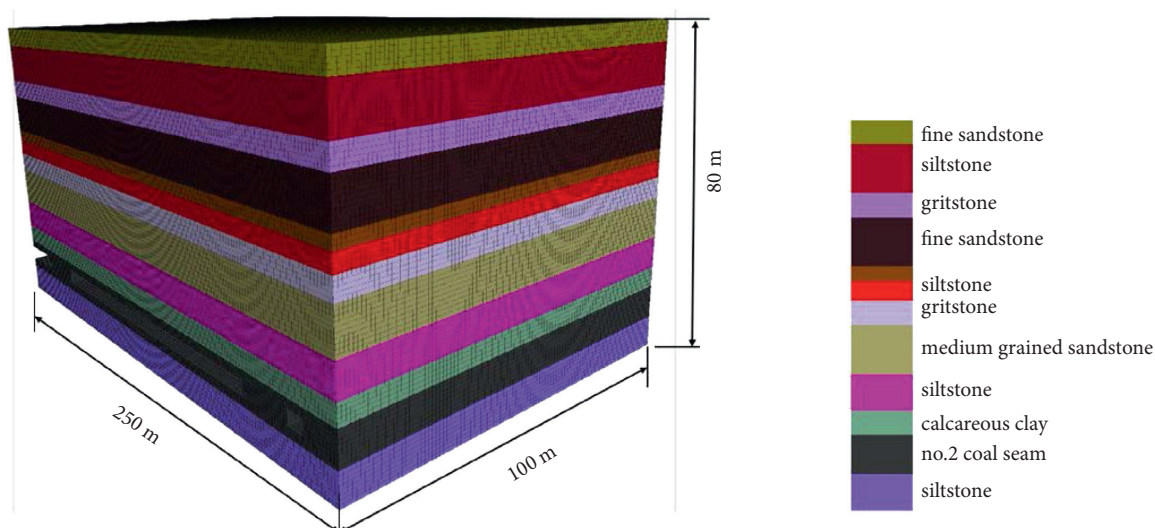


FIGURE 4: Numerical calculation model.

TABLE 2: Some rock mechanics parameters of the numerical model.

Strata	Bulk modulus (K/GPa)	Shear modulus (K/GPa)	Cohesion (C/MPa)	Internal friction angle ($\varphi/^\circ$)	Density ($\rho/\text{kg/m}^3$)
Coarse-grained sandstone	3.5	1.5	2.31	32	2680
Medium-grained sandstone	4.2	2.1	2.9	37	2670
Siltstone	4.0	1.9	3.2	38	2670
Carbonaceous mudstone	3.6	2.0	2.8	36	2680
2# coal seam	2.5	1.2	1.56	30	1380
Siltstone	4.0	1.9	3.2	38	2670

The relatively high-stress (above 11 MPa) areas are mainly concentrated in the upper 30 m of the model, and the concentrated stress of the 20 m coal pillar is even as high as 20 MPa. As shown in Figure 7(b), due to the existence of cutting slot after the roof hydraulic fracturing, the low-stress (less than 6 MPa) area increases significantly, mainly concentrated in the excavation roadway and the upper 50 m

range of goaf. At the same time, the stress between 20 m coal pillars decreases from the original 20 MPa above to 12–15 MPa, decreasing by about 40%. The relatively high-stress (16 MPa) areas are mainly concentrated in the upper 10 m of the model. On the whole, after hydraulic fracturing, the area of high-stress concentration above the rubber-tire haulage gateway and in the direction of the coal pillar is

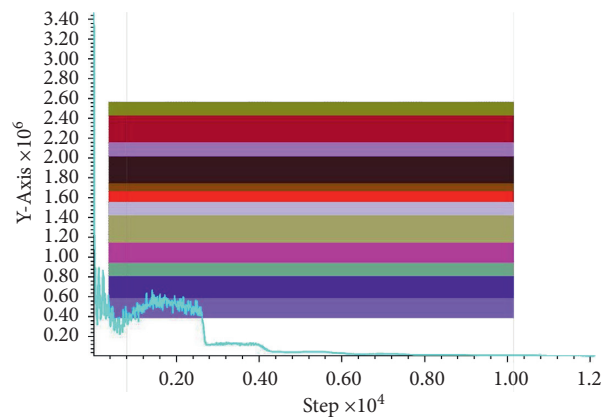


FIGURE 5: Numerical calculation model in the equilibrium state.

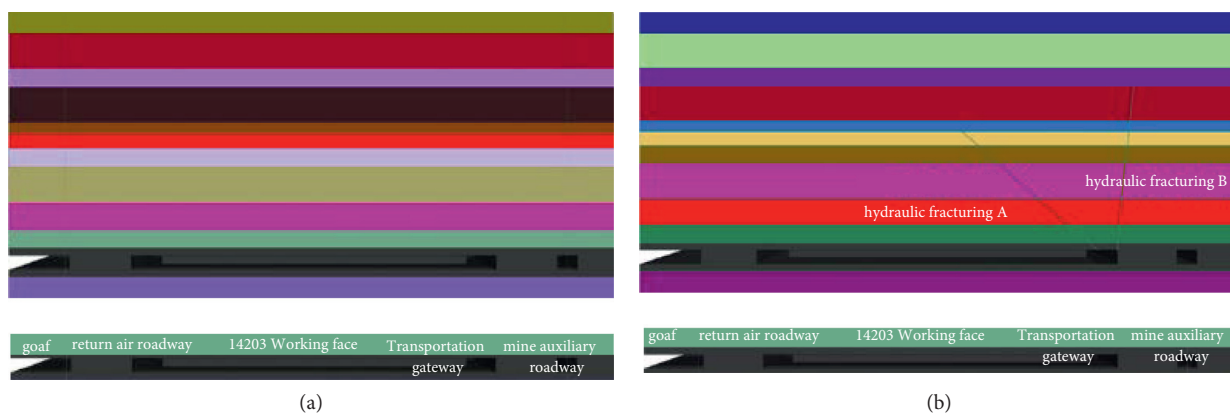


FIGURE 6: Excavation space relationship diagram of the model. (a) Nonhydraulic fracturing. (b) Hydraulic fracturing.

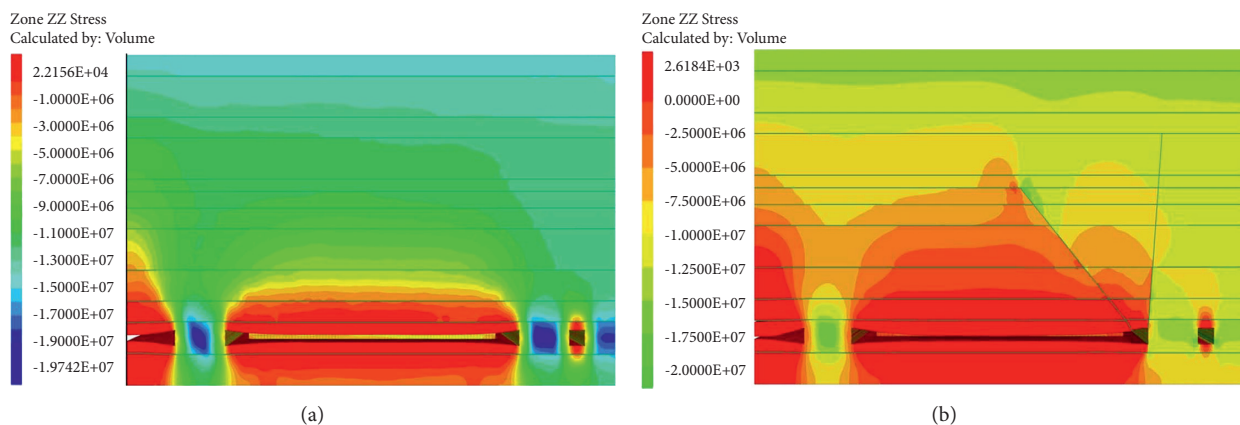


FIGURE 7: Nephogram of vertical stress of roadway surrounding rock (a) before and (b) after hydraulic fracturing.

obviously reduced. As a result, the damage degree of the area is greatly reduced, and the stability of the roadway is significantly enhanced.

(2) *Influence of Hydraulic Fracturing Pressure Relief on the Plastic Zone of Surrounding Rock.* Figure 8 shows the change of plastic zone of surrounding rock in the roadway before

and after hydraulic fracturing pressure relief. As shown in Figure 8(a), the roof subsidence in the nonhydraulic fracturing section is not sufficient, and the plastic zone is about 15 m in the upper part. The plastic zone of coal pillar is fully developed on the side of the rubber-tire haulage gateway, and there is a range of 2–5 m free of plastic failure in the middle of the 20 m coal pillar. The development range of the

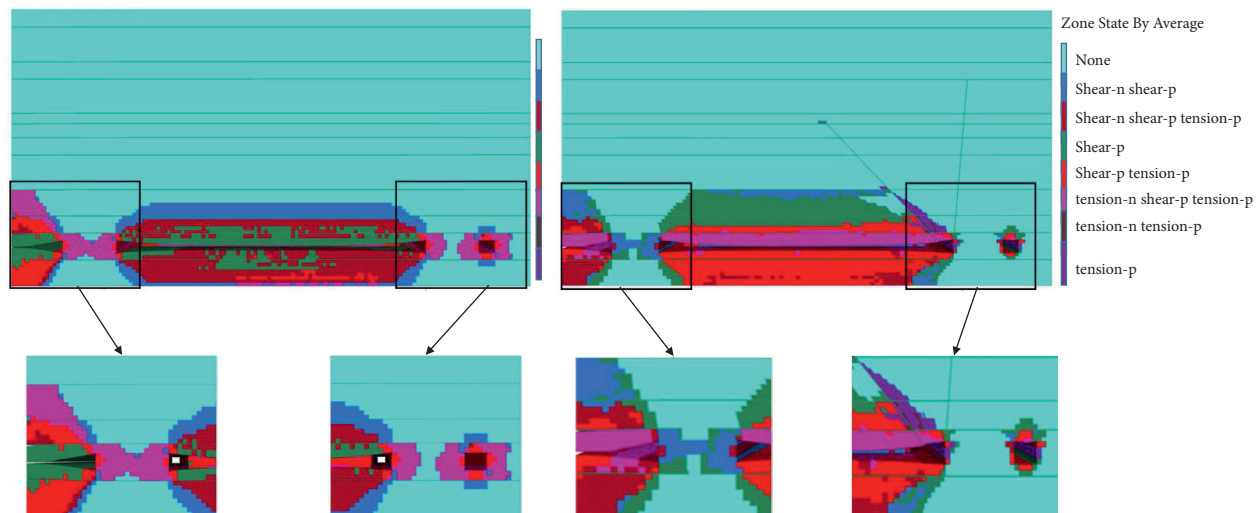


FIGURE 8: Variation cloud map of plastic zone of surrounding rock in the roadway (a) before and (b) after hydraulic fracturing.

plastic zone in the upper roof is 8 m, and the plastic zone in the shallow roof and floor is dominated by tensile failure and the two sides and other deep areas by shear failure. It indicates that the deformation and failure of the surrounding rock of the rubber-tire haulage gateway are also serious. At the same time, the plastic zone in the two sides of the auxiliary haulage gateway is affected by the vertical stress, and the influence range is more than 8 m. The influence range in the roof and floor is more than 5 m.

As shown in Figure 8(b), due to the existence of hydraulic fractures, the plastic zone in the upper part of the mined roof is fully developed and the roof subsidence is sufficient. The plastic zone on the side of the rubber-tire haulage gateway changes obviously. The plastic zone of the 20 m coal pillar is less than 5 m, and the plastic zone of the roof is reduced by about 50%, which greatly reduces the deformation and failure of the roof and coal wall. The plastic zone of the two sides of the auxiliary haulage gateway is reduced to less than 4 m, and the development range of the roof and floor is less than 4 m. Compared with the non-hydraulic fracturing section, the reduction of plastic zone is obvious in the hydraulic fracturing section. It indicates that hydraulic fracturing is more conducive to reducing the mining influence and roadway deformation and maintaining the stability of the roadway.

(3) *Influence of Hydraulic Fracturing Pressure Relief on the Deformation of Surrounding Rock.* Figure 9 shows the distribution of displacement and deformation curve of rubber-tire haulage gateway 14203 in the two schemes. Through the comparison, it can be seen that the displacement of surrounding rock of roadway in hydraulic fracturing section decreases significantly, with an overall decrease of about 45.8%. The floor and the left and right sides have the most prominent decrease. The left side decreases from about 435 mm to about 377 mm, and the right side decreases from about 434 mm to about 174 mm. The change of floor is the biggest, and the decrease is about 365 mm before and after hydraulic fracturing. The displacement of surrounding rock

decreases obviously, which is positively correlated with the plastic zone distribution of surrounding rock. It shows that hydraulic fracturing technology reduces the influence of mining on roadway deformation and maintains the stability of the roadway.

4. Engineering Practice

4.1. Hydraulic Fracturing Parameter Design. To ensure the normal production of the working face, the drilling was carried out at the position of rubber-tire haulage gateway 14203, which was 120 m away from the working face. Figure 10 shows the hydraulic fracturing parameters and roadway support parameters of the rubber-tire haulage gateway in the working face 14203. The construction sequence was as follows: observation of roof rock structure with a peep scope → in situ test of roof rock strength → determination of fracturing parameters → fracturing drilling operation → implementation of fracturing → fracturing monitoring. The underground construction started on July 20, 2019, and ended on January 20, 2020. The length of the test roadway in the working face 14203 was 300 m, and a total of 60 boreholes were constructed:

- (1) The fracturing boreholes were arranged along the axial direction of the haulage gateway. The opening position was about 1 m away from the coal pillar, and the included angles with the roadway were 45° and 5°, respectively, as shown in Figures 10(a) and 10(b). The actual angle and opening position were adjusted according to the field space.
- (2) The length of boreholes was 50 m, the dip angle was 50°, and the spacing was 10 m, as shown in Figure 10(c).
- (3) Roadway support parameters: two corners of the roadway roof were supported by the $\varnothing 21.98 \text{ mm} \times 4300 \text{ mm}$ (1 × 19) anchor cables. The dip angle of anchor cables was 15°, the preload was more than 200 kN, and the row spacing between anchor cables

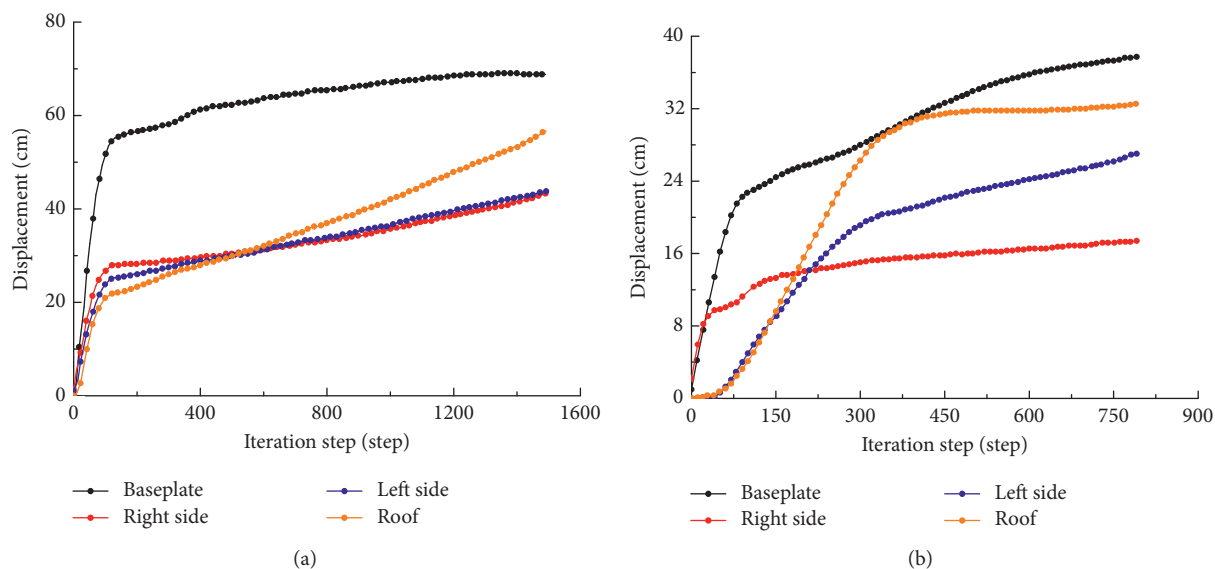


FIGURE 9: Displacement curve distribution of rubber-tire haulage gateway 14203 in two schemes. (a) Nonhydraulic fracturing. (b) Hydraulic fracturing.

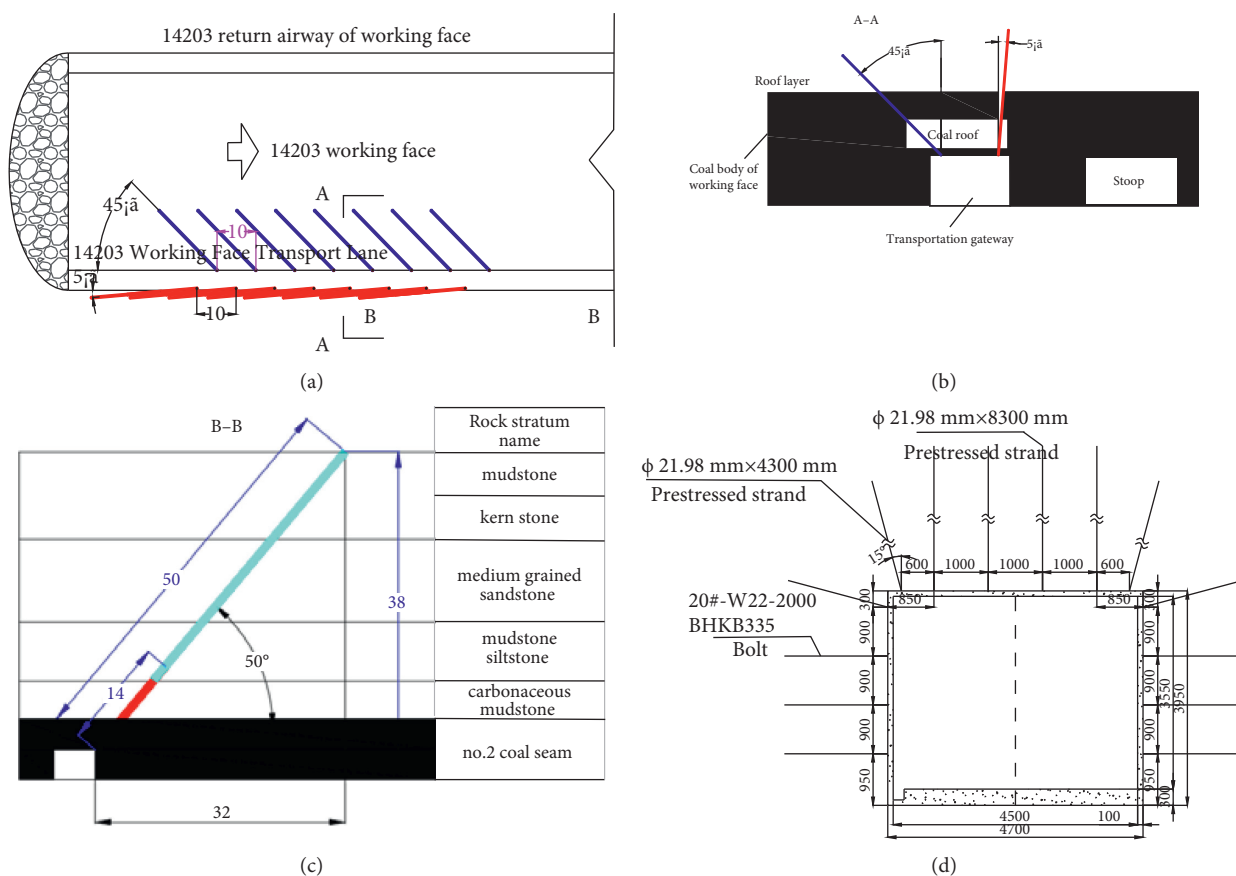


FIGURE 10: Hydraulic fracturing and supporting parameters of rubber haulage gateway 14203. (a) Drilling layout plan. (b) Section A-A. (c) Section B-B. (d) Sectional view of rubber-tire haulage gateway support.

was 1000/600 × 900 mm. The top of the cable truss was arranged for support, the specification of this cable was 21.98 mm × 8300 mm, and the cable

preload was greater than 200 kN. The anchor cable trusses $L = 3800$ mm were arranged symmetrically along both sides of the center line, and the row

spacing was 900 mm. The $W280 \times 5 \times 4700-1000/600-6$ type W steel strip was used for the top support. The $\phi 6.5$ mm round steel welded steel mesh was hung at the top of the roadway, and the mesh size was 100×100 mm. The 20#-M22-2000 BHRB335 left-handed rebar bolt without longitudinal bar was adopted at the side of the roadway. The tensile force of the bolt at the side was greater than 50 kN, the row spacing between the bolts was 900×900 mm, and the spray layer with a thickness of 400 mm was laid on the bottom plate, as shown in Figure 10(d).

4.2. Monitoring Content and Scheme. In the working face 14203, three measuring stations were respectively arranged in the hydraulic fracturing section and nonhydraulic fracturing section, with a total of six measuring stations. The interval of stations was 100 m, as shown in Figure 11. The hydraulic fracturing section was 120 m away from the working face. The surface displacement of the roadway, roof separation, and anchor cable stress were mainly monitored.

4.3. Engineering Effect. The monitoring results of 5# station in the nonhydraulic fracturing section and 2# station in the hydraulic fracturing section of the rubber-tire haulage gateway in the working face 14203 were compared and analyzed.

4.3.1. Roadway Surface Displacement. According to the monitoring results of 5# station and 2# station, the roadway surface displacements of nonhydraulic fracturing section and hydraulic fracturing section in the working face 14203 are plotted respectively, as shown in Figures 12 and 13. The maximum roof subsidence of the nonhydraulic fracturing section is 310 mm, the maximum floor heave is 760 mm, the maximum displacement of the left side is 607 mm, and the maximum displacement of the right side is 409 mm. When the hydraulic fracturing section is 110 m away from the working face, the surrounding rock of the roadway has obvious displacement changes. When it is 80 m away from the working face, the displacement of surrounding rock rapidly increases. However, compared with the nonhydraulic fracturing section, the roof subsidence, floor heave, left side, and right side of the hydraulic fracturing section decrease by 52.2%, 53.8%, 59.2%, and 44.5%, respectively. At the same time, when the hydraulic fracturing section is 90 m away from the working face, the displacement of the surrounding rock of the roadway changes; when it is 80 m away from the working face, the displacement of surrounding rock of roadway increases rapidly. Therefore, hydraulic fracturing has an obvious effect on the roadway stability control.

4.3.2. Roof and Floor Separation of Roadway. The separation amount of roof and floor in the roadway is also the rock movement amount at the roof and floor of the roadway. According to the monitoring results of 5# station and 2# station, the roof and floor separation of nonhydraulic fracturing section and hydraulic fracturing section in

working face 14203 are drawn, as shown in Figures 14 and 15. When the distance from the working face is 130 m, the roof separation of roadway occurs in the nonhydraulic fracturing section (monitored by 5# station), which is consistent with the response of roof subsidence. It indicates that the separation and roof subsidence have a positive correlation. When the distance from the working face is 60 m, the amount of roof separation begins to increase rapidly. When the distance from the working face is 0 m, the maximum value of the deep base point is 186 mm, and the maximum value of the shallow base point is 68 mm. However, in the hydraulic fracturing section, when the distance is 100 m away from the working face, the roof separation occurs (monitored by 2# station). When the distance from the working face is 65 m, the amount of roof separation is significant. When the distance from the working face is 0 m, the maximum values are obtained. The maximum value of the deep base point is 164.7 mm, and that of the shallow base point is 22 mm in the hydraulic fracturing section, which is 22.6% and 60% less than that of the nonhydraulic fracturing section. The amount of roof separation presents the characteristics of decreasing from deep to shallow.

4.3.3. Bolt Stress

(1) Stress Analysis of Side Bolt of Coal Pillar. Figures 16 and 17 show the stress curves of the bolts at the coal pillar side of 5# and 2# stations, respectively. It can be seen that the stress of the upper 2# bolt in the nonhydraulic fracturing section is less than that of the lower 1# bolt, and the stress of the two bolts shows a gradually increasing trend. This suggests that the lower bolt is obviously affected by the floor heave, and the stress is obviously larger. With the advance of the working face, the stress of the bolt increases gradually. When the distance from the working face is 0 m, the stress of the upper 2# bolt reaches the maximum value of 163.8 kN, and the stress of the lower 1# bolt increases to 105.3 kN and does not change. When the distance is 100 m away from the working face in the hydraulic fracturing section, the bolt stress on the side of the coal pillar begins to increase, in which 2# bolt increases more rapidly than the lower 1#. It indicates that the pressure on the upper part of the coal pillar is faster. When it is 65 m away from the working face, the stress of the upper 2# bolt reaches the maximum value of 112 kN and suddenly decreases to 0 kN. The actual observation shows that the bolt tail breaks off. The stress of the lower 1# bolt increases continuously until it reaches 85 kN and does not change. Compared with the nonhydraulic fracturing section, the stress of the side bolt of the coal pillar in the hydraulic fracturing section is reduced by 12.3%–31.9% on average.

(2) Stress Analysis of Side Bolt in the Mining Face. Figures 18 and 19 show the stress curves of the bolts at the mining face of 5# and 2# stations, respectively. As shown in Figure 18, the stress of 3# bolt in the nonhydraulic fracturing section decreases slowly at the later stage, while the stress of the lower 4# bolt increases greatly at the later

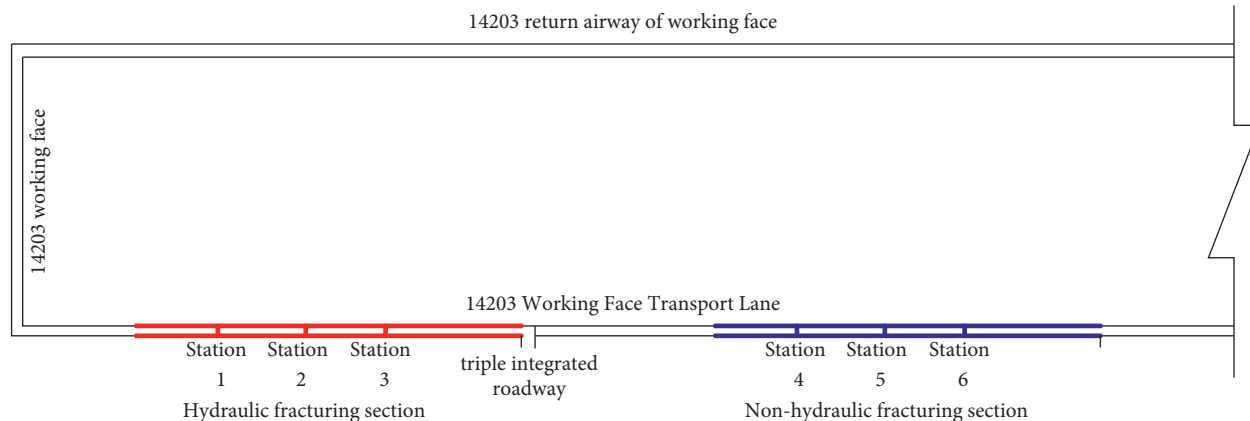


FIGURE 11: Hydraulic fracturing parameters of rubber haulage gateway 14203.

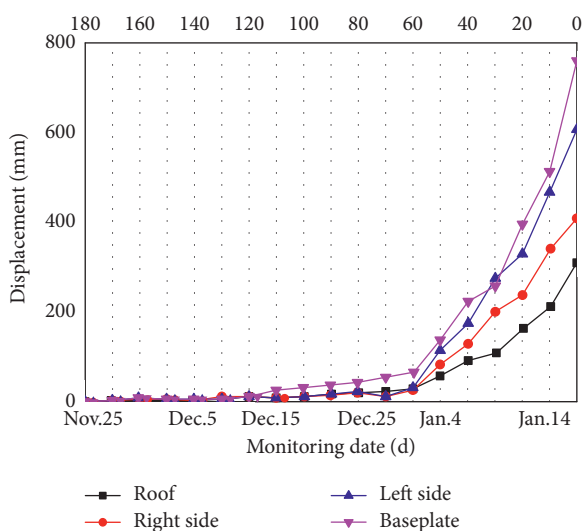


FIGURE 12: Nonhydraulic fracturing section: displacement variation of surrounding rock monitored by 5# station.

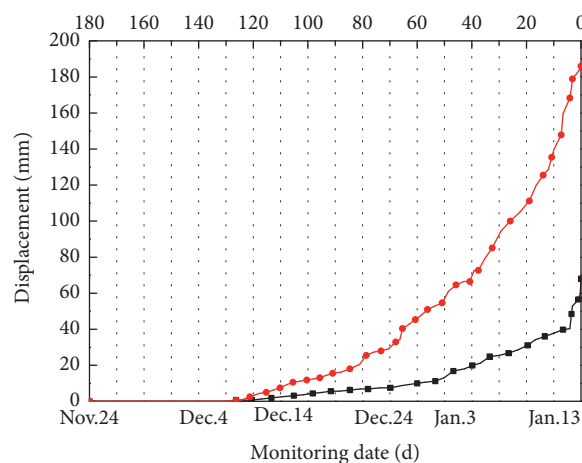


FIGURE 14: Nonhydraulic fracturing section: roof separation curve of 5# station.

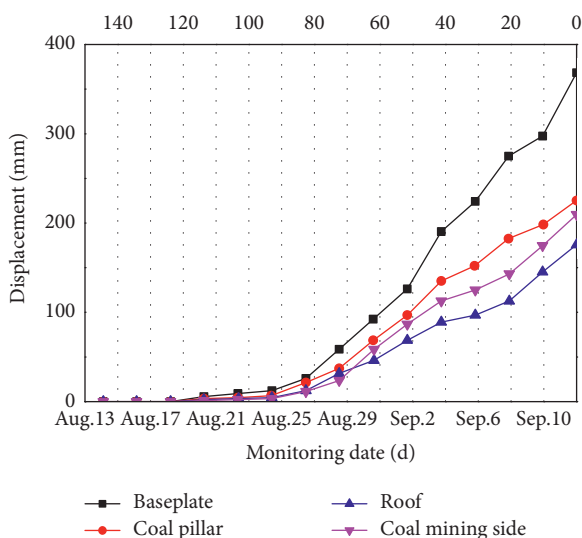


FIGURE 13: Hydraulic fracturing section: displacement variation of surrounding rock monitored by 2# station.

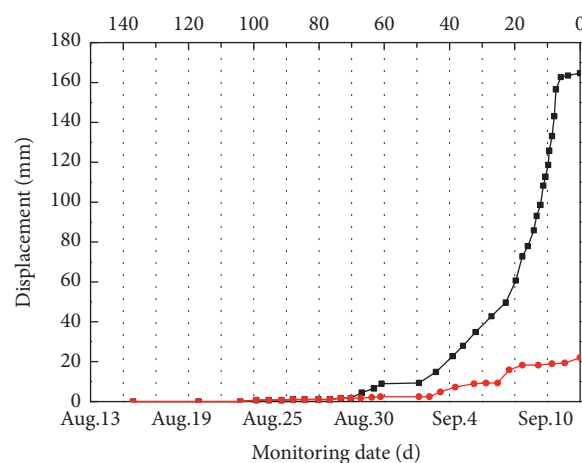


FIGURE 15: Hydraulic fracturing section: roof separation curve of 2# station.

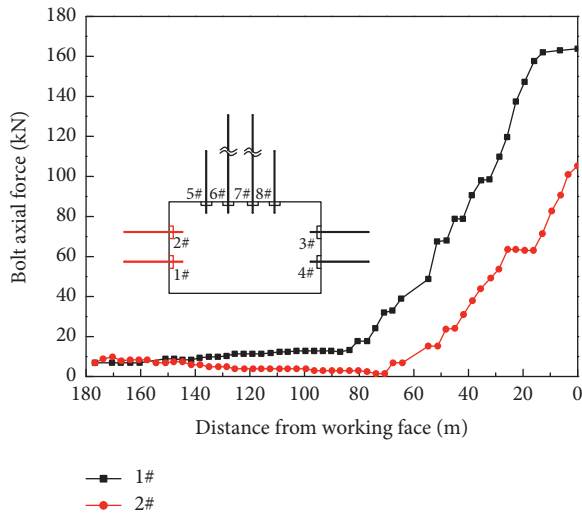


FIGURE 16: Nonhydraulic fracturing section: stress of side bolt of coal pillar at 5# station.

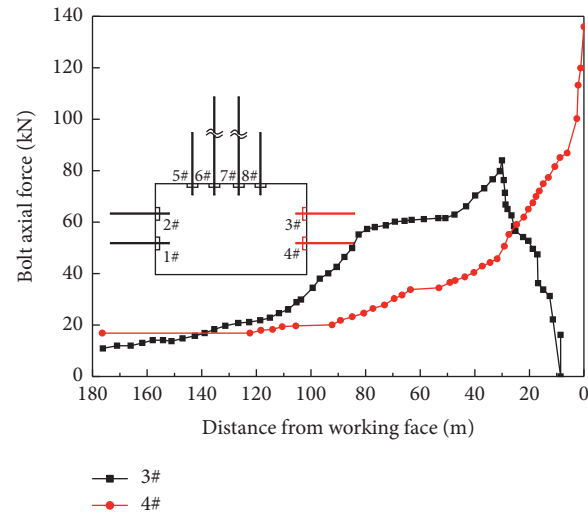


FIGURE 18: Stress of side bolt at 5# station in the nonhydraulic fracturing section.

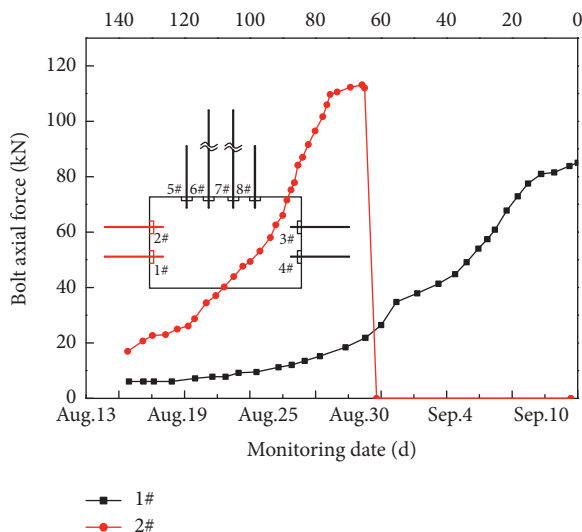


FIGURE 17: Hydraulic fracturing section: stress of side bolt of coal pillar at 2# station.

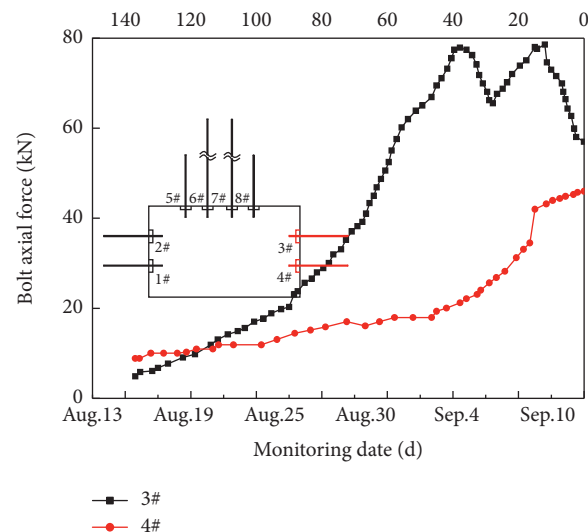


FIGURE 19: Stress of side bolt at 2# station in the hydraulic fracturing section.

stage. When the distance from the working face is 30 m, the stress of the upper 3# bolt reaches the maximum value of 84 kN, and the stress drops sharply to 0, and the stress of the lower 4# bolt begins to rise rapidly. When the distance from the working face is 0 m, the stress of the lower 4# bolt reaches 136 kN. As shown in Figure 19, the supporting force of 3# bolt in the hydraulic fracturing section fluctuates strongly in the later stage, while that of 4# bolt increases steadily. When it is 15 m away from the working face, the maximum stress of the upper 3# and lower 4# bolts is 78 kN and 42 kN. Then the stress of the upper 3# bolt decays. Finally, the upper 3# bolt is stable at about 57 kN, and the lower 4# bolt reaches the maximum value of 46 kN. The stress of the side bolt in the hydraulic fracturing section is 56.1%–51.8% less than that in the nonhydraulic fracturing section.

4.3.4. Anchor Cable Stress

(1) *Stress Analysis of the Anchor Cable at Coal Pillar Side.* Figures 20 and 21 show stress curves of anchor cable at coal pillar side of 5# and 2# measuring stations, respectively. As shown in Figure 20, with the advance of the working face, the stress of anchor cable in the nonhydraulic fracturing section increases continuously. When it is 30 m away from the working face, the stress of anchor cable decreases rapidly. With the decreasing distance to the working face, the stress of anchor cable increases continuously until the distance is about 0 m. The stress of 5# anchor cable reaches the maximum value of 239 kN and that of 6# anchor cable reaches more than 500 kN. These conditions are consistent with the characteristics of roof subsidence. As shown in Figure 21, when hydraulic fracturing technology is adopted and the distance

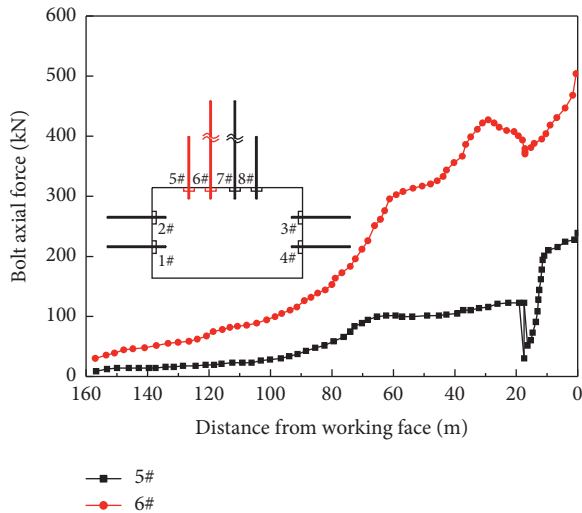


FIGURE 20: Nonhydraulic fracturing section: stress of the anchor cable at coal pillar side of 5# station.

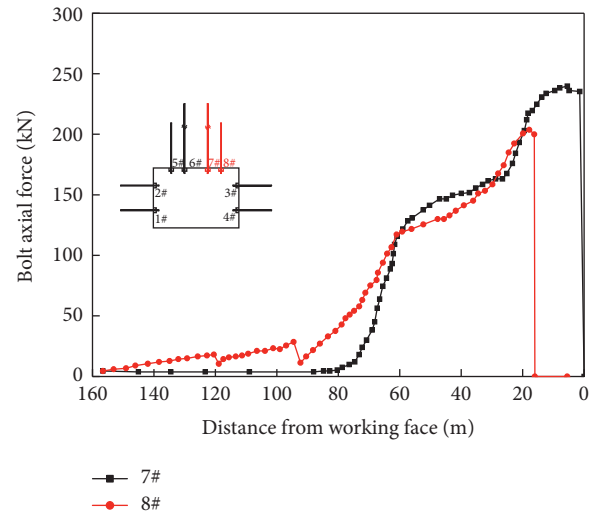


FIGURE 22: Nonhydraulic fracturing section: stress of the anchor cable at 5# station.

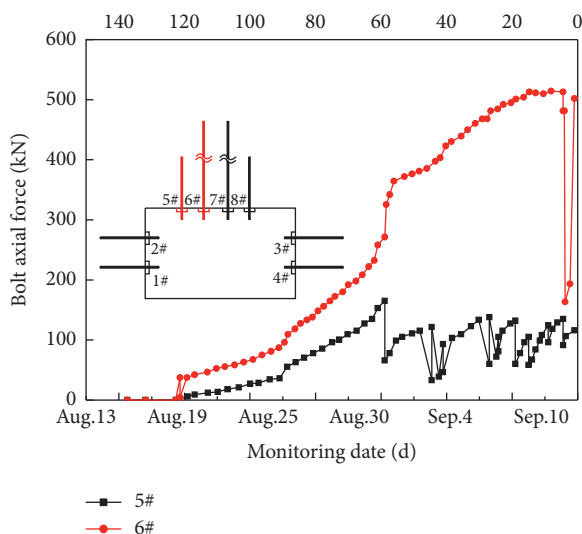


FIGURE 21: Hydraulic fracturing section: stress of the anchor cable at coal pillar side of 2# station.

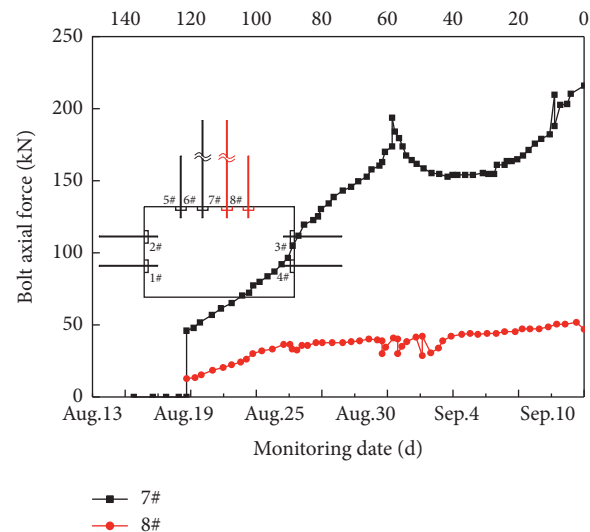


FIGURE 23: Hydraulic fracturing section: stress of the anchor cable at 2# station.

from the working face is 60 m, the stress of 6# and 5# fluctuates, indicating that the roof failure fluctuates. When the distance is 1 m away from the working face, the stress reaches the maximum value of 502 kN and 116 kN, with an average reduction of 44.8% and 16.4%.

(2) *Stress Analysis of the Side Anchor Cable in Mining Face.* Figures 22 and 23 show the stress curves of the anchor cable at the mining face of 5# and 2# measuring stations, respectively. As shown in Figure 22, for the nonhydraulic fracturing section, when the distance is 100 m away from the working face, the stress of the anchor cable begins to increase, which synchronizes with the increase of roof subsidence and separation amount. With the advance of the working face, the stress of the anchor cable continues to increase until the distance is 0 m away from the working

face and then the stress remains relatively stable. The stress of the outer 8 # anchor cable is 205 kN and the inner 7 # anchor cable is 242 kN. As shown in Figure 23, for the hydraulic fracturing section, with the advance of the working face, the stress of the anchor cable increases and remains stable until the distance is 10 m away from the working face. The stress of the 7 # anchor cable is 216 kN and that of the 8 # anchor cable is 47 kN. Compared with the nonhydraulic fracturing section, the stress of anchor cable is reduced by 48% and 51.3% on average in the hydraulic fracturing section.

5. Conclusion

- (1) On the premise of not destroying the stability of roadway in working face, the fracture position of the roof can be artificially controlled, and the high-stress

from the lateral cantilever beam of the working face to the coal pillar of the retained roadway can be unloaded or transferred to improve the stress state of the retained roadway.

- (2) Hydraulic fracturing pressure relief technology changes the deformation and failure mode of roof and restricts the development of the plastic zone of surrounding rock in the roadway. As a result, the deformation and failure of roof and coal sides are greatly alleviated, and the stress of anchor bolt and anchor cable is reduced to varying degrees.

References

- [1] J. B. Bai and C. J. Hou, "Control principle of surrounding rocks in deep roadway and its application," *Journal of China University of Mining & Technology*, vol. 35, no. 2, pp. 145–148, 2006.
- [2] L. Yuan, J. H. Xue, Q. S. Liu, and B. Liu, "Surrounding rock stability control theory and support technique in deep rock roadway for coal mine," *Journal of the China Coal Society*, vol. 36, no. 4, pp. 535–543, 2011.
- [3] T. Xiao, X. Wang, and Z. Zhang, "Stability control of surrounding rocks for a coal roadway in a deep tectonic region," *International Journal of Mining Science and Technology*, vol. 24, no. 2, pp. 171–176, 2014.
- [4] J. Chang and G. Xie, "Research on space-time coupling action laws of anchor-cable strengthening supporting for rock roadway in deep coal mine," *Journal of Coal Science and Engineering*, vol. 18, no. 2, pp. 113–117, 2012.
- [5] D. S. Kong and Y. P. Chen, "Stability prediction of surrounding rocks and optimum design of roof-bolt parameters in deep roadway," *Applied Mechanics and Materials*, vol. 353–356, pp. 436–439, 2013.
- [6] X. Y. Zhang, "Pressure releasing technology with borehole drilling and blasting for mine roadway in high stressed strata," *Coal Science and Technology*, vol. 37, pp. 74–77, 2009.
- [7] X. Yang, C. Hu, M. He et al., "Study on presplitting blasting the roof strata of adjacent roadway to control roadway deformation," *Shock and Vibration*, vol. 2019, Article ID 3174898, 16 pages, 2019.
- [8] S. Yang, M. He, W. Liu, and X. Ma, "Mechanics and application research on the floor anchor to control the floor heave of deep soft rock roadway," *Chinese Journal of Rock Mechanics and Engineering*, vol. 27, pp. 2913–2920, 2008.
- [9] M. C. He, G. Qi, C. Cheng, Z. Guofeng, and S. Xiaoming, "Deformation and damage mechanisms and coupling support design in deep coal roadway with compound roof," *Journal of Rock Mechanics and Engineering*, vol. 26, no. 5, pp. 987–993, 2007, in Chinese.
- [10] X. M. Sun, M. C. He, and X. J. Yang, "Study on nonlinear design method of coupling support of anchor, mesh and cable in deep soft rock roadway," *Rock and Soil Mechanics*, vol. 27, no. 7, pp. 1061–1065, 2006, in Chinese.
- [11] J. Zuo, J. Wang, and Y. Jiang, "Macro/meso failure behavior of surrounding rock in deep roadway and its control technology," *International Journal of Coal Science & Technology*, vol. 6, no. 3, pp. 301–319, 2019.
- [12] Z. Xiao, J. Liu, S. Gu et al., "A control method of rock burst for dynamic roadway floor in deep mining mine," *Shock and Vibration*, vol. 2019, Article ID 7938491, 16 pages, 2019.
- [13] Y. D. Wei, L. H. Chen, X. U. Chang-Yu, and J. H. Liu, "Mechanism and application of coupling grouting reinforcement for crossing of deep soft rock roadway," *Value Engineering*, vol. 38, no. 4, pp. 133–136, 2019, in Chinese.
- [14] X. Guo and D. Hao, "Deformation characteristics of surrounding rock of deep soft rock roadway and mechanism of full anchor cable supporting," *China Mining Magazine*, vol. 28, no. 12, pp. 123–127, 2019, in Chinese.
- [15] W. Liu, X. Zhang, and C. Huang, "Surrounding rock supporting technology in deep roadway of xingdong coal mine," *Safety In Coal Mines*, vol. 50, no. 6, pp. 86–90, 2019.
- [16] T. Z. Zhang and C. Company, "Research and application of floor heave collaborative control technology in deep mine high stress coal-winning roadway," *Coal Science & Technology Magazine*, vol. 40, no. 3, pp. 54–57, 2019, in Chinese.
- [17] J. Han, "Analysis on pressure relief process of coal mine hydraulic fracturing," *Energy and Energy Conservation*, no. 12, pp. 102–103, 2019, in Chinese.
- [18] C. Zhai, M. Li, C. Sun, J. Zhang, W. Yang, and Q. Li, "Guiding-controlling technology of coal seam hydraulic fracturing fractures extension," *International Journal of Mining Science & Technology*, vol. 22, no. 6, pp. 831–836, 2012.
- [19] J. Zhao and G. Li, "Pressure-relief mining of the working face under the coal pillar in the close distance coal seams," *Geotechnical & Geological Engineering*, vol. 34, no. 4, pp. 1067–1077, 2016.
- [20] J. Guo, "Application of hydraulic fracturing and cutting top pressure relief technology in the roadway along the goaf," *Coal and Chemical Industry*, vol. 3, pp. 47–49, 2019.
- [21] Y. Li, "Study on hydraulic fracturing roof cutting and pressure relief technology of removal channel in fully mechanized caving face," *Datong Coal Science & Technology*, no. 4, pp. 21–23, 2019, in Chinese.

Evaluation of heating performance of the PVC earth-air tubular heat exchanger applied to a greenhouse in the coastal area of west Syria: An experimental study

Niranjan Behera, *Department of Mechanical Engineering, Raajdhani Engineering College, Bhubaneswar, niranjanbehera2514@gmail.com*

Abinash Sahoo, *Department of Mechanical Engineering, Capital Engineering College, Bhubaneswar, abinashsahoo719@yahoo.co.in*

Shakyasingha Sahoo, *Department of Mechanical Engineering, NM Institute of Engineering & Technology, Bhubaneswar, shakyasinghasahoo@gmail.com*

Himanshu Sekhar Moharana, *Department of Mechanical Engineering, Aryan Institute of Engineering & Technology, Bhubaneswar, hsmoharana26@gmail.com*

Abstract

The Earth-to-Air Heat Exchanger (EAHE) system is a geothermal environmental approach that uses the ground's undisturbed temperature to condition air, reducing energy consumption and costs for heating and cooling. The goal of this research is to employ a tubular heat exchanger to heat an agricultural greenhouse in Baniyas in a straightforward, cost-effective, and ecologically friendly manner. In addition, determine the length, diameter, and flow velocity characteristics that influence the heat exchanger's efficiency. The tests were conducted in a Mediterranean climate in the Tartous Governorate, which is located on the coast of western Syria. The 20-meter-long exchanger pipes were buried at a depth of one metre. For each exchanger studied, the diameters used were 10.16 and 15.24 cm, with two velocities of 1.5 and 2 m/s. Two heat exchangers were installed along the length of a plastic greenhouse. Beginning on December 1, 2020, tests were conducted for a month. The results revealed that the parameters had a substantial impact on the heating performance of both exchangers. The soil temperature averaged 18 to 19 °C during the heating period, while the input air temperature averaged 11 to 12 °C. The heating performance increased by 56 percent and 36.28 percent for 10.16 cm and 15.24 cm diameter tubes, respectively, when the tube length was increased to 20 m. As a result, the smaller diameter tube was preferable, and decreasing airflow velocity from 2 to 1.5 m/s led a temperature increase from 5.5 to 6.99 °C.

Keywords: Air-ground tube heat exchanger; Thermal performance; Heating efficiency; PVC.

Nomenclature

COP	Coefficient of performance	T_i	Inlet temperature ($^{\circ}\text{C}$)
C_p	Specific heat capacity ($\text{J/ kg.}^{\circ}\text{C}$)	T_o	Outlet temperature ($^{\circ}\text{C}$)
d	Diameter (m)	T_s	Soil temperature ($^{\circ}\text{C}$)
E	East	V	Volume flow rate (m^3/s)
EAHE	Earth-to-air heat exchanger	v	Air velocity (m/s)
EUT	Earth's undisturbed temperature	π	Pi constant
m	Mass flow rate (kg/s)	ΔT	Temperature difference ($^{\circ}\text{C}$)
N	North	ϵ	Efficiency (%)
PVC	Polyvinyl chloride	ρ	Density (kg/m^3)
Q	Heat amount (J)		

1. Introduction

Greenhouses consider one of the most energy-intensive sectors in the agricultural field [1], as temperatures drop in the winter season, which affects the productivity of crops. Therefore, farmers resort to expensive heating processes that consume a lot of energy, which depend mostly on fossil fuels with environmentally harmful combustion products, which increases the energy crisis [2]. Thus, the trend was towards searching for other alternative clean and renewable energy sources [3] to meet the increasing energy requirements in the agricultural sector [4].

The earth's temperature at a depth often greater than 1 m below the soil surface is almost constant throughout the year and is called Earth's Undisturbed Temperature (EUT) [5]. It remains higher than the ambient temperature in winter and lower than in summer, but this stable depth varies from one region to another [6, 7]. This feature can be beneficial in greenhouse heating in a simple, economical, and clean way by means of tubular heat exchangers [8]. Tubular heat exchangers (air-ground) systems consist of an air blower device that draws and pushes air through a network of pipelines of various shapes made of durable materials that bear the pressure of the soil above them (steel, plastic, cement, etc.), where the cold air entering the exchanger is heated by heat exchange between the air and the soil through the pipe walls [9].

The tubular (air-ground) exchanger is classified according to two main classifications: First, according to the airflow circuit, there is the open-circuit [10], and there is the closed-circuit [11]. Second, depending on the position of the tubes, there is the horizontal position [12] which is the most common, and there is the vertical position, which requires a large depth in the soil often greater than 15 m and thus large digging costs, as the most expensive in installing the exchanger is the drilling process and the pipe costs, which amount to about 70% of the total cost of the exchanger [13]. In addition, the vertical exchangers are not suitable for all areas, such as places with rock layers, due to the difficulty of drilling [14]. It should be mentioned that the exchanger tubes could be installed next to or under the greenhouse [15].

Many experimental and numerical analyzes of the exchanger performance and the parameters affecting its performance in many countries of the world had been conducted, each of them under

the conditions of the studied region of climate, geographic location, and different soil nature, thus each had a different amount of impact on performance. Yang et al. [16] found that the exchanger system is an efficient, low-cost method that reduces fuel consumption and the associated environmental damage, in addition to increasing productivity, and saving costs compared to traditional fossil fuel air conditioning systems, as they found that it provides about 561.6 kW/h in summer, which saves energy by 74.3%, and 177.6 kW/h in winter by saving 67.3%.

Le et al. [17] confirmed that geothermal energy at a depth of 1 to 4 m below the surface of the soil could be employed in greenhouse conditioning in China (Shouguang), as they noticed a large thermal difference between the air and the subsoil of 5 to 15 °C in summer, and of 10 to 25 °C in winter. In the study of Onder Ozgener and Leyla Ozgener [18], the exchanger system was highly efficient in winter when used to heat greenhouses in Turkey (Izmir), as it raised the temperature to 24.76 °C at a rate of 18.67 °C.

Ghosal and Tiwari [19] conducted a study in India (Delhi), on the effect of tube length and diameter on the performance of the air-ground heat exchanger for greenhouse air conditioning. They found that the temperature decreases in summer by increasing the length of the pipe and reducing the diameter, where the pipe used was made of PVC plastic with a length of 39 m and a diameter of 0.06 m. This exchanger increased the temperature at a rate of 7 to 8 °C in winter and decreased it at a rate of 5 to 6 °C in the summer compared to a greenhouse without the air-ground heat exchanger. Abbaspour-Fard et al. [20] studied, in the northeast of Iran, the effect of tube length on the performance of an air-ground tubular exchanger system made of galvanized mild steel with a diameter of 0.1 m and a length of 18 m. They found that the highest temperature difference for the system was at total tube length and the measured minimum velocity is 4 m/s and resulted in a temperature difference of 9.4 °C for heating and 14.4 °C for cooling.

The tube diameter plays an important role in the performance of the exchanger, and Sobti and Singh [21] confirm this in their study of the exchanger performance in India (Chandigarh). They found that as the diameter of the tube increases, the pressure decreases, and thus the performance efficiency decreases while the thermal performance and performance efficiency increase for a longer pipe with a smaller diameter buried at a greater depth and lower airflow velocity.

Rosa et al. [22] also concluded in their study conducted in Portugal (Coimbra) that increasing the velocity of airflow in the exchanger tubes leads to a decrease in the heat exchange to and from the ground for both heating and cooling modes, but at different rates. Deldan et al. [23] observed in their study on a heat exchanger with a length of 42 m in length and a diameter of 0.25 m buried at a depth of 3.5 m, by testing the system in both open and closed positions for a range of velocities between 2.3 to 24 m/s, that the difference between inlet and outlet increased with reduced speed in both systems. Namgial et al. [24] in their study in India (Ludhiana) found the performance of an (air - earth) exchanger consisting of a single line of PVC of length 42 m and diameter 0.25 m buried at a depth of 3.5 m, where the minimum and maximum mean tube efficiency was 18.4% and 64.9% for airflow velocities 24 and 2.3 m/s, respectively. The performance efficiency of the exchanger system decreases with the increase in airflow velocity through the tubes.

It has been observed from the literature that there are many factors that affect the performance of the exchanger, but the amount of their impact on the performance varies according to the circumstances of each region and the fluid type used through exchanger tubes [25]. Therefore, in

this research, a study has been made to study the effect of some factors related to the specifications of the PVC pipes of the exchanger under the conditions of the studied area on the Syrian coast, which are the length, diameter, and airflow velocity within it.

According to our knowledge, this is the first study to be conducted in the Baniyas area on the Syrian coast. Therefore, this study aims to use a tubular heat exchanger (air-ground) to heat an agricultural greenhouse in the Baniyas area in a simple, more economical, and environmentally friendly way that limits the use of fossil fuels. In addition, to assess the main parameters (length, diameter, and flow velocity) that affect the efficiency of the heat exchanger.

2. Experimentation and methodology

2.1. The site of the experiment

The experimental study was carried out in the Harisoun agricultural area located between the Baniyas Refinery and the Al-Sain Lake ($35^{\circ} 58' 14''$ E, $35^{\circ} 14' 07''$ N) with a Mediterranean coastal climate as it rises about 5 m from the sea level as shown in Fig. 1 on a plastic house consisting of iron bars covered with plastic sheets. Its dimensions are 2, 5, and 19 m as shown in Fig. 2. The heating mode was tested during the period from 1 December 2020 to 31 December 2020 when the soil temperature was higher than the outside air temperature.

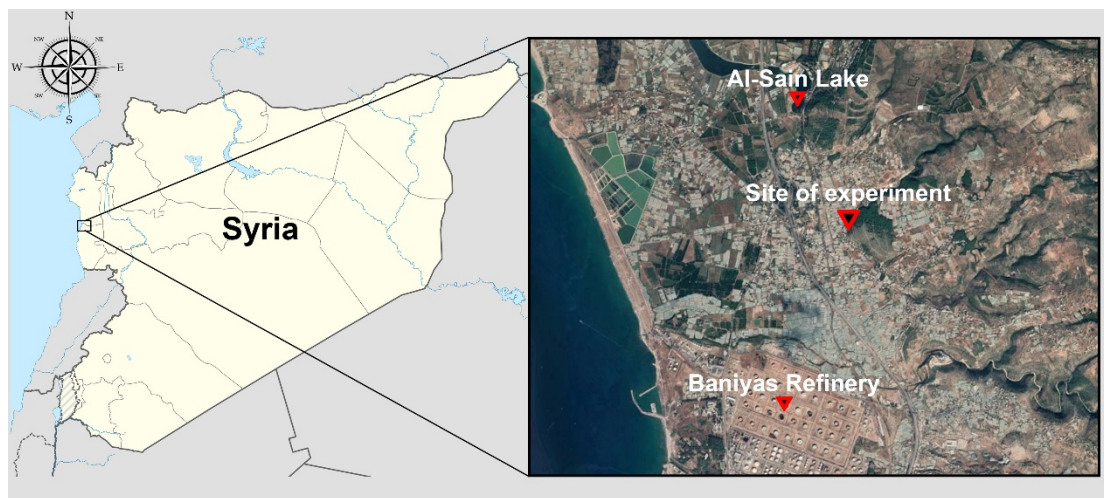


Fig. 1. Site of the experiment.

2.2. Apparatus description

A tubular (air-ground) heat exchanger was installed for the conditioning of a greenhouse and then its performance effectiveness was tested, and for that, the following devices and tools were used: Two air intake devices of capacity 85 and 125 W, PVC pipes, and elbows with a length of 20 m per line, having a diameter of 10.16 and 15.24 cm, two Arduino devices (MEGA, UNO), air temperature sensors (DHT22) with measurement precision of $\pm 0.5^{\circ}\text{C}$, and soil temperature

sensor (DS18B20) has a temperature range from $-55\text{ }^{\circ}\text{C}$ to $+125\text{ }^{\circ}\text{C}$ with a resolution from 9 to 12 bit. The air velocity was measured by an Anemometer device that has wind speed accuracy of ± 5 percentage and wind speed resolution of 0.1 m/s .

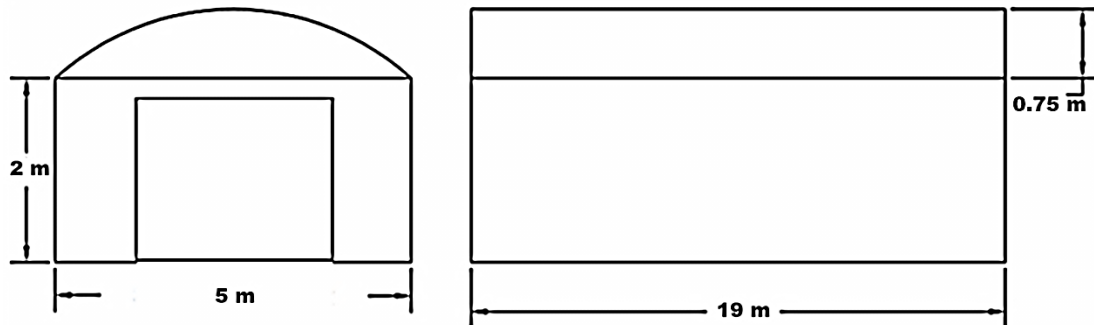


Fig. 2. Greenhouse dimensions (length, width, and height).

2.3. Parameters

The positions 10 m and 20 m of the tube length were chosen to know the amount of thermal difference resulting from each of them under the conditions of the studied area. The two diameters 10.16 and 15.24 cm were chosen to test the effectiveness of the exchanger performance in each of them. The appropriate depth varies from one region to another and is related to the geography of the place, thus the depth of 1 m was chosen due to the lack of height of the study area above sea level. Fig. 3 illustrates a diagram of the exchanger line where the tubes were placed on both sides of the greenhouse 1 m deep below the soil surface. As for the air velocity through the tubes, the two speeds of 1.5 and 2 m/s were chosen for the experimentation. Polyvinyl chloride (PVC) pipes were chosen in the research with a thickness of 3 mm on the one hand, in addition to their availability and cheapness on the other hand.

2.4. Methodology

First, a trench of 1 m deep was dug on both sides of the greenhouse and two pipelines were placed in it. Then, an air intake device of 85 and 125 W was installed at the inlet to each line, respectively. Fig. 4 shows the stages of the test implementation. For each line, a group of sensors connected to the Arduino device was placed in order to measure the temperatures every hour, and store them on a memory card (SD Card), where the sensors were installed at the inlet, middle, and outlet of the tube, in addition to a sensor that measures the temperature of the soil in general, and another one sensitive to the temperature of the outside air. Fig. 5 shows the block diagram of how to connect the sensors to the two Arduino devices.

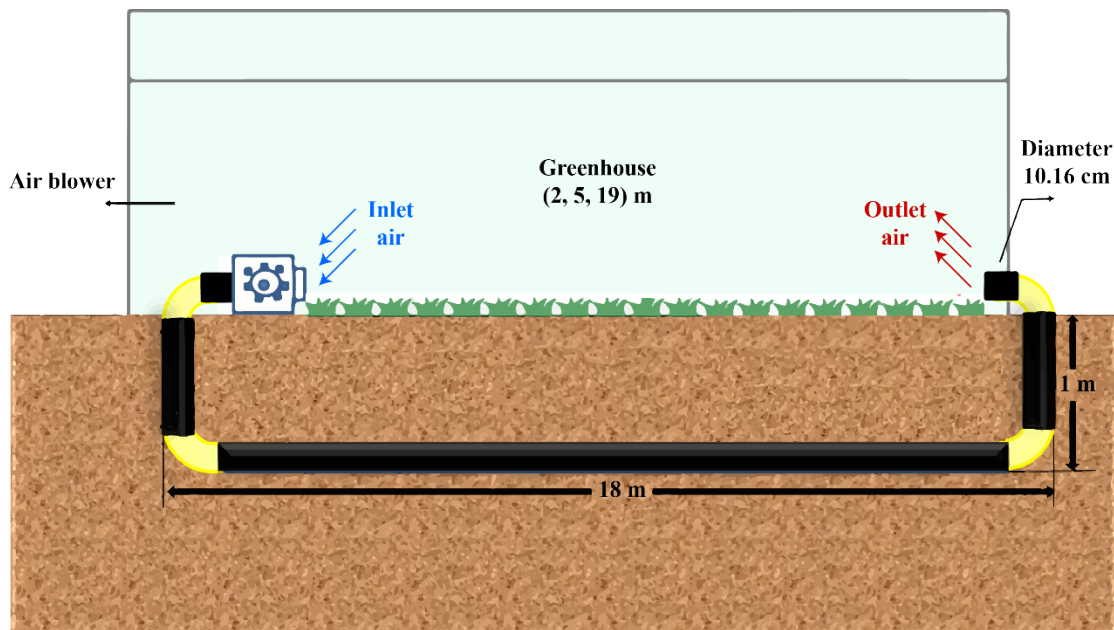


Fig. 3. Typical diagram of the 10.16 cm diameter exchanger.

After verifying the correct functioning of the devices and sensors, the soil over the two pipelines was backfilled, and then the exchanger was started on 1 December 2020. Hourly temperature data were collected at the three positions (inlet, middle, and outlet of the tube) for both lines throughout the month using 1.5 and 2 m/s speeds, and then classified to study the effect of length, diameter, and airflow velocity parameters on the exchanger performance.



Fig. 4. Stages of conducting the experiment: (A) Excavate the first side, (B) Excavate the second side, (C) Pipes installation, (D) Connecting the wires to the sensors to the tubes, (E) and to the Arduino devices, (F) Connecting with a laptop, and (G) Installation of air intake devices.

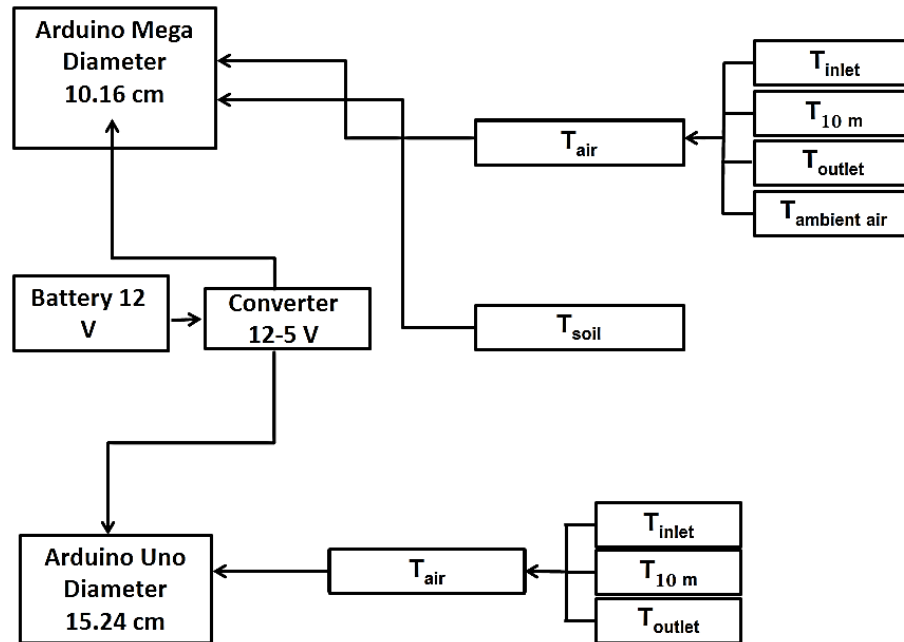


Fig. 5. Diagram of the connection of sensors with measuring devices.

The work of the tubular heat exchanger (air-ground) depends mainly on the surrounding daily and seasonal heat exchanges of the surrounding environment and their transfer through the soil layers and their storage in them [6], as it uses the subsoil as a source to provide the heating in winter [7]. The pulled air is pushed by an air blower to flow through the tubes of the exchanger as a mediator heat carrier to the medium required to be conditioned by a process of heat exchange between it and the soil through the walls of the tubes [26], where the heat is transferred from the air flowing through the tube to its walls by convection and then transmitted through it by conduction to the surrounding soil as shown in Fig. 6. The performance of the exchanger depends largely on the thermal differences between the air entering the pipes and the soil, and the higher the temperature difference, the greater the performance efficiency [27].

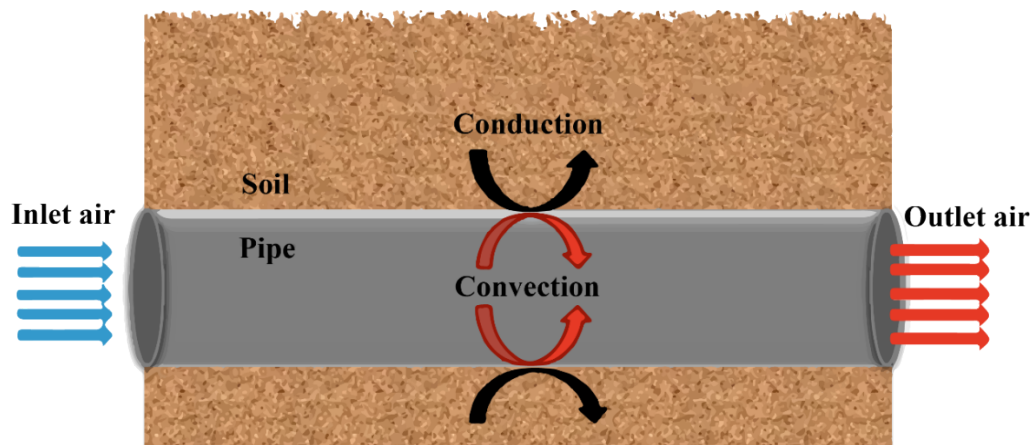


Fig. 6. Heat exchange between tube air and soil.

To evaluate the heating performance of the exchanger system, the performance efficiency (ϵ) as a percentage was calculated that expressing the difference between inlet air temperature (T_i) and outlet air temperature (T_o) divided by the difference between inlet air temperature and soil temperature (T_s) as shown in Eq. 1 [28]:

$$\epsilon = (T_i - T_o) / (T_i - T_s) \quad (1)$$

2.5. Statistical analysis

One-way analysis of variance (ANOVA) was performed to compare the means of the independent groups in order to determine whether there are any statistically significant differences between the means [29]. Then, it followed by a T-test, and a threshold ($p < 0.05$) was used to indicate the significance of the results using IBM SPSS® Statistics V27.

3. Results and discussion

During the month of December of 2020, the average outdoor temperature of 13 °C, and the average temperature recorded at the inlet of the two lines of the exchanger was 11.5 ± 5 °C. The lowest and highest value recorded at 2 and 24 °C respectively, and the soil temperature was stable between 18 and 19 °C as shown in Fig. 7.

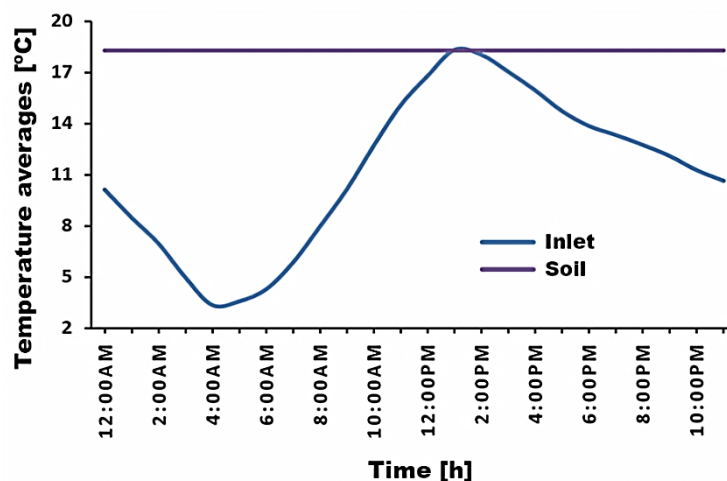


Fig. 7. Hourly temperature averages for the month of December / 2020 at the inlet of the exchanger lines, and the average soil temperature.

Hourly average temperatures during the month of December 2020 recorded at the inlet, middle, and outlet of the tube were calculated for each of the two lines 10.16 and 15.24 cm, as shown in Fig. 8 and Fig. 9. The temperature difference made by the two lines during the periods (after

midnight between 12:00 and 5:00 in the morning, during the day between 6:00 in the morning and 6:00 in the evening, at night between 7:00 and 11:00 in the evening) was the same as shown in Table 1. After midnight between 12:00 and 5:00 in the morning, it was the most intense hour of the day that the heating effect of the exchanger appeared. The line with a diameter of 10.16 cm raised the temperature by 3 and 7.21 °C at the middle and the end of its length, while the line with a diameter of 15.24 cm raised it by 1.93 and 4.74 °C, respectively.

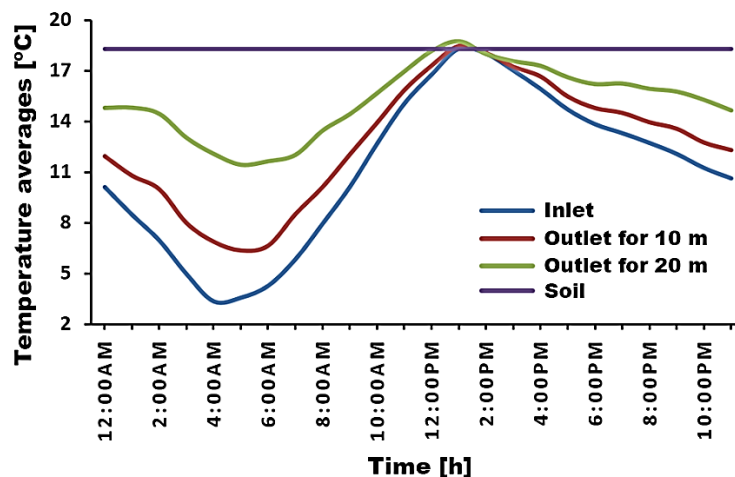


Fig. 8. Hourly average temperatures at the middle and outlet of the line with a diameter of 10.16 cm.

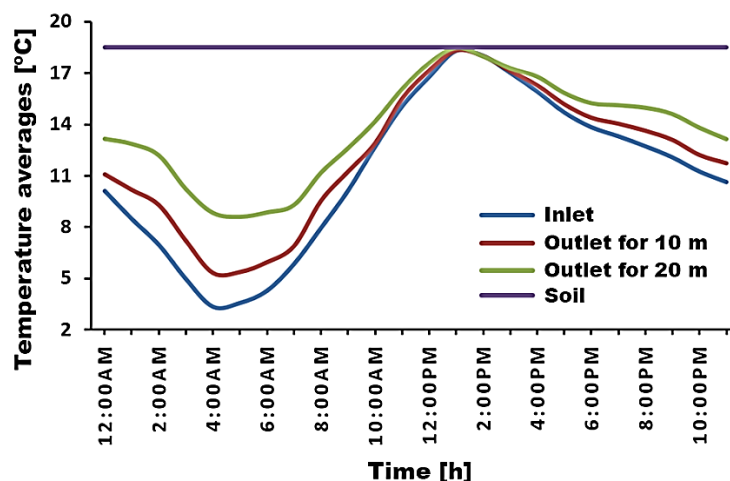


Fig. 9. Hourly average temperatures at the middle and outlet of the line with a diameter of 15.24 cm.

During the day between 6:00 am and 6:00 pm, the difference between the inlet air and soil temperatures decreased, leading to a slight increase in the air exiting from the exchanger lines of 1.13 and 2.77 °C at the middle and the end of the line (diameter of 10.16 cm), respectively, and an increase of 0.6 and 1.57 °C for the middle and the end of the line (diameter of 15.24 cm) respectively.

Between 7:00 pm and 11:00 pm, the line with a diameter of 10.16 cm raised the temperature by 1.41 and 3.47 °C at the middle and the end of its length respectively, while a line with a diameter of 15.24 cm raised it by 0.92 and 2.31 °C. Consequently, the full length of the 20 m tube led to a decrease in the temperature of the air exiting from both lines compared to the half-length of 10 m. The line with a diameter of 10.16 cm at the full length was the best as it increased the temperature by 7.21°C after midnight.

Table 1. Average hourly temperatures divided into three periods during the day.

Time periods [h]	Tube's diameter [cm]	Average inlet temperature [°C]	Average outlet temperature according to the length [°C]	
			10 m	20 m
12:00 am - 5:00 am	10.16	6.24±2.92	9.25±2.5	13.4±1.73
	15.24		8.17±2.76	10.98±2.25
6:00 am - 6:00 pm	10.16	13.13±5.19	14.26±4.22	15.9±2.6
	15.24		13.74±4.6	14.7±3.66
7:00 am - 11:00 pm	10.16	12.03±0.7	13.44±1.4	15.5±0.95
	15.24		12.95±1.5	14.34±1.22

The seventeenth of December 2020 is considered the imaginary day which represents any day during the month and is determined mathematically by calculating the average hourly external temperatures throughout the month to subtract from them the hourly temperatures for each day at the same time, and then these hourly differences are squared and added to each other for each day, thus the day with the least difference is the typical day [30]. On this day, the inlet temperatures ranged between two minimum and maximum values 2.5 and 18 °C with an average of 10.84 ± 4.66 °C. Fig.10 and Fig.11 show the average hourly temperatures during the typical day of the inlet, the middle and the end of the two lines 10.16 and 15.24 cm at the two positions 10 and 20 m of them. The day was divided into three periods according to the heat effect of the exchanger as shown in Table 2.

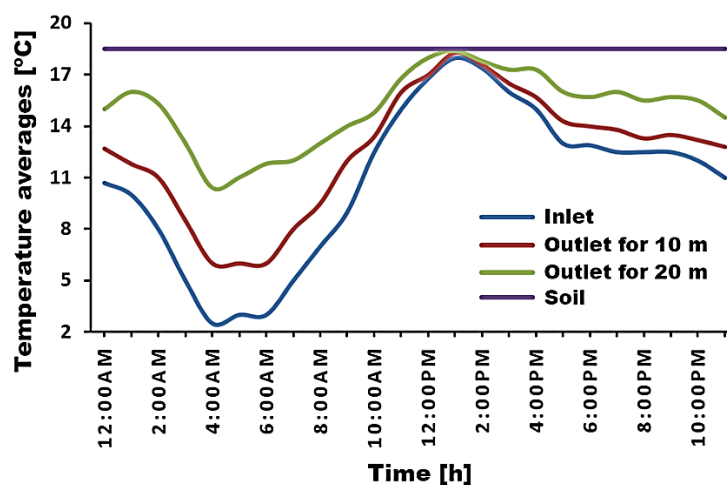


Fig. 10. The hourly temperature recorded on 17 December for the inlet, middle, and outlet of the line is 10.16 cm.

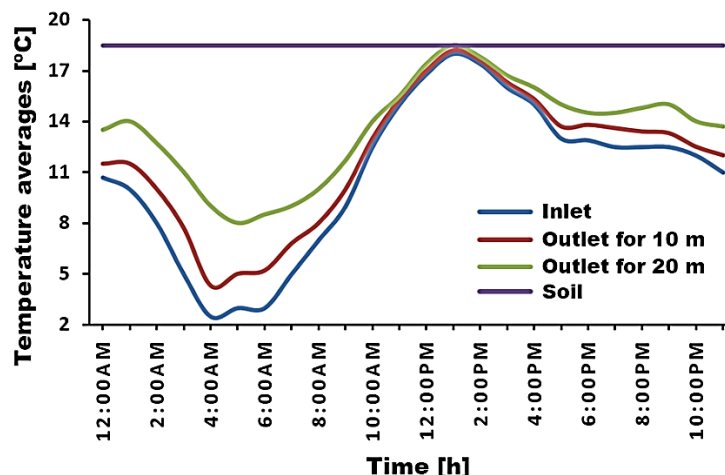


Fig. 11. The hourly temperature recorded on 17 December for the inlet, middle, and outlet of the line is 15.24 cm.

Table 2. Hourly temperature averages for the typical day divided into three periods during the day.

Time periods [h]	Tube's diameter [cm]	Average inlet temperature [°C]	Average outlet temperature according to the length [°C]	
			10 m	20 m
12:00 am - 5:00 am	10.16	6.53±3.5	9.33±2.9	13.45±2.35
	15.24		8.3±3.18	11.4±2.46
6:00 am - 6:00 pm	10.16	12.35±4.88	13.7±3.8	15.6±2.3
	15.24		13±4.3	14.2±3.38
7:00 am - 11:00 pm	10.16	12±0.65	13.32±0.37	15.44±0.56
	15.24		12.96±0.68	14.4±0.54

From Table 2, we find that between 12:00 am and 5:00 am, the greatest heating effect was shown by 2.8 and 6.92 °C for the 10.16 cm diameter line and 1.77 and 4.87 °C for the 15.24 cm diameter line, at the two lengths 10 and 20 m, respectively. Between 6:00 am and 6:00 pm, the heating effect of the exchanger system appeared, but in smaller degrees 1.35 and 3.25 °C for the line of diameter 10.16 cm, in addition to the values 0.97 and 1.85 °C for the line of diameter 15.24 cm, at lengths 10 and 20 m respectively.

In the evening, between 7:00 and 11:00, the heating effect of the temperature drop increased by 1.32 and 3.44 °C for the line of 10.16 cm diameter, and 0.96 and 2.4 °C for the 15.24 cm line, at lengths 10 and 20 m respectively. The most hours of the day during which the heating effect appeared to be between 12:00 am and 9:00 am, when the temperature at the inlet ranged between 2.5 and 10.7 °C.

Based on the results of One Way ANOVA with the Least Significant Difference (LSD) test that shown in Table 3, the level of statistical significance was $0.000 < 0.05$, and the significant difference between the mean inlet and outlet air temperature at the two positions 10 and 20 m for the 10.16 cm diameter exchanger line was 2.83 and 6.8 °C, respectively. As for the 15.24 cm line, it was 1.68 and 4.42 °C as shown in Fig. 12.

For the tube of 10.16 cm diameter, the performance efficiency was 23.23% at 10 m position, while it was 56% at 20 m position with the least significant difference of 2.35. However, for the tube of 15.24 cm diameter, the performance efficiency was 13.79% at 10 m position, while it was 36.28% at 20 m position with the least significant difference of 2.43.

The results could be supported and attributed to the fact that the rate at which heat is exchanged between air and soil, which is the heating capacity of EAHE, is expressed by the equation of heat exchange as shown in Eq. 2.

$$Q_{out} = m \cdot C_p \cdot \Delta T \quad (2)$$

The mass flow rate of the air, the volume flow rate of the air, and the thermal difference between outlet and inlet air temperature of the system and the coefficient of heating performance (COP) shown in Eq. 3, Eq. 4, and Eq. 5, Eq. 6, respectively.

$$m = \rho \cdot V \quad (3)$$

$$V = (\pi/4) \cdot d^2 \cdot v \quad (4)$$

$$\Delta T = T_o - T_i \quad (5)$$

$$COP = Q_{out} / Q_{in} \quad (6)$$

The highest temperature differences obtained at the velocity of 1.5 m/s for 10.16 cm pipe diameter at 10 m and 20 m lengths were 5 °C and 12.5 °C, respectively. Thus at the inlet temperature of 2 °C, the air density was $\rho=1.28 \text{ kg/m}^3$ and specific heat $C_p=1003.2 \text{ J/kg} \cdot ^\circ\text{C}$. From Eq. 4, the volume flow rate of the air is $0.012 \text{ m}^3/\text{s}$, and the mass flow rate of the air is 0.0153 kg/s according to Eq. 3. Therefore, the rates of gaining or losing heat by convection were 77.045 W and 192.614 W , according to Eq. 2, respectively. The coefficient of heating performance (COP) was 0.9 and 2.266 according to Eq. 6 for 10 m and 20 m lengths, respectively.

At the same conditions for 15.24 cm pipe diameter and at 10 m and 20 m lengths, the highest temperature differences obtained between the inlet and outlet were 3 °C and 7.5 °C, respectively. The volume flow rate of the air is $0.0273 \text{ m}^3/\text{s}$ according to Eq. 4, and the mass flow rate of the air is 0.0349 kg/s according to Eq. 3. Therefore, the rates of gaining or losing heat by convection were 105.155 W and 262.888 W according to Eq. 2, respectively. The coefficient of heating performance (COP) was 0.841 and 2.1, for 10 m and 20 m lengths according to Eq. 6, respectively.

It is observed that the pipe with a smaller diameter and a longer length gives a larger thermal difference between the inlet and outlet of the pipe, but the increase in the pipe diameter increases the airflow rate, which gives more energy output by the system. However, compared to the input power consumed, the coefficient of heating performance (COP) of the smaller diameter is better.

These results agree with the findings of Sharan and Jadhav study [31] on a single tubular heat exchanger with a length of 50 m and a diameter of 10 cm buried at a depth of 3 m in India (Ahmedabad), the velocity of air inside the tube was 11 m/s, and the soil temperature at the depth studied in January was 24.2°C , where the highest heating values obtained at the middle and end of the tube were 13.2°C and 14.7°C , and the lowest values 2.5°C and 3.6°C , respectively.

Table 3. The results of One Way ANOVA with the Least Significant Difference (LSD).

Tube's diameter [cm]	Tube's length [m]	Average temperature [°C]	Standard deviation	Significance level	Mean difference [°C]	Least Significant Difference	ϵ efficiency [%]
10.16	Inlet	6.32	3.04	0.000	inlet-10 m 2.83	2.35	-
	10 m	9.15	2.64		inlet-20 m 6.83		23.23
	20 m	13.15	1.89		m-2010 m 4		56
15.24	inlet	6.32	3.04	0.003	inlet-10 m 1.68	2.43	-
	10 m	8	2.67		inlet-20 m 4.42		13.79
	20 m	10.74	2.16		m-2010 m 2.74		36.28

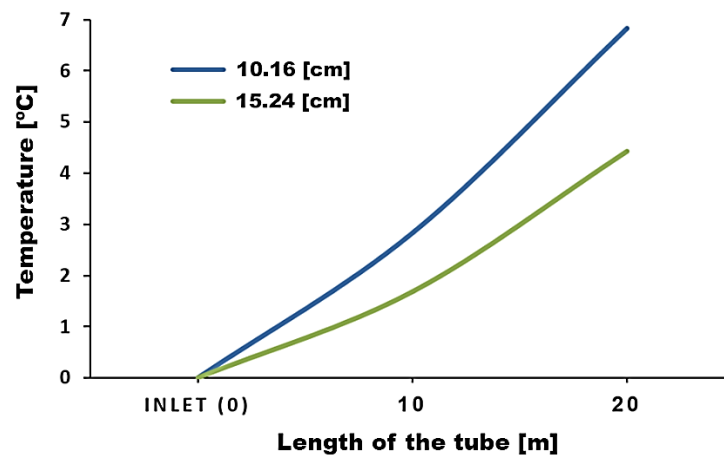


Fig. 12. The amount of temperature raised by the height difference.

The results indicate a significant effect of the tube's length and its diameter on the temperatures, as increasing the length and reducing the diameter led to an increase in the outlet air temperature. The effect of airflow velocity on the heating performance of the exchanger during the periods of 1st to 7th of December for a velocity of 2 m/s, and from 25th to 31st of December 2020 for a velocity of 1.5 m/s were studied for the line of the exchanger with a diameter of 10.16 cm. The hourly average temperatures were taken from 12:00 to 9:00 am, in which the best performance of the exchanger was during the aforementioned period, and a T-test was then performed on them.

Table 4. The results of the T-test.

Soil temperature [°C]	Velocity [m/s]	T _{outlet} [°C]	Standard deviation	T	Sig.(2-taild) Significance level	$\Delta T_{outlets}$ [°C]	ΔT_{in-out} [°C]
18-19	1.5	12.15	1.64	3.69	0.002	2.12	6.99
	2	14.27	0.77				5.5

By comparison between the results of the two velocities 1.5 and 2 m/s, it was found that the value of $T = 3.69$ with a significance value of 0.002 is smaller than the significance level of 5% as shown in Table 4. Therefore, there are significant differences between the mean temperatures of the line of diameter 10.16 cm at the two different speeds, and the difference value is 2.12 °C in favor of the lower velocity is 1.5 m/s as the two velocities 1.5 and 2 m/s raised the air temperature by 6.99 and 5.5 °C respectively. This is in agreement with the simulation and experimental results of Bansal et al. study [32] of an exchanger consists of two different materials pipes (PVC and mild steel) with 23.42 m length and 0.15 m diameter buried at 2.7 m depth in India (Ajmer), and the airflow velocities were 2, 3.2, 4, and 5 m/s. The maximum increases in temperatures for both two pipes were 4.5 °C and 4.8 °C at an air velocity of 2 m/s.

The result of our study also is in agreement with Deldan et al. study [23] on heating a greenhouse using a single-tube heat exchanger of PVC with a length of 42 m and a diameter of 0.25 m at a depth of 3.5 m in India (Ludhiana). The study was carried out from October 2014 to February 2015 at speeds from 2.3 to 24 m/s. The best performance was at the lowest speed, meaning that with increasing speed, performance decreased.

It was found that increasing the length of the tubes caused an increase in the contact surface area between the air and the soil (the heat exchange surface), which allowed for greater heat exchange, while increasing the diameter decreased the air pressure inside the tubes, which negatively affected the heat exchange process and increased the intake fan requirements. Moreover, using slow velocities of airflow through the pipes gave better performance because decreasing the air velocity to a certain extent increases the time of air contact with the tube surface and thus improves the heat transfer to and from the soil surrounding the pipes of the exchanger.

As previously mentioned, the highest temperature difference obtained at the velocity of 1.5 m/s for the pipe diameter 10.16 cm was 12.5 °C, the volume flow rate of the air is 0.012 m³/s, and the mass flow rate of the air is 0.0153 kg/s according to Eq. 4 and Eq. 3, respectively. Therefore, the output energy is 192.614 W, according to Eq. 2, and the coefficient of heating performance (COP) was 2.266, according to Eq. 6.

At the air velocity of 2 m/s for the same pipe diameter (10.16 cm), the highest temperature differences obtained at the inlet and outlet temperatures were 3.7°C and 12.3°C, respectively. The air density was $\rho=1.26$ kg/m³ and the specific heat was $C_p=1003.2$ J/ kg.°C. From Eq. 4, the volume flow rate of the air is 0.016 m³/s, and the mass flow rate of the air is 0.02 kg/s according to Eq. 3. Therefore, the output energy is 172.55 W, according to Eq. 2, and the coefficient of heating performance (COP) was 2.03, according to Eq. 6.

Based on these results, it is observed that the lower velocity gives a higher outlet temperature for the constant pipe diameter; this may be because the air remains within the pipe for a longer time, which allows for greater heat exchange and gives more temperature rise of the outlet air. This rise in temperature increases the output energy of the system and the coefficient of heating performance (COP).

4. Conclusion

From the results of this study, it was found that the heating efficiency of the 10.16 cm line increased by 56% when its length was increased to 20 m. The heating efficiency of the 15.24 cm

diameter line increased by 36.28%. Decreased airflow velocity inside the tubes increased heating by 6.99°C. Accordingly, it is recommended to use tubular heat exchangers (air-ground) for conditioning agricultural greenhouses on the Syrian coast, but it is preferable to use thin plastic tubes with a length of not less than 15 m, with small diameters, and to use slow airflow velocities through the pipes, which gives better performance. Further investigations should focus on conducting more experimental studies on other parameters that affect the performance of the exchanger and in different regions to reach a reliable database. In addition, through modeling and simulation programs to predict the effectiveness of the thermal performance and behavior of the system.

Conflict of interest

All authors were fully involved in the study and preparation of the manuscript and declare that there is no conflict of interest.

Acknowledgment

The authors are grateful for University of Miskolc (Institute of Machine and Product Design) for its unlimited support.

References

- [1] A. Vadiée, V. Martin, Solar blind system-solar energy utilization and climate mitigation in glassed buildings, *Energy Procedia*. 57 (2014) 2023-2032.
- [2] S. Hamdane, C. Mahboub, A. Moumami, Numerical approach to predict the outlet temperature of earth-to-air-heat-exchanger, *Thermal Science and Engineering Progress*. 21 (2021) 100806.
- [3] A. Chel, G. Kaushik, Renewable energy for sustainable agriculture, *Agronomy for Sustainable Development*. 31 (2011) 91-118.
- [4] J. Xamán, I. Hernández-Pérez, J. Arce, G. Álvarez, L. Ramírez-Dávila, F. Noh-Pat, Numerical study of earth-to-air heat exchanger: The effect of thermal insulation, *Energy and buildings*. 85 (2014) 356-361.
- [5] H. Faridi, A. Arabhosseini, G. Zarei, M. Okos, Degree-Day Index for Estimating the Thermal Requirements of a Greenhouse Equipped with an Air-Earth Heat Exchanger System, *Journal of Agricultural Machinery*. 11 (2021), 83-95.
- [6] R.K. Singh, R.V. Sharma, Mathematical Investigation of Soil Temperature Variation for Geothermal Applications, *International Journal of Engineering*. 30 (2017) 1609-1614.

- [7] T.S. Bisoniya, A. Kumar, P. Baredar, Experimental and analytical studies of earth–air heat exchanger (EAHE) systems in India: a review, *Renewable and Sustainable Energy Reviews*. 19 (2013) 238-246.
- [8] H. Faridi, A. Arabhosseini, G. Zarei, M. Okos, Utilization of Soil Temperature Modeling to Check the Possibility of Earth-Air Heat Exchanger for Agricultural Building, *Iranian (Iranica) Journal of Energy & Environment*. 10 (2020) 260-268.
- [9] S.C. Kaushik, S. Lal, P.K. Bhargava, Earth–air tunnel heat exchanger for building space conditioning: a critical review, *Nanomaterials and energy*. 2 (2013) 216-227.
- [10] T.G. Manik, M.L. Panjaitan, T.B. Sitorus, Simulation of fluid flow in an earth-air heat exchanger with the open loop system. In *IOP Conference Series: Materials Science and Engineering*. 420 (2018) 012026.
- [11] N. Naili, M. Hazami, S. Kooli, A. Farhat, Energy and exergy analysis of horizontal ground heat exchanger for hot climatic condition of northern Tunisia, *Geothermics*. 53 (2015) 270-280.
- [12] K.K. Agrawal, R. Misra, G.D. Agrawal, M. Bhardwaj, D.K. Jamuwa, Effect of different design aspects of pipe for earth air tunnel heat exchanger system: A state of art, *International Journal of Green Energy*. 16 (2020) 598-614.
- [13] K.K. Agrawal, R. Misra, G.D. Agrawal, Improving the thermal performance of ground air heat exchanger system using sand-bentonite (in dry and wet condition) as backfilling material, *Renewable Energy*. 146 (2020) 2008-2023.
- [14] Y. Yuan, X. Cao, L. Sun, B. Lei, N. Yu, Ground source heat pump system: A review of simulation in China, *Renewable and Sustainable Energy Reviews*. 16 (2012) 6814-6822.
- [15] G.N. Tiwari, M.A. Akhtar, A. Shukla, M.E. Khan, Annual thermal performance of greenhouse with an earth–air heat exchanger: An experimental validation, *Renewable Energy*. 31 (2006) 2432-2446.
- [16] L.H. Yang, B.H. Huang, C.Y. Hsu, S.L. Chen, Performance analysis of an earth–air heat exchanger integrated into an agricultural irrigation system for a greenhouse environmental temperature-control system, *Energy and Buildings*. 202 (2020) 109381.
- [17] A.T. Le, L. Wang, Y. Wang, D. Li, Measurement investigation on the feasibility of shallow geothermal energy for heating and cooling applied in agricultural greenhouses of Shouguang City: Ground temperature profiles and geothermal potential, *Information Processing in Agriculture*. (2020) in press.
- [18] O. Ozgener, L. Ozgener, Determining the optimal design of a closed loop earth to air heat exchanger for greenhouse heating by using exergoeconomics, *Energy and Buildings*. 43 (2011) 960-965
- [19] M.K. Ghosal, G.N. Tiwari, Modeling and parametric studies for thermal performance of an earth to air heat exchanger integrated with a greenhouse, *Energy conversion and management*. 47 (2006) 1779-1798.

- [20] M.H. Abbaspour-Fard, A. Gholami, M. Khojastehpour, Evaluation of an earth-to-air heat exchanger for the north-east of Iran with semi-arid climate, *International Journal of Green Energy*. 8 (2011) 499-510.
- [21] J. Sobti, S.K. Singh, Earth-air heat exchanger as a green retrofit for Chandigarh-a critical review, *Geothermal Energy*. 3 (2015) 1-9.
- [22] N. Rosa, P. Santos, J.J. Costa, H. Gervásio, Modelling and performance analysis of an earth-to-air heat exchanger in a pilot installation, *Journal of Building Physics*. 42 (2018) 259-287.
- [23] N. Deldan, A. Rajan, V.S. Hans, A. Kaushal, Evaluation of thermal performance of single pass earth–air heat exchanger in heating mode, *Environmental Progress & Sustainable Energy*. 36 (2017) 1253-1261.
- [24] D. Namgial, K.G. Singh, V.S. Hans, R. Aggarwal, A. Singh, Performance of Thermo Hydraulic Designed Single Pass Earth Air Heat Exchanger, *International Journal of Agriculture, Environment and Biotechnology*. 12 (2020) 55-62.
- [25] M.E. Nakhchi, J.A. Esfahani, CFD approach for two-phase CuO nanofluid flow through heat exchangers enhanced by double perforated louvered strip insert, *Powder Technology*. 367 (2020) 877-888.
- [26] K.K. Agrawal, G.D. Agrawal, R. Misra, M. Bhardwaj, D.K. Jamuwa, A review on effect of geometrical, flow and soil properties on the performance of Earth air tunnel heat exchanger, *Energy and Buildings*. 176 (2018) 120-138.
- [27] M.K. Rodrigues, R. da Silva Bru, J. Vaz, L.A.O. Rocha, E.D. dos Santos, L.A. Isoldi, Numerical investigation about the improvement of the thermal potential of an Earth-Air Heat Exchanger (EAHE) employing the Constructal Design method, *Renewable Energy*. 80 (2015) 538-551.
- [28] F. Al-Ajmi, D.L. Loveday, V.I. Hanby, The cooling potential of earth–air heat exchangers for domestic buildings in a desert climate, *Building and Environment*. 41 (2006) 235-244.
- [29] M.E. Nakhchi, Experimental optimization of geometrical parameters on heat transfer and pressure drop inside sinusoidal wavy channels, *Thermal Science and Engineering Progress*. 9 (2019) 121-131.
- [30] W. Morshed, L. Leso, L. Conti, G. Rossi, S. Simonini, M. Barbari, Cooling performance of earth-to-air heat exchangers applied to a poultry barn in semi-desert areas of south Iraq, *International Journal of Agricultural and Biological Engineering*. 11 (2018) 47-53.
- [31] G. Sharan, R. Jadhav, Performance of Single Pass Earth-Tube Heat Exchanger: An Experimental Study, *Journal of Agricultural Engineering*. 40 (2003) 1-8.
- [32] V. Bansal, R. Misra, G.D. Agrawal, J. Mathur, Performance analysis of earth–pipe–air heat exchanger for winter heating, *Energy and Buildings*. 41 (2009), 1151-1154.

“Relief-Retaining” Control Technology of Floor Heave in Mining Roadway with Soft Rock

Bipash Mohanty, *Department of Civil Engineering, Capital Engineering College, Bhubaneswar, bipashmohanty784@gmail.com*

S. C. Mishra, *Department of Civil Engineering, NM Institute of Engineering & Technology, Bhubaneswar, scmishra11@yahoo.co.in*

Sourav Debasish, *Department of Civil Engineering, Aryan Institute of Engineering & Technology, Bhubaneswar, souravdebasish1@gmail.com*

Mdaras Aras Ansari, *Department of Civil Engineering, Raajdhani Engineering College, Bhubaneswar, mdarasansari2578@gmail.com*

ABSTRACT

The floor heave problem is one of the important factors affecting the stability and safety of surrounding rocks of roadways, especially in deep high-stress mining roadway with soft rock. The return airway of no. 130203 working face in Zaoquan Coal Mine of Ningdong Mining Area in Northwest China is the research object in this study. Firstly, an innovative “relief-retaining” control scheme of floor heave is proposed, which is the comprehensive measure of “cutting groove in floor + drilling for pressure relief at roadway side + setting retaining piles at the junction of roadway side and floor.” Then, the specific parameters suitable for floor heave control of no. 130203 return airway are determined using numerical simulation method. Finally, the yield monitoring results show that both the deformation of surrounding rocks and the cable force are significantly reduced. The roof falling capacity, floor heave displacement, and thickness increasing value of 0–2 m floor strata are 596 mm, 410 mm, and 82 mm, respectively, which are 43.67%, 67.49%, and 75.38% less than those of the control section. The maximum force of cables at roadway sides is 140.13 kN, about 32.54% less than that of the control section. The results verify the reliability of the proposed “relief-retaining” control scheme and can provide some reference for the floor heave control of similar roadways.

1. Introduction

After excavation of mining roadway, the phenomenon of upward heave of roadway floor is called floor heave. Floor heave will reduce the roadway section, hinder pedestrians and transportation, and hinder the mine ventilation. Many mines have to invest a lot of manpower and material resources to do temporary processing work such as “digging the bottom.” Seriously, it will cause the whole roadway to be scrapped and affect the safety of mine production [1–5]. Therefore, it is of great significance to study the floor heave control of mining roadway.

In order to control the floor heave problem effectively, many scholars have conducted a lot of exploration, and many floor heave prevention and control technologies are proposed. For example, He et al. [6] proposed the bolt, steel mesh, and anchor coupling support technology for the floor heave of deep coal roadway, which controlled the large deformation and floor heave of deep coal roadway

effectively. Sun and Wang [7] studied the control method of floor heave by the way of roadway cutting groove to relieve pressure, which improved the stress state of the floor effectively. Aiming at the deformation and failure characteristics of mining roadway, Bai et al. [8] put forward to strengthen the floor and reduce the stress environment of surrounding rocks for the control measures of floor heave, and the control effect is remarkable. Li [9] proposed reinforcement floor and bottom angle control method for floor heave of roadway, which laid the foundation for further study of floor heave control. Wang et al. [10] studied the floor heave control method of high-stress soft rock roadway, took the triple roadway of the main belt conveyor roadway in the west wing of Panyidong Mine as the research object, and proposed the floor heave control scheme based on end anchor cable bundle, which provided solutions and ideas for the floor heave problem of high-stress soft rock roadway. Chen et al. [11] proposed the floor heave control technology of soft rock roadway with “floor anchor + floor

hardening + relief groove + roof and side anchor (cable) supplement” and achieved good engineering application results. Wang et al. [12] proposed the support concept of strong bottom reinforcement and modified the support parameters in a timely manner by dynamic analysis according to the degree of floor heave, which provided a theoretical basis for the treatment of floor heave. Stankus and Peng [13] proposed the supporting theory of coupling of yielding support and rigid support and designed and applied the retractable floor beam, which achieved good economic and technical results. Many scholars have done a lot of research on floor heave control, mainly focused on the aspects of reducing surrounding rocks stress [14–17] and increasing floor integrity [18–23], and achieved good control results.

However, due to the complex diagenetic conditions of Ningdong Mining Area in northwest China, the cohesion of coal and rock is low, the internal friction angle is small, the stress level of surrounding rocks is high, the roadway floor has continuous deformation, and the floor heave is very large [24–27]. The application effect of the existing floor heave control method in Ningdong Mining Area is limited. The method of floor heave control suitable for high-stress roadway with soft rock needs further exploration, especially in Ningdong Mining Area.

Based on the typical large deformation roadway with soft rock in Zaoquan Coal Mine of Ningdong Mining Area, this paper puts forward the innovative “relief-retaining” control scheme of floor heave, and the specific parameters suitable for floor heave control of no. 130203 return airway are determined using numerical simulation method. Field monitoring results verify the reliability of the proposed “relief-retaining” control scheme and can provide some reference for the floor heave control of similar roadways.

2. Engineering Background

Zaoquan Coal Mine in Ningdong Mining Area, as the main production mine of Ningmei Group with an annual output of 8 million tons, is located at the edge of Maowusu Desert 62 km southeast of Lingwu City, Ningxia, and the specific geographical location is shown in Figure 1. The length of the minefield is 13 km from north to south, and the width from east to west is about 4 km on average. The minefield area is 56.6982 km², and the geological reserves are 10.6574 million tons.

The research object of this paper is no. 130203 return airway in Zaoquan Coal Mine. The depth of roadway is 670 m, the vertical stress is about 16.75 MPa, the recoverable length of strike is 2832 m, and the inclined length is 198~225 m. There are 5~15 m coal pillars on the east side of the working face adjacent to the goaf of no. 130202 working face. The west side is the no. 130205 preparation face under excavation, the south side is the undeveloped area, and the north side is the extension section of 13 mining areas. Through the in situ stress test of the return airway in 130203 working face, the results show that the maximum horizontal principal stress of the roadway is 11.65 MPa, which belongs to the area of medium stress value.

The strata of no. 130203 working face coal seam are Middle Jurassic Yan'an Formation. The floor is a typical soft stratum, which is mainly the carbonaceous mudstone and argillaceous sandstone, and the uniaxial strength is between 17 MPa and 23 MPa. The soft strata of the floor lead to the serious floor heave problem of the roadway under the influence of the high surrounding rocks stress of the floor during the tunneling and mining of the no. 130203 roadway, which affects the normal mining of the mine. The floor heave deformation of the roadway is shown in Figure 2.

3. “Relief-Retaining” Control Scheme of Floor Heave

3.1. Control Scheme

3.1.1. Cutting Groove in the Floor. The loose pressure relief groove is arranged near the center of roadway floor in the test area. In order to minimize the disturbance of surrounding rocks outside the pressure relief groove, the pressure relief groove is produced by smooth blasting, and the sectional drawing and vertical view are as shown in Figure 3.

3.1.2. Setting Retaining Piles at the Junction of Roadway Side and Floor. The retaining pile is inclined to the outside of the roadway at a certain angle in the horizontal direction. The retaining pile is made of steel pipe, cement, and sodium silicate slurry. By drilling a hole at a predetermined position, installing a steel pipe in the hole and installing an anchor cable inside the steel pipe, injecting cement and water glass, and then applying a certain preload to the anchor cable after solidification, the fabrication of retaining pile can be completed. The sectional drawing and vertical view are as shown in Figure 4.

3.1.3. Drilling for Pressure Relief at Roadway Side. Large-diameter pressure relief boreholes are arranged in the solid coal side to transfer the peak value of lateral abutment pressure to the deep coal side. At a certain height from the floor of the roadway, two rows of large-diameter boreholes are constructed along the roadway direction, which are arranged in three-flower-hole layout. For the convenience of site construction, a certain elevation angle can be brought in the borehole construction. The borehole diameter is generally 130 mm, and the sectional drawing and vertical view are as shown in Figure 5.

3.2. Parameter Selection

3.2.1. Simulation Scheme and Modeling. The “relief-retaining” control scheme of floor heave mainly involves the following parameters: the depth and width of pressure relief grooves, the length and spacing of retaining pile, and the depth and spacing of large-diameter pressure relief boreholes in solid coal side. By comparing the construction examples of mines with similar geological conditions, the numerical simulation scheme is shown in Table 1. Physical

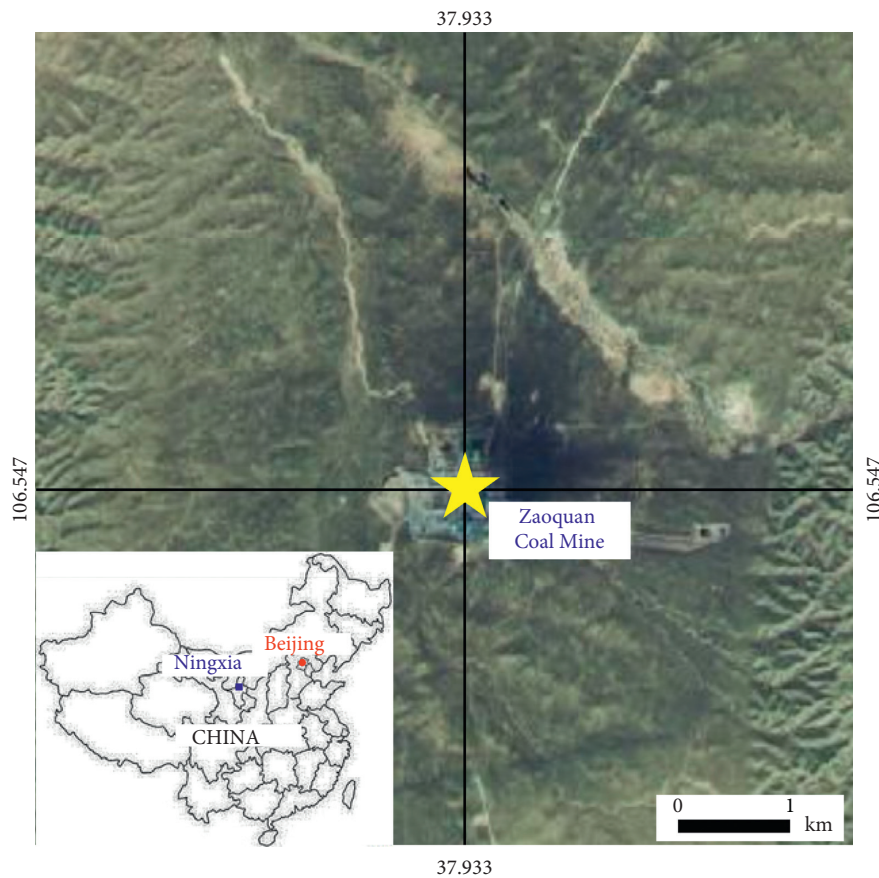


FIGURE 1: Floor heave of return airway in no. 130203 working face.

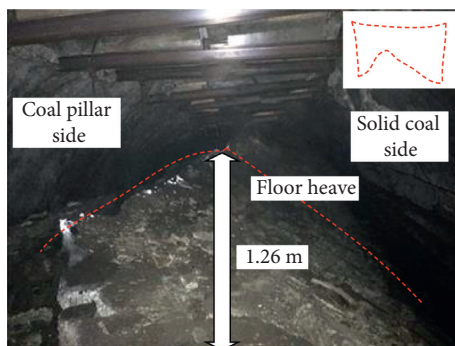


FIGURE 2: Floor heave of return airway in no. 130203 working face.

and mechanical parameters of retaining pile are shown in Table 2.

This section takes the geological and mining conditions of no. 130203 return airway in Zaoquan Coal Mine as the background, adopts FLAC3D numerical software, selects no. 130203 working face as the engineering prototype, and selects the length of X horizontal direction 200 m, the length of Y horizontal direction 50 m, and the length of Z vertical direction 150 m to establish the numerical calculation model. The coarse sandstone is the upper boundary of the model, and the medium sandstone is the lower boundary of the model. The strata from top to bottom are coarse sandstone, siltstone, coal, mudstone, fine sandstone, and

medium sandstone. The buried depth of field roadway is about 700 m, and 17.5 MPa uniform compressive stress is applied on the upper boundary of the model. The specific shape of roadway section is selected as rectangular roadway, and the roadway size is 5.0 m × 4.0 m. The specific model is shown in Figure 6.

The left and right, front and back, and lower boundaries of the model are displacement boundaries, and the top of the model is stress boundary conditions. The mechanical parameters of coal and rock in the model are shown in Table 3.

3.2.2. Modeling Results

(1) *Cutting Groove in the Floor.* The deformation and stress distribution of roadway surrounding rocks with different width of cutting grooves in the floor are shown in Figure 7.

It can be seen from Figure 7 that when the depth of cutting groove is constant, with the increase of the width of cutting groove, the deformation compensation space of the floor surrounding rocks increases, and the floor heave displacement of the roadway decreases gradually. In particular, when the width of cutting groove is not more than 0.6 m, the floor heave displacement decreases rapidly. When the width of cutting groove is more than 0.6 m, the floor heave displacement decreases slowly with the increase of the width of cutting groove. It can be seen that when the cutting

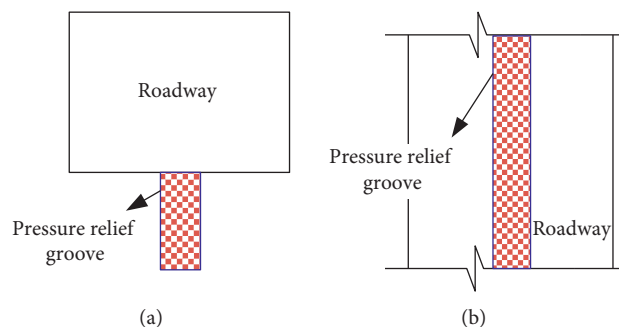


FIGURE 3: Schematic diagram of cutting groove in the floor. (a) Sectional drawing; (b) vertical view.

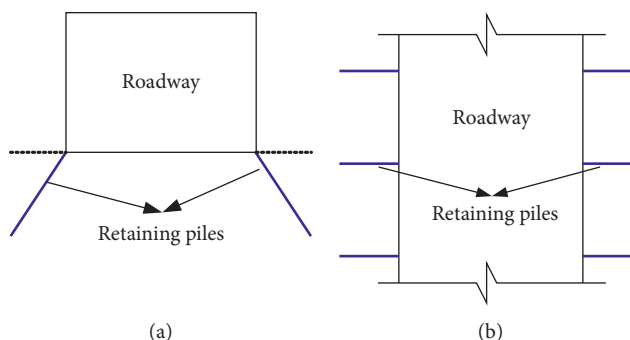


FIGURE 4: Indication diagram of retaining pile arrangement. (a) Sectional drawing; (b) vertical view.

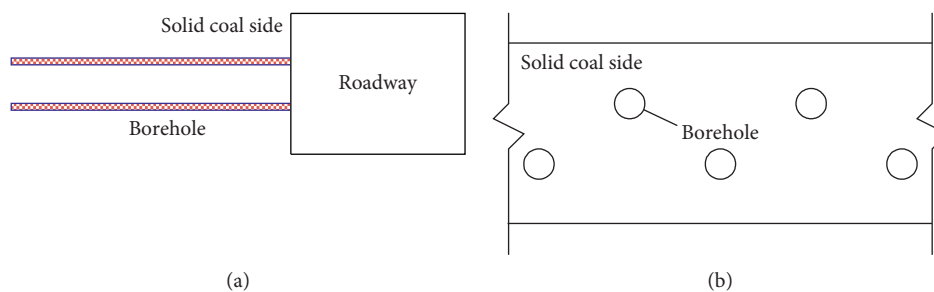


FIGURE 5: Large-diameter pressure relief drilling schematic diagram of solid coal side. (a) Sectional drawing; (b) vertical view.

TABLE 1: Numerical simulation scheme for control scheme of floor heave.

Control technologies and parameters		Scheme 1	Scheme 2	Scheme 3
Pressure relief grooves	Depth (m)	2.0	2.0	2.0
	Width (m)	0.4	0.6	0.8
Retaining piles	Depth (m)	3.0	3.0	3.0
	Spacing (m)	0.5	1.0	1.5
Large-diameter pressure relief boreholes	Depth (m)	10	10	10
	Spacing (m)	0.8	1.0	1.2

groove is set to control the floor heave, the width of cutting groove should not exceed 0.6 m.

(2) *Setting Retaining Piles at the Junction of Roadway Side and Floor.* The deformation and stress nephogram of roadway surrounding rocks with different spacings of retaining piles are shown in Figure 8.

From Figure 8, it can be seen that the floor heave displacement increases with the increase of the spacing of retaining piles, and the increase trend decreases gradually. When the spacing of retaining piles exceeds 1.0 m, the increase of the spacing of retaining piles has little effect on the improvement of floor heave control. From the economic point of view, too small spacing of retaining piles will also

TABLE 2: Physical and mechanical parameters of retaining pile.

Name	Diameter (mm)	Density ($\text{kg}\cdot\text{m}^{-3}$)	Elastic modulus (GPa)	Poisson ratio
Retaining piles	50	2500	35	0.2

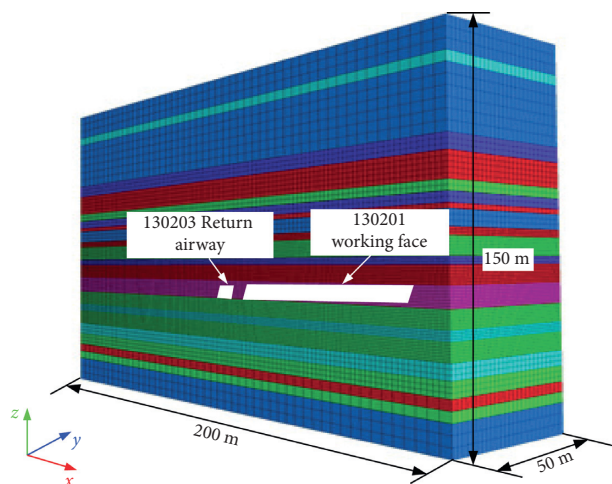


FIGURE 6: Numerical calculation model diagram of no. 130203 working face.

TABLE 3: Physical and mechanical parameter table of numerical model materials.

Lithology	Density ($\text{kg}\cdot\text{m}^{-3}$)	Compressive strength (MPa)	Tensile strength (MPa)	Elastic modulus (GPa)	Internal cohesion (MPa)	Internal friction angle ($^{\circ}$)	Poisson ratio
Medium grained sandstone	2300	21.76	0.61	11.73	1.62	32	0.25
Gritstone	2360	28.39	0.83	21.35	1.83	36	0.21
Siltstone	2860	27.62	0.71	19.04	1.24	37	0.23
Mudstone	2620	17.36	0.56	9.60	0.86	34	0.24
Fine-sandstone	2510	23.30	0.96	14.37	1.36	47	0.21
Carbon mudstone	2650	17.36	0.56	8.03	0.47	27.25	0.24
Coal	1310	11.65	0.47	8.71	0.50	26.36	0.23
Siltstone	2860	27.62	0.71	19.04	1.42	37	0.23

cause the increase of floor heave control cost. Therefore, the simulation of the spacing of retaining piles in the no. 130203 working face of Zaoquan Coal Mine in Ningdong Mining Area shows that the spacing of retaining piles is 1.0 m.

(3) *Drilling for Pressure Relief at Roadway Side.* The deformation and stress nephogram of surrounding rocks of roadway with different spacings of pressure relief boreholes are shown in Figure 9.

Figure 9 shows that the floor heave displacement increases with the increase of the spacing of pressure relief boreholes, and the increasing trend decreases gradually. When the spacing of pressure relief boreholes exceeds 1.0 m, the effect of pressure relief boreholes on floor heave control is not obvious. At the same time, when the spacing is reduced, the setting of dense drilling will further increase the control cost. Therefore, considering the control cost and control effect, the spacing of pressure relief boreholes in no. 130203 working face of Zaoquan Coal Mine in Ningdong Mining Area is 1.0 m.

In summary, the main parameters for determining the “relief-retaining” control scheme of floor heave are as follows: the depth and width of pressure relief groove are 2.0 m and 0.5 m, respectively. The length and spacing of retaining piles are 3.0 m and 1.0 m, respectively. The depth and spacing of large-diameter pressure relief boreholes at the roadway side are 10.0 m and 1.0 m, respectively.

4. Analysis of Result

The scheme is implemented outside 200 m of advanced working face, and the roadway with similar geological structure, surrounding rocks property, and coal pillar sizes should be selected for test. The length of the test area is 200 m. The test area division and the corresponding station layout are shown in Figure 10. The original support scheme was used as the control section in the first 100 m, and the last 100 m was the test section of the “relief-retaining” control scheme of floor heave in this paper. The monitoring results are as follows.

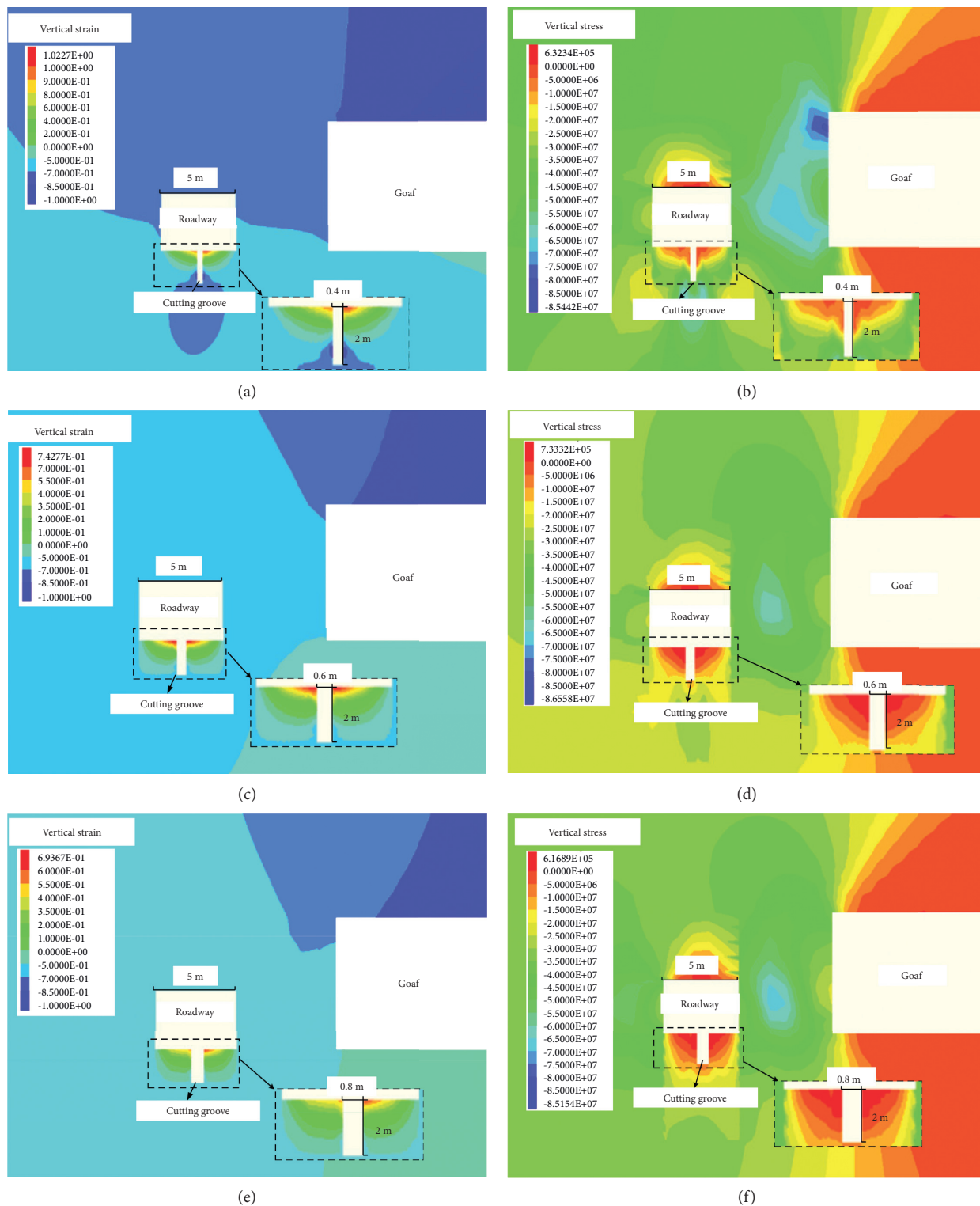


FIGURE 7: Deformation and stress distribution of roadway surrounding rock with different floor cutting groove width. (a) Vertical strain of 0.4 m; (b) vertical stress of 0.4 m; (c) vertical strain of 0.6 m; (d) vertical stress of 0.6 m; (e) vertical strain of 0.8 m; (f) vertical strain of 0.8 m.

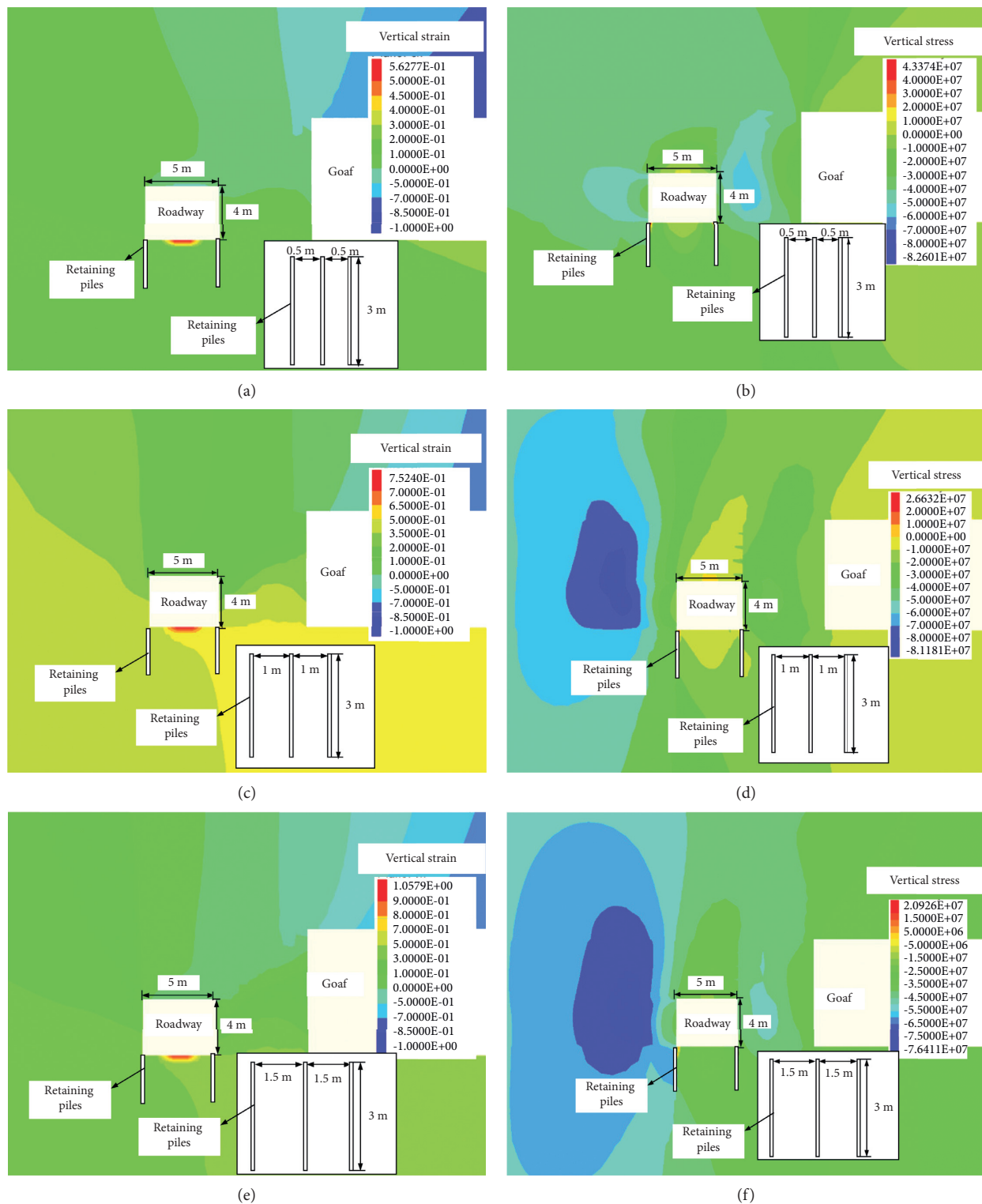


FIGURE 8: Deformation and stress distribution of roadway surrounding rocks with different spacings of retaining piles. (a) Vertical strain of 0.5 m; (b) vertical stress of 0.5 m; (c) vertical strain of 1.0 m; (d) vertical stress of 1.0 m; (e) vertical strain of 1.5 m; (f) vertical stress of 1.5 m.

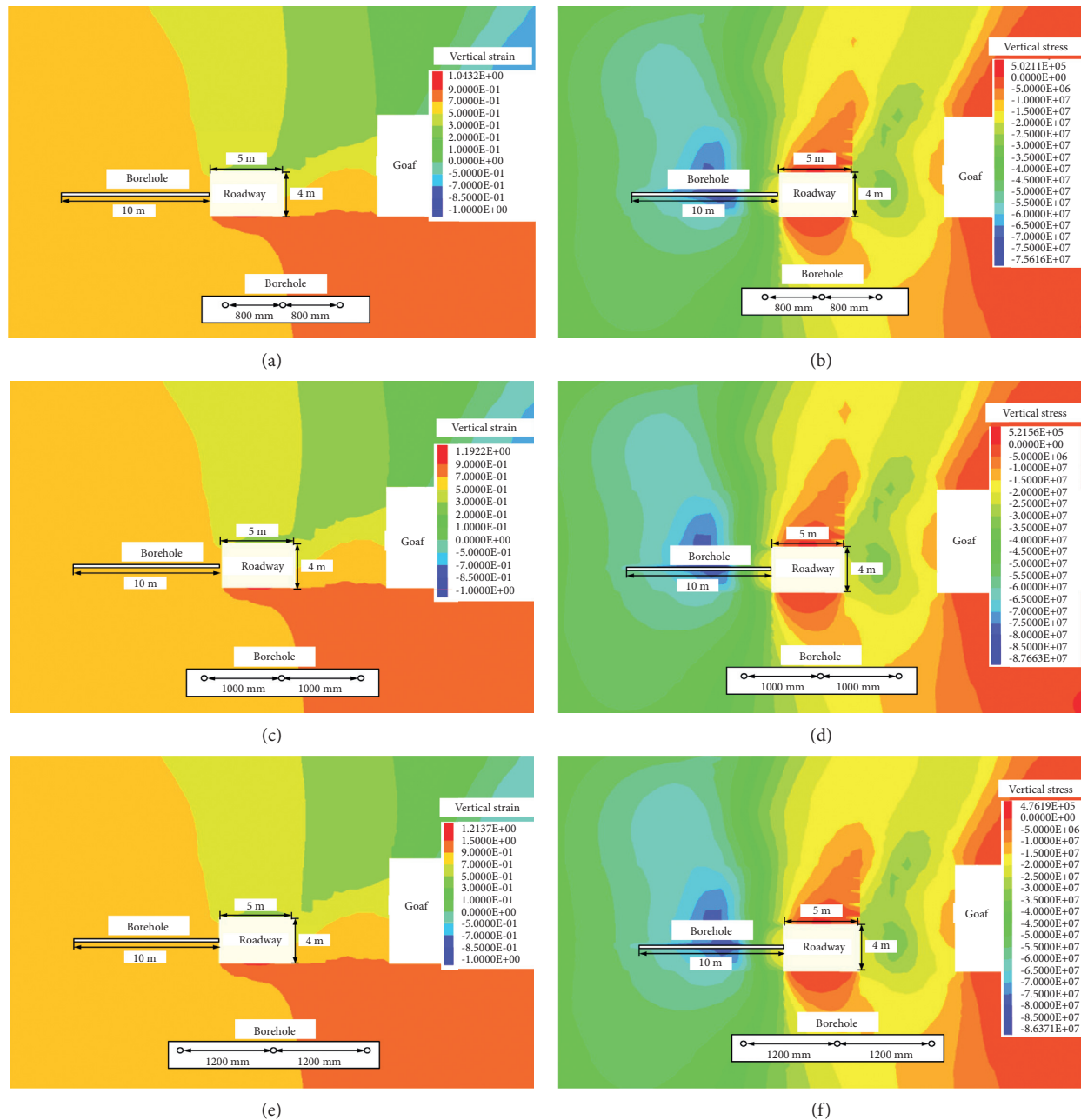


FIGURE 9: Deformation and stress distribution of surrounding rocks in mining roadway with different spacings of pressure relief boreholes. (a) Vertical strain of 0.8 m; (b) vertical stress of 0.8 m; (c) vertical strain of 1.0 m; (d) vertical stress of 1.0 m; (e) vertical strain of 1.2 m; (f) vertical stress of 1.2 m.

4.1. Deformation Law of Roadway Surrounding Rocks.

The "cross-bonded method" was used to observe the surface displacement of roadway surrounding rocks, the multipoint displacement meter was used to observe the deep displacement of roadway surrounding rocks, and the roof and floor of roadway are the main monitoring object. The main monitoring results are as follows.

(1) Deformation law of roadway roof and floor

With the mining of no. 130203 working face, the surrounding rocks deformation of return airway shows different changes. The monitoring results of roof falling capacity and floor heave displacement of each station are shown in Figures 11 and 12, respectively. In order to facilitate data comparison, the

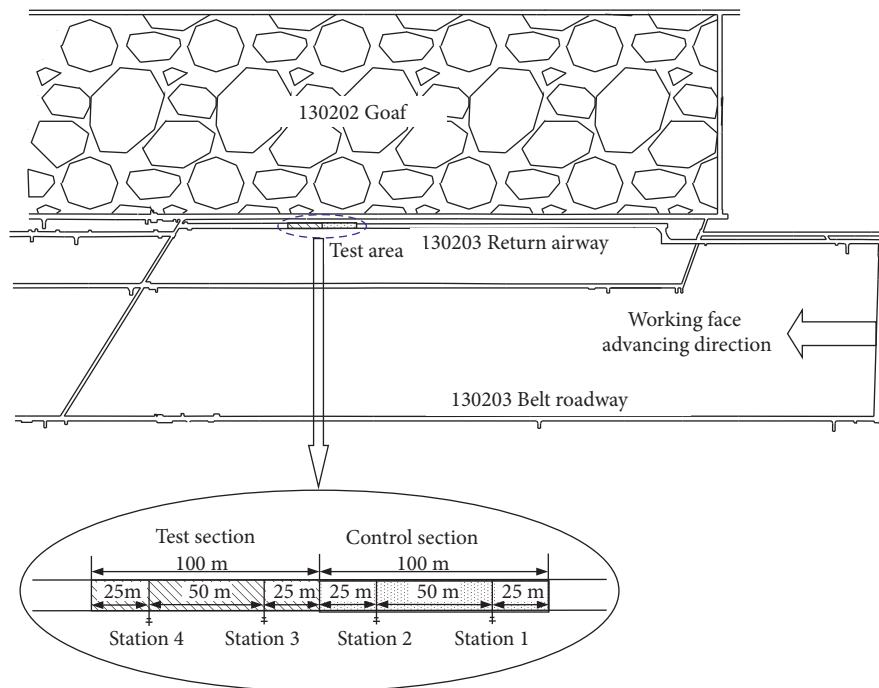


FIGURE 10: Test area and station layout diagram.

data of each station are recorded at 120 m from the working face.

It can be seen from Figure 11 that when the measuring point is 80 m away from the working face, the roof falling capacity of roadway is small. Within the range of 80–30 m from the working face, the surrounding rocks of the roadway are affected by the advanced abutment pressure, and the roof falling capacity begins to increase significantly. When the distance from the working face is within 30 m, the roof falling capacity of the control section is still increased, and the speed of the roof falling capacity of the test section is gradually slowed down. Thus, the mining roadway is less affected by the mining of the working face outside 80 m and is in the slow deformation stage. The influence range of the advanced abutment pressure of the working face is 80 m ahead of the working face.

At the same time, by comparing the change of roof falling capacity of each station, the maximum values of the control section are 1366 mm and 1364 mm, respectively, with an average of 1365 mm. The maximum values of roof falling capacity in the test section were 598 mm and 594 mm, respectively, with an average of 596 mm, which were 43.67% lower than those in the control section, and the control effect was obvious.

By comparing the change of floor heave displacement of each station, it can be seen from Figure 12 that the deformation of floor heave in the initial test section is slightly larger than that in the control section, which is because the integrity of the floor is

reduced due to the initial construction. In the process of approaching the working face, the floor heave displacement of the control section increases rapidly, while the increase of the test section is slow, indicating that the measures of the test section begin to play a key role. In addition, compared with the monitoring data of each station, the maximum values of the control section were 1257 mm and 1267 mm, with an average of 1262 mm. The maximum floor heave displacement of the test section was 414 mm and 406 mm, with an average of 410 mm, which was 852 mm lower than that of the control section, and the decrease was 67.49%, indicating that the floor heave displacement of the test section was significantly lower than that of the control section.

At the same time, it can be seen from the control section that the floor heave displacement accounts for a large proportion in the deformation of roadway roof and floor. When the deformation of roadway roof and floor is the largest, the floor heave displacement accounts for about 48.16% of the roof to floor convergence, while the floor heave displacement of the test section accounts for about 40.99% of the deformation of roadway, indicating that the floor heave displacement of the test section is effectively reduced due to the implementation of the “relief-retaining” control scheme of floor heave, which has a good control effect on the floor heave of roadway.

- (2) Deformation law of thickness increasing value of 0–2 m floor strata

With the mining of working face, the deformation of surrounding rocks of roadway floor has different

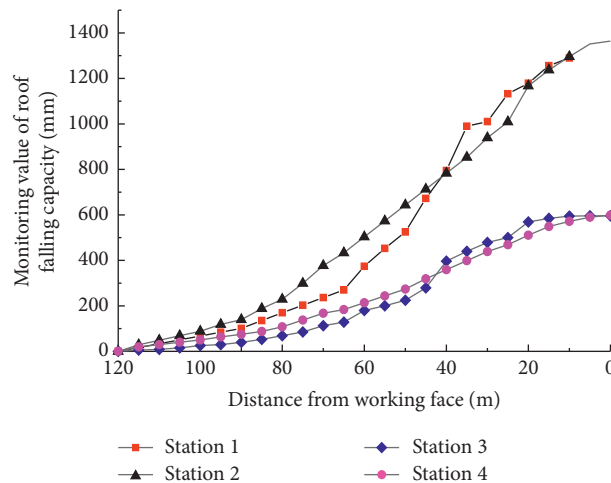


FIGURE 11: Curve diagram of roof falling capacity of each station.

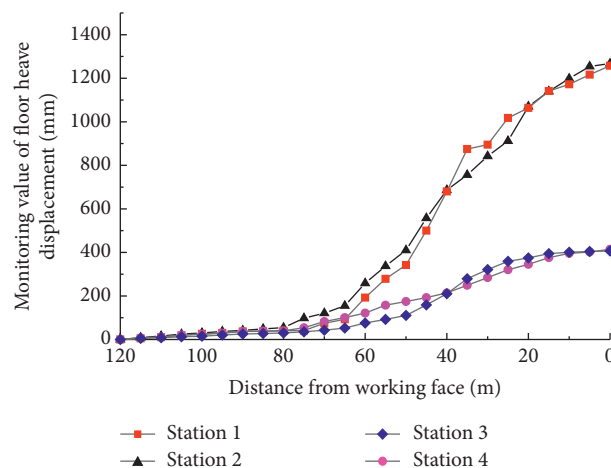


FIGURE 12: Curve diagram of floor heave displacement at each station.

changes. The monitoring results of the average deformation of the surrounding rocks of the roadway floor in the control section and the test section are shown in Figure 13. Because the depth of the cable claw at the deepest point of the multipoint displacement meter of the roadway floor is 2 m, the monitoring data of the deep 2 m position of the roadway floor are compared and analyzed. At the same time, in order to facilitate data comparison, the data of each station are recorded from 120 m away from the working face.

Comparing the average change of surrounding rocks of roadway floor between the control section and the test section, it can be seen that before 80 m from the working face, the deformation trend of surrounding rocks of roadway floor in the test section and the control section is similar, but the deformation speed of the test section is slightly smaller than that of the control section. In the range of 80–50 m from the working face, the deformation of the test section is still very stable, but the deformation of the control

section increases sharply, and the deformation of the surrounding rocks of the roadway floor in the test section is much smaller than that of the control section. Within 50 m, the deformation of the control section slightly slowed down, while the deformation of the test section was still relatively stable and maintained at a low growth state.

From the monitoring data, it can be seen that during the period from 120 m from the measuring station to the working face until the working face is pushed past the measuring station, the deformation of roadway floor surrounding rocks in the test section was significantly reduced compared with that in the control section. The maximum deformation value of roadway floor surrounding rocks in the control section was 333 mm, and the deformation value of roadway floor surrounding rocks in the test section was 82 mm, which was reduced by 75.38%, indicating that the effect of the “relief-retaining” control scheme of floor heave was significant.

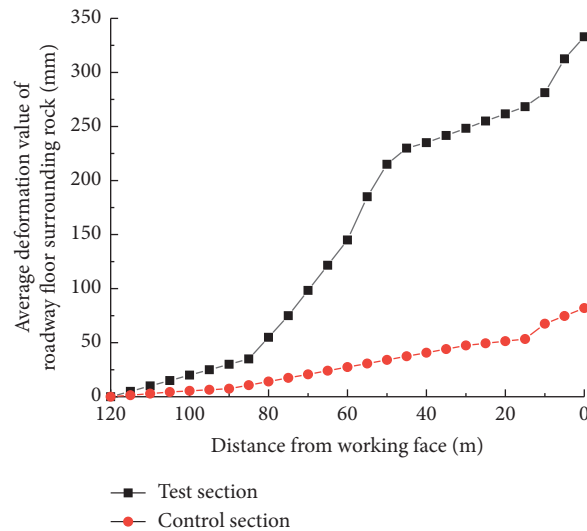


FIGURE 13: The average deformation curves of 0–2 m floor strata of control section and test section.

After monitoring the station, the deformation of surrounding rocks in different layers of roadway floor is counted, and the deformation of surrounding rocks in different layers of roadway floor is shown in Figure 14. It can be seen from Figure 14 that whether the test section or the control section, the deformation of surrounding rocks of roadway floor gradually decreases with the increase of depth. By comparing the deformation of surrounding rocks in different layers of the test section and the control section, it is found that the deformation of the test section in each layer is smaller than that in the corresponding layer of the control section. The shallower the layer is, the more obvious the reduction effect of the test section scheme is. In particular, the effect is the most obvious when the shallow part is 0–0.5 m. The deformation reduction of the test section is 155 mm, which is 75.61% lower than that of the control section.

4.2. Stress Variation Law of Roadway Surrounding Rocks.

In the mining process of no. 130203 working face, the stress of roadway surrounding rocks shows a certain change rule. The MSC-400 cable dynamometer is used to monitor the average stress of roadway surrounding rocks. The monitoring results of the control section and the test section are shown in Figure 15. In order to facilitate data comparison, the data of each station are recorded from 190 m away from the working face.

It can be seen from the monitoring data that within the range of 30–35 m from the working face, the cable force in the control section and the test section appears to be the maximum. The maximum force of cable in the control section appears at about 35 m from the working face, which is about 206.06 kN. The maximum force of the cable in the test section appears at about 30 m from the working face, which is about 140.13 kN. Compared with the control

section, the test section is reduced by 32.54%, indicating that the “relief-retaining” control scheme of floor heave has a certain effect on reducing the force of surrounding rocks.

4.3. Discussion. The analysis of the above monitoring results shows that the deformation of the surrounding rocks of the mining roadway is effectively controlled after the “relief-retaining” control scheme of floor heave. The floor displacement is reduced by 67.49%, and the cable force is reduced by 32.54%. The stress environment and stability of the surrounding rocks are significantly improved, which has played a good demonstration role. The main reason is that the “relief-retaining” control scheme of floor heave liberates the deformation of floor, reduces the stress of surrounding rocks, and effectively blocks the transmission of horizontal stress, which will greatly reduce the deformation and stress of floor.

Many studies have been carried out by many scholars on the floor heave control of roadways with similar conditions [4, 16, 28–31]. For example, Gu et al. [28] proposed the combined support of bolt grouting and grooving to control floor heave for the floor of return airway in 2407 working face of high-stress roadway with soft rock in Yuhua Coal Mine, Tongchuan, and the field monitoring showed that the floor heave displacement was reduced by 61.5%. This not only reduces the impact of horizontal stress but can also lead to difficulty in repairing the floor. Compared with the above scheme, the “relief-retaining” control scheme of floor heave proposed in this paper can effectively reduce the stress concentration degree of roadway side and resist the transmission of horizontal stress of floor, so as to reduce the influence of horizontal stress on floor strata. At the same time, it can provide certain free space for floor deformation and liberate the deformation of roadway floor, so the control effect is better than the above scheme.

In summary, it can be seen that the mechanism of floor heave is likely to be related to the horizontal stress and the

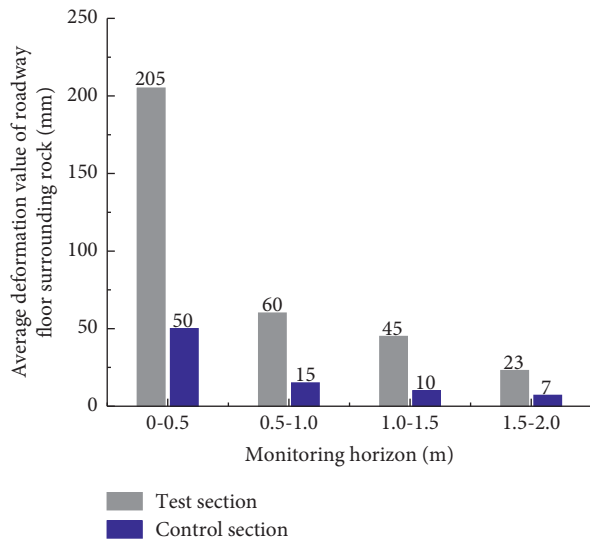


FIGURE 14: Histogram of average deformation value of roadway floor surrounding rocks in different layers.

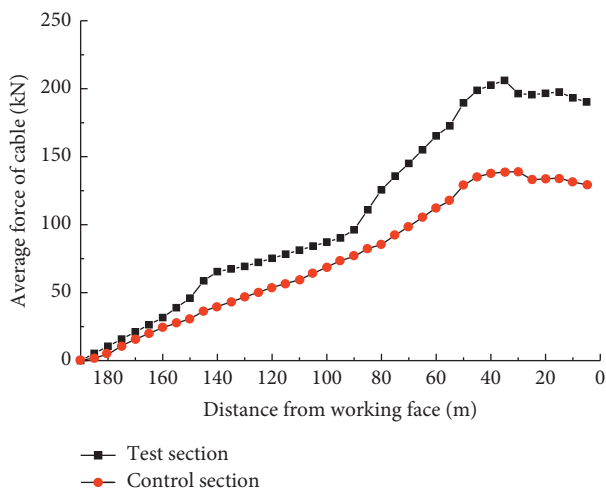


FIGURE 15: Average stress curve of anchor of surrounding rocks of solid coal side of roadway in control section and test section.

stress concentration degree of roadway side and floor. For example, the floor heave can be reduced to a certain extent by reducing the stress concentration by implementing the pressure relief of large-diameter boreholes on roadway side. The next step will focus on these three factors to carry out the related research on the mechanism of floor heave in high-stress roadway with soft rock.

5. Conclusions

Based on the serious floor heave problem of no. 130203 working face return airway in Zaoquan Coal Mine of Ningdong Mining Area, an innovative "relief-retaining" control scheme of floor heave is designed, and the specific parameters suitable for floor heave control of no. 130203 return airway are determined; then the feasibility of the

technical scheme is verified by engineering practice in the field. The main conclusions are as follows.

- (1) Taking the typical high-stress soft rock roadway with large deformation in Zaoquan Coal Mine of Ningdong Mining Area as the background, the "relief-retaining" control scheme of floor heave is proposed, which is the comprehensive measure of "cutting groove in floor+drilling for pressure relief at roadway side+setting retaining piles at the junction of roadway side and floor."
- (2) The specific parameters suitable for floor heave control of no. 130203 return airway are determined using numerical simulation method. The depth and width of pressure relief groove are 2.0 m and 0.5 m, respectively. The length and spacing of retaining piles are 3.0 m and 1.0 m, respectively. The depth and spacing of large-diameter pressure relief boreholes are 10.0 m and 1.0 m, respectively.
- (3) By conducting "relief-retaining" control scheme, field monitoring results show that the average roof falling capacity is 596 mm, and the average floor heave displacement is 410 mm, which are, respectively, 43.67% and 67.49% less than the control section. The maximum force of cable is about 140.13 kN, which is 32.54% less. The deformation and failure of roadway surrounding rocks, especially floor heave, are well controlled.

References

- [1] J. Shi and D. Kong, "Floor heave mechanism and anti-slide piles control technology in deep and large-span chamber," *Applied Sciences*, vol. 11, no. 10, p. 4576, 2021.
- [2] H. Jia, L. Wang, K. Fan, B. Peng, and K. Pan, "Control technology of soft rock floor in mining roadway with coal pillar protection: a case study," *Energies*, vol. 12, no. 15, p. 3009, 2019.
- [3] C. Wang, Y. P. Wu, S. J. Chen et al., "Analysis and application on inverted arch support of cross-cut floor heave," *Journal of Physics: Conference Series*, vol. 2002, no. 1, pp. 713–720, 2021.
- [4] X. Kang, D. Guo, and Z. Lu, "Mechanism of roadway floor heave controlled by floor corner pile in deep roadway under

- high horizontal stress," *Advances in Civil Engineering*, vol. 2021, Article ID 6669233, 10 pages, 2021.
- [5] W. Zheng, Y. Zhao, Q. Bu, and S. I. Kundalwal, "The coupled control of floor heave based on a composite structure consisting of bolts and concrete antiarches," *Mathematical Problems in Engineering*, vol. 2018, Article ID 3545423, 14 pages, 2018.
 - [6] M. C. He, G. F. Zhang, G. L. Wang, Y. L. Xu, C. Z. Wu, and Q. D. Tang, "Research on mechanism and application to floor heave control of deep gateway," *Chinese Journal of Rock Mechanics and Engineering*, vol. 28, pp. 2593–2598, 2009.
 - [7] J. Sun and L. Wang, "Numerical simulation of grooving method for floor heave control in soft rock roadway," *Mining Science and Technology (China)*, vol. 21, no. 1, pp. 49–56, 2011.
 - [8] J. B. Bai, W. F. Li, X. Y. Wang, X. U. Ying, and L. J. Huo, "Mechanism of floor heave and control technology of road way induced by mining," *Journal of Mining and Safety Engineering*, vol. 28, pp. 1–5, 2011.
 - [9] Y. J. Li, "Study on mechanism analysis and control technology of roadway floor heave," *Coal Chemical Industry*, vol. 40, pp. 31–33, 2017.
 - [10] X. Q. Wang, J. G. Kan, and J. K. Jiao, "Mechanism of floor heave in the roadway with high stress and soft rock and its control practice," *Journal of Mining and Safety Engineering*, vol. 38, pp. 215–226, 2021.
 - [11] G. M. Chen, Y. T. Zhang, H. H. He, and H. W. Zhang, "Research on mechanism and control technology of floor heave in soft rock roadway in Dafosi mine," *China Coal*, vol. 39, pp. 59–61, 2013.
 - [12] C. Wang, Y. Wang, and S. Lu, "Deformational behaviour of roadways in soft rocks in underground coal mines and principles for stability control," *International Journal of Rock Mechanics and Mining*, vol. 37, 2000.
 - [13] J. C. Stankus and S. S. Peng, "Floor bolting for control of mine floor heave," *Mining Engineering*, vol. 46, pp. 1099–1102, 1994.
 - [14] P. T. Xie, "Reinforcement design and application on close roadway below mined - out area," *Shanxi Coking Coal Science Technology*, vol. 37, pp. 8–10+14, 2013.
 - [15] X. S. Liu, D. Y. Fan, Y. L. Tan et al., "Failure evolution and instability mechanism of surrounding rock for close-distance parallel chambers with super-large section in deep coal mines," *International Journal of Geomechanics*, vol. 21, 2021.
 - [16] L. Shi, H. D. Zhang, and P. Wang, "Research on key technologies of floor heave control in soft rock roadway," *Advances in Civil Engineering*, vol. 2020, Article ID 8857873, 13 pages, 2020.
 - [17] W. X. Zheng, Q. W. Bu, and Y. Q. Hu, "Plastic failure analysis of roadway floor surrounding rocks based on unified strength theory," *Advances in Civil Engineering*, vol. 2018, Article ID 7475698, 10 pages, 2018.
 - [18] X. Liu, S. Song, Y. Tan et al., "Similar simulation study on the deformation and failure of surrounding rock of a large section chamber group under dynamic loading," *International Journal of Mining Science and Technology*, vol. 31, no. 3, pp. 495–505, 2021.
 - [19] X. S. Liu, D. Y. Fan, Y. L. Tan et al., "New detecting method on the connecting fractured zone above the coal face and a case study," *Rock Mechanics and Rock Engineering*, vol. 54, no. 8, pp. 4379–4391, 2021.
 - [20] H. Zhang, H. P. Kang, and Y. L. Xu, "Study on rapid reinforced technology with pre-stressed anchor for floor of mine roadway in deep mine," *Coal Science and Technology*, vol. 41, pp. 16–19+23, 2013.
 - [21] L. Z. Xu and S. J. Wei, "Control technology and simulation study of floor heave in high stress soft rock roadway," *Geotechnical & Geological Engineering*, vol. 38, pp. 1–14, 2020.
 - [22] H. P. Kang, J. H. Wang, and J. Lin, "Study and applications of roadway support techniques for coal mines," *Journal of China Coal Society*, vol. 35, pp. 1809–1814, 2010.
 - [23] T. Yang and J. Zhang, "Research on the treatment technology of soft rock floor heave based on a model of pressure-relief slots," *Arabian Journal Geosciences*, vol. 14, 2021.
 - [24] D. Y. Fan, X. S. Liu, Y. L. Tan et al., "Roof cutting parameters design for gob-side entry in deep coal mine: a case study," *Energies*, vol. 12, 2019.
 - [25] M. G. Qian, P. W. Shi, and J. L. Xu, *Ground Pressure and Strata Control*, China University Min Techno Press, Beijing, China, 2010.
 - [26] S. G. Liu, J. B. Bai, X. Y. Wang, B. W. Wu, W. D. Wu, and Z. X. Li, "Mechanisms of floor heave in roadways adjacent to a goaf caused by the fracturing of a competent roof and controlling technology," *Shock and Vibration*, vol. 2020, Article ID 5632943, 17 pages, 2020.
 - [27] D. Y. Fan, X. S. Liu, Y. L. Tan, S. L. Song, J. G. Ning, and Q. Ma, "Numerical simulation research on response characteristics of surrounding rock for deep super-large section chamber under dynamic and static combined loading condition," *Journal of Central South University*, vol. 27, no. 12, pp. 3544–3566, 2020.
 - [28] S. C. Gu, X. M. Wang, R. B. Huang, and H. W. He, "Analysis on mechanism and control technique of floor heave deformation in high stress roadway," *Journal Safety Science and Technology*, vol. 16, pp. 57–63, 2020.
 - [29] J. Yang, K. Zhou, Y. Cheng, Y. Gao, Q. Wei, and Y. Hu, "Mechanism and control of roadway floor heave in the paleogene soft rock surroundings," *Geotechnical & Geological Engineering*, vol. 37, no. 6, pp. 5167–5185, 2019.
 - [30] G. Y. Yu, J. Wang, J. Z. Hu et al., "Innovative control technique for the floor heave in goaf-side entry retaining based on pressure relief by roof cutting," *Mathematical Problems in Engineering*, vol. 2021, Article ID 7163598, 17 pages, 2021.
 - [31] G. R. Feng, S. Y. Li, P. F. Wang et al., "Study on floor mechanical failure characteristics and stress evolution in double predriven recovery rooms," *Mathematical Problems in Engineering*, vol. 2020, Article ID 9391309, 13 pages, 2020.

Gas Drainage Based on Multifield Coupling Model of Gas-Bearing Coal

Ram Narayan Mishra, *Department of Civil Engineering, Aryan Institute of Engineering & Technology, Bhubaneswar, ramnmishra@outlook.com*

Jagruiti Swain, *Department of Civil Engineering, Capital Engineering College, Bhubaneswar, jagrutiswain26@yahoo.co.in*

Jyotikusum Acharya, *Department of Civil Engineering, NM Institute of Engineering & Technology, Bhubaneswar, jyotikusumacharya@yahoo.co.in*

Binapani Mohapatra, *Department of Civil Engineering, Raajdhani Engineering College, Bhubaneswar, binapanimohapatra@yahoo.co.in*

ABSTRACT

Gas drainage through long seam boreholes is an effective method to prevent gas disasters in coal mines. In this paper, a multi field coupling model of gas migration in gas-bearing coal was first established. Then, a quantitative characterization method of gas drainage effect was put forward. Finally, the extraction effect of long boreholes was obtained under different layouts and drilling lengths. The research results show that, under the arrangement of long boreholes along the seam, the gas pressure around the borehole decreases significantly with the extraction time. There is no extraction blank in the middle of the working face. However, it is easy to cause uneven gas drainage in the combined arrangement of the long boreholes along the seam and the penetrating boreholes. Furthermore, it is found that the drainage volume of the long boreholes along the seam is similar to that of the joint layout under the same drainage time. As the length of the borehole increases, the influencing range of gas drainage increases. When the borehole lengths are 150 m and 240 m, the drainage volumes are about 1.31 and 2.50 times that of the 90 m boreholes, respectively. The research achievements could provide a specific reference for the layout of long boreholes along the bedding and the determination of reasonable parameters for gas drainage on site.

1. Introduction

Gas drainage is an effective way to eliminate the danger of coal and gas outbursts in China at present [1–4]. In recent years, with the development of drilling rig equipment and drilling technology, gas drainage technology with long boreholes has made rapid progress [5–7]. Gas migration significantly affects the gas drainage effect of long boreholes. Therefore, a correct understanding of the law of coal gas migration is of great significance for preventing and controlling coal mine gas disasters and promoting long drilling technology [8–12].

At present, many scholars have studied the multifield coupling model of coal seam gas migration. The coal reservoir is a typical double pore system composed of interlaced fractures and coal matrices [13–15]. Coal seam gas migration

mainly includes two processes: diffusion and seepage. First, the gas is desorbed from the coal matrix and diffused into the fissures under the action of a concentration gradient. This process conforms to Fick's law of diffusion. Then, the gas in the fissure flows to the borehole under the action of the pressure gradient, and this process conforms to Darcy's law [16]. Su et al. [17] described a dual pore model that paralleled coal seam gas migration. The diffusion and seepage of gas in gas drainage are simulated, and the influence of diffusion coefficient on gas pressure evolution and permeability in fractures is analyzed. Dong et al. [18] analyzed the mechanism of negative pressure in gas drainage through a gas-solid coupling model and put forward a method to reduce the negative pressure of drainage to improve gas drainage efficiency. Mora and Wattenbarger [19] summarized the

correct shape factor formulas considering constant drainage rate from a matrix block and constant pressure in the adjacent fractures through numerical simulation. However, the above research mainly analyzed the gas drainage effect in conventional borehole gas drainage. There are few studies on gas drainage with long boreholes along the seam.

On the other hand, to evaluate the effect of long borehole gas drainage, it is necessary to study the reasonable length of the borehole for long borehole drainage [20–22]. If the length of the borehole is too large, due to the attenuation of the negative pressure in the borehole, the gas content at the bottom of the long borehole will be high, making it difficult to reach the drainage index. If the length of the borehole is too short, it will result in low efficiency of gas drainage measures [23–25]. At present, the methods to determine the effective gas drainage radius include on-site measurement and theoretical calculation methods [26, 27]. The on-site measurement mainly determines the residual gas content of the gas after the gas drainage. In terms of theoretical calculations, the effective gas drainage radius is determined mainly based on the gas flow theory in the borehole and the characteristics of coal seam gas seepage. [28, 29] The practice of predecessors in gas drainage has achieved remarkable results. In the case of a short borehole length, the negative pressure of gas drainage in the borehole does not decrease significantly, and there is still a large negative pressure for gas drainage at the bottom of the borehole. After a period of time of extraction, there is little difference in residual gas content before and after the borehole. However, for long boreholes along the bedding, when the negative pressure attenuation is apparent, the residual gas content at the bottom of the borehole is still relatively large. Therefore, it is necessary to study the reasonable length of the borehole for long borehole drainage.

This paper first elaborates and establishes a multifield coupling model of gas migration in coal which considers coal matrix gas diffusion, fissure gas seepage, permeability evolution law, and coal deformation law. Then, the change value of the residual gas content per unit time is used to calculate the gas drainage volume and then quantify the gas drainage effect of the long borehole. Finally, the COMSOL software was adopted, and the fully coupled numerical simulation method was used to analyze the drainage effects of different layouts and lengths of long boreholes along the bedding. The research results are expected to provide a theoretical basis for gas drainage from long boreholes along the bedding.

2. Multifield Coupling Model for Gas-Bearing Coal Seams

2.1. Model Assumptions. The multifield coupling model for gas-bearing coal seams is established based on the following assumptions:

- Coal seam is a homogeneous, isotropic, double-porosity elastic medium
- The influence of water on gas migration in coal seams is ignored
- The coal seam is an isothermal system, and gas is an ideal gas

- The strain of the coal skeleton is infinitesimal [14, 16, 17]

2.2. Effective Stress Principle. In order to better describe the mechanical response of pore and fissure dual media under gas pressure, the effective stress law of dual porous media is introduced when establishing the permeability model [16]:

$$\sigma_{ij}^e = \sigma_{ij} - (\beta_f p_f + \beta_m p_m) \delta_{ij}, \quad (1)$$

where σ_{ij}^e is the effective stress, MPa; σ_{ij} is the total stress, MPa; δ_{ij} is the Kronecker delta (1 for $i=j$ and 0 for $i \neq j$); p_f and p_m are pressure in the fractures and matrix blocks, respectively, Pa; and β_f and β_m are the effective stress coefficients for pore and fracture, respectively.

The effective stress coefficients β_f and β_m of the cracks in (1) can be calculated by the following formulas, respectively:

$$\begin{aligned} \beta_f &= 1 - \frac{K}{K_m}, \\ \beta_m &= \frac{K}{K_m} - \frac{K}{K_s}, \end{aligned} \quad (2)$$

where K is the bulk modulus of the coal body, MPa; K_m is the bulk modulus of the coal matrix, MPa; and K_s is the bulk modulus of the coal body skeleton, MPa.

The following formulas can calculate the above three bulk moduli:

$$\begin{aligned} K &= \frac{E}{3(1-2\nu)}, \\ K_m &= \frac{E_m}{3(1-2\nu)}, \\ K_s &= \frac{K_m}{1 - 3\phi_m(1-\nu)/[2(1-2\nu)]}, \end{aligned} \quad (3)$$

where E is the elastic modulus of the coal body, MPa; E_m is the elastic modulus of the coal matrix, MPa; ν is Poisson's ratio of the coal; and ϕ_m is the coal matrix porosity, %.

2.3. Dynamic Evolution Equation of Coal Porosity and Permeability. Palmer and Mansoori [30] proposed a widely used permeability model (PM model) suitable for uniaxial strain conditions. However, the PM model was established based on the coal seam containing only cracks. The coal seam is usually modeled as a dual-porosity medium containing both cracks and pores. Therefore, this study adopts the dual-porosity poroelasticity theory. The revised crack porosity model is shown in the following equation:

$$\begin{aligned} \frac{\phi_f}{\phi_{f0}} &= \frac{\varepsilon_L}{\phi_{f0}} \left(\frac{K}{M} - 1 \right) \left(\frac{p_m}{p_L + p_m} - \frac{p_0}{p_L + p_0} \right) + 1 \\ &+ \frac{1}{M\phi_{f0}} (\beta_f(p_f - p_0) + \beta_m(p_m - p_0)), \end{aligned} \quad (4)$$

where ϕ_f is the fracture porosity, %; ϕ_{f0} is the initial fracture porosity, %; ε_L is Langmuir volumetric strain constant, Pa; p_0 is the initial pressure in the matrix Langmuir pressure constant; M is block length, m.

According to the Kozeny–Carman equation [31, 32], the coal seam permeability k is

$$\frac{k}{k_0} = \left(1 + \frac{1}{M\phi_{f0}} (\beta_f(p_f - p_0) + \beta_m(p_m - p_0)) + \frac{\varepsilon_L}{\phi_{f0}} \left(\frac{K}{M} - 1 \right) \left(\frac{p_m}{P_L + p_m} - \frac{p_0}{P_L + p_0} \right) \right)^3, \quad (5)$$

where k_0 is the coal seam permeability, m^2 .

2.4. Diffusion Equation of Gas in Coal. The mass exchange between the matrix and the fissures in the coal body can be expressed by the following equation:

$$Q_m = D\chi \frac{M_C}{RT} (p_m - p_f), \quad (6)$$

where Q_m is the mass exchange between coal pores and cracks, $\text{kg}/(\text{m}^3 \cdot \text{s})$; χ is the matrix shape factor, m^{-2} ; M_C is the molar mass of methane, kg/mol ; D is gas diffusion coefficient, m^2/s ; R is the universal gas constant, $\text{J}/(\text{mol} \cdot \text{K})$; and T is the coal seam temperature, K .

The following formula can calculate the diffusion coefficient:

$$D = D_0 \exp(-\xi t), \quad (7)$$

where ξ is the attenuation coefficient of the dynamic diffusion coefficient, s^{-1} , and D_0 is the initial gas diffusion coefficient, m^2/s .

According to the Langmuir equation, the gas content per unit volume of coal matrix can be obtained as

$$m_p = \frac{abp_m\rho_c M_C}{(1 + bp_m)V_m} + \phi_m \frac{M_C p_m}{RT}, \quad (8)$$

where m_p is the gas content per unit mass of the coal matrix, kg/m^3 ; ρ_c is the apparent density of the coal, kg/m^3 ; ϕ_m is the matrix porosity, %; a is the Langmuir volume constant, m^3/kg ; b is the reciprocal of Langmuir pressure constant, Pa^{-1} ; and V_m is the molar volume of methane under standard conditions, m^3/mol .

From the conservation of mass, it can be seen that the relationship between the amount of change in matrix gas content and Q_m is

$$\frac{\partial m_p}{\partial t} = -Q_m. \quad (9)$$

Substituting (6) ~ (8) into (9), the governing equation for gas diffusion is

$$\frac{\partial p_m}{\partial t} = -\frac{b\chi V_m (p_m - p_f) (p_m + P_L)^2}{aRT\rho_c + b\phi_m V_m (p_m + P_L)^2} D_0 \exp(-\xi t). \quad (10)$$

2.5. The Seepage Equation of Gas in Coal. According to the law of conservation of mass, the change in gas mass in a fracture is equal to the gas diffused into the fracture by the pore minus the gas flowing into the borehole from the fracture; namely,

$$\frac{M_C}{RT} \frac{\partial \phi_f p_f}{\partial t} = Q_m (1 - \phi_f) - \nabla \left(\frac{M_C}{RT} p_f v_f \right), \quad (11)$$

where v_f is the gas flow velocity in the crack, m/s .

Moreover, the flow of gas in the cracks of the coal body conforms to Darcy's law; then,

$$v_f = -\frac{k}{\mu} \nabla p_f, \quad (12)$$

where μ is the dynamic viscosity of the gas, $\text{Pa} \cdot \text{s}$.

By combining the above equations, the governing equation of gas percolation can be obtained as

$$\phi_f \frac{\partial p_f}{\partial t} + p_f \frac{\partial \phi_f}{\partial t} - \nabla \left(p_f \frac{k}{\mu} \nabla p_f \right) = D\chi (p_m - p_f) (1 - \phi_f). \quad (13)$$

2.6. Deformation Equation of Gas-Bearing Coal. The deformation equation of gas-containing coal is composed of the stress balance equation, geometric deformation equation, and stress-strain relationship [33], which can be expressed as

$$Gu_{i,jj} + \frac{G}{1 - 2\nu} u_{j,ji} - \beta_f p_{f,i} - \beta_m p_{m,i} + F_i = 0, \quad (14)$$

where G is the coal's shear modulus, MPa , and u_i is the displacement component in the i -direction.

The above control equations constitute a multifield coupling model for gas-containing coal seams that comprehensively consider the coal skeleton compression effect (effective stress effect) and matrix shrinkage effect. The coupling relationship between the physical fields is shown in Figure 1.

3. Geometric Model and Definite Solution Conditions

3.1. Geometric Model. In order to analyze the effect of gas drainage with long boreholes along the seam, two gas

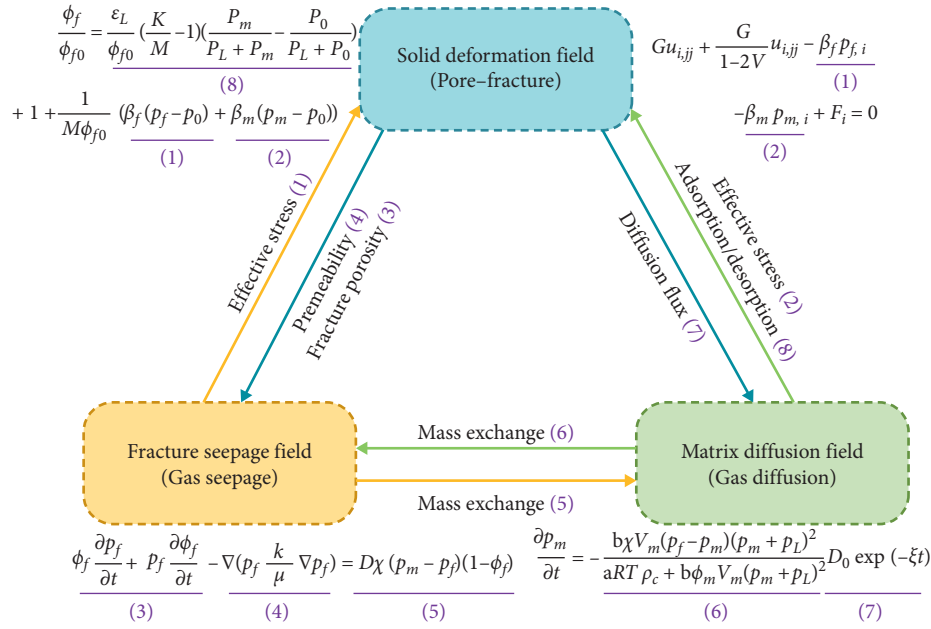


FIGURE 1: Schematic diagram of physics coupling relationship.

drainage schemes under two conditions have been established :

- (1) Gas drainage with long boreholes along the seam
The geometric model is shown in Figure 2. The 240 m long boreholes along the seam were constructed in the direction of the coal seam's inclination in the machine roadway or wind roadway in the working face. The borehole spacing distance is 2 m, and ten long boreholes along the seam were constructed.
- (2) The combination of long boreholes along the seam and penetrating boreholes
The geometric model is shown in Figure 3. The 90 m long boreholes along the seam were constructed in the machine lane and the winding lane in the working face along the direction of the inclination of the coal seam. The borehole spacing distance is 2 m, and 20 long boreholes along the seam were constructed. Moreover, the penetrating boreholes were constructed in the middle of the working face of the bottom-drawing roadway, and the position of the final hole of the penetrating boreholes is shown in Figure 3. The boreholes are spaced 2 m apart in both the strike and inclination directions, and a total of 290 penetrating boreholes have been constructed.

The size of the coal seam under these two drainage schemes is 400×240 m.

The numerical simulation software used in this study is COMSOL Multiphysics. The simulation uses the PDE module and the solid mechanics module in COMSOL to calculate the model. The parameters used in the numerical simulation are shown in Table 1 [17].

3.2. Model Validation. To verify the correctness of the multi-field coupling model of gas-bearing coal seams established in this paper, the use of mathematical models of Liu et al. [16] coal seam gas pressure data was compared to verify. A model consisting of three horizontal coal layers was established. There is a coal seam with a width of 40 meters and a height of 4 meters between the two rock layers. The drill hole is located in the center of the coal seam. The other parameters used in the model are consistent with those in the Liu model. After COMSOL numerical calculation, the experimental results are shown in Figure 4. It can be seen from Figure 4 that the gas-solid coupling model established in this paper is in good agreement with Liu's model.

4. Quantitative Characterization of Gas Drainage Effect in Boreholes

It can be seen from Section 1 that, at time t and $t + \Delta t$, the gas content in the coal seam is

$$m_t = \frac{V_L p_m(t)}{p_m(t) + P_L} \frac{M_c}{V_M} \rho_c + \phi_m \frac{M_c}{RT} p_m(t),$$

$$m_{t+\Delta t} = \frac{V_L p_m(t + \Delta t)}{p_m(t + \Delta t) + P_L} \frac{M_c}{V_M} \rho_c + \phi_m \frac{M_c}{RT} p_m(t + \Delta t). \quad (15)$$

In the formula, m_t and $m_t + \Delta m_t$ represent the gas content in the coal seam when the drainage time is t and $t + \Delta t$, respectively.

According to the above formula, the gas content extracted from the coal seam after the gas drainage of Δt time is as follows:

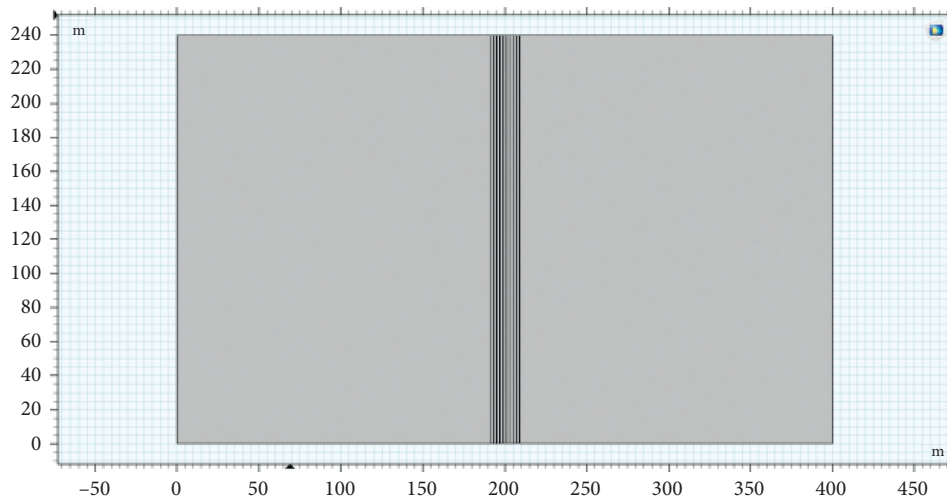


FIGURE 2: The arrangement of long boreholes along the seam.

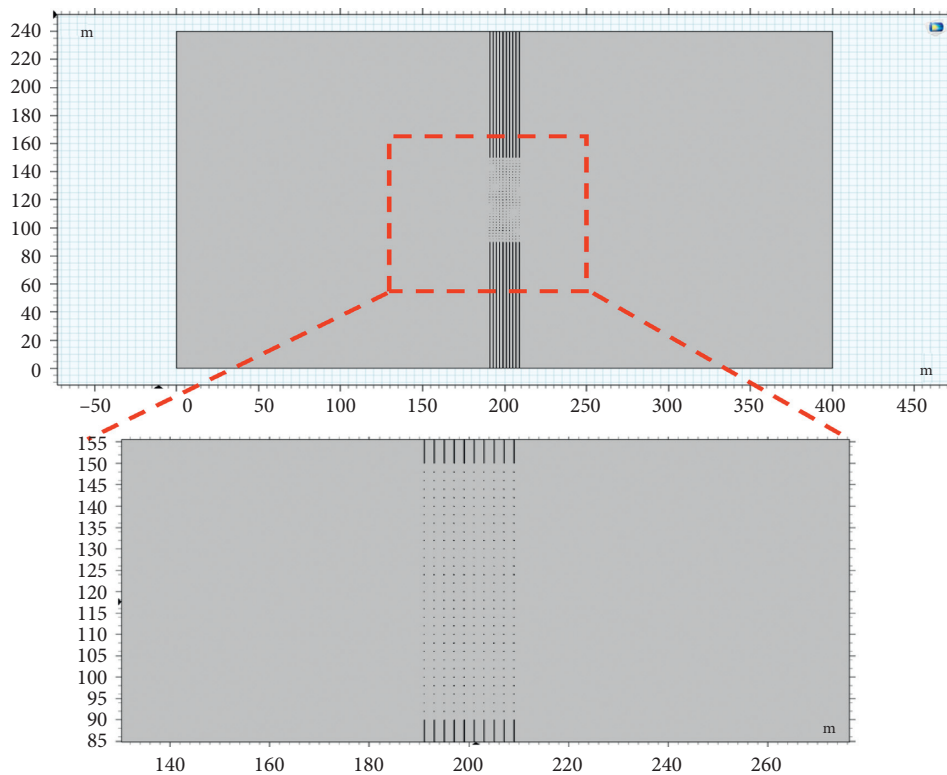


FIGURE 3: Borehole layout method for gas drainage combined with long boreholes along the seam and penetrating boreholes.

$$m_{\Delta t} = \iint_{\Omega} (m_t - m_{t+\Delta t}) dv. \quad (16)$$

Based on the above formula, the gas content extracted within a certain period can be obtained by integration with COMSOL software.

5. Results and Discussion

5.1. Influence of Drilling Layout on the Effect of Gas Drainage.

Figure 5 is a cloud map of coal seam gas content under different drainage times in long boreholes along the seam. It can be seen from Figure 5 that, under the action of negative

TABLE 1: Parameters used in numerical simulation [17].

Parameter	Value
Modulus of elasticity of coal	2713 MPa
Poisson's ratio of coal	0.339
Initial porosity	0.072
Initial gas pressure	1.08 MPa
Initial coal permeability	0.02 mD
Coal initial diffusion coefficient	$1 \times 10^{-12} \text{ m}^2/\text{s}$
Attenuation coefficient	$2 \times 10^{-8} \text{ s}^{-1}$
Langmuir pressure constant	1.8672 MPa^{-1}
Langmuir volume constant	$14.4348 \text{ m}^3/\text{t}$
Coal density	1250 kg/m^3
The molar mass of methane	0.016 kg/mol
Drainage time	360 d
Time step	1 d
Ambient temperature	293 K

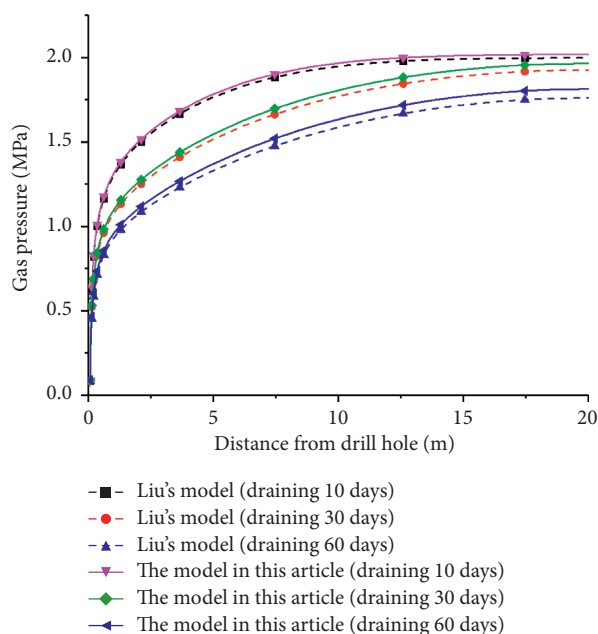


FIGURE 4: Data comparison between the model in this article and Liu's model at different extraction times.

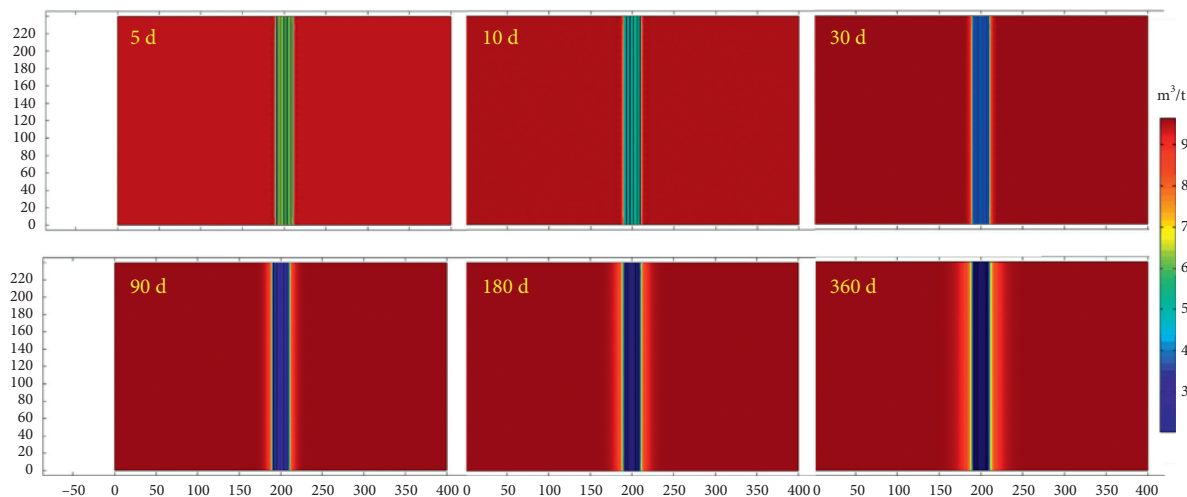


FIGURE 5: Cloud map of coal seam gas content under different drainage time in the case of long boreholes along the seam.

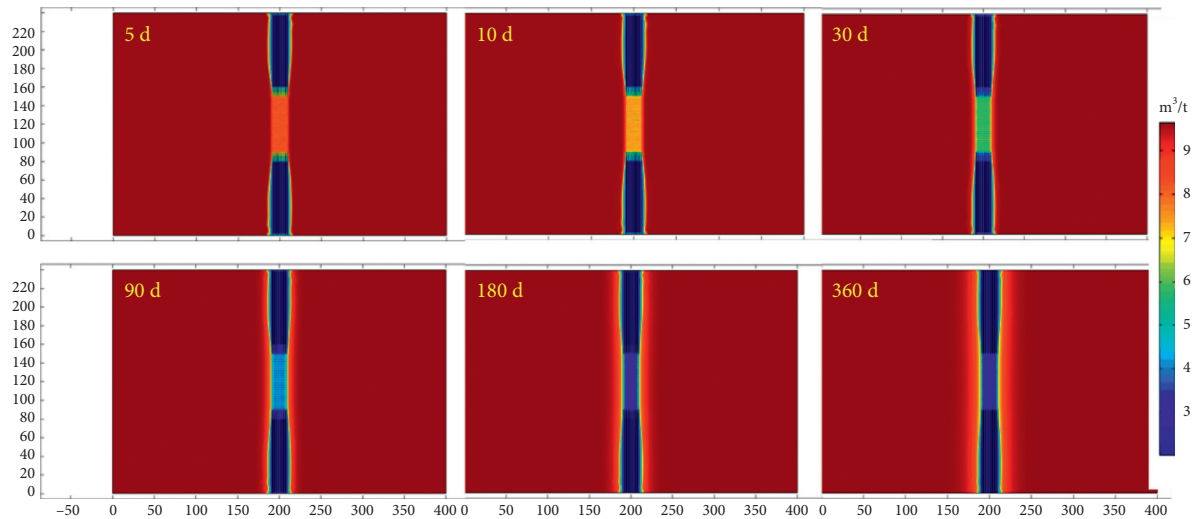


FIGURE 6: Cloud map of coal seam gas content under different drainage times under the combined drainage of long boreholes along the seam and penetrating boreholes.

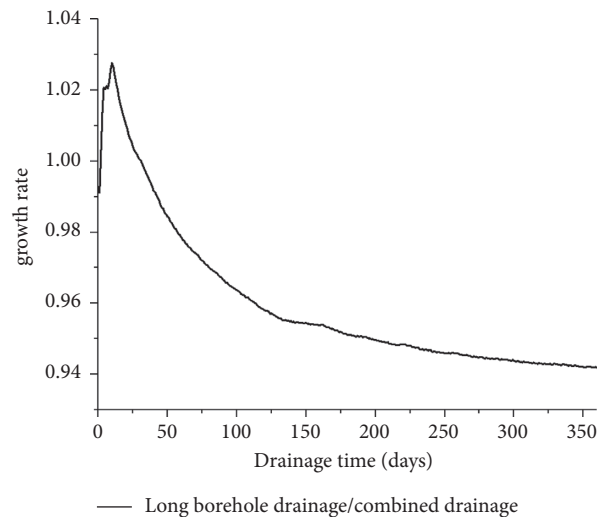


FIGURE 7: Long boreholes drainage growth rate.

pressure in the borehole, the gas pressure around the borehole is significantly lower than that of the distant coal body. Furthermore, because the borehole spacing distance is only 2 m, the gas pressure between the drill holes is significantly reduced, and there is no apparent blank zone. In addition, the length of the borehole reaches 240 meters and runs through the entire working face. Therefore, the contact area between the borehole and the coal body is large, and the drainage effect is good. On the other hand, as the drainage time increases, the gas content around the borehole gradually decreases, and the influence range of borehole drainage gradually increases. For example, after 360 days of drainage, the gas content of the coal body covered by the borehole was significantly reduced to $3 \text{ m}^3/\text{t}$, which was significantly lower than the gas content of 5 days of drainage.

At present, due to limited drilling rig equipment in some domestic mining areas, the construction length of long boreholes along the seam is limited, so there must be a blank

zone of gas drainage in the middle of the working face. To ensure the safety of the working face during the mining period, penetrating boreholes are usually used to extract the coal seam gas in the middle of the working face. The boreholes arrangement in this section is based on the above facts.

Figure 6 is a cloud map of coal seam gas content under different drainage times in combined drainage with long boreholes along the seam and penetrating boreholes. It can be seen from Figure 6 that the distribution of residual gas content in coal seams is different from that in Figure 5. The gas content in long boreholes along the seam drainage area is significantly lower than that of penetrating boreholes drainage area. For example, at five days of drainage, the gas content in the area covered by the long boreholes along the seam has dropped to $4 \text{ m}^3/\text{t}$, while the gas content in the penetrating boreholes covering the coal seam is about $8 \text{ m}^3/\text{t}$. According to the analysis in Section 1, the gas drainage

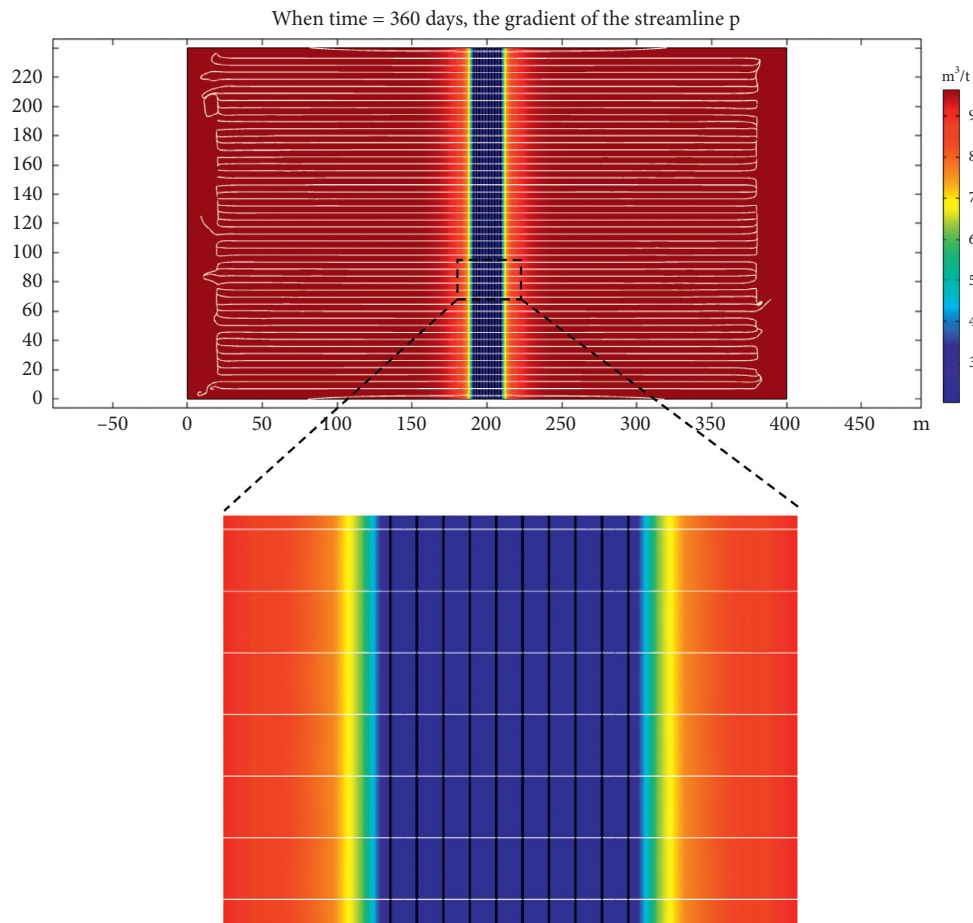


FIGURE 8: Streamline diagram of the long boreholes along the seam.

volume per unit time of a borehole is mainly determined by the permeability and the contact area of the borehole. Therefore, the gas drainage effect of long boreholes along the seam is significantly higher than that of penetrating boreholes. In addition, with the increase of the extraction time, the gas content of the coal body around the borehole is consistent with the previous analysis. One point that needs to be particularly pointed out is that, with the increase of the drainage time, the difference between the gas drainage effect of the long boreholes along the seam and the penetrating boreholes gradually decreases.

For example, at 360 days of drainage, the gas content in the long boreholes along the seam area is about $2.5 \text{ m}^3/\text{t}$, and the gas content in the penetrating boreholes area is also reduced to about $3 \text{ m}^3/\text{t}$.

It can be seen that the drainage effect of the long boreholes along the seam arrangement is significantly higher than that of the combined long boreholes along the seam and penetrating boreholes. However, it is difficult to intuitively compare the drainage effects of the two drilling arrangements based on the distribution cloud map of the residual gas content after coal seam drainage. To solve the problems mentioned above, this paper proposes a quantitative characterization method for the effect of borehole gas drainage in Section 3. Based on this quantitative characterization

method, the gas drainage volume under different borehole layouts can be obtained. This paper takes the combined drainage volume of long boreholes along the seam and penetrating boreholes as the benchmark. It can be concluded that there is an increase in drainage under the condition of long boreholes along the seam relative to the combined drainage, as shown in Figure 7. It can be seen from Figure 7 that the gas drainage volume in the bedding long borehole layout is similar to the gas drainage volume under the combined layout under the same drainage time. For example, in the early stage of drainage, the drainage volume under the long borehole layout is 1.025 times that of the combined drainage, and it gradually decreases in the later stage, down to 0.94 times at the lowest level. In addition, considering the construction cost of tunnel extraction and drilling through layers, it can be considered that the long boreholes along the seam can reduce the pressure and content of coal seam gas faster in the process of gas drainage in coal mines. The danger of gas outbursts in the working face is eliminated, and construction costs are reduced.

Figures 8 and 9 are the streamline diagram of the long boreholes along the seam and the streamline diagram of the combined boreholes through bedding during the 360-day drainage. It can be seen from Figure 8 that the gas migration streamlines of the long boreholes along the seam are

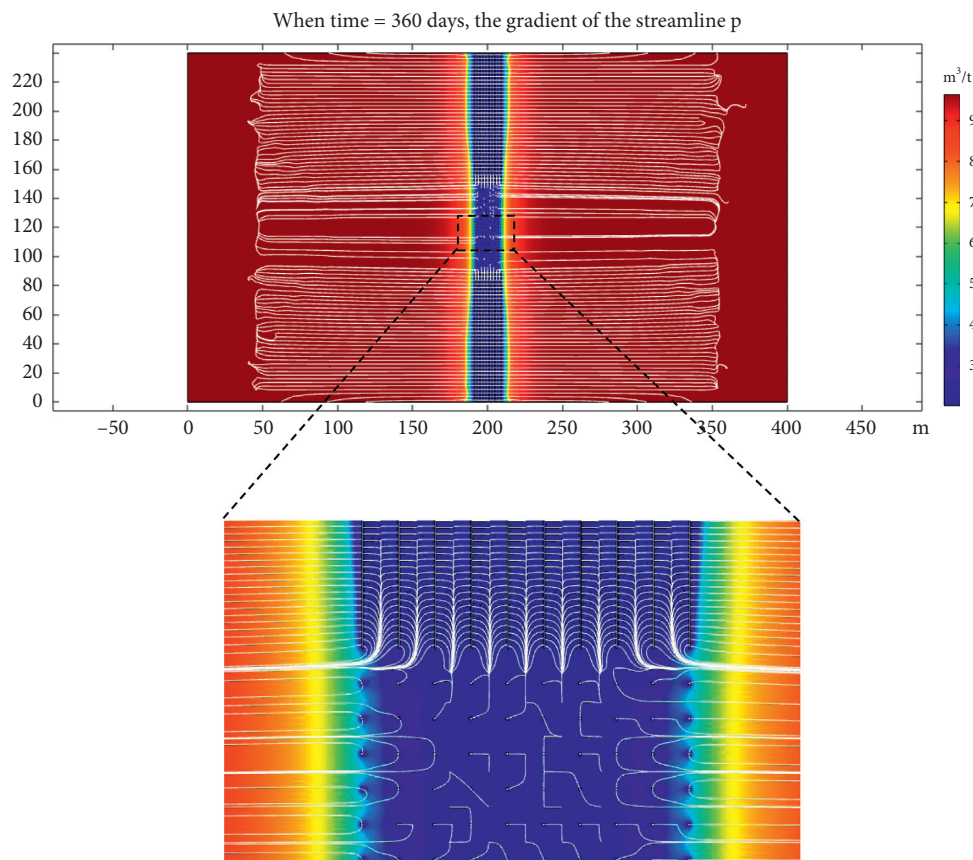


FIGURE 9: Streamline diagram of the combined layout of penetrating boreholes and the long boreholes along the seam.

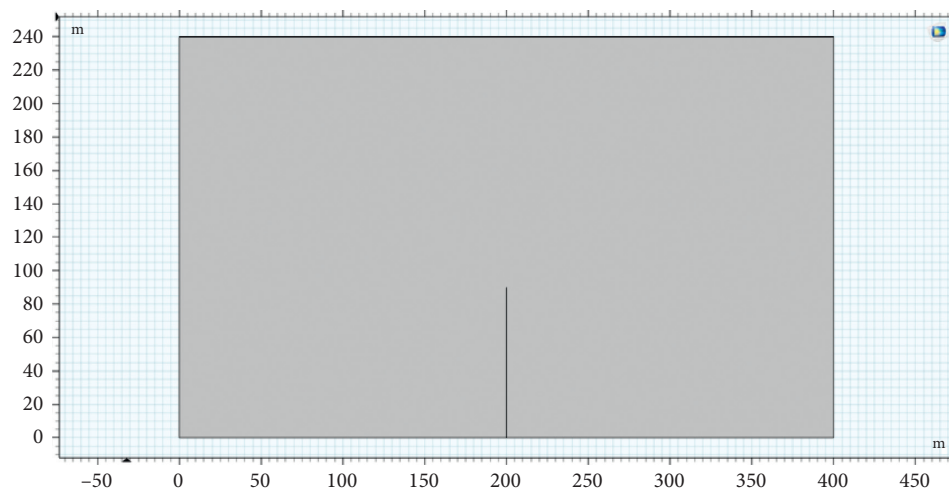


FIGURE 10: 90 m drilling geometry model.

perpendicular to the borehole. The gas flows neatly and orderly to the boreholes, with almost no influence on each other, conforming to radial flow. It can be seen from Figure 9 that the gas streamlines in the long boreholes along the seam area still show a radial flow, while the gas flow in the penetrating boreholes area is messy. In addition, the turbulent gas streamlines interfere with each other at the intersection of the long boreholes along the seam and

penetrating boreholes. The gas migration between boreholes is subject to drainage forces in multiple directions, not conducive to gas drainage.

The above analysis compares and analyzes the drainage effect of the arrangement of long boreholes along the seam and the combined arrangement of penetrating boreholes and the long boreholes along the seam from the three aspects of gas drainage volume, gas flow line, and drilling construction

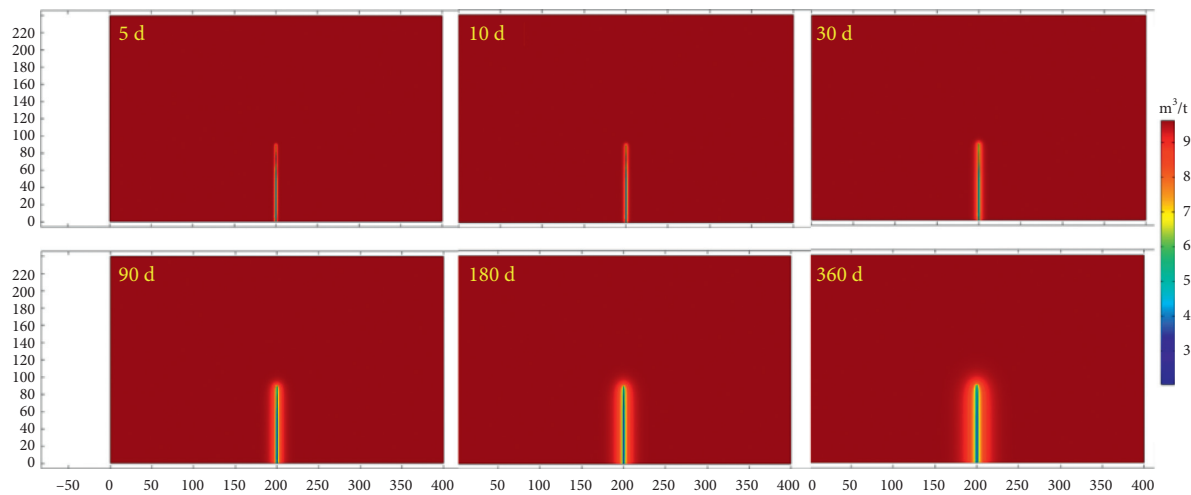


FIGURE 11: Cloud map of coal seam gas content distribution under different drainage time of 90-meter borehole.

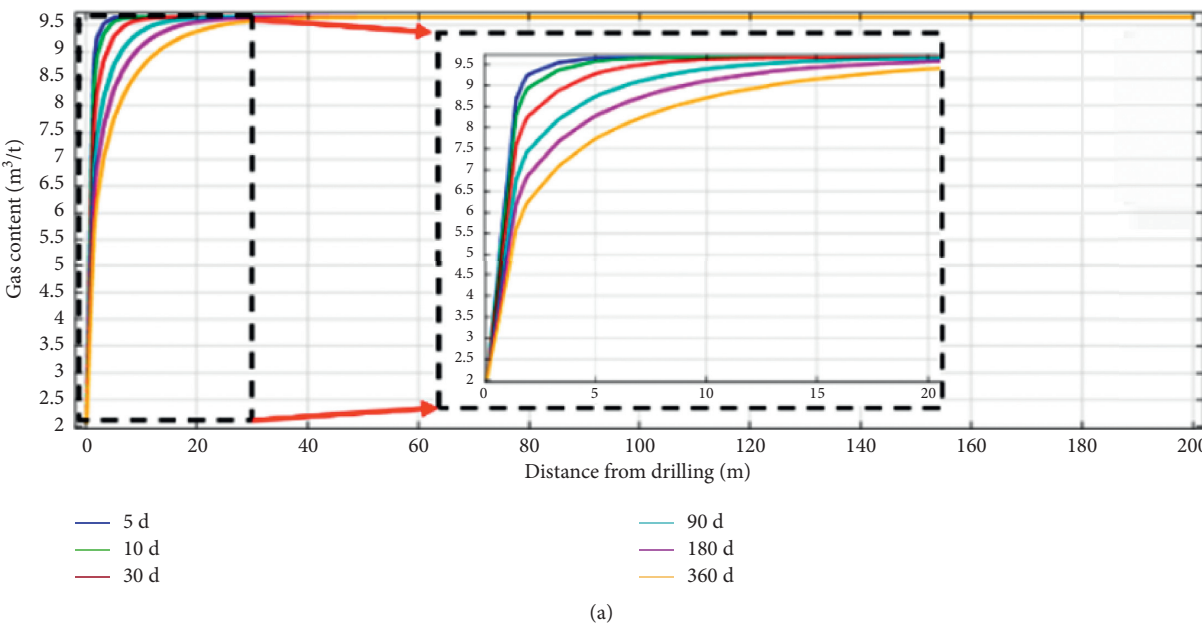


FIGURE 12: Continued.

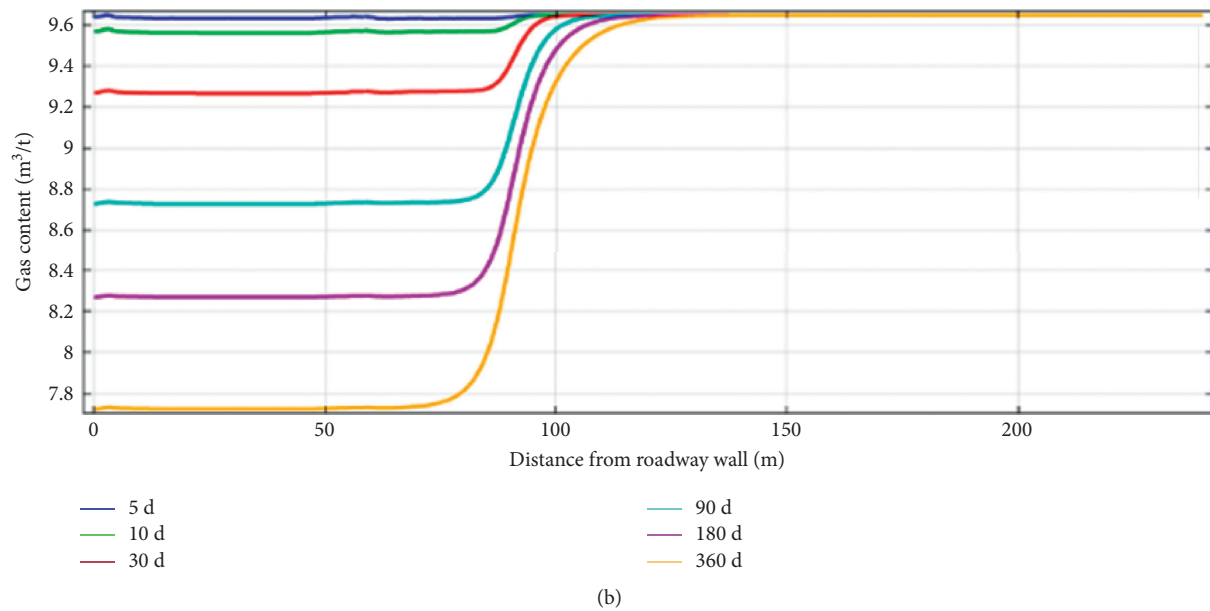


FIGURE 12: Distribution of gas content in 90 m borehole with different drainage time: (a) gas content distribution on the monitoring line in the strike direction; (b) distribution of gas content in the trend direction monitoring line.

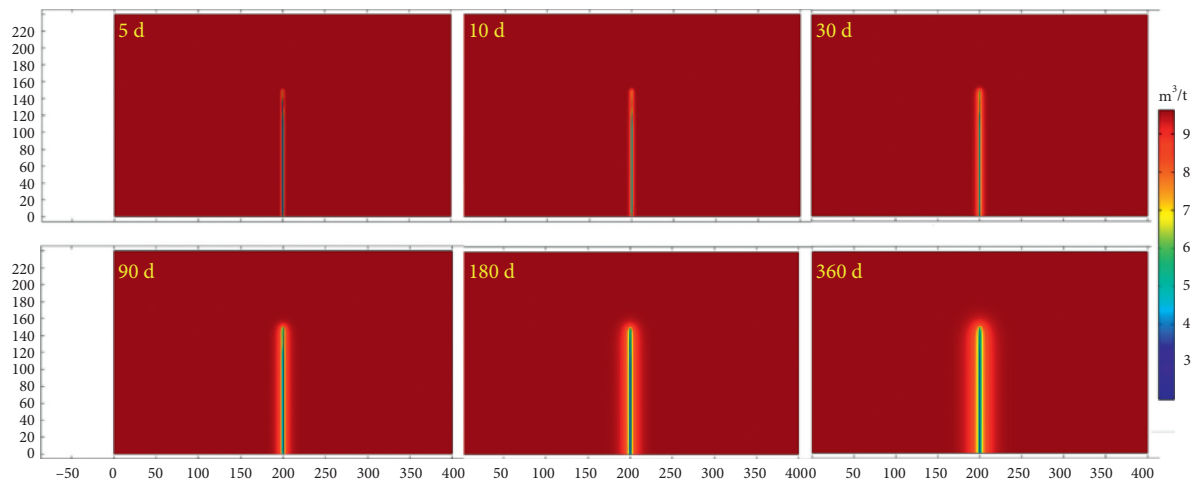


FIGURE 13: Cloud map of coal seam gas content under different drainage time of 150-meter borehole.

cost. It can be seen that long boreholes along the seam have advantages in all aspects. Therefore, it is recommended that the arrangement of long boreholes along the seam is used in gas drainage in the working face.

5.2. Influence of Drilling Length on the Effect of Gas Drainage.

To study the impact of the length of the long borehole along the bedding on gas drainage, numerical simulations of gas drainage with borehole lengths of 90 m, 120 m, 150 m, 180 m, 210 m, and 240 m were carried out. The geometric model is shown in Figure 10.

When the borehole length is 90 m, the gas content distribution around the borehole at different extraction times is shown in Figure 11. It can be seen from Figure 11 that, under the action of the borehole negative pressure, as

the drainage time increases, the gas content around the borehole gradually decreases, and the range of influence of borehole drainage gradually increases.

To quantitatively analyze the distribution of gas content around the borehole under different extraction times, a monitoring line is selected along the direction and inclination of the working face, and the gas content change law on it is analyzed. The monitoring line in the strike direction is 45 m away from the roadway wall, and the monitoring line in the inclined direction is first 5 m away from the borehole. Figure 12 shows the distribution of gas content on the monitoring line under different extraction times. From Figure 12(a), when the borehole length is 90 m, in the strike direction, as the drainage time increases, the gas content of the coal seam gradually decreases. At a distance of 5 m from the borehole, the gas content at a drainage time of 180 days is

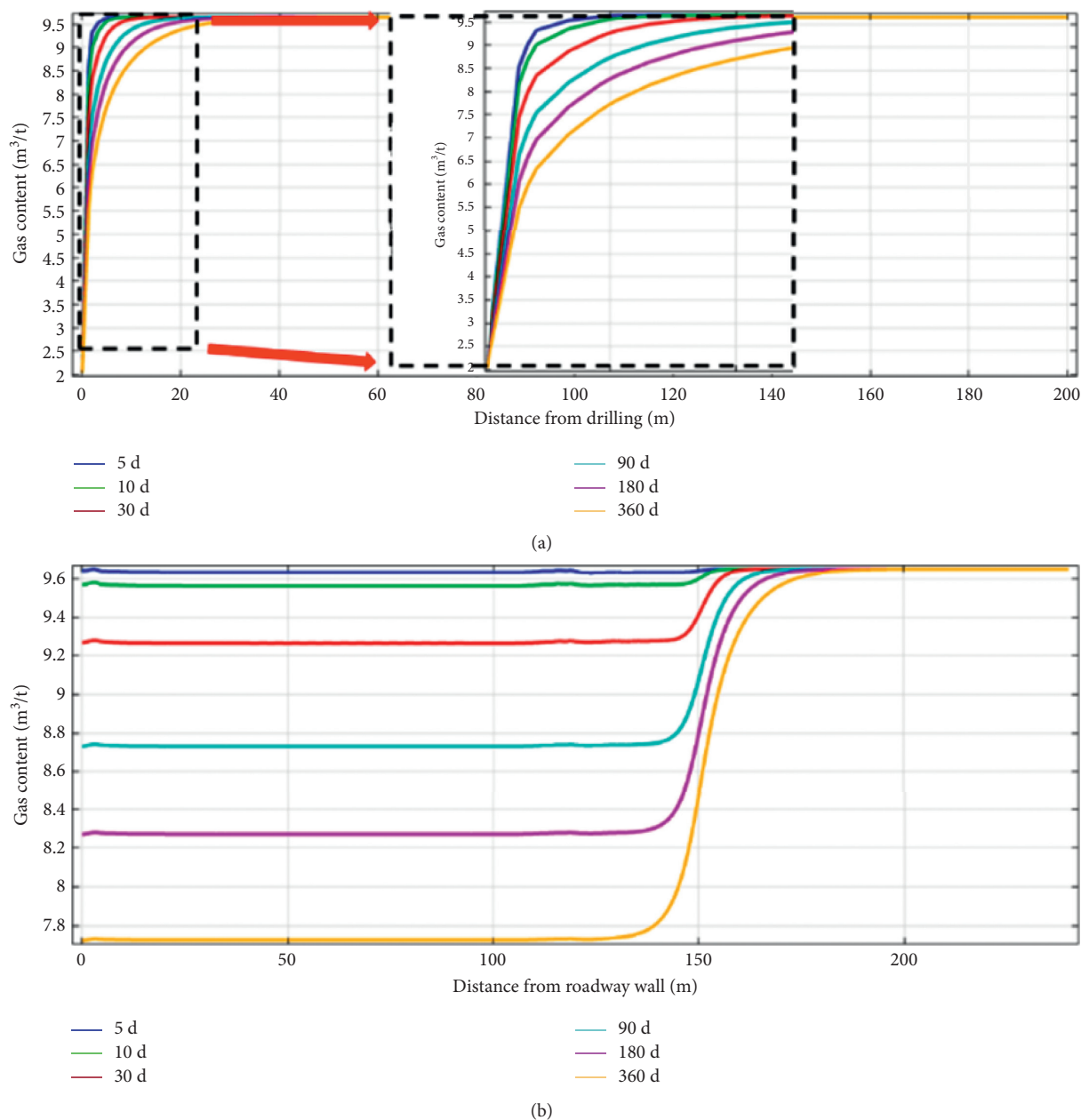


FIGURE 14: Distribution of gas content in 150 m borehole with different drainage time: (a) gas content distribution on the monitoring line in the strike direction; (b) distribution of gas content in the trend direction monitoring line.

reduced by $1.0 \text{ m}^3/\text{t}$ and $1.3 \text{ m}^3/\text{t}$ compared with the gas content at a drainage time of 30 days and five days. In the direction of the trend, the gas content of the coal seam gradually decreases with the increase of the extraction time. However, because the length of the borehole is only 90 m, part of the gas in the middle and back of the coal seam has not been effectively drained.

When the borehole length is 150 m, the gas content distribution around the borehole under different extraction time is shown in Figure 13. It can be seen from Figure 13 that, under the action of borehole negative pressure, as the drainage time increases, the gas content around the borehole gradually decreases, and the range of influence of borehole

drainage gradually increases. Compared with the 90 m borehole, the 150 m borehole has a broader range of drainage, and the drainage effect is more significant.

In the strike direction, as the drainage time increases, the coal seam gas content gradually decreases. At a distance of 5 m from the borehole, the gas content at 180-day drainage is reduced by $0.94 \text{ m}^3/\text{t}$ and $1.26 \text{ m}^3/\text{t}$ compared with the gas content at the drainage time of 30 days and five days, and the change is small compared to the 90 m borehole, as shown in Figure 14.

When the borehole length is 240 m, the gas content distribution around the borehole under different extraction time is shown in Figure 15. It can be seen from Figure 15

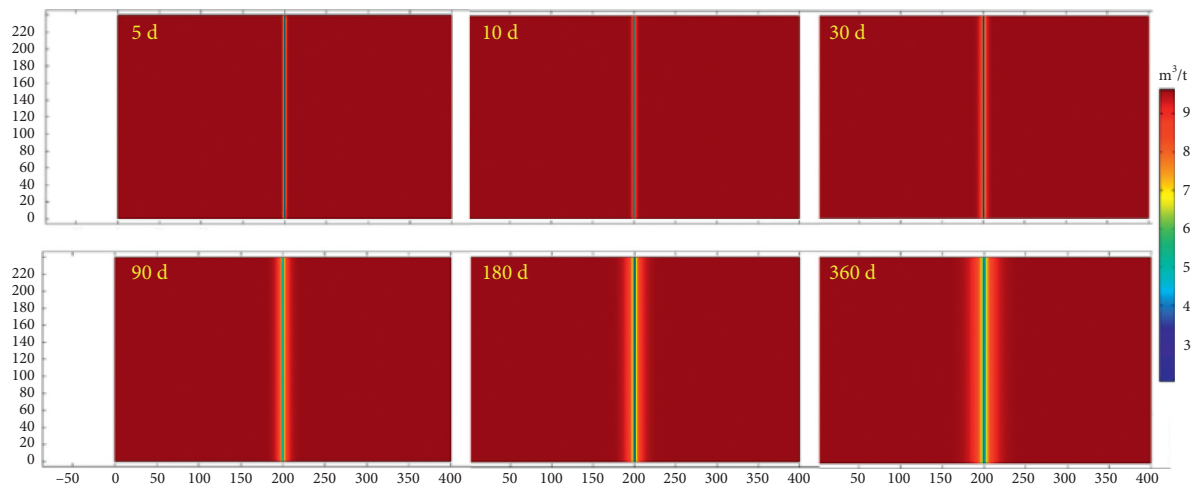


FIGURE 15: Cloud map of coal seam gas content under different drainage time of 240-meter borehole.

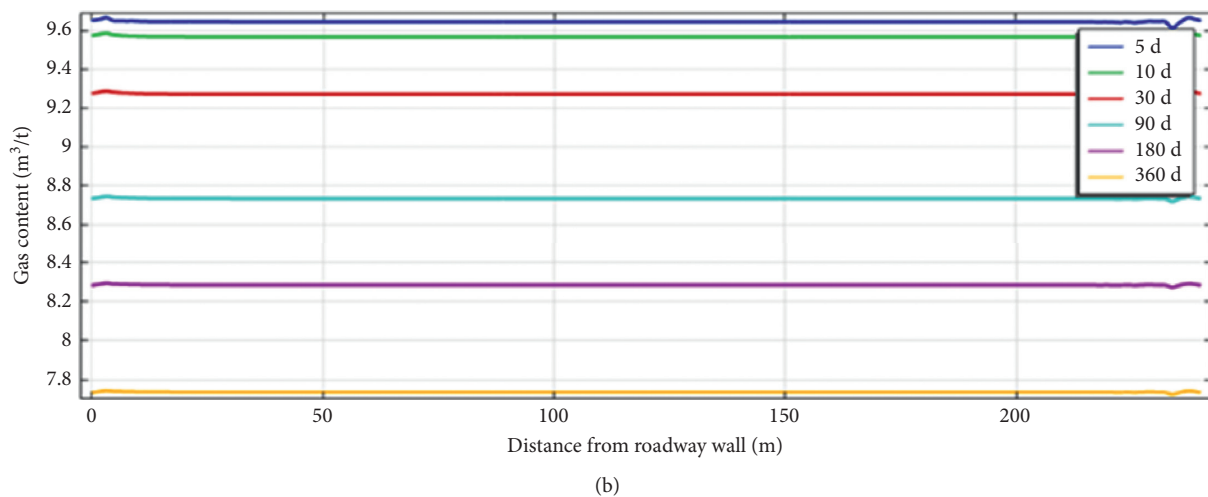
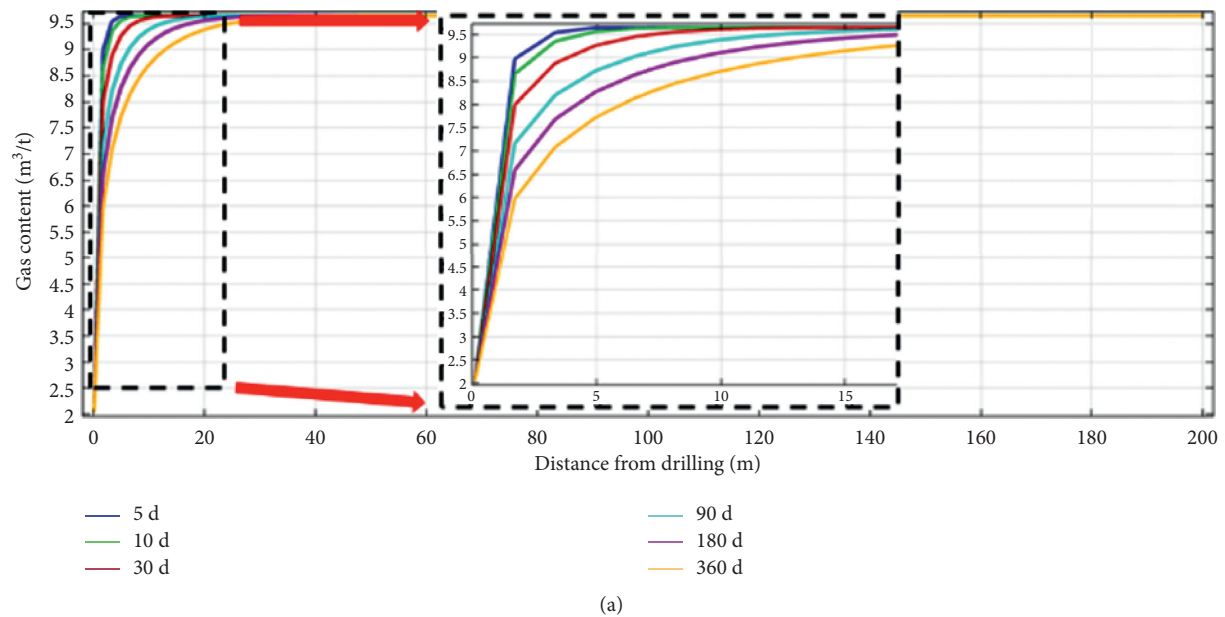


FIGURE 16: Distribution of gas content in 240 m borehole with different drainage time: (a) gas content distribution on the monitoring line in the strike direction; (b) distribution of gas content in the trend direction monitoring line.

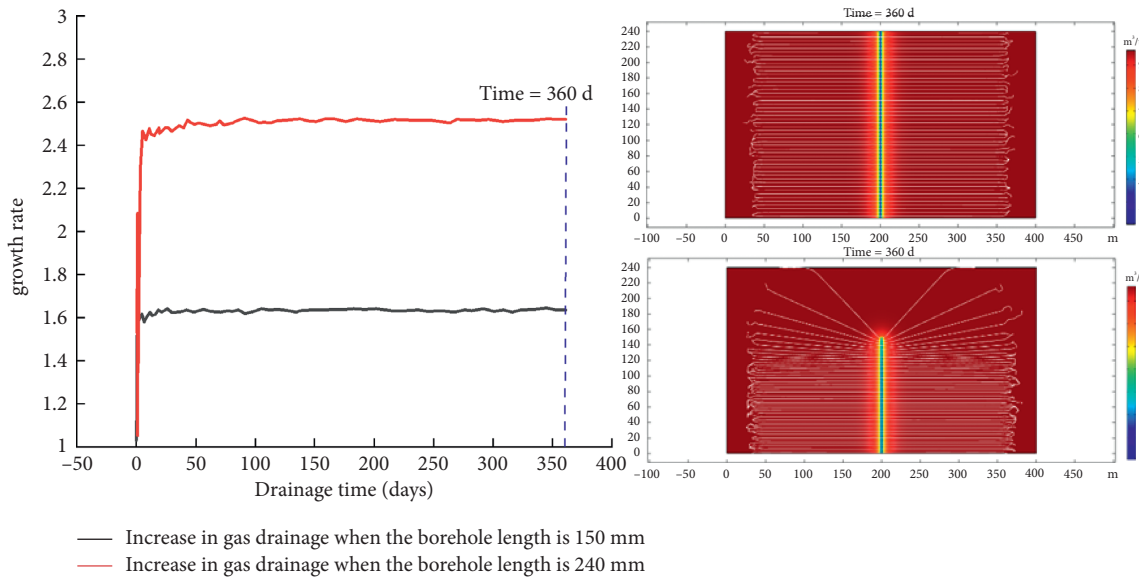


FIGURE 17: Gas drainage ratio under different borehole lengths.

that, under the action of borehole negative pressure, as the drainage time increases, the gas content around the borehole also shows a gradual decrease, and the influence range of borehole drainage further increases.

In the strike direction, as the drainage time increases, the coal seam gas content gradually decreases. In the trend direction, the gas content in the coal seam gradually decreases with the increase of the extraction time, and the gas content at the bottom of the borehole decreases significantly. With the increase of drilling depth, the upward trend value changes less. As the drilling depth increases, the gas at the bottom of the drilling hole can be drained, and the gas content decreases significantly, as shown in Figure 16.

To quantitatively analyze the impact of borehole length on the gas drainage effect, the drainage volume when the borehole length is 90 m is used as the benchmark. The increase in the drainage of the 150 m and 240 m borehole lengths relative to the 90 m borehole can be obtained, as shown in Figure 17. It can be seen from Figure 17 that the longer the borehole length, the better the drainage effect and the greater the impact range of the borehole. When the borehole length is 150 m, the drainage volume is about 1.31 times that of the 90 m borehole; when the borehole length is increased to 240 m, the drainage volume is about 2.50 times that of the 90 m borehole. It can be seen from Figure 17 that the flow line after drilling is perpendicular to the drilling, the gas migration at the tip of the slot conforms to the law of spherical flow, and the gas migration in the middle and rear parts conforms to the radial flow. With the increase of drilling length, the streamline area and the influence range of drilling increase significantly.

6. Conclusions

This paper first elaborates and establishes a multifield coupling model of gas migration in coal. Then, the change value of the residual gas content per unit time is used to

quantify the gas drainage effect of the long borehole. Finally, the COMSOL software was adopted to analyze the drainage effects of different layouts and drilling lengths of long boreholes along the bedding. The main conclusions are as follows:

- (1) A multifield coupling model for gas-containing coal seams was established. The model considers the gas diffusion in the coal matrix, the gas seepage through fractures, the evolution of permeability, and the deformation of coal. At the same time, the dynamic equation of coal diffusion is introduced to make the simulation results more in line with the actual situation.
- (2) By integrating the space of the coupled model and then making the difference in time, the change value of the residual gas content per unit time can be obtained to calculate the gas drainage volume. Furthermore, the gas drainage effect of long boreholes can be quantified.
- (3) Under the combined layout of long boreholes along the seam and penetrating boreholes, the gas content of the long boreholes along the seam area is significantly lower than that of the interbedded borehole drainage area.
- (4) The drainage volume is similar to that under the combined arrangement under the same drainage time. In the early stage of drainage, the drainage volume under the long borehole layout is 1.025 times that of combined drainage, and it gradually decreases in the later stage, down to 0.94 times at the lowest level.
- (5) As the length of the borehole increases, the scope of influence of borehole drainage increases. When the borehole length is 150 m and 240 m, the drainage volume is about 1.31 and 2.50 times that of the 90 m borehole.

References

- [1] G. W. Cheng, T. H. Yang, H. Y. Liu et al., "Characteristics of stratum movement induced by downward longwall mining activities in middle-distance multi-seam," *International Journal of Rock Mechanics and Mining Sciences*, vol. 136, pp. 1365–1609, 2020.
- [2] J. Liu, J. Wang, Z. Chen, S. Wang, D. Elsworth, and Y. Jiang, "Impact of transition from local swelling to macro swelling on the evolution of coal permeability," *International Journal of Coal Geology*, vol. 88, no. 1, pp. 31–40, 2011.
- [3] J. Y. Fan, P. Liu, J. J. Li, and D. Jiang, "A coupled methane/airflow model for coal gas drainage: model development and finite-difference solution," *Process Safety and Environmental Protection*, vol. 141, pp. 288–304, 2020.
- [4] D. L. Fu, G. S. Xu, M. Li et al., "Gas generation from coal: taking Jurassic coal in the Minhe Basin as an example," *International Journal of Coal Science & Technology*, vol. 7, no. 3, pp. 611–622, 2020.
- [5] G. Z. Hu, J. L. Xu, T. Ren, Y. Dong, W. Qin, and Z. Shan, "Field investigation of using water injection through in-seam gas drainage boreholes to control coal dust from the longwall face during the influence of abutment pressure," *International Journal of Mining, Reclamation and Environment*, vol. 30, no. 1, pp. 48–63, 2016.
- [6] H. B. Zhao, J. Y. Li, Y. H. Liu, Y. Wang, T. Wang, and H. Cheng, "Experimental and measured research on three-dimensional deformation law of gas drainage borehole in coal seam," *International Journal of Mining Science and Technology*, vol. 30, no. 3, pp. 397–403, 2020.
- [7] C. S. Zheng, M. Kizil, Z. W. Chen, and A. Saïed, "Effects of coal damage on permeability and gas drainage performance," *International Journal of Mining Science and Technology*, vol. 27, no. 5, pp. 783–786, 2017.
- [8] Y. Xue, P. G. Ranjith, F. N. Dang, and J. Liu, "Analysis of deformation, permeability, and energy evolution characteristics of coal mass around borehole after excavation," *Natural Resources Research*, vol. 29, no. 5, pp. 3159–3177, 2020.
- [9] F. B. Zhou, T. Q. Xia, X. X. Wang, Y. Zhang, Y. Sun, and J. Liu, "Recent developments in coal mine methane extraction and utilization in China: a review," *Journal of Natural Gas Science and Engineering*, vol. 31, pp. 437–458, 2016.
- [10] J. J. Hu, C. Gao, H. P. Xie, J. Wang, M. Li, and C. Li, "Anisotropic characteristics of the energy index during the shale failure process under triaxial compression," *Journal of Natural Gas Science and Engineering*, vol. 95, Article ID 104219, 2021.
- [11] C. B. Li, D. C. Yang, H. P. Xie, L. Rin, and J. Wang, "Research on the anisotropic fracture behavior and the corresponding fracture surface roughness of shale," *Engineering Fracture Mechanics*, vol. 255, no. 5, Article ID 107963, 2021.
- [12] Y. K. Ma, E. Y. Wang, D. Xiao, and Z. Li, "Acoustic emission generated during the gas sorption-desorption process in coal," *International Journal of Mining Science and Technology*, vol. 22, no. 3, pp. 391–397, 2012.
- [13] S. Harpalani and R. A. Schraufnagel, "Shrinkage of coal matrix with release of gas and its impact on permeability of coal," *Fuel*, vol. 69, no. 5, pp. 551–556, 1990.
- [14] Z. D. Liu, Y. P. Cheng, L. Wang, H. Wang, J. Jiang, and W. Li, "Analysis of coal permeability rebound and recovery during methane extraction: implications for carbon dioxide storage capability assessment," *Fuel*, vol. 230, pp. 298–307, 2018.

Determination of Shear Strength in RC Beams Using ANN Trained with Tabu Search Training Algorithm

Atul, *Department of Civil Engineering, Aryan Institute of Engineering & Technology, Bhubaneswar, atul226@outlook.com*

Ajaya Kumar Beura, *Department of Mechanical Engineering, Aryan Institute of Engineering & Technology, Bhubaneswar, akbeura25@gmail.com*

Shradha Jena, *Department of Civil Engineering, Capital Engineering College, Bhubaneswar, shradhajena98@gmail.com*

Deepika Priyadarshini Palai, *Department of Civil Engineering, NM Institute of Engineering & Technology, Bhubaneswar, deepikadalai2561@gmail.com*

ABSTRACT

The shear failure of reinforced concrete (RC) beams is a critical issue and has attracted the attention of researchers. The specific challenges of shear failure are the numerous factors affecting shear strength, the nonlinear behavior, and the nonlinear relationship between affecting parameters and the concrete properties. This study tackles this challenge by employing Artificial Neural Network (ANN) models. Since, according to No Free Lunch theorem, the performance of optimization algorithms is problem-dependent, this paper aims to assess the feasibility of modeling the shear strength of RC beams using ANNs trained with the Tabu Search Training (TST) algorithm. To this end, 248 experimental results were collected from the literature, and a feed-forward ANN model was employed to predict the shear strength. To assess its feasibility, the ANNs were also modeled using the Particle Swarm Optimization, and Imperialist Competitive Algorithms. As a traditional technique, the multiple regression model was also employed. The shear design equations of ACI-318-2019 were also investigated and compared with Tabu Search Trained ANN model. The analysis of results suggests the superiority of Tabu Search Trained ANNs in comparison to other suggested models in literature and the ACI-318-2019 design code.

1. Introduction

The shear strength of reinforced concrete (RC) beams can be predicted by multiple methods. Their precision, however, remains very limited because of the number and complex nature of affecting parameters such as aggregate interlock and concrete in compression region. In addition, the cross section and the axial load of the beam (if any) could have an effect on the shear strength of the RC beams [1]. The design strength and shear behavior of members are of central concern in structural design. In concrete members, there are many types of failure, and shear failure is one of the most critical and unwanted types of failure because of the fragility of concrete systems. Thus, to withstand shear failure, RC members are employed [2]. The literature and concrete codes suggest many empirical formulas for RC beam strength. In structural design, the American Concrete

Institute (ACI) code has been used extensively. Furthermore, each of the analytical formulas proposed in concrete codes delivers good results for a given data set only [2].

There have been numerous studies on the use of soft computing techniques, especially artificial neural networks (ANNs) to assess properties of concrete. Artificial neural network models have proved to be outstanding for determination of shear strength of RC beams as shown by Mansour et al. They employed 176 experimental results and built a 9-input ANN. For the 176 test results, they achieved a 1.003 experimental-to-predicted shear strength ratio. The results indicate that ANNs have the potential to be used as a practical tool in determining the ultimate shear strength of reinforced concrete beams with stirrups in the range of parameters studies [3]. Olalusi and Awoyera investigated the shear failure in reinforced concrete beams by utilizing machine learning techniques. They employed Gaussian

process regression and random forest techniques to develop an ML-based model high accuracy [4]. ANNs have also been shown to be accurate in predicting the shear strength of concrete beams with stirrups. Based on the observed behavior, Cladera and Mari proposed new design equations for normal and high-strength concrete beams [5]. Abdalla et al. employed the shear strength, compressive strength, shear and longitudinal reinforcement, beam depth and width, and shear span-to-depth ratio parameters to predict and model the shear strength of RC beams using the artificial neural networks. The effective parameters help guide further research in narrowing parameter list. They modeled a backpropagation-based ANN with various transfer functions and provided shear response surfaces and curves [6]. Although being fast, the backpropagation using gradient descent technique is prone to get stuck in local optima and therefore not suitable in predicting the best performing model. To predict the torsional strength of reinforced concrete beams, Arslan collected 76 test results published in the literature and based the ANN models on the compressive strength, beam cross section area, steel ratio of longitudinal bars and stirrups, closed stirrup dimensions, reinforcement yield strengths, stirrup spacing, and cross section area for one leg of closed stirrups. The researcher concluded that ANN models predict the torsional strength of concrete beams more accurately than formulas provided in codes [7].

Oreta utilized the ANN model to measure the effect of size on the shear strength of RC beams without stirrups. The researcher modeled an ANN using five input variables and concluded that the ANN model performs superior to existing equation [8]. To predict the shear strength of RC joints, Naderpour and Nagai employed seven input variables to develop an ANN model. They compared the developed model with existing equations and calculated the relative importance of input parameters on the shear strength by employing a sensitivity analysis. The results indicated that the reinforcement ratio is the most influential parameter on shear strength of RC joints [9], which is helpful in guiding further research in selecting effective parameters. Feng and Fu predicted the shear strength of internal RC beam-column joints by developing a gradient boosting regression tree built by integrating several machine learning models including ANNs and support vector machines. The researchers concluded that the utilized model predicts the shear strength more accurately than the existing models [10]. Jeon et al. proposed a multivariate adaptive regression splines model for predicting the shear strength of RC beam-column joints. They compared the model against symbolic regression and multivariate linear regression models and showed that the proposed model is more accurate [11]. Salehi and Burgueño investigated the use of Artificial Intelligence (AI) techniques in structural engineering. They evaluated traditional machine learning methods, deep learning, and pattern recognition techniques for the structural engineering use case [12]. The results of their analysis make the case for using AI techniques in structural engineering problems.

Despite their utility and attractiveness, RC deep beams are challenging to design, because various parameters nonlinearly affect their behavior and shear strength.

Remarkably, shear stress is a dominant failure mode of RC deep beams that tends to result in sudden, severe collapse and human loss [13]. To predict the shear strength of deep reinforced concrete beams, Zhang et al. employed the support vector regression method hybridized with the genetic algorithm. The model inputs were the mechanical, material, and dimensional properties of beam. In comparison to ANN and gradient boosted tree models, the employed model proved to be more accurate for shear strength prediction of deep RC beams [14]. Although being powerful, the genetic algorithm method requires a lot of trial-and-error to find the optimum values of hyperparameters and therefore is used less often. Shahnewaz et al. reviewed the proposed methods for predicting the shear strength of deep reinforced concrete beams in the literature. They concluded that the design equations are conservative in predicting the shear strength of deep RC beams. The researchers proposed an improved model based on genetic algorithm and reliability analysis [15]. This makes the case for further investigation of shear strength using contemporary techniques to get a clearer picture of the phenomenon. To predict the shear strength of prestressed and reinforced deep concrete beams, Pal and Deswal employed a support vector regression-based model. To evaluate the model accuracy relative to other models, they additionally used a backpropagation-based ANN and three empirical models from the literature. The researchers concluded that the support vector regression-based approach performance is superior to empirical and ANN models [16]. Chou et al. combined the smart artificial firefly colony algorithm with least squares support vector regression method to predict the shear strength of deep RC beams. The researchers calibrated the proposed model by using a dataset of experimental data collected from literature. The comparison of the model with existing equations leads researchers to conclude that the proposed method performs more accurately than the methods proposed in the literature for predicting the shear strength of deep RC beams [17]. In the realm of metaheuristic approaches, Gandomi et al. employed a hybrid search algorithm combined with genetic programming and simulated annealing, called the genetic simulated annealing for predicting the shear strength of deep RC beams. The comparison of the proposed model with ACI and CSA codes indicated the superiority of the method relative to these codes [18]. For shear strength of deep RC beams, Sanad and Saka proposed a predictive model based on artificial neural networks. The researchers concluded that ANN model performs more accurately than empirical equations [19]. Prayogo et al. utilized a hybrid model composed of two support vector machine models and symbiotic organisms search algorithm, called optimized support vector machines with adaptive ensemble weighting to predict the shear strength of deep RC beams. The researchers demonstrated the feasibility of the proposed algorithm in predicting the shear strength of deep reinforced concrete beams [13].

The purpose of this study is to assess the feasibility of using Tabu Search Training (TST) algorithm to calibrate the weights of an artificial neural network model for predicting the shear strength of reinforced concrete beams. The input

parameters of the model include physical, geometric, and material properties. The dataset utilized is composed of 248 experimental results collected from literature. Section 2 summarizes the artificial neural network model and the tabu search training algorithm in a general context. The model training and development are detailed in Section 3, followed by results and conclusion in Sections 4 and 5. The general outline of the paper is given in Figure 1 [20].

2. Background

2.1. Artificial Neural Networks. As one of the most lively fields of current research, Artificial Neural Networks (ANNs) offer valuable features and capabilities including learning and adapting to existing knowledge, generalization, parallel processing, and therefore higher processing speed, and high error tolerance [21–23]. The bioinspired feed-forward artificial neural network is an algorithm that consists of neurons organized in layers. Each neuron in a layer is connected to all neurons of the previous layers. The signals are transmitted between neurons through connection lines, and the weight of each connection shows its strength. In fact, the knowledge of the ANN is stored using these weights. To

The weights of an ANN are typically randomly initialized, and the network output is thus different from the target values. The weights and biases of the network need to be optimized in a process called neural network training to minimize the model error [25, 26]. Generally, the strategies for addressing this problem of optimization can be divided into two categories: gradient-based and metaheuristic. Gradient-based methods are quick; however, they can get stagnated in local minima. The algorithm does not get stuck in the local minima using metaheuristic methods; however, the solution obtained is not necessarily the global minimum. The metaheuristic approaches are designed to explore and exploit the solution space to provide accurate results [25–27]. Figure 2 displays an ANN with 9 neurons in the input layer, one hidden layer with 16 neurons, and one output layer. This is the top performing architecture utilized in this study.

2.2. Tabu Search Training Algorithm. Tabu search (TS) is a discrete optimization algorithm proposed by Glover in 1986 [28], and its modern form is ascertained by the researcher in 1989 and 1990 [29, 30]. Being a metaheuristic optimization algorithm, it is designed to guide the search operator from being trapped in local minima. It employs a short-term memory to move in the search space by a controlled randomization and thus avoid cycling on previously visited solutions by setting as tabu every step that has led to an improvement of the cost function and a long-term memory to diversify and explore the search space [31, 32].

Additionally, intermediate-term memory structures could be introduced to lead moves toward promising areas [28, 33].

To make it usable for training artificial neural networks, Dengiz et al. [31] introduced a modified version of Tabu Search algorithm later on. The proposed algorithm is named Tabu Search Training (TST) algorithm. TST commences by generating an initial vector of weights, i.e., W_{cur} for the artificial neural network. It then generates a neighborhood around the current solution by changing one of the elements (w_i) of W_{cur} by a randomly generated number drawn from a uniform distribution. The weight w_i is then changed by the amount $v_{i,j}$ if the value of $v_{i,j}$ is not in a tabu-value-start list for V (tabu value list size) iterations. Each weight w_i is updated K times resulting in nK number of neighbor weight vectors, where n is the size of weights vector W_{cur} . Then, for each of the neighbors, the cost function is evaluated, and if the move is allowed through the tabu mechanism, the weights vector W_{cur} is updated, and if the move is not allowed, the next best neighbor in terms of cost function is chosen if allowed.

The tabu search training algorithm employs a short-term memory to allow for intensification of search and a long-term memory to allow for diversification of search and thus avoiding local minima. The details of the algorithm are given in Dengiz et al. [31]. The outline of the TST algorithm is depicted in Figure 3.

3. Methods and Materials

3.1. Dataset. The database in this paper is based on data collected by Baghi and Barros [1]. The collected data consist of 248 experimental samples gathered from numerous published papers [34–44]. Baghi and Barros identified 9 effective parameters on the shear strength of reinforced concrete T-beams, namely, flange width (b), flange thickness (h_f), concrete compressive strength (f'_c), web width (b_w), effective depth (d), yield stress of stirrups times transverse reinforcement ratio ($f_{st,y} \cdot \rho_{st}$), shear span-to-depth ratio (a/d), flexural reinforcement ratio (ρ_{sl}), and k_f coefficient that takes the influence of flanges of the T-beam on shear capacity into account and is defined by using Equations (1) and (2) [1, 45].

$$k_f = 1 + n \cdot \left(\frac{h_f}{b_w} \right) \cdot \left(\frac{h_f}{d} \right) \leq 1.5, \quad (1)$$

where

$$n = \frac{b - b_w}{h_f} \leq 3. \quad (2)$$

The descriptive statistics of experimental dataset are given in Table 1. The histogram of the shear strength of reinforced concrete T-beams is displayed in Figure 4.

Various ranges of input variables to an artificial neural network (ANN) may have unfavorable effects on the model such as optimization algorithm divergence and an added training time [25]. Therefore, the input and output variables

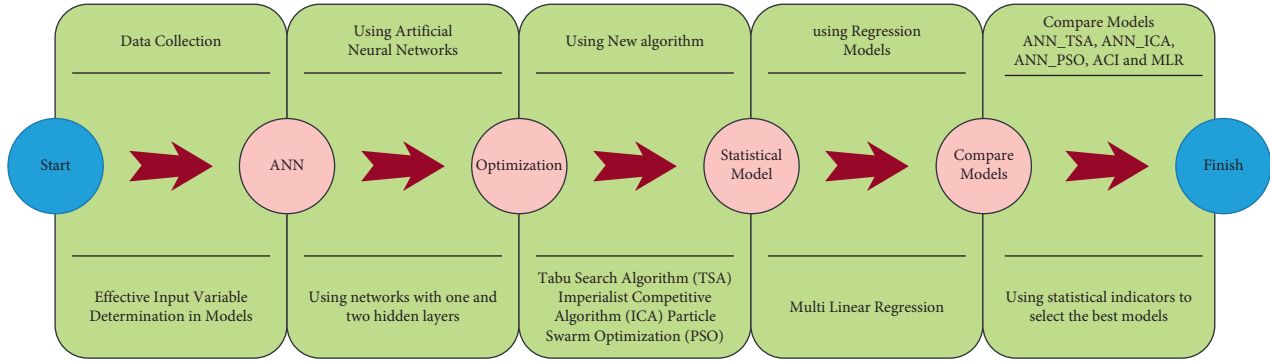


FIGURE 1: Outline of the paper.

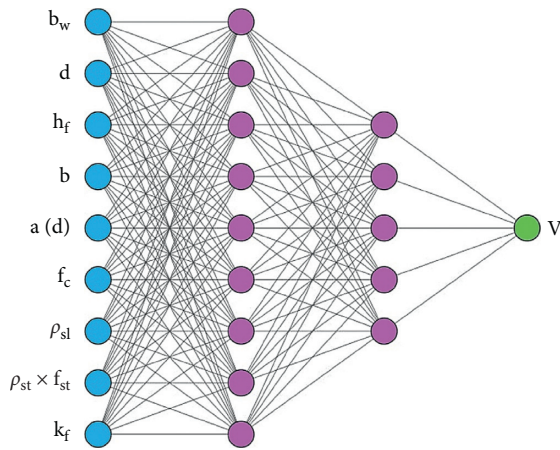


FIGURE 2: Architecture of the optimum artificial neural network used in this study with 9 input neurons, 16 neurons in the hidden layer, and one neuron in output layer.

of the dataset were transformed (normalized) into a range of $[-1 \ 1]$ using Equation (3) as follows:

$$X_n = \frac{2(X - X_{\min})}{X_{\max} - X_{\min}} - 1, \quad (3)$$

where X_n is the normalized value of the variable, X_{\max} is the maximum, and X_{\min} is its minimum value. X is the original (nontransformed) value of the variable. The minimum and maximum values of each of the 9 input parameters and the target value of shear strength are given in Table 1. Since ANN is trained on normalized data, it should be noted that when using ANN, the network should be fed with normalized values of variables, and the output of the network should be denormalized, i.e., transferred into its original range [46].

3.2. Performance Measures. The benchmarks by which the model's performance and prediction accuracy are evaluated should be described in order to evaluate and compare models. The performance measure selected is the fitness value (or cost) of objective function on test data. The explanation for the performance evaluation based on test data is the selection of a model with the most generalization capability.

The statistical measures used to evaluate the performance of different predictive models are the Mean Error (ME), Mean Absolute Error (MAE), Mean Squared Error (MSE), Root Mean Squared Error (RMSE), Average Absolute Error (AAE), Model Efficiency (EF), and Variance Account Factor (VAF) that are defined as Equations (4)–(8) [47]:

$$ME = \frac{1}{n} \sum_{i=1}^n (P_i - O_i), \quad (4)$$

$$MAE = \frac{1}{n} \sum_{i=1}^n |P_i - O_i|, \quad (5)$$

$$MSE = \frac{1}{n} \sum_{i=1}^n (P_i - O_i)^2, \quad (6)$$

$$RMSE = \left[\frac{1}{n} \sum_{i=1}^n (P_i - O_i)^2 \right]^{1/2}, \quad (7)$$

$$AAE = \frac{\left| \sum_{i=1}^n (O_i - P) / O_i \right|}{n} \times 100. \quad (8)$$

3.3. Empirical Model Development Using ANNs and TSO. As mentioned in Section 3.1, there are 9 parameters influencing the shear strength of reinforced concrete T-beams. So, the artificial neural networks trained will all have 9 neurons in the input layer, and one neuron in the output layer as shown in Figure 2. Feed-forward networks, as described in Section 2.1, were used for ANNs.

The overfitting phenomenon affects artificial neural networks. An overfitted network is highly accurate in the training phase but is unable to produce a good performance on test data not encountered before and therefore does not have generalization capability. In order to minimize the overfitting effects, data were randomly divided into two sets, as recommended in literatures [26, 46]. 70% (174 cases) were used to train the network, and the remaining 30% (74 cases) were used to test the performance of the network.

The number of hidden layers and total neurons in hidden layers is problem-dependent for an artificial neural network

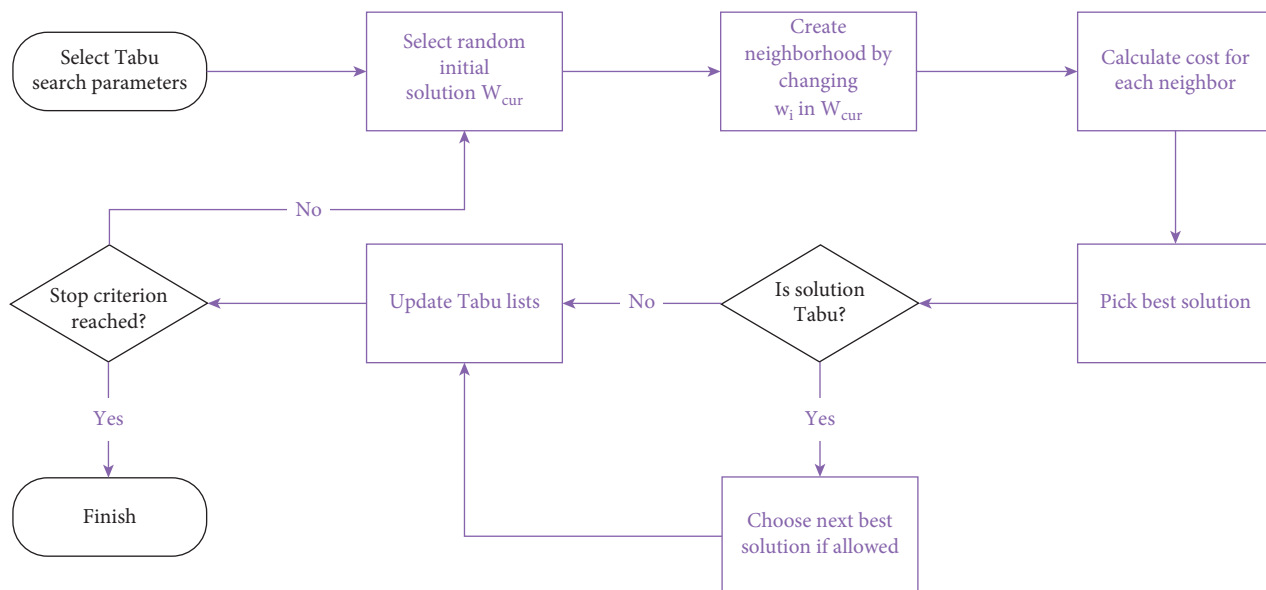


FIGURE 3: Flowchart of the tabu search training algorithm.

TABLE 1: Descriptive statistics of collected experimental data.

Parameter	Unit	Type	Max	Min	Average	STD
b_w	mm	Input	457.00	50.00	204.21	89.20
d	mm	Input	1200.00	198.00	425.21	217.44
h_f	mm	Input	152.00	0.00	36.95	47.37
b	mm	Input	1200.00	125.00	387.14	222.27
a/d		Input	5.40	2.53	3.45	0.56
f_{co}	MPa	Input	125.00	10.00	44.01	22.47
ρ_{sl}	%	Input	15.61	0.49	3.10	2.16
$\rho_{st} \times f_{st,y}$	–	Input	9.60	0.00	1.18	1.48
k_f	–	Input	1.50	1.00	1.10	0.13
V	kN	Output	1330.00	33.00	255.93	224.12

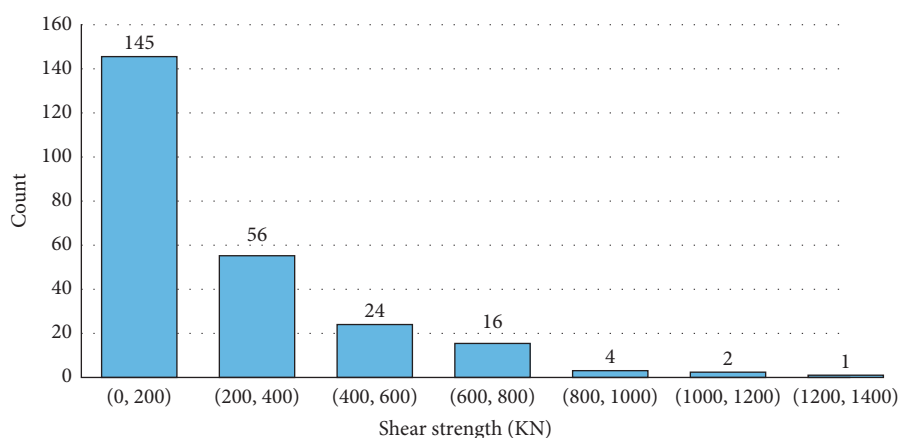


FIGURE 4: Shear strength distribution of experimental data.

model [48]. A trial-and-error approach was therefore used to obtain the optimal architecture, i.e., the architecture that best represents data. Equation (9) provides a commonly used heuristic for the total number of neurons of an artificial neural network by using Equation (9) [49]:

$$N_H \leq 2N_I + 1, \quad (9)$$

where N_H is the number of hidden layer nodes, and N_I is the number of inputs. Since the number of effective parameters is 9, the empirical equation suggests that the number of

hidden layer nodes can be chosen to be less than 19. Therefore, different architectures having one and two hidden layers and less than a total of 19 neurons were trained. A total of 30 different ANN architectures were trained, and the selected architectures are given in Table 2. The hyperbolic tangent and the logistic functions were chosen as the activation function of the hidden layers, and identity function was chosen as the activation function of the output layer.

The process of adjusting the weights and biases of an artificial neural network, i.e., training, is a minimization process, where the optimal solution is one with weights and biases that minimize the cost function, i.e., the prediction error of the network. To this end, the tabu search training (TST) algorithm described in Section 2.2 was applied. MATLAB [50] software package was used to code the ANNs and tabu search training algorithm. The optimum parameters of the tabu search training algorithm were found using trial-and-error, and the parameters used for training various ANN architectures are given in Table 3.

4. Results

4.1. Empirical Model Evaluation. As described in Section 3, 30 different architectures of artificial neural networks (ANNs) having one and two hidden layers were trained using the tabu search training (TST) algorithm. The networks had the hyperbolic tangent, and logistic function as the activation function of the hidden layers, and the activation function of the output layer was chosen to be the identity function. In the remaining sections, the ANNs will be referred to by designation ANN-ALG nL ($n_1 - n_2$), where ALG designates the training algorithm used, nL signifies that the ANN has n hidden layers, and n_1 and n_2 designate the number of neurons in the first and second hidden layers, respectively.

Of the 30 models trained to predict the shear strength of reinforced concrete T-beams, the top four based on their values of Mean Squared Error (MSE) were chosen. The ANNs along with their performance measures on training data are given in Table 4, and the performance measures on testing data of the same top four networks are given in Table 5.

Referring to Table 5, the network ANN-TST 2L (9-5) has the least values of MSE (and RMSE) for testing data; therefore, it is chosen as the top model trained using the TST for further analysis. The activation function of this model is the hyperbolic tangent function. On training data, ANN-TST 2L (9-5) has AAE, MSE, R^2 , RMSE, and MAE values of 0.07, 520.70, 0.9903, 22.82, and 14.16, respectively.

For testing data, ANN-TST 2L (9-5) has AAE, MSE, R^2 , RMSE, and MAE values of 0.16, 2217.08, 0.9475, 47.09, and 32.72, respectively. It should be noted that the error metrics for training and testing data were calculated using the data values in the original range of the variables and not in the normalized range of $[-1, 1]$ as is sometimes used in literature.

For a visual representation of the performance of ANN-TST 2L (9-5), the predicted values of the empirical model vs. their values found from experiment are depicted in Figures 5–7 for training data, testing data, and all data,

TABLE 2: Trained artificial neural network architectures.

Num	Topology	Num	Topology	Num	Topology
1	4-4	11	6-4	21	8-4
2	4-5	12	6-5	22	8-5
3	4-6	13	6-6	23	8-6
4	4-7	14	6-7	24	8-7
5	4-8	15	6-8	25	8-8
6	5-4	16	7-4	26	9-4
7	5-5	17	7-5	27	9-5
8	5-6	18	7-6	28	9-6
9	5-7	19	7-7	29	9-7
10	5-8	20	7-8	30	9-8

TABLE 3: Optimum tabu search algorithm parameters used in training artificial neural network models.

Algorithm	Parameter	Value
Tabu search algorithm	Maximum iterations	100
	K	2
	Lower bound	0
	Upper bound	0.001
	Tabu value list size	10
	Bound increment	0.001
	Tabu increase decrease list size	12
	Tabu frequency list size	5
	Maximum frequency	10

TABLE 4: Error metrics of the top four artificial neural networks on training data.

Network designation	MAE	MSE	RMSE	AAE
ANN-TST 2L (9-5)	14.16	520.70	22.82	0.07
ANN-TST 2L (6-8)	16.73	590.98	24.31	0.09
ANN-TST 2L (9-4)	62.82	8292.82	91.06	0.34
ANN-TST 2L (5-7)	22.90	1117.06	33.42	0.11

TABLE 5: Error metrics of top four artificial neural networks on testing data.

Network designation	MAE	MSE	RMSE	AAE
ANN-TST 2L (9-5)	32.72	2217.08	47.09	0.16
ANN-TST 2L (6-8)	38.40	4281.70	65.43	0.16
ANN-TST 2L (9-4)	67.37	7757.97	88.08	0.37
ANN-TST 2L (5-7)	45.63	8438.66	91.86	0.19

respectively. It is evident that the values predicted by the model are close to the line $y = x$, signifying the accuracy of the model. The comparison between experimental results and ANN-TST 2L (9-5) predictions on testing data is displayed in Figure 8.

4.2. Comparison with Other Methods. To evaluate the performance of tabu search training algorithm for training an artificial neural network for the purpose of predicting the shear strength of reinforced concrete T-beams, three different models are also developed. One artificial neural

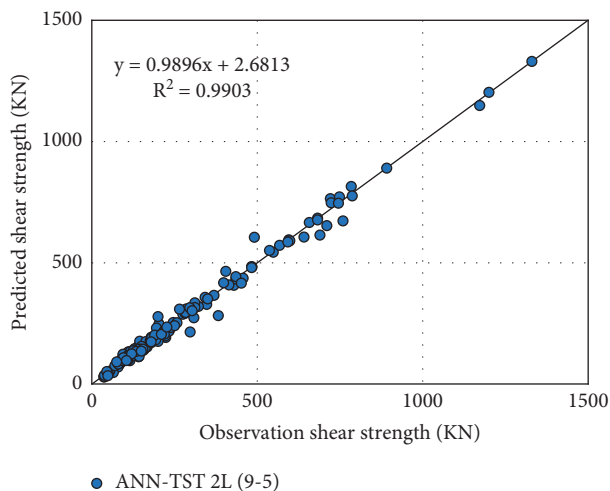


FIGURE 5: Target (experimental) versus predicted values of shear strength for ANN-TST 2L (9-5) model using training data.

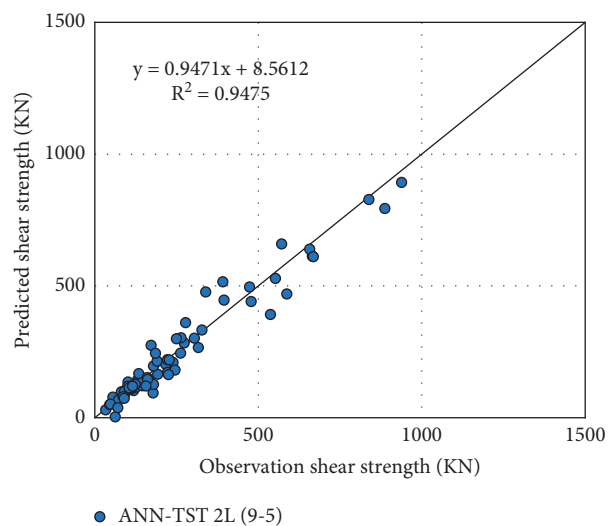


FIGURE 6: Target (experimental) versus predicted values of shear strength for ANN-TST 2L (9-5) model using testing data.

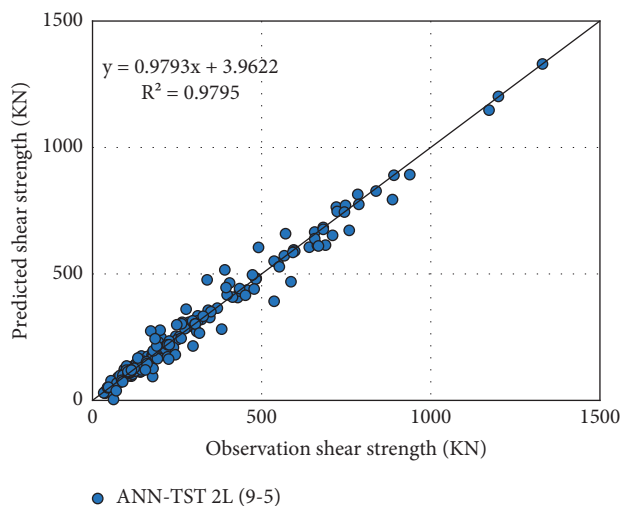


FIGURE 7: Target (experimental) versus predicted values of shear strength for ANN-TST 2L (9-5) model using all data.

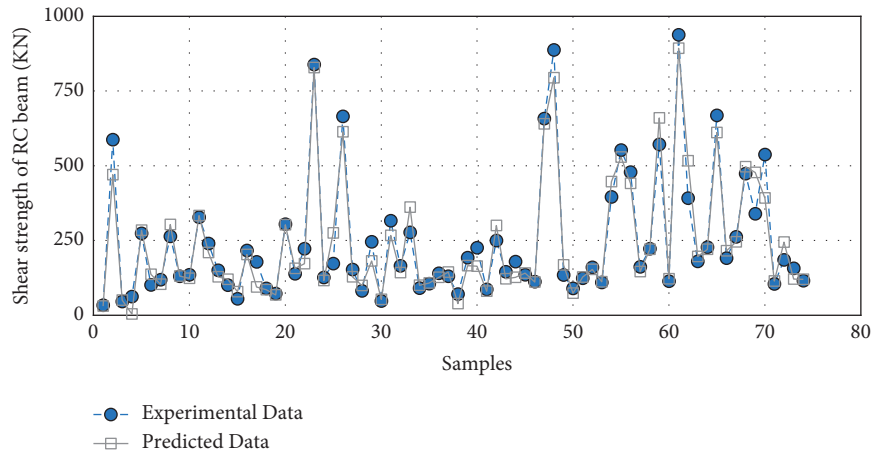


FIGURE 8: Comparison between the experimental results and ANN-TST 2L (9-5) predictions for testing data.

network model is trained using the imperialist competitive algorithm (ICA), one trained using the particle swarm optimization (PSO) algorithm, one multivariable linear regression model, and ACI standard code.

4.2.1. Imperialist Competitive Algorithm Model. The ANN-ICA 2L (9-5) architecture was trained using the imperialist competitive algorithm (ICA), and the optimum ICA parameters used to train the network were found by trial-and-error, and their values are given in Table 6. Compared to TST-trained neural network, this network has much higher prediction error. For a visual representation of the performance of this model, the predicted values of shear strength vs. their experimental values are shown in Figure 9. It is evident that the points on the plot are much farther from the $y=x$ line in comparison to the ANN-TST 2L (9-5) model.

4.2.2. Particle Swarm Optimization Model. The same ANN-PSO 2L (9-5) architecture was used to train the network

using particle swarm optimization (PSO) algorithm, the optimum PSO parameters used to train the network were found by trial-and-error, and their values are given in Table 6. Compared to ICA-trained network, this model performs relatively better; however, compared to TST-trained neural network, it has much higher prediction error. The performance of this model is visually represented in Figure 10 that depicts the predicted values of shear strength vs. their experimental values.

4.2.3. Multiple Regression Model. A Multiple Linear Regression (MLR) model [51] was developed as a classical model to provide an easy-to-use model. The model was developed in Minitab 19 software package using the same data. The influence of each variable can be approximated by checking the values of regression coefficients [52, 53]. The resulting regression equation (10) is

$$V = 560 + (1.17b_w) + (0.144 d) + (2.27h_f) + (0.0296b) - (26.9 a/d) + (1.35 f'_c) + (25.9\rho_{sl}) + (78.5\rho_{st} \cdot f_{st,y}) - 763k_f. \quad (10)$$

where b is the flange width, h_f is the flange thickness, f'_c is the concrete compressive strength, b_w is the web width, d is the effective depth, $f_{st,y}$ is the yield stress of stirrups times transverse reinforcement ratio, a/d is the shear span-to-depth ratio, ρ_{sl} is the flexural reinforcement ratio, and k_f is the coefficient.

4.2.4. ACI-318. The model presented by the ACI 318-14 standard code estimates the shear strength of RC beams. However, it does not provide any information concerning their rotation capability. In this case, the nominal shear resistance is reached:

$$(V_c = \phi \times 0.17 \times \gamma \times f'_c \times 0.5 \times b_w \times d), \quad (11)$$

where V_c is the shear resistance; $\phi = 0.75$; $\lambda = 0.75$ for lightweight concrete and 1 for normal weight concrete; f'_c is the 28-d cylinder compressive strength of concrete in MPa; b_w is the web width; d is the effective depth of the beam in mm.

Compared to TST-trained, PSO-trained, and ICA-trained ANNs, multiple linear regression model performs far less accurately. The experimental vs. predicted values of these models on all data are depicted in Figures 10–12.

A useful diagram for evaluating the performance of ANN-TST is the Taylor diagram depicted in Figure 13. The Taylor diagram depicts the adequacy of model based on root mean square centered difference, the correlation coefficient, and the standard deviation [54].

TABLE 6: Optimum ICA and PSO parameters used in training artificial neural network models.

Optimum parameters of imperialist competitive algorithm			Optimum parameters of particle swarm optimization			
Number of countries	Number of imperialists	Number of decades	Swarm size	Iterations	C1	C2
500	50	150	100	150	2	2

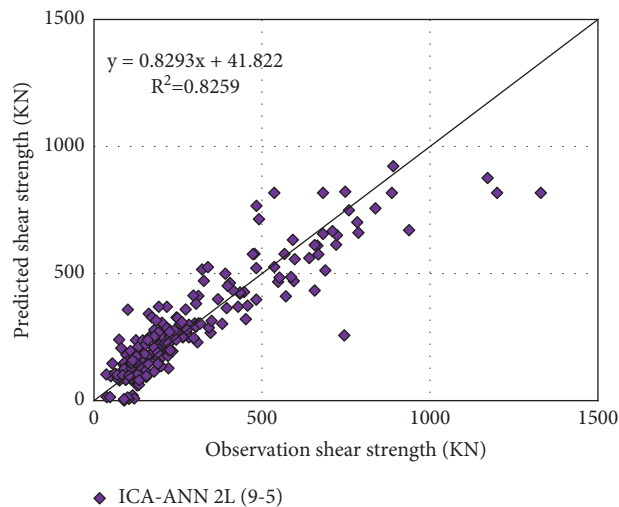


FIGURE 9: Target (experimental) versus predicted values of shear strength for ANN-ICA 2L (9-5) model using all data.

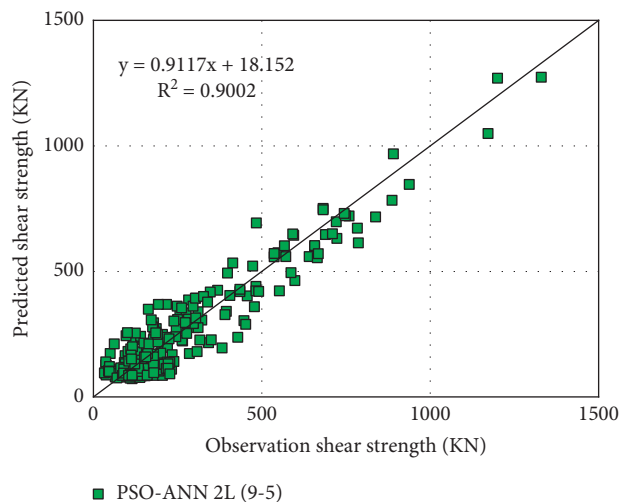


FIGURE 10: Target (experimental) versus predicted values of shear strength for ANN-PSO 2L (9-5) model using all data.

The statistical indices of ME, MAE, MSE, RMSE, AAE, EF, and VAF on all data for ANN-TST 2L (9-5), ANN-PSO 2L (9-5), ANN-ICA 2L (9-5), ACI, and the multiple linear regression model are given in Table 7. Comparing these values, the top performing empirical model is the ANN-TST 2L (9-5), the second-best performing model is the ANN-PSO 2L (9-5) model, multiple linear regression, and ANN-ICA 2L(9-5), and the least accurate model is the ACI standard code.

4.3. Sensitivity Analysis. Because of the improved results in ANN-TST 2L (9-5) model relative to ANN-PSO 2L (9-5), ANN-ICA 2L (9-5), and multiple linear regression model, the sensitivity analysis for determining the relative contribution of each of the 9 input variables was performed using this analytical model. The profile method proposed by Lek [53, 55] was implemented in MATLAB [50] software package and used for sensitivity analysis. This approach is based on analyzing each of the inputs while holding others

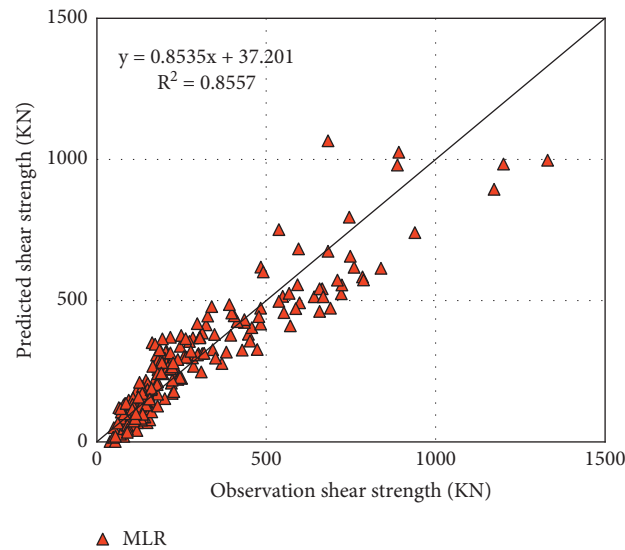


FIGURE 11: Target (experimental) versus predicted values of shear strength for multiple linear regression model using all data.

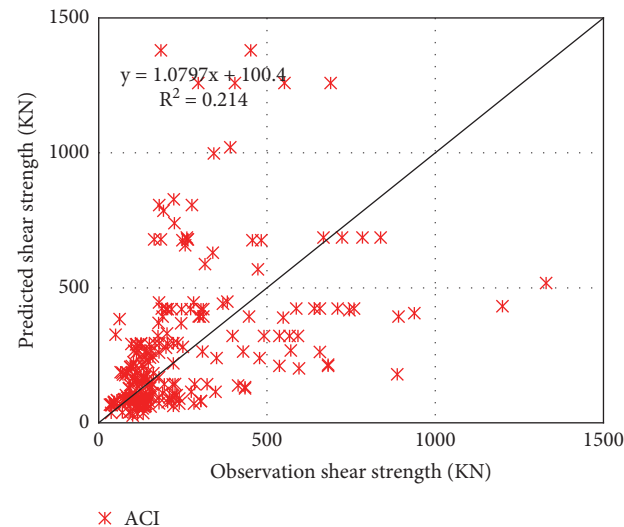


FIGURE 12: Target (experimental) versus predicted values of shear strength for ACI-318 model using all data.

fixed. The input variable ranges were divided into several equal intervals called the scale. While setting the values of other variables to m different fixed values, the output of the network was calculated for the entire range of the selected variable, which resulted in m groups of outputs. Eventually, m groups of outputs were combined by calculating the median output for every single input case. The fixed values selected for each of the variables were their min, Q1, median, Q3, and max. The implementation and the theory are clearly explained by Lek [53, 55]. In this study, the 192 scale was used as suggested by Lek [53, 55].

The relative importance and contribution of explanatory variables (9 inputs) on the response variable (shear strength of reinforced concrete T-beams) were calculated, and the resulting contribution is plotted in Figure 14. The most influential parameter is $\rho_{st} \times f_{st,y}$, where 25% of the variation in the response variable is

attributed to it. The next three most influential parameters are h_f , b_w and d that are 23%, 22%, and 15%. The least influential parameters are shear span-to-depth ratio (a/d) that is 1%.

4.4. Predictive Model and ANN Weights. The top empirical model produced in this study is the ANN-TST 2L (9-5). This model is not useful for the end user unless its source file is provided to them. So, in this section, the weights and biases of this network are provided. As mentioned in Section 3.1, the input data to the network must be first normalized using Equation (3) and using the maximum and minimum values given in Table 1 for each variable, and the output of the network must be denormalized using Equation (14). The input is a 9×1 vector called $a^{(1)}$. The shear strength is calculated using equations (12)–(14):

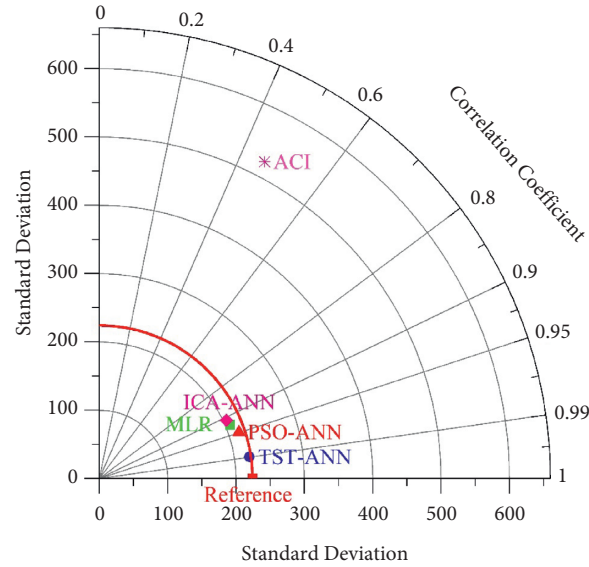


FIGURE 13: Taylor diagram visualization of model performance, in terms of shear strength.

TABLE 7: Error metrics of top ANN-TST, ANN-PSO, ANN-ICA, and MLR models on all data.

Network designation	RMSE	AAE	R^2	$y = ax + b$
ANN-TST 2L (9-5)	32.04	0.10	0.9795	$y = 0.9793x + 3.9622$
MLR	84.96	0.34	0.8557	$y = 0.8535x + 37.201$
ACI	478.63	0.96	0.214	$y = 1.0797x + 100.4$
PSO-ANN 2L (9-5)	70.84	0.34	0.9002	$y = 0.9117x + 18.152$
ICA-ANN 2L (9-5)	93.35	0.36	0.8259	$y = 0.8293x + 41.822$

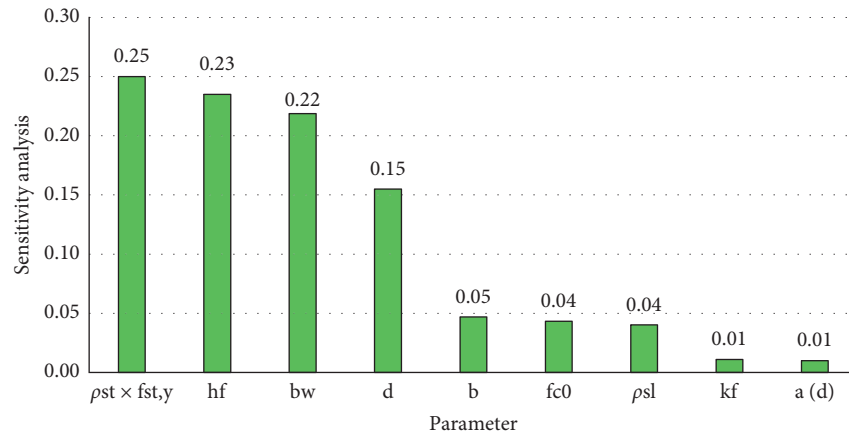


FIGURE 14: Relative contribution of input parameters on the shear strength of reinforced concrete T-beams.

$$a^{(2)} = \tanh(\vartheta^{(1)} \times a^{(1)} + b_1), \quad (12)$$

$$v^{\text{predict (normalized)}} = \tanh(\vartheta^{(2)} \times a^{(2)} + b_2), \quad (13)$$

$$v^{\text{predict}} = \frac{v^{\text{predict (normalized)}} + 1}{2} \times (v_{\max} - v_{\min}) + v_{\min}, \quad (14)$$

where \tanh is the hyperbolic tangent function, $v^{\text{predicted}}$ is the predicted value of shear strength, and v_{\max} and v_{\min} are the minimum and maximum shear strength values in database

given in Table 1. The weight (θ) and bias (b) matrices are as follows:

$$\begin{aligned} \theta^{(1)} &= 10^{-1} \times \begin{bmatrix} 0.048 & 0.035 & -0.538 & -0.288 & -0.218 & -0.411 & 0.268 & 0.797 & -0.373 \\ -0.126 & 0.085 & 0.306 & -0.309 & 0.147 & 0.398 & -0.046 & 0.153 & -0.321 \\ 0.088 & -0.269 & 0.113 & -0.462 & -0.044 & -0.188 & -0.385 & -0.653 & -0.632 \\ -0.230 & 0.360 & 0.404 & 0.281 & -0.096 & 0.076 & -0.301 & -1.320 & 0.289 \\ -0.229 & -0.151 & -0.532 & 0.062 & 0.118 & -0.559 & 0.348 & 0.721 & -0.042 \\ 0.513 & 0.541 & 0.536 & 0.352 & 0.077 & 0.404 & 0.710 & 0.812 & -0.704 \\ -0.207 & -0.957 & -0.057 & -0.339 & 0.012 & 0.308 & 0.220 & 0.015 & 0.203 \\ 0.184 & -0.300 & 0.291 & 0.375 & 0.254 & 0.102 & -0.030 & 0.050 & -0.268 \\ 0.083 & 0.121 & 0.311 & 0.002 & 0.167 & 0.253 & -0.482 & -0.666 & -0.511 \end{bmatrix}, \\ \theta^{(2)} &= 10^{-1} \times \begin{bmatrix} 0.459 & 0.246 & -0.737 & -0.252 & -0.543 & 0.488 & -0.239 & -0.422 & 0.100 \\ -0.005 & -0.187 & 0.354 & 0.578 & 0.415 & -0.071 & 0.459 & -0.043 & 0.093 \\ 0.484 & 0.389 & -0.136 & -0.795 & -0.621 & 0.449 & -0.222 & -0.067 & 0.451 \\ -0.612 & -0.335 & 0.444 & -0.061 & -0.243 & -1.124 & -0.329 & 0.199 & 0.283 \\ -0.364 & 0.139 & 0.450 & -0.234 & -0.373 & -0.211 & 0.273 & 0.057 & -0.348 \end{bmatrix}, \\ \theta^{(3)} &= 10^{-1} \times [1.252 \quad -0.492 \quad 0.816 \quad -1.193 \quad -0.313], \\ b_1 &= 10^{-1} \times [0.030 \quad -0.544 \quad -0.861 \quad 0.351 \quad 0.884 \quad 0.356 \quad 0.463 \quad -0.623 \quad 0.318], \\ b_2 &= 10^{-1} \times [0.935 \quad 0.172 \quad 0.535 \quad -0.197 \quad -0.239], \\ b_3 &= 10^{-1} \times [0.092]. \end{aligned} \quad (15)$$

5. Conclusion

To assess the feasibility of using Tabu Search Training (TST) algorithm to train Artificial Neural Networks (ANNs) for predicting the shear strength of reinforced concrete specimens, 248 experimental test results were collected from published results. After training the artificial neural network model with the lowest MSE on test dataset was selected, a sensitivity analysis was conducted on the model, and to assess its accuracy, other ANN models trained using particle swarm optimization and imperialist competitive algorithm were employed. The analysis of the results suggests the following:

- (1) The trained ANN-TST 2L (9-5) model predicted the shear strength more accurately than other artificial neural networks. The mean squared error and model efficiency of this model on test data were 2217.08 and 0.9475, respectively.
- (2) A multiple regression model was provided as an easy-to-use model to predict the shear strength.
- (3) An imperialist competitive algorithm-based and a particle swarm optimization-based artificial neural network were trained using the same data. The comparison of ANN-TST 2L (9-5), ANN-ICA 2L (9-5), ANN-PSO 2L (9-5), ACI code, and multiple

regression models suggests that the TST-based ANN is the most accurate, followed by particle swarm optimization-based and imperialist competitive algorithm-based ANNs, and then the multiple regression model.

- (4) The shear design formula of ACI-318-2019 was also investigated, and its accuracy was compared with that of ANN-TST 2L (9-5) model. The Tabu Search based ANN was shown to be superior in accuracy.
- (5) Sensitivity analysis results suggest that the top three most influential parameters on shear strength of reinforced concrete T-beams are flexural reinforcement ratio, effective depth, and web width. The least influential parameters are shear span-to-depth ratio and concrete compressive strength.
- (6) A predictive model based on the weights and biases of the top trained model, ANN-TST 2L (9-5), was provided to make the trained model available without the need for a computer source file.

References

- [1] H. Baghi and J. A. O. Barros, "Design-oriented approach to predict shear strength of reinforced concrete beams," *Structural Concrete*, vol. 19, no. 1, pp. 98–115, 2018.
- [2] J. A. Mani and R. Moeini, "Prediction of shear strength of reinforced concrete beams using adaptive neuro-fuzzy inference system and artificial neural network," *Scientia Iranica*, vol. 19, no. 2, pp. 242–248, 2012.
- [3] M. Y. Mansour, M. Dicleli, J. Y. Lee, and J. Zhang, "Predicting the shear strength of reinforced concrete beams using artificial neural networks," *Engineering Structures*, vol. 26, no. 6, pp. 781–799, 2004.
- [4] O. B. Olalusi and P. O. Awoyera, "Shear capacity prediction of slender reinforced concrete structures with steel fibers using machine learning," *Engineering Structures*, vol. 227, Article ID 111470, 2021.
- [5] A. Cladera and A. R. Marí, "Shear design procedure for reinforced normal and high-strength concrete beams using artificial neural networks. Part II: beams with stirrups," *Engineering Structures*, vol. 26, no. 7, pp. 927–936, 2004.
- [6] J. A. Abdalla, A. Elsanosi, and A. Abdelwahab, "Modeling and simulation of shear resistance of R/C beams using artificial neural network," *Journal of the Franklin Institute*, vol. 344, no. 5, pp. 741–756, 2007.
- [7] M. H. Arslan, "Predicting of torsional strength of RC beams by using different artificial neural network algorithms and building codes," *Advances in Engineering Software*, vol. 41, no. 7–8, pp. 946–955, 2010.
- [8] A. W. C. Oreta, "Simulating size effect on shear strength of RC beams without stirrups using neural networks," *Engineering Structures*, vol. 26, no. 5, pp. 681–691, 2004.
- [9] H. Naderpour and K. Nagai, "Shear strength estimation of reinforced concrete beam-column sub-assemblages using multiple soft computing techniques," *The Structural Design of Tall and Special Buildings*, vol. 29, no. 9, Article ID e1730, 2020.
- [10] D.-C. Feng and B. Fu, "Shear strength of internal reinforced concrete beam-column joints: intelligent modeling approach and sensitivity analysis," *Advances in Civil Engineering*, vol. 2020, Article ID 8850417, 19 pages, 2020.
- [11] J.-S. Jeon, A. Shafieezadeh, and R. DesRoches, "Statistical models for shear strength of RC beam-column joints using machine-learning techniques," *Earthquake Engineering & Structural Dynamics*, vol. 43, no. 14, pp. 2075–2095, 2014.
- [12] H. Salehi and R. Burgueño, "Emerging artificial intelligence methods in structural engineering," *Engineering Structures*, vol. 171, pp. 170–189, 2018.
- [13] D. Prayogo, M.-Y. Cheng, Y.-W. Wu, and D.-H. Tran, "Combining machine learning models via adaptive ensemble weighting for prediction of shear capacity of reinforced-concrete deep beams," *Engineering with Computers*, vol. 36, no. 3, pp. 1135–1153, 2020.
- [14] G. Zhang, Z. H. Ali, M. S. Aldlemy et al., "Reinforced concrete deep beam shear strength capacity modelling using an integrative bio-inspired algorithm with an artificial intelligence model," *Engineering with Computers*, 2020.
- [15] M. Shahnewaz, A. Rteil, and M. S. Alam, "Shear strength of reinforced concrete deep beams - a review with improved model by genetic algorithm and reliability analysis," *Structure*, vol. 23, pp. 494–508, 2020.
- [16] M. Pal and S. Deswal, "Support vector regression based shear strength modelling of deep beams," *Computers & Structures*, vol. 89, no. 13–14, pp. 1430–1439, 2011.
- [17] C. Jui-Sheng, N. Ngoc-Tri, and P. Anh-Duc, "Shear strength prediction in reinforced concrete deep beams using nature-inspired metaheuristic support vector regression," *Journal of Computing in Civil Engineering*, vol. 30, no. 1, Article ID 4015002, 2016.
- [18] A. H. Gandomi, A. H. Alavi, D. M. Shadmehri, and M. G. Sahab, "An empirical model for shear capacity of RC deep beams using genetic-simulated annealing," *Archives of Civil and Mechanical Engineering*, vol. 13, no. 3, pp. 354–369, 2013.
- [19] A. Sanad and M. P. Saka, "Prediction of ultimate shear strength of reinforced-concrete deep beams using neural networks," *Journal of Structural Engineering*, vol. 127, no. 7, pp. 818–828, 2001.
- [20] N. Aalimahmoodi, C. Bedon, N. Hasanzadeh-Inanlou, A. Hasanzade-Inallu, and M. Nikoo, "BAT algorithm-based ANN to predict the compressive strength of concrete-a comparative study," *Infrastructure*, vol. 6, no. 6, p. 80, 2021.
- [21] S. Shekhar, M. B. Amin, and P. Khandelwal, *Generalization Performance of Feed-Forward Neural Networks*, E. B. T.-N. N. Gelenbe, Ed., North-Holland, Amsterdam, 1992.
- [22] G. Ellis, "Feed-forward," in *Control System Design Guide*, Butterworth-Heinemann, Oxford, United Kingdom, 2004.
- [23] A. Pourdayaei, H. Mokhlis, H. A. Illias, S. H. A. Kaboli, S. Ahmad, and S. P. Ang, "Hybrid ANN and artificial co-operative search algorithm to forecast short-term electricity price in de-regulated electricity market," *IEEE Access*, vol. 7, pp. 125369–125386, 2019.
- [24] M. Fan, Z. Zhang, and C. Wang, "Optimization method for load frequency feed forward control," in *Mathematical Models and Algorithms for Power System Optimization*, Elsevier Science, Amsterdam, The Netherlands, 2019.
- [25] S. Haykin, *Neural Networks and Learning Machines*, Vol. 3, Pearson Education India, London, United Kingdom, 2008.
- [26] A. Géron, *Hands-on Machine Learning with Scikit-Learn and TensorFlow: Concepts, Tools, and Techniques to Build Intelligent Systems*, O'Reilly Media, Inc., Newton, Massachusetts, United States, 2017.
- [27] M. Nikoo, Ł. Sadowski, F. Khademi, and M. Nikoo, "Determination of damage in reinforced concrete frames with shear walls using self-organizing feature map," *Applied Computational Intelligence and Soft Computing*, vol. 2017, Article ID 3508189, 10 pages, 2017.
- [28] F. Glover, "Future paths for integer programming and links to artificial intelligence," *Computers & Operations Research*, vol. 13, 1986.
- [29] F. Glover, "Tabu search-Part I," *ORSA Journal on Computing*, vol. 1, no. 3, pp. 190–206, 1989.
- [30] F. Glover, "Tabu search-Part II," *ORSA Journal on Computing*, vol. 2, no. 1, pp. 4–32, 1990.
- [31] B. Dengiz, C. Alabas-Uslu, and O. Dengiz, "A tabu search algorithm for the training of neural networks," *Journal of the Operational Research Society*, vol. 60, no. 2, pp. 282–291, 2009.

- [32] O. Hajji, S. Brisset, and P. Brochet, "A new tabu search method for optimization with continuous parameters," *IEEE Transactions on Magnetics*, vol. 40, no. 2, pp. 1184–1187, 2004.
- [33] X.-S. Yang, "Metaheuristic optimization: nature-inspired algorithms and applications," *Studies in Computational Intelligence*, vol. 427, pp. 405–420, 2013.
- [34] S. J. E. Dias and J. A. O. Barros, "Shear strengthening of RC beams with NSM CFRP laminates: experimental research and analytical formulation," *Composite Structures*, vol. 99, pp. 477–490, 2013.
- [35] P. Y. Kong and B. V. Rangan, "Shear strength of high-performance concrete beams," *ACI Structural Journal*, vol. 95, no. 6, 1998.
- [36] R. J. Frosch, "Behavior of large-scale reinforced concrete beams with minimum shear reinforcement," *ACI Structural Journal*, vol. 97, no. 6, 2000.
- [37] W. D. C. Young-Soo Yoon and D. Mitchell, "Minimum shear reinforcement in normal, medium, and high-strength concrete beams," *ACI Structural Journal*, vol. 93, no. 5, 1996.
- [38] J. J. Roller and H. G. Russel, "Shear strength of high-strength concrete beams with web reinforcement," *ACI Structural Journal*, vol. 87, no. 2, 1990.
- [39] K.-H. Reineck, E. Bentz, B. Fitik, D. A. Kuchma, and O. Bayrak, "ACI-DAFStb databases for shear tests on slender reinforced concrete beams with stirrups," *ACI Structural Journal*, vol. 111, no. 5, 5 pages, 2014.
- [40] A. G. Mphonde, "Use of stirrup effectiveness in shear design of concrete beams," *ACI Structural Journal*, vol. 86, no. 5, 1989.
- [41] U. E. Guney Ozcebe and T. Tankut, "Evaluation of minimum shear reinforcement requirements for higher strength concrete," *ACI Structural Journal*, vol. 96, no. 3, 1999.
- [42] B. Bresler and A. C. Scordelis, "Shear strength of reinforced concrete beams," *ACI Journal Proceedings*, vol. 60, no. 1, 1963.
- [43] I.-J. C. Jung-Yoon Lee and S.-W. Kim, "Shear behavior of reinforced concrete beams with high-strength stirrups," *ACI Structural Journal*, vol. 108, no. 5, 2011.
- [44] W. J. Krefeld and C. W. Thurston, "Studies of the shear and diagonal tension strength of simply supported reinforced concrete beams," *ACI Journal Proceedings*, vol. 63, no. 4, 1966.
- [45] L. Vandewalle, D. Nemegeer, G. Balázs, and B. Barr, "Rilem tc 162-TDF: 'test and design methods for steel fibre reinforced concrete' σ - ϵ -design method," *Mater. Struct. Constr.* vol. 36, no. 262, pp. 560–567, 2003.
- [46] A. Hasanzade-Inallu, P. Zarfam, and M. Nikoo, "Modified imperialist competitive algorithm-based neural network to determine shear strength of concrete beams reinforced with FRP," *Journal of Central South University*, vol. 26, no. 11, pp. 3156–3174, 2019.
- [47] J. Li and A. D. Heap, *A Review of Spatial Interpolation Methods for Environmental Scientists*, Australian Government, Canberra, 2008.
- [48] A. Hasanzade-Inallu, P. Hassanzadeh Inallou, and B. Eskandarinezhad, "Prediction of compressive strength of concrete with manufactured sand using neural networks and bat algorithm," *Soil Struct. Interact. J.* vol. 4, pp. 52–63, 2019.
- [49] G. J. Bowden, G. C. Dandy, and H. R. Maier, "Input determination for neural network models in water resources applications. Part 1-background and methodology," *Journal of Hydrology*, vol. 301, no. 1-4, pp. 75–92, 2005.
- [50] Matlab, *Mathworks*, Mathematical Computing Software, Natick, Massachusetts, U.S.A, 2018.
- [51] M. Nikoo, F. Torabian Moghadam, and Ł. Sadowski, "Prediction of concrete compressive strength by evolutionary artificial neural networks," *Advances in Materials Science and Engineering*, vol. 2015, Article ID 849126, 8 pages, 2015.
- [52] D. K. Panesar, M. Aqel, D. Rhead, and H. Schell, "Effect of cement type and limestone particle size on the durability of steam cured self-consolidating concrete," *Cement and Concrete Composites*, vol. 80, pp. 175–189, 2017.
- [53] M. Gevrey, I. Dimopoulos, and S. Lek, "Review and comparison of methods to study the contribution of variables in artificial neural network model," *Ecological Modelling*, vol. 160, 2003.
- [54] I. Faridmehr, M. Nikoo, M. H. Baghban, and R. Pucinotti, "Hybrid krill herd-ANN model for prediction strength and stiffness of bolted connections," *Buildings*, vol. 11, no. 6, pp. 229–6, 2021.
- [55] S. Lek, M. Delacoste, P. Baran, I. Dimopoulos, J. Lauga, and S. Aulagnier, "Application of neural networks to modelling nonlinear relationships in ecology," *Ecological Modelling*, vol. 90, no. 1, pp. 39–52, 1996.

Design of Backfill Highway Subgrade on the Lower Bearing Capacity Foundation By Finite Element Method

Nilgrib Mohanty, *Department of Civil Engineering, Aryan Institute of Engineering & Technology, Bhubaneswar, nilgribmohanty25@outlook.com*

Saruk Mallick, *Department of Civil Engineering, Raajdhani Engineering College, Bhubaneswar, sarukmallik57@yahoo.co.in*

Satyaprakash Mishra, *Department of Civil Engineering, Capital Engineering College, Bhubaneswar, satyaprakash_m25@gmail.com*

Suryaleen Rout, *Department of Civil Engineering, NM Institute of Engineering & Technology, Bhubaneswar, suryaleenrout@yahoo.co.in*

ABSTRACT

The purpose of this study is to look into the stability of the backfill subgrade on a foundation with a lower bearing capacity. To simulate the high-filled road subjected to the actual self-weight load, a finite element (FE) model was built. The strength reduction method was used to create a slope stability analysis model. Simultaneously, parametric studies were used to conduct a sensitivity analysis of the elements impacting slope stability, such as elastic modulus, cohesion, internal friction angle, and slope rate. The results revealed that by computing the slope safety coefficient, the slope stability analysis model created using the strength reduction approach can characterise the slope's stability. The criterion can be the mutation point of the relationship curve between the displacement caused in the slope and the reduction coefficient. The calculated findings acquired from FE modelling can be used under the condition of a particular strength reduction coefficient.

1. Introduction

Road slope refers to the infrastructure constructed or modified to meet the needs of road construction [1–5]. The slope formed under certain conditions (topography and geology) will break the previous mechanical balance into an unstable body due to changes in external factors. Under the action of its own weight or other loads, it will follow a certain relatively weak surface [4, 6, 7]. A landslide is a kind of bad geological phenomenon such as sliding downwards as a whole, intermittently slowly, and sometimes even suddenly. The factors that cause landslides include excavation of side slopes, rapid embankment filling, earthquakes, river erosion, sudden drops in reservoir water levels, and heavy rains [6, 8–10]. The slope is not only a special geological environment but also an important part of engineering construction. Due to the construction demand for a large number of highway projects in recent years, the stability of the slope during the construction process is a link that cannot be ignored [11–14].

In the past, there were various approximate methods and specialized methods, which can be used to calculate the global safety factor that depends on the slope height, the steepness, and the constitutive properties of the soil constituting the slope. Nash [15] conducted a comprehensive review of many classic slope stability analysis methods. The limitation of many of these classical methods is that Mohr–Coulomb shear strength behavior with a fixed friction angle is usually assumed because of the inherent application of simple statistical methods to the soil. Approximately, the calculation of stress and related shear strength is a continuous mechanical problem with static uncertainties [16–18]. To reduce manual trials and errors associated with these technologies, such as slicing methods, many engineering software packages have been developed, but most software packages still use simple static methods to approximate soil stress and strength [19–22].

In the FE analysis, the method of increasing the external load or reducing the material strength of the rock-

soil mass is the earlier method adopted [23, 24]. The stability analysis of these slopes mainly includes the judgment basis of slope instability, the stability of the excavated slope, the comparative analysis of the selection of different software, and the analysis of the internal force of the slope with the supporting structure [25, 26]. In recent years, the FE method has been increasingly used to predict the displacement and stress in statically indeterminate slopes, dams, and embankments [5, 13, 14, 27–45]. The potential attractiveness of calculating slope stability in a continuum/finite element framework lies in many previous studies [7]. The equilibrium stress, strain, and related shear strength in the soil have been calculated accurately in the studies conducted by Aryal and Duncan [41, 44]. The general material models of soil (including Mohr–Coulomb and many other models) have been employed in the studies conducted by Ardah et al. [46]. The FEM method has been applied in 2D or 3D with complex slope combinations and soil sediments to model almost all types of mechanisms [47]. The FEM method has also been extended to address the damage caused by leakage, brittle soil behavior, random “yield soil” properties, and interventions such as engineering geotextiles, soil nails, drainage ditches, and retaining walls [5, 38, 40, 42–45]. To fully understand the stability condition of the backfill soil on the high-filled road with lower foundation bearing capacity, this article adopts the classic slope stability analysis method. In this method, the inclined soil is subjected to the actual self-weight load, and the purpose is to find a continuous surface through the soil that has the smallest safety coefficient against the slip or shear failure. The safety coefficient is defined as the degree to which the shear strength of the soil is reduced so that the slope has just reached the critical failure state.

2. Research Objective and Overview

The present study is to investigate the stability condition of the backfill soil on the high-filled road with lower foundation bearing capacity, as shown in Figure 1. A FE model was constructed to simulate the high-filled road subjected to the actual self-weight load. The strength reduction method was adopted to establish an analysis model of slope stability. At the same time, the sensitivity analysis of the factors affecting the slope stability was carried out through parametric studies, including the elastic modulus, cohesion, internal friction angle, and slope rate. Under the condition of a given strength reduction coefficient, the simulation results obtained by ABAQUS software show the development of the equivalent plastic zone in the way of cloud maps. The slope is stable under the reduction factor when the failure of transfixion or local yield failure occurs. If the reduction coefficient continues to increase, the slope is in a critical failure state when the plastic strain between adjacent iterative steps increases too much or the equivalent plastic strain reaches the yield limit at some nodes, and the strength reduction coefficient is positioned as the minimum safety factor of the overall stability of the slope.

3. Model Construction

In the present study, the FE method was adopted. In this method, a structure is regarded as a whole composed of a finite number of elements through nodes [5, 14, 30]. Except for the nodes which are fixed on the boundary, the displacement of each node that can produce displacement can be calculated by using equilibrium conditions, and then the internal forces of each element can be calculated by the node displacement [33–35].

In the finite element analysis of the strength reduction of the slope, the stability of the slope usually adopts the non-convergence of the solution as the failure criterion [48]. Within the maximum number of iterations, if the calculation fails to converge, it means that no stress distribution that can satisfy both the failure criterion and the overall balance is found, which means that the soil has been damaged. Specifically, the actual strength parameters c' and ϕ' of the backfilled roadbed are divided by a reduction factor F_{trial} at the same time to obtain a set of new values of c'' and ϕ'' after reduction, i.e.,

$$\begin{cases} c'' = \frac{c'}{F_{\text{trial}}}, \\ \phi'' = \arctan \left| \frac{1}{F_{\text{trial}}} \tan \phi' \right|. \end{cases} \quad (1)$$

Then, the reduced values of c'' and ϕ'' are taken into the trial calculation of finite elements as new material parameters [49, 50]. When the finite element calculation converges, the value of F_{trial} is slightly larger, and then the trial calculation is carried out until the finite element no longer converges, which indicates that the soil reaches the critical limit state and the slope shear failure occurs. At this time, the critical slip surface and safety factors are obtained.

The gravity load is determined by the following method [51, 52]. On each one of the finite elements, the gravitational load generated by the weight of the soil can be obtained by the following equation:

$$p^{(e)} = \gamma \int S^{eN^T} dS, \quad (2)$$

in which S is the area of the element; e is the element number. The result of this integration is to take the product of the area of each element and the weight of the soil as the element's gravity load and then distribute it to each node. Various complex constitutive models can be considered in the FE analysis, but the most common in engineering analysis is the ideal elastoplastic model because the results of the ideal elastoplastic model are the most comparable to the results of the limit equilibrium method. For general road slopes, the shear failure of the soil is mainly controlled, and the calculation accuracy of the distribution and size of the plastic zone is relatively high, and the requirements for the displacement are relatively low.

In the present study, the Mohr–Coulomb plastic model was employed to characterize the constitutive property of the soil. The yield criterion of the Mohr–Coulomb model is assumed as follows. When the shear stress acting on a certain point is equal to the shear strength of that point, the point

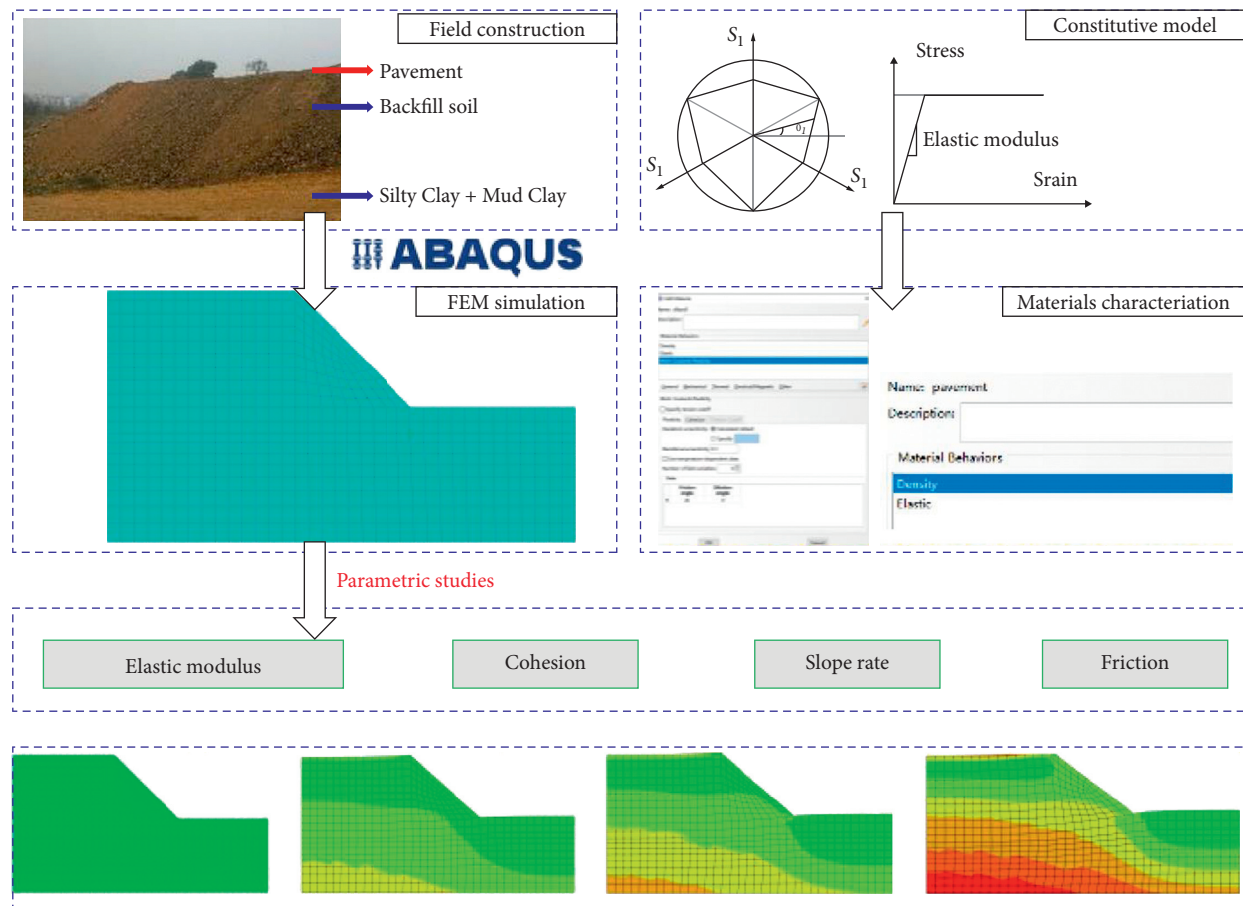


FIGURE 1: Research objective and overview.

will be broken, and the shear strength has a linear relationship with the normal stress acting on the surface. The yield surface equation of the Mohr–Coulomb model [53, 54] can be presented as follows:

$$F = R_{mc}q - p \tan \varphi - c = 0, \quad (3)$$

in which $\varphi(\theta, f^\alpha)$ is the friction angle on the meridian plane; $c(\varepsilon^{-pl}, \theta, f^\alpha)$ represents the changing process of the cohesive force of the material according to the isotropic hardening model. p is the equivalent compressive stress. q is the Mises equivalent stress. R_{mc} is the deviatoric stress coefficient of the Mohr–Coulomb model [55, 56], which can be defined as

$$R_{mc}(\theta, \varphi) = \frac{1}{\sqrt{3} \cos \varphi} \sin\left(\theta + \frac{\pi}{3}\right) + \frac{1}{3} \cos\left(\theta + \frac{\pi}{3}\right) \tan \varphi, \quad (4)$$

in which φ is the bevel angle of the yield surface of the Mohr–Coulomb model on the P-RMCQ plane, and it generally refers to the internal friction angle of the material. θ is the direction angle of the generalized shear stress.

3.1. Material Properties. Four types of civil engineering materials were adopted in the present simulation [48]. Table 1 gives the material properties.

The bounding and unbound pavement materials (including the surface layer, base layer, and subbase layer) were simplified to one type of material property [57]. Elastic behavior without plastic deformation characterized by Young's modulus and Poisson's ratio was adopted for the pavement materials. The density of the backfill soil was determined as 1800 kg/m^3 . Regarding the Mohr–Coulomb parameters of the backfill soil, the cohesion was determined as 15, 20, and 25 kPa, respectively. The internal friction angle was selected as 25° and 30° , and two elastic moduli of 50 MPa and 100 MPa were determined. The foundation with the lower bearing capacity was characterized by silty clay and mud clay [48]. The corresponding Mohr–Coulomb parameters are shown in Table 1 as well.

3.2. Physical Size of the Whole Model. Figure 2 gives the physical size of the whole model, including the pavement, subgraded by the backfill soil, and the foundation with lower bearing capacity [48].

These physical sizes were determined according to earlier studies [36–42]. The slope angle α is an important parameter considered in the present study, and it varied for different values ($\tan \alpha = 1:1; 1:1.25; 1:1.5; 1:1.75; 1:2$) to evaluate the effects on the slope stability. To reduce computations, only half of the high-filled subgrade FEM model (symmetric model) was constructed. The width of the pavement was

TABLE 1: Material properties.

Materials	Density, ρ (kg/m ³)	Cohesion, c (kPa)	Internal friction angle, φ (°)	Elastic modulus, E (MPa)	Poisson's ratio, μ
Pavement materials	2100	—	—	1200	0.35
Backfill soil	1800	15, 20, and 25	25 and 30	40, 60, 80, and 100	0.35
Silty clay	1750	14	22	45	0.4
Mud clay	1700	12	20	40	0.45

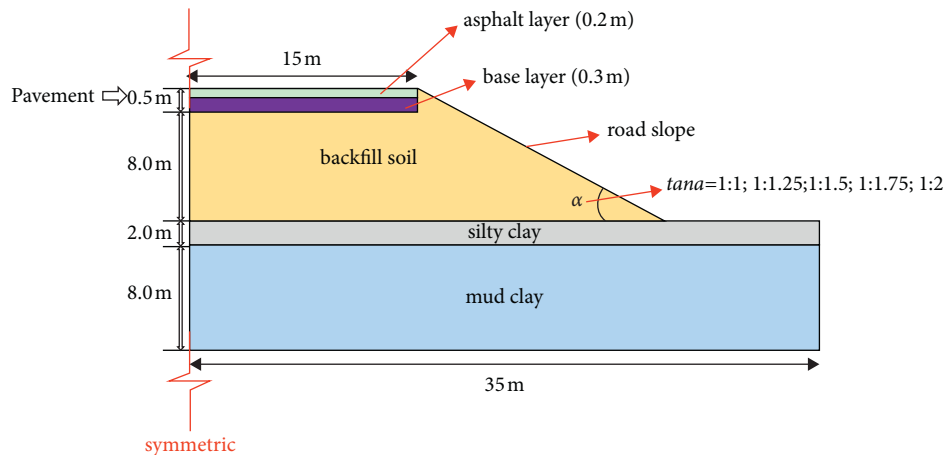


FIGURE 2: High-filled road with the backfill soil.

selected as 15 m according to the design of the conventional highway. The length of the foundation was determined as 35 m to support the subgrade by the backfill soil. The dimension of the FE model in the longitudinal direction can be regarded as infinite since only the 2D model was employed in this study. Under such conditions, the cross section of the road structure was regarded as the research object of the study, and the longitudinal length of the road structure was considered infinite [48].

3.3. Meshing and Element Selection. Figure 3 gives the FE meshing for different slopes used in the present study.

Element selection is the foundation for the FE analysis. For the same FE model, different calculation results can be obtained by using different elements. Regarding the FE model in the present study, the solid element was the optimized one to simulate one part of the whole model. Since a solid element can be connected to other elements through any of its surfaces, it can construct almost any shape and bear any load in the FE model.

To reduce the computations and improve the calculating accuracy, the 8-node plane-strain-reduced (CPE8R) element was adopted in the present FE simulation. It is a general plane strain element, in fact, a special plane stress element, which can be used to simulate a section of a very long structure, such as a dam. It is understood that the plate or shell element may be more efficient to solve the plane strain problem considering the high efficiency during the application. However, it should be noted that the research objective in the present study is about the subgrade and road pavement, which are not satisfying the premise of plate or shell theory. Therefore, the solid element, CPE8R, was

employed in the present study. Also, it should be noted that the structure containing the plane strain element should be defined in the global X - Y plane, that is, for all nodes $z = 0$.

4. Parametric Studies

4.1. Effects of Slope Angle. The soil was defined by the Mohr–Coulomb model, which is the so-called rigid plastic model or Saint-Venant model. Regarding the Mohr–Coulomb model, when the stress of the soil is less than the yield stress, the soil will not deform, just like a rigid body. When the stress reaches the soil yield stress, the plastic deformation will increase until the soil failure occurs. Therefore, the equivalent plastic strain (PEEQ) should be evaluated first, considering the proposed models. Figure 4 gives the results of PEEQ when the slopes are 1 : 1, 1 : 1.25, 1 : 1.5, 1 : 1.75, and 1 : 2, respectively.

As shown in Figure 4, under the conditions of a given strength reduction coefficient, the calculation results obtained through the FE simulation can show the development of the equivalent plastic zone in the form of cloud diagrams. When the slopes were 1 : 5, 1 : 1.75, and 1 : 2, respectively, failure to achieve penetration or local yield failure indicates that the slope is stable under this reduction factor, while when the slopes equal 1 : 1.25 and 1 : 1, the plastic deformation between adjacent iteration steps at some nodes increases too much or the equivalent plastic strain reaches the yield limit. From the displayed results (Figure 4), the plastic zone has penetrated the top of the slope, and the equivalent plastic strain and displacement have an infinite development trend, with obvious sudden changes, indicating that the slope is already in a critical failure state at this time.

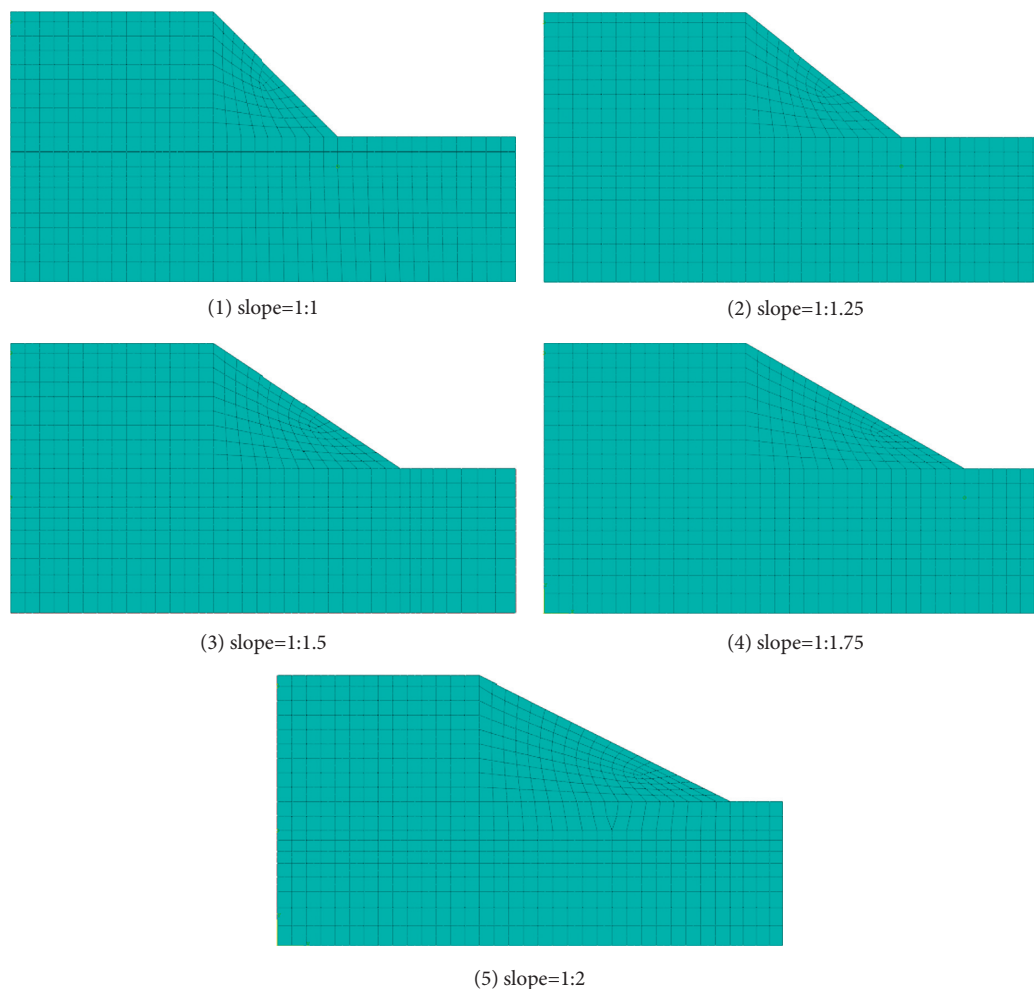


FIGURE 3: FEM meshes for the five types of slopes. (a) Slope = 1 : 1. (b) Slope = 1 : 1.25. (c) Slope = 1 : 1.5. (d) Slope = 1 : 1.75. (e) Slope = 1 : 2.

Also, it can be observed that when the slopes are 1 : 1, 1 : 1.25, 1 : 1.5, 1 : 1.75, and 1 : 2, the maximum PEEQ are $1.058e-2$, $9.026e-3$, $8.999e-3$, $6.556e-3$, and $6.807e-3$. Basically, as the slope decreases, the maximum PEEQ decreases, as shown in Figure 4. It can be indicated that reducing the slope can improve the stability of the road slope. Also, it can be observed that when the slope is lower than 1 : 1.75, the maximum PEEQ tends to converge.

4.2. Effects of Cohesion and Internal Friction Angle. It can be observed that, as the cohesion equals 15 kPa, the maximum PEEQ for internal friction angles 25° and 30° are 1.058×10^{-2} and 1.022×10^{-2} , respectively. A higher internal friction angle can increase the value of maximum PEEQ. As the cohesion equals 20 kPa, the maximum PEEQ when the internal friction angles equal 25° and 30° are 1.019×10^{-2} and 1.023×10^{-2} , respectively. However, as the cohesion increases to 30 kPa, the maximum PEEQ when the internal friction angles equal 25° and 30° are still 1.019×10^{-2} and 1.023×10^{-2} , respectively. This means that, as the internal friction angles equal 25° and 30° , even the cohesion increases, and the maximum PEEQ will remain the same.

Also, it can be observed that when the internal friction angle equals 25° , the maximum PEEQ when the cohesions equal 15 kPa, 20 kPa, and 30 kPa are $1.058e-2$, $1.019e-2$, and $1.019e-2$, respectively. The result proves that 20 kPa is the split point of the maximum PEEQ. When the internal friction angle equals 30° , the maximum PEEQ when the cohesions equal 15 kPa, 20 kPa, and 30 kPa are $1.022e-2$, $1.023e-2$, and $1.023e-2$, respectively. This result can also prove that 20 kPa is the split point of the maximum PEEQ. It can further be observed that the increase rate of the maximum PEEQ between 15 kPa and 20 kPa is very small (about 0.1%). Therefore, it can conclude that higher cohesion and internal friction angle can decrease the maximum PEEQ, but when the cohesion or internal friction angle is higher than one constant value, the maximum PEEQ will remain the same.

The cohesive force of the backfill has a great influence on the overall stability of the slope. With the increase of the cohesion of the backfill, the safety and stability factor also greatly increases, indicating that when the cohesive force of the subgrade soil is high, the stability of the roadbed slope is also high. It can be seen from Figure 5 that the cohesion is increased by 5 kPa, and the stability coefficient can be

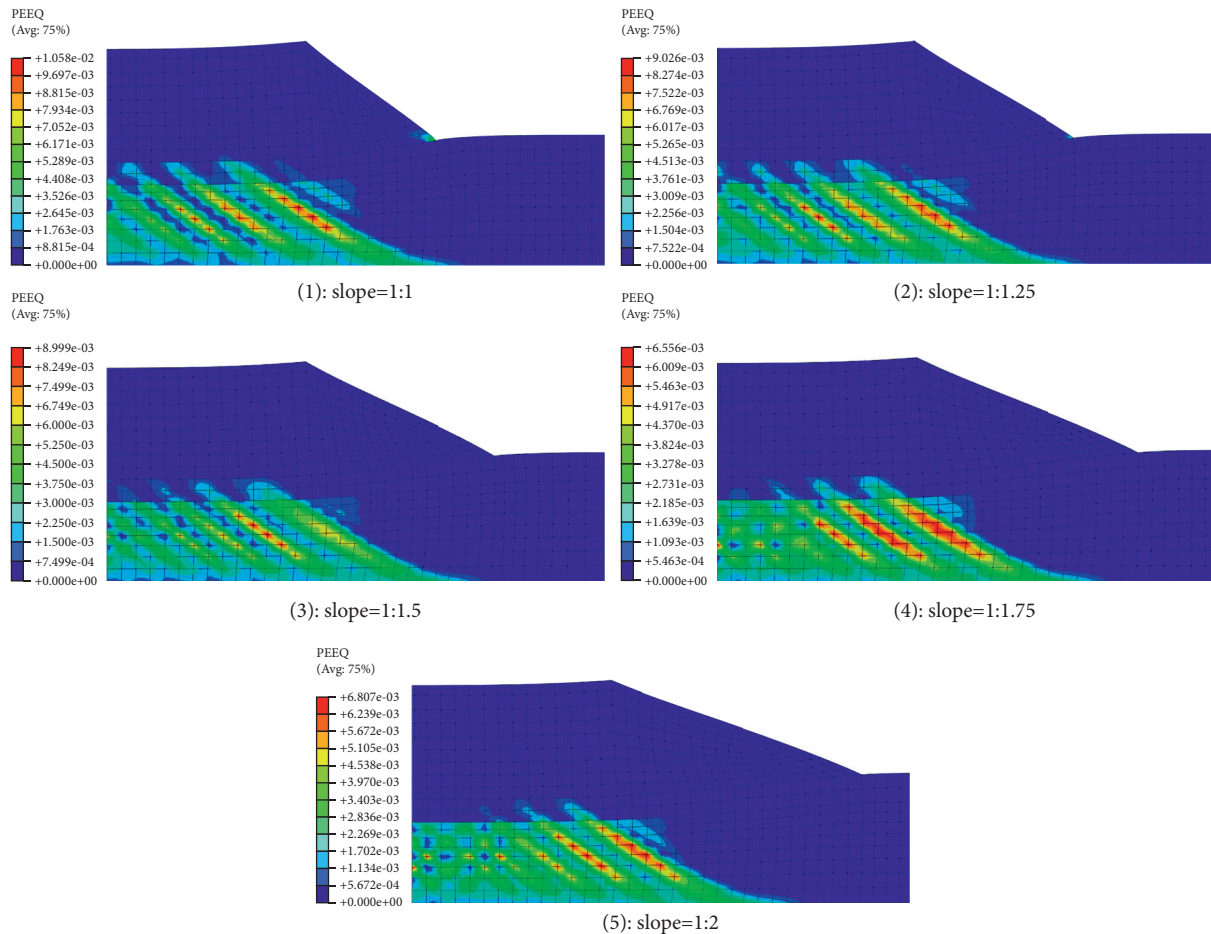


FIGURE 4: Effects of road slopes on PEEQ. (a) Slope = 1 : 1. (b) Slope = 1 : 1.25. (c) Slope = 1 : 1.5. (d) Slope = 1 : 1.75. (e) Slope = 1 : 2.

increased by about 10%. When the cohesion is large, the contribution to the safety and stability coefficient gradually decreases. It can also be seen that if the backfill material with greater cohesion is selected, the stability of the roadbed slope can be significantly improved. The safety and stability factor remains unchanged as the cohesive force of the weak foundation changes. The main reason may be related to the high fill height of the roadbed. Because when the height of the roadbed is large, the additional stress generated by the external load has a limited range, that is, the working area of the roadbed does not penetrate deep into the soil foundation, the influence of the change of the soil foundation material parameters on the results can be almost ignored. Through the above analysis, we can know the importance of subgrade soil cohesion in highway engineering, and foundation cohesion has little effect on stability.

4.3. Effects of Elastic Modulus. According to the strength reduction theory, when the finite element calculation does not converge due to the reduction of strength parameters, the slope shear failure occurs. Therefore, the reduction coefficient of the strength parameter corresponding to the last convergence calculation can be defined as the safety coefficient of the slope. Based on this determination criterion, Figure 6 gives the relationship between the elastic

modulus and safety coefficient when the cohesion and internal friction angle equal 15 kPa and 25°, respectively.

It can be found from Figure 6 that the elastic modulus of the backfill soil has little effect on the safety and stability coefficient of the slope. In the case of a lower modulus of elasticity, the safety and stability coefficient of the slope is higher than that of the high modulus of elasticity. The possible reason is that the plastic expansion zone is generated, and when the elastic modulus of the subgrade that occupies most of the entire embankment is small, the overall settlement displacement of the structure increases, which causes the center of gravity of the plastic zone to decrease, which will reduce the sliding force. On the contrary, the safety and stability coefficient of the slope is increased, and this kind of situation cannot be attributed to the improvement of the safety and stability of the slope.

Figure 7 gives the safety coefficients of the road slope for varying cohesion and internal friction angle.

The slight effect of the elastic modulus on the safety coefficient of the road slope can also be found since the slope safety coefficients were almost the same for different elastic moduli. However, it should be noted that the slope safety coefficient was obviously improved when the internal friction angle increased from 25° to 30°. The internal friction angle is the representative of the internal friction of the soil,

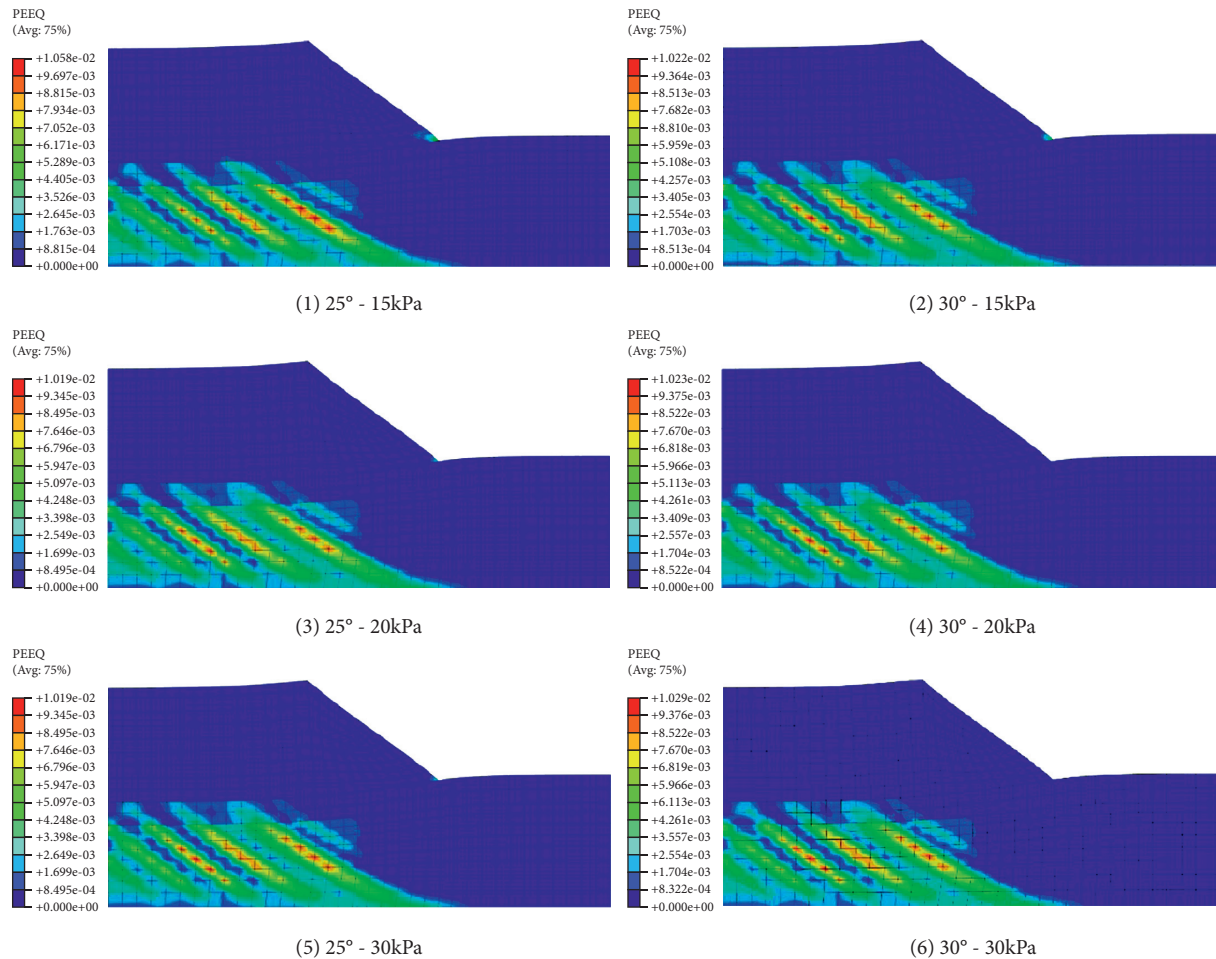


FIGURE 5: Effects of cohesion and internal friction angle. (a) 25°-15 kPa. (b) 30°-15 kPa. (c) 25°-20 kPa. (d) 30°-20 kPa. (e) 25°-30 kPa. (f) 30°-30 kPa.

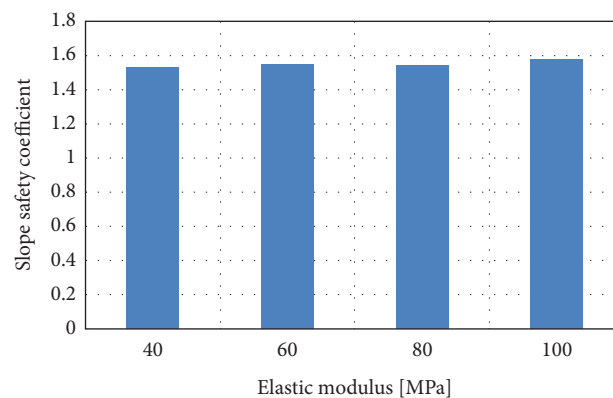


FIGURE 6: Relationship between the elastic modulus and safety coefficient ($c = 15$ kPa; $\phi = 25^\circ$).

which specifically includes the surface friction between the soil particles and the bite force generated by the interlocking action between the soil particles. The larger the internal friction angle, the greater the internal friction force, so as the internal friction angle increases, the maximum equivalent plastic strain value becomes smaller, resulting in a higher value of the slope safety factor.

Figure 8 gives the safety coefficients of the road slope when the cohesion was 15 kPa and 20 kPa, respectively.

A slight effect of the elastic modulus on the safety coefficient of the road slope can also be found because of the similar values of slope coefficients. Besides, the cohesion increased the values of the slope safety coefficient. Various physical and chemical forces between soil particles

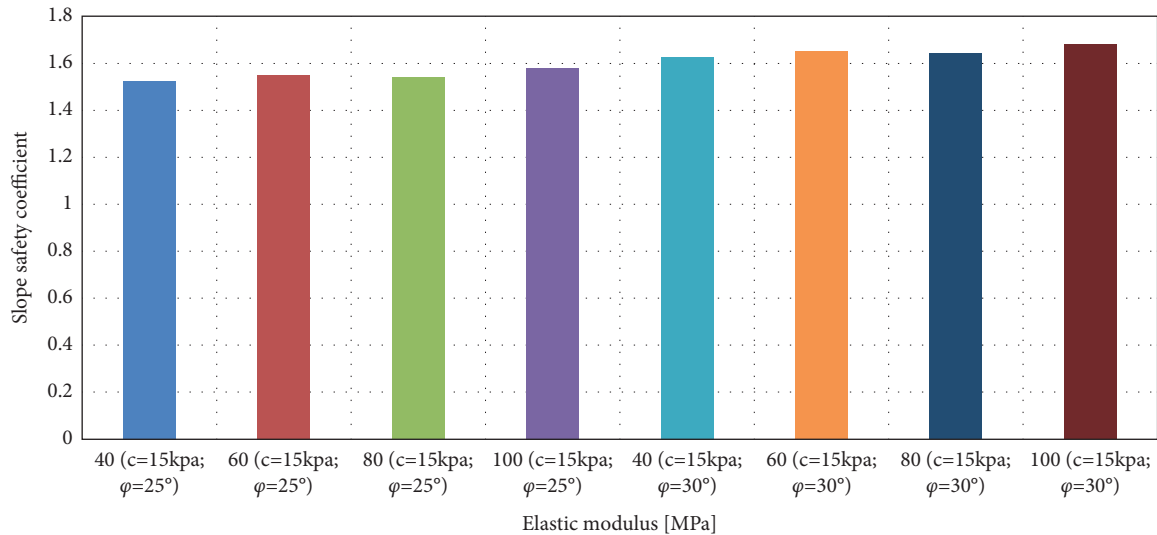


FIGURE 7: Safety coefficients of the road slope for varying cohesion and internal friction angle.

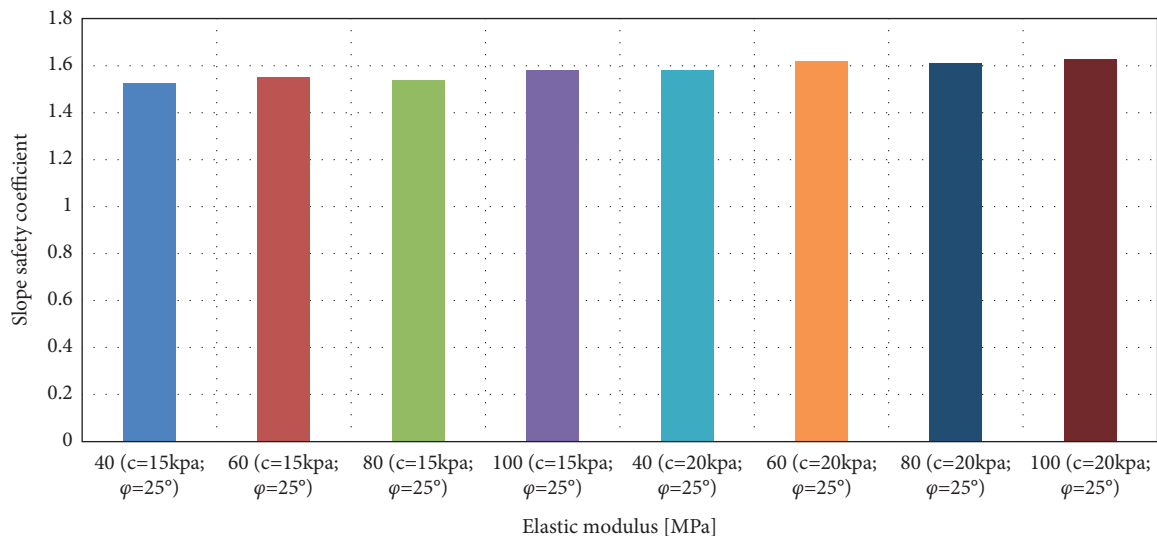


FIGURE 8: Safety coefficients of the road slope when the cohesion was 15 kPa and 20 kPa.

determine the value of soil cohesion, including Coulomb force, static force, van der Waals force, and cementation. The greater the cohesive force, the greater the suction force between the particles so that only when the external force is given greater pulling force can plastic strain occur, and the corresponding antisliding force is greater.

5. Conclusions

According to the current construction requirements of the process of backfilling the subgrade on the weak foundation, this paper conducted a FE analysis on the slope of this special engineering condition based on the commonly used strength reduction method in the stability analysis of the road slope. To accurately investigate the influence of slope and the mechanical properties of the soil on the stability of the backfill subgrade during the construction process, the slope

stability model based on the strength reduction method is established in this study. At the same time, the influence analysis of the slope, cohesion, and internal friction angle on the slope stability was carried out. The research process can highlight the following conclusions:

- (1) The slope stability analysis model established by the strength reduction method can characterize the stability of the slope by calculating the slope safety coefficient. In the analysis process, the mutation point of the relationship curve between the displacement generated in the slope and the reduction coefficient is used as the criterion.
- (2) As the slopes were lower than 1:1.5, failure to achieve penetration or local yield failure indicates that the slope is stable under this reduction factor, while as the slopes were higher than 1:1.5, the plastic

References

- [1] A. W. Bishop, "The use of the slip circle in the stability analysis of slopes," *Géotechnique*, vol. 5, no. 1, pp. 7–17, 1955.
- [2] Y. Sebsadji, S. Glaser, S. Mammari, and J. Dakhallallah, "Road slope and vehicle dynamics estimation," in *Proceedings of the 2008 American Control Conference*, June 2008.
- [3] P. Lingman and B. Schmidtbauer, "Road slope and vehicle mass estimation using Kalman filtering," *Vehicle System Dynamics*, vol. 37, no. sup1, pp. 12–23, 2002.
- [4] H. Ohnishi, J. Ishii, M. Kayano, and H. Katayama, "A study on road slope estimation for automatic transmission control," *JSAE Review*, vol. 21, no. 2, pp. 235–240, 2000.
- [5] J. Huang, T. Duan, Y. Lei, and M. Hasanipanah, "Finite element modeling for the antivibration pavement used to improve the slope stability of the open-pit mine," *Shock and Vibration*, vol. 2020, Article ID 6650780, 11 pages, 2020.
- [6] W. Shan, C. C. Zhang, and Y. Guo, "Mechanism of shallow slide on soil road cutting slope during spring in seasonal frozen region," *Applied Mechanics and Materials*, Trans Tech Publication, Bäch SZ, Switzerland, 2012.
- [7] J. Huang, Y. Sun, and J. Zhang, "Reduction of computational error by optimizing SVR kernel coefficients to simulate concrete compressive strength through the use of a human learning optimization algorithm," *Engineering with Computers*, vol. 37, 2021.
- [8] F. J. Swanson and C. T. Dyrness, "Impact of clear-cutting and road construction on soil erosion by landslides in the western Cascade Range, Oregon," *Geology*, vol. 3, no. 7, pp. 393–396, 1975.
- [9] D. Tarchi, G. Antonello, N. Casagli, and P. Farina, *On the Use of Ground-Based SAR Interferometry for Slope Failure Early Warning: The Cortenova Rock Slide (Italy)*, pp. 337–342, Springer, New York USA, 2005.
- [10] J. Huang, J. Zhang, J. Ren, and H. Chen, "Anti-rutting performance of the damping asphalt mixtures (DAMs) made with a high content of asphalt rubber (AR)," *Construction and Building Materials*, vol. 271, Article ID 121878, 2021.
- [11] H. Luo, T. Zhao, M. Dong et al., "Field studies on the effects of three geotextiles on runoff and erosion of road slope in Beijing, China," *Catena*, vol. 109, pp. 150–156, 2013.
- [12] J. L. Clayton, *Evaluating Slope Stability Prior To Road Construction*, Vol. 307, US Department of Agriculture, Forest Service, Intermountain Forest and Range, Ogden, UT, USA, 1983.
- [13] J. Huang, M. Losa, P. Leandri, S. G. Kumar, J. Zhang, and
[a] Sun, "Potential anti-vibration pavements with damping layer: finite element (FE) modeling, validation, and parametrical studies," *Construction and Building Materials*, vol. 281, Article ID 122550, 2021.
- [14] Z. Cai and X. Zheng, "A private and efficient mechanism for data uploading in smart cyber-physical systems," *IEEE Transactions on Network Science and Engineering*, vol. 7, no. 2, pp. 766–775, 2018.
- [15] J. Huang, Y. Sun, and J. Zhang, "Reduction of computational error by optimizing SVR kernel coefficients to simulate concrete compressive strength through the use of a human learning optimization algorithm," *Engineering with Computers*, vol. 37, 2021.
- [16] W. Wei, Y. M. Cheng, and L. Li, "Three-dimensional slope failure analysis by the strength reduction and limit equilibrium methods," *Computers and Geotechnics*, vol. 36, no. 1-2, pp. 70–80, 2009.
- [17] M. Prokurov, A. Indykin, and A. Alekseyev, "Increasing the reliability of the soil slopes design using evolutionary modelling," *MATEC Web of Conferences*, vol. 251, no. 3, Article ID 04017, 2018.
- [18] J. T. Christian, C. C. Ladd, and G. B. Baecher, "Reliability applied to slope stability analysis," *Journal of Geotechnical Engineering*, vol. 120, no. 12, pp. 2180–2207, 1994.
- [19] C. H. Juang, Y.-Y. Jhi, and D.-H. Lee, "Stability analysis of existing slopes considering uncertainty," *Engineering Geology*, vol. 49, no. 2, pp. 111–122, 1998.
- [20] B. Yang, X. Li, Y. Hou et al., "Non-invasive (non-contact) measurements of human thermal physiology signals and thermal comfort/discomfort poses—a review," *Energy and Buildings*, vol. 224, Article ID 110261, 2020.
- [21] S. Xie, Z. Yu, and Z. Lv, "Multi-disease prediction based on deep learning: a survey," *Computer Modeling in Engineering and Sciences*, vol. 127, no. 3, pp. 1–34, 2021.
- [22] Z. Wan, Y. Dong, Z. Yu, H. Lv, and Z. Lv, "Semi-supervised support vector machine for digital twins based brain image fusion," *Frontiers in Neuroscience*, vol. 15, p. 802, 2021.
- [23] Z. Lv, S. Zhang, and W. Xiu, "Solving the security problem of intelligent transportation system with deep learning," *IEEE Transactions on Intelligent Transportation Systems*, vol. 22, no. 7, pp. 1–10, 2020.
- [24] Z. Lv, L. Qiao, K. Cai, and Q. Wang, "Big data analysis technology for electric vehicle networks in smart cities," *IEEE Transactions on Intelligent Transportation Systems*, vol. 22, no. 3, pp. 1–10, 2020.
- [25] M. Jahanbakht, W. Xiang, L. Hanzo, and M. R. Azghadi, "Internet of underwater Things and big marine data analytics—a comprehensive survey," *IEEE Communications Surveys & Tutorials*, vol. 23, pp. 904–956, 2021.
- [26] X. Cheng, B. Yang, A. Hedman, T. Olofsson, H. Li, and
[a] G. Van, "NIDL: a pilot study of contactless measurement of skin temperature for intelligent building," *Energy and Buildings*, vol. 198, pp. 340–352, 2019.
- [27] Z. Cai and Z. He, "Trading private range counting over big IoT data," in *Proceedings of the 2019 IEEE 39th International Conference on Distributed Computing Systems (ICDCS)*, July 2019.
- [28] M. Hudson, I. Idriss, and M. Beikae, *User's Manual for QUAD4M: A Computer Program to Evaluate the Seismic Response of Soil Structures Using Finite Element Procedures and Incorporating a Compliant Base*, University of California, Los Angeles, CA, USA, 1994.

Measurements of Heart Rate and Facial Expression to Assess Human Reactions in Glass Structures

Anand Mandal, *Department of Civil Engineering, Raajdhani Engineering College, Bhubaneswar, anandmandal1@gmail.com*

Alivasakhi Mishra, *Department of Civil Engineering, Capital Engineering College, Bhubaneswar, alivasakhimishra258@gmail.com*

Sudepta Kishor Dash, *Department of Civil Engineering, NM Institute of Engineering & Technology, Bhubaneswar, sudeptakishordash1@gmail.com*

Murari Prasad Panda, *Department of Civil Engineering, Aryan Institute of Engineering & Technology, Bhubaneswar, muraripanda25@outlook.com*

ABSTRACT

Human comfort is difficult to achieve in engineering applications because it is dependent on various factors that can be statistically controlled and maximised, such as structural, energy, or thermal difficulties, among others. Major issues might arise from a combination of human emotions that are tied to a variety of factors. Part of the problem is the so-called "emotional architecture" and its uneasy sentiments. As a result of the interaction of objective and subjective criteria, the "ideal" building design might become complicated. The results of a pilot experiment conducted remotely to quantify the reactions and nerve states of ten volunteers exposed to structural glass environments are presented in this publication. As is well known, intrinsic material properties (transparency, brittleness, and so on) necessitate specific engineering knowledge for safe mechanical design, but they can also elicit strong subjective feelings in customers, affecting their psychological comfort and, as a result, their behaviour and movements. This research uses static and dynamic Virtual Reality (VR) environments, as well as facial recognition software.

1. Introduction

It is generally recognized that human comfort in the built environment is a target for a multitude of aspects [1,2]. Engineering tools that can be used to optimize comfort are able to account for a great number of factors and parameters which can affect comfort levels severely. Typical applications are focused on thermal comfort, indoor air quality, visual comfort, noise nuisance, ergonomics, vibrations, and others. In addition, it is also recognized that other aspects (like, for example, personal factors, nervous states, and architectural parameters) should be also properly considered in the list of influencing indicators for comfort. There are no doubts about the correlation of built environment characteristics and its impact on the occupants' emotions, behaviours, and physical well-being [2]. The same behaviours can also affect

typical engineering issues and indirectly influence the building design and detailing [3–6].

Structurally speaking, vibration serviceability issues and the consequent risk of user discomfort are, for example, usually addressed in terms of acceleration peaks and recommended limit parameters. Their satisfaction ensures possible annoyance for customers or suggests a design retrofit/modification [7–12]. As a matter of fact, however, there are no doubts that human reactions to vibrations strongly depend on the physiological perception of frequency and amplitude of vibrations. The operational context and the nervous state of users have thus a severe impact on the degree of human tolerance of vibration issues [9]. Most importantly, such a set of feelings can be maximized in presence of uncomfortable architectures and building components.

The well-known psychological effect of architecture can have both positive and negative effects on users and thus can evoke subjective feelings that could possibly interact with mechanical choices and technical detailing of structural design [13]. This is typical of architects that evoke nervous states in the so-called “emotional buildings” [14–19]. Pilot literature studies, in this regard, proved that experimental measures can be carried out to quantify users emotions [20]. Smart sensors for real or Virtual Reality (VR) walks proved also to represent useful tools in support of the quantitative analysis of human reactions and emotions to building stimuli [21,22]. In this paper, a special care is spent for structural glass applications in buildings. Known as versatile but vulnerable constructional material, glass transparency and capacity to adapt to various setup configurations make it a largely used solution [23]. The high aesthetic impact of glass structures can be thus sometimes in contrast with the need of more efficient feeling of protection for the occupants, as it could be for extreme accidents, pedestrian systems, or uncomfortable configurations (Figure 1). Glass walkways are in fact often known as “architectures of vertigo” [26], where transparent structures are conceived as spaces of visceral thrills and intense psychophysiological stimuli with deep sensory experience and sociospatial implications. Additionally, glass pedestrian systems can be highly demanding in engineering terms, due to the mutual interaction of mechanical dynamic parameters, complex Human-Structure Interaction (HSI) phenomena, and even severe subjective reactions [9]. The analytical analysis and quantitative measure of emotional states for customers can thus represent a useful tool in the whole design process.

2. Research Goals and Experimental Strategy

A virtual experimental study is presented and assessed in this paper, in support of structural glass design. The goal of the proposed method is to quantify the prevailing human reactions and comfort levels for occupants that are exposed to different virtual built environments made of/with a primary role of glass. The measured reactions are then compared to address the psychological comfort level of volunteers under imposed visual stimuli. In accordance with Figure 2, the process takes advantage of a quantitative analysis of emotions based on the analysis of facial microexpressions (Action Units (AUs) of nervous states) and also heart rate (HR) parameters for volunteers exposed to several glass built scenarios.

While the use of glass material in buildings is largely increasing and further demanded in the post-Covid-19 stage [27,28], its impact on the psychological comfort of customers can be severely affected by transparency, intrinsic brittleness, lack of technical knowledge on its structural performance, vulnerability risk, etc. [29,30].

Glass material for structural applications is in fact known to require specific engineering knowledge for optimal and safe mechanical design. Besides, discomfort for building in occupants can still arise and thus affect their behaviour and movements inside/onto a glass system. Typical examples can be related to glass pedestrian systems or structural glass barriers with risk of shards/fall.

In this regard, under the limits of remote experimental measures, and based on the herein presented research outcomes, it is expected that building structural design could take advantage of subjective measurements in support of classical mathematical tools and engineering models. Besides, real in situ experimental procedures should be also carried out for a further extension of the methodology.

More in detail, the pilot experimental investigation was carried out with the active contribution of 10 participants and the FaceReader™ automatic facial expression recognition software [31]. The number of volunteers was chosen based on the availability of individual participants and on the number of experimental records to process for each participant/stimulus/time interval. The group of participants was selected from a class of volunteers preliminary involved in measurement trials discussed in [25]. The class of volunteers included 60% females and 40% males, with an average age of 28 years. No preliminary technical knowledge on structural glass in constructions was required at the time of the experiment.

The remote experimental procedure was planned as in Figure 3, as an adaptation and extension of [25]. Two different stimuli were designed to address nervous states and human reactions of volunteers, namely, a VR set of “static” items and a “dynamic” video clip of virtual walks. A special attention was paid for the selection of stimuli, so as to capture different facial microexpressions and emotions. For this reason, a preliminary Computer Assisted Web Interviewing (CAWI) survey was also distributed in Winter 2020 and used to explore the prevailing subjective reactions for the selected participants asked to virtually deal with buildings or open spaces characterized by a prevailing role of structural glass. At the end of the remote experiments, moreover, the participants were asked to comment about their feelings.

There are several literature studies which confirm the potential of human emotions as a guide for designers in different research fields [32,33]. Besides, such a result can be achieved in different ways. Facial microexpressions are, for example, considered essential for the quantitative analysis of basic emotions, because human faces provide useful information about feelings and the inner individual states. At the same time, there is a large number of literature experiments that confirm the strict correlation between human reactions and emotions with HR data and their variations over time [34–36], as well as the useful feedback that can be derived from biosignals [37–39]. In the present study, both facial expressions and optical HR data are recorded for volunteers exposed to virtual glass structures.

As shown in Sections 3–5, the analysis of experimental results confirms that the use of glass in buildings is still largely affected by scattered human reactions. For selected stimuli, a rather close match can be observed for most of participants. It is worth to be noted that a good trend in facial microexpressions/emotions and HR data can be found for the imposed scenarios. Such an outcome, consequently, suggests the comparative analysis of remote facial measures with possible in situ experimental records.

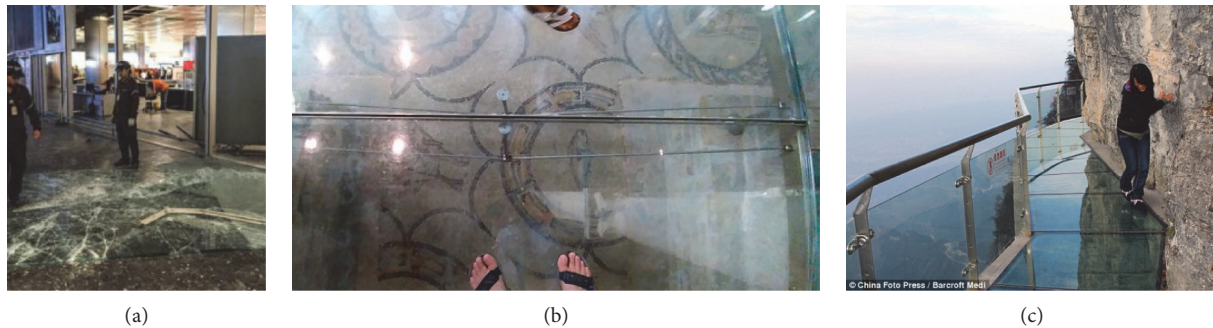


FIGURE 1: Selection of glass built scenarios: (a) cracks and shards in glass walls and windows under hazard (reproduced from [24] with permission from Elsevier®, copyright license agreement n. 5042381253637, April 2021); (b) indoor pedestrian system (walkway in Aquileia, IT; reproduced from [9] under the terms and conditions of CC-BY license); (c) Cliffside skyway, CN (reproduced from [25] under the terms and conditions of CC-BY license).

3. Virtual Experimental Analysis

3.1. Remote Testing. The procedure schematized in Figure 4 was repeated twice for each volunteer, first with a static VR input and later with a VR video clip of virtual walks. All the experiments were carried out remotely, under Covid-19 restrictions to mobility, with the support of laptops, a shared screen for the input stimuli, and a web cam for recording the face of participants.

The invited subjects were preliminary informed about how the experiment would be conducted. To this aim, the setup was properly checked, so as to avoid disturbing effects for the record acquisition and for the postprocessing analysis. A special attention was given to ensure an optimal and mostly uniform ambient illumination and face exposure for the participants. The position of the screen for each participant was also checked, so as to avoid distortions or introduce misleading inclination values for the experimental acquisition. Finally, the presence of participants with glasses or beard was allowed but separately noted, for a more refined analysis of collected data. Once the operational conditions were verified, the input source was shared to all the participants. During the presentations, audio communication was allowed to provide additional comfort to the participants. No audio source was indeed introduced in addition to the visual input. During each one of the presentations, the webcam of controlling machine was used to record the facial expressions of the participants, while looking at the shared screen. For this purpose, a preliminary tentative to capture the best cam resolution and sampling rate was carried out. The final choice resulted in high quality records with minimum 1280×720 (or 1920×1028) video resolution and a total of frames in the range of 4300 for each signal (30–60, the range of frame rate; 12432 kbits/s, the average bitrate). The software analysis was based on all the collected frames for each record, thus requiring an average of 10 minutes/setup.

3.2. Measurement of Raw Signals. The analysis and interpretation of facial expressions and heart rate data for the participants exposed to VR stimuli was carried out with a hybrid approach. A fundamental role was assigned to the

automatic analysis offered by FaceReader™, for the quantification of basic human reactions, emotional states, and HR data as in Figure 2. Furthermore, the manual elaboration of software results represented a key step of analysis.

The selected commercial software was used because it is based on Artificial Intelligence tools and can efficiently detect subjective emotions, human reactions, and HR parameters from input video records. Based on 500 key points for the description of facial movements, the output classifications of $N = 7$ nervous states based on facial expressions include “happy”, “sad”, “scared”, “disgusted”, “surprised”, “angry”, and “neutral” feelings. These states are normalized and quantified in terms of instantaneous evaluation of Action Units (AU) for basic emotions. Among others, an additional intrinsic advantage of the used software is represented by the optical measure of HR of subjects, based on complex remote photoplethysmography (rPPG) optical techniques. The rPPG module analyzes HR data and HR variability from input videos of participants, by quantifying the amount of light that is reflected by their face. The latter relates to cardiac cycles and changes in blood volume based on video captured by the camera [40]. Different literature studies proved that the remote HR analysis can be powerful and efficient [41–44]. The limit requirement is that setup conditions for the experiments are properly addressed. Possible movements of participants (i.e., while walking, talking, etc.) may result in overestimates or underestimates for real HR data [45,46].

In the present study, the implicit advantage was represented by constant ambient conditions for all the participants and by their mostly fixed position during the whole experimental analysis (sitting on a chair). Moreover, a preliminary check of setup features resulted in input video records for the software generally classified as “high quality” video sources for remote analysis (Figure 5). An example of resulting AUs and HR records is shown in Figure 6 for one of the involved participants. The experimental measurements for each participant/virtual experiment/inner state were in fact collected in the form of AU charts of single basic emotions (in the range from 0 to 1) and HR data (bpm), as a function of time.

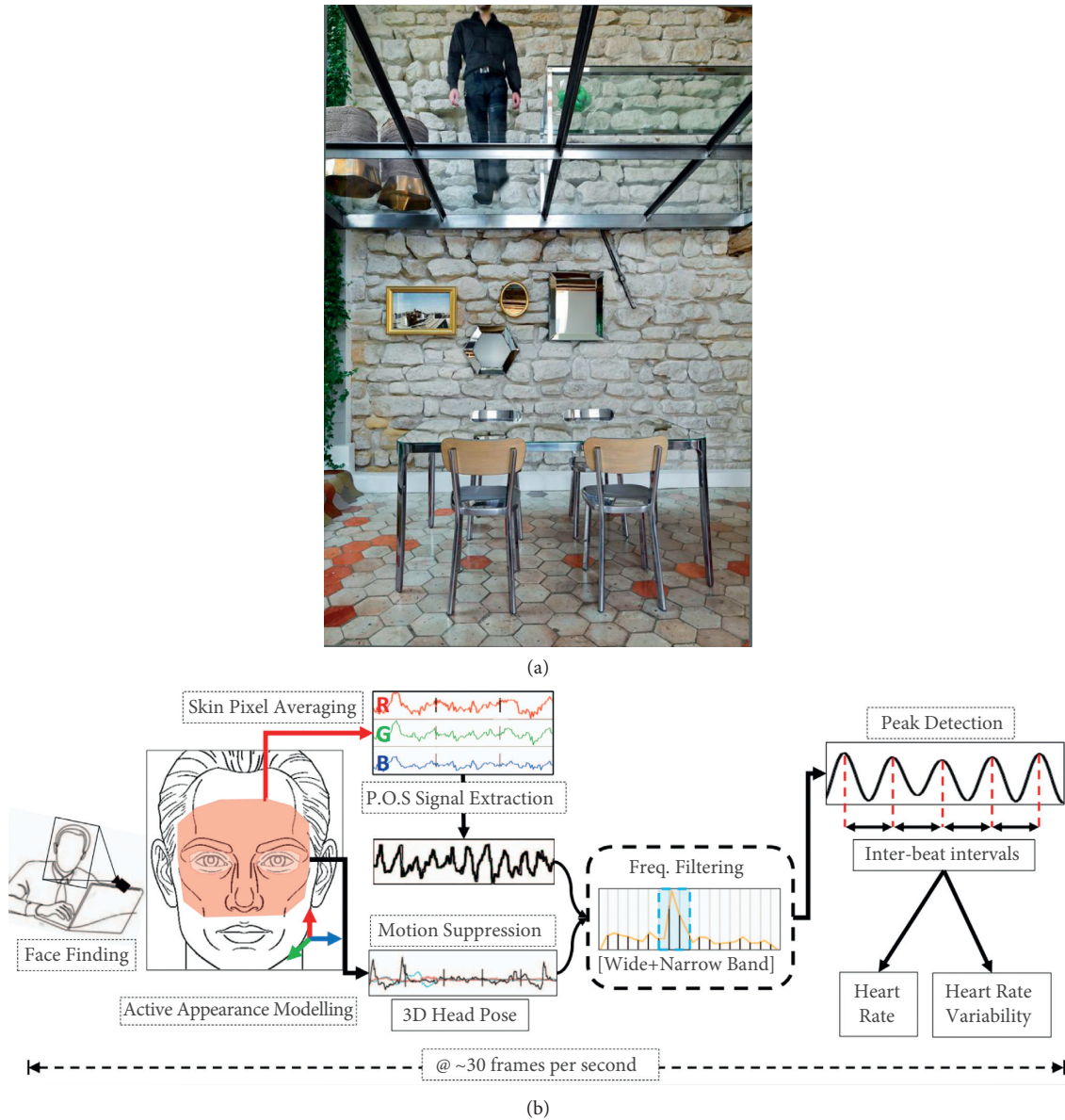


FIGURE 2: Example of (a) glass structure used as input stimulus (apartment floor in Paris, FR, ©Jerry Jacobs Design) and (b) remote facial expression analysis.

3.3. Postprocessing Strategy for Measured Raw Signals. A set of charts agreeing with Figure 6 was used for the interpretation of human reactions and for the analysis of their possible correlations with the imposed VR stimuli. To this aim, postprocessing feedback from volunteers was also used to double-check the emotional states. It is worth to be noted that the chart in Figure 6 omits the first instants of records, where a preliminary discussion was carried out with each participant to provide instructions and create a comfortable condition.

3.3.1. Action Units and Emotions. Given that multiple AU records were collected for each participant/state/VR stimulus, the first postprocessing step consisted in the detailed analysis of single AUs. The first effort was spent for the

normalization of AU records in time, so as to offer a more independent analysis and comparison of AU records for multiple participants. This was measured as

$$AU_{\text{norm}}(t) = AU_{\text{original}}(t) - AU_{\text{initial,avg}}(t). \quad (1)$$

with $0 \leq t \leq 120$ s and $AU_{\text{norm}}(t)$, the normalized record for each participant, emotion, and VR scenario, at the time instant t ; $AU_{\text{original}}(t)$, the original signal record for each participant, emotion, and VR scenario, at the time instant t ; $AU_{\text{initial,avg}}$ the mean value of each emotion, participant, and VR scenario (preliminary stage).

Following equation (1), the individual records of basic emotions, $AU_{\text{norm}}(t)$, were successively grouped in basic pos * (t) and neg * (t) plots. In the pos * (t) set, the AU data in time for feelings marked as “happy” were considered only:

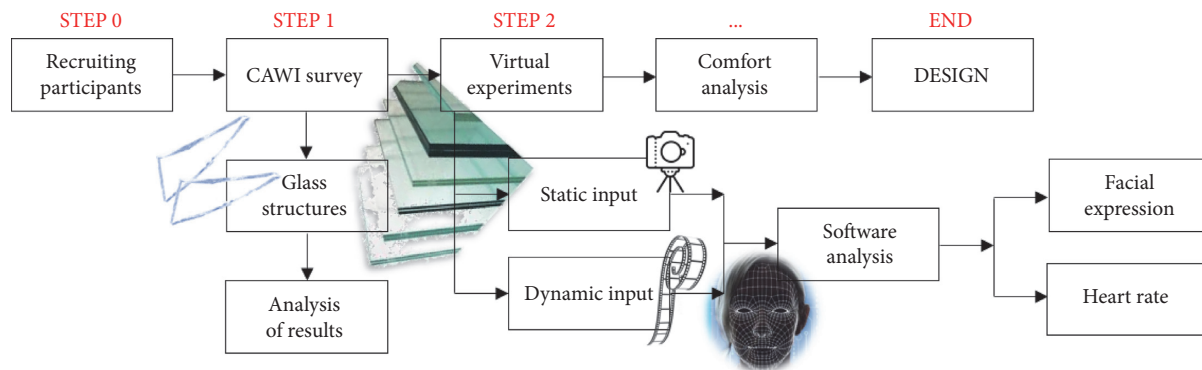


FIGURE 3: Flowchart of the virtual experimental analysis.

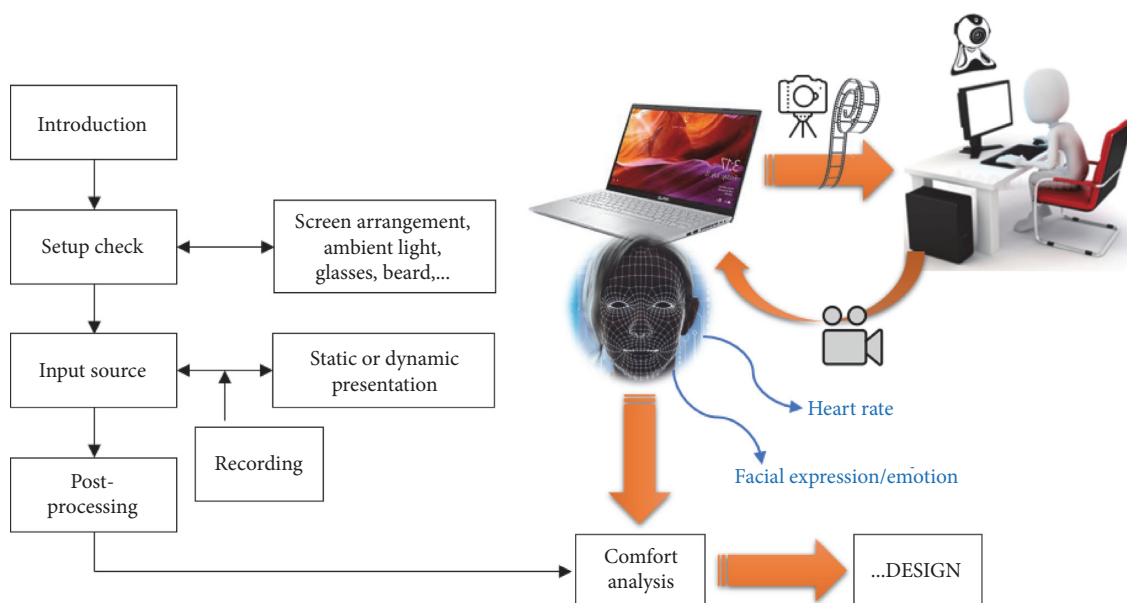


FIGURE 4: Flowchart for the virtual experimental investigation.

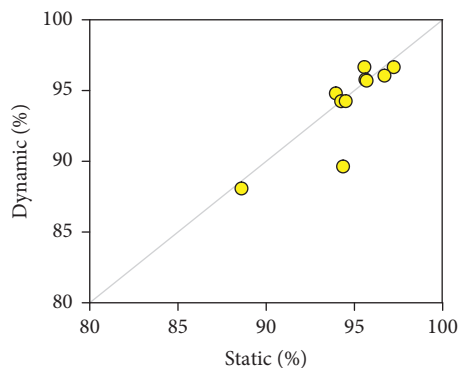


FIGURE 5: Quality level for the input video records of each participant, under static or dynamic VR input stimuli.

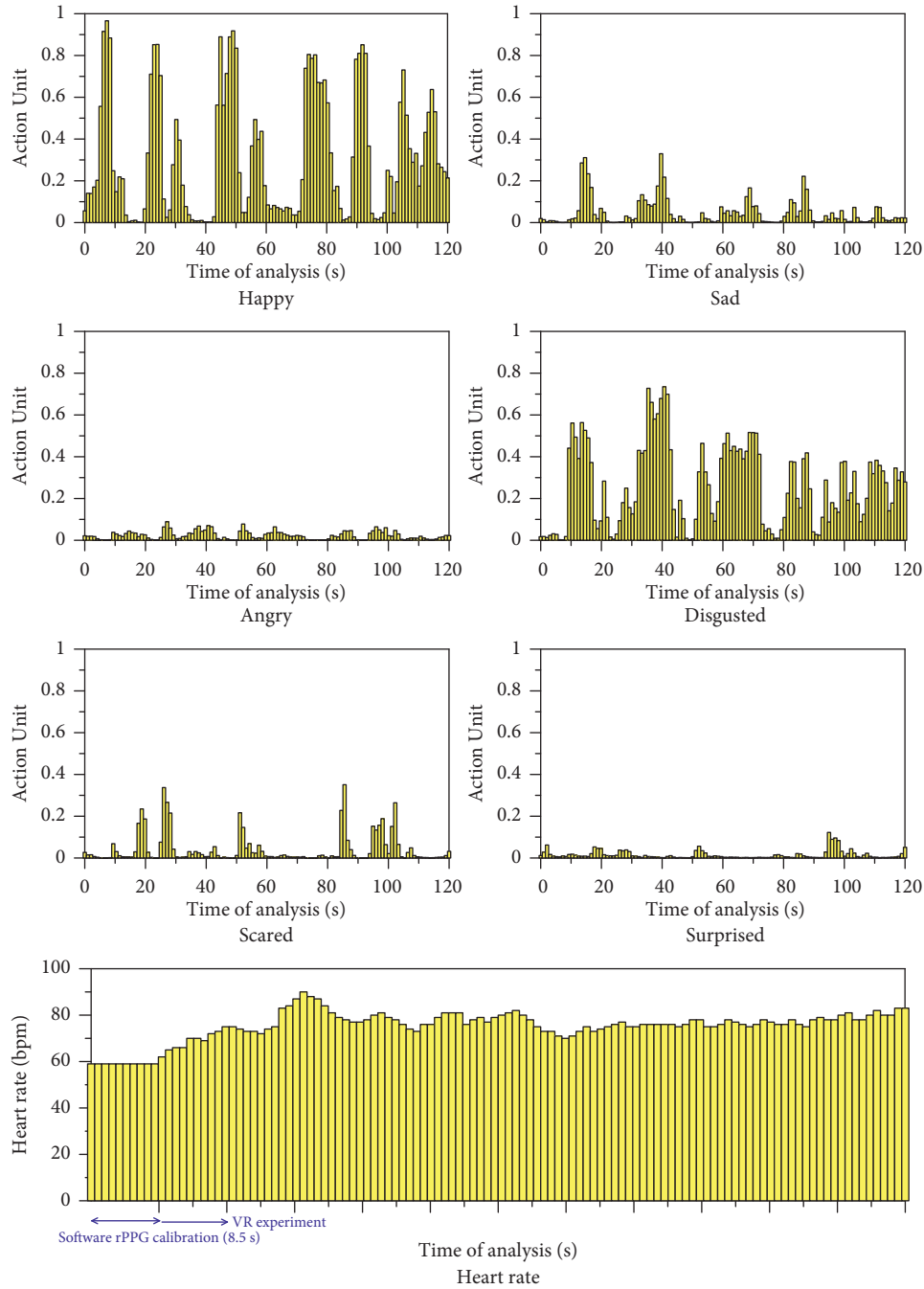


FIGURE 6: Example of AU (0–1 range) records of facial expressions and HR data (bpm), over the time of the experimental analysis, as obtained for one of the participants under VR stimuli.

$$\text{pos}^*(t) = \sum_{i=1}^{N-1} \text{AU}_{\text{norm}}(t) = f(\text{happy}). \quad (2)$$

$$\text{neg}^*(t) = \sum_{i=1}^{N-1} \text{AU}_{\text{norm}}(t) = f(\text{sad, angry, scared, disgusted}). \quad (3)$$

Similarly, the $\text{neg}^*(t)$ set included the input data from feelings marked as “sad”, “angry”, “scared”, and “disgusted”:

The “surprised” AU data (“SUR(t)”) was disregarded in the so-calculated $\text{pos}^*(t)$ and $\text{neg}^*(t)$ signals but analyzed

separately. Depending on the individual subject, context, and stimulus, “surprised” states can be in fact typically associated with both positive or negative feelings [25]. For the same reason, “neutral” states were omitted from the study, due to the virtual remote setup. The final marking of emotional data was based on the analysis of prevailing AUs at a given time instant t , where the $SUR(t)$ input was superimposed as

$$POS^*(t) = \begin{cases} pos^*(t) + SUR(t) & \text{if } pos^*(t) > neg^*(t), \\ pos^*(t) & \text{if } pos^*(t) < neg^*(t), \end{cases} \quad (4)$$

or

$$NEG^*(t) = \begin{cases} neg^*(t) + SUR(t) & \text{if } neg^*(t) > pos^*(t), \\ neg^*(t) & \text{if } neg^*(t) < pos^*(t). \end{cases} \quad (5)$$

In conclusion, the final detection of comfort trends for a given visual stimulus was carried out based on the percentage variation of elaborated signals, over the time of analysis. At each increment t of the experiment, the emotional variation was calculated for both $POS^*(t)$ and $NEG^*(t)$ data as

$$\Delta\% = 100 \frac{Y(t_n) - Y(t_{n-1})}{Y(t_{n-1})}, \quad (6)$$

with $Y = POS^*(t)$ or $NEG^*(t)$, respectively, as in the example of Figure 7.

The prevailing emotional state (and thus comfort trend) was established analytically, in terms of absolute maximum values of nervous feelings and max/min percentage variations. Each time instant t was classified with a final POS or NEG mark, uniquely detected from data elaboration. A unitary “comfort weight” value $C(t) = POS$ or NEG (based on the prevailing nervous state) was assigned to each participant/instant/scenario, to facilitate the comparative analysis of multiple signals and stimuli. More precisely,

for static VR, the primary/prevailing emotion based on AUs was calculated for each one of the 27 input items and

for dynamic VR input, the attention was still focused on primary emotions based on AUs, but for specific frames only that were detected and selected from absolute AU peaks and building configurations.

3.3.2. Heart Rate and Emotions. The elaboration of HR data derived from rPPG techniques was based on the analysis of single measures over the time of the experiment. Studies of literature (see, for example, [21] and Figure 8) demonstrated that HR measures can offer useful feedback for the quantification of emotions and human feelings. In the present study, based also on the relatively short duration of stimuli, the attention was focused on the comparison of HR data trends with facial expression measurements, for a given participant/stimulus. In the present study, the HR variation

in time was labelled as $HR^+(t)$ or $HR^-(t)$, respectively (with $0 \leq t \leq 120s$), with $HR^+(t)HR(t) > HR(t-1)$, (7a)

or

$$HR^-(t)HR(t) < HR(t-1). \quad (7b)$$

As in Section 3.3.1, a unitary “comfort weight” $C(t)$ was assigned to the HR^+ and HR^- parameters, so that each instant t could be quantified as in equation (7) with a POS or NEG reaction. Care was paid especially for HR^+ data, so as to detect possible discomfort/NEG feelings of volunteers, while the HR decrease (HR^-) was related to comfortable situations. Furthermore, a null comfort weight was assigned to the limit condition $HR(t) = HR(t-1)$.

3.3.3. Correlation of Heart Rate and Facial Expression Measurements. The combined analysis of AUs and HR outcomes for the comfort quantification of participants was carried out by comparison of normalized weights over the time of the experiment. In this manner, the attention was focused

On the analysis of single elaborated signals for a given participant and stimulus (HR or facial AU)

On the synchronized analysis of HR and facial expression data for a single participant, over the time of experiment; in this case, the attention was focused on the potential agreement of AU and HR data and trends at a given time instant t

On the analysis of reaction trends from the whole group of volunteers

4. Discussion of Stimuli and Results

4.1. Static VR Input. The participants were subjected to a selection of 27 pictures, equally spaced at time intervals of 5 seconds. Figure 9 shows some examples, where labels $\#n$ denote the order of items. For each subject, the stimuli sequence was kept fixed. The items were selected from magazines, scientific journals, construction companies webpages, and newspapers. Major advantage for the selection of items was taken from the preliminary CAWI survey (Step 1 in Figure 3).

4.2. Analysis of Prevailing Reactions Based on AUs and HR Data. Average POS and NEG reactions were first calculated for each static item and participant. Figure 10 shows the prevailing reactions in the group of volunteers, giving emphasis on measured (a) discomfort (NEG and HR^+ data) or (b) comfort (POS and HR^-), respectively.

As far as a different time instant is selected in Figure 10, it is worth of interest to note the variation of POS/NEG and HR^+/HR^- data for volunteers. The chart shows a clear variation of emotions and human reactions for an assigned stimulus, with marked fluctuations of POS and NEG data. Rather balanced POS/NEG conditions can be noticed for

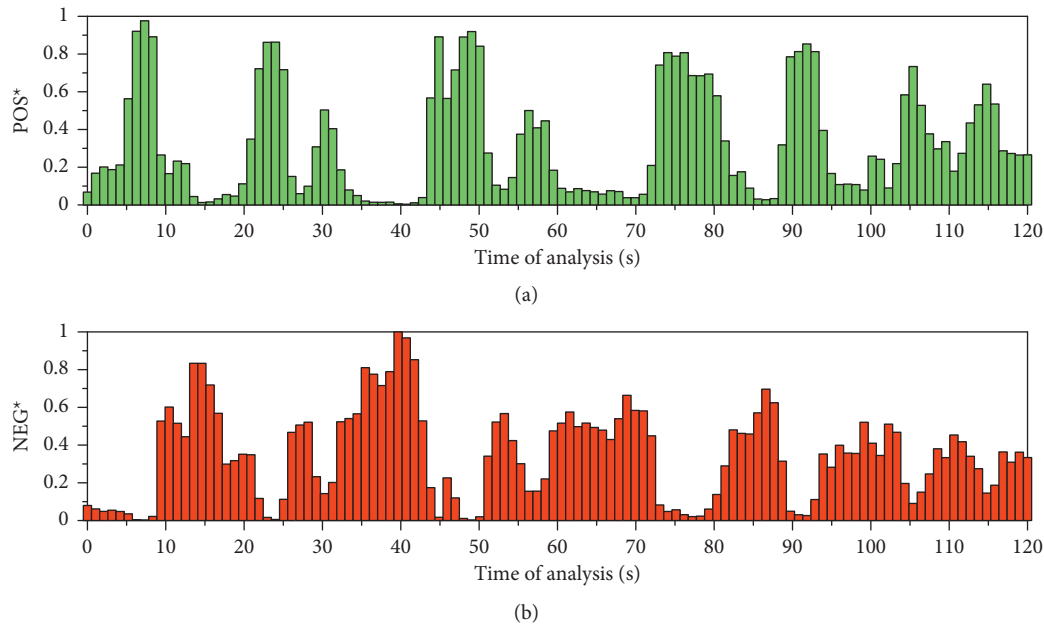


FIGURE 7: Example of calculated (a) POS* and (b) NEG* measurements of AU signals, as obtained for one of the participants under the VR input source.

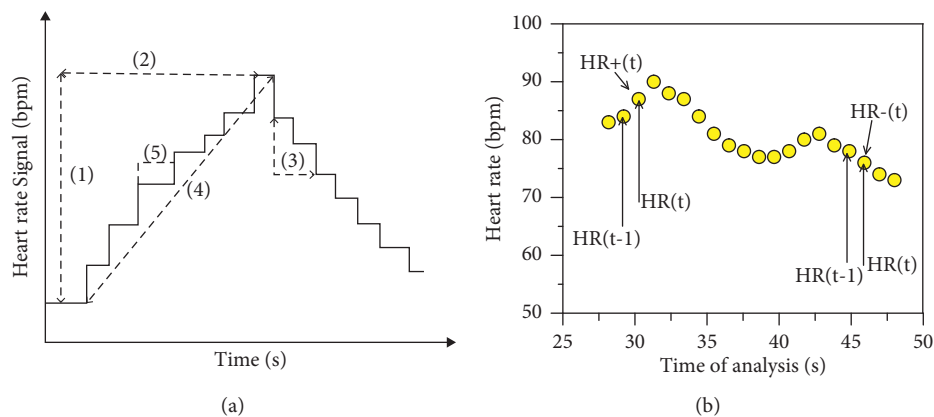


FIGURE 8: Heart rate analysis over the time of VR experiment: (a) procedure presented in [21] (figure reproduced under the terms and conditions of a CC-BY license) and (b) current study.

some instants of the experiment. Moreover (at least for some intervals), a good correlation of NEG/HR⁺ trends can be observed, in the same way of POS/HR⁻ variations in time. Within the limitations of the study, such a finding confirms that HR increases corresponding to discomfort and negative feelings for participants, while the HR decrease can be related to a more comfortable situation and nervous state.

A more concise analysis of measured AUs and HR data for each stimulus can be indeed carried out based on Figure 11, where average experimental outcomes are proposed for the 27 items (5 seconds each). The good match of NEG and HR⁺ data for most of the pictures is worth to be noted. Rather close agreement (but for a limited number of items) can be observed also for POS and HR⁻ trends, thus enforcing the potential of the procedure.

In this regard, some first conclusions about the experimental method can be derived when global results are grouped and analyzed as for items characterized by

- prevailing NEG reactions (#14, #19, #25, #27),
- prevailing POS reactions (#1, #10, #20, #21),
- mostly “balanced” NEG and POS reactions (#2, #3, #5, #15, #16),
- prevailing NEG values with a good match of HR⁺ reactions, to denote discomfort (#19, #25), and
- prevailing POS values with a good match of HR⁺ reactions (#10, #20, #21, #24).

Selected items with marked NEG and POS reactions are proposed in Figures 12 and 13, respectively.

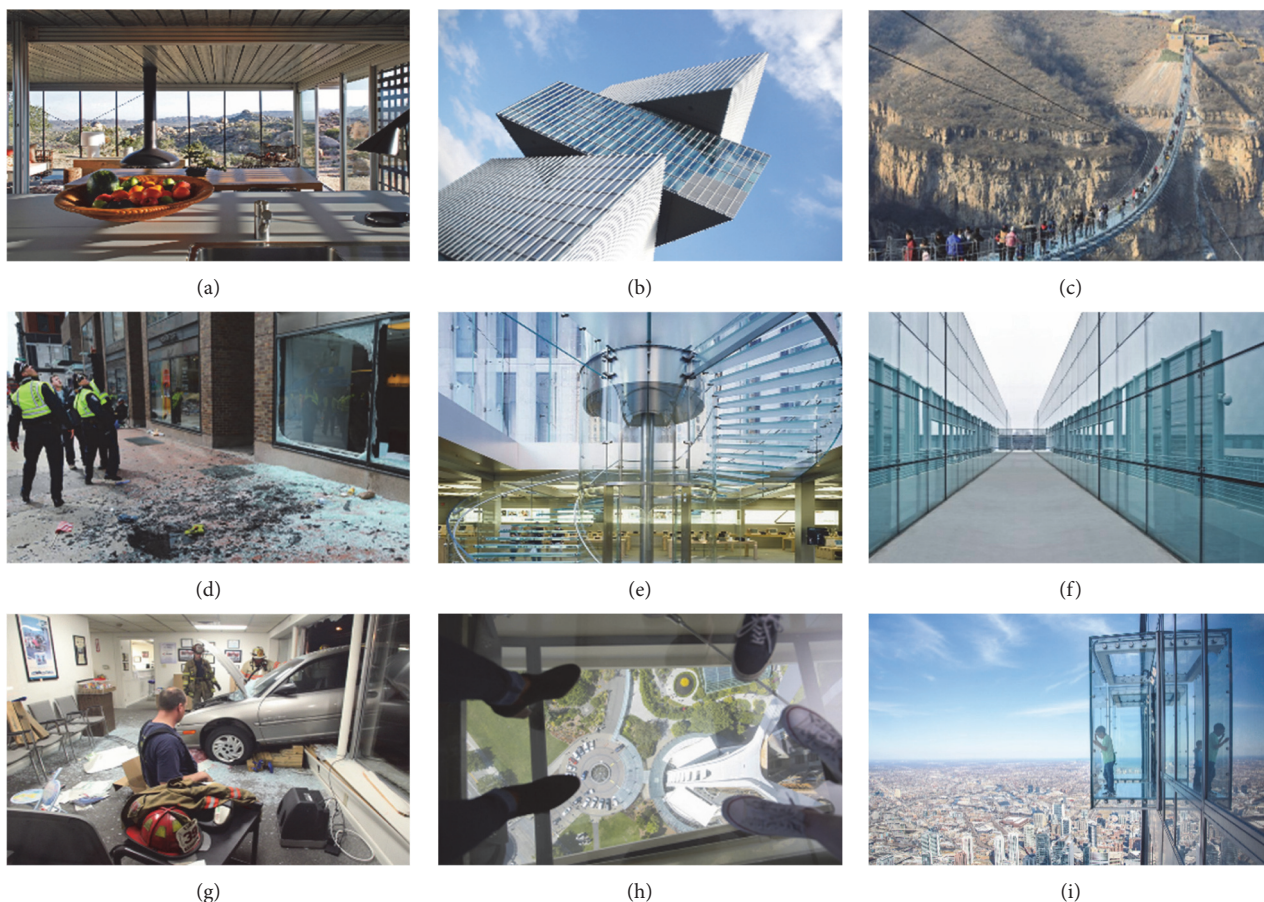


FIGURE 9: Selection of static input sources for the static VR experiment: (a) private room (Off-grid itHouse, Pioneertown, USA; © Airbnb); (b) Amsterdam RAI Hotel, NL (courtesy of © A Bakker); (c) Hongyagu bridge, Hebei, CN (© REUTERS/Stringer); (d) windows under blast hazard; (e) stair (Apple Cube, New York, USA, © Sedak GmbH & Co KG); (f) facade and walls; (g) window under vehicle impact; (h) Space Needle tower (Seattle, WA, USA); (i) skyscraper (Willis Tower, Chicago, USA). (a) Item #1; (b) item #2; (c) item #4; (d) item #6; (e) item #8; (f) item #11; (g) item #12; (h) item #15; (i) item #20.

4.3. Analysis of Reactions Based on the Subject of Items. A special care was paid for the analysis of experimental measurements for grouped static pictures. The attention was focused on glass structures and components representative of major categories of items and built environments, namely:

Group A: pedestrian glass systems and structures or glass elements characterized by risk of fall for the occupants (items #4, #8, #10, #13, #15, #17, #18, #20, #22, #23, and #27).

Group B: glass systems or elements with damage and/or under hazard (items #6, #9, #12, and #25).

Group C: others (#1, #2, #3, #5, #7, #11, #14, #16, #19, #21, #24, and #26).

Figure 14 reports the residual static items from the full set of 27 pictures, while Table 1 presents a summary of prevailing reactions based on facial expressions and heart rate parameters (% of prevailing measurements for grouped items).

It is worth to be noted that there is a marked NEG response for groups A and B that are characterized by a major risk for the participants. In particular, the presence of damage (B) evokes

high discomfort in the majority of the involved volunteers. Besides, for the set of pictures in group C, a more balanced response was measured. For the pictures in group A, the experimental outcome suggests that pedestrian glass systems involve the highest human reaction and intrinsic discomfort, compared to other glazing solutions in buildings. The effect can be justified by the fact that the human interaction with the structure becomes predominant. It is important to notice the POS effect of occupants in the pictures, as, for example, in the case of item #10.

Even under the limitations of the experimental study herein presented, the collected results suggest that as far as the structural design of the glass system is optimally designed to preserve robustness, stability, and overall protective feedback for the occupants, the first human reaction is slightly on the side of POS feelings. In this regard, it is necessarily required to explore further this kind of scenario and extend the VR experimental stage with field experiments, so as to capture the human reactions of active pedestrians and combine these emotional feelings with the structure vibrations and other mechanical parameters of primary interest for the dynamic

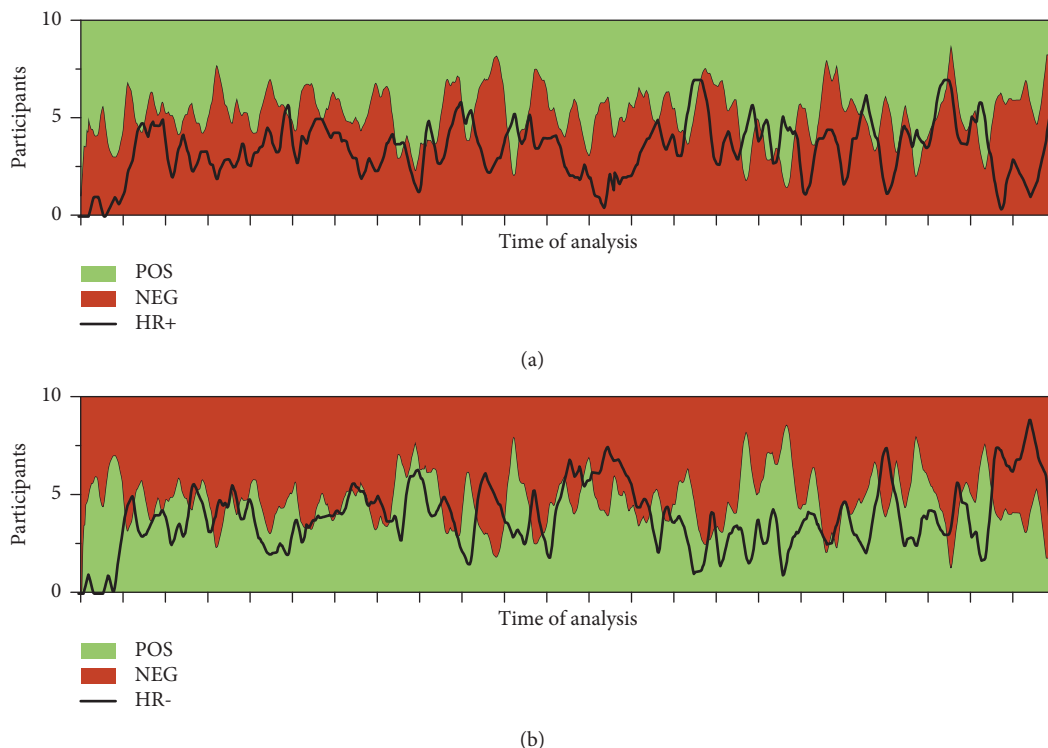


FIGURE 10: Detection of prevailing reactions (for the whole group of participants), as a function of the time of analysis, based on facial expression or heart rate data. In evidence, the measured (a) discomfort or (b) comfort of participants.

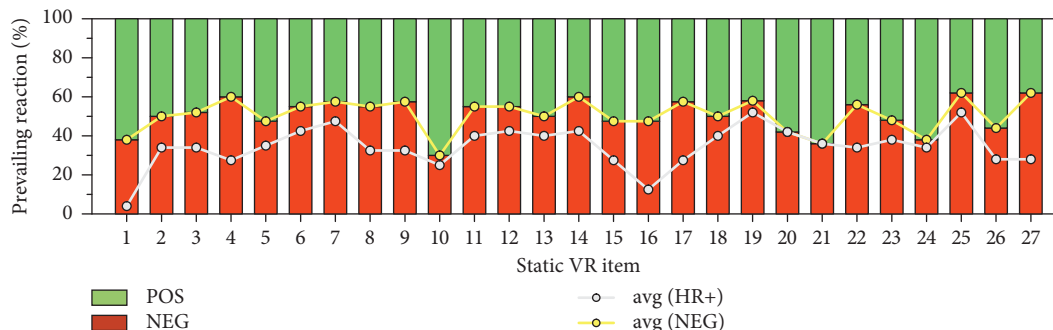


FIGURE 11: Detection of prevailing reactions (for the whole group of participants), as a function of the input stimulus, based on facial expression or heart rate data. In evidence, the discomfort of participants.

characterization of the structure itself under the effects of walking occupants.

In terms of HR+ and HR- correlations in Table 1, finally, the collected results suggest some agreement with facial expression outcomes but also recommend the need of a more extended analysis in this direction (i.e., number of volunteers/stimuli).

5. Discussion of Results from Dynamic VR Experiment

The second stage of remote investigation was carried out with the same group of participants exposed to a virtual walk in a glazing environment. Major benefit was taken from the

adaptation of a VR clip representative of a real case-study building (Generali Real Estate French Branch) located in Paris. The building, as shown in Figure 15, is currently under renovation and is characterized by a large amount of structural glass in facades, roofs, and floors. In order to preserve a total duration of 120 seconds for the whole experimental analysis, the selection of clips for the case-study building was divided into three different virtual walks (40 seconds/each), realized at the roof/terrace level (W1), at the ground level, from the main entrance of the building (W2), and at the first level (W3), within the internal open space. More in detail, the walks were characterized by the following:

W1 (outdoor): risk of fall (glass balustrades) and presence of glass facades.



(a)



(b)



(c)



(d)

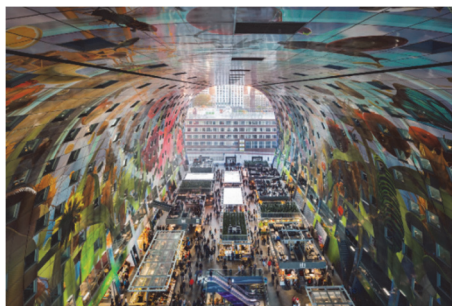


(e)



(f)

FIGURE 12: Static input items with prevailing (a)-(b) NEG, (c)-(d) POS reactions, or (e)-(f) balanced NEG-POS reactions: (a) Zhangjiajie bridge, Hunan, CN (© Getty Images); (b) cliff concept boutique hotel (© Hayri Atak); (c) mock-up of glass floor system (© Vitroplena bvba, BE); (d) walls (Amsterdam, NL (© A'DAM Lookout)); (e) walls (Glass Pavilion Rheinbach, DE (from [47] (© (F) Wellershoff)); (f) roof (Botanical Garden, Amsterdam, NL). (a) Item #25; (b) item #27; (c) item #10; (d) item #21; (e) item #3; (f) item #16.



(a)



(b)

FIGURE 13: Static input items with good match of NEG (or POS) and HR variation: (a) Markthal, Rotterdam, NL (© MVRDV); (b) Hubertus Hotel (Valdaora, IT, © Design & Contract). (a) Item #19; (b) item #24.

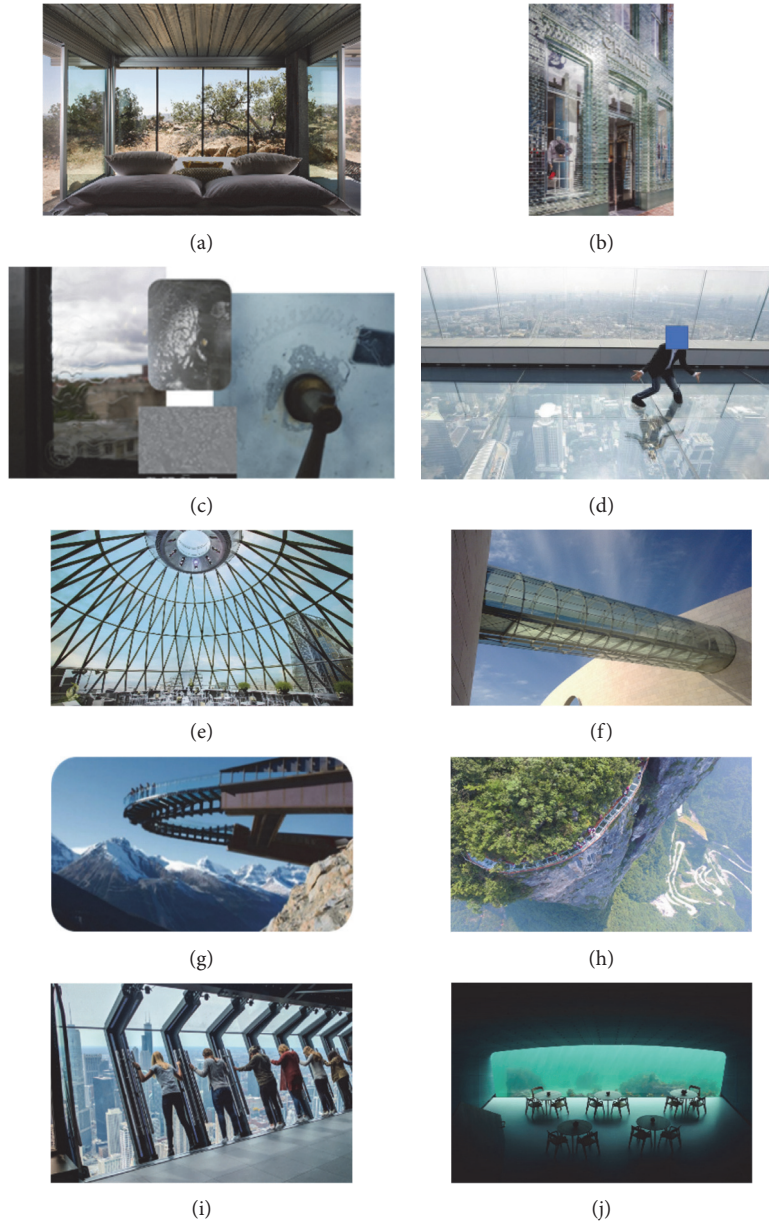


FIGURE 14: Static input items: (a) private room (Off-grid itHouse, Pioneertown, USA; © Airbnb); (b) glass bricks (Chanel Amsterdam Store, NL, © MVRDV); (c) delamination (reproduced from [48] under the terms and permissions of a CC-BY license); (d) skywalk (Mahanakhon, Bangkok, THA, © Tripadvisor); (e) roof (30 St Mary Axe Tower, London, UK, © ArchDaily); (f) footbridge (glass bridge, Lisbon, PT, © Schlaich Bergermann Partner, DE); (g) skywalk (Jasper National Park, CA, © Getty Images); (h) walkway (Cliffside skyway, CN, © Global Times); (i) observation deck (360 Chicago Tilt, Chicago, USA, © Tripster); (j) underwater restaurant (N) © Dezeen. (a) Item #5; (b) item #7; (c) item #9; (d) item #13; (e) item #14; (f) item #17; (g) item #18; (h) item #22; (i) item #23; (j) item #26.

TABLE 1: Analysis of prevailing reactions for static VR items by subject (% values given for the items).

	Prevailing reaction (facial expression) (%)		Prevailing reaction (heart rate) (%)	
	POS	NEG	HR ⁻	HR ⁺
Group A (11 items)	18	82	37	63
Group B (4 items)	0	100	50	50
Group C (12 items)	48	52	70	30

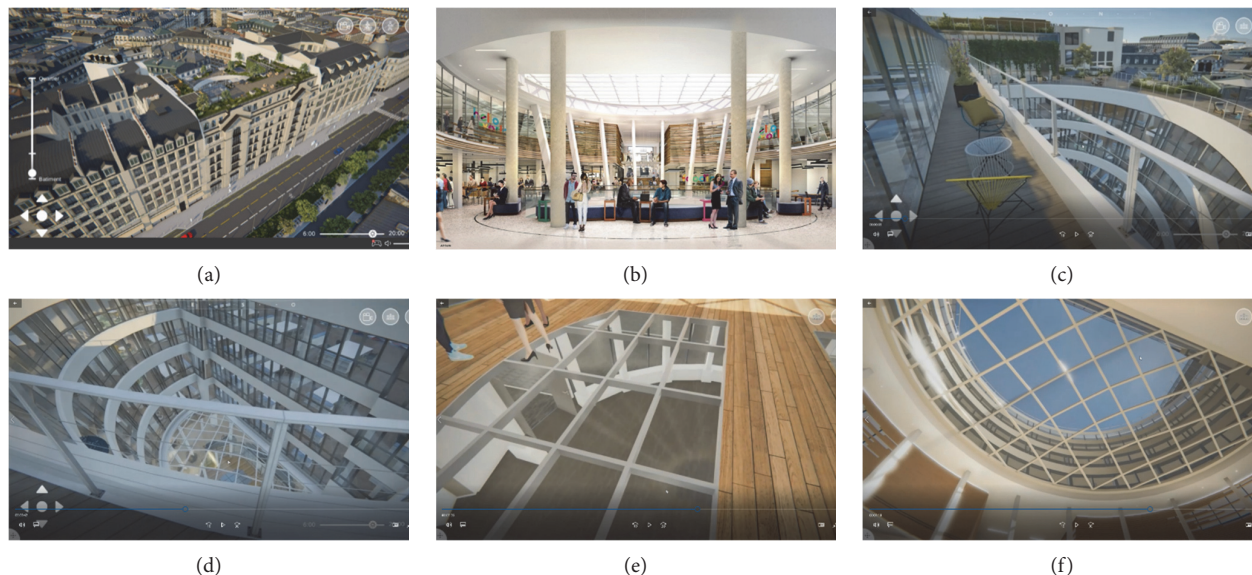


FIGURE 15: Selection of screenshot frames from the VR video clip (courtesy of © Generali Real Estate French Branch, adapted from <http://www.helloworldparis.com>) inspired by the case-study palace in Paris, FR: (a) view of the building (from Rue Réaumur); (b) internal open space; (c) top terrace; (d) glass conical envelope/facade; (e) glass floor (from the top/ground level); (f) glass roof (from the bottom/ground level).

W2 (indoor): risk of fall (glass floor), but also glass roof on the top, glass walls, and internal partitions.

W3 (indoor): risk of falls (glass balustrades) and presence of a glass floor (visual stimulus only).

Figure 16 shows the analysis of POS, NEG, and HR⁺ data for the group of volunteers. The dynamic VR scenario gave evidence of scattered emotional responses from the volunteers. Furthermore, the HR⁺ trend for the group of volunteers was observed to have close correlation with NEG data, thus confirming and enforcing, under the limitations of the present setup, the experimental findings from Section 4.

Worth of interest in Figure 16 is the local and global fluctuation of POS or NEG peaks (and thus HR⁺ data) and their correlation with visual stimuli. Major NEG/HR⁺ peaks of discomfort were in fact detected for conditions characterized by the presence of

outdoor or indoor balustrades (risk of fall) and floors (risk of fall),

while major comfortable responses were calculated for scenarios with

facades/walls (no direct contact) and

roof components (no direct contact),

thus suggesting again an agreement with the experimental outcomes from the static VR scenario.

On the other side, a more scattered and weak evolution of HR⁺ data with NEG values was noticed in Figure 16, compared to Section 4. A reason for such an outcome could be found in the dynamic nature of the stimulus itself [20,21].

Certainly, a direct comparison of human reactions under static or dynamic VR stimuli is not possible. The context features as well as the subjective response of participants in a given remote scenario could be affected by several aspects. In Figure 17, to this aim, the analysis of heart rate parameters is shown for all the volunteers exposed to the two experimental conditions. A mostly uniform response under static or dynamic stimuli can be observed only for a few participants.

In this regard, future investigations will be carried out to quantify more in detail the subjective reaction of occupants in glass building scenarios, as well as the correlation of design parameters and quantitative data of human reactions. Most importantly, instrumented experimental configurations will be examined under field scenarios with real walks from the participants and a new calibration of their subjective feelings.

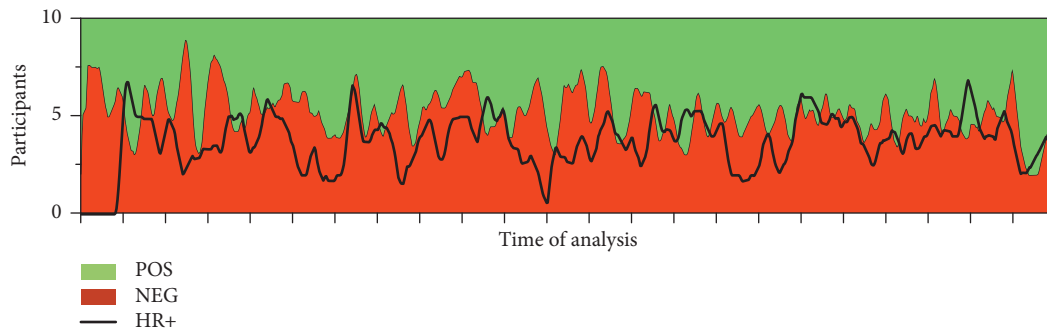


FIGURE 16: Detection of prevailing reactions (for the whole group of participants), as a function of the time of analysis for the dynamic VR scenario.

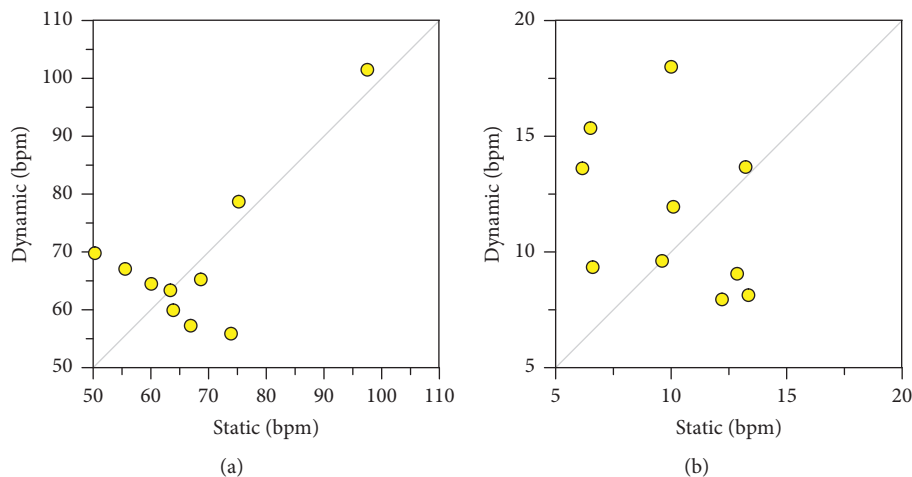


FIGURE 17: HR data (bpm) for the involved participants under static or dynamic VR setup: (a) average and (b) standard deviation.

6. Conclusions

The analysis, quantification, and optimization of human comfort in the built environment is a target for several design fields and depends on several engineering aspects that can be mathematically controlled to satisfy specific performance indicators. Typical examples relate to structural, energy, and thermal design issues. On the other side, human reactions are also sensitive to a multitude of parameters that find origin in subjective feelings of users, in the same way in which the so-called “emotional architecture” aims at evoking positive responses of building occupants.

In this paper, an experimental analysis was presented and addressed in support of the quantitative measure and analysis of emotional and nervous states of users for selected built scenarios, towards the definition of enhanced design strategies that could combine engineering targets/methods with architectural concepts, technological solutions, and evocation of subjective feelings of customers. In doing so, major advantage was taken from the use of virtual experimental techniques and a facial expression commercial software able to capture both microexpressions and nervous states of participants (based on facial Action Units (AUs)), as well as heart rate (HR) parameters. A group of 10 volunteers was in fact exposed to visual stimuli of static and dynamic glazing environments.

By designing an input stimulus characterized by a prevailing role of structural glass elements (i.e., roofs, floors, balustrades, etc.), the attention was focused on the quantification of the herein called “positive” (POS) or “negative” (NEG) feelings of participants based on their facial microexpressions and feedback, as well as to address the possible correlation of heart rate modifications with the so-detected POS and NEG emotions. As shown, the analysis of remote experimental measurements gave evidence of some good correlations of facial expression parameters, HR trends, and input stimuli, and this was found in agreement with preliminary expectations at the time of the experimental planning. Postprocessing feedback also suggested the use of remote tools and facial measurements in support of comfort analysis, as a direct quantitative measure of nervous states evoked by virtual stimuli. The remote measurement of HR variations for participants was then addressed to explore their potential correlation with selected input stimuli and corresponding facial expression/emotional state. Well promising outcomes were observed through the post-processing analysis, with general HR trends in correlation with facial microexpressions outcomes, for most of the stimuli. On the other side, while proving the efficiency of the approach, the same experimental outcomes highlighted scattered human reactions for some of the stimuli, thus

enforcing the need of additional in situ experimental procedures to address more in detail the emotional state and trend of glazing customers. [49].

References

- [1] H. Levin, *Designing for People: What Do Building Occupants Really Want? Keynote Lecture*, Healthy Buildings, Singapore, 2003.
- [2] S. Colenberg, T. Jylha, and M. Arkesteijn, "The relationship between interior office space and employee health and well-being – a literature review," *Building Research & Information*, vol. 49, no. 3, pp. 352–366, 2020.
- [3] D. Li, C. C. Menassa, and V. R. Kamat, "Personalized human comfort in indoor building environments under diverse conditioning modes," *Building and Environment*, vol. 126, pp. 304–317, 2017.
- [4] G. R. Oldham and N. L. Rotchford, "Relationships between office characteristics and employee reactions: a study of the physical environment," *Administrative Science Quarterly*, vol. 28, no. 4, pp. 542–556, 1983.
- [5] G. Y. Yun and J. T. Kim, "Creating sustainable building through exploiting human comfort," *Energy Procedia*, vol. 62, pp. 590–594, 2014.
- [6] A. M. G. Abdel, "Human thermal comfort and heat stress in an outdoor urban arid environment: a case study," *Advances in Meteorology*, vol. 2013, Article ID 693541, 7 pages, 2013.
- [7] G. Busca, A. Cappellini, S. Manzoni, M. Tarabini, and M. Vanali, "Quantification of changes in modal parameters due to the presence of passive people on a slender structure," *Journal of Sound and Vibration*, vol. 333, no. 21, pp. 5641–5652, 2014.
- [8] B. Davis and O. Avci, "Simplified vibration serviceability evaluation of slender monumental stairs," *Journal of Structural Engineering*, vol. 141, no. 11, 2015.
- [9] C. Bedon and M. Fasan, "Reliability of field experiments, analytical methods and pedestrian's perception scales for the vibration serviceability assessment of an in-service glass walkway," *Applied Sciences*, vol. 9, no. 9, p. 1936, 2019.
- [10] M. D. Burton, K. C. S. Kwok, and A. Abdelrazaq, "Wind-Induced motion of tall buildings: designing for occupant comfort," *International Journal of High-Rise Buildings*, vol. 4, no. 1, pp. 1–8, 2015.
- [11] R. O. Denoon, R. D. Roberts, C. W. Letchford, and M. C. S. Kwok, "Field experiments to investigate occupant perception and tolerance of wind-induced building motion," Research Report No. R803, Department of Civil Engineering, University of Sydney, Sydney, Australia, 2000.
- [12] K. C. S. Kwok and P. A. Hitchcock, "Occupant comfort test using a tall building motion simulator," in *Proceedings of the Fourth International Conference on Advances in Wind and Structures*, Jeju, Korea, May, 2008.
- [13] I. Bower, R. Tucker, and P. G. Enticott, "Impact of built environment design on emotion measured via neurophysiological correlates and subjective indicators: a systematic review," *Journal of Environmental Psychology*, vol. 66, Article ID 101344, 2019.
- [14] F. J. Vidal and S. I. Abad, "Introducing emotions in the architectural design process," in *Proceedings of the 1st International Conference on Higher Education Advances*, June 2015.
- [15] G. Shearcroft, "The joy of architecture: evoking emotions through building," *Architectural Design*, vol. 91, no. 1, pp. 108–117, 2021.
- [16] C. Suri, "Inside the Rise of Emotional Design," *Architectural Digest*, <https://www.architecturaldigest.com/story/emotional-design>, 2017.
- [17] M. Shahid, "The Different Emotions Architecture (Buildings) Can Express, Rethinking the Future, New Delhi," <https://www.re-thinkingthefuture.com/fresh-perspectives/a2586-the-different-emotions-architecture-buildings-can-express/>.
- [18] R. Kozlovsky, "Architecture, emotions and the history of childhood," in *Childhood, Youth and Emotions in Modern History*. Palgrave Studies in the History of Emotions, S. Olsen, Ed., Palgrave Macmillan, London, England, 2015.
- [19] N. Ricci, "The psychological impact of architectural design," Claremont McKenna College, CA, USA, 2018, https://scholarship.claremont.edu/cmc_theses/1767 CMC Senior Theses.
- [20] E. Canepa, V. Scelsi, A. Fassio, L. Avanzino, G. Lagravinese, and C. Chiorri, "Atmospheres: Feeling Architecture by Emotions - Preliminary Neuroscientific Insights on Atmospheric Perception in Architecture," *Ambiances*, vol. 5, 2019 <http://journals.openedition.org/ambiances/2907>.
- [21] L. Shu, Y. Yu, W. Chen et al., "Wearable emotion recognition using heart rate data from a smart bracelet," *Sensors*, vol. 20, no. 3, p. 718, 2020.
- [22] Mordor Intelligence, "Europe flat glass market - growth, Trends, COVID-19 Impact, and Forecasts," Morodor Intel-ligence Hyderabad, Telangana 500008, India, 2020, <https://www.mordorintelligence.com/industry-reports/europe-flat-glass-market> Technical Report.
- [23] G. Creating, "Safe, sustainable spaces: how building materials will evolve post COVID-19," 2020, <https://www.gauzy.com/creating-safe-sustainable-spaces-how-building-materials-will-evolve-post-covid-19/>.
- [24] C. Bedon and L. Kruszka, "An Insight on the Mitigation of Glass Soft Targets and Design of Protective facades," in *Critical Infrastructure Protection. Best Practices and Innovative Methods of Protection*, NATO Science for Peace and Security Series D: Information and Communication Security, M. Kruszka and Muzolf, Eds., vol. 52, pp. 107–117, IOS Press, Amsterdam Netherlands, 2019.
- [25] C. Bedon, "Transparent materials and new design strategies in the covid-19 era," in *Proceedings of the International Conference on Central European Critical Infrastructure Protection*, M. Nyikes and Molnar, Eds., p. 39, Budapest (Hungary), November 2020.

Designing a Large Marine Two-Stroke Diesel Engine with Cylinder Bypass Valve and EGR System

Shaik Mozammil, *Department of Mechanical Engineering, Aryan Institute of Engineering & Technology, Bhubaneswar, smozammil157@gmail.com*

Deepikarani Swain, *Department of Mechanical Engineering, NM Institute of Engineering & Technology, Bhubaneswar, depika_r19@yahoo.co.in*

Nalinikanta Swain, *Department of Mechanical Engineering, Capital Engineering College, Bhubaneswar, nalini_526@yahoo.co.in*

Abstract:

A two-stroke turbocharged marine diesel engine's nonlinear mean value engine model (MVEM) is built, parameterized, and verified against measurement data. The goal is to construct a computationally quick and accurate engine model that captures the major dynamics and can be utilised to develop control systems for the recently implemented EGR system. The tuning technique is described, and the outcome is a six-state MVEM with seven control inputs that captures the system's primary dynamics.

Keywords: Engine modeling, diesel engines, parametrization, validation, nonlinear systems

1. INTRODUCTION

The upcoming Tier III regulation (International Maritime Organization, 2013) is the next milestone for EGR technology in large two-stroke engines. The EGR system is used to reduce NO_x emissions by recirculating a fraction of the exhaust gas into the scavenging manifold. This results in a lower combustion peak temperature and consequently a reduction in NO_x formation. Due to the high financial costs of performing tests on a real engine, a reliable and fast dynamic engine model is an important tool for the development of new EGR control systems.

A lot of research can be found in literature about Mean Value Engine Models (MVEM) with EGR systems for automotive engines, e.g., Wahlström and Eriksson (2011) and Nieuwstadt et al. (2000). However, much less research has been done in the same area with large marine two-stroke diesel engines. A few examples are Blanke and Anderson (1985), Theotokatos (2010) where an MVEM of a marine engine was developed, and Hansen et al. (2013) where a similar model of the engine used here was proposed.

In this study the proposed MVEM is based on the 4T50ME-X test engine from MAN Diesel & Turbo, which is a turbocharged two-stroke diesel engine with direct injection, uniflow scavenging and variable valve timing. It can provide a maximum rated power of 7080 kW at 123 RPM. It is equipped with an EGR system and a Cylinder Bypass Valve (CBV). The purpose of the valve is to keep the desired turbocharger speed when the engine operates under high EGR rates. In those situations less energy is transferred through the turbine, thus part of the compressor air mass flow is bypassed to boost the turbine.

2. MODELING

The MVEM consists of six states and seven control inputs. The states are scavenging manifold pressure and oxygen

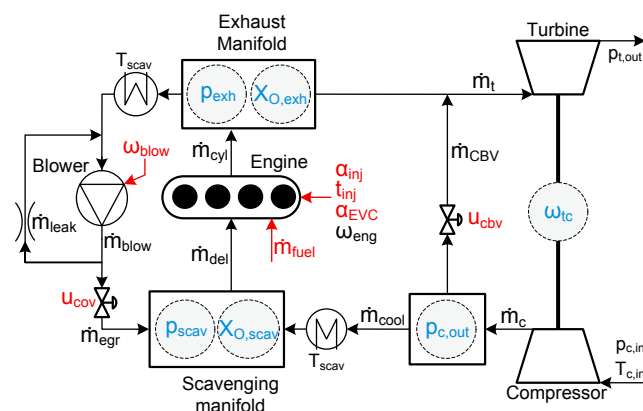


Fig. 1. Structure of system with state variables (blue) and control inputs (red)

mass fraction, p_{scav} and $X_{O,scav}$, compressor outlet pressure, $p_{c,out}$, exhaust manifold pressure and oxygen mass fraction, p_{exh} and $X_{O,exh}$ and turbocharger speed, ω_{tc} . The control inputs are fuel mass flow, \dot{m}_{fuel} , EGR blower speed, ω_{blow} , fuel injection time, t_{inj} , fuel injection angle α_{inj} , exhaust valve closing angle, α_{EVC} , cut-out valve (COV) position, u_{cov} , and CBV position, u_{cbv} . Figure 1 gives an overview of the model. The engine model consists of several interconnected submodels which are introduced in the following subsections.

2.1 Turbocharger

The turbocharger model includes submodels for the compressor, the turbine and the connecting shaft.

Compressor

The mass flow and efficiency models of the compressor are based on the parameterization of the performance maps in SAE format. The turbocharger speed and the compressor mass flow in the performance map are corrected in order to take into account changes in ambient conditions. The com-

pressor mass flow is modeled using super-ellipses centred at the origin. A similar approach is found in Leufvén and Eriksson (2013). The explicit expression of a super-ellipse is

$$\dot{m}_{c,corr} = a \left(1 - \left(\frac{\Pi_c}{b} \right)^n \right)^{\frac{1}{n}} \quad (1)$$

where Π_c is the pressure ratio over the compressor, $p_{c,out}/p_{c,in}$. The variables a , b and n are described by third order polynomials of the corrected turbocharger speed, so the model has 12 tuning parameters.

The compressor efficiency is modeled by parameterizing the manufacturer performance map with rotated and translated ellipses. The implicit expression of an ellipse rotated α and translated from the origin to (a_0, b_0) is as follows

$$\left(\frac{(x - a_0) \cos \alpha - (y - b_0) \sin \alpha}{a} \right)^2 + \left(\frac{(x - a_0) \sin \alpha + (y - b_0) \cos \alpha}{b} \right)^2 = 1 \quad (2)$$

where in this case x corresponds to \dot{m}_c and y corresponds to η_c . The coefficients a_0 , b_0 , a , b , and α are described using second order polynomials of Π_c so the model consists of 15 parameters to estimate.

Turbine

The turbine corrected mass flow is described as in Eriksson and Nielsen (2014)

$$\dot{m}_{t,corr} = C_t \sqrt{1 - \Pi_t^{k_t}} \quad (3)$$

where Π_{turb} is the pressure ratio over the turbine, $p_{t,out}/p_{exh}$. Moreover, k_t and C_t are parameters to be estimated.

The turbine efficiency is commonly modeled using the Blade Speed Ratio (BSR), e.g. Wahlström and Eriksson (2011) and Eriksson and Nielsen (2014)

$$BSR = \frac{R_t \omega_t}{\sqrt{2 c_{p,e} T_{t,in} \left(1 - \Pi_t^{1 - \frac{1}{\gamma_e}} \right)}} \quad (4)$$

where R_t is the turbine blade radius. The turbine efficiency is again modeled with rotated and translated ellipses using (2). In this case x corresponds to the BSR and y corresponds to the η_t . The coefficients a_0 , b_0 , a , b , and α are described as second order polynomials of the corrected turbocharger speed, thus 15 parameters need to be determined.

Connecting Shaft

The turbocharger shaft speed is described by Newton's second law using the power recovered from the exhaust gas by the turbine and transferred to the compressor

$$\frac{d}{dt} \omega_{tc} = \frac{P_t - P_c}{J_t \omega_{tc}} \quad (5)$$

where the parameter J_t corresponds to the overall turbocharger inertia. P_t and P_c are the turbine and compressor powers, respectively. Note that the mechanical efficiency is not included in (5), it is already included in the turbine efficiency of the SAE map.

The power generated by the turbine and the power consumed by the compressor are defined as in Dixon (1998)

$$P_t = \eta_t \dot{m}_t c_{p,e} T_{t,in} \left(1 - (\Pi_t)^{\frac{\gamma_e - 1}{\gamma_e}} \right) \quad (6)$$

$$P_c = \frac{\dot{m}_c c_{p,a} T_{c,in}}{\eta_c} \left((\Pi_c)^{\frac{\gamma_a - 1}{\gamma_a}} - 1 \right) \quad (7)$$

2.2 Control Volumes

The model consists of three control volumes. The compressor outlet and the two manifolds, they are all modeled with standard isothermal models as proposed in Heywood (1988) and Eriksson and Nielsen (2014).

The pressure at the compressor outlet is described by

$$\frac{d}{dt} p_{c,out} = \frac{R_a T_{c,out}}{V_{c,out}} (\dot{m}_c - \dot{m}_{cool} - \dot{m}_{cbv}) \quad (8)$$

where $V_{c,out}$ is the control volume size, and it has to be estimated and $T_{c,out}$ is described in (14).

At the scavenging manifold, the temperature is assumed to be constant since the cooler is considered to be ideal and capable of maintaining a constant scavenging temperature. Two states are needed to fully characterize the manifold, the pressure and the oxygen mass fraction. The pressure is governed by the following differential equation

$$\frac{d}{dt} p_{scav} = \frac{R_a T_{scav}}{V_{scav}} (\dot{m}_{cool} + \dot{m}_{egr} - \dot{m}_{del}) \quad (9)$$

where V_{scav} is the volume of the manifold and has to be estimated. The oxygen mass fraction is described as in Wahlström and Eriksson (2011)

$$\begin{aligned} \frac{d}{dt} X_{O,scav} = & \frac{R_a T_{scav}}{p_{scav} V_{scav}} (X_{O,exh} - X_{O,scav}) \dot{m}_{egr} + \\ & \frac{R_a T_{scav}}{p_{scav} V_{scav}} (X_{O,a} - X_{O,scav}) \dot{m}_{cool} \end{aligned} \quad (10)$$

where $X_{O,a}$ is the mass fraction of oxygen in dry air.

As in the previous manifold, two states characterize the exhaust manifold, the pressure and the oxygen mass fraction. The exhaust pressure is driven by the following differential equation

$$\frac{d}{dt} p_{exh} = \frac{R_e T_{exh}}{V_{exh}} (\dot{m}_{cyl} - \dot{m}_{egr} - \dot{m}_{exh,out}) \quad (11)$$

with

$$\dot{m}_{exh,out} = \dot{m}_t - \dot{m}_{cbv} \quad (12)$$

and where V_{exh} is the exhaust manifold volume and a tuning parameter, and $\dot{m}_{cyl} = \dot{m}_{del} + \dot{m}_{fuel}$. The oxygen mass fraction is defined in a similar manner as in the scavenging manifold

$$\frac{d}{dt} X_{O,exh} = \frac{R_e T_{exh}}{p_{exh} V_{exh}} (X_{O,cyl} - X_{O,exh}) \dot{m}_{cyl} \quad (13)$$

where $X_{O,cyl}$ is the oxygen mass fraction coming out from the cylinders. Since the injected fuel combustion is assumed to be ideal and complete, $X_{O,cyl}$ is calculated as equation (16) in Wahlström and Eriksson (2011).

2.3 CBV

The CBV model consists of a submodel for the compressor outlet temperature, a submodel for the flow through the CBV valve and a submodel for the flow through the cooler.

The temperature at the compressor outlet is calculated using the definition of the adiabatic efficiency of the compressor from Dixon (1998)

$$T_{c,out} = T_{c,in} \left(1 + \frac{(\Pi_c)^{\frac{\gamma_a - 1}{\gamma_a}} - 1}{\eta_c} \right) \quad (14)$$

The mass flow through the CBV is modeled as a compressible turbulent restriction. A generic formulation of the model is presented as follows

$$\dot{m} = \frac{A_{eff} p_{in}}{\sqrt{R_i T_{in}}} \sqrt{\frac{2 \gamma_i}{\gamma_i - 1} \left(\Pi^{\frac{2}{\gamma_i}} - \Pi^{\frac{\gamma_i + 1}{\gamma_i}} \right)} \quad (15)$$

for this case, \dot{m} is the mass flow through the CBV, Π is the pressure ratio $p_{exh}/p_{c,out}$, γ_i and R_i are the heat capacity ratio and the specific gas constant of air, respectively. A_{eff} corresponds to the CBV effective area A_{cbv} , which in this case is variable depending on the control input u_{cbv} , and it is defined as follows

$$A_{cbv} = A_{max} \left(1 - \cos(u_{cbv} \frac{\pi}{2}) \right) \quad (16)$$

where A_{max} is a tuning parameter that corresponds to the maximum area of the restriction.

The mass flow through the cooler is described by an incompressible turbulent restriction, described in Eriksson and Nielsen (2014)

$$\dot{m}_{cool} = k_{cool} \sqrt{\frac{p_{c,out} (p_{c,out} - p_{scav})}{T_{c,out}}} \quad (17)$$

where k_{cool} is a parameter to be estimated.

In situations where the CBV is open, the turbine inlet temperature cannot be assumed to be equal to the exhaust temperature. To consider the temperature drop caused by the CBV flow, the perfect mixing model described in Eriksson and Nielsen (2014) is used

$$T_{t,in} = \frac{T_{exh} c_{p,e} \dot{m}_{exh,out} + T_{c,out} c_{p,a} \dot{m}_{cbv}}{c_{p,e} \dot{m}_{exh,out} + c_{p,a} \dot{m}_{cbv}} \quad (18)$$

With this formulation, an algebraic loop is encountered between the $T_{t,in}$ and the \dot{m}_t calculations. In order to break the algebraic loop, it is assumed that $\dot{m}_{exh,out}$ in (18) can be approximated by its steady state value $\dot{m}_{exh,out} = \dot{m}_{cyl} - \dot{m}_{egr}$.

The exhaust oxygen measurement equipment is installed downstream of the turbine. When the CBV is open, it affects the measurement. Therefore, a new oxygen mass fraction is calculated in (19) for validation purposes.

$$X_{O,t} = \frac{X_{O,exh} \dot{m}_{exh,out} + X_{O,a} \dot{m}_{cbv}}{\dot{m}_t} \quad (19)$$

In this expression, the $\dot{m}_{exh,out}$ used is described by equation (12).

2.4 Cylinders

The mass flow through four-stroke engines is commonly modeled with the volumetric efficiency as in Wahlström and Eriksson (2011) and Heywood (1988). For two-stroke engines, the mass flow through all cylinders can be approximated with the flow through a compressible turbulent restriction. The continuous flow represents the average

flow through all cylinders. The same approach is found in Hansen et al. (2013) and Theotokatos (2010). The same generic equation (15) is used, and in this case the \dot{m} is the delivered mass flow \dot{m}_{del} through the cylinders, Π is the pressure ratio over the cylinders p_{exh}/p_{scav} , γ_i and R_i correspond to the heat capacity ratio and the specific gas constant of air. A_{eff} is the effective area of the restriction, and has to be estimated.

It is common to characterize the scavenging process in two-stroke engines with the scavenging efficiency η_{scav} and the trapping efficiency η_{trap} . Their definitions can be found in Heywood (1988). The delivery ratio (DR) is defined as the ratio between the delivered flow and the ideal flow at the scavenging manifold density

$$DR = \frac{2\pi \dot{m}_{del}}{n_{cyl} \omega_{eng} V_1} \left(\frac{R_a T_{scav}}{p_{scav}} \right) \quad (20)$$

The model proposed here is a combination of the two limited ideal models introduced in Heywood (1988), the perfect displacement and the complete mixing. The perfect displacement assumes that the burned gases are displaced by the fresh gases without mixing, on the other hand, the complete mixing model assumes instantaneous mixing of the gases when fresh mixture enters the combustion chamber. By introducing the tuning parameters K_{se1} and K_{se2} in the complete mixing model (21) and (22), an intermediate formulation is obtained, with the purpose of taking into account the late exhaust valve closing.

$$\eta_{scav} = 1 - e^{-K_{se1} DR} \quad (21)$$

$$\eta_{trap} = \frac{1 - e^{-K_{se2} DR}}{DR} \quad (22)$$

Limited pressure diesel cycle

As an overview, six changes to the cycle presented in Wahlström and Eriksson (2011) have been incorporated.

(i) The constant volume burned ratio x_{cv} is considered variable. The maximum pressure rise in the cylinders is regulated by the control system as a safety measure. The regulation is accomplished by delaying the injection. To be able to model late injection, the x_{cv} is considered a linear function of the start crank angle and duration of the injection. The model is shown in (23). A similar model for x_{cv} is shown in Lee et al. (2010).

$$x_{cv} = c_1 + c_2 \alpha_{inj} + c_3 t_{inj} \quad (23)$$

where the three parameters c_i have to be estimated.

(ii) The compression process is considered to start when the exhaust valve closes. In that instant the crank angle is given by α_{EVC} . The volume of the combustion chamber based on the crank angle is used in the limited pressure cycle calculations, and it is defined as equation (4.3) from Eriksson and Nielsen (2014). Also, the expansion process is assumed to last until the bottom dead center.

(iii) Both the compression and the expansion processes are considered polytropic Jiang et al. (2009) in order to consider heat exchange with the cylinder walls, both polytropic exponents of the compression and expansion are tuning parameters.

(iv) The delivered mass flow is assumed to be heated by a tuning factor dT_{cyl} before the cycle starts. The heating

affects both the trapped and the short-circuited flows (25). The pressure of the trapped gas when the combustion chamber is sealed is assumed to be the scavenging pressure, while the temperature is described by

$$T_1 = T_{cyl} (1 - \eta_{scav}) + \eta_{scav} (T_{scav} + dT_{cyl}) \quad (24)$$

The algebraic loop between the initial cycle temperature, T_1 and the cylinder out temperature, T_{cyl} , is solved using the previous sample value for T_{cyl} similar to what is done in Wahlström and Eriksson (2011).

(v) The $c_{v,a}$ before the constant volume combustion starts and the $c_{p,a}$ at the beginning of the constant pressure combustion are calculated based on the temperatures at the respective crank angles. To perform such calculation, the NASA polynomials are used to describe these parameters in terms of temperature. The same polynomials found in Goodwin et al. (2014) are used here.

(vi) To determine the exhaust temperature T_{exh} , characterized by the mixture of the short-circuited flow and the trapped flow in the cylinder at their respective temperatures, the perfect mixing model is used again in the same manner as (18). The short-circuited flow is defined as

$$\dot{m}_{sh} = \dot{m}_{del} - \dot{m}_{trap} \quad (25)$$

Using the pressures and the volumes of each process in the thermodynamic cycle, the indicated power of the cycle is computed using equations (2.14) and (2.15) in Heywood (1988). To sum up, the limited pressure cycle has eight parameters to determine.

2.5 EGR loop

The EGR loop model consists of a blower to overcome the pressure difference between exhaust and scavenge manifolds, a recirculation valve and a cut-out valve (COV) to manage the start-up of the EGR system. The flow is considered ideally cooled to scavenging temperature.

EGR Blower

The performance map is expressed in a non-dimensional space described by the Head Coefficient (Ψ) and the Flow Coefficient (Φ), their definitions are shown in (26) and (28) respectively

$$\Psi = \frac{2 T_{scav} c_{p,e} \left(\Pi_{blow}^{\frac{\gamma-1}{\gamma}} - 1 \right)}{(\omega_{blow} R_{blow})^2} \quad (26)$$

where ω_{blow} is the blower angular speed, R_{blow} is the blower blade radius and Π_{blow} is the pressure ratio over the blower p_{scav}/p_{exh} .

The non-dimensional performance map is modeled with the same approach as the compressor mass flow, but here only one speed line is parameterized. Therefore, the parameters a , b , and n are constants and need to be estimated.

$$\Phi = a \left(1 - \left(\frac{\Psi}{b} \right)^n \right)^{\frac{1}{n}} \quad (27)$$

Rearranging the definition of Φ , the mass flow through the blower \dot{m}_{blow} is obtained

$$\dot{m}_{blow} = \frac{p_{exh}}{R_e T_{scav}} (\Phi \omega_{blow} \pi R_{blow}^3) \quad (28)$$

The existence of a leak in the recirculation valve is known, however, its magnitude is unknown. The leak mass flow \dot{m}_{leak} is modeled as a compressible turbulent restriction, like in (15). But in this case, the Π is the pressure ratio over the recirculation valve p_{exh}/p_{scav} , γ_i , and R_i corresponds to the heat capacity ratio and the specific gas constant of exhaust gas respectively. A_{eff} corresponds to the leak effective area. The resulting mass flow through the EGR system is

$$\dot{m}_{egr} = (\dot{m}_{blow} - \dot{m}_{leak}) f(u_{cov}) \quad (29)$$

where $f(u_{cov})$ describes the valve dynamics as

$$f(u_{cov}) = \left(1 - e^{-\frac{1}{\tau_{cov}} u_{cov}} \right) \quad (30)$$

u_{cov} only regulates the flow during start-up of the system, then the flow is controlled using the blower speed.

3. EXPERIMENTAL DATA AND TUNING PROCEDURE

The parameters in the submodels are estimated using engine measurements. The measured signals: $p_{c,in}$, $p_{t,out}$, $T_{c,in}$ and ω_{eng} are used in the estimation and in the validation of the model in the same manner as if they were inputs to the model.

Unfortunately, the oxygen sensors were not properly calibrated before the measurements. Thus the stationary values cannot be trusted and will not be used for estimation purposes. More information (types, starts and stops and number of steps) about each of the dynamic datasets can be found in the top part of Table 2.

The following relative error is used to quantify the difference between the modeled signals, y_{mod} , and the measured signals, y_{meas}

$$e_{rel}[k] = \frac{y_{mod}[k] - y_{meas}[k]}{1/N \sum_{j=1}^N y_{meas}[j]} \quad (31)$$

the euclidean norm of this relative error is used as the objective function to minimize in the tuning procedure.

3.1 Submodels initialization

Some of the submodels are initialized using the maps provided by the component manufacturer. Table 1 presents the stationary errors of the submodels that are initialized.

Table 1. Relative errors of the initialized submodels

Model	\dot{m}_c	η_c	\dot{m}_t	η_t	\dot{m}_{blow}
Mean rel. error [%]	3.11	0.69	0.19	0.31	0.47
Max rel. error [%]	14.5	3.24	0.45	1.03	0.87

To get an initial guess and to avoid overparametrization in the pressure limited cycle submodels, e.g. (23), a few extra stationary measurements are used, which are not used later in the model simulation, e.g., the maximum cylinder pressure and ordered cylinder compression pressure. This initialization is based on a least-squares optimization with T_{exh} and the indicated power of the cycle as objectives. Since some of the submodel inputs are not measured, e.g., \dot{m}_{del} , those submodels have to be used in this initialization.

3.2 Overall stationary estimation

Since there are no mass flow measurements apart from \dot{m}_{egr} , some submodels cannot be properly initialized, e.g., the \dot{m}_{eng} or the \dot{m}_{cbv} . Therefore all the parameters have to be estimated together, since the optimization problem cannot be separated. Another reason for estimating all parameters at the same time is that it is difficult to attain the same stationary levels for the modeled and the measured signals by fixing the previously estimated parameters. The overall estimation is performed with 27 different stationary points extracted from the estimation datasets. A point is considered stationary when the pressure and temperature signals are stabilized.

The measured states are used as inputs in the optimization since they cannot be integrated for isolated stationary points. To ensure that the model outputs are stationary at the stationary points, the derivative terms of (5), (8), (9) and (11) are added into the objective function weighted by the mean of the measured state to provide fair comparison. The objective function is defined as

$$V_{stat}(\theta) = \frac{1}{NM} \sum_{i=1}^M \sum_{n=1}^N \frac{(\dot{x}^i[n])^2}{1/N \sum_{j=1}^N x_{meas}^i[j]} \quad (32)$$

$$+ \frac{1}{NS} \sum_{i=1}^S \sum_{n=1}^N (e_{rel}^i[n])^2$$

where the first row minimizes the residuals of the dynamic models. With $x^1 = p_{scav}$, $x^2 = p_{exh}$, $x^3 = p_{c,out}$ and $x^4 = \omega_t$, the second row minimizes the relative error of the EGR mass flow, the exhaust temperature and the engine indicated power. N is the number of stationary points available. The vector θ represents the parameters to be estimated, which in this case are all the static parameters, except for the compressor parameters and the turbine efficiency parameters. This selection has proven to be a good trade-off between objective function complexity and model accuracy.

3.3 Dynamic estimation

Keeping the static parameters already estimated fixed, the next step is to tune the parameters of the dynamic models (5), (8), (9), (11) and (30). From the available datasets, 13 step responses were extracted and used in the estimation. These steps consist of EGR blower speed steps, fuel flow steps and CBV steps. In the same manner as it is done in Wahlström and Eriksson (2011), the measurements and the model outputs are normalized so the stationary errors have no effect on this estimation. The objective function used is

$$V_{dyn}(\theta) = \sum_{i=1}^J \sum_{z=1}^D \frac{1}{L_z} \sum_{l=1}^{L_z} (x_{meas,n}^i[l] - x_{mod,n}^i[l])^2 \quad (33)$$

where x^i are the control volume pressures and the turbocharger speed, J , is the number of states (excluding oxygen mass fractions), D is the number of steps used, and L_z is the length of each step. The parameter vector is thus $\theta = [J_t, V_{scav}, V_{exh}, V_{c,out}, \tau_{cov}]^T$.

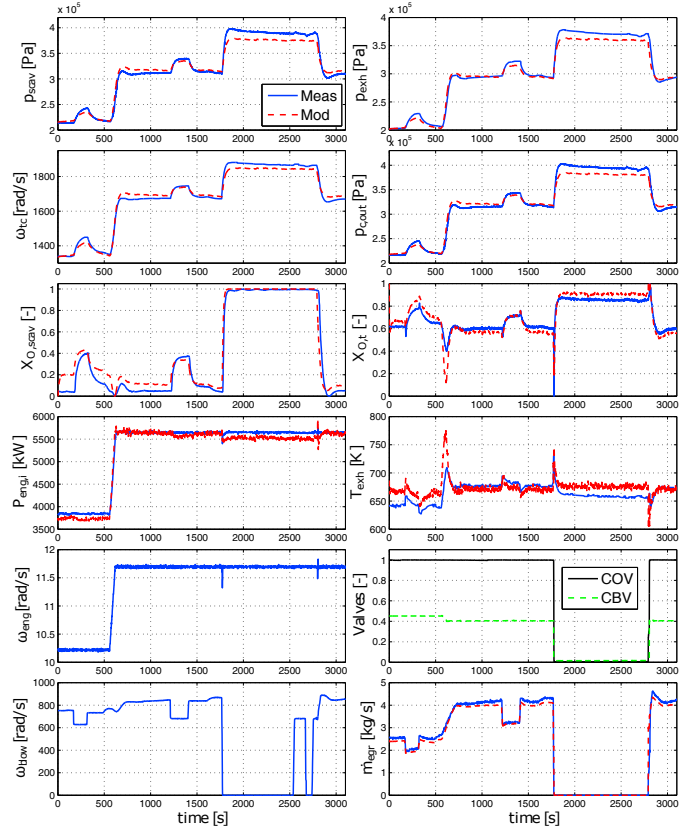


Fig. 2. Model simulation vs measurements of dataset 11.

4. MODEL VALIDATION

Table 2 presents the mean relative errors in percentage for all dynamic datasets. The 27 extracted stationary points are used to compute the mean required in the denominator of (31). This is done to provide a fair comparison between them, so all errors for different datasets are weighted with the same mean value. Excluding the EGR mass flow, the model errors are below 6.28% and in general below 3%. A higher error is observed for the EGR mass flow, where the mean for all datasets is 7.34%.

Figure 2 shows the states of the model compared to the measurements for dataset 11. Since the oxygen measurements are not calibrated, the modeled and the measured signals are normalized to compare only the dynamic behavior. This dataset has a load step, several EGR blower speed steps and a start and stop of the EGR system which is coupled to the CBV operation. It can be observed that the model captures the dynamics of the system.

5. CONCLUSION

An MVEM for a large marine two-stroke engine is proposed and validated. The estimation is done with part of the datasets available while the validation against measurements is done for another set of datasets. The overall agreement of the states is good, and the model is able to capture the general state dynamics.

Nevertheless this model is the first step towards a more general model to be used for development of control strategies. The next step is low load modeling, where new components need to be introduced.

Table 2. Top: number and type of steps contained in each dataset. Bottom: mean relative errors in % of the tuned model for the absolute measured signals in the estimation and validation datasets.

	Estimation Datasets										Validation Datasets				
	DS1	DS2	DS3	DS4	DS5	DS6	DS7	DS8	DS9	DS10	DS11	DS12	DS13	DS14	DS15
\dot{m}_{fuel} steps	1	1	5	1	1	0	1	4	3	6	1	0	0	0	7
ω_{blow} steps	9	1	<i>fixed</i>	5	7	1	8	9	11	<i>fixed</i>	9	9	5	7	<i>fixed</i>
u_{CBV} steps	0	0	0	0	0	0	2	1	3	2	3	4	3	4	5
EGR start/stop	1	1	0	0	0	1	3	0	0	0	3	4	3	5	0
CBV start/stop	0	0	0	0	0	0	2	1	3	0	3	4	3	4	0
p_{scav}	1.34	3.03	1.71	2.25	2.71	1.27	2.36	2.32	1.92	2.47	2.67	3.12	3.22	6.23	2.94
$p_{c,out}$	1.32	2.94	1.71	2.24	2.70	1.24	2.31	2.39	1.96	2.51	2.49	2.88	2.98	6.28	2.96
p_{exh}	1.72	3.07	2.36	1.80	3.10	1.60	2.16	2.78	2.36	3.11	2.18	2.52	2.69	6.13	3.68
ω_{tc}	0.92	4.21	0.91	0.96	2.03	0.83	1.44	1.13	1.04	1.27	1.14	1.23	1.23	4.61	1.96
T_{exh}	1.36	4.22	1.39	1.48	1.10	0.77	2.66	1.39	1.96	1.91	1.93	1.60	1.61	2.37	2.83
$P_{eng,i}$	1.57	1.41	1.76	2.11	2.52	2.70	1.66	1.44	2.01	1.73	1.85	1.95	2.24	1.58	2.29
\dot{m}_{egr}	7.23	8.35	10.15	6.54	4.77	6.07	5.62	6.40	8.88	7.82	6.58	7.87	9.34	7.31	7.14

REFERENCES

- Blanke, M. and Anderson, J.A. (1985). On modelling large two stroke diesel engines: new results from identification. *IFAC Proceedings Series*, 2015–2020.
- Dixon, S. (1998). *Fluid Mechanics and Thermodynamics of Turbomachinery*. Butterworth-Heinemann.
- Eriksson, L. and Nielsen, L. (2014). *Modeling and Control of Engines and Drivelines*. John Wiley & Sons.
- Goodwin, D.G., Moffat, H.K., and Speth, R.L. (2014). Cantera: An object-oriented software toolkit for chemical kinetics, thermodynamics, and transport processes. <http://www.cantera.org>. Version 2.1.2.
- Hansen, J.M., Zander, C.G., Pedersen, N., Blanke, M., and Vejlgård-Laursen, M. (2013). Modelling for control of exhaust gas recirculation on large diesel engines. *Proceedings of the 9th IFAC conference on Control Applications in Marine Systems*.
- Heywood, J.B. (1988). *Internal Combustion Engine Fundamentals*. McGraw-Hill.
- International Maritime Organization (2013). *MARPOL: Annex VI and NTC 2008 with Guidelines for Implementation*. IMO.
- Jiang, L., Vanier, J., Yilmaz, H., and Stefanopoulou, A. (2009). Parameterization and simulation for a turbocharged spark ignition direct injection engine with variable valve timing. *SAE Technical Paper 2009-01-0680*.
- Lee, B., Jung, D., Kim, Y.W., and Nieuwstadt, M. (2010). Thermodynamics-based mean value model for diesel combustion. *Engineering for Gas Turbines and Power*, 135(9), 193–206.
- Leufvén, O. and Eriksson, L. (2013). A surge and choke capable compressor flow model - validation and extrapolation capability. *Control Engineering Practice*, 21(12), 1871–1883.
- Nieuwstadt, M., Kolmanovsky, I., Moraal, P., Stefanopoulou, A., and Jankovic, M. (2000). EGR-VGT control schemes: experimental comparison for a high-speed diesel engine. *IEEE Control Systems Mag.*, 20(3), 63–79.
- Theotokatos, G. (2010). On the cycle mean value modelling of a large two-stroke marine diesel engine. *Proceedings of the Institution of Mechanical Engineers, Part M: Journal of engineering for the maritime environment*, 224(3), 193–206.

- Wahlström, J. and Eriksson, L. (2011). Modelling diesel engines with a variable-geometry turbocharger and exhaust gas recirculation by optimization of model parameters for capturing non-linear system dynamics. *Proceedings of the Institution of Mechanical Engineers, Part D: Journal of Automobile Engineering*, 225, 960–986.

Appendix A. NOMENCLATURE

Table A.1. List of symbols

A	Area	$[m^2]$
B	Bore	$[m]$
c	Connecting rod length	$[m]$
c_p	Specific heat at constant pressure	$[J/(kgK)]$
c_v	Specific heat at constant volume	$[J/(kgK)]$
J	Inertia	$[kg\ m^2]$
\dot{m}	Mass flow	$[kg/s]$
n_{cyl}	number of cylinders	$[]$
p	Pressure	$[Pa]$
P	Power	$[kW]$
R	Gas constant	$[J/(kgK)]$
s	Stroke	$[m]$
T	Temperature	$[K]$
V	Volume	$[m^3]$
X_O	Oxygen mass fraction	$[]$
α	angle	$[rad]$
γ	Specific heat capacity ratio	$[]$
η	Efficiency	$[]$
Π	Pressure ratio	$[]$
Φ	Flow Coefficient	$[]$
Ψ	Head Coefficient	$[]$
ω	Rotational speed	$[rad/s]$

Table A.2. Subscripts

a	air	inj	injection
$blow$	blower	$meas$	measured
c	compressor	mod	modeled
$cool$	cooler	$scav$	scavenging manifold
cyl	cylinder	t	turbine
del	delivered	$trap$	trapped
e	exhaust gas	$x, corr$	corrected quantity
egr	EGR gas	x, in	inlet of x
eng	engine	x, out	outlet of x
exh	exhaust manifold	x, n	normalized x

Experimental Investigation of an RC Slab Culvert Rehabilitated with Grouted CSPs

Shradhanjali Moharana, *Department of Civil Engineering, Raajdhani Engineering College, Bhubaneswar, shradhanjalimoharana1@gmail.com*

Akashprava Panda, *Department of Civil Engineering, Aryan Institute of Engineering & Technology, Bhubaneswar, a_panda12@gmail.com*

Raushan Gupta, *Department of Civil Engineering, Capital Engineering College, Bhubaneswar, raushangupta26@yahoo.co.in*

Debi Prasad Singh, *Department of Mechanical Engineering, Raajdhani Engineering College, Bhubaneswar, deboprasad_1159@gmail.com*

ABSTRACT

The rehabilitation of an existing culvert with corrugated steel plates (CSPs) has been an emerging technology in recent years, but engineers and researchers are not particularly clear about the working principle of the rehabilitated structure. To investigate the mechanical properties of reinforced concrete (RC) slabs rehabilitated with CSPs, laboratory tests were carried out to explore the calculation method and influencing factors of load-carrying capacity of RC slab culverts rehabilitated with grouted CSPs. The results revealed the following: the flexural failure of the prerehabilitated RC slab has little influence on the test-loading capacity of the rehabilitated system; shear failure will occur in the RC slab and grout, and an arch effect will be formed in the CSP and grout after rehabilitation; the higher the shear strength of the concrete of the RC slab and grout, the greater the test-loading capacity of the rehabilitated system; the RC slab and grout greatly contribute to the test-loading capacity of the rehabilitated system; CSP changes the ductility of the rehabilitated system at the failure stage. It was found that the estimation method for the test-loading capacity of the rehabilitated system based on the shear capacities of the RC slab and grout and the flexural capacity of the CSP is reasonable; the maximum difference between the theoretical and experimental results was less than 30%, and the minimum difference between them was 0%.

1. Introduction

Most small bridges and culverts built early in China are mostly coming into overhaul period. Among many repair methods, the rehabilitation of small bridges and culverts with grouted corrugated steel plates (CSPs) is a very convenient technology that only requires the insertion of CSPs into the bridge or culvert and then grouting the space between them [1, 2]. However, this technology introduces new challenges to structural analysis as the mechanical mechanism of the structure changes from a single system to a composite system of the existing bridge or culvert, grout, and corrugated steel arch after rehabilitation; the existing bridge or culvert, grout, and CSPs may play very different roles in the rehabilitated system.

A large amount of research has been conducted to investigate the performance of slip-lined pipes, and post-rehabilitated pipes fixed with different materials have been found to exhibit different mechanical properties. For

example, a cast-iron pipe rehabilitated with a liner has been found to act as a "pipe within a pipe" system [3], whereas a rehabilitated concrete sewer has been found to act as a composite system [4]. Moreover, the compressive strength of the grout has been found to have an important influence on the test-loading capacity of the rehabilitated pipe [5]. Both full and partial interactions have been found to occur between the existing pipe, grout, and liner, and the design of the liner should not rely on the assumption of a bond between the two components [6, 7]. Furthermore, the level of corrosion of CSPs has been found to have no impact on structural behavior, and paving the invert has been found to improve the structural performance [8]. Generally, a rehabilitated pipe can carry higher loads than a pipe before rehabilitation [9, 10]. If a CSP is used to rehabilitate a reinforced concrete (RC) pipe, the load-sharing theory can be used to estimate the test-loading capacity of the rehabilitated pipe, and the level of corrosion of the RC pipe has little impact on the test-loading capacity [11, 12].

Some facets of the existing research on slip-lined pipes, for example, the influencing factors of the strength of the rehabilitated structure and the contact state between different materials, can provide a reference for the research of rehabilitated RC slab culverts; however, the mechanical properties of an RC slab are very different from those of an RC pipe. Some field tests have proven that the stress state of a concrete bridge or a brick culvert rehabilitated with CSPs was effectively reduced and that the CSPs achieved a good reinforcement effect [13–15]. However, the investigations of RC slabs rehabilitated with CSPs remain insufficient. RC slabs rehabilitated with a CSP exhibit the following characteristics: (1) the CSP is constrained by the RC slab culvert and grout, which are stronger than soil, and the deformation of the CSP is limited; (2) the interface of the RC slab, grout, and CSP is characterized by contact and slippage that are different from those of the composite structure, and the CSP has an arch effect, which increases the difficulty of structural analysis; (3) with the transformation of the structural system, the failure mode of the rehabilitated structure changes, as does the corresponding mechanical model; (4) the grout cannot transfer tension but can only transfer pressure, thereby increasing the complexity of the role of cracked grout in the reinforcement system.

Recently, increasingly more CSPs have been used to rehabilitate RC slab culverts in China, but engineers only design a CSP as a new culvert, and the working principle of the rehabilitated structure is not clear. Therefore, it is necessary to investigate the mechanical characteristics of the rehabilitated structure to provide a reference for engineering applications. Against this background, in the present research, a series of destructive tests were conducted to explore the calculation method and influencing factors of load-carrying capacity of RC slab culverts rehabilitated with grouted CSPs. The research results of this paper can provide effective theoretical guidance for engineering application, so that designers can reasonably design the rehabilitation project according to the calculation formula and realize the target load-carrying capacity of the rehabilitated system.

2. Experiment Description

2.1. RC Slabs. Five laboratory-manufactured RC slabs were used in this experiment, each of which had a length of 2600 mm, a width of 500 mm, and a thickness of 150 mm. Double-layer steel bars (HRB400) were arranged in the RC slabs with a protective layer thickness of 30 mm; a 3 ϕ 12 arrangement was adopted for the upper steel bars, while a 6 ϕ 16 arrangement was adopted for the lower steel bars. The strength grade of the RC slabs was C40, which represents a compressive strength of 40.375 MPa and an elastic modulus of 32.5 GPa. The strength grade of the steel bars was HRB400 with a minimum yield strength of 400 MPa and a tensile strength of 575 MPa, and the elastic modulus of the steel bars was 210 GPa. The RC slabs were placed directly on the integral foundations, and the lap length was 150 mm.

2.2. Integral Foundation. The integral foundation, which had a length of 3000 mm and a height of 1500 mm, was a U-shaped foundation formed by two piers connected with a bottom plate. The piers had a thickness of 350 mm and a width of 500 mm, and three layers of 6 ϕ 18 steel bars were arranged in the piers. The bottom plate had a thickness of 200 mm and a width of 500 mm, and two layers of 6 ϕ 18 steel bars were arranged in the plate. A groove was arranged at the top of the pier to place the RC slab, which had a length of 170 mm and a depth of 150 mm.

2.3. CSPs. The CSPs were semicircular with an inner diameter of 1000 mm and were purchased from the manufacturer. The corrugation amplitude of the CSPs was 55 mm with a period of 200 mm and an intact wall thickness of 3 mm. The designation of the CSPs was Q235, and they had a minimum yield strength of 235 MPa, a minimum tensile strength of 370 MPa, and an elastic modulus of 210 GPa. Unbalanced channels were used to connect the CSPs and the foundation, and the channel was connected with the foundation and CSPs by M20 expansion bolts and high-strength bolts, respectively.

2.4. Grout. Many materials can be used for grout, including foamed cement banking, cement mortar, fine aggregate concrete, and ordinary concrete. Considering that concrete is usually used in China [16–18], two types of grouts were used, namely, C30 concrete and M5 cement mortar. The C30 concrete had a compressive strength of 30.35 ± 2.00 MPa and an elastic modulus of 30 GPa, while the M5 cement mortar had a compressive strength of 3.37 MPa and an elastic modulus of 6.08 GPa. The thickness of the grout at both the foot and the crown of the CSPs was 95 mm.

2.5. Specimens. A total of five specimens were used in this experiment: (1) an RC slab rehabilitated with a grouted CSP (RRCS1 hereafter), (2) an RC slab rehabilitated with a grouted CSP (RRCS2 hereafter), (3) a preloaded RC slab rehabilitated with a grouted CSP (RRCS3 hereafter), (4) a preloaded RC slab rehabilitated with a grouted CSP (RRCS4 hereafter), and (5) an RC slab rehabilitated only with grout (RRCS5 hereafter). The grout used in RRCS1 was M5 cement mortar, whereas the grout used for the other specimens was C30 concrete. The difference between RRCS3 and RRCS4 was that the RC slab used in RRCS3 was preloaded to failure, whereas that used in RRCS4 was not. The details of the specimens are presented in Figure 1, and the loading scheme is illustrated in Figure 2.

2.6. Loading. This study enables a better understanding of the performance of RC slabs rehabilitated with grouted CSPs. A midspan single-point loading experiment was conducted in this study, and a string potentiometer with an accuracy of 0.1 mm was used to measure the vertical displacement of the midspan.

A load was applied to the specimens using a 1500 kN hydraulic actuator that was attached to a reaction frame over

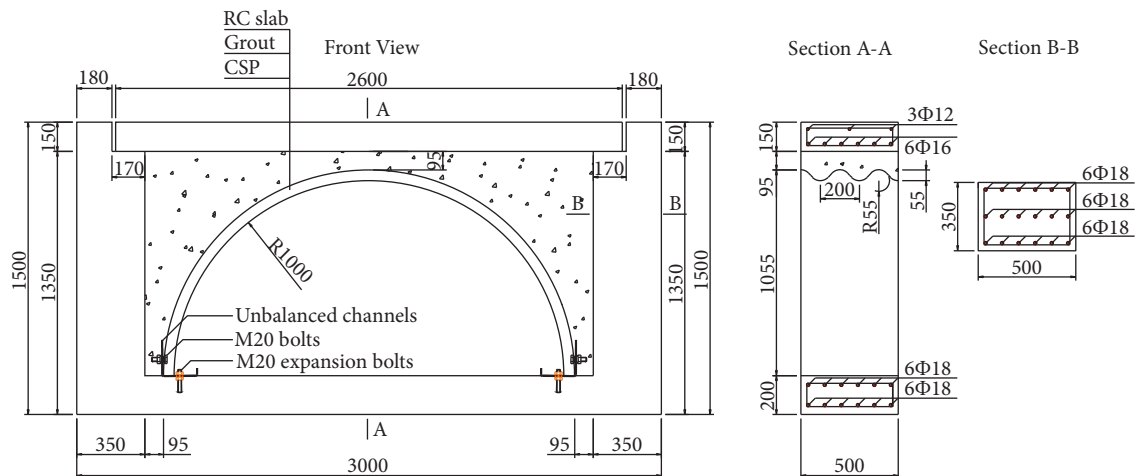


FIGURE 1: The details of the test specimens.

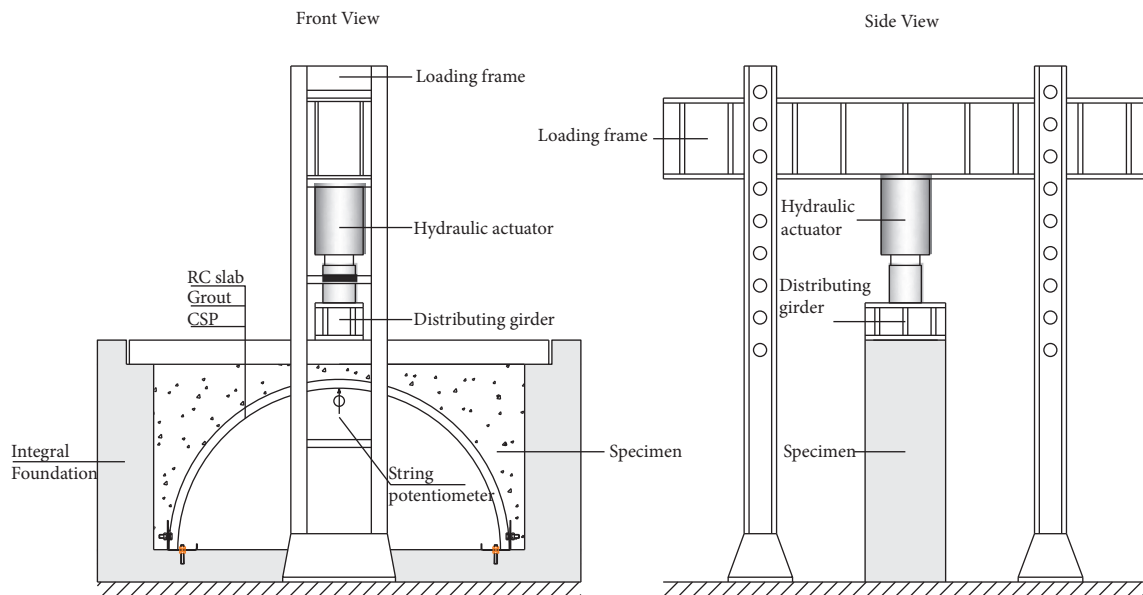


FIGURE 2: The schematic diagram of the loading frame.

the specimens. A distributing girder was used to ensure that the concentrated load could not cause the deterioration of the specimens or stress concentration. The specimens were loaded to the ultimate test-loading capacity at a loading rate of 15 kN/min, and the loading was paused at various stages to observe the experimental phenomena.

3. Experimental Results

3.1. RC Slab. In this single-point experiment, the RC slab, which was a flexural member, was mainly subjected to a bending moment before rehabilitation. The RC slab exhibited good ductility throughout the experimental process, which conformed to the failure characteristics of the underreinforced beam. It can be seen from the load-displacement curve shown in Figure 3 that the RC slab had a yield strength of 116.52 kN and an ultimate strength of 130 kN.

3.2. Rehabilitated System. Specimens RRCS1-5 were all RC slabs rehabilitated with grouted CSPs, and their load-displacement curves had the same shape; that is, each curve was basically a straight line before point (a). After point (a) was reached, the grout began to crack, and the slope of the load-displacement curve decreased and the curve was slightly inclined.

The experimental results of specimens RRCS3, RRCS4, and RRCS2 revealed that the preloading truly reduced the test-loading capacity of the rehabilitated system (667.03 kN and 683.89 kN versus 735.4 kN, respectively), but preloading to failure or not to failure had little effect on the test-loading capacity (667.03 kN versus 683.89 kN). However, the RC slab preloaded to failure (RRCS3) had a lower vertical displacement in the midspan of its rehabilitated system than the RC slab not preloaded to failure (RRCS4) when the maximum test-loading capacity of the rehabilitated system was reached (9.59 mm versus 14.17 mm, respectively). Moreover,

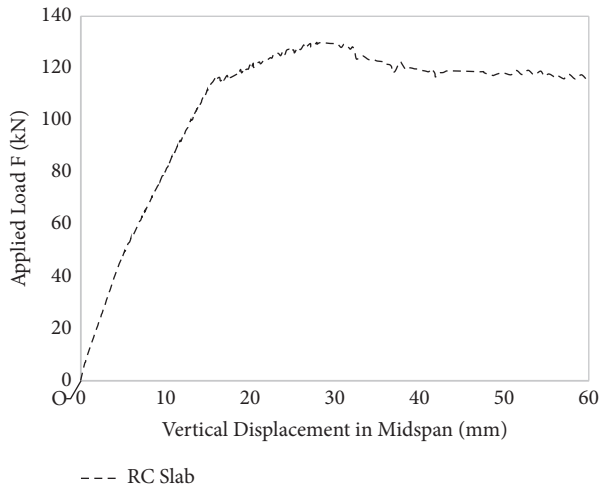


FIGURE 3: The relationship between the load and displacement for the RC slab.

it can be seen from Figure 4 that the vertical displacements of the midspans of the preloaded rehabilitated systems (RRCS3 and RRCS4) were both lower than that of the unpreloaded rehabilitated system (RRCS2) (9.59 mm and 14.17 mm versus 17.21 mm, respectively) when they reached the maximum test-loading capacity.

Generally, the load-displacement curves of the three specimens were similar in shape, and their grout-cracking points (point (a)) were close to each other. However, the ductilities of the three specimens after failure were quite different; that of RRCS3 (preloaded to failure) was the worst, followed by that of RRCS4 (not preloaded to failure), and that of RRCS2 (unpreloaded) was the best.

It can be seen from Figure 5 that the maximum test-loading capacity of RRCS5 (the rehabilitated system without a CSP) was much lower than that of RRCS2 (536.64 kN versus 735.4 kN, respectively), and the difference between them was 198.76 kN (this represents the test-loading capacity provided by the CSP). This finding indicates that the CSP did indeed play a role in the rehabilitated system, but the main contribution of the test-loading capacity of the rehabilitated system was provided by the RC slab and grout (73%), whereas the CSP contributed 27% of the test-loading capacity. The two curves for RRCS2 and RRCS5 were found to be strikingly similar before reaching the maximum test-loading capacity but had different amplitudes. From this point, the grout played an important role in strengthening the RC slab. The biggest difference between the two curves was that the ductility of RRCS2 was better than that of RRCS5 after reaching the maximum test-loading capacity due to the internal support of the CSP. Interestingly, the vertical displacements of the midspans of RRCS2 and RRCS5 were basically the same when the maximum test-loading capacity was reached. This indirectly indicates that the RC slab, grout, and CSP all reached their maximum test-loading capacities when the rehabilitated system reached its ultimate test-loading capacity.

Figure 6 reveals that the maximum test-loading capacity of RRCS1 was lower than that of RRCS2. Based on this, it can

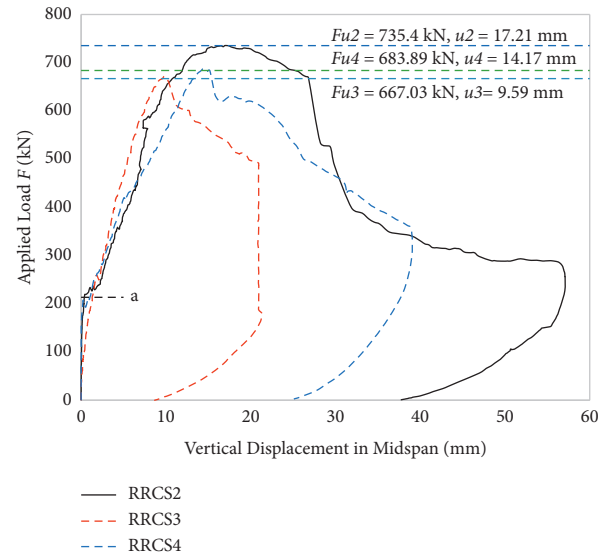


FIGURE 4: The relationship between the load and displacement for RRCS2, RRCS3, and RRCS4.

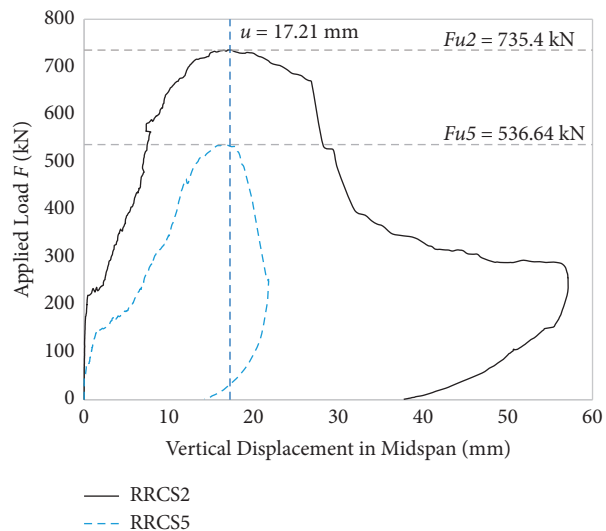


FIGURE 5: The relationship between the load and displacement for RRCS2 and RRCS5.

be concluded that the low grout strength resulted in the low test-loading capacity of the rehabilitated system. Moreover, the vertical displacements of the midspans of RRCS1 and RRCS2 were basically the same when the specimens reached the maximum test-loading capacity, and these specimens had the same ductility after reaching their maximum test-loading capacity.

3.3. Strain and Curvature of CSPs. The cross-sectional strains of CSPs are helpful for distinguishing the bonded condition of the RC slab, grout, and CSP. If the RC slab, grout, and CSP are fully bonded in the midspan, the strains of the CSP should be an oblique straight line, and the strains at the crest and valley of the CSP should be tensile strains; if there is no

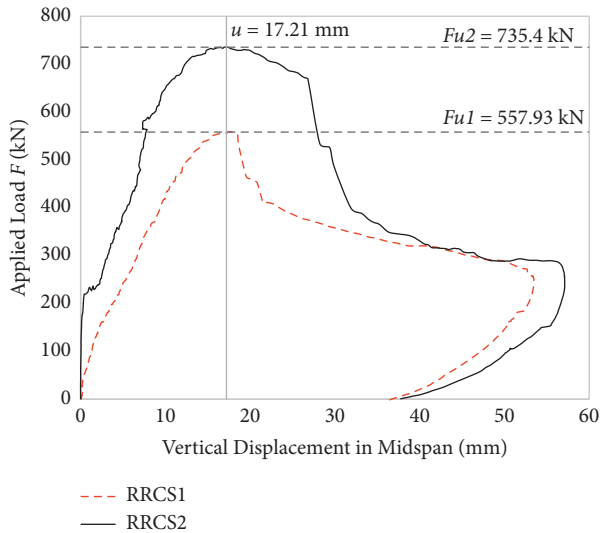


FIGURE 6: The relationship between the load and displacement for RRCS1 and RRCS2.

bonding between the CSP and grout, the strains at the crest and valley should be compressive and tensile strains, respectively. These two cases correspond to the strain distributions of full and partial bonding, as shown in Figure 7.

Figure 8 presents the strain distributions at the crest and valley of the CSP in RRCS2 at four different loading stages, namely, before grout cracking ($F = 100$ kN), during grout cracking ($F = 216.39$ kN), before the rehabilitated system reached the ultimate test-loading capacity ($F = 600$ kN), and at the point at which the rehabilitated system reached the ultimate test-loading capacity ($F = 735.4$ kN). It can be seen from Figure 8 that the strains at the vault of the CSP were all tensile, and the crest strain was less than the valley strain, which indicates that the CSP and grout were bonded before and during grout cracking (similar to the full bonding case exhibited in Figure 7). In contrast, at the crown of the CSP, the crest strain was compressive and the valley strain was tensile, which indicates that the CSP and grout slipped, and the CSP began to act independently before and at the point at which the ultimate test-loading capacity was reached.

The yield strain of steel was about 0.0011 (1100×10^{-6}), so when the specimen reached its ultimate test-loading capacity, the strains at the crown of the CSP already exceeded the yield strain of steel; this indicates that a plastic hinge had been formed at this time. If the test-loading capacity estimation is based on the ultimate test-loading capacity, the contribution of the CSP should be calculated via the use of a plastic theory.

The curvatures reflect the bending deformation of the CSP. When the strains of the CSP are less than the yield strains, the bending moment can be calculated by transforming the strains into stresses via Hooke's law; however, once the strains of the CSP are greater than the yield strains, Hooke's law is no longer applicable. Moreover, the stress-strain relationship of a cold-pressed CSP is unknown, and it is difficult to obtain the stresses. Therefore, the mechanical performance of the CSP after yielding was analyzed via the curvature, which was calculated as follows [19]:

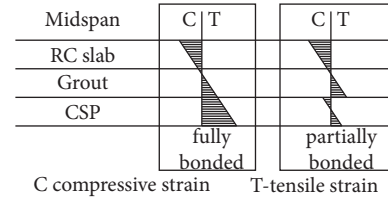


FIGURE 7: The strain distributions of different bonding conditions.

$$\kappa = \frac{\varepsilon_2 - \varepsilon_1}{h}, \quad (1)$$

where κ is the curvature ($10^{-6}/\text{mm}$) and ε_1 and ε_2 are, respectively, the crest and valley strains.

Figure 9 presents the curvature distributions of the CSP in two stages, namely, the yield stage of the CSP and the ultimate stage. The curvature was found to increase with the increase of the applied loads, and the curvature distributions were the largest when the specimens reached the ultimate test-loading capacity. The curvature distributions of the cross sections in the two loading stages were similar. The crown of the CSP was subjected to a positive bending moment, resulting in downward deformation, while the other sections were subjected to a negative bending moment, resulting in upward deformation. This phenomenon indirectly indicates that the CSP may have only carried applied loads (active action) directly at the crown, while the other sections were constrained by the grout (passive action) and not directly subjected to applied loads. If a two-hinged semicircular arch without the restraint of grout is subjected to vertical load, the inflection point will appear in the inclined direction at an angle of 45° relative to the vault. However, the inflection point shown in Figure 8 was less than 45° ; this indicates that the grout provided stronger lateral restraint for the foot and shoulder of the CSP than soil; that is, the foot of the CSP cannot rotate outward.

4. Failure Characteristics of the Rehabilitated System

Specimens RRCS1-5 had the same failure characteristics. Taking RRCS2 as an example, Figure 10 presents the crack distributions of the rehabilitated system. When RRCS2 was loaded to 230 kN, vertical bending cracks appeared at the crown of the grout, and horizontal bending cracks appeared at the middle height of the side of the grout. When loaded to 300 kN, vertical bending cracks appeared at the midspan of the RC slab. When loaded to 310 kN, shear cracks appeared in the RC slab and developed obliquely downward from the edge of the distributing girder at an approximate angle of 45° . When loaded to 550 kN, shear cracks appeared in the grout and also developed obliquely downward at an approximate angle of 45° . When loaded to the ultimate test-loading capacity, the width of the shear cracks in the RC slab and grout increased, the vertical deformation of the CSP also increased, and the shoulders buckled plastically. It can be inferred from the experimental phenomena that shear failure occurred in the RC slab and grout, whereas bending failure occurred in the CSP, and plastic hinges appeared at the crown and shoulders of the CSP. Thus, the ultimate test-

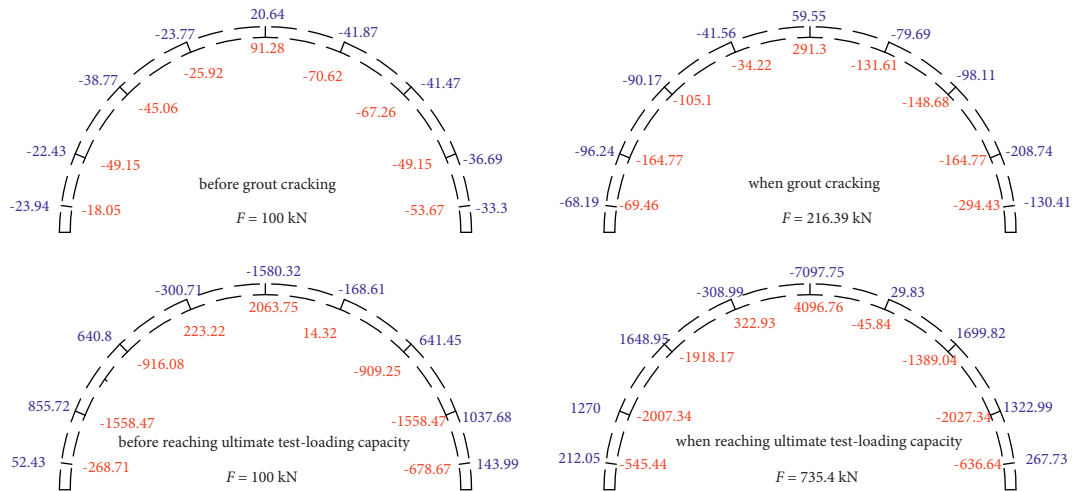


FIGURE 8: The cross-sectional strains of the CSP (unit: 10^{-6}).

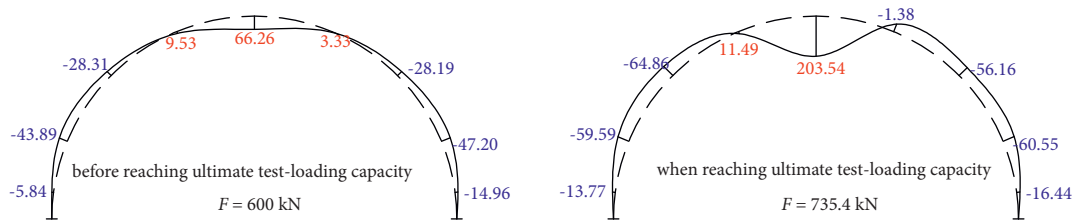


FIGURE 9: The sectional curvatures of the CSPs.

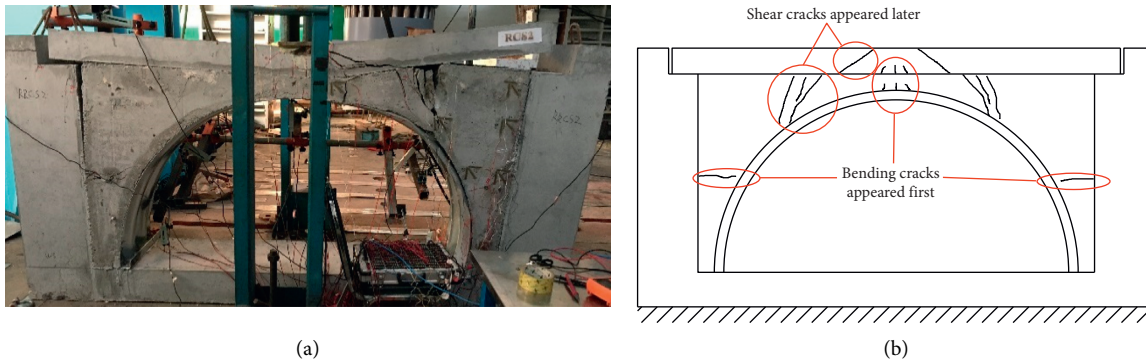


FIGURE 10: The failure characteristics: (a) overall failure pattern; (b) schematic diagram of cracks.

loading capacity of the rehabilitated system may depend on the shear capacity of the RC slab and grout and the flexural carrying capacity of the CSP.

5. Estimation of the Test-Loading Capacity

Based on the experimental phenomena, shear failure occurred in the RC slab and grout, and horizontal slippage occurred at their interface; thus, they did not bond together. In addition, Figure 5 shows that the deformations of specimens RRCS5 and RRCS2 were the same, which indicates that the rehabilitated system reached its ultimate test-loading capacity when the RC slab and grout were damaged.

Moreover, because bending failure occurred in the CSP, it can be concluded that the RC slab and grout were

subjected to shear forces, while the CSP was separately subjected to a bending moment, and the rehabilitated system reached its ultimate test-loading capacity when the RC slab and grout reached their shearing strengths. The maximum test-loading capacity of the rehabilitated system was the sum of the shear capacities of the RC slab and grout and the bending capacity of the CSP. Therefore, the calculation sketch in Figure 11 was used to estimate the test-loading capacity of the rehabilitated system. The shear failure surface was an oblique section downward from the edge of the distributing girder to the crown of CSPs with a hypothetical angle of 45° , and the applied load F should satisfy the following equation:

$$F = F_1 + F_2 + F_3, \quad (2)$$

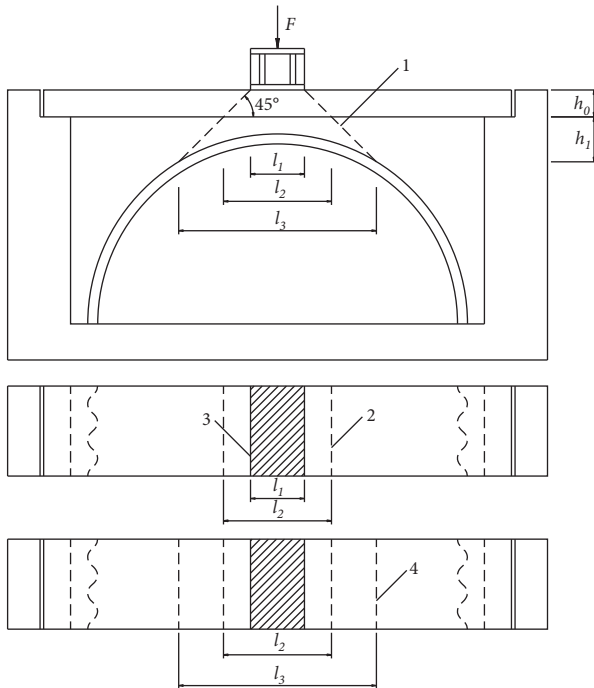


FIGURE 11: The calculation sketch of the rehabilitated system. (1) Shear surface of the RC slab and grout; (2) shear failure bottom line of the RC slab; (3) distributing girder side line; (4) shear failure bottom line of the grout.

where F is the applied load carried by the rehabilitated system, F_1 is the shear capacity of the RC slab, F_2 is the shear capacity of the grout, and F_3 is the bending capacity of the CSPs.

The shear capacity of the RC slab and grout can be calculated using the approach specified in the Concrete Structures Design Code [20] as follows:

$$\begin{aligned} F_1 &= 0.5f_{t1}A_1 + 0.8f_{yv}A_{sv}, \\ F_2 &= 0.7\beta_h f_{t2}A_2, \end{aligned} \quad (3)$$

where f_{t1} is the characteristic tensile strength of the concrete in the RC slab, f_{t2} is the characteristic tensile strength of the grout, and β_h is the influence coefficient of the cross-sectional height, which should be 1.0 when the cross-sectional height is not more than 800 mm and 0.9 when the cross-sectional height is not less than 2000 mm. Moreover, A_1 is the total area of the shear surface of the RC slab, which is equal to $(l_2 - l_1)/\cos 45^\circ$, and A_2 is the total area of the shear surface of the grout, which is equal to $(l_3 - l_2)/\cos 45^\circ$. Furthermore, f_{yv} is the characteristic tensile strength of the stirrup, A_{sv} is the section area of the stirrups intersecting the shear surface of the RC slab, l_1 is the width of the distributing girder, l_2 is the length of the applied load diffused to the bottom of the RC slab, and l_3 is the length of the applied load diffused to the bottom of the grout.

In a soil-steel system, the CSP is usually simplified as a two-hinged arch. However, due to the lateral restraint of the grout, the rotation of the foot of the CSP is restrained, thereby greatly improving the test-loading capacity of the CSP. Thus, in the rehabilitated system, the CSP was simplified as a fixed arch, the flexural capacity of which

can be calculated using the approach specified for arch bridges [21]. At this time, the bending moment at the crown of the CSP can be calculated by equation (4) and should be less than the plastic bending capacity $f_{csp}Z$. Moreover, F_3 can be calculated by equation (5).

$$M_c = \frac{F_3 R}{8} = f_{csp} Z, \quad (4)$$

$$F_3 = \frac{8f_{csp}Z}{R}, \quad (5)$$

where F_3 is the bending capacity of the CSP, which is the resultant force of uniformly distributed loads acting on the crown of the CSP, R is the mean radius of the CSP, f_{csp} is the characteristic yield strength of the CSP, and Z is the plastic section modulus of the CSP.

Specimen RRCS2 was taken as an example to illustrate the calculation process of the test-loading capacity; while the characteristic material strength was used in this process, the design values of material strength should be adopted for structural design. The characteristic tensile strengths of C40 concrete, C30 concrete, and M5 mortar were, respectively, 2.39, 2.01, and 0.1 MPa, and the characteristic yield strength and cross-sectional area of the stirrups were, respectively, 400 MPa and 123 mm². Because the horizontal projection length of the shear cracks (150 mm) in the RC slab was less than the spacing of the stirrups (180 mm), the shear cracks would not intersect with the stirrups, and the stirrups would not provide any shear capacity. Moreover, the values of l_1 , l_2 , and l_3 of the specimens were, respectively, 183, 483, and 847 mm (these values can be measured by drawing software, such as AUTO CAD). The characteristic yield strength of the CSP was 235 MPa, the plastic section modulus was 62.351 mm³/mm, the mean radius of the CSP was 0.5 m, the widths of the RC slab and CSP were 500 mm, and the value of β_h was 1.0.

$$\begin{aligned} F_1 &= 0.5f_{t1}A_1 + 0.8f_{yv}A_{sv} \\ &= 0.5 \times 2.39 \times 500 \times (483 - 183) \times \sqrt{2} \times 10^{-6} + 0 \\ &= 253.5 \text{ kN}, \\ F_2 &= 0.7\beta_h f_{t2}A_2 \\ &= 0.7 \times 1.0 \times 2.01 \times 500 \times (847 - 483) \times \sqrt{2} \times 10^{-6} \\ &= 362 \text{ kN}, \\ F_3 &= \frac{8f_{csp}Z}{R} \\ &= \frac{8 \times 235 \times 62.351 \times 500 \times 10^{-6}}{0.5} \\ &= 117.3 \text{ kN}, \\ F &= F_1 + F_2 + F_3 \\ &= 732.8 \text{ kN}. \end{aligned}$$

The calculated test-loading capacity of RRCS2 (732.8 kN) was very close to the experimental result (735.4 kN), and the calculated and experimental results of other specimens are summarized in Table 1. It is evident that the maximum difference between the theoretical and experimental results was less than 30%, and the minimum difference between them was 0%, which indicates that the calculation method is reasonable and can be used to estimate the test-loading capacity of a rehabilitated system. If the design value of material strength was adopted, the calculated results would be more conservative.

6. Discussion

It can be concluded that the test-loading capacity of the RC slab depends on its flexural capacity, while that of the rehabilitated system depends on the shear capacity of the RC slab and grout after rehabilitation, which can be determined based on the test-loading capacity of these specimens and the failure phenomena. Because preloading will cause the RC slab to have different residual flexural capacities, if the test-loading capacity of the rehabilitated system depends on the flexural capacity of the RC slab, it should be substantially different from the test-loading capacity of the original system. However, this was not the case with the experimental results; the test-loading capacities of RRCS2, RRCS3, and RRCS4 were found to be very close. The rehabilitated systems consisted of an RC slab, grout, and a CSP, and an arch effect was produced by the CSP and grout. This arch effect greatly improved the test-loading capacity of the rehabilitated system, resulting in the flexural strengths of the RC slab and grout being higher than the shearing strengths; thus, the rehabilitated system can only undergo shear failure.

Specimen RRCS2 represents an RC slab rehabilitated with a grouted CSP, whereas specimen RRCS5 represents an RC only rehabilitated with only grout. However, RRCS2 and RRCS5 had the same vertical deformation when they reached their ultimate test-loading capacities. This phenomenon indicates that, regardless of the presence of a CSP, once the RC slab and grout undergo shear failure, the rehabilitated system will be damaged. Before reaching the ultimate test-loading capacity, the flexible CSP does not change the ductility of the rehabilitated system; on the contrary, it changes the ductility at the failure stage, and, consequently, the rehabilitated system will not collapse suddenly. In these experiments, the CSP and grout were found to, respectively, contribute 27% and 73% to the improvement in the test-loading capacity, from which it can be inferred that the ultimate test-loading capacity of the rehabilitated system was mainly provided by the grout. However, whether the CSP can play a greater role is related to its own bending stiffness; the greater the bending stiffness, the greater the role it will play.

The flexural strength of the existing RC slab should be ignored when the slab is rehabilitated with a semicircular CSP, as the rehabilitated slab and grout will undergo shear failure instead of flexural failure. In such a rehabilitated system, due to the arch effect of the CSP and grout, the failure of the RC slab and grout will be changed from flexural

TABLE 1: The calculated and experimental results of the test-loading capacity.

Specimen	f_c (kN)	f_t (kN)	$ f_c - f_t /f_t$ (%)
RRCS1	388.9	557.93	30
RRCS2	732.8	735.4	0
RRCS3	732.8	667.03	10
RRCS4	732.8	683.89	7
RRCS5	615	536.64	15

Note. f_t : experimental results; f_c : calculated results.

failure (before rehabilitation) to shear failure (after rehabilitation). Therefore, the shear strengths of the RC slab and grout were used to estimate the test-loading capacity of the rehabilitated system. However, the CSP underwent flexural failure, so the bending strength should be used to estimate the test-loading capacity of the rehabilitated system. The restraint of the grout on the CSP resulted in differences from a soil-CSP system; the side wall and grout provided strong lateral restraint for the CSP in the rehabilitated system, which caused the test-loading capacity of the CSP to be much higher than that of a soil-CSP structure. The horizontal restraint of the grout and side wall was found to be very beneficial to the restriction of the foot deformation of the CSP; consequently, the arch foot should be simplified to a fixed constraint. In addition, the applied load acting on the midspan will be diffused into a range at the crown of the CSP by the RC slab and grout, and the grout at the shoulders of the CSP will also restrain the vertical deformation of the CSP, which appears as vertical loads acting on the shoulders of the CSP. Taking these two factors into consideration, the load acting on the CSP was simplified as a uniform load distribution across the full span of the CSP. For this reason, a CSP with small corrugation can provide a high test-loading capacity in the rehabilitated system, which is very different from the analysis principle of the soil-CSP structure.

It is noteworthy that a semicircular arch was used to rehabilitate the RC slabs in this research, and the test-loading capacity estimation was based on the experimental results and phenomena. If an RC slab with a large span is rehabilitated with a box-type CSP, the failure mechanism of the rehabilitated system will be different; the flexural failure of the RC slab, grout, and CSP will be more likely to occur in the midspan (at the crown of the arch), and the ultimate test-loading capacity of the rehabilitated system may primarily depend on the flexural capacities of the RC slab, grout, and CSP.

7. Conclusions

The current investigation was undertaken to ascertain the influencing factors and propose the practical calculation method of load-carrying capacity of RC slabs rehabilitated with grouted CSPs. Five specimens were tested in single-point loading experiments of the midspans of the RC slabs. The following key conclusions were drawn from this research:

- (1) Regardless of whether the RC slab undergoes flexural failure, it will have little influence on the test-loading

capacity of the rehabilitated system. After rehabilitation, shear failure will occur in the RC slab and grout, and the arch effect will be formed in the CSP and grout. Moreover, the ultimate test-loading capacity of the rehabilitated system will depend on the shear capacity of the RC slab and grout, as well as the flexural capacity of the CSP. In addition, the CSP will be subjected to strong horizontal restraint, which will also improve the flexural capacity of the semicircular CSP arch. Therefore, the flexural capacity of an RC slab culvert can be greatly improved via rehabilitation with a grouted CSP.

- (2) The specimens with high-strength grout exhibited significant increases in their test-loading capacities; the greater the strength of the grout, the higher the test-loading capacity of the rehabilitated system. In other words, the higher the shear strength of the concrete of the RC slab and the grout, the greater the test-loading capacity of the rehabilitated system. This means that the RC slab and grout greatly contribute to the test-loading capacity of the rehabilitated system. Moreover, the CSP changes the ductility of the rehabilitated system at the failure stage.
- (3) The estimation method of the test-loading capacity of the rehabilitated system based on the shear capacity of the RC slab and grout and the flexural capacity of the CSP is reasonable. The maximum difference between the theoretical and experimental results was found to be less than 30%, and the minimum difference between them was 0%. The designers can effectively design the rehabilitation project according to this practical calculation method.

Abbreviations

RRCS1:	RC slab rehabilitated with a grouted CSP; M5 cement mortar was used as grout
RRCS2:	Unpreloaded RC slab rehabilitated with a grouted CSP; C30 concrete was used as grout
RRCS3:	RC slab preloaded to failure rehabilitated with a grouted CSP; C30 concrete was used as grout
RRCS4:	RC slab not preloaded to failure rehabilitated with a grouted CSP; C30 concrete was used as grout
RRCS5:	RC slab rehabilitated with grout; C30 concrete was used as grout
F_{u1} :	Maximum test-loading capacity of RRCS1
F_{u2} :	Maximum test-loading capacity of RRCS2
F_{u3} :	Maximum test-loading capacity of RRCS3
F_{u4} :	Maximum test-loading capacity of RRCS4
F_{u5} :	Maximum test-loading capacity of RRCS5
u_1 :	Midspan vertical displacement corresponding to F_{u1}
u_2 :	Midspan vertical displacement corresponding to F_{u2}
u_3 :	Midspan vertical displacement corresponding to F_{u3}

u_4 :	Midspan vertical displacement corresponding to F_{u4}
u_5 :	Midspan vertical displacement corresponding to F_{u5}
κ :	Curvature ($10^{-6}/\text{mm}$)
ε_1 :	Crest strains of CSP
ε_2 :	Valley strains of CSP
F :	Applied load carried by the rehabilitated system
F_1 :	Shear capacity of the RC slab
F_2 :	Shear capacity of the grout
F_3 :	Bending capacity of the CSP, which is the resultant force of uniformly distributed loads acting on the crown of the CSP
f_{t1} :	Characteristic tensile strength of the concrete in the RC slab
f_{t2} :	Characteristic tensile strength of the grout
β_h :	Influence coefficient of the cross-sectional height, which should be 1.0 when the cross-sectional height is not more than 800 mm and 0.9 when the cross-sectional height is not less than 2000 mm
A_1 :	Total area of the shear surface of the RC slab $= (l_2 - l_1)/\cos 45^\circ$
A_2 :	total area of the shear surface of the grout $= (l_3 - l_2)/\cos 45^\circ$
f_{yv} :	Characteristic tensile strength of the stirrup
A_{sv} :	Section area of the stirrups intersecting the shear surface of the RC slab
l_1 :	Width of the distributing girder
l_2 :	Length of the applied load diffusing to the bottom of the RC slab
l_3 :	Length of the applied load diffusing to the bottom of the grout
R :	Mean radius of CSP
f_{CSP} :	Characteristic yield strength of CSP
Z :	Plastic section modulus of CSP
f_i :	Experimental results
f_c :	Calculated results.

Acknowledgments

This work was supported by the National Natural Science Foundation (Grant no. 52108142). The authors are grateful to Guangzhou Communication Investment Group Co., Ltd., and Hunan Jindi Corrugated Pipe Co., Ltd., for providing funds and experimental specimens.

References

- [1] Astm, *Standard Guide for Insertion of Flexible Polyethylene Pipe into Existing Sewers*, ASTM F585, West Conshohocken, PA, USA, 2013.
- [2] SnapTite, *Design Guide*, SnapTite, Erie, PA, USA, 2013, http://www.culvert-rehab.com/pdfs/2013_manual.pdf.
- [3] J. Q. Zhao and L. Daigle, "Structural performance of sliplined watermain," *Canadian Journal of Civil Engineering*, vol. 28, no. 6, pp. 969–978, 2001.
- [4] G. McAlpine, "Structural rehabilitation of semi elliptical concrete sewers," in *Proceedings of Pipelines*, pp. 1–7, ASCE, Reston, VA, USA, 2006.
- [5] T. Smith, N. A. Hoult, and I. D. Moore, "Role of grout strength and liners on the performance of slip-lined pipes," *Journal of Pipeline Systems Engineering and Practice*, vol. 6, no. 4, Article ID 04015007, 2015.
- [6] D. Becerril García and I. D. Moore, "Performance of deteriorated corrugated steel culverts rehabilitated with sprayed-on cementitious liners subjected to surface loads," *Tunnelling and Underground Space Technology*, vol. 47, pp. 222–232, 2015.
- [7] I. D. Moore and D. B. García, "Ultimate strength testing of two deteriorated metal culverts repaired with spray-on cementitious liners," *Transportation Research Record: Journal of the Transportation Research Board*, vol. 2522, no. 1, pp. 139–147, 2015.
- [8] J. Tetreault, N. A. Hoult, and I. D. Moore, "Pre- and post-rehabilitation behaviour of a deteriorated horizontal ellipse culvert," *Canadian Geotechnical Journal*, vol. 55, no. 3, pp. 329–342, 2018.
- [9] B. Simpson, I. D. Moore, and N. A. Hoult, "Experimental investigation of rehabilitated steel culvert performance under static surface loading," *Journal of Geotechnical and Geo-Environmental Engineering*, vol. 142, no. 2, Article ID 04015076, 2016.
- [10] B. Simpson, N. A. Hoult, and I. D. Moore, "Rehabilitated reinforced concrete culvert performance under surface loading," *Tunnelling and Underground Space Technology*, vol. 69, pp. 52–63, 2017.
- [11] B. J. Li, L. S. Zhu, and X. S. Fu, "Influence of grout strength and residual deformation on performance of rehabilitated RC pipes," *Journal of Pipeline Systems Engineering and Practice*, vol. 11, no. 2, Article ID 04020003, 2020.
- [12] B. J. Li, L. S. Zhu, and X. S. Fu, "Investigation of the load-sharing theory of the rc pipes rehabilitated with slip liners," *Advances in Civil Engineering*, vol. 2019, no. 8, Article ID 9594379, 2019.
- [13] J. Vaslestad, A. Madaj, L. Janusz, and B. Bednarek, "Field measurements of old brick culvert slip lined with corrugated steel culvert," in *Proceedings of the 83rd Annual Meeting of the Transportation-Research-Board*, pp. 227–234, Washington, DC, USA, January 2004.
- [14] J. Vaslestad, A. Madaj, L. Janusz et al., "Field measurements of long-span corrugated steel culvert replacing corroded concrete bridge," in *Proceedings of the 82nd Annual Meeting of the Transportation-Research-Board*, pp. 164–170, Washington, DC, USA, January 2002.
- [15] S. Syachrani, H. S. Jeong, V. Rai, M. J. Chae, and T. Iseley, "A risk management approach to safety assessment of trenchless technologies for culvert rehabilitation," *Tunnelling and Underground Space Technology*, vol. 25, no. 6, pp. 681–688, 2010.
- [16] C. Chen, "On consolidation of steel corrugated pipe culvert on expressways," *Shanxi Architecture*, vol. 42, no. 17, pp. 142–143, 2016.
- [17] P. P. Shang, "Defect culvert reinforcement technology using corrugated plate on existing heavy haul railway," *Railway Engineering*, vol. 57, no. 8, pp. 50–53, 2017.
- [18] Z. H. Wang, "On application of corrugated steel pipe culvert in road construction," *Shanxi Architecture*, vol. 38, no. 25, pp. 186–188, 2012.
- [19] H. W. Liu, *Mechanics of Materials (I)*, Higher Education Press, Beijing, China, 4th edition, 2004.
- [20] Mohurd (Ministry of Housing and Urban-Rural Development), *Code for Design of Concrete Structures, GB 50010-2010*, National Standards of People's Republic of China, Beijing, China, 2011.
- [21] CGDMHBC (Compile Group of Design Manual for Highway Bridge and Culvert), *Arch Bridge*, China Communication Press, Beijing, China, 1984.

Experimental Analysis on Axial Compression of Reinforced Concrete Short Circular Columns Strengthened with Prestressed Semicircular Steel Plates

Ranjan Kumar, *Department of Mechanical Engineering, NM Institute of Engineering & Technology, Bhubaneswar, kumarranjan75@gmail.com*

Sagarika Pasayat, *Department of Civil Engineering, Aryan Institute of Engineering & Technology, Bhubaneswar, s.pasayat@gmail.com*

Satchidananda Mohanty, *Department of Mechanical Engineering, Aryan Institute of Engineering & Technology, Bhubaneswar, s_mohanty234@gmail.com*

Suchampa Bagchi, *Department of Civil Engineering, NM Institute of Engineering & Technology, Bhubaneswar, suchampabagchi@yahoo.co.in*

ABSTRACT

China's total area of various existing buildings, according to relevant department estimates, is at least 10 billion m², with roughly one-third of the homes having exceeded their design life and having insufficient safety reserves. It is not economically feasible to demolish and rebuild these homes, and the benefits of new building are far less than the benefits of reinforcing existing structures to extend their service life. As a result, the importance of reinforcement technology is growing. Various methods for prestressed concrete column strengthening are now being investigated, however they are not generally viable. Prestressed semicircular steel plate is used to support concrete columns in a new prestressed strengthening technology. This article uses a combination of experimental and numerical modelling approaches to investigate the axial compression of a reinforced concrete circular section short column enhanced with prestressed semicircular steel plate.

1. Introduction

The application of prestress reinforcement in a building structure improves the force performance of the original structure by enhancing crack resistance, structural carrying capacity, and durability [1–3]. Currently varying methods for the prestressed reinforcement of concrete columns are developed comprising prestressed rod, prestressed strip, and prestressed steel strand reinforcement methods [4–7]. However, the application of prestressed reinforcement technology in practical engineering is still in the preliminary stage. Zhang et al. [8] explored the anchorage-reinforced concrete column (similar to the clamp method) by the quasistatic test to find the circumferential prestressed steel strands and demonstrated good repair and improvement effect on the seismic performance of damaged columns. Prestressed steel strand has the advantages of convenient

construction and short cycle and does not affect the use of the original structure during construction. It can also improve the bearing capacity, stiffness, and energy dissipation capacity of reinforced concrete columns. After reinforcement, the fire resistance, corrosion resistance, and aging resistance of the components are improved [9, 10]. Ge et al. [11] studied the seismic behavior of concrete columns strengthened by prestressed steel strand tensioning and anchoring. The test results show that the yield load and ultimate load were improved, but the concrete of the protective layer of the original column exposed to the prestressed steel strand is in the three-dimensional stress state, and the exposed concrete is still in the two-dimensional stress state, which makes the mechanical state of the concrete column more complex, which brings complexity to the design calculation, and the prestress of the steel strand is limited. Sun et al. [12] found a prestressed steel plate hoop to

reinforce bridge and effectively improve axial compression bearing capacity and deformation capacity of pier column. The axial compression performance tests of 16 reinforced columns and 2 contrast columns were carried out by Sun et al. [13] and Yong et al. [14]. The results show that the bearing capacity and deformation capacity of reinforced columns are improved under the conditions of constant spacing of steel strips, increasing or unchanged number of layers, and decreasing spacing. However, the column concrete between steel strips is exposed outside, which is not constrained by steel strips, leading to increased potential of early explosion [8, 15]. From the above research status, can we find a prestressed reinforcement method? It can not only improve the deformation resistance and bearing capacity of reinforced concrete columns, but also ensure that the stress of new and old structural layers is synchronized, the original structure is not destroyed, and the implementation is convenient.

Therefore, the prestressed semicircular steel plate is firstly proposed as a feasible solution toward the increased demand as shown in Figure 1. The main novelty is that two prestressed semicircular steel plates are installed on the side of the required strengthened cylinder, and the circumferential prestress is applied to the two semicircular steel plates by tightening the bolts. The prestress can be adjusted by tightening the bolts, so as to improve the bearing capacity of concrete columns without damaging the original column, and to achieve the purpose of rapid repair and reinforcement of concrete columns. As a result, compared to traditional reinforcement methods such as increasing section method [16, 17], steel casing method [18, 19], and CFRP reinforcement method [20, 21], the advantage can be concluded as follows: ①It does not increase the section of the column, nor add steel bars to the original column. ②Its core concrete is in the active three-way stress state before the force. ③The original concrete column has reinforcement according to the original bearing requirements. The reinforced concrete column is equivalent to the prestressed reinforced concrete-filled steel tube column, and its bearing capacity is higher than that of the concrete-filled steel tube column. ④The prestress can be adjusted to ensure the force synchronization of the original structure and the reinforced structure, and there will be no echelon damage. ⑤The reinforcement does not damage the structure of the original concrete column, nor does it reduce its bearing capacity. ⑥It is not necessary to unload the original concrete column and does not affect the use of the structure. The reinforcement construction can be implemented online and can be carried immediately after reinforcement. The structure demonstrates promising potential in intelligence manufacture owing to its superior advantages especially in the 3D printing domain [22–24].

In this article, the experimental study on the axial compression of the reinforced concrete circular section short column strengthened with prestressed semicircular steel plate is carried out by combining experimental and numerical simulation methods, and the calculation formula of bearing capacity of the reinforced short column is established by finite element analysis. In order to study the axial

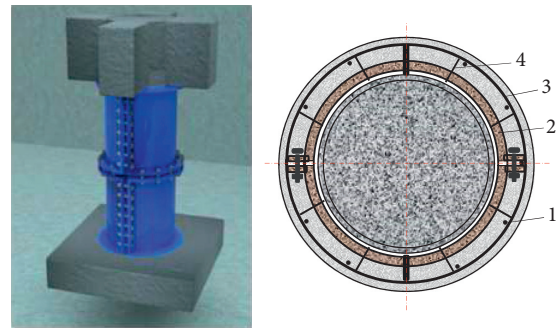


FIGURE 1: Schematic diagram of the reinforcement method. (1) Longitudinal bar; (2) semicircular steel plate; (3) stirrup; (4) radial structural bars.

bearing capacity of strengthened concrete columns, the axial compression tests of 20 concrete columns were completed, including 5 comparative columns and 15 concrete columns. All specimens were strengthened by steel casing with varying prestressing values. The test results show that the bearing capacity of the reinforced concrete column is greatly improved by prestressed steel casing, and the ultimate bearing capacity is increased by 72.1%–109.9%. On the basis of the experimental study, the finite element models of the prestressed semicircular steel plate strengthened column were established by ABAQUS. The correctness of the finite element model is verified by the experimental results. Finally, the bearing capacity of the reinforced concrete column is analyzed theoretically, to propose the calculation formula for axial compression bearing capacity; compared with the experimental data, the theoretical calculation formula has outstanding accuracy. Through this test, it can provide experimental data for the eccentric compressive test, earthquake-resistant test, shear test, resistant explosion experiment, fatigue test, and stability test of the prestressed steel casing reinforcement method for strengthening the concrete column.

2. Materials and Methods

2.1. Materials and Specimen Design. The concrete in this test is C30. According to Chinese Standard Test Method (GB/T50081-2016) [25], the same batch of concrete with the cylinder was selected for the compressive performance test of a concrete cube, and the average compressive strength of the concrete cube was 30.75 MPa.

As shown in Figure 2(a), 6C14HRB400E was selected as the longitudinal bar. According to the Steel Test Method for Reinforced Concrete (GB/T28900-2012) [26], the yield strength of the longitudinal bar was measured to be 541 MPa. The yield strength of the stirrup A6HPB300 is 332 MPa.

The test column is circular, 256 mm in diameter, and 1000 mm in height (Figure 2(b)). A total of 20 columns were designed in this experiment, of which 5 were the contrast columns, numbered RC-1 (the specific column numbers are RC-11 to RC-15), and the remaining 15 were divided into three groups of different prestressed reinforced concrete columns, numbered RC-2-1–RC-2-3 (the specific column numbers of each group are RC-2-11~RC-2-15).

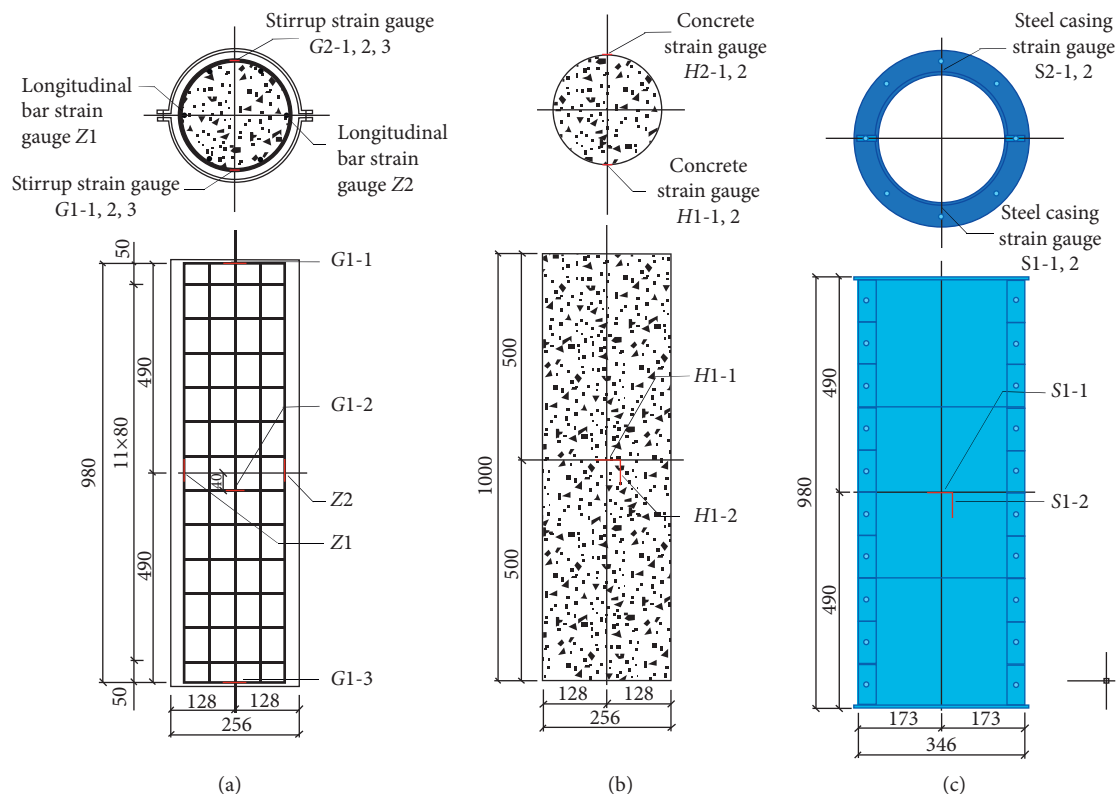


FIGURE 2: Details of specimens.

As shown in Figure 2(c), the inner diameter of the steel casing wall is 256 mm, the length is 980 mm, and the thickness of the steel plate is 5 mm. In order to make the steel casing successfully impose circumferential prestress on the concrete cylinder, the two semicircular steel plates cannot be closed into a complete circle, and the two semicircular steel plates should leave 6 mm ($256 \times \pi \times 0.01 \times 1.5 = 12$ mm, 0.01 is the ultimate tensile strain of steel, and 1.5 is the surplus coefficient) gaps in advance.

The nominal diameter was 12 mm, and the stress cross-sectional area of M12 bolt was 84.3 mm².

In order to measure the internal stress and deformation of the steel bar, concrete, and steel casing, strain gauges are affixed at the specific position of the specimen, and the specific position of the strain gauge is shown in Figure 2.

2.2. Loading Program. In order to study the mechanical properties and reinforcement effect of concrete columns strengthened with steel casting (steel cylinder formed by closing two semicircular steel plates) under precompression stress, four groups of axial compression tests of strengthened columns were carried out:

- (1) Contrast column test of the unreinforced original column.
- (2) According to the prestress value, the test of the reinforced column can be divided into the following three categories:
 - ① In Scheme 1, the prestress value is 0, which means tightening the bolt gently with a common wrench so that the steel casing is just close to the surface of the concrete cylinder; therefore, reinforced columns are equivalent to reinforced concrete-filled steel tubular columns.
 - ② In Scheme 2, the confining pressure of the semicircular steel plate on the concrete column is equivalent to that of the unreinforced column stirrup on core concrete. As shown in Figure 3, $p = \sigma_r$ (p is shown in Figure 3(c), and σ_r is the confining pressure of steel casing on concrete columns); therefore, $\sigma_3 = \sigma_r$ (Figure 3(c)). Because the thickness of the semicircular steel plate is far less than the diameter of the concrete column, and the thickness of the steel plate is $t = 5$ mm, the cross-sectional area of the steel tube wall is $A_{s1} = 4097.70 \text{ mm}^2$. When the diameter of the

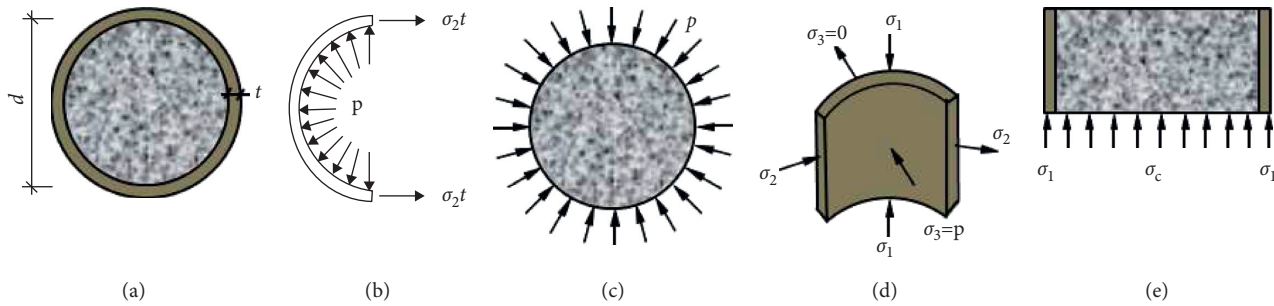


FIGURE 3: Stress diagram after reinforcement.

column is $d = 256$ mm and the thickness of the concrete cover is 25 mm, the diameter of core concrete (stirrup spacing) is 194 mm and the area of core concrete is $A_{cor} = 29544.26 \text{ mm}^2$. The cross-sectional area of concrete column $A = 51445.76 \text{ mm}^2$, and the stirrup conversion area is $A_{ss0} = 215.19 \text{ mm}^2$. Therefore, the constraint stress (σ_{r1}) of stirrup on the core concrete column can be calculated by the following formula [27, 28]:

$$\sigma_{r1} = \frac{f_{yv} \cdot A_{ss0}}{2A_{cor}} = \frac{270 \times 215.19}{2 \times 29544.26} = 0.983 \frac{\text{N}}{\text{mm}^2}, \quad (1)$$

where f_{yv} is the design value of stirrup tensile strength, $f_{yv} = 270$ MPa. When the confining pressure of steel casing on the surface of the concrete column is equal to that of stirrup on core concrete before column reinforcement, there should be

$$\sigma_r = \sigma_{r1}. \quad (2)$$

At this time, the circumferential tensile stress in the steel casing plate can be obtained as follows:

$$\sigma_\theta = 2\sigma_r \frac{A}{A_{s1}} = 2 \times 0.983 \times \frac{51445.76}{4097.70} = 24.68 \frac{\text{N}}{\text{mm}^2}. \quad (3)$$

- ③ In Scheme 3, the prestress value is equivalent to the prestress value required to make the bolt reach its tensile strength design value. At this time, the tensile force of the steel casing is larger than that of Scheme 2. The design value of the axial tensile connection bearing capacity of a single bolt is set as N_t^b :

$$N_t^b = A_{\text{eff}} f_t^b = 84.3 \times 400 = 33270 \text{ N}, \quad (4)$$

where A_{eff} is the stress section area of a single bolt, $A_{\text{eff}} = 84.3 \text{ mm}^2$. f_t^b is the tensile design strength of the bolt, $f_t^b = 400$ MPa. In addition, the number of bolts per row is 10:

$$\sigma_\theta = \frac{N_t^b \times 10}{t \cdot l} = \frac{33270 \times 10}{5 \times 980} = 67.90 \frac{\text{N}}{\text{mm}^2}, \quad (5)$$

where t is the thickness of the steel casing plate, $t = 5$ mm and l is the height of steel casing, $l = 980$ mm. Therefore, the grouping scheme and the corresponding prestress values are listed in Table 1.

The loading method is full-section axial compression. The test is carried out on the microcomputer controlled electro-hydraulic servo press-shear testing machine. The strain of steel bars, steel casings, and concrete is measured by the static resistance strain gauge DH3818Y and dynamic signal acquisition and analysis system DHDAS. The cracks are observed with the naked eye of the magnifying glass and the flashlight. The testing machine is shown in Figure 4.

The test loading was carried out according to the *Standard Test Method for Concrete Structures* (GB/T50152-2012) [29]. After the reinforcement column is aligned, the preloading of $0.3N_u$ (predicted ultimate load value) was carried out, and the preloading was carried out 2-3 times. During the preloading period, the number of test equipment indicators needs to be carefully checked, and the abnormal phenomena should be eliminated in time. After the preload is completed. Then, remove all loads and start the formal test. The test device is shown in Figure 5. Pressurized loading was used in the test. Each stage was kept for 10 min, and the loading value of each stage was $0.2N_u$ (predicted ultimate load value) [30, 31]. The loading speed was 2 kN/s. When the loading value reached $0.8N_u$, the loading value of each stage was $0.1N_u$. When the last stage was loaded, the loading speed was 1 kN/s. Until the ultimate load was reached and the pressure was kept, the loading was continuously and slowly until the specimen was destroyed. Among them, the strain data take the average value of 1 minute before the pressure was kept. Because the concrete column has 10 mm exposure in the upper and lower ends of the steel casing (Figure 5), the loading stops when the upper and lower loading plates contact the steel casing.

3. Results and Discussion

3.1. Main Results of the Test. The main test results are shown in Table 2. It can be seen from Table 2 that the ultimate load of strengthened columns increases differently with different prestress values. Compared with the contrast column, when the prestress value is 0 N/mm^2 , the ultimate load of the strengthened column increases by 72.1%–92.4%; when the

TABLE 1: Details of specimens.

Methods	Number	Scheme	σ_{θ} (MPa)	Quantity (pillar)
No reinforcement	RC-1	No steel casing	0	5
Reinforcement	RC-2-1	Scheme 1	0	5
	RC-2-2	Scheme 2	24.68	5
	RC-2-3	Scheme 3	67.90	5
Total				20



FIGURE 4: Testing machine.

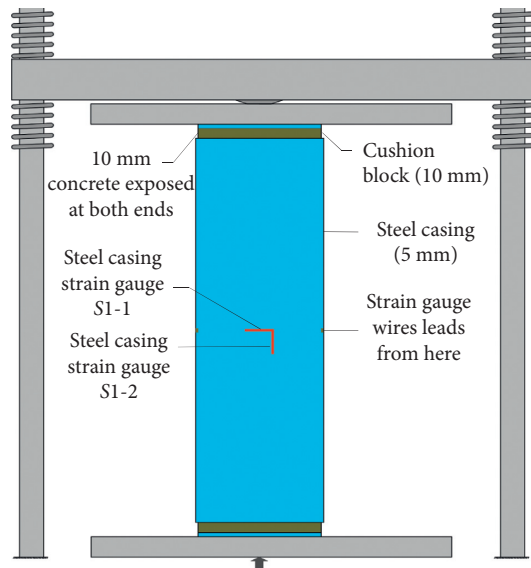


FIGURE 5: Diagram of specimen.

confining pressure of the semicircular steel plate on the concrete column is equivalent to that of the unreinforced column stirrup on core concrete, the ultimate load of the strengthened column increases by 95.0%–102.7%; when the prestress value is equivalent to the prestress value required to make the bolt reach its tensile strength design value, the ultimate load of the strengthened column increases by 97.5%–109.9%. It can be seen that, with the increase in the

prestress value, the confinement effect of steel casing on concrete is more obvious, and the bearing capacity of concrete columns after reinforcement is slightly improved.

3.1.1. Phenomena. As shown in Figure 6, for RC-1, at the beginning of loading, two ends of the column due to stress concentration distribution crack. With the increase of load, because there is no restriction of steel casing, vertical cracks gradually appear in the surface of concrete cover. When the axial load reaches about 90% of its peak load, the vertical cracks continued to extend vertically, and the crack width increased. With a slight click, some cover concrete spalling. When the load reaches the maximum value, the head of the concrete column collapses in a large area, and the upper part of the specimen is bulging. Then, the bearing capacity decreases sharply. From the crack of the concrete column to the complete failure of the reinforced column, the whole process is relatively short, and the compression process shows the characteristics of brittle failure. For the three groups of concrete columns strengthened with steel casing, they have no obvious change at the initial stage of loading. When the load gradually increases, the appearance of steel casing has no obvious change, but its two vertical flanges have corrugated changes. Then, there was a crackling sound, which was due to the joint action of rib angle and bolt to make the vertical flange yield first. When the reinforced column reaches the ultimate bearing capacity, the weld position of the rib angle of the vertical flange is tear. Because the steel casing is restrained by the transverse flange during loading, the appearance of the steel casing still has no obvious change.

Figure 7 shows the internal failure mode diagram of the concrete cylinder after removing the steel plate. It can be seen that the failure of the ends of the column is more serious, which is due to the cushion plate that directly acts on the top of the concrete column during loading, and the end is not restrained by the steel casing. The ultimate compressive strain of concrete ϵ_{cu} is 0.0033; from this, the ultimate displacement value is 3.3 mm. Two ends of the reinforced column are compressed more than 10 mm, indicating that the confined concrete in the concrete column has been compressed. However, due to the circumferential constraint of the steel casing, the concrete column can still withstand axial pressure. Therefore, the prestressed steel casing can effectively restrict the concrete column. After loading, the steel casing is closely connected with the surface of the concrete cylinder, and it is very difficult to separate them. This shows that the Poisson displacement or lateral displacement of the concrete in the steel casing is obvious, and the steel casing ensures the integrity of the specimen and the effectiveness of the pressure transfer.

3.1.2. Failure Patterns of Specimens. There are two typical failure modes of concrete column: ①The top concrete is crushed and peeled off. ②Due to the constraint effect of the steel casing on the core concrete, the whole shearing destruction of the concrete will not appear, and even the cracked concrete will be re-extrusion under the constraint of

TABLE 2: Main results of the test.

Number	N_u (kN)	Increase rate (%)	Failure mode
RC-1	1	1471.50	Cover concrete spalling, concrete crushing, upper column drumming
	2	1553.30	
	3	1548.53	
	4	1612.32	
	5	1526.23	
RC-2-1	1	2654.89	Concrete cracking, no obvious phenomenon in the steel casing
	2	2910.25	
	3	2967.48	
	4	2938.08	
	5	2781.00	
RC-2-2	1	3017.00	Vertical flange weld cracking, concrete splitting
	2	3008.29	
	3	3026.02	
	4	3110.64	
	5	3125.31	
RC-2-3	1	3133.54	Bolt fracture, steel casing failure
	2	3146.81	
	3	3046.87	
	4	3237.70	
	5	3304.70	



FIGURE 6: Failure modes of typical specimens.

the axial pressure and the steel casing. Due to the continuous occurrence of new corrugated bending of the vertical flange of the steel casing, cracks appear at the welds of the vertical flange, and the confining pressure is gradually weakened. On the premise of ensuring that no shear failure occurs, the reinforced column mainly occurs in two types of failure forms: the first type is axial compression failure; concrete

columns in the compression zone are crushed and peeled off. The second type is the failure of the vertical flange of steel casing. From the cracking of reinforced columns under failure, two failure modes are ductile failure. Because the reinforced column has concrete spalling and clicking sound before failure, it shows that there are obvious signs before failure, and the failure form is reasonable.

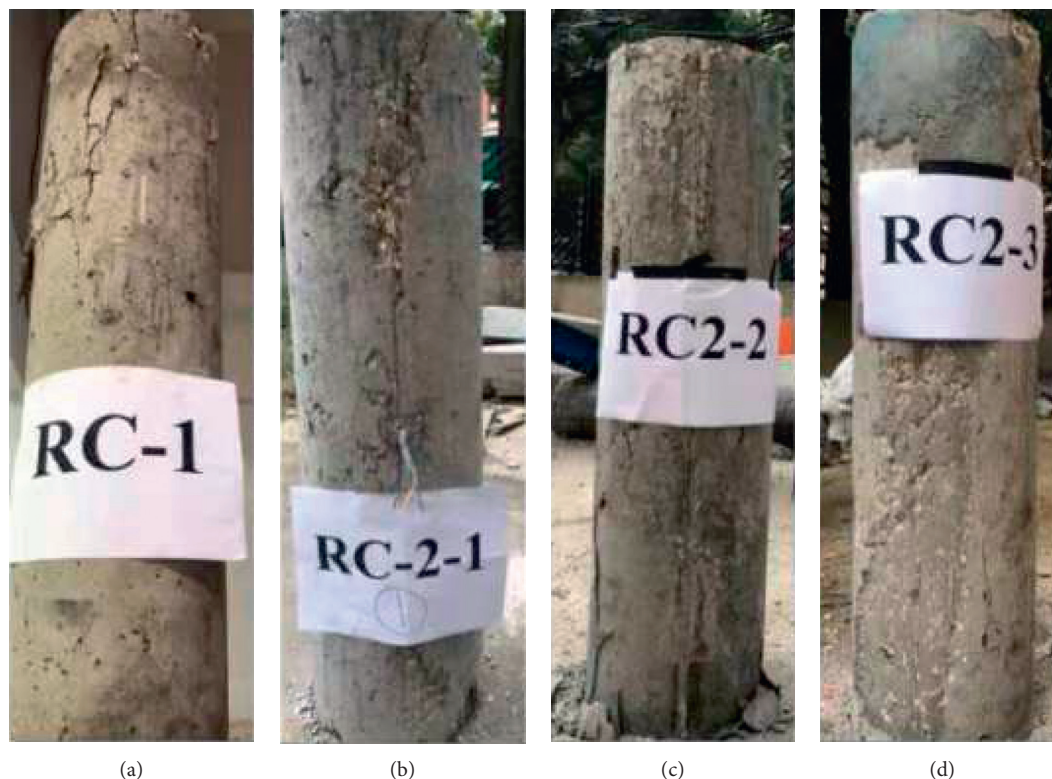


FIGURE 7: Internal failure mode of test column.

3.1.3. Load-Displacement Curve. Figure 8 shows the load-displacement curve of reinforced column. The curve can be divided into elastic section at the beginning of loading, inelastic section at 80% of ultimate load, and descending section after ultimate load. During the initial loading, all columns are in the elastic stage. Because fine stone concrete is poured between the steel casing and the concrete column to make them fit closely, the steel casing has a constraint effect on the core concrete. Therefore, with the increase of load, the greater the prestress value, the greater the slope of the strengthened column. As the load continues to increase, the constraint effect of steel casing on concrete becomes more obvious, and the bearing capacity of reinforced columns is also larger. Compared with the contrast column, the bearing capacities of RC2-1, RC2-2, and RC2-3 of the reinforced column were increased by 85%, 98%, and 106%, respectively. Because the steel casing has a strong constraint on concrete, the ultimate bearing capacity decreases slowly when it is destroyed, and for the specimens RC-1, RC2-1, RC2-2, and RC2-3, $\Delta_{\max}/\Delta_{\text{elastic}}$ is 1.06, 2.57, 2.77, 3.48, respectively (Δ_{\max} is the ultimate displacement, and Δ_{elastic} is the elastic displacement). It shows that the ductility of the new concrete structure increases with the increase of steel casing prestress.

3.1.4. Load-Material Strain Curve. Figure 9 shows the load-strain curve of the concrete and steel casing. In the early stage of loading, the load-strain is linear, which indicates that the reinforced column is in the elastic stage. The strain

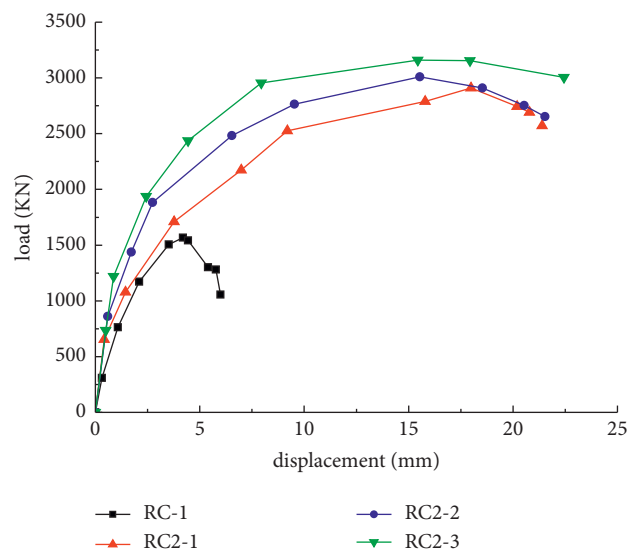


FIGURE 8: Load-displacement curves.

of concrete and steel casing increases proportionally with the increase of load. When the load increases to 50%, the column cracks and works with cracks. With the increase of load, the strain of concrete increases and the transverse strain of steel casing also increases. The longitudinal strain of steel casing increases mainly due to the increase of transverse strain of steel casing. When the load is close to N_u , the slope of the curve continues to decrease, the stiffness of the specimen

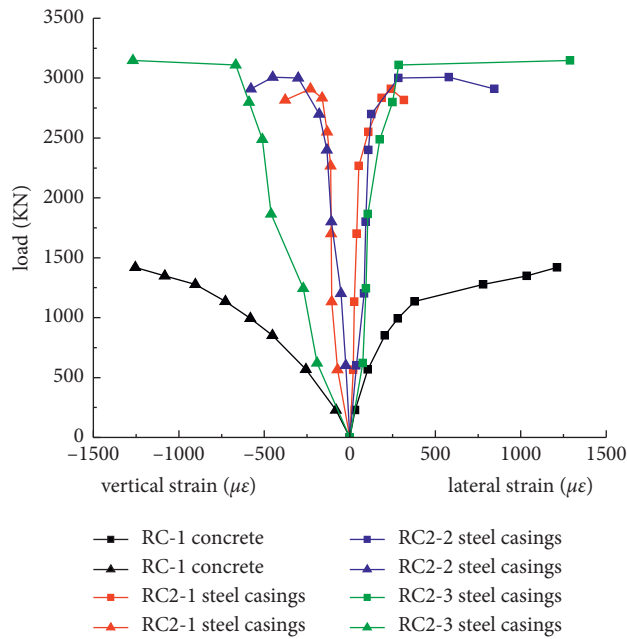


FIGURE 9: Load-strain curves of concrete and steel casings.

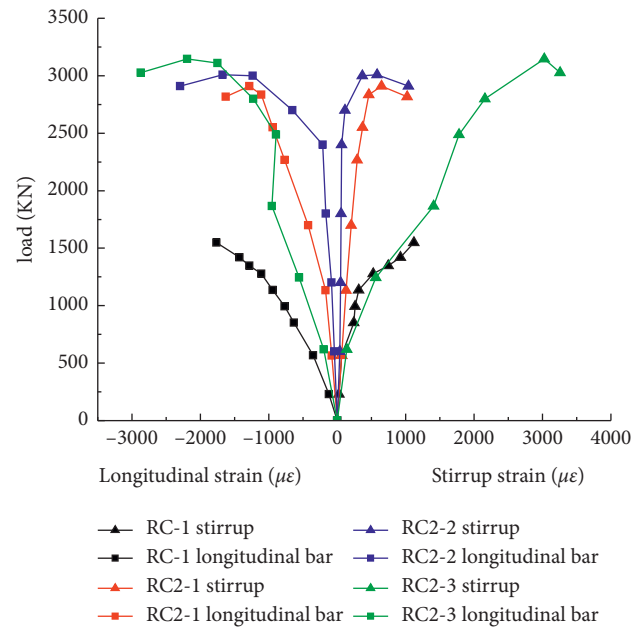


FIGURE 10: Load-strain curve of steel bar.

decreases, and the reinforced column is destroyed. When specimens RC2-1, RC2-2, and RC2-3 reach the ultimate load, the transverse strains of steel casing are 241, 580, and 1288 $\mu\epsilon$, and the longitudinal strains are 231, 450, and 1268 $\mu\epsilon$, respectively.

Figure 10 shows the load-strain curve of the steel bar of the reinforced column. With the increase in the steel casing prestress value, the constraint effect on the concrete column is stronger, and the increase of the peak strain of the steel bar (the strain corresponding to the ultimate load) is greater. When the specimens RC-1, RC2-1, RC2-2, and RC2-3 reach the ultimate load, the stirrup strains are 1120, 650, 584, and 3025 $\mu\epsilon$, and the longitudinal reinforcement strains are 1767, 1284, 1675, and 2292 $\mu\epsilon$, respectively. Comparing the reinforced columns RC2-1, RC2-2, and RC2-3, it is known that the prestressed semicircular steel plate reinforcement can improve the ultimate strain of concrete, and the concrete strain is related to the size of reinforcement prestress. The greater the prestress, the greater the ultimate strain of the reinforcement column. And the strain growth rate of the reinforced column is accelerated after the peak load, indicating that the prestressed semicircular steel plate reinforcement gives full play to the material properties of steel and concrete. It can be seen from the figure that the steel strain of the contrast column RC-1 decreases directly after reaching the ultimate load. Due to the transverse constraint force provided by the prestressed semicircular steel plate, the steel strain of the reinforced column decreased slowly after reaching the ultimate load.

3.2. Finite Element Analysis

3.2.1. Finite Element Modeling. In this article, ABAQUS software is used for finite element analysis. The steel skeleton and concrete are contacted by the embedded

region without considering the influence of bond-slip, and it is assumed to be coordinated deformation. Although the steel casing and concrete column surface will produce relative slip in the actual test, many research results show that this relative slip has little effect on the constraint ability, so this article assumes that they are ideally connected and use tie contact. In the existing research field, the application method of steel casing prestress is still relatively rare. High strength bolts are used to apply prestress in the test, but, in the simulation, the equivalent substitution method is used to control prestress, and the prestress is equivalent to the pressure generated around the concrete column; that is, the contact element between the steel casing and the concrete transfers the interface pressure p , and the pressure perpendicular to the contact surface can be completely transferred between the interfaces. Only normal contact is considered between the cushion plate and the top surface of the concrete. Among them, the steel casing and two ends of the cushion plate are simulated by shell element S4R, and the concrete is simulated by three-dimensional solid element C3D8R.

The constitutive model of the concrete column strengthened with prestressed steel casing is similar to that of the concrete-filled steel tubular column. Therefore, the constitutive model of concrete in this simulation adopts the compression constitutive model of the concrete-filled steel tubular column in Liu Wei's study on the working mechanism of the concrete-filled steel tubular column under local compression [32]. The loading method adopts the vertical displacement loading of the upper part of the model. It is assumed that the lower part of the model is completely fixed, and the upper part constrains two translational and rotational degrees of freedom. The finite element model is shown in Figure 11.

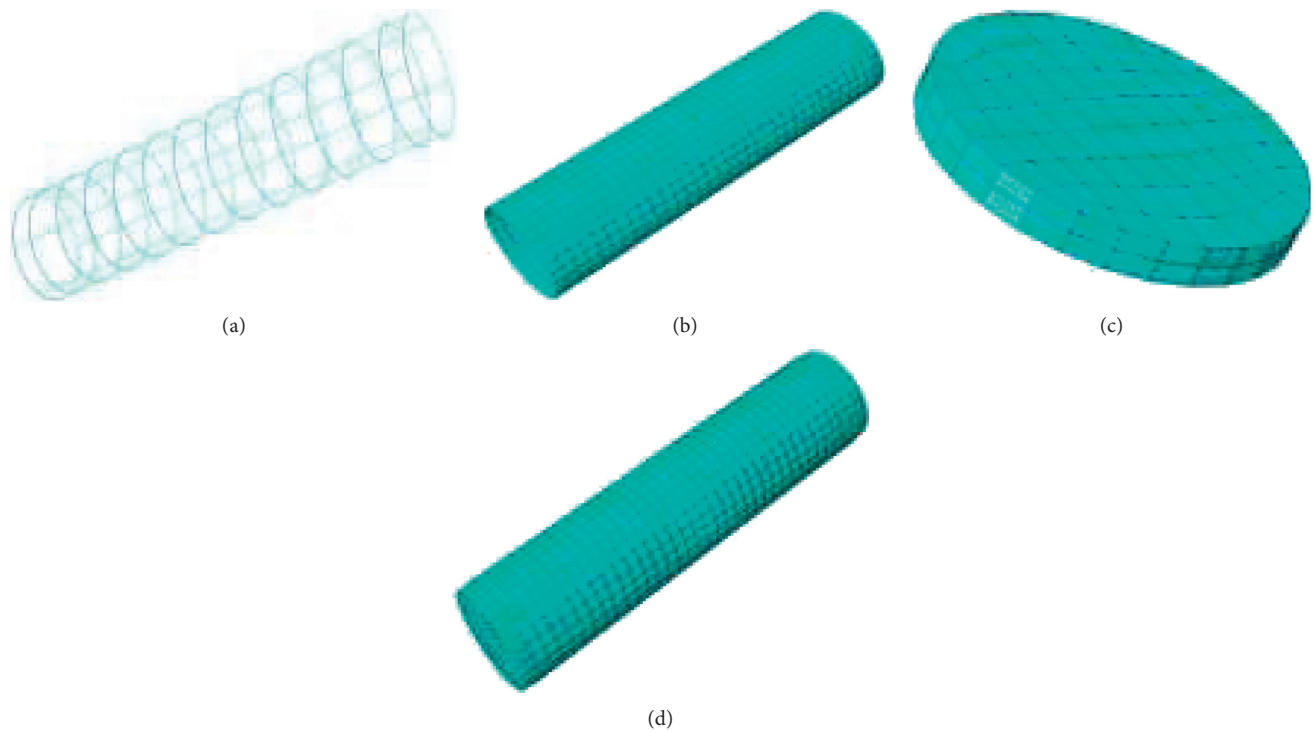


FIGURE 11: Model mesh subdivision. (a) Steel frame. (b) Steel casings. (c) Cushion block. (d) The whole specimen.

3.2.2. Results of Finite Element. Figure 12 shows the stress distribution nephogram of the steel casing when the reinforced column reaches the ultimate load when the prestress of the steel casing is 0 N/mm^2 , 24.68 N/mm^2 , and 67.90 N/mm^2 , respectively. It can be seen from the figure that with the increase in the prestress value, the coverage of the maximum stress of the steel casing increases and is distributed in the middle area of the reinforced column. And with the increase in the prestress value, the compressive stress value increases, it shows that the steel casing has a good restraint effect, and the restraint effect is also obvious. There is a certain error between the finite element simulation and the test results; the main reason for the error is that there is a deviation between the application mode of prestress of reinforced columns and the actual situation during modeling. Moreover, the contact between steel casing and concrete is also complete contact in the ideal state, which is difficult to achieve in the actual project.

Figure 13 shows the load-displacement curve of the specimen obtained by the test and the finite element method. The real line represents the finite element value. The imaginary line represents the experimental value. It can be seen that the calculation results of the finite element model are consistent with the test results. The finite element analysis tends to be idealized. Therefore, the finite element analysis results are better than the test results. The comparison of specimen bearing capacity is shown in Table 3, $N_{FEM}/\overline{N}_{EXP}$ mean value is 1.026, and the standard deviation is 0.012, indicating that the finite element model established in this article can better simulate the stress characteristics of

reinforced concrete columns strengthened with prestressed steel casing.

4. Calculation of Axial Compression Bearing Capacity

The prestressed steel casing reinforcement method studied in this article is a new reinforcement method. By prestressing the steel casing, the steel casing and the column needed to be strengthened are connected into a whole, so that they work together, thus significantly improving the bearing capacity of concrete columns.

Referring to the research results of Si et al. [33] in the axial compression test of damaged reinforced concrete columns strengthened with prestressed steel wires, after reinforcement, the bearing capacity of the reinforced column is composed of longitudinal reinforcement and confined concrete, and thus, the calculation formula of the bearing capacity of the reinforced column with prestressed steel wires is proposed:

$$N_u = \phi \cdot f_{c,c} A_c + f_y' A_s', \quad (6)$$

$$f_{c,c} = b \cdot f_c,$$

where N_u is the ultimate bearing capacity of the composite strengthened member, kN; $f_{c,c}$ is the axial compressive strength of confined concrete, MPa; b is the prestressed winding improvement coefficient; f_c is the axial compressive strength of unconstrained concrete, MPa; A is the damage coefficient; A_c is the section area of compressive concrete, mm^2 ; f_y is the longitudinal reinforcement compressive

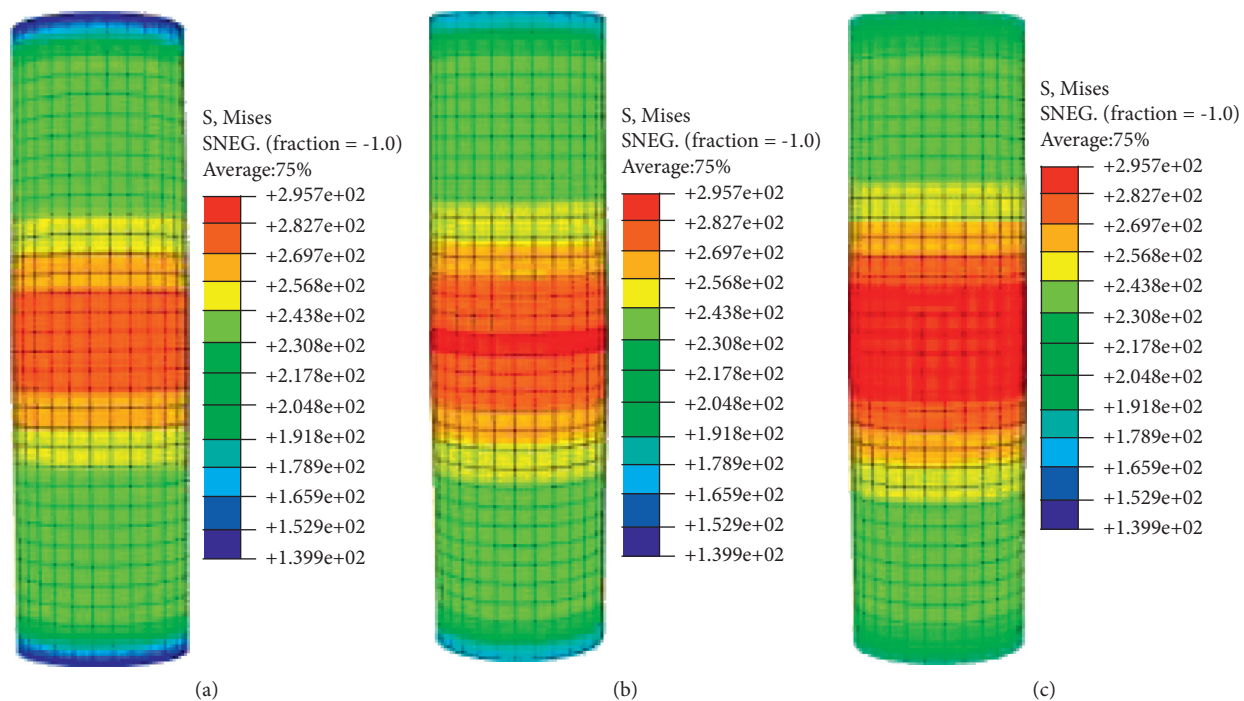


FIGURE 12: Strain cloud picture (MPa). (a) RC2-1. (b) RC2-2. (c) RC2-3.

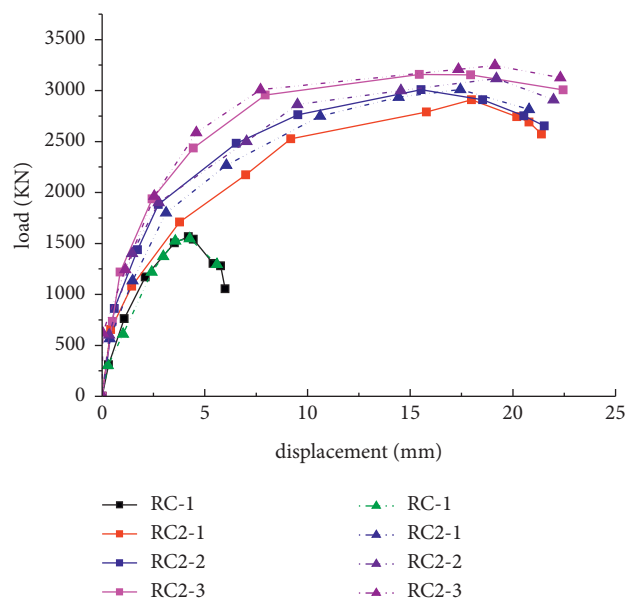


FIGURE 13: Load-displacement curve.

strength design value, MPa; and A_s is the longitudinal section area, mm^2 .

Based on the derivation of Si Jianhui's calculation formula for the bearing capacity of reinforced members, it can be seen from Figure 5 that there are 10 mm left at the upper and lower ends of the concrete column without the constraint of steel plate. Therefore, the steel casing does not provide axial bearing capacity, but only provides one circumferential constraint force for the concrete column in this experiment. It can be seen that the increase in the bearing

capacity of concrete columns strengthened with prestressed steel casing is mainly caused by the increase in the bearing capacity of concrete after being constrained [30, 34–36]. Due to the different prestress value, the ultimate compressive strain of confined concrete is different, and the strain of the steel bar is also different, so it is necessary to set up a composite reinforcement improvement coefficient. Since the specimens used in the test are all not under pressure before the test, the damage coefficient A can be taken as 1. Then calculation formula of the bearing capacity of concrete

TABLE 3: Comparison of experimental and calculated values.

Number	N_{EXP} (kN)					Average	N_{FEM} (kN)	N_c (kN)	
	1	2	3	4	5			Formula (7)	Error (%)
RC-1	1471.50	1553.30	1548.53	1612.32	1526.23	1542.38	1548.53	1419.67	8
RC-2-1	2654.89	2910.25	2967.48	2938.08	2781.00	2850.34	3010.25	2833.62	0.6
RC-2-2	3017.00	3008.29	3026.02	3110.64	3125.31	3057.45	3118.29	2921.90	4.4
RC-2-3	3133.54	3146.81	3046.87	3237.70	3304.70	3173.92	3246.81	3083.75	2.8

Note. N_{EXP} is the test bearing capacity. N_{FEM} is the bearing capacity of finite element analysis. N_c is the calculated bearing capacity.

columns strengthened with prestressed steel casing can be simplified as follows:

$$N_u = b f_c A_c + f_y' A_s', \quad (7)$$

where b is the prestress increase coefficient, which is obtained by fitting from the relationship between prestress f and bearing capacity of steel casing by Origin software, $b = 0.005f + 3.40$.

The calculated results of formula (7) are compared with the experimental data and summarized in Table 3. It can be seen from Table 3 that the calculation results of formula (7) are in good agreement with the measured values.

5. Conclusions

In this article, the prestressed steel casing reinforcement method was proposed. Through the axial compression test and numerical simulation of 20 columns, the following preliminary conclusions can be drawn:

- (1) Compared with the original column, the ultimate bearing capacity of reinforced concrete columns strengthened with prestressed steel casing is increased by 72.1%–109.9%, and the ductility is also greatly improved.
- (2) The calculation formula of the axial compression bearing capacity of reinforced concrete columns strengthened with prestressed steel casing provided in this article has good applicability. Compared with the experimental values, the theoretical calculation formula has sufficient accuracy.
- (3) The reinforcement effect of the prestressed steel casing reinforcement method is obvious, which is suitable for rapid repair and reinforcement of concrete columns that need to greatly improve the bearing capacity in a short time.
- (4) ABAQUS software was used to model and analyze the test process. The results show that the finite element results are in good agreement with the test results. The comparative analysis results of models under different prestress levels show that when the prestress of steel casing is 0 N/mm^2 , 24.68 N/mm^2 , and 67.90 N/mm^2 , the simulated bearing capacity increases by 94%, 101%, and 110%, respectively.

Data Availability

All data used to support the study are included within the article.

References

- [1] Z. Ren, X. Zeng, and J. Sun, "Using two-way prestressed semicircular steel plate for construction of reinforced concrete cylinder column," *Complexity*, vol. 2018, Article ID 1481837, 10 pages, 2018.
- [2] Y. Tang, W. Feng, Z. Chen, Y. Nong, S. Guan, and J. Sun, "Fracture behavior of a sustainable material: recycled concrete with waste crumb rubber subjected to elevated temperatures," *Journal of Cleaner Production*, vol. 318, Article ID 128553, 2021.
- [3] Z. Ren, X. Zeng, J. Sun, and J. Wang, "Fracture properties of wide-notch concrete beams strengthened with near-surface mounted CFRP rebar," *KSCE Journal of Civil Engineering*, vol. 23, no. 11, pp. 4735–4746, 2019.

- [4] B. Zhou, M. Zhang, L. Wang, and G. Ma, "Experimental study on mechanical property and microstructure of cement mortar reinforced with elaborately recycled GFRP fiber," *Cement and Concrete Composites*, vol. 117, Article ID 103908, 2021.
- [5] X. Tan, Z. Hu, C. Chen, and M. Zhao, "3D DEM-FDM coupled analysis of the behavior of an isolated geogrid-encased stone column under axial loading," *Journal of Geotechnical and Geoenvironmental Engineering*, vol. 147, no. 6, Article ID 04021028, 2021.
- [6] L. Hu and P. Feng, "Prestressed CFRP-reinforced steel columns under axial and eccentric compression," *Composite Structures*, vol. 268, Article ID 113940, 2021.
- [7] L. Hu, P. Feng, and X. L. Zhao, "Fatigue design of CFRP strengthened steel members," *Thin-Walled Structures*, vol. 119, pp. 482–498, 2017.
- [8] J. Zhang, Y. Sun, G. Li, Y. Wang, J. Sun, and J. Li, "Machine-learning-assisted shear strength prediction of reinforced concrete beams with and without stirrups," *Engineering with Computers*, vol. 36, pp. 1–15, 2020.
- [9] W. Yayong, "Fire Resistance Test of RC Beam Retrofitted with Cover of High Strength Steel Mesh and Polymetric Motar," *Building Structure*, vol. 37, no. 1, pp. 112–113, 2007.
- [10] Y. Sun, G. Li, and J. Zhang, "Developing hybrid machine learning models for estimating the unconfined compressive strength of jet grouting composite: a comparative study," *Applied Sciences*, vol. 10, no. 5, 2020.
- [11] W. Ge, W. Song, A. F. Ashour, W. Lu, and D. Cao, "Flexural performance of FRP/steel hybrid reinforced engineered cementitious composite beams," *Journal of Building Engineering*, vol. 31, Article ID 101329, 2020.
- [12] Y. Sun, G. Li, and J. Zhang, "Investigation on jet grouting support strategy for controlling time-dependent deformation in the roadway," *Energy Science & Engineering*, vol. 8, no. 6, pp. 2151–2158, 2020.
- [13] Y. Sun, R. Bi, Q. Chang et al., "Stability analysis of roadway groups under multi-mining disturbances," *Applied Sciences*, vol. 11, no. 17, 2021.
- [14] Y. Yong, L. Hui, and C. Wei, "Experimental study on seismic behavior of reinforced concrete frame structure retrofitted by prestressed steel strips," *Engineering Mechanics*, vol. 34, no. 10, pp. 53–60, 2017.
- [15] Y. Sun, L. Guichen, Z. Junfei, S. Junbo, and X. Jiahui, "Development of an ensemble intelligent model for assessing the strength of cemented paste backfill," *Advances in Civil Engineering*, vol. 2020, Article ID 1643529, 6 pages, 2020.
- [16] C. X. C. C. Yun-peng, "On reliable analysis of section-enlarging reinforcing method in strengthening frame structure," *Shanxi Architecture*, vol. 2, 2010.
- [17] J. Sun, Y. Huang, F. Aslani, and G. Ma, "Electromagnetic wave absorbing performance of 3D printed wave-shape copper solid cementitious element," *Cement and Concrete Composites*, vol. 114, Article ID 103789, 2020.
- [18] C. J. X. Jin, "Ultimate strength of reinforced concrete columns strengthened by circular steel jacketing," *Journal of South China University of Technology*, vol. 35, no. 10, pp. 78–83, 2007.
- [19] Y. Sun, G. Li, J. Zhang, J. Sun, J. Huang, and R. Taherdangkoo, "New insights of grouting in coal mass: from small-scale experiments to microstructures," *Sustainability*, vol. 13, no. 16, 2021.
- [20] L. Hu, Y. Wang, P. Feng, H. Wang, and H. Qiang, "Debonding development in cracked steel plates strengthened by CFRP laminates under fatigue loading: experimental and boundary element method analysis," *Thin-Walled Structures*, vol. 166, Article ID 108038, 2021.
- [21] L. L. Hu, X. L. Zhao, and P. Feng, "Fatigue behavior of cracked high-strength steel plates strengthened by CFRP sheets," *Journal of Composites for Construction*, vol. 20, no. 6, Article ID 04016043, 2016.
- [22] G. Ma, J. Sun, F. Aslani, Y. Huang, and F. Jiao, "Review on electromagnetic wave absorbing capacity improvement of cementitious material," *Construction and Building Materials*, vol. 262, Article ID 120907, 2020.
- [23] J. Sun, Y. Huang, F. Aslani, X. Wang, and G. Ma, "Mechanical enhancement for EMW-absorbing cementitious material using 3D concrete printing," *Journal of Building Engineering*, vol. 41, Article ID 102763, 2021.
- [24] J. Sun, "Fresh and mechanical behaviour of developed fibre-reinforced lightweight engineered cementitious composites for 3D concrete printing containing hollow glass microspheres," *Ceramics International*, vol. 47, no. 19, pp. 27107–27121, 2021.
- [25] *Standard for Test Method of Mechanical Properties on Ordinary concrete*, Ministry of Construction of the People's Republic of China, Beijing, China, 2002.
- [26] W. Ge, Y. Wang, A. Ashour, W. Lu, and D. Cao, "Flexural performance of concrete beams reinforced with steel-FRP composite bars," *Archives of Civil and Mechanical Engineering*, vol. 20, pp. 1–17, 2020.
- [27] W. Ge, K. Chen, Z. Guan, A. Ashour, W. Lu, and D. Cao, "Eccentric compression behaviour of concrete columns reinforced with steel-FRP composite bars," *Engineering Structures*, vol. 238, Article ID 112240, 2021.
- [28] J. Sun, F. Aslani, J. Wei, and X. Wang, "Electromagnetic absorption of copper fiber oriented composite using 3D printing," *Construction and Building Materials*, vol. 300, Article ID 124026, 2021.
- [29] "Standard test methods for concrete structures," 2012.
- [30] J. Li, Q. Qin, J. Sun, Y. Ma, and L. Qia, "Mechanical and conductive performance of electrically conductive cementitious composite using graphite, steel slag, and ggbs," *Structural Concrete*, Wiley, NJ, USA, 2020.
- [31] J. Sun, Y. Wang, S. Liu et al., "Mechanical, chemical and hydrothermal activation for waste glass reinforced cement," *Construction and Building Materials*, vol. 301, Article ID 124361, 2021.
- [32] W. Liu, *Research on Mechanism of concrete-filled Steel Tubes Subjected to Local Compression*, pp. 64–65, Fuzhou University, Fuzhou, China, 2005.
- [33] J. Si, L. Wu, and W. Guo, "Axial compression of reinforced concrete columns strengthened by composite of prestressed plastic-steel strip and angle steel: an experimental study," *Structural Concrete*, Wiley, NJ, USA, 2021.
- [34] W. Ma, X. Wang, J. Wang, J. Sun, and X. Xiang, "Generative design in building information modelling (BIM): approaches and requirements," *Sensors*, vol. 21, no. 16, 2021.
- [35] J. Sun, Y. Wang, X. Yao et al., "Machine-Learning-Aided prediction of flexural strength and ASR expansion for waste glass cementitious composite," *Applied Sciences*, vol. 11, no. 15, p. 6686, 2021.
- [36] J. Sun, Y. Ma, J. Li, J. Zhang, Z. Ren, and X. Wang, "Machine learning-aided design and prediction of cementitious composites containing graphite and slag powder," *Journal of Building Engineering*, vol. 43, Article ID 102544, 2021.

Alternative Load Path Analysis for Assessing the Geometric Agreement of a Cable-Stayed Bridge with Steel Truss Girders

Sharadhananda Ghadei, *Department of Civil Engineering, Aryan Institute of Engineering & Technology, Bhubaneswar, sharadhananda@outlook.com*

Swarup Sahoo, *Department of Civil Engineering, Capital Engineering College, Bhubaneswar, swarupsahoo26@outlook.com*

Ajaya Kumar Beura, *Department of Mechanical Engineering, Aryan Institute of Engineering & Technology, Bhubaneswar, akbeura25@gmail.com*

Saswati Nayak, *Department of Mechanical Engineering, Capital Engineering College, Bhubaneswar, saswatinayak2574@gmail.com*

ABSTRACT

The geometric agreement, also known as load-transferring routes within bridge structures, is critical to the mechanical performance of bridge structures, such as capacity, deformation, and collapse behaviour. The collapse behaviour of a double-pylon cable-stayed bridge with steel truss girders subjected to excessive vehicle loading is investigated using a methodology based on different load routes. A series-parallel load-bearing arrangement simplifies the cable-stayed bridge with steel truss girders. In diverse load-structure conditions, this research shows that enforced vehicle loading can be moved to alternative routes of cable-stayed bridges. To investigate the collapse route of a cable-stayed bridge with steel truss girders, a 3-D finite element model is created using the computer software ANSYS, taking into consideration chord failure, cable loss, and corrosion in steel truss girders. The findings demonstrate that chord failures in the main span's middle section cause brittle damage to truss girders or potentially bridge collapse. Furthermore, ductile degradation occurs when long cables are lost.

1. Introduction

Bridge structural collapse is characterized with collapse of an entire structure or a disproportionate portion in structure resulting from initial local failure in an individual member. The failures of critical members in bridge structures typically occur due to overloading. Cable-stayed bridges with steel truss girders are widely applied for bridge constructions spanning rivers and valleys. The truss girders can provide sufficient and harmonious space for vehicles and trains individually due to double-layer driving, and also the cables can supply adequate tension on truss girders to maximize the bridge span, as shown in Figure 1. Unfortunately, some of these bridges have collapsed commonly originated from damage produced by heavy live loads. For example, the chords and joints can be damaged by fatigue, such as the I-35W Highway Bridge over the Mississippi River in Minneapolis, which collapsed suddenly, resulting in

the death of 13 and injury to 145 people, as shown in Figure 2 [1]. Similarly, the sudden failure of a single rod led to the fracture of several other rods, causing the collapse of the Silver Bridge over the Ohio River between Ohio and West Virginia, resulting in the death of 46 people.

Bridge systems are vulnerable to collapse under extremely heavy loads due to the complicated connections of components and low robustness. Existing assessment approaches fall into three categories: the deterministic method, the probability and reliability method, and the risk-based approach [2].

The deterministic method assesses structural safety in terms of displacement under loads, structural capacity, and energy and component sensitivity. Pandey and Barai proposed the structural response sensitivity to measure redundancy for continuum and discrete structures and assess structural damage [3]. Nafday proposed the minimum difference between the stiffness matrix and singular matrices and the correlation between the stiffness matrix and column vector as



FIGURE 1: Yu Men Kou Huanghe River Bridge.

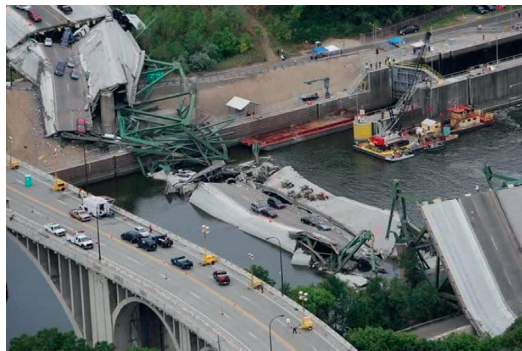


FIGURE 2: Collapse of the I-35W Highway Bridge.

safety indices for discrete structures. In addition, methods for determining the key structural components and the failure path were also proposed [4]. Hunley and Harik investigated the redundancy of double-steel box curved beam bridges, considering the effects of the span, continuity, curvature, damage location of the beam, external supports, and girder spacing on bridge failure. The study indicated that additional criteria to those in the American Association of State Highway and Transportation Officials (AASHTO) Load and Resistance Factor Design (LRFD) code were required to ensure the redundancy of the double-steel box curved beam bridge system [5]. NCHRP 406 is a study of the collapse resistance of various structural systems [6]. A system factor table was developed for common-type bridges, including simple and continuous bridges with multiple girders, and step-by-step calculations are provided to assess the redundancy of bridges with complex structures. The collapse behavior of long-span bridges was analyzed using experiments and numerical simulations [7–11]. In the literature [7], the collapse behavior of a suspension bridge and cable-stayed bridge due to sudden cable loss was investigated. A dynamic amplification factor (DAF) of 2.0 was required to meet the safety requirements of the cable design; the cable-stayed bridge did not survive the sudden loss of more than two cables. The bending moments enforced on the cross sections of bridge girders were computed to determine the importance in ultimate limit state of failure at a stay location in cable-stayed bridge. The average DAF values of the undamped and damped movements were 3.35 and 2.52, respectively, for the positive bending moments [8]. The average DAF values of the axial stress in the pylon cross-sections and the stays of a

cable-stayed bridge were smaller than 2.0 and 1.68 for the undamped movement and 1.47 for 2% of the critical damping, respectively [9]. A model describing large displacement effects and internal damage and time-dependent damage functions were established to describe the constitutive relationships. The results showed that the sudden failure of cables resulted in DAF values of 2.5–3.5 for vertical displacement, 5.5–8.5 for the bending moment, and 1.3–2.8 for torsional rotation in the midspan [10]. The cable system of a hybrid cable-stayed/suspension (HCS) bridge can redistribute the additional stresses produced by internal damage of the bridge components [11].

Four reliability indices were developed for the four limit states of a bridge under heavy static loads, namely, member failure, ultimate limit state, functionality limit state, and damage limit state. The differences in the reliability indices of the member failure in the latter three limit states are the structural redundancies, as demonstrated with a standard TS-20 truck load. Consequently, several approaches based on reliability have been developed to assess structural redundancy and failure probability due to insufficient capacity and overload [12–16]. In [12, 13], the geometric configuration and safety of a truss bridge system were analyzed using system reliability, considering the uncertainties of the critical members and future loads. It was shown that the system safety, which influences public security and national defense, depended on the number of girders, the girder spacing, and the presence of diaphragms. The target reliability index was calculated by considering the expected life of the structure, importance of individual members, design experience, and material costs. This index was used to determine the members' strength and applicability and prevent fatigue damage [14]. The redundancy concept has been applied to many types of infrastructures. The target reliability index provides a good balance between safety and costs in infrastructure networks [15, 16].

Many significant results have been obtained from studies focusing on redundancy and collapse of structures. However, it is necessary to extend the current methodologies to long-span bridges. The simplified deterministic approach for assessing the collapse behavior of suspension bridges has been extended to complex bridge systems, such as arch bridges and cable-stayed bridges. In this study, the deformation and cable force of a double-pylon cable-stayed bridge with steel truss girders are considered using a series-parallel load-bearing system to investigate the transfer of the absorbed loads to alternative paths in different scenarios. The collapse behavior of the bridge is analyzed using increasing traffic loads to determine the optimal structural system. It is shown that the series-parallel load-bearing system of the structural members affects the mechanical behavior of the cable-stayed bridge system.

2. Selection and Description of Cable-Stayed Bridge

The cable-stayed bridge has a total length of 700 m, with 360 m between the two pylons and 170 m on each side of the pylons, as shown in Figure 3. The main beam consists of 2 truss girders with a height of 6 m and spacing of 26 m. The chords have box sections, and the vertical and diagonal bars have H-shaped sections; 104 steel-wire cables are anchored

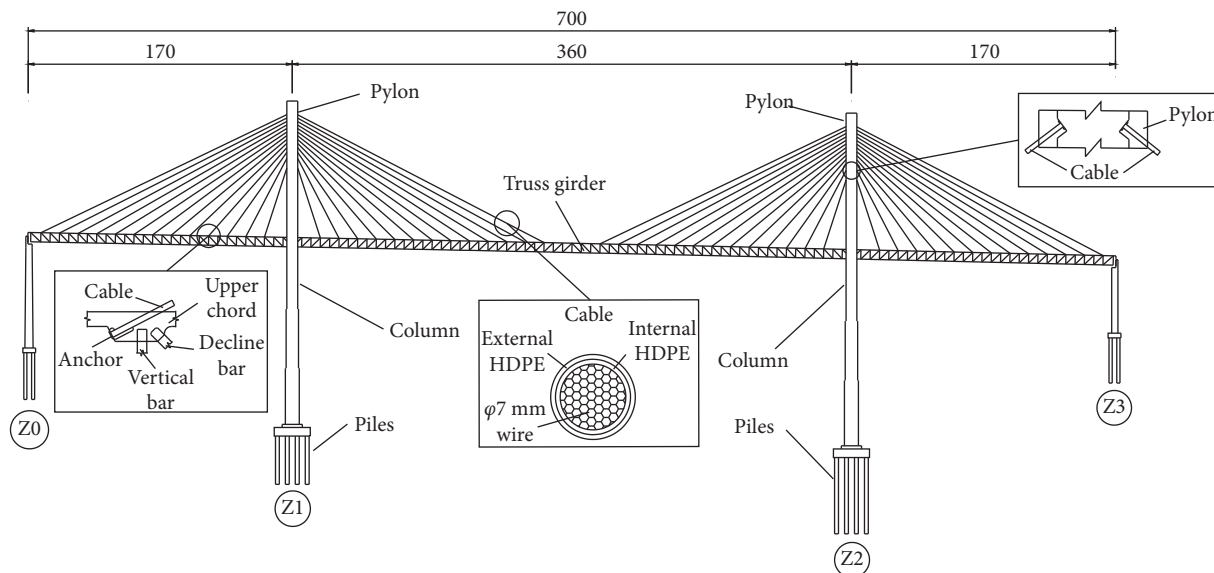


FIGURE 3: Double-pylon cable-stayed bridge with steel truss girders (Units: m).

in the truss girder and the pylons. Each pylon consists of 3 parts, with lengths of 133.5 m, 38 m, and 38 m or 44 m. The material properties are listed in Table 1.

3. Numerical Model

The alternative load paths of the bridge during the failure of individual members are investigated to study the collapse behavior of the cable-stayed bridge. A numerical model is established to simulate the performance of the bridge under vehicle loads in different cases and is verified by an experiment using live loads.

3.1. Analysis Details. Without alternative load paths, a bridge can collapse entirely or partially under a load. If a cable-stayed bridge consisting of a steel truss girder and cables collapses entirely when the girder fails, the girder lacks alternative load paths, as depicted in Figure 4(a). In contrast, the bridge does not collapse when one cable fails if the adjacent cables act as alternative load paths and bear the absorbed load from the failed cable, as shown in Figure 4(b). For the analysis of the structural load paths, the cable-stayed bridge can be simplified as a conceptual model that includes series and parallel systems, as shown in Figure 5. The girder segments, which lack alternative load paths, comprise the series system, whereas the cables with many alternative load paths form the parallel system.

The conceptual collapse model of the series-parallel system depicts the configuration of the alternative load paths in the cable-stayed bridge. These load paths significantly affect the collapse behavior. The loss of chords in the truss girder and the failure of cables correspond to the series and parallel systems, respectively. The truss girder segments of the two trusses are illustrated in Figure 5. Each truss section with upper and lower chords and bars provides limited alternative load paths, indicating that the failures of the

upper and lower chords would significantly decrease the capacity of a truss section. If the chords fail, the limit alternative load paths in the truss girder represent the series system. Thus, if a small deformation occurs before the collapse, the cable-stayed bridge is prone to global collapse, indicating an insufficient number of alternative load paths to absorb the loads from the lost chords. In contrast, the cables represent a parallel system, providing a sufficient number of alternative load paths, which is reflected by changes in the forces in the adjacent cables in the damage model of the cable loss scenario. A change in the cable forces and the large deformation before total collapse indicate that the loading of the failed cables is absorbed by the other cables.

The series and parallel system model is used to assess the collapse behavior of the bridge. A three-dimensional finite element model (3D FEM) is established to simulate the bridge under different load scenarios and is verified using a live load experiment. The mechanical behavior of the bridge (force and deformation) after the removal of individual members and the corrosion of the truss girder is investigated. In addition, the damaged bridge after the removal of chords and cables is thoroughly analyzed to investigate its capacity and collapse behavior. The mechanical behavior is assessed with the series-parallel structural system to determine alternative load paths. The flowchart of the analysis is shown in Figure 6.

3.2. Numerical Discretization. The 3D FEM is established in the ANSYS software to study the structural collapse behavior. The pylons and truss girder are discretized using BEAM189 elements, and the cables are modeled with LINK180 elements. MPC184 rigid link/beam elements are used to connect the cables and pylons. BEAM189 has three nodes with six degrees of freedom at each node, i.e., three translations in the nodal x -, y -, and z -directions and three rotations around the x -, y -, and z -axes [17]. The beam element is based on the Timoshenko beam theory, which

TABLE 1: Material properties of the cable-stayed bridge.

Members	Material	Modulus of elasticity (MPa)	Sectional area (m ²)
Pylon	Concrete ($f_{cu} \cdot k = 32$ MPa)	3.45×10^4	16.04~27.0
Deck	Concrete ($f_{cu} \cdot k = 26$ MPa)	3.25×10^4	4.70
Truss girder	Steel ($\sigma_s = 370$ MPa)	2.06×10^5	0.10
Horizontal and lateral bars	Steel ($\sigma_s = 345$ MPa)	2.06×10^5	0.27×10^{-1}
Cables (per)	$\phi 7$ mm wire ($f_{pk} = 1670$ MPa)	1.95×10^5	$(0.53 \sim 1.34) \times 10^{-2}$

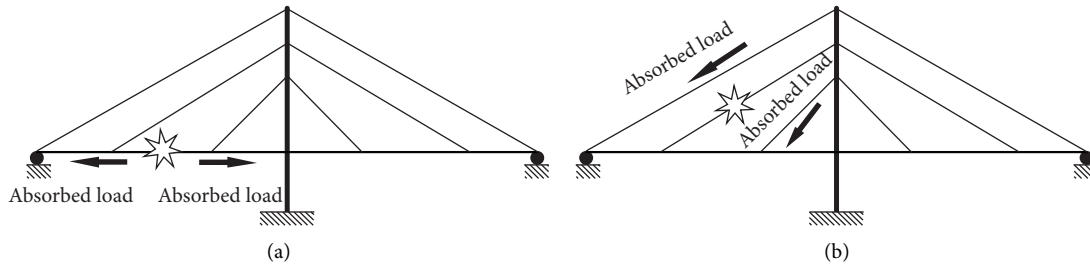


FIGURE 4: Failures of individual members of the cable-stayed bridge: (a) load transfer after girder failure; (b) load transfer after cable failure.

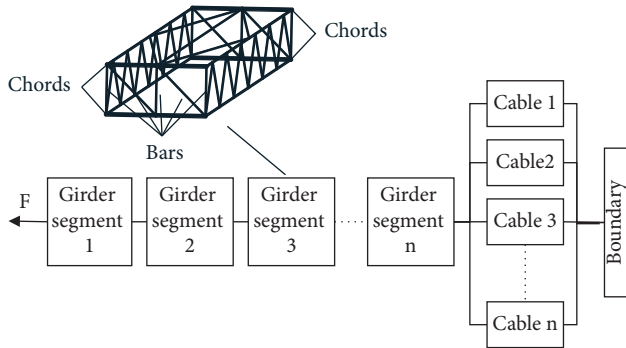


FIGURE 5: Series and parallel system of the cable-stayed bridge.

includes shear deformation effects; thus, it is suitable for analyzing 3D slender to moderately stubby/thick beam structures. LINK 180 has two nodes with three degrees of freedom per node, i.e., translations in the nodal x -, y -, and z -directions [18]. This element does not bend or rotate, making it suitable for modeling 3D cables, links, and springs. The MPC184 rigid link/beam has two nodes with six degrees of freedom at each node, i.e., three translations in the nodal x -, y -, and z -directions and three rotations around the x -, y -, and z -axes.

This element models a rigid constraint or a rigid component. The material stiffness properties are not required; thus, it can be used to simulate a rigid constraint between two deformable bodies or a rigid component that transmits forces and moments. To simplify the supports on the pylons, the translations of the nodes of the tie beam of the pylons and the nearby nodes of the truss girder are coupled in the nodal x - and z -directions. The ends of the pylons are constrained in all degrees of freedom, i.e., three translations in the nodal x -, y -, and z -directions and three rotations around the x -, y -, and z -axes. The supports at the ends of the truss girder are simulated by constraining some degrees of freedom, i.e., translations in the nodal z -direction and x -direction with an allowance of ± 500 mm.

The node-to-node interactions are modeled to discretize the structural model and account for the common action of the cable-stayed bridge [19]. Nodes are shared between the beam elements of the truss girder and the link elements of the cables, between the link elements of the cables and the rigid link/beam elements of the rigid connections, and between the beam elements of the pylons and the rigid link/beam elements of the rigid connections [20]. The 3D structural model, the mesh, and the constraints for the structural analysis are shown in Figure 7.

Inelastic material properties are adopted in the FEM for the structural collapse analysis under extremely heavy vehicle loading. The cables and truss girder have ideal elastic-plastic properties with yield strengths of 1670 MPa and 370 MPa, respectively (Table 2). All the failures of the chords and bars of the steel truss girder subjected to considerable compression are considered in the analysis since they may lead to bridge collapse. As the static load increases, the data on the member failure and the changes in the forces are recorded until the analysis is terminated when the bridge collapses.

3.3. Calibration of Numerical Model. The selected bridge is subjected to a live load test to calibrate the 3D FEM of the cable-stayed bridge (Figure 8). Thirty-two strain gauges are attached to the upper and lower chords to determine the mechanical performance of the truss girder, and the bridge is subjected to a standard truck load (Figure 9). The strain gauges are connected to a wired data acquisition system to collect the data.

According to the influence line of the cable-stayed bridge, three load cases are designed to obtain the critical bending moments in the side and main spans. Three-axle dump trucks with a combined axial weight of 300 kN are used to apply the loading. The axle weights of the trucks are 60 kN for the front axle and 120 kN for each of the two rear axles, and the axial spacing is 3.5 m at the front and 1.35 m at

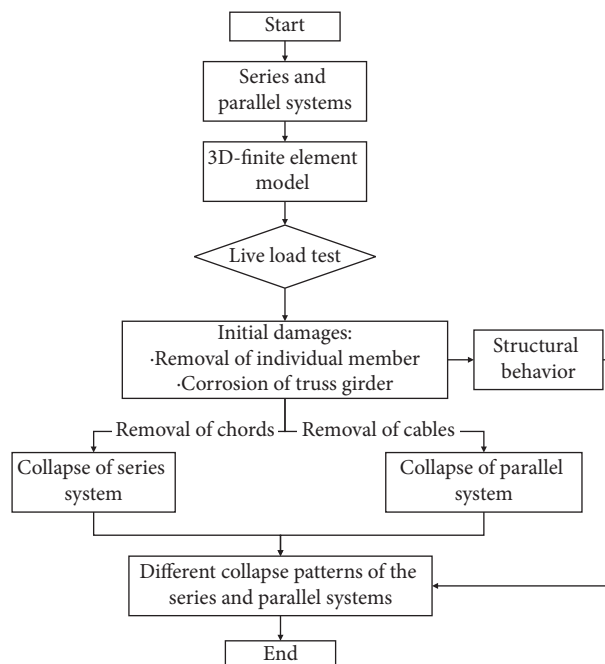


FIGURE 6: Flowchart of the collapse analysis of the cable-stayed bridge.

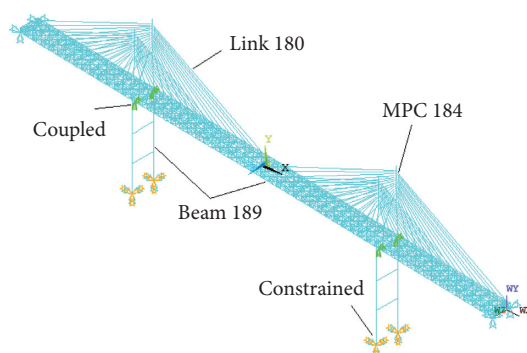


FIGURE 7: Finite element model of the cable-stayed bridge.

TABLE 2: Strain of the chords for the three load cases.

Load case	Section	Strain gauge location	Strain ($\mu\epsilon$)		Ratio
			Measured	FE model result	
1	I-I	Upper chord	-134	-150	0.89
		Lower chord	159	165	0.96
2	II-II	Upper chord	-87	-90	0.97
		Lower chord	75	79	0.95
3	III-III	Upper chord	-228	-231	0.99
		Lower chord	190	204	0.93

the back, as shown in Figure 9. Figures 9 and 10 show the location of applying the truck load in a cross-sectional and longitudinal view and the locations of the deflection points. The data are used to obtain the vertical deformation of the truss girder.

Table 2 shows the three load cases, the strain gauge locations, the measured strain, and the strain obtained from the FEM. Similarly, the vertical displacement values

obtained from the measurements and the FEM for the three load cases are listed in Table 3.

The ratios of the measured strain and vertical displacement to the FEM model results in Tables 2 and 3 range from 0.89 to 0.99 for the three load cases, indicating a good agreement between the measured and modeled results. Therefore, the FEM accurately simulates the behavior of the cable-stayed bridge with steel truss girders subjected to heavy truck loading.



FIGURE 8: Live load test.

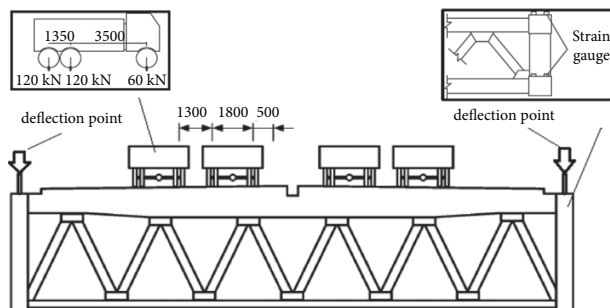


FIGURE 9: Cross-sectional view and load paths (units: mm).

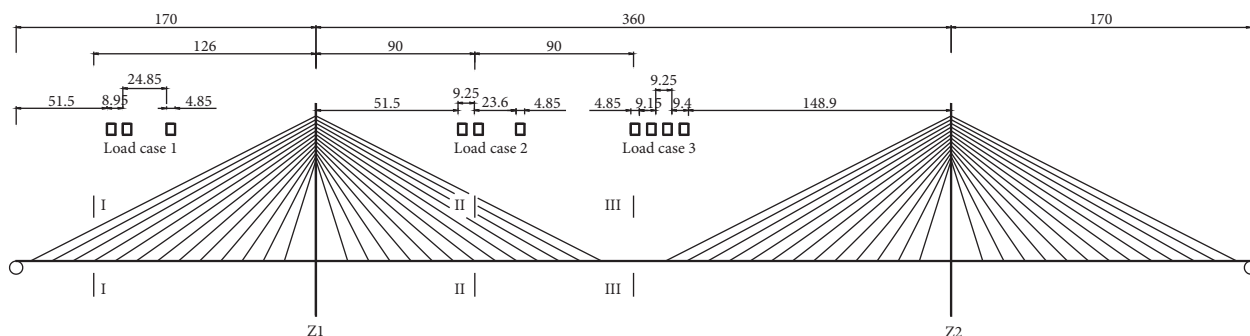


FIGURE 10: Longitudinal view and load paths (units: m).

TABLE 3: Vertical displacement of sections for the three load cases.

Load case	Section	Vertical displacement (mm)		Ratio
		Measured	FE model result	
1	I-I	87	92	0.95
2	II-II	101	104	0.97
3	III-III	214	221	0.97

3.4. Analysis Procedure. The instability of the truss girder and the failure of the cables can result in the collapse of the cable-stayed bridge subjected to high vertical loading. Steel corrosion can significantly change the material properties, such as the elastic modulus and yield strength, potentially causing failure of the members or bridge collapse. We analyzed the ultimate capacity of the bridge by removing individual members. Without alternative load paths, the cable-

stayed bridge collapses, resulting in the automatic termination of the analysis in the software. The effect of corrosion of the truss girder on the mechanical behavior of the bridge is assessed by changing the cable forces and the deformation level of the truss girder. The removed members and the corroded sections of the cable-stayed bridge are depicted in Figure 11.

According to the influence line of the members of the bridge, it is assumed that chords A8-A9, A29-A30, A44-A45, and A59-A58' and cables S9, M8, and M13 failed. According to the Technical Standards for Highway Engineering (JTG B01-2014), the Highway-I lane loading is combined with a concentrated force of 360 kN and a uniformly distributed load of 10.5 kN/m. The loading types and placements causing bridge collapse are shown in Figure 12 and Table 4.

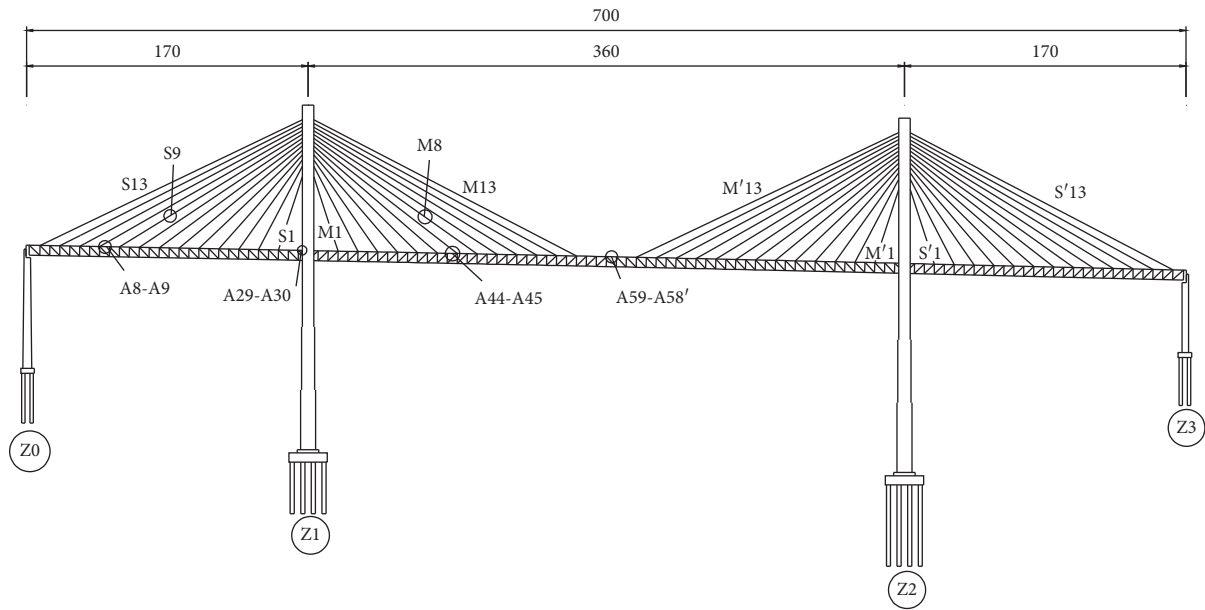


FIGURE 11: Failed members and corroded bridge sections (units: m).

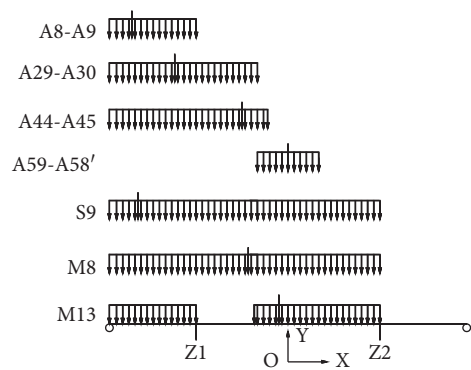


FIGURE 12: Loading location for the loading scenarios.

TABLE 4: Load types and placement for different loading scenarios.

Failed members	Loading location	
	Uniform load	Concentrated load
A8-A9	Entire side span	-306 m
A29-A30	-350 m to -60 m	-218 m
A44-A45	-350 m to -40 m	-90 m
A59-A58'	-60 m to 60 m	0 m
S9	Side span and main span	-294 m
M8	Side span and main span	-78 m
M13	-66 m to 180 m and side span	-18 m

4. Results and Discussion

Two load scenarios, the removal of individual chords and cables, and corrosion of the truss girder sections are considered to conduct an in-depth analysis of the response of the collapsing cable-stayed bridge. The relationship between the load and displacement and the collapse patterns are investigated.

4.1. Damage to the Cable-Stayed Bridge. The failures of the chords A8-A9, A29-A30, A44-A45, and A59-A58' and the cables S9, M7, and M13 change the internal forces of the truss girder and cables, as depicted in Figures 13 and 14. Compared to the intact bridge, the forces of cables S6, S7, S8, S9, and S10 increase by 0.3% to 4.4%, while the forces of cables S1 to S5 and S11 to S13 decrease by 0.3%–1.7%. The loss of chords A29-A30 reduces the force of cables M1 and

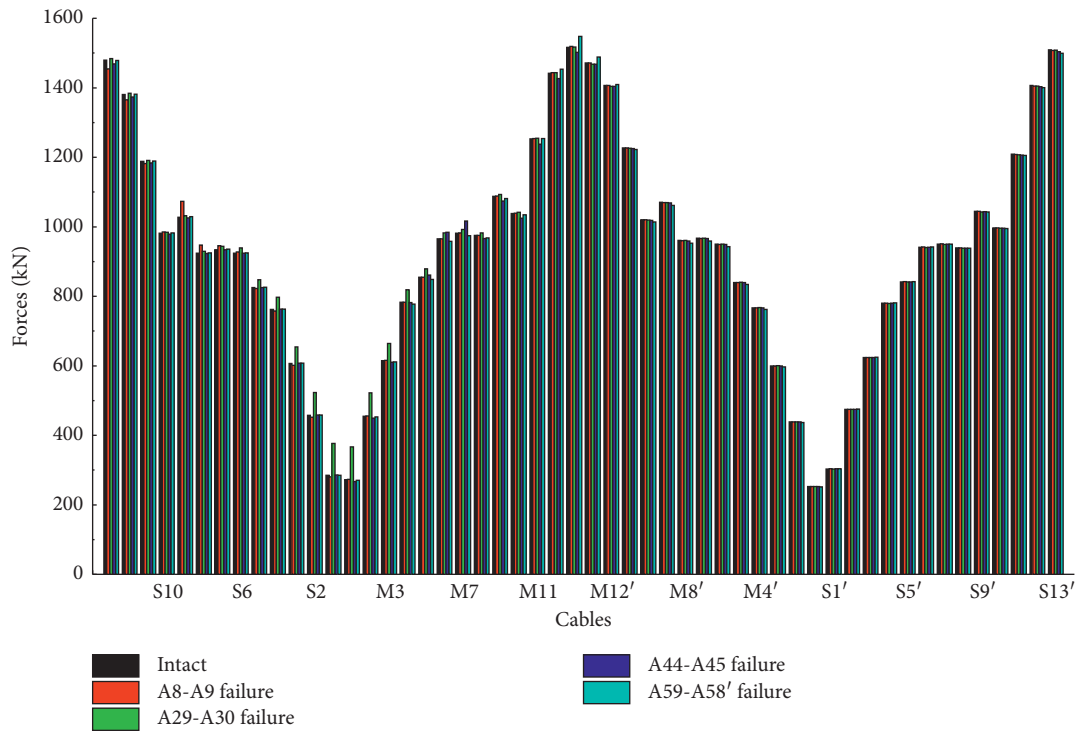


FIGURE 13: The cable forces in the chord loss scenarios.

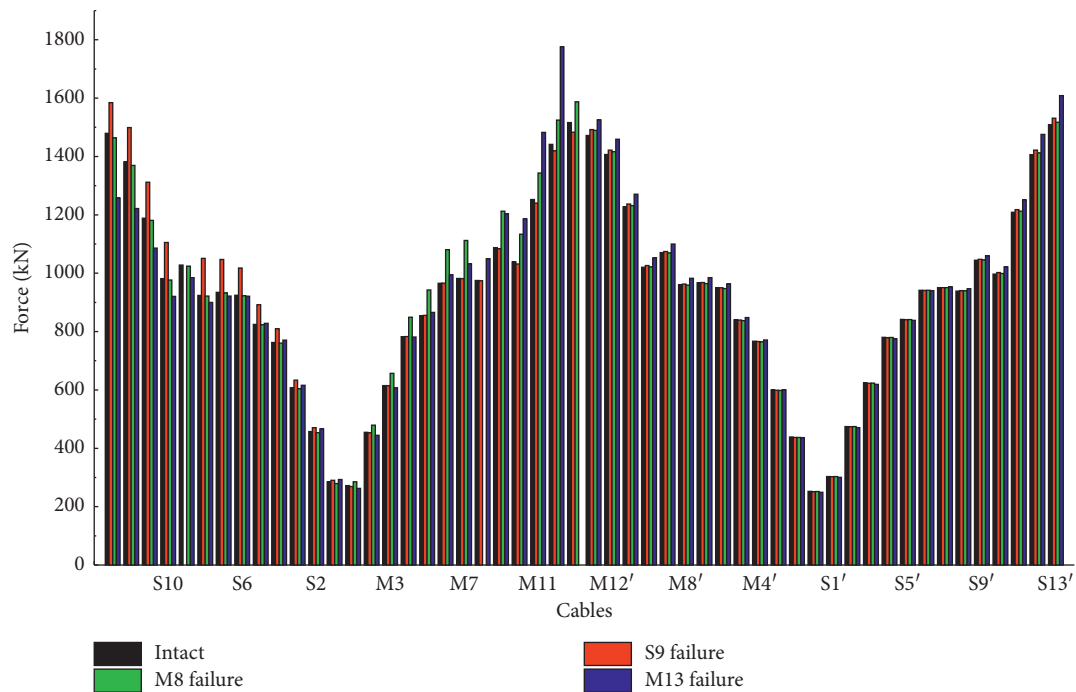


FIGURE 14: The cable forces in the cable loss scenario.

S1 anchored in the girder of the side span by a maximum of 34.7% and 32.1%, respectively, and the proportion increases toward the pylon. In contrast, the failures of chords A29-A30 or A59-A58' do not significantly increase the cable forces (a maximum increase of 3.5%). Since the truss girder is a series bearing system with a lack of alternative load paths, the

absorbed load is not transferred to the cables, resulting in small changes in the cable forces.

In the cable S9 loss scenario, the increase in the axial force of the cables in the side span ranges from 1.9% to 13.8%, and the force of the other cables changes only slightly. The failure of cable M8 results in an increase in the cable

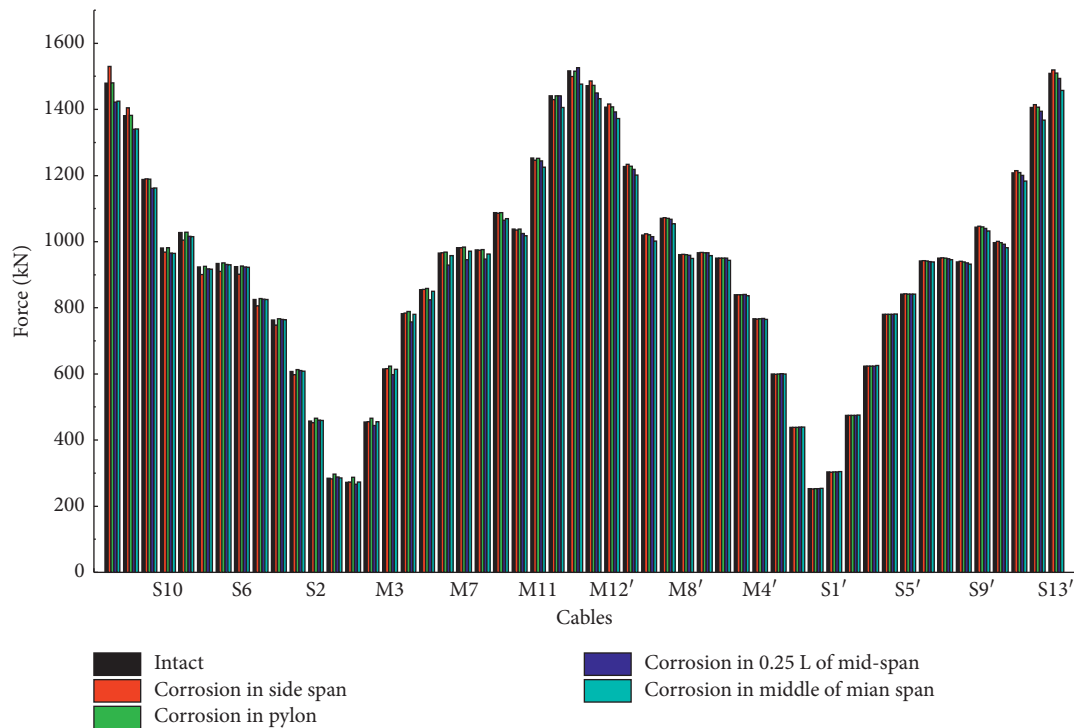


FIGURE 15: The cable forces in the corroded truss girder scenario.

force ranging from 4.7% to 13.3%. The decrease in the axial force of cables S6 to S13, M1 to M4, and M2' to S6' is a minimum of 15% in the cable S13 loss scenario, while the increase in the axial forces of cables S5 to S1, M5 to M3', and S7' to S13' ranges from 0.1% to 23.2%. Since the cables are a parallel bearing system with many alternative load paths, the absorbed load is transferred to the other cables, reflected in the changes in the cable forces.

The material properties can be changed by the corrosion of members, resulting in different properties for different corrosion rates. It is assumed that the corrosion rate equals 10% of the bars and chords in sections I, II, III, and IV of the truss girder (Figure 11). The calculated values of the elastic modulus and tensile strength of the materials are 146.26 GPa and 292.3 MPa, respectively. These values lead to the changes in the forces of the cables subjected to a dead load, as depicted in Figure 15.

Compared to the cable forces of the intact bridge, the forces in cables S5, S6, S7, S9, and S10 decrease from 2.2% to 2.6%, with a 3.4% increase in the force of cable 13 in section I corrosion scenario. Similarly, the force in cable M1 increases by 5.7% in section II corrosion scenario, while the corrosion in section III leads to a reduction in the forces of cables M1 to M10 and S9 to S13 of 2.0% to 3.7% and 1.1 to 3.9%, respectively. The forces of cables S13, M13, and S13 decrease by 3.7%, 2.7%, and 3.4%, respectively, in section IV corrosion scenario. In contrast, the corrosion of the girder has a negligible effect on its vertical displacement, with a maximum value of 14 mm (Figure 16). The truss girder, a series bearing system, does not transfer the absorbed load to the cables if the main beam is corroded due to an insufficient number of alternative paths.

4.2. Collapse Behavior. The loss of chords A8-A9, A29-A30, A44-A45, and A59-A58 causes a decrease in the ultimate capacity and ductility of the remaining structures. Figure 17 depicts the axial and vertical displacements of the girder of the remaining structures subjected to increasing traffic loading.

In the chord loss scenarios A8-A9, A29-A30, A44-A45, and A59-A58, the vertical displacement values of the degraded structures are much larger than the lateral values when the bridge is subjected to high traffic loading. The remaining structures exhibit significant deflection and collapse when chords A8-A9, A44-A45, and A59-A58 are lost. In the chord loss scenario A59-A58, the axial displacement of the girder increases rapidly, whereas the vertical displacement is very small. The degraded bridge can bear 12 times the design load, but its deflection, including the vertical and axial displacement, is very small. The collapse patterns of the bridges for different loading cases are depicted in Figure 18, and the maximum displacements and load factors are listed in Table 3. The brittle collapse of the damaged bridge occurs without deformation. Since the truss girder is a series bearing system, the load is transferred in limited paths to the truss girder after the individual chords fail.

The loss of cables S9, M8, and M13 leads to a decrease in the ultimate capacity and ductility of the remaining structures. Figure 19 depicts the axial and vertical displacements of the girder of the remaining structure subjected to increasing traffic loading. Under the critical loading, the remaining structure exhibits significant vertical displacement before it collapses, indicating insufficient ductility of the degraded bridge. The axial and vertical displacement values increase to

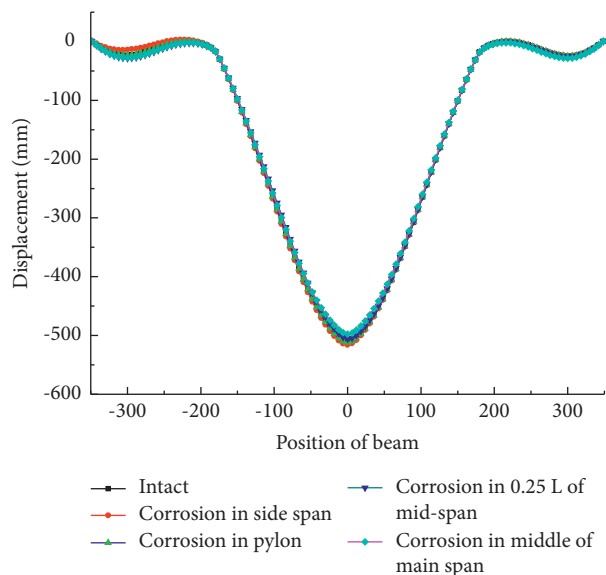


FIGURE 16: Vertical displacement in the corroded truss girder scenario.

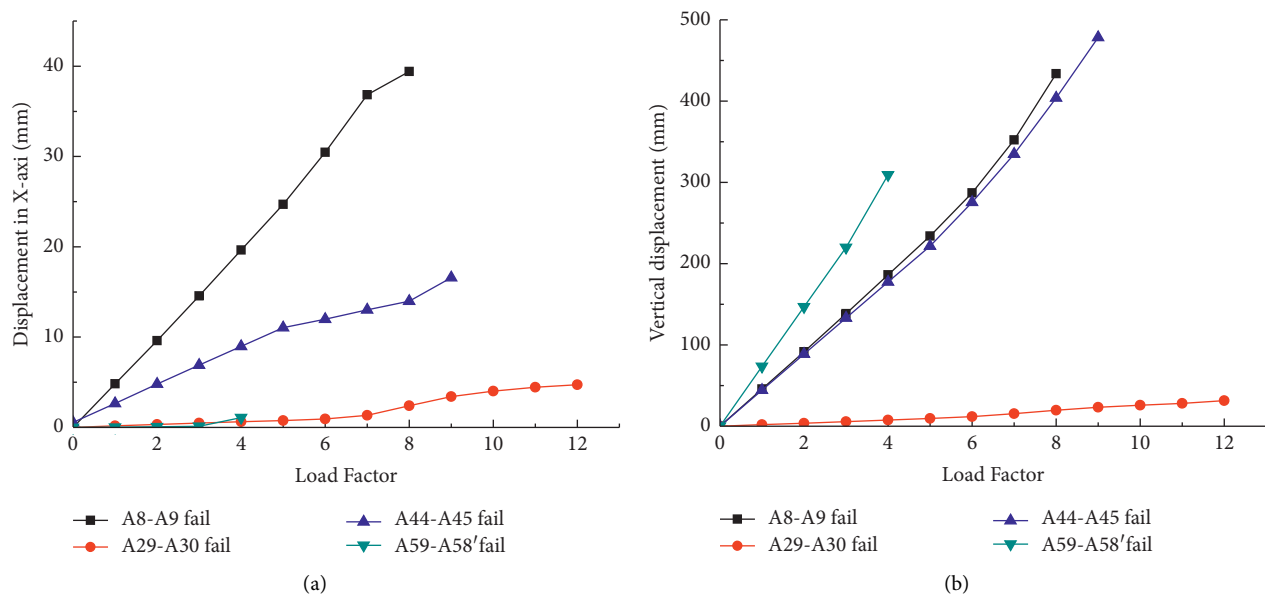


FIGURE 17: Displacement of the girder in the chord loss scenarios: (a) axial displacement-load response obtained from the finite element model; (b) vertical displacement-load response obtained from the finite element model.

29 mm and 580 mm, respectively, when the bridge is subjected to the most critical loading in the cable S9 loss scenario. These are the minimum values in the three cable loss scenarios. On the other hand, once a displacement of 4.7 mm is reached, the axial displacement value increases to 20 mm in the opposite direction when the bridge collapses in the cable S13 loss scenario. The collapse patterns of the bridge for the different load scenarios are shown in Figure 20. The vertical displacement reaches 1150 mm, which is the maximum value in the three cable loss scenarios (Table 5). The large deformation before the bridge collapse in the cable loss scenario shows that the parallel bearing system provides ample alternative paths for absorbing the load after the cable loss.

The chord loss does not result in a change in the cable forces under a dead load; however, the cable failure leads to a redistribution of the cable forces. A chord failure close to the pylon results in brittle damage of the entire bridge under a critical loading, whereas a cable loss leads to outstanding ductility of the remaining structure. In addition, the corrosion of the truss girder does not significantly influence the cable force and vertical displacement of the beam. Overall, the truss girder, a series bearing system, provides limited alternative load paths after the bridge is damaged by a chord loss. In contrast, the cables, a parallel bearing system, provide sufficient load paths for the bridges damaged by a cable loss.

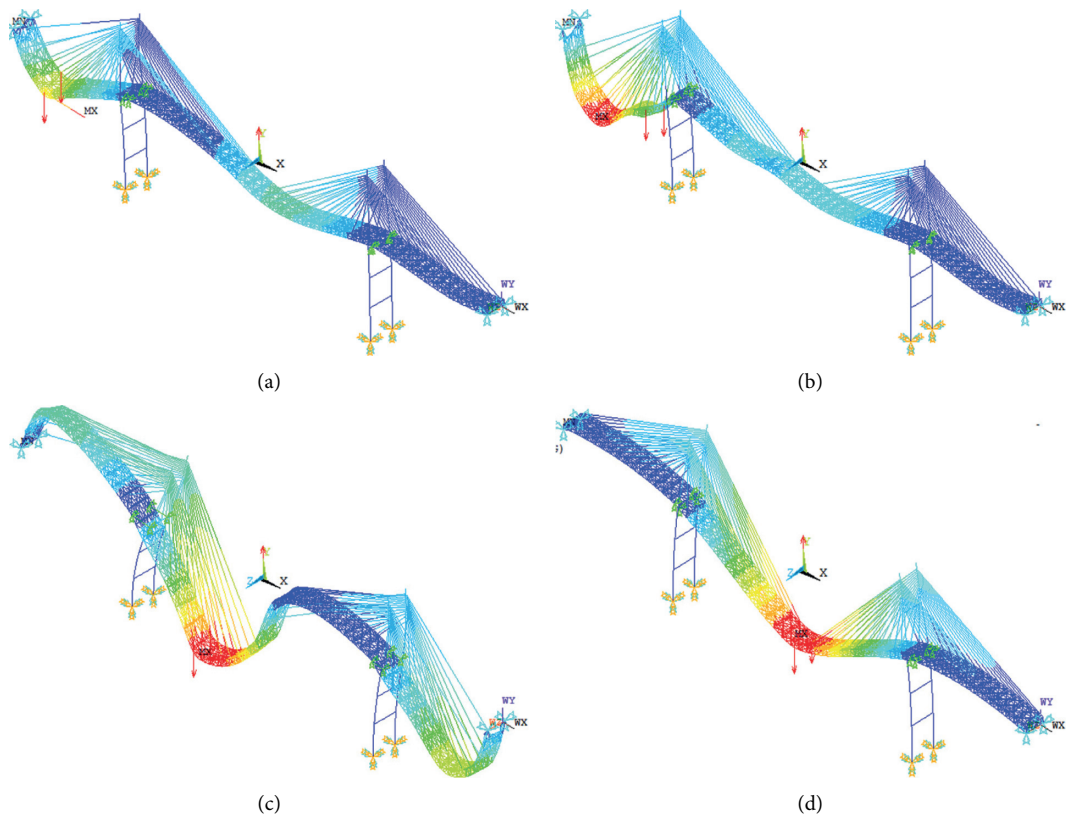


FIGURE 18: Collapse patterns of the bridge in different chord loss scenarios: (a) loss of chords A8-A9; (b) loss of chords A29-A30; (c) loss of chords A44-A45; (d) loss of chords A59-A58.

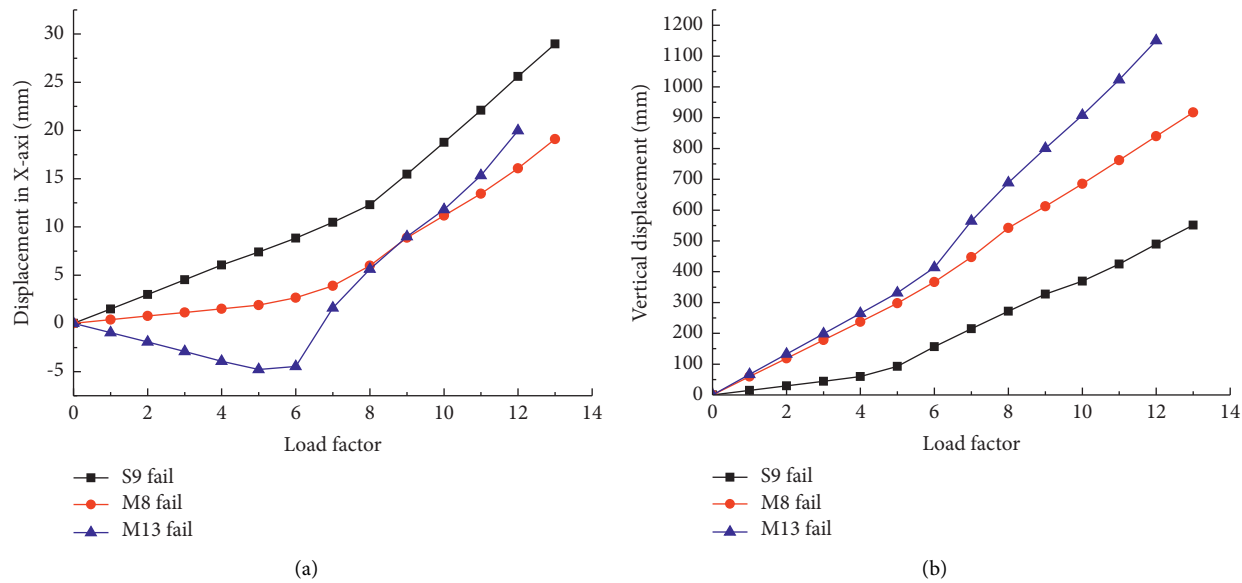


FIGURE 19: Displacement of the girder in the cable loss scenarios: (a) axial displacement-load response obtained from the finite element model; (b) vertical displacement-load response obtained from the finite element model.

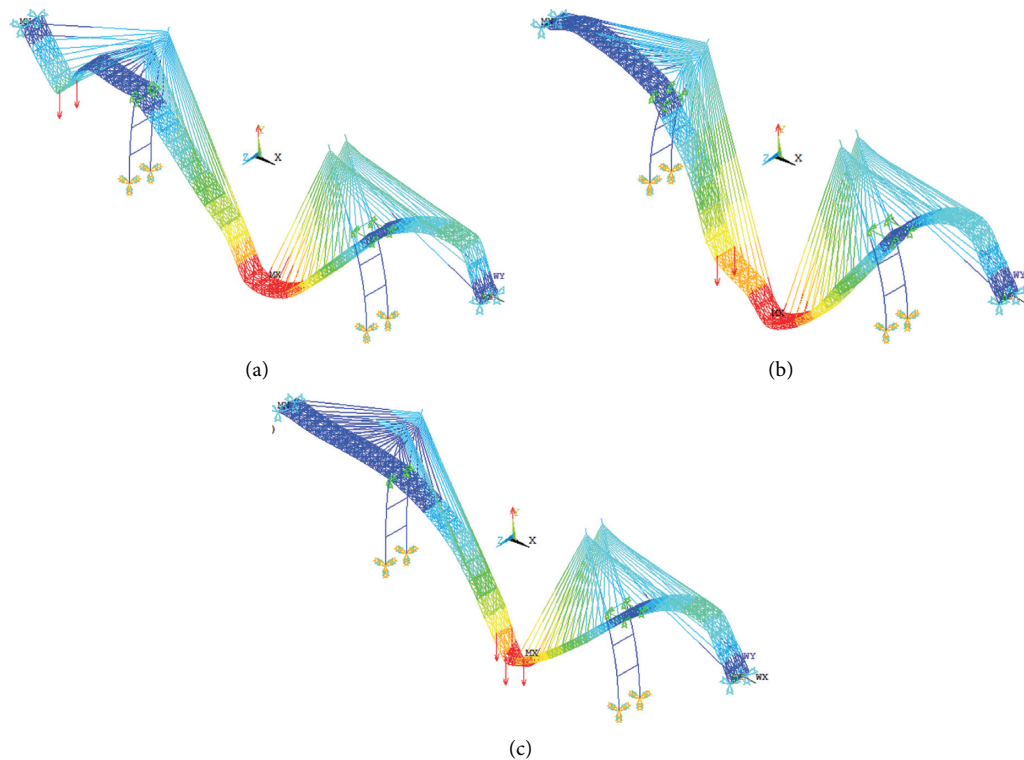


FIGURE 20: Collapse patterns of the bridge in different cable loss scenarios: (a) loss of cable S9; (b) loss of cable M8; (c) loss of cable M13.

TABLE 5: The collapse performance of the bridge in the cable loss scenarios.

Failed members	Node	Load factor	Maximum displacement (mm)	
			Axial	Vertical
S9	18	12.9	29	580
M8	90	13.1	21	960
M13	110	12.3	21	1150
A8-A9	14	7.9	40	434
A29-A30	54	12.0	5	31
A44-A45	86	5.1	-25	406
A59-A58'	116	2.9	1	309

5. Conclusions

An approach, taking into consideration a series-parallel load-bearing system and alternative load paths, is proposed to investigate collapse behavior of cable-stayed bridge with steel truss girders. This approach reveals structural load paths and collapse behavior. The load-bearing systems can also be used to evaluate and determine the damage to cable-stayed bridge and further improve their structural-performance design. The conclusions are drawn as follows:

- (1) A series-parallel load-bearing system of a cable-stayed bridge is proposed to assess and determine alternative load paths in damaged bridges and attain structural ultimate bearing capacity.

- (2) As a series bearing system, the loss of an individual chord in truss girders has negligible effects on the cable forces; thus, the truss girder can bear most of the load without required alternative loading paths. Similarly, corrosion in truss girder has highly slight effects on cable forces and vertical displacement in the main beam. In contrast, as a parallel bearing system, cables provide alternative paths to transfer the load when forces changed due to cable loss.
- (3) After individual chord failure, a brittle collapse of the damaged bridge occurs, with a maximum displacement of 40 mm along the longitudinal axis. The series bearing system of truss girders can transfer load in limited paths to other members in truss girder after failure of individual chords. Thus, additional bars should be recommended to add into truss girder to create more alternative load paths at mid-span and near pylon.
- (4) Unlike the chord loss scenarios, the damaged bridges collapse after exhibiting significant deformation in cable loss scenarios due to the fact that the other cables absorbed loading; this effect is more pronounced when a long cable fails. As a parallel bearing system, cables provide various alternative paths to absorb loading if individual cables fail. For cable-stayed bridges with steel truss girders, bearing capacity in cables is required to be twice dead and live loads, which is less than 2.5 times recommended in specification.

References

- [1] 2017, <https://www.mprnews.org/story/2017/08/01/looking-back-photos-of-the-bridge-collapse>.
- [2] M. Ghosn, J. Yang, D. Beal, and B. Sivakumar, "Bridge system safety and redundancy," *No. Project*, vol. 12-86, 2014.
- [3] P. C. Pandey and S. V. Barai, "Structural sensitivity as a measure of redundancy," *Journal of Structural Engineering*, vol. 123, no. 3, pp. 360–364, 1998.
- [4] A. M. Nafday, "System safety performance metrics for skeletal structures," *Journal of Structural Engineering*, vol. 134, no. 3, pp. 499–504, 2018.
- [5] C. T. Hunley and I. E. Harik, "Structural redundancy evaluation of steel tub girder bridges," *Journal of Bridge Engineering*, vol. 17, no. 3, pp. 481–489, 2011.
- [6] M. Ghosn and F. Moses, "Redundancy in highway bridge superstructures," *Transportation Research Board*, vol. 406, 1998.
- [7] J. Scheller and U. Starossek, "A new energy-efficient device for active control of bridge vibrations," *International Association for Bridge and Structural Engineering*, vol. 17, no. 12, pp. 310–311, 2008.
- [8] C. M. Mozos and A. C. Aparicio, "Parametric study on the dynamic response of cable stayed bridges to the sudden failure of a stay, part II: bending moment acting on the pylons and stress on the stays," *Engineering Structures*, vol. 32, no. 10, pp. 3301–3312, 2010.
- [9] C. M. Mozos and A. C. Aparicio, "Parametric study on the dynamic response of cable stayed bridges to the sudden failure of a stay, part II: bending moment acting on the pylons and stress on the stays," *Engineering Structures*, vol. 32, 2010.
- [10] F. Greco, P. Lonetti, and A. Pascuzzo, "Dynamic analysis of cable-stayed bridges affected by accidental failure mechanisms under moving loads," *Mathematical Problems in Engineering*, vol. 20, pp. 130–137, Article ID 302706, 2013.
- [11] P. Lonetti and A. Pascuzzo, "Vulnerability and failure analysis of hybrid cable-stayed suspension bridges subjected to damage mechanisms," *Engineering Failure Analysis*, vol. 45, pp. 470–495, 2014.
- [12] T. N. Kudsi and C. C. Fu, "Redundancy analysis of existing truss bridges: a system reliability-based approach," in *Proceedings of the First International Conference Bridge Maintenance, Safety and Management*, 2002.
- [13] M. Ghosn, F. Moses, and D. M. Frangopol, "Redundancy and robustness of highway bridge superstructures and substructures," *Structure and Infrastructure Engineering*, vol. 6, no. 1-2, pp. 257–278, 2010.
- [14] J. Yang, "Structural redundancy and system reliability of highway bridges," Doctoral dissertation, The City College of, New York, 2015.
- [15] M. Ghosn, D. M. Frangopol, T. P. McAllister et al., "Reliability-based performance indicators for structural members," *Journal of Structural Engineering*, vol. 142, no. 9, Article ID F4016002, 2016.
- [16] M. Ghosn, L. Duenas-Osorio, D. M. Frangopol et al., "Performance indicators for structural systems and infrastructure networks," *Journal of Structural Engineering*, vol. 142, no. 9, Article ID F4016003, 2016.
- [17] G. Zhang, V. K. R. Kodur, W. Hou, and S. H. He, "Evaluating fire resistance of prestressed concrete bridge girders," *Structural Engineering & Mechanics*, vol. 62, no. 6, pp. 663–674, 2017.
- [18] G. Zhang, V. K. R. Kodur, W. F. Yao, and Q. Huang, "Behavior of composite box bridge girders under localized fire exposure," *Structural Engineering & Mechanics*, vol. 69, no. 2, pp. 193–204, 2019.
- [19] G. Zhang, M.-C. Zhu, V. Kodur, and G.-Q. Li, "Behavior of welded connections after exposure to elevated temperature," *Journal of Constructional Steel Research*, vol. 130, pp. 88–95, 2017.
- [20] X. M. Wang, *Structural Analysis Element and Application* (In Chinese), China Communication Publishing & Media Management Co., Ltd., 2011.

Use of nanofluids to improve heat exchanger performance

Ranjan Kumar, *Department of Mechanical Engineering, NM Institute of Engineering & Technology, Bhubaneswar, kumarranjan75@gmail.com*

Saswati Nayak, *Department of Mechanical Engineering, Capital Engineering College, Bhubaneswar, saswatinayak2574@gmail.com*

Chinmay Swain, *Department of Mechanical Engineering, Raajdhani Engineering College, Bhubaneswar, chinmayswain1972@gmail.com*

Subhasis Sarkar, *Department of Mechanical Engineering, NM Institute of Engineering & Technology, Bhubaneswar, subhasissarkar14@yahoo.co.in*

ARTICLE INFO

Keywords:

Nanofluids
Heat exchangers
Heat transfer intensification
Thermal performance
Pressure drop

ABSTRACT

Heat exchangers are widely used in a variety of thermal systems for a variety of industrial applications. The thermal efficiency, operational load, size, flexibility in operation, compatibility with working fluids, superior temperature and flow controls, and comparatively inexpensive capital and maintenance expenses all factor into the decision to use HEx. Heat exchanger heat transfer intensification can be achieved through passive, active, or combination methods. Nanofluids have lately been used as working fluids in heat exchangers. The performance of heat exchangers using various nanofluids is primarily determined by the thermophysical properties of the fluids and their improvement. Researchers have made significant progress in understanding the peculiar behaviour of several nanofluids. The current paper examines and summarises recent developments in the use of nanofluids in various heat exchanger types, such as plate heat exchangers, double-pipe heat exchangers, shell and tube heat exchangers, and cross-flow heat exchangers. The findings revealed that nanofluids with increased thermal conductivity, despite a significant drop in heat capacity and an increase in viscosity, improved the performance of several heat exchanger types. To correctly evaluate the total performance of any type of heat exchanger, a performance evaluation criterion that combines thermal improvement and increases pumping power is required. The problems and potential for future heat transfer and fluid flow research using nanofluids for various types of heat exchangers are reviewed and presented.

1. Introduction

Nowadays, the rapid progress in thermal technologies for different heat exchangers (HEXs) applications, associated with power-saving and intensification of heat transfer, is a critical issue for scientists. The heat transfer intensification (HTI) may be assorted to active, passive, or compound approaches based on the necessity of an external power device such as a pump or fan [1–3]. The active techniques of performance intensification may be accomplished either utilizing the electrostatic fields, vibrate the surface or the working fluid, or supplying nanofluids rather than conventional fluids [4–6]. However, the

passive approach uses coiled tubes with different geometries, swirling flow devices, processed, rough and extended surfaces, and utilizing phase-change or nanoparticles materials. In the compound systems, two or more passive or active individual methods can be employed synchronously to practically intensify the heat transfer using a rough surface with twisted tapes [7,8]. One of the promising active methods to enhance the heat transfer in HEXs is modifying the surface roughness [9,10]. The synthetic techniques of surface roughness include sandpaper [11], erosion-corrosion [12], V-grooves [13] and square rib [14,15]. The inference of height of the rough element, size of rough elements, pitch to height ratio, etc., significantly impacts the performance of HEx.

Utilizing conventional working fluids in different HEXs is not adequate to remove the required heat rate for various applications. Adding nanoparticles (NPs) or phase-change materials into the base working fluids such as gasses or liquids belong to passive

Nomenclature

b	corrugation depth (m)
cp	specific heat capacity (J/m K)
D_{sh}	shell diameter (mm)
d_t	tube diameter (mm)
De	Dean number (—)
f	friction factor (—)
h	convective heat transfer coefficient (W/m ² K)
k	thermal conductivity (W/m ² K)
L	plate length (m)
L_p	port to port length (m)
\dot{m}	mass flow rate (kg/s)
n	number of turns (—)
NTU	number of transfer unit (—)
Nu	Nusselt number (—)
p_i	vortex generator pitch (mm)
p	pressure (N/m ²)
Re	Reynolds number (—)
U	overall heat transfer coefficient (W/m ² K)
\dot{V}	volume flow rate (Lit/min)
W	plate width (m)

Subscripts

c	coil
i	inner
nf	nanofluid
o	outer
sh	shell
t	tube

Greek symbols

ε	effectiveness (%)
θ	chevron angle (degree)
λ	corrugation pitch (m)
γ	curvature ratio
ρ	density (kg/m ³)
δ	plate thickness (m)
ϕ	volume fraction of nanoparticles
μ	dynamic viscosity (Ns/m ²)

Abbreviations

DPHEX	double-pipe heat exchanger
HEX	heat exchanger
HTC	heat transfer coefficient
MWCNT	multi-walled carbon nanotubes
NPs	nanoparticles
PEC	performance evaluation criterion
PHEx	plate heat exchanger
RSM	response surface methodology
STHEX	shell and tube heat exchanger

intensification methods [16–18]. Nanofluids (NFs), as formed by dispersing nanoparticle (NPs) to conventional heat transfer fluids, i.e., base fluids (BF), have higher thermal conductivity compared and high intensity of the thermal performance, should be employed to achieve the thermal engineering requirements in various application such as water desalination, heat storage, heat exchangers [19–24]. This in return provides a very promising approach to increase the energy efficiency in many applications at lower environmental impacts [25]. One of the promising applications for the use of nanofluid is to harness renewable and sustainable energies, which are usually characterized by being diffusive and diluted, hence energy conversion enhancement present one of the major activates [26–28].

The application of various NFs has an intensive potential for augmenting the heat transfer of HEXs. Utilizing traditional working fluids such as air or water has low thermal conductivities restricting the heat transfer rates. The main parameters that influence the thermophysical properties of NFs and hence the thermal performance of HEX are the size of NPs and their morphology and concentration and other parameters involved in the preparation of nanofluids such as the aggregation of nanoparticles into the nanofluids and sonication and agitation time [29–31], pH of nanofluids [32,33], adding surfactants [34]. However, the stability of NPs in the base working fluid is a critical issue that impacts the rheological and the thermophysical properties of NFs. As well, for diverse applications of NFs, there are a number of serious issues that should be taken into consideration such as sedimentation, erosion, and fouling. Utilizing NFs in HEXs as working fluids is a promising solution to augment the thermal performance. However, it increases the pressure drop through the heat exchanger. Hence, the improvement of thermal performance of HEXs due to using NFs relative to the corresponding pressure drop is investigated by studying the performance evaluation criterion (PEC) [35,36].

Elevating conventional fluids' thermal conductivity by dispersing NPs changes the thermophysical properties, leads to augmenting the heat transfer rate. However, the increase in NPs volume fraction ϕ , i.e., concentration, raises the viscosity of NF, resulting in higher pressure drop and hence high pumping power [37–39]. Several studies have been conducted to investigate the thermophysical properties of different NFs to obtain higher thermal conductivity at lower viscosity raise [40–43]. The heat transfer augmentation utilizing NFs in HEXs is due to the different generated forces [44]. Recently, the thermophysical properties of NFs can be determined using computer-aids such as artificial neural networks [45–47], least squares support vector machines [48], genetic algorithm optimization [49,50], and neuro-fuzzy models [51].

Qiu et al. have comprehensively reviewed the recent advances in manufacturing NPs with different materials and thermophysical properties measuring and modeling [31]. Mahian et al. reviewed the synthesis, thermophysical properties, and applications of NFs [44]. The group studied the various generated forces due to dispersing nanoparticles into the based fluids such as van der Waals, drag, lift, Brownian, electrostatic forces, and thermophoretic. Afterward, the physical models of the fluid flow and heat transfer of NFs in single- and two-phase were introduced. The rheological behavior and the thermophysical properties of different NFs, i.e., copper oxide CuO, silicon dioxide SiO₂, and aluminum oxide Al₂O₃ in ethylene glycol/water (60/40%) were measured by Vajjha et al. [52].

The hybrid NFs are produced by dispersing NPs of two or more material into a BF and result in higher thermophysical properties than the NFs with a single nanoparticle material, i.e., mono NF [53,54]. The hybrid NFs improve the heat transfer at a reduced pressure drop by trading-off the advantages and disadvantages of single NPs [55,56]. The detailed information on characterization, preparation, thermophysical properties, and stability of the hybrid NFs were introduced by Kumar and Valan Arasu [57]. Munkhbayar et al. shown that the thermal conductivity of the hybrid NF was lower than that of mono NF due to the lack of collaboration between pair nanoparticles [58]. Utilizing NFs in HEXs as promising working fluids are a promised solution for augmenting the heat transfer however it increase the pressure drop through the heat exchanger.

The present study reviews and summarizes the recent implementations of utilizing NFs in different HEXs types, including plate heat exchangers (PHExs), double-pipe heat exchangers (DPHEXs), shell and tube heat exchangers (STHEXs), and cross-flow heat exchangers (CFHEXs). The effect of NFs on the thermal efficiency and performance along with pressure drop for each type of HEX is investigated. Moreover, the thermophysical properties of nanoparticles (NPs) such as thermal conductivity, density, heat capacity, and viscosity and

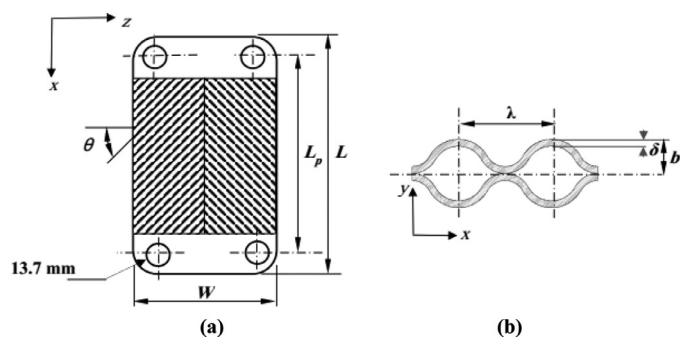


Fig. 1. Plate heat exchanger (a) representational outline (b) corrugated plate [67], reused with permission from Elsevier license number 5016670637890.

their effect on the properties of NFs are addressed. The performance evaluation criterion (PEC) that combines the improvement in heat transfer effectiveness and raising the pumping power in HEx is investigated to evaluate the overall performance precisely. The challenges and future work for the intensification of heat transfer and fluid flow for different types of HExs utilizing NFs are thoroughly discussed and presented.

2. Applications of nanofluids in heat exchangers

Due to the significant improvement in the thermal conductivity, the nanofluids are promised to enhance the heat transfer coefficients in HEx. While, the suspensions of NPs in the base working fluids impacts all thermophysical properties other than the thermal conductivity (k) such as the thermal capacity (cp), density (ρ) and viscosity (μ) of NFs. So in this section, the effects of utilizing different nanofluids with various thermophysical properties on a number of heat exchangers i.e., plate heat exchangers (PHEs), double-pipe heat exchangers (DPHEs), shell and tube heat exchangers (STHEs), and cross-flow heat exchangers (CFHEs) will be introduced.

2.1. Plate heat exchangers (PHEs)

The high thermal efficiency, operating at variable load, size compactness, operation flexibility, compatibility with different working fluids, better temperature control, and comparatively low

maintenance cost are the main advantages of the plate heat exchangers (PHEs) [59–62]. So, the PHEs are excessively utilized in different cooling/heating applications such as pharmaceutical, chemical, food industries, air-conditioning systems, etc. Passing the cold and hot streams through the parallel channels in PHEx generates high turbulence, thus intensify the heat transfer rate, and consequently, it improves the HEx effectiveness [63–66]. The fundamental geometry of PHEs and its configuration are illustrated in Fig. 1 [67].

Pantzali et al. explored the effect of the surface modulation on the heat transfer of miniature PHEx using 4 vol.% of Cu/water NF as represented in Fig. 2 [68]. The results indicated that a lower NF flowrate than that of water maintained a low-pressure drop and low-pumping power. Sun et al. studied the flow characteristics and convective heat transfer of PHEx using Fe_2O_3 , Al_2O_3 , and Cu/water at 0.1, 0.2, and 0.3 wt.% [69]. The results revealed that the convective HTC (h) was enhanced compared with that of water, with Cu/water NF performing better, while the stability of Al_2O_3 /water NF was the best. Pandey and Nema investigated the influence of Al_2O_3 /water NF at 2, 3, and 4 vol.% on the heat transfer, friction factor, and exergy loss for a counter-flow PHE [70]. The experiments were carried out at flowrate ranges of 2–5 Lit/min for the NF and water. The results revealed that for Al_2O_3 /water NF with 2 vol.% introduced the most effective heat transfer and lowest exergy loss at 3.7 Lit/min as a result of its enhanced thermophysical properties compared with water.

Taws et al. examined the effect of utilizing the CuO/water NF on heat transfer and fluid flow of chevron type two-channel PHEx experimentally [71]. The results indicated that the heat transfer of the CuO/water NF with 2 vol.% concentration was higher than that for 4.65 vol.%. Similarly, Barzegarian et al. investigated the heat transfer and pressure drop in a smooth brazed PHEx using TiO_2 /water NF [72]. The results indicated heat transfer was enhanced by increasing the Reynolds number Re and increasing the weight fraction of NPs. The maximum overall heat transfer coefficient (U) enhancement obtained were 2.2, 4.6, and 8.5%, for 3, 0.8, and 1.5 wt.%, respectively. Moreover, the pressure drop through the HEx increased insignificantly due to using NF compared with the considerable augmentation of U .

The heat transfer and pressure drop of PHEx using Al_2O_3 and multi-wall carbon nanotubes (MWCNT)/water NFs were evaluated by Huang et al. [73]. The experimental results concluded that as a result of improving thermophysical properties of Al_2O_3 rather than that for MWCNT, the heat transfer enhancement for the Al_2O_3 /water NF was

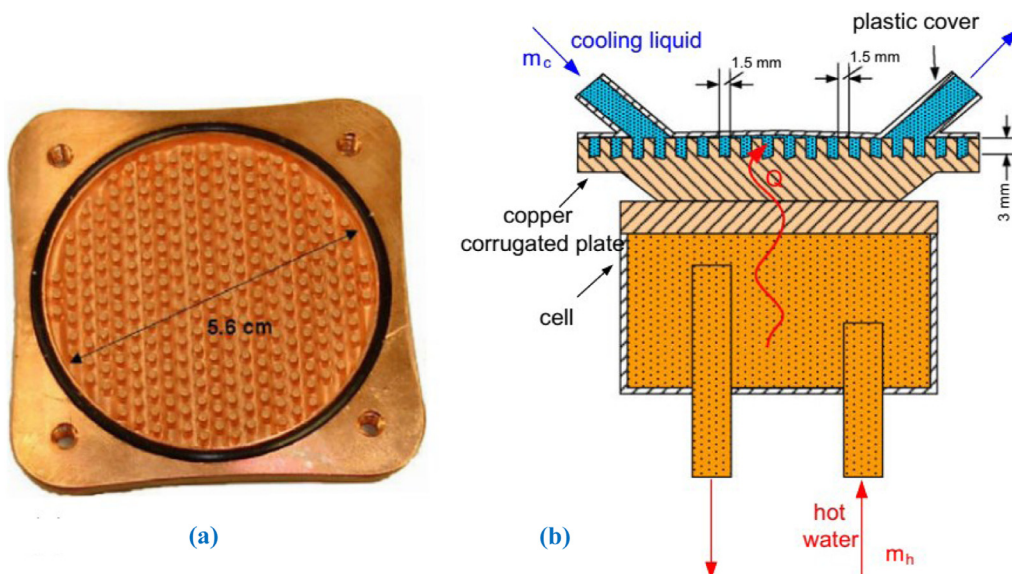


Fig. 2. Plate heat exchanger (a) modulated copper plate (b) heat exchanging unit [68], reused with permission from Elsevier license number 5016671006737.

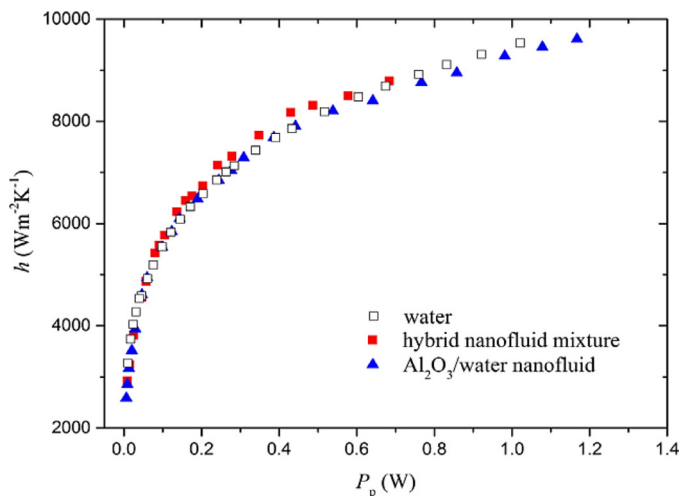


Fig. 3. Heat transfer coefficient (h) versus the pumping power (P_p) [74], reused with permission from Elsevier license number 5016671200098.

higher than that of MWCNT/water NF. Moreover, correlations for the Nusselt number (Nu) and the friction factor (f) were proposed based on the obtained results. Huang et al. tested the hybrid Al_2O_3 –MWCNT/water NF on the convective heat transfer coefficient (h) and pumping power (P_p) of PHEX [74]. The results revealed that (h) for the hybrid NF was slightly greater than the corresponding value of Al_2O_3 /water NF, contrary to the (P_p) as illustrated in Fig. 3. Goodarzi et al. studied the influence of the covalent functional groups such as cysteine and silver on the thermal properties of MWCNT/water NF [75]. The water as BF, and MWCNT with Gum arabic (GA), MWCNT with cysteine (Cys), and with silver (Ag) in water were examined. The experimental results indicated that increasing the (Re), Peclet number (Pe), and the ϕ enhanced the heat transfer as well as increased the pumping power compared to water.

The thermal efficiency as well as the pressure drop of PHEX employing Al_2O_3 /water NF considering the surface roughness were examined experimentally by Attalla et al. [76]. The results showed that the increase of the ϕ enhanced the heat transfer rate, while it increased the pressure drop in PHEX. Furthermore, increasing ϕ in the laminar flow region has a slight effect on the heat transfer

enhancement. On the other hand, Pantzali et al. investigated the effectiveness of PHEX using different NFs, concluding that for industrial HEXs, high ϕ and turbulent flow were necessary, making the substitution of the conventional fluids by NFs impractical [77]. Tiwari et al. studied the performance of PHEX using CeO_2 /, Al_2O_3 /, TiO_2 /, and SiO_2 /water at various ϕ values and flow rates experimentally [78]. The results demonstrated that at low ϕ , the TiO_2 / and CeO_2 /water NFs maintained higher heat transfer, while at high ϕ , the Al_2O_3 / and SiO_2 /water NFs were more efficient. The highest obtained overall HTC (U) was for CeO_2 /water NF, followed by Al_2O_3 /water, TiO_2 /water, and lastly SiO_2 /water. Furthermore, at the optimum ϕ value for each, the maximum improvement of PHEX effectiveness was 13.5, 9.6, 7.9, and 5.0% for CeO_2 /, Al_2O_3 /, TiO_2 /, and SiO_2 /water NFs, respectively as shown in Fig. 4.

Barzegarian et al. experimentally investigated the effect of (Re) for TiO_2 /water NF on the heat transfer augmentation and pressure drop of a PHEX [79]. The results demonstrated that the maximum (h) enhancement for TiO_2 /water NF at 0.3, 0.8, and 1.5 wt.% were 6.6, 13.5, and 23.7%, respectively. Meanwhile, the pressure drop increase was negligible compared to the improvement in the heat transfer. Similarly, Kabeel et al. studied the impact of ϕ on the performance of PHEX [80]. The results show a 13% heat transfer improvement at 4 vol.% compared to water, but at a 90% increase in pumping power, as shown in Fig. 5. Summary of PHEXs performance enhancement utilizing different NF, and the main findings is listed in Table 1.

2.2. Double pipe heat exchangers (DPHEXs)

The double-pipe heat exchanger (DPHEX) is considered as the simplest HEXs utilized for low heat duty in industrial applications, simply consists of one tube inside another, i.e., concentric, with the inner one is finned or plain [16,81,82]. One fluid passes through the inner pipe, while the other fluid passes into the annulus space of the two pipes. The counter-flow configuration helps to achieve the best thermal performance, while parallel or concurrent flow is utilized for application in which constant wall temperature is required. The DPHEX has the advantages of simplicity, compactness, ease of manufacturing, ease of maintenance, etc. [83–85].

Rennie et al. studied the DPHEX for parallel- and counter-flow configurations, with the Wilson plot, was employed to evaluate the h in inner and annulus tubes and the) [86]. The results indicated that

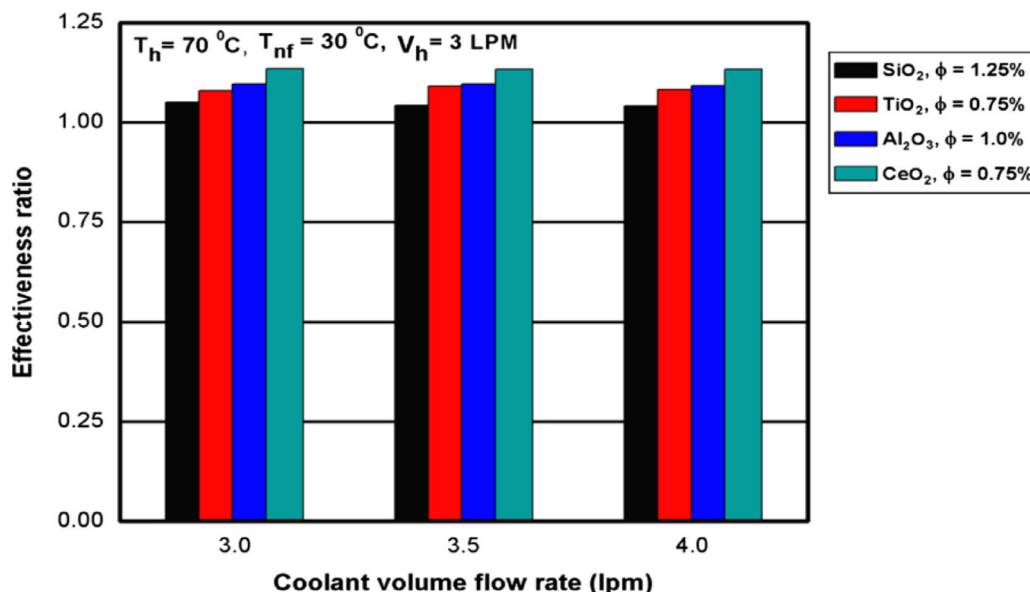


Fig. 4. Effectiveness ratio versus coolant flow rate for different NFs [78], reused with permission from Elsevier license number 5016671436964.

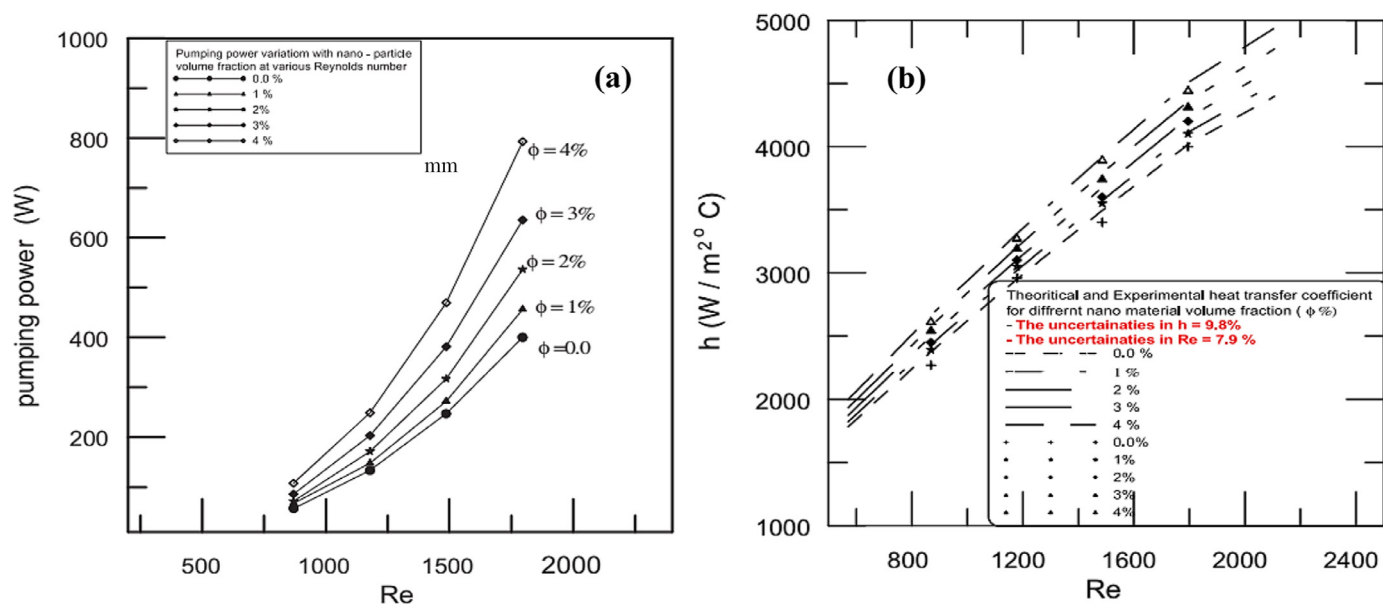


Fig. 5. (a) Pumping power and (b) convective heat transfer coefficient (h) versus Reynolds number for different volume fractions [80], reused with permission from Elsevier license number 5016680167876.

the experimental and numerical results of the Nusselt number (Nu) in the annulus for large coil were matched with a high deviation, while this deviation is less for small scale HEX. Khedkar et al. studied the impact of Al_2O_3 /water NF on the heat transfer of DPHEX, showing an increase h by about 16% at 3 vol.% [87]. The heat transfer characteristics and friction of turbulent flow in DPHEX using Al_2O_3 and TiO_2 /water with a size of 13 nm and 27 nm, respectively, were investigated experimentally by Pak and Cho [88]. The results concluded that a better selection of particles with large size and better thermophysical properties such as thermal conductivity improves the thermal performance of the NF. Additionally, the viscosity increase of NFs resulted in a 30% additional power consumption at a 3 vol.% NF.

The heat transfer and fluid flow performance using Cu/water NF at different ϕ values were investigated experimentally by Xuan and Li [89]. The authors evaluated and correlated the h for the NF considering the micro-diffusion and -convection effects. Similarly, the heat transfer and friction factor characteristic in a counter-flow DPHEX using SiO_2 /water NF were studied by Kassim and Lahij, obtaining the maximum Nu was achieved at 0.3 vol.% [90]. The results Gnanavel et al. improved the heat transfer in DPHEX using a twisted tape HEX as a passive technique, as shown in Fig. 6 [91,92]. The numerical results show that the thermal performance of NFs was larger than unity and significantly higher than those of water. The thermal performance for TiO_2 /water NF was the highest with 1.879 in the laminar flow region, followed by BeO /, ZnO /, and CuO /water NFs at 1.795, 1.798, and 1.601, respectively.

The optimization and thermal performance of a mini HEX using a hybrid NF containing tetra-methylammonium hydroxide (TMAH) coated by magnetite (Fe_3O_4) NPs and gum arabic (GA) coated CNTs were investigated numerically by Shahsavari et al. [93]. The results indicated that low entropy generation with high heat transfer was achieved at low Re values with a high ϕ of CNT and Fe_3O_4 . Utilizing the objective functions, the optimum values of ϕ_{CNT} , $\phi_{magnetite}$, and Re were 0.88%, 1.1%, and 500, respectively as illustrated in Fig. 7. Jafarzad and Heyhat studied experimentally the injection of air bubbles into NF flow inside the annulus of DPHEX in a vertical orientation as illustrated in Fig. 8 [94]. The authors evaluated the thermal performance, exergy efficiency, and pressure drop of the proposed system. Additionally, a multi-objective optimization based on the artificial neural network and the genetic algorithm was carried out to evaluate the

best HEX performance according to its thermal performance and exergy efficiency. The results indicated that the proposed combined method increased the NF surface tension that responsible for creating a stream of smaller air bubbles with high frequency, that improved the performance rather than each method separately. Additionally, the Air bubble injection reduced the pressure drop by 94%, where the gas bubbles replaced the liquid momentum near the contact wall. Consuming additional power to supply air flow was considered as the fundamental reason for reducing the exergy efficiency in the proposed system.

Bezaatpour and Goharkhah proposed a method to improve the convective heat transfer in DPHEX and reduce the pressure drop using NF exposed to an external magnetic field, inducing a swirling flow [95]. The results revealed that applying an external magnetic field intensified the heat transfer up to 320% with an inconsiderable pressure drop increase, which was attributed to the generated swirling flow disrupted the thermal boundary layer and consequently improved the inside flow mixing of the HEX, as shown in Fig. 9. Alternatively, Singh and Sarkar proposed a novel enhancing technique in a DPHEX using wire coil turbulator and Al_2O_3 -MgO/water hybrid NF for turbulent flow [96]. The effect of coil configurations such as converging (C), diverging (D), and converging-diverging (C-D) types were examined. The results indicated that the D-type of the wire coil produced better hydrothermal performance compared with the other types. The Nu of the hybrid NF using D-type, C-D type, and C-type wire improved up to 84, 47, and 57%, respectively than that of HEX using water without insert in a tube, while the corresponding values of the friction factor (f) were 71, 68, and 46%, respectively. For all types of coil inserts, the thermal performance factor due to using hybrid NF was found more than unity.

Arjmandi and Pour studied the impact of employing combined vortex generators and twisted tape turbulator with Al_2O_3 /water NF flowing through the inner tube of DPHEX as illustrated in Fig. 10 [97]. The response surface methodology (RSM) was employed to acquire the combined vortex generator's optimum geometry and the twisted tape turbulator. The pitches ratio, angle of vortex generator, annulus Re were assessed. The numerical results indicated that increasing the number of vortex generators, the vortex generator angle, and Re improved the heat transfer. While, increasing the of vortex generators raised the pressure drop. Accordingly, the performance

Table 1
Summary of plate heat exchangers (PHEs) performance enhancement using different nanofluids (NFs) with base water.

Ref.	Study	PHE Type	Nanoparticles	Size, nm	Concentration (ϕ)	Main findings
Pantzali et al. [68]	Exp. and Num.	Counter-flow miniature	CuO		0.4 vol.%	<ul style="list-style-type: none"> The k_{eff} increased by 10%. The ρ_{eff} increased by 25%. The cp_{eff} decreased by 20%. Al_2O_3/water is the most stable. Cu/water is the most effective. The maximum rate of heat transfer was maintained at the lowest ϕ.
Sun et al. [69]	Exp.	Brazed	Cu, Fe_2O_3 and Al_2O_3	50	0.1 - 0.5 wt.%	
Pandey and Nema [70]	Exp.	Counter flow with corrugated plates	Al_2O_3	40–50	2 - 4 vol.%	
Taws et al. [71]	Exp.	Three corrugated plates with heringbone pattern	CuO	29	2 – 4.65 vol.%	<ul style="list-style-type: none"> CuO/water increased the friction factor. Heat transfer decreased for 4.65 vol.% nanofluid compared with that for 2 vol.%.
Barzegarian et al. [72]	Exp.	Brazed	TiO_2	20	0.3 - 1.5 wt.%	<ul style="list-style-type: none"> The heat transfer coefficient for 0.3, 0.8 and 1.5% increased by 6.6, 13.5 and 23.7%.
Huang et al. [73]	Exp.	Corrugated with 10 channels	Al_2O_3 , MWCNT	40 1.5 μm (length), 9.5 nm (diameter)	2.18 - 10.36 wt.% 0.02 - 0.1 wt.%	<ul style="list-style-type: none"> The HTC for MWCNT/water nanofluid decreased with increasing the ϕ.
Huang et al. [74]	Exp.	Chevron corrugated with 5 channels	Al_2O_3 , MWCNT	40	1.89 vol.% 0.0111 vol.%	<ul style="list-style-type: none"> The pressure drop of hybrid NF was less than Al_2O_3/water and slightly higher than water.
Goodarzi et al. [75]	Exp. and Num.	Counter flow corrugated PHE	FWMCNT-Ca, FWMCNT-Cys, and FWMCNT-Ag	diameter of 10–20 nm, and length of 5–15 μm	0.5% - 1.0%	<ul style="list-style-type: none"> Water had the lowest Nusselt Nu number, while the maximum value was maintained by 1 vol.% MWCNT-Ca/water. The viscosity of working fluids was a crucial factor for the heat exchanger performance.
Pantzali et al. [77]	Exp.	Corrugated PHE with 16 stainless steel plates	Al_2O_3 , CuO, CNT	11 30–50 3–5 nm (dia) 8–15 μm (length)	4 vol.% 3 vol.% 0.5 vol.%	
Tiwari et al. [78]	Exp.	Chevron PHE	CeO_2 , Al_2O_3 , TiO_2 , SiO_2 , TiO_2	30 45 10 10 20	0.5 - 3 vol.%	<ul style="list-style-type: none"> The CeO_2/water at 0.75 vol.% result in the best performance with 16% performance index enhancement.
Barzegarian et al. [79]	Exp.	Brazed PHE			0.3 - 1.5 wt.%	<ul style="list-style-type: none"> The U was enhanced by 2.2, 4.6 and 8.5% for 0.3, 0.8 and 1.5% wt, respectively.
Kabeel et al. [80]	Exp.	Corrugated chevron-type with 6 plates	Al_2O_3	47	1 – 4 vol.%	<ul style="list-style-type: none"> Heat transfer coefficient was increased by 13% for 4 vol.%. The increase in Δp was 45% at 4% vol.%

*Exp. = experimental, Num. = Numerical, ϕ = volume fraction, CNT = carbon nanotube, MWCNT = multi-wall CNT, FWMCNT = functionalized-MWCNT, Ca = gum Arabic, Cys = cysteine, U = overall heat transfer coefficient.

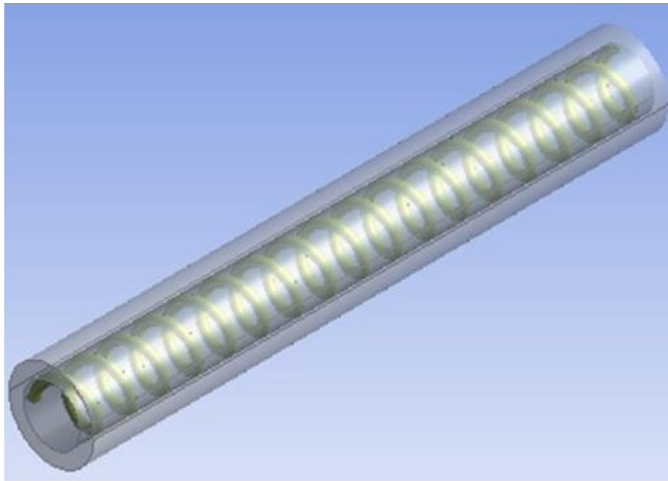


Fig. 6. Three-dimensional model of DPHEx with spring inserts [91], reused with permission from Elsevier license number 5016680360745..

evaluation criterion (PEC) and the overall performance of DPHEx combined with vortex generator was enhanced. The optimal performance of the HEX was maintained at pitch vortex generator ratio, angle, and annulus Re of 0.18, 0.5235 (rad), and 20,000, respectively. Poongavanam et al. analyzed the heat transfer and pressure drop in the DPHEx, where the inner surface was modified rough surface [98]. The experimental results indicated that the roughened tube surface had an appreciable effect on the HEX performance. The HTC of the MWCNT/ethylene glycol at 0.6% was enhanced by about 115% at 0.04 kg/s mass flow rate. The summary of the DPHExs performance enhancement with respect to different parameters such as the geometry of HEX, material, size, ϕ are presented in Table 2.

2.3. Shell and helically coiled tube heat exchangers (SHCTHExs)

The compact size and relatively high operating temperatures are the main advantages of the shell and helically coiled tube HEX

(SHCTHEx) than the conventional shell and tube HEX. The SHCTHEx ensures a high turbulence flow intensity, so it magnifies the HTC as compared to that for the straight tube HEX [99,100–102]. The SHCTHEx is preferred for the medium and high heat duties [16]. The flow of the working fluid into the helically coiled tube produces a centrifugal force, thus generating a secondary flow that improves the heat transfer characteristics; however, it elevates the pressure drop compared to a straight tube [103–106]. Different technologies employ the SHCTHEx, such as heat recovery processes, food processing, refrigeration, air-conditioning systems, etc. [107–109].

Jamshidi et al. studied the intensification of heat transfer rate in the SHCTHEx shown in Fig. 11 [110]. The Taguchi-method was utilized to study the effect of the fluid flow and the geometrical parameters on the thermal performance of the HEX. The optimum operating and geometrical parameters were 0.0116 mm, 0.018 mm, 3 Lit/min, and 3 Lit/min for the coil diameter, pitch, cold flowrate, and hot flow-rate, respectively. The convective heat transfer and pressure drop of a double-pipe HCTHEx for both laminar and turbulent flow using Al_2O_3 /water NF at different ϕ were investigated by Wu et al. [111]. The results showed that increasing ϕ from 0.78 to 7.04 wt.% improved the heat transfer by 0.37 and 3.43% for laminar and turbulent flow, respectively. Similarly, Kumar et al. studied the heat transfer and friction factor of a SHCTHEx employing NF of Al_2O_3 /water at ϕ of 0.1 – 0.8 vol.% [112]. The experimental results showed that the U , h , and Nu number for the NF with 0.8 vol.% were enhanced by 24, 25, and 28%, respectively, however increasing the ϕ raised the friction factor.

Srinivas and Venu Vinod studied the heat transfer of a SHCTHEx utilizing CuO/water NF with different ϕ of 0.3 – 2 wt.% experimentally [113]. The results revealed that utilizing CuO/water NF enhanced the heat transfer by increasing the Dean number (De) and ϕ . Kannadasan et al. experimentally studied the heat transfer and pressure drop of a SHCTHEx with different orientations utilizing CuO/water NF with variable ϕ [114]. The results indicated that increasing the De and ϕ improved the Nu . Whereas increasing the ϕ and decreasing the De increased the friction factor (f) as illustrated in Fig. 12. Furthermore, suggested correlations to compute the coil Nu were developed for the turbulent fluid flow. Srinivas and Venu Vinod experimentally investigated the heat transfer and effectiveness of a SHCTHEx utilizing CuO/water, Al_2O_3 /water, and TiO_2 /water NFs at different ϕ of 0.3 –

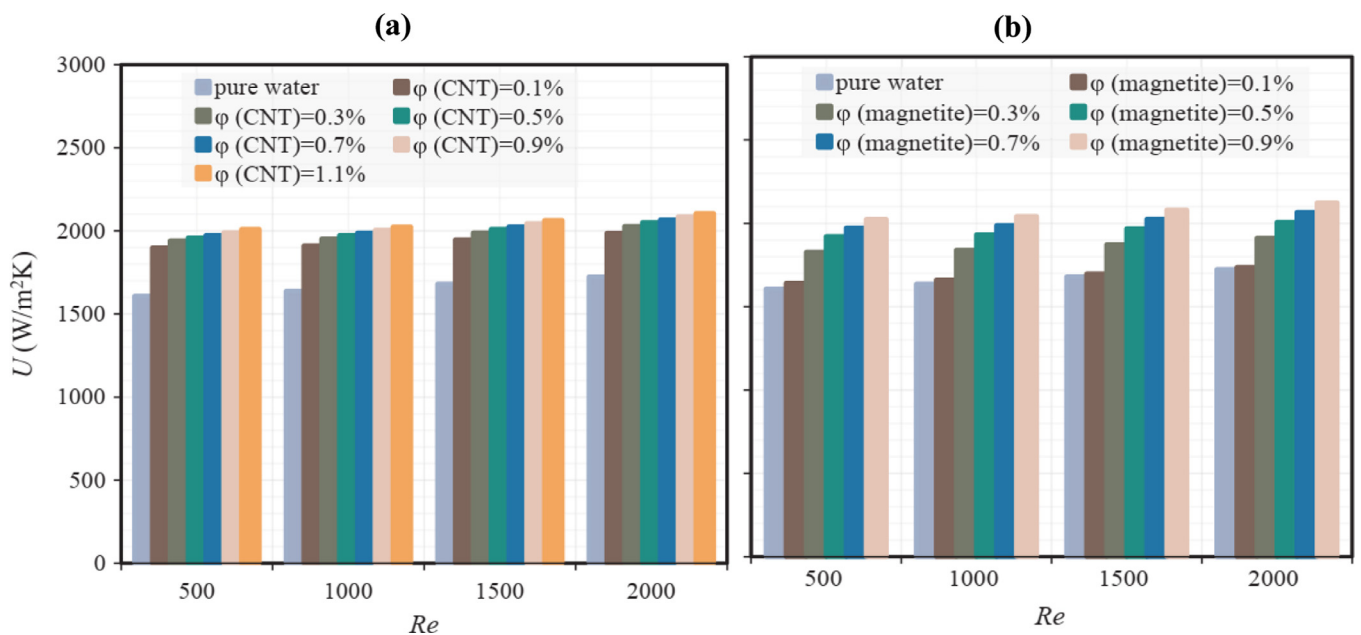


Fig. 7. Overall heat transfer coefficient (U) versus Reynolds number (Re) with the effect for of (a) CNT concentration of 0.7 vol.% (b) magnetite concentration of 0.7 vol.% [93], reused with permission from Elsevier license number 5016680952574.

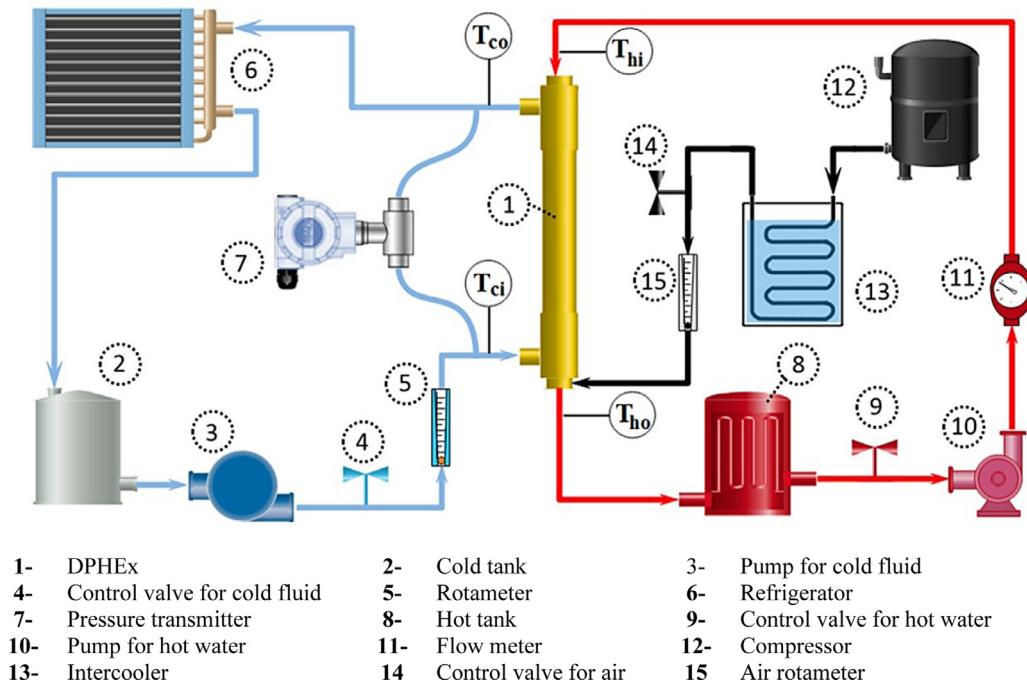


Fig. 8. Experimental setup of the proposed system [94], reused with permission from Elsevier license number 5016681103231.

2 wt.% [115]. The results showed that regarding to the thermophysical properties of different NFs, the effectiveness of the SHTHEx employing Al_2O_3 , CuO, and TiO_2 /water NF were increased by 30.37, 32.7, and 26.8%, respectively.

Elshazly et al. studied the performance of a horizontal SHCTHEx utilizing a $\gamma\text{-Al}_2\text{O}_3$ /water NF [116]. During the study, the coil torsion ($p_c/\pi D_c$) was varied from 0.0442 to 0.1348, and ϕ up to 2 vol.%. The experimental results showed that reducing the coil torsion enhanced the heat transfer but raised the friction factor. Additionally, correlations were developed based on the experimental results to compute the average Nu , and friction factor. Fule et al. studied the heat transfer performance of the SHCTHEx using CuO/water NF with variable ϕ as

illustrated in Fig. 13 [117]. The experimental results revealed that employing CuO/water NF at 0.1 and 0.5 vol.% enhanced h by 37.3% and 77.7%, respectively. Additionally, increasing Re from 812 to 1895 improved increased h about 4.4 times.

Bhanvase et al. studied the performance of a SHCTHEx in the vertical direction using polyaniline (PANI) nanofibers at ϕ of 0.1 - 0.5 vol.% [118]. The experimental results revealed that the h for 0.1 and 0.5 vol.% PANI was enhanced by 10.52% and 69.62%, respectively. Jamshidi et al. explored the performance and friction factor of SHCTHEx utilizing Al_2O_3 /water NF at ϕ of 1 and 2 vol.% numerically

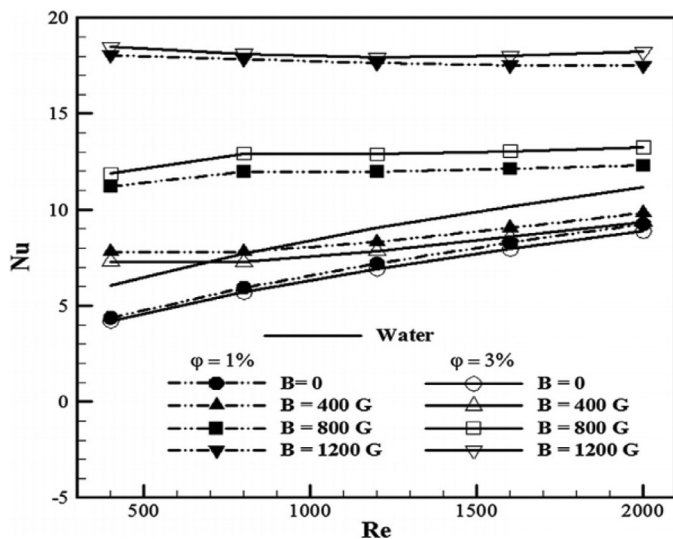


Fig. 9. Nusselt number (Nu) versus Reynold number (Re) at different magnetic field intensities and volume fractions [95], reused with permission from Elsevier license number 5016681342022.

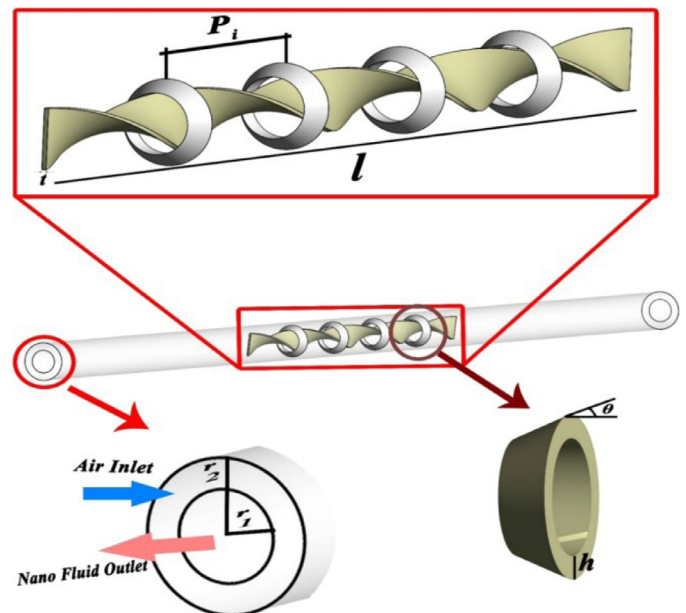


Fig. 10. Geometry details of the combined vortex generators and the twisted tape turbulator [97], reused with permission from Elsevier license number 5016681495129..

Table 2
Summary of the performance of double-pipe heat exchanger (DPHEX).

Ref.	Study	Flow direction	Nanoparticles	Size, nm	Concentration (φ)	Based fluid	Main findings
Kassim and Lahij [90]	Num. and Exp.	Counter-flow	SiO ₂	15–20	0.1–3 vol.%	water	<ul style="list-style-type: none"> The Nu_c and performance factor enhanced by 15.72%, 11.51%, and 11.57% due to using SiO₂/water NF.
Gnanavel et al. [91]	Num.	Spiral Spring insert	TiO ₂ , CuO, BeO, ZnO	NA	NA	water	<ul style="list-style-type: none"> The thermal performance factor due to using TiO₂, BeO, CuO, ZnO/water NFs was 1.879, 1.795, 1.798, and 1.601, respectively.
Shahsavari et al. [93]	Num.	Counter-flow	Hybrid nanofluid of CNT-Fe ₃ O ₄	NA	0.01–0.9 vol.%, (Fe ₃ O ₄) 0.05–1.35 vol.%, (CNT) 0.1 and 0.5 vol.%	water	<ul style="list-style-type: none"> The optimum concentration values of Fe₃O₄ and CNT were 0.88% and 1.1%, respectively.
Jafarizad and Heyhat [94]	Exp.	Counter-flow	SiO ₂	12	0.1 and 0.5 vol.%	water	<ul style="list-style-type: none"> The maximum heat transfer enhancement was achieved at 0.5% concentration.
Bezaatpour and Goharkhah [95]	Num.	Mini HEx	Fe ₃ O ₄	20 nm	1 and 3 vol.%	water	<ul style="list-style-type: none"> Air bubble injection enhanced the exergy efficiency up to 58.1%.
Singh and Sarkar [96]	Num.	With wire coil turbulator	Al ₂ O ₃ –MgO	50 (Al ₂ O ₃) 90 (MgO)	0.1 vol.%	water	<ul style="list-style-type: none"> Utilizing external magnetic field enhanced the heat transfer up to 320% with a little increase of pressure drop.
Arjmandi et al. [97]	Num.	With twisted tape and vortex generators	Al ₂ O ₃	NA	0.04 vol.%	water	<ul style="list-style-type: none"> The Nu and f of Al₂O₃–MgO/water NF using D-, C-D, and C-types wire inserts increased up to 84%, 71% and 47%, and 68%, 57%, and 46%, respectively.
Poongavanam et al. [98]	Exp.	Counter-flow with an inner roughened surface	MWCNT	20–30	0.2–0.6 vol.%	ethylene glycol	<ul style="list-style-type: none"> The pitch ratio of vortex had a prevalent impact on Nu and f, which increased the efficiency up to five times compared with the original case. Using 0.6 vol.% MWCNT enhanced the h up to 115%.

*Exp. = experimental, Num. = Numerical, φ = volume fraction, NA: not applicable or value not directly available.

[119]. Taguchi-method was used to investigate the effect of geometrical parameters and fluid flow behavior, as shown in Fig. 14. The results indicated that the essential geometrical parameters were the constant tube diameter and length of the helically coiled tube. Moreover, increasing the φ and Re enhanced Nu , while increasing the friction factor. Similarly, Bahrehmand and Abbassi numerically studied the heat transfer and pressure drop in a SHCTHEX using Al₂O₃/water NF at φ of 0.1 to 0.3 vol.% [120]. During the experiments, the Reynolds number in coil (Re_c) changed from 9000 to 36,000, while for the shell (Re_{sh}) it varied from 600 to 2600. The results showed that the heat transfer rate was enhanced, while the pressure drop was elevated at higher φ . Additionally, the HEx effectiveness was enhanced by increasing the diameters of coil and tube and increasing the φ , whereas it reduced with increasing the mass flow rate.

Akbaridoust et al. studied numerically and experimentally the heat transfer and pressure drop characteristics for a coiled tube with different curvature ratios utilizing CuO/water NF [121]. The results revealed that the increased coil curvature ratio, Re , and φ enhanced the h and the pressure drop. Furthermore, the heat transfer rate of the helically coiled tube was greater as compared to the straight tube. Moreover, the performance index of the helical coil was enhanced with increasing the coil curvature ratio. Rakhsha et al. investigated the thermal performance and pressure drop of through a helically coiled tube in a horizontal direction utilizing CuO/water NF at 0.1 vol.% [122]. The results showed an increased pressure drop (Δp) and h by 16–17% and 14–16%, respectively.

Maghrabie et al. studied the effect of the inclination angle of a SHCTHEX on its performance employing water and SiO₂/ and Al₂O₃/water NFs [123]. The results showed that changing the HEx orientation from horizontal to vertical positions enhanced the Nu_c by 11%, 8.3%, and 7.5% for water, Al₂O₃/water, and SiO₂/water NFs at φ of 0.1 vol.%, respectively. Additionally, due to the superior thermophysical properties of Al₂O₃ NPs, the HEx vertical orientation and Re_c of 6000 for 0.1 vol.% Al₂O₃/water, the enhancements in Nu_c and HEx effectiveness (ε) increased by 35.7% and 35.5%, respectively. While, for 0.1 vol.% SiO₂/water were 16.2% and 15.6%, respectively. Wang et al. proposed an intelligent optimization design for a SHCTHEX utilizing the genetic algorithm [124]. The results indicated that at the optimal SHCTHEX structure, the heat transfer rate and flux were increased by 101% and 110%, respectively.

Mirgolbabaie et al. assessed the effects of tube diameter, coil pitch, and shell mass flow rate on h_{sh} in SHCTHEX based on the fluid-to-fluid HEx boundary conditions [125]. The results indicated that increasing the coil pitch in the medium range decreased the h while increasing it up to twice the tube diameter increased the h . Moreover, the h decreased by elevating the tube diameter for the same coil pitch. Wanga et al. proposed a new design of cylindrical SHCTHEX with a finned tube, as shown in Fig. 15, and analyzed the effect of shell mass flow rate and the fin geometry on exergy analysis [126]. The numerical results indicated that increasing the number and height of fins, and shell mass flow rate improved the number of the transfer unit (NTU) and the exergy loss. The exergy loss was found to be only 23.4% of the heat transfer rate. Additionally, correlations to identify the optimum values of the geometrical and operational parameters of SHCTHEX with fins were presented. The thermal performance and friction factor of horizontal SHCTHEX with segmental baffles using γ -Al₂O₃/water NF with sodium dodecylbenzene sulphate as a surfactant were studied by Barzegarian et al. [127]. The experimental results revealed that using NF at φ of 0.03, 0.14, and 0.3 vol% enhanced the Nu up to 9.7%, 20.9%, and 29.8%, respectively, while U was improved by 5.4, 10.3, and 19.1%, respectively. Additionally, the thermal performance factor was enhanced up to 6.5 and 18.9%, for 0.03 and 0.3 vol%, respectively.

Kumar et al. investigated experimentally the increase in heat transfer and pressure drop of the SHCTHEX using Al₂O₃/water NF at variable φ [128]. The results indicated that the Nu for φ of 0.1, 0.4, and

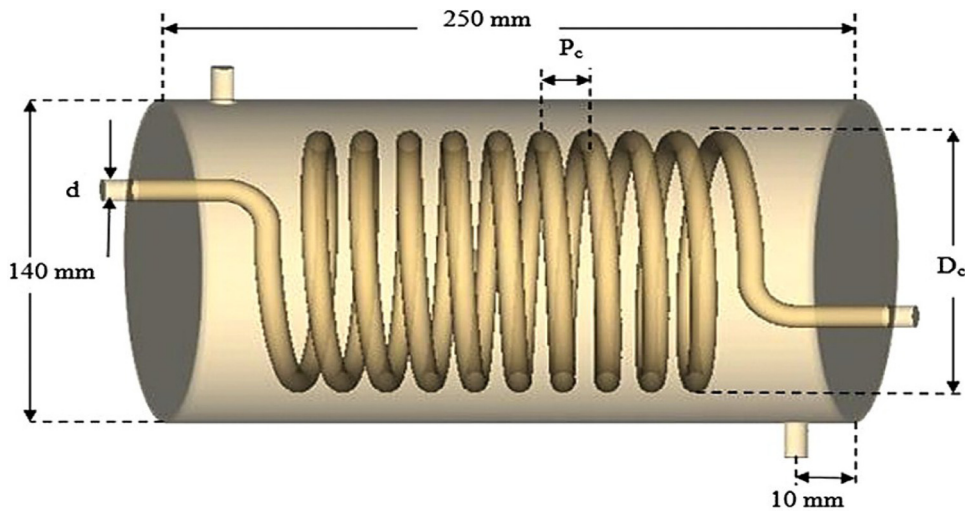


Fig. 11. Geometrical details of the SHCTHEX [110], reused with permission from Elsevier license number 5016690153179.

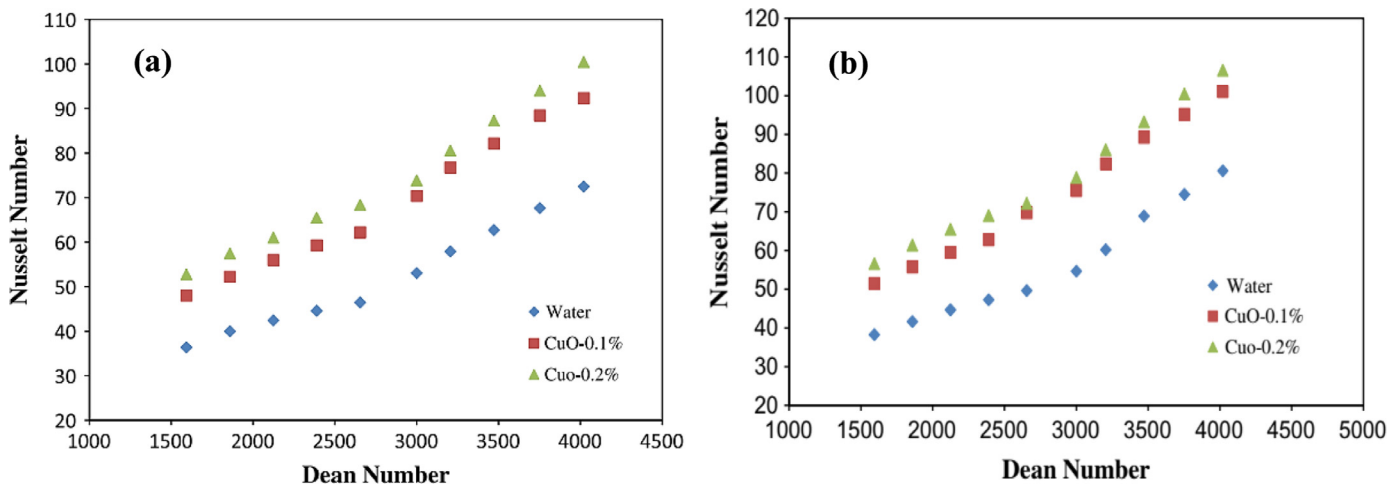


Fig. 12. Coil Nusselt number (Nu) versus Dean number (De) for (a) horizontal position (b) vertical position [114], reused with permission from Elsevier license number 5016690459229.

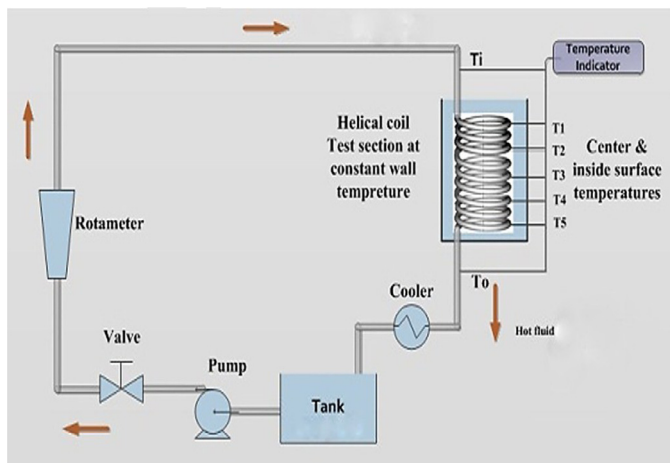


Fig. 13. Schematic of experimental setup proposed by [117], reused with permission from Elsevier license number 5016690619277.

0.8 vol.% was improved by 28, 36, and 56%, respectively. While the pressure drop was raised by 4, 6, and 9%, respectively, at the same ϕ values. The h , Nu , ε , and entropy generation of SHCTHEX using the three-dimensional analysis were assessed numerically. The ϕ of CuO and TiO_2 and mass flow rate were assessed numerically. The results revealed the maximum values of ε for CuO/water and TiO_2 /water NFs at 2 vol.% were 91% and 80%, respectively. The impact of utilizing different nanoparticles of Al_2O_3 , CuO, SiO_2 , and ZnO with different thermophysical properties at various ϕ of 1 - 4 vol.% dispersed into different base fluids such as water, ethylene glycol, and engine oil on the performance of the SHCTHEX was numerically investigated by Narrein and Mohammed [130]. The results indicated that the highest Nu obtained value was for CuO/water NF. Additionally, the engine oil as base fluid with large viscosity had the highest pressure drop (Δp) compared to water and ethylene glycol. Table 3 presents the correlations developed to evaluate the Nu number for coiled tube showing the range of applicable parameters and its error in previous works are listed in. Additionally, the summary of the thermal performance of SHCTHEX using different NFs are listed in Table 4.

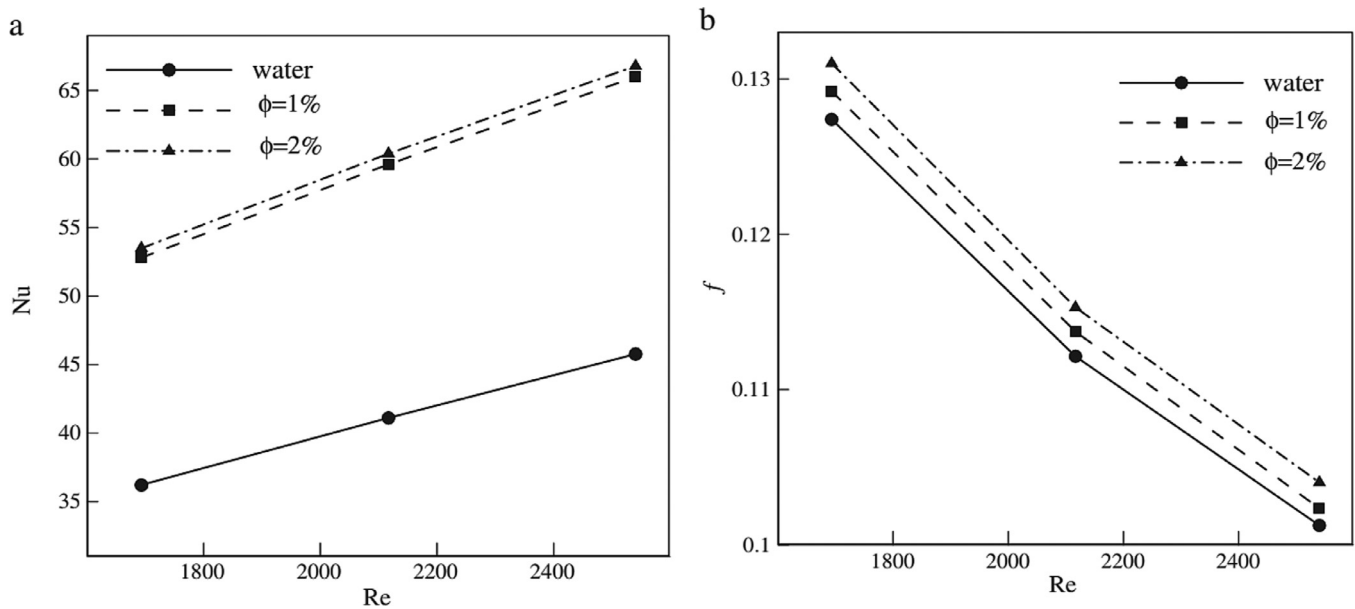


Fig. 14. Effect of suspending Al_2O_3 NPs on (a) Nusselt number (Nu) and (b) friction factor (f) [119], reused with permission from Elsevier license number 5016690787667.

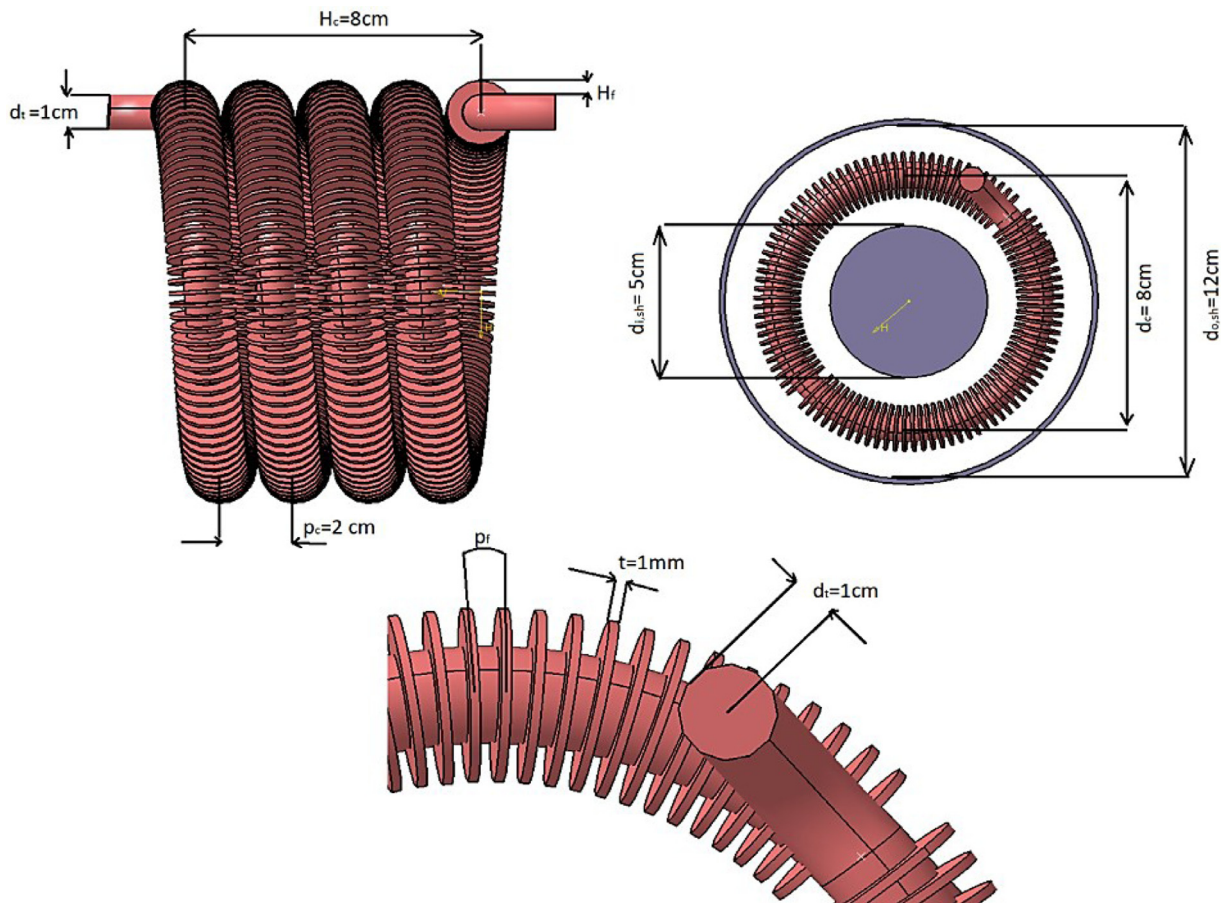


Fig. 15. The finned helical tube proposed by Wanga et al. [126], reused with permission from Elsevier license number 5020220465594.

2.4. Cross-flow heat exchangers (CFHExs)

Due to the manufacturing simplicity, possibly design, low maintenance cost, the cross-flow heat exchangers (CFHExs) are extensively

used in various industrial applications, e.g., petrochemical processes, refrigeration and air conditioning applications, food processing and storage, car radiators, etc. [134–136]. The CFHExs constitute flow across a bundle of cylinders developing flow separation, boundary

Table 3

Correlations for estimating the coil Nusselt number in shell helically coiled tube heat exchangers SHCTHExs.

Ref.	Correlation	Range of parameters	NF
Kannadasan et al. [114]	For vertical orientation: $Nu_c = 1.5De^{0.827} + (d/D)^{0.0008} \phi^{1.1694}$ For horizontal orientation: $Nu_c = 3.6De^{0.67} + (d/D)^{0.0009} \phi^{1.004}$	$1,600 \leq De \leq 4,000$ $0.1\% \leq \phi \leq 0.2\%$	CuO/water
Elshazly et al. [116]	$Nu_c = 0.01974Re^{0.928}Pr^{1.302}\lambda^{-0.04775}\phi^{0.603}$	$5,702 \leq Re \leq 55,101$ $0.1\% \leq \phi \leq 0.2\%$ $0.0442 \leq \lambda \leq 0.1348$ $1.92 \leq Pr \leq 3.9$	γ -Al ₂ O ₃ /water
Maghrabie et al. [123]	For Al ₂ O ₃ /water NF: $Nu_c = 0.0344Re^{0.681}Pr^{0.0144}\phi^{0.2567}$ For SiO ₂ /water NF: $Nu_c = 0.062Re^{0.596}Pr^{0.0168}\phi^{0.2522}$	$1,600 \leq Re \leq 4,000$ $0.017 \leq \theta \text{ (rad.)} \leq 1.571$ $0.005\% \leq \phi \leq 0.02\%$	Al ₂ O ₃ /water SiO ₂ /water
Rakhsha et al. [122]	$Nu_c = 0.061Re^{0.77}Pr^{0.4}(1 + \phi)^{0.22}$	$10,000 \leq Re \leq 90,000$ $4 \leq Pr \leq 5$ $0\% \leq \phi \leq 1\%$	CuO/water
Kahani et al. [131]	For TiO ₂ /water NF: $Nu_c = 0.5He^{0.522}Pr^{0.613}\phi^{0.0815}$ For Al ₂ O ₃ /water NF: $Nu_c = 0.7068He^{0.514}Pr^{0.563}\phi^{0.112}$ $He = De[1 + (\frac{p}{\sigma D})^{2.05}]$	$115.3 \leq He \leq 1311.4$ $5.89 \leq Pr \leq 8.95$ $0.25\% \leq \phi \leq 1\%$	TiO ₂ /water Al ₂ O ₃ /water
Hashemi and Akhavan-Behabadi [132]	$Nu_c = 41.73Re^{0.346}Pr^{0.286}(1 + \phi)^{0.18}$	$Re \leq 125$ $7 \leq Pr \leq 2050$ $0\% \leq \phi \leq 2\%$	CuO/water
Mahdi et al. [133]	$Nu_c = 0.0104De^{0.92}Pr^{0.12}(1 + \phi)^{-0.09}$	$De \leq 2000$ $0.08\% \leq \phi \leq 0.3\%$	Al ₂ O ₃ /water

NA: not applicable or value not directly available.

layer, and vortex formation. The intensification of CFHEs is accomplished using fins on the tubes with different pitch ratios and geometries as well as using a vortex generator or winglet to augment the turbulence intensity [137,138]. Various fin configurations plain fin, slit fin, fin with winglets, and crimped spiral, were investigated experimentally and numerically as illustrated in Fig. 16 by Tang et al. [139]. The performance of the air-side HEX with the above-mentioned configurations of fins was evaluated, and it was found that the HEX with mixed fin had the best performance than that for a fin with vortex generators.

Hussein et al. examined the heat transfer enhancement of car radiators using SiO₂/ and TiO₂/water experimentally [140]. The results showed that according to the thermophysical properties of

each NF, the heat transfer of SiO₂/ and TiO₂/water NFs was enhanced by 32% and 20%, respectively. Moreover, there was an insignificant effect of ϕ of SiO₂/ and TiO₂/water on the friction factor. Hussein et al. [141] discussed the effect of using the SiO₂/water NF on the convective heat transfer of car radiator at ϕ of 1 - 2.5 vol.% both numerically and experimentally. The results showed that the thermal performance intensified with increasing the NF flow rate, ϕ , and inlet temperature, as shown in Fig. 17, achieving the maximum heat transfer enhancement of 46% with 2.5 vol.% SiO₂/water NF.

Hussein et al. [142] examined the thermal performance of the automotive cooling system using SiO₂/ and TiO₂/water at ϕ of 1 - 2 vol.% experimentally. In addition, a statistical model for cooling components based on the input and output parameters was

Table 4

Summary of previous studies of SHCTHEx using nanofluids.

Ref.	Study	Orientation	Nanoparticles	Size, nm	ϕ	Heat exchanger dimensions
Wu et al. [111]	Exp.	Horizontal double pipe	Al ₂ O ₃	40	0.78 - 7.04 wt.%	$d_t = 13.28$ mm, $D_{sh} = 44.4$ mm, $D_c = 254$ mm, $n = 4.5$, $p = 34.5$, $L = 3.591$ m, $Re_t = 3019 - 4824$
Kumar et al. [112]	Exp.	Horizontal	Al ₂ O ₃	13	0.1 - 0.8 vol.%	$d_t = 10.5$ mm, $D_{sh} = 124$ mm, $D_c = 93$ mm, $p = 19$ mm, $L_t = 3.7$ m, $Re_t = 5100 - 8700$
Kannadasan et al. [114]	Exp.	Vertical and horizontal	CuO	10 - 15	0.1 and 0.2 vol.%	$d_t = 9$ mm, $D_{sh} = 124$ mm, $D_c = 93$ mm, $n = 13$, $p = 17$ mm, $L_{sh} = 370$ mm, $De_t = 1600 - 4000$
Srinivas and Venu Vinod [115]	Exp.	Vertical	Al ₂ O ₃ CuO TiO ₂	20-30 40 10	0.3 - 2 wt.%	$d_t = 9.8$ mm, $D_{sh} = 275$ mm, $D_c = 165$ mm, $n = 10$, $p = 32$ mm, $L_t = 6$ m, $\dot{V}_t = 0.5 - 5$ Lit/min
Elshazly et al. [116]	Exp.	Horizontal	γ -Al ₂ O ₃	40	0.5 - 2 vol.%	$D_c = 131$ mm, $n = 10$, p and $L_t =$ variable, $Re_t = 5702 - 55,101$
Fule et al. [117]	Exp.	Vertical	CuO	10	0.1 - 0.5 vol.%	$d_t = 13$ mm, $n = 10$, $p = 35$ mm, $L_t = 10$ m, $Re_t = 812 - 1895$
Bhanvase et al. [118]	Exp.	Vertical	Poly aniline PANI	< 100	0.1 - 0.5 vol.%	$d_t = 13$ mm, $D_{sh} = 275$ mm, $D_c = 290$ mm, $n = 10$, $p = 35$ mm, $L_t = 10$ m, $Re_t = 812 - 1896$
Bahreghmand et al. [120]	Num.	Vertical	Al ₂ O ₃	20	0.1 - 0.3 vol.%	$d_t, 13$ mm, $D_{sh} = 80$ mm, $n = 19.25$, $p = 20$ mm, $L_{sh} = 420$ m, $Re_t = 9000 - 36,000$, $Re_{sh} = 600 - 2600$
Akbaridoust et al. [121]	Exp. and Num.	Helically coiled tube	CuO	68	0.1 - 0.2 vol.%	d_t and n are variables, $\dot{V}_t = 0.1 - 2.5$ Lit/min
Barzegarian et al. [127]	Exp.	Horizontal with segmental baffles	γ -Al ₂ O ₃	15	0.03 - 0.3 vol.%	$d_t = 5$ mm, $D_{sh} = 71.4$ mm, $n = 48$, $L_t = 202$ mm, $Re_t = 200 - 1200$
Kumaret al. [128]	Exp.	Horizontal	Al ₂ O ₃	45 - 50	0.1 - 0.8 vol.%	$d_t = 12$ mm, $D_{sh} = 130$ mm, $n = 48$, $p = 20$ mm, $L_t = 3.7$ m, $D_c = 95$ mm, $Re_t = 9500 - 13,000$

*Exp. = experimental, Num. = Numerical, ϕ = volume fraction.

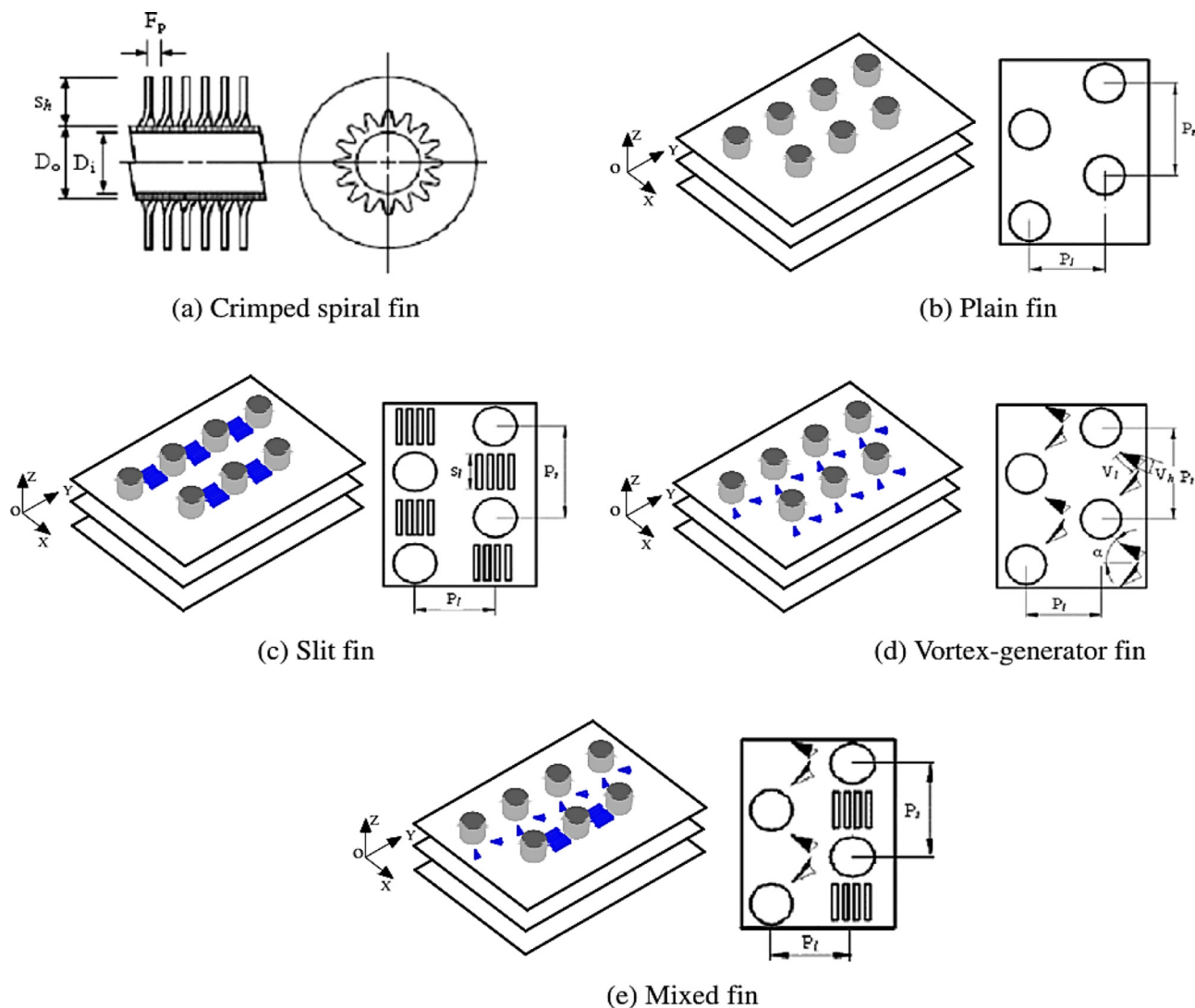


Fig. 16. Heat exchanger with different fin configurations [139], reused with permission from Elsevier license number 5016691432059.

developed. The experimental and the statistical results revealed that the Nu strongly depended on the NFs flowrate, inlet temperature and ϕ . Moreover, the maximum increase in Nu was 22.5% and 11% for SiO_2 / and TiO_2 /water NFs, respectively. Peyghambarzadeh et al. [143] investigated the convective heat transfer of CFHEX as shown in Fig. 18, using Al_2O_3 in water and ethylene glycol (EG) as base fluids at ϕ up to 1 vol.% experimentally. The results showed that the highest Nu enhancement was 40% at the best conditions for both Al_2O_3 /water and Al_2O_3 / ethylene glycol NFs.

Ray and Das studied the cooling of cross-flow, mixed (air)/ unmixed using Al_2O_3 , CuO , and SiO_2 in ethylene glycol/water (60EG/ 40 W wt./wt.) mixture computationally [144]. The authors coded the effectiveness-number of transfer unit method in MATLAB with variable ϕ of 1 – 6 vol.%. The results showed superior cooling performance was obtained at 1 vol.% of NFs, the high inlet temperature of the coolant, low turbulent flow for coolant-side ($Re \leq 5, 500$), and high air-side ($Re \geq 1000$). Furthermore, the SiO_2 -based NF showed the least performance gain, but could still reduce the pumping power. Esfe et al. evaluated the thermal conductivity of ZnO /DWCNT hybrid NF at ϕ of 0.045 - 1.9 vol.% and at inlet temperature of 30 - 50 °C experimentally [145]. The results showed that the thermal conductivity of the hybrid NF was enhanced by increasing the ϕ and

temperature of the NF. The maximum enhancement in thermal conductivity of 24.9% was achieved at a temperature of 50 °C and ϕ of 1.9%. An experimental study to evaluate the thermal performance of car radiator using ZnO /water NF at ϕ of 0.01 - 0.3 vol.% was carried out by Ali et al. [146]. The results indicated that increasing the ϕ enhanced the thermal performance, where at ϕ of 0.2 vol.% the maximum enhancement of heat transfer was 46% as illustrated in Fig. 19.

3. Challenges and future work

Utilizing NFs is a promising practical solution for designing effective HEXs, predominantly when the equipment volume is an essential issue. The sole drawbacks of employing different NFs are its extensive and possible instability. There are some challenges and future work directions that have to be implemented to well assess the intensification of heat transfer and the corresponding possible pressure drop due to the use of NFs in various HEXs for different engineering application such as follow:

- Due to the higher cost of NF relative to BF, experiments should be accomplished taking into consideration the techno-economic of NFs to adjusted the best use of various NFs under different

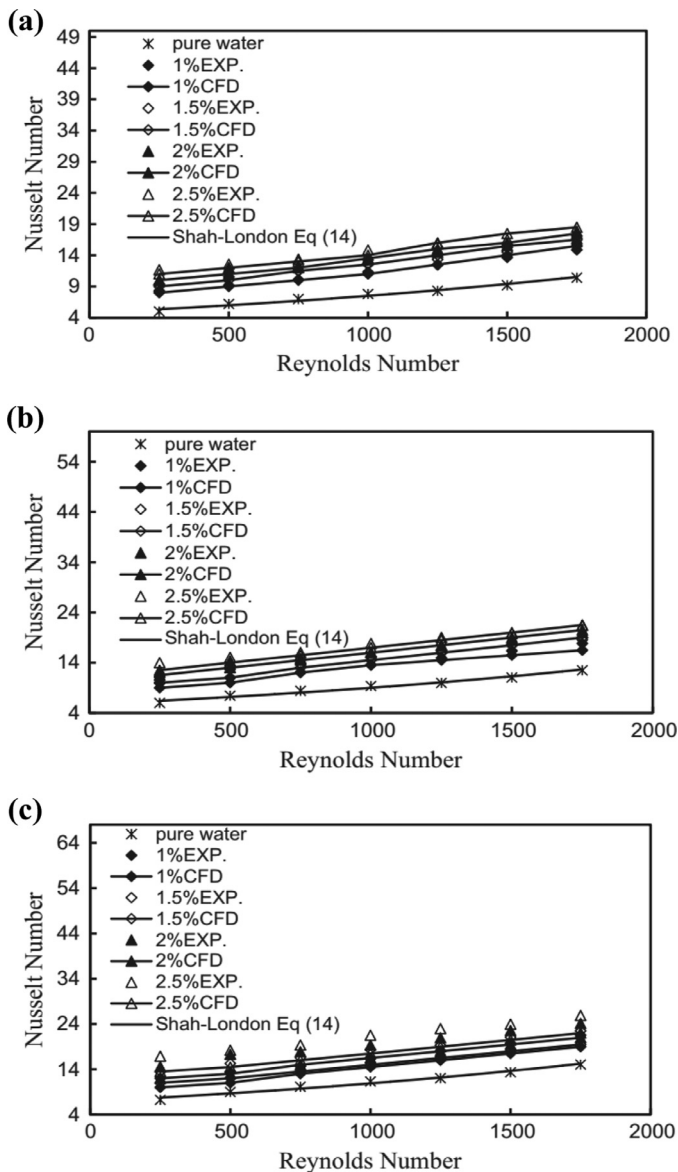


Fig. 17. Nusselt number (Nu) versus Reynolds number (Re) for different inlet temperature (a) 60 °C (b) 70 °C (c) 80 °C [141], reused with permission from Elsevier license number 5016700106544.

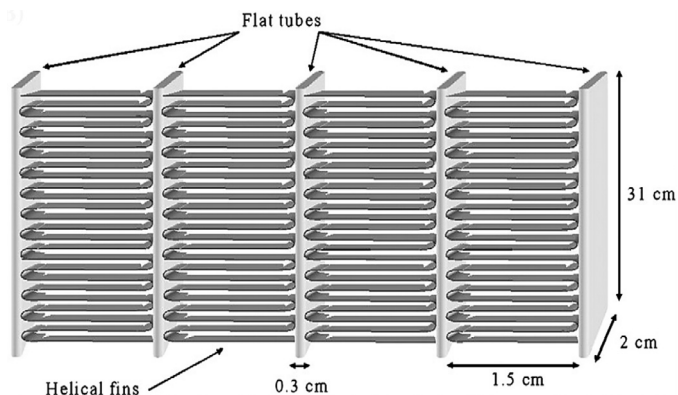


Fig. 18. Schematic of louvered aluminum fin and flat tube in cross-flow heat exchanger [143], reused with permission from Elsevier license number 5016700267568.

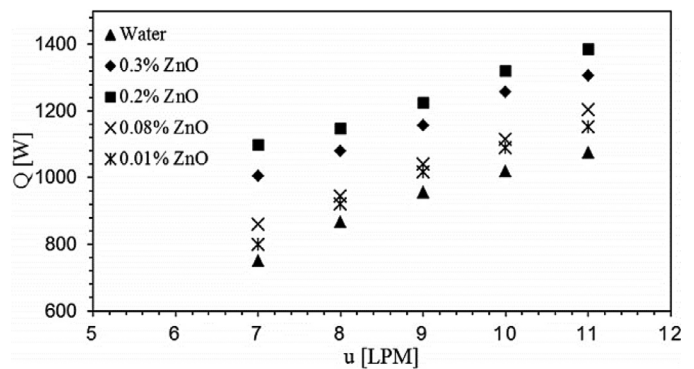


Fig. 19. Heat transfer rate versus the coolant flow rate [146], reused with permission from Elsevier license number 5016700485629.

operating and geometrical conditions of HEx, material and size of NPs, environments, and base fluid.

- Various examined NFs should be tested to assess the best material of NPs for each particular application considering the heat transfer rate, pressure drop, and exergy loss.
- The major challenge behind the applications of the NF in various HExs is the selection of suitable nanomaterials with optimum concentration, long term NF stability, manufacturing, and effective cost of NPsmaterial. It is required to determine the optimum value of volume fraction ϕ to obtain the best thermal performance, lower pressure drop, and NF stability.
- The stability of NFs is a crucial issue, so maintaining the NF stability requires proper NFs preparation and might require the addition of surfactant.
- Hybrid NFs of two different NPs materials with various shapes and sizes may cause higher viscosity leading to a higher pressure drop, increasing the pumping power. Accordingly, attention must be paid to selecting the different materials for hybrid NFs.
- The suitable aspect ratio of nanomaterials pair in hybrid NFs must be selected properly to improve the thermal path between NPs and the synergistic effect, leading to a high heat transfer rate.
- Most of the published investigations were dedicated to water and ethylene glycol as base fluids, while literature is limited concerning other base fluids such as engine oil, silicone oil, refrigerants, etc.
- Heat transfer intensification in HExs based on the active methods such as maintaining the rough surface needs a further precaution to avoid the sedimentation and accumulation of NPs, leading to the deterioration of thermophysical properties of NFs.
- The optimization criterion of HEx indicating the maximized heat transfer rate and reduced cost is required when studying the HExs. In addition, using various optimizing methods based on numerical results, reliable correlations considering the design and operating parameters are required to facilitate optimizing different types of HExs.

4. Conclusions

As a rapid progress report in the applications, NFs for different heat exchangers would be highly useful to the designers, researchers, and engineers working in this critical area to understand the up-to-date achieved efforts properly and identify the advances of utilizing NF for HExs. With this aim, the current work comprehensively reviews the thermal and fluid flow characteristics for different types of HExs, considering the thermophysical properties of NFs, with the following points concluded:

- The thermophysical properties of NFs were systematically investigated, emphasizing the common trends reported of increasing

the thermal conductivity, decreasing the heat capacity, increasing the density, increasing the viscosity, and the possibility of generating a non-Newtonian behavior.

- Utilizing NFs is a promising solution for designing an efficient HEX, specifically when the equipment footprint is critical.
- The superior heat transfer performance of NFs is due to the generation of various forces such as lift, drag, electrostatic, Brownian, van der Waals, and thermophoretic forces.
- Hybrid NFs introduce a better improvement in thermophysical properties, particularly the thermal conductivity compared with that for single/mono NF.
- The pressure drop and pumping power in HEXs increased due to the use of NF and increased with the increase of the concentration of NPs.
- Using different nanofluids with air bubble injection, rough surface, etc., enhances additionally the effectiveness of heat exchange.
- Inducing swirling flow in a HEXs using a magnetic field, twisted tape turbulators, vortex generators, etc., is favorable for a small size heat exchanger at low Reynolds numbers, and high volume concentrations of nanofluid.

References

- [1] D. Reay, C. Ramshaw, A. Harvey, *Process Intensification: Engineering for Efficiency, Sustainability and Flexibility*, Elsevier, 2013.
- [2] M.J. Nee, *Heat Exchanger Engineering Techniques*, ASME Press, 2003.
- [3] J.C. Charpentier, Process intensification by miniaturization, *Chem. Eng. Technol.* 28 (2005) 255–258, doi: [10.1002/ceat.200407026](https://doi.org/10.1002/ceat.200407026).
- [4] F.I. Gómez-Castro, G. Segovia-Hernández, *Process Intensification: Design Methodologies*, Berlin, 2019.
- [5] A. Stankiewicz, T. van Gerven, S. Giorgos, *The Fundamentals of Process Intensification*, Wiley, 2019.
- [6] H. Jouhara, A. Żabnieńska-Góra, N. Khordehghah, D. Ahmad, T. Lipinski, Latent thermal energy storage technologies and applications: a review, *Int. J. Thermofluids*. (2020) 5–6, doi: [10.1016/j.ijft.2020.100039](https://doi.org/10.1016/j.ijft.2020.100039).
- [7] S. Kakac, A.E. Bergles, W.O. Fernandes, Two-phase flow heat exchangers: thermal-hydraulic fundamentals and design, 1st ed., Eds. Hemisphere, Washington, D.C. 1988. <https://books.google.com/books?id=2yrOCAAQBAJ&pgis=1>.
- [8] V. Guichet, N. Khordehghah, H. Jouhara, Experimental investigation and analytical prediction of a multi-channel flat heat pipe thermal performance, *Int. J. Thermofluids*. 5–6 (2020) 100038, doi: [10.1016/j.ijft.2020.100038](https://doi.org/10.1016/j.ijft.2020.100038).
- [9] A.E. Bergles, Some perspectives on enhanced heat transfer second generation heat transfer technology, *J. Heat Transf. Trans. ASME*. 110 (1988) 1082–1096.
- [10] M. Attalla, H.M. Maghrabie, E. Specht, An experimental investigation on fluid flow and heat transfer of rough mini-channel with rectangular cross section, *Exp. Therm. Fluid Sci.* 75 (2016) 199–210, doi: [10.1016/j.expthermflusci.2016.01.019](https://doi.org/10.1016/j.expthermflusci.2016.01.019).
- [11] S.A. Lolja, Momentum and mass transfer on sand paper-roughened surfaces in pipe flow, *Int. J. Heat Mass Transf.* 48 (2005) 2209–2218.
- [12] J. Postlethwaite, U. Lotz, Mass transfer at erosion-corrosion roughened surfaces, *Can. J. Chem. Eng.* 66 (1988) 75–78.
- [13] A.K. Barik, A. Mukherjee, P. Patro, Heat transfer enhancement from a small rectangular channel with different surface protrusions by a turbulent cross flow jet, *Int. J. Therm. Sci.* 98 (2015) 32–41.
- [14] F.P. Berger, K.F. Hau, F.L. Hau, Local mass/heat transfer distribution on surfaces roughened with small square ribs, *Int. J. Heat Mass Transf.* 22 (1979) 1645–1656, doi: [10.1016/0017-9310\(79\)90081-4](https://doi.org/10.1016/0017-9310(79)90081-4).
- [15] S. Alfarawi, S.A. Abdel-Moneim, A. Bodalal, Experimental investigations of heat transfer enhancement from rectangular duct roughened by hybrid ribs, *Int. J. Therm. Sci.* 118 (2017) 123–138, doi: [10.1016/j.ijthermalsci.2017.04.017](https://doi.org/10.1016/j.ijthermalsci.2017.04.017).
- [16] R.K. Shah, D.P. Sekulic, *Fundamentals of Heat Exchanger Design*, John Wiley & Sons, Inc., Hoboken, New Jersey, 2003.
- [17] R.L. Webb, N.H. Kim, *Principles of Enhanced Heat Transfer*, 2nd ed., Taylor & Francis, 2006.
- [18] A.G. Olabi, T. Wilberforce, E.T. Sayed, K. Elsaid, H. Rezk, M.A. Abdelkareem, Recent progress of graphene based nanomaterials in bioelectrochemical systems, *Sci. Total Environ.* 749 (2020) 141225.
- [19] P. Koblinski, R. Philpot, S. Choi, A. Eastman, Mechanisms of heat flow in suspensions of nano-sized particles (nanofluids), *Int. J. Heat Mass Transf.* 45 (2002) 855–863.
- [20] A.G. Olabi, K. Elsaid, M.K.H. Rabaia, A.A. Askalany, M.A. Abdelkareem, Waste heat-driven desalination systems: perspective, *Energy* 209 (2020) 118373, doi: [10.1016/j.energy.2020.118373](https://doi.org/10.1016/j.energy.2020.118373).
- [21] D. Grohmann, Design and Characterization of a Compact Heat Exchanger for use with Nanofluids, Southern Illinois University - Carbondale, 2014.
- [22] M. Bahiraei, Particle migration in nanofluids: a critical review, *Int. J. Therm. Sci.* 109 (2016) 90–113.
- [23] K. Elsaid, E. Taha Sayed, B.A.A. Yousef, M. Kamal Hussien Rabaia, M. Ali Abdelkareem, A.G. Olabi, Recent progress on the utilization of waste heat for desalination: a review, *Energy Convers. Manag.* 221 (2020) 113105, doi: [10.1016/j.enconman.2020.113105](https://doi.org/10.1016/j.enconman.2020.113105).
- [24] M.A. Abdelkareem, M.E.H. Assad, E.T. Sayed, B. Soudan, Recent progress in the use of renewable energy sources to power water desalination plants, *Desalination* 435 (2018) 97–113.
- [25] K. Elsaid, A. Olabi, T. Wilberforce, M.A. Abdelkareem, E. Taha, Environmental impacts of nanofluids: a review, *Sci. Total Environ.* 763 (2021) 144202.
- [26] E.T. Sayed, T. Wilberforce, K. Elsaid, M.K.H. Rabaia, M.A. Abdelkareem, K.J. Chae, A.G. Olabi, A critical review on environmental impacts of renewable energy systems and mitigation strategies: wind, hydro, biomass and geothermal, *Sci. Total Environ.* 766 (2021) 144505, doi: [10.1016/j.scitotenv.2020.144505](https://doi.org/10.1016/j.scitotenv.2020.144505).
- [27] M.K.H. Rabaia, M.A. Abdelkareem, E.T. Sayed, K. Elsaid, K.J. Chae, T. Wilberforce, A.G. Olabi, Environmental impacts of solar energy systems: a review, *Sci. Total Environ.* 754 (2021) 141989, doi: [10.1016/j.scitotenv.2020.141989](https://doi.org/10.1016/j.scitotenv.2020.141989).
- [28] M.A. Abdelkareem, K. Elsaid, T. Wilberforce, M. Kamil, E.T. Sayed, A. Olabi, Environmental aspects of fuel cells: a review, *Sci. Total Environ.* 752 (2021) 141803, doi: [10.1016/j.scitotenv.2020.141803](https://doi.org/10.1016/j.scitotenv.2020.141803).
- [29] A. Afzal, I. Nawfal, I.M. Mahbubul, S.S. Kumbar, An overview on the effect of ultrasonication duration on different properties of nanofluids, *J. Therm. Anal. Calorim.* 135 (2019) 393–418, doi: [10.1007/s10973-018-7144-8](https://doi.org/10.1007/s10973-018-7144-8).
- [30] A.I. Khan, A. Valan Arasu, A review of influence of nanoparticle synthesis and geometrical parameters on thermophysical properties and stability of nanofluids, *Therm. Sci. Eng. Prog.* 11 (2019) 334–364, doi: [10.1016/j.tsep.2019.04.010](https://doi.org/10.1016/j.tsep.2019.04.010).
- [31] L. Qiu, N. Zhu, Y. Feng, E.E. Michaelides, G. Żyła, D. Jing, X. Zhang, P.M. Norris, C.N. Markides, O. Mahian, A review of recent advances in thermophysical properties at the nanoscale: from solid state to colloids, *Phys. Rep.* 843 (2020) 1–81, doi: [10.1016/j.physrep.2019.12.001](https://doi.org/10.1016/j.physrep.2019.12.001).
- [32] P. Selvakumar, S. Suresh, Use of Al₂O₃-Cu/water hybrid nanofluid in an electronic heat sink, *IEEE Trans. Components Packag. Manuf. Technol.* 2 (2012) 1600–1607, doi: [10.1109/TCPMT.2012.2211018](https://doi.org/10.1109/TCPMT.2012.2211018).
- [33] M.H. Al-Kashed, G. Dzido, M. Korpys, J. Smolka, J. Wójcik, Investigation on the CPU nanofluid cooling, *Microelectron. Reliab.* 63 (2016) 159–165, doi: [10.1016/j.microrel.2016.06.016](https://doi.org/10.1016/j.microrel.2016.06.016).
- [34] J. Wang, G. Li, T. Li, M. Zeng, B. Sundén, Effect of various surfactants on stability and thermophysical properties of nanofluids, *J. Therm. Anal. Calorim.* (2020), doi: [10.1007/s10973-020-09381-9](https://doi.org/10.1007/s10973-020-09381-9).
- [35] H.M. Maghrabie, M. Attalla, H.E. Fawaz, M. Khalil, Impingement/effusion cooling of electronic components with cross-flow, *Appl. Therm. Eng.* 151 (2019) 199–213, doi: [10.1016/j.applthermaleng.2019.101.06](https://doi.org/10.1016/j.applthermaleng.2019.101.06).
- [36] H.M. Maghrabie, M. Attalla, H.E. Fawaz, M. Khalil, Numerical investigation of heat transfer and pressure drop of in-line array of heated obstacles cooled by jet impingement in cross-flow, *Alexandria Eng. J.* 56 (2017) 285–296, doi: [10.1016/j.aej.2016.12.022](https://doi.org/10.1016/j.aej.2016.12.022).
- [37] M. Corcione, Empirical correlating equations for predicting the effective thermal conductivity and dynamic viscosity of nanofluids, *Energy Convers. Manag.* 52 (2011) 789–793, doi: [10.1016/j.enconman.2010.06.072](https://doi.org/10.1016/j.enconman.2010.06.072).
- [38] A.O. Borode, N.A. Ahmed, P.A. Olubambi, A review of heat transfer application of carbon-based nanofluid in heat exchangers, *Nano-Struct. Nano-Objects* 20 (2019) 100394, doi: [10.1016/j.nanoso.2019.100394](https://doi.org/10.1016/j.nanoso.2019.100394).
- [39] M. Attalla, Experimental investigation of heat transfer and pressure drop of SiO₂/water nanofluid through conduits with altered cross-sectional shapes, *Heat Mass Transf. Und Stoffuebertragung*. 55 (2019) 3427–3442, doi: [10.1007/s00231-019-02668-0](https://doi.org/10.1007/s00231-019-02668-0).
- [40] S.K. Das, U.S. Choi, W. Yu, T. Pradeep, *Nanofluids: Science and Technology*, John Wiley & Sons, Inc., Hoboken, New Jersey, 2007.
- [41] A.M. Fsadni, J.P.M. Whitty, A.A. Adeniyi, J. Simo, H.L. Brooks, A review on the application of nanofluids in coiled tube heat exchangers, in: M.J. Jackson, W. Ahmed (Eds.), *Micro and Nanomanufacturing Volume II*, Springer International Publishing AG, 2018, doi: [10.1007/978-3-319-67132-1](https://doi.org/10.1007/978-3-319-67132-1).
- [42] B. Sundén, Z. Wu, Performance of heat exchangers using nanofluid, in: V. Bianco, O. Manca, S. Nardini, K. Vafai (Eds.), *Heat Transfer Enhancement with Nanofluids*, CRC Press, Taylor & Francis Group, New York, 2015.
- [43] A. Iqbal, M.S. Mahmoud, E.T. Sayed, K. Elsaid, M.A. Abdelkareem, H. Alawadhi, A.G. Olabi, Evaluation of the nanofluid-assisted desalination through solar stills in the last decade, *J. Environ. Manag.* 277 (2021) 111415.
- [44] O. Mahian, L. Kolsi, M. Amani, P. Estellé, G. Ahmadi, C. Kleinstreuer, J.S. Marshall, M. Siavashi, R.A. Taylor, H. Niazmand, S. Wongwises, T. Hayat, A. Kolanjiyil, A. Kaseaia, I. Pop, Recent advances in modeling and simulation of nanofluid flows-Part I: fundamentals and theory, *Phys. Rep.* 790 (2019) 1–48, doi: [10.1016/j.physrep.2018.11.004](https://doi.org/10.1016/j.physrep.2018.11.004).
- [45] F. Yousefi, Z. Amoozandeh, new model to predict the densities of nanofluids using statistical mechanics and artificial intelligent plus principal component analysis, *Chin. J. Chem. Eng.* 25 (2017) 1273–1281.
- [46] M. Hassanpour, B. Vaferi, M.E. Masoumi, Estimation of pool boiling heat transfer coefficient of alumina water-based nanofluids by various artificial intelligence (AI) approaches, *Appl. Therm. Eng.* 128 (2018) 1208–1222.

- [47] M. Afrand, M.H. Esfe, E. Abedini, H. Teimouri, Predicting the effects of magnesium oxide nanoparticles and temperature on the thermal conductivity of water using artificial neural network and experimental data, *Phys. E Low-Dimens. Syst. Nanostruct.* 87 (2017) 242–247.
- [48] M.K. Meybodi, S. Naseri, A. Shokrollahi, A. Daryasafar, Prediction of viscosity of water-based Al_2O_3 , TiO_2 , SiO_2 , and CuO nanofluids using a reliable approach, *Chemom. Intell. Lab. Syst.* 149 (2015) 60–69.
- [49] H. Karimi, F. Yousefi, M.R. Rahimi, Correlation of viscosity in nanofluids using genetic algorithm-neural network (GA-NN), *Heat Mass Transf.* 47 (2011) 1417–1425.
- [50] M.H. Esfe, M. Bahiraei, O. Mahian, Experimental study for developing an accurate model to predict viscosity of CuO –ethylene glycol nanofluid using genetic algorithm based neural network, *Powder Technol.* 338 (2018) 383–390.
- [51] M. Mehrabi, M. Sharifpur, J.P. Meyer, Application of the FCM-based neuro-fuzzy inference system and genetic algorithm-polynomial neural network approaches to modelling the thermal conductivity of alumina–water nanofluids, *Int. Commun. Heat Mass Transf.* 39 (2012) 971–977.
- [52] R.S. Vajha, D.K. Das, D.P. Kulkarni, Development of new correlations for convective heat transfer and friction factor in turbulent regime for nanofluids, *Int. J. Heat Mass Transf.* 53 (2010) 4607–4618, doi: [10.1016/j.jheatmasstransfer.2010.06.032](https://doi.org/10.1016/j.jheatmasstransfer.2010.06.032).
- [53] R. Saidur, K.Y. Leong, H.A. Mohammad, A review on applications and challenges of nanofluids, *Renew. Sustain. Energy Rev.* 15 (2011) 1646–1668, doi: [10.1016/j.rser.2010.11.035](https://doi.org/10.1016/j.rser.2010.11.035).
- [54] K. Abdul Hamid, W.H. Azmi, R. Mamat, K.V. Sharma, Heat transfer performance of TiO_2 – SiO_2 nanofluids in a tube with wire coil inserts, *Appl. Therm. Eng.* 152 (2019) 275–286, doi: [10.1016/j.applthermaleng.2019.02.083](https://doi.org/10.1016/j.applthermaleng.2019.02.083).
- [55] J. Sarkar, P. Ghosh, A. Adil, A review on hybrid nanofluids: recent research, development and applications, *Renew. Sustain. Energy Rev.* 43 (2015) 164–177, doi: [10.1016/j.rser.2014.11.023](https://doi.org/10.1016/j.rser.2014.11.023).
- [56] T.R. Shah, H.M. Ali, Applications of hybrid nanofluids in solar energy, practical limitations and challenges: a critical review, *Sol. Energy.* 183 (2019) 173–203.
- [57] D. Dhinesh Kumar, A. Valan Arasu, A comprehensive review of preparation, characterization, properties and stability of hybrid nanofluids, *Renew. Sustain. Energy Rev.* 81 (2018) 1669–1689, doi: [10.1016/j.rser.2017.05.257](https://doi.org/10.1016/j.rser.2017.05.257).
- [58] B. Munkhbayar, M.R. Tanshen, J. Jeoun, H. Chung, H. Jeong, Surfactant-free dispersion of silver nanoparticles into MWCNT-aqueous nanofluids prepared by one-step technique and their thermal characteristics, *Ceram. Int.* 39 (2013) 6415–6425, doi: [10.1016/j.ceramint.2013.01.069](https://doi.org/10.1016/j.ceramint.2013.01.069).
- [59] K. Thulukkanam, *Heat Exchanger Design Handbook*, Marcel Dekker, New York, New York, 2000.
- [60] R.K. Shah, W.W. Focke, Plate heat exchanger and their design theory, "Heat Transf. Equipment Desing.", R. K. Shah, E. C. Subbarao, and R. A. Mashelkar, eds. Hemisphere, Washington, pp. 227–254, 1988.
- [61] L. Wang, Bengt Sundén, R.M. Manglik, *Plate Heat Exchangers: Design, Applications and Performance*, Wit Press, Boston, 2007.
- [62] J.E. Hesselgreaves, *Compact Heat Exchangers: Selection, Design and Operation*, Elsevier Science Ltd., Pergamon, Oxford, UK, 2001.
- [63] L. Wang, B. Sundén, R.M. Manglik, *Plate Heat Exchangers: Design, Applications and Performance*, Wit Press, 2010, doi: [10.1081/E-EAFE](https://doi.org/10.1081/E-EAFE).
- [64] S. Kakaç, H. Liu, A. Pramuanjaroenkij, *Heat Exchangers Selection, Rating, and Thermal Design*, third edit, CRC Press, 2010 www.mhhe.com.
- [65] M.M. Abu-Khader, Plate heat exchangers: recent advances, *Renew. Sustain. Energy Rev.* 16 (2012) 1883–1891, doi: [10.1016/j.rser.2012.01.009](https://doi.org/10.1016/j.rser.2012.01.009).
- [66] T.M. Abou Elmaaty, A.E. Kabeel, M. Mahgoub, Corrugated plate heat exchanger review, *Renew. Sustain. Energy Rev.* 70 (2017) 852–860, doi: [10.1016/j.rser.2016.11.266](https://doi.org/10.1016/j.rser.2016.11.266).
- [67] M. Attalla, H.M. Maghrabie, Investigation of effectiveness and pumping power of plate heat exchanger with rough surface, *Chem. Eng. Sci.* 211 (2020) 115277, doi: [10.1016/j.ces.2019.115277](https://doi.org/10.1016/j.ces.2019.115277).
- [68] M.N. Pantzali, A.G. Kanaris, K.D. Antoniadis, A.A. Mouza, S.V. Paras, Effect of nanofluids on the performance of a miniature plate heat exchanger with modulated surface, *Int. J. Heat Fluid Flow.* 30 (2009) 691–699, doi: [10.1016/j.jheatfluidflow.2009.02.005](https://doi.org/10.1016/j.jheatfluidflow.2009.02.005).
- [69] B. Sun, C. Peng, R. Zuo, D. Yang, H. Li, Investigation on the flow and convective heat transfer characteristics of nanofluids in the plate heat exchanger, *Exp. Therm. Fluid Sci.* 76 (2016) 75–86, doi: [10.1016/j.expthermflusci.2016.03.005](https://doi.org/10.1016/j.expthermflusci.2016.03.005).
- [70] S.D. Pandey, V.K. Nema, Experimental analysis of heat transfer and friction factor of nanofluid as a coolant in a corrugated plate heat exchanger, *Exp. Therm. Fluid Sci.* 38 (2012) 248–256, doi: [10.1016/j.expthermflusci.2011.12.013](https://doi.org/10.1016/j.expthermflusci.2011.12.013).
- [71] M. Taws, C.T. Nguyen, N. Galanis, I. Gherasim, Experimental investigation of nanofluid heat transfer in a plate heat exchanger, in: *Proceedings of the ASME Summer Heat Transfer Conference HT2012*, 2012, pp. 1–8.
- [72] R. Barzegarian, M.K. Moraveji, A. Aloueyan, Experimental investigation on heat transfer characteristics and pressure drop of BPHE (brazen plate heat exchanger) using TiO_2 –water nanofluid, *Exp. Therm. Fluid Sci.* 74 (2016) 11–18, doi: [10.1016/j.expthermflusci.2015.11.018](https://doi.org/10.1016/j.expthermflusci.2015.11.018).
- [73] D. Huang, Z. Wu, B. Sunden, Pressure drop and convective heat transfer of Al_2O_3 /water and MWCNT/water nanofluids in a chevron plate heat exchanger, *Int. J. Heat Mass Transf.* 89 (2015) 620–626, doi: [10.1016/j.applthermaleng.2013.06.051](https://doi.org/10.1016/j.applthermaleng.2013.06.051).
- [74] D. Huang, Z. Wub, B. Sunden, Effects of hybrid nanofluid mixture in plate heat exchangers, *Exp. Therm. Fluid Sci.* 72 (2016) 190–196.
- [75] M. Goodarzi, A. Amiri, M. Shahab, M. Reza, A. Karimipour, E. Mohseni, M. Dahari, Investigation of heat transfer and pressure drop of a counter flow corrugated plate heat exchanger using MWCNT based nanofluids, *Int. Commun. Heat Mass Transf.* 66 (2015) 172–179.
- [76] M. Attalla, H.M. Maghrabie, An experimental study on heat transfer and fluid flow of rough plate heat exchanger using Al_2O_3 /water nanofluid, *Exp. Heat Transf.* 33 (2020) 261–281, doi: [10.1080/08916152.2019.1625469](https://doi.org/10.1080/08916152.2019.1625469).
- [77] M.N. Pantzali, A.A. Mouza, S.V. Paras, Investigating the efficiency of nanofluids as coolants in plate heat exchangers (PHE), *Chem. Eng. Sci.* 64 (2009) 3290–3300, doi: [10.1016/j.ces.2009.04.004](https://doi.org/10.1016/j.ces.2009.04.004).
- [78] A.K. Tiwari, P. Ghosh, J. Sarkar, Performance comparison of the plate heat exchanger using different nanofluids, *Exp. Therm. Fluid Sci.* 49 (2013) 141–151, doi: [10.1016/j.expthermflusci.2013.04.012](https://doi.org/10.1016/j.expthermflusci.2013.04.012).
- [79] R. Barzegarian, M. Keshavarz, A. Aloueyan, Experimental investigation on heat transfer characteristics and pressure drop of BPHE (brazen plate heat exchanger) using TiO_2 – water nanofluid, *Exp. Therm. Fluid Sci.* 74 (2016) 11–18, doi: [10.1016/j.expthermflusci.2015.11.018](https://doi.org/10.1016/j.expthermflusci.2015.11.018).
- [80] A.E. Kabeel, T. Abou El Maaty, Y. El Samadony, The effect of using nano-particles on corrugated plate heat exchanger performance, *Appl. Therm. Eng.* 52 (2013) 221–229, doi: [10.1016/j.applthermaleng.2012.11.027](https://doi.org/10.1016/j.applthermaleng.2012.11.027).
- [81] N. Afgan, E.U. Schlünder, *Heat Exchangers: Design and Theory Sourcebook*, McGraw-Hill, New York, 1974.
- [82] M.S. Alias, *Design of Small Heat Exchanger (double Pipe Type)*, UMP, 2010.
- [83] T.J. Rennie, V.G.S. Raghavan, Numerical studies of a double-pipe helical heat exchanger, *Appl. Therm. Eng.* 26 (2006) 1266–1273, doi: [10.1016/j.applthermaleng.2005.10.030](https://doi.org/10.1016/j.applthermaleng.2005.10.030).
- [84] K.M. Shirvan, Numerical investigation of heat exchanger effectiveness in a double pipe heat exchanger filled with nanofluid: a sensitivity analysis by response surface methodology, *Powder Technol.* 313 (2017) 99–111.
- [85] R.W. Serth, *Process Heat Transfer: Principles, Applications*, Elsevier Academic Press, 2007.
- [86] T.J. Rennie, V.G.S. Raghavan, Experimental studies of a double-pipe helical heat exchanger, *Exp. Therm. Fluid Sci.* 29 (2005) 919–924, doi: [10.1016/j.expthermflusci.2005.02.001](https://doi.org/10.1016/j.expthermflusci.2005.02.001).
- [87] R.S. Khedkar, S.S. Sonawane, K.L. Wasewar, Water to nanofluids heat transfer in concentric tube heat exchanger: experimental study, *Procedia Eng.* 51 (2013) 318–323, doi: [10.1016/j.proeng.2013.01.043](https://doi.org/10.1016/j.proeng.2013.01.043).
- [88] B.C. Pak, Y.I. Cho, Hydrodynamic and heat transfer study of dispersed fluids with submicron metallic oxide particles, *Exp. Heat Transf.* 11 (1998) 151–170, doi: [10.1016/j.compstruct.2012.07.019](https://doi.org/10.1016/j.compstruct.2012.07.019).
- [89] Y. Xuan, Q. Li, Investigation on convective heat transfer and flow features of nanofluids, *J. Heat Transf.* 125 (2003) 151–155, doi: [10.1115/1.1532008](https://doi.org/10.1115/1.1532008).
- [90] M. Sabah Kassim, S.Fahad Lahij, Numerical and experimental study the effect of (SiO_2) nanoparticles on the performance of double pipe heat exchanger, *J. Eng. Sustain. Dev.* 23 (2019) 148–171, doi: [10.31272/jeasd.23.5.11](https://doi.org/10.31272/jeasd.23.5.11).
- [91] C. Gnanavel, R. Saravanan, M. Chandrasekaran, Heat transfer augmentation by nano-fluids and Spiral Spring insert in Double Tube Heat Exchanger-A numerical exploration, *Mater. Today Proc.* 21 (2020) 857–861, doi: [10.1016/j.matpr.2019.07.602](https://doi.org/10.1016/j.matpr.2019.07.602).
- [92] C. Gnanavel, R. Saravanan, M. Chandrasekaran, Heat transfer enhancement through nano-fluids and twisted tape insert with rectangular cut on its rib in a double pipe heat exchanger, *Mater. Today Proc.* 21 (2020) 865–869, doi: [10.1016/j.matpr.2019.07.606](https://doi.org/10.1016/j.matpr.2019.07.606).
- [93] A. Shahsavari, Z. Rahimi, M. Bahiraei, Optimization of irreversibility and thermal characteristics of a mini heat exchanger operated with a new hybrid nanofluid containing carbon nanotubes decorated with magnetic nanoparticles, *Energy Convers. Manag.* 150 (2017) 37–47, doi: [10.1016/j.enconman.2017.08.007](https://doi.org/10.1016/j.enconman.2017.08.007).
- [94] A. Jafarzad, M.M. Heyhat, Thermal and exergy analysis of air–nanofluid bubbly flow in a double-pipe heat exchanger, *Powder Technol.* 372 (2020) 563–577, doi: [10.1016/j.powtec.2020.06.046](https://doi.org/10.1016/j.powtec.2020.06.046).
- [95] M. Bezaatpour, M. Goharkhah, Convective heat transfer enhancement in a double pipe mini heat exchanger by magnetic field induced swirling flow, *Appl. Therm. Eng.* 167 (2020) 114801, doi: [10.1016/j.applthermaleng.2019.114801](https://doi.org/10.1016/j.applthermaleng.2019.114801).
- [96] S.K. Singh, J. Sarkar, Improving hydrothermal performance of hybrid nanofluid in double tube heat exchanger using tapered wire coil turbulator, *Adv. Powder Technol.* 31 (2020) 2092–2100, doi: [10.1016/j.apt.2020.03.002](https://doi.org/10.1016/j.apt.2020.03.002).
- [97] H. Arjmandi, P. Amiri, M. Saffari Pour, Geometric optimization of a double pipe heat exchanger with combined vortex generator and twisted tape: a CFD and response surface methodology (RSM) study, *Therm. Sci. Eng. Prog.* 18 (2020) 100514, doi: [10.1016/j.tsep.2020.100514](https://doi.org/10.1016/j.tsep.2020.100514).
- [98] G.K. Poongavanam, K. Panchabikesan, R. Murugesan, S. Duraisamy, V. Ramalingam, Experimental investigation on heat transfer and pressure drop of MWCNT – Solar glycol based nanofluids in shot peened double pipe heat exchanger, *Powder Technol.* 345 (2019) 815–824, doi: [10.1016/j.powtec.2019.01.081](https://doi.org/10.1016/j.powtec.2019.01.081).
- [99] D.G. Prabhajan, G.S.V. Raghavan, T.J. Rennie, Comparison of heat transfer rates between a straight tube heat exchanger and a helically coiled heat exchanger, *Int. Commun. Heat Mass Transf.* 29 (2002) 185–191, doi: [10.1016/S0735-1933\(02\)00309-3](https://doi.org/10.1016/S0735-1933(02)00309-3).
- [100] R. Beigzadeh, M. Rahimi, Prediction of thermal and fluid flow characteristics in helically coiled tubes using ANFIS and GA based correlations, *Int. Commun. Heat Mass Transf.* 39 (2012) 1647–1653, doi: [10.1016/j.icheatmasstransfer.2012.10.011](https://doi.org/10.1016/j.icheatmasstransfer.2012.10.011).
- [101] G. Huminic, A. Huminic, Heat transfer and flow characteristics of conventional fluids and nano fluids in curved tubes: a review, *Renew. Sustain. Energy Rev.* 58 (2016) 1327–1347, doi: [10.1016/j.rser.2015.12.230](https://doi.org/10.1016/j.rser.2015.12.230).
- [102] A.C. Mueller, *Thermal Design of Shell-and-tube Heat Exchangers for Liquid-to-liquid Heat Transfer*, American Society for Metals, Metals Park, OH., 1954.

- [103] S.S. Pawar, V.K. Sunnapwar, Studies on convective heat transfer through helical coils, *Heat Mass Transf.* 49 (2013) 1741–1754, doi: [10.1007/s00231-013-1210-3](https://doi.org/10.1007/s00231-013-1210-3).
- [104] H. Shokouhmand, M.R. Salimpour, M.A. Akhavan-Behabadi, Experimental investigation of shell and coiled tube heat exchangers using wilson plots, *Int. Commun. Heat Mass Transf.* 35 (2008) 84–92, doi: [10.1016/j.icheatmasstransfer.2007.06.001](https://doi.org/10.1016/j.icheatmasstransfer.2007.06.001).
- [105] L.C. Gómez, V. Manuel, *Advances in Heat Exchangers*, IntechOpen, 2019.
- [106] H.M. Maghrabie, M. Attalla, A.A.A. Mohsen, International Journal of Thermal Sciences Performance of a shell and helically coiled tube heat exchanger with variable inclination angle : experimental study and sensitivity analysis, *Int. J. Therm. Sci.* 164 (2021) 106869, doi: [10.1016/j.ijthermalsci.2021.106869](https://doi.org/10.1016/j.ijthermalsci.2021.106869).
- [107] A.N. Dravid, K.A. Smith, E.W. Merrill, P.L.T. Brian, Effect of secondary fluid motion on laminar flow heat transfer in helically coiled tubes, *J. Heat Transf.* 17 (1971) 1114–1122, doi: [10.1002/aic.690170517](https://doi.org/10.1002/aic.690170517).
- [108] A. Alimoradi, F. Veysi, Prediction of heat transfer coefficients of shell and coiled tube heat exchangers using numerical method and experimental validation, *Int. J. Therm. Sci.* 107 (2016) 196–208, doi: [10.1016/j.ijthermalsci.2016.04.010](https://doi.org/10.1016/j.ijthermalsci.2016.04.010).
- [109] B. Delpech, M. Milani, L. Montorsi, D. Boscardin, A. Chauhan, S. Almahmoud, B. Axcell, H. Jouhara, Energy efficiency enhancement and waste heat recovery in industrial processes by means of the heat pipe technology: case of the ceramic industry, *Energy* 158 (2018) 656–665, doi: [10.1016/j.energy.2018.06.041](https://doi.org/10.1016/j.energy.2018.06.041).
- [110] N. Jamshidi, M. Farhadi, D.D. Ganji, K. Sedighi, Experimental analysis of heat transfer enhancement in shell and helical tube heat exchangers, *Appl. Therm. Eng.* 51 (2013) 644–652, doi: [10.1016/j.applthermaleng.2012.10.008](https://doi.org/10.1016/j.applthermaleng.2012.10.008).
- [111] Z. Wu, L. Wang, B. Sunden, Pressure drop and convective heat transfer of water and nanofluids in a double-pipe helical heat exchanger, *Appl. Therm. Eng.* 60 (2013) 266–274, doi: [10.1016/j.applthermaleng.2013.06.051](https://doi.org/10.1016/j.applthermaleng.2013.06.051).
- [112] P.C.M. Kumar, J. Kumar, S. Suresh, Experimental investigation on convective heat transfer and friction factor in a helically coiled tube with $\text{Al}_2\text{O}_3/\text{water}$ nanofluid, *J. Mech. Sci. Technol.* 27 (2013) 239–245, doi: [10.1007/s12206-012-1206-9](https://doi.org/10.1007/s12206-012-1206-9).
- [113] T. Srinivas, A. Venu Vinod, Heat transfer enhancement using CuO/water nanofluid in a shell and helical coil heat exchanger, *Procedia Eng.* 127 (2015) 1271–1277, doi: [10.1016/j.proeng.2015.11.483](https://doi.org/10.1016/j.proeng.2015.11.483).
- [114] N. Kannadasan, K. Ramanathan, S. Suresh, Comparison of heat transfer and pressure drop in horizontal and vertical helically coiled heat exchanger with CuO/water based nano fluids, *Exp. Therm. Fluid Sci.* 42 (2012) 64–70, doi: [10.1016/j.expthermflusci.2012.03.031](https://doi.org/10.1016/j.expthermflusci.2012.03.031).
- [115] T. Srinivas, A. Venu Vinod, Heat transfer intensification in a shell and helical coil heat exchanger using water-based nanofluids, *Chem. Eng. Process. Process Intensif.* 102 (2016) 1–8, doi: [10.1016/j.cep.2016.01.005](https://doi.org/10.1016/j.cep.2016.01.005).
- [116] K.M. Elshazly, R.Y. Sakr, R.K. Ali, M.R. Salem, Effect of $\gamma\text{-Al}_2\text{O}_3/\text{water}$ nanofluid on the thermal performance of shell and coil heat exchanger with different coil torsions, *Heat Mass Transf.* 53 (2017) 1893–1903, doi: [10.1007/s00231-016-1949-4](https://doi.org/10.1007/s00231-016-1949-4).
- [117] P.J. Fule, B.A. Bhanvase, S.H. Sonawane, Experimental investigation of heat transfer enhancement in helical coil heat exchangers using water based CuO nanofluid, *Adv. Powder Technol.* 28 (2017) 2288–2294, doi: [10.1016/j.appt.2017.06.010](https://doi.org/10.1016/j.appt.2017.06.010).
- [118] B.A. Bhanvase, S.D. Sayankar, A. Kapre, P.J. Fule, S.H. Sonawane, Experimental investigation on intensified convective heat transfer coefficient of water based PANI nanofluid in vertical helical coiled heat exchanger, *Appl. Therm. Eng.* 128 (2018) 134–140, doi: [10.1016/j.applthermaleng.2017.09.009](https://doi.org/10.1016/j.applthermaleng.2017.09.009).
- [119] N. Jamshidi, M. Farhadi, K. Sedighi, D.D. Ganji, Optimization of design parameters for nanofluids flowing inside helical coils, *Int. Commun. Heat Mass Transf.* 39 (2012) 311–317, doi: [10.1016/j.icheatmasstransfer.2011.11.013](https://doi.org/10.1016/j.icheatmasstransfer.2011.11.013).
- [120] S. Bahrehmand, A. Abbassi, Heat transfer and performance analysis of nanofluid flow in helically coiled tube heat exchangers, *Chem. Eng. Res. Des.* 109 (2016) 628–637, doi: [10.1016/j.cherd.2016.03.022](https://doi.org/10.1016/j.cherd.2016.03.022).
- [121] F. Akbaridoust, M. Rakhsha, A. Abbassi, M. Saffar-Avval, Experimental and numerical investigation of nanofluid heat transfer in helically coiled tubes at constant wall temperature using dispersion model, *Int. J. Heat Mass Transf.* 58 (2013) 480–491, doi: [10.1016/j.appt.2015.08.006](https://doi.org/10.1016/j.appt.2015.08.006).
- [122] M. Rakhsha, F. Akbaridoust, A. Abbassi, S. Majid, Experimental and numerical investigations of turbulent forced convection flow of nano-fluid in helical coiled tubes at constant surface temperature, *Powder Technol.* 283 (2015) 178–189, doi: [10.1016/j.powtec.2015.05.019](https://doi.org/10.1016/j.powtec.2015.05.019).
- [123] H.M. Maghrabie, M. Attalla, A.A.A. Mohsen, Performance assessment of a shell and helically coiled tube heat exchanger with variable orientations utilizing different nanofluids, *Appl. Therm. Eng.* 182 (2021) 116013, doi: [10.1016/j.applthermaleng.2020.116013](https://doi.org/10.1016/j.applthermaleng.2020.116013).
- [124] C. Wang, Z. Cui, H. Yu, K. Chen, J. Wang, Intelligent optimization design of shell and helically coiled tube heat exchanger based on genetic algorithm, *Int. J. Heat Mass Transf.* 159 (2020) 120140, doi: [10.1016/j.ijheatmasstransfer.2020.120140](https://doi.org/10.1016/j.ijheatmasstransfer.2020.120140).
- [125] Y. Bazilevs, M. Hsu, J. Kiendl, R. Wüchner, K. Bletzinger, Numerical estimation of mixed convection heat transfer in vertical helically coiled tube heat exchangers, *Int. J. Numer. Methods Fluids.* 65 (2011) 236–253, doi: [10.1002/flid](https://doi.org/10.1002/flid).
- [126] J. Wang, S.S. Hashemi, S. Alahgholi, M. Mehri, M. Safarzadeh, A. Alimoradi, Analysis of Exergy and energy in shell and helically coiled finned tube heat exchangers and design optimization, *Int. J. Refrig.* 94 (2018) 11–23, doi: [10.1016/j.ijrefrig.2018.07.028](https://doi.org/10.1016/j.ijrefrig.2018.07.028).
- [127] R. Barzegarian, A. Aloueyan, T. Yousefi, Thermal performance augmentation using water based Al_2O_3 -gamma nanofluid in a horizontal shell and tube heat exchanger under forced circulation, *Int. Commun. Heat Mass Transf.* 86 (2017) 52–59, doi: [10.1016/j.icheatmasstransfer.2017.05.021](https://doi.org/10.1016/j.icheatmasstransfer.2017.05.021).
- [128] P.C.M. Kumar, J. Kumar, R. Tamilarasan, S. Sendhil Nathan, S. Suresh, Heat transfer enhancement and pressure drop analysis in a helically coiled tube using $\text{Al}_2\text{O}_3/\text{water}$ nanofluid, *J. Mech. Sci. Technol.* 28 (2014) 1841–1847, doi: [10.1007/s12206-014-0331-z](https://doi.org/10.1007/s12206-014-0331-z).
- [129] G. Huminic, A. Huminic, Heat transfer and entropy generation analyses of nanofluids in helically coiled tube-in-tube heat exchangers, *Int. Commun. Heat Mass Transf.* 71 (2016) 118–125, doi: [10.1016/j.icheatmasstransfer.2015.12.031](https://doi.org/10.1016/j.icheatmasstransfer.2015.12.031).
- [130] K. Narrein, H.A. Mohammed, Influence of nanofluids and rotation on helically coiled tube heat exchanger performance, *Thermochim. Acta.* 564 (2013) 13–23, doi: [10.1016/j.tca.2013.04.004](https://doi.org/10.1016/j.tca.2013.04.004).
- [131] M. Kahani, S. Zeinali Heris, S.M. Mousavi, Comparative study between metal oxide nanopowders on thermal characteristics of nanofluid flow through helical coils, *Powder Technol.* 246 (2013) 82–92, doi: [10.1016/j.powtec.2013.05.010](https://doi.org/10.1016/j.powtec.2013.05.010).
- [132] S.M. Hashemi, M.A. Akhavan-Behabadi, An empirical study on heat transfer and pressure drop characteristics of CuO -base oil nanofluid flow in a horizontal helically coiled tube under constant heat flux, *Int. Commun. Heat Mass Transf.* 39 (2012) 144–151, doi: [10.1016/j.icheatmasstransfer.2011.09.002](https://doi.org/10.1016/j.icheatmasstransfer.2011.09.002).
- [133] Q.S. Mahdi, S.A. Fattah, F. Juma, Experimental investigation to evaluate the performance of helical coiled tube heat exchanger with using TiO_2 nanofluid, *Adv. Mater. Res.* 1036 (2014) 2013–2014, doi: [10.1115/IMECE2013-62230](https://doi.org/10.1115/IMECE2013-62230).
- [134] T. Bes, Thermal performance of codirected cross-flow heat exchangers, *Heat Mass Transf.* 31 (1996) 215–222.
- [135] H.A. Navarro, L. Cabezas-Gómez, A new approach for thermal performance calculation of cross-flow heat exchangers, *Int. J. Heat Mass Transf.* 48 (2005) 3880–3888, doi: [10.1016/j.ijheatmasstransfer.2005.03.027](https://doi.org/10.1016/j.ijheatmasstransfer.2005.03.027).
- [136] J. Ramos, A. Chong, H. Jouhara, Experimental and numerical investigation of a cross flow air-to-water heat pipe-based heat exchanger used in waste heat recovery, *Int. J. Heat Mass Transf.* 102 (2016) 1267–1281, doi: [10.1016/j.ijheatmasstransfer.2016.06.100](https://doi.org/10.1016/j.ijheatmasstransfer.2016.06.100).
- [137] M. Benkhedda, T. Boufendi, T. Tayebi, A.J. Chamkha, Convective heat transfer performance of hybrid nanofluid in a horizontal pipe considering nanoparticles shapes effect, *J. Therm. Anal. Calorim.* 140 (2020) 411–425, doi: [10.1007/s10973-019-08836-y](https://doi.org/10.1007/s10973-019-08836-y).
- [138] A. Zukauskas, Heat transfer from tubes in cross flow, *Adv. Heat Transf.* 8 (1972) 93–160.
- [139] L.H. Tang, M. Zeng, Q.W. Wang, Experimental and numerical investigation on air-side performance of fin-and-tube heat exchangers with various fin patterns, *Exp. Therm. Fluid Sci.* 33 (2009) 818–827, doi: [10.1016/j.expthermflusci.2009.02.008](https://doi.org/10.1016/j.expthermflusci.2009.02.008).
- [140] A.M. Hussein, R.A. Bakar, K. Kadirgama, K.V. Sharma, Heat transfer augmentation of a car radiator using nanofluids, *Heat Mass Transf.* 50 (2014) 1553–1561, doi: [10.1007/s00231-014-1369-2](https://doi.org/10.1007/s00231-014-1369-2).
- [141] A.M. Hussein, R.A. Bakar, K. Kadirgama, Study of forced convection nanofluid heat transfer in the automotive cooling system, *Case Stud. Therm. Eng.* 2 (2014) 50–61, doi: [10.1016/j.csite.2013.12.001](https://doi.org/10.1016/j.csite.2013.12.001).
- [142] A.M. Hussein, R.A. Bakar, K. Kadirgama, K.V. Sharma, Heat transfer enhancement using nanofluids in an automotive cooling system, *Int. Commun. Heat Mass Transf.* 53 (2014) 195–202, doi: [10.1016/j.icheatmasstransfer.2014.01.003](https://doi.org/10.1016/j.icheatmasstransfer.2014.01.003).
- [143] S.M. Peyghambarzadeh, S.H. Hashemabadi, S.M. Hoseini, M. Seifi Jamnani, Experimental study of heat transfer enhancement using water/ethylene glycol based nanofluids as a new coolant for car radiators, *Int. Commun. Heat Mass Transf.* 38 (2011) 1283–1290, doi: [10.1016/j.icheatmasstransfer.2011.07.001](https://doi.org/10.1016/j.icheatmasstransfer.2011.07.001).
- [144] D.R. Ray, D.K. Das, Superior performance of nanofluids in an automotive radiator, *J. Therm. Sci. Eng. Appl.* 6 (2014) 041002, doi: [10.1115/1.4027302](https://doi.org/10.1115/1.4027302).
- [145] M.H. Esfe, S. Esfandeh, M. Afrand, M. Rejvani, S.H. Rostamian, Experimental evaluation, new correlation proposing and ANN modeling of thermal properties of EG based hybrid nanofluid containing ZnO -DWCNT nanoparticles for internal combustion engines applications, *Appl. Therm. Eng.* 133 (2018) 452–463, doi: [10.1016/j.applthermaleng.2017.11.131](https://doi.org/10.1016/j.applthermaleng.2017.11.131).
- [146] H.M. Ali, H. Ali, H. Liaquat, H.T. Bin Maqsood, M.A. Nadir, Experimental investigation of convective heat transfer augmentation for car radiator using ZnO -water nanofluids, *Energy* 84 (2015) 317–324, doi: [10.1016/j.energy.2015.02.103](https://doi.org/10.1016/j.energy.2015.02.103).

Strength Analysis of Flat and Folded Fly Ash-Based Geopolymer Ferrocement Panels under Flexure and Impact

Sikendar Sharma, *Department of Civil Engineering, Raajdhani Engineering College, Bhubaneswar, sikendarsharma92@gmail.com*

Biswa Ranjan Pradhan, *Department of Civil Engineering, Capital Engineering College, Bhubaneswar, biswaranjanpradhan78@gmail.com*

Saleema Panda, *Department of Civil Engineering, NM Institute of Engineering & Technology, Bhubaneswar, saleemapanda25@gmail.com*

Sampad Kumar Pradhan, *Department of Civil Engineering, Aryan Institute of Engineering & Technology, Bhubaneswar, s_kumar6@gmail.com*

ABSTRACT

The impact of fibre and wire mesh layers on the strength behaviour of flat and folded fly ash-based geopolymer ferrocement panels is discussed in this research. Flexural strength, impact strength, ductility, stiffness, and cracking patterns are all observed behaviours. Concrete makes use of wastes such as fly ash discarded by industrial sectors in order to reduce CO₂ emissions. In addition to two panels of each kind for the impact investigation, six panels (three flat and three folded) were cast using a fly ash-dependent geopolymer mortar with dimensions of 1000 mm 400 mm 30 mm. After 24 hours of resting, heat curing was performed in a temperature-controlled chamber at 75°C to 80°C for 24 hours. The number of wire mesh layers increased the flexural strength by 33%, but the ductility of the flat panels fell by 30%, according to the data.

1. Introduction

Ferrocement is a type of reinforced concrete with wire mesh layers and/or small diameter rings, completely coated or encapsulated in mortar. In 1940, the first ferrocement operation of aircraft hangars, ships, and buildings was carried out by Pier Luigi Nervi, Italy's engineer, architect, and builder. This material is extremely durable, cost-effective, and flexible. Geopolymer ferrocement panels have been developed widely as a common building material in the past decades because its manufacturing operation could minimize carbon dioxide emissions by 80 percent relative to the conventional Portland cement production. Davidovits [1] formulated a concrete mixture geopolymer composite material, which could be manufactured through incorporation of a pozzolanic element and often alumina silicate from a high alkaline solution. Fly ash, which is readily accessible

from coal power plants, has become an ideal primary substance for alumina silicate. It also exhibits ceramic-like properties, such as good fire resistance at high temperatures. In addition to this, the advantages compared to OPC concrete include resistance to acid attack, strong bonding intensity, and higher corrosion resistance, as well as reduced creep and shrinkage. Abdulla et al. [2] quantitatively illustrated the functioning and chemical reactivity of fly ash-based geopolymer concrete.

Ferrocement is also an environmentally sustainable innovation that has outstanding special features like higher tensile strength, increased durability, elevated cracking resistance, fire resistance, and the capacity to withstand massive deformation prior to actually collapsing. It also proves to be an energy-efficient building material. According to ACI Committee 549 [3], ferrocement is a form of slender wall of moderate thickness built using the hydraulic concrete

mixture that is combined with wire mesh layers. Two essential parameters are widely used in the characterization of ferrocement, such as the volume fraction of reinforcement and overall bonded reinforcement area per unit composite length. Hexagonal wire mesh, welded wire mesh, woven wire mesh, and three-dimensional mesh are the major categories of wire mesh used in the construction sector. The mesh can be constructed using an appropriate metal or some other products. Thickness varies from 25 mm to 50 mm. The updated ACI code allows the use of nonmetallic insulation and fiber. Ferrocement finds its application in construction sector, agriculture, water supply systems, etc.

Research suggests that in the scenario of earthquake resistance buildings, this tends to be an outstanding combination. Temuujin et al. [4] investigated experimentally the formulation and characterization of geopolymer mortar made of fly ash by altering the binding material as well as aggregate proportion. Hardjito et al. [5] focused on the low calcium fly ash-dependent geopolymer mortar and its setting duration.

Mahmood and Majeed [6] performed theoretical as well as experimental investigations on the flexural behavior of cement-based ferrocement panels. The work explained the impact of overall strength as well as ductility using varied wire mesh materials. Rajendran and Soundarapandian [7] addressed the theoretical research on the flexural behavior of flat geopolymer ferrocement slabs. The variables investigated were wire mesh layers and the concentration of alkaline solution. Rahman et al. [8] conducted a review on the behavior of polymer fiber as a substitute to metal wire mesh. Their study revealed that the utilization of fiber as the ferrocement reinforcement is technologically feasible and does not have any negative impact on flexural strength.

The influence of curing temperature upon these flexural characteristics of silica-based carbon-reinforced composites was discussed (Tran et al.) [9]. Curing temperature in the range of 70°C and 100°C was established as an optimum temperature for obtaining a good flexural strength. Hago et al. [10] experimentally studied the flexural strength of optimal and service loaded ferrocement roof slab panels.

Nagan and Mohana [11] studied experimentally the behavior of geopolymer ferrocement slabs subjected to impact by varying the wire mesh layers and concluded that an increase in the volume fraction of reinforcement increases the impact strength. Murali et al. [12] performed an investigation on the impact resistance and strength of fiber-reinforced concrete, and the results indicated that the concrete containing fiber gave the best performance under impact loading. Kaliraj et al. [13] investigated the impact strength of geopolymer ferrocement trough panels and found that trough panels are stronger than flat panels.

Due to its high viscosity, a fresh fly ash-based geopolymer's workability could be a major disadvantage. Xie and Kayali [14] investigated the influence of superplasticizer on the workability of fly ash-based geopolymers in Class F and Class C. It found that superplasticizers based on polycarboxylates were successful for Class C fly ash, while superplasticizers based on naphthalene were effective for Class F fly ash.

The primary purpose of this research is to establish an environmentally friendly composite material for construction that can be employed as multipurpose building element that incorporates industrial by-products by exploiting the advantages of both geopolymer as well as ferrocement technologies. Moreover, an attempt is made to study the strength behavior of ferrocement panels under flexure and impact by adjusting the wire mesh layers and integrating fibers into the geopolymer matrix.

2. Materials and Methods

2.1. Specimen Geometry. The geometry of the geopolymer ferrocement (GF) panels used in the experimental investigation is shown in Figure 1. The panels had a constant thickness of 30 mm, and the description of the panels is given in Table 1.

2.2. Materials. The constituents of the geopolymer ferrocement are shown in Figure 2.

2.2.1. Geopolymer Mortar. Geopolymer mortar was obtained by synthesizing the pozzolanic component with a combination of activator solution. The ingredients of the freshly prepared concrete consist of fly ash, fine aggregate, and the liquid alkaline activator. Low calcium fly ash (Class F) conforming to IS 3812 (Part 1) [15] and ASTM C618-5 [16], acquired from Tuticorin thermal power plant, has been used as a pozzolanic component, and the chemical properties of fly ash used are provided in Table 2. Specific gravity as well as fineness of fly ash used is 2.32 and 390.40 m²/kg, respectively.

24 hours before application, an activator solution was prepared using sodium hydroxide granules and sodium silicate. The amount of sodium hydroxide solids, including the water used to generate sodium hydroxide solution of the specified molarity was extracted in accordance to the guidance provided in Perry's Chemical Engineers' Handbook [17].

River sand passing through 2.36 mm IS sieve and retained on 150 μ IS sieve of specific gravity 2.57 with a fineness modulus of 2.89 adhering to Zone II of IS 383 [18] was used as the fine aggregate. A water reduction admixture, such as Fosroc Conplast SP430, a chloride free superplasticizing admixture based on selected sulphonated naphthalene polymers, conforming to ASTM-C-494, Type 'F', and Type 'A', is employed to provide the required workability. Table 3 shows the mix proportions and the strength of the geopolymer mortar specimens.

2.2.2. Wire Mesh. Wire meshes made of steel were used as prime mesh reinforcement. The characteristics of the resulting ferrocement component are influenced by the size of the mesh, ductility, fabrication, and treatment of the mesh used in the panel [19]. This form of mesh is easily available, affordable, and easy to handle. This mesh is made up of cold drawn wire that is normally twisted into hexagonal patterns.

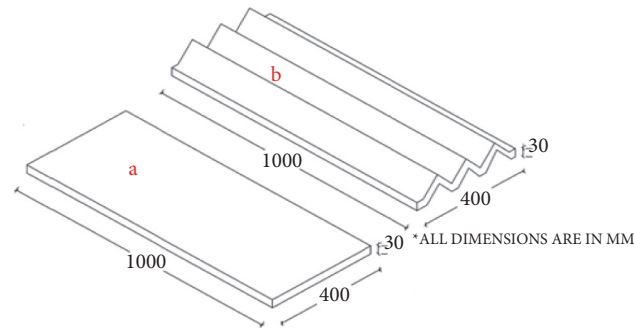


FIGURE 1: Geometry of GF panels. (a) Flat panel. (b) Folded panel.

Hexagonal mesh including longitudinal wires may contain unique designs. For this work, a galvanized sheet metal wire mesh (termed as chicken wire mesh) with hexagon-shaped grid was used as shown in Figure 2(d). The wire separation distance is 12.50 mm c/c with a width of 0.72 mm and of about 20 gauges. The steel mesh wire was kept in the optimal position as shown in Figure 3, using a binding string prior to inserting it into the panel mould. The yield strength for chicken wire is 310 N/mm². The density fraction of the mesh intensification was determined using the relationship as follows:

$$Vr = \frac{Nw_r}{h\delta_r} \quad (1)$$

Here, 'N' signifies the number of mesh layer, 'w_r' denotes the reinforcement mesh weight, 'h' represents the element thickness, and 'δ_r' denotes the reinforcement density.

2.2.3. Steel Fiber. Steel fiber was employed as a secondary reinforcement material. Steel fiber in comparison to prolonged reinforcing bars is short and closely distributed. As a result, additional reinforcing zones could be accomplished by using a reinforcing steel bar grid. Additionally, steel fiber helps in controlling the crack and enhancing the flexural strength, rigidity, and elastic modulus. Crimped steel fiber of length 10 mm and thickness 0.4 mm with an aspect ratio of 25 as shown in Figure 2(e) was used.

2.2.4. Skeletal Reinforcement. Skeletal reinforcement (Figure 3) was used on which chicken wire layers would be placed.

2.2.5. Preparation of Geopolymer Mortar. Before mixing, all material quantities were weighed according to the mix design. Alkaline activator solutions (AAS) were made 24 hours ahead of time and allowed to cool to room temperature before mixing and casting. With the aim of combining the weighted materials, a pan mixer was employed. After 3 minutes of dry mixing (fly ash, sand, and fiber), alkaline liquid was added to the combination. In addition, a superplasticizer was added to the solution after being diluted in extra water. The wet mixing took another 4 minutes. It was then poured into the moulds to make geopolymer mortar specimens.

TABLE 1: Description of GF panels.

Description of the panels	Panel ID
GF flat panel with single layer mesh	GFP-FT-01-OC
GF flat panel with double layer mesh	GFP-FT-02-OC
Fiber-reinforced GF flat panel with single layer mesh	GFP-FR-FT-OC
GF-folded panel with single layer mesh	GFP-FD-01-OC
GF-folded panel with double layer mesh	GFP-FD-02-OC
Fiber-reinforced GF-folded panel with single layer mesh	GFP-FR-FD-OC

2.3. Specimen Casting and Curing. Steel moulds (Figure 4), which are properly lubricated were used for flat as well as folded panels. After setting the reinforcement in place, the prepared geopolymer mortar was poured and compacted well. A consistency test was performed using flow table testing according to BS:EN 1015-3 [20]. Mortar cubes of dimensions 70.6 mm × 70.6 mm × 70.6 mm were also cast to evaluate the characteristic stiffness of the geopolymer mixture. After 24 hours, the panels were demoulded and exposed to heat curing in a custom-designed heat curing chamber (Figure 5) for 24 hours at 75°C to 80°C.

2.4. Experiment Methods

2.4.1. Compressive Strength Test. The compressive strength of geopolymer mortar cubes representing corresponding mixes was done in accordance with IS 4031 (Part 6) [21] in a compressive testing machine of 1000 kN capacity (Figure 6(a)).

2.4.2. Ultrasonic Pulse Velocity Test. To check the quality and homogeneity of the panels, an ultrasonic pulse velocity test was carried out (Figure 7). This test was conducted by passing ultrasonic pulses through the panels and by measuring the time taken by the pulse to get through the structure. Higher velocities indicate good quality and continuity of the material, while lower velocities may indicate that the panel have cracks or voids.



FIGURE 2: Constituents of geopolymer ferrocement. (a) Fly ash. (b) Sodium hydroxide. (c) Sodium silicate. (d) Wire mesh. (e) Steel fiber. (f) River sand.

TABLE 2: Chemical compositions of low calcium fly ash.

Characteristics	Composition by % weight	Specifications as per IS 3812 : 2003
Aluminium dioxide (Al_2O_3) plus iron oxide (as Fe_2O_3)	35.99	Minimum 70
Silicon oxide (as SiO_2)	59.10	
Magnesium oxide (as MgO)	1.29	—
Total sulphur as sulphur trioxide (SO_3)	0.61	Max 3
Alkalis as sodium oxide (Na_2O)	0.20	Max 1.5
Calcium oxide as CaO	2.25	Max 5
Loss on ignition	0.48	Max 5

TABLE 3: Mix proportions of the geopolymer mortar.

Mortar type	Proportions	Compressive strength (N/mm^2), after 24 hours of curing at 75°C to 80°C
<i>(A) Geopolymer mortar (GM)</i>		
Fly ash to fine aggregate ratio	1 : 1	
Alkaline activator to fly ash ratio	0.45	
Sodium hydroxide (NaOH) concentration	10 molarity	46.98
Sodium hydroxide to sodium silicate ratio	1 : 1.5	
Superplasticizer Conplast SP430	1% of wt. of fly ash	
<i>(B) Fiber-reinforced geopolymer mortar</i>	GM + steel fiber 0.50% of wt. of total composite	49.44

2.4.3. Flexural Test. The fabricated panels were tested in a hydraulic power packed loading frame employing load cells and 16 channel LVDT under two-point loading conditions. While loading, the crack pattern obtained was also observed

and marked. Furthermore, the yield strength and corresponding deflection were recorded.

The flexure testing carried out on the flat panel is shown in Figure 8.

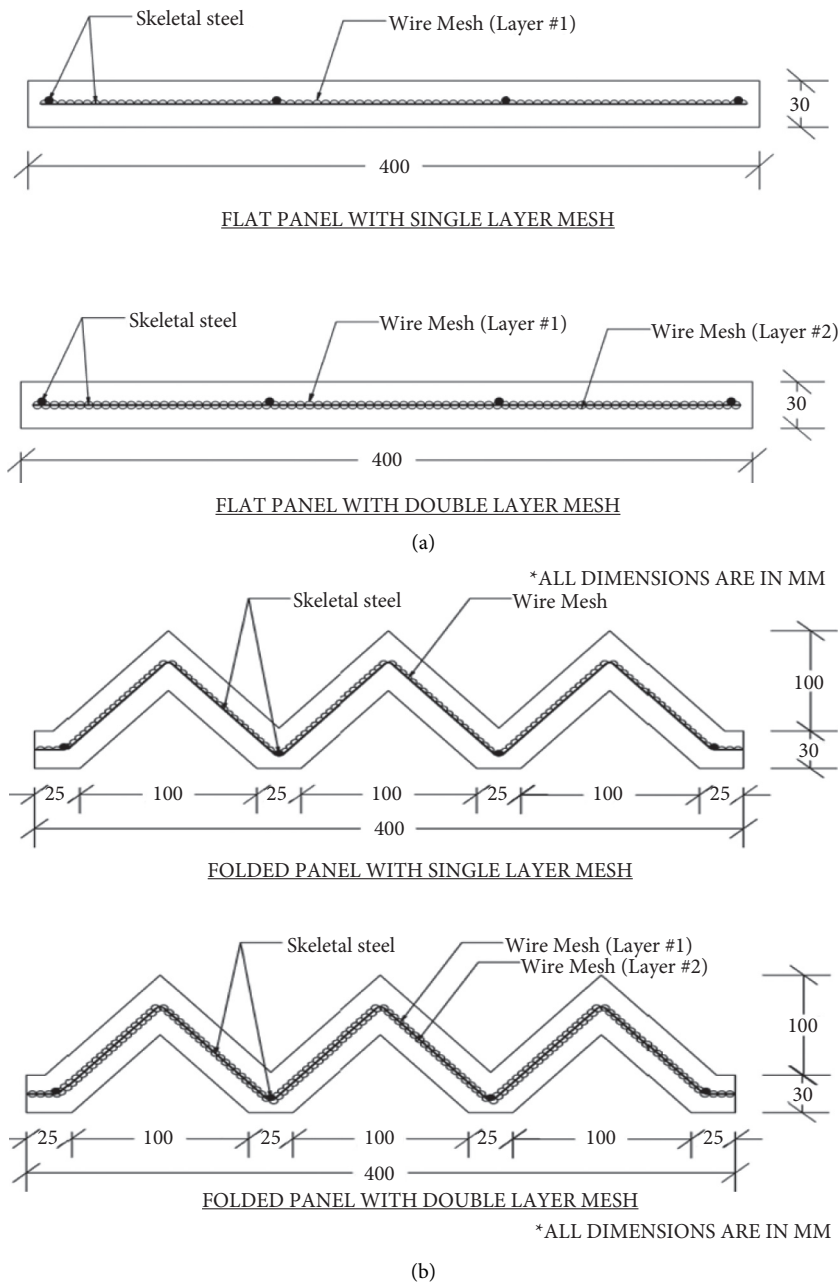


FIGURE 3: Geopolymer ferrocement panels with single and double layer wire mesh. (a) Flat panels. (b) Folded panels.

Flexure testing carried out on the folded panel is shown in Figure 9.

2.4.4. Drop-Weight Impact Test. The ability to absorb energy referred to as 'toughness' is of importance in the case of mesh-reinforced composites subjected to static, dynamic, and fatigue loads. The drop-weight impact test is a test meant for evaluating the impact characteristics of concrete/cement composites. The impact test was conducted using a 4.5 kg hammer, which was allowed to fall freely from a constant height of 460 mm through a guide at the center of the panel as per ASTM D2794-93 [22]. Specimens were placed in their position on a rigid platform. The mass was then dropped

repeatedly, and the number of blows required to cause the first crack was recorded for each panel. The process was continued until the crack propagated further and appeared at the top surface of the specimen. At this point, the corresponding numbers of blows were noted. The impact test setup is shown in Figure 10.

3. Experimental Results and Analysis

3.1. Compressive Strength of the Geopolymer Mortar. Figure 11 shows the compressive strength of fly ash-based geopolymer mortar specimens in contrast to the control specimens. The geopolymer mortar comprised mostly of fly ash has a maximum compressive strength of 46.98 N/mm^2 ,

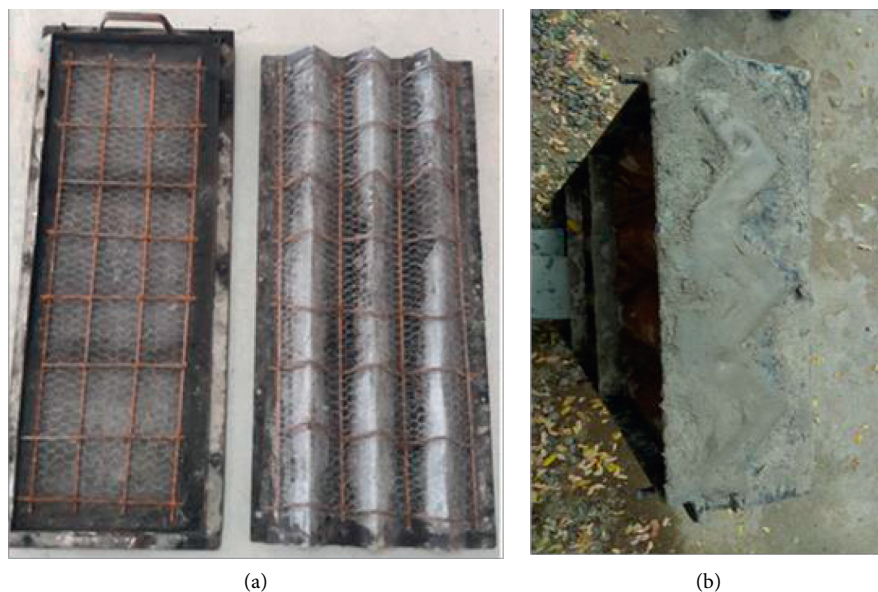


FIGURE 4: Fabrication and casting specimens. (a) Fabrication of reinforcement. (b) Casting specimens.

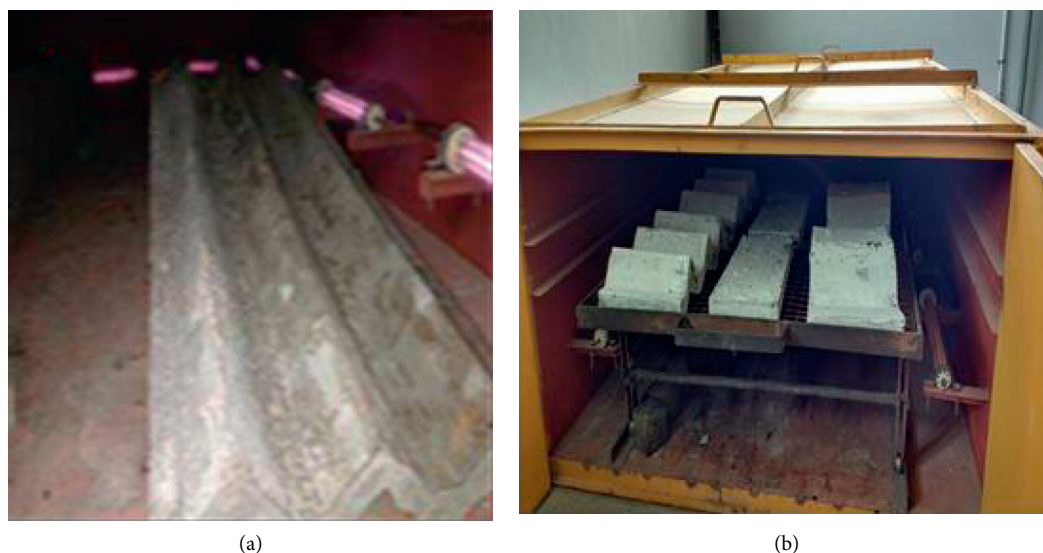


FIGURE 5: Curing specimens. (a) Specimens under curing. (b) Temperature-controlled heat curing chamber.

which is 19% higher than the compressive strength of control specimens. This increase may be attributed to the potential of the geopolymer in filling the pores, which eventually results in a closely packed microstructure. However, the specimens showed ductile behavior.

3.2. Flexural Strength of GF Panels. The load and corresponding deflection of GF panels are given in Table 4. Moreover, the stiffness, ductility, and the amount of energy absorbed are included.

The obtained load-deflection variation for GF flat and folded panels is shown in Figure 12.

The volume, type, orientation, and inherent geometry of the strengthening mesh are the factors affecting the ultimate strength in relation to the position and the neutral axis. The

strengthening properties consequently affect the ultimate strength. Table 4 shows the rise in ultimate strength as the number of wire mesh layers for flat and folded panels increases.

In flat geopolymer ferrocement panels, due to the increase in the number of wire mesh layers, the flexural strength has increased by 33%. However; there is a 30% reduction in ductility. In the folded geopolymer ferrocement panel, there is no considerable effect on the flexural strength due to the increase in wire mesh layers. However, there is a 10% reduction in ductility.

Boosting the number of wire mesh layers has little impact on cracking, ultimate load, deflection, stiffness, ductility, and the level of energy absorption. This is because the wire mesh has been positioned in a zigzag plane to align the geometry of the folded panel as seen in Figure 3(b). Moreover, it does not complement the horizontal bending plane. However, the

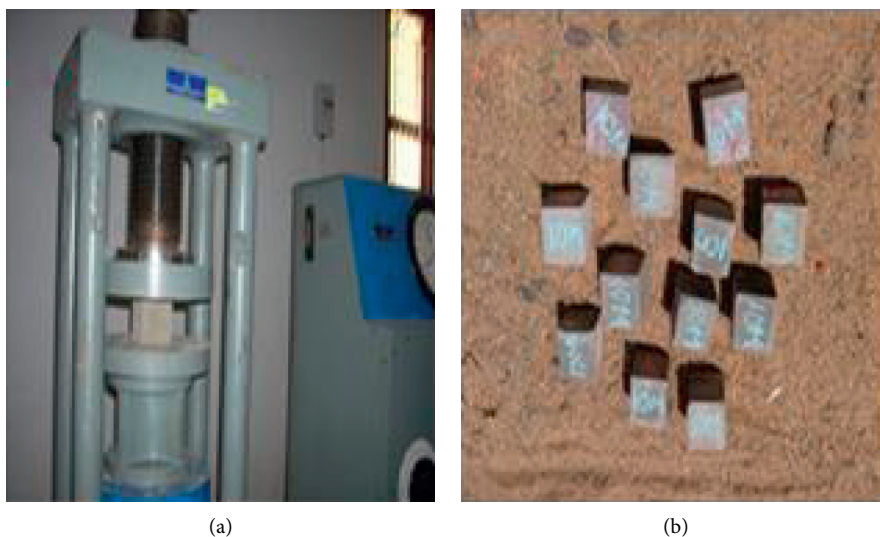


FIGURE 6: Compressive strength test. (a) Compression test on a mortar cube. (b) Geopolymer mortar cubes.



FIGURE 7: Ultrasonic pulse velocity test.



FIGURE 8: Flexural test on the GF flat panel.

cracking sequence has been altered by creating extra consistent cracks all along its span. As in the case of the portion, under compression, the load-deflection and stress-strain correlation for loading segments are defined by three phases (Kadhim

Sallal) [23], such as the elastic, elastic to plastic and plastic stages. The ending of the steeper linear part of the load-deflection curve correlates to the panel's first crack. Until this stage, no fracturing was noticed visually, although cracking was



FIGURE 9: Flexural test on the GF folded panel.



FIGURE 10: Drop-weight impact test on GF panels. (a) Test on flat panel. (b) Test on folded panel.

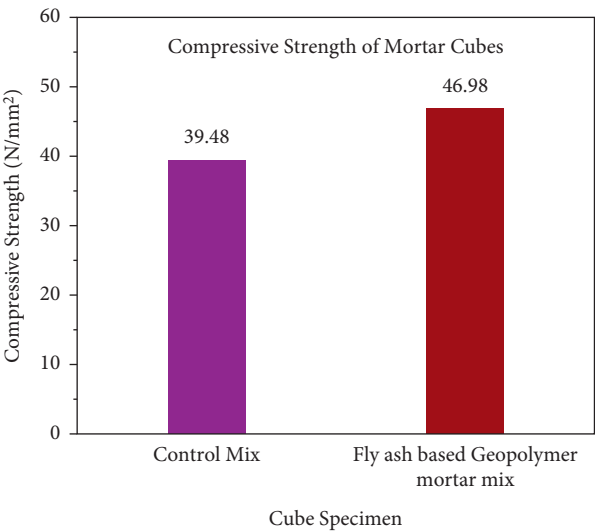


FIGURE 11: Compressive strength of the geopolymer mortar.

TABLE 4: Load, deflection, and flexural strength of GF panels.

Panel ID	Cracking		Ultimate		Stiffness (N/mm)	Ductility	Energy absorption (joule)
	Load (kN)	Deflection (mm)	Load (kN)	Deflection (mm)			
GFP-FT-01-OC	1.70	3.20	2.70	7.70	350.65	2.41	13.20
GFP-FT-02-OC	2.10	3.50	3.10	5.90	525.42	1.69	10.60
GFP-FR-FT-OC	2.30	3.70	2.90	6.30	460.32	1.70	11.40
GFP-FD-01-OC	5.30	4.70	12.60	15.00	840.00	3.19	105.50
GFP-FD-02-OC	4.60	5.10	13.00	14.90	872.48	2.92	104.00
GFP-FR-FD-OC	7.20	4.90	13.90	11.00	1263.64	2.25	88.00

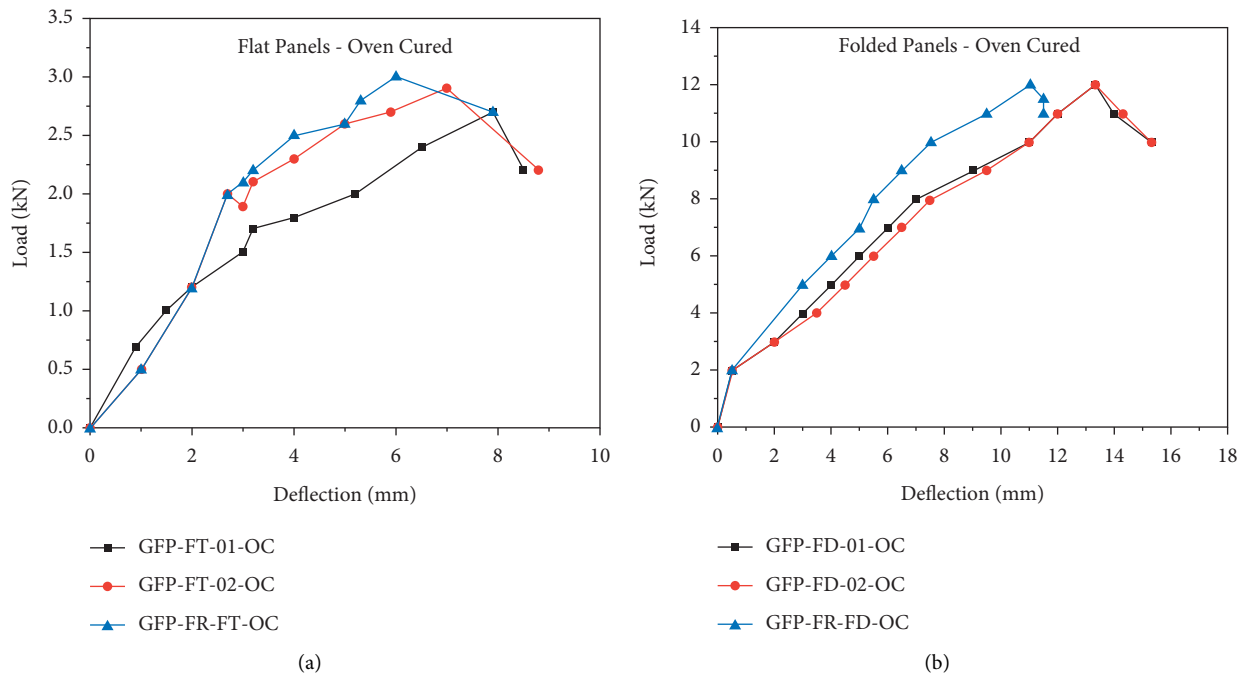


FIGURE 12: Load-deflection of GF panels. (a) Flat panels. (b) Folded panels.

always observed shortly after the load. In the second section of the curve (elastic to plastic level), multiple cracks are noticed and the steel stress is lower than the yield strain. At this point, as the steel quality increases, the distance and slope also increase. Steel yielding marks the conclusion of this stage and the beginning of the plastic stage.

With regard to fiber-reinforced GF panels, folded panels prove to be 3 times stiffer than the flat panels of wire mesh. In fiber-reinforced folded panels of single layer mesh, the crackings as well as ultimate load have increased by 35% and 10%. The ultimate deflection and ductility, on the other hand, have decreased by 26% and 30%, respectively, compared to the folded panels of a single and double layer mesh. In addition to this, the crack propagation and ultimate loads of fiber-reinforced folded panels were found to be 3.13 and 4.8 times greater than those of flat panels.

The cracking behavior of the ferrocement is explored by the observation of the number of cracks at the very first cracking and the aspects that induced their failure. Consequently, no observational results are available to trigger or validate the calculations for crack width estimation. Recently, there have been tests in relation to the variables known to calculate the crack width.

The cracking characteristics of flat as well as folded panels' geopolymer ferrocement could be seen in Figure 13.

Due to the weak compression field, preterm compression degradation was observed in flat panels having a single layer mesh at the upper end of the panel. However, the sequence of cracks was altered by increasing the number of wire mesh layers twice and by arranging the mesh far from the neutral axis. As a result, few other cracks occurred in the panel until it failed. Furthermore, as the fiber was inserted, consistent cracks were noticed across the length of the structure, and a desirable compression failure occurred at the final phase. Doubling the number of wire meshes resulted in a desirable compression failure in folded panels at the ultimate phase. This, however, did not influence the strength of the panel. Nevertheless, when the fiber is incorporated, the ultimate load improves significantly and the deflection at the ultimate phase reduces.

3.3. Impact Strength of GF Panels. The total energy absorbed by the GF panels when struck by a hard impactor depends on the local energy absorbed in the contact zone as well as by the impactor. The impact energy absorption can be obtained by using the following formula [11,12]:

TABLE 5: Impact resistance, impact energy absorption, and residual impact strength of GF panels.

Panel ID	Impact resistance (no. of blows)			Impact energy absorption (joules)		Residual impact strength ratio (I_{rs})
	Cracking	Ultimate	% increase	Cracking	Ultimate	
GFP-FT-01-OC	4	12	2	77.69	233.08	3.00
GFP-FT-02-OC	6	16	1.6	116.54	310.78	2.66
GFP-FD-01-OC	20	132	5.6	388.47	2563.94	5.17
GFP-FD-02-OC	28	145	4.2	543.86	2816.45	6.60



FIGURE 13: Cracking behavior of GF panels under flexure. (a) Flat panels. (b) Folded panels.

Impact energy absorption, $E = (N.m.v^2)/2$, where, the mass of the hammer, $m = w/g$; w = weight of the hammer; g = acceleration due to gravity; and impact velocity, $v = g.t$. Height of fall, $h = (g.t)^2/2$.

Time required for the hammer to fall from a height of h ,

$$t^2 = \frac{2h}{g}.$$

$$\begin{aligned} \text{Therefore, } E &= \frac{[N.w/g \cdot (g.t)^2]}{2} \\ &= \frac{(N.w.g.t^2)}{2} = \frac{N.w.g.(2h/g)}{2} \\ &= N(w.h), \end{aligned} \quad (2)$$

where E = energy in joules; w = weight in Newton; h = drop height in meter; and N = blows in numbers.

The ratio of energy absorbed at the failure of specimens to the energy absorbed at the initiation of the first crack is defined as the 'residual impact strength ratio' (I_{rs}). The impact resistance, energy absorption, and residual impact strength ratio of GF panels at first crack and at ultimate are presented in Table 5, and the variation is shown in Figures 14 and 15.

3.3.1. Cracking Behavior of GF Panels due to Impact. From the impact test, the number of blows required to initiate the first crack was determined by visual observation, and the ultimate failure was determined based on the number of blows required for the crack to propagate to the sides of the panels. The impact energy absorbed by the GF panels was computed based on the number of blows required to cause the ultimate failure. The impact energy per blow as seen in Figure 14 shows the cracking behavior of GF flat and folded panels due to the impact load.

Moreover, the ultimate crack resistance generally increases with an increase in the volume fraction of reinforcement of the panels. This may be due to its higher ductility and lesser susceptibility to embrittlement of reinforcement. It is also observed that the failure pattern of the specimens exhibited localized failure at the point of contact of the drop weight. It is also noticed that no fragments detached from the specimens because various layers of the mesh reinforcement helped to hold different fragments together.

It can thus be inferred that the meshes used as reinforcement play a major role in not only improving the impact energy absorption, but also retaining/holding various fragments together. All panels failed due to spalling at the top face and scabbing at the bottom face. It is also observed that the crack patterns of all panels were similar. The failure pattern of GF panels is shown in Figure 16.

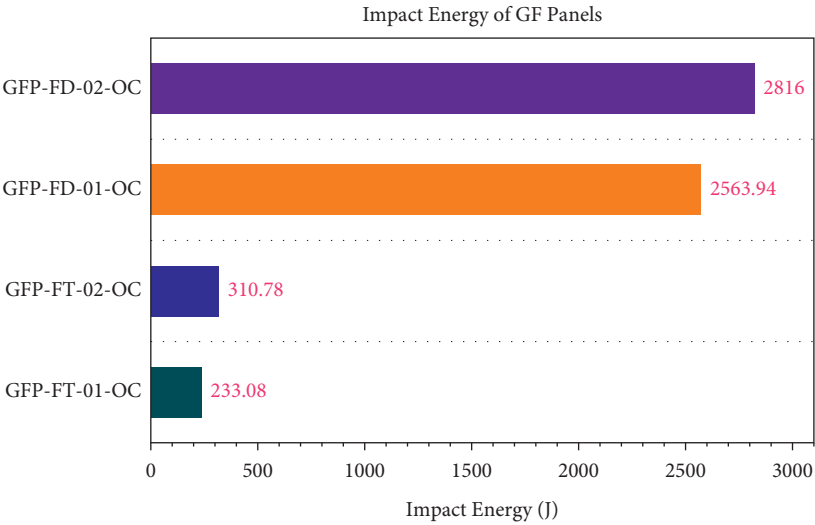


FIGURE 14: Energy absorption of GF panels under impact load.

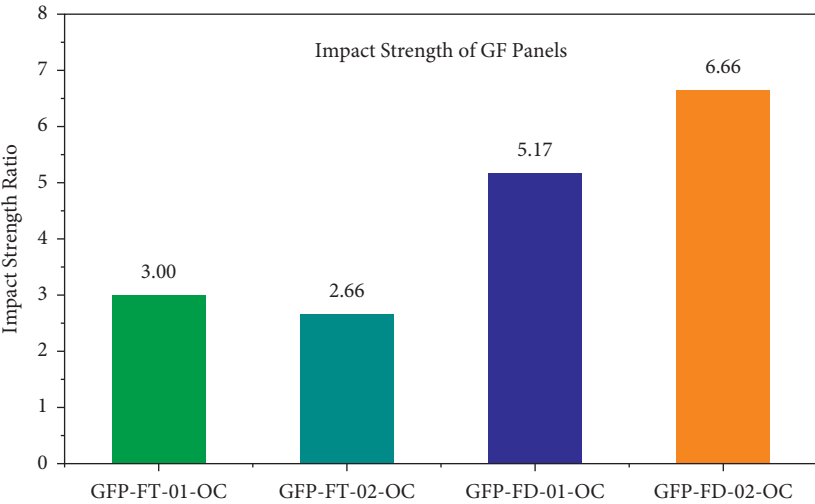


FIGURE 15: Residual impact strength of flat and folded GF panels.



FIGURE 16: Cracking behavior of GF panels under impact. (a) GF flat panels. (b) GF folded panels.

4. Conclusions

Based on the experimental test results of the geopolymer flat and folded ferrocement panels, the following conclusions are drawn:

- (1) In flat geopolymer ferrocement panels, by increasing the number of wire mesh layers, the flexural strength increases by 33% and the ductility reduces by 30%. In the folded geopolymer ferrocement panel, increasing the wire mesh layer has no considerable effect on the flexural strength. However, the ductility reduces by 10%.
- (2) The flexural strength of the folded geopolymer ferrocement panel is three times more than that of the flat panels. Moreover, the ductility of folded panels with single layer mesh and the fiber-reinforced panel increases by 32%. It is also observed that the ductility of the panel with double layer mesh is 73% more than that of flat panels.
- (3) In terms of cracking and ultimate load, flat and folded geopolymer ferrocement panels with double layer wire mesh and fiber-reinforced panels with single layer mesh behave similarly.
- (4) When compared to the flat geopolymer ferrocement panels, the impact strength of the folded panels increased by 90%, and the energy absorbed at failure due to the impact is directly proportional to the volume of the reinforcement provided in the panels.
- (5) Due to the higher volume fraction of reinforcement, the failure pattern in the tested panels due to impact is found to be punching shear.

References

- [1] J. Davidovits, "Global warming impact on the cement and aggregates industries," *World Resource Review*, vol. 6, no. 2, pp. 263–278, 1994.
- [2] M. M. A. Abdullah, K. Hussin, M. Bnhussain, K. N. Ismail, and W. M. W. Ibrahim, "Mechanism and chemical reaction of fly ash geopolymer cement—a review," *International Journal of Pure and Applied Sciences and Technology*, vol. 6, no. 1, pp. 35–44, 2011.
- [3] ACI Committee 549, *State-of-the-Art Report on Ferrocement*, Report ACI 549-R97, American Concrete Institute, Michigan, USA, 1997.
- [4] J. Temuujin, A. V. Riessen, and K. J. D. Mackenzie, "Preparation and characterisation of fly ash based geopolymer mortars," *Construction and Building Materials*, vol. 24, no. 10, pp. 1906–1910, 2010.
- [5] D. Hardjito, C. C. Cheak, and C. H. Lee Ing, "Strength and setting times of low calcium fly ash-based geopolymer mortar," *Modern Applied Science*, vol. 2, no. 4, pp. 3–11, 2008.
- [6] N. M. Mahmood and S. A. Majeed, "Flexural behavior of flat and folded ferrocement panels," *Al-Rafidain Engineering*, vol. 17, no. 4, pp. 1–11, 2009.
- [7] M. Rajendran and N. Soundarapandian, "An experimental investigation on the flexural behavior of geopolymer ferrocement slabs," *Journal of Engineering and Technology*, vol. 3, no. 2, pp. 97–104, 2013.
- [8] M. M. Rahman, S. Sameen, R. Hafiza, and M. A. Sadeque, "Behavior of polymeric fiber as an alternative reinforcement to iron wire mesh in ferrocement elements under flexural load," *International Journal of Chemical, Environmental & Biological Sciences*, vol. 1, no. 5, 2013.
- [9] S. Kaliraj, P. Madasamy, and S. Dharmar, "Impact behaviour of geopolymer ferrocement trough panel," *SSRG International Journal of Civil Engineering*, pp. 496–500, 2017.
- [10] J. Xie and O. Kayali, "Effect of superplasticiser on workability enhancement of Class F and Class C fly ash-based geo-polymers," *Construction and Building Materials*, vol. 122, pp. 36–42, 2016.
- [11] IS 3812 (Part 1), *Pulverized Fuel Ash - Specification for Use as Pozzolana in Cement, Cement Mortar and Concrete*, Bureau of Indian Standards, New Delhi, India, 2003.
- [12] ASTM C618-5, *Standard Specification for Coal Fly Ash and Raw or Calcined Natural Pozzolan for Use in Concrete*, ASTM Standards, USA, 2005.
- [13] R. H. Perry, *Perry's Handbook for Chemical Engineers*, McGraw-Hill, New York, USA, 1997.
- [14] IS 383, *Specification for Coarse and Fine Aggregates from Natural Sources for Concrete*, Bureau of Indian Standards, New Delhi, India, 1997.
- [15] "ferrocement Slab panels using welded square mesh by in-corporating Steel Fibers," *International Journal of Renewable Energy Technology*, vol. 3, no. 5, 2014.
- [16] R. J. Phalke and D. G. Gaidhankar, "Flexural behaviour of
- [17] D. H. Tran, D. Kroisova, P. Louda, O. Bortnovsky, and [a] Bezucha, "Effect of curing temperature on flexural properties of silica-based geopolymer-carbon reinforced composite," *Journal of Achievements in Materials and Manufacturing Engineering*, vol. 37, no. 2, pp. 492–497, 2009.
- [18] A. W. Hago, K. S. Al-Jabri, A. S. Alnuaimi, H. Al-Moqbali, and [a] A. Al-Kubaisy, "Ultimate and service behavior of ferrocement roof slab panels," *Construction and Building Materials*, vol. 19, no. 1, pp. 31–37, 2005.

Modeling of a Ballastless Track System Resulting from Early-Aged Relative Humidity for the Construction Process

Subrat Kumar Panda, *Department of Civil Engineering, Aryan Institute of Engineering & Technology, Bhubaneswar, spanda226@gmail.com*

Barsa Priyadarshini Sahoo, *Department of Civil Engineering, Raajdhani Engineering College, Bhubaneswar, barsap_sahoo@gmail.com*

Bipash Mohanty, *Department of Civil Engineering, Capital Engineering College, Bhubaneswar, bipashmohanty784@gmail.com*

S. C. Mishra, *Department of Civil Engineering, NM Institute of Engineering & Technology, Bhubaneswar, scmishra11@yahoo.co.in*

ABSTRACT

For bi-block ballastless track systems consisting of foundation, precast sleepers, and cast-in-place track slab, drying-induced cracks are a significant issue that not only impacts the comfort and safety of rapid transit railways but also limits the service life of ballastless track. This paper proposes an evolution model of relative humidity (RH) in the CRTS I bi-block ballastless track system, which takes into account the actual construction sequence and ambient variables to simulate crack propagation caused by a nonuniform RH field. First, a three-step RH transfer process is designed based on the node coupling technique to investigate the influence of the construction sequence on the early humidity field in the foundation, sleepers, and cast-in-place track slab separately, and then the nonuniform distribution of the early humidity field in the ballastless track system is determined.

1. Introduction

Since the operation of Beijing-Tianjin intercity high speed railway in 2008, Chinese rapid transit railway has made a rapid development and remarkable achievement [1]. Ballastless track has become the main structural type of rapid transit railway because of its good stability and less maintenance. By the end of April 2021, the total mileage of rapid transit railway has reached about 38,000 kilometers in China [2, 3]. As the most widely used type of ballastless track, the CRTS (Chinese Railway Track System) I bi-block ballastless track has been applied on more than 44 rapid transit railways

such as Wuhan-Guangzhou, Xi'an-Chengdu, and Lanzhou-Xinjiang lines [4]. According to the difference of structures built on the subgrade, bridge, and tunnel, the CRTS I bi-block ballastless track can be divided into three types. The schematic diagram of CRTS I bi-block ballastless track in tunnel is shown in Figure 1, which consists of rail, fastener, sleeper, track slab, and tunnel foundation [5]. However, the ballastless track, as the basis for rapid transit railway, is directly exposed to the atmosphere and eroded by the complex environment factors. These influencing factors make the component materials of the ballastless track in a continuous deterioration process [6–8]. Through the field

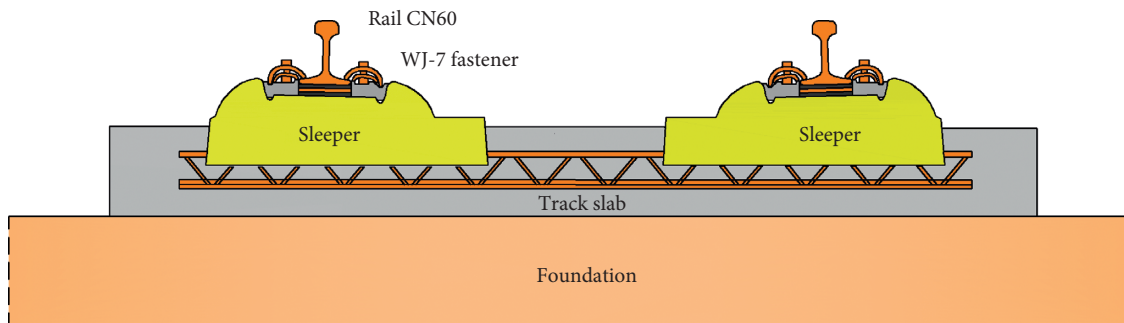


FIGURE 1: Diagram of CRTS I bi-block ballastless track in tunnel.

investigation, it is found that the early cracks are more likely to occur on the surface of track slab due to the bad construction and inadequate design, and then these cracks would rapidly develop into obvious water diseases in abundant rain or poor drainage areas, as shown in Figures 2(c) and 2(d).

The bi-block ballastless track has large contact area with the external environment, and thus the transport of moisture from concrete to environment is significantly affected by the environmental humidity. After concreting the track slab, the hydration of concrete materials will lead to the overall decrease of relative humidity inside the structure. Then, the higher humidity diffuses from track slab to sleepers and ambient dry air, as shown in Figure 2(b). Due to the slow transport rate of moisture in concrete materials, the nonlinear humidity gradient is formed in the ballastless track by the difference of low surface humidity and high internal humidity. On account of the wetting expansion and drying contraction of concrete materials, the shrinkage deformation and stress will occur under the nonlinear humidity gradient. Once the stress is greater than the ultimate tensile strength of concrete, the early cracks will form in the structure, as shown in Figure 2(c).

Figure 3 shows the distribution of early cracks on the track slab of bi-block ballastless track, which was discovered during the investigation of a new bi-block ballastless track. Combined with existing reports [9], the characteristics of cracks on the track slab of bi-block ballastless track can be described as follows: (1) the majority of cracks occurred at the age of 2~3 days or 2 months after the initial setting of track slab; (2) the splayed crack first appeared at the corner of sleeper, and its initial angle is about 40°; (3) the crack angle decreases with the propagation of crack and gradually tends to 0°; (4) the cracks at corner of adjacent sleepers would be coalesced and finally form a transverse through-wall crack in the track slab. Currently, the formation mechanism of early drying-induced cracks on the track slab is not clear.

In view of the causes of early cracks in the ballastless track, Wang [9] firstly conducted a statistical analysis of the early crack characteristics on the track slab under construction and pointed out that the temperature and drying shrinkage deformation could be the main reasons for the early cracks. Over the next decade, the related researches [10, 11] mainly focus on the strength and stability caused by temperature load and seldom consider the influence of

shrinkage deformation resulting from internal relative humidity. Based on the heat-moisture-deformation coupling analysis, Chen [12] found that the shrinkage deformation of concrete with a 1% drop in humidity is equivalent to a 2°C drop in temperature. The research results of Li et al. [4] and Yang et al. [6] indicate that the maximum humidity gradient on the surface of the concrete in a dry environment is dozens of times the temperature gradient. That is, the drying shrinkage deformation is much greater than the temperature deformation. Han et al. [13] believe that the contribution of drying shrinkage deformation to early crack can reach 80%. In the control of early-age cracks of track slab, the addition of anticrack steel bars can reduce the early splayed cracks, while the film-forming moisture curing can effectively reduce the irregular cracks [14]. The crack resistance test of concrete slab indicates that adding the 6% TK-ICM anticrack materials in cementitious materials can maintain the internal humidity of concrete for a long time and reduce the risk of cracking [15].

As a main component material of ballastless track, the influence of water on concrete is first reflected in its internal moisture distribution. At present, the moisture transfer model based on Fick's law is widely used to describe the moisture exchange between concrete and environment [16]. Liu et al. [17] used the finite difference method to conduct the concrete humidity. By programming the finite element program, Akika et al. [18] analyzed the humidity field of solid structure with a simplified boundary. In the aspect of experimental research, Parrott [19] fitted the formula for calculating the humidity field in a unilateral drying condition based on experimental data. Combining the theoretical and test results, Gao [20] proposed a calculation model for the concrete humidity field under dry-wet cycles. For the problem of humidity distribution in complex environment, Wang et al. [21] qualitatively analyzed the problem of parameter values affecting the calculation accuracy of humidity field. Subsequently, Gao and Wei [22] put forward the quantitative analysis method of humidity gradient in concrete slab by comprehensively considering the influencing factors such as water/cement ratio, ambient air humidity, and moisture diffusion property of concrete material. To predict the relative humidity of early-age concrete under sealed and unsealed conditions, the models for early-age relative humidity are proposed in consideration of water/cement ratio, critical time, and age of concrete [23]. In view

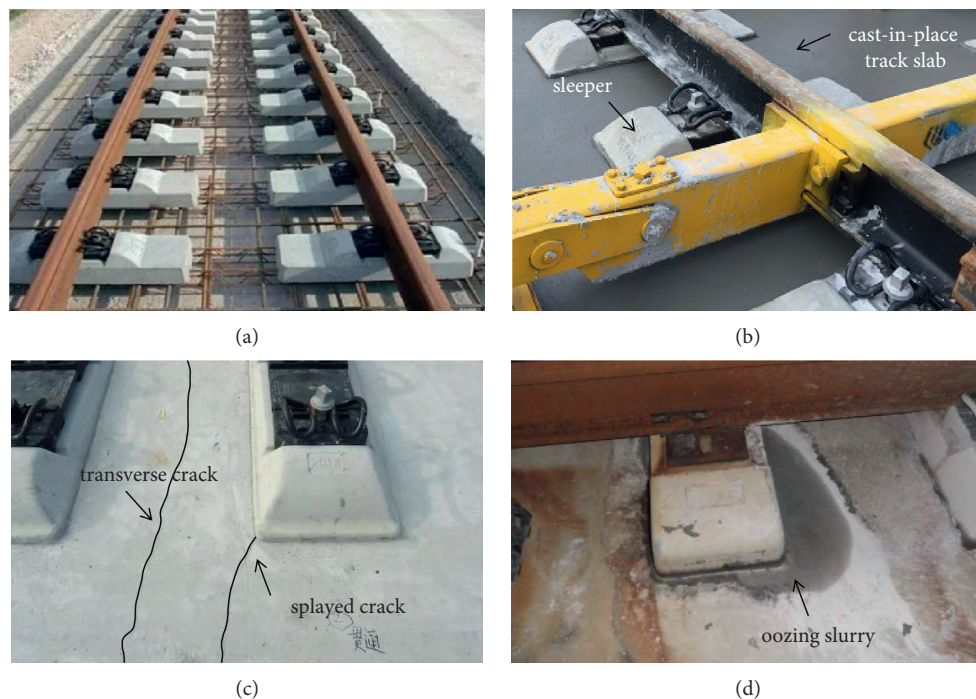


FIGURE 2: State of bi-block ballastless track at different stages. (a) Accurately adjusted and positioned sleepers [4]. (b) Cast-in-place track slab. (c) Early cracks. (d) Oozing slurry.



FIGURE 3: Distribution of cracks on the surface of track slab. (a) Initial crack. (b) Crack coalescence.

of the disadvantages of the complex numerical calculation method of humidity field which is not conducive to engineering application, Wang et al. [24] proposed a conventional method to calculate the concrete humidity field based on the temperature field module by comparing the differential equation, initial and boundary conditions of the temperature, and humidity fields. Although the scholars have studied the distribution characteristics of humidity field in concrete materials, these research results can neither consider the influence of construction characteristics of ballastless track on humidity field nor satisfy the complex humidity environment acting on ballastless track. Up to now, there are few reports on the research of early humidity field of ballastless track. To realize the early humidity analysis of the bi-block ballastless track, the following obstacles need to be resolved firstly: (1) after concreting the track slab, the three separated layers of bi-block ballastless

track bond to adjacent layers, (2) affected by the construction sequence, the initial humidity field of each layer is inconsistent, and (3) the initial humidity conditions of sleepers and foundation are unknown. Therefore, the early humidity prediction presents a considerable challenge when construction sequence is taken into consideration.

In this paper, a finite element computational model of humidity distribution in ballastless track was established by introducing the complex environmental influence and construction process. Based on the node coupling technique, a three-step calculation process including one steady-state and two transient analyses was designed to realize the influence of the construction sequence on the early humidity field. Then according to the construction sequence, the early humidity field of each layer of bi-block ballastless track was analyzed, and the effects of controlling parameters related to external ambient air drying, internal hydration self-

desiccation, and local wetting time on early humidity distribution in ballastless track were analyzed. The distribution characteristics and development law of early humidity field of bi-block ballastless track were defined. Moreover, the formation mechanism of shrinkage crack was analyzed on the basis of strength theory, and the crack propagation path was predicted by using the mixed-mode fracture criterion. The research results can provide theoretical basis for optimizing track structure design and improving track construction technology.

2. Computational Model of Humidity Field in Concrete

In the complex environment, the internal relative humidity field of the ballastless track is in a state of dynamic equilibrium under the combined action of wetting on the bottom, moisture exchange between the exposed surface and the ambient air, internal moisture diffusion from high humidity region to low humidity region, and self-desiccation due to hydration of cement. To serve the practical analysis of the ballastless track, here the computational theory of humidity field is firstly reviewed.

Assuming that the RH at the position (x, y, z) and time t is $H(x, y, z, t)$, the moisture change within a closed domain Ω caused by the RH variation from $H(x, y, z, t_1)$ to $H(x, y, z, t_2)$ is

$$Q_1 = \int_{t_1}^{t_2} \left[\iiint_{\Omega} \frac{\partial H}{\partial t} dV \right] dt. \quad (1)$$

Considering the effect of self-desiccation of material, the moisture change from time t_1 to t_2 is

$$Q_2 = - \int_{t_1}^{t_2} \left[\iiint_{\Omega} G(x, y, z, t) dV \right] dt, \quad (2)$$

where $G(x, y, z, t)$ is the function of hydration self-desiccation of material, and the relationship between the hydration self-desiccation and the water-cement ratio w/c can be described as follows [24]:

$$G(t) = \frac{0.002 \cdot \exp[-(w/c)/0.3068]}{(1 + 0.43t)^{1.2}}. \quad (3)$$

The moisture in the structure will diffuse from high humidity region to low humidity region under the action of humidity gradient, and the moisture diffused through a tiny surface is proportional to the time dt , surface area dA , and humidity gradient along the surface normal direction; that is,

$$dQ_3 = -D(x, y, z, t) \frac{\partial H}{\partial n} dA dt, \quad (4)$$

where $\partial H / \partial n$ is the change rate of humidity along the normal direction of surface and $D(x, y, z, t)$ is the coefficient of moisture diffusion which is a function of the internal RH [22]:

$$D(H) = D_1 \left[\alpha + \frac{1 - \alpha}{1 + (1 - H/1 - H_c)^\beta} \right]. \quad (5)$$

In equation (5), D_1 is the maximum moisture diffusion coefficient, α is the ratio of minimum to maximum moisture diffusion coefficient, H_c is the relative humidity when $D(H) = 0.5D_1$, and β is the material constant.

Therefore, the total amount of water diffused through the closed surface from time t_1 to t_2 can be written as

$$Q_3 = \int_{t_1}^{t_2} \left[\iiint_{\Omega} D \nabla^2 H dV \right] dt. \quad (6)$$

According to the law of conservation of mass, $Q_1 = Q_2 + Q_3$, we have

$$\int_{t_1}^{t_2} \left[\iiint_{\Omega} \frac{\partial H}{\partial t} dV \right] dt = - \int_{t_1}^{t_2} \left[\iiint_{\Omega} G(x, y, z, t) dV \right] dt + \int_{t_1}^{t_2} \left[\iiint_{\Omega} D \nabla^2 H dV \right] dt. \quad (7)$$

The humidity boundary condition for the ballastless track can be divided into the following two categories.

- (1) The humidity on the material surface is a known function related to time; that is,

$$H_m = H(t). \quad (8)$$

- (2) The moisture exchange coefficient between the exposed surface and ambient air is known; then,

$$-D \frac{\partial H}{\partial n} = a_m (H_m - H_s), \quad (9)$$

where H_s is the RH of the ambient air, H_m is the RH of the exposed surface, and a_m is the moisture exchange coefficient.

In order to verify the correctness of the computation model of concrete early humidity field, a concrete specimen from casting to curing stage is considered, as shown in Figure 4. A serial of monitoring points A, B, C, D, and E were set in the calculation model, and the corresponding distance to the upper surface is 2, 8, 15, 25, and 28 cm, respectively. The calculation conditions were set as follows: within 28 days after casting the concrete specimen, the upper surface of specimen is exposed to the ambient air with a RH of 65%. After this, the bottom is in contact with water directly.

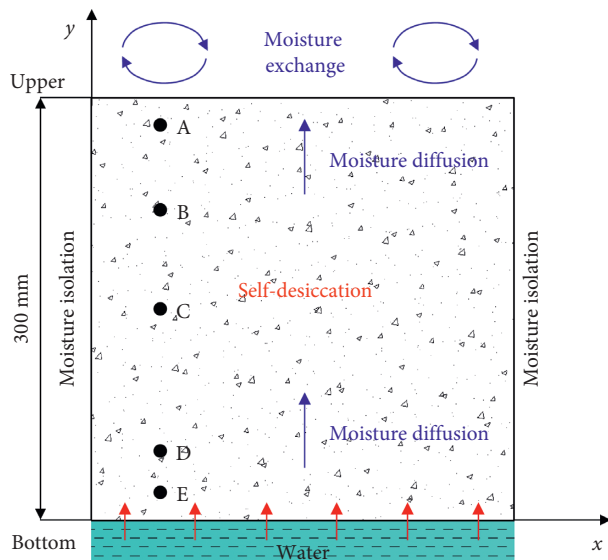


FIGURE 4: Early humidity field calculation model of concrete specimen ($w/c = 0.4$).

Furthermore, both the left and right sides of the concrete specimen keep isolated from the ambient air. Using ANSYS Workbench 18.0, the concrete specimen is discretized by 900 elements. The resulting humidity distribution in the specimen is shown in Figures 5 and 6.

As can be seen from Figure 5, since the monitoring point A is close to the upper surface and greatly affected by the dry ambient air, the relative humidity declines rapidly over time. For the deeper monitoring point B and below, due to the slow rate of moisture diffusion in the concrete material, the declining rate and amplitude of humidity are significantly smaller than those at monitoring point A, and the humidity reduction is mainly caused by the hydration self-desiccation. At the age of 28 days, the specimen bottom is beginning to contact with the water directly, and the relative humidity of monitoring points adjacent to the bottom increases to a different degree. Due to the fast rate of capillary water absorption, the relative humidity at monitoring point E increases rapidly, while the relative humidity at monitoring point D increases with a delay amplitude and slow rate but still shows a rising trend. From Figures 6 and 7, it can be seen that, under the combined action of upper drying air, bottom wetting environment, and internal hydration self-desiccation, the moisture variation in the concrete specimen can be divided into three regions along depth: (1) the influence area of the ambient drying air is about 8 cm away from the upper surface; (2) the influence area of the wetting environment is within 7.5 cm from the bottom; (3) the influence area of hydration self-desiccation is the intermediate region with a uniform humidity distribution. In addition, the numerical calculation value of relative humidity is in good agreement with the test result, so it can be considered that the transient calculation model of humidity field established in this paper can be used to predict the humidity distribution of ballastless track under the complex environment.

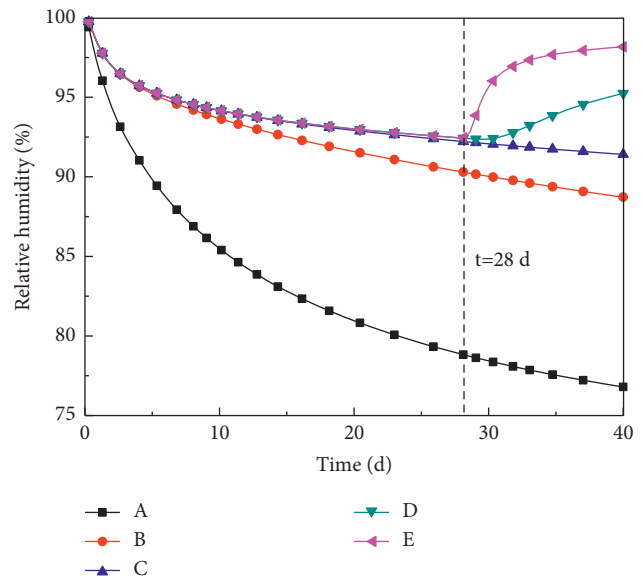


FIGURE 5: Variations of RH at different monitoring points.

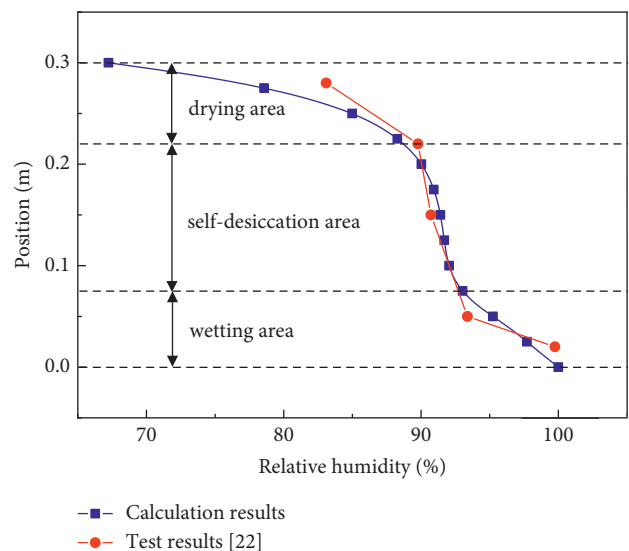


FIGURE 6: RH distribution along the vertical direction ($t = 40$ d).

3. Early Humidity Field Calculation Model and Process of Ballastless Track

3.1. Calculation Model. In this paper, the CRTS I bi-block ballastless track in tunnel is focused on to establish the humidity field calculation model, as shown in Figure 8. The model consists of bi-block sleepers ($800 \text{ mm} \times 140 \text{ mm} \times 300 \text{ mm}$), track slab ($2800 \text{ mm} \times 260 \text{ mm} \times 6250 \text{ mm}$), and foundation ($5800 \text{ mm} \times 2000 \text{ mm} \times 6250 \text{ mm}$). The corresponding material parameters are shown in Table 1 [20, 22, 25]. In order to solve the unsteady moisture diffusion problem, the internal moisture source with negative value is used to control the hydration self-desiccation of early-age concrete, as shown in equation (3). Meanwhile, the convective moisture flux is applied on the exterior boundaries of ballastless track to realize the moisture

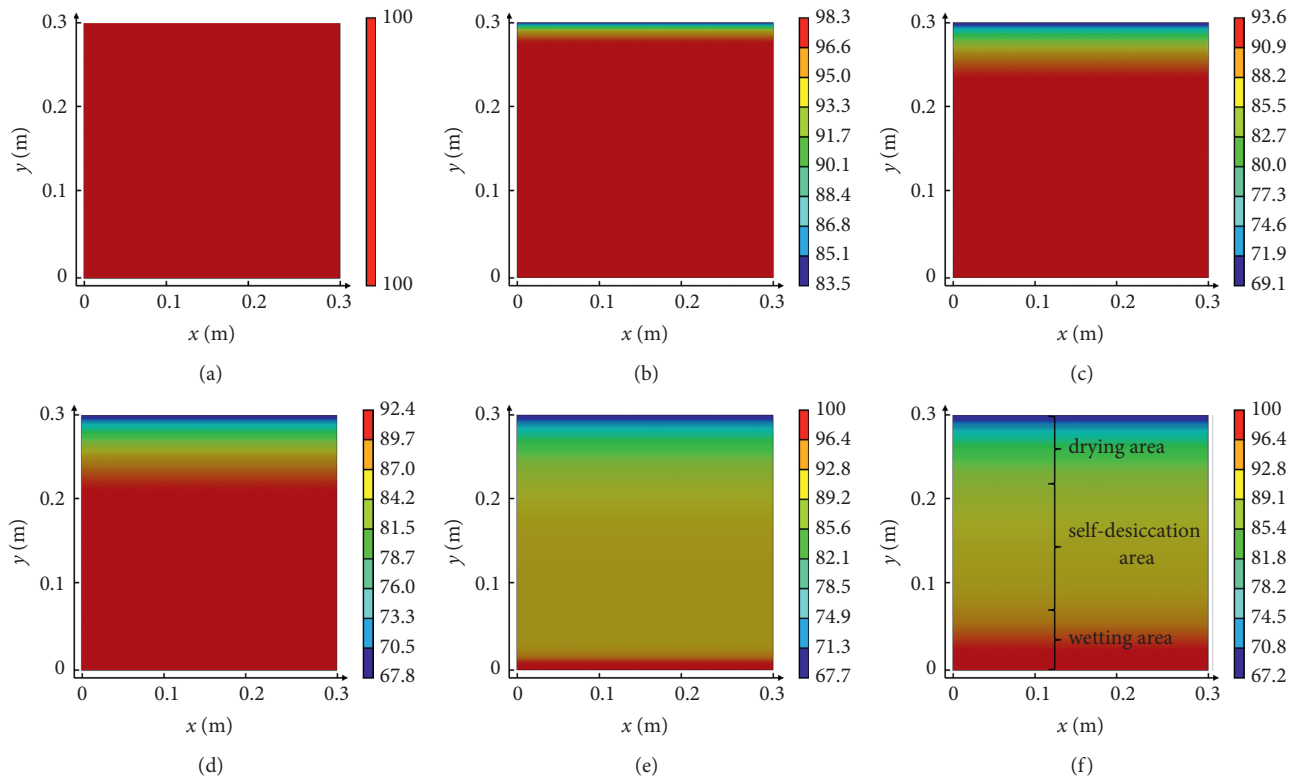


FIGURE 7: RH contour of concrete specimen at different times. (a) $t = 0$ d, (b) $t = 1$ d, (c) $t = 14$ d, (d) $t = 28$ d, (e) $t = 29$ d, and (f) $t = 40$ d.

exchange between exterior boundaries and ambient air. The external ambient relative humidity is set to be 65%, and the moisture transfer coefficient a_m is listed in Table 1. In addition, the wet boundary is specified as constant relative humidity of 100%.

3.2. Calculation Process. CRTS I bi-block ballastless track is a kind of track structure which is one-time cast-in-place after assembling the prefabricated bi-block sleepers into track panels. It is important to notice that the three separated layers of bi-block ballastless track will be bonded to adjacent layer after concreting the track slab. Meanwhile, the initial humidity conditions of three layers are nonuniform and inconsistent. In order to overcome the above technical obstacles, based on the node coupling technique, the three-step calculation process including one steady-state and two transient analyses was designed to realize the influence of the construction sequence on the early humidity field, as shown in Figure 9.

- (1) Step 1: Under the long-term action of groundwater infiltration and external ambient air drying, the humidity field of foundation is in equilibrium. First, the steady humidity field of foundation is obtained by conducting a steady-state humidity field analysis. This steady result will be used as the initial humidity condition of foundation for the transient humidity field analysis of ballastless track in step 3.

- (2) Step 2: The sleepers are precast at the factory and maintained to $t = 60$ d. In this case, their humidity distribution is mainly affected by the external ambient air drying and internal hydration self-desiccation. In this step, the variation of humidity field is obtained by carrying out a transient humidity field analysis of sleepers. The last-time result is used as the initial humidity condition of sleepers for the transient humidity field analysis of ballastless track in step 3.

- (3) Step 3: To control the interface state transition before and after concreting the track slab, the node coupling technique is applied at the interfaces between track slab and sleepers, track slab and foundation, as shown in Figure 10. Before concreting the track slab, the node coupling technique is deactivated, and the interface state keeps separated. After concreting the track slab, the node coupling technique is activated, and the interface state translates from separated state to bonded state. Then, the initial high humidity will diffuse from track slab to sleepers and foundation through the bonded interfaces.

According to the above calculation process, the early humidity distribution characteristics of CRTS I bi-block ballastless track can be defined. The initial conditions, boundary conditions, and result analysis of the above three steps are described in detail in Section 4.

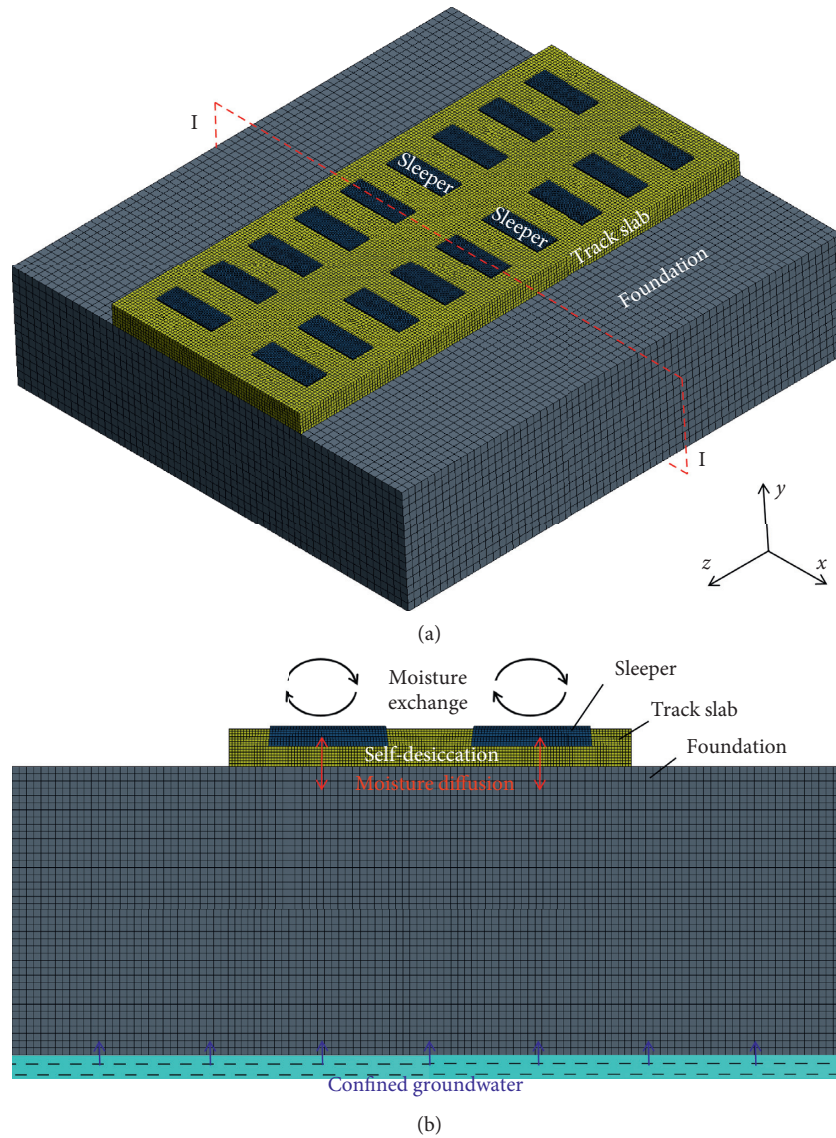


FIGURE 8: Early humidity field calculation model of CRTS I bi-block ballastless track. (a) Overall FE model and (b) local schematic for the cross section I-I.

TABLE 1: Material parameters.

Component	E_{28} (GPa)	ν	w/c	f_t (MPa)	$D_1 \times 10^{-10}$ ($\text{m}^2 \cdot \text{s}^{-1}$)	α	β	H_c (%)	a_m ($\text{m} \cdot \text{d}^{-1}$)
Sleeper	36.0	0.2	0.3	1.54	0.25	0.018	1.3	98	0.0038
Track slab	32.5	0.2	0.4	2.39	0.5	0.022	1.1	98	0.0055
Foundation	25.5	0.2	0.6	2.74	2.02	0.071	0.8	98	0.0105

4. Early Humidity Analysis in the Ballastless Track

4.1. Steady-State Humidity Analysis of Foundation. In the tunnel, it is assumed that the groundwater exists at a depth of 2 m, and the relative humidity of the ambient air is 65%. Under the long-term action of groundwater and ambient air, the steady humidity distribution of tunnel foundation was calculated by steady-state analysis, as shown in Figures 11 and 12.

Up to now, the linear interpolation is still a common approach used to deal with the initial conditions of sub-structures such as tunnel foundation and subgrade bed during a transient physical field analysis of ballastless track [26]. However, in view of the nonlinear relationship between moisture diffusivity and humidity, the steady humidity distribution along the depth follows a cubic polynomial, as shown in Figures 11 and 12. The relative humidity of the upper surface is about 65.1%, which is very close to that of the ambient air in tunnel. At the depth of 1 m, the maximum

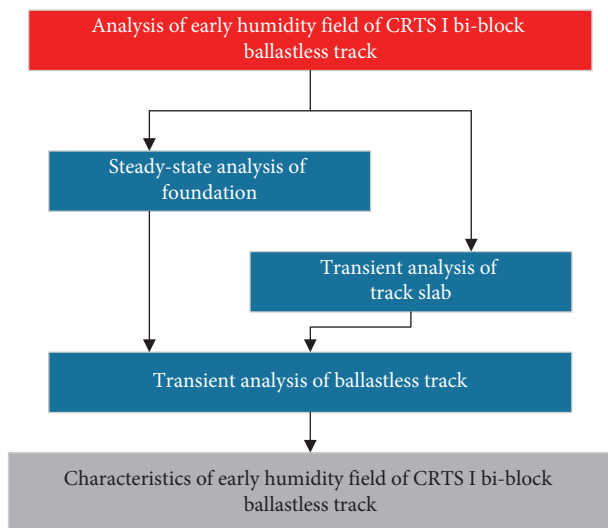


FIGURE 9: Early humidity field calculation process of CRTS I bi-block ballastless track.

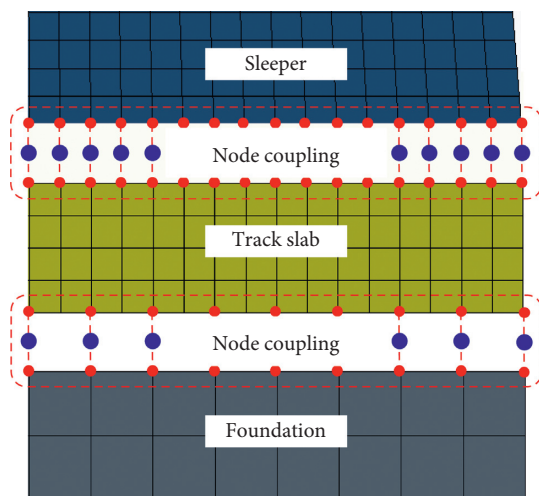


FIGURE 10: Node coupling technique applied at the interfaces.

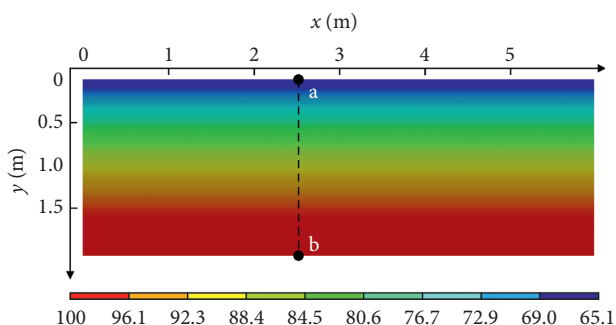


FIGURE 11: Steady RH contour of foundation.

difference between numerical result and linear interpolation is 7.5%. Therefore, the steady-state humidity analysis of foundation is essential, and the steady result will be as the initial humidity condition of foundation for the transient humidity field analysis of ballastless track in Section 4.3.

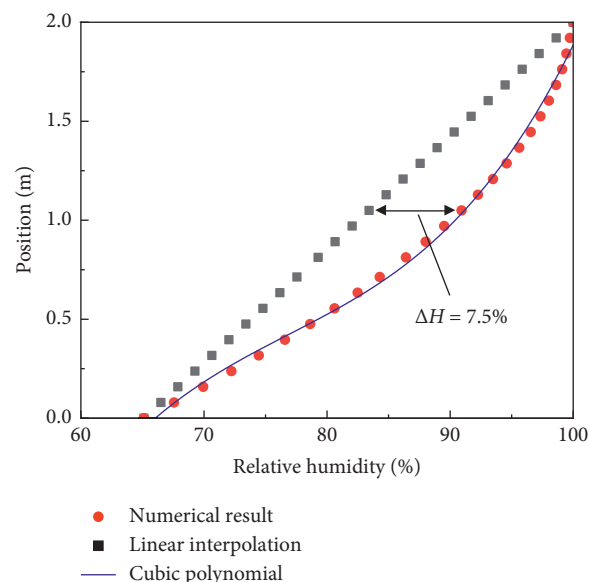


FIGURE 12: Distribution of RH along the path ab.

4.2. Transient Humidity Analysis of Sleeper. After concreting sleepers at the factory, the sleepers were stored in the ambient air with an average RH of 65% and RH amplitude of 50%, as shown in Figure 13, and kept for 60 days. Under the action of external ambient air drying and internal hydration self-desiccation, the humidity distribution of sleeper was calculated, as shown in Figures 14–16.

Figure 14 shows that, under the coupling effect of external air drying and internal hydration self-desiccation, the relative humidity in the sleeper shows a steady decline. On the 60th day after the sleepers have been precast, the surface relative humidity decreases to 66.6%, and the intermediate relative humidity decreases to 80.1%. The relative humidity of the surface layer of the sleeper is mainly affected by the ambient air, while the interior of the sleeper is mainly controlled by hydration self-desiccation. In order to further study the distribution of sleeper's relative humidity, the relative humidity and relative humidity gradient (RHG) along line ab shown in Figure 14(b) were calculated, as shown in Figures 15 and 16, respectively.

According to Figures 15 and 16, it is found that the typical nonlinear relative humidity gradient is formed inside the sleeper due to the slow transfer of moisture in concrete materials, which can also be approximated by a five-segment linear distribution. As a result of diurnal fluctuations of ambient relative humidity, the maximum relative humidity gradient appears around 6 mm beneath the surface of sleeper, and the limit influence depth of diurnal fluctuations of ambient relative humidity is about 8 mm. In this section, the last-time transient result will be as the initial humidity condition of sleepers for the transient humidity field analysis of ballastless track in Section 4.3.

4.3. Transient Humidity Analysis of Ballastless Track. Sixty days after the sleepers had been precast, the sleepers were transported to the construction site. Then, the track slab was poured after the sleepers had been assembled into

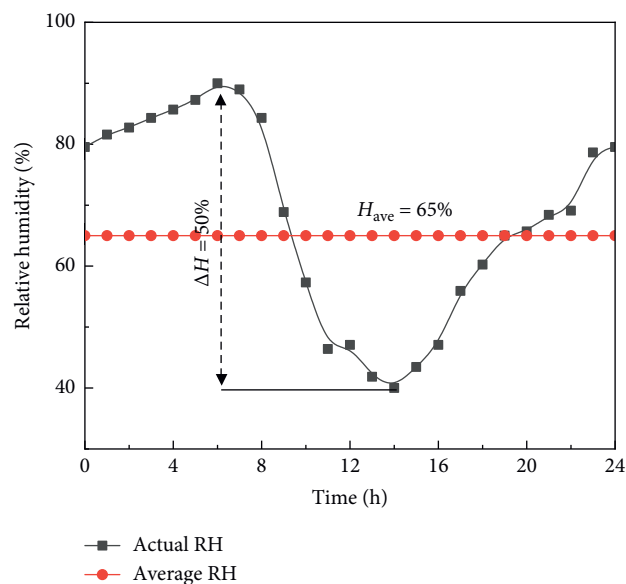


FIGURE 13: Daily periodic fluctuations of ambient relative humidity applied on the surface of sleeper.

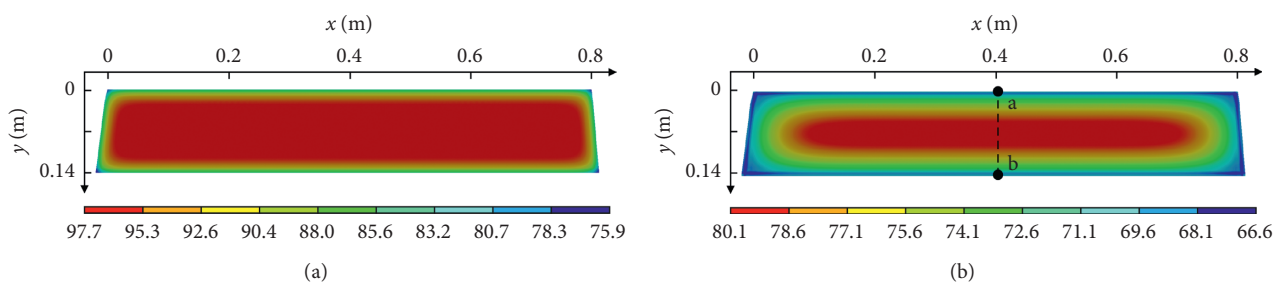


FIGURE 14: RH contour of sleeper at different times. (a) $t = 1$ d and (b) $t = 60$ d.

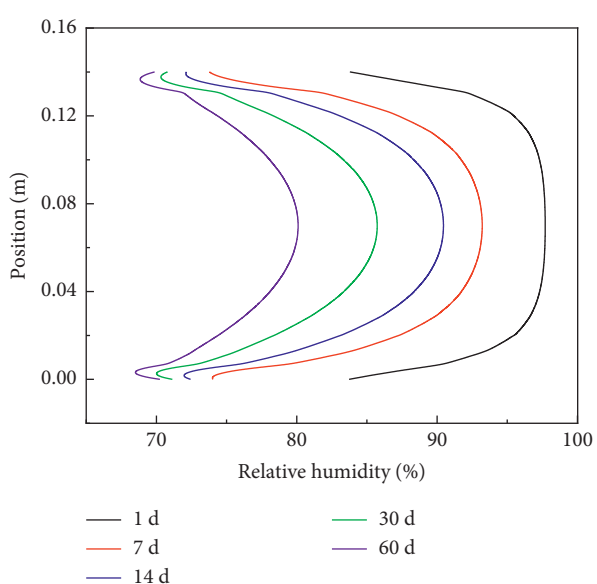


FIGURE 15: Distribution of RH along the path ab.

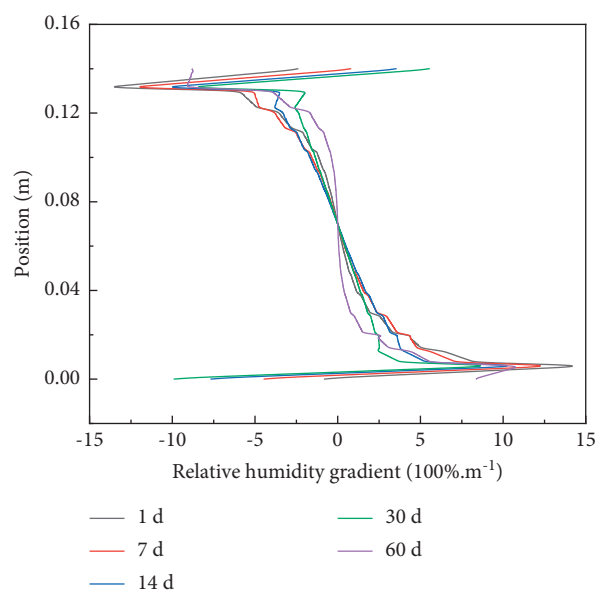


FIGURE 16: Distribution of RHG along the path ab.

track panels and maintained for 90 days. In this transient analysis, the initial humidity state of ballastless track is shown in Figures 17(a) and 17(b). The initial humidity of foundation used the steady-state result in Section 4.1, the initial humidity of track slab was set to be 100%, and the initial humidity of sleepers adopted the transient result in Section 4.2. In the first seven days, the exposed surfaces of ballastless track were specified as wet boundaries ($H = 100\%$) according to the construction requirements and replaced by a convective moisture flux condition ($H = 65\%$) in the days that followed. Under the water wetting, external ambient air drying, and internal hydration self-desiccation, the humidity distribution of the ballastless track was calculated, as shown in Figure 17.

It can be seen from Figure 17 that, at the initial phase after concreting the track slab, the significant difference of humidity forms on both sides of the interface. Under the driving action of humidity difference, the moisture in the structure diffuses from high humidity to low humidity areas and forms a higher relative humidity gradient at the interface, as shown in Figures 17(c), and 17(d). Subsequently, the relative humidity field inside the whole ballastless track gradually becomes stable under the continuous effect of moisture diffusion, as shown in Figures 17(c), 17(e), and 17(g). Finally, the maximum relative humidity gradient of each region appears at the surface interface, shown as points A and B in Figure 17(h). In order to further study the humidity distribution at the interface, the relative humidity and relative humidity gradient along the line ab shown in Figure 17(h) were calculated, as shown in Figures 18 and 19. Interface 1 represents the interface between sleeper and track slab, and interface 2 represents the interface between track slab and foundation.

From Figures 18 and 19, a large relative humidity gradient will occur at the interface between track slab and sleeper or the track slab and foundation. On the 1st, 3rd, 7th, 14th, 30th, 45th, 60th, and 90th days after concreting the track slab, the relative humidity gradients at the interface between the track slab and sleeper are 24.46, 14.45, 8.69, 4.17, 2.26, 1.65, 1.39, and $1.09 \times 100\%/m$, respectively. The results show that the relative humidity gradient decreases rapidly in the first week after concreting the track slab, and then the descending rate tends to be slow over time.

5. Crack Formation

5.1. Cracking Criterion. Due to the apparent characteristics of wetting expansion and drying contraction of concrete materials, the cracks in concrete structures may be caused by the nonuniform internal relative humidity. Based on the beam warping test, the relation between drying-induced strain ε and internal relative humidity H in concrete can be written as follows [27]:

$$\varepsilon = 8.14 \times (1 - H) \times 10^{-4}, \quad (10)$$

from which it is found that the nonuniform RH field leads to the nonuniform strain and then stress.

Besides, as a key parameter that affects the deformation of material, the elastic modulus of concrete increases with

age, and the increase rate in early age is higher than that in the later age. In this paper, the constant elastic modulus E_{28} of sleeper and foundation listed in Table 1 is adopted, and the elastic modulus of track slab is described by exponential formula [28]:

$$E(t) = E_{28} \times [1 - \exp(-0.4t^{0.34})], \quad (11)$$

where t is the time in day and E_{28} is the elastic modulus of the concrete at the equivalent age of 28 days.

For brittle materials such as concrete, its failure is mainly caused by the maximum tensile stress. The cracking risk of concrete can be defined as the ratio of the maximum principal stress to the tensile strength [29]; that is,

$$\zeta = \frac{\sigma_{1,\max}}{f_t}, \quad (12)$$

where ζ is the cracking risk, $\sigma_{1,\max}$ is the maximum principal stress, and f_t is the tensile strength.

Considering the fluctuating characteristics of the mechanical properties of concrete materials, it is generally believed that the crack will be caused when the cracking risk reaches 0.7 [30].

5.2. Results and Analysis. After concreting the track slab, the distributions of maximum principal stress at different times were calculated without taking into account wet curing, as shown in Figure 20.

It can be seen from Figure 20 that, in the curing stage of track slab, a certain tensile stress will be generated due to the drying shrinkage property of concrete materials, and the stresses that occur at the interface between sleeper and track slab are greater than those at other areas. When the stress exceeds the tensile strength of the interface, the interface crack will be generated.

After the interface crack between sleeper and track slab has been generated, shown as white lines ab and cd in Figure 20(b), the released energy of interface crack will be transferred to the corner of sleeper and intensifies the stress concentration effect. When the maximum principal stress exceeds the tensile strength of the track slab, the splayed crack with an initial angle of about 45° will be generated at the sleeper corner. Finally, the cracks at corner of adjacent sleepers would be coalesced and form a transverse through-wall crack of track slab, as shown in Figures 3(b) and 20(b).

6. Crack Propagation

6.1. Mixed-Mode Fracture Criterion. In order to clarify the propagation mechanism of track slab crack, the mixed-mode fracture criterion was selected to predict the propagation direction of track slab crack by considering the combined effect of tensile and shear stresses. The previous studies have shown that the maximum circumferential tensile stress criterion is in good agreement with the test data of brittle materials such as concrete and rock. Therefore, this criterion is often used to analyze the fracture mechanism of concrete structures. For the mixed-mode crack, the equivalent stress

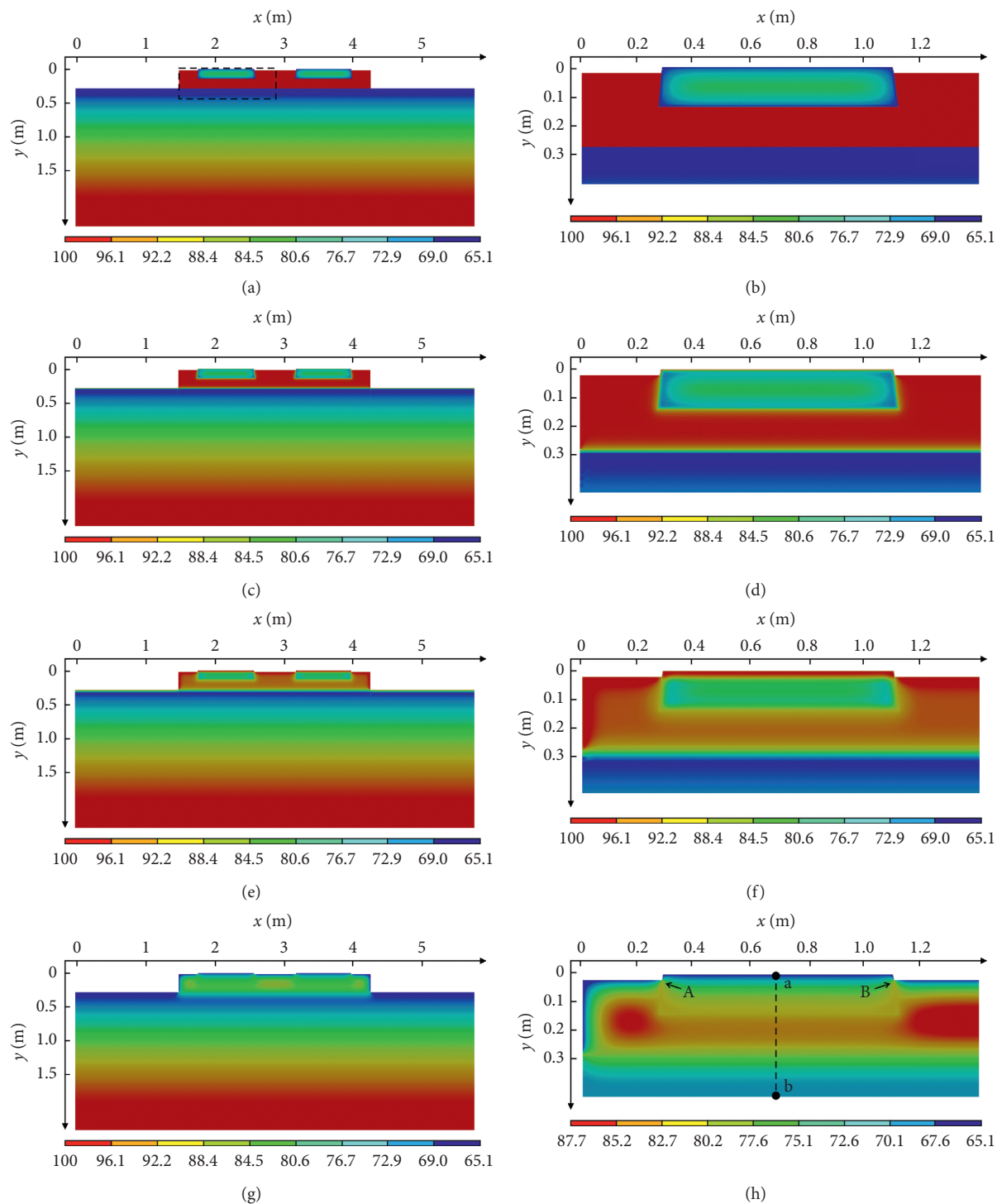


FIGURE 17: RH contour of ballastless track at different times. (a) $t = 0$ d, entire contour; (b) $t = 0$ d, local contour; (c) $t = 1$ d, entire contour; (d) $t = 1$ d, local contour; (e) $t = 7$ d, entire contour; (f) $t = 7$ d, local contour; (g) $t = 60$ d, entire contour; (h) $t = 60$ d, local contour.

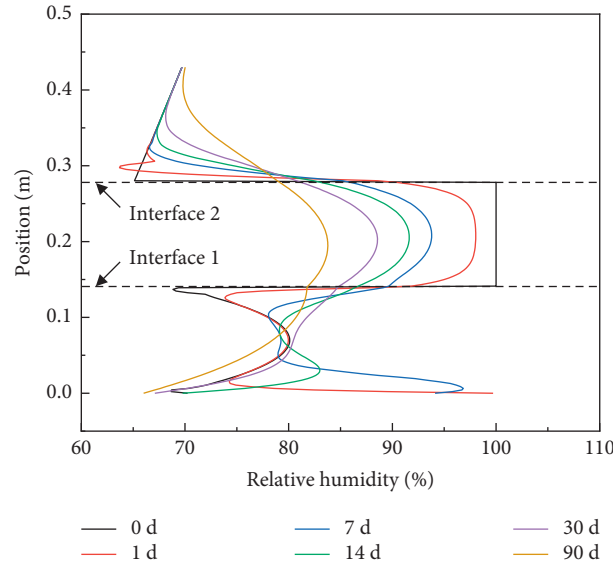


FIGURE 18: Distribution of RH along the path ab.

intensity factor K_{eff} can be evaluated by the following equation [31]:

$$K_{eff} = \sqrt{(K_I + K_{II})^2 + \frac{1}{1-2\nu} K_{III}^2}, \quad (13)$$

where ν is Poisson's ratio and K_I , K_{II} , and K_{III} are the stress intensity factors in modes I, II, and III, respectively, which can be computed based on the displacement extrapolation method [32]; that is,

$$\begin{cases} K_I = \frac{G(v_c - v_e)}{\kappa + 1} \sqrt{\frac{2\pi}{r}}, \\ K_{II} = \frac{G(u_c - u_e)}{\kappa + 1} \sqrt{\frac{2\pi}{r}}, \\ K_{III} = \frac{G(w_c - w_e)}{\kappa + 1} \sqrt{\frac{2\pi}{r}}. \end{cases} \quad (14)$$

G is the shear modulus, κ is the coefficient related to Poisson's ratio, r is the element length, and u , v , and w are the node displacements in the x , y , and z directions, respectively, as shown in Figure 21.

When the equivalent stress intensity factor K_{eff} exceeds the fracture toughness K_C , the crack will lose the stability and fracture rapidly. The fracture condition can be expressed as

$$K_{eff} \geq K_C. \quad (15)$$

The maximum circumferential tensile stress criterion assumes that the crack propagates along the direction of the maximum circumferential tensile stress [33]:

$$\theta = 2 \tan^{-1} \left[\frac{1}{4} \frac{K_I}{K_{II}} + \frac{1}{4} \sqrt{\left(\frac{K_I}{K_{II}} \right)^2 + 8} \right], \quad (16)$$

where θ is the turning angle of the crack, as shown in Figure 21.

The fracture models described above have been implemented in the ANSYS Workbench 18.0, and the flowchart of numerical procedure for the fatigue crack growth simulation is shown in Figure 22.

6.2. Results and Analysis. Based on the maximum circumferential tensile stress criterion, the propagation path of crack with an initial length $L_{in} = 0.1$ m and angle $\theta_{in} = 45^\circ$ was predicted, as shown in Table 2 and Figure 23. The results show that, under the action of drying shrinkage deformation of early-age concrete, the initial crack tip is subject to the combined action of tensile and shear stresses. In this case, the initial crack belongs to a mixed-mode crack, and the ratio of K_{II} and K_{III} to K_I is 31.37% and 7.6%, respectively. Under the combined action of stress intensity factors including K_I , K_{II} , and K_{III} , the initial crack direction will turn an angle of 30.06° , as shown in Figure 23(b). After the propagation path of initial crack has been turned, the ratio of K_{II} to K_I drops to 1.34%, and then the crack propagation path further turns an angle of 1.53° , as shown in Figure 23(c). Due to the continuous turning of crack propagation path, the final propagation path tends to be along the transverse direction of track slab, and the corresponding failure mode gradually transforms from mixed-model into pure opening-mode. When there are initial cracks at the corner of adjacent sleepers, the cracks would be coalesced

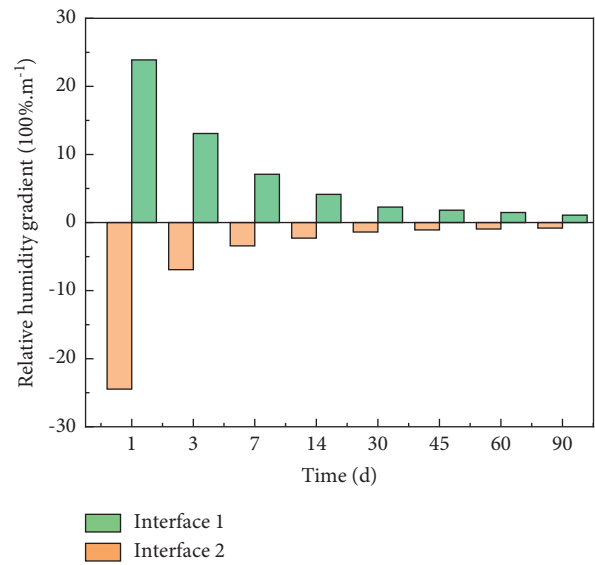
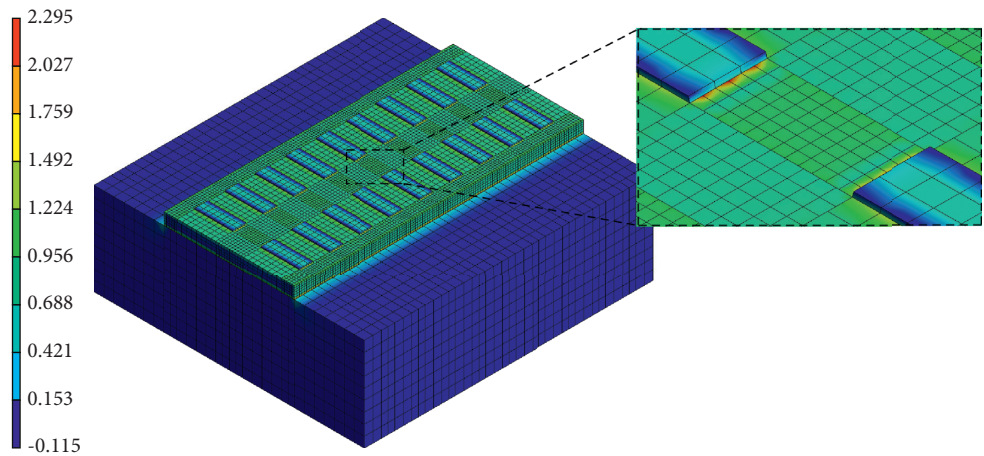


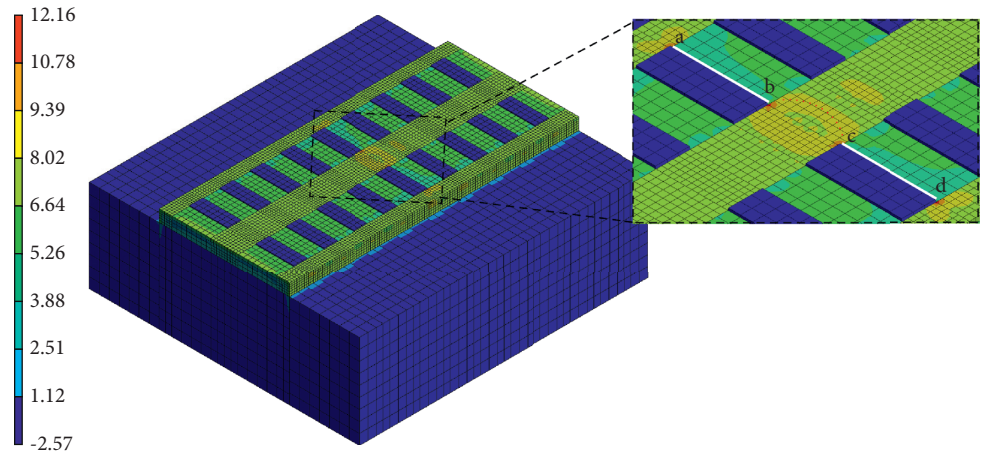
FIGURE 19: RHG at the interfaces.

TYPE: Maximum principal stress
Unit: MPa
Time: 1 d



(a)

TYPE: Maximum principal stress
Unit: MPa
Time: 90 d



(b)

Modeling of a Ballastless Track System... 492 S. K. Panda et al.
FIGURE 20: Maximum principal stress contour of ballastless track. (a) $t = 1$ d and (b) $t = 90$ d.

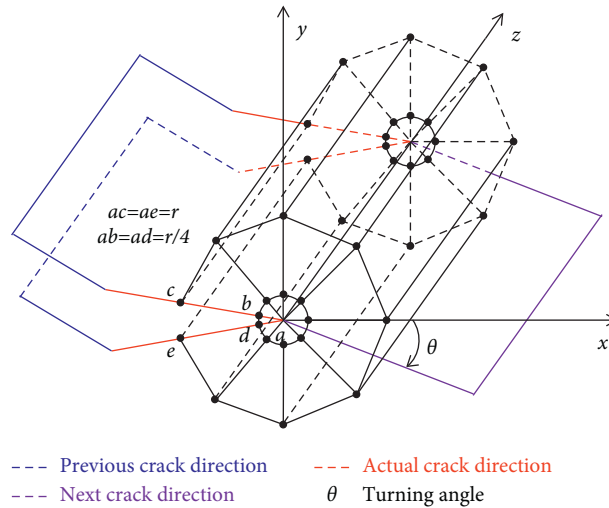


FIGURE 21: Singularity elements at the crack tip and crack propagation path.

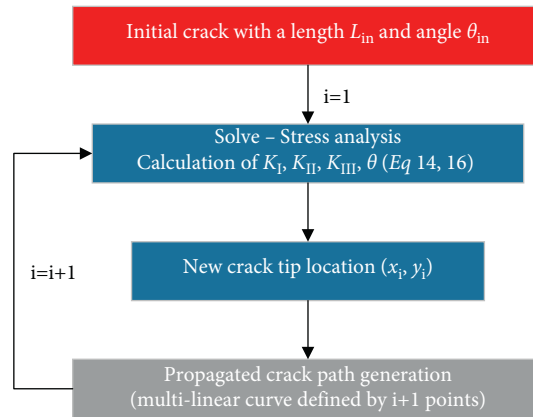


FIGURE 22: Numerical procedure for the fatigue crack growth simulation.

TABLE 2: Turning angle of the crack propagation path.

Crack length (m)	K_I (MPa.m ^{0.5})	K_{II} (MPa.m ^{0.5})	K_{III} (MPa.m ^{0.5})	K_{eff} (MPa.m ^{0.5})	Initial angle (°)	Previous angle (°)	Actual angle (°)	Turning angle (°)
0.1	3.8659	1.2128	0.2960	5.0930	45	—	45	30.06
0.2	5.2919	0.0709	0.0072	5.3637	45	45	14.94	1.53
0.3	5.4932	0.1268	0.0009	5.6200	45	14.94	13.41	2.65

and further form the transverse through-wall crack of track slab, as shown in Figures 3(b) and 23(d). The transverse through-wall crack not only significantly

affects the comfortableness and safety of rapid transit railway, but also reduces the service life of ballastless track.

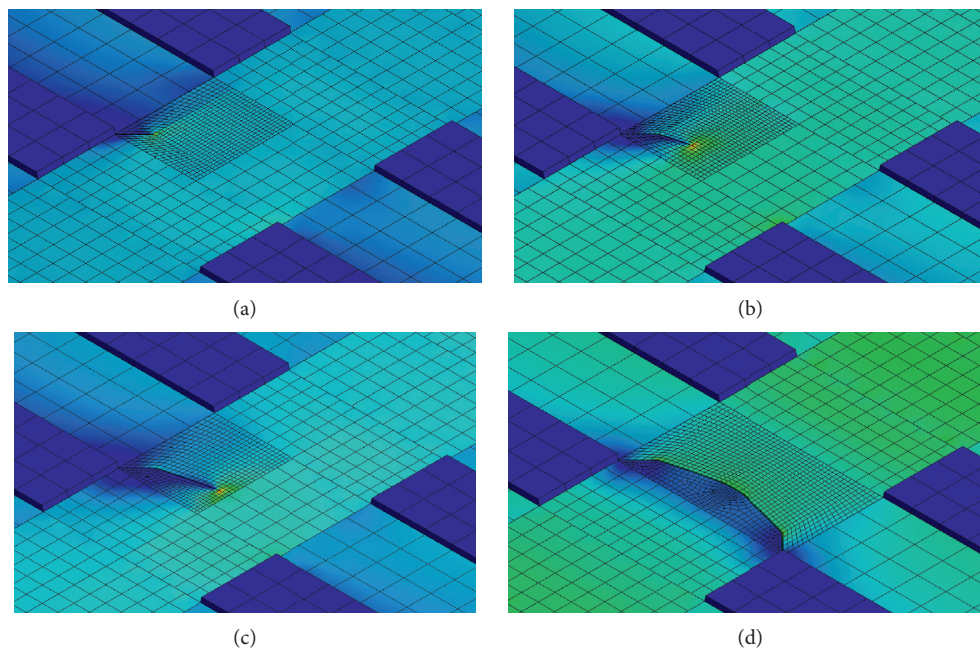


FIGURE 23: Predicted propagation paths of the crack with an initial angle of 45° . (a) $\theta = 30.06^\circ$, (b) $\theta = 1.53^\circ$, (c) $\theta = 2.65^\circ$, and (d) crack coalescence.

7. Conclusions

This paper focuses on the drying-induced crack mechanism of the CRTS I bi-block ballastless track system induced by early-aged internal relative humidity. Considering the construction sequence and environmental conditions of the ballastless track system, the RH distribution in the system is simulated, and the crack propagation induced by the nonuniform RH is predicted. The following conclusions can be drawn:

- (1) Under the long-term action of groundwater infiltration and external ambient air drying, the steady humidity of foundation along the depth obeys a cubic polynomial distribution. The steady result can provide an accurate initial humidity condition of foundation for the transient humidity field analysis of ballastless track relative to the linear interpolation method.
- (2) After precasting the sleeper, the nonuniform humidity field is formed inside the sleeper. The surface relative humidity of sleeper is mainly affected by the ambient air drying, and the interior relative humidity is mainly controlled by the hydration self-desiccation. The transient result can provide a nonuniform initial humidity condition of sleepers for the transient humidity field analysis of ballastless track.
- (3) After concreting the track slab in the site, the high humidity diffuses from track slab to sleepers and foundation through the bonded interfaces, and the maximum relative humidity gradient appears at the interface between track slab and sleeper. The maximum value rapidly decreases from $24.46 \times 100\%/m$

to $8.69 \times 100\%/m$ in the first week, and then the descending rate tends to be slow over time.

- (4) Due to the drying shrinkage property of concrete materials, the stresses that occur at the interface between sleeper and track slab are greater than those at other areas. When the maximum principal stress exceeds the ultimate tensile strength of the track slab, the splayed crack with an initial angle of about 45° will be generated at the sleeper corner.
- (5) Under the action of drying shrinkage deformation of early-age concrete, the initial splayed crack belongs to a mixed-mode crack, and the direction of crack tip turns an angle of 30.06° . Then, the final propagation path tends to be along the transverse direction of track slab due to the continuous turning of crack propagation path, and the corresponding failure mode gradually transforms from mixed-model into pure opening-mode. When there are initial cracks at the corner of adjacent sleepers, the cracks would be coalesced and further form the transverse through-wall crack of track slab. The transverse through-wall crack not only significantly affects the comfortableness and safety of rapid transit railway, but also reduces the service life of ballastless track.

Data Availability

All data used to support this study are available from the corresponding author upon reasonable request.

References

- [1] W. Zhai, K. Wang, Z. Chen, S. Zhu, C. Cai, and G. Liu, "Full-scale multi-functional test platform for investigating mechanical performance of track-subgrade systems of high-speed railways," *Railway Engineering Science*, vol. 28, no. 3, pp. 213–231, 2020.
- [2] Q. Luo, M. Wei, Q. Lu, and W. Tengfei, "Simplified analytical solution for stress concentration ratio of piled embankments incorporating pile-soil interaction," *Railway Engineering Science*, vol. 29, no. 2, pp. 1–12, 2021.
- [3] J. Zhu, H. Hu, Z. He, X. Guo, and W. Pan, "A power-quality monitoring and assessment system for high-speed railways based on train-network-data center integration," *Railway Engineering Science*, vol. 29, no. 1, pp. 30–41, 2021.
- [4] X. Li, J. Ren, J. Wang, Y. Rongshan, S. Luhui, and L. Xueyi, "Drying shrinkage of early-age concrete for twin-block slab track," *Construction and Building Materials*, vol. 243, pp. 1–9, 2020.
- [5] S. Yan, L. Ding, and S. Wang, "Key construction technology for CRTS I double-block ballastless track in tunnel," *Journal of Railway Engineering Society*, vol. 12, no. 11, pp. 13–16, 2009.
- [6] R. Yang, J. Li, W. Kang, L. Xueyi, and C. Shihao, "Temperature characteristics analysis of the ballastless track under continuous hot weather," *Journal of Transportation Engineering, Part A: Systems*, vol. 143, no. 9, pp. 1–10, 2017.
- [7] Z. Chen, J.-L. Xiao, X.-K. Liu, X.-Y. Liu, R.-S. Yang, and J.-J. Ren, "Effects of initial up-warp deformation on the stability of the CRTS II slab track at high temperatures," *Journal of Zhejiang University-Science*, vol. 19, no. 12, pp. 939–950, 2018.
- [8] P. Zhao, C. Ding, L. Guo, Y. A. Zhang, and X. Liu, "A prototype fatigue test for slab track subjected to the coupling action of wheel load, temperature variation, and water erosion," *Proceedings of the Institution of Mechanical Engineers-Part F: Journal of Rail and Rapid Transit*, vol. 233, no. 5, pp. 566–579, 2019.
- [9] S. Wang, R. Yang, X. Liu, P. Wang, and Z. Qian, "Discussion on ballastless track about the bring cause of crack and renovation measure," *Railway Engineering*, vol. 47, no. 9, pp. 76–79, 2007.
- [10] Z. Zeng, Z. Huang, H. Yin, M. Xiaobai, W. Weidong, and W. Jundong, "Influence of track line environment on the temperature field of a double-block ballastless track slab," *Advances in Mechanical Engineering*, vol. 10, no. 12, pp. 1–16, 2018.
- [11] S. Zhu, J. Luo, M. Wang, and C. Cai, "Mechanical characteristic variation of ballastless track in high-speed railway: effect of train-track interaction and environment loads," *Railway Engineering Science*, vol. 28, no. 4, pp. 408–423, 2020.
- [12] D. Chen, "Multi-physical field coupling simulation of hygro-thermal deformation of concrete," *Journal of Southeast University (Natural Science Edition)*, vol. 43, no. 3, pp. 582–587, 2013.
- [13] Y. Han, J. Zhang, and Q. Yue, "Review on shrinkage of modern concrete," *Concrete*, vol. 29, no. 2, pp. 1–12, 2019.
- [14] C. He, G. Miao, and X. Li, "Control measures for crack on ballastless track bed slab of plateau railway," *Railway Engineering*, vol. 61, no. 4, pp. 129–132, 2021.
- [15] Y. Tan, Y. Zheng, and L. Kang, "Crack resistance performance of cast-in-situ concrete for double-block ballastless track," *Railway Engineering*, vol. 61, no. 2, pp. 91–94, 2021.
- [16] J. Li, F. Xie, G. Zhao, and L. Li, "Experimental and numerical investigation of cast-in-situ concrete under external sulfate attack and drying-wetting cycles," *Construction and Building Materials*, vol. 249, Article ID 118789, 2020.
- [17] P. Liu, W. Yu, W. Wang, and C. Ying, "Moisture transmission boundary condition between concrete and artificial simulation environment," *China Journal of Highway and Transport*, vol. 28, no. 5, pp. 108–116, 2015.
- [18] H. Akita, T. Fujiwara, and Y. Ozaka, "A practical procedure for the analysis of moisture transfer within concrete due to drying," *Magazine of Concrete Research*, vol. 49, no. 179, pp. 129–137, 1997.
- [19] L. J. Parrott, "Moisture profiles in drying concrete," *Advances in Cement Research*, vol. 1, no. 3, pp. 164–170, 1988.
- [20] Y. Gao, "Studies on shrinkage and shrinkage induced stresses of concrete under dry-wet cycles," Dissertation, Tsinghua University, Beijing, China, 2013.
- [21] J. Wang, H. Dai, and C. Gu, "Summary on numerical calculation of moisture transfer in concrete," *Journal of Hydroelectric Engineering*, vol. 24, no. 2, pp. 85–89, 2015.
- [22] X. Gao and Y. Wei, "Modeling and analysis of moisture gradients in concrete pavements," *Engineering Mechanics*, vol. 31, no. 8, pp. 183–188, 2014.
- [23] D. Shen, B. Zhou, M. Wang, Y. Chen, and G. Jiang, "Predicting relative humidity of early-age concrete under sealed and unsealed conditions," *Magazine of Concrete Research*, vol. 71, no. 22, pp. 1151–1166, 2019.
- [24] Y. Wang, Y. Jia, and R. Zhao, "Calculation of internal humidity field of concrete based on ANSYS," *Journal of Southwest Jiaotong University*, vol. 52, no. 1, pp. 54–60, 2017.
- [25] S. F. Wong, T. H. Wee, S. Swaddiwudhipong, and S. L. Lee, "Study of water movement in concrete," *Magazine of Concrete Research*, vol. 53, no. 3, pp. 205–220, 2001.
- [26] W. Kang, S. Chen, and C. Wei, "Temperatures of ballastless track and effect of continuous hot weather," *Journal of the China Railway Society*, vol. 41, no. 7, pp. 127–134, 2019.
- [27] Y. Wei, W. Hansen, J. J. Biernacki, and E. Schlagen, "Unified shrinkage model for concrete from autogenous shrinkage test on paste with and without ground-granulated blast-furnace slag," *ACI Materials Journal*, vol. 108, no. 1, pp. 13–20, 2011.
- [28] G. Liu, "The mechanical analysis of CRST I Bi-block Track's process," Dissertation, Southwest Jiaotong University, Chengdu, China, 2015.
- [29] J. H. Hattel and J. Thorborg, "A numerical model for predicting the thermomechanical conditions during hydration of early-age concrete," *Applied Mathematical Modelling*, vol. 27, no. 1, pp. 1–26, 2003.

Machine Learning Algorithms to Predict Uniaxial Compressive Strength for Soft Sedimentary Rocks

P. Paulpandian, *Department of Mechanical Engineering, Aryan Institute of Engineering & Technology, Bhubaneswar, p_pandian@gmail.com*

Suchismita Satpathy, *Department of Civil Engineering, Aryan Institute of Engineering & Technology, Bhubaneswar, suchismita@outlook.com*

Chinmay Swain, *Department of Mechanical Engineering, Raajdhani Engineering College, Bhubaneswar, chinmayswain1972@gmail.com*

Subhasis Sarkar, *Department of Mechanical Engineering, NM Institute of Engineering & Technology, Bhubaneswar, subhasissarkar14@yahoo.co.in*

Mdaras Aras Ansari, *Department of Civil Engineering, Raajdhani Engineering College, Bhubaneswar, mdarasansari2578@gmail.com*

Jagruiti Swain, *Department of Civil Engineering, Capital Engineering College, Bhubaneswar, jagrutiswain26@yahoo.co.in*

ABSTRACT

The use of NSM FRP for concrete structure strengthening has become a popular choice for retrofitting existing structures against shear and flexure. In previous review articles, only the use of NSM for shear was discussed. To evaluate the existing design formulas for computing the NSM contribution in shear, a database of testing of NSM strengthened beams in shear is presented. These formulas corresponded to the database's experimental results. The shape of NSM FRP bars, the combined effects of existing steel stirrups, and NSM FRP reinforcement and analytical formulations are among the other study subjects mentioned. Brazilian tensile strength (BTS) in MPa, moisture in percent, and dry density (d) in g/cm^3 . Then, for each method, a 106-point dataset was divided into 70% training and 30% testing. The XGBoost algorithm outperformed the GBR, Catboost, and LightGBM algorithms in the training phase, with R^2 0.99, MAE 0.00062, MSE 0.0000006, and RMSE 0.00079, and R^2 0.99, MAE 0.00054, MSE 0.0000005, and RMSE 0.00069 in the testing phase. BTS and w are favourably connected with the UCS, while moisture and d are adversely correlated with the UCS, according to the sensitivity analysis. As a result, the XGBoost algorithm was found to be the best accurate approach for UCS prediction of soft sedimentary rocks in this study, out of the four algorithms evaluated.

1. Introduction

The uniaxial compressive strength (UCS) of rock is one of the important data in engineering planning and design. Correctly testing UCS of rock to ensure its accuracy and authenticity is a prerequisite for ensuring the design of any rock engineering project. UCS of rock has a wide range of

applications in mining, geotechnical, petroleum, geomechanics, and other fields of engineering. The study of rock mechanical properties is the basis for innovative advances associated with energy supply. The significance of rock mechanics is acknowledged in the advancement of natural assets, for example, the protection of energy sources (petroleum products: oil, coal, and natural gas), as well as the

protection of the surrounding rock environment. In addition, protective waste removal and hydroelectric energy assets require further examination of rocks and soils, which are dependent on the mechanical properties of rocks [1, 2]. Unconfined UCS of rocks plays a significant role in tackling issues associated with rock mechanics and the design of geostructures [3–6]. Various researchers have proposed empirical equations in order to estimate the UCS of different rock mass databases as tabulated in Table 1.

Some researchers have employed indirect testing methods, i.e., multiple linear regression (MLR) [17, 22, 23], artificial neural network (ANN) [23, 24], adaptive neuro-fuzzy inference system (ANFIS) [25], and other machine learning algorithms to estimate the accuracy and reliability of rock data [26–28], rather than using direct tests recommended by international standards, which are considered time-consuming, expensive, and unreliable [29, 30]. While these frameworks are appropriate, fast, and favorable techniques to tackle difficult problems, in most cases, they are simply capable of understanding the complex interactions among variables to estimate an objective and do not provide any intuition about the interrelationships among predictors and a return value [31]. Abidi et al. predicted the UCS of intact rocks with 196 data points, i.e., sandstone, marl, limestone, and conglomerate, using the intelligent ANN method and MLR. According to the results of their study, the ANN model performed better than the MLR model in terms of correlation coefficient (R^2), mean absolute error (MAE), and root mean square error (RMSE) [23]. Abidi et al. employed both ANN and ANFIS models to predict UCS of 136 sandstone rock samples because laboratory testing methods are time-consuming and complex. Based on the results of several performance metrics, i.e., R^2 , RMSE, and variance accounted for (VAF), the ANFIS model showed the best performance over ANN [32]. Ceryan et al. adopted soft computing methods, i.e., extreme learning machine (ELM) and minimax probability machine regression (MPMR), to predict the UCS of volcanic rocks. In addition, the least-square support vector machine (LS-SVM) model was incorporated to compare its performance with the proposed soft computing models. Thus, ELM and MPMR outperformed the LS-SVM [33]. Ceryan et al. developed the fuzzy interface system (FIS), ANN, and LV-SVM to predict the UCS of rocks. According to their results, LV-SVM performed better than the other developed models [34]. Neurogenetic and multiple regression (MR) methods were developed by Monjezi et al. to estimate the UCS of rocks. The neurogenetic approach was best applied compared to MR [35]. Aboutaleb et al. predicted the UCS of carbonate rocks using nondestructive tests, namely, simple regression analysis (SRA), multiple regression analysis (MRA), ANN, and support vector regression (SVR). As reported by the SVR model, it performed best among all the models studied [36]. Ghasemi et al. developed a soft computing (model tree) approach to predict the UCS of carbonate rocks, which proved to have the best performance [37]. Barzegar et al. used ensemble tree-based machine learning approaches such as “random forest (RF), M5 model tree, and multivariate adaptive regression splines (Mars)” for

predicting UCS of travertine rocks. In parallel, an ensemble committee-based ANN model was developed to correlate the returns of proposed models to determine the predicted UCS in accuracy. According to the results, Mars outperformed all studied models [38]. Matin et al. used RF for variable selection and UCS prediction, and the proposed RF for UCS prediction was satisfactory [39]. Zhong et al. predicted rock mechanical property, i.e., UCS with an established XGBoost model of machine learning, which proved to have the best performance in results [40].

According to the above literature, the application of the gradient boosting machine learning algorithms has been rarely used for UCS prediction. In this work, we proposed an innovative adaptation of four gradient boosting machine learning algorithms such as gradient boosted regression (GBR), Catboost, light gradient boosting machine (LightGBM), and extreme gradient boosting (XGBoost) that improves the handling of concept drift. The database employed in this work has been collected from soft sedimentary rocks of the Block-IX at Thar Coalfield, Pakistan. Previously, researchers considered wet density (ρ_w) [41]; moisture [41]; dry density (ρ_d) [42]; and Brazilian tensile strength (BTS) [43] as input variables for evaluating the UCS. Based on the literature, the four significant input parameters ρ_w in g/cm³; moisture in %; dry ρ_d in g/cm³; and BTS in MPa are used for each developed algorithm. Moreover, 106-point dataset was allocated identically for each algorithm into 70% for the training phase and 30% for the testing phase. Figure 1 illustrates the flowchart of this study.

2. Overview of the Study Area and Dataset

Thar Coalfield is the 7th world's biggest coal mine in the Sindh Province of Pakistan [44]. Thar Coal is demarcated to be 175.5 billion tons of lignite or brown coal which can be utilized for the fuel and generation of electricity purpose. As shown in Figure 2, the Thar Coalfield is divided into 12 different blocks. Open-pit and underground mining methods can be used to extract coal from the area. Specifically, Block-II of the 12 blocks is fully developed for the open-pit mining method by Sindh Engro Coal Mining Company (SECMC), while some areas of Block-1 and Block-IX are being prepared for the underground mining method. The coal seam thickness of Block-IX at Thar Coalfield is about 12 m with an inclination of 0° to 7°, and the top-bottom plate is siltstone-claystone to claystone. However, for the first time in the history of Pakistan, Shahani et al. recommended the use of mechanized longwall top coal caving (LTCC) method in the Thar Coalfield, Pakistan [44,45]. At the same time, accurate determination of the mechanical properties of the Thar Coalfield, especially the UCS, plays an important role in providing a good understanding of the behavior of the roof and ground prior to mining operations. In this study, 106 samples of soft sedimentary rocks were initially collected randomly from Block-IX at Thar, as shown in Figure 2 of the yellow-colored area. The collected rock samples were then arranged and subdivided according to the recommended standards of the

TABLE 1: Empirical equations proposed by the researchers for estimating UCS.

S. no	Country of origin	Rock type	No. of data	R^2	References
1	Turkey	Sedimentary	18	0.82	[7]
2	USA	Mixed	86	0.81	[8]
3	Spain	Mixed	194	0.81	[9]
4	Japan and Indonesia	Mixed	33	0.77	[10] Based on part of dataset by [11]
5	Turkey	Sedimentary	150	0.65	[12]
6	India	Sedimentary	13	0.87	[13]
7	Iran	Sedimentary	40	0.94	[14]
8	Israel and USA	Mixed	7	0.96	[15]
9	UK, France, and Denmark	Sedimentary	7	0.9	[16]
10	England and Turkey	Mixed	44	0.11	[17]
11	Greece	Metamorphic	32	0.82	[18]
12	Spain	Sedimentary	99	0.94	[19]
13	Turkey	Sedimentary	19	0.78	[20]
14	Portugal	Igneous	9	0.72	[21]
15	UK, France, and Denmark	Sedimentary	7	0.87	[16]
16	United Kingdom	Igneous	171	0.53	[21]

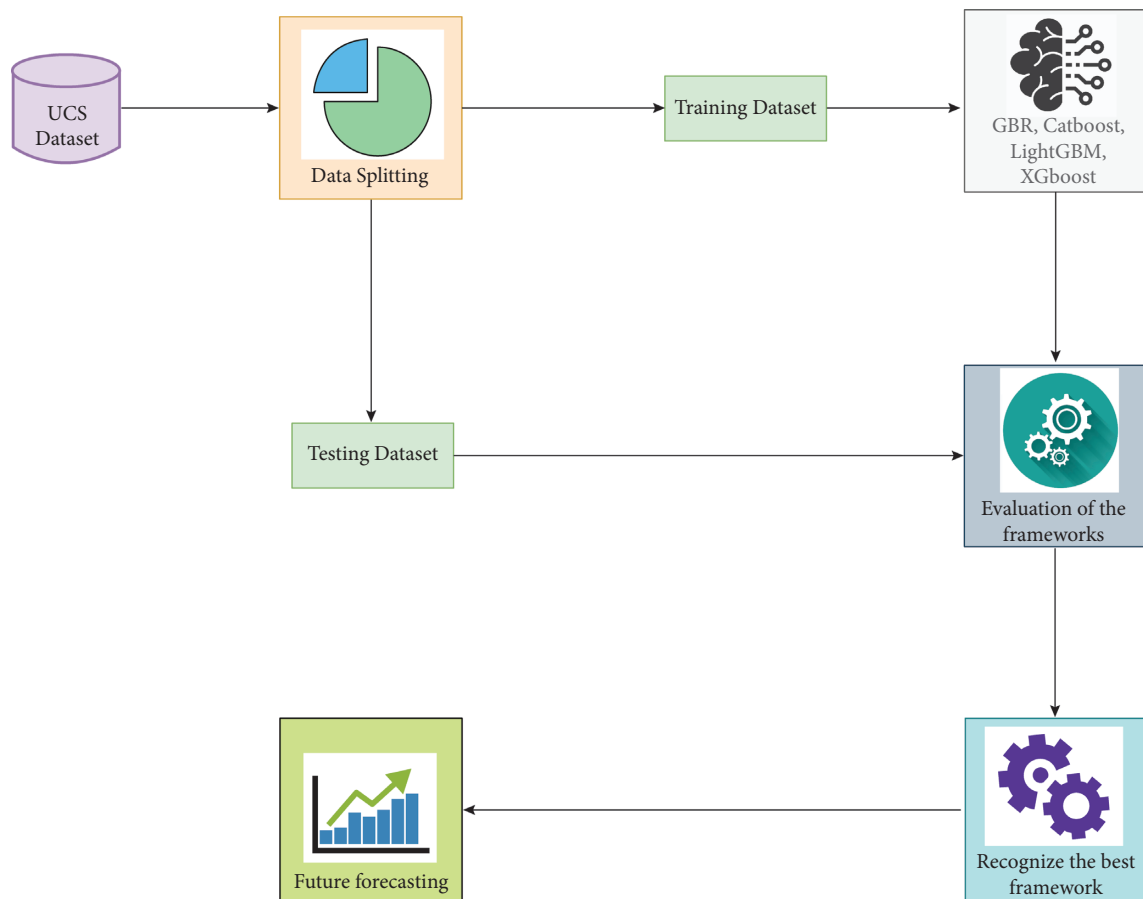


FIGURE 1: Flowchart of the study.

International Society of Rock Mechanics (ISRM) [46] and the American Society for Testing Methods (ASTM) [47] in order to maintain the same core size and geological and geometric characteristics. The experimental work on the studied rock samples was carried out in the laboratory of the Department of Mining Engineering, Mehran University of Engineering and Technology (MUET), to determine the

physical and mechanical properties like ρ_w (g/cm³); moisture (%); ρ_d (g/cm³); BTS (MPa); and UCS (MPa). In Figure 3(a), a universal testing machine (UTM) was used to perform the UCS as shown in Figure 3(b) and a BTS as shown in Figure 3(c). Table 2 illustrates the entire dataset employed in the study. Table 3 denotes the statistical distribution of the UCS dataset.

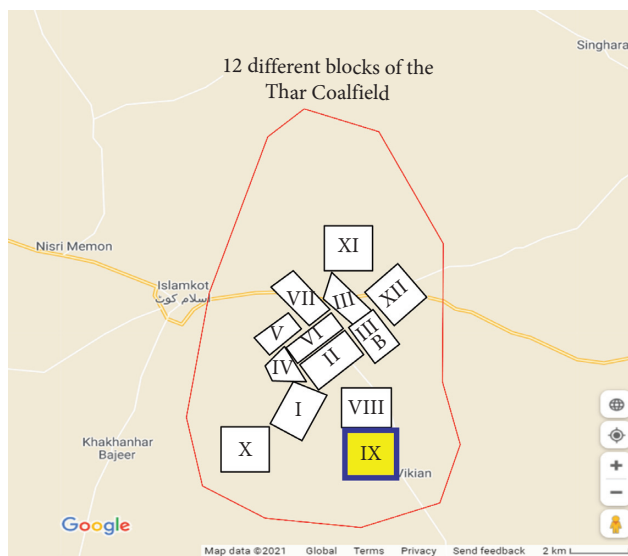


FIGURE 2: Location map of study area (Block-IX) of Thar Coalfield, Pakistan.

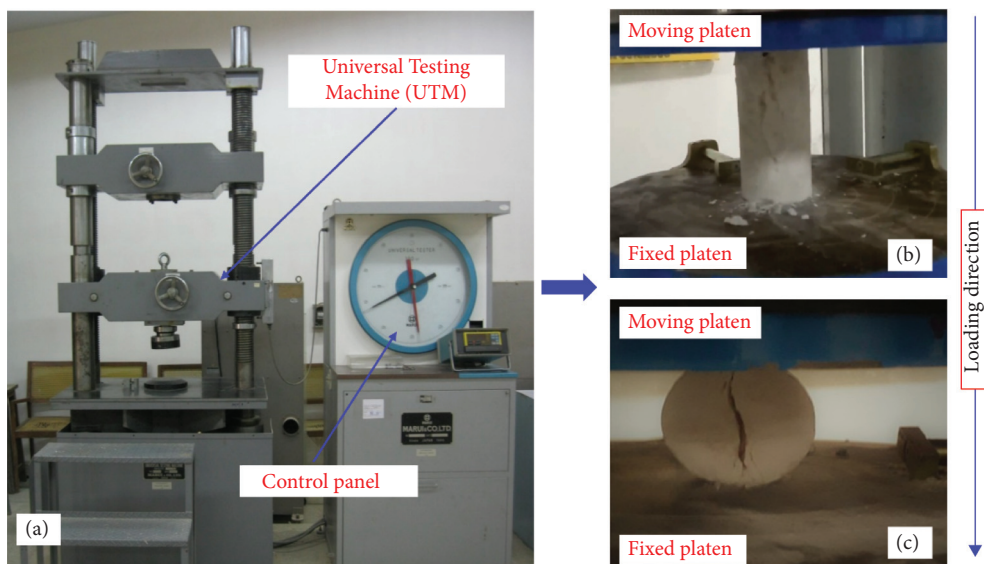


FIGURE 3: (a) Universal testing machine (UTM), (b) deformed rock core specimen for Brazilian tensile strength test, and (c) deformed rock core specimen for UCS test.

TABLE 2: Brief summary of UCS dataset.

Serial no.	ρ_w (g/cm ³)	Moisture (%)	ρ_d (g/cm ³)	BTS (MPa)	UCS (MPa)
1	2.132	11.78747	1.90719	0.305	0.404
2	2.013	15.07577	1.749282	0.217402	0.491
3	2.112	14.08254	1.851291	0.259	0.579
4	2.119	17.0949	1.809643	0.394188	0.485
5	2.034	15.59792	1.759547	0.336	0.52
....
102	2.003	20.67989	1.659763	0.502	3.35
103	1.823	14.17769	1.596634	0.452715	2.46
104	1.964	20.07648	1.635624	0.358732	3.448
105	1.993	16.44345	1.71156	0.516271	3.549
106	1.97	12.14405	1.756669	0.627239	3.28

Figure 4 represents the pairwise distribution of various features and UCS. It can be seen that moisture and BTS are moderately correlated to the UCS whereas ρ_w and ρ_d are negatively correlated to the UCS. It is important to mention that each feature does not correlate well with UCS independently; hence all the features together are evaluated to predict the UCS.

3. Methods

3.1. Gradient Boosted Regressor (GBR). The gradient boosted regression (GBR) tree incorporates the weak learners; i.e., the learner algorithms moderately perform well as compared to random algorithms, into a strong learner in a repetitive technique [48]. In contrast to the bagging technique, the boosted mechanism produces the base frameworks consecutively. The robustness of the prediction model is enhanced by generating several frameworks in a series by focusing priority on this learning information that is complicated to evaluate. In the boosting mechanism, the previous base frameworks that are inappropriate to estimate are frequently developed in the training datasets compared to those models that are precisely evaluated. Each supplementary base framed is directed to rectify the errors produced by its preceding base framework. The existence of the boosting mechanism is from the response of Schapire to Keran's inquiry [49, 50] (Kearns): Is a combination of a weak learner an alternative to distinguish strong learner? Weak Learner is defined as the algorithm that is working well as compared to random approximation; a strong base framework is a more authentic classification or regression algorithm that is inconsistent that is efficiently corresponding with the problem. The response to such an inquiry is very significant. The evaluation of a weak framework is often unchallenging as compared with a strong framework. Schapire demonstrated that the response to Kearns' inquiry is "Yes" manifesting that many weak frameworks are combined into a high and single robust framework.

The main difference between boosted and bagging mechanism is that in boosting method the training datasets are systematically resampled in order to anticipate the most convenient instruction for each succeeding framework. The modified dissemination in each stage of training is contingent on the error generated by the preceding framework. In contrast, in the bagging mechanism, each trail is consistently designated to generate a training dataset, and the uncertainty of designating a single trail is divergent for the boosting mechanism. The trails that are incorrectly evaluated or misclassified have more probability to be set with higher weights. Hence, each freshly developed framework emphasizes the trail that has been incorrectly evaluated or misclassified by succeeding frameworks.

Boosting arranges the secondary frameworks that reduce a certain loss function averaged over the learning datasets,

e., mean absolute error or squared mean error. The loss function calculates the aggregate of the forecasted value that varies from the measured value. A forward stage-wise modeling technique is one of the estimated solutions to the problem. This modeling technique consecutively adjoins new base frameworks without replacing the coefficient and

parameter of the model that has previously been attached. With reference to the regression models, the boosting mechanism is a configuration of "functional gradient descent." Functional gradient descent is an optimization mechanism that reduces a certain loss function by attaching a base framework at each stage that minimizes well the loss function. Figure 5 shows the description of GBR employed in this study [51, 52].

Friedman suggested an improvement to the gradient boosted regression models by employing a predetermined amount of regression tree to the base framework. The modified framework enhances the performance of the Friedman model [53]. In order to predict the UCS of sedimentary rocks, the modified version of gradient boosted regression has been used. Table 4 illustrates the execution of a GBR framework in python. Consider that the leaves number for each tree is l , each tree splitting the input space into l separate territory $T_{1p}, T_{2p}, \dots, T_{lp}$ and forecasting a constant value k_{lp} for territory T_{lp} . The gradient boosting regression tree is given by

$$f_p(a) = \sum_{l=1}^L k_{lp} F(a \in T_{lp}), \quad (1)$$

$$\text{where } F(a \in T_{lp}) = \begin{cases} 1, & \text{if } a \in T_{lp} \\ 0, & \text{otherwise} \end{cases}$$

By employing a regression tree to reinstate $f_p(a)$ in the generic gradient boosting mechanism, the framework gradient descent stage size and updating equation are given by equation (2) and (3), respectively.

$$f_p(a) = f_{p-1}(a) + \rho_p g_p(a). \quad (2)$$

$$\rho_p = \operatorname{argmin}_\rho \sum_{i=1}^L M(b_i, f_{p-1}(a_i) + \rho g_p(a_i)). \quad (3)$$

Hence, equations (2) and (3) fit as equations (4) and (5):

$$f_p(a) = f_{p-1}(a) + \sum_{l=1}^L \rho_p k_{lp} F(a \in T_{lp}). \quad (4)$$

$$\rho_p = \operatorname{argmin}_\rho \sum_{i=1}^L M\left(b_i, f_{p-1}(a_i) + \sum_{l=1}^L \rho_p k_{lp} F(a \in T_{lp})\right). \quad (5)$$

By employing discrete ideal ρ_{lp} for each territory T_{lp} k_{lp} are supposed to be detached. The updated framework equations (6) and (7) are given by

$$f_p(a) = f_{p-1}(a) + \sum_{l=1}^L \rho_p F(a \in T_{lp}). \quad (6)$$

$$\rho_p = \operatorname{argmin}_\rho \sum_{i=1}^L M\left(b_i, f_{p-1}(a_i) + \sum_{l=1}^L \rho_p F(a \in T_{lp})\right). \quad (7)$$

The framework overfitting can be restrained through managing the gradient boosting repetitions number, or

TABLE 3: Statistical distribution of UCS dataset.

	ρ_w (g/cm ³)	Moisture (%)	ρ_d (g/cm ³)	BTS (MPa)	UCS (MPa)
Mean	1.93	18.28	1.66	0.29	1.31
Standard deviation	0.37	8.93	0.39	0.12	0.93
Minimum	1.005	6.63	0.76	0.02	0.26
Maximum	2.38	43.3	2.15	0.62	3.623

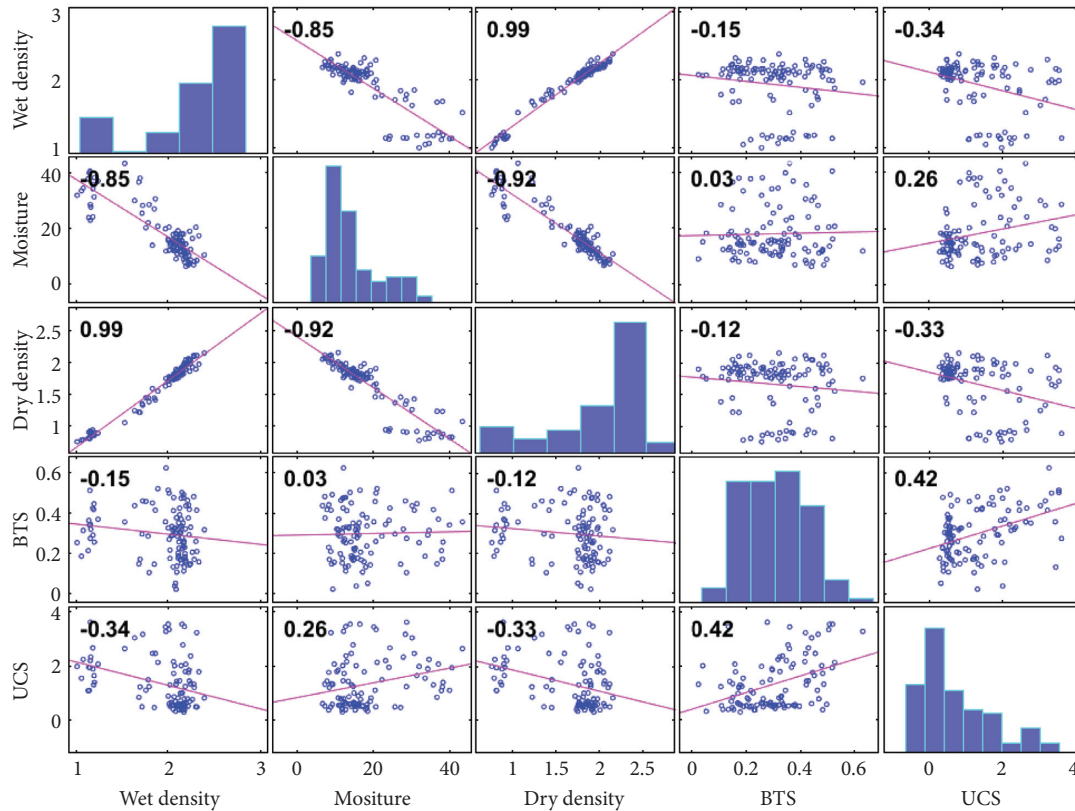


FIGURE 4: Pairwise correlation between the input variables and output in the original dataset.

more competent, appraising the beneficiation of each tree by $J \in (0, 1)$. Hence, the updated model is given by

$$f_p(a) = f_{p-1}(a) + L \sum_{l=1}^L \rho_p F(a \in T_{lp}). \quad (8)$$

3.2. Catboost. Catboost is a type of gradient boosting algorithm that is succeeded in recent times by Dorogush et al. [54]. Catboost tackles both the regression and classification problems and has been publicized in a new free open-source multiplatform gradient boosting library [54, 55]. Decision trees are employed as a base weak learner in the Catboost algorithm and gradient boosting to sequentially fit on the decision tree. In order to enhance the execution of the Catboost algorithm and to avoid overfitting, the inconsistent permutation of the learning information of the gradient is employed [54].

The Catboost algorithm aims to minimize the forecasting relocation that happens during the learning stage. The

dissemination relocation is the removal of $F(y_i) | (y_i)$ with y_i being a learning sample, with relation to $F(y_i) | (y_i)$ for a test sample y . At the learning stage, gradient boosting employs the same sample for the calculation of gradient and the framework that reduces that gradient. The concept of Catboost is to establish $j \dots n$, the base framework for individual P boosting repetition. The i th framework of the m th repetition is learnt of initial i th samples of the permutation and is applicable to calculate the gradient of the $j+1$ sample for $p+1$ repetition. Succeeding, to be unrestrained of the start arbitrary permutation, this technique employs s reciprocated arbitrary permutation. A distinguish framework is constructed per repetition that manages all permutations and frameworks. Symmetric trees work as a foundation for the frameworks. The trees are extended by growing all the leaf nodes level-wise by using the same splitting criteria.

The mechanism introduced in the Catboost algorithm is to calculate the contemporary character that is identical to the one imitated for establishing the network. Thus, for a specified arbitrary permutation of the samples, the data sample $< i$ is used to calculating the character value for each

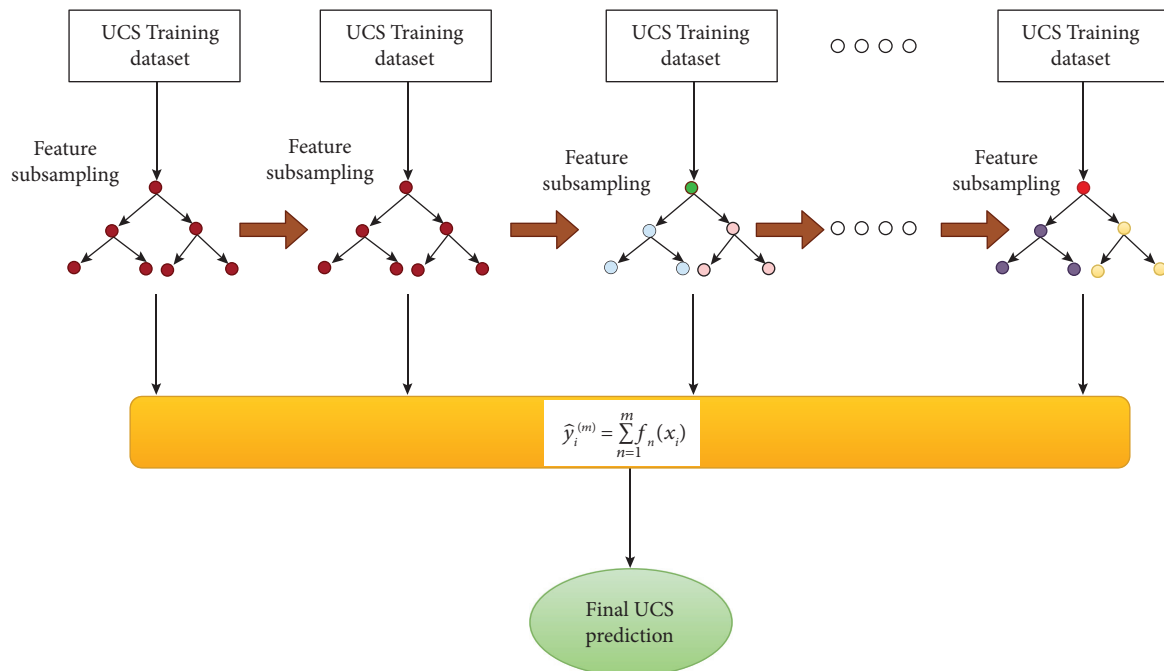


FIGURE 5: Description of GBR employed in this study.

sample i . Later on, various permutations are executed and the acquired character value for each sample is averaged. Catboost is a large-scale and comprehensive library that is composed of various elements as standard boosting, GPU learning and consists of tenfold hyperparameters optimization to modify to several practicable investigation circumstances. Standard gradient boosting is also a part of the Catboost algorithm. Figure 6 depicts the description of Catboost employed in this study.

It should be noted that the training capability of the Catboost algorithm is supervised by its framework hypermeter, namely, the number of iterations, learning rate, maximum depth, etc. The determination of the best hyperparameters for a model is a difficult, time-consuming, challenging, and tedious task contingent on the user's skills and expertise. Table 5 illustrates the execution of a Catboost framework in python employed in this study.

3.3. Light Gradient Boosting Machine (LightGBM). Light Gradient Boosting Machine, abbreviated as LightGBM, is an open-source gradient boosting machine learning framework by Microsoft that uses a decision tree as a based training algorithm [56]. LightGBM inserts consecutive element value buckets into discrete bins with higher efficiency and faster training speed. It employs the histogram-based algorithms [57,58] in order to enhance the learning stage, minimize memory consumption, and incorporate an updated communication network to improve training uniformity, known as parallel voting decision tree machine learning algorithm. The learning information is split into multiple trees, the local voting technique is implemented to choose the top-k element, and the globing voting technique is acquired in each repetition. LightGBM manipulates the leaf-wise strategy to

perceive a leaf with maximum splitter gain as shown in Figure 7. It can be used for classification, regression, sorting, and numerous machine learning projects. LightGBM builds a sophisticated tree compared with the level-wise distribution technique by the leaf-wise distribution technique, which is the principal component for executing the algorithm with higher efficiency. Even so, it gives rise to overfitting; however, it can be prohibited by using the max-depth element in LightGBM.

LightGBM [56] is a comprehensive library that executes gradient boosting and intends some modification. The execution of gradient boosting has been mainly concentrated on building a computationally systematic algorithm. The library comprises tenfold training hyperparameters that authenticate this framework to implement in the diverse scenario. LightGBM execution also suggests advanced features both in CPU and in GPU; it can operate as gradient boosting and has multifold combinations including bootstrap subsampling and column randomization. LightGBM is broadly featured by Gradient-based One-Side Sampling and Exclusive Feature Bundling. Gradient-based One-Side Sampling is a subsample mechanism employed to build the learning information as a base tree in the ensemble. In the Adaboost machine learning algorithm, the objective of this mechanism is to enhance the importance of the sample with a higher probability, which is associated with the sample having a higher gradient. When the Gradient-based One-Side Sampling is implemented, the learning information for the base learner is formulated on the top fraction of the sample with a higher gradient (a) plus an arbitrary instance fraction (b) reacquired from the samples with a smaller gradient. To remunerate for the variation of measured dissemination, the sample in the lower gradient category is arranged together and weighed up by $(1 - x)/y$ when

TABLE 4: Executing a GBR framework in python employing the gradient boost regressor.

Description	Python script
Import the python packages	<pre>from sklearn.ensemble import GradientBoostingRegressor from sklearn.model_selection import cross_val_score, RepeatedKFold Framework = GradientBoostingRegressor() # Interpretation of the evaluation mechanism cv = RepeatedKFold(n_splits = 10, n_repeats = 3, random_state = 1) # Framework assessment</pre>
Interpretation of the framework attributes	<pre>n_scores = cross_val_score(Framework, x_train, UCS_train, scoring = 'neg_mean_absolute_error', cv = cv, n_jobs = -1) # Performance Report print('MAE: %.8f (%.8f)' % (mean(n_scores), std(n_scores))) # fit the framework on training dataset Framework.fit(x, UCS)</pre>
Training dataset	<pre>Train_dataset_Forecasting = Framework.predict(x_train)</pre>
Testing dataset	<pre>Test_dataset_Forecasting = Framework.predict(x_test)</pre>

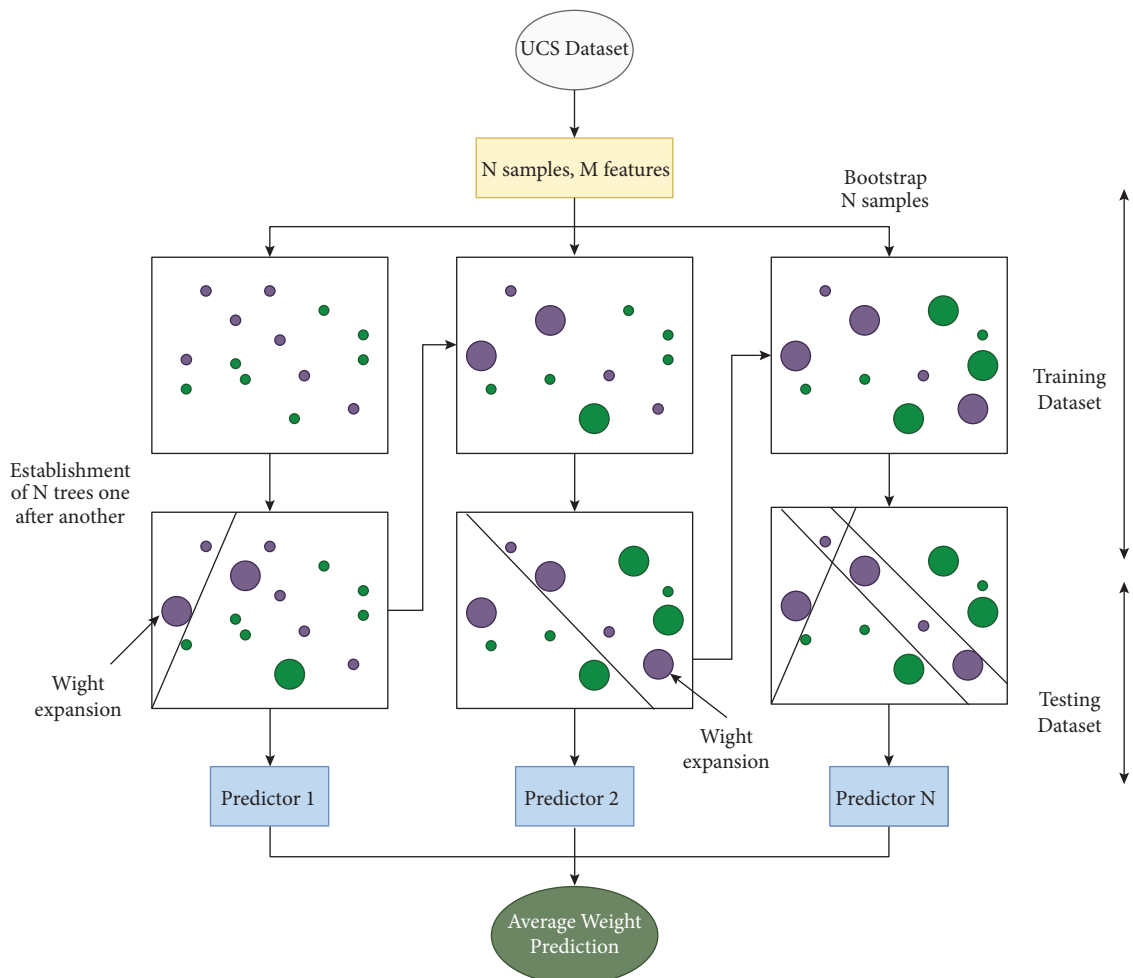


FIGURE 6: Description of Catboost employed in this study.

calculating the data gain. On the other hand, the Exclusive Feature Bundling mechanism accumulates the sparse element into a single element. This can be accomplished without preventing any knowledge when those elements do not consist of a nonzero number coincidentally. The mechanism anticipates supplementary learning rate gain. Table 6

illustrates the execution of a LightGBM framework in python employed in this study.

3.4. *Extreme Gradient Boosting (XGBoost)*. Extreme gradient boosting (XGBoost) is one of the significant types of

TABLE 5: Executing a catboost framework in python employing the catboost regressor.

Description	Python script
Import the python packages	<pre> from catboost import CatBoostRegressor from sklearn.model_selection import RepeatedKFold, cross_val_score Framework = CatBoostRegressor(verbose=0, n_estimators=100) # Interpretation of the evaluation Mechanism cv = RepeatedKFold(n_splits=10, n_repeats=3, random_state=1) # Framework assessment n_scores = cross_val_score(Framework, x_train, UCS_train, scoring='neg_mean_absolute_error', cv=cv, n_jobs=-1, error_score='raise') # Performance Report print('MAE: %.8f (%.8f)' % (mean(n_scores), std(n_scores))) # fit the framework on training dataset Framework = CatBoostRegressor(verbose=0, n_estimators=100) Framework.fit(x, UCS) </pre>
Interpretation of the framework attributes	
Training dataset	train_dataset_Forecasting = Framework.predict(x_train)
Testing dataset	test_dataset_Forecasting = Framework.predict(x_test)

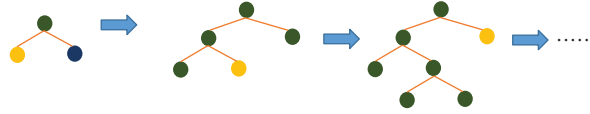


FIGURE 7: Description of LightGBM employed in this study.

ensemble learning algorithms in machine learning methods [59]. It comprises ordinary regression and classification trees by incorporating analytical boosting techniques. Boosting enhances the precision estimation of the framework by building various trees as a substitution to establish a targeted tree and later on adding them to determine a coherent forecasting model [60]. XGBoost initiates the tree by sequentially retaining the residuals of past trees as influences on the consequence tree. Due to this, the consequence tree establishes comprehensive forecasting by generating the error of past trees. At the stage when the loss function is reduced, the sequential framework structure relation can be segmented as a gradient descent type that improves the prediction by adding an extra tree at each step to lower the reduction [61]. Tree growth ends when a preestablished number of the most extraordinary tree is gained, or when the error of the training stage cannot be augmented to a predicted sequential tree number. The performance promptness and evaluation accuracy of the gradient boosting can be significantly increased by attaching arbitrary investigation. Particularly for each tree in a symmetry, an arbitrary training data subsample is considered from the entire training dataset, excluding the replacement. Instead of the entire sample, this arbitrarily described subsample is then utilized to fit the tree and is ascertained to update the framework. XGBoost is a state-of-the-art redistributed gradient boosting algorithm that can manage and achieve up-to-date forecasting demonstration [62]. The second-order evaluation of the loss function is employed in the XGBoost algorithm which is expeditious and speedy as compared to the conventional gradient boosting algorithms. It has been extensively

adopted to mine gene coupling features. Figure 8 depicts the description of XGBoost employed in this study.

Consider \bar{u}_i is the forecasted result of i th number of data for which the characteristics vector is V_i ; E shows the estimators number for each estimator f_k (with k from 1 to E) corresponding to individual tree anatomy, and u_i^0 depicts the preliminary assumption that is the average of the measured characteristics in the learning information. The following equation implements various expansion functions to forecast the results:

$$\bar{u}_i = u_i^0 + \eta \sum_{k=1}^E f_k(V_i), \quad (9)$$

whereas the η parameter is the learning rate that is adjoined to improve the model implementation to enhance the model, to execute rhythmically while linking the latest tree and confront overfitting.

Concerning Eq. 9, at k th state, a character k th is connected to the model and the k th forecasted value u_i^{-k} is implemented from the forecasted value at the preceding state $u_i^{-(k-1)}$ and the augmented f_k of the character of the attached k th character is depicted in

$$u_i^{-k} = u_i^{-(k-1)} + \eta f_k, \quad (10)$$

whereas f_k shows the weight of leaves that are developed by reducing the objective function of the k th tree represented by

$$\text{obj} = \gamma N + \sum_{a=1}^N \left[G_a \omega_a + \frac{1}{2} (H_a + \lambda) \omega_a^2 \right], \quad (11)$$

TABLE 6: Executing a lightgbm algorithm in python employing the lightgbm regressor.

Description	Python script
Import the python packages	<pre>from lightgbm import LGBMRegressor from sklearn.model_selection import cross_val_score, RepeatedKFold Framework = LGBMRegressor() # Interpretation of the evaluation Mechanism cv = RepeatedKFold(n_splits=10, n_repeats=3, random_state=1) # Framework assessment</pre>
Interpretation of the framework attributes	<pre>n_scores = cross_val_score(Framework, x_train, UCS_train, scoring='neg_mean_absolute_error', cv=cv, n_jobs=-1, error_score='raise') # Performance Report print('MAE: %.8f (%.8f)' % (mean(n_scores), std(n_scores))) # fit the framework on training dataset Framework.fit(x, UCS)</pre>
Training dataset	train_dataset_Forecasting = Framework.predict(X_train)
Testing dataset	test_dataset_Forecasting = Framework.predict(X_test)

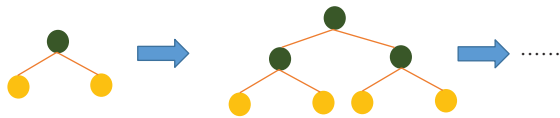


FIGURE 8: Description of XGBoost employed in this study.

whereas N designates the leaves of the k th tree and ω_a represent the weight of the leaves from 1 to N , and γ and λ are the uniformity features that are utilized to implement the coherence to the anatomy to evade the overfitting in the model. The parameters H_a and G_a are the aggregate of entire information attached with data a leaf of the prior and subsequent loss function gradient, respectively.

In sequence to build the k th tree, a single leaf is split into different numeration leaves. Eq. 12 indicates the anatomy of utilizing the gain parameters. Consider C_R and D_R depict the interdependent right leaf, and C_L and D_L are interdependent left leaf attaining the divergence. At the time, the gain parameter is close by zero, and the diverging benchmark is traditionally assumed. The γ and λ are the uniformity features that are periphrastically susceptible on the gain feature; i.e., higher the regularization parameter will decrease the gain parameter which in result will avoid the convolution of the excruciating of the leaf. But it will decrease the ability of the framework in order to apt to the training dataset.

$$\text{gain} = \frac{1}{2} \left[\frac{C_L^2}{D_L + \lambda} + \frac{C_R^2}{D_R + \lambda} + \frac{(C_L + C_R)^2}{D_L + D_R + \lambda} \right]. \quad (12)$$

XGBoost is a widely used machine algorithm that assembles an articulated and logical accomplishment of gradient boosting machine learning algorithm. A numerical value is the outcome of the regression prediction model problems. XGBoost can be practiced promptly to probabilistic regression frameworks. The ensembles are established from the decision tree model. Ensembles successively link trees and adjust the forecasting imprecision models. These types of ensemble machine learning techniques are known as boosting. The frameworks are established by implementing any arbitrary gradient descent optimization technique and distinct loss function. When the model is implemented, the

gradient loss function is decreased, and therefore this mechanism is recognized as “gradient boosting.” Table 7 illustrates the execution of an XGBoost framework in python employed in this study. XGBoost framework performed well on the UCS datasets as compared to GBR, Catboost, and LightGBM with the same parameter $n_splits=10$, $n_repeats=3$, $random_state=1$ (all the other parameters were used as a default in python). However, in order to further enhance the performance of the XGBoost framework, gbm_param_grid was further implemented in this study.

3.5. Performance Indices. In order to accurately and approximately assess the performance of machine learning algorithms, various researchers have employed different evaluation criteria, i.e., coefficient of correlation (R^2) [63], mean absolute error (MAE), mean square error (MSE) [64], and root mean square error (RMSE) [65]. The higher value of R^2 and the lower MAE, MSE, and RMSE indicate that the predicted target values perform better in each proposed model. In this study, four estimation criteria are employed to narrate the association between measured and predicted UCS values, i.e., R^2 , MAE, MSE, and RMSE as shown in Table 8.

4. Results and Discussion

UCS plays a significant role in the stability of geostuctures. In this study, the use of novel machine learning methods to estimate the accuracy of the UCS is necessary. This is because the accuracy of the studied UCS can help in designing any type of rock engineering project. Therefore, this study aims to incorporate these gradient boosting machine learning algorithms, namely, GBR, Catboost, LightGBM, and XGBoost to predict the UCS of soft sedimentary rocks of Block-IX at Thar Coalfield, Pakistan, by using four input variables, i.e., ρ_w (g/cm^3); moisture (%); ρ_d (g/cm^3); and BTS (MPa). Then, the 106-point dataset for each model was identically assigned as 70% for the training phase to train the model and 30% for the testing phase to test the model. In the end, the ultimate output of predicted UCS is as follows.

TABLE 7: Executing a xgb framework in python employing the XGBoost.

Description	Python script
Import the python packages	<pre> import xgboost as xgb from xgboost import XGBRegressor from sklearn.model_selection import train_test_split, cross_val_score, RepeatedKFold from sklearn.metrics import mean_squared_error as MSE Framework = XGBRegressor(objective = 'reg:squarederror') # Interpretation of the evaluation Mechanism cv = RepeatedKFold(n_splits = 10, n_repeats = 3, random_state = 1) # Framework assessment n_scores = cross_val_score(Framework, x_train, UCS_train) print('MAE: %.8f (%.8f)' % (mean(n_scores), std(n_scores))) # fit the framework on training dataset Framework = XGBRegressor(objective = 'reg:squarederror') Framework.fit(x, UCS) gbm_param_grid = { "eta": [0.2, 0.25, 0.3, 0.35, 0.4, 0.5, 0.65, 0.7, 0.8, 0.9], "max_depth": [1,2,3,4,5,6,7,8,9,10], "colsample_bytree": [0.5,0.55,0.6,0.62,0.65,0.7,0.8,0.9,0.95,1], "subsample": [0.5,0.55,0.6,0.62,0.65,0.7,0.8,0.9,0.95,1], } # Instantiate the regressor: gbm gbm = xgb.XGBRegressor(objective = 'reg:squarederror') # Implement grid search: grid_mse randomized_mse = RandomizedSearchCV(estimator = gbm, param_distributions = gbm_param_grid, scoring = "neg_mean_squared_error", cv = 3, verbose = 1,) # Fit grid_mse to the UCS training dataset randomized_mse.fit(x, UCS) train_dataset_forecasting = randomized_mse.predict(x_train) test_dataset_forecasting = randomized_mse.predict(x_test) </pre>
Interpretation of the framework features	
Create the parameter grid	
Training dataset	
Testing dataset	

Figures 9(a) to 9(d) and 10(a) to 10(d) show the scatter plots of the predicted UCS as opposed to the measured UCS in the training and testing phases, respectively, employing various algorithms. In Figures 9(a) to 9(d), the correlation coefficient (R^2) values of the GBR, Catboost, LightGBM, and XGBoost are 0.97, 0.95, 0.40, and 0.99 in the training phase, respectively. At the same time, Figures 10(a) to 10(d) demonstrate the R^2 values of the GBR, Catboost, LightGBM, and XGBoost are 0.94, 0.91, 0.39, and 0.99 in the testing phase, respectively. Figures 11 and 12 reveal the performance plots of predicted UCS as opposed to measured UCS in the training phase. Figure 12 reveals the performance plots of predicted UCS as opposed to measured UCS in the testing phase.

Figure 13 shows the various performance indices of proposed algorithms such as R^2 , MAE, MSE, and RMSE. The performance indices can tell us the evaluation of the developed model by which we can distinguish the most suitable model. In this study, the performance indices of the proposed algorithms are tabulated in Table 9.

Taylor diagram describes a concise statistical description of how well the frameworks match their standard deviation and correlation. The following equation [66] represents the formula of the Taylor diagram:

$$R = \frac{1/P \sum_P (r_n - \bar{r})(f_n - \bar{f})}{\sigma_r \sigma_f}, \quad (13)$$

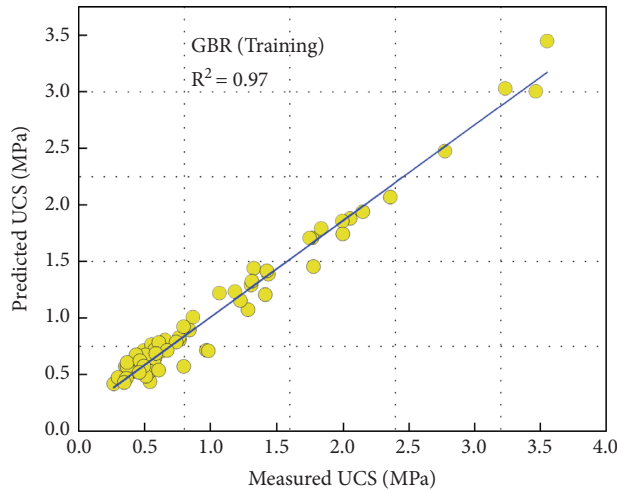
where R represents a correlation, P is the discrete point number, r_n and f_n are two vectors, σ_r and σ_f show the standard deviation of r and f , and \bar{r} and \bar{f} depict the average value of vectors r_n and f_n , respectively.

Figure 14 shows the association among the standard deviation, RMSE, and correlation of predicted UCS and measured UCS of GBR, Catboost, LightGBM, and XGBoost algorithms, respectively, from Figure 13. According to the results, the UCS of the XGBoost prediction algorithm was highly correlated with the measured UCS compared to the other studied algorithms. In addition, the standard deviation of the XGBoost is nearest to the original value of the standard deviation. As a result, the XGBoost demonstrates high accuracy as compared to the existing publicly available literature [7, 21, 40], and is proved to be the high accurate algorithm among all for UCS prediction. The GBR also has a standard deviation nearer to the original standard deviation but shows the smallest R^2 value. Meantime, Catboost and LightGBM have the smallest correlation and are further away from the original standard deviation values.

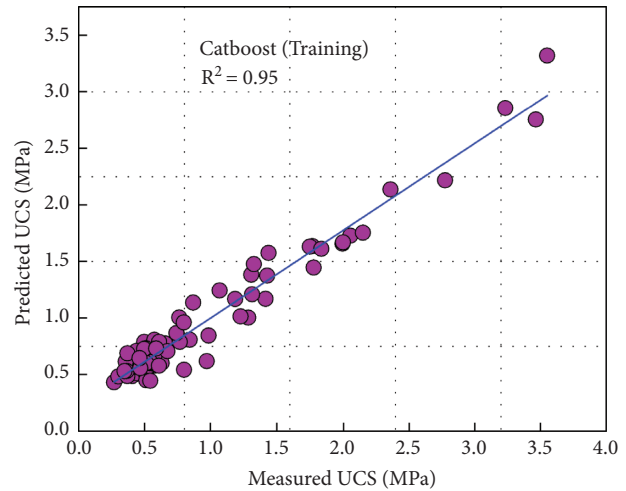
TABLE 8: Performance indices employed in this work.

Performance indices	Definition	Mathematical formula
R^2	R^2 is an aggregate bench used to compute how significant the association between measured and predicted UCS values is.	$R^2 = 1 - \frac{\sum_{i=1}^n (UCS_{\text{measured}} - UCS_{\text{predicted}})^2}{\sum_{i=1}^n (UCS_{\text{measured}} - UCS_{\text{mean}})^2}$
MAE	MAE shows the mean absolute error, which is a conventionally employed statistical feature that can inspect the real scenario of the predicted UCS value error.	$MAE = \sum_{i=1}^n UCS_{\text{mean}} - UCS_{\text{measured}} $
MSE	MSE as shown by equation (15) is a broadly practiced mathematical standard that shows the appropriate standard deviation of the error relative to the measured and predictive UCS value.	$MSE = 1/T \sum_{i=1}^n (UCS_{\text{measured}} - UCS_{\text{mean}})^2$
RMSE	RMSE is a statistical measure used to compute the mean of square error in UCS database.	$RMSE = \sqrt{1/2 \sum_{i=1}^n (UCS_{\text{measured}} - UCS_{\text{mean}})^2}$

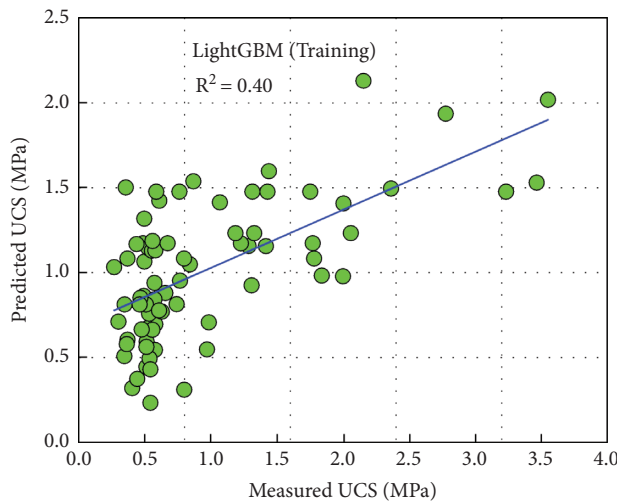
$UCS_{\text{predicted}}$ and UCS_{mean} represent the predicted values and the mean values, T shows the total number of datasets, and UCS_{measured} is the measured value.



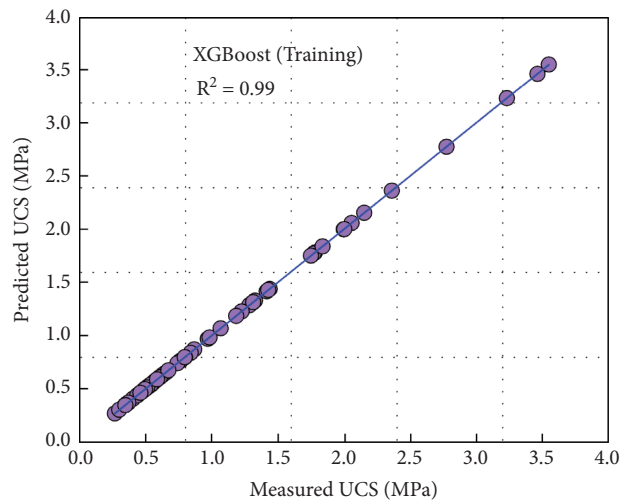
(a)



(b)



(c)



(d)

FIGURE 9: Scatter plots of predicted UCS as opposed to measured UCS of different models in the training stage: (a) GBR, (b) Catboost, (c) LightGBM, and (d) XGBoost.

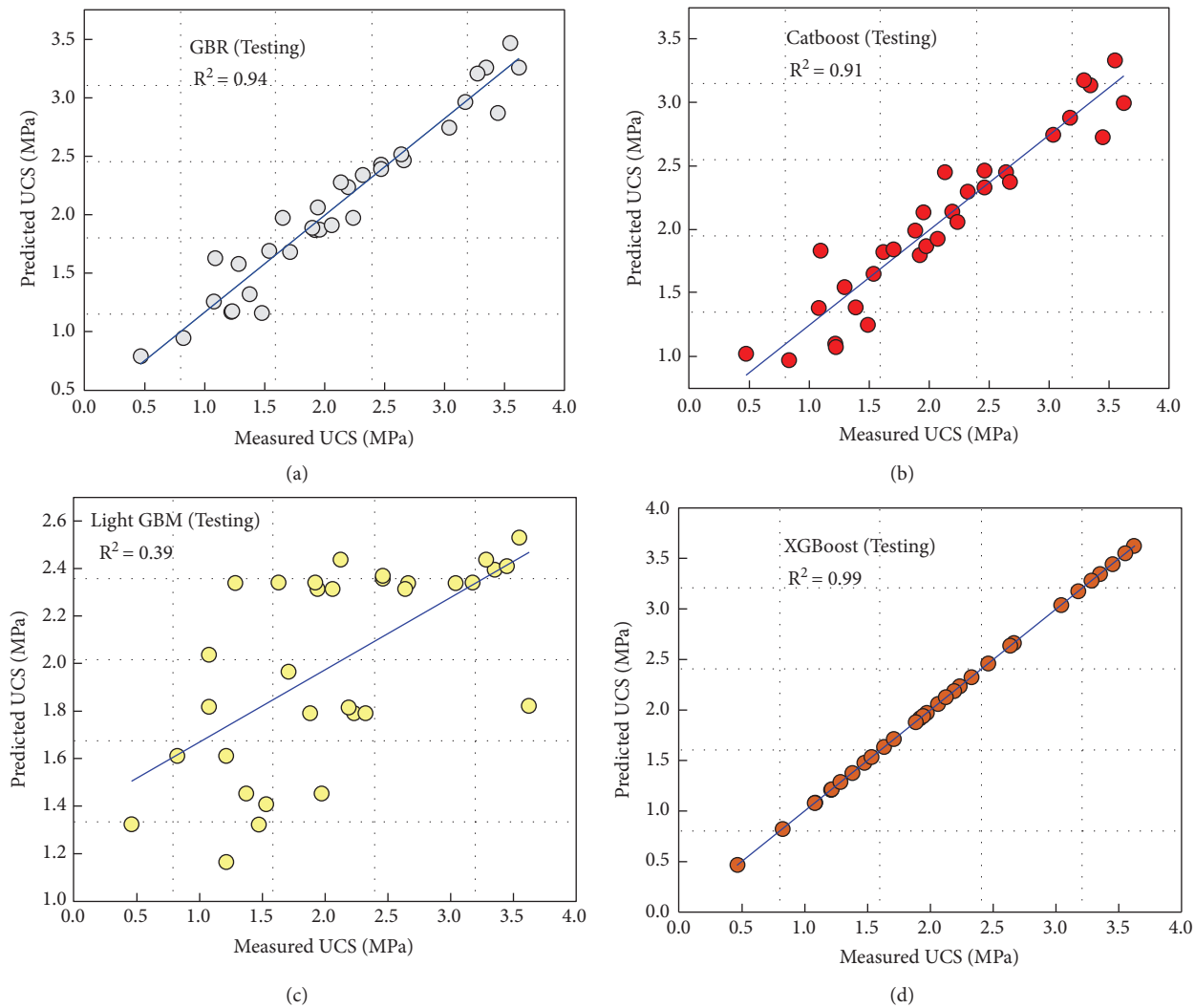


FIGURE 10: Scatter plots of predicted UCS as opposed to measured UCS of different models in the testing stage: (a) GBR, (b) Catboost, (c) LightGBM, and (d) XGBoost.

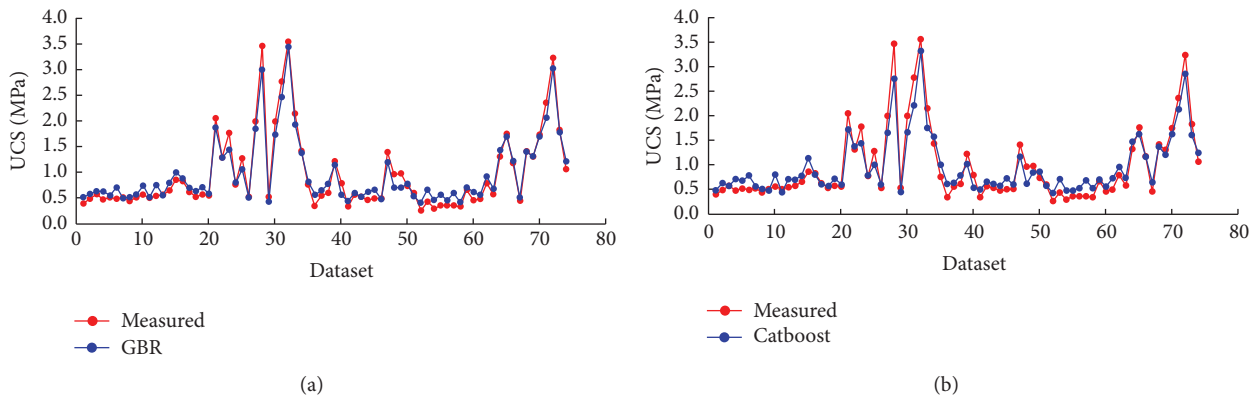
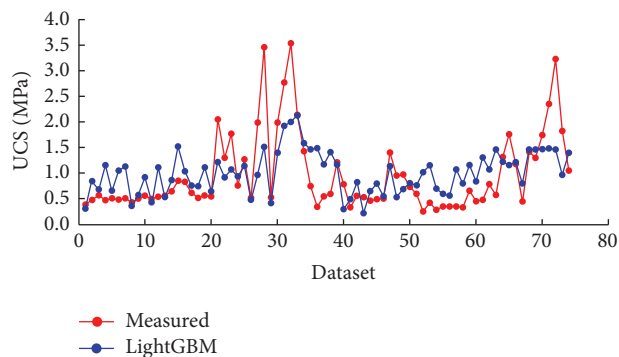
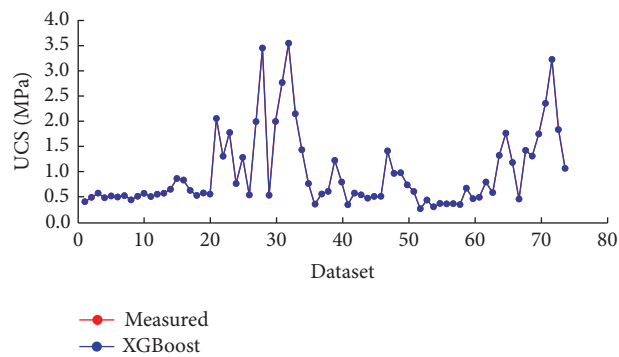


FIGURE 11: Continued.

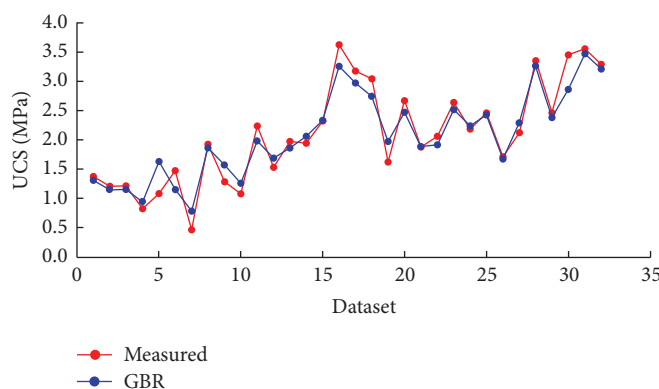


(c)

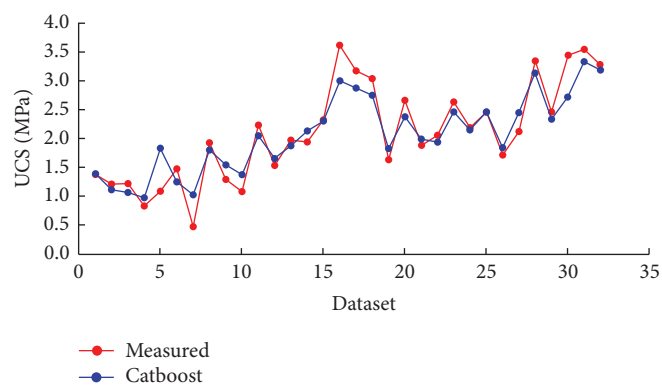


(d)

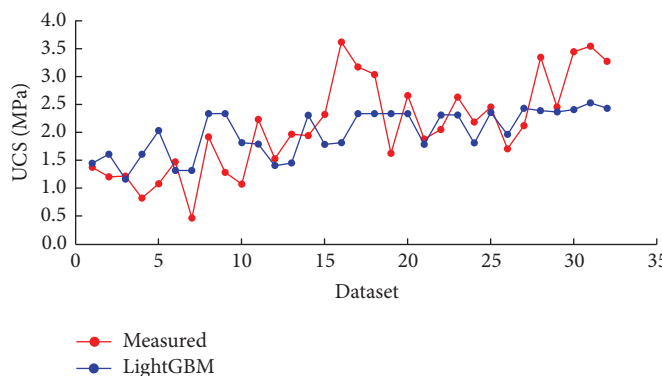
FIGURE 11: Performance plots of predicted UCS as opposed to measured UCS in the training stage phase: (a) GBR, (b) Catboost, (c) LightGBM, and (d) XGBoost.



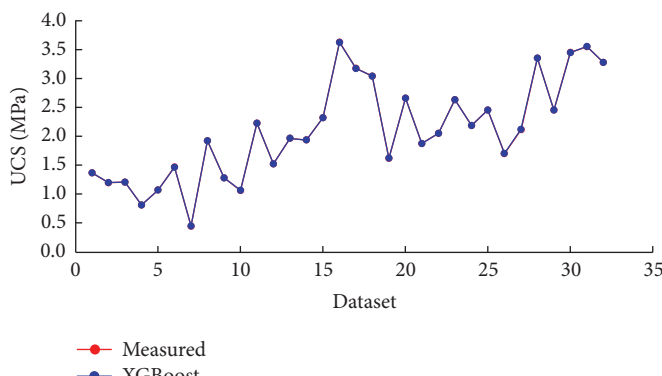
(a)



(b)



(c)



(d)

FIGURE 12: Performance plots of predicted UCS as opposed to measured UCS in the testing stage phase: (a) GBR, (b) Catboost, (c) LightGBM, and (d) XGBoost.

The results of the present study are similar to a previous study in the literature where Zhong et al. [40] also developed the XGBoost algorithm for predicting of rock mechanical

properties, i.e., UCS, in their study, which proved to have the best performance in results with maximum R^2 and smallest MAE and RMSE.

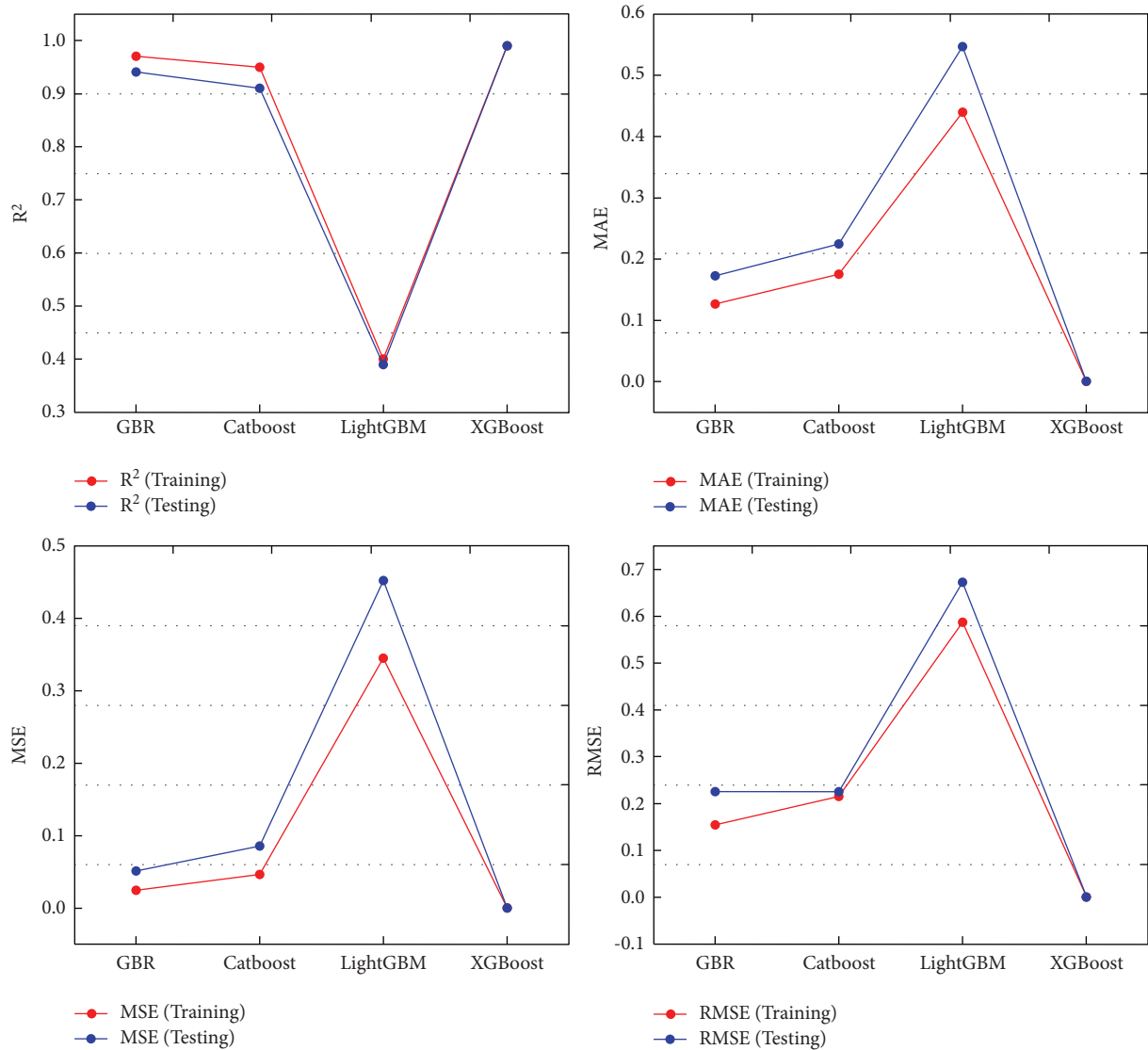


FIGURE 13: Evaluation criteria of the proposed algorithms R^2 , MAE, MSE, and RMSE in the training phase and testing phase, respectively.

TABLE 9: Performance indices of the proposed algorithms in this study.

Proposed algorithms	Training				Testing			
	R^2	MAE	MSE	RMSE	R^2	MAE	MSE	RMSE
GBR	95.7146	0.1266	0.0241	0.1554	92.7812	0.1726	0.0507	0.2253
Catboost	91.7856	0.17521	0.0463	0.2152	87.8611	0.2244	0.0853	0.2921
LightGBM	38.8687	0.43944	0.3448	0.5872	35.7219	0.5468	0.4521	0.6723
XGBoost	99.99	0.00062	0.00000062	0.00079	99.99	0.00054	0.0000047	0.00069

5. Sensitivity Analysis

Sensitivity analysis is a statistical tool that evaluates how target features are influenced based on changes in input features [67]. In this work, sensitivity analysis has been carried out by implementing “feature importance” module in python programming language on the superior performed XGBoost testing data. The following equation [68] depicts the formula of the feature importance:

$$\text{XGboostfm}_m = \frac{\sum_{l \in \text{alltree}} \text{fm}_{mn}}{T}, \quad (14)$$

where XGboostfm_m = the importance of feature m estimated from all trees in the XGBoost testing dataset, fm_{mn} = the feature importance for m tree in n , and T indicates the entire number of trees.

From Figure 15, it is clear that BTS and ρ_w are positively correlated, and the moisture and ρ_d are negatively correlated

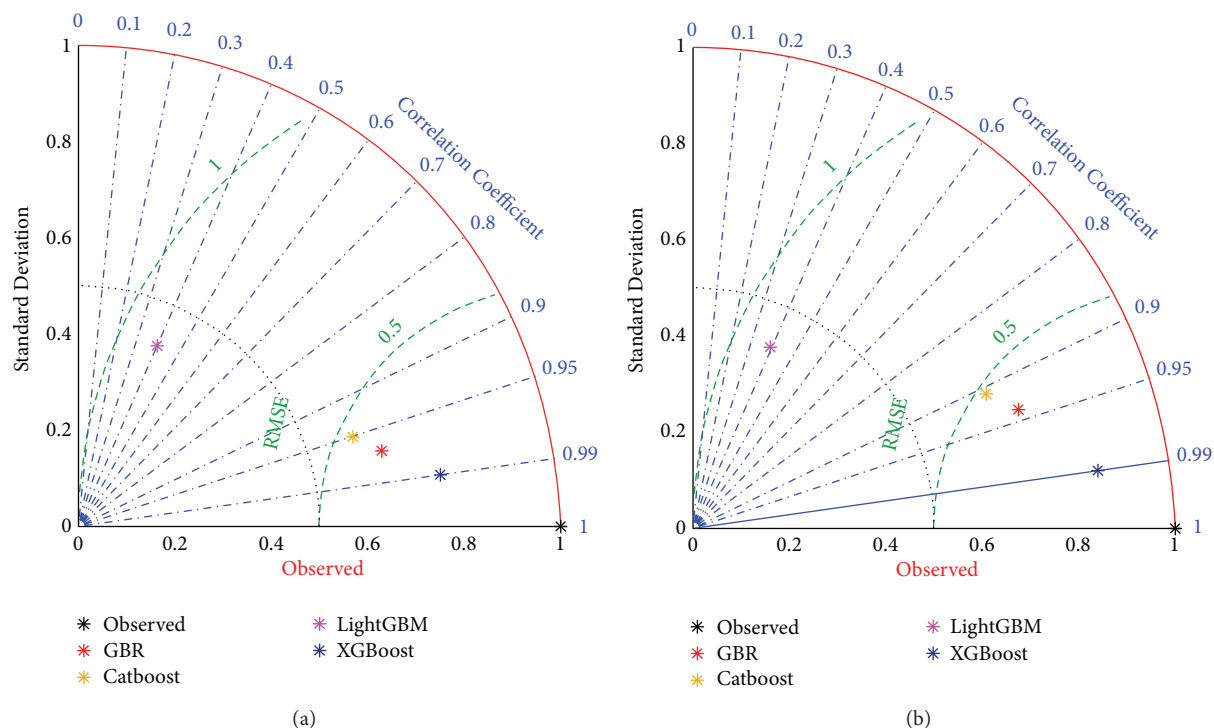


FIGURE 14: Taylor diagrammatic representation of GBR, XGBoost, Catboost, and LightGBM models in the (a) training phase and (b) testing phase.

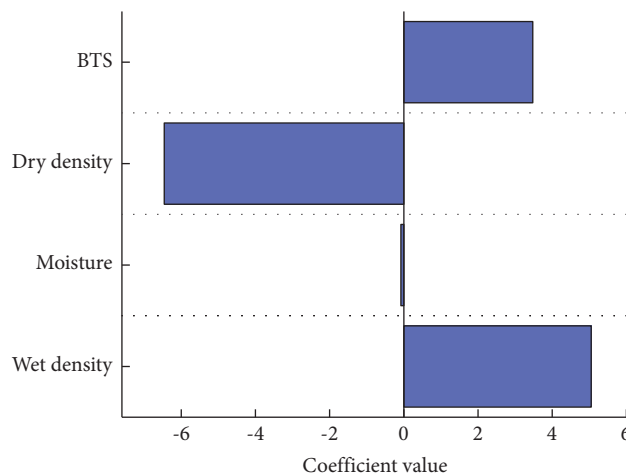


FIGURE 15: Sensitivity analysis of UCS dataset.

with the UCS. The feature importance of each input feature is given as:

BTS = 5.050, $\rho_w = -0.078$, moisture = -6.457, and $\rho_d = 3.475$.

6. Conclusion

UCS is one of the significant rock strength parameters and has various applications in mining, geology, geotechnical engineering, etc. An advanced data visualization model has been established in order to depict the research findings of various indirect tests to UCS. This study developed the four

gradient boosting machine learning algorithms such as GBR, Catboost, LightGBM, and XGBoost for predicting UCS of soft sedimentary rocks of Block-IX at Thar Coalfield. The application of these developed algorithms has rarely been employed for the prediction of rock mechanical parameters, especially UCS. In order to execute the gradient boosting machine learning algorithms, the four significant input parameters ρ_w in g/cm^3 ; moisture in %; dry ρ_d in g/cm^3 ; and BTS in MPa are used as input parameter and the corresponding UCS is employed as output parameter. Moreover, 106-point dataset was split identically for each algorithm into 70% for the training phase and 30% for the testing

phase. The developed models were executed in python programming language. In this study, the performance of each developed algorithm was computed and as a result, XGBoost outperformed the GBR, Catboost, and LightGBM with $R^2 = 0.99$, MAE = 0.00062, MSE = 0.0000006, and RMSE = 0.00079 in the training phase and $R^2 = 0.99$, MAE = 0.00054, MSE = 0.0000005, and RMSE = 0.00069 in the testing phase. In addition, according to the Taylor diagram, the standard deviation of the XGBoost is nearest to the original value of the standard deviation. Therefore, the XGBoost exhibits high accuracy in the training and testing phases, respectively. In this study, the developed XGBoost algorithm proved to be the best-fit algorithm for predicting the UCS of soft sedimentary rocks of the Block-IX at Thar Coalfield, Pakistan. Future work can be expanded employing different datasets to verify the more accuracy of the proposed algorithms.

References

- [1] D. C. Washington, *Limitations of Rock Mechanics in Energy-Resource Recovery and Development*, National Academy of Science, Washington, DC, USA, 1978.
- [2] S. Demirdag, K. Tufekci, R. Kayacan, H. Yavuz, and R. Altindag, "Dynamic mechanical behavior of some carbonate rocks," *International Journal of Rock Mechanics and Mining Sciences*, vol. 47, no. 2, pp. 307–312, 2010.
- [3] D. Jahed Armaghani, E. Tonnizam Mohamad, E. Momeni, M. S. Narayanasamy, and M. F. Mohd Amin, "An adaptive neuro-fuzzy inference system for predicting unconfined compressive strength and Young's modulus: a study on Main Range granite," *Bulletin of Engineering Geology and the Environment*, vol. 74, no. 4, pp. 1301–1319, 2015.
- [4] E. Hakan and D. Kanik, "Multicriteria decision-making analysis based methodology for predicting carbonate rocks' uniaxial compressive strength," *Earth Sciences Research Journal*, vol. 16, no. 1, pp. 65–74, 2012.
- [5] D. J. Armaghani, E. T. Mohamad, E. Momeni, M. Monjezi, and M. S. Narayanasamy, "Prediction of the strength and elasticity modulus of granite through an expert artificial neural network," *Arabian Journal of Geosciences*, vol. 9, no. 1, pp. 1–16, 2016.
- [6] Á. Török and B. Vásárhelyi, "The influence of fabric and water content on selected rock mechanical parameters of travertine, examples from Hungary," *Engineering Geology*, vol. 115, no. 3–4, pp. 237–245, 2010.
- [7] N. Yilmaz, "The influence of testing procedures on uniaxial compressive strength prediction of carbonate rocks from Equotip hardness tester (EHT) and proposal of a new testing methodology: hybrid dynamic hardness (HDH)," *Rock Mechanics and Rock Engineering*, vol. 46, no. 1, pp. 95–106, 2013.
- [8] J. S. Lee, L. Smallwood, and E. Morgan, "New application of rebound hardness numbers to generate logging of unconfined compressive strength in laminated shale formations," in *Proceedings of the 48th US rock mechanics/geomechanics symposium*, (ARMA), vol. 2, pp. 972–978, Minneapolis, MN, USA, June 2014.
- [9] F. Meulenkamp and M. A. Grima, "Application of neural networks for the prediction of the unconfined compressive strength (UCS) from Equotip hardness," *International Journal of Rock Mechanics and Mining Sciences*, vol. 36, no. 1, pp. 29–39, 1999.
- [10] H. Aoki and Y. Matsukara, "Estimating the unconfined compressive strength of intact rocks from Equotip hardness," *Bulletin of Engineering Geology and the Environment*, vol. 67, no. 1, pp. 23–29, 2008.
- [11] W. Verwaal and A. Mulder, "Estimating rock strength with the Equotip hardness tester: technical note," *International Journal of Rock Mechanics and Mining Science & Geomechanics Abstracts*, vol. 30, no. 6, pp. 659–662, 1993.
- [12] I. Cobanoglu and S. Celik, "Estimation of uniaxial compressive strength from point load strength, Schmidt hardness and P-wave velocity," *Bulletin of Engineering Geology and the Environment*, vol. 67, no. 4, pp. 491–498, 2008.
- [13] A. K. Ghose and S. Chakraborti, "Empirical strength indices of Indian coals," in *Proceedings of the 27th US symposium on rock mechanics Balkema*, Rotterdam, Netherlands, June 1986.
- [14] A. Azimian, R. Ajalloeian, and L. Fatehi, "An Empirical correlation of uniaxial compressive strength with P-wave velocity and point load strength index on Marly rocks using statistical method," *Geotechnical & Geological Engineering*, vol. 32, no. 1, pp. 205–214, 2014.
- [15] O. Katz, Z. Reches, and J. C. Roegiers, "Evaluation of mechanical rock properties using a Schmidt Hammer," *International Journal of Rock Mechanics and Mining Sciences*, vol. 37, no. 4, pp. 723–728, 2000.

Numerical Analysis and Simulation of Maximum Turbidity Zone Formation at Inlet to River

Jyotikusum Acharya, *Department of Civil Engineering, NM Institute of Engineering & Technology, Bhubaneswar, jyotikusumacharya@yahoo.co.in*

Binapani Mohapatra, *Department of Civil Engineering, Raajdhani Engineering College, Bhubaneswar, binapanimohapatra@yahoo.co.in*

Shradha Jena, *Department of Civil Engineering, Capital Engineering College, Bhubaneswar, shradhajena98@gmail.com*

Rakesh Kumar Panda, *Department of Civil Engineering, Aryan Institute of Engineering & Technology, Bhubaneswar, rakeshpanda116@gmail.com*

ABSTRACT

A river's estuary can be thought of as a relatively open and partially closed coastal body. It is a transitional zone of rivers that contains processes from land to sea and from fresh water to salt water. It is connected to the ocean. Due to natural processes such as runoff and tides, the estuary is one of the most productive natural environments on the planet, and it contains a significant amount of sediments. As a result, many coastal locations with river estuaries have become the human population's most densely populated areas. The RSM (Reynolds stress model) turbulence model and the PID (proportional integral derivative) algorithm are successfully used in this paper to simulate the dynamic model and numerical simulation of the formation of the turbidity maximum zone in the estuary, providing a theoretical basis for the continuation of similar research studies.

1. Introduction

The estuary of a river is a free and partially enclosed coastal waters that can freely exchange water with the deep sea [1, 2]. Due to the influence of marine civilization, the coast of the estuary is already one of the most densely populated areas in the world [3], and more than half of the world's population lives in estuaries and coastlines [4]. As a result, many estuary areas have been damaged in many ways, including deforestation, overgrazing, and agricultural farming [5]. The estuarine area has been damaged in many ways, which makes the soil barren and loose and easy to be washed away by water [6]. Together with urban life and industrial drainage and filling wetlands, sewage and animal face result in too many nutrients in the body of the sea, which is the primary cause of eutrophication [7, 8]. The sediment movement at the bottom of a river or estuary is one of the key factors affecting the hydrodynamic force [9]. Waves will be generated under the interaction between water and

seabed sediments, which in turn will create a free surface with the air [10]. As an important factor of coastal hydrodynamic environment, waves control the dynamic processes of sediment liquefaction, suspension, transport, deposition, and consolidation [11]. Because of the important influence of sediments on the seabed, it is very important to study the effects of flow and sediment on the Haikou Port waterway project [12]. From the upper reaches to the lower reaches of the river, deposition processes continue to form throughout the entire process until reaching the sea, and the speed is slowed down under the influence of ocean forces [13]. With the slow deposition of sediments near the estuary, different forms of deltas emerge as the times require [14]. Previous scholars have studied the dynamic model and numerical simulation of the formation of the maximum turbidity zone in the estuary, which provides the necessary theoretical support for its future development [15].

Because the river estuary is closely related to human life, the hydrodynamics of the estuary has always been a topic of

interest among domestic and foreign researchers [16]. At present, the related research work is mainly carried out from the following aspects. Some scholars have studied the research methods of hydrodynamic problems [17]. In the theoretical study, under certain conditions, the activity of upper water in shallow water area is very regular. At the same time, the activity of the upper water affects the fluid in the lower sediment and is penetrated by the two-fluid model [18, 19]. The researchers introduced longitudinal irregularity into the model, refined mud in the multilayer structure, and studied laminar flow sediment. In the aspect of experimental research, researchers from the research institute have completed the experimental research on the interaction between waves and sediments [20, 21]. In the process of wave attenuation and sediment transport, scholars have observed the final results under different conditions [22]. In the aspect of numerical simulation, some researchers use the numerical simulation method to study the wave motion under the action of waves and use numerical simulation method to study the submarine flow with a lot of soil [23, 24]. A finite difference method is used to calculate the two-layer structure of a viscous fluid system under pulsating action [25]. Generally speaking, the numerical study of free surface water sediment interaction in estuaries is rarely applied [26].

In this paper, the RSM turbulence model and the PID algorithm are used to study the dynamic model and numerical simulation of the formation of turbidity maximum zone in the estuary. The research work of these two aspects has been completed. The research is divided into three parts. Firstly, the multiresolution mesh subdivision model of

turbidity maximum zone in digital estuary is established. Secondly, the RSM turbulence model is optimized by PID algorithm. Finally, the simulation calculation is carried out and good results are obtained.

2. Methodology

2.1. RSM Turbulence Model. The RSM turbulence model is often used to solve the Reynolds pressure for the second-order moment turbulent flow equation, as shown in Figure 1 [27]. In the RSM turbulence model, the constant of an equation is $\overline{u'_i u'_j}$. This constant is mainly used to further improve the accuracy of the Reynolds pressure solution for the second-order moment turbulent flow equation [28]. By setting different $\overline{u'_i u'_j}$ values, the purpose of precisely adjusting the fluctuation coefficient of the flow equation of the second-order moment turbulent flow is achieved [29] so that the Reynolds pressure of the flow Equation of the second-order moment turbulent flow can be more accurately obtained in the calculation process [30]. It is worth noting that there are many unstable factors in the flow equation of the second-order moment turbulence. These unstable factors make the calculation result of the second-order moment turbulent flow equation biased, so some effective measures must be taken to close the flow equation [31].

The RSM turbulence model mathematical calculation equation is as follows, and the obtained outputs are shown in Figure 2:

$$\begin{aligned} \frac{\partial}{\partial t}(\rho \overline{u'_i u'_j}) + \underbrace{\frac{\partial}{\partial x_k}(\rho u_k \overline{u'_i u'_j})}_{C_{ij}} = & - \underbrace{\frac{\partial}{\partial x_k}[\rho \overline{u'_i u'_j u'_k} + p(\delta_{kj} u'_i + \delta_{ik} u'_j)]}_{D_{T,ij}} + \underbrace{\frac{\partial}{\partial x_k}[\mu \frac{\partial}{\partial x_k}(\overline{u'_i u'_j})]}_{D_{L,ij}} \\ & - \underbrace{\rho \left(\overline{u'_i u'_k} \frac{\partial u_j}{\partial x_k} + \overline{u'_j u'_k} \frac{\partial u_i}{\partial x_k} \right)}_{P_{ij}} - \underbrace{\rho \beta (g_i \overline{u'_j \theta} + g_j \overline{u'_i \theta})}_{G_{ij}} + \underbrace{p \left(\frac{\partial'_i}{\partial x_j} + \frac{\partial'_j}{\partial x_i} \right)}_{\varphi_{ij}} - \underbrace{2\mu \frac{\partial u'_i}{\partial x_k} \frac{\partial u'_j}{\partial x_k}}_{\varepsilon_{ij}} \\ & - \underbrace{2\nu \Omega_k (\overline{u'_j u'_m} \varepsilon_{ikm} + \overline{u'_i u'_m} \varepsilon_{jkm})}_{F_{ij}}. \end{aligned} \quad (1)$$

In equation (1), only $D_{T,ij}$, G_{ij} , φ_{ij} , and ε_{ij} need to establish a corresponding mode to close the aspect, and variables C_{ij} , $D_{L,ij}$, P_{ij} , and F_{ij} do not need to sealing treatment.

According to the RSM turbulence model, the following model of gradient divergence can be established:

$$D_{T,ij} = C_s \frac{\partial}{\partial x_k} \left(\rho \frac{\overline{u'_k u'_k}}{\varepsilon} \frac{\partial \overline{u'_i u'_j}}{\partial x_l} \right). \quad (2)$$

However, due to the existence of many uncertainties in the gradient divergence model itself, the stability of the

equation is not satisfactory. Therefore, the equation is simplified as follows:

$$D_{T,ij} = \frac{\partial}{\partial x_k} \left(\frac{\mu_t}{\sigma_k} \frac{\partial \overline{u'_i u'_j}}{\partial x_k} \right). \quad (3)$$

The simplified equation can be obtained using plane shear flow.

After obtaining the σ_k value, the linear stress-strain φ_{ij} value in the equation can be further obtained:

$$\varphi_{ij} = \varphi_{ij,1} + \varphi_{ij,2} + \varphi_{ij,\omega}, \quad (4)$$

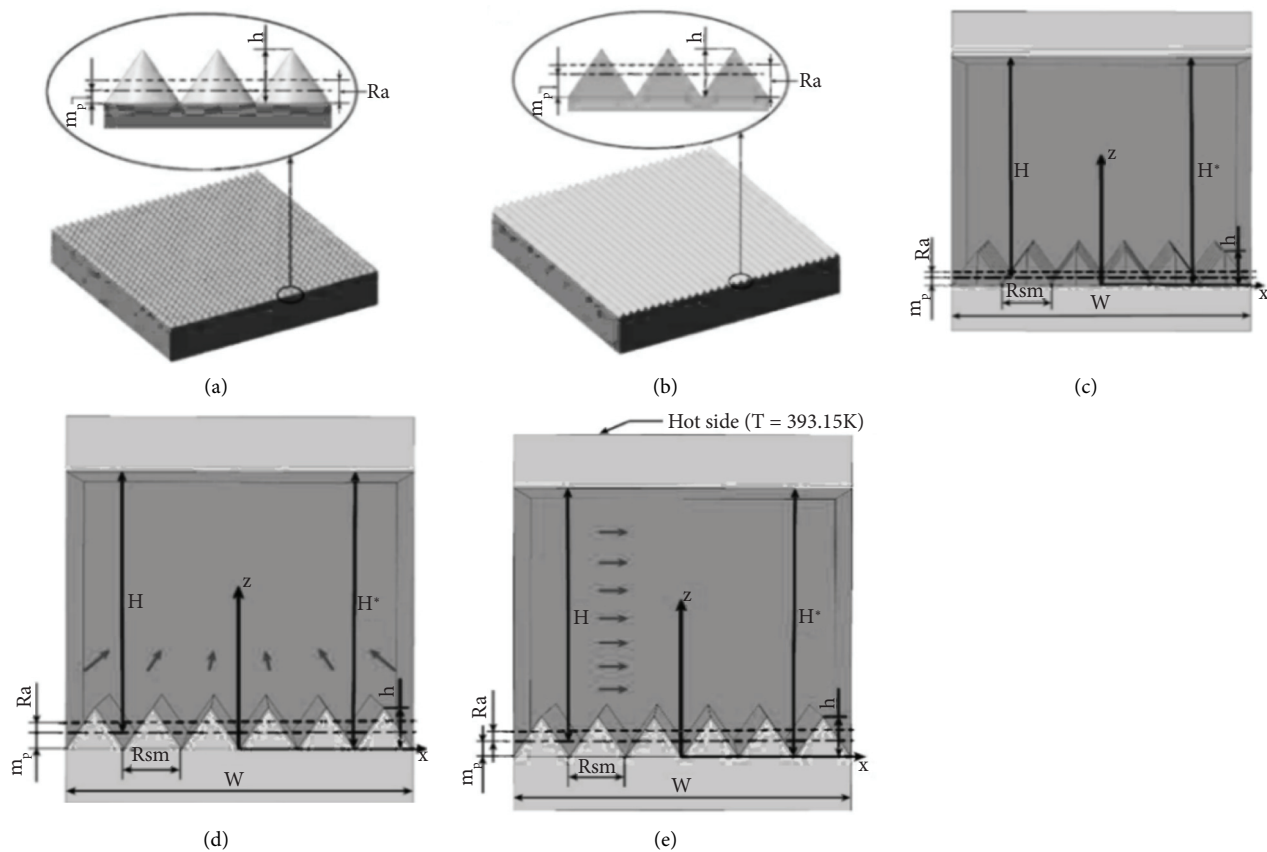


FIGURE 1: RSM turbulence model diagram.

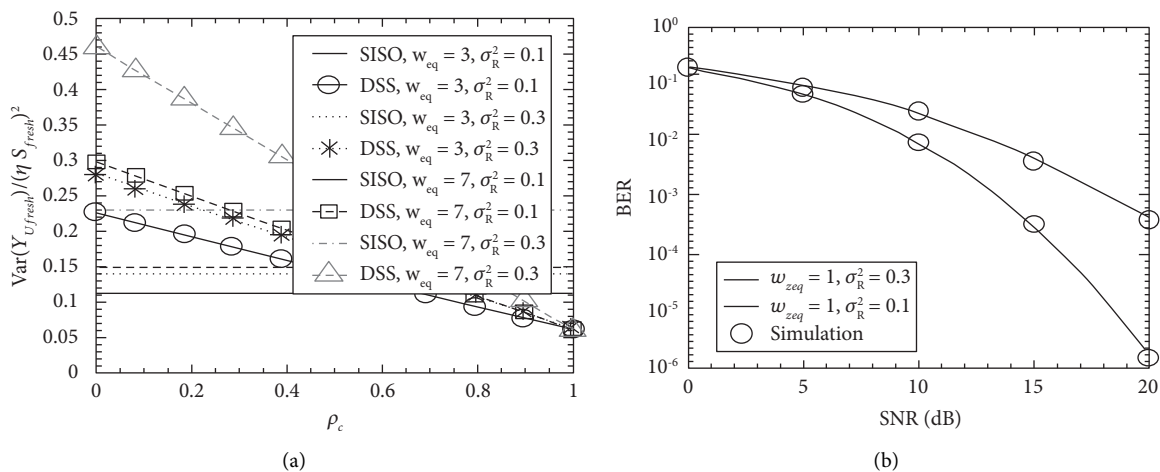


FIGURE 2: Continued.

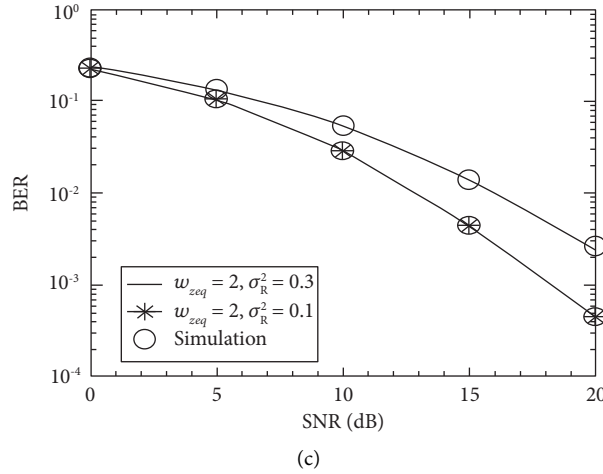


FIGURE 2: The calculation process between different variables of the RSM turbulence model.

In equation (4), the variable $\varphi_{ij,1}$ is mainly used to express the slow pressure strain term, the variable $\varphi_{ij,2}$ is mainly used to express the fast stress-strain term, and the variable $\varphi_{ij,\omega}$ is mainly used to represent the wall reflection term. The variables in the above equation are calculated as follows.

The calculation equation for the slow pressure strain item $\varphi_{ij,1}$ is as follows:

$$\varphi_{ij,1} = -C_1 \rho \frac{\varepsilon}{k} \left[\overline{u_i u_j'} - \frac{2}{3} \delta_{ij} k \right]. \quad (5)$$

The calculation equation for the stress-strain item $\varphi_{ij,2}$ is as follows:

$$\varphi_{ij,2} = -C_2 \left[(P_{ij} + F_{ij} + G_{ij} - C_{ij}) - \frac{2}{3} \delta_{ij} (P + G - C) \right]. \quad (6)$$

Among them, P_{ij} , F_{ij} , C_{ij} , and G_{ij} are given in equation (6). Moreover, $P = 1/2 P_{kk}$, $G = P = 1/2 G_{kk}$, and $C = 1/2 C_{kk}$.

The calculation equation of the wall reflection term $\varphi_{ij,\omega}$ is more complicated than the calculation equation of the slow pressure strain term $\varphi_{ij,1}$ and the calculation equation of the fast stress-strain term $\varphi_{ij,2}$. The specific calculation equation is as follows:

$$\begin{aligned} \varphi_{ij,\omega} = & C_1' \frac{\varepsilon}{k} \left(\overline{u_k u_m'} n_k n_m \delta_{ij} - \frac{3}{2} \overline{u_i u_k'} n_k n_j - \frac{3}{2} \overline{u_j u_k'} n_k n_i \right) \frac{k^{3/2}}{C_1 \varepsilon d} \\ & + C_2' \frac{\varepsilon}{k} \left(\varphi_{km,2} n_k n_m \delta_{ij} - \frac{3}{2} \varphi_{ik,2} n_k n_j - \frac{3}{2} \varphi_{jk,2} n_k n_i \right) \frac{k^{3/2}}{C_1 \varepsilon d}, \end{aligned} \quad (7)$$

where n_k is mainly used to represent a unit in the wall and d is the distance to the wall.

The calculation equation for the variable G_{ij} is as follows:

$$G_{ij} = \beta \frac{\mu_t}{Pr_t} \left(g_i \frac{\partial T}{\partial x_j} + g_j \frac{\partial T}{\partial x_i} \right), \quad (8)$$

where the variable Pr_t is mainly the actual Prandtl number used to represent turbulence. In general, the value of Pr_t is mainly 0.85. The variable β is used to represent the thermal expansion coefficient of turbulent flow. Turbulence in the ideal state can be calculated directly by using the following equation:

$$G_{ij} = \frac{\mu_t}{\rho Pr_t} \left(g_i \frac{\partial \rho}{\partial x_j} + g_j \frac{\partial \rho}{\partial x_i} \right). \quad (9)$$

The calculation equation for the divergent tensor ε_{ij} is as follows:

$$\varepsilon_{ij} = \frac{2}{3} \delta_{ij} (\rho \varepsilon + Y_M), \quad (10)$$

In the above equation, variable $Y_M = 2\rho \varepsilon M_t^2$ belongs to a diffusion term, so the actual calculation equation of its trickle Mach number is as follows:

$$M_t = \sqrt{\frac{k}{a^2}}, \quad (11)$$

where the variable a is mainly used to express the speed of sound. The ideal turbulent divergence rate ε can be calculated directly by using the following equation $k - \varepsilon$:

$$\begin{aligned} \frac{\partial}{\partial t} (\rho \varepsilon) + \frac{\partial}{\partial x_i} (\rho \varepsilon u_i) = & \frac{\partial}{\partial x_j} \left[\left(\mu + \frac{\mu_t}{\sigma_\varepsilon} \right) \frac{\partial \varepsilon}{\partial x_j} \right] \\ & + C_{\varepsilon 1} \frac{1}{2} [P_{ii} + C_{\varepsilon 3} G_{ii}] \frac{\varepsilon}{k} - C_{\varepsilon 2} \rho \frac{\varepsilon^2}{k}. \end{aligned} \quad (12)$$

The calculation equation for the eddy viscosity coefficient μ_t is as follows:

$$\mu_t = \rho C_\mu \frac{k^2}{\varepsilon}. \quad (13)$$

2.2. PID Algorithm. As early as in the 1930s, researchers proposed PID algorithms. After years of development, their practical application in industrial control has been quite abundant. Because of its relatively simple organizational structure, it is easy to improve. It is adaptable to all kinds of complicated situations. The related supporting control methods are also very efficient. In the process of industrial control, there are a lot of factors that will affect it [14]. The control process is adjusted at any time according to the actual situation, and the supporting control parameters are constantly changing, so it is very suitable to use the PID algorithm to control it, and the PID development process is also relatively easy. In the process of development, the parameters can be changed at any time according to the actual situation, which shows a very good flexibility, and it can adapt to any excessively redundant, as shown in Figure 3 [15].

The PID algorithm is a linear regulator. By linear combination, this regulator constitutes the control quantity by the ratio (*P*), integral (*I*), and derivative (*D*) of the control deviation $c = r - y$, which is composed of the set point r of the system and the actual output value y . Therefore, it is abbreviated as PID algorithm. The simulation PID control law in the continuous control system is

$$u(t) = K_p \left[e(t) + \frac{1}{T_I} \int_0^t e(t) dt + T_D \frac{de(t)}{dt} \right], \quad (14)$$

where $u(t)$ is the output of the algorithm, $e(t)$ is the deviation of the system's given quantity and output, K_p is the proportional coefficient, T_I is the integral time constant, and T_D is the differential time constant. The corresponding transfer function is

$$G(s) = K_p \left(1 + \frac{1}{T_I s} + T_D s \right). \quad (15)$$

The functions of the proportional regulator, integral regulator, and differential regulator are as follows. Firstly, the proportional regulator: the proportional regulator is to prevent the control parameters from deviating during the control process, thus causing the control error to occur [16]. If a control error occurs in the actual control process, the proportional regulator controls and adjusts according to the corresponding principle to minimize the deviation [17]. Secondly, proportional-integral regulator: in the process of proportional adjustment, there will be a static difference [18]. In order to compensate for the influence of the control caused by the static difference, a proportional-integral regulator is required for adjustment. It adjusts the control quantity by the deviation, and the deviation can also accumulate, that is to say there is regulation as long as the deviation is not zero. The greater the deviation, the greater the score and the larger the adjustment range [19]. The adjustment process is completed when the deviation is zero. In the actual adjustment process, it is also possible to slightly reduce the adjustment range in order to ensure the stability of the control. Thirdly, a proportional-integral derivative regulator exists to allow the control process to be completed in the shortest possible time. The deviation in the control

process is analyzed. According to the predicted deviation situation, the control is adjusted, which can minimize the adjustment range and ensure the normal operation of the system [20].

Because of the control characteristics of the industrial system itself, deviation analysis should be performed according to the sampling conditions at the time when the system is running. Therefore, the circumscribed rectangular method is used for numerical integration, and the first-order backward difference is used for numerical differentiation [21]:

$$u_i = K_p \left[e_i + \frac{T}{T_I} \sum_{j=0}^i e_j + \frac{T_D}{T} (e_i - e_{i-1}) \right]. \quad (16)$$

If the sampling period is small enough, this discrete approximation is quite accurate. In equation (16), u_i is the full output, which corresponds to the position that the actuator of the controlled object should reach at the sampling time of the i th time. Therefore, equation (16) is called a PID position type control equation, as shown in Figure 3.

It can be seen that when u_i is calculated as above, the output value is related to all the past states. When what the actuator needs is not the absolute value of the control quantity but its increment, the following equation can be derived:

$$\Delta u_i = u_i - u_{i-1} = K_p \left[e_i - e_{i-1} + \frac{T}{T_I} e_i + \frac{T_D}{T} (e_i - 2e_{i-1} + e_{i-2}) \right] \quad (17)$$

or

$$u_i = u_{i-1} + K_p \left[e_i - e_{i-1} + \frac{T}{T_I} e_i + \frac{T_D}{T} (e_i - 2e_{i-1} + e_{i-2}) \right]. \quad (18)$$

Equation (4) is called an incremental PID control equation. Equation (5) is called a recursive PID control equation. The quantitative control equation has the following advantages. First, the computer only outputs the control increment, that is, the change in the position of the actuator, so the influence of the malfunction is small. Second, the output u_i at time i only needs to use the deviation at this moment, the previous moment, the deviation e_{i-1} and e_{i-2} of the first two moments, and the previous output value u_{i-1} , which greatly saves memory and calculation time [22]. Third, when the manual-automatic switching is performed, the control volume has a small impact and can be smoothly transitioned. The computer of the control process requires strong real-time performance. When the microcomputer is used as a digital algorithm, the necessary methods must be used to speed up the calculation due to the restrictions on word length and operation speed. The method of simplifying the equation is described below [23].

According to the recursive PID Equation represented by equation (5), each time the computer outputs u_i , four additions, two subtractions, four multiplications, and two divisions are performed. The equation is slightly consolidated and written as follows:

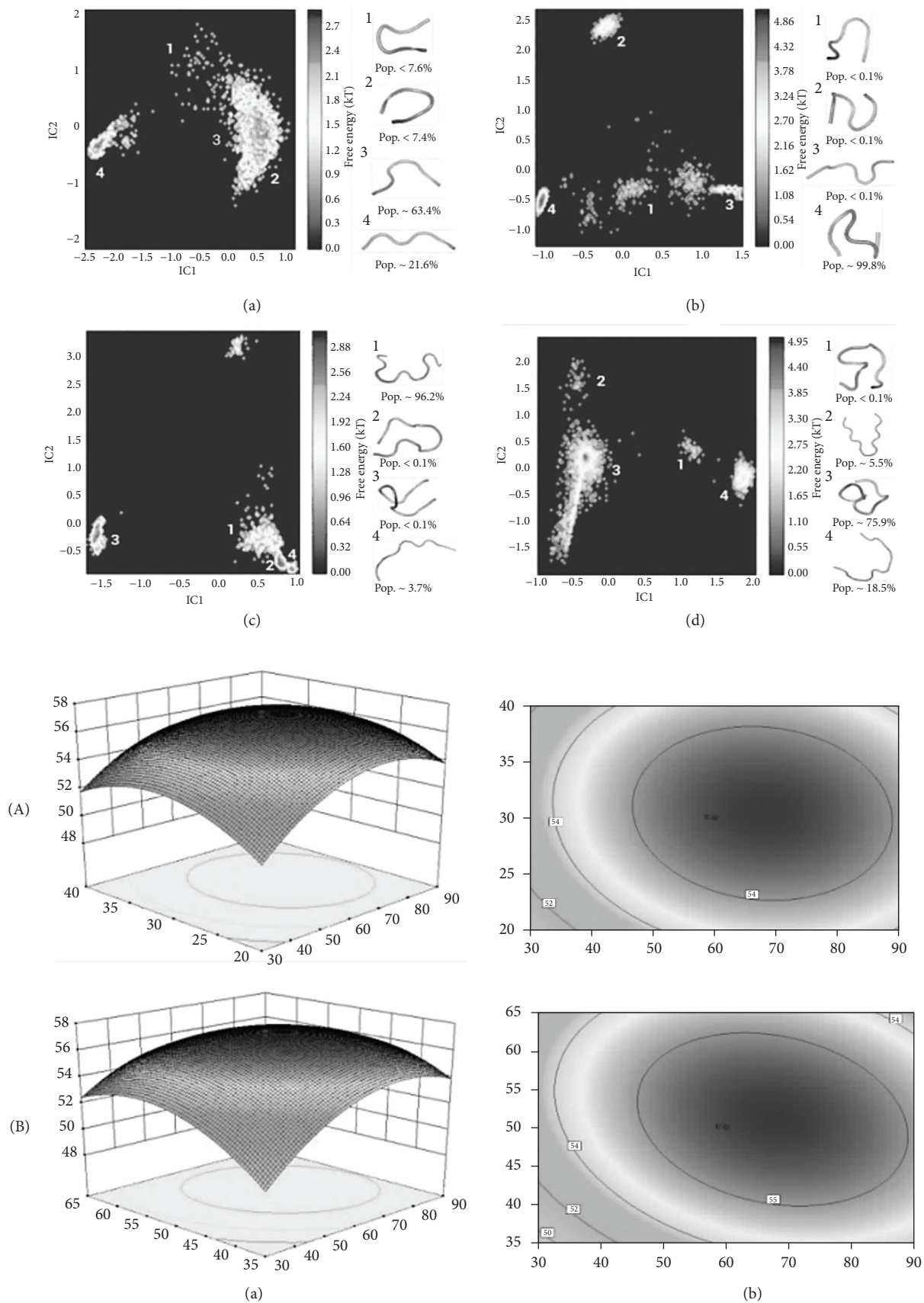


FIGURE 3: PID algorithm. (a) PID algorithm linear adjustment process. (b) PID position control algorithm.

$$u_i = u_{i-1} + K_p \left(1 + \frac{T}{T_I} + \frac{T_D}{T} \right) e_i - K_p \left(1 + \frac{2T_D}{T} \right) e_{i-1} + K_p \frac{T_D}{T} e_{i-2} = u_{i-1} + a_0 e_i - a_1 e_{i-1} + a_2 e_{i-2}. \quad (19)$$

In equation (19), the coefficient a_0 , a_1 , and a_2 can be calculated discretely, thereby speeding up the operation of the algorithm program.

3. Results and Discussion

The RSM turbulence model and the PID algorithm are mainly used to simulate and study the dynamic model and numerical experiment of turbidity maximum zone in estuary. The specific contents of the numerical simulation study include the following aspects. Firstly, a multiresolution grid subdivision model for the largest turbid zone of the digital river inlet is constructed. Secondly, the PID algorithm is used to optimize the RSM turbulence model and for simulation calculation [24].

Before conducting the research, the digital modeling of river estuaries is required. According to the distribution and characteristics of the river bodies in the study area, one or more satellite remote-sensing data sources, such as GF-1, GF-2, Landsat TM/ETM+, HJ-1A, and HJ-1B, can be selected. The single-wavelength threshold method, the water body index method, the classification method based on statistics and machine learning, the decision tree classification method based on prior knowledge or the object-oriented classification method are used to extract water, and the extracted water body is vectorized. The remote-sensing image data are used to effectively identify the river boundary line, as shown in Figure 4 [25].

Considering that the river channel is long and narrow, in the visualization process, the spatial position of the viewpoint changes, and only the local river area can be observed. The other areas are outside the computer window. If the river is modeled uniformly and the river is carefully observed during the process of roaming, the proportion of rivers outside the field of view is large [26]. If this part of the river is synchronized, it will inevitably affect the real-time interaction. Therefore, the river is first partitioned. If during the change of viewpoint, the river is not in the window, and it

will be unloaded without rendering [27]. Partition can be conducted through the aspect ratio of the window. The multiresolution grid subdivision model of the largest turbid zone in the digital river inlet is shown in Figure 4.

After completing the digital modeling of the river estuary, the corresponding sensor equipment can be used to collect data on the most turbid zone of the river inlet. The AT89S52 chip is mainly used to make the corresponding data acquisition device placement, and all-weather data acquisition is conducted in the key position identified in Figure 4 [28]. AT89S52 is a small and has high performance and low power chip introduced by STC. The chips use the main features of flash memory technology, reducing the cost of production. Its software and hardware are fully compatible with the MCS-51-related manufacturing technology, making development and testing easier and providing intelligent flexibility and cheap solutions for many embedded control systems. The AT89S52 has the following features [29]. First, the AT89S52 and MCS-51 microcontrollers are fully compatible with the instruction set and pins. Second, an on-chip 4k byte line can reprogram Flash program memory. The working range of AT89S52 is 0 Hz~24 MHz. In addition, it also has the following characteristics: three-level program memory encryption, with 128×8 bit internal RAM with 32 bit bidirectional input and output lines. It has not only two 16 bit timers/counters but also five interrupt sources and two interrupt priorities and full duplex asynchronous serial ports [30].

After obtaining a large amount of data, it is necessary to use the corresponding mathematical model to excavate the contents of these data, thus obtaining the dynamic model of the formation of the largest turbid zone in the river mouth [31]. For river data mining, the most common in the industry is the use of RSM turbulence models for mathematical modeling. However, this model not only is computationally complex but also lacks accuracy in the calculation of low Reynolds pressures. Therefore, the PID algorithm is used to optimize the RSM turbulence model to obtain a simpler and more accurate turbulence model. The optimization process is as follows.

The equation for the RSM turbulence model is shown below:

$$\begin{aligned} \frac{\partial}{\partial t} (\rho \overline{u'_i u'_j}) + \underbrace{\frac{\partial}{\partial x_k} (\rho u'_k \overline{u'_i u'_j})}_{C_{ij}} = & - \underbrace{\frac{\partial}{\partial x_k} [\rho \overline{u'_i u'_j u'_k} + p(\delta_{kj} u'_i + \delta_{ik} u'_j)]}_{D_{T,ij}} + \underbrace{\frac{\partial}{\partial x_k} \left[\mu \frac{\partial}{\partial x_k} (\overline{u'_i u'_j}) \right]}_{D_{L,ij}} \\ & - \underbrace{\rho \left(\overline{u'_i u'_k} \frac{\partial u_j}{\partial x_k} + \overline{u'_j u'_k} \frac{\partial u_i}{\partial x_k} \right)}_{P_{ij}} - \underbrace{\rho \beta (g_i \overline{u'_j \theta} + g_j \overline{u'_i \theta})}_{G_{ij}} + \underbrace{p \left(\frac{\partial u'_i}{\partial x_j} + \frac{\partial u'_j}{\partial x_i} \right)}_{\varphi_{ij}} - \underbrace{2\mu \frac{\partial u'_i}{\partial x_k} \frac{\partial u'_j}{\partial x_k}}_{\varepsilon_{ij}} \\ & - \underbrace{2\nu \Omega_k (\overline{u'_j u'_m} \varepsilon_{ikm} + \overline{u'_j u'_m} \varepsilon_{jkm})}_{F_{ij}}. \end{aligned} \quad (20)$$

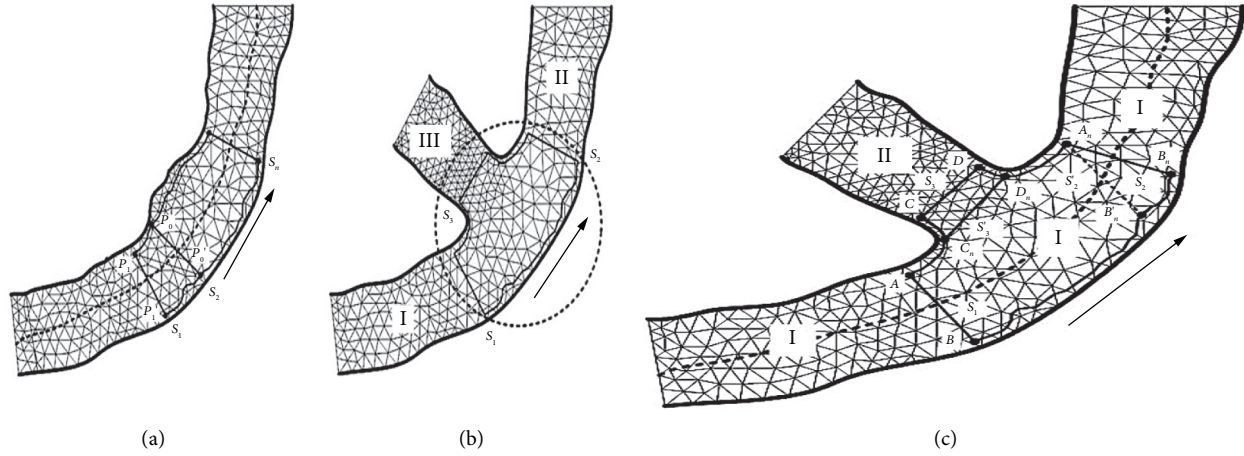


FIGURE 4: Digital estuary. (a) Remote-sensing image of river boundary. (b) Multiresolution mesh subdivision model for maximum turbidity zone. (c) Dynamic model simulation results of the maximum turbidity zone formed in the estuary of the river.

In equation (20), the variables $D_{T,ij}$, G_{ij} , φ_{ij} , and ε_{ij} need to establish a corresponding mode for closing operation, and the variables C_{ij} , $D_{L,ij}$, P_{ij} , and F_{ij} do not need sealing treatment.

For this model, the PID equation can be used to optimize the derivative. It is supposed that there is a quadratic polynomial as follows:

$$p_2(x) = a_0 + a_1x^1 + a_2x^2. \quad (21)$$

The difference f is at points x_0, x_1 , and x_2 , that is, the local coordinate system is used to make $x_i = 0$, $x_{i+1} = h$, and $x_{i+2} = 2h$; then,

$$\begin{aligned} f(x_i) &= a_0 + a_1x_i + a_2x_i^2 = a_0, \\ f(x_{i+1}) &= a_0 + a_1x_{i+1} + a_2x_{i+1}^2 = a_0 + a_1h + a_2h^2, \\ f(x_{i+2}) &= a_0 + a_1x_{i+2} + a_2x_{i+2}^2 = a_0 + a_1(2h) + a_2(2h)^2. \end{aligned} \quad (22)$$

These three equations with three unknowns can be converted into

$$\begin{aligned} a_0 &= f(x_i) = f(0), \\ a_1 &= \frac{-f(x_{i+2}) + 4f(x_{i+1}) - 3f(x_i)}{2h} \\ &= \frac{-f(2h) + 4f(h) - 3f(0)}{2h}, \\ a_2 &= \frac{f(x_{i+2}) - 2f(x_{i+1}) + f(x_i)}{2h^2} \\ &= \frac{f(2h) - 2f(h) + f(0)}{2h^2}, \end{aligned} \quad (23)$$

where $a_i, i = 1, 2, 3$, are obtained, and equation (1) is derived:

$$f'(x) = a_1 + 2a_2x. \quad (24)$$

Then, the expression is calculated in A; then, we obtain

$$f'(x) = \frac{-f(x_{i+2}) + 4f(x_{i+1}) - 3f(x_i)}{2h}. \quad (25)$$

Regarding the point x , f is smooth enough; then, the Taylor series expansion of f can be expressed as

$$f(x+h) = f(x) + h \frac{d}{dx} f(x) + \frac{h^2}{2!} \frac{d^2}{dx^2} f(x) + \frac{h^3}{3!} \frac{d^3}{dx^3} f(x) + \dots \quad (26)$$

The function $f(x)$ on the right side of (10) is moved to the left side of (10); then, it is divided by h to get the standard deviation quotient:

$$\frac{f(x+h) - f(x)}{h} = \frac{df(x)}{dx} + \left\{ \frac{h}{2!} \frac{d^2f(x)}{dx^2} + \frac{h^2}{3!} \frac{d^3f(x)}{dx^3} + \dots \right\}. \quad (27)$$

Let $h \rightarrow 0$; the items in braces disappear. Defined by derivative, then

$$f'(x) \approx \frac{f(x+h) - f(x)}{h}. \quad (28)$$

At this time, the difference quotient $(f(x+h) - f(x))/h$ is used to replace $f'(x)$, resulting in an error:

$$\left| f'(x) - \frac{f(x+h) - f(x)}{h} \right| = \left| \frac{h}{2!} \frac{d^2f(x)}{dx^2} + \frac{h^2}{3!} \frac{d^3f(x)}{dx^3} + \dots \right|. \quad (29)$$

A linear operator from equation (29) is extracted:

$$T(f) = \left(\frac{h}{2!} \frac{d^2}{dx^2} + \frac{h^2}{3!} \frac{d^3}{dx^3} + \dots \right) f(x). \quad (30)$$

At the same time, according to different representatives, the error between the corresponding differential operator $Df = df/dx$ and the approximate linear operator $D_h f = (f(x+h) - f(x))/h$ is constructed. The truncation error obtained here represents the error in the linear operator L .

Let L_h be a discrete approximation on the neighborhood of the maximum h defined by the linear differential operator L . If there are constants $C > 0$, $p > 0$, and $h_0 > 0$, then

$$T(\varphi) = |(L - L_h)\varphi| \leq Ch^p, \forall \varphi \in C^m, \forall h < h_0. \quad (31)$$

Then, L_h has a truncation error of $O(h^p)$.

In equation (32), the limit value for any smooth f and sufficiently small h is calculated:

$$\lim_{h \rightarrow 0} T(f) = h \left| \frac{f''}{2} \right|. \quad (32)$$

Formally, because of this, when the variable approaches infinity to zero, the truncation error can be defined by the convergence given by the method given in (31). Formally because of this, truncated error is $T(f)$. When the variable h approaches infinity to zero, the convergence of $O(h)$ can be defined by the method given in (31).

When $h^3 f^{(4)}/6 + \dots$ is much smaller than $hf''/2$, f is calculated to find its approximate value. If the second derivative of function f is much less than the other derivative within the effective range, then

$$0 < |f''(x)| \ll |f^{(n)}(x)|, \quad n > 2. \quad (33)$$

The Taylor series of function B is solved at point A :

$$\begin{aligned} f(x+h) &= f(x) + hf'(x) + \frac{h^2}{2!} f''(x) \\ &+ \frac{h^3}{3!} f'''(x) + \frac{h^4}{4!} f^{(4)}(x) + \dots \end{aligned} \quad (34)$$

The simulation equation for the dynamic model formed by the largest turbid zone in the river inlet is obtained:

$$\begin{aligned} \frac{Dk}{Dt} &= P_k + \frac{\partial}{\partial x_j} \left(\left(v + \frac{v_t}{\sigma_k} \right) \frac{\partial k}{\partial x_j} \right), \\ \frac{D\varepsilon}{Dt} &= \frac{C_{\varepsilon 1} P_k - C_{\varepsilon 2} \varepsilon}{T} + \frac{\partial}{\partial x_j} \left(\left(v + \frac{v_t}{\sigma_\varepsilon} \right) \frac{\partial \varepsilon}{\partial x_j} \right), \\ \frac{Dv^2}{Dt} &= kf - 6v^2 \frac{\varepsilon}{k} + \frac{\partial}{\partial x_j} \left(\left(v + \frac{v_t}{\sigma_k} \right) \frac{\partial v^2}{\partial x_j} \right), \\ L^2 \nabla^2 f - f &= \frac{(C_1 - 1)}{T} + \left[\frac{v^2}{k} - \frac{2}{3} \right] - C_2 \frac{P_k}{k} - \frac{5}{T} \frac{v^2}{k}. \end{aligned} \quad (35)$$

At this time, the data information acquired by the sensing device is substituted into the simulation equation of the power mode to calculate, and the results can be obtained.

In this paper, through numerical simulation and theoretical analysis, the dynamic flow formed by the solid-liquid turbid zone in the estuary is simulated and calculated, and the best operating parameters are obtained through industrial test, and the automatic control of numerical prediction is realized. The specific conclusions are as follows.

The RSM turbulence model and PID algorithm are used to calculate the dynamic model and numerical simulation of

the formation of turbidity maximum zone in the estuary, and the turbulent flow is studied. The results show that only the Reynolds stress model can give the correct tangential, axial, and radial velocity distribution. The RSM model can also give the results close to the actual results in a certain range, but the numerical prediction results for the radial and conical sections of the dynamic model are not reasonable. In order to describe the turbulent internal flow accurately, the Reynolds stress model must be used.

4. Conclusions

Due to the influence of marine civilization, estuarine and coastal areas have become one of the most densely populated areas in the world. More than half of the world's population live in estuaries and coastlines. Due to the influence of human activities and the natural movement of the river itself, a very complex water environment is produced at the estuary. The rich diversity of sediments and the changes of water flow bring great challenges to the management of estuaries. The RSM turbulence model and PID algorithm are used to study the dynamic model and numerical simulation of the formation of the turbidity maximum zone in the estuary. The research work of these two aspects has been completed. Firstly, the multiresolution mesh subdivision model of turbidity maximum zone in digital estuary is established. Secondly, the PID algorithm is used to optimize the RSM turbulence model, and the simulation results are good. Based on the RSM turbulence model and PID algorithm, a multiresolution mesh subdivision model for turbidity maximum area of digital estuary is studied. It has its unique advantages. In order to overcome the shortcomings of static hydraulic control, it is necessary to improve the real-time control. The real-time performance of turbulence simulation control system is related to the accuracy of output and the synchronization of multichannel, which determines the performance of the system to a certain extent. At present, there are still some problems in the synchronization of the model, which leads to the instability of the start-up and stop of the system. In order to solve this problem, on the one hand, we need to improve the real-time performance of the system and, on the other hand, we need to develop new software algorithms to solve this problem.

References

- [1] J. Bang, Z. Fu, and H. Qiao, "Assessment of eutrophication and water quality in the estuarine area of Lake Wuli, Lake Taihu, China," *The Science of the Total Environment*, vol. 650, pp. 1392–1402, 2019.

- [2] Y. Chi, Z. Zhang, J. Gao, Z. Xie, M. Zhao, and E. Wang, "Evaluating landscape ecological sensitivity of an estuarine island based on landscape pattern across temporal and spatial scales," *Ecological Indicators*, vol. 101, pp. 221–237, 2019.
- [3] J. Chen, T. Cui, Z. Qiu, and C. Lin, "A three-band semi-analytical model for deriving total suspended sediment concentration from HJ-1A/CCD data in turbid coastal waters," *ISPRS Journal of Photogrammetry and Remote Sensing*, vol. 93, no. 7, pp. 1–13, 2014.
- [4] B. Chen, J. Liu, J. Qiu, X. Zhang, S. Wang, and J. Liu, "Spatio-temporal distribution and environmental risk of sedimentary heavy metals in the Yangtze River Estuary and its adjacent areas," *Marine Pollution Bulletin*, vol. 116, no. 1–2, pp. 469–478, 2017.
- [5] S. Clayton, S. Dutkiewicz, O. Jahn, C. Hill, P. Heimbach, and M. J. Follows, "Biogeochemical versus ecological consequences of modeled ocean physics," *Biogeosciences*, vol. 14, no. 11, pp. 2877–2889, 2017.
- [6] L. Chen, W. Hu, C. Ye, J. Wang, W. W. Wei, and Y. Deng, "Research progress on ecological models in the field of water eutrophication: CiteSpace analysis based on data from the ISI web of science database," *Ecological Modelling*, vol. 410, Article ID 108779, 2019.
- [7] W. Di, "Water eutrophication evaluation based on semi-supervised classification: a case study in Three Gorges Reservoir," *Ecological Indicators*, vol. 81, pp. 362–372, 2017.
- [8] L. De, M. R. Casas, K. T. Alfredsen, and A. H. McCluskey, "Key hydraulic drivers and patterns of fine sediment accumulation in gravel streambeds: a conceptual framework illustrated with a case study from the Kiewa River, Australia," *Geomorphology*, no. 299, pp. 152–164, 2017.
- [9] T. Dysarz, E. Szalkiewicz, and J. Wicher-Dysarz, "Long-term impact of sediment deposition and erosion on water surface profiles in the Ner river," *Water*, vol. 9, no. 3, p. 168, 2017.
- [10] X. Dou, J. Jiao, X. Dou, and X. Gao, "Numerical model study of panjin port waterway back-silting," in *Proceedings of the International Conference on Asian and Pacific Coasts*, pp. 317–324, Springer, Hanoi, Vietnam, 2019.
- [11] G. Gaillot, P. Hamilton, and K. Strom, "Linking hydraulic properties in supercritical submarine distributary channels to depositional-lobe geometry," *Journal of Sedimentary Research*, vol. 87, no. 9, pp. 935–950, 2017.
- [12] M. Helstab, P. D. Powers, and S. L. Niezgoda, "A process-based approach to restoring depositional river valleys to Stage 0, an anastomosing channel network," *River Research and Applications*, vol. 35, no. 1, pp. 3–13, 2019.
- [13] R. F. Hesse, A. Zorndt, and P. Fröhle, "Modelling dynamics of the estuarine turbidity maximum and local net deposition," *Ocean Dynamics*, vol. 69, no. 4, pp. 489–507, 2019.
- [14] Z. Jiang, Z. Shi, J. Xu, X. Huang, F. Ye, and X. Liang, "Relationship between nutrients and plankton biomass in the turbidity maximum zone of the Pearl River Estuary," *Journal of Environmental Sciences*, vol. 57, pp. 72–84, 2017.
- [15] A. P. Krelling, M. M. Souza, A. T. Williams, and A. Turra, "Transboundary movement of marine litter in an estuarine gradient: evaluating sources and sinks using hydrodynamic modelling and ground truthing estimates," *Marine Pollution Bulletin*, vol. 119, no. 1, pp. 48–63, 2017.
- [16] I. Kulikov, I. Chernykh, and A. Tutukov, "A new hydrodynamic code with explicit vectorization instructions optimizations that is dedicated to the numerical simulation of astrophysical gas flow. I. Numerical method, tests, and model problems," *The Astrophysical Journal - Supplement Series*, vol. 243, no. 1, p. 4, 2019.
- [17] A. Kadiric, A. Hajishafiee, S. Ioannides, and D. Dini, "A coupled finite-volume CFD solver for two-dimensional elasto-hydrodynamic lubrication problems with particular application to rolling element bearings," *Tribology International*, vol. 109, pp. 258–273, 2017.
- [18] C. Moliner, F. Marchelli, N. Spanachi, A. Martinez-Felipe, B. Bosio, and E. Arato, "CFD simulation of a spouted bed: comparison between the discrete element method (DEM) and the two fluid model (TFM)," *Chemical Engineering Journal*, vol. 377, Article ID 120466, 2019.
- [19] T. A. McMahon, A. W. Western, B. L. Finlayson, and I. O'Neill, "A method for characterising longitudinal irregularity in river channels," *Geomorphology*, vol. 21, no. 1, pp. 39–51, 1997.
- [20] A. J. Mehta, A. Sheremet, B. Liu, and B. W. Stone, "Wave-sediment interaction on a muddy inner shelf during Hurricane Claudette. Estuarine," *Coastal and Shelf Science*, vol. 63, no. 1–2, pp. 225–233, 2005.
- [21] V. Miles and Barnhart, "Experimental demonstration of a dissipative multi-resonator metamaterial for broadband elastic wave attenuation," *Journal of Sound and Vibration*, vol. 43, no. 8, pp. 1–12, 2018.
- [22] B. Mondon, D. A. Sear, A. L. Collins, P. J. Shaw, and T. Sykes, "The scope for a system-based approach to determine fine sediment targets for chalk streams," *Catena*, vol. 206, no. 206, Article ID 105541, 2021.
- [23] M. McKenzie, J. England, I. D. L. Foster, and M. A. Wilkes, "Abiotic predictors of fine sediment accumulation in lowland rivers," *International Journal of Sediment Research*, 2021, In press.
- [24] D. J. Mehta and S. M. Yadav, "Hydrodynamic simulation of river ambica for riverbed assessment: a case study of navsari region," *Advances in Water Resources Engineering and Management*, Springer, New York, NY, USA, 2020.
- [25] C. Rocha, C. E. Robinson, I. R. Santos, H. Waska, H. A. Michael, and H. J. Bokuniewicz, "A place for subterranean estuaries in the coastal zone," *Estuarine, Coastal and Shelf Science*, vol. 250, Article ID 107167, 2021.
- [26] Z. Sun, S. A. Hashmi, H. Dai, and G. Li, "Safety of a high-speed train passing by a windbreak breach under different wind speeds," *Proceedings of the Institution of Mechanical Engineers-Part F: Journal of Rail and Rapid Transit*, 2021.
- [27] A. Scagliarini, J. L. A. Hegele, M. Sbragaglia et al., "High-Reynolds-number turbulent cavity flow using the lattice Boltzmann method," *Physical Review*, vol. 98, no. 4, Article ID 043302, 2018.
- [28] I. Shevchuck, F. Ries, P. Obando, J. Janicka, and A. Sadiki, "Numerical analysis of turbulent flow dynamics and heat transport in a round jet at supercritical conditions," *International Journal of Heat and Fluid Flow*, vol. 66, pp. 172–184, 2017.
- [29] Y. Zhang, Y. Liu, Z. Chen, and L. Zhou, "Hydrodynamic modeling of swirling binary mixture gas-particle flows using a second-order-moment turbulence model," *ACS Omega*, vol. 5, no. 49, pp. 31490–31501, 2020.
- [30] L. Zhou, Y. Liu, and Y. Zhang, "Numerical simulation of bubble-liquid two-phase turbulent flows in shallow bioreactor," *Energies*, vol. 12, no. 12, pp. 22–69, 2019.

Analysis of Resilient Modulus Inversion and Evaluation of Different Asphalt Pavement Structures

Flora Das, *Department of Civil Engineering, Aryan Institute of Engineering & Technology, Bhubaneswar, floradas22@yahoo.co.in*

Priyadarshan Mahana, *Department of Mechanical Engineering, Aryan Institute of Engineering & Technology, Bhubaneswar, priyadarshan_mahana@gmail.com*

Deepika Priyadarshini Palai, *Department of Civil Engineering, NM Institute of Engineering & Technology, Bhubaneswar, deepikadalai2561@gmail.com*

Saruk Mallick, *Department of Civil Engineering, Raajdhani Engineering College, Bhubaneswar, sarukmallik57@yahoo.co.in*

Satyaprakash Mishra, *Department of Civil Engineering, Capital Engineering College, Bhubaneswar, satyaprakash_m25@gmail.com*

ABSTRACT

Based on the modulus inversion theory and the equivalent principle of deflection basin, the obtained equivalent resilient moduli of different structural layers in three different structures (a semi rigid type Asphalt pavement and two inverted asphalt pavements) were compared by analyzing the deflection basin data of each structure layer measured by the FWD. Simultaneously, the inversion approach was employed to change the current theory formula using the computed equivalent resilience modulus of the top surface of the structural layer. The results show that the calculated equivalent resilient modulus of the top surface of the cushion layer has a small error using both the inversion method and the theoretical calculation method, but the theoretical calculation method overestimates the equivalent resilient modulus of the top surface of the cement stabilized crushed stone layer and the top surface of the graded crushed stone transition layer, especially for the inverted asphalt pavement. The comparable result of the inversion method, on the other hand, is closer to the value in real engineering. The influence of the thickness of the cement stabilized crushed stone layer on the equivalent resilient modulus of the cushion layer must be considered when determining the equivalent resilient modulus of the cushion layer, and the inverted asphalt pavement structure should adopt a thicker asphalt layer to reduce modulus deviation; at the same time, the more structural layers and the larger the difference in the interlayer modulus ratio, the larger the deviation of the equivalent resilient modulus of the top surface. The inversion method may be used to calculate the equivalent resilience modulus of each structural layer of an inverted and semi rigid asphalt pavement, and the results can be used to build an asphalt pavement structure reconstruction.

1. Introduction

During the road reconstruction design of pavement, it is necessary to know the equivalent resilient modulus of the existing pavement or the top surface of the foundation. In fact, the equivalent resilient modulus is characterized by the ability to resist the load of a multilayer system composed of soil foundation, graded crushed stone, and cement stabilized crushed stone; these materials have different modulus and thicknesses. Therefore, it is necessary to transform the multilayer structure system into a 2-layer or 3-layer equivalent semi-infinite homogeneous space system according to the equivalent physical principle of deflection value and flexural stress [1–3]. At present, most studies

mainly focus on solving the equivalent resilient modulus of the foundation or the cement concrete. The conversion formula of the equivalent resilient modulus of the foundation was modified according to the equivalent principle of deflection and introduced the correction coefficient of the influence of the load action radius; this formula is suitable for conversion of equivalent resilient modulus of the top surface of the base layer [4–6]. A method to calculate the equivalent resilient modulus of the top surface of the cement concrete pavement base layer was proposed based on different equivalence principles such as deflection, flexural stress, and temperature [7–11]. Besides, the influence of the contact situation between layers on the calculation results was also considered, but the calculation result based on the

bending-tension stress and temperature was poor; particularly, it is difficult to effectively monitor bending-tension stress, and the equivalent principle based on the deflection value has a wide range of applications. Jiang and Yao [12] and Tan et al. [13] proposed the approximate conversion formula of the multilayer structure under different load forms (single circle, double circle wheel load) and regressed the calculation formula of the equivalent modulus of the top surface of the double-layer structure under different inter-layer contact conditions (smooth, continuous). Vakili [14] established an equivalent modulus calculation model for simple pavement structure layer (the pavement structure layer on the subgrade is regarded as a two-layer elastic layered system) and verified the accuracy of the model using the inversion method (the ratio of pavement equivalent modulus to subgrade modulus).

In the structure design of cement concrete pavement, the equivalent resilient modulus of the top surface of the structural layer needs to be solved; the existing research mainly focuses on the equivalent resilient modulus of the top surface of the cement concrete pavement or soil foundation [15–20], but the asphalt material pavement has obvious viscoelastic properties; the influence of temperature must be considered in calculation or correction; besides, due to the high complexity of structural and material properties, there are relatively few studies on the equivalent resilient modulus of asphalt pavement. Based on the design method of the overlay layer, Guo et al. [21] calculated the minimum equivalent resilience modulus of the top surface of the crushed layer under different structural combinations and did not study the calculation method of the equivalent resilience modulus. According to the theory of section bending stiffness, Tan and Yu [22] studied the equivalent resilient modulus of asphalt surface layer and considered the contact conditions between different layers. In addition, by comparing the inverse calculated modulus of the indoor dynamic triaxial test, rotary compaction molding, and the test road structure, Xu et al. [23] studied the correction coefficient of the modulus inversion value. Cao et al. [24] research showed that the structure of the inverse asphalt pavement was more complex, and the traditional modulus inversion error was larger than the inversion value of the semirigid asphalt pavement; besides, the layer-by-layer inversion method can improve the accuracy of the modulus inversion. Considering the current equivalent resilience modulus research is mainly based on the theoretical calculation and analysis of semirigid asphalt pavement, without too much field verification, in this paper, by testing the dynamic deflection of three pavement structures by layer, the equivalent resilient modulus of the top surface of the cushion layer, the top surface of the base layer, and the top surface of the transition layer was determined using the inversion method, which was also used to correct theoretical calculation formula, providing the basis for the road overlay design of the semirigid asphalt pavement and inverted asphalt pavement.

2. The Test Pavement Structure and Equivalent Resilient Modulus Inversion Method

2.1. The Test Pavement Structure. The test section of Sui-Guang Expressway adopted two kinds of structural forms, the semirigid asphalt pavement (S1) and inverted asphalt pavement (S2 and S3), as shown in Table 1. The traffic grade of Sui-Guang Expressway is heavy traffic grade.

2.2. Theoretical Calculation Method for Determining Equivalent Resilient Modulus. While using the theoretical calculation method to calculate the equivalent resilient modulus, firstly, the structural layer is converted into an equivalent single-layer structure (Figure 1); then, the equivalent resilient modulus of the top surface of the cement stabilized crushed stone layer is calculated as follows [1]:

$$E_t = ah_x^b E_0 \left(\frac{E_x}{E_0} \right)^{1/3},$$

$$a = 6.22 \left[1 - 1.51 \left(\frac{E_x}{E_0} \right)^{-0.45} \right],$$

$$b = 1 - 1.44 \left(\frac{E_x}{E_0} \right)^{-0.55},$$

where E_t represents the equivalent resilient modulus of the top surface of the cement stabilized crushed stone layer (MPa), E_x represents the modulus of cement stabilized crushed stone layer (MPa), H_x represents the thickness of cement stabilized crushed stone layer (m), E_0 represents the resilient modulus of the top surface of the graded crushed stone cushion layer (MPa), and a and b are regression coefficients relating to E_x/E_0 .

In addition, the equivalent modulus of the top surface of the graded crushed stone cushion layer is calculated using formulas (2) and (3) in the “Standard for Design of Highway Cement Concrete JTG D40-2011.”

$$E_{2t} = \left(\frac{E_3}{E_4} \right)^\alpha E_4,$$

$$\alpha = 0.86 + 0.26 \ln h_3,$$

where E_{2t} represents the equivalent modulus of the top surface of the graded crushed stone cushion layer (MPa), E_3 and h_3 represent the modulus (MPa) and thickness (m) of the graded crushed stone cushion layer, respectively, E_4 represents the modulus of the soil foundation (MPa), and a is the regression coefficient. Besides, while calculating the equivalent modulus of the top surface of the graded gravel transition layer using (2) and (3), the lower structure is used as the base.

TABLE 1: The structure of the test section.

Pavement structure	S1 (semirigid structure)	S2 (inverted structure 1)	S3 (inverted structure 2)
The asphalt mastic macadam SMA upper surface layer (cm)		4	
The SBS modified asphalt AC-20C middle surface layer (cm)		6	
The lower surface layer	The type Asphalt AC-20C	The SBS modified asphalt AC-20C	ATB-25
The thickness (cm)	8	8	12
The graded crushed stone transition layer (cm)	—	12	
The cement stabilized crushed stone base (cm)	28	20	
The cement stabilized crushed stone subbase (cm)	28	24	20
The graded crushed stone cushion layer (cm)	15	15	15
The total pavement thickness (cm)	89	89	89

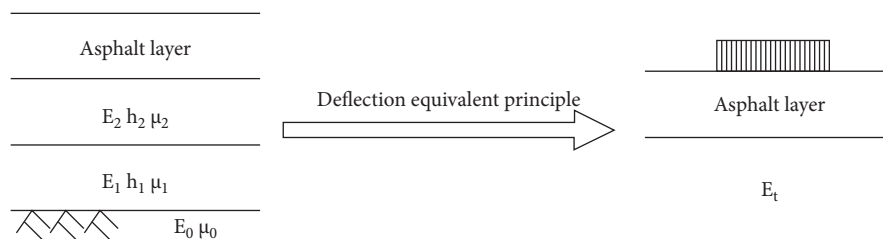


FIGURE 1: Conversion model of equivalent principle of deflection.

2.3. The Method of Determining the Equivalent Resilient Modulus Based on Deflection. During the calculation of the equivalent resilient modulus, the calculated theoretical equivalent modulus through multiple double-layer conversion is greater than the result of one double-layer conversion [8, 25], and it was believed that the deviation of the calculation results of these two conversion methods is mainly due to the difference in load distribution on the top surface of different structural layers, which means the actual load effect is smaller and the load distribution on the top surface of each structural layer is mostly in the shape of bell rather than the uniform distribution. Therefore, in order to prevent the overestimation of equivalent modulus using multiple double-layer conversions and to make it conform to the actual field value, the inversion method was proposed in this paper. Based on the theory of elastic layered system, the inversion method adopts the tested deflection of the top surface of each structural layer by FWD as the basic data and regards the modulus of each structural layer calculated with the aid of the inversion program as the structural layer modulus; moreover, the designated structural layer and lower structural layer are considered as one layer, to determine the equivalent resilient modulus of the top surface of the designated structural layer using the inversion method again. While using the inversion method to determine the equivalent resilient modulus, the variable is only the equivalent resilient modulus, which avoids the tedious process of multiple double-layer conversions, reduces the variable number, and improves inversion accuracy. The existing pavements are often unable to test the top surface

deflection and sink of the top surface of each structural layer, and the modulus can be inverted based on the deflection and sink of road surface.

A more advanced iteration method was adopted, in which based on the assumed structural layer modulus, the theoretical deflection basin is calculated using the mechanical calculation method. By analyzing the difference in deflection basin between the actual measurement and the theoretical calculation, the new assumed combination of structural layer modulus is determined; then, the calculation is repeated until the mean square error between the measured and the theoretical deflection basin reached the minimum value, and the ending condition is set as the iterations number or the preassumed convergence accuracy [26].

3. Deflection Data of Different Pavement Structures

Following the “Field Test Regulations of Highway Subgrade and Pavement” (JTGE60-2008), the PRIMAX1500 FWD (Figure 2) was used to test the dynamic deflection basin of the top surface of the base layer, the graded crushed stone transition layer, the lower layer, the middle layer, and the upper layer. The distance between the sensor and the center of the loading plate is shown in Table 2. The FWD test of the cement stabilized crushed stone base layer is performed 30 days after its construction is completed, and the subsequent test intervals of each layer are within 48h.



FIGURE 2: FWD field testing.

TABLE 2: The distance between the sensor and the center of the loading plate.

The distance between the sensor and the center of the loading plate (cm)											
0	20	30	40	50	60	90	120	150	180	210	

4. Comparison of Calculated Equivalent Modulus of Different Structures

4.1. Calculation and Comparison of Equivalent Resilient Modulus of Top Surface of Cushions with Different Structures. Based on the deflection basin data of the top surface in the FWD test, the inversion method and theoretical calculation method were used to determine the equivalent resilient modulus of the cushion top surface, as shown in Tables 3 and 4. For the three test sections, the roadbed and graded crushed stone cushions layers all adopt the same construction technology, raw materials, and construction team. The tested roadbed is uniformly compacted, and its compaction is greater than 96%, with a maximum of 98.3%, and an average of 97.4%. The compaction of graded crushed stone cushions layer is greater than 97%, with a minimum of 97.9%, a maximum of 108.4%, and an average of 102%. In theory, the equivalent resilience modulus of the top surface of any cushion in the test section should be basically the same. However, the equivalent resilience modulus determined by the inversion method or theoretical calculation method is not the same, structure $S3 < \text{structure } S2 < \text{structure } S1$. At the same time, the thickness values of the cement stabilized crushed stone layer of structure S1, structure S2, and structure S3 are 56 cm, 44 cm, and 40 cm, respectively. It can be inferred that the thickness of the cement stabilized crushed stone layer affects the inversion result of the equivalent resilient modulus. With the theoretical calculation method, the calculated equivalent modulus of the top surface of structure S1 cushion layer is 1.11 times that of structure S2 and 1.28 times that of structure S3; at the same time, with the inversion method, the determined equivalent modulus of the top surface of structure S1 cushion layer determined is 1.16 times that of structure S2

and 1.40 times that of structure S3; it can be seen that when the thickness of the cement stabilized crushed stone layer is thin, for the same decrease of the thickness of the cement stabilized crushed stone layer, the reduction in the equivalent modulus of the cushion top surface is greater than that of thick cement stabilized crushed stone layer. Besides, the decrease of the equivalent modulus of the cushion top surface determined by the inversion method is more than the result of the theoretical calculation method, suggesting it is important to accurately test the thickness of the cement stabilized gravel layer for using the inversion method to determine the equivalent modulus of the top surface of cushion layer.

The difference in the determined equivalent resilient modulus of the cushion top surface between the theoretical calculation method and the inversion method was structure $S3 < \text{structure } S2 < \text{structure } S1$, but the absolute values of the deviation were all within 10%, so it can be concluded that the equivalent resilient moduli determined by these two methods are basically the same, and they can be used to determine the equivalent resilient modulus of the top surface of cushion layer of semirigid asphalt pavement and inverted asphalt pavement.

4.2. Calculation and Comparison of Equivalent Resilient Modulus of the Top Surface of Different Base Structures. Based on the FWD deflection basin data, the equivalent resilient modulus of the top surface of the base layer was determined using the inversion method and theoretical calculation method, as shown in Tables 5 and 6. It can be seen that the equivalent resilient modulus of the top surface of the base layer of structure S1 was greater than that of structures S2 and S3, and the value of structure S3 was the smallest. When FWD is subjected to the top surface of the asphalt layer, the thickness and characteristics of the asphalt layer (such as temperature) will affect the equivalent resilient modulus value of the top surface of the base layer. According to Table 6, for structure S1, based on the deflection basin data of the top surface of the lower layer tested by FWD, the equivalent resilient modulus of the base layer top surface determined by the inversion method was 1.38 and 1.37 times that based on deflection basin data of the top surface of the middle layer and the upper layer; at the same time, its value determined by the theoretical calculation method was 1.64 times and 1.59 times that based on deflection basin data of the top surface of the middle layer and the upper layer.

In addition, compared with the theoretical calculation method, the deviation value of the equivalent resilient modulus of the top surface of the cushion determined by the inversion method (Table 3) is significantly smaller than that of the equivalent resilient modulus of the base layer top surface (Tables 5 and 6). The equivalent resilient modulus of the top surface of the cushion is the equivalent of the modulus of the subgrade and the graded crushed stone cushion layer, their modulus ratio was less than 3, and the thickness of the cushion layer was small. The subgrade is a half-space infinite elastic body, and the equivalent resilience modulus of the top surface of the cushion layer is

TABLE 3: The calculation of equivalent resilient modulus of the top surface of the cushion layer when FWD is loaded on the top surface of the base layer.

Structural layer	Determined method	Base layer	Cushion layer	Roadbed
S1	Inversion modulus value (MPa)	8417	309	206
	Theoretical calculation method (MPa)	—	239	
	Equivalent resilient modulus Inversion method (MPa)	—	243	
	Deviation value (%)	—	-2	
S2	Inversion modulus value (MPa)	6330	309	175
	Theoretical calculation method (MPa)	—	216	
	Equivalent resilient modulus Inversion method (MPa)	—	206	
	Deviation value (%)	—	5	
S3	Inversion modulus value (MPa)	4762	309	139
	Theoretical calculation method (MPa)	—	186	
	Equivalent resilient modulus Inversion method (MPa)	—	174	
	Deviation value (%)	—	7	

TABLE 4: Determination of equivalent resilient modulus of cushion top surface based on road surface deflection.

Structural layer	Determined method	Cushion layer	Roadbed
S1	Inversion modulus value (MPa)	309	141
	Theoretical calculation method (MPa)	188	
	Equivalent resilient modulus Inversion method (MPa)	195	
	Deviation value (%)	-4	
S2	Inversion modulus value (MPa)	309	138
	Theoretical calculation method (MPa)	185	
	Equivalent resilient modulus Inversion method (MPa)	197	
	Deviation value (%)	-6	
S3	Inversion modulus value (MPa)	309	152
	Theoretical calculation method (MPa)	197	
	Equivalent resilient modulus Inversion method (MPa)	181	
	Deviation value (%)	9	

mainly determined by the subgrade modulus; while determining the equivalent resilience modulus of the top surface of the base layer, the thickness of the cement stabilized crushed stone layer is large, its modulus is more than 10 times that of the subgrade or graded crushed stone, and the load is mainly borne by the roadbed and the cement stabilized crushed stone layer. Therefore, the determined equivalent resilient modulus of the top surface of the base layer is far greater than the subgrade modulus and smaller than the modulus of the cement stabilized crushed stone layer, and thicker cement-stabilized crushed stone layer or larger subgrade modulus can improve the equivalent resilience modulus of the top surface of the base layer. At the same time, while calculating the equivalent resilient modulus of the top surface of the base layer with the theoretical calculation method, the three-layer system of cement-stabilized crushed stone layer, cushion layer, and subgrade is transformed into a one-layer system, and more conversion times will increase the deviation of the calculated equivalent resilient modulus of the top surface of the base layer. Besides, the more the structural layers in the inversion or calculation of the equivalent resilient modulus, the greater the modulus ratio of the interlayer, and the greater the deviation of the equivalent modulus of elasticity determined by the inversion method compared with the theoretical calculation method.

4.3. Comparison and Calculation of Equivalent Resilient Modulus of the Top Surface of Transition Layer with Different Structure. Based on the FWD test deflection basin data of asphalt upper layer, middle surface layer, and lower layer of structure S2 and structure S3, the inversion method and theoretical calculation method were used to determine the equivalent resilient modulus of the top surface of the graded gravel transition layer, as shown in Table 7. It can be seen that the equivalent resilient modulus obtained by the theoretical calculation method was about 1.7~2.4 times that of the inversion method. Based on the FWD test deflection basin data of the lower layer of the asphalt, compared to the result of the theoretical calculation method, the deviation of equivalent resilient modulus of structure S2 determined by the inversion method was greater than that of structure S3, and this deviation value decreased with the increase of the number of asphalt surface layers; besides, a thick asphalt layer can reduce this deviation. Therefore, while determining the equivalent resilient modulus of the top surface of the transition layer, it is better to use FWD to test the deflection basin data of the asphalt upper layer. This is because the increase of the thickness of the asphalt layer increases the weight of the superstructure so as to improve the confining pressure of the loaded part of the graded crushed stone, making the modulus of the graded crushed stone layer become higher and the internal force of the graded crushed

TABLE 5: The calculation of the equivalent resilient modulus of the top surface of the base layer when FWD is loaded on the top surface of the transition layer.

Structural layer	S2				S3			
	Inversion modulus value (MPa)	Equivalent resilient modulus			Inversion modulus value (MPa)	Equivalent resilient modulus		
		Theoretical calculation method (MPa)	Inversion method (MPa)	Deviation value (%)		Theoretical calculation method (MPa)	Inversion method (MPa)	Deviation value (%)
Transition layer	243	—	—	—	243	—	—	—
Base layer	6330				4762			
Cushion layer and roadbed	134	1121	762	47	101	780	360	117

TABLE 6: Calculation of equivalent resilient modulus of the top surface of structure S1.

Load layer	Determined method			Base layer	Cushion layer and roadbed
Lower layer	Equivalent resilient modulus	Inversion modulus value (MPa)		8417	489
		Theoretical calculation method (MPa)			3039
		Inversion method (MPa)			1845
		Deviation value (%)			65
Middle layer	Equivalent resilient modulus	Inversion modulus value (MPa)		8417	185
		Theoretical calculation method (MPa)			1858
		Inversion method (MPa)			1336
		Deviation value (%)			39
Upper layer	Equivalent resilient modulus	Inversion modulus value (MPa)		8417	195
		Theoretical calculation method (MPa)			1913
		Inversion method (MPa)			1344
		Deviation value (%)			42

TABLE 7: Calculation of the equivalent resilient modulus of the top surface of the graded gravel transition layer.

Structural layer	S2				S3			
	Inversion modulus value (MPa)	Equivalent resilient modulus			Inversion modulus value (MPa)	Equivalent resilient modulus		
		Theoretical calculation method (MPa)	Inversion method (MPa)	Deviation value (%)		Theoretical calculation method (MPa)	Inversion method (MPa)	Deviation value (%)
FWD loading on the top surface of the lower layer								
Transition layer	243				243			
Base layer	6330	837	351	138	4762	546	270	102
Cushion layer and roadbed	212				102			
FWD loading on the top surface of the middle layer								
Transition layer	243				243			
Base layer	6330	684	356	92	4762	578	278	108
Cushion layer and roadbed	127				117			
FWD loading on the top surface of the upper layer								
Transition layer	243				243			
Base layer	6330	813	467	74	4762	685	358	91
Cushion layer and roadbed	197				181			

TABLE 8: Determination of the equivalent resilient modulus of the top surface of the structural layer.

Structure	Structural layer	Equivalent resilient modulus (MPa)		
		Theoretical calculation method	Corrected theoretical calculation method	Inversion method
Semirigid structure	Base layer	835	585	535
	Base layer	483	217	211
Inverted structure	Transition layer	532	239	233

stone layer more uniform; furtherly, the effect of the error on the equivalent resilient modulus is reduced, and the accuracy of the inversion of the equivalent resilient modulus of the top surface of the transition layer is improved.

5. Modification of the Theoretical Calculation Formula of Equivalent Resilient Modulus

According to the analysis above, it can be known that the determination of the equivalent resilient modulus of the top surface of the cushion layer is less affected by the pavement structure, and the existing calculation method has high accuracy. Formulas (2) and (3) are recommended. For the equivalent resilient modulus of the top surface of the base layer, when $E_d/E_s \approx 47$, the deviation of the resilient modulus of structure S3 determined by theoretical calculation method and the inversion method is up to 117%, while the deviation of structure S2 is 47%, so except the modulus ratio, factors such as the type of pavement structure and the FWD loading layer position should also be considered while deriving the calculation formula of the equivalent modulus of the base layer. Due to the different structure types and the different FWD loading position, the equivalent resilient modulus of the top surface of each structural layer determined by the calculation method and the inversion method is different. Therefore, by regressively and comparatively analyzing the equivalent resilient modulus of the top surface of each structural layer determined by the theoretical calculation and inversion, their difference is eliminated by introducing the correction coefficient k_1 to formula (1), which is 0.65~0.75 for semirigid asphalt pavement, and 0.35~0.55 for inverted asphalt pavement. The large difference in structural characteristics results in a significant difference in the correction coefficient of equivalent modulus theoretical calculation formula of semirigid asphalt pavement and inverted asphalt pavement. The specific value of k_1 depends on the thickness of the asphalt layer and the FWD loading position; the closer the FWD loading position to the top surface of the base layer, the closer the value to the upper limit. After the correction, the calculation of the equivalent modulus of the top surface of the base is shown in formula (2), in which the regression parameters a and b are calculated as before. Compared to the inversion method, the deviation of the equivalent resilient modulus of the top surface of the base layer determined by the corrected calculation method is within 20%, with a maximum value of 19%.

$$E_t = k_1 a h_x^b E_0 \left(\frac{E_x}{E_0} \right)^{1/3} \quad (4)$$

While using modified formulas (2)–(4) to calculate the equivalent resilient modulus of the top surface of the graded crushed stone transition layer, k_1 was taken as 0.35 to obtain the deviation within 20% compared with the inversion method, and the maximum deviation is 16%; this calculation accuracy meets the requirements of engineering applications.

In order to verify the reliability of the calculation formula for the equivalent resilience modulus of the top surface of the structural layer based on the corrected measured deflection basin data, two kinds of asphalt pavement structures in Sichuan were selected [27], and the determined equivalent resilient modulus of the top surface of the base layer with different methods is shown in Table 8. The correction coefficient k_1 of the semirigid structure was 0.7, and the correction coefficient k_1 of the inverted structure was 0.45. Compared with the inversion method, the deviation of using the corrected theoretical calculation method is within 10%, which is much decreased. It can be seen that using the modified theoretical calculation formula to calculate the equivalent resilient modulus of the top surface of the structure layer is more in line with the actual value.

6. Conclusions

- (1) The equivalent resilient modulus is influenced by factors such as pavement structure characteristics (thickness of adjacent layers, structure type, etc.), material characteristics, and loading layer position. The thin cement stabilized crushed stone layer or asphalt surface layer in the inverted asphalt pavement is not conducive to accurately determining the equivalent resilient modulus value of the structural layer.
- (2) Generally, in terms of the deviation of the equivalent resilient modulus of the top surface of the cushion layer determined by the theoretical calculation method and the inversion method, the semirigid asphalt pavement is smaller than the inverted asphalt pavement, and the deviation using these two methods is less than 10%. However, for the equivalent resilience modulus of the top surface of the base layer and the equivalent resilience modulus of the top surface of the transition layer, this deviation is larger than 40% and 70%, respectively. Therefore, these two methods can be used to determine the equivalent resilience modulus of the top surface of the cushion layer, but the inversion method should be preferred while determining the equivalent resilient modulus under other working conditions.

- (3) With using the corrected calculation formula of the equivalent resilient modulus of the top surface of the cement stabilized crushed stone layer, the calculated equivalent resilient modulus of the top surface of the transition layer is close to that obtained by the inversion method, which means the distortion of equivalent resilient modulus calculated by theoretical calculation method comes from the calculation formula of equivalent modulus of the top surface of cement-stabilized crushed stone layer; based on this, the correction coefficient of structure type is introduced.
- (4) The accuracy of the equivalent resilient modulus determined by the inversion method is higher than that of the theoretical calculation method and more in line with the actual value. While determining the equivalent resilient modulus of the asphalt pavement structure, the inversion method is more suitable; when the test conditions are insufficient, the modulus of the structural layer of similar engineering can be considered to be substituted into the correction formula to calculate the equivalent resilient modulus of the top surface of the structural layer.

References

- [1] Z. H. Wang, L. C. Cai, Q. K. Gu, X. J. Liu, and A. H. Wu, "Modified calculation method of equivalent modulus of elasticity of foundation," *Journal of Air Force Engineering University (Natural Science Edition)*, vol. 10, no. 6, pp. 23–27, 2009.
- [2] X. S. Mao and X. L. Zhi, "Checking method of construction deflection of semi-rigid base," *Journal of Xi'an Highway University (Natural Science Edition)*, vol. 23, no. 2, pp. 37–40, 2003.
- [3] X. Liu, S. Song, Y. Tan et al., "Similar simulation study on the deformation and failure of surrounding rock of a large section chamber group under dynamic loading," *International Journal of Mining Science and Technology*, vol. 31, no. 3, pp. 495–505, 2021.
- [4] Y. J. Jiang, J. L. Dai, and Z. D. Chen, "Calculation method of equivalent modulus of elasticity of foundation under principles of different equivalence," *Journal of Chang'an University (Natural Science Edition)*, vol. 25, no. 3, pp. 1–6, 2005.
- [5] Y. Zhou, D. Zhao, B. Li, H. Wang, and Q. Zhang, "Fatigue damage mechanism and deformation behaviour of granite under ultrahigh-frequency cyclic loading conditions," *Rock Mechanics and Rock Engineering*, vol. 54, no. 9, pp. 4723–4739, 2021.
- [6] X. Liu, D. Fan, Y. Tan et al., "New detecting method on the connecting fractured zone above the coal face and a case study," *Rock Mechanics and Rock Engineering*, vol. 54, no. 8, pp. 4379–4391, 2021.
- [7] H. P. Wang, "Research on the revised coefficient of the recommended value for earth subgrade rebound modulus in the design of rigid pavement," *China Journal of Highway and Transport*, vol. 11, no. 4, pp. 1–20, 1998.
- [8] Z. M. Tan and L. Wang, "Equivalent resilient modulus of subgrade based on principle of flexural-tensile stress equivalence," *Journal of Highway and Transportation Research and Development*, vol. 32, no. 3, pp. 46–50, 2015.
- [9] Y. J. Jiang, C. L. Hou, X. F. Qin, and Z. D. Chen, "Calculation method of composite resilient modulus of foundation under cement concrete pavement," *Journal of Highway and Transportation Research and Development*, vol. 22, no. 5, pp. 38–42, 2005.
- [10] Y. J. Jiang and J. L. Dai, "Calculation method of equivalent modulus of elasticity of foundation under principles of thermal stress equivalence," *Journal of Highway and Transportation Research and Development*, vol. 23, no. 7, pp. 10–13, 2006.
- [11] Y. Sun, G. Li, N. Zhang, Q. Chang, and J. Zhang, "Development of ensemble learning models to evaluate the strength of coal-grout materials," *International Journal of Mining Science and Technology*, vol. 31, no. 2, pp. 153–162, 2021.
- [12] A. F. Jiang and Z. K. Yao, "Calculation of surface equivalent modulus of subgrade in the pavement structure," *Journal of Tongji University: Natural Science Edition*, vol. 29, no. 5, pp. 536–540, 2001.
- [13] Z. M. Tan, Z. K. Yao, and B. Y. Liu, "Approximate calculation of equivalent modulus of end face of layered structures," *Highways*, vol. 48, no. 8, pp. 5–8, 2003.
- [14] J. Vakili, "A simplified method for evaluation of pavement layers moduli using surface deflection data," *Proceedings of the 12th International Conference of International Association for Computer Methods and Advances in Geomechanics (IAC-MAG)*, vol. 16, pp. 4314–4319, 2008.
- [15] Q. K. Gu, R. Y. Zhang, B. Qu, and Y. Li, "Method on the calculation of compressive modulus based on loading test," *Journal of Chang'an University (Natural Science Edition): Natural Science Edition*, vol. 35, no. 1, pp. 56–60, 2015.
- [16] J. M. Wu, R. Y. Du, and X. F. Wang, "Design method of asphalt pavement's overlay based on valid modulus," *Journal of Chang'an University (Natural Science Edition)*, vol. 32, no. 4, pp. 1–6, 2012.
- [17] S. Shao, C. Wu, M. Hao et al., "A novel coating technology for fast sealing of air leakage in underground coal mines," *International Journal of Mining Science and Technology*, vol. 31, no. 2, pp. 313–320, 2021.
- [18] Y. Zhang, Y. Xie, Y. Zhang, J. Qiu, and S. Wu, "The adoption of deep neural network (DNN) to the prediction of soil liquefaction based on shear wave velocity," *Bulletin of Engineering Geology and the Environment*, vol. 80, no. 6, pp. 5053–5060, 2021.
- [19] H. Rafezi and F. Hassani, "Drilling signals analysis for tricone bit condition monitoring," *International Journal of Mining Science and Technology*, vol. 31, no. 2, pp. 187–195, 2021.

- [20] X. S. Liu, D. Y. Fan, Y. L. Tan et al., "Failure evolution and instability mechanism of surrounding rock for close-distance parallel chambers with super-large section in deep coal mines," *International Journal of Geomechanics*, vol. 21, no. 5, 2021.
- [21] L. Guo, Y. Zhou, and Z. Tan, "Loading stress of asphalt overlay on rubblized cement concrete pavement and related resilient modulus," *Journal of Highway and Transportation Research and Development*, vol. 5, no. 1, pp. 7–12, 2012.
- [22] Z. M. Tan and X. H. Yu, "Calculation of sectional flexural stiffness equivalent modulus of asphalt pavement," *China Journal of Highway and Transport*, vol. 25, no. 6, pp. 37–42, 2012.
- [23] Y. L. Xu, B. M. Tang, G. D. Xie, and S. Chen, "Back calculated modulus correction coefficient for asphalt concrete layer based on fwd," *Journal of Chang'an University (Natural SciEnce Edition)*, vol. 32, no. 3, pp. 24–29, 2012.
- [24] M. Cao, W. Huang, Y. Zou, and Y. Liu, "Modulus inversion layer by layer of different asphalt pavement structures," *Advances in Civil Engineering*, vol. 2021, pp. 1–10, Article ID 1928383, 2021.
- [25] Z. M. Tan, "Simplified calculation of bi-layer plate bending with semi-continue condition," *Highways*, vol. 4, pp. 25–26, 2001.
- [26] P. Li, "Study of the pavement modulus backanalysis using the database of FWD" Qingdao: Master's degree thesis of Shandong University of Science and Technology, 2007.
- [27] C. Xiao, Y. J. Qiu, J. Zeng, and B. X. Li, "Measured dynamic response of asphalt pavement under fwd load," *Journal of Highway and Transportation Research and Development*, vol. 8, no. 4, pp. 1–9, 2012.

Method for Construction of an Extra-Long Underwater Tunnel in Soft Soils.

Sourav Debasish, *Department of Civil Engineering, Aryan Institute of Engineering & Technology, Bhubaneswar, souravdebasish1@gmail.com*

Sidhanta Behera, *Department of Civil Engineering, Raajdhani Engineering College, Bhubaneswar, sidhantabehera29@outlook.com*

Bijayalaxmi Behera, *Department of Civil Engineering, Capital Engineering College, Bhubaneswar, bijayalaxmi759@gmail.com*

Binoda Bihari Sahoo, *Department of Civil Engineering, NM Institute of Engineering & Technology, Bhubaneswar, bionod_bihari231@yahoo.co.in*

ABSTRACT

Because of its simple construction technology, great operating efficiency, and low cost, the cut-and-cover technique is commonly utilised in tunnel engineering. However, the foundation pit's safety and the influence on the environment during excavation are major concerns, particularly for tunnels that pass through lakes and/or rivers. The Taihu tunnel, China's largest lake-crossing tunnel, is the subject of this research, which details a revolutionary excavation and construction approach. A cofferdam made of double-row steel sheet piles (DSSPs) was used to partition the underlying excavation into numerous closed zones in this procedure. During construction, four zones were treated as a single entity, with distinct construction phases being carried out in each zone at the same time. As a result, a tunnel excavation assembly line was constructed to speed up the construction process. The most notable benefit of this procedure is that the excavation did not cut off the regular flow of water.

1. Introduction

Underwater tunnels are inevitably constructed in the highway projects that cross rivers and/or lakes using the drill-and-blast, shield-bored tunnelling, and immersed tube methods [1–4]. Compared with the above methods, the cut-and-cover technique may be more suitable for tunnel construction in soft soils [5–8] owing to its simple construction technology, high working efficiency, and low cost. However, the deformation behaviours and the environmental impacts caused by excavation are of great concern for both engineering safety and ecological protection.

Retaining structures, such as diaphragm walls, cement mixed piles, jet grouting columns, and bored piles, can effectively control deformation behaviour. Many studies have focused on the performance of diaphragm walls during excavation. However, few researchers have

documented the deflection of bored piles caused by lateral soil movements. Ong et al. [9] examined the large deflections of bored piles as a direct result of lateral soil movements due to slope failure. Cui et al. [10] investigated the behaviour of a large-scale foundation pit supported by bored piles and inclined steel struts. Chong and Ong [11] discussed the field observations of a contiguous bored pile wall system affected by accidental groundwater drawdown. They showed that the accidental groundwater leakage led to small wall deflection. Zhou et al. [12] presented a field study on the compressive bearing capacity of a prebored grouted planted (PGP) pile and a bored pile embedded in deep soft clay. However, for foundation pits supported by various piles (i.e., bored piles, cement mixed piles, and cut-off walls), the relationship between the deflection of bored piles and the excavation depth has seldom been investigated.

Another key factor for controlling tunnel deformations is the excavation and construction method, especially when the soil parameters are determined at the design phase. Zoned and staged construction methods, including the parallel isolation excavation method [13], the perpendicular partitioned excavation method [14], and the divided alternate excavation method [15], are commonly used in cut-and-cover tunnelling. In these methods, by dividing a large pit into several small zones, the excavation can be significantly shortened, and the rigid floor slabs can be cast as early as possible. However, for an extra-long underwater tunnel with a larger excavation depth and a high unload ratio, the tunnel deformation may not be controlled with conventional construction schemes. More importantly, the normal flow of the surface water and the shipping routes are affected by these construction methods, with potentially severe environmental impacts. Therefore, novel excavation and construction methods should be further explored.

Field monitoring data can provide a less accurate but more readily applicable prediction of tunnel deformations induced by deep excavations, and these data are useful for a preliminary estimate of excavation performance. Compared with empirical results, numerical simulation is the most effective tool for evaluating the three-dimensional time-space effect and characterizing the tunnel stiffness [6, 8, 16–18]. Moreover, numerical solutions can predict the actual development of stress-strain in soft soils under complex construction conditions [6, 15]. Therefore, using various methods (i.e., field monitoring and numerical analysis) to investigate deformation behaviours is vital for the construction of practical projects.

The objective of this study is to put forward a novel excavation and construction method, which is employed for the Taihu tunnel, the longest lake-crossing tunnel in China. To this end, the site characterization is introduced. Then the novel excavation and construction method is described in detail. The effects of the new construction method on the tunnel deformation were evaluated using finite element analysis combined with field monitoring data. The results revealed that the proposed method could effectively control the tunnel deformation and enhance the overall stability. This work provides an innovative idea for the design and construction of tunnel engineering, especially for extra-long underwater tunnels in soft soils.

2. Site Characterization

2.1. Project Overview. The Taihu tunnel crossing the Tai Lake, which is the third largest freshwater lake in China [19], is the longest lake-crossing tunnel in China, with a total length of 10.79 km and a width of 43.6 m. The tunnel is an important part of the Su-Xi-Chang South Expressway, which connects the cities of Suzhou, Wuxi, and Changzhou (i.e., the Su-Xi-Chang area) in China. Figure 1 shows the location of the Taihu tunnel. The cut-and-cover technique was adopted in the construction of the tunnel, combined with a cofferdam of double-row steel sheet piles (DSSPs). Three sections, including the west shore section (WSS) (K23 + 900–K24 + 410), the lake section (LS) (K24 + 410–K41 + 561), and the east shore

section (ESS) (K41 + 561–K43 + 560), comprised the tunnel excavation. Moreover, the depth from the water surface to the tunnel roof was in the range of 4–8 m, and the thickness of the overburden soil beneath the lakebed ranged from 2 m to 6 m. The maximum excavation depth was 20.3 m.

2.2. Geological and Hydrogeological Conditions. Figure 2 shows the soil profile along the tunnel alignment, and Figure 3 summarizes the physical and mechanical properties of the main soil layers in the project area. The soil parameters were obtained with typical geotechnical tests (i.e., direct shear test, triaxial test, pumping tests, standard penetration tests, and oedometer tests), following the Chinese standard [20]. The stratigraphic units at the tunnel site are mainly composed of Quaternary Holocene miscellaneous fill and mucky clay layers, Upper Pleistocene clay, and silty clay and silt layers, as well as Devonian strongly weathered sandstone at the ESS. The site investigation identified three major soft soil layers along the tunnel alignment, namely, ①₂, ②₄, and ③₂. The pile foundation was suggested for crossing through these weak layers. In addition, there were no obvious large faults and folds in the project area.

The groundwater in the study area could be divided into pore water in the Quaternary Holocene formation, confined water in the silt layer, and fracture water in the strongly weathered sandstone. The silt layer is the main aquifer in the study area, for which the permeability coefficient is 1–2 orders of magnitude higher than that of the upper and lower layers. Moreover, the hydrochemical type of the surface water in the project area was $\text{Cl}\cdot\text{SO}_4\text{-Na}$, and that of the groundwater was $\text{HCO}_3\cdot\text{SO}_4\text{-Na}\cdot\text{Ca}$.

3. Excavation and Construction Method

The traditional construction methods are not suitable for the Taihu tunnel, because of the unfavourable soil conditions, the stringent environmental requirements of Tai Lake, and the design request of the complex project. Therefore, an innovative excavation and construction method was proposed for the construction of the Taihu tunnel. Figure 4 schematically shows the proposed construction method. The construction steps are described in detail as follows:

Step 1: DSSPs were used to form several closed zones, that is, WSS and Zone #1 (Figure 4(a)). Following the drainage of the lake water and the dredging work, the bored piles, cut-off walls, and cement mixed piles are prepared for the excavation of the closed zones.

Step 2: the levee and transverse DSSPs were removed for maintaining the smooth flow of construction vehicles, the space was excavated to the desired level along with the foundation dewatering, and the retaining structures were constructed to ensure the stability of foundation pits in WSS and Zone #1 (Figure 4(b)). Meanwhile, Zone #2 was formed by referring to Step 1.

Step 3: the tunnel ancillary structures in WSS and Zone #1 were installed and Steps 1 and 2 were implemented

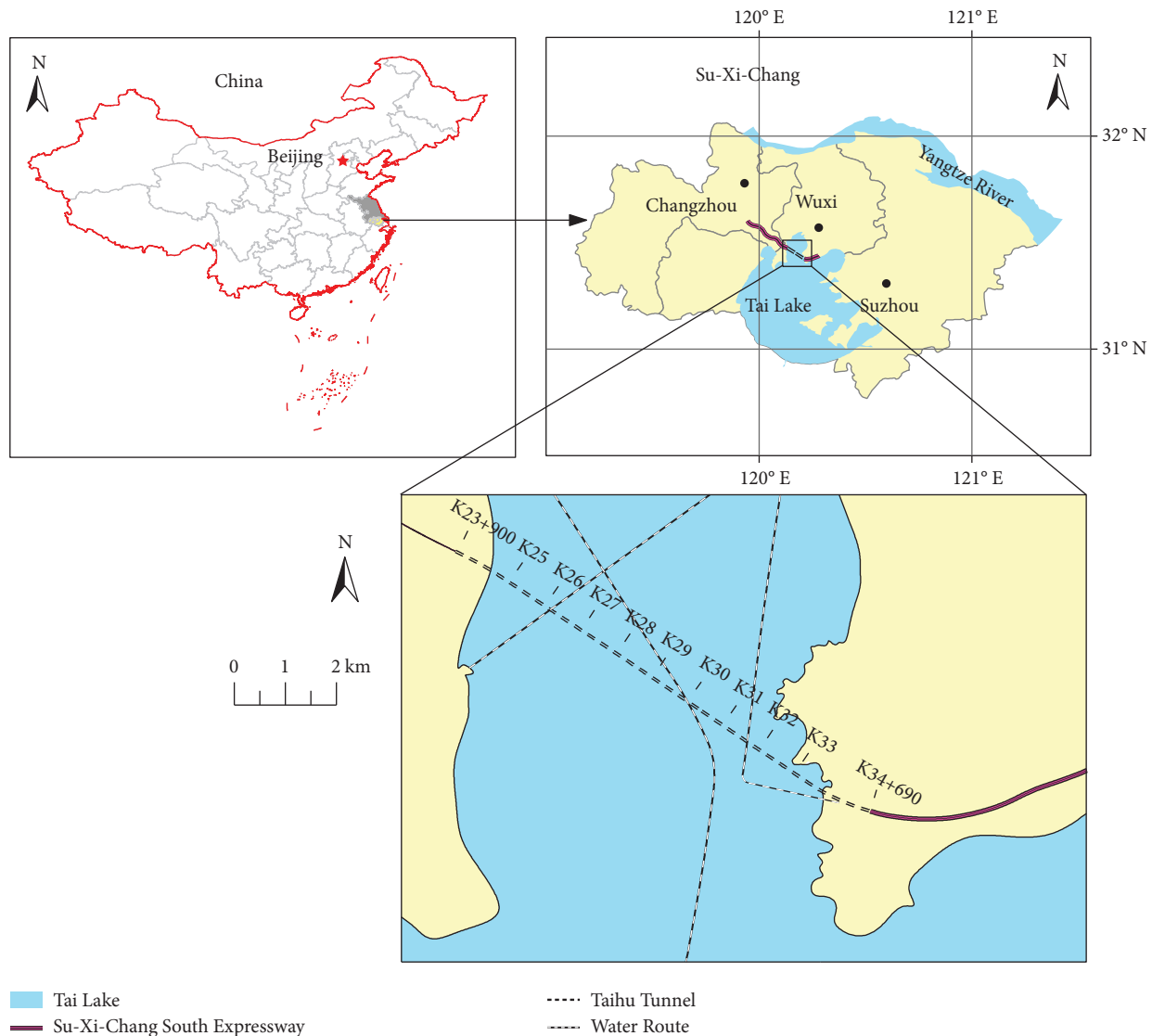


FIGURE 1: Location of the Taihu tunnel.

in Zone #3 and Zone #2, respectively (Figure 4(c)). Similarly, the transverse DSSPs located between Zone #1 and Zone #2 were removed.

Step 4: The gap between the tunnel roof and the ground surface was filled in WSS and Zone #1, the first earth cofferdam between WSS and Zone #1 was constructed along the location of the transverse DSSPs in Step 2, and the truncated levee was backfilled (Figure 4(d)). Simultaneously, Steps 1, 2, and 3 were carried out in Zone #4, Zone #3, and Zone #2, respectively. It should be noted that the earth cofferdam was constructed at the frequency of two zones.

Step 5: the longitudinal DSSPs of the WSS were removed to allow the lake water to flow normally, the soils in Zone #2 were backfilled, the tunnel ancillary structures in Zone #3 were constructed, and the soils in Zone #4 were excavated (Figure 4(e)). In addition, the second earth cofferdam was built between Zone #2 and Zone #3.

In the proposed method, four zones were regarded as a unit, and different construction steps were carried out simultaneously in each zone. Hence, an assembly line for the tunnel excavation was established to accelerate the construction speed. The excavation did not cut off the normal flow of the lake water and the shipping routes because of the installation and removal of the DSSPs. Therefore, the proposed method had the advantages of low environmental impact, usage of recycled materials, and quick construction.

4. Field Monitoring

To monitor the deformation behaviour of the tunnel, a long-term comprehensive field instrumentation program was conducted along the tunnel alignment. Taking Zone #1 as an example, the observed deformation behaviours included vertical and horizontal movements of the DSSPs, vertical movements at the tops of the bored piles, deflections of the bored piles, ground surface settlements, and settlements of the earth cofferdam.

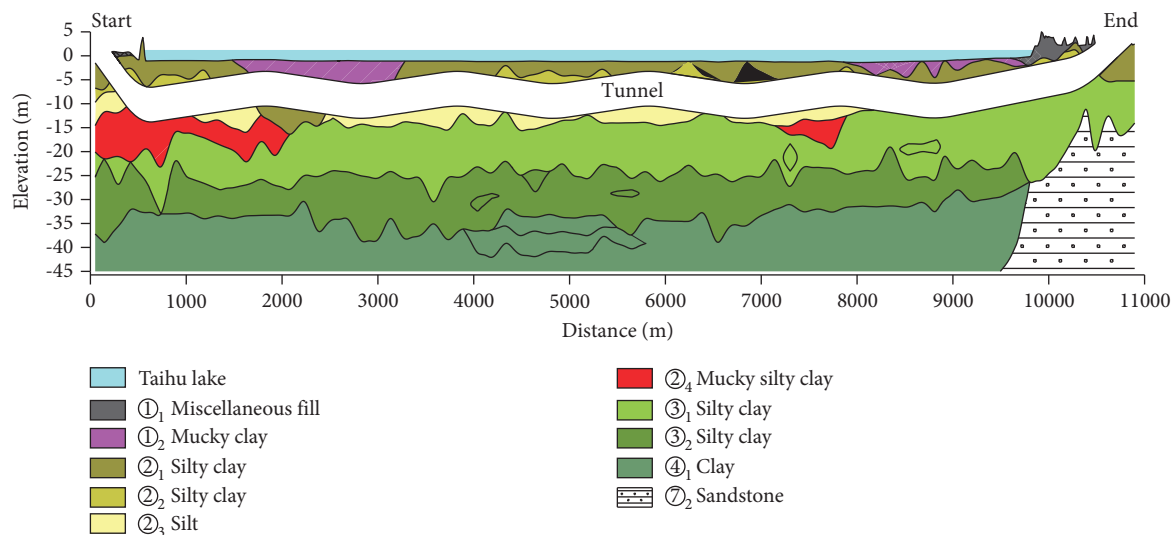


FIGURE 2: Soil profile along the tunnel alignment.

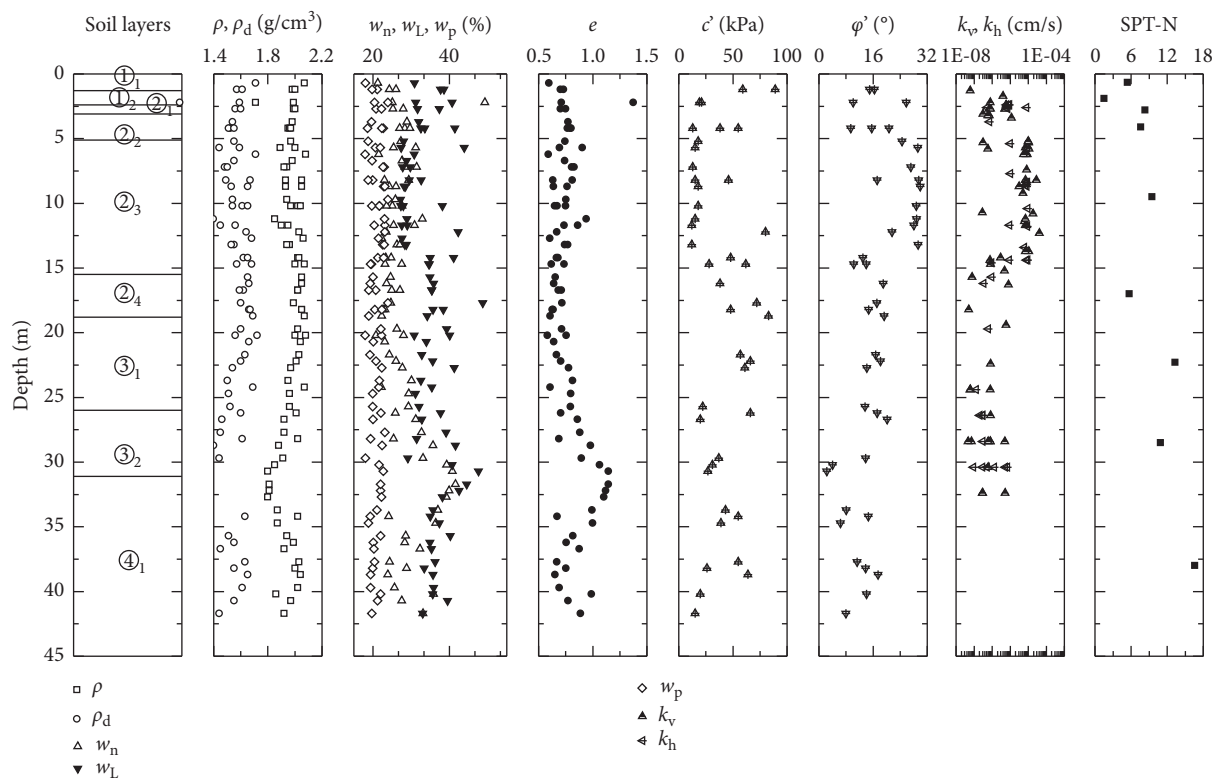


FIGURE 3: Geotechnical parameters of soft soils.

4.1. Retaining Structures. Figure 5 presents a typical cross section on the north side of Zone #1. Clearly, the DSSPs connected by the reinforcement were 15 m long, and the embedded length was 10 m. The space above the ground surface with a 6 m width was filled with cohesive soil whose compaction was at least 90%. The cut-off wall was set at the top of the slope with a length of 16.3 m and a width of 0.85 m. The height of the two-level slope was 7.2 m with a slope ratio

of 1:1.5, while the depth supported by the bored piles was 8.9 m. The reinforcement ratio of the normal section of the bored piles was 0.45%, and the bending moment capacity was 550 kNm. To restrain the lateral deflections of the bored piles, two levels of struts were constructed. The first level strut was made of C30 concrete with a diameter of 0.8 m and a spacing of 1.2 m, whereas $\Phi 609 @ 16$ steel tubes were used for the second level. Moreover, the cement mixed piles were

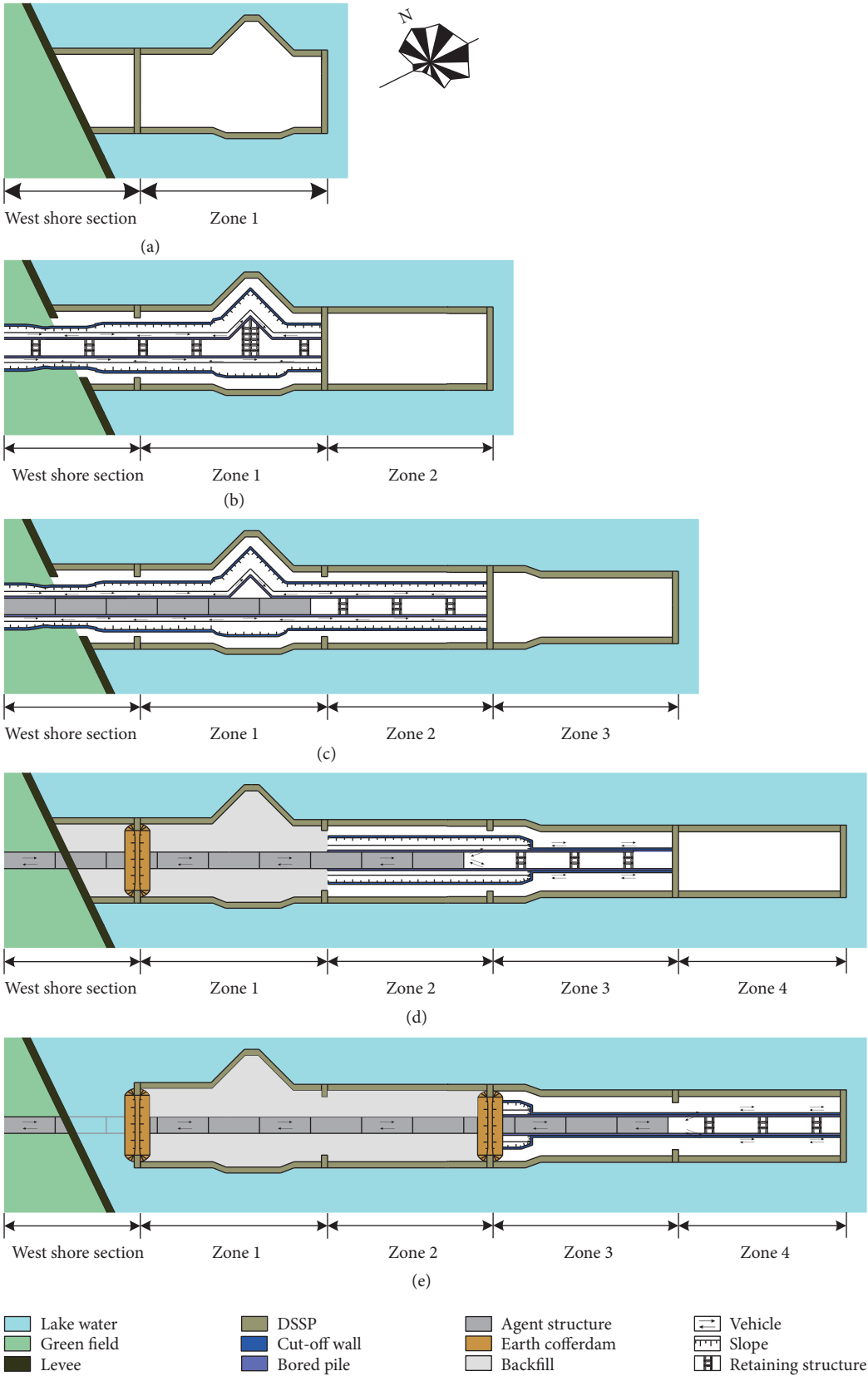


FIGURE 4: Schematic diagram of the novel construction method. (a) Step 1, (b) Step 2, (c) Step 3, (d) Step 4, and (e) Step 5.

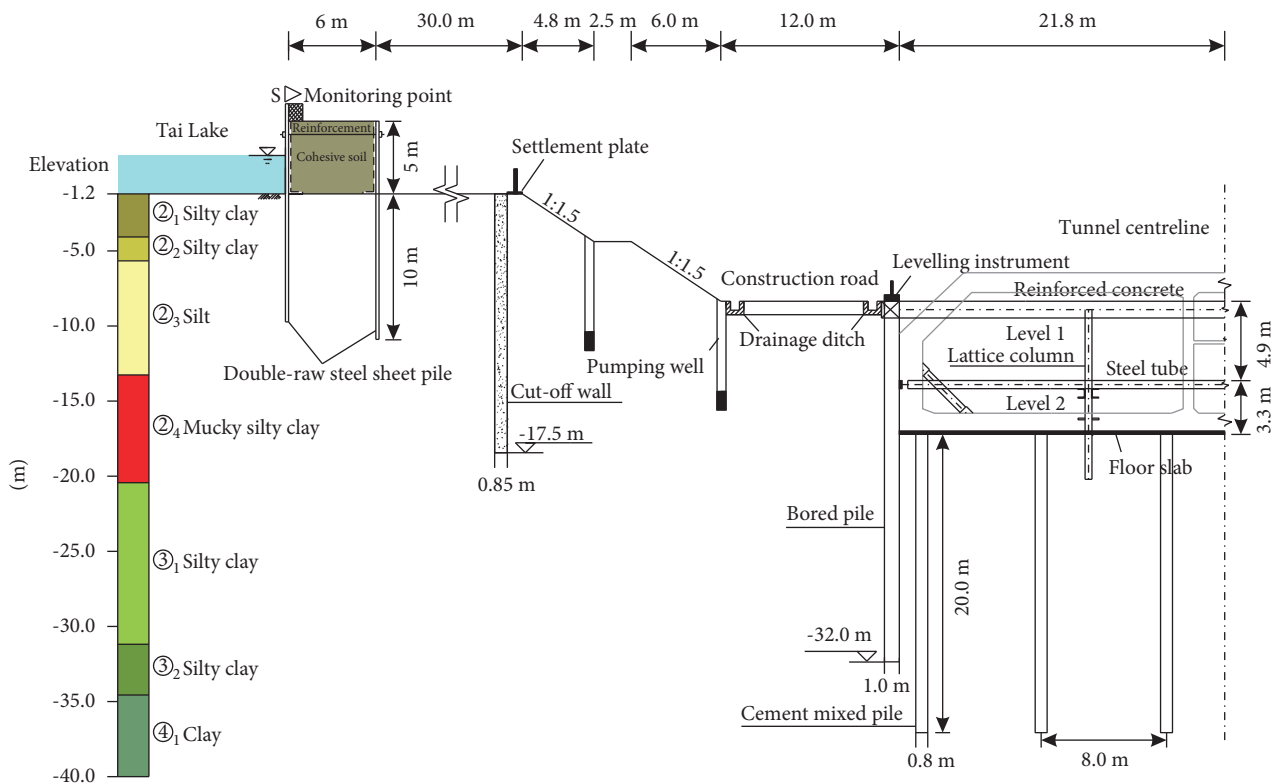


FIGURE 5: Typical cross section on the north side of Zone #1.

arranged to reinforce the subsoil beneath the bottom of the foundation pit, with a pile spacing of 8.0 m, a diameter of 0.8 m, and a length of 20.0 m.

The earth cofferdam, as a secondary transverse cofferdam, was used to prevent the lake water from entering the excavation after the removal of the DSSPs. The height, top width, bottom width, and slope ratio of the earth cofferdam located between WSS and Zone #1 were 5.0 m, 3.0 m, 33.0 m, and 1 : 3, respectively, as shown in Figure 6.

4.2. Construction Stages. Table 1 summarizes the main construction stages of Zone #1. The site work began with the construction of the DSSPs, followed by the drainage of the lake water and the dredging work in the zone. After the construction of the bored piles, cut-off walls, and cement mixed piles, the excavation activities started on September 10, 2018, and ended on April 13, 2019. To reduce the tunnel deformation, two-level struts were installed promptly after the corresponding soil layer was excavated. The tunnel ancillary structures were constructed with the casting of floor slabs and the removal of the struts, and the soil was backfilled from the tunnel roof to the ground surface. Finally, the earth cofferdam was completed on May 13, 2020, and was monitored after the removal of the longitudinal DSSPs of the WSS.

4.3. Instrumentation. Figure 7 displays the instrumentation layout of Zone #1. The movements of the DSSPs were observed by 74 monitoring points, numbered as S1 to S74 with

approximately 15 m intervals. The deflections of bored piles were monitored by 40 inclinometer tubes (designated as B1 to B40 and spaced approximately 20 m apart) that were fixed to the reinforcement cage for each instrumented panel before concreting. The resolution of each inclinometer was 0.1 mm/500 mm gauge length. Moreover, the vertical movements at the tops of bored piles were measured using levelling instruments. To survey the ground settlements, 44 monitoring points, designated as G1 to G44 and at approximately 20 m intervals, were set at the top of the slope in Zone #1. Twelve monitoring points for the settlements of the earth cofferdam are shown in Figure 7. The data reading for the earth cofferdam had to be taken after removing the longitudinal DSSPs of the WSS, and the frequency of data reading was once every three days.

Unfortunately, some inclinometer tubes and settlement points were damaged during the construction. Therefore, the remaining available data are provided in the electronic supplementary files, which can be found online at <https://www.researchgate.net/publication>.

5. Observed Deformation Behaviours

5.1. Vertical Movements of DSSPs. The DSSPs acting as a cofferdam were used to prevent lake water from entering the excavation, which was directly related to the stability and safety of the whole project. Therefore, it was necessary to monitor both the vertical and horizontal movements of the DSSPs during excavation. Figure 8 shows the development of the vertical movements of the longitudinal DSSPs during

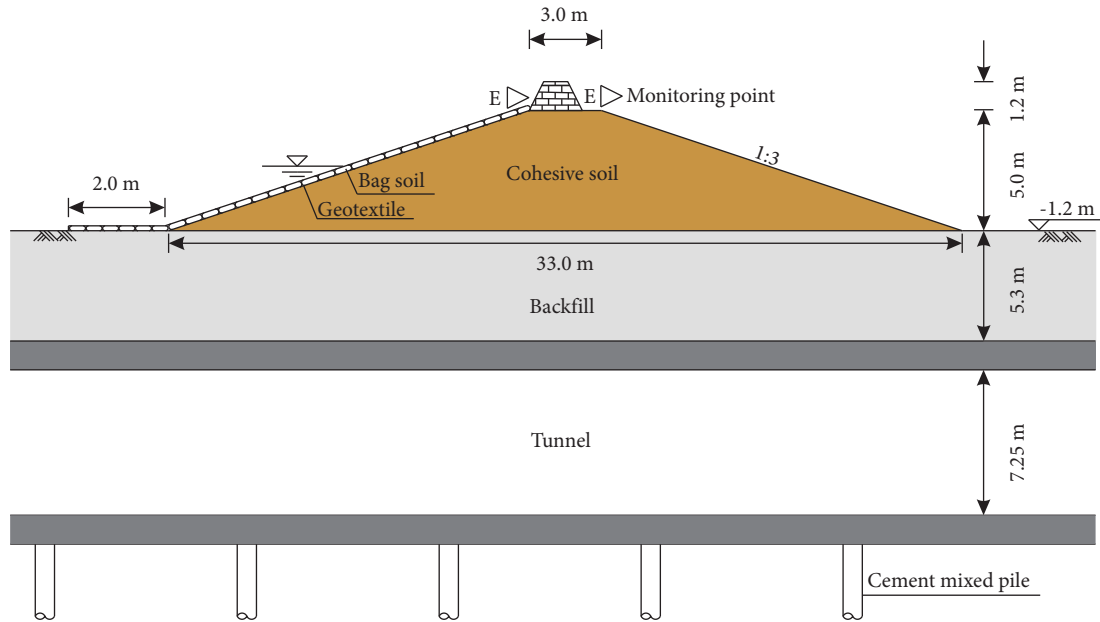


FIGURE 6: Cross section of the earth cofferdam located between WSS and Zone #1 along the tunnel centreline.

TABLE 1: Main construction stages of Zone #1.

Stages	Construction activity	Date (mm/dd/year)
1(a)	Construction of DSSPs	04/01/2018–06/27/2018
1(b)	Discharge of lake water and dredging work	06/28/2018–07/07/2018
1(c)	Construction of bored piles, cut-off walls, and cement mixed piles	07/18/2018–09/08/2018
2(a)	Removal of embankment or transverse DSSPs	09/09/2018
2(b)	Excavation of the first layer of subsoil with thickness of 3.2 m	09/10/2018–10/16/2018
2(c)	Excavation of the second layer of subsoil with thickness of 4 m	10/17/2018–12/19/2018
2(d)	Installation of struts at Level 1	12/20/2018–12/31/2018
2(e)	Excavation of the third layer of subsoil with thickness of 5.3 m	01/01/2019–03/05/2019
2(f)	Installation of struts at Level 2	03/06/2019–03/14/2019
2(g)	Excavation of the fourth layer of subsoil with thickness of 3.6 m	03/15/2019–04/13/2019
3(a)	Casting of floor slabs	04/14/2019–06/19/2019
3(b)	Removal of struts at Level 2	06/20/2019–06/27/2019
3(c)	Construction of side walls of tunnel	06/28/2019–09/09/2019
3(d)	Construction of inclined steel struts	09/09/2019–09/18/2019
3(e)	Removal of struts at Level 1	09/19/2019–09/26/2019
3(f)	Construction of tunnel roof	09/27/2019–05/07/2020
3(g)	Removal of inclined steel struts	05/08/2020–05/21/2020
4(a)	Backfilling of soils	05/22/2020–05/29/2020
4(b)	Construction of earth cofferdam or truncated embankment	06/01/2020–06/09/2020
5	Removal of longitudinal DSSPs	06/20/2020–06/27/2020

excavation. Obviously, the longitudinal DSSPs at both sides of Zone #1 experienced significant settlements during construction. Following the casting of floor slabs and the installation of ancillary structures, the settlements tended to stabilize with time, implying that the floor slabs and the ancillary structures could help stabilize the vertical movements of the DSSPs. The measured maximum movement was approximately 28.05 mm along S12 on the north side of Zone #1, still being controlled within the permitted value (i.e., 30 mm).

Figure 9 shows the development of the vertical movements of the transverse DSSPs located between Zone #1 and

Zone #2 during the excavation. Compared with the vertical movements of the longitudinal DSSPs, those of the transverse DSSPs along S41 to S45 were relatively small, approximately –10 to 15 mm. This suggests that the excavation of the foundation pit strongly affects the longitudinal DSSPs more than the transverse DSSPs.

5.2. Horizontal Movements of DSSPs. Figure 10 presents the variation in the horizontal movements of the longitudinal DSSPs during excavation. Overall, the horizontal movements of the longitudinal DSSPs were positive, indicating

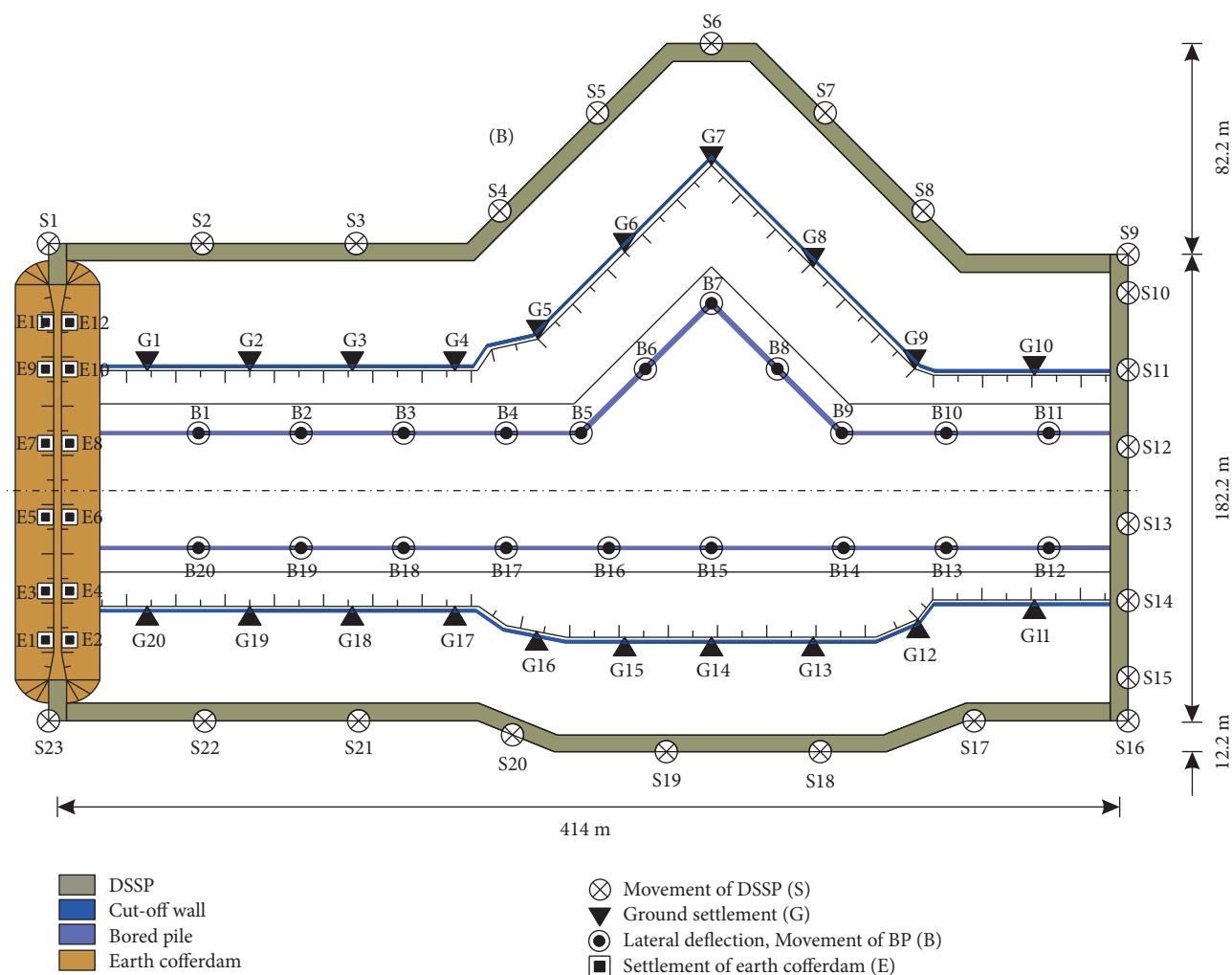


FIGURE 7: Instrumentation layout of Zone #1.

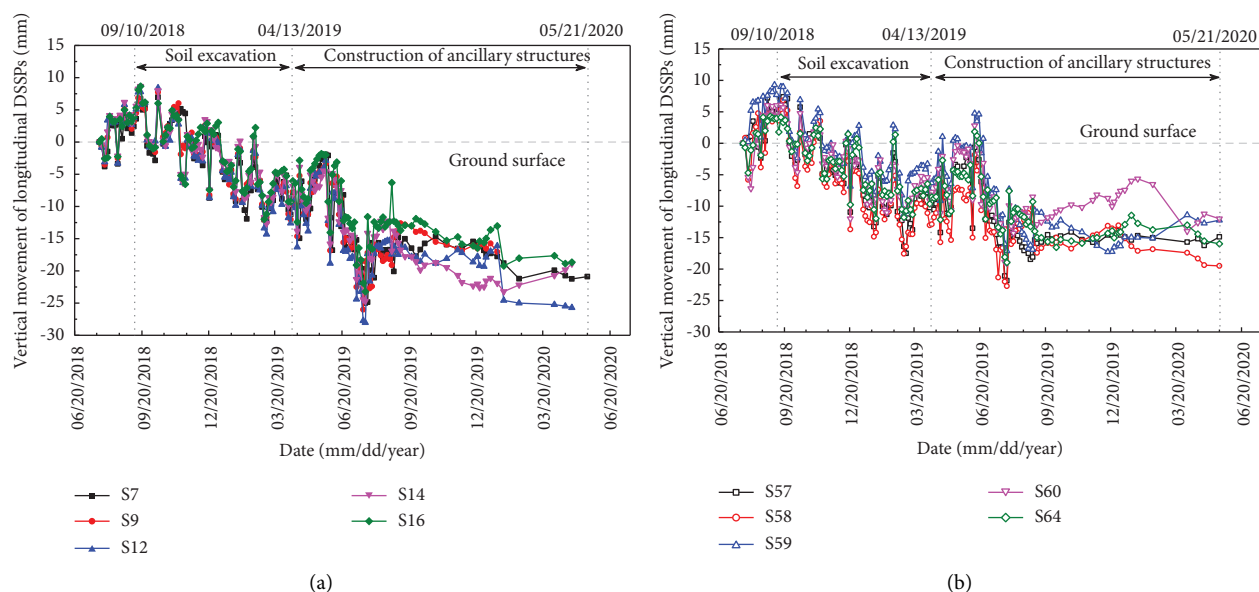


FIGURE 8: Development of the vertical movements of the longitudinal DSSPs during construction. (a) On the north side of Zone #1 and (b) on the south side of Zone #1.

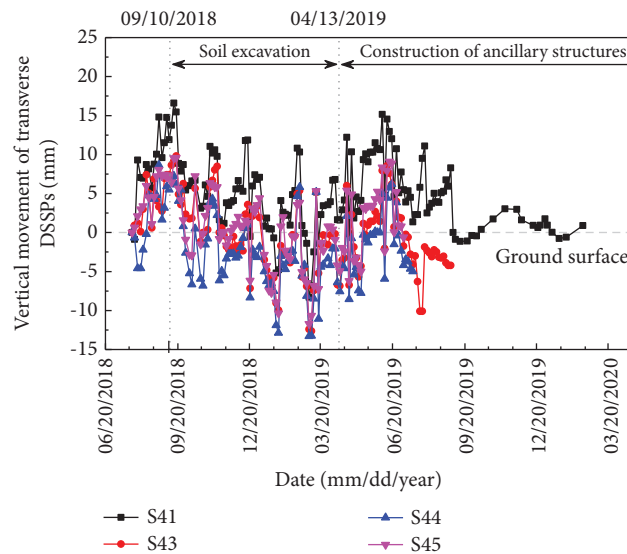


FIGURE 9: Development of the vertical movements of the transverse DSSPs.

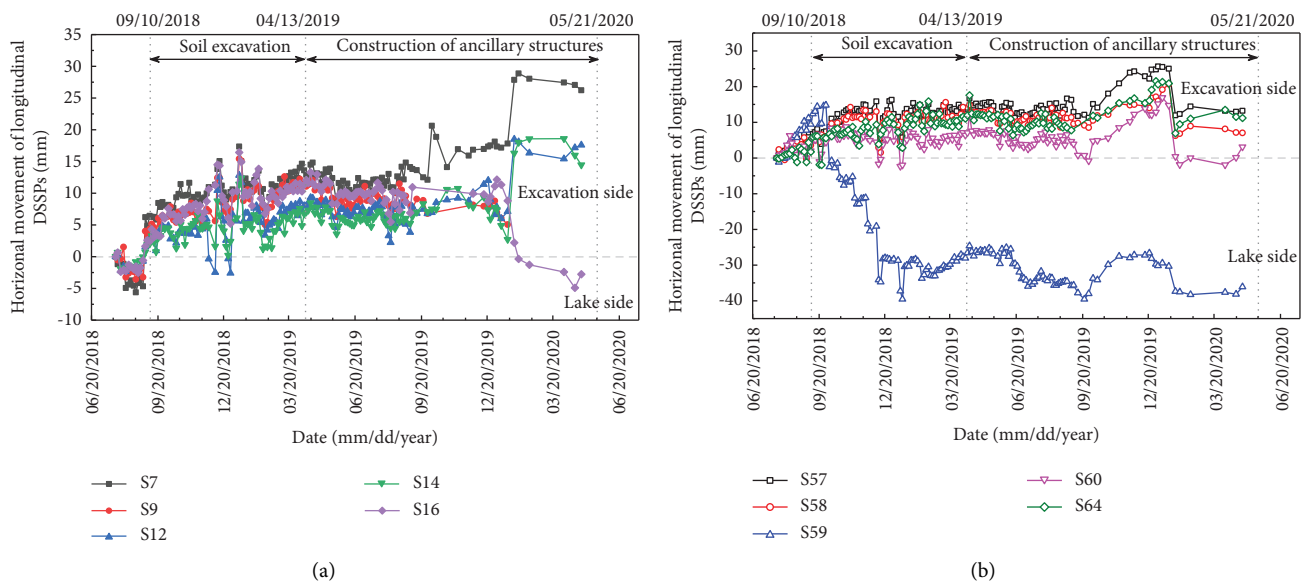


FIGURE 10: Development of the horizontal movements of the longitudinal DSSPs during construction. (a) On the north side of Zone #1 and (b) on the south side of Zone #1.

that the longitudinal DSSPs moved to the excavation side in the horizontal direction. The horizontal movements increased rapidly in Stages 1(b) and 1(c) (Table 1) and then fluctuated widely during the soil excavation, which revealed that the soil excavation had less influence on the horizontal movements than on the vertical movements of the longitudinal DSSPs. Some factors have contributed to these horizontal movements: (1) the hydrostatic pressure of the lake water, (2) the hydrodynamic pressure caused by the wave action, and (3) the force unbalance because of the excavation. However, the data for the monitoring point S59 exceeded the control value (i.e., 30 mm). Thus, the corresponding measures had to be taken to control the deformation.

Figure 11 shows the development of the horizontal movements of the transverse DSSPs during excavation. Obviously, the magnitudes of the horizontal movements of the transverse DSSPs were smaller than those of the longitudinal DSSPs. This likely occurred because the drainage of lake water in Zone #2 reduced the unbalance force on the transverse DSSPs. Some rapid drops occurred around January 20, 2019, indicating that the transverse DSSPs moved to the lake side. The bagged soil arranged behind the DSSPs might have contributed to this phenomenon.

5.3. Deflections of Bored Piles. The lateral deflection of the bored piles could be related to the site excavation and the

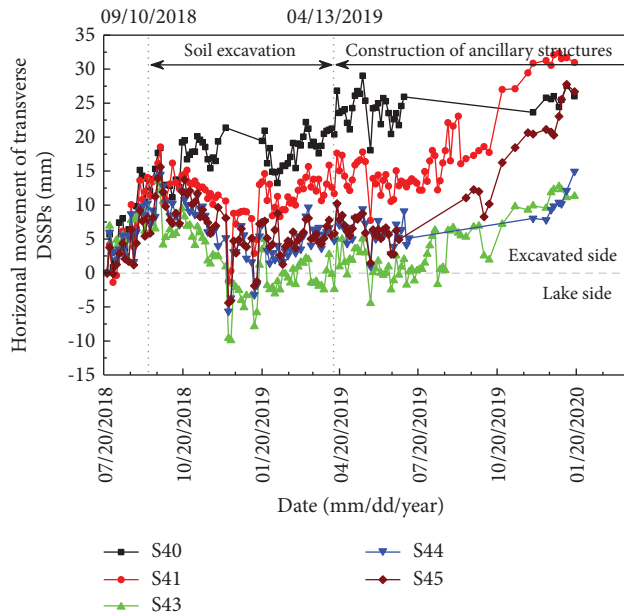


FIGURE 11: Development of the horizontal movements of the transverse DSSPs.

casting of the floor slabs. The development of the lateral deflections of the bored piles at B36 and the maximum deflections at several monitoring points is presented in Figure 12. The bored piles began to develop deep-seated movements toward the excavation side as the excavation proceeded to lower levels in Stages 2(e) and 2(f). The lateral deflection reached its maximum during the subsequent construction of the floor slab at Stage 3(a). The maximum deflection of the bored piles was 8.95 mm at B36 on the south side of Zone #1.

Figure 13 shows the relationship between the measured maximum deflection at each excavation level, δ_{hm} , and the excavation depth, H_e . Obviously, the measured δ_{hm} was distributed between $\delta_{hm} = 0.006\%H_e$ and $\delta_{hm} = 0.06\%H_e$. Some case histories are presented in Figure 13 for the purpose of comparison. These case histories indicate that the upper and lower boundaries of δ_{hm} at this site are significantly smaller than those reported by Clough and O'Rourke [21] for excavations in stiff clay, by Hashash et al. [22] for excavations in medium-stiff Boston clay, and by Tan and Wei [6] for excavations in soft Shanghai clay. Therefore, the deformations of the bored piles were relatively smaller than those reported in the literature. The extensive use of underground structures such as cut-off walls and cement mixed piles, the rapid cast of floor slabs, and the quick construction of bored piles may contribute to this phenomenon. It is noteworthy to mention that the influence of the seepage force on the lateral deflection of bored piles is not considered because of the waterproofing structures.

Figure 14 summarizes the normalized maximum deflection, δ_{hm}/H_e , and the normalized retaining system stiffness, $EI/(\gamma_w h^4)$, at this site, in which $EI/(\gamma_w h^4)$ was defined by Clough et al. [23]. The factor of safety against the basal heave FOS_{base} was calculated based on the method used by Terzaghi [24]. The six case histories reported by Wang

et al. [25] are also included in this figure for comparison. As illustrated, the observed δ_{hm}/H_e from the excavation fell within the ranges proposed by Clough et al. [23], and it appeared to be independent of FOS_{base} .

5.4. Vertical Movements at the Top of Bored Piles.

Figure 15 illustrates the distribution of the vertical movements at the top of bored piles during construction. Beyond expectation, the bored piles experienced significant heaves rather than settlements during the excavation. The excavation of upper soils and the release of stress resulted in the swelling of soils at the bottom of the foundation pit, and then the elastic and plastic rebound of soils happened [6]. Beyond that, the soil movements around the bored piles might have also caused this phenomenon. The measured maximum movement was approximately 21.51 mm along B4 on the north side of the excavation.

5.5. Ground Surface Settlements.

Figure 16 summarizes the development of the ground settlements δ_{vm} at G3, G39, G40, G41, G42, and G43. The ground settlements increased with the excavation of the pit until the casting of floor slab and then tended to be stable. The settlement on the north side of the pit exhibited a similar tendency to that on the south side. The fluctuation in the settlement at the slope top of the pit was observed during the excavation of the subsoil, which may be due to two factors: (1) rainfall and (2) vehicles frequently passing at approximately 13.3 m. Moreover, the measured ground settlement was in the range of 5–15 mm, with the maximum value of 11.25 mm at G42. Therefore, based on the new construction method, the ground settlements of the foundation pit were controlled within the permitted value, i.e., 30 mm.

Figure 17 plots the relationships between the measured maximum ground settlement, δ_{vm} , and each excavation depth, H_e , in which three-case histories from Taipei [21], Boston [22], and Shanghai [6] were introduced for the purpose of comparison. It can be shown that δ_{vm} was bounded by $\delta_{vm} = 0.01\%H_e$ and $\delta_{vm} = 0.1\%H_e$. The developed boundaries of δ_{vm} for Zone #1 were much lower than those of Clough and O'Rourke [21] for excavations in stiff Taipei clay, Tan and Wei [6] in soft Shanghai clay, and Hashash et al. [22] in medium-stiff Boston clay.

To better illustrate the characteristics of the settlement profiles, the ground surface settlement was normalized by its corresponding δ_{vm} , as plotted in Figure 18. Two common profiles and several available data collected by Wang et al. [26] in Shanghai soft clay are also shown for comparison in the same figure. It can be seen that the δ_v/δ_{vm} measured from the excavation ranged from 0.21 to 0.98, which confirmed the effectiveness of the construction scheme and the related measures.

5.6. Settlements of Earth Cofferdam.

After the removal of the longitudinal DSSPs of the WSS, the earth cofferdam was constructed to prevent the lake water from entering the excavation site, on June 10, 2020. Figure 19 shows the

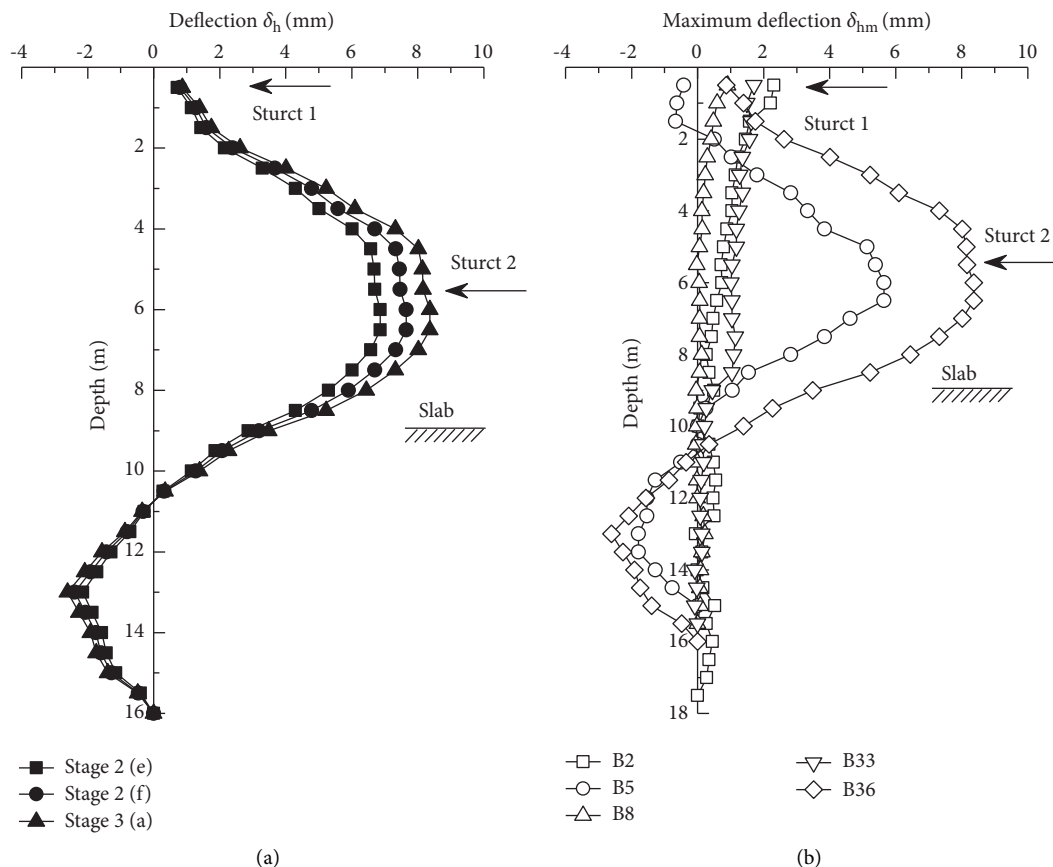


FIGURE 12: Lateral deflection of bored piles along depth. (a) Development of deflections at B36 and (b) maximum deflections at B2, B5, B8, B33, and B36.

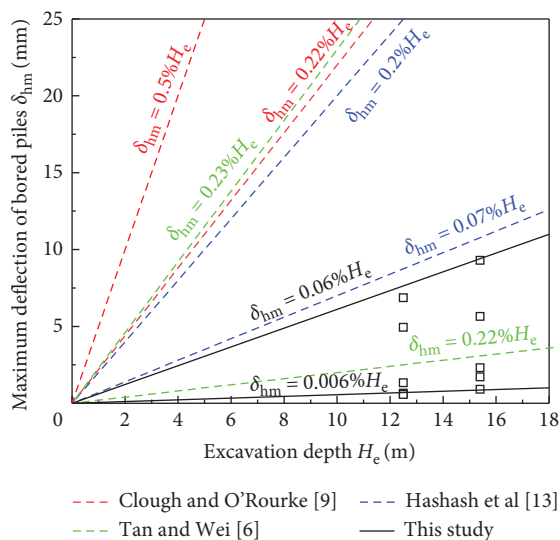


FIGURE 13: Relationship between the maximum deflections of bored piles and the excavation depths.

measured surface settlements of the earth cofferdam. The settlements on the upstream side were found to be in the range of 11–26 mm, while that on the excavation side ranged from 0.5 mm to 14.0 mm.

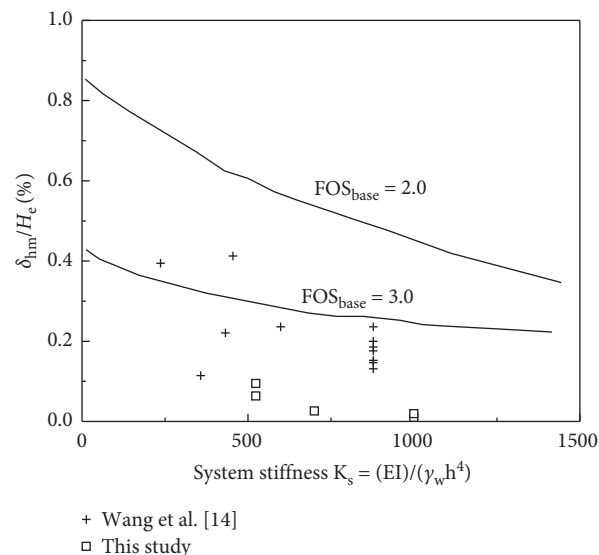


FIGURE 14: Relationship between the normalized maximum deflection and the system stiffness.

6. Numerical Simulation

Based on the field monitoring data in this study, it is found that the magnitudes of the vertical movements of the DSSPs

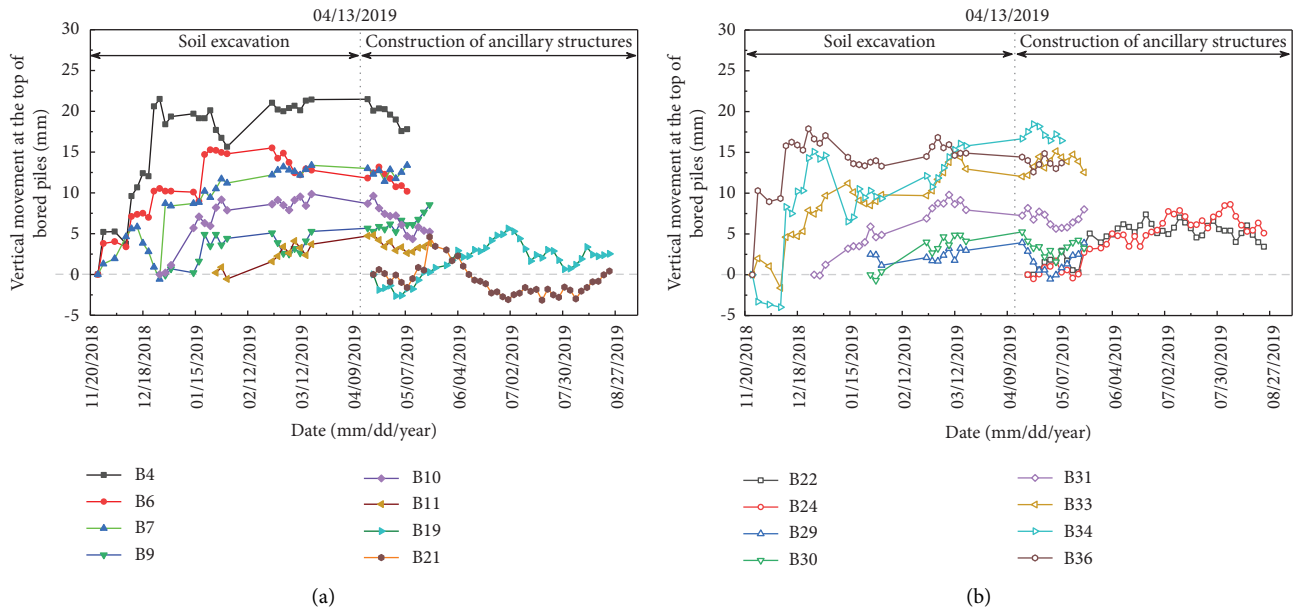


FIGURE 15: Distribution of the vertical movements at the top of bored piles. (a) On the north side of Zone #1 and (b) on the south side of Zone #1.

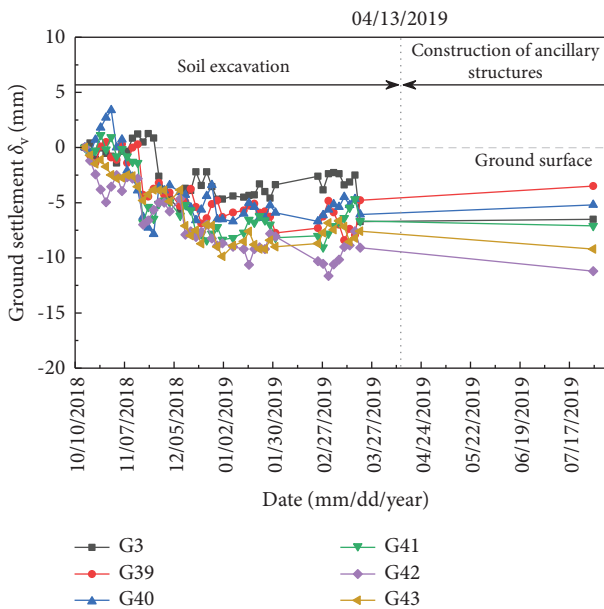


FIGURE 16: Ground surface settlements at G3, G39, G40, G41, G42, and G43.

were larger than those of the horizontal movement. Additionally, the maximum deflection and settlement were atypical to those reported in the literature. To better show the performance of the foundation pit, a plane-strain numerical model was established based on the field case study.

6.1. Finite Element Numerical Model. A finite element model, solved with PLAXIS 2D software, was built as shown in Figure 20. The length and the depth of the model

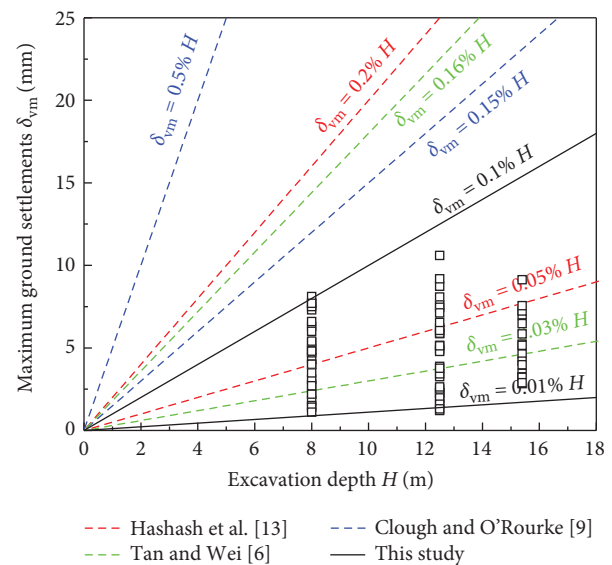


FIGURE 17: Relationship between the maximum ground settlement and the excavation depth.

were 100 m and 42 m, respectively. The displacements were constrained in both directions at the bottom, and zero horizontal displacement was imposed at the lateral boundaries. The silt layer was simulated as being in the drained condition, whereas the clay layers were modeled as being in the undrained condition. Moreover, the hydrostatic pressure load had a linear relationship with the water depth on the DSSPs. The Mohr-Coulomb constitutive model was adopted in the numerical analysis. The retaining structures (e.g., bored piles, mixed cement piles, and cut-off wall) were assumed to be linear elastic materials, referring

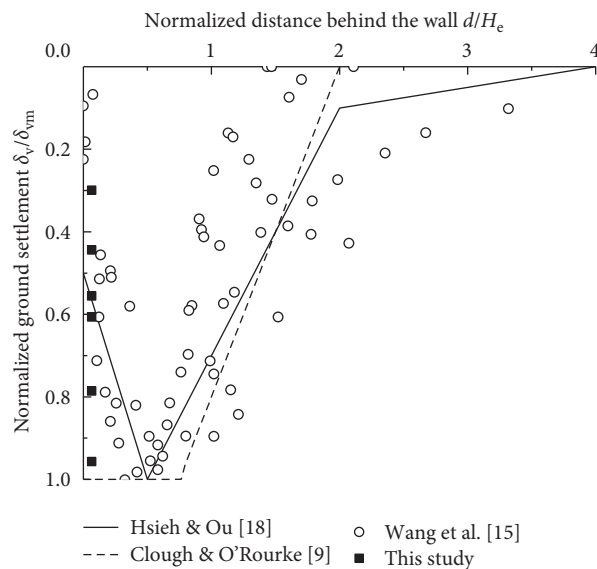


FIGURE 18: Normalized ground surface settlement perpendicular to the excavation area.

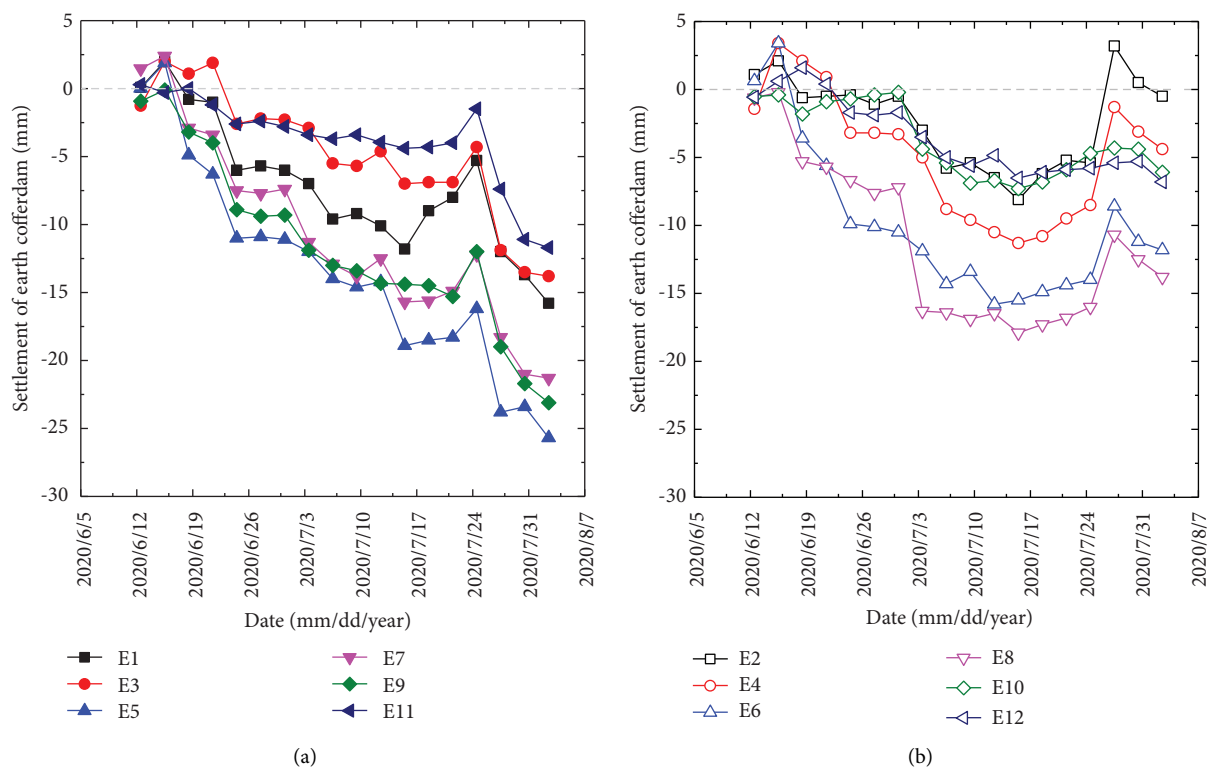


FIGURE 19: Variation of the measured ground settlements of the earth cofferdam with time. (a) Upstream side and (b) excavation side.

to the literature [9, 10, 18]. The parameters of each layer used in the numerical model are shown in Table 2. The constitutive parameters of the retaining structures are shown in Table 3.

6.2. Lateral Soil Movement. Figure 21(a) displays a comparison of the vertical movement of the DSSPs between the

FEM and the measurements. It is found that the numerical results have a similar tendency to those of the measurements. The difference between the FEM and the measurements is in the range of 10.02%–45.01%, which validates the correctness of the numerical model. The distribution of lateral soil movement of the foundation pit at Stage 3(a) is shown in Figure 21(b). It is clearly seen that the value of lateral soil movement reaches 2.87 cm, which appears in the mucky silty clay.

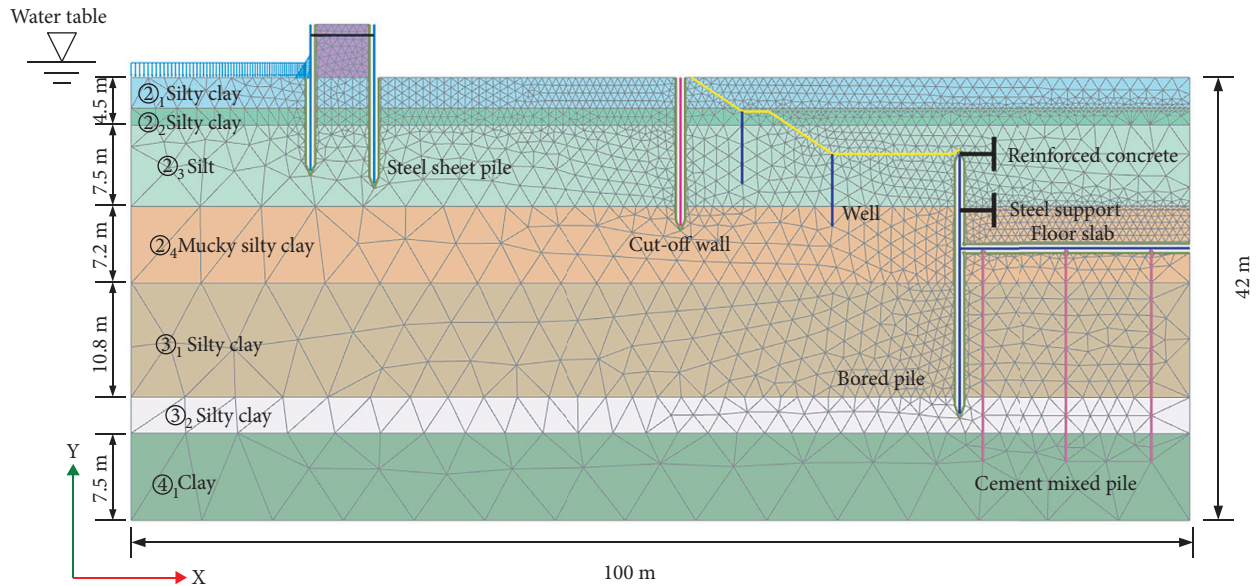


FIGURE 20: Two-dimensional finite element model and mesh generation.

TABLE 2: Summary of main geotechnical properties of soil layers.

Soil layer	γ_{unsat} (kN/m ³)	γ_{sat} (kN/m ³)	E_s (kN/m ²)	ν	c (kPa)	ϕ (°)	k (cm/s)
① Silty clay	16.8	19.4	20000	0.31	34.4	34.7	4.39E-06
② Silty clay	17.7	18.9	20000	0.31	22.6	12.2	1.08E-05
③ Silt	18.1	19.1	30000	0.30	12.6	26.5	1.79E-04
④ Mucky silty clay	16.7	17.8	10000	0.35	13.7	5.3	7.35E-06
③ Silty clay	18.9	19.7	23000	0.33	36.2	14.2	3.77E-06
③ Silty clay	17.3	18.2	23000	0.33	19.0	13.0	1.78E-06
④ Clay	18.5	19.5	35000	0.35	46.6	14.7	8.27E-07
Cohesive soil	18.5	19.5	35000	0.35	45	15	1.0E-07

Note: γ_{unsat} = unsaturated unit weight; γ_{sat} = saturated unit weight; E_s = Young's ground modulus; ν = Poisson's ratio; c = cohesion; ϕ = friction angle; k = permeability.

TABLE 3: Constitutive parameters of retaining structures.

Structure type	EA (kN/m)	EI (kN m ² /m)	ν	W (kN/m ²)
Steel sheet piles	4.8×10^7	2.5×10^5	0.25	20
Bored piles	7.5×10^6	4.0×10^5	0.2	24
Cut-off walls	6.5×10^6	5.5×10^5	0.2	24
Cement mixed piles	7.0×10^6	—	—	24
Steel strut	2.0×10^7	—	—	—
Reinforced concrete	3.5×10^7	—	—	—
Floor slab	6.0×10^6	4.0×10^4	0.2	24

Note: EA = axial stiffness; EI = bending stiffness; W = weight; ν = Poisson's ratio.

6.3. Effect of Seepage Force. A hypothetical numerical case was examined to reveal the effect of groundwater on the deformation of bored piles. In the hypothetical case, the pumping wells were neglected so that the groundwater was assumed to be undrained in the soil layers. Figure 22 shows a comparison of the pile deformations between the actual case and the hypothetical case. The maximum

deflection of the bored piles in the actual case is 2.12 cm, while that of the bored piles affected by groundwater is 4.11 cm. Using the strength reduction method, the safety coefficients of the foundation pit for the two cases are 1.61 and 1.39. Therefore, the seepage force leads to the large pile deflection and the low foundation pit stability.

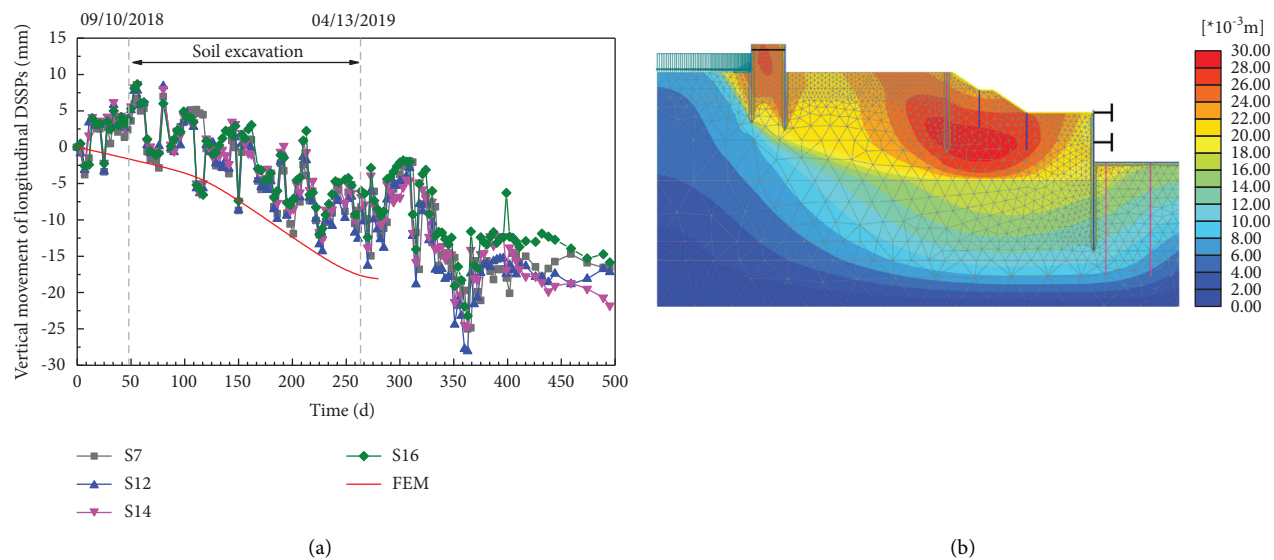


FIGURE 21: (a) Comparison of the vertical movements of DSSPs between FEM and measurements and (b) lateral soil movements of the foundation pit at Stage 3(a) calculated with the FEM.

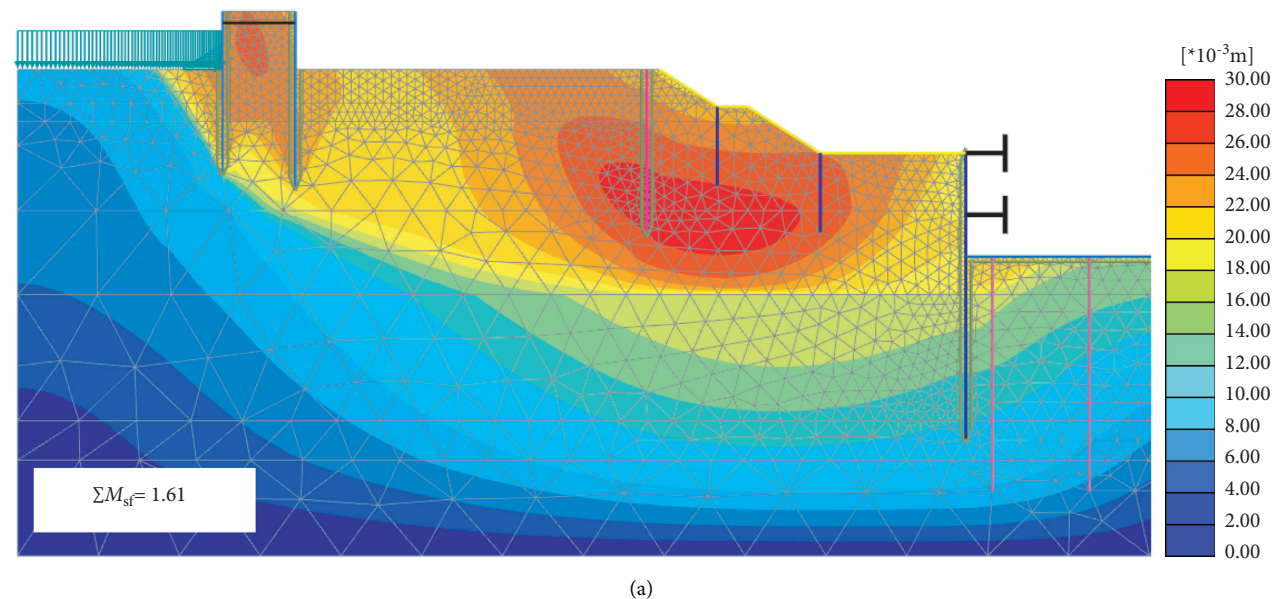


FIGURE 22: Continued.

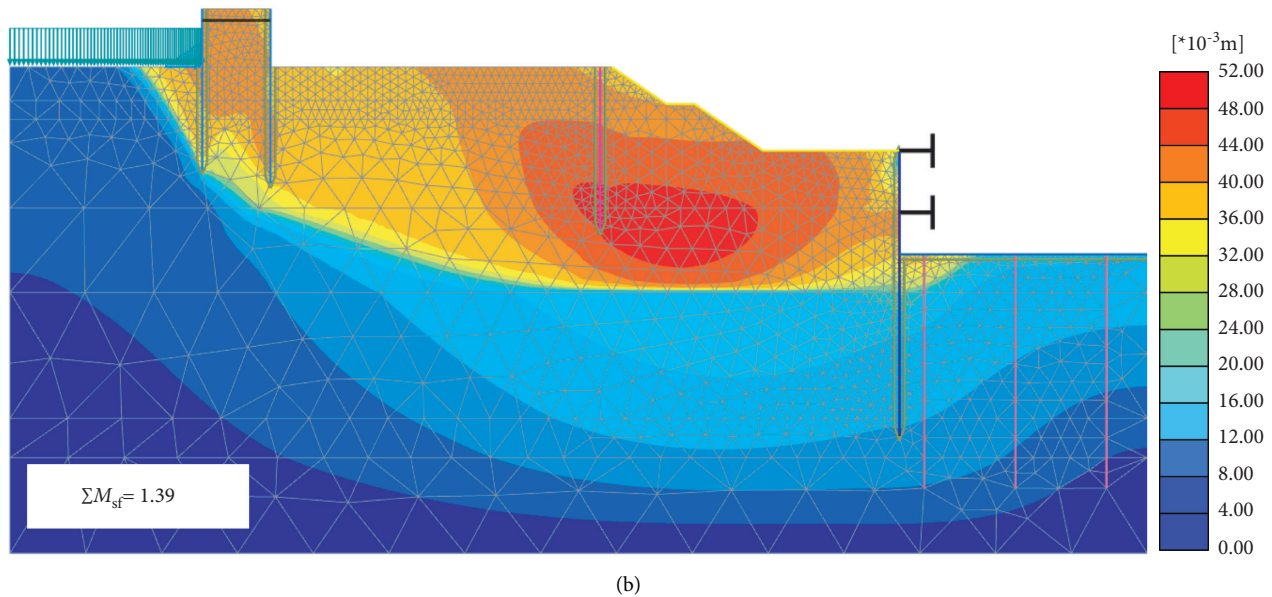


FIGURE 22: Effect of seepage force on the deformation of piles. (a) Actual numerical case and (b) hypothetical numerical case.

7. Conclusions

This paper presents a novel excavation and construction method for the Taihu tunnel, which is the longest lake-crossing tunnel in China. In the new method, an assembly line for the tunnel excavation was established to accelerate the construction speed, and the excavation did not cut off the normal flow of the lake water and the shipping routes. To investigate the tunnel deformation, a finite element analysis combined with field monitoring data was adopted. The following conclusions can be drawn:

- (1) The DSSPs experienced settlements in the vertical direction and movements toward the excavation side in the horizontal direction. The maximum vertical and horizontal movements were 28.05 mm and -39.53 mm, respectively. In addition, the magnitudes of the deformations of the transverse DSSPs were smaller than those of the longitudinal DSSP. Three factors might have contributed to such deformations: (1) the hydrostatic pressure of lake water, (2) wave action, and (3) soil excavation.
- (2) The maximum lateral deflections of the bored piles along excavation depth were between $\delta_{hm} = 0.006\%H_e$ and $\delta_{hm} = 0.06\%H_e$. However, the values of δ_{hm} were significantly smaller than the measurements reported by Clough and O'Rourke [21] for excavations in stiff clay, by Hashash et al. [22] for excavations in soft-to-medium clay, and by Tan and Wei [6] for excavations in soft Shanghai clay. The extensive use of underground structures, such as cut-off walls and cement mixed piles, the rapid cast of floor slabs, and the quick construction of bored piles might have contributed to this phenomenon.
- (3) The bored piles unexpectedly experienced heaves instead of settlements, and the maximum vertical movement at the top of bored piles was approximately 21.51 mm along B4 on the north side of the foundation pit. The elastic and plastic rebound of soils at the bottom of the foundation pit and the soil movements around the bored piles might have contributed to such upward movements [6].
- (4) The ground settlements increased with time during the excavation and then tended to be stable after the construction of floor slabs. Therefore, the casting of floor slabs and the construction of tunnel ancillary structures stabilized the retaining structures and surrounding soils. The upper and lower boundaries of the maximum ground settlements at each excavation depth were bounded by $\delta_{vm} = 0.01\%H_e$ and $\delta_{vm} = 0.1\%H_e$, which were lower than those reported in the literature [6, 21, 22]. Finally, the settlements of the earth cofferdam, which was located between WSS and Zone #1, were shown in this study.
- (5) To compare the field performance for revealing the greater impact of the tunnel excavation, a plain-strain numerical model was established based on the Mohr-Coulomb failure criterion. Two numerical cases were performed to study the effect of groundwater on the deformation of the piles, showing that the seepage force led to large pile deflection. Based on the strength reduction method, the safety coefficient of the foundation pit was 1.61, satisfying the safety requirement during tunnel excavation. The finite element analysis combined with field monitoring data reveals that the excavation and construction method could effectively control the tunnel deformations and enhance the overall stability.

References

- [1] C. Shi, C. Cao, and M. Lei, "Construction technology for a shallow-buried underwater interchange tunnel with a large span," *Tunnelling and Underground Space Technology*, vol. 70, pp. 317–329, 2017.
- [2] M. Alp and A. Apaydin, "Assessment of the factors affecting the advance rate of the Tunnel Gerede, the longest and one of the most problematic water transmission tunnels of Turkey," *Tunnelling and Underground Space Technology*, vol. 89, pp. 157–169, 2019.
- [3] Z.-N. Hu, Y.-L. Xie, and J. Wang, "Challenges and strategies involved in designing and constructing a 6 km immersed tunnel: a case study of the Hong Kong-Zhuhai-Macao Bridge," *Tunnelling and Underground Space Technology*, vol. 50, pp. 171–177, 2015.
- [4] Y. Miao, X. Li, L. Kong, D. Wu, X. Chen, and J. Sun, "Study on the symmetric bilinear initiating technique of deep-hole boulder blasting in the TBM tunnel excavation," *Tunnelling and Underground Space Technology*, vol. 111, Article ID 103871, 2021.
- [5] X. Xiao, J.-J. Chen, M.-G. Li, and J. H. Wang, "Field monitoring of an existing cut-and-cover tunnel between two large-scale deep excavations," *Journal of Aerospace Engineering*, vol. 31, no. 6, Article ID 04018082, 2018.
- [6] Y. Tan and B. Wei, "Observed behaviors of a long and deep excavation constructed by cut-and-cover technique in Shanghai soft clay," *Journal of Geotechnical and Geo-environmental Engineering*, vol. 138, no. 1, pp. 69–88, 2012.
- [7] C. Lou, T. Xia, N. Liu, and X. Gong, "Investigation of three-dimensional deformation behavior due to long and large excavation in soft clays," *Advances in Civil Engineering*, vol. 2019, Article ID 4187417, 12 pages, 2019.
- [8] C. Cao, C. Shi, L. Liu et al., "Novel excavation and construction method for a deep shaft excavation in ultrathick aquifers," *Advances in Civil Engineering*, vol. 2019, Article ID 1827479, 15 pages, 2019.
- [9] D. E. L. Ong, C. F. Leung, Y. K. Chow, and T. G. Ng, "Severe damage of a pile group due to slope failure," *Journal of Geotechnical and Geoenvironmental Engineering*, vol. 141, no. 5, Article ID 04015014, 2015.
- [10] X. Cui, M. Ye, and Y. Zhuang, "Performance of a foundation pit supported by bored piles and steel struts: a case study," *Soils and Foundations*, vol. 58, no. 4, pp. 1016–1027, 2018.
- [11] E. E.-M. Chong and D. E.-L. Ong, "Data-Driven field observational method of a contiguous bored pile wall system affected by accidental groundwater drawdown," *Geosciences*, vol. 10, no. 7, p. 268, 2020.
- [12] J.-j. Zhou, J.-l. Yu, X.-n. Gong, and T.-l. Yan, "Field tests on behavior of pre-bored grouted planted pile and bored pile embedded in deep soft clay," *Soils and Foundations*, vol. 60, no. 2, pp. 551–561, 2020.
- [13] M.-G. Li, Z.-J. Zhang, J.-J. Chen, J.-H. Wang, and A.-J. Xu, "Zoned and staged construction of an underground complex in Shanghai soft clay," *Tunnelling and Underground Space Technology*, vol. 67, pp. 187–200, 2017.
- [14] D. Li and C. Yan, "Building deformation prediction based on ground surface settlements of metro-station deep excavation," *Advances in Civil Engineering*, vol. 2018, Article ID 6050353, 11 pages, 2018.
- [15] J.-J. Chen, Y.-F. Zhu, M.-G. Li, and S. L. Wen, "Novel excavation and construction method of an underground highway tunnel above operating metro tunnels," *Journal of Aerospace Engineering*, vol. 28, no. 6, Article ID A4014003, 2015.
- [16] M. N. Houhou, F. Emeriault, and A. Belounar, "Three-dimensional numerical back-analysis of a monitored deep excavation retained by strutted diaphragm walls," *Tunnelling and Underground Space Technology*, vol. 83, pp. 153–164, 2019.
- [17] P.-G. Hsieh, C.-Y. Ou, and Y.-L. Lin, "Three-dimensional numerical analysis of deep excavations with cross walls," *Acta Geotechnica*, vol. 8, no. 1, pp. 33–48, 2013.
- [18] H. Liu, K. Li, J. Wang, and C. Cheng, "Numerical simulation of deep foundation pit construction under complex site conditions," *Advances in Civil Engineering*, vol. 2021, Article ID 6669466, 11 pages, 2021.
- [19] W. An, L. Duan, Y. Zhang et al., "Occurrence, spatiotemporal distribution, seasonal and annual variation, and source apportionment of poly- and perfluoroalkyl substances (PFASs) in the northwest of Tai Lake Basin, China," *Journal of Hazardous Materials*, vol. 416, Article ID 125784, 2021.
- [20] Ministry of Water Resources of the People's Republic of China (MWRC). Specification of Soil Test (SL237-1999) China Water Power Press, Beijing, China, 1999, in Chinese.
- [21] G. W. Clough and T. D. O'Rourke, "Construction induced movements of in-situ walls," in *Design and Performance of Earth Retaining Structures*, pp. 439–470, ASCE, Reston, VA, USA, 1990.
- [22] Y. M. A. Hashash, A. Osouli, and C. Marulanda, "Central artery/tunnel project excavation induced ground deformations," *Journal of Geotechnical and Geoenvironmental Engineering*, vol. 134, no. 9, pp. 1399–1406, 2008.
- [23] G. W. Clough, E. M. Smith, and B. P. Sweeney, "Movement control of excavation support systems by iterative design," *Proc., Foundation engineering: Current Principles and Practices*, vol. 2, pp. 869–884, 1989.
- [24] K. Terzaghi, *Theoretical Soil Mechanics*, Wiley, New York, 1943.
- [25] Z. W. Wang, C. W. Ng, and G. B. Liu, "Characteristics of wall deflections and ground surface settlements in Shanghai," *Canadian Geotechnical Journal*, vol. 42, no. 5, pp. 1243–1254, 2005.
- [26] J. H. Wang, Z. H. Xu, and W. D. Wang, "Wall and ground movements due to deep excavations in Shanghai soft soils," *Journal of Geotechnical and Geoenvironmental Engineering*, vol. 136, no. 7, pp. 985–994, 2010.

Effect of various factors influencing thermal conductivity of building insulation materials

Sarat Kumar Mishra, *Department of Mechanical Engineering, Aryan Institute of Engineering & Technology, Bhubaneswar, skmishra784@gmail.com*

Debi Prasad Singh, *Department of Mechanical Engineering, Raajdhani Engineering College, Bhubaneswar, deboprasad_1159@gmail.com*

Ranjan Kumar, *Department of Mechanical Engineering, NM Institute of Engineering & Technology, Bhubaneswar, kumarranjan75@gmail.com*

Saswati Nayak, *Department of Mechanical Engineering, Capital Engineering College, Bhubaneswar, saswatinayak2574@gmail.com*

ARTICLE INFO

Keywords:

Building insulation
materials Thermal
conductivity Influencing
factors Temperature
difference Moisture
content
Density

ABSTRACT

Solving the problem of traditional energy usage and identifying appropriate alternative supplies are critical components of a long-term development strategy. Many new thermal insulation materials have been developed in recent years to improve energy efficiency and reduce environmental impact. Due to characteristics such as low density, good heat resistance, and cost effectiveness, these items have proven their value in buildings. Thermal insulation's effectiveness is determined by its thermal conductivity and capacity to maintain its thermal properties over time. This research examines the elements that influence the thermal conductivity coefficient of three types of materials: traditional, alternative, and new advanced materials. Moisture content, temperature difference, and bulk density are the most typical contributors. Other parameters, such as airflow velocity, thickness, pressure, and material ageing, are discussed in certain dependent research. The experimentally determined relationship - between thermal conductivity values and mean temperature, moisture content, and density has also been summarised. Finally, uncertainty about the thermal conductivity value of some common insulation materials is also reviewed as the basis of selecting or designing the products used in building envelopes.

1. Introduction

1.1. Energy consumption in the building sector

The global energy expenditure in industrial and residential construction has become one of the most important concerns in the third decade of the 21st century. Building construction, raw material processing, and product manufacturing are the largest sources of greenhouse gas emissions. Carbon dioxide compounds are the main by-products of fossil fuel consumption, and since buildings are among the biggest consumers of energy, they are also major contributors to global warming which is accelerating climate change and threatening the survival of millions of people, plants and animals. According to Directive 2010/31/EU of the European Parliament and of the Council of 19 May 2010, on the energy performance of buildings, new construction will have to consume nearly zero energy and that energy will be to a very large extent from renewable resources, because the construction sector has been identified as the largest energy consumer, generating up to 1/3

of global annual greenhouse gas emissions (GHG), contributing up to 40% of global energy, and consuming of 25% of global water worldwide [1]. Global energy consumption is predicted to grow by 64% until the year 2040 from the considerable increase in residential, industrial, commercial, and urban construction due to the industrial development and growth of population, according to the Energy Information Association in 2018 [2]. As a result, environmental disasters and climate change are becoming more apparent. For instance, global warming from the greenhouse effect (45% carbon dioxide emissions in which buildings and construction industry are major contributors, [3]) is predicted to raise the Earth's average surface temperature from 1.1° to 6.4 °C by the end of 2100 [4,5]. The increased consumption of natural resources for lighting, refrigeration, ventilation, recycling, heating, and cooling system in commercial buildings due to the acceleration of urbanization, causes an enormous expenditure for energy. Therefore, it is necessary to use insulation materials for better energy conservation, and to enhance sustainable energy strategies in the building sector.

Nomenclature

PS	Polystyrene
EPS	Expanded polystyrene
XPS	Extruded polystyrene
PUR	Polyurethane
PIR	Polyisocyanurate
PE	Polyethylene
ENR	Expanded nitrile rubber
EVA	Ethylene vinyl acetate
VIPs	Vacuum insulation panels
GFPs	Gas filled panels
LWAC	Lightweight aggregate concrete
PCM	Phase change materials
OIT	Optimum insulation thickness

Greek symbols

λ	Thermal conductivity (W/(m.K))
ρ	Density (kg/m ³)
p	Pressure (Pa)
w	Moisture content (%)

1.2. The use of thermal insulation materials

As the energy becomes more precious, the use of thermal insulation materials is being enforced in buildings. Thermal insulation is a material or combination of materials that retard the rate of heat flow by conduction, convection, and radiation when properly applied [6]. Using thermal insulation products helps in reducing the dependence on heating, ventilation, and air conditioning (HVAC) systems to manage buildings comfortably. Therefore, it conserves energy and decreases the use of natural resources. Other advantages are profits, environmentally friendly materials, extending the periods of indoor thermal comfort, reducing noise levels, fire protection, and so on [7]. These materials will enable systems to achieve energy efficiency. They also have many applications in food cold storage, refrigeration, petroleum and liquefied natural gas pipelines [8]. Sustainable insulation products with lower embodied energy and reduced environmental emissions are also increasing in popularity and a large number of innovative types of insulation are constantly entering the market [9].

Some former detailed reviews of thermal insulation materials and their application in the building sector include Aditya et al. [10], and D'Alessandro et al. [11]. Insulation materials are applied in some groups including the walls, the roofs, the ceilings, the windows, and the floors. Their types, properties, benefits, and drawbacks were also discussed. The work of Abu-Jdayil et al. [12] has reviewed the different types, methods of manufacturing, and features in both the traditional and state-of-the-art thermal insulation materials in the last decades. Thermal insulating materials are generally comprised of a solid matrix material with a gaseous material interspersed randomly or regularly within the cells, pores or interstices [13].

Most of the available thermal insulation materials can be classified in four general groups including inorganic, organic, combined, and advanced materials. They are created in several forms including porous, blanket or batt form, rigid, natural form, and a reflective structure [14]. Inorganic materials (glass wool and rock wool) account for 60% of the market, whereas organic insulation materials are 27%. Conventional materials such as polyurethane (PUR), polyisocyanurate (PIR), extruded polystyrene (XPS), expanded polystyrene (EPS) are preferred in many buildings and thermal energy storage applications due to their low thermal conductivity and low cost [15].

Mineral wool includes a variety of inorganic insulation materials such as rock wool, glass wool, and slag wool. The average range of

thermal conductivity for mineral wool is between 0.03 and 0.04 W/(m.K) and the typical λ -values of glass wool and rock wool are 0.03–0.046 W/(m.K) and 0.033–0.046 W/(m.K), respectively. These materials have the low thermal conductivity value, are non-flammable, and highly resistant to moisture damage. However, it can affect health problems, for example, skin and lung irritation [12]. Organic insulation materials are derived from natural resources which are currently used in buildings due to their attractiveness, renewable, recyclable, environmentally friendly and required energy to manufacture is less than that of traditional materials [10].

To retard the heat transfer in building envelopes, various of new insulation materials has produced to achieve the highest possible thermal resistance. They are vacuum insulation panels (VIPs), gas filled panels (GFPs), aerogels, and phase change materials (PCM). Among them, VIPs exhibit one of the lowest thermal conductivity values (lower than 0.004 W/(m.K)) and have a high life expectancy (over 50 years). This super-insulated material is created inside the panel which decreases the thickness of the thermal insulation materials, but the thermal conductivity will increase irreversible over time due to diffusion of water vapor and air through the envelope [12]. Aerogels are also considered as one of the state-of-the-art thermal insulators with the range of thermal conductivity values from 0.013 to 0.014 W/(m.K) and the density for buildings is usually 70–150 kg/m³ [11]. However, its commercial availability is very limited due to the high cost production [16]. GFPs and PCM are the thermal insulation materials of tomorrow due to their low thermal conductivity values, 0.013 W/(m.K) and 0.004 W/(m.K), respectively. While GFPs are made of a reflective structure containing a gas insulated from the external environment by an envelope impermeable as possible, PCM stores and releases heat as the surrounding change by transforming from a solid state to liquid when heated and turning into a solid state when the ambient temperature drops [10,11,16].

Table 1 shows the thermal properties of some common insulation materials. The data are collected and synthesized according to the literature and practical experiment. Thermal insulating materials are usually tested which covered by standards such as EN 12664 (low thermal resistance) [17], EN 12667 (high thermal resistance) [18], EN 12939 (thick materials) [19], ASTM C518 (heat flow meter apparatus) [20], and ASTM C177 (guarded hot plate apparatus) [21]. Nevertheless, as a result of the wide range of thermal properties of insulation materials, there is no single measurement method for all thermal conductivity measurements [22].

There is uncertainty about the thermal conductivity values for inorganic, organic, and advanced materials which are 0.03–0.07 W/(m.K), 0.02–0.055 W/(m.K), and lower than 0.01 W/(m.K), respectively. Generally, the nominal thermal conductivity of porous materials range from 0.02 to 0.08 W/(m.K), while the thermal conductivity values of alternative insulation materials made from natural fibers vary from 0.04 to 0.09 W/(m.K). Conventional materials such as mineral wool, foamed polystyrene are mainly used in thermal energy storage systems due to long term usage, and low cost. Natural fibers-based insulation materials derived from agricultural waste such as coconut, rice straw, bagasse, etc., currently applied in some building applications due to the environmentally friendly properties [33,34]. However, the main disadvantage is their relatively high-water absorption, resulting in high thermal conductivity. Therefore, the use of VIPs or PUR-PIR foams with lower thermal conductivity can be a good choice for reducing energy consumption as well as cost savings [15]. Additionally, there are efforts to make thermal insulation from wood waste products [35], but they should be protected against saturation, especially when used externally. Another new development material is aerogel and VIPs with a low thermal conductivity of just 0.017–0.021 W/(m.K) and 0.002–0.008 W/(m.K), respectively, which exhibits excellent thermal insulation properties. In fibrous insulating materials, the fineness of the fibers and their orientation play a main role. In foam insulating materials, the thermal conductivity is determined by the fineness and distribution of the cells and particularly by the gases in those cells. Insulating materials

Table 1

Classification of the commonly used insulation materials and uncertainty about their thermal conductivity.

Main group	Subgroup	Insulation Material	Temperature (°C)	Density (kg/m ³)	Thermal conductivity (W/(m.K))	Reference
Inorganic	Fibrous	Glass wool	-100–500	13–100	0.03–0.045	[11,12,23]
		Rock wool	-100–750	30–180	0.033–0.045	[7,11,12,23–26]
	Cellular	Calcium silicate	300	115–300	0.045–0.065	[24]
		Cellular glass	-260–430	115–220	0.04–0.06	[24]
		Vermiculite	700–1600	70–160	0.046–0.07	[7,24,27]
Organic	Foamed	Ceramic	N.A.	120–560	0.03–0.07	[24]
		EPS	-80–80	15–35	0.035–0.04	[7,11,16,23,24]
		XPS	-60–75	25–45	0.03–0.04	[7,11,15,16,23,24,28]
		PUR	-50–120	30–100	0.024–0.03	[11,16,23,24,29]
		PIR	-20–100	30–45	0.018–0.028	[11,30]
	Foamed, expanded	Cork	110–120	110–170	0.037–0.050	[11,16,24]
		Melamine foam	N.A.	8–11	0.035	[24]
		Phenolic foam	150	40–160	0.022–0.04	[11,24]
		Polyethylene foam	-40–105	25–45	0.033	[24]
		Fiberglass	-4–350	24–112	0.033–0.04	[7,28]
	Fibrous	Sheep wool	130–150	25–30	0.04–0.045	[24]
		Cotton	100	20–60	0.035–0.06	[24]
		Cellulose fibers	60	30–80	0.04–0.045	[7,11,16,24]
		Jute	N.A.	35–100	0.038–0.055	[11]
		Rice straw	24	154–168	0.046–0.056	[11]
		Hemp	100–120	20–68	0.04–0.05	[24]
		Bagasse	160–200	70–350	0.046–0.055	[11,31]
		Coconut	180–220	70–125	0.04–0.05	[11,24,31]
		Flax	N.A.	20–80	0.03–0.045	[24]
		Gypsum foam	N.A.	N.A.	0.045	[24]
Combined	Boards	Wood wool	110–180	350–600	0.09	[24]
		Wood fibers	110	30–270	0.04–0.09	[24]
Advanced materials		VIPs	N.A.	150–300	0.002–0.008	[11,24]
		Aerogel	N.A.	60–80	0.013–0.014	[11,16,24,32]

made from wood fibers or wood wool, the density factor is critical for the insulating capacity. The range of temperature shows the minimum and maximum service temperatures based on manufacturers information. Insulating materials can react very differently to hot and cold environment and there is no uniform test method that enables a direct comparison between insulating materials [24].

Previous studies have carried out the thermal conductivity coefficient strongly depends on the temperature, moisture content, density [7, 11,12,16]. Some research gaps can be identified from existing literature and published studies. Firstly, there has been no detailed overview of all factors influencing in the thermal properties of building insulation materials. Secondly, few empirical data evaluates the thermal performance of insulation materials considering cost, environment impact, personal comfort and lessen attention to other properties such as embodied energy, embodied carbon, hygroscopic and fire protection. Furthermore, thermal properties of insulation materials are mainly determined by thermal conductivity, specific heat capacity, thermal diffusivity, coefficient of thermal expansion, and mass loss. However, most studied in the field of heat and moisture transport have only focused on the thermal conductivity for the steady state without evaluating the other properties. Hence, it is imperative to understand the combined influence of the many factors to gain useful insights into the actual performance of insulation materials for practical applications.

This review aims to provide a fundamental understanding of different building insulation materials and their thermal conductivities. The main research question is to discuss the factors influencing thermal conductivity coefficients of insulation materials used in building envelopes. Another object is to synthesize the relationship between mean temperature, moisture content, and density with thermal conductivity as a linear function. This article also exhibits the λ -values of some common traditional and state-the-art materials to understand insulating materials used in building construction.

This paper has been structured as follows. Section 2 explores the main role of the thermal conductivity coefficient when studies the heat transport in buildings as well as the values of various common building insulation materials are displayed. The effects of factors including

temperature, moisture content, density, thickness, pressure, aging, and air surface velocity in the thermal conductivity are presented in section 3. Then, section 4 discussed how these factors influencing in the thermal conductivity. Finally, section 5 concludes the present study.

2. Thermal conductivity coefficient

Insulation materials are supposed to conduct heat badly in order to prevent large heat losses. The lower the heat conduction in a material, the less heat flows through it. The thermal performance of a building envelope depends to a great extent on the thermal effectiveness of the insulation layer which is mainly determined by its λ -value. Thermal conductivity is the time rate of steady-state heat flow through a unit area of a homogeneous material in a direction perpendicular to its isothermal planes, induced by a unit temperature difference across the sample [36]. At the microscopic level, the apparent thermal conductivity depends on numerous factors such as cell size, diameter and arrangement of fibers or particles, transparency to thermal radiation, type and pressure of the gas, bonding materials, etc. A specific combination of these factors produces the minimum thermal conductivity. At the macroscopic level, the apparent thermal conductivity largely depends on various factors, namely mean temperature, moisture content, density, and aging. Therefore, thermal conductivity coefficient is always a primary parameter measuring in every thermal calculation.

Thermal insulating materials can reduce the energy losses as well as minimize the emissions of the greenhouse gases from buildings. The choice of insulation material can have a great effect on energy efficiency in both cooling and heating, and on health problems. Heat transfer in thermal insulation materials is generally divided into heat conduction through the solid material, conduction through its gas molecules and radiation through its pores. Convection is insignificant because of the small size of the air bubbles. To develop insulation materials in an environmentally friendly manner, it is important to know their apparent thermal conductivity [14]. According to the DIN 4108, “Thermal insulation and energy economy in buildings”, materials with a λ -value lower 0.1 W/(m.K) may be classed as thermal insulating materials. Materials

with thermal conductivity values lower 0.03 W/(m.K) can be regarded as very good, whereas values from 0.03 to 0.05 W/(m.K) are only moderate, and higher 0.07 W/(m.K) are less effective [16,24,37,38]. The published thermal conductivity of insulation materials are usually specified by manufactures and normally investigated under standard laboratory conditions [39–42], for example, a standardized mean temperature around 24 °C and relative humidity of $50 \pm 10\%$ [43].

3. Factors influence thermal conductivity coefficient

It is essential to examine the thermal properties of any insulation materials due to its important role affecting the heat transfer in building envelopes. Thermal properties are mainly defined by thermal conductivity, specific heat, thermal diffusivity, thermal expansion, and mass loss [44]. Among them, the thermal conductivity coefficient is the main key to measure the ability of a material to transfer or restrain heat flows through building insulation materials. At the macroscopic level, thermal conductivity largely depends on three main factors: operating temperature, moisture content, and density [33,37,42]. Other factors are a thickness, pressure, air surface velocity, and aging.

3.1. Temperature

The temperature dependency of thermal conductivity in building insulation materials has been investigated by a large number of theoretical and practical studies. Based on these results, the λ -value usually increases with increasing temperature [28,37,39,42,45–62].

3.1.1. Inorganic materials

Abdou and Budaiwi elucidated the dependence of thermal conductivity of inorganic materials under mean temperatures ranging from 4° to 43 °C. Their first study was conducted for rock wool and fiberglass with different densities [57]. Their results showed an increase in thermal conductivity values as a linear relation with mean temperatures. The variation was clearer with less density materials. An equivalent analysis of rock wool, mineral wool, and fiberglass with a thickness ranging from 5 to 100 mm in their next study indicated that higher operating temperatures are associated with higher λ -values, and the relationship is presented by a linear regression with temperature for most insulation materials [42]. Experiments with fiberglass and rock wool were observed in their third article in accordance with the impact of moisture content [63]. They assessed the changes in thermal conductivity with different densities not only the variation of operating temperatures ranging from 14° to 34 °C but also the effect of moisture content. Examination of their results continues to confirm that a higher operating temperature is always associated with higher thermal conductivity. The effective thermal conductivity of some conventional materials such as mineral wool and foam glass as a linearly increasing function at mean temperatures varying from 0° to 100 °C was studied with a protected heating plate device [47]. The λ -values of these insulation materials were 0.04 W/(m.K), 0.045 W/(m.K), and 0.05 W/(m.K) at mean temperature of 10 °C. Occasionally, inorganic open-cell materials, such as fiberglass or rock wool, have been proposed the linear temperature-dependent law that displays a decreased thermal conductivity at low temperatures [45].

3.1.2. Organic materials

The change of thermal conductivity of polystyrene (PS) and polyethylene (PE) with mean temperatures was evaluated [42,57]. The rate of heat exchanges of PE was the most sensitive to temperature, while PS insulation was the least affected, approximately of 0.000384 (W/(m.C)/°C) and 0.0001 (W/(m.C)/°C), respectively. According to the statistical data of expanded polystyrene (EPS) material in determining the impact of the temperature on thermal conductivity, Gnip et al. [64] calculated the λ -value at any point in a range temperature from 0° to 50 °C by using a calculated value of thermal conductivity at 10 °C. The

relationships presented a slight increase with a rise of temperature. The changes in temperature have always been ascribed to the variation of thermal conductivity. Khoukhi et al. [65] showed that higher temperatures increase thermal conductivity for three types of polystyrene materials. Their next study demonstrated a linear rise in thermal conductivity with increasing temperatures in four PE insulation specimens with densities from low to super high [49]. Testing the effect of temperature on thermal conductivity on EPS and polyurethane (PUR) materials by using the hot wire method, Song et al. [56] revealed that at the same density, the thermal conductivity coefficient increases with increasing ambient temperature.

A series of empirical observations of some insulation materials including EPS, extruded polystyrene (XPS), PUR have shown the influence of temperature on their effective thermal conductivity [47]. The data shows the relationship between λ -values and temperatures is a linear function. An evaluation of alternative insulation materials based on sheep wool has also shown the linear increase with increasing temperature from 10° to 40 °C [66]. Koru [37] studied the effects of temperature on thermal conductivity closed-cell thermal insulation materials, namely EPS, XPS, expanded nitrile rubber (ENR), PUR, PE, and ethylene vinyl acetate (EVA) with a heat flow meter using the standards EN 12664, 12667, and ASTM C518. The results revealed that thermal conductivity increases with the rise of the range temperature between– 10° and 50 °C. Based on the empirical data, the author expressed the relationships among the λ -values and the temperature as linear equations. A similar assertion also comes from the experimental investigation of Berardi et al. [28]. Zhang et al. [8] investigated the change of thermal conductivity of five polyurethane foams occurs at temperatures varying from– 40° to 70 °C. Resembling the previous publication, Khoukhi also affirmed the incremental increases of thermal conductivity of polystyrene expanded insulation materials as the operating temperature increases when studying the combined impact of heat and moisture transfer on building energy performance [39]. Next, he continued to investigate the dynamic thermal effect of thermal conductivity at different temperatures of the same insulation materials. The experimental data showed that thermal conductivity increases linearly with temperature [67].

Besides the studies on temperature-dependent thermal conductivity of various traditional materials, there is an interesting in manufacturing natural fiber-based insulation materials with high thermal resistance. These insulators are derived from natural materials such as hemp, cotton, rice straw, or wood waste products. Manohar et al. [68] tested the apparent thermal conductivity of coconut and sugarcane fiber at a mean temperature of 24 °C with different densities. The λ -value of both biodegradable materials increased with an increase in temperature. The minimum thermal conductivity of coconut and sugarcane ranged from 0.048 to 0.049 W/(m.K) and 0.046 to 0.049 W/(m.K) showing low values when compared to some conventional insulation materials. Wood-based fiberboards are also used as thermal insulation materials due to their low density, and high thermal resistance, etc. However, they are sensitive to changes in environmental conditions because of their porous internal structures. Hence, the thermal conductivity will increase by approximately 50% as the temperature goes up from– 10° to 60 °C [50].

3.1.3. Combined materials

Bio-based materials can be used as an effective alternative product in buildings which reduce energy consumption and optimize the utilization of fossil fuels for the sake of sustainable development. Some natural materials such as hemp, flax, jute or rice straw can be combined with concrete to create material with high thermal resistance, low density, and high durability. According to the study of Rahim et al. [69], the effect of temperature on λ -values is important. The thermal conductivity of bio-based materials rose slightly with increasing temperature from 10° to 40 °C and the relationship is a linear function. The same trend was demonstrated in the work of Srivaro et al. [70], with empirical tests of

some rubberwood specimens which had a linear change between their thermal conductivity and the varying temperatures. The thermal conductivity of three different samples sheep wool, goat wool, and horse mane increases significantly by approximately 55% with increases in temperature [46].

Lightweight aggregate concrete (LWAC) shows better thermal performance than conventional concrete, so, it is currently used in the construction sector [71]. The study of twelve mixtures of LWAC proved that its thermal conductivity increases with the temperature range between 5° and 35 °C [72]. A novel multilayer reflecting thermal insulation material called “mirror-panel” made from aluminum foil and coated paper using in building envelope was developed and tested to determine the temperature dependency of its thermal resistance. Experimental results showed that its thermal conductivity increases almost linearly with an increase of temperature [73].

A series of practical observations studied the temperature-dependent thermal conductivity of the composite materials [74–76]. Using water-based nanofluids, the results from measurements of Das et al. [77] and Mints et al. [78] showed a linear increase of effective thermal conductivity with temperature varying between 20° and 50 °C. Working with nanotube specimens, Khordad et al. [75] found that thermal conductivity increases as temperature increases. The same upward trend was also documented in a paper of Wang et al. [79] with the composite phase change materials. The data is expressed by a highly accurate linear fit. The recent study of Guo et al. [80] on aerogel blankets, phenolic, and polyisocyanurate foams has shown a linear increase in thermal conductivity by 24%, 13%, and 14% respectively when the mean temperature varies from 280° to 300 K.

3.1.4. New technology materials

The combination of technical development and advanced materials produced state-of-the-art thermal building insulation including vacuum insulation panels (VIPs), aerogels, gas filled panels (GFPs), phase change material (PCM), and closed-cell foam [10]. Among them, VIPs exhibit the lowest thermal conductivity. Its main benefit is the reduction of the required thickness of the insulation layers compared to conventional materials in buildings [81].

Fantucci et al. [82], investigated the temperature dependence of thermal conductivity in fumed silica-based VIPs. The main advantage is its relatively low thermal conductivity in the case of a complete loss of vacuum. Experimental analyses of two samples with different thickness showed an increase up to 45% when the temperature increases from 2° to 50 °C. The next study noted that a 53% increase in thermal conductivity of the raw VIPs from 0.0049 to 0.0075 W/(m.K), and from 0.0021 to 0.0028 W/(m.K) in fumed silica over the range of temperatures between 7.5° and 55 °C [48].

Aerogel is one of the thermal building insulations of tomorrow due to its low density, high porosity, small average pore size, and very low thermal conductivity. They have found potential practical applications for thermal insulation systems including energy storage, construction and building [83]. Several studies have investigated the effect of temperature on thermal models of aerogel composite insulation materials [84–86]. The data of Liu et al. [87], showed a low effective thermal conductivity of silica aerogels from 0.014 to 0.044 W/(m.K) and a nonlinear increasing correlation with increasing temperature from 28° to 108 K. There was the same result of three samples of silica aerogel but different densities with temperature ranges from 300° to 700 K [86]. Thermal conductivity of aerogel blankets increased from 0.0135 to 0.0175 W/(m.K) at mean temperatures varying from 20° to 80 °C and the relationship was almost linear [32]. Same conclusions with increasing slightly were also shown in the study of Nosrati et al. [88].

Table 2 shows practical equations to illustrate the temperature-dependent thermal conductivity of different insulation materials using data collected from articles.

A higher operating temperature is always associated with higher thermal conductivity for most insulation materials. As the temperature

Table 2

Temperature-dependent thermal conductivity shown as a linear function of insulation materials.

Main group	Insulation Materials	Relationship	Mean temperature (°C)	Reference
Inorganic materials	Rock wool	$1.915e-4 \times T + 0.0336$	4–43	[42]
	Fiberglass	$3.01e-4 \times T + 0.0281$	14–39	[89]
		$3.368e-4 \times T + 0.0414$	4–43	[42]
		$1.476e-4 \times T + 0.0356$	0–50	[64]
Organic materials	EPS	$5e-5 \times T + 0.0347$	10–43	[67]
		$6e-5 \times T + 0.033$	10–43	[39]
	XPS	$1.045e-4 \times T + 0.0276$	10–43	[42]
	EVA	$8.46e-5 \times T + 0.03746$	–10–50	[37]
	PE	$3.19e-4 \times T + 0.04589$	–10–50	[37]
	PIR	$2e-4 \times T + 0.0273$	7–27	[80]
	PUR	$1.71e-4 \times T + 0.027$	0–100	[90]
	Hemp	$2e-4 \times T + 0.047$	10–40	[69]
	Sheep wool	$2e-4 \times T + 0.0349$	10–40	[66]
	Coconut	$2.84e-6 \times T + 0.0487$	10–40	[68]
	Bagasse	$2.38e-4 \times T + 0.0456$	10–40	[68]
	Rubberwood	$4e-4 \times T + 0.1246$	–10–40	[70]
	Wood wool	$3.06e-4 \times T + 0.0607$	4–43	[42]
	VIPs	$4e-5 \times T + 0.0049$	–15–63	[48]
	Aerogel blanket	$5e-5 \times T + 0.0166$	–10–50	[88]

risers, the rate of heat conduction increases, then increasing the λ -value but within the limited temperature range, usually from 10° to 50 °C and typically up to 20%–30%. This is the case with inorganic fiber insulation and some petrochemical insulating materials which show lower thermal conductivity at lower temperatures [45]. Additionally, the relationship between thermal conductivity and temperature is almost linear. Firstly, the measurements are focused separately on the effect of these influencing factors. Secondly, the experimental conditions are set up in a steady-state condition. According to the American Society for Testing and Materials ASTM-C518 standard, thermal conductivity is only given for standardized conditions and most of the published thermal conductivity values from experimental investigations as well as from manufacturers from laboratory work [37]. However, weather conditions, exterior temperature, and moisture values vary over the course of a day. Therefore, it is important to determine the thermal conductivity of insulation materials and their dependence on temperature.

3.2. Moisture content

In the normal environmental conditions around buildings, all these three stages of moisture (solid, liquid, gas) can be dangerous for building materials. Excessive moisture causes the following five problems: deteriorated habitation quality, reduced thermal resistance, additional mechanical stresses, salt transport, and material decay. This phenomenon is due to both obvious as well as more inconspicuous causes: moisture intrusion into building interior due to contact with liquid water, moisture deposition on the building surface due to contact with water vapor,

moisture intrusion into the building due to contact with water vapor and built-in moisture [91]. For building envelopes, insulated walls, and roofs, moisture can diminish their effective thermal properties. Additionally, moisture migrating through building envelopes can also lead to poor interior air quality as high ambient moisture levels cause microbial growth, which may seriously affect human health and be a cause of allergies and respiratory symptoms [92]. As the thermal conductivity of water is about 20 times greater than that of stationary air, water absorption is always connected with an increase in thermal conductivity [24]. Therefore, it is crucial to study the impact of moisture on thermal performance, especially in building insulating materials.

It is essential to measure the initial and the increased moisture content of building insulation materials. Various techniques have been suggested for each type of measurement such as drilling techniques, electrical techniques, environmental monitoring, thermographic imaging [93]. Zhang et al. measured the moisture content from the change in volumetric heat capacity before and after the moisture acquirement using a hot wire [94]. The same method was adopted in another investigation but using the transient temperature [95]. The moisture content of a building material is calculated based on the weight of absorbed moisture to the dry weight of the material. According to the ASTM C1616, the moisture content of organic and inorganic insulation materials by mass is calculated from the following equation:

$$w = \frac{m - m_d}{m_d} \quad (1)$$

where w is the moisture content (%), m_d is the mass of the dried sample (kg), m is the mass of damped sample (kg).

3.2.1. Conventional materials

Some experimental investigations in building insulation materials including mineral wool, fiberglass, and polystyrene have found that an increase of thermal conductivity is always associated with rising moisture content [50,96–98]. Lakatos observed a slight increase of up to 0.2 W/(m.K) for mineral wool and fiberglass samples with varying of moisture content from 0 to 100% [98]. His previous study with extruded polystyrene (XPS) confirmed the influence of moisture content on thermal conductivity [99]. Jerman et al. [97] concluded that thermal conductivity of mineral wool rises quickly from 0.041 W/(m.K) to approximately 0.9 W/(m.K) with rising moisture content. Another investigation was concluded, in which the thermal conductivity of mineral wool increased from 0.037 to 0.055 W/(m.K) with increasing moisture content from 0% to 10% by volume [16]. Conversely, expanded polystyrene (EPS) is only slightly affected by an increase of moisture content. Its value was 0.037 W/(m.K) in a dry state and 0.051 W/(m.K) in saturated conditions. Another study investigated thermal performance by cooling polystyrene insulation materials documented the rise of thermal conductivity due to the increases in moisture content [39]. An increase of thermal conductivity of mineral wool can reach a maximum of 446% with increasing moisture content of 15% [63], compared to the thermal conductivity of rock wool which can increase 312.8% with an increase in moisture content of 13.6% in the latest study of Gusyachkin et al. [96], and thermal conductivity of fiberglass increases nearly 300% by the time if it gained 3% moisture [100]. It can be explained by the initial moisture content. Samples with higher initial moisture content always show higher percentage change of thermal conductivity.

Most of building insulation materials are normally porous and their the coefficient of thermal conductivity usually ranges from 0.02 to 0.08 W/(m.K) [101]. Due to the high porosity, porous materials can absorb large amounts of moisture under high humidity conditions resulting in an increase in the thermal conductivity coefficient [54]. A study of Liu et al. [102] showed that thermal conductivity of foam concrete rose rapidly in the low volumetric fraction of moisture content and slowly increased with increased moisture. The authors later measured the

influence of water content on the thermo-acoustic performance of building insulation materials [103]. Samples of high porosity insulation materials were treated by heat treatment through some steps before measuring with the transient plane method to assess how thermal conductivity is influenced by water content. This showed a linear increase for four types of specimens including mineral wool, melamine foam, polyurethane, and cork. When the building materials are moistened, wet insulation can increase to the maximum ratio of thermal conductivity between the dry and wet samples by 3.51 with a maximum moisture content of 15.1% in the ambient temperature ranged from 24.9° to 38.6 °C after 55 days [104]. Thermal conductivity increases by approximately 200% when the moisture content reaches 10% in foam concrete [102]. In contrast to the above conclusions, another study with wood frame insulation walls made of spruce-pine-fir concluded that there was no obvious effect on thermal conductivity since moisture content was less than 19% [105].

A study carried out by Gawin et al. [106] measured the impact of the initial moisture content on the thermal conductivity of wood-concrete and EPS-concrete materials using a heat flow meter. The results showed an increase of thermal conductivity with increasing the water content in the range of 70%–85% relative humidity. Using the same lightweight specimens but with different densities, Taoukil et al. [107] also confirmed the influence of relative humidity on thermal properties. Thermal conductivity rose rapidly with water content and was presented as an exponential equation. The next laboratory study from Nguyen L.H. et al. [72] contributed to the assumption of the moisture dependence of thermal conductivity of lightweight concretes. In this case, the result showed a linear relationship.

3.2.2. Alternative materials

In recent years, thermal protection used of natural fibrous materials, agricultural wastes, forest product wastes as the raw materials of thermal insulation products. Therefore, the amount of harmful waste gas caused by petrochemical insulating materials in the atmosphere will decrease. However, these kinds of materials are more sensitive to moisture, so, it is necessary to evaluate their thermal performance due to the change of relative humidity. The moisture dependence of thermal conductivity values of different insulating materials made from hemp, jute, and flax was investigated in the study [108]. Results showed a high increase of thermal conductivity with increasing moisture content. Data for the effect of water content in thermal conductivity of three bio-based concretes derived from hemp, jute, flax noted that there is a linear increase in λ -values as the moisture content increases and its effect is more crucial due to the increase of thermal conductivity of air and water at high temperature [69]. An experimental study on the effect of humidity on thermal conductivity of binderless board made from date palm fibers was investigated in a study of Boukhattem et al. [109]. It showed a significant increase with volumetric water content ranges from 0 to 40% and the relationship was expressed as a polynomial function. As a result, date palm fiberboard can be used as insulation materials in buildings due to its low thermal conductivity of 0.033 W/(m.K) in a dry state. The effect of moisture content due to the changes of relative humidity on thermal performance of wood-based fiberboards was evaluated. Thermal conductivity increased almost linearly with increasing moisture content [50]. The tests carried out on twenty-four soft fiberboards made from wood fibers also showed that thermal conductivity increases linearly with increasing moisture content [110]. Abdou and Budaiwi [63] investigated the thermal performance of eleven different fibrous materials at different percentages of moisture content. The results showed that higher moisture content is always associated with higher thermal conductivity for different densities. The data fit a linear relationship for almost all the specimens except for mineral wool which was expressed by a non-linear function.

The natural insulators show a low value of thermal conductivity and better thermal technical characteristics than other conventional materials. However, a major drawback is their high wettability and

absorbability due to an open structure of natural fiber, which can negatively affect the mechanical and thermal properties. Natural fiber can be activated with silane surfactant to combat effectively hydrophilicity and prevent rotting [111]. Some different products for hydrophobic treatment were chosen to deal with the water absorption and hygroscopicity of hemp fibers in the study. It was found that the hydrophobic-treated fibers have shown lower short-term absorbability compared to untreated ones [112].

3.2.3. Advanced materials

Aerogel is one of the new insulating materials, commonly used in construction due to its nano-porous structure and excellent thermal conductivity between 0.014 and 0.022 W/(m.K). In these studies [113, 114], there are some experimental steps, in which the thermal conductivity of aerogel in the form of blankets is significantly affected by the moisture content. The first one documented that the thermal conductivity increases by up to 15% as the relative humidity increases from 0% to 90%. Whereas the second study showed an increase by 36% in thermal conductivity in the same range of relative humidity. An increase in the thermal conductivity of aerogel-enhanced insulation materials due to high levels of moisture content was observed in the study [88]. Results showed that the thermal conductivity increased in a wide range of relative humidity from 0% to 95%. Additionally, there was a correlation between the density distribution and the increase in the λ -values in which the lower the density the lower the increasing rate of thermal conductivity.

The most beneficial conclusion from numerous studies mentioned above, is to elucidate the crucial impact of moisture content on thermal conductivity. As a result, thermal conductivity increases with increasing moisture content due to the presence of liquid phase. Moisture content is related to thermal conductivity in accordance with a linear law for most insulation materials. However, some experimental investigations of mineral wool and foamed insulation materials showed non-linear equations [46,66]. It could be caused by an increase in the quantity of air from the increasing the number and size of cells. Another reason could be the accuracy of experimental measurements and variable laboratory conditions or the imperfections of the materials. Supposing that higher moisture content increases thermal conductivity, Table 3 presents the increased linear between the λ -values and the moisture content of building insulation materials.

Table 3
Thermal conductivity as a linear function of moisture content.

Main group	Insulation Materials	Relationship	Moisture range (%)	Reference
Conventional materials	Fiberglass	$4.6e-5 \times w + 0.0372$	0–50	[63]
		$1.023e-3 \times w + 0.0323$	0–35	[89]
	Rock wool	$1e-5 \times w + 0.0398$	0–50	[63]
	EPS	$7e-4 \times w + 0.035$	0–80	[99]
		$0.017 \times w + 0.039$	0–40	[67]
	PUR	$0.00187 \times w + 0.039$	0–80	[100]
Alternative materials	Fiberboard	$2.31e-4 \times w + 0.0383$	0–14	[110]
	Bagasse	$7.2e-4 \times w + 0.08807$	5–30	[115]
	Hemp	$0.298 \times w + 0.118$	0–80	[69]
	Flax	$0.365 \times w + 0.157$	0–80	[69]
	Straw	$0.239 \times w + 0.088$	0–80	[69]
	Aerogel	$0.2 \times w + 0.01859$	0–6	[114]

3.3. Heat and moisture transport

Both operating temperature and relative humidity have a significant influence on the thermal energy performance of insulation materials. Employing experimental analyses, most of the studies have focused on determining the influencing temperature and moisture content in thermal conductivity in a steady state in which its value can be determined independently at a mean temperature and specific humidity. In reality, it is essential to determine a simultaneous calculation of the effect of influencing factors such as temperature, moisture levels, air velocity, and thickness in thermal conductivity due to the heat transport transient process. Therefore, many scholars focused on the combined effect of heat and moisture transfer simultaneously on the insulation λ -values of materials, based on numerical simulation and experimental investigation [50,72,92,99,116–119].

A numerical problem was modeled to study four stages of heat and moisture transfer in porous insulation materials [120]. The result showed that the effective thermal conductivity increases with increasing ambient humidity. The energy transfer in a multilayered building envelope was investigated through the coupled heat and moisture transfer. Modeling the problem in two dimensions and using the Comsol program [121], Liu et al. analyzed the change of temperature due to the change of moisture transfer with space and time in both horizontal and vertical directions. In order to obtain the actual thermal conductivity in the combined heat and moisture transfer mechanism of porous materials, i. e., normal concrete, clay brick and aerated concrete, Wang et al. [122] built a mathematical model calculating the actual thermal conductivity caused by moisture, different temperatures, and humidity. From the numerical model, there is an increase in the actual thermal conductivity when the temperature decreases, and the water vapor pressure increases. Khoukhi examined the combined effect of temperature and moisture content on the change of thermal conductivity of polystyrene materials and their impact on the energy performance of building [43]. The findings confirmed the increase of thermal conductivity as temperature and moisture content increase and the results can be used for reference to other insulation materials.

3.4. Density

3.4.1. Traditional materials

The density dependence of thermal conductivity of polystyrene, fiberglass, and mineral wool was investigated at various mean temperatures [42]. The thermal conductivity of expanded polystyrene (EPS) decreases from 0.043 and reached the minimum value of 0.032 W/(m.K) with rising density from 14 to 38 kg/m³ at a mean temperature of 10 °C [64]. There was no discussion for this behavior in the article, however, it may be explained by the air bubble sizes of porous materials in case of low density which are bigger than in the higher density foam materials. The higher bubbles provide more intense heat transfer through the material. As the density increases the air bubbles will be smaller and the frame structure become more complex. In the smaller bubble the heat transfer is lower, and additionally the more complex solid matrix system has a higher thermal resistance. By increasing the density, the solid content of the system will be higher consequently the thermal conductivity of solid parts become more dominant. These three phenomena (bubble size, complexity of the frame, amount of solid content) results an effective thermal conductivity which can reach a minimum value. Another study also found that the thermal conductivity of EPS decreases with increasing density in the range of 10 and 25 kg/m³ and the relationship was expressed by a linear function [123]. It is known that increasing density of the foam materials led to decreasing air content and size of the air inclusions. In this case, the convection of air and gas conduction are insignificant, and the heat flow is directed by the conduction of the solid particles resulting the decreased thermal conductivity. The experimental data of Khoukhi and Tahat contributed to the assumption that higher density produces lower thermal conductivity. In

their first study [65], they measured thermal conductivity of three polystyrene samples with different densities at four different temperatures varying from 10° to 43 °C using the guarded hot plate method. The result showed that lower material density leads to higher thermal conductivity values. An equivalent experiment was conducted to support this hypothesis in their next studies [49,124]. When testing four heat-insulated EPS and PU samples at the same temperature, the thermal conductivity first went down and then increased with an increase in density and reached its minimum value at 0.029 W/(m.K) and 0.026 W/(m.K) in the range of 17 to 18 kg/m³ and 30 to 45 kg/m³, respectively [56]. Experimental studies of 17 different inorganic samples were investigated with changing densities from 8.9 to 60 kg/m³ [37]. It is seen that the thermal conductivity decreases with increasing density for the same types of materials. Furthermore, the thermal conductivity of specimens having lower densities increased faster the others.

3.4.2. Alternative materials

Although conventional materials are mainly used in buildings, alternative materials derived from natural sources also show the same performance requirements in heating. A study with open-cell insulation materials which are made from hemp fibers found that a reduction of thermal conductivity with an increase of density due to the condensation inside the sample [125]. Whereas, the thermal conductivity of concrete-based hemp fibers increases by about 54% when the density increases by 2/3 [126]. The test of sheep wool showed the thermal conductivity decreases by up to 21% at 40 °C when the bulk density increases 50%, from 20 to 40 kg/m³ [66]. However, Sekino concluded the opposite trend in his experiment with cellulose fibers [127]. The λ -values increase slightly by approximately 5% with increasing density from 20 to 110 kg/m³. To explain this conclusion, a parameter named “the apparent thermal conductivity” was created to elucidate how density affects λ -values. The number of heat bridges formed by cellulose fibers increases with rising material density which causes increased thermal conductivity. The same result in investigating the effect of moisture on thermal conductivity at various of densities was obtained experimentally with three bio-based materials: hemp concrete, flax concrete, and rape straw concrete. It is showed that dry thermal conductivity was expressed as a linearly increasing function of the dry density [69]. Another study of G. Balciunas et al. [128] demonstrated that the thermal conductivity of hemp shives composites depends on 97% of density and the relationship shown as a multiple regression equation. Also, this specimen had low thermal conductivity from 0.055 to 0.076 W/(m.K) within the range of 210 to 410 kg/m³ due to the low density of the sapropel binder additive. Among the different types of natural fibers, coconut fiber has been used as the potential lightweight material when using as reinforcement in a composite. A study of three types of coconut samples exhibited that thermal conductivity decreased from 0.052 to 0.024 W/(m.K) with an increase in density from 30 to 120 kg/m³ [129].

Table 4 shows the increased linear of some fibrous insulation materials.

3.4.3. New technology materials

A model consisting of aerogel, calcium silicate and xonotlite-aerogel composite insulation materials was built to determine the effect of their

densities on their thermal conductivity [86]. In the range of optimal density from 110 to 160 kg/m³, the thermal conductivity of aerogel reached the minimum value of approximately 0.016 W/(m.K) and the density of calcium silicate was the key factor to affect the λ -values of the aerogel composite. Moreover, with an increase of the density of the silicate up to 250 kg/m³, the thermal conductivity of the aerogel composite increased by 200%. The relation between thermal conductivity and density is nonlinear, the limiting low value of thermal conductivity is 0.012 W/(m.K) which is denoted for density as 150 kg/m³ [131]. Investigation of VIPs with wood fiber core materials noted that their thermal conductivity increases slowly with increasing density less than 240 kg/m³ and rapidly increases since the density reaches 260 kg/m³ [132].

3.5. Thickness

It is a common understanding that the thicker the insulation, the lower the heat transfer through it [133]. However, thermal conductivity is not dependent on the thickness of insulation, which instead affects its thermal resistance [134].

Lakatos et al. investigated the dependence of the thermal conductivity on the thickness of the expanded materials [123]. They proved that thermal conductivity does not depend on the thickness of the specimens, contrary to the R-values. The thermal resistance increased regarding to the calculated data from the measurement. In another study with sheep wool, the thermal resistance showed an increase with increasing thickness of samples from 40 to 80 mm at varying of mean temperature [66]. Mahlia et al. evaluated the correlation between the thickness and the thermal resistance of fiberglass, urethane, EPS through the thermal conductivity values [135]. The main objective of the research was to point out the optimum thickness to achieve the highest thermal conductivity or the lowest thermal resistance.

The impact of thickness on the thermal transmittance of expanded polystyrene, glass wool, and wood cement board for the external wall structure has been investigated [136]. For construction, the thermal transmittance and its thermal resistance have a reciprocal relationship; the lower the thermal transmittance, the higher the thermal resistance; and consequently, the higher thermal insulation of wall structure. The results indicated that the thermal resistance increased for all three types of insulation material as the thickness increased up to 0.2 m. In addition, there is a critical thickness for the thermal insulation of the external wall. One of the popular ways to improve thermal performance is to use an enclosed air layer in exterior building envelopes since the air has low thermal conductivity. Zhang et al. found that the thermal resistance increased by 14.77% when the thickness of the air layer increased from 10 to 20 mm, but the effect was limited when the thickness exceeded 20 mm [137].

Insulation thickness with material costs, energy saving, and energy consumption was investigated in some studies whose data is shown in Table 5.

3.6. Air surface velocity

Air surface velocity can affect the heat transfer coefficients, and therefore, it can affect the heat transfer process. Higher the rate of air movement across a surface, higher is the rate of heat transfer, and consequently, higher the surface coefficient [141]. The outside surface convective heat transfer coefficient is a function of windward speed which varied from 1 to 10 m/s in a study. From this relationship, the higher the rate of air speed across a surface, the higher the rate of heat transfer through the building envelope. Consequently, the higher heat transfer coefficient resulted in the moderation in the temperature difference between outdoor and indoor temperature. Therefore, it influences the thermal performances of insulation materials. Effects of wind velocity and orientation were investigated considering four surface-to-air temperature differences [142]. Results showed that the

Table 4
Thermal conductivity as a linear function of density.

Insulation Materials	Relationship	Density range (kg/m ³)	Reference
Cellulose fiber	$1.73e-4 \times \rho + 0.0262$	20–110	[127]
Hemp concrete	$2.37e-4 \times \rho + 0.0196$	200–600	[69]
Flax concrete	$2.48e-4 \times \rho + 0.0192$	200–600	[69]
Straw concrete	$1.61e-4 \times \rho + 0.0221$	200–600	[69]
Straw bale	$1.9e-4 \times \rho + 0.045$	50–130	[130]

Table 5

Insulation thickness with material cost energy saving, and energy consumption of various thermal insulation materials.

Insulation Materials	Thermal conductivity (W/(m.K))	Thickness (mm)	Material cost (\$/m ³)	Energy Saving (\$/m)	Energy Consumption (MJ/f. u. kg)	Reference
Rock wool	0.04	50	95	6.2	53.09	[134,138,139]
Glass wool	0.038	50	155	5.6	229.02	[15,139]
Fiberglass	0.05	50	350	25.6	–	[139,140]
XPS	0.035	50	224	27.2	127.31	[37,134,139]
EPS	0.035	50	155	28.4	80.8–127	[15,30,37,139]
PUR	0.022	50	156	–	99.63	[15,139,140]
PIR	0.025	25	152	–	69.8	[15,139]
VIPs	0.008	5	247	–	149–226	[15,139]
Aerogels	0.015	20	547	–	53.9	[15,139]

wind velocity strongly affects the convective heat transfer coefficient, in which the wind direction had a notable effect for vertical walls and roofs, but the surface-to-air temperature difference had a negligible effect for wind velocity higher than 2 m/s. The obtained results are also useful for designing appropriate building envelopes. Moreover, when calculating the thermal properties of buildings and constructions, surface resistance should be considered on the outside and inside of the structure. Surface resistance generally comprises of the combined heat transfer by radiation and convection, it can be increased by decreasing the air velocity and can be used to calculate the energy need for heating or cooling [143].

In the laboratory, where sample is well-insulated and well-protected from the wind, there is negligible influence on the permeability of the insulation materials. However, in real climate conditions, there is a significant impact of wind on thermal performances of building envelopes, which has not yet been determined. Excellent thermal performance can be achieved by using thicker layer, higher airflow velocity, or lower thermal conductivity of porous material. The heat flux entering the indoor space can be reduced to practically zero, when the exhaust airflow velocity in porous layer reaches to 0.003 m/s [101].

3.7. Pressure

The most commonly used insulation materials in buildings are fibrous insulations. Heat transfers through a fibrous insulation involves combined modes of heat transfer: solid conduction through fibers, gas conduction and natural convection in the space between fibers, radiation interchange through participating media. If solid and radiative contributions are independent of gas pressure, changing pressure affects the effect of gas conduction to the effective thermal conductivity. This contribution investigated by Zhao et al. [144]. The results noted a significant increase in effective thermal conductivity of fibrous insulation materials from 0.01 to 0.04 W/(m.K) with an increase of pressure from 10^{-2} to 10^5 Pa.

Vacuum insulation panels (VIPs) are effective thermal insulators due to their lower thermal conductivity compared to other traditional insulation materials. The thermal conductivity coefficient of VIPs at vacuum pressure varied in the range of 0.001 to 0.002 W/(m.K). Some conventional materials used as the core in VIPs such as glass fiber, polyurethane foam, or polystyrene foam showed an increase in λ -values with increasing pressure in the range from 10 to 10^5 Pa [145]. For instance, the thermal conductivity of extruded polystyrene showed an increase from 0.006 W/(m.K) at 10 Pa to 0.031 at 10^5 Pa [146]. A possible explanation is that the thermal conductivity of air inside the pore structures increases when the pressure increases from vacuum to ambient over the time [147]. Another potential insulation material, aerogel, has low thermal conductivity of approximately 0.0135 W/(m.K) at ambient pressure and can be reduced to 0.004 W/(m.K) at a pressure reduced to 50 mbar [83]. Liu Hua et al. [87] documented the effective thermal conductivity of silica aerogel increased nonlinearly from 0.014 to 0.044 W/(m.K) with raising the pressure using the inverse method.

The other specimens of aerogel and xonotlite calcium silicate also showed a considerable decrease in thermal conductivity with a drop of pressure, and approach to a constant when pressure is less than 10^4 Pa, and 10^2 Pa, respectively [86]. The same trend was also derived from the experimental study of Tang et al. [61].

3.8. Aging

It is generally known that the mechanical properties and thermal performances of insulation materials alter significant over the time. One of the most impactful aging influences on the thermal conductivity is the diffusion of the highly insulating blowing agents, and the infusion of air from the environment which may absorb moisture into the material [148]. Bhattacharjee et al. has first given the model of thermal conductivity of foam insulation materials which experience three stages throughout their aging process [149]. The impact of environmental aging, through exposure to high temperature and moisture on the temperature and humidity dependent conductivity of polyurethane (PUR) and polyisocyanurate (PIR) foam materials has investigated in the study [148]. Results showed that the thermal conductivity of closed-cell PUR is much higher after the aging from 1 to 4.5 months and the change in the first month is greater than the rate change later in the process. Whereas the effect of aging in the open-cell PUR is minimal but the initial λ -value is higher than the measured closed-cell materials. In case of determining the moisture dependent conductivity, all samples were stored in the chamber to expose the materials from dry state to relative humidity of 90%. The effective thermal conductivity was subsequently observed that there was a slightly increase with higher humidity, especially at very low temperature. In the latest study of Winkler-Skalna et al. [90], the changes in the effective thermal conductivity of five PUR samples with the effects of density, thickness, and average temperature after the aging was analyzed. The first stage is to determine the initial thermal conductivity values at different mean temperature before heating for 7 days, 21 days, 90 days, and 175 days. For most PUR types, the highest increment in the value of λ coefficient with mean temperature was noted in the 7 days and 21 days of conditioning. Meanwhile, there was a distinct drop in the rise of the λ coefficient with increasing density from 40 kg/m³ to 80 kg/m³. To investigate the effect of the age of materials on the effective thermal conductivity of foam insulation, Berardi observed the impact of temperature and moisture content on thermal conductivity in a pristine condition and after heating for 4.5 months [148]. As a result, there is a minimal increase in thermal conductivity with temperature of polyurethane materials after aging. It is explained by the diffusion of gas in the material of lower density, because the lower is the apparent density of the foam material, the higher the percentage of gas filling up the cells, and thus the higher the impact of aging.

The main aging mechanism of VIPs are moisture penetration and air impact in which air causes the pressure growth inside the materials and moisture can penetrate the core structure [131]. The influence of aging on thermal properties was also tested for VIPs in some studies [146,

150]. Fantucci et al. [48] evaluated the changes in thermal conductivity of VIPs with aging. It showed a rapid increase of λ -values from 0.0048 to 0.0051 W/(m.K) after the first 20 months and a slow increase between 8% and 10% for the next 20 months. Generally, in order to predict the aging influence and further exceed the service life of VIPs, it is essential to determine the gas and water vapor permeance velocity as well as the relation between these parameters and the materials properties, size, and temperature of the VIPs.

In general, evaluation of the effects of aging through the temperature, moisture, density on the dependence of thermal conductivity is very useful to develop the hygrothermal models in order to assess how insulation materials perform over the life cycle of a building under real environmental conditions.

4. Discussion

Insulation materials can be classified as conventional and state-of-the-art materials. Specifically, conventional materials are fibrous materials including inorganic such as fiber glass, mineral wool (rock wool, glass wool) or natural/bio-based insulation materials and organic, like, polystyrene, polyurethane (PUR), polyisocyanurate (PIR). Besides, recent applications in building envelopes are using innovative materials such as vacuum insulation panels (VIPs), aerogel due to their high thermal resistance. Most of commonly used building insulation materials considerable influenced by the environmental conditions due to their porous structure and the proportional of air or other gas filling up the cells. The heat conduction of an insulator is strongly influenced by several factors: temperature, moisture content, density, aging time, along with secondary factors such as raw material, cell gases, nature and microstructural of solid component, air surface velocity, pressing, and sample thickness. A comparison of thermal conductivity and density in common building insulation materials collected from published studies are shown in Fig. 1 [8,12,28,32,35,37,42,46–48,63–66,80,89,96,151–157]. Materials having low thermal conductivity (below 0.05 W/(m.K)) and low density (below 100 kg/m³) are placed in the first group. These are the most commonly used insulation materials in buildings today. The second group with aerogel and VIPs also has low thermal conductivity, but higher density than that in the first group. The last group shows materials with the highest thermal conductivity and the highest density.

Due to the fact that molecule movements is the basic of heat conduction, the temperature has a huge impact on thermal conductivity of insulation materials. Fig. 2 shows an increase in thermal conductivity for four groups of insulation materials with increasing mean temperature

from -10° to 50 °C [28,37,42,48,66,68,69,88]. Fibrous insulation materials such as fiberglass, hemp fibers, flax fibers, cellulose fibers, sheep wool are more affected by temperature than other insulation materials. Besides, thermal conductivity of samples having lower densities increased faster in relation to the increase in temperature. In other words, low density implies large pore volume and much more air content which causes a greater effect of operating temperature on λ -values. Additionally, the starting thermal conductivity of the open cell materials (fiberglass, rockwool) is much higher than that of the closed-cell materials (XPS, EPS, PUR). due to the high initial moisture content of the samples. Also, the thermal conductivity of aerogel and VIPs may be 2–3 times lower than that of conventional insulating materials. The increase in the thermal conductivity of new advanced materials is subjected to high levels of temperature, moisture content, and aging effect. Combined insulation materials also exhibit temperature-dependence due to the high density and water absorption from surroundings. It is reported that the temperature-dependent laws is linear.

Changes in thermal conductivity due to moisture variations can be explained by a shift in the division of the thermal and humidity distribution in the structure, which alters the sorption properties of the material. Fig. 3 [63,66,88,115,158] illustrates the changes in thermal conductivity as the moisture content increases. The thermal conductivity of natural fibrous insulating materials rises more sharply than that of foam materials for the same increase in moisture content at the same temperature of 24 °C. Since the fibrous materials are naturally hygroscopic and have a porous structure, they can accumulate moisture by adsorption from the air. The ability of moisture to penetrate into the internal open pore system at increased relative humidity significantly affects the temperature distribution as well as the thermal conductivity. Examination of results revealed that higher moisture content is always related to higher thermal conductivity for all densities. In addition, samples with higher density generally exhibit larger changes in λ -values at the same moisture content. Materials having similar density but conditioned at different initial moisture content exhibit different relationships between the thermal conductivity and moisture content. The rate of change in thermal conductivity with moisture content is higher at higher initial moisture content. The lower the density of open-cell insulation materials, the higher the effect of moisture content on the thermal conductivity. An increasing in thermal conductivity of aerogel with increasing moisture content reflects that the hydrophilic properties of the materials need to be investigated for use in building and construction.

Recent studies confirmed that thermal building materials are considerably influenced by moisture and to a lesser degree, by ambient

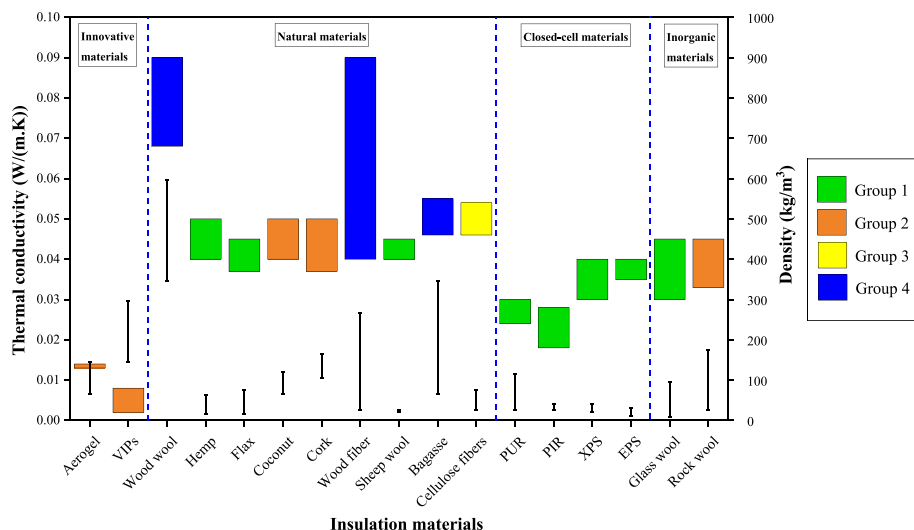


Fig. 1. Comparison of thermal conductivity and density in common insulating materials.

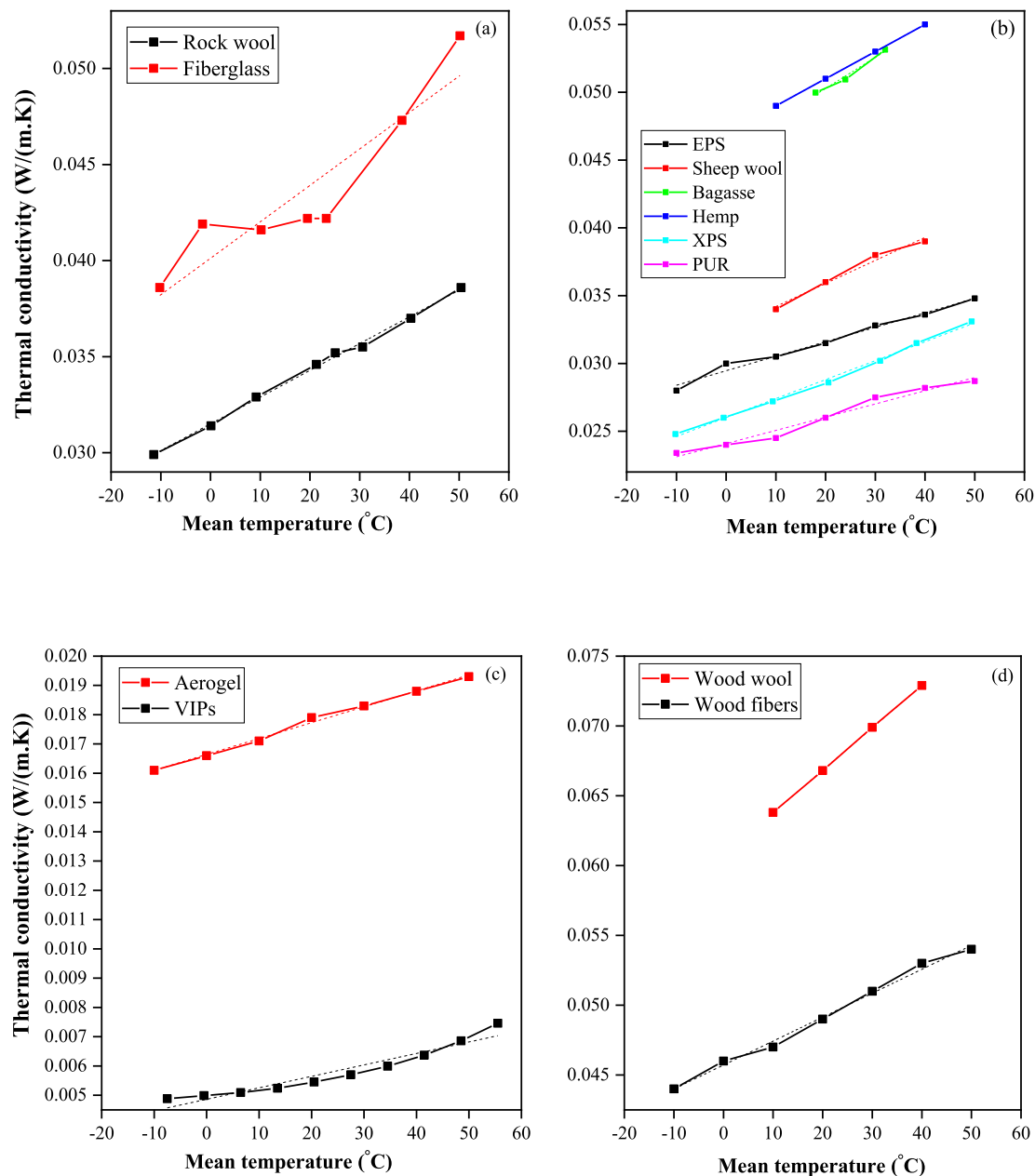


Fig. 2. Effect of mean temperature on thermal conductivity of various building insulation materials: (a) inorganic materials; (b) organic materials; (c) advanced materials; (d) combined materials.

temperature. Due to the accumulation of moisture on the surface of a building envelope, some vapor condenses into liquid and changes the relative humidity. This leads to an increase in thermal conductivity by an extent greater than that caused by the temperature variation. However, these studies have primarily focused on foam insulation materials with a large moisture content and latent heat storage capacity. Hence, it is crucial to study the combined effect of heat and moisture transfers on the thermal conductivity of building components.

The density is critical for the thermal performance of an insulating material. Fig. 4 illustrates the variation in thermal conductivity at mean temperature of 24 °C with density of conventional insulation materials (Fig. 4a) and natural fibrous insulating materials (Fig. 4b). Generally, the most favourable densities range for practical investigation falls between 20 and 140 kg/m³.

For closed-cell materials, it can be stated that high density shows low thermal conductivity. At densities range from 20 to 40 kg/m³, the thermal conductivity of EPS, XPS, and PUR insulation materials shows

the trend that decreases as density increases as shown in Fig. 4a [37,42, 63]. It is because higher density means smaller pores and less than air volume, resulting in the heat flow through the materials is mainly governed by the thermal conduction of the solid particles, while the effect of the heat transfer by convection and radiation becomes insignificant. This causes a decrease in λ -values. Besides, the variation in thermal conductivity values of EPS and PUR can be explained by the difference of microstructure, porosity, and pore dimensions of the foam insulation materials. The thermal conductivity of open-cell materials also shows the linear decrease as the density increases in the range of 40 and 140 kg/m³ and the changes in thermal conductivity values of mineral wool and fiberglass can be explained by the air bubbles present in the porous structures. Besides, the effect of density on thermal conductivity of open-cell materials is generally lesser than that of closed-cell materials. It is because the diffusion of gas in the foam materials; the higher the apparent density the lower the proportional of gas filling up the cells, and thus the lower the impact of other influencing factors like

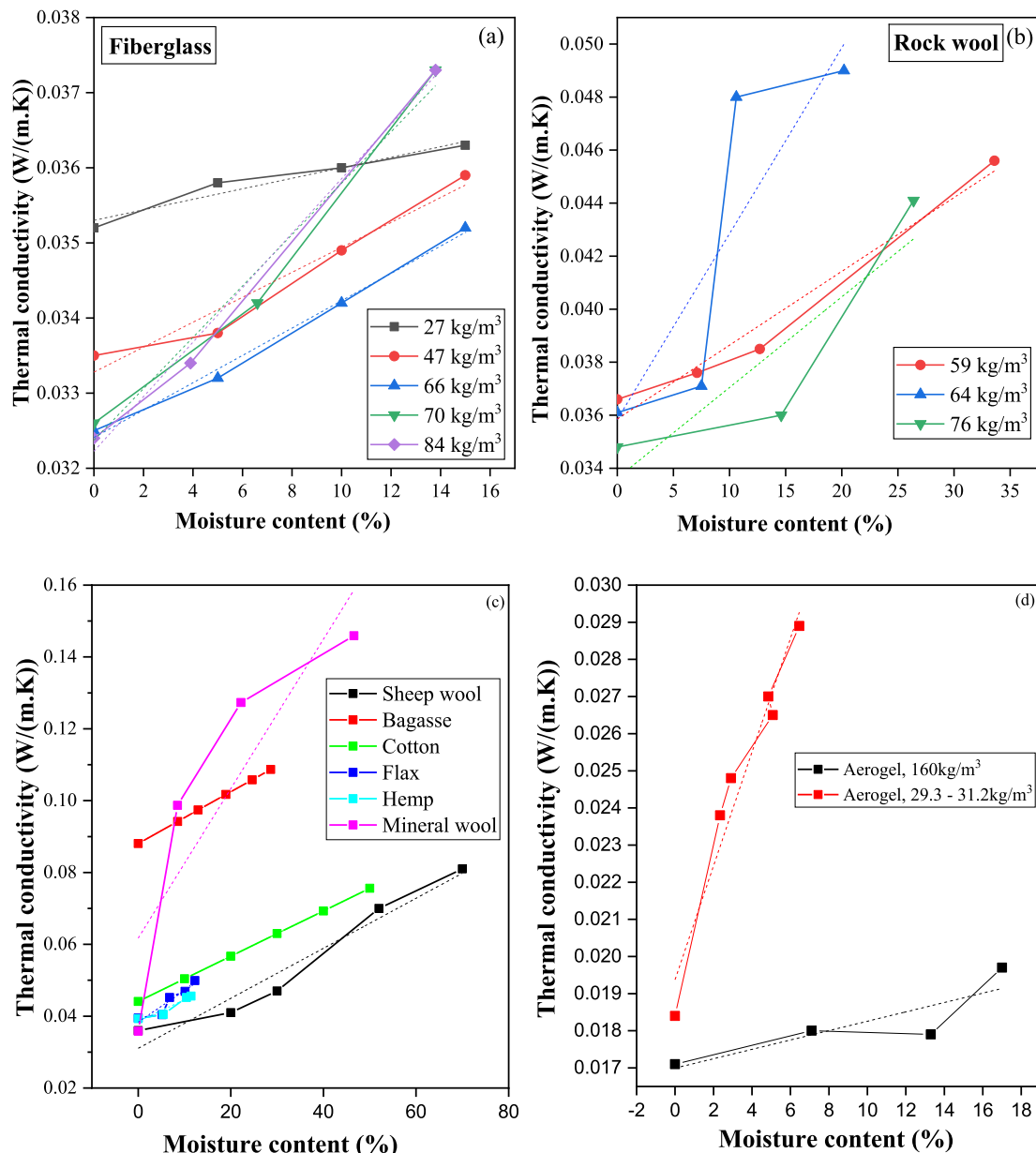


Fig. 3. Effect of moisture content on thermal conductivity of various building insulation materials: (a) fiberglass, (b) rockwool; (c) natural materials; (d) aerogel.

mean temperature, moisture content, or aging. On the other hand, fibrous materials such as bagasse, palm, coconut fibers showed the variation in which the thermal conductivity decreased to a minimum and then increased as density increased from the minimum possible value upwards [66,129,155]. This behavior shows the same reaction with the result in article [64], therefore, it can be explained by three phenomenon include bubble size, complexity of the frame, and the amount of solid particles. Besides, the non-linear decrease may come from the reduction of wettability and absorbability due to a reduction of the voids in open structure of the natural fiber since increased density. The decreased thermal conductivity may be explained by the heat conduction mechanism, if fibrous materials are high density, thermal conductance through the solid particles is more important than both radiation and convection. In this conduction, the thermal conductivity is decreased while the density increases. Additionally, it is also shown that an increase in solid fiber density reflected an increase in thermal conductivity values of the fibrous batt after reaching the minimum value and it is consistent with loose fill materials having higher thermal conductivity than closed-cell insulation materials.

5. Conclusions

This comprehensive review provides a detailed discussion on the factors influencing the thermal conductivity of insulation materials. Temperature, moisture content, and bulk density are the primary factors significantly affecting the thermal conductivity coefficient, depending on the material. Other factors such as thickness, airflow velocity, pressure, aging also influence the thermal performances. In most cases, the thermal conductivity shows a linearly increasing trend with temperature. The moisture content strongly affects the thermal conductivity of both organic and inorganic materials. Bulk density also plays an important role in determining the thermal conductivity with opposite trends, it may exhibit a linear decrease for conventional materials and nonlinear variation for organic materials. This function seems to be linear decrease in types of conventional materials or shows a non-linear with natural fiber materials. Depending on the relationship between thermal conductivity and influencing factors, fibrous insulation materials show more sensitivity to temperature, moisture, and density compared to the other conventional materials. Understanding the

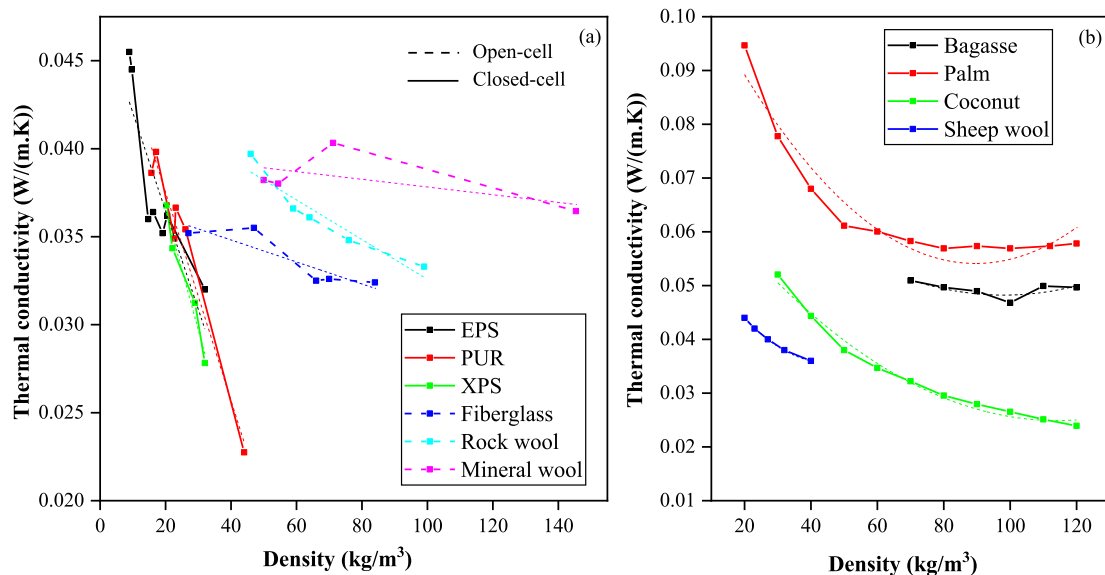


Fig. 4. Effect of density on thermal conductivity of various building insulation materials: (a) conventional insulation materials; (b) natural fibrous insulation materials.

quantitative relationship between the effective thermal conductivity and the influencing factors of the insulation materials is fundamental in determining the envelope heat, mass transfer, and building energy consumption.

Published studies demonstrate that influencing factors cannot be ignored. Recently, the design methods calculate with a standardized value, measured in ideal laboratory conditions and these results are shown in marketing products. However, reality is much more transient. With the increasing importance of energy savings and decreasing the embodied energy of insulation materials, more sophisticated calculation methods will be needed in the near future. These new methods can rearrange the evaluation aspects, but undoubtedly will need more complex technical equipment and calculation processes. In fact, new calculation methods could not determine the perfect values, but they provide a better approximation of the performance of insulation. Furthermore, the research gaps found in some publications and existing empirical studies should be considered in future works.

In further investigations, it would be interesting to compare the calculated thermal performance and the real performance on the site of an insulated structure. This finding provides the following insights for future research to examine the dependence of thermal properties including thermal conductivity, thermal diffusivity, heat specific capacity, coefficient of thermal expansion on their moisture content, temperature differences, density, and air velocity of the thermal insulators derived from natural fibers.

Declaration of competing interest

The authors declare that they have no known competing financial interests or personal relationships that could have appeared to influence the work reported in this paper.

Acknowledgement

The work was carried out as part of the "Sustainable Raw Material Management Thematic Network – RING 201", EFOP-3.6.2-16-2017-00010 project in the framework of the Széchenyi 2020 Program. The realization of this project was supported by the European Union, and co-financed by the European Social Fund.

References

- [1] S. Lemmet, *Buildings and Climate Change. Summary for Decision-Makers*, UNEP SBCI, 2009.
- [2] E. Useia, *International energy outlook 2018 - highlights*. https://www.eia.gov/pressroom/presentations/capuno_07242018.pdf, 2018.
- [3] J.G. Olivier, K. Schure, J. Peters, *Trends in Global CO2 and Total Greenhouse Gas Emissions*, PBL Netherlands Environmental Assessment Agency, 2017, p. 5.
- [4] S. Solomon, *IPCC (2007): Climate Change the Physical Science Basis vol. 2007*, AGU, 2007. U43D-U01.
- [5] R. Pachauri, A. Reisinger, *Climate Change 2007. Synthesis Report. Contribution of Working Groups I, II and III to the Fourth Assessment Report*, Cambridge University Press, Cambridge, 2008.
- [6] R. American Society of Heating, I. Air Conditioning Engineers, *ASHRAE Fundamentals Handbook 2001* (SI, American Society of Heating, Refrigerating & Air Conditioning Engineers, Incorporated, 2001.
- [7] M.S. Al-Homoud, *Performance characteristics and practical applications of common building thermal insulation materials*, *Build. Environ.* 40 (3) (2005) 353–366.
- [8] H. Zhang, W.-Z. Fang, Y.-M. Li, W.-Q. Tao, *Experimental study of the thermal conductivity of polyurethane foams*, *Appl. Therm. Eng.* 115 (2017) 528–538.
- [9] R. Walker, S. Pavia, *Thermal performance of a selection of insulation materials suitable for historic buildings*, *Build. Environ.* 94 (2015) 155–165.
- [10] L. Aditya, T. Mahlia, B. Rismanchi, H. Ng, M. Hasan, H. Metselaar, O. Muraza, H. Aditya, *A review on insulation materials for energy conservation in buildings*, *Renew. Sustain. Energy Rev.* 73 (2017) 1352–1365.
- [11] F. D'Alessandro, S. Schiavoni, F. Bianchi, F. Asdrubali, *Insulation materials for the building sector: a review and comparative analysis*, *Renew. Sustain. Energy Rev.* 62 (2016) 988–1011.
- [12] B. Abu-Jdayil, A.-H. Mourad, W. Hittini, M. Hassan, S. Hameedi, *Traditional, state-of-the-art and renewable thermal building insulation materials: an overview*, *Construct. Build. Mater.* 214 (2019) 709–735.
- [13] B. Peavy, *A heat transfer note on temperature dependent thermal conductivity*, *J. Therm. Insul. Build. Envelopes* 20 (1) (1996) 76–90.
- [14] N. Yüksel, *The Review of Some Commonly Used Methods and Techniques to Measure the Thermal Conductivity of Insulation Materials*, *Insulation Materials in Context of Sustainability*, IntechOpen, 2016.
- [15] W. Villasmil, L.J. Fischer, J. Worlitschek, *A review and evaluation of thermal insulation materials and methods for thermal energy storage systems*, *Renew. Sustain. Energy Rev.* 103 (2019) 71–84.
- [16] B.P. Jelle, *Traditional, state-of-the-art and future thermal building insulation materials and solutions—Properties, requirements and possibilities*, *Energy Build.* 43 (10) (2011) 2549–2563.
- [17] E.C.f. Standardization, *Thermal Performance of Building Materials and Products - Determination of Thermal Resistance by Means of Guarded Hot Plate and Heat Flow Meter Methods - Dry and Moist Products of Medium and Low Thermal Resistance*, 2001.
- [18] E.C.f. Standardization, *Thermal Performance of Building Materials and Products - Determination of Thermal Resistance by Means of Guarded Hot Plate and Heat Flow Meter Methods - Products of High and Medium Thermal Resistance*, 2001.
- [19] E.C.f. Standardization, *Thermal Performance of Building Materials and Products - Determination of Thermal Resistance by Means of Guarded Hot Plate and Heat Flow Meter Methods - Thick Products of High and Medium Thermal Resistance*, 2000.

- [20] A.C.- ASTM International, Standard Test Method for Steady-State Thermal Transmission Properties by Means of the Heat Flow Meter Apparatus.
- [21] A.C.- ASTM International, Standard Test Method for Steady-State Heat Flux Measurements and Thermal Transmission Properties by Means of the Guarded-Hot-Plate Apparatus, pp.
- [22] Y. N, The Investigation of Structure and Operating Parameters Effect on the Heat Transfer Coefficient in Porous Structures, Uludag University, Bursa, 2010.
- [23] A.M. Papadopoulos, State of the art in thermal insulation materials and aims for future developments, *Energy Build.* 37 (1) (2005) 77–86.
- [24] M. Pfundstein, R. Gellert, M. Spitzner, A. Rudolphi, *Insulating Materials: Principles, Materials, Applications*, Walter de Gruyter, 2012.
- [25] A. Karamanos, S. Hاديarakou, A. Papadopoulos, The impact of temperature and moisture on the thermal performance of stone wool, *Energy Build.* 40 (8) (2008) 1402–1411.
- [26] H. Wieland, D.P. Murphy, H. Behring, C. Jäger, P. Hinrichs, F.-J. Bockisch, Perspektiven für Dämmstoffe aus heimischen nachwachsenden Rohstoffen, *Landtechnik* 55 (1) (2000) 22–23, 22–23.
- [27] H. Zhang, *Building Materials in Civil Engineering*, Elsevier, 2011.
- [28] U. Berardi, M. Naldi, The impact of the temperature dependent thermal conductivity of insulating materials on the effective building envelope performance, *Energy Build.* 144 (2017) 262–275.
- [29] J.-W. Wu, W.-F. Sung, H.-S. Chu, Thermal conductivity of polyurethane foams, *Int. J. Heat Mass Tran.* 42 (12) (1999) 2211–2217.
- [30] S. Omer, S. Riffat, G. Qiu, Thermal insulations for hot water cylinders: a review and a conceptual evaluation, *Build. Serv. Eng. Technol.* 28 (3) (2007) 275–293.
- [31] S. Panyakaew, S. Fotios, New thermal insulation boards made from coconut husk and bagasse, *Energy Build.* 43 (7) (2011) 1732–1739.
- [32] A. Hoseini, C. McCague, M. Andisheh-Tadbir, M. Bahrami, Aerogel blankets: from mathematical modeling to material characterization and experimental analysis, *Int. J. Heat Mass Tran.* 93 (2016) 1124–1131.
- [33] F. Domínguez-Muñoz, B. Anderson, J.M. Cejudo-López, A. Carrillo-Andrés, Uncertainty in the thermal conductivity of insulation materials, *Energy Build.* 42 (11) (2010) 2159–2168.
- [34] A. Bakatovich, F. Gaspar, Composite material for thermal insulation based on moss raw material, *Construct. Build. Mater.* 228 (2019) 116699.
- [35] I. Cetiner, A.D. Shea, Wood waste as an alternative thermal insulation for buildings, *Energy Build.* 168 (2018) 374–384.
- [36] A.S. C168, Terminology Relating to Thermal Insulating Materials, 2013.
- [37] M. Koru, Determination of thermal conductivity of closed-cell insulation materials that depend on temperature and density, *Arabian J. Sci. Eng.* 41 (11) (2016) 4337–4346.
- [38] P. Čech, D. Tesárová, J. Hadačová, E. Jerábková, The quality of indoor air in wooden based buildings and the factors with impact of them, *Wood Res.* 61 (4) (2016) 583–598.
- [39] M. Khoukhi, The combined effect of heat and moisture transfer dependent thermal conductivity of polystyrene insulation material: impact on building energy performance, *Energy Build.* 169 (2018) 228–235.
- [40] C. ASTM, 518, Standard Test Method for Steady-State Thermal Transmission Properties by Means of the Heat Flow Meter Apparatus, Annual Book of ASTM Standards, 2008.
- [41] ISO, Thermal Insulation-Determination of Steady-State Thermal Resistance and Related Properties-Heat Flow Meter Apparatus, International Standards Organization Geneva, Switzerland, 1991.
- [42] A.A. Abdou, I.M. Budaiwi, Comparison of thermal conductivity measurements of building insulation materials under various operating temperatures, *J. Build. Phys.* 29 (2) (2005) 171–184.
- [43] M. Khoukhi, Simultaneous changes of temperature and moisture of thermal conductivity of EPS insulation material and its impact on building energy performance, *Int. J. Smart Grid Clean Energy* 8 (2) (2019).
- [44] N.F. Shahedan, M.M.A.B. Abdullah, N. Mahmed, A. Kusbiantoro, M. Binhussain, S.N. Zailan, Review on Thermal Insulation Performance in Various Type of Concrete, AIP Conference Proceedings, AIP Publishing LLC, 2017, 020046.
- [45] U. Berardi, The impact of temperature dependency of the building insulation thermal conductivity in the Canadian climate, *Energy Procedia* 132 (2017) 237–242.
- [46] A. Ahmed, A. Qayoum, F.Q. Mir, Investigation of the thermal behavior of the natural insulation materials for low temperature regions, *J. Build. Eng.* 26 (2019) 100849.
- [47] F. Ochs, H. Müller-Steinhagen, Temperature and Moisture Dependence of the Thermal Conductivity of Insulation Materials, NATO Advanced Study Institute on Thermal Energy Storage for Sustainable Energy Consumption (TESSEC), Izmir, Csmes, 2005.
- [48] S. Fantucci, A. Lorenzati, A. Capozzoli, M. Perino, Analysis of the temperature dependence of the thermal conductivity in Vacuum Insulation Panels, *Energy Build.* 183 (2019) 64–74.
- [49] M. Khoukhi, M. Tahat, Effect of temperature and density variations on thermal conductivity of polystyrene insulation materials in Oman climate, *J. Eng. Phys. Thermophys.* 88 (4) (2015) 994–998.
- [50] E. Troppová, M. Švehlík, J. Tippner, R. Wimmer, Influence of temperature and moisture content on the thermal conductivity of wood-based fibreboards, *Mater. Struct.* 48 (12) (2015) 4077–4083.
- [51] B. Suleiman, J. Larfeldt, B. Leckner, M. Gustavsson, Thermal conductivity and diffusivity of wood, *Wood Sci. Technol.* 33 (1999) 465–473.
- [52] R. Besant, E. Miller, Thermal Resistance of Loose-Fill Fiberglass Insulation Spaces Heated from below, Thermal Performance of the Exterior Envelope of Building II, ASHRAE/DOE Conference, 1982, pp. 720–733.
- [53] D. Aldrich, R. Bond, Thermal Performance of Rigid Cellular Foam Insulation at Subfreezing Temperatures, Thermal Performance of the Exterior Envelopes of Buildings III, ASHRAE/DOE/BTECC Conference, 1985, pp. 500–509.
- [54] F. Ochs, W. Heidemann, H. Müller-Steinhagen, Effective thermal conductivity of moistened insulation materials as a function of temperature, *Int. J. Heat Mass Tran.* 51 (3–4) (2008) 539–552.
- [55] Y. Xu, Z. Zeng, H. Lv, Temperature dependence of apparent thermal conductivity of compacted bentonites as buffer material for high-level radioactive waste repository, *Appl. Clay Sci.* 174 (2019) 10–14.
- [56] H.Y. Song, X.X. Cheng, L. Chu, Effect of Density and Ambient Temperature on Coefficient of Thermal Conductivity of Heat-Insulated EPS and PU Materials for Food Packaging, *Applied Mechanics and Materials*, Trans Tech Publ, 2014, pp. 152–155.
- [57] I. Budaiwi, A. Abdou, M. Al-Homoud, Variations of thermal conductivity of insulation materials under different operating temperatures: impact on envelope-induced cooling load, *J. Architect. Eng.* 8 (4) (2002) 125–132.
- [58] Z. Misri, M. Ibrahim, A. Awal, M. Desa, N. Ghadzali, Review on Factors Influencing Thermal Conductivity of Concrete Incorporating Various Type of Waste Materials, IOP Conference Series: Earth and Environmental Science, IOP Publishing, 2018, 012141.
- [59] S.B. Coşkun, M.T. Atay, Fin efficiency analysis of convective straight fins with temperature dependent thermal conductivity using variational iteration method, *Appl. Therm. Eng.* 28 (17–18) (2008) 2345–2352.
- [60] Q. Zhong, H. Kou, L. Yang, Y. Tao, C. Luo, Z. Xu, Factors influencing variations in the thermal conductivity of polycrystalline ZnS and Cr²⁺: ZnS, *Mater. Lett.* 158 (2015) 222–224.
- [61] Q. Tang, J. He, W. Zhang, Influencing factors of thermal contact conductance between TC4/30CrMnSi interfaces, *Int. J. Heat Mass Tran.* 86 (2015) 694–698.
- [62] Y. Xu, Z. Zeng, H. Lv, Effect of temperature on thermal conductivity of lateritic clays over a wide temperature range, *Int. J. Heat Mass Tran.* 138 (2019) 562–570.
- [63] A. Abdou, I. Budaiwi, The variation of thermal conductivity of fibrous insulation materials under different levels of moisture content, *Construct. Build. Mater.* 43 (2013) 533–544.
- [64] I. Gnip, S. Vėjelis, S. Vaitkus, Thermal conductivity of expanded polystyrene (EPS) at 10 °C and its conversion to temperatures within interval from 0 to 50 °C, *Energy Build.* 52 (2012) 107–111.
- [65] M. Khoukhi, M. Tahat, Effect of Operating Temperatures on Thermal Conductivity of Polystyrene Insulation Material: Impact on Envelope-Induced Cooling Load, *Applied Mechanics and Materials*, Trans Tech Publ, 2014, pp. 315–320.
- [66] J. Zach, A. Korjenic, V. Petránek, J. Hroudová, T. Bednar, Performance evaluation and research of alternative thermal insulations based on sheep wool, *Energy Build.* 49 (2012) 246–253.
- [67] M. Khoukhi, A. Hassan, S. Al Saadi, S. Abdelbaqi, A dynamic thermal response on thermal conductivity at different temperature and moisture levels of EPS insulation, *Case Stud. Therm. Eng.* 14 (2019) 100481.
- [68] K. Manohar, D. Ramalakhan, G. Kochhar, S. Haldar, Biodegradable fibrous thermal insulation, *J. Braz. Soc. Mech. Sci. Eng.* 28 (1) (2006) 45–47.
- [69] M. Rahim, O. Douzane, A.T. Le, T. Langlet, Effect of moisture and temperature on thermal properties of three bio-based materials, *Construct. Build. Mater.* 111 (2016) 119–127.
- [70] S. Srivaro, Z. Börcsök, Z. Pásztor, Temperature Dependence of Thermal Conductivity of Heat-Treated Rubberwood, *Wood Material Science & Engineering*, 2019, pp. 1–4.
- [71] H.-K. Kim, J. Jeon, H.-K. Lee, Workability, and mechanical, acoustic and thermal properties of lightweight aggregate concrete with a high volume of entrained air, *Construct. Build. Mater.* 29 (2012) 193–200.
- [72] L. Nguyen, A.-L. Beaucour, S. Ortola, A. Noumowé, Experimental study on the thermal properties of lightweight aggregate concretes at different moisture contents and ambient temperatures, *Construct. Build. Mater.* 151 (2017) 720–731.
- [73] Z. Pásztor, T. Horváth, S.V. Glass, S. Zelinka, Experimental investigation of the influence of temperature on thermal conductivity of multilayer reflective thermal insulation, *Energy Build.* 174 (2018) 26–30.
- [74] K. Chu, C. Jia, X. Liang, H. Chen, Temperature dependence of thermal conductivity in SiCp based metal–matrix composites, *Mater. Sci. Technol.* 27 (1) (2011) 91–94.
- [75] R. Khordad, F. Razi, Effect of temperature and distribution function of depolarization factor on thermal conductivity of carbon nanotube-based composites, *Superlattice. Microsc.* 64 (2013) 439–450.
- [76] M. Zain-ul-Abidin, S. Azeem, S.M. Shah, Computational investigation of factors affecting thermal conductivity in a particulate filled composite using finite element method, *Int. J. Eng. Sci.* 56 (2012) 86–98.
- [77] S.K. Das, N. Putra, P. Thiesen, W. Roetzel, Temperature dependence of thermal conductivity enhancement for nanofluids, *J. Heat Tran.* 125 (4) (2003) 567–574.
- [78] H.A. Mints, G. Roy, C.T. Nguyen, D. Doucet, New temperature dependent thermal conductivity data for water-based nanofluids, *Int. J. Therm. Sci.* 48 (2) (2009) 363–371.
- [79] X. Wang, H. Yu, L. Li, M. Zhao, Research on temperature dependent effective thermal conductivity of composite-phase change materials (PCMs) wall based on steady-state method in a thermal chamber, *Energy Build.* 126 (2016) 408–414.
- [80] H. Guo, S. Cai, K. Li, Z. Liu, L. Xia, J. Xiong, Simultaneous test and visual identification of heat and moisture transport in several types of thermal insulation, *Energy* 197 (2020) 117–137.

Unified Failure Strength Analysis for Terrace Slope Reinforcement Materials

Akashprava Panda, *Department of Civil Engineering, Aryan Institute of Engineering & Technology, Bhubaneswar, a_panda12@gmail.com*

Nalinikanta Swain, *Department of Mechanical Engineering, Capital Engineering College, Bhubaneswar, nalini_526@yahoo.co.in*

Tapan Kumar Mohanty, *Department of Mechanical Engineering, Aryan Institute of Engineering & Technology, Bhubaneswar, tapankmohanty789@yahoo.co.in*

Jyotikusum Acharya, *Department of Civil Engineering, NM Institute of Engineering & Technology, Bhubaneswar, jyotikusumacharya@yahoo.co.in*

ABSTRACT

The failure strength criterion of terrace slope reinforcement materials, such as lean cemented sand and gravel (LCSG) material, under a tri axial stress state is investigated in this research. Based on experimental results and literature data, cement content and confining pressure were chosen as main components to evaluate their influence on the peak stress of terrace slope reinforcement materials. Under four confining pressure levels, the mechanical characteristics of LCSG samples with cement contents of 60, 80, and 90 kg/m³ and non cemented sand and gravel materials were tested (namely, 300, 600, 1000, and 1500 k Pa). The results reveal that as the confining pressure is increased, the strength of the LCSG material improves. When the confining pressure exceeds 1200 k Pa, the rate of strength increase for LCSG and other cemented grained materials often slows. The material strength increases in a linear fashion as the cement content rises. Damage will occur at the particle cemented site along the shear plane when the axial load reaches a particular value, and the resistive stress caused by the cementation will display a tendency of growth first and then attenuation, while the friction between particles will increase by degrees. Based on the found strength properties of LCSG material under various cement contents and confining pressures, a new strength criteria for LCSG and other comparable materials is presented that includes frictional and cementing strengths. The findings of this study can be used as a theoretical foundation for calculating the stability of terrace slopes and LCSG dams.

1. Introduction

In China, most regions from the south of the Qinling Mountains and to the north of the Bashan Mountains are earth-rock mountainous areas where 81% of the cultivated land is sloping land. Owing to the climatic conditions in these regions, heavy rainfall and frequent rainstorms occur for extended periods of time, resulting in severe soil erosion. Accordingly, the local government has implemented measures to transform the sloping farmlands and build level terraces to prevent soil and water loss. These level terraces are of concern to the production growth of local grains and for guaranteeing the satisfactory livelihoods of local residents. However, most terraced ridges are formed by artificial tamping that are liable to collapse considering the characteristics of soil and stone materials, the slope condition, the

construction technology adopted, and unreasonable human activities. The material solidification method, which involves the addition of materials such as cement [1], high polymer [2], zeolite stabilizer [3], natural calcarene [4], lime [5], bacteria, and other microorganisms [6] to improve the strength and stability of the gravel or soil, is used to reinforce the slopes [7]. The materials formed on the basis of the aforementioned method are essentially cemented sand and gravel, cemented coarse soil, and other cemented granular materials.

The mechanical properties of the reinforcement materials are utilized to analyze the stability of a slope theoretically, especially the strength criterion, which is used to analyze the failure criteria of the materials under various stress states and is helpful for the structural calculation of terrace slopes. Previous studies have revised the existing

classical strength criteria and proposed several new strength criteria by carrying out triaxial tests on specific reinforcement materials. Mola-Abasi et al. [3] investigated the potential of a zeolite stabilizer known as an additive material to improve the unconfined compression strength, failure, and chemical properties of cemented sand. Coop and Atkinson [4] investigated strength properties of artificially cemented carbonate by triaxial tests at confining pressures of up to 9 MPa. With the increase of the cement content of artificially cemented carbonate, the peak strength increases which agrees well with this framework of other cemented soils. Ding et al. [8] conducted triaxial compression tests aiming at analyzing the relationship among the shear strength characteristics of solidified dredged materials, cement content, and confining pressure and then proposed a strength criterion for solidified dredged materials that accounted for the strength evolution mechanism. Li et al. [9] modified the Mohr-Coulomb (M-C) criterion through triaxial compression tests of artificially cemented sand and elaborated on the influence of the cement content. Kongsukprasert et al. [10] conducted a triaxial compression strength test on lean cemented sand and gravel (LCSG) materials and studied the effects of factors such as water content, curing agent content, dry density, curing period, and shear force on their strength. Wu et al. [11] analyzed the influence of curing age and confining pressure on the shear strength of LCSG materials through triaxial tests, modified the M-C criterion, and then developed a strength criterion considering curing age. Amini and Hamidi [12] researched the effect of the cement content on the cohesion and internal friction angle values based on the M-C criterion and triaxial compression tests on LCSG. Clough et al. [13] and Wang [14] took the aggregate contents and confining pressures as the variables to determine their impact on the shear strength values of LCSG; however, no strength criterion that accounted for the aggregate content was proposed. Yang et al. [15, 16] found the influence of cement content, confining pressure, and aggregate content on the strength according to test research results and not only modified the M-C criterion but also proposed a new strength criterion for LCSG materials. Wei et al. [17] concluded from triaxial tests on LCSG materials under confining pressures of 0–2500 kPa that the peak strength increased as the confining pressure increased, but the magnitude of the increment decreased gradually. According to the aforementioned studies, the strength criteria of LCSG materials, cement soil, and other reinforcement materials are typically directly revised according to various forms of the classical strength criteria. The strength criterion above has different forms, and most of them are obtained by directly fitting the strength and confining pressure. For the areas with abundant soil and stone materials, it is difficult to reasonably verify the slope reinforcement there based on the strength criterion of a specific cemented soil material or improved stone material given by existing references. Therefore, it is indispensable to establish a unified strength criterion.

M-C strength criterion is widely utilized because of its simple mathematical expression and clear physical meaning. To accurately reflect the decay law of slope strength, the

respective reduction factors of cohesive force c and friction angle ϕ are applied for the M-C strength criterion. Chen et al. [18, 19] assumed that slope stability coefficient F_s was the weighted average of cohesion reduction coefficient and friction angle reduction coefficient, whose weight was used to represent the proportion of cohesion and friction angle, and thus proposed an improved double-strength reduction method. Various modifications to the M-C strength criterion have been proposed to reflect the characteristics of geotechnical materials [11, 20–24]. For instance, in some studies, the linear criteria were revised to nonlinear criteria according to material test results, while in others, the M-C strength criterion was modified, and binary medium models for structural soil and other similar materials were proposed. The binary medium model [23, 25–27] considers the material as a binary medium composed of a cementation element (structure) and a friction element (damaged body). The structural change in the deformation process is abstracted as structural gradual damage, which is then transformed into a damaged body. Similar to structural soil, LCSG materials have certain cemented properties. However, they are mainly provided by cemented materials such as cement and fly ash, rather than produced by structural action. Whether it is appropriate to directly simulate the strength characteristics of LCSG via binary medium modeling remains to be discussed.

Aiming at providing a theoretical basis for the stability calculation of the terrace slope of reinforcement materials such as LCSG material, the strength and failure characteristics of these cemented materials under different cement contents and confining pressures were analyzed in this study. Based on the M-C strength criterion and binary medium theory, a new strength criterion that incorporates the frictional strengths and the cementing strengths was proposed for the LCSG material and cemented soil.

2. Materials and Methods

2.1. Raw Materials and Mix Ratio. Natural sand and gravel, as shown in Figure 1(a), were employed as the aggregates in the large-scale triaxial consolidated drained shear test of the LCSG material. The gradation of the aggregates is shown in Figure 2. The aggregate particle size was varying from 0.075 mm to 60 mm, and the aggregate distributions are exhibited in Table 1. The sample preparation density for the aggregates was maintained at 2.29 g/cm^3 . The LCSG materials containing cementing agents of 60, 80, and 90 kg/m^3 were researched, respectively, in order to accurately determine the degree of improvement of the cement content on the mechanical properties of the sand and gravel material. The cemented materials, as shown in Figure 1(a), consisted of dry cement (PO 42.5R) and secondary dry fly ash collected from power plants around Nanjing, China, respectively, which were mixed in accordance with a mass ratio of 3:2. The cement contents for the LCSG materials with cementing agents of 60, 80, and 90 kg/m^3 are 36, 48, and 54 kg/m^3 , respectively, and the fly ash contents are 24, 32, and 36 kg/m^3 , respectively. The water-binder ratio was fixed at 0.8.

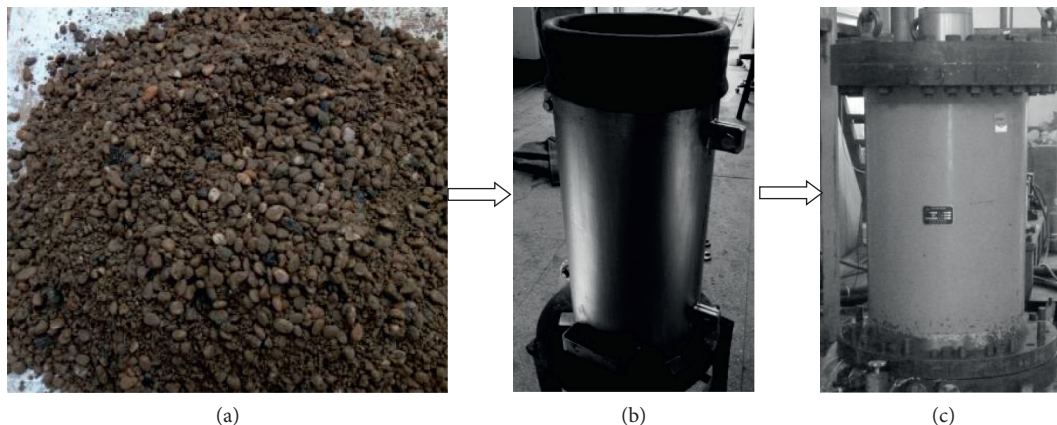


FIGURE 1: Raw materials and mix ratio. (a) Raw materials. (b) Cylindrical mold. (c) The static and dynamic triaxial test instrument.

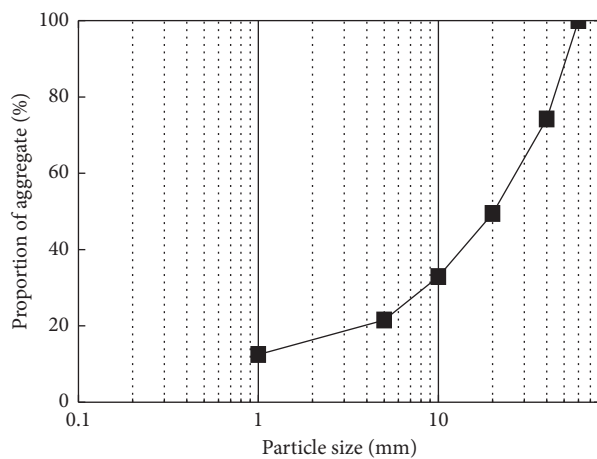


FIGURE 2: Gradation of the aggregates.

2.2. Test Sample Preparation. A cylindrical LCSG specimen with a diameter of 300 mm and a height of 700 mm was prepared. The specimen preparation procedure is detailed below, which has a comprehensive precision index higher than 1%.

- (1) The amounts of cement, fly ash, sand, gravel, and water required for each specimen were calculated according to the mix proportion requirements of cemented sand, and then these components were mixed.
- (2) The mixture was divided into five layers into the cylindrical mold, as shown in Figure 1(b). Each layer was vibrated, grounded, and compacted. After the fifth mixture layer was rolled, the sample of LCSG material was formed.
- (3) Two specimens were prepared for each test to improve the accuracy of the test results. The specimens were cured at $20 \pm 2^\circ\text{C}$ for 28 days. Wu et al. [11] believed that the strength of LCSG materials had met the engineering requirements after curing for 28 days, and the strength of materials beyond 28 days had not been substantially improved. Therefore, the

experimental curing age of such materials was generally set as 28 days. The specimens were fixed with a rubber sleeve to prevent them from falling or damaging the testing machine.

2.3. Test Equipment and Process. The large-scale triaxial consolidated drained shear test on LCSG was carried out using the static and dynamic triaxial test instrument as shown in Figure 1(b). The test instrument consisted of five parts, namely, the hydraulic station and digital signal element, load cell, triaxial pressure chamber, pressure/volume controller, and cylinder software. The maximum confining pressure and axial load were 4 MPa and 1500 kN, respectively. The test was conducted according to the guidelines specified in SL237-1999 [28]. The comprehensive accuracy index of the instrument was greater than 1%. In this study, the axial displacement was measured by a grating displacement sensor with an accuracy of 0.01 mm, and the axial strain was obtained by the ratio of axial displacement to axial dimension. The volumetric strain can be calculated by the ratio of the drained volume of the specimen to its own volume.

The specimens were allowed to stand for 2 or 3 h prior to the triaxial tests. They were then saturated using the vacuum pumping saturation method [29] for LCSG materials, thereby ensuring that the saturation exceeded 95%. The large-scale triaxial consolidated drained shear tests were launched under four confining pressures: 300, 600, 1000, and 1500 kPa, respectively. The reason for selecting these values of confining pressures is that they conform to the state of stress for all engineering applications of LCSG material including slope reinforcement and dam construction at present. Furthermore, it was ensured that the loading would be halted once the axial strain reached a value of 15%. The specimen after the test is shown in Figure 3.

3. Results and Discussion

Figure 4 gives the triaxial shear test results for the non-cemented sand and gravel and LCSG with cement contents of 60, 80, and 90 kg/m³, respectively, under different

TABLE 1: Details of the aggregates.

Name	Content					
	0-1 (mm)	1-5 (mm)	5-10 (mm)	10-20 (mm)	20-40 (mm)	40-60 (mm)
Sand and gravel (kg/m^3)	286.25	206.1	261.06	377.85	567.92	590.82



FIGURE 3: The specimen after the large-scale triaxial consolidated drained shear test.

confining pressures. The deviatoric stress, especially peak deviatoric stress called peak shear strength of LCSG material, grew significantly larger as the cement content increased under a fixed confining pressure. The stress-strain curves of the LCSG material under different cement contents are strain softening, which differ from the hardening curves of noncemented sand and gravel material. In contrast, the stress-strain curve of the structural loess is similar to that of the remolded loess without the strain-softening phenomenon [30]. The main reason for this difference is that the LCSG materials contain cement and fly ash, which can cement the particles and improve the strength of the sand and gravel materials, while the internal resistance of the structural loess is mainly the frictional resistance, and the damage resistance of the cement in it is negligible. To further study the strength characteristics of the LCSG material, it is necessary to understand its failure mechanism. In recent studies, Huo [31] used Particle Flow Code (PFC) software to simulate the uniaxial shear tests of the cemented coarse-grained soil, and the shear process is shown in Figure 5. Chen [32] used the multiphysics lattice discrete particle

model (M-LDPM) to conduct a microscopic numerical simulation of a triaxial shear test of the cemented sand and gravel materials, the failure process of which is shown in Figure 6. Combined with the aforementioned numerical simulation results of those similar materials and the macroscopic variation characteristics of the specimen for LCSG material observed by those large-scale triaxial consolidated drained shear tests, we believe that the failure process of LCSG materials and similar materials should be shown in Figure 7. The LCSG material begins to undergo cementation damage under a certain confining pressure, and then the damaged loose particles are subjected to extrusion and friction until the LCSG material is destroyed. Macroscopically, the damaged area gradually becomes larger, forming a shear zone.

To explore the reasons of this strength enhancement, referred to the treatment method of triaxial test curves of the hardfill material at different curing ages by Wu et al. [11], the difference of the deviatoric stress between LCSG materials and noncemented sand and gravel material under the same axial strain is calculated and shown in Figure 8. At the initial stage of axial loading, the difference of the deviatoric stress of LCSG material with varying confining pressure or cemented content exists, which indicates that the cemented material in the LCSG material rapidly begins to act as a cohesive component under small strains. With the increase of axial strain, the difference of the deviatoric stress becomes greater, explaining that the cemented part of LCSG resists the load from the initial stage of loading, and the resistance increases as the loading adds. When the difference of deviatoric stress reaches the peak value of the curve, the resistance of the cemented part is the most obvious. Then, the difference of the deviatoric stress starts attenuation, reflecting that the effect of the cemented part reduces, and the deviatoric stress is mainly caused by friction. Thus, the gradual destruction of the cemented material enhances the influence of the friction between particles. The cohesive and internal frictional forces in the LCSG material develop stepwise with variations in the axial stress, the phenomenon of which resembles the properties of structural loess [30]. In addition, under the same confining pressure, the difference of the deviatoric stress corresponding to the same axial strain enlarges with the increase of the cement content. The results show that the greater the amount of cementation, the stronger the cementation resistance with the same deformation.

Combined with the deviatoric stress in Figures 4 and 8, it is seen that the differences of the peak deviatoric stress between noncemented sand and gravel and LCSG material with cement contents of 60, 80, and 90 kg/m^3 under a confining pressure of 300 kPa are 1.31%, 1.51%, and 1.29%, respectively, while the corresponding differences of the peak deviatoric stress in Figure 8 are 1.28%, 1.34%, and 1.17%,

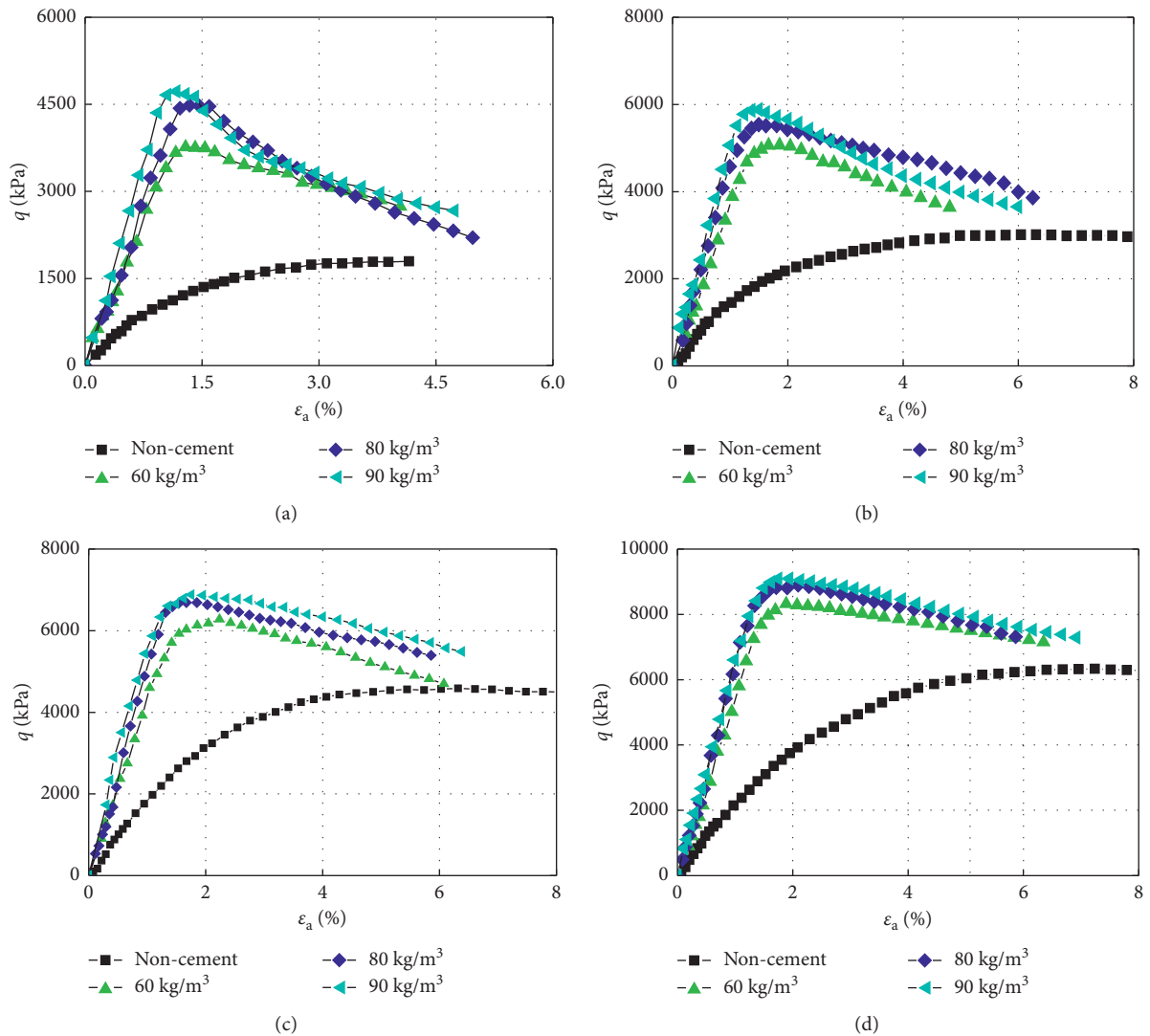


FIGURE 4: The stress-strain curves for different confining pressures. (a) 300 kPa. (b) 600 kPa. (c) 1000 kPa. (d) 1500 kPa.

respectively, indicating that, under a confining pressure of 300 kPa, the differences of the peak deviatoric stress of cemented sand and gravel are greater than those of the specimen under failure. The partial cementation and other partial contacts of the LCSG material particles at low pressure mainly reflect that the cementation and frictional resistance increase with the growth of the deformation. However, when the confining pressure is over 600 kPa, the differences of the peak deviatoric stress of LCSG material are smaller than those of the specimen under failure. It can be explained that the weak cementation resistance of the LCSG material attains the limit earlier, and the frictional resistance becomes the main force earlier than that of the LCSG material. Therefore, as the confining pressure augments, more particles near the shear zone can resist the external force, and the macroscopic strength value becomes greater. When the confining pressure is at a certain value, the higher the cement content of LCSG material is, the harder it is to separate the cemented particles, and the macroscopic strength value increases as well.

Figure 9 shows the relationship between the failure strength and the confining pressure of LCSG material. The strengths of the cemented and noncemented sand and gravel materials differ distinctly under the same confining pressure, illustrating that the cementation of the LCSG material significantly affects the shear strength from the beginning and contributes toward the cohesive component of shear resistance. The cemented block between the grains is compressed and damaged under the influence of the external load. Although the cemented strength of the LCSG mixture plays an important role when subjected to a low confining pressure, the residual cemented material acts as a cohesive component in the LCSG material with increasing confining pressure. The strength of the LCSG material improves nonlinearly. Wei et al. [17] increased the confining pressure to 3000 kPa in their tests and observed that the shear strength of the LCSG mixture increased with increasing confining pressure; however, the magnitude of the increment decreased significantly, which is consistent with the results of this study. Moreover, the strength of other reinforcement materials, such as high polymer rockfill and cement

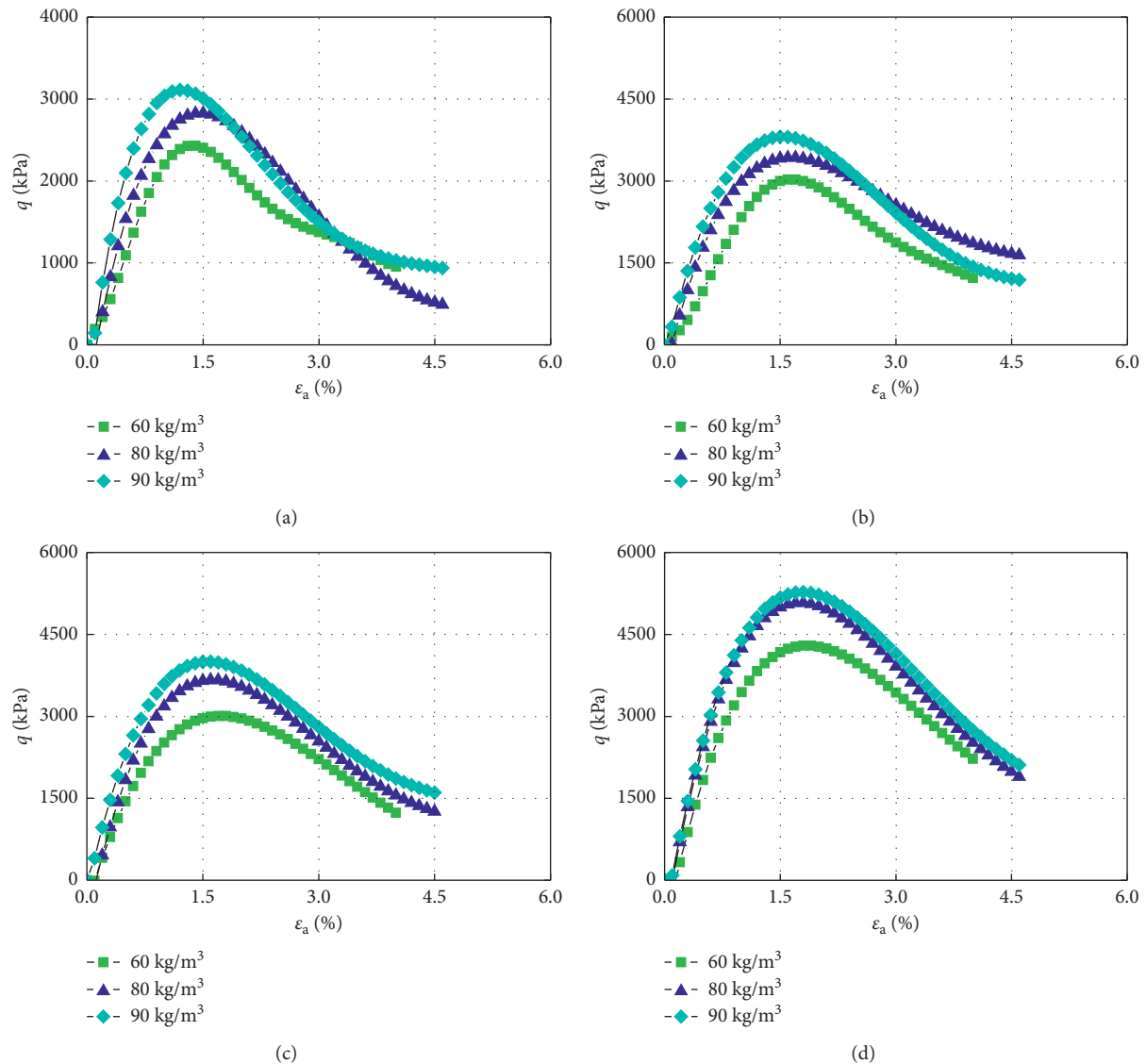


FIGURE 5: Difference of deviatoric stress between LCSG and noncemented sand and gravel. (a) 300 kPa. (b) 600 kPa. (c) 1000 kPa. (d) 1500 kPa.

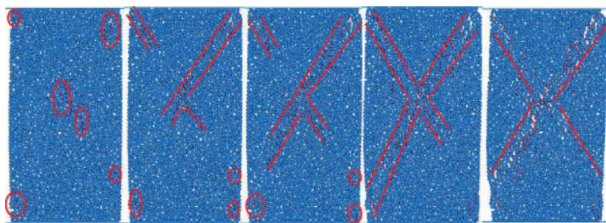


FIGURE 6: The shear failure process of cemented coarse-grained soil [31].

soil, also increases as the confining pressure accumulates, albeit accompanied by a slight reduction in the increment magnitude. Material particles are more prone to damage, and the bonding damage resistance near the failure point of these materials tends a diminution; hence, the peak strength of these materials increases nonlinearly as the confining pressure grows. The

linear relationship between strength and confining pressure under the same cement content reported by Yang et al. [15] was suitable for a small range of confining pressure lower than 1200 kPa. In summary, when the confining pressure is small, a straight line can reflect the relationship between the shear strength of the LCSG material and the confining pressure. However, when the confining pressure is high, the calculated value using the linear equation is greater than the real test value, such as in the test results of Wei et al. [17]. In order to put forward a general strength criterion, we believe the nonlinear relation could reflect its strength characteristics better.

4. Strength Criterion

The results and discussion of LCSG material demonstrate that the shear strengths of the cemented sand and gravel mixture, the cemented soil, and other reinforcement materials are composed of resistance to cementation and friction between particles. The effect of cementation on the strength of LCSG material is much

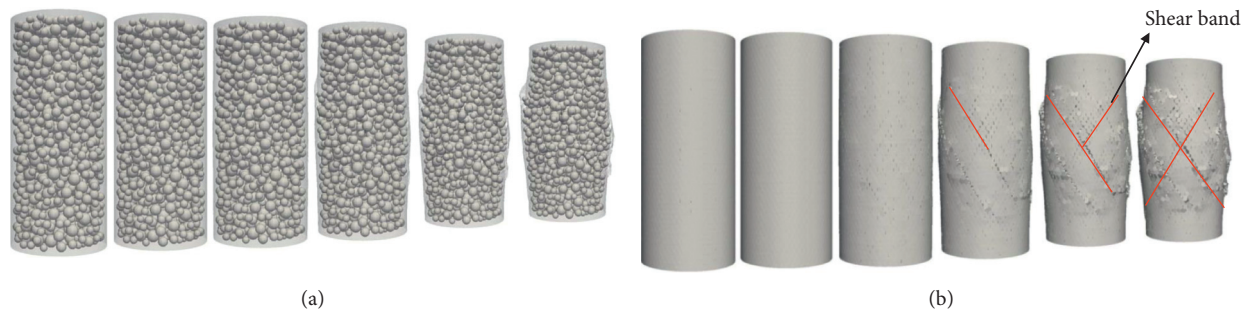


FIGURE 7: The shear failure process of cemented coarse-grained soil. (a) Internal particles. (b) The surface of the specimen [32].

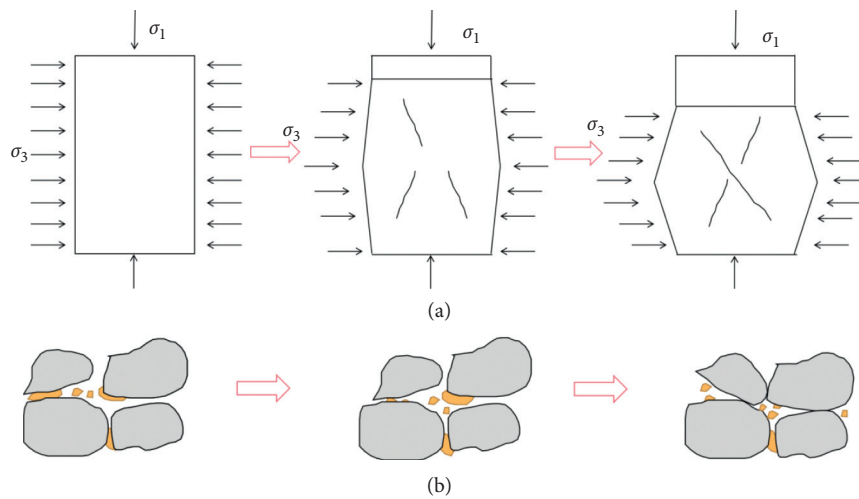


FIGURE 8: (a) The failure mode and (b) the failure mechanisms of the LCSG.

greater than the effect of damage resistance on the strength of loess [30]. And it is untoward to determine the shear contribution in the binary medium model. Hence, the binary medium model for structured soil is not the optimal choice to reflect the strength characteristics of LCSG material. It is essential to seek a simple and reasonable strength criterion that can describe the bonding and frictional strengths of LCSG material.

On the basis of the foregoing results as shown in Figures 4–9, the strength q_f of the LCSG material, the cemented soil, and other reinforcement materials can be expressed as follows:

$$q_f = f + A, \quad (1)$$

where f is the stress value caused by resistance to friction and A is the cementation factor which is the stress value resisting the cementation of the cement.

As indicated by Figure 9, the relationship between the strength of cemented granular materials including LCSG material and the confining pressure can be described as

$$q_f = B \cdot Pa \left(\frac{\sigma_3 + Pa}{Pa} \right)^n + A. \quad (2)$$

Here, B , n , and A are dimensionless parameters; Pa is the standard atmospheric pressure; $B \cdot Pa$ is the product of B with Pa , representing the strength of the material without

cementation ($A = 0$) when the confining pressure is 0; n represents the growth index of the initial modulus.

In order to verify the accuracy of equation (3), the test results of various reinforcement materials and their corresponding calculated values are shown in Figure 10. It can be observed from the figure that, according to equation (3), the strength calculation values of LCSG material, high polymer rockfill material, and cemented soil are roughly the same as the corresponding experimental results. This indicates that the new nonlinear strength criterion is suitable for the strength prediction of different types of reinforcement materials.

The influence of parameters A , B , and n from equation (3) on the strength was studied by utilizing the data from the LCSG material by Wei et al. [17]. The values of A , B , and n were equal to 601.2 kPa, 18.24, and 0.51, respectively. During the analysis of one parameter, the other parameters were kept constant. The influence of strength parameters A , B , and n on the variations in the peak strength of the cemented sand and gravel under the confining pressure is shown in Figure 11. Increasing the value of parameter A results in an augment in the predicted value of the corresponding strength, as shown in Figure 11(a); however, the form of the strength criterion remains unchanged. It is evident from Figure 11(b) that the predicted strength increases as the value of B adds. With the increment of the confining

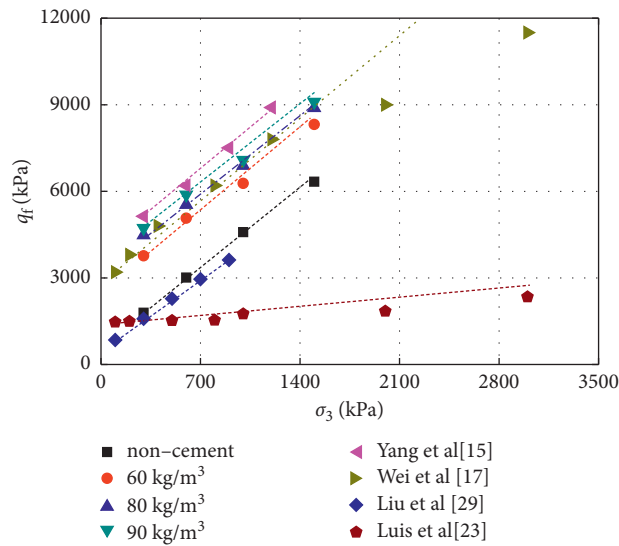


FIGURE 9: The relationship of the peak strength and confining pressure.

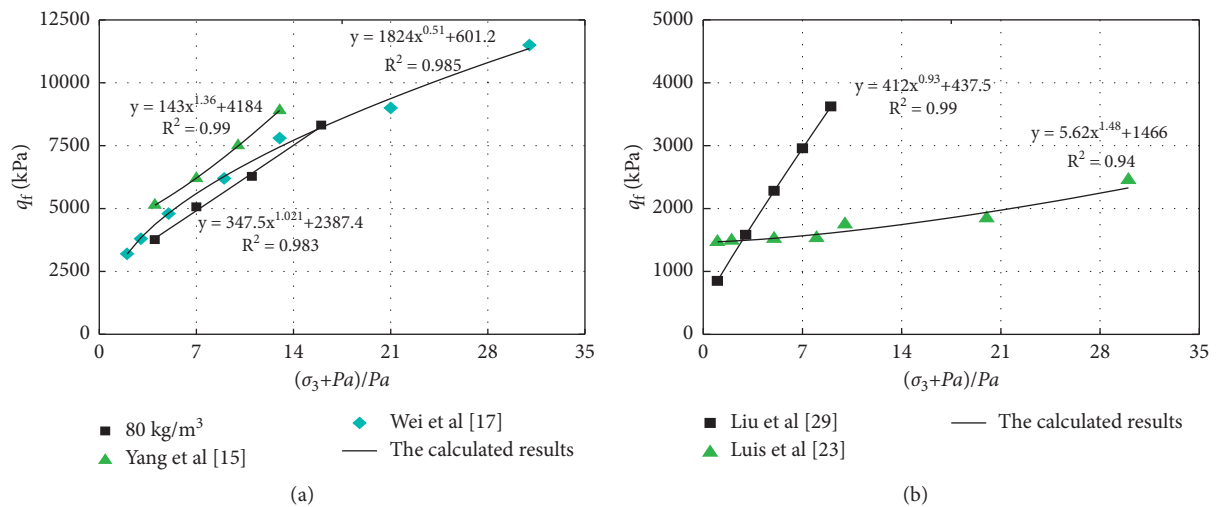


FIGURE 10: Strength criterion verification for different kinds of the reinforcement materials. (a) LCSG material. (b) Other similar reinforcement materials.

pressure, the effect of parameter B on the strength of the LCSG material exceeds that of parameter A . Thus, the magnitude of the strength increment gradually increases. Magnifying the value of n under small confining pressures leads to a slight increase in the corresponding predicted strength, as exhibited in Figure 11(c). The predicted strength value increases noticeably as the confining pressure grows. In conclusion, parameter A is only related to the cementitious content, while parameters B and n are affected by the confining pressure, especially the high confining pressure.

Considering the effect of the cement content, A in equation (2) can be rewritten as the function of cementing strength considering the influence of the cement content C_c ; when C_c is 0, A is 0; $B \cdot Pa(\sigma_3 + Pa/Pa)^n$ is the function of the strength due to friction.

In order to reveal the relationship between A and C_c , take LCSG material as an example. The peak strength of the

noncemented sand and gravel was subtracted from the peak strengths of LCSG material with different cement contents to determine the difference of peak strength Δq_f as shown in Figure 12. And the difference of peak strength Δq_f of LCSG material with a specific cement content under different confining pressures is essentially the same. Therefore, the average value of the difference of peak strength Δq_f can be considered as A as shown in Figure 13. The relationship between A and C_c can be expressed as

$$A(C_c) = k_1 \frac{C_c}{C_{c0}}, \quad (3)$$

where k_1 is the increase intensity of the relative cement content, with the unit of kPa, and C_{c0} is the reference cement content, taken as 1 kg/m^3 .

The linear relation of equation (3) shows that the function A increases linearly with the increase of the

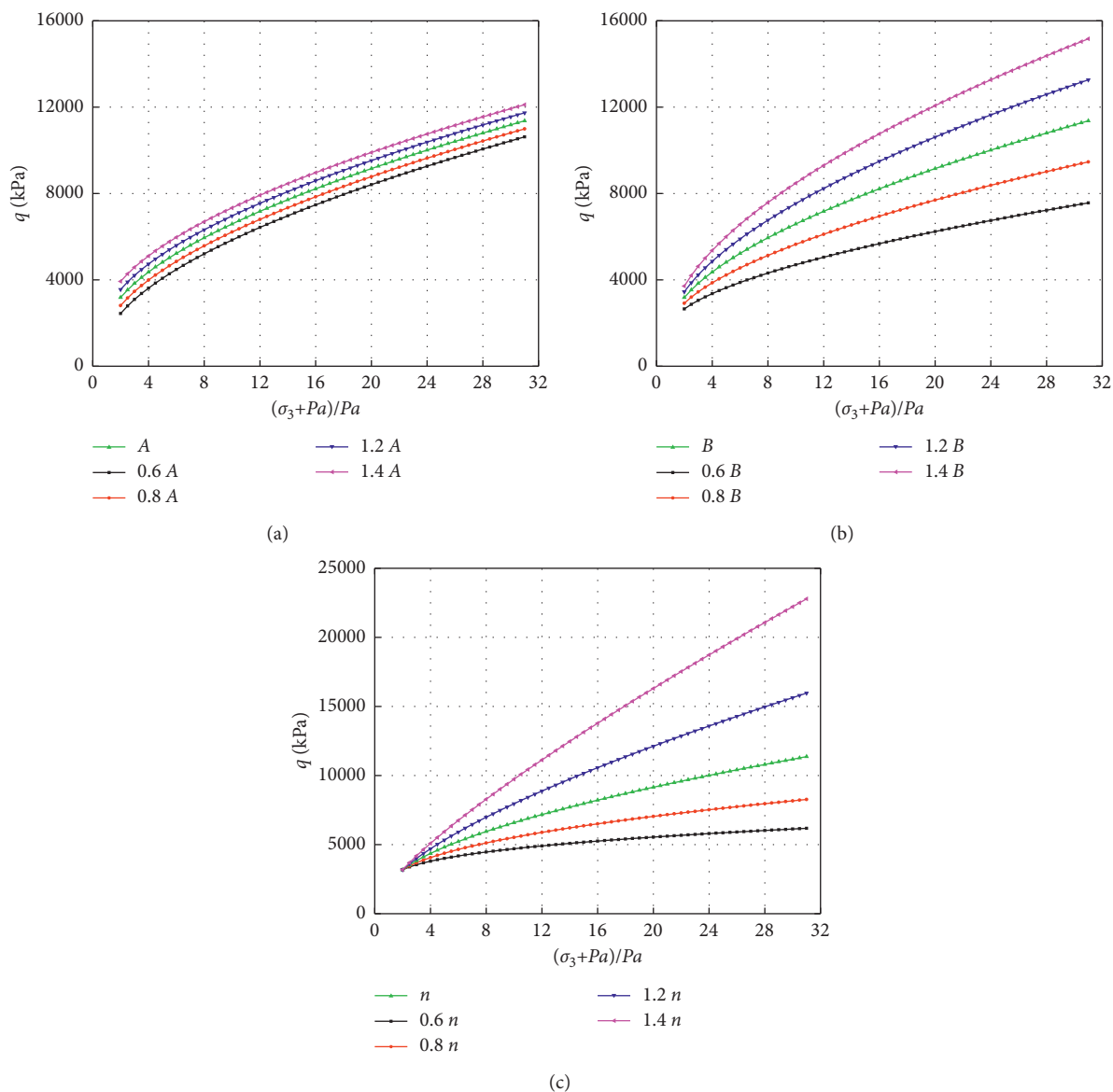


FIGURE 11: Influence of strength parameters on prediction results of the strength criteria. (a) Parameter A. (b) Parameter B. (c) Parameter n .

cement content, and only A in equation (3) is affected by the cement content. Thus, the strength of LCSG material increases linearly with the increase of the cement content under the same confining pressure.

A comparison between the experimental and the predicted strength values of the LCSG material with different

cement contents is illustrated in Figure 14. The predicted values of the nonlinear strength criterion, which account for the influence of the cement content, are consistent with the experimental values. This confirms that the proposed strength criterion can accurately predict the strengths of the LCSG material with different cement contents under

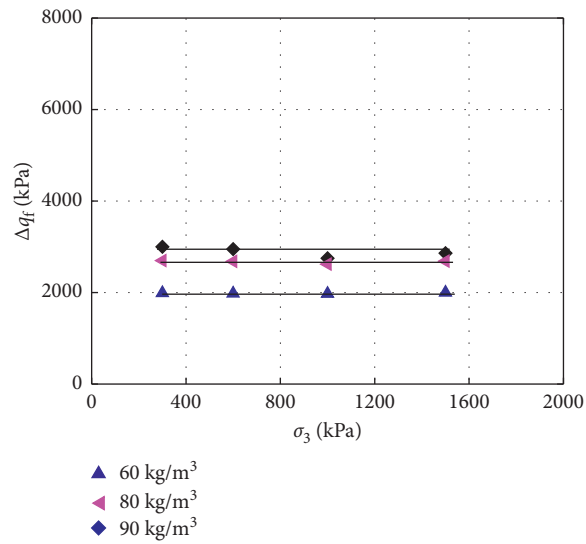


FIGURE 12: The relationship of the difference of peak strength and cement content.

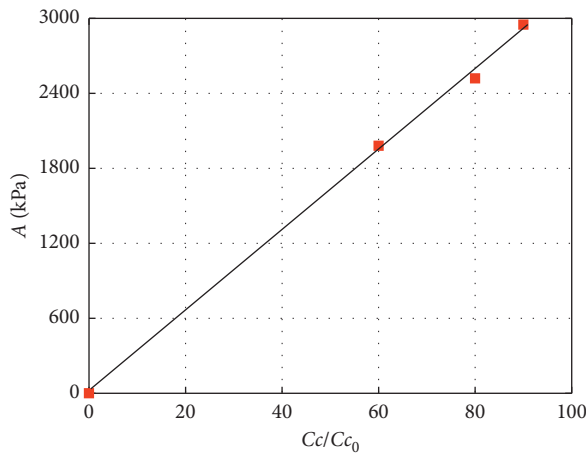


FIGURE 13: The relationship of A and Cc.

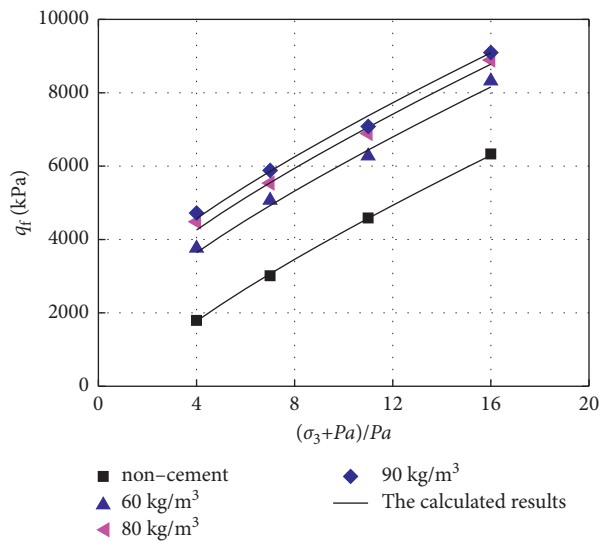


FIGURE 14: Strength criterion verification of LCSG material for different cement contents.

References

varying confining pressures. In addition, it reflects that the strength increases linearly with the augment of the cement content.

5. Conclusions

In this study, by conducting a laboratory triaxial consolidated drained shear test of cemented granular materials such as LCSG materials and noncemented sand and gravel materials, the strength variation law of such materials under different cement contents and confining pressures was examined. The main conclusions are drawn as follows:

- (1) When the stress between particles is greater than its cemented strength, failure occurs at the cementation of particles. Then, the particle friction resists the continued load, while the remaining cemented particles continue to provide cohesion against the continued load. The constantly increasing axial loading gradually damages the internal cementation point of the cylindrical specimen, resulting in the formation of an internal cross shear band.
- (2) With an increase in confining pressure, failure readily occurs at the cementation of the LCSG material particles. When the stress of the LCSG material reaches the peak strength, the strength generated by the cementation first increases and then declines, and the frictional strength keeps a gradual growth.
- (3) The relationship between the peak strength and the confining pressure should be nonlinear. The peak strength of the LCSG material increases linearly as the cement content adds, and the rate of increase is not affected by the confining pressure.
- (4) Based on the experimental analysis and discussion results, combined with the M-C criterion and the binary medium model, a nonlinear relation between the strength and the confining pressure of cemented granular materials including LCSG, which can reveal the cementing property and friction, is proposed in this paper. By changing the cement content, a strength criterion of cemented gravel material considering the effect of cement content and con-fining pressure was obtained.

- [1] H. Fu, S. S. Chen, H. Q. Han, H. Ling, and X. Cai, "Experimental study on static and dynamic properties of cemented sand and gravel," *Chinese Journal of Geotechnical Engineering*, vol. 37, no. 2, pp. 357–362, 2015.
- [2] G. Yang, X. Sun, and Y. Y. Wang, "Tests on resilient behaviour of polymer rockfill materials," *Rock and Soil Mechanics*, vol. 39, no. 5, pp. 1669–1674, 2018.
- [3] H. Mola-Abasi, B. Kordtabar, and A. Kordnaeij, "Effect of natural zeolite and cement additive on the strength of sand," *Geotechnical & Geological Engineering*, vol. 34, no. 5, pp. 1539–1551, 2016.
- [4] M. R. Coop and J. H. Atkinson, "Discussion: the mechanics of cemented carbonate sands," *Géotechnique*, vol. 44, no. 3, pp. 533–537, 1994.
- [5] A. F. Cabalar, Z. Karabash, and W. S. Mustafa, "Stabilising a clay using tyre buffings and lime," *Road Materials and Pavement Design*, vol. 15, no. 4, pp. 872–891, 2014.
- [6] A. M. Sharaky, N. S. Mohamed, M. E. Elmashad, and N. M. Shredah, "Application of microbial biocementation to improve the physico-mechanical properties of sandy soil," *Construction and Building Materials*, vol. 190, pp. 861–869, 2018.
- [7] A. Yildiz and F. Uysal, "Numerical modelling of Haarakjoki test embankment on soft clays with and without PVDs," *Geomechanics and Engineering*, vol. 8, no. 5, pp. 707–726, 2015.
- [8] J. W. Ding, M. L. Shi, W. Z. Liu, and Z. S. Hong, "In situ stabilization of problematic mixtures in a failed roadway subbase," *Journal of Performance of Constructed Facilities*, vol. 31, no. 3, pp. 707–726, 2017.
- [9] D. Li, X. Liu, and X. Liu, "Experimental study on artificial cemented sand prepared with ordinary Portland cement with different contents," *Materials*, vol. 8, no. 7, pp. 3960–3974, 2015.
- [10] L. Kongsukprasert, F. Tatsuoka, and M. Tateyama, "Several factors affecting the strength and deformation characteristics of cement-mixed gravel," *Soils and Foundations*, vol. 45, no. 3, pp. 107–124, 2005.
- [11] M. Wu, B. Du, Y. Yao, and X. He, "An experimental study on stress-strain behavior and constitutive model of hardfill material," *Science China Physics, Mechanics and Astronomy*, vol. 54, no. 11, pp. 2015–2024, 2011.
- [12] Y. Amini and A. Hamidi, "Triaxial shear behavior of a cement-treated sand-gravel mixture," *Journal of Rock Mechanics and Geotechnical Engineering*, vol. 6, no. 5, pp. 455–465, 2014.
- [13] G. W. Clough, N. Sitar, R. C. Bachus, and N. S. Rad, "Cemented sands under static loading," *Journal of the Geotechnical Engineering Division*, vol. 107, no. 6, pp. 799–817, 1981.

- [14] Q. Wang, "Experimental study on behavior of strength a deformation of cemented coarse-grained soil," Master thesis, Dalian University of Technology, Dalian, China, 2010.
- [15] J. Yang, X. Cai, Q. Pang, X.-w. Guo, Y.-l. Wu, and J.-l. Zhao, "Experimental study on the shear strength of cement-sand-gravel material," *Advances in Materials Science and Engineering*, vol. 2018, pp. 1–11, Article ID 2531642, 2018.
- [16] J. Yang, X. Cai, X. W. Guo, and J. L. Zhao, "Effect of cement content on the deformation properties of cemented sand and gravel material," *Applied Sciences-Basel*, vol. 9, pp. 1–16, Article ID 2369, 2019.
- [17] K. M. Wei, S. S. Chen, and G. Y. Li, "Elastoplastic model for cemented coarse-grained materials and its application," *Chinese Journal of Geotechnical Engineering*, vol. 41, no. no5, pp. 797–805, 2019.
- [18] Y. Chen, H. Lin, Y. Wang, R. Cao, C. Zhang, and Y. Zhao, "Modified double-reduction method considering strain softening and equivalent influence angle," *KSCE Journal of Civil Engineering*, vol. 24, no. 11, pp. 3257–3266, 2020.
- [19] Y. F. Chen, H. Lin, R. H. Cao, and C. Y. Zhang, "Slope stability analysis considering different contributions of shear strength parameters," *International Journal of Geomechanics*, vol. 21, no. 3, pp. 1–9, Article ID 04020265, 2021.
- [20] M. C. Liu, Y. F. Gao, and X. M. Huang, "Study on elasto-plastic constitutive model of rockfills with nonlinear strength characteristics," *Chinese Journal of Geotechnical Engineering*, vol. 27, no. 3, pp. 294–298, 2005.
- [21] B. A. Lingga and D. B. Apel, "Shear properties of cemented rockfills," *Journal of Rock Mechanics and Geotechnical Engineering*, vol. 10, no. 4, pp. 635–644, 2018.
- [22] C. J. Deng, G. J. He, and Y. R. Zheng, "Studies on drucker-prager yield criterions based on M-C yield criterion and application in geotechnical engineering," *Chinese Journal of Geotechnical Engineering*, vol. 6, pp. 735–739, 2006.
- [23] A. Luis, L. Deng, L. Shao, and H. Li, "Triaxial behaviour and image analysis of edmonton clay treated with cement and fly ash," *Construction and Building Materials*, vol. 197, pp. 208–219, 2019.
- [24] X. L. Li, Q. W. Li, and C. Yang, "A nonlinear failure strength criterion for rocks based on the peak value of deviatoric stress from triaxial tests," *Journal of China Society*, vol. 44, pp. 517–525, 2019.
- [25] E. L. Liu and Z. J. Shen, "Binary medium model for structured soils," *Journal of Hydraulic Engineering*, vol. 36, no. 4, pp. 391–395, 2005.
- [26] D. Zhang, E. Liu, X. Liu, G. Zhang, and B. Song, "A new strength criterion for frozen soils considering the influence of temperature and coarse-grained contents," *Cold Regions Science and Technology*, vol. 143, pp. 1–12, 2017.
- [27] J. Fu, J. Wang, and W. Song, "Damage constitutive model and strength criterion of cemented paste backfill based on layered effect considerations fill based on layered effect Considerations," *Journal of Materials Research and Technology*, vol. 9, no. 3, pp. 6073–6084, 2020.
- [28] SL237-1999, *Specification of Soil Test*, Ministry of Water Resources of the People's Republic of China, Beijing, China, 1999.
- [29] P. Liu, H. L. Liu, Y. Xiao, and G. Yang, "Experimental study on mechanical properties of the PFA-reinforced rockfill materials," *Rock and Soil Mechanics*, vol. 36, no. 3, pp. 749–754, 2015.
- [30] B. Zhi, Y. X. Wang, B. T. Deng, and W. Liu, "Shear strength criterion for structured loess under high stress based on geobinary medium model," *Coal Engineering*, vol. 50, no. 10, pp. 41–45, 2018.
- [31] W. L. Huo, "Study on failure mechanism of cement sandy gravel material based on particle flow code," Master thesis, North China University of Water Conservancy and Electric Power, Zhengzhou, China, 2018.
- [32] J. J. Chen, "Meso-mechanical characteristics study and multiscale analysis of cemented sand and gravel material," Doctor thesis, Hohai University, Nanjing, China, 2020.

Steady-State Response Analysis of the Incompressible Nonlocal Saturated Poroelastic Beam under a Vertical Harmonic Load

Nalinikanta Swain, *Department of Mechanical Engineering, Capital Engineering College, Bhubaneswar, nalini_526@yahoo.co.in*

Sthitiprajanya Satpathy, *Department of Civil Engineering, Aryan Institute of Engineering & Technology, Bhubaneswar, sthiti_p93@yahoo.co.in*

Saleema Panda, *Department of Civil Engineering, NM Institute of Engineering & Technology, Bhubaneswar, saleemapanda25@gmail.com*

Barsa Priyadarshini Sahoo, *Department of Civil Engineering, Raajdhani Engineering College, Bhubaneswar, barsap_sahoo@gmail.com*

ABSTRACT

Based on the nonlocal theory and the theory of saturated porous media, the mathematical and physical model and governing equations of the steady-state response of the incompressible nonlocal saturated poroelastic beam under vertical harmonic loading are established with assumption of the movement of the liquid-phase fluid only in the axial direction of the beam and considering the nonlocal effects such as particle size, pore size, and pore dynamic stress. The dynamic response of a saturated poroelastic cantilever beam with permeability at both ends under a vertical harmonic concentrated force at the free end is studied. In the frequency domain, the analytical expressions of deflection amplification factor and equivalent couple amplification factor of liquid fluid pressure are given. The effects of nonlocal coefficient τ , mechanical parameter α , and geometric parameter β on the deflection amplification factor and equivalent couple amplification factor at the midpoint of the nonlocal saturated poroelastic cantilever beam are studied. The results show that the steady-state vibration of the incompressible nonlocal saturated poroelastic cantilever beam has resonance. When the nonlocal effect is considered, the deflection amplification factor and the equivalent couple amplification factor are larger, so the influence of the nonlocal effect on the steady-state response of the beam should not be ignored. The geometric parameter β has significant effect on the peak positions of the curves of the deflection amplification factor and the equivalent couple amplification factor varying with frequency.

1. Introduction

Saturated porous structures are widely used in civil engineering, aviation, transportation, and other engineering fields because of their good sound absorption and energy consumption. The research on the mechanical behavior of saturated porous structures has significant engineering application value and academic value. Therefore, since Biot put forward the theory of saturated porous media [1, 2], the research on vibration and wave propagation in saturated porous media has attracted the attention of many scholars [3–9]. Since Biot theory assumes that the wave length of saturated porous media is larger than the pore size, the influence of pore size effect on wave propagation is not considered and the influence of pore size is very significant at high frequency [10]. As a method of engineering description, Biot theory has some defects in the model [11] and it is difficult to determine the elastic constant and inertial

coupling coefficient in the Biot dynamic equation. The porous media theory based on the mixture axiom and the concept of volume fraction is more rigorous and reasonable. The concept of volume fraction in porous media theory can avoid the incompatibility of the model and can also consider the effects of dynamic, material, and geometric nonlinearity. Aiming at the static and dynamic problems of saturated porous structures, Busse et al. [12] established the dynamic mathematical model of the saturated poroelastic Mindlin plate based on Biot theory and gave the virtual work principle with rotation angle, deflection, and pore stress as basic unknowns. Iesan and Nappa [13] studied the thermal stress of poroelastic cylinders and circular tubes. Li et al. [14] studied the transverse vibration of fluid saturated poroelastic beams and obtained the solutions of free vibration and forced vibration. Cederbaum et al. [15] studied the mechanical behavior of saturated poroelastic beams and rods and pointed out that Mandel–Cryer phenomenon also exists

in the deformation response of poroelastic beams and rods. Xiao and Chen [16] established the nonlinear governing equation of large deflection of the incompressible saturated poroelastic beam under the constraint that the pore fluid only diffuses along the axial direction of the beam and studied the nonlinear bending problem of the saturated poroelastic cantilever beam with fixed impermeability at one end and free permeability at another end under a sudden constant transverse concentrated load at the free end. However, in the analysis of mechanical behavior of saturated porous structures, the scale effects such as solid skeleton particle size, pore size, and pore stress are not considered. As the engineering structure is developing towards miniaturization and intelligence, it is more and more important to consider the influence of structural scale effect on mechanical properties. The nonlocal theory in [17, 18] believes that the stress at a point in the continuum is related not only to the strain at that point but also to the strain and deformation history of all points in the area near the point. The nonlocal theory considering the scale effect is mainly used to study the mechanical problems of nanostructures. In recent years, scholars began to combine the nonlocal theory with the Biot saturated soil theory [19, 20] and apply it to the field of geotechnical engineering. In this paper, the dynamic control equation of the incompressible nonlocal saturated poroelastic beam under a vertical simple harmonic load is established by combining the porous medium theory and nonlocal theory and the steady-state response of the saturated poroelastic cantilever beam with permeable ends under simple harmonic concentrated force at the free end is studied.

2. Mathematical Model and Basic Equation

The incompressible two-phase saturated poroelastic cantilever beam under the action of vertical simple harmonic force shown in Figure 1 is studied, where i is an imaginary unit, ω is the frequency of the simple harmonic force, Q_0 is the amplitude, and the surface of the cantilever beam is impermeable. If the mechanical properties of saturated poroelastic beams are described by using the porous medium theory without considering the influence of volume force, the governing equation is

$$\text{div} \sigma^{SE} - \text{grad} p - (\rho^S + \rho^F) \ddot{\mathbf{u}}^S - \rho^F \dot{\mathbf{v}}^{FS} = 0, \quad (1)$$

$$-n^F \text{grad} p - \rho^F (\ddot{\mathbf{u}}^S + \dot{\mathbf{v}}^{FS}) - \kappa \mathbf{v}^{FS} = 0, \quad (2)$$

$$\text{div} (\dot{\mathbf{u}}^S + \mathbf{v}^{FS}) = 0. \quad (3)$$

Here, σ^{SE} is the effective stress of the solid skeleton, p is the pressure of the liquid phase, ρ^S is the macroscopic density of the solid phase, ρ^F is the macroscopic density of the liquid phase, κ is the solid-liquid phase coupling coefficient, \mathbf{u}^S is the displacement tensor of the solid phase, \mathbf{v}^{FS} represents the velocity of the liquid phase relative to the solid phase, and n^F is the volume fraction of the liquid phase, from which the volume fraction of the solid phase is $n^S = 1 - n^F$.

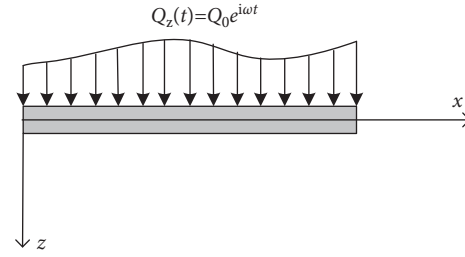


FIGURE 1: Incompressible nonlocal saturated poroelastic beam under vertical harmonic loading.

The nonlocal theory proposed by Eringen holds that the stress at a point depends not only on the strain at that point but also on the weighted average of all point strains in the whole region. Here, considering the influence of nonlocal effects such as particle size, pore size, and pore dynamic stress of the solid skeleton of the saturated poroelastic beam, it is assumed that the solid skeleton of the saturated poroelastic beam is linear elastic, uniform, and isotropic material. Without the influence of physical force, the basic equation of Eringen's nonlocal theory is [17]

$$\sigma_{ij,j}(r) = \int_V \chi(|r - r'|, \tau) C_{ijkl} \varepsilon_{kl} dV(r'), \quad (4)$$

$$\varepsilon_{ij} = \frac{1}{2} (u_{i,j} + u_{j,i}), \quad (5)$$

where σ_{ij} is the nonlocal stress tensor, ε_{ij} and u_i are the nonlocal strain and displacement tensor, respectively, C_{ijkl} is the fourth-order elastic tensor, and $\int_V \chi(|r - r'|, \tau)$ is the nonlocal modulus, which determines the weight coefficient of the corresponding point strain, where τ is the nonlocal kernel function. The influence of the pore dynamic stress, pore size, and particle size of the saturated poroelastic beam is reflected by the nonlocal kernel function; $|r - r'|$ is the Euclidean distance. At the same time, Eringen also gave the differential formula of Equation (4), that is,

$$[1 - (e_0 a)^2 \nabla^2] \sigma_{ij}^{SE} = \sigma_{ij}^{LSE}, \quad (6)$$

where σ_{ij}^{SE} and σ_{ij}^{LSE} represent the nonlocal stress tensor and classical stress tensor, respectively. e_0 represents the nonlocal material constants, a is the internal characteristic length which is related to solid skeleton particle size and pore size, and ∇^2 is the Laplace operators.

The constitutive equation of solid skeleton under small deformation is

$$\sigma^{LSE} = \lambda^S (\varepsilon^S \cdot \mathbf{I}) \mathbf{I} + 2\mu^S \varepsilon^S. \quad (7)$$

where σ^{LSE} is the classical effective stress of the solid skeleton, ε^S is the strain tensor of phase skeleton, \mathbf{I} is the identity matrix, and λ^S , μ^S are the Lamé constants.

3. Dynamic Control Equation of the Incompressible Nonlocal Saturated Poroelastic Beam

The dynamic problem of the incompressible nonlocal saturated poroelastic beam under a vertical simple harmonic

load is one-dimensional, and the displacement of the saturated poroelastic beam is

$$\begin{aligned} u_x^S(x, y, z, t) &= -z \frac{\partial w^S(x, t)}{\partial x}, \\ u_z^S(x, y, z, t) &= w^S(x, t), \end{aligned} \quad (8)$$

where $w^S(x, t)$ is the vertical displacement of the solid phase of the saturated poroelastic beam. Assuming that the liquid phase moves only along the axial direction, the velocities in x , y , and z directions satisfy

$$\begin{aligned} v_x^{FS} &= v_x^{FS}(x, y, z, t), \\ v_y^{FS} &= v_z^{FS} = 0. \end{aligned} \quad (9)$$

Assuming a small amount of stress $\sigma_{zz}^{SE} = \sigma_{yy}^{SE} \approx 0$, it can be obtained from equations (6) and (7) that

$$\epsilon_{kk}^S = \frac{1}{3\lambda^S + 2\mu^S} [1 - (e_0 a)^2 \nabla^2] T_{xx}^{SE}, \quad (10)$$

$$[1 - (e_0 a)^2 \nabla^2] \sigma_{xx}^{SE} = -E^S z \frac{\partial^2 w^S}{\partial x^2}, \quad (11)$$

$$[1 - (e_0 a)^2 \nabla^2] \sigma_{xz}^{SE} = G \frac{\partial w^S}{\partial x}, \quad (12)$$

where ϵ_{kk}^S is the volume strain of the solid skeleton, σ_{xx}^{SE} and σ_{xz}^{SE} are the normal stress and shear stress on the cross section of the saturated poroelastic beam, respectively, and E^S and G are the elastic modulus and shear modulus of the solid phase of the saturated poroelastic beam, respectively. λ^S and μ^S are the lame constants and satisfy

$$E^S = \frac{3\lambda^S + 2\mu^S}{\lambda^S + \mu^S} \mu^S. \quad (13)$$

Let

$$M_x^{SE} = \iint_A z T_{xx}^{SE} dy dz, Q_x^{SE} = \iint_A T_{xz}^{SE} dy dz, M_p = \iint_A z p dy dz. \quad (14)$$

Here, M_x^{SE} and Q_x^{SE} are the solid bending moment and shear force on the cross section of saturated poroelastic beam, respectively, and M_p is the equivalent couple of the pore fluid pressure.

Ignoring the rotational inertia of the pore liquid to the solid skeleton, multiplying the equation in the ox direction of equation (1) by z and integrating it on the cross-sectional area A of the beam, one obtains

$$\frac{\partial M_x^{SE}}{\partial x} - \frac{\partial M_p}{\partial x} - Q_x^{SE} = 0. \quad (15)$$

If the equation in the oz direction of equation (1) is integrated on the cross-sectional area A of the beam, we have

$$\frac{\partial Q_x^{SE}}{\partial x} + q_z - (\rho^S + \rho^F) A \frac{\partial^2 w^S}{\partial t^2} = 0. \quad (16)$$

Here, $q_z(x, t) = \phi_A (\sigma_{zz}^{SE} - p) n_z ds$. For the rotational inertia of the solid skeleton, multiplying the equation in the ox direction of equation (2) by z and integrating it on the cross-sectional area A of the beam, we obtain

$$-n^F \frac{\partial M_p}{\partial x} - \kappa \iint_A z v_x^{FS} dy dz = 0. \quad (17)$$

It can be obtained from equations (3) and (10) that

$$\frac{1}{3\lambda^S + 2\mu^S} \frac{\partial [1 - (e_0 a)^2 \nabla^2] \sigma_{xx}^{SE}}{\partial t} + n^F \frac{\partial v_x^{FS}}{\partial x} = 0. \quad (18)$$

Both ends of equation (18) are multiplied by z and integrated on the cross-sectional area A of the beam, and we have

$$\frac{1}{3\lambda^S + 2\mu^S} \frac{\partial [1 - (e_0 a)^2 \nabla^2] M_x^{SE}}{\partial t} + n^F \frac{\partial}{\partial x} \iint_A z v_x^{FS} dy dz = 0. \quad (19)$$

It can be obtained from equations (17) and (19) that

$$\frac{1}{3\lambda^S + 2\mu^S} \frac{\partial [1 - (e_0 a)^2 \nabla^2] M_x^{SE}}{\partial t} + \frac{(n^F)^2}{\kappa} \frac{\partial^2 M_p}{\partial x^2} = 0. \quad (20)$$

Multiplying both ends of equation (11) by z and integrating it on area A , we have

$$[1 - (e_0 a)^2 \nabla^2] M_x^{SE} = -E^S I \frac{\partial^2 w^S}{\partial x^2}, \quad (21)$$

where $I = \iint_A z^2 dy dz$ is the moment of inertia of the cross section. Integrating both ends of equation (12) on area A , we can obtain

$$[1 - (e_0 a)^2 \nabla^2] Q_x^{SE} = G \frac{\partial w^S}{\partial x}. \quad (22)$$

Calculating $1 - (e_0 a)^2 \nabla^2$ on both ends of equations (15) and (16), respectively, and considering equations (21) and (22), we obtain

$$E^s I \frac{\partial^3 w^s}{\partial^3 x} + \frac{\partial [1 - (e_0 a)^2 \nabla^2] M_p}{\partial x} + G \frac{\partial w^s}{\partial x} = 0, \quad (23)$$

$$G \frac{\partial^2 w^s}{\partial x^2} + [1 - (e_0 a)^2 \nabla^2] q_z - (\rho^s + \rho^F) A \frac{\partial^2 [1 - (e_0 a)^2 \nabla^2] w^s}{\partial t^2} = 0. \quad (24)$$

It can be obtained from equations (20) and (21) that

$$-(1 - 2\nu) I \frac{\partial^3 w^s}{\partial^2 x \partial t} + \frac{(n^F)^2}{\kappa} \frac{\partial^2 M_p}{\partial x^2} = 0. \quad (25)$$

Sorting out equations (24)–(26), one obtains

$$E^s I \frac{\partial^4 w^s}{\partial^4 x} + \frac{(1 - 2\nu) I \kappa}{(n^F)^2} [1 - (e_0 a)^2 \nabla^2] \frac{\partial^3 w^s}{\partial^2 x \partial t} - [1 - (e_0 a)^2 \nabla^2] q_z + (\rho^s + \rho^F) A [1 - (e_0 a)^2 \nabla^2] \frac{\partial^2 w^s}{\partial t^2} = 0. \quad (26)$$

Equations (25) and (26) are the vertical dynamic control equations of the incompressible nonlocal saturated poroelastic beams.

4. Steady-State Response of the Incompressible Nonlocal Saturated Poroelastic Cantilever Beam under a Vertical Simple Harmonic Load

Here, taking the steady-state response of the incompressible nonlocal saturated poroelastic cantilever beam shown in Figure 2 as an example, the same method can be used to analyze the steady-state response of the incompressible nonlocal saturated poroelastic cantilever beam with other boundaries. A simple harmonic concentrated force $Q(t) = q_0 e^{i\omega t}$ is acting on the free end of an incompressible nonlocal saturated poroelastic cantilever beam. The corresponding boundary conditions are

$$\begin{aligned} w^s &= 0, \\ \frac{\partial w^s}{\partial x} &= 0, \\ M_p &= 0, \\ x &= 0, \\ M_x^{SE} - M_p &= 0, \\ M_p &= 0, \\ Q_x^{SE} &= 0, \\ x &= L. \end{aligned} \quad (27)$$

$$\left[E^s I - \frac{i\omega(1 - 2\nu)I\kappa}{(n^F)^2} (e_0 a)^2 \right] \frac{\partial^4 \tilde{w}^s}{\partial^4 x} + \left[\frac{i\omega(1 - 2\nu)I\kappa}{(n^F)^2} + \omega^2 (\rho^s + \rho^F) A (e_0 a)^2 \right] \frac{\partial^2 \tilde{w}^s}{\partial^2 x} - \omega^2 (\rho^s + \rho^F) A \tilde{w}^s = 0, \quad (28)$$

$$-i\omega(1 - 2\nu)I \frac{\partial^2 \tilde{w}^s}{\partial^2 x} + \frac{(n^F)^2}{\kappa} \frac{\partial^2 \tilde{M}_p}{\partial x^2} = 0, \quad (29)$$

$$\begin{aligned} \tilde{w}^s &= 0, \\ \frac{\partial \tilde{w}^s}{\partial x} &= 0, \\ \tilde{M}_p &= 0, \\ x &= 0, \end{aligned} \quad (30)$$

$$\begin{aligned}\tilde{M}_x^{SE} - \tilde{M}_p &= 0, \\ \tilde{M}_p &= 0, \\ Q_x^{SE} &= q_z, \\ x &= L.\end{aligned}\quad (31)$$

Under the action of the simple harmonic load, the incompressible nonlocal saturated poroelastic cantilever beam vibrates in a steady state. Considering the harmony of the problem, the parameters meet $w^S = \tilde{w}^S e^{i\omega t}$, $M_p = \tilde{M}_p e^{i\omega t}$, and $M_x^{SE} = \tilde{M}_x^{SE} e^{i\omega t}$, where \tilde{w}^S , \tilde{M}_p , and \tilde{M}_x^{SE} are the amplitudes of w^S , M_p , and M_x^{SE} , respectively. The following equations can be obtained by substituting w^S , M_p , and M_x^{SE} into vertical dynamic control equations (25) and (26) of the incompressible nonlocal saturated poroelastic beam:

We introduce the dimensionless variables and parameters as follows: $\bar{x} = x/L$, $\bar{\omega} = \omega/T = \omega L/\nu$, $\tau = e_0 a/L$, $T = \nu/L$, $\nu = \sqrt{E^S/\rho^S}$, $\bar{w} = \tilde{w}^S/L$, $\bar{M}_p = LM_p/E^S I$, $q = L^2 Q/E^S I$, $\alpha = (1 - 2\nu)\kappa L^2 T / E^S n^{F2} = (1 - 2\nu)\kappa L / \sqrt{E^S \rho^S} n^{F2}$, and $\beta = (\rho^S + \rho^F)AL^4 T^2 / E^S I = (\rho^S + \rho^F)AL^2 / \rho^S I$. The parameter α mainly reflects the influence of mechanical parameters such as liquid-solid coupling coefficient and elastic modulus on the steady-state response of the beam, the parameter β mainly reflects the influence of geometric parameters such as the size of the saturated porous cantilever beam. Substituting the above dimensionless quantity into dimensionless equations (30)–(32), we obtain the following initial value problem:

$$\frac{\partial^4 \bar{w}^S}{\partial \bar{x}^4} + \alpha_1 \frac{\partial^2 \bar{w}^S}{\partial \bar{x}^2} + \beta_1 \bar{w}^S = 0, \quad (32)$$

$$\frac{\partial^2 \bar{M}_p}{\partial \bar{x}^2} - i\bar{\omega}\alpha \frac{\partial^2 \bar{w}^S}{\partial \bar{x}^2} = 0, \quad (33)$$

$$\begin{aligned}\bar{w}^S &= 0, \\ \frac{\partial \bar{w}^S}{\partial \bar{x}} &= 0, \\ \bar{M}_p &= 0, \\ \bar{x} &= 0,\end{aligned}\quad (34)$$

$$\begin{aligned}\frac{\partial^2 \bar{w}^S}{\partial \bar{x}^2} + \bar{M}_p &= 0, \\ \bar{M}_p &= 0, \\ \frac{\partial}{\partial \bar{x}} \left(\frac{\partial^2 \bar{w}^S}{\partial \bar{x}^2} + \bar{M}_p \right) &= -q_z, \\ \bar{x} &= 1,\end{aligned}\quad (35)$$

where $\alpha_1 = i\bar{\omega}\alpha + \bar{\omega}^2 \tau^2 \beta / 1 - i\bar{\omega}\alpha \tau^2$ and $\beta_1 = -\beta \bar{\omega}^2 / 1 - i\bar{\omega}\alpha \tau^2$. By solving equations (32) and (33), the general solutions are

$$\begin{aligned}\bar{w}^S &= A_1 e^{\gamma_1 \bar{x}} + A_2 e^{-\gamma_1 \bar{x}} + A_3 e^{\gamma_2 \bar{x}} + A_4 e^{-\gamma_2 \bar{x}}, \\ \bar{M}_p &= -i\bar{\omega}\alpha A_1 e^{\gamma_1 \bar{x}} - i\bar{\omega}\alpha A_2 e^{-\gamma_1 \bar{x}} - i\bar{\omega}\alpha A_3 e^{\gamma_2 \bar{x}} - i\bar{\omega}\alpha A_4 e^{-\gamma_2 \bar{x}} + A_5 \bar{x} + A_6,\end{aligned}\quad (36)$$

where $r_1 = \sqrt{-\alpha_1 \pm \sqrt{\alpha_1^2 - 4\beta_1/2}}$, $r_2 = \sqrt{-\alpha_1 \pm \sqrt{\alpha_1^2 - 4\beta_1/2}}$, and A_1, A_2, A_3, A_4, A_5 , and A_6 are undetermined coefficients. The undetermined coefficients can be determined by boundary condition equations (34) and (35). The deflection amplification factor g , w and the equivalent couple amplification factor of liquid pore pressure are introduced as follows:

$$\begin{aligned}w &= \left| \frac{\bar{w}^S}{q} \right|, \\ g &= \left| \frac{\bar{M}_p}{q} \right|.\end{aligned}\quad (37)$$

5. Numerical Examples

Based on the obtained deflection amplification factor w and equivalent couple amplification factor g of the incompressible

nonlocal saturated poroelastic cantilever beam under vertical simple harmonic concentrated force, the steady-state dynamic response characteristics of the incompressible nonlocal saturated poroelastic cantilever beam are analyzed through numerical examples. If there is no special description, the dimensionless quantities are $\tau = 0.05$, $\alpha = 20$, and $\beta = 10$. Figures 3–8 show the curves of mid-span deflection amplification factor w and equivalent couple amplification factor g of the incompressible nonlocal saturated poroelastic cantilever beam varying with dimensionless frequency $\omega L/\nu$ for different values of nonlocal coefficient τ , mechanical parameter α , and geometric parameter β . Evidently, there are obvious peaks and troughs in the curves, which shows that there is resonance in the vertical vibration of the incompressible nonlocal saturated poroelastic cantilever beam under a simple harmonic load. When the frequency is large, because the structure has no time to reflect, the deflection amplification factor of the cantilever beam gradually approaches zero, while the equivalent couple amplification factor tends to a stable value. Figures 9–14 show the variation curves of the deflection amplification factor and

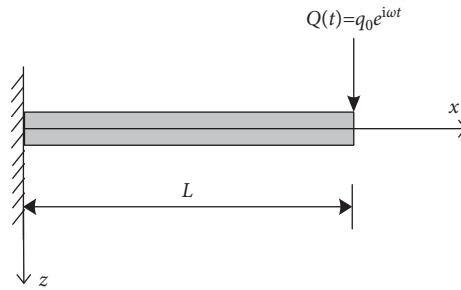


FIGURE 2: Incompressible nonlocal saturated poroelastic cantilever beam under vertical harmonic concentrated loading.

equivalent couple amplification factor at different positions of the beam varying with x/L when the dimensionless frequency $\omega L/\nu = 1.0$ for different values of nonlocal coefficient τ , mechanical parameter α , and geometric parameter β . Since the external concentrated force acts at $x/L = 1$, the deflection amplification factor increases gradually with the increase in x/L and the equivalent couple amplification factor in the middle of the span is the largest, which has a certain relationship with its boundary conditions.

The influence of nonlocal coefficient τ on the deflection amplification factor and equivalent couple amplification factor is shown in Figures 3, 4, 9, and 10; $\tau = 0$ is the result of ignoring the influence of nonlocal effects such as solid particle size and pore size. The deflection amplification factor and equivalent couple amplification factor are larger when nonlocal effects are considered than when they are not considered. Therefore, the influence of nonlocal effects on the steady-state response of the beam should not be ignored, and the deflection amplification factor and equivalent couple amplification factor increase with the increase of nonlocal factors. In addition, when τ is small, because the left end of the beam is a fixed end, the influence of the nonlocal coefficient τ on the deflection amplification factor and the equivalent couple amplification factor is relatively small.

The influence of the mechanical parameter α on the deflection amplification factor and equivalent couple amplification factor is shown in Figures 5, 6, 11, and 12. When the dimensionless frequency is small ($\omega L/\nu < 1.0$), the larger the parameter α is, the smaller the deflection amplification factor and the larger the valley value will be. When the dimensionless frequency is large ($\omega L/\nu > 1.0$), the larger the parameter α is, the larger the deflection amplification factor and the greater the peak value will be. The equivalent couple amplification factor increases with the increase in parameter α . But parameter α has little effect on the peak position of the curve of the deflection amplification factor and equivalent couple amplification factor varying with frequency.

The influence of the geometric parameter β on the deflection amplification factor and equivalent couple amplification factor is shown in Figures 7, 8, 13 and 14. The larger the parameter β is, the larger the deflection amplification factor and the smaller the valley value will be, when the dimensionless frequency is small. The larger the parameter β is, the smaller the deflection amplification factor and the smaller the peak value will be, when the dimensionless frequency is large. When the

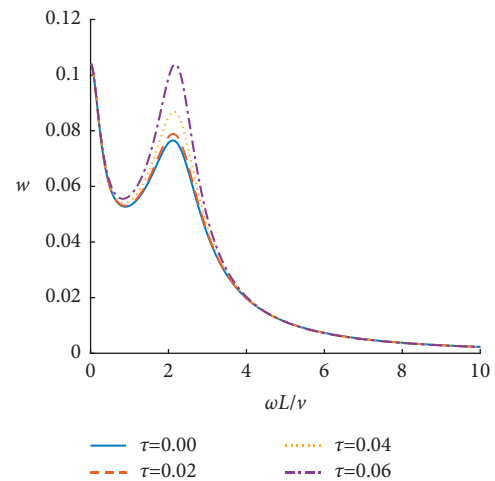


FIGURE 3: Influence of the nonlocal coefficient on the deflection amplification factor at the midpoint of the beam.

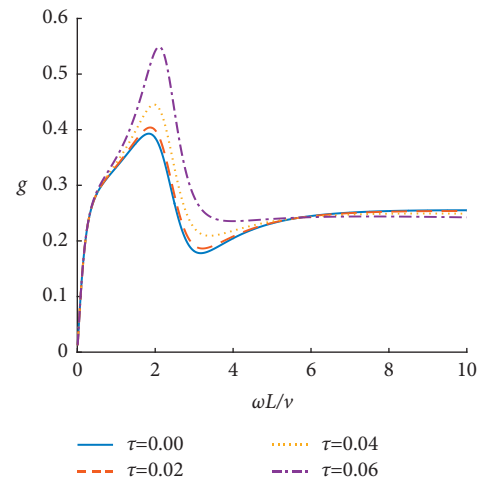


FIGURE 4: Influence of the nonlocal coefficient on the equivalent couple amplification factor at the midpoint of the beam.

dimensionless frequency is small, the equivalent couple amplification factor increases with the parameter β ; when the frequency is large, it shows the opposite, but the difference is relatively small. Different from the parameter α , the parameter β has a significant influence on the peak position of the curve of the deflection amplification factor and equivalent couple amplification factor varying

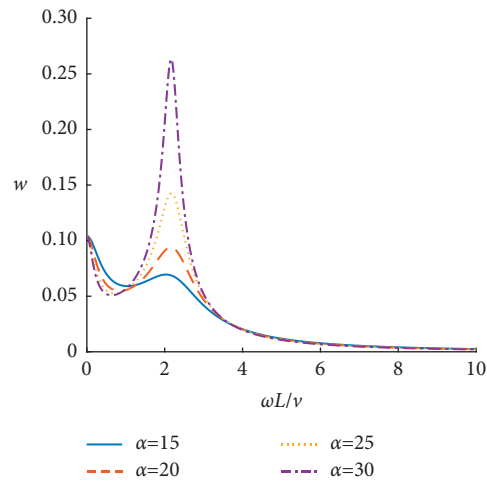


FIGURE 5: Influence of the parameter α on the deflection amplification factor at the midpoint of the beam.

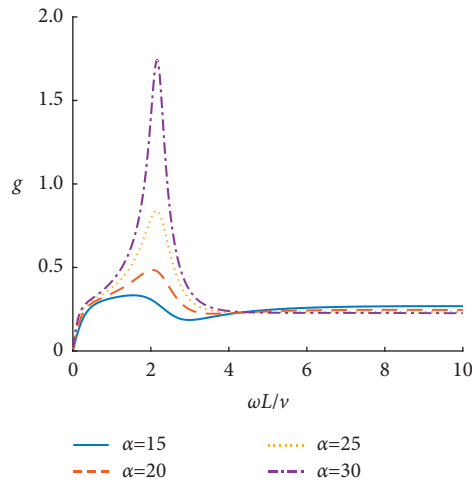


FIGURE 6: Influence of the parameter α on the equivalent couple amplification factor at the midpoint of the beam.

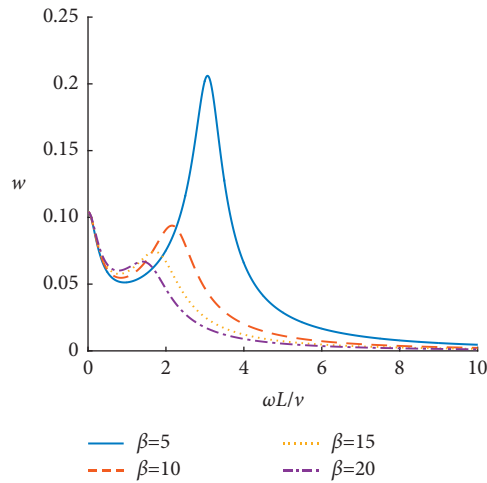


FIGURE 7: Influence of the parameter β on the deflection amplification factor at the midpoint of the beam.

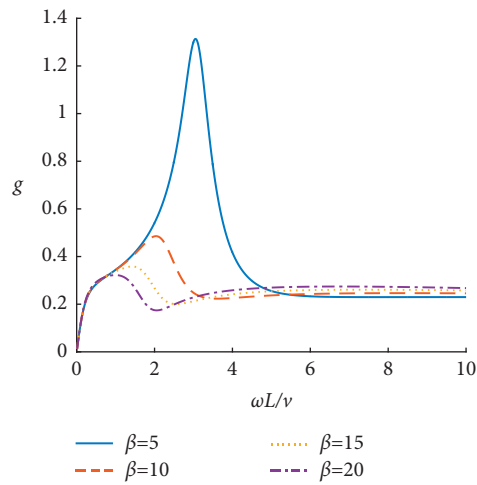


FIGURE 8: Influence of the parameter β on the equivalent couple amplification factor at the midpoint of the beam.

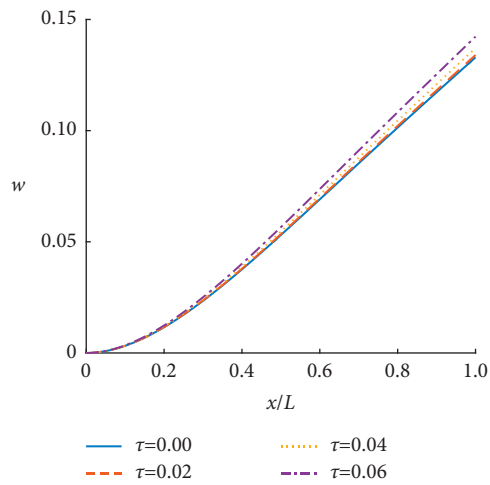


FIGURE 9: Influence of the nonlocal coefficient on the deflection amplification factor at different locations of the beam.

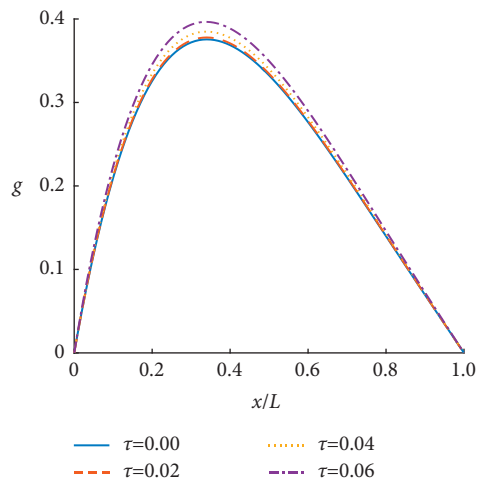


FIGURE 10: Influence of the nonlocal coefficient on the equivalent couple amplification factor at different locations of the beam.

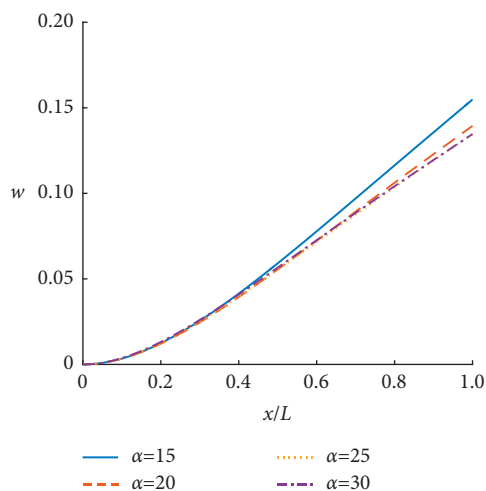


FIGURE 11: Influence of the parameter α on the deflection amplification factor at different locations of the beam.

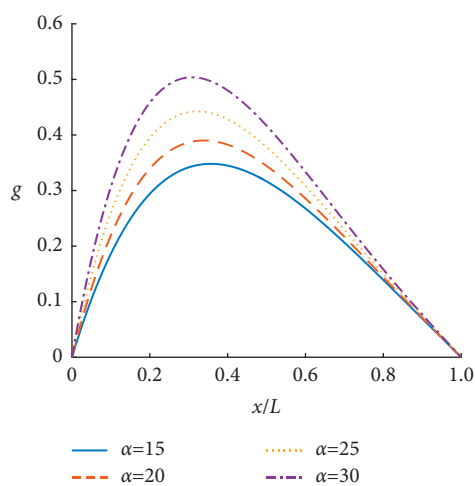


FIGURE 12: Influence of the parameter α on the equivalent couple amplification factor at different locations of the beam.

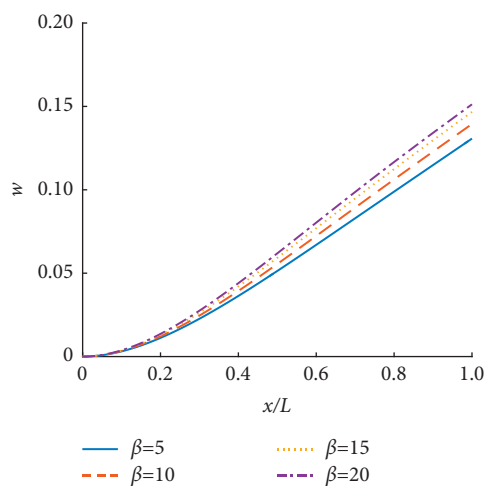


FIGURE 13: Influence of the parameter β on the deflection amplification factor at different locations of the beam.

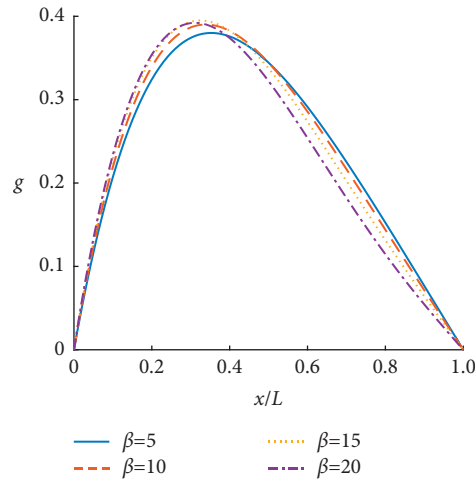


FIGURE 14: Influence of the parameter β on the equivalent couple amplification factor at different locations of the beam.

with frequency. With the increase in the parameter β , the frequency corresponding to the peak value of the curve of the deflection amplification factor and equivalent couple amplification factor will increase.

6. Conclusions

Combining the nonlocal elastic theory with the porous medium theory and considering the nonlocal effects such as solid skeleton particle size, pore size, and pore dynamic stress, the dynamic control equation of the incompressible nonlocal saturated poroelastic cantilever beam is established. Taking the saturated porous cantilever beam as an example, the response of the beam under the vertical harmonic concentrated force at the free end is studied. The main conclusions are as follows: (1) there is resonance in the vertical vibration of the incompressible nonlocal saturated poroelastic cantilever beam under a simple harmonic load; (2) the deflection amplification factor and equivalent couple amplification factor with nonlocal effect are larger than those without nonlocal effect, so the influence of the nonlocal effect on the steady-state response of the beam should not be ignored; (3) the mechanical parameter α and geometric parameter β have a significant influence on the deflection amplification factor and the equivalent couple amplification factor, and the influence law has a certain relationship with the frequency; (4) the parameter β has a significant influence on the peak position of the curve of the deflection amplification factor and equivalent couple amplification factor varying with frequency, and α has little effect on the peak position.

References

- [1] M. A. "Theory of propagation of elastic waves in a fluid-saturated porous solid.I. low-frequency range," *Journal of the Acoustical Society of America*, vol. 28, no. 2, pp. 168–178, 1956.
- [2] M. A. "Theory of propagation of elastic waves in a fluid-saturated porous solid. II. Higher-frequency range," *The Journal of the Acoustical Society of America*, vol. 28, no. 2, pp. 179–191, 1956.
- [3] V. W. Lee and M. D. Trifunac, "Response of tunnels to incident SH-waves," *Journal of the Engineering Mechanics Division*, vol. 105, no. 4, pp. 643–659, 1979.
- [4] V. W. Lee and J. Karl, "On deformation near a circular underground cavity subjected to incident plane P waves," *European Earthquake Engineering*, vol. 7, no. 1, pp. 29–41, 1993.
- [5] Y. S. Karinski, V. V. Shershnev, and D. Z. Yankelevsky, "Analytical solution of the harmonic waves diffraction by a cylindrical lined cavity in poroelastic saturated medium," *International Journal for Numerical and Analytical Methods in Geomechanics*, vol. 31, no. 5, pp. 667–689, 2007.
- [6] Z. Yuan, Y. Cai, and Z. Cao, "An analytical model for vibration prediction of a tunnel embedded in a saturated full-space to a harmonic point load," *Soil Dynamics and Earthquake Engineering*, vol. 86, no. 7, pp. 25–40, 2016.
- [7] L. H. Tong, Y. S. Liu, D. X. Geng, and S. K. Lai, "Nonlinear wave propagation in porous materials based on the Biot theory," *Journal of the Acoustical Society of America*, vol. 142, no. 2, pp. 756–770, 2017.
- [8] M. Ciarletta, B. Straughan, and V. Tibullo, "Acceleration waves in a nonlinear Biot theory of porous media," *International Journal of Non-linear Mechanics*, vol. 103, no. 7, pp. 23–26, 2018.
- [9] Z. Yuan, A. Boström, Y. Cai, and Z. Cao, "Closed-form analytical solution for vibrations from a tunnel embedded in a saturated poroelastic half-space," *Journal of Engineering Mechanics*, vol. 143, no. 9, Article ID 04017079, 2017.

- [10] K. I. Lee, V. F. Humphrey, B. N. Kim, and S. W. Yoon, "Frequency dependencies of phase velocity and attenuation coefficient in a water-saturated sandy sediment from 0.3 to 1.0 MHz," *Journal of the Acoustical Society of America*, vol. 121, no. 1, pp. 2553–2560, 2007.
- [11] I. Edelman and K. Wilmanski, "Asymptotic analysis of surface waves at vacuum/porous medium and liquid/porous medium interfaces," *Continuum Mechanics and Thermodynamics*, vol. 14, no. 1, pp. 25–44, 2002.
- [12] A. Busse, M. Schanz, and H. Antes, "A poroelastic mindlin-plate," *Pammattone*, vol. 3, no. 1, pp. 260–261, 2003.
- [13] D. Iesan and L. Nappa, "Thermal stresses in plane strain of poroelastic solid," *Meccanica*, vol. 39, no. 2, pp. 125–138, 2004.
- [14] L. P. Li, G. Cederbaum, and K. Schulgasser, "Vibration of poroelastic beams with axial diffusion," *Euro J Mech*, vol. 15, no. 6, pp. 1077–1094, 1996.
- [15] G. Cederbaum, K. Schulgasser, and L. P. Li, "Interesting behavior patterns of poroelastic beams and columns," *International Journal of Solids and Structures*, vol. 35, no. 34–35, pp. 4931–4943, 1998.
- [16] Y. Xiao and W. Chen, "A nonlinear mathematical model for large deflection of incompressible saturated poroelastic beams," *Applied Mathematics and Mechanics*, vol. 28, no. 11, pp. 1587–1595, 2007.
- [17] A. C. Eringen, "On differential equations of nonlocal elasticity and solutions of screw dislocation and surface waves," *Journal of Applied Physics*, vol. 54, no. 9, pp. 4703–4710, 1983.
- [18] A. C. Eringen and D. G. B. Edelen, "On nonlocal elasticity on nonlocal elasticity," *International Journal of Engineering Science*, vol. 10, no. 3, pp. 233–248, 1972.
- [19] L. Tong, Y. Yu, W. Hu, Y. Shi, and C. Xu, "On wave propagation characteristics in fluid saturated porous materials by a nonlocal Biot theory," *Journal of Sound and Vibration*, vol. 379, pp. 106–118, 2016.
- [20] H. B. Dinga, L. H. Tong, C. J. Xua, X. S. Zhao, and Q. X. Nie, "Dynamic responses of shallow buried composite cylindrical lining embedded in saturated soil under incident P wave based on nonlocal-Biot theory," *Soil Dynamics and Earthquake Engineering*, vol. 121, no. 6, pp. 25–40, 2019.

Using response surface methods (RSM), the effect of alumina nanoparticles as additive with diesel–biodiesel blends has been studied on performance and emission characteristic of a six-cylinder diesel engine

Pili Kumari Sahoo, *Department of Mechanical Engineering, Aryan Institute of Engineering & Technology, Bhubaneswar, p.kumari4gmail.com*

Rajaram Sahu, *Department of Mechanical Engineering, Raajdhani Engineering College, Bhubaneswar, rajaramsahu65@gmail.com*

Sidharth Pradhan, *Department of Mechanical Engineering, Capital Engineering College, Bhubaneswar, sidharthpradhan265@gmail.com*

Subhasis Sarkar, *Department of Mechanical Engineering, NM Institute of Engineering & Technology, Bhubaneswar, subhasissarkar14@yahoo.co.in*

ARTICLE INFO

Keywords:

IC engine
Performance
Exhaust emission
Nanoparticle
Biodiesel
Response surface methodology

ABSTRACT

The impact of alumina nanoparticle concentration in diesel–biodiesel blended fuels and engine speed on the performance and emission characteristics of a six-cylinder, four-stroke diesel engine was explored in this study. Alumina nanoparticles (40, 80, 120, and 160 ppm) were made and put to a diesel–biodiesel blended fuel as an additive. These mixtures were used to fuel a diesel engine that ran at various speeds (800, 850, 900, 950 and 1000 rpm). Following that, using response surface approach, the interaction of variables on diesel engine emissions and performance was examined (RSM). For a nanoparticle concentration of 160 ppm and an engine speed of 1000 rpm, the maximum brake power and torque were 42.82 kW and 402.8 N.m, respectively. The minimal BSFC, CO, and HC were also determined to be 207.21 gr/kWh, 1.15 percent, and 9%, respectively. For a nanoparticle concentration of 160 ppm and an engine speed of 1000 rpm, the maximum CO₂ and NO_x values were 11.76 percent and 1899 ppm, respectively. The findings of the experiments demonstrated that alumina nanoparticles are a good addition to diesel–biodiesel blends to increase engine performance and reduce emissions. It was discovered that the mathematical model established can be utilised to accurately estimate engine performance and emissions.

1. Introduction

Diesel engine is widely used in agriculture, industry, transportation and other fields. Due to the global warming threat, governments have strict rules regarding emissions to the environment. Therefore, efforts to increase the quality of combustion and reduce environmental pollutants along with the use of alternative fuels as well as conducting research in this field are crucial [1,2].

The global need for alternative energy resources is on the rise as a result of the diminution of fossil fuels and due to their negative environmental effects. In this domain, strict rules and regulations regarding emission have been adopted by the state organizations that oblige scholars and practitioners to opt for alternatives for fossil fuels. In fact, the main aim is to decrease environmental destruction and have different renewable fuels at disposal to be used in internal combustion engines [3,4,5]. Therefore, it is necessary to provide unconventional fuels like

the conventional petroleum-based ones so that the environment can be protected against pollution. Non-stop attempts have also been being made in this area in order to reduce the use of petroleum-based fuels all over the world [6,7,8]. CI engines produce pollutants such as CO, CO₂, HC, NO_x, smoke and particulate matter [9,10]. So, the harmful effects of fossil fuel consumption have made it essential to find renewable fuels to be used in diesel engines [11,12].

Some advantages of using biodiesel or its blends on engine emissions are decrease in the emissions of CO, HC and PM [13,14]. Biodiesel is considered as an accessible, eco-friendly, non-toxic, and low-sulfur recyclable fuel with the potential to be directly used in diesel engines without the need for any change [15]. A large bulk of literature has been reported regarding the application of nanoparticles in biodiesel engines. Additives are usually used to improve fuel properties. Aluminum, silver, cerium, iron, manganese, copper, graphene quantum dot (GQD) and magnesium are some metal additives that improve engine performance and fuel combustion with their more catalytic activity in combination

Nomenclature

RSM	Response Surface Methodology
ASTM	American Society for Testing and Materials
B	Biodiesel
B ₂₀	20% Biodiesel
D100	Pure diesel
CI	Compressed Ignition
IC	Internal Combustion
CO	Carbon Monoxide
CO ₂	Carbon Dioxide
NO _x	Nitrogen Oxides
O ₂	Oxygen
HC	Hydrocarbons
BSFC	Brake Specific Fuel Consumption
PM	Particulate Matter

FAME	Fatty Acid Methyl Ester
kW	kilo Watt
Nm	Newton meter
MPa.s	Mega Pascal second
ppm	part per million
rpm	Revolutions per minute
WCO	Waste Cooking Oil
SEM	Scanning Electron Microscopy
Cm	Centimeter
°C	Centigrade Degree
g	gram
h	hour
CCD	Central Composite Design
GQD	Graphene Quantum Dot
GC	Gas Chromatography

with biodiesel [16,17,18].

In recent years, it has been found that adding nanoparticles to the biodiesel fuel improves the fuel features, combustion and engine performance and decreases the exhaust emissions from a diesel engine [19]. Moreover, nanoparticles are practical additives for increasing the octane number. In a research, the amino-functionalized carbon nanotubes were added to gasoline. According to the results of octane number examination, it has been proved that such additives would lead to the rise of the octane number [20]. Tyagi et al. examined the impact of Al₂O₃ nanoparticles on the diesel fuel of a diesel engine. Experiments have shown that heat transfer to the fuel and probability of ignition increases by adding nanoparticles [21]. Solero investigated the influence of Al₂O₃ nano-additive to diesel fuel on diesel combustion spray and flame characteristics. Results showed that Alumina nanoparticle can increase the fuel penetration length and improve the flame and combustion [22].

In a study, the effect of three metal nanoparticles (A1, B1, and F1) in the fuel on diesel engine was investigated. According to the results, the brake thermal efficiency increased for 9, 4, and 2% in A1, B1, and F1, respectively. Researchers discovered that carbon monoxide and unburned hydrocarbon emissions declined for 4 and 8% in F1 and A1 fuels, respectively. A small increase was also reported in nitrogen oxide emissions [23]. Adding nanoparticles to biodiesel fuel has the potential to enhance the engine performance and decline CO and HC emissions, while increasing CO₂ and NO_x emissions [24]. Among the various methods for reducing emissions from the exhaust of combustion engines, the use of catalysts has become common due to their advantages in reducing greenhouse gases [25]. The effect of nano-blended fuels on the performance of diesel engine was also investigated. The results showed that by using nanoparticles in diesel and biodiesel fuels and by increasing nanoparticle concentration in fuels at all engine speeds, power and torque increased and the consumption of brake specific fuel decreased. Also, the influence of nanoparticles on the exhaust gas emission was investigated. It was observed that by using nano additives in diesel and biodiesel blend fuels, CO and HC emissions decreased and CO₂ and NO_x emissions increased [26]. Effects of adding carbon nanotubes (CNT) and Ag nano particles to diesel and diesel-biodiesel blends on the emission and performance parameters of diesel engines was also investigated and it was shown that adding nanoparticles to diesel and biodiesel fuels led to increase in torque output and engine power by 2% while a 7.08% decrease happened to the brake specific fuel consumption in comparison with pure diesel fuel. Carbon dioxide emission was maximised by a 17.03% growth and carbon monoxide emission in a diesel-biodiesel fuel with nanoparticles decreased significantly by a 25.17% drop compared to pure diesel fuel. With the addition of nano particles to blended fuels, NO_x emission rose by 25.32% in

comparison with the pure diesel [27]. In another study, effects of CNT nanoparticles added to biodiesel fuel on the performance and emission parameters of a diesel engine was investigated and the results showed that the brake power was increased and brake specific fuel consumption was decreased. Moreover, they concluded that CO and HC emissions were decreased [28].

Experimental works on performance and emission parameters of engines are so complicated and it is not very effective in terms of being expensive and time consuming. For this reason, optimization of engine performances, combustion and emissions using the input factors such as engine load, engine speed, fuel blend, etc. has become of significant attention recently [29]. RSM have been chosen by numerous researchers to diminish the number of tests. Also, RSM is a common technique to optimize the output factors and engineering based modeling by test variables. Unlike other optimization techniques, RSM needs lowest period to finish the process through reducing the number of tests and making suitable matrix for tests [30,31]. Some researchers used RSM to explore the impact of engine operating parameters on the desired responses. Lee and Reitz [32] showed the reduction of pollutants and changes in other engine parameters in an injection diesel engine, which had a common rail system where they employed the RSM. Ileri et al. [33] predicted engine performance and exhaust emission characteristics of a diesel engine that used canola oil methyl ester as an alternative fuel. Bharadwaz et al. [34] predicted that engine performance variables such as compression ratio, load and fuel mixture to enhanced the performance characteristics of diesel engines using alternative fuels. In another study, the amount of ignition advance of a gasoline engine was predicted using fuel filters with different lifespan by the RSM [35].

In this study, according to the recommendations in the applications of biodiesel nano-additives [36], alumina nanoparticles were selected as nano-additives in biodiesel fuel due to their oxygenated composition to improve the combustion process. Then, the stable diesel-biodiesel blends were prepared using WCO methyl ester and Al₂O₃ nanoparticles with new concentrations (40, 80, 120 and 160 ppm) were added in diesel-biodiesel blends. RSM was used for mathematical modelling of engine performance and exhaust emissions at different engine speeds from 800 to 1000 rpm. Since there is lack of knowledge in the literature on the effect of different nano-alumina additives on biodiesel blends, the utilization of further nano alumina concentrations in diesel-biodiesel blends was addressed in this research study to assess the performance and emission characteristics of a six-cylinder diesel engine. Therefore, this study was conducted to discover the effect of combining biodiesel fuel with alumina nanoparticle additives in different concentrations on improving combustion, increasing performance and reducing emissions from IC engines and the results were analyzed by RSM method.

Table 1

Technical specifications of the diesel engine.

Engine type	IC engine, Six-cylinder
Combustion order	1-5-3-6-2-4
Bore × Stroke (mm)	98.6 × 127
Compression ratio	17:1
Displacement volume (l)	5.8
Max. Torque (N.m/rpm)	410 / 1300
Max. Power (kW/rpm)	82 / 2300

Table 2

Technical specifications of the exhaust gas analyzer.

Parameters	Unit	Measurement range	Accuracy
CO	vol, %	0–15	±0.3
CO ₂	vol, %	0–20	±0.2
HC	Ppm	0–20000	±0.2
NO _x	Ppm	0–5000	±0.2

2. Materials and methods

2.1. Experimental

In the present research, the tests were conducted on a six-cylinder diesel engine whose specifications have been described in Table 1. A 190 kW SCHENCK-WT190 eddy-current dynamometer was employed in the research. In doing so, fuel consumption was evaluated by means of laminar type flow meter (Pierburg model) in the range of 0.4–45 kg/h. The amount of exhaust emissions (CO, CO₂, HC and NO_x) were recorded by an online and calibrated exhaust gas analyzer (AVL DiGas 4000). The technical specifications of the emission tester are reported in Table 2. Also, a special fuel tank was installed and used for fuel mixtures in the diesel engine. Fig. 1 illustrates the engine test and schematics of the experimental setup.

In this research, five types of fuels were utilized in the experiments. The required base diesel was provided from Tehran Oil Refinery Company. In Table 3, the features of the produced biodiesel and the results of comparing it with ASTM D6751 standard have been presented. Fatty acid methyl ester (FAME) was prepared from WCO through conventional transesterification process using lab-scale stirring tank reactor (Fig. 2).

The Gas Chromatography (GC) was applied for evaluating the transesterification reaction yield as well as the final FAME content in the purified product. Metcalf method was used to analyze the purified FAME and, then, the profile of fatty acids and the molecular weight of WCO were determined by injecting the already obtained sample into the GC device.

Four alumina nano-additive concentrations of 40, 80, 120 and 160 ppm were used in this study. Dynamic light scattering (DLS) device was

used to evaluate the size and zeta potential of Al₂O₃ nanoparticles (Fig. 3). The particle size and surface charge of the nanoparticles were examined using DLS (Malvern instruments, Westborough, MA, USA) in three replications. The results of DLS showed that the average size of Al₂O₃ nanoparticles was 72.51 ± 8.7 nm. Moreover, these results revealed that the zeta potential of Al₂O₃ nanoparticles was 37.5 ± 4.2 mV.

After the start of the engine, it was given enough time to warm up. Then, it reached the steady state condition. Engine tests were performed at 800, 850, 900, 950 and 1000 rpm and full load condition. Prior to running the engine via a new fuel mixture, 15 min was given to the engine to keep running so that the remainder of the fuel from the prior experiment could be consumed. Thereafter, engine speed, fuel consumption, and load were recorded, and the brake power and BSFC were also evaluated. After the engine reached the steady state, concentrations of exhaust emissions (HC, CO, CO₂ and NO_x) from an online and accurately calibrated exhaust gas analyzer were measured.

2.2. Uncertainty analysis

Uncertainty analysis is the systematic and symmetric set of procedures followed for calculation of errors in experimental data. The percentage of uncertainty for various parameters was analyzed based on the square root method. The overall percentage of uncertainty was calculated by using the following equation [15,39]:

Table 3

The biodiesel properties produced in comparison with the ASTM D 6751 standard.

Property	Test method	Limits	Units	Measured property
Water and sediment	ASTMD 2709	0.05 max	% vol	0.048
Kinematical viscosity (40 °C)	ASTMD 445	1.9–6.0	mm ² /s	4.5
Sulphated ash	ASTMD 874	0.02 max	% mass	0.02
Sulphur S15 grade	ASTMD 5453	0.0015 max	% mass	0.002
Copper strip corrosion	ASTMD 130	No. 3 max		No. 2
Flash point, Closed cup	D93	130 min	°C	185
Cetane number	ASTMD 613	–	–	48
Carbon residue	ASTMD 4530	0.05 max	% mass	0.025
Acid number	ASTMD 664	0.50 max	mg KOH/g	0.43
Total glycerin	ASTMD 6584	0.24	% mass	0.015
Methanol content	EN14110	0.20 max	% vol	0.18

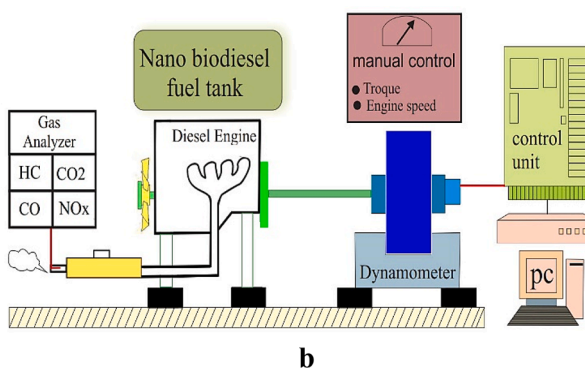
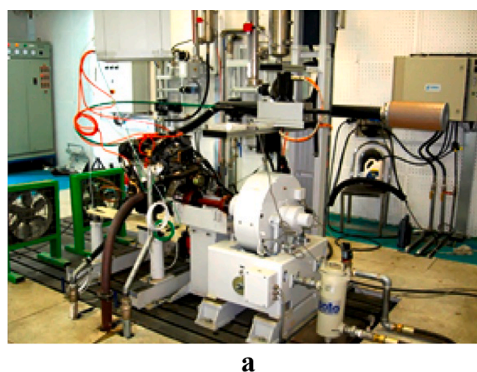


Fig. 1. Engine test setup (a) and schematics of the experimental setup (b).

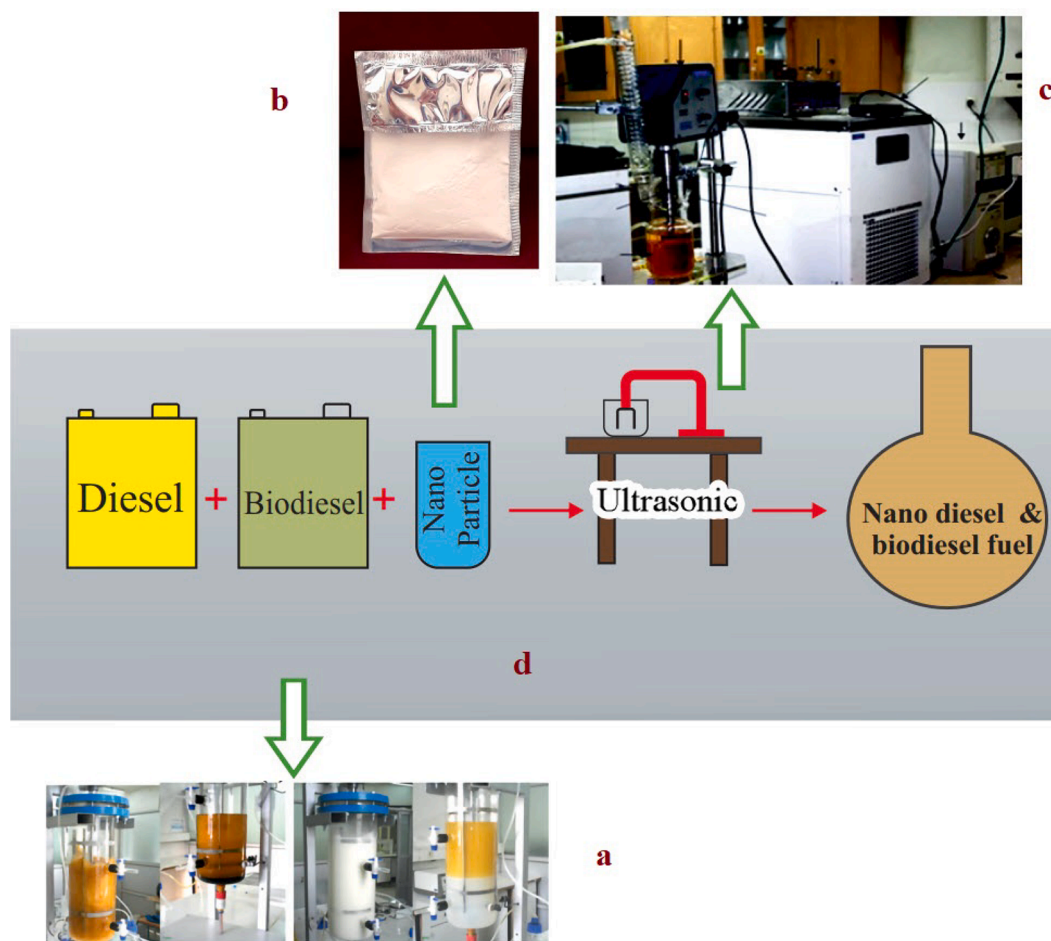


Fig. 2. (a) Transesterification reaction, (b) Al_2O_3 nanoparticles, (c) Ultrasonication of Al_2O_3 nanoparticles into biodiesel fuel and (d) Schematic layout of the experimental setup.

Percentage of uncertainty = $\pm \text{Square root of } \{(\text{uncertainty of CO})^2 + (\text{uncertainty of CO}_2)^2 + (\text{uncertainty of HC})^2 + (\text{uncertainty of NO}_x)^2 + (\text{uncertainty of BT})^2 + (\text{uncertainty of BP})^2 + (\text{uncertainty of BSFC})^2\}$
 $= \pm \text{Square root of } (0.3^2 + 0.2^2 + 0.2^2 + 0.2^2 + 0.4^2 + 0.5^2 + 0.6^2) = \pm 0.98$.

2.3. Statistical analysis by RSM

Response Surface Method (RSM) is a common route for designing experiments and finding the optimum values of dependent variables (responses) through the statistical model between independent variables (experimental factors). RSM significantly decreases the number of required experimental runs and based on the selected model, can also identify the effect of interaction between factors. RSM was employed for statistical analysis using Design-Expert® Software (version10). To this end, the influence of the independent variables on the performance and exhaust emission parameters were assessed by using the central composite design (CCD). Independent variables were the fuel blend (nano-additive concentration) and engine speed at 5 levels. The experiments matrix and the proposed experimental design by software are tabulated in Tables 4 and 5, respectively.

3. Results and discussion

Table 6 presents the analysis of variance (ANOVA) results for the conducted experiments. The probability value (p value) for all models is <0.01 . Therefore, ANOVA shows that the model is statistically significant.

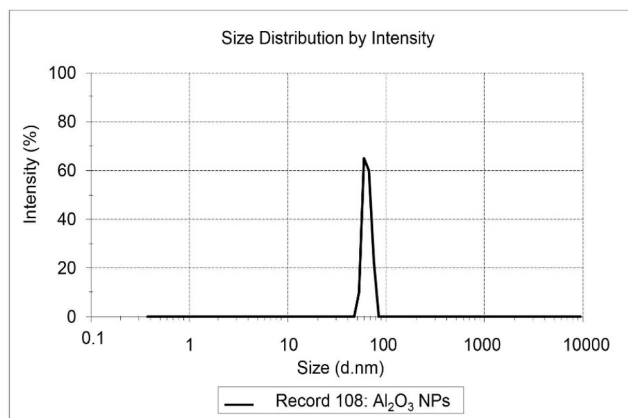
3.1. Brake torque

The interaction effect of nanoparticles concentration in B_{20} fuel and engine speed on the brake torque is illustrated in Fig. 4. The contour surface plot shows that the addition of nano particles and their mixture with B_{20} fuel increased brake torque for all engine speeds. In fact, with increasing concentration of nanoparticles in the fuel and increasing engine speed, the brake torque has increased. This is due to the fact that the performance of alumina nanoparticles is similar to oxygen buffers as they both increase the combustion quality of diesel fuel sample [39]. Moreover, it can be seen that as the concentration of nanoparticle increases, a slight improvement in brake torque is observed. According to Fig. 4 and the results of ANOVA shown in Table 6, it is evident that the engine speed and concentration of nanoparticles in B_{20} fuel has a significant effect (at a level of 0.01) on brake torque. The regression equation generated for estimation of brake torque (using the coded values) is given by Eq. (1).

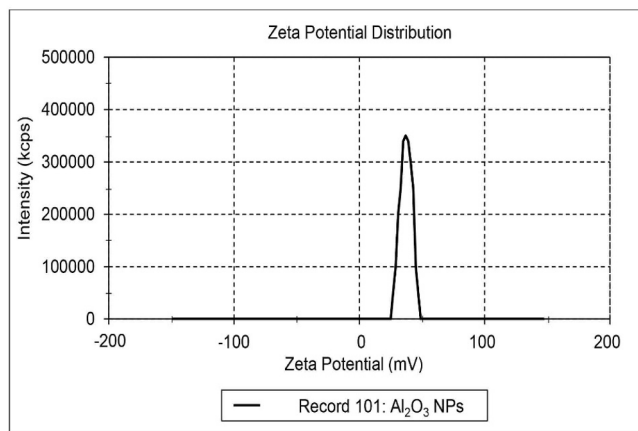
$$\text{Brake Torque} = 380.51 + 20.36A + 4.40B + 0.89A^2 - 3.08B^2 \quad (1)$$

3.2. Brake power

The change trend of brake power along with engine speed and concentration of nanoparticles are shown in Fig. 5. The contour surface plot shows that by increasing the nano content in the B_{20} fuel, the engine brake power experienced a small increase for all engine speeds, which means the combustion is tuned to be completed [22]. As the nano-alumina load increases, the density of the blend and the engine



(A)



(B)

Fig. 3. A) Particle size and B) zeta potential of Al_2O_3 nanoparticles.

Table 4
The experiment matrix.

				Independent variables	Symbols	Levels of each factor
Engine speed (rpm)	A	800	850	900	950	1000
Concentration of nanoparticles (ppm)	B	0	40	80	120	160

Table 5
Experimental design proposed by RSM.

Std	Run	Engine speed (Rpm)	Nano-additive concentration of (ppm)	Brake torque (N. m)	Brake power (kW)	BSFC (gr/ kWh)	CO (%) vol)	CO ₂ (%) vol)	HC (ppm)	NO _x (ppm)
8	1	900	160	383.60	35.99	212.34	1.41	11.18	14.00	1690
13	2	900	80	379.50	35.64	214.89	1.47	10.00	16.00	1517
9	3	900	80	380.30	35.84	214.99	1.50	10.25	15.00	1525
10	4	900	80	381.60	35.74	215.68	1.42	10.00	15.50	1508
12	5	900	80	380.80	34.99	214.69	1.48	10.56	15.00	1485
2	6	1000	0	395.00	41.36	218.44	1.30	11.30	14.00	1370
4	7	1000	160	402.80	42.82	207.21	1.15	11.76	9.00	1899
7	8	900	40	377.10	35.58	217.86	1.50	10.31	17.00	1525
5	9	750	80	353.10	27.84	225.87	1.80	8.88	19.00	1447
6	10	1000	80	400.90	42.00	210.82	1.21	11.52	12.00	1689
3	11	800	160	360.80	29.99	223.13	1.70	9.05	18.00	1639
11	12	900	80	380.40	35.81	214.75	1.49	10.30	15.20	1512
1	13	800	0	353.00	29.57	231.29	1.90	8.70	20.00	1025

volumetric efficiency also increase and this is why the power increases [37]. Adding nano-alumina to fuel leads to higher peak pressure which subsequently causes higher brake power [27,38,40]. The results showed that an increase in nano additive content, would also lead to an increase in the engine torque. The cylinder pressure increased with nano-diesel-biodiesel fuels compared to biodiesel fuel (B_{20}) because ignition delays were reduced and combustion quality was improved. This can be attributed to the improvement of the surface-to-volume ratio of the alumina nanoparticles in the fuel mixture which in turn improves the combustion quality due to the catalytic effect of the nanoparticles [41]. At this stage, a highly advanced timing was made possible by means of the improved antiknock behavior, which led to a higher combustion pressure and, thereby, a larger torque [42,43]. According to Fig. 5 and the results of ANOVA shown in Table 6, it is obvious that the engine speed and concentration of nanoparticles in B_{20} fuel have significant effects on the brake power. The regression equation generated for brake power (using the coded values) is given in Eq. (2).

$$\text{Brake power} = 35.63 + 6.05 A + 0.46B + 0.26 AB + 0.51 A^2 - 0.17 B^2 \quad (2)$$

3.3. Brake specific fuel consumption (BSFC)

Fig. 6 shows the effects of engine speed and nano-alumina load on the BSFC values. It was observed that by increasing the nano-alumina content in the B_{20} fuel, the BSFC decreased for all engine speeds. It is because adding nanoparticles to the fuel enhances the combustion completion [44]. According to Fig. 6 and the results of ANOVA shown in Table 6, it is obvious that the engine speed and load of nanoparticles in B_{20} fuel have significant effects (at the level of 0.01) on BSFC. Eq. 3 presents the regression model obtain by Design Expert Software for the estimation of brake specific fuel consumption (using the coded values) .

$$\text{BSFC} = 214.94 - 6.45 A - 5.08B - 0.77 AB + 1.07 A^2 + 3.67 B^2 \quad (3)$$

3.4. CO emission

The variation of CO emission with engine speed and concentration of nanoparticles in B_{20} fuel has been depicted in Fig. 7. It can be easily noticed that when the concentration of nanoparticles increases in fuel, the CO concentration decreases. This phenomenon indicates that the combustion is tuned to be completed [15,27,45]. According to Fig. 7 and the results of ANOVA shown in Table 6, it is obvious that the engine speed and concentration of nanoparticles in B_{20} fuel has a significant effect (at a level of 0.01) on CO emission. The proposed regression model based on ANOVA (using the coded values) is presented by Eq. (4).

$$\text{CO} = 1.48 - 0.26 A - 0.082B \quad (4)$$

Table 6
Analysis of variance (ANOVA).

Source	Model	A - Engine speed	B - Concentration of nano	AB	A ²	B ²	
Brake Torque	F. Value	381.74	1676.23	61.65	0.00	2.50	15.68
	p-value Prob > F	< 0.0001	< 0.0001	0.0001	1.00	0.1582	0.0055
Brake Power	F. Value	537.29	2466.19	11.35	2.85	13.68	0.79
	p-value Prob > F	< 0.0001	< 0.0001	0.0119	0.13	0.0077	0.0077
BSFC	F. Value	84.43	227.45	111.24	2.02	4.84	30.13
	p-value Prob > F	< 0.0001	< 0.0001	< 0.0001	0.20	0.0637	0.0009
CO	F. Value	150.01	279.78	19.77	–	–	–
	p-value Prob > F	< 0.0001	< 0.0001	0.0012	–	–	–
CO ₂	F. Value	61.26	116.39	5.96	–	–	–
	p-value Prob > F	< 0.0001	< 0.0001	0.0347	–	–	–
HC	F. Value	72.74	176.73	35.90	5.08	–	–
	p-value Prob > F	< 0.0001	< 0.0001	0.0002	0.0506	–	–
NO _x	F. Value	39.63	19.60	59.43	–	–	–
	p-value Prob > F	< 0.0001	0.0013	< 0.0001	–	–	–

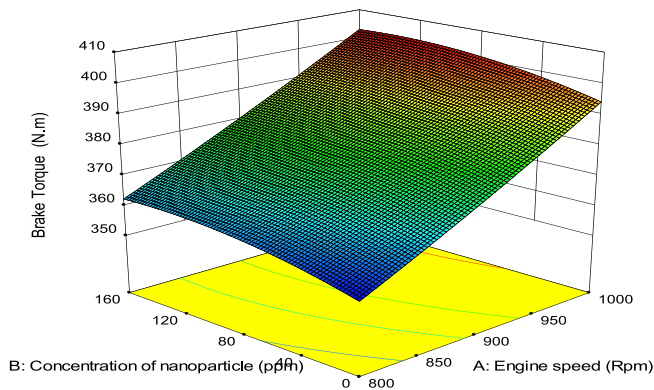


Fig. 4. Effect of engine speeds and concentration of nanoparticles in B₂₀ fuel on brake torque.

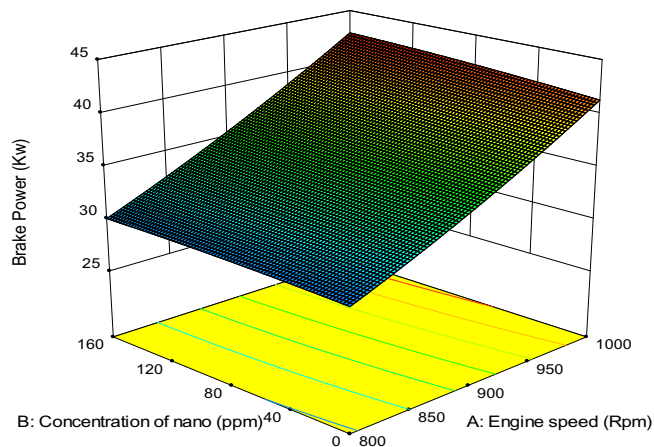


Fig. 5. Effect of engine speeds and concentration of nanoparticles in B₂₀ fuel on brake power.

3.5. CO₂ emission

The effect of the interaction of engine speed and concentration of nanoparticles in biodiesel fuel on CO₂ greenhouse gas is shown in Fig. 8. The results of the experimental test revealed that CO₂ content witnesses an increase with increase in the nanoparticles concentration. The amount of CO₂ emission is dependent upon relative air–fuel ratio and concentration of CO emission [46,47]. The increase in CO₂ is due to the improvement in combustion [13,14,16,47]. According to Fig. 8 and the results of statistical analysis shown in Table 6, it is obvious that the

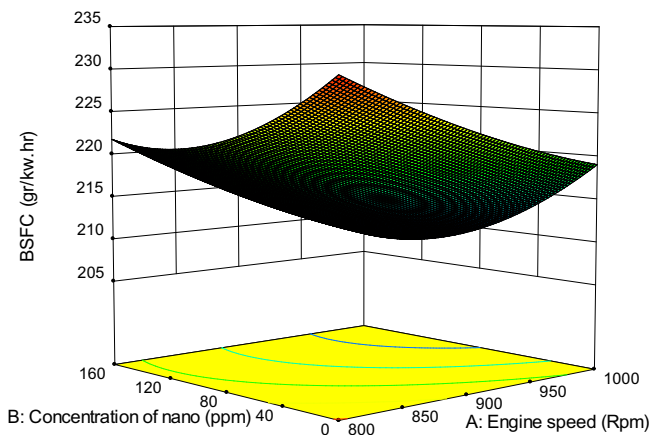


Fig. 6. Effect of engine speeds and concentration of nanoparticles in B₂₀ fuel on BSFC.

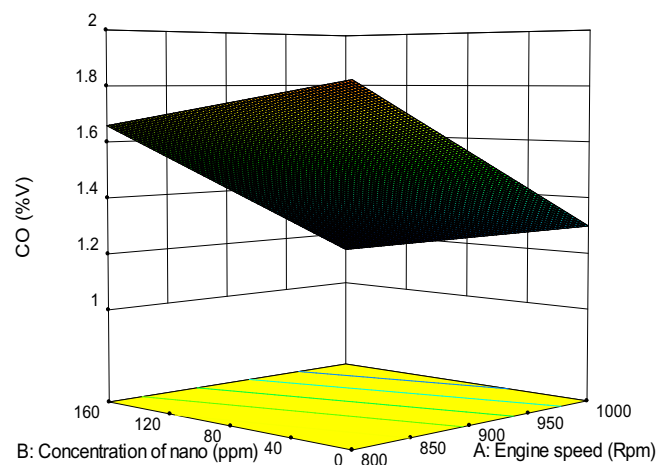


Fig. 7. Effect of engine speeds and concentration of nanoparticles in B₂₀ fuel on CO emission.

engine speed and concentration of nanoparticles in B₂₀ fuel has a significant effect (at a level of 0.01 and 0.05) on CO₂ emission respectively. The obtained regression equations for CO₂ emission (using the coded values) is given by Eq. 5.

$$\text{CO}_2 = 10.33 + 1.20 \text{ A} + 0.32 \text{ B} \quad (5)$$

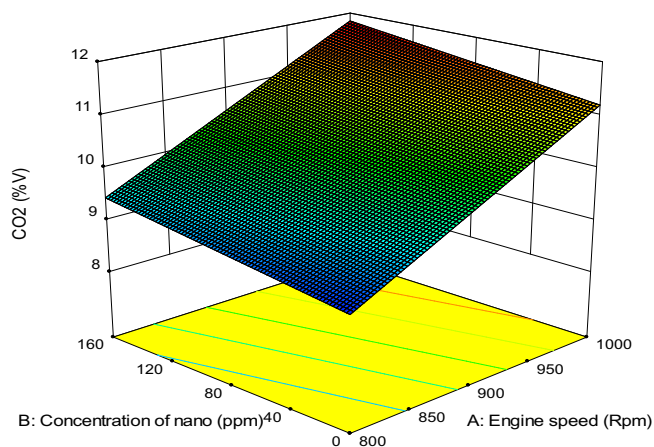


Fig. 8. Effect of engine speeds and concentration of nanoparticles in B₂₀ fuel on CO₂ emission.

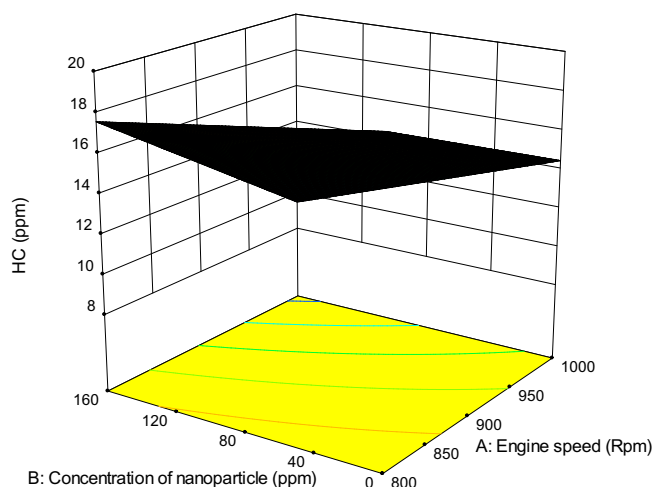


Fig. 9. Effect of engine speeds and concentration of nanoparticle in B₂₀ fuel on HC emission.

3.6. HC emission

The effect of the interaction of engine speed and concentration of nanoparticles in B₂₀ fuel on HC emission is presented in Fig. 9. It is observed that when nanoparticle concentration increases, the HC emission decreases. This is due to the fact that the addition of nanoparticles to fuel reduces the activation temperature of carbon and improves combustion [36]. According to Fig. 9 and the results of ANOVA shown in Table 6, it is obvious that the engine speed and concentration of nanoparticles have significant effects (at a level of 0.01) on HC emission. The regression equations generated for HC emission (using the coded values) are given in Eq. 6.

$$HC = 15.30 - 3.29 A - 1.74 B - 0.75 AB \quad (6)$$

3.7. NO_x emission

The change trend of NO_x emission with engine speed and concentration of nanoparticle in B₂₀ fuel is shown in Fig. 10. The surface plot shows the elevation of NO_x concentration with the increase in nanoparticle concentration. There is a smaller degree of NO_x emission for the neat B₂₀ fuel in comparison with nano-alumina fuel blends. The reason is the increased adiabatic flame temperature. The influence of oxygenated

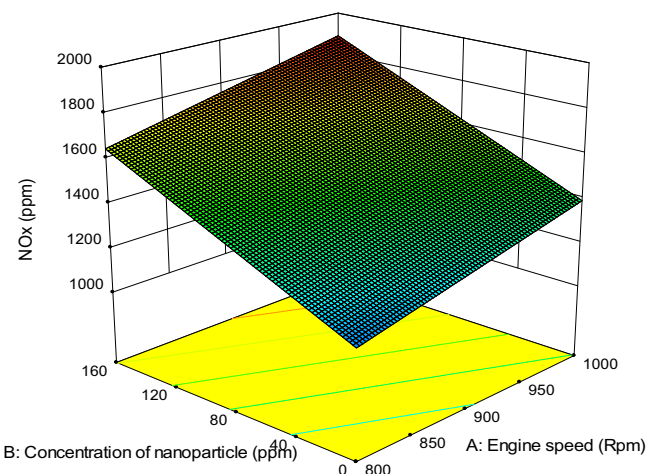


Fig. 10. Effect of engine speeds and concentration of nanoparticle in B₂₀ fuel on NO_x emission.

nanoparticles intensifies combustion and lengthens the ignition delay because nanoparticles addition leads to quicker fulfillment of premixed combustion as well as an increase in the combustion temperature and thus more NO_x emissions [16,48–53]. According to Fig. 10 and the ANOVA results, it is obvious that the engine speed and concentration of nanoparticles in B₂₀ fuel have significant effects (at a level of 0.01) on NO_x emission. Eq. 7 presents the regression equations generated for NO_x emission (using the coded values) by Design Expert Software.

$$NO_x = 1520.55 + 121.90 A + 249.57 B \quad (7)$$

4. Conclusion

In this study, alumina nanoparticles were added to the diesel–biodiesel fuel blend as an additive due to the oxygen content of these particles in order to increase the combustion quality. By using RSM, an empirical relationship was developed to model engine performance and exhaust emissions of a diesel engine fueled with nano biodiesel fuel blends. The maximum values of brake power and torque were predicted as 42.82 kW and 402.8 N.m for 160 ppm concentration of nanoparticle at 1000 rpm engine speed respectively. The minimum values of BSFC, CO and HC were recorded as 207.21 gr/kW.hr, 1.15 V% and 9 V.% within the same engine condition, respectively. With increasing concentration of nanoparticles in the fuel mixture, the average amounts of CO₂ and NO_x increased. In addition, the results proved that RSM is a good method for analyzing experimental data. Statistical analysis showed that the results of experimental tests are very close to the predicted results and can be used to predict engine performance and emissions. The R-squared values obtained for brake torque, brake power, BSFC, CO, CO₂, HC and NO_x were equal to 0.99, 0.99, 0.98, 0.96, 0.92, 0.96 and 0.88, respectively. Results showed that alumina nanoparticles is a good addition for diesel–biodiesel fuel blend to increase performance and decrease emissions of diesel engine that with a little change in engine design, it can be used as an alternative fuel to reduce air pollution in big cities.

CRedit authorship contribution statement

Mani Ghanbari: Conceptualization, Methodology, Investigation, Supervision, Data curation, Software, Validation, Writing - original draft. **Lotfali Mozafari-Vanani:** Supervision, Methodology, Validation, Writing - review & editing. **Masoud Dehghani-Soufi:** Supervision, Investigation, Software, Validation, Writing - review & editing. **Ahmad Jahanbakhshi:** Supervision, Methodology, Investigation, Validation,

Writing - original draft.

Declaration of Competing Interest

The authors declare that they have no known competing financial interests or personal relationships that could have appeared to influence the work reported in this paper.

References

- [1] Mesri Gundoshmian T, Heidari-Maleni A, Jahanbakhshi A. Evaluation of performance and emission characteristics of a CI engine using functional multi-walled carbon nanotubes (MWCNTs-COOH) additives in biodiesel-diesel blends. *Fuel* 2021;287:119525. <https://doi.org/10.1016/j.fuel.2020.119525>.
- [2] Samadi S, Heidarbeygi K. Acoustic analysis of a single-cylinder diesel engine using magnetized biodiesel-diesel fuel blends. *Heliyon* 2020;6(9):e05113. <https://doi.org/10.1016/j.heliyon.2020.e05113>.
- [3] Zhang Z, Li L. Investigation of in-cylinder steam injection in a turbocharged diesel engine for waste heat recovery and NOx emission control. *Energies* 2018;11(4):936. <https://doi.org/10.3390/en11040936>.
- [4] Shekofteh M, Gundoshmian TM, Jahanbakhshi A, Heidari-Maleni A. Performance and emission characteristics of a diesel engine fueled with functionalized multi-wall carbon nanotubes (MWCNTs-OH) and diesel-biodiesel-bioethanol blends. *Energy Rep* 2020;6:1438–47. <https://doi.org/10.1016/j.egy.2020.05.025>.
- [5] Jahanbakhshi A, Salehi R. Processing watermelon waste using *Saccharomyces cerevisiae* yeast and the fermentation method for bioethanol production. *J Food Process Eng* 2019;42(7):e13283. <https://doi.org/10.1111/jfpe.13283>.
- [6] Lenin AH, Thyagarajan K. Performance evaluation of a diesel engine fueled with methyl ester of pongamia oil. *Int J Energy Environ* 2012;3(6):939–48.
- [7] Salehi R, Taghizadeh-Alisaraei A, Shahidi F, Jahanbakhshi A. Potentiometric of bioethanol production from cantaloupe waste (Magassi Neishabouri Cultivar). *J Saudi Soc Agric Sci* 2020;19(1):51–5. <https://doi.org/10.1016/j.jssas.2018.05.006>.
- [8] Salehi R, Taghizadeh-Alisaraei A, Jahanbakhshi A, Shahidi F. Evaluation and measurement of bioethanol extraction from melon waste (Qassari cultivar). *Agric Eng Int: CIGR J* 2018;20(3):127–31.
- [9] Mahmudul HM, Hagos FY, Mamat R, Adam AA, Ishak WFW, Alenezi R. Production, characterization and performance of biodiesel as an alternative fuel in diesel engines—A review. *Renew Sustain Energy Rev* 2017;72:497–509. <https://doi.org/10.1016/j.rser.2017.01.001>.
- [10] Ghanbari M. Technology and design of internal combustion engines. Technical and Vocational University; 2019. p. 279–93. 9786008820598. (book.tvu.ac.ir), (In Farsi).
- [11] D'Alessandro B, Bidini G, Zampilli M, Laranci P, Bartocci P, Fantozzi F. Straight and waste vegetable oil in engines: review and experimental measurement of emissions, fuel consumption and injector fouling on a turbocharged commercial engine. *Fuel* 2016;182:198–209. <https://doi.org/10.1016/j.fuel.2016.05.075>.
- [12] Gren L, Malmberg VB, Falk J, Markula L, Novakovic M, Shamun S, et al. Effects of renewable fuel and exhaust aftertreatment on primary and secondary emissions from a modern heavy-duty diesel engine. *J Aerosol Sci* 2021;156:105781. <https://doi.org/10.1016/j.jaerosci.2021.105781>.
- [13] Heidari-Maleni A, Gundoshmian TM, Karimi B, Jahanbakhshi A, Ghobadian B. A novel fuel based on biocompatible nanoparticles and ethanol-biodiesel blends to improve diesel engines performance and reduce exhaust emissions. *Fuel* 2020;276:118079. <https://doi.org/10.1016/j.fuel.2020.118079>.
- [14] Heidari-Maleni A, Mesri Gundoshmian T, Jahanbakhshi A, Ghobadian B. Performance improvement and exhaust emissions reduction in diesel engine through the use of graphene quantum dot (GQD) nanoparticles and ethanol-biodiesel blends. *Fuel* 2020;267:117116. <https://doi.org/10.1016/j.fuel.2020.117116>.
- [15] Ghanbari M, Najafi G, Ghobadian B. Experimental studying the effect of nano particles additives in diesel-biodiesel blends on the emission characteristics of a CI engine. *Automotive Science and Engineering* 2020;10(4):3408–20. <http://tx.doi.org/10.22068/ijae.10.4.3408>.
- [16] Heidari-Maleni A, Mesri-Gundoshmian T, Jahanbakhshi A, Karimi B, Ghobadian B. Novel environmentally friendly fuel: The effect of adding graphene quantum dot (GQD) nanoparticles with ethanol-biodiesel blends on the performance and emission characteristics of a diesel engine. *NanoImpact* 2021;21:100294. <https://doi.org/10.1016/j.impact.2021.100294>.
- [17] Ghanbari M, Najafi G, Ghobadian B, Mamat R, Noor M. M., & Moosavian, A. (2015, November). Adaptive neuro-fuzzy inference system (ANFIS) to predict CI engine parameters fueled with nano-particles additive to diesel fuel. In IOP Conference Series: Materials Science and Engineering (Vol. 100, No. 1, p. 012070). IOP Publishing.
- [18] Suhel A, Abdul Rahim N, Abdul Rahman MR, Bin Ahmad KA, Teoh YH, Zainal Abidin N. An experimental investigation on the effect of ferrous ferric oxide nano-additive and chicken fat methyl ester on performance and emission characteristics of compression ignition engine. *Symmetry* 2021;13(2):265. <https://doi.org/10.3390/sym13020265>.
- [19] Shaafi T, Sairam K, Gopinath A, Kumaresan G, Velraj R. Effect of dispersion of various nanoadditives on the performance and emission characteristics of a CI engine fuelled with diesel, biodiesel and blends—a review. *Renew Sustain Energy Rev* 2015;49:563–73. <https://doi.org/10.1016/j.rser.2015.04.086>.
- [20] Kish SS, Rashidi A, Aghabozorg HR, Moradi L. Increasing the octane number of gasoline using functionalized carbon nanotubes. *Appl Surf Sci* 2010;256(11):3472–7. <https://doi.org/10.1016/j.apsusc.2009.12.056>.
- [21] Tyagi H, Phelan PE, Prasher R, Peck R, Lee T, Pacheco JR, et al. Increased hot-plate ignition probability for nanoparticle-laden diesel fuel. *Nano Lett* 2008;8(5):1410–6. <https://doi.org/10.1021/nl080277d>.
- [22] Solero G. Experimental analysis of the influence of inert nano-additives upon combustion of diesel sprays. *Nanosci Nanotechnol* 2012;2(4):129–33. <https://doi.org/10.5923/j.nn.20120204.07>.
- [23] Mehta RN, Chakraborty M, Parikh PA. Nanofuels: Combustion, engine performance and emissions. *Fuel* 2014;120:91–7. <https://doi.org/10.1016/j.fuel.2013.12.008>.
- [24] Ghanbari M, Najafi G, Ghobadian B, Mamat R, Noor M. M., & Moosavian, A. (2015, November). Support vector machine to predict diesel engine performance and emission parameters fueled with nano-particles additive to diesel fuel. In IOP Conference Series: Materials Science and Engineering (Vol. 100, No. 1, p. 012069). IOP Publishing.
- [25] Jung H, Kittelson DB, Zachariah MR. The influence of a cerium additive on ultrafine diesel particle emissions and kinetics of oxidation. *Combust Flame* 2005;142(3):276–88. <https://doi.org/10.1016/j.combustflame.2004.11.015>.
- [26] Cline C, Micklow G. A. “literature review of chemical additives in diesel and biodiesel fuels for improved combustion”, *Journal of Multidisciplinary Engineering Science and Technology*. Vol. 7, No. 5, (2020), 11791–11807.
- [27] Ghanbari M, Najafi G, Ghobadian B, Yusuf T, Carlucci AP, Kiani MKD. Performance and emission characteristics of a CI engine using nano particles additives in biodiesel-diesel blends and modeling with GP approach. *Fuel* 2017;202:699–716. <https://doi.org/10.1016/j.fuel.2017.04.117>.
- [28] Ghafoori M, Ghobadian B, Najafi G, Layeghi M, Rashidi A, Mamat R. Effect of nanoparticles on the performance and emission of a diesel engine using biodiesel-diesel blend. *Int J Autom Mech Eng* 2015;12:3097–108.
- [29] Ganji, P. R., Raju, R. K. V., & Rao, S. S. (2017). Computational optimization of biodiesel combustion using response surface methodology. *Thermal Science*, 21(1 Part B), 465–473. <https://doi.org/10.2298/TSIC161229031G>.
- [30] Uslu S. Optimization of diesel engine operating parameters fueled with palm oil-diesel blend: Comparative evaluation between response surface methodology (RSM) and artificial neural network (ANN). *Fuel* 2020;276:117990. <https://doi.org/10.1016/j.fuel.2020.117990>.
- [31] Kumar S, Dinesha P. Optimization of engine parameters in a bio diesel engine run with honge methyl ester using response surface methodology. *Measurement* 2018;125:224–31. <https://doi.org/10.1016/j.measurement.2018.04.091>.
- [32] Lee T, Reitz RD. Response surface method optimization of a high-speed direct-injection diesel engine equipped with a common rail injection system. *J. Eng. Gas Turbines Power* 2003;125(2):541–6. <https://doi.org/10.1115/1.1559900>.
- [33] Ileri E, Karaoglan AD, Atmanli A. Response surface methodology based prediction of engine performance and exhaust emissions of a diesel engine fuelled with canola oil methyl ester. *J Renewable Sustainable Energy* 2013;5(3):033132. <https://doi.org/10.1063/1.4811801>.
- [34] Bharadwaz YD, Rao BG, Rao VD, Anusha C. Improvement of biodiesel methanol blends performance in a variable compression ratio engine using response surface methodology. *Alexandria Engineering Journal* 2016;55(2):1201–9. <https://doi.org/10.1016/j.aej.2016.04.006>.
- [35] Ghanbari M, Mozafari Vanani L, Najafi G. Investigating the effect of gasoline fuel filter lifetime on fuel pressure and ignition advance using the RSM method. *Fluid Mech Aerodyn J* 2020;9(1):135–50.
- [36] Krupakaran RL, Hariprasad T, Gopalakrishna A, Babu P. The performance and exhaust emissions investigation of a diesel engine using γ -Al₂O₃ nanoparticle additives to biodiesel. *Carbon Manage* 2016;7(3–4):233–41. <https://doi.org/10.1080/175833004.2016.1218713>.
- [37] Al-Hasan M. Effect of ethanol-unleaded gasoline blends on engine performance and exhaust emission. *Energy Convers Manage* 2003;44(9):1547–61. [https://doi.org/10.1016/S0196-8904\(02\)00166-8](https://doi.org/10.1016/S0196-8904(02)00166-8).
- [38] Ghanbari M. Experimental study on the effect of Al₂O₃ nanoparticles in diesel fuel on the performance and emission characteristics of a diesel engine. *The Journal of Engine Research* 2021;61(61):35–45.
- [39] Anchupogu P, Rao LN, Banavathu B. Effect of alumina nano additives into biodiesel-diesel blends on the combustion performance and emission characteristics of a diesel engine with exhaust gas recirculation. *Environ Sci Pollut Res* 2018;25(23):23294–306. <https://doi.org/10.1007/s11356-018-2366-7>.
- [40] Chintala V, Subramanian KA. Experimental investigation on effect of enhanced premixed charge on combustion characteristics of a direct injection diesel engine. *Int J Adv Eng Sci Appl Math* 2014;6(1–2):3–16. <https://doi.org/10.1007/s12572-014-0109-7>.
- [41] Shaafi T, Velraj R. Influence of alumina nanoparticles, ethanol and isopropanol blend as additive with diesel-soybean biodiesel blend fuel: Combustion, engine performance and emissions. *Renewable Energy* 2015;80:655–63. <https://doi.org/10.1016/j.renene.2015.02.042>.
- [42] Adzmi MA, Abdullah A, Abdullah Z, Mrwan AG. Effect of Al₂O₃ and SiO₂ metal oxide nanoparticles blended with POME on combustion, performance and emissions characteristics of a diesel engine. *Int J Autom Mech Eng* 2019;16(3):6859–73.
- [43] Agarwal AK. Biofuels (alcohols and biodiesel) applications as fuels for internal combustion engines. *Prog Energy Combust Sci* 2007;33(3):233–71. <https://doi.org/10.1016/j.peccs.2006.08.003>.
- [44] Selvan VAM, Anand RB, Udayakumar M. Effects of cerium oxide nanoparticle addition in diesel and diesel-biodiesel-ethanol blends on the performance and emission characteristics of a CI engine. *J Eng Appl Sci* 2009;4(7):1819–6608.

- [45] Sajith V, Sobhan CB, Peterson GP. Experimental investigations on the effects of cerium oxide nanoparticle fuel additives on biodiesel. *Adv Mech Eng* 2010;2: 581407. <https://doi.org/10.1155/2010/581407>.
- [46] Celik MB. Experimental determination of suitable ethanol-gasoline blend rate at high compression ratio for gasoline engine. *Appl Therm Eng* 2008;28(5-6): 396-404. <https://doi.org/10.1016/j.applthermaleng.2007.10.028>.
- [47] Wu CW, Chen RH, Pu JY, Lin TH. The influence of air-fuel ratio on engine performance and pollutant emission of an SI engine using ethanol-gasoline-blended fuels. *Atmos Environ* 2004;38(40):7093-100. <https://doi.org/10.1016/j.atmosenv.2004.01.058>.
- [48] Heydari-Maleny K, Taghizadeh-Alisaraei A, Ghobadian B, Abbaszadeh-Mayvan A. Analyzing and evaluation of carbon nanotubes additives to diesohol-B2 fuels on performance and emission of diesel engines. *Fuel* 2017;196:110-23. <https://doi.org/10.1016/j.fuel.2017.01.091>.
- [49] Nematizade, P., Ghobadian, B., & Najafi, G. (2012). Investigation of fossil fuels and liquid biofuels blend properties using artificial neural network. *International Journal of Automotive and Mechanical Engineering*, 5, 639-47. <http://dx.doi.org/10.15282/ijame.5.2012.10.0051>.
- [50] Ganesan P, Rajakarunakaran S, Thirugnanasambandam M, Devaraj D. Artificial neural network model to predict the diesel electric generator performance and exhaust emissions. *Energy* 2015;83:115-24. <https://doi.org/10.1016/j.energy.2015.02.094>.
- [51] Ganesan P, Rathna SJ, Saidur R. Application of artificial neural network to map the performance characteristics of boiler using different algorithms. *Int J Green Energy* 2021;1-13. <https://doi.org/10.1080/15435075.2021.1891908>.
- [52] Elkelawy M, Alm-Eldin Bastawissi H, El Shenawy EA, Taha M, Panchal H, Sadasivuni KK. Study of performance, combustion, and emissions parameters of DI-diesel engine fueled with algae biodiesel/diesel/n-pentane blends. *Energy Convers Manage: X* 2021;10:100058. <https://doi.org/10.1016/j.ecmx.2020.100058>.
- [53] Sandesh K, Ujwal P. Trends and perspectives of liquid biofuel-process and industrial viability. *Energy Convers Manage: X* 2021;10:100075. <https://doi.org/10.1016/j.ecmx.2020.100075>.

Use of Steel Slag-Superfine Blast Furnace Slag Composite Mineral Admixture on Mortar and Concrete

Binoda Bihari Sahoo, *Department of Civil Engineering, NM Institute of Engineering & Technology, Bhubaneswar, bionod_bihari231@yahoo.co.in*

Shradhanjali Moharana, *Department of Civil Engineering, Raajdhani Engineering College, Bhubaneswar, shradhanjalimoharana1@gmail.com*

Raushan Gupta, *Department of Civil Engineering, Capital Engineering College, Bhubaneswar, raushangupta26@yahoo.co.in*

Subrat Kumar Panda, *Department of Civil Engineering, Aryan Institute of Engineering & Technology, Bhubaneswar, spanda226@gmail.com*

ABSTRACT

Steel slag and superfine blast furnace slag were used to make a composite mineral admixture. The effects of superfine blast furnace slag in the composite mixture on the mortar and concrete were studied. The findings reveal that while the composite mineral addition may reduce concrete strength at first, it improves strength growth with time. The early strength can be reduced by increasing the quantity of superfine blast furnace slag. When a composite mineral admixture is introduced, autogenous shrinkage and adiabatic temperature rise are significantly reduced. When the water-to-solid ratio (w/s) is low, the reduction is more noticeable. The results suggest that a composite mineral admixture containing steel slag and superfine blast furnace slag as complimentary elements can be employed as an effective cement alternative.

1. Introduction

To combat halt global warming, the emission of CO₂ and other greenhouse gases needs to be zero or even negative [1]. Cement production is a process with high energy consumption and high carbon emission. CO₂ emission from the cement industry accounts for 7% of the world's total emissions [1]. The production of 1t cement clinker emits about 1t CO₂, 0.74 kg SO₂ and 1.15 kg NO_x (including the emissions from the use of fossil fuel during cement production) [2–4]. Using renewable energy is an important technology to reduce CO₂ emission. But this method cannot completely reduce the CO₂ emission of the cement industry. The CO₂ emission of energy consumption accounts for 40–60% of the total emission in cement production [5, 6]. The chemical reaction occurring in the production of cement is a process that inherently emits CO₂. Therefore, substituting cement by pozzolanic materials or other materials with hydration activity to reduce clinker usage is important. In recent decades, different kinds of supplementary cementitious materials (SCMs) were developed [7]. Some SCMs have not been extensively used yet, and new

SCMs are still being developed [7]. Compared to the plain cement concrete, the concrete mixed with SCMs might have several pros and cons. The mechanical properties, chemical resistance, and interfacial transition zone (ITZ) are usually improved [8]. However, some SCMs degrade the properties of concrete, so these SCMs are not extensively used on a large scale. For instance, the addition of fly ash and steel slag decreases the early strength of concrete. Therefore, eliminating the negative effects and fully utilizing the properties of these SCMs is a strategy for reducing clinker usage. One of the important technical routes is to use composite SCMs, which can take advantage of performance characteristics of different admixtures and fully utilize them. Wang et al. [9] found that the composite admixture of steel slag and ground blast furnace slag can eliminate the negative effect of steel slag on the pore structure of concrete. Han et al. [10] found that the pore structure of cement is refined when using fly ash-steel slag composite admixtures. The temperature rise and later age compressive strength were also improved [10]. From those literatures, it is obvious that composite admixture has several advantages compared to single admixture. Fineness is reported as an important factor on the

reactivity of admixture [11, 12]. However few studies were conducted on the composite admixture with ultrafine SCMs. Therefore, the study on the composite admixture with ultrafine SCMs is worth conducting.

Steel slag (SS) is a byproduct in the process of steel production [13]. The world's annual output of steel slag exceeds 1.6 billion tons every year [14]. Steel slag mainly consists of CaO, SiO₂, MgO, and Fe₂O₃ [15–18]. The main mineral compositions of steel slag are C₂S, C₃S, C₂F, C₄AF, and RO phase and f-CaO [15–17]. At present, steel slag has been studied for producing bricks [18], ceramics [19], pavement materials [20], and aggregates of concrete [21]. Due to the existence of Ca-containing minerals and amorphous phase in steel slag, it shows a certain level of hydration activity [16, 17]. Consequently, steel slag is considered as a potential mineral admixture. Researches have shown that the addition of steel slag in concrete can reduce the reaction heat of cement hydration, the adiabatic temperature rises, and the early autogenous shrinkage of concrete [22]. However, adding steel slag can also reduce the compressive strength of concrete [23]. Steel slag has less cementitious minerals compared to cement, which makes the degree of hydration lower than that of cement particles [24]. The larger particles in the steel slag have few cementitious properties due to the high content of RO phase. The interface between the large steel slag particles and the C-S-H is relatively weak [25]. Therefore, the addition of steel slag in concrete can decrease both the mechanical and durability properties of concrete.

Blast furnace slag (BFS) is a mineral admixture with pozzolanic activity, which has been used as common supplementary cementitious materials in concrete [26]. However, the “effective utilization” of BFS is low. Wu et al. [26] found that the pozzolanic reaction mainly occurred on the surface of slag. The reaction rate of large particles in BFS was higher than the small particles [27]. This means that increasing the fineness and specific surface area of slag can improve the utilization efficiency of BFS. Zhu et al. [28] found that the fineness significantly affected the reaction activity of BFS. Thus, superfine blast furnace slag (SBFS) can be a better alternative than blast furnace slag (BFS) as mineral admixture. According to Luo et al. [29], using SBFS as a supplementary material for cement accelerated the cement hydration. Besides, the filler effect of ultrafine powder can increase or at least not decrease the strength of the concrete [30]. The SBFS acted as microfiller [31] in the interface transition zone (ITZ). The filling effect of finer particles increases the packing density of the cement matrix and improves the pore structure of the concrete. Therefore, using SS and SBFS as complementary parts in the mineral admixture to replace parts of cement in concrete can be an effective way to reduce the amount of cement production.

In this paper, a composite mineral admixture was produced by adding the SBFS to SS. The workability and the compressive strength of the mortar were tested under different w/s. The compressive strength of the concrete mixed with composite mineral admixture was tested. The workability, compressive strength, and adiabatic temperature rise and autogenous shrinkage of the self-compacting concrete were tested in this paper.

2. Materials and Methods

2.1. Raw Materials. The cement used in this study was ordinary Portland cement (OPC) with the strength grade of 42.5 complying with the Chinese National Standard GB 175-2007. The specific surface area of OPC is 350 m²/kg. The specific surface areas of SS and SBFS used in this study are 455 m²/kg and 639 m²/kg, respectively. The chemical compositions of OPC, SS, and SBFS are presented in Table 1. The polycarboxylate (PCE) superplasticizer was used to adjust the concrete fluidity.

2.2. Test Method. The mortar and concrete were prepared to test the compressive strength. The mortars were mixed by a planet mixer. After adding the water, the pastes were mixed at a low speed for 30 seconds, followed by the addition of sands, and then a 4-minute mixing was conducted. The mortars were cast in 40 mm × 40 mm × 160 mm molds and cured under the standard curing conditions (20 ± 2°C, 95% RH).

The concrete was mixed using a pan mixer. The powder materials were dry-mixed for 5 minutes in order to make the powder more homogeneous. Water-PCE suspension was gradually added into the mixer after the dry-mixing. The whole mixing process had lasted for 15 minutes. The concrete was cast in 100 mm × 100 mm × 100 mm molds and cured under the standard curing conditions. The mix proportions of different concrete are described in the following sections.

Adiabatic temperature rises of the concrete were measured by a specific temperature measuring instrument. The measurement accuracy of the instrument is 0.1°C. The concrete was put into the instrument after the mixing.

A horizontal noncontact autogenous shrinkage measurement was carried out to measure the autogenous shrinkage of the concrete. The noncontact autogenous shrinkage measurement of concrete can measure the shrinkage of the cement of concrete at the early age.

3. Results and Discussion

3.1. Mortar Performance

3.1.1. Fluidity of the Mortar. Fluidity is one of the important properties of concrete. The fluidity of concrete is affected by complex factors such as particle size distribution, surface humidity of the aggregate, and overall environment when mixing. Therefore, in this paper, the fluidity ratio experiment of mortar is conducted to characterize the impact of the composite mineral admixture on the fluidity. The test was carried out according to the Chinese national standard GB/T 2419-2016. The w/s ratio of the mortar is fixed at 0.47 and the cementitious material-to-sand ratio is 1 : 3. The total content of the composite admixture was set as 30%. The fluidity of mortar is correlated to the packing density of mortar solid particles [32]. Generally, the higher the packing density is, the more water is released on the particle surface to form a so-called “water film” [32]. The thickness of the water film plays an important role in lubricating between particles,

TABLE 1: Chemical compositions of the material (w.t.%).

Sample	CaO	SiO ₂	Al ₂ O ₃	Fe ₂ O ₃	MgO	K ₂ O	NaO	SO ₃	Loss
OPC	57.21	22.36	7.73	3.66	3.10	0.23	0.73	3.54	2.31
SS	43.37	19.10	7.46	18.01	5.17	0.63	0.41	—	1.36
SBFS	40.26	34.39	13.78	0.19	7.43	0.44	0.3	1.92	3.5

affecting the rheology and adhesiveness of mortar [32]. Different particle sizes of admixtures have great influences on the packing density of the mortar. Theoretically, if the particle size is smaller than the cement particle size, the packing density of cementitious material is higher, and the thickness of “water film” increases. But the actual situation is not necessarily the case. Because the small particles have larger specific surface area and greater adhesion to water, the thickness of “water film” does not necessarily become greater. SBFS used in this study has a smaller particle size than SS powder. Therefore, in order to explore the influence of different components in the composite admixture on the fluidity, five groups of experiments with different SBFS content were set in this section (total content of composite admixture is 30%). The component of the composite admixture and the fluidity ratio are shown in Table 2.

Table 2 demonstrates that when the total content of composite admixture is fixed, the fluidity ratio of mortar gradually decreases as the content of SBFS increases from 0 to 25% of the total amount of the composite mineral admixture. This indicates that the fluidity of mortar decreases with the addition of the SBFS. The reason of this is that the SBFS (639 m²/kg) used in this study has a larger specific surface area and stronger adhesion to water than SS (455 m²/kg); therefore, the “water film” on the particle surface is thinner, resulting in the decrease of fluidity. Although more water is released due to the small particle size of SBFS, it cannot offset the loss of water film thickness due to the high specific surface.

3.1.2. Compressive Strength of the Mortar. In order to investigate the influence of composite admixtures on the compressive strength, two w/s (0.5 and 0.4) and two total contents of composite admixtures (20% and 30%) were set. Additionally, in order to study the effect of SBFS content on the mortar strength, four groups with different SBFS content were set. The content of these four groups is the same as S-1, S-2, S-3, and S-4 in Table 2. The mix proportions of the mortar are shown in Table 3 (w/s is 0.5) and Table 4 (water-to-cement ratio is 0.4).

Figure 1 shows that the 3 d compressive strength of mortar mixed with composite admixture is lower than that of pure cement mortar. This is mainly due to the fact that the addition of the mineral admixture reduces the cementitious materials, which can undergo hydration reaction in the early stage. Therefore, the strength decreases because of less hydration products providing strength in the early stage. However, with the increase of curing age, the strength development of mortar mixed with composite mineral admixture grows higher than that of pure cement mortar. At

TABLE 2: The component of the composite admixture and the fluidity ratio of the mortar for fluidity ratio experiment.

Group	SS (%)	SBFS (%)	Fluidity ratio
S0	100	0	107
S1	90	10	102
S2	85	15	100
S3	80	20	98
S4	75	25	96

TABLE 3: Mix proportion (w/s is 0.5) of mortar containing composite mineral admixture for compressive strength test (kg).

Group	Cement	SS	SBFS	Sand	Water
C1	450	0	0		
S1-20%		81	9		
S2-20%		76.5	13.5		
S3-20%	360	72	18		
S4-20%		67.5	22.5	1350	225
S1-30%		121.5	13.5		
S2-30%		114.7	20.3		
S3-30%	315	108	27		
S4-30%		101.2	33.8		

TABLE 4: Mix proportion (w/s is 0.5) of mortar containing composite mineral admixture for compressive strength test (kg).

Group	Cement	SS	SBFS	Sand	Water
C1	450	0	0		
S1-20%		81	9		
S2-20%		76.5	13.5		
S3-20%	360	72	18		
S4-20%		67.5	22.5	1350	180
S1-30%		121.5	13.5		
S2-30%		114.7	20.3		
S3-30%	315	108	27		
S4-30%		101.2	33.8		

90 d, the strength of mortar mixed with composite admixture becomes even higher than pure cement mortar.

The 3 d and 28 d strength of pure cement mortar reach 41.5% and 81.4% of the 90 d strength, respectively. While the strengths of 3 d and 28 d of the highest composite admixture mortar group only account for 38.6% and 78.8% of that of 90 d. This indicates that although the early strength of composite admixture mortar is lower, it shows a better performance in the later strength development. This can be explained by the fact that the activity of SS and SBFS is lower than that of cement in early hydration. The main active components of SS are similar to that of cement, while the

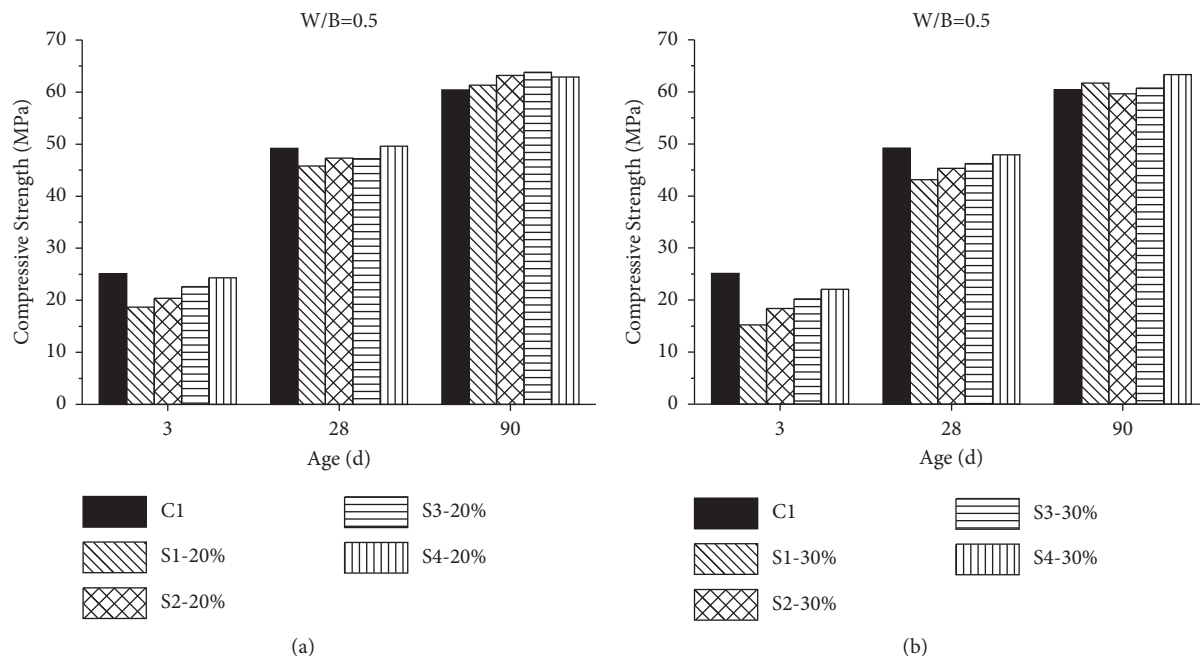


FIGURE 1: Compressive strength of pure cement mortar and composite admixture mortar (w/s ratio is 0.5). The total content of composite admixture is (a) 20% and (b) 30%.

hydration rate is lower than cement [15, 16]. The main component of SBFS is amorphous aluminosilicate. These amorphous phases can react with the $\text{Ca}(\text{OH})_2$, which is the byproducts of cement hydration. This reaction produces gel materials that create bonding on particle interface, enhancing mortar strength. The reaction is called “pozzolanic reaction.” These two minerals react in the later stage, which improves the later strength of mortar.

Comparing Figures 1(a) and 1(b), it can be found that when the composition of the composite admixture is fixed, with the increase of the composite admixture content, the early strength is lower, but the later strength is higher. This also indicates that although adding more composite admixture reduces the early strength, it has little impact on the 90 d strength. This is because at a high w/s ratio (0.5 in this case), cement particles have enough water to undergo hydration reaction and produce plenty of products to fill the pores of the paste. Consequently, the weakest position is the interface between the paste and SS as well as SBFS. With the development of curing age, SS and SBFS gradually react and produce cementitious products to enhance their interfaces, so that the microstructure of the weakest position can be refined. However, because the total pore structure is mainly determined by w/s, there is little difference in strength at 90 d.

Figure 1 also shows that when the composite admixture content is fixed, the mortar strength of 3 d gradually grows with the increase of the content of SBFS. This phenomenon is not obvious at the later age. The result shows that SBFS can improve the early strength of mortar compared to SS. The reason of this is that SBFS with a small particle size can fill in the small pores of cementitious material, therefore improving the compactness of mortar [31, 32]. Besides, the

filling of SBFS also releases water in pores so that more water can be consumed for cement hydration. Thus, the degree of early hydration of cement is higher. SBFS can also promote the nucleation of C-S-H and the early hydration of cement [33, 34]. In addition, the activity of SBFS is higher than SS. SS reacts with $\text{Ca}(\text{OH})_2$ at the early age because of its high specific surface area. The reaction improves the pore structure of the matrix, which can also enhance the strength of mortar. This indicates that the addition of SBFS can significantly mitigate the negative effect of SS on the strength of mortar at the early age. Therefore, mixing SBFS and SS in the composite mineral admixture is more efficient and effective than using only one of them. With the utilization of this kind of composite mineral admixture, the cement usage is expected to be reduced.

Figure 2 shows the mortar strength with w/s of 0.4. The phenomenon of the compressive strength is similar to that with w/s of 0.5. However, compared with the group w/s of 0.5, the difference between pure cement mortar and composite admixture mortar at 3 d is significantly narrowed. This shows that when the w/s ratio is low, the negative effect of composite admixture on early strength is less. This can be explained from two perspectives. (1) When the w/s ratio is low, the space between particles is small. Although the addition of SS can reduce the generation of hydration products, the hydration products of cement are enough to fill the pores between SS and cement when the reaction degree is high. Therefore, the adverse effect of SS on pore structure is insignificant. (2) The addition of SS increases the actual water-to-cement ratio and raises the degree of hydration. This phenomenon is not obvious when the water-to-cement ratio is high. However, when the w/s is low, the water-release effect of SS is more obvious, therefore promoting the cement hydration.

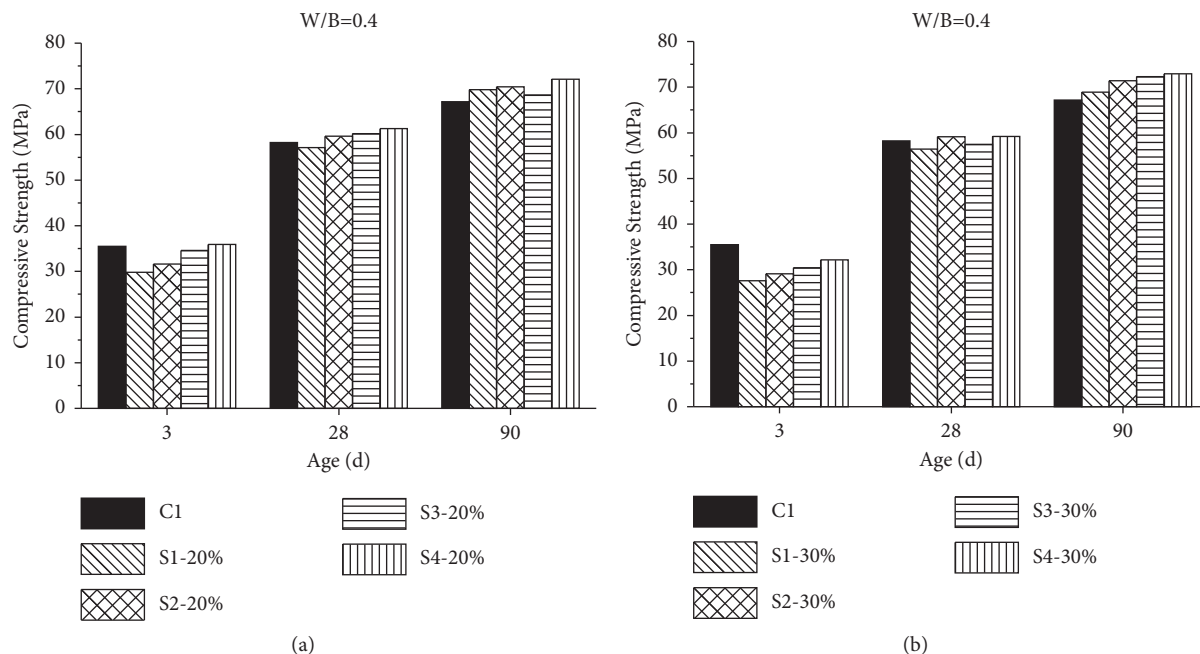


FIGURE 2: Compressive strength of pure cement mortar and composite admixture mortar (water-to-solid ratio is 0.4). The total content of composite admixture is (a) 20% and (b) 30%.

Comparing Figures 2(a) and 2(b), it can also be found that when the w/s is 0.5, with the development of age, the tendency of the strength increasing as the content of SBFS increases becomes less obvious. When the w/s is 0.4, with the addition of SBFS, the enhancement of strength is still observable at the 90 d. This shows when the w/s is low, SBFS can not only improve the early mortar strength but also improve the later mortar strength. When the w/s is 0.5, the pore structure development is weak. The later strength is determined by the w/s. The result shows that the composite mineral admixture is more efficient at a low w/s ratio.

3.2. Compressive Strength of the Ordinary Concrete. Two different grades of concrete (C30 and C40) were designed. In order to use cement more efficiently, two types of concrete with different cement content were also designed for each grade. The mix proportion of the concrete is shown in Table 5.

Figure 3 shows the compressive strength of concrete mixed with composite mineral admixture. It can be seen from Figure 3 that with the addition of the SBFS, 28 d and 90 d strength of concrete are increased. This indicates that SBFS can increase the compressive strength of concrete, which is consistent with the compressive strength of mortar. The reason for that is that the addition of SBFS can improve the hydration of cement and the pore structure of the matrix. For C40 concrete, the addition of SBFS increases both the 28 d and 90 d strength. But for C30 concrete, with the addition of SBFS, the increase in strength of 28 d is greater than that of 90 d, which is also consistent with the phenomenon of mortar. This is due to the lower w/s of C40 compared to that of C30. Therefore, the addition of SBFS increases the strength development of the concrete at the lower w/s ratio.

Figure 3 also shows that for the same grade concrete, when the amount of cement is reduced, the 28 d strength decreases significantly, while the 90 d strength has little difference. This indicates that reducing the cement content can damage the 28 d strength, but improve strength development. The results of compressive strength show that reducing the amount of cement poses a negative effect on strength at the early age, while increasing the content of SBFS can improve the 28 d strength.

3.3. Performance of Self-Compacting Concrete. Two strength grades (C50 and C60) of self-compacting concrete were designed in this section to study the feasibility of preparing self-compacting concrete with composite admixture. Table 6 shows the mix proportion of self-compacting concrete. Self-compacting concrete is often used in the pouring of mass concrete. Pure cement concrete (group C) was set as the control group.

Figure 4 shows the adiabatic temperature rise curve of C50 self-compacting concrete. The adiabatic temperature rises of concrete with pure cement, Z1, and Z2 at 7 days are 50.9°C, 45.95°C, and 46.67°C, respectively. The adiabatic temperature rises of concrete mixed with composite admixture are lower than that of pure cement concrete. This shows that the composite admixture of ultrafine slag and steel slag powder can significantly reduce the adiabatic temperature rise of concrete.

When the content of SBFS is increased, the adiabatic temperature rise grows higher. This indicates that SBFS can slightly increase the adiabatic temperature rise, which is the result of the smaller particle size of SBFS. The addition of SBFS can release the water in the pores, increasing the water around the cement and thus promoting the early hydration

TABLE 5: Mix proportion of concrete containing composite mineral admixture for compressive strength test (kg/m³).

Grade	Group	w/s	Cement	SS	SBFS	Sand	Aggregate	Water
C30	S-1	0.47	200	120	30	780	1035	165
	S-2			112.5	37.5			
	S-3	0.45	175	145	35	790	1025	161
	S-4			131.2	43.8			
C40	SS-1	0.395	250	120	30	730	1055	158
	SS-2	0.385	200	112.5	37.5	720	1070	154
	SS-3			160	40			
	SS-4			150	50			

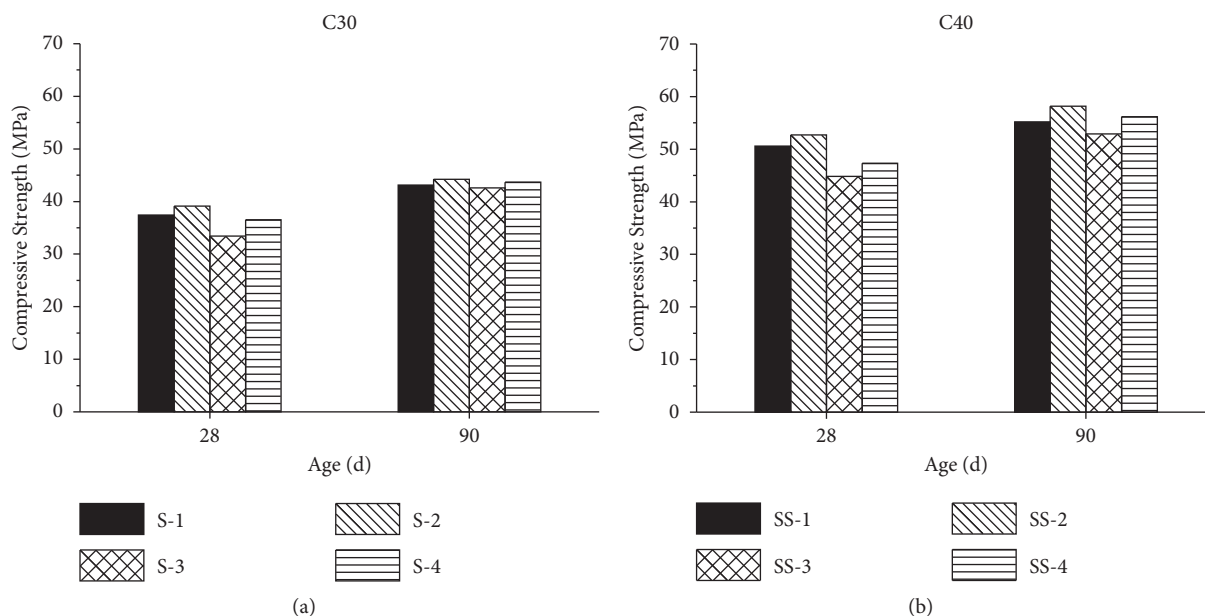


FIGURE 3: Compressive strength of concrete with composite admixture mortar: (a) C30 and (b) C40.

TABLE 6: Mix proportion of self-compacting concrete containing composite mineral admixture (kg/m³).

Grade	Group	w/s	Cement	SS	SBFS	Sand	Aggregate	Water
C50	Z1	0.31	340	128	32	810	890	157
	Z2			120	40			
C60	ZZ1	0.278	380	144	36	780	880	156
	ZZ2			135	45			

degree of the cement. The larger specific surface area and the activity of SBFS can promote the nucleation of the C-S-H [32]. In addition, the pozzolanic reaction of SBFS can also release heat. Figure 4 also shows that the adiabatic temperature rises of group Z2 and ZZ2 are higher than group C at 1 d. While the adiabatic temperature rises of Z1 and ZZ1 at 1 d is lower than pure cement concrete at 1 d, the concrete mixed with higher SBFS increases the heat release before 1 d. This proves that the addition of SBFS can improve the early hydration of cement.

Figure 5 shows the autogenous shrinkage of the self-compacting concrete. The autogenous shrinkage of

concrete mixed with composite admixture is less than that of pure concrete because less cement content was used. For C50 concrete, when the proportion of SBFS is increased from 20% to 25%, the autogenous shrinkage is increased by 7.8%. While for C60 concrete, with the same addition of SBFS, the autogenous shrinkage is only increased by 2.1%. This indicates that the influence of the proportion of SBFS on the autogenous shrinkage decreases with the increase of concrete grade, which can be attributed to the fact that SBFS has better performance in promoting the hydration of cement at a low w/s.

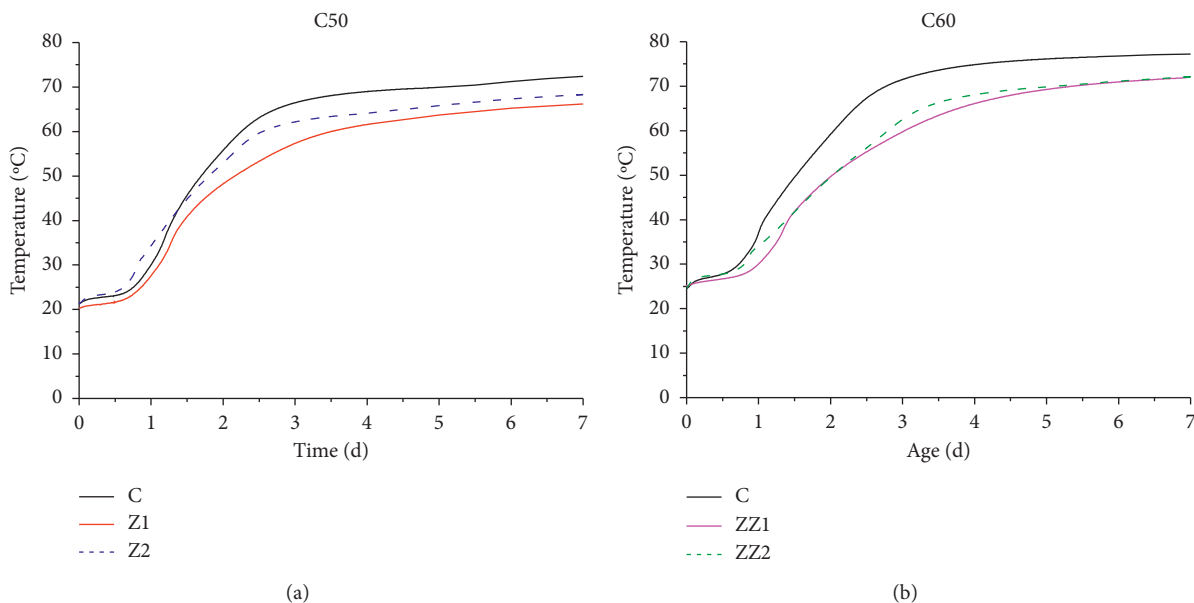


FIGURE 4: Adiabatic temperature rises of the self-compacting concrete: (a) C50 and (b) C60.

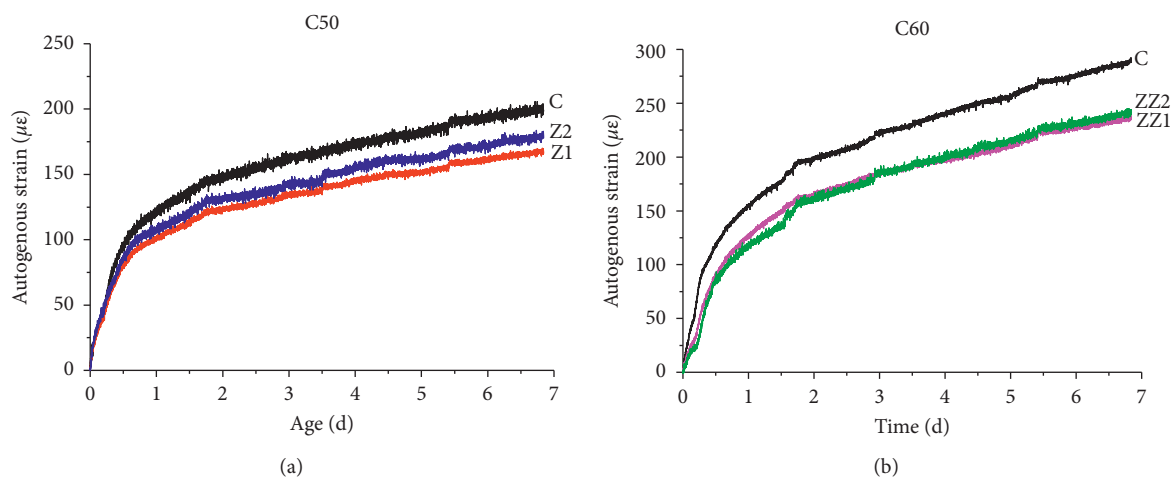


FIGURE 5: Autogenous shrinkage of the self-compacting concrete: (a) C50 and (b) C60.

4. Conclusions

In this study, a composite mineral admixture was used to replace cement. The fluidity and strength of the mortar, the strength of ordinary concrete, and the adiabatic temperature rise as well as the autogenous shrinkage of the self-compacting concrete were studied in this paper. The main conclusions are as follows:

- (1) The addition of composite mineral admixture decreases the early strength of the mortar. Increasing the SBFS content of the composite admixture can reduce degradation of the early strength. This may contribute to the pozzolanic reaction of SBFS, enhancing interface transition zone.

- (2) Composite admixture significantly reduces the adiabatic temperature rise of self-compacting concrete up to 7 days. For C50 concrete, the adiabatic temperature rise increases with the addition of SBFS content. While for C60 concrete, the SBFS content has little effect on adiabatic temperature rise.
- (3) Composite admixture significantly influences the autogenous shrinkage behavior of self-compacting concrete. The addition of composite admixture reduces autogenous shrinkage by 10%–15% for C50 concrete and 15%–20% for C60 concrete, respectively. The reduction effect of SBFS content on the autogenous shrinkage is prominent for C50 concrete compared to C60 concrete. This may be attributed to

the reason that SBFS promotes the early hydration of cement at low w/s in C60 concrete and thus increases the autogenous shrinkage.

References

- [1] H. Ostovari, L. Müller, J. Skocek, and A. Bardow, "From ussa cement industry based on CO₂ mineralization," *Environmental Science & Technology*, vol. 55, no. 8, pp. 5212–5223, 2021.
- [2] Y. Cancio Díaz, S. Sánchez Berriel, U. Heierli et al., "Limestone calcined clay cement as a low-carbon solution to meet expanding cement demand in emerging economies," *Development Engineering*, vol. 2, pp. 82–91, 2017.
- [3] N. Mahasenan, S. Smith, and K. Humphreys, "The cement industry and global climate ChangeCurrent and potential future cement industry CO₂ emissions," in *Proceedings of the Greenhouse Gas Control Technologies—6th International Conference*, pp. 995–1000, Kyoto, Japan, October 2003.
- [4] B. Ma, X. Li, X. Wang, R. Dong, and H. Zhu, "Study on environmental load and the control approach in cement industry," *Cement Engineering*, vol. 2, pp. 79–82, 2005.
- [5] D. Xu, Y. Cui, H. Li, K. Yang, W. Xu, and Y. Chen, "On the future of Chinese cement industry," *Cement and Concrete Research*, vol. 78, pp. 2–13, 2015.
- [6] X. Chai, H. Kao, T. Guo, and Q. Zhang, "Study on thermal energy recovery methods of cement industry basing on the energy balance methods," *Journal of Bulletin China Ceramic*, vol. 32, no. 4, pp. 692–698, 2013.
- [7] M. C. G. Juenger, F. Winnefeld, J. L. Provis, and J. H. Ideker, "Advances in alternative cementitious binders," *Cement and Concrete Research*, vol. 41, no. 12, pp. 1232–1243, 2011.
- [8] J. Sun and P. Zhang, "Effects of different composite mineral admixtures on the early hydration and long-term properties of cement-based materials: a comparative study," *Construction and Building Materials*, vol. 294, Article ID 123547, 2021.
- [9] Q. Wang, P. Yan, and G. Mi, "Effect of blended steel slag-GBFS mineral admixture on hydration and strength of cement," *Construction and Building Materials*, vol. 35, pp. 8–14, 2012.
- [10] X. Han, J. Feng, Y. Shao, and R. Hong, "Influence of a steel slag powder-ground fly ash composite supplementary cementitious material on the chloride and sulphate resistance of mass concrete," *Powder Technology*, vol. 370, pp. 176–183, 2020.
- [11] P. Chindaprasirt, S. Homwuttivong, and V. Sirivivatnanon, "Influence of fly ash fineness on strength, drying shrinkage and sulfate resistance of blended cement mortar," *Cement and Concrete Research*, vol. 34, no. 7, pp. 1087–1092, 2004.
- [12] P. Chindaprasirt, C. Jaturapitakkul, and T. Sinsiri, "Effect of fly ash fineness on compressive strength and pore size of blended cement paste," *Cement and Concrete Composites*, vol. 27, no. 4, pp. 425–428, 2005.
- [13] C. Shi, "Steel slag-its production, processing, characteristics, and cementitious properties," *Journal of Materials in Civil Engineering*, vol. 16, no. 3, pp. 230–236, 2004.
- [14] İ. Yüksel, "A review of steel slag usage in construction industry for sustainable development," *Environment, Development and Sustainability*, vol. 19, no. 2, pp. 369–384, 2017.
- [15] T.-S. Zhang, F.-T. Liu, S.-Q. Liu, Z.-H. Zhou, and X. Cheng, "Factors influencing the properties of a steel slag composite cement," *Advances in Cement Research*, vol. 20, no. 4, pp. 145–150, 2008.
- [16] S. Kourounis, S. Tsvivilis, P. E. Tsakiridis, G. D. Papadimitriou, and Z. Tsibouki, "Properties and hydration of blended cements with steelmaking slag," *Cement and Concrete Research*, vol. 37, no. 6, pp. 815–822, 2007.
- [17] T. Zhang, Q. Yu, J. Wei, J. Li, and P. Zhang, "Preparation of high performance blended cements and reclamation of iron concentrate from basic oxygen furnace steel slag," *Resources, Conservation and Recycling*, vol. 56, no. 1, pp. 48–55, 2011.
- [18] K. Wang, C. Qian, and R. Wang, "The properties and mechanism of microbial mineralized steel slag bricks," *Construction and Building Materials*, vol. 113, pp. 815–823, 2016.
- [19] R. J. Galán-Arboledas, J. Álvarez de Diego, M. Dondi, and S. Bueno, "Energy, environmental and technical assessment for the incorporation of EAF stainless steel slag in ceramic building materials," *Journal of Cleaner Production*, vol. 142, pp. 1778–1788, 2017.
- [20] L. D. Poulikakos, C. Papadaskalopoulou, B. Hofko et al., "Harvesting the unexplored potential of European waste materials for road construction," *Resources, Conservation and Recycling*, vol. 116, pp. 32–44, 2017.
- [21] J. J. Feng, S. S. Wang, and X. Q. Wang, "Usage of steel slag in concrete as coarse aggregates," *Advanced Materials Research*, vol. 887–888, pp. 801–804, 2014.
- [22] S. Liu and L. Li, "Influence of fineness on the cementitious properties of steel slag," *Journal of Thermal Analysis and Calorimetry*, vol. 117, no. 2, pp. 629–634, 2014.
- [23] S. Zhuang and Q. Wang, "Inhibition mechanisms of steel slag on the early-age hydration of cement," *Cement and Concrete Research*, vol. 140, Article ID 106283, 2021.
- [24] Y.-C. Peng and C.-L. Hwang, "Carbon steel slag as cementitious material for self-consolidating concrete," *Journal of Zhejiang University - Science*, vol. 11, no. 7, pp. 488–494, 2010.
- [25] Q. Wang, D. Wang, and S. Zhuang, "The soundness of steel slag with different free CaO and MgO contents," *Construction and Building Materials*, vol. 151, pp. 138–146, 2017.
- [26] M. Wu, Y. Zhang, Y. Ji et al., "Reducing environmental impacts and carbon emissions: study of effects of superfine cement particles on blended cement containing high volume mineral admixtures," *Journal of Cleaner Production*, vol. 196, pp. 358–369, 2018.
- [27] P. Z. Wang, R. Trettin, and V. Rudert, "Effect of fineness and particle size distribution of granulated blast-furnace slag on the hydraulic reactivity in cement systems," *Advances in Cement Research*, vol. 17, no. 4, pp. 161–167, 2005.
- [28] J. Zhu, Q. Zhong, G. Chen, and D. Li, "Effect of particlesize of blast furnace slag on properties of P," *Procedia Engineering*, vol. 27, pp. 231–236, 2012.
- [29] T. Luo, Q. Wang, and S. Zhuang, "Effects of ultra-fine ground granulated blast-furnace slag on initial setting time, fluidity

- and rheological properties of cement pastes,” *Powder Technology*, vol. 345, pp. 54–63, 2019.
- [30] B. Lothenbach, G. Le Saout, E. Gallucci, and K. Scrivener, “Influence of limestone on the hydration of Portland cements,” *Cement and Concrete Research*, vol. 38, no. 6, pp. 848–860, 2008.
- [31] T. Zhang, Q. Yu, J. Wei, P. Zhang, and P. Chen, “A gap-graded particle size distribution for blended cements: analytical approach and experimental validation,” *Powder Technology*, vol. 214, no. 2, pp. 259–268, 2011.
- [32] A. K. H. Kwan and Y. Li, “Effects of fly ash microsphere on rheology, adhesiveness and strength of mortar,” *Construction and Building Materials*, vol. 42, pp. 137–145, 2013.
- [33] E. Berodier and K. Scrivener, “Understanding the filler effect on the nucleation and growth of C-S-H,” *Journal of the American Ceramic Society*, vol. 97, no. 12, pp. 3764–3773, 2014.
- [34] X. Ouyang, D. A. Koleva, G. Ye, and K. van Breugel, “Insights into the mechanisms of nucleation and growth of C-S-H on fillers,” *Materials and Structures*, vol. 50, p. 513, 2017.

Thermodynamic analysis and optimization of a water-cooled multi-split heat pipe system in finite time (MSHPS)

Himanshu Sekhar Moharana, *Department of Mechanical Engineering, Aryan Institute of Engineering & Technology, Bhubaneswar, h.moharana26@gmail.com*

Debi Prasad Singh, *Department of Mechanical Engineering, Raajdhani Engineering College, Bhubaneswar, deboprasad_1159@gmail.com* Nalinikanta

Swain, *Department of Mechanical Engineering, Capital Engineering College, Bhubaneswar, nalin_526@yahoo.co.in*

Sikendar Sharma, *Department of Civil Engineering, Raajdhani Engineering College, Bhubaneswar, sikendarsharma92@gmail.com*

Biswa Ranjan Pradhan, *Department of Civil Engineering, Capital Engineering College, Bhubaneswar, biswaranjanpradhan78@gmail.com*

ARTICLE INFO

Keywords:

Thermodynamic simulation
Finite time thermodynamic analysis
Exergy method
IDC room
Heat pipe air-conditioning system
SIMULINK software
Refrigerant flow distribute characteristic
Energy saving potential

ABSTRACT

The heat transfer properties of the evaporation terminal, cool distribute unit (CDU), and refrigerant flow distribution of a water cooled multi-split heat pipe system (MSHPS) utilised in data centres are the focus of this research. The integrated system simulation model was built using finite time thermodynamic analysis, the exergy method, and the software SIMULINK. The findings reveal that IT servers should focus on organising themselves at a distance of less than 1.3 m. The heat transfer rate of the CDU is around 74 J per second. And the CDU's optimal flow rate is 0.82 kg/s. The working fluid is R22, and the flow distribution characteristic of a CDU that connects two 6 kW heat pipe evaporator terminals was computed. Then, in important Chinese cities, the free cooling time, part-time free cooling, and energy-saving potential were examined. The potential for energy savings ranges from 61% to 25%. The findings have significant implications for the operation and practical use of MSHPS and comparable pipe-net systems.

1. Introduction

Given the rise of cloud computing, communication, big data, finance, e-commerce, e-government, and other data-driven methods, the role of data centers will become more prominent. To maintain the normal operation of the run, air-conditioning system is needed. The energy of the air - conditioning take more than 40% of the total energy consumption of the room [1]. The heat load of the IDC room has those characteristics: (1) There are high sensible heat ratio, it is bigger than 0.9 in most cases. Because there are big heat load in IDC room, the wet load is very low and almost to zero. (2) It needs refrigerating all the year. Because the traditional air-conditioning system cooling down the whole IDC room, there are about 20–30% of the energy is used to reduce the humidity of the IDC room at the same time. Then to keep the humidity of the room, the reheat component is added after the air-conditioning process. The process wastes a lot of energy. On the other hand, the cooled air is distributed by the wind pipe. The distance is long and there are cooling capacity loss in the process. To tackle these problems, the air-cooled heat pipe air-conditioner is developed. The heat pipe has high heat transfer efficiency. Then with the heat density of the IDC room grows, the air-cooled heat pipe air-conditioner cannot meet the demand. Then the water-cooled technique is employed in the design of the high efficiency cooling process. But for the safety of the IDC room, the water pipe are prohibited to go into the IDC room, some are even not promised to the

corridor of the room. So the water cooled multi-split heat pipe system (MSHPS) was developed, the heat pipe evaporator terminal absorb the heat and condensing in the CDU, then the heat was taken away by the cooling water through the CDU. The heat pipe system tackle the heat exhaust by the IT equipment locally, and the cold and heat channel closed technical was employed to the system. The PUE of the IDC room can reach about 1.3 [2].

The energy performance of MSHPS are studied by many scholars. In the heat source and evaporator model: Yue. et al. developed a complete CFD model for the parallel tubes with simplified louvered fins of the evaporator structure was established to consider the thermal enhancement while reduce the computing costs. The CFD model was validated by comparing the cooling capacity and outlet temperature of MSHPS with experiments [3]. Zou. et al., focused on the onsite test about self-adaptive capacity of a MSHPS in a real data center under 25%, 50%, 75% and 100% heating loads and various fan failures. The results show that the MSHPS abnormally operated under low heating loads, but it still met the cooling demands due to its superior self-adaptive capacity [4]. Ling et al., carried out experimental research on the MSHPS, and pointed out that the optimal filling rate of the system is between 33% and 42% [5]. Zeng. et al., mainly studies the heat transfer performance of the micro-channel backplane heat pipe air conditioning system and conducts heat transfer performance experiments in a standard enthalpy difference laboratory [6]. Zou had done Experimental investigation on

Nomenclature

Abbreviations

MSHPS	multi-split heat pipe system
CDU	cooling deliver unit
IDC	information data center
IT	information technique
EDL	enthalpy difference laboratory
COP	coefficient of performance
PUE	power use efficiency
CFD	calculated fluid design

Symbols

A	linear diversion coefficient
BL	boiling number
D	diameter(m)
e	exergy(J)
t	time (s)
T	temperature (K)
h	heat transfer coefficient ($W/m^2 \cdot K$)
height	high degree (m)
H	enthaphy,(J)
i	exergy loss (J)
I	total exergy loss (J)
j	colburn j factor
k	thermal conductivity ($W/m \cdot K$)
m	Mass flow (kg/h)
P	pressure (Pa)
Pr	prandtl number
q	flow rate (m^3/s)
Q	total heat(J)
Re	reynolds number
s	entropy ($J/(mol \cdot K)$)
V	velocity vector (m/s)
v	volume flow
W	work input(J)
We	weber number
x	gas to liquid degree

Green letters

ρ	density (kg/m^3)
λ	resistance coefficient
ε	local resistance coefficient
σ	relative error
τ	period
η	efficiency

Subscripts

n, i, j	phase n, i and j
l	liquid
g	gas
gen	entropy generation
o	out
out	out door
sat	saturation
ev	evaporator
exp	expansion valve
a	air-side
tp	two phase
com	compressor
cond	condenser
ref	refrigerant
w	water
0	mbient temperature

.	hourly
-	average

the thermal performance of a water-cooled loop thermosyphon system under fan failure conditions. It is showed that is better to choose a high optimal filling ratio to ensure the good operating performance and anti-failure capability of loop thermosyphon system [7]. Further more, many scholars have down many research to check the pipe network characteristics such as liquid separation parameters. A novel multi-branch heat pipe was investigated by experiment. The proposed heat pipe consists of three branches—two with an evaporator and one with a condenser. the optimal working fluid filling ratio and ideal heat load was obtained [8]. Chen, et al., used the thermodynamic simulation software cyclepad to simulate and calculate the thermodynamic properties and energy saving characteristics of 72 backplane heat pipes connected by 6 CDU in a telecommunication room in Changde city. The results show that the annual average energy saving of heat pipe is more than 26% [9]. However, the simulation method is steady-state. There are few researches on the influence of environment on heat pipe system of IDC room and energy efficiency evaluation: A thermodynamic approach for evaluating energy performance (productivity) of information technology (IT) servers and data centers is presented. This approach is based on the first law efficiency to deliver energy performance metrics defined as the ratio of the useful work output (server utilization) to the total energy expanded to support the corresponding computational work. These energy performance metrics will facilitate proper energy evaluation and can be used as indicators to rank and classify IT systems and data centers regardless of their size, capacity or physical location [10]. A distribute parameter annual energy consumption model with considering the effect of the dynamic heat dissipation characteristics of servers, lake water temperature, outdoor weather conditions, and cooling plant thermal performance, will be established to evaluate the performance and energy efficiency of this cooling plant under different load factors [11].

They simulation model is complex, and the task of the experiment is large, to build a simple method to evaluate the heat-pipe combined system, a thermodynamic simulation software *SIMULINK* is employed. In this paper, the finite time thermodynamic method is applied to establish an hourly simulation model of CDU, which can reflect the actual operation of the system, such as the influence of inlet water temperature fluctuation on the heat transfer performance of CDU. To solve the refrigerant flow distribute characteristic and the key parameters of the water cooled multi-split heat pipe system used in data center, based on the two term flow model, the network node model of the system will be established and solved by MATLAB simulation method in this paper. Then the energy and exergy efficiency will be calculated and compared with the traditional air-conditional system.

2. The physical model of the water cooled multi-split heat pipe system

2.1. The system model of water cooled multi-split heat pipe system

A typical heat pipe air-conditioning system can be seen in Fig. 1. The area of the IDC room is $384 m^2$, the indoor temperature demand is about $24^\circ C$, and the humidity is about 50%. 72 backboard heat pipe air conditioners were designed in the system. The dimension of the gas pipe is about 19mm, and the liquid pipe is about 16mm. The distance between the two pipe is about 600mm. The average outdoor temperature is $35.4^\circ C$ in summer, and $-2.6^\circ C$ in winter. The temperature of the chiller water in and outlet to the CDU is $12/17^\circ C$ [12]. And when the gap of outdoor temperature and IDC room is larger than $10^\circ C$ in winter or transition season, the free cooling mode can be used, the chilling wa-

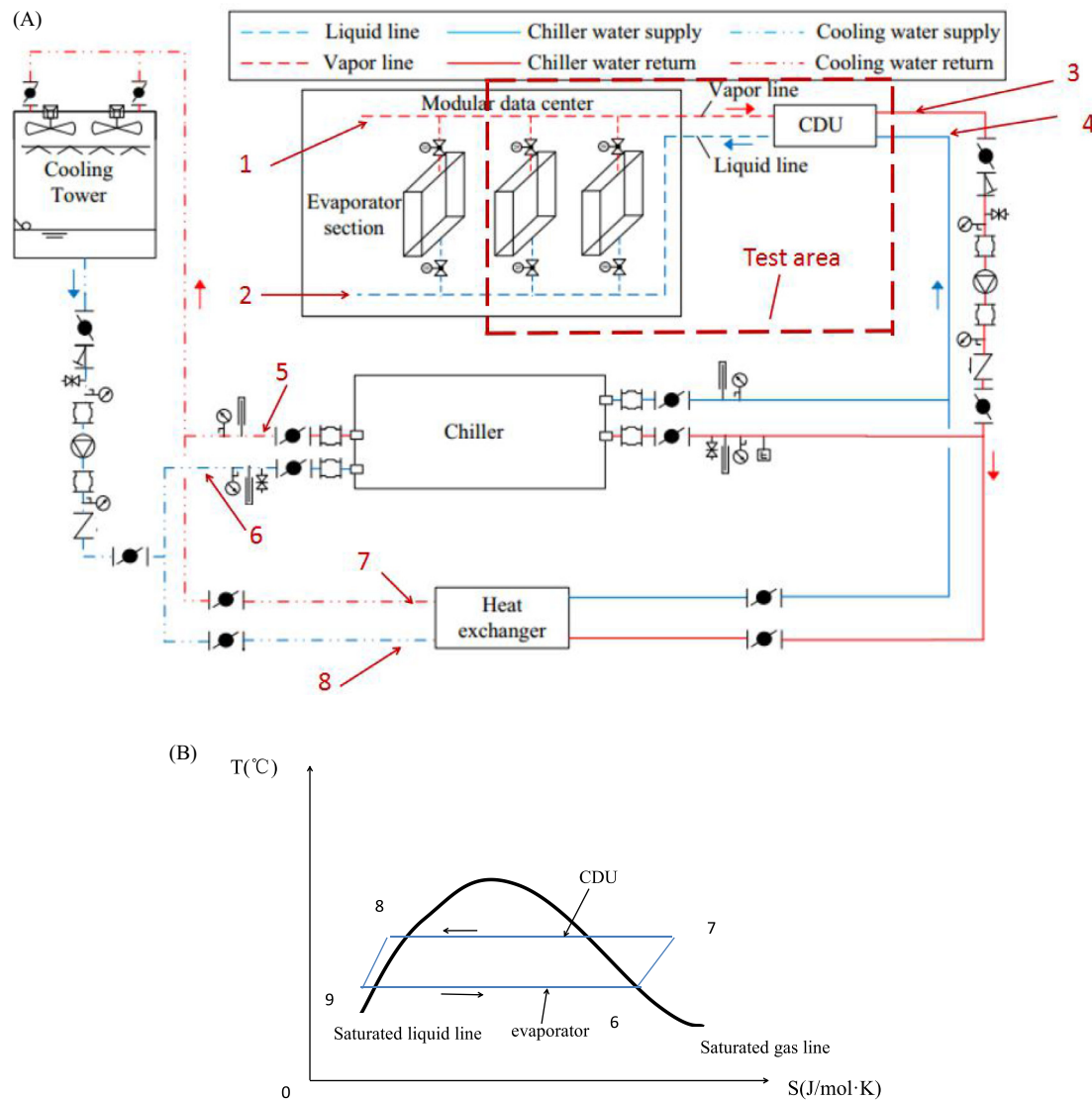


Fig. 1. (A) The backboard heat pipe air-conditioning system in the IDC room [14]. (B) The T-S diagram of the evaporator and CDU of the heat pipe system.

Table 1

The percentage of average outdoor temperature zone of a year of Wuhan city.

\bar{T}_{out} (°C)	≥ 30	$\geq 20, < 30$	$\geq 10, < 20$	$\geq 0, < 10$	< 0
Percentage of the time	11.5%	33.3%	27.1%	26.2%	1.9%

ter machine can be shut down [13]. The refrigerant absorb heat in the evaporator and form liquid (state 9) to gas (state 6), then exhaust heat at the CDU and from gas (7) to liquid (8). See in Fig. 1(B).

1-refrigerant (gas) out of evaporate and into CDU; 2-refrigerant (liquid) out of CDU and into evaporate; 3- chilled water in to CDU; 4- chilled water out of CDU; 5-cooling water out of cooling tower and in to Chiller; 6- cooling water out of Chiller and into cooling tower; 7- cooling water out of cooling tower and in to heat exchanger (free cooling mode); 8-cooling water out of heat exchanger and in to cooling tower (free cooling mode)

The percentage of average outdoor temperature zone of a year of Wuhan city is showed in the Table 1 [15]. For example, the time of the outdoor temperature \bar{T}_{out} which is over 30 °C is about 11.5% of the whole year.

2.2. The physical model of heat pipe evaporator

The heat pipe evaporator of 6 kW in a company is taken as the calculate object. The heat pipe evaporator is microchannel heat exchanger. The height of the heat pipe evaporator is 2 m, and the width is 600 mm. The wind rate of the fan of the heat pipe evaporator is 2000 m³/s, and the refrigerant of the heat pipe evaporator is R22 [16].

2.3. The physical model of CDU

The parameter of the CDU is show in Table 2 [17].

2.4. The physical model of the network

The MSHPS has three operation model: 1, when the gap of outdoor temperature and IDC room is larger than 10 °C in winter or transition season, the free cooling mode is used; 2, when the gap of outdoor temperature and IDC room is larger than 0 °C and smaller than 10 °C, the refrigerating main engine and the heat pipe operate at the same time; 3, When the gap of outdoor temperature and the IDC room is less than 0 °C, the refrigerating main engine operate, and the heat emitted from the IDC room is taken away, and discharged into the outdoor environment by the condenser [18].

Table 2

The parameter of the CDU.

Parameter	Side of refrigerant	Water side
Mass flow (kg/h)	187.6	1714
Pressure drop (kPa)	2.100	-
Working pressure(bar)	8.85	0.1
Temperature(°C)	20	12/17
Tracheal branch(mm)	19	
Liquid pipe branch(mm)	16	
The heat transfer area(m^2)	0.9	
CDU outline size		
(high)×(wide)×(thick)	0.525×0.111×0.12	
Installation height(m)	1.8	

2.5. The physical model of the cooling source

The cooling capacity of the compressor is about 130 kW; the condensing temperate is about 35 °C; the temperate of the cold water is about 12 °C [19].

3. The mathematical model of the heat-pipe air-conditioning system

3.1. The mathematical model of the evaporator of the heat-pipe

Referring to the micro channel heat exchanger model, based on the new Gungor-Winterton correlation formula [20], the hourly simulation model of the heat pipe evaporator is established.

$$h_{tp} = 0.0455(S + F)Re_1 P_r^{-1} W_{e_{lo}}^{-0.17} \frac{k_l}{D_h} \quad (1)$$

$$S = 1 + 4400 BL^{0.86} Fr_{lo}^{-0.22} \quad (2)$$

$$F = 1.12 \left(\frac{x}{1-x} \right)^{0.86} \left(\frac{\rho_l}{\rho_g} \right)^{0.41} \quad (3)$$

In the formula, Re_1 is Liquid Reynolds number; P_r is Liquid Prandt number; BL is Boiling number; $W_{e_{lo}}$ is Liquid Weber number; k_l is Liquid thermal conductivity; D_h is heat pipe diameter; x is hourly gas to liquid degree; ρ_l is liquid density; ρ_g is gaseous density.

The total heat exchange:

$$Q = m \cdot \int_0^1 h_{tp} dx \quad (4)$$

In the formula: h_{tp} : Hourly two current heat transfer coefficient; x is gas to liquid degree.

The efficiency of the system:

$$\eta = \frac{Q}{\tau} \quad (5)$$

In the formula, τ : the heat transfer time of the working fluid in the heat pipe evaporator.

$$\tau = \frac{h_{ev}}{V} \quad (6)$$

In the formula, h_{ev} is high degree of the evaporator ; V is the velocity of the working fluid:

$$V = \frac{v}{\pi \cdot \left(\frac{D}{2} \right)^2} \quad (7)$$

In the formula, v is volume flow.

The formula (1) - (7) constitutes a heat transfer model for heat pipe microchannel heat exchangers.

3.2. The mathematical model of the CDU

See in Fig. 2. The heat exchange of the CDU is equal to the enthalpy drop from the state point 7 to the state point 8 [21].

$$Q_{cond} = \dot{H}_7 - \dot{H}_8 \quad (8)$$

In the formula, Q_{cond} is the heat transfer for CDU by time. The \dot{H}_7, \dot{H}_8 are enthalpy value at the state point 7 and 8.

The points 7 and 8 can be determined according to T-S diagram (Fig. 1(B)) and the designed evaporation and condensation temperature.

The exergy loss of the CDU:

$$I_{cond} = \dot{m}_{ref} \cdot i_{cond} \quad (9)$$

And:

$$i_{cond} = \dot{m}_{ref} \cdot (h_7 - h_8) - T_0 \cdot (\dot{s}_7 - \dot{s}_8) \quad (10)$$

In the formula, i_{cond} : the hourly loss of refrigerant for unit quality; I_{cond} : the loss of working hours; \dot{m}_{ref} : the mass flow rate of working medium; T_0 : the hourly ambient temperature; \dot{s}_7, \dot{s}_8 : hourly entropy.

The formula (8) - (10) constitutes a finite time thermodynamic model of CDU.

3.3. The mathematical model of network system

According to the law of conservation of mass, the sum of the flow of each pressure node in the fluid network is 0:

$$\sum_{i=1}^m q_i = 0 \quad (11)$$

In the formula, q is the flow of the branch into the node.

Momentum equation based on fluid motion:

$$p_i - p_{i+1} = R_i \cdot q_i^2 \quad (12)$$

The R is resistance coefficient of the pipeline, and P is the pipe inlet and outlet pressure, Pa.

It should be linearized and the computing equations of network nodes are obtained.

In the process of computing, the following assumptions are made:

- (1) The branch has a fixed intercepting area;
- (2) There is no heat exchange with the outside world;
- (3) The working fluid of the node is incompressible;
- (4) The diversion coefficient of the branch is variable. It is depends on the parameters of fluid pressure, flow rate and valve opening.

Because the momentum equation contains a square term, the software can not be directly solved and linearized.

$$q_i = \frac{\sqrt{p_i - p_{i+1}}}{\sqrt{R_i}} \quad (13)$$

Calculation of boundary and local resistance:

$$p_i - p_{i+1} = \left(\lambda_i \frac{l_i}{d_i} + \epsilon_i \right) \cdot V_i^2 \cdot \rho / 2 \quad (14)$$

Where, λ_i is the resistance coefficient along the way; l_i is the length of I pipe; d_i is the diameter of I pipe; ϵ_i is the local resistance coefficient of I pipe; V_i is the flow velocity of I pipe; ρ is the density of working medium, which is ρ_l in liquid state and ρ_g is in gas state.

Among them, A is a linear diversion coefficient:

$$\sqrt{\frac{\pi^2 \cdot d_i^4}{2 \cdot \rho \cdot (\lambda_i \frac{l_i}{d_i} + \epsilon_i) \cdot (p_i - p_{i+1})}}$$

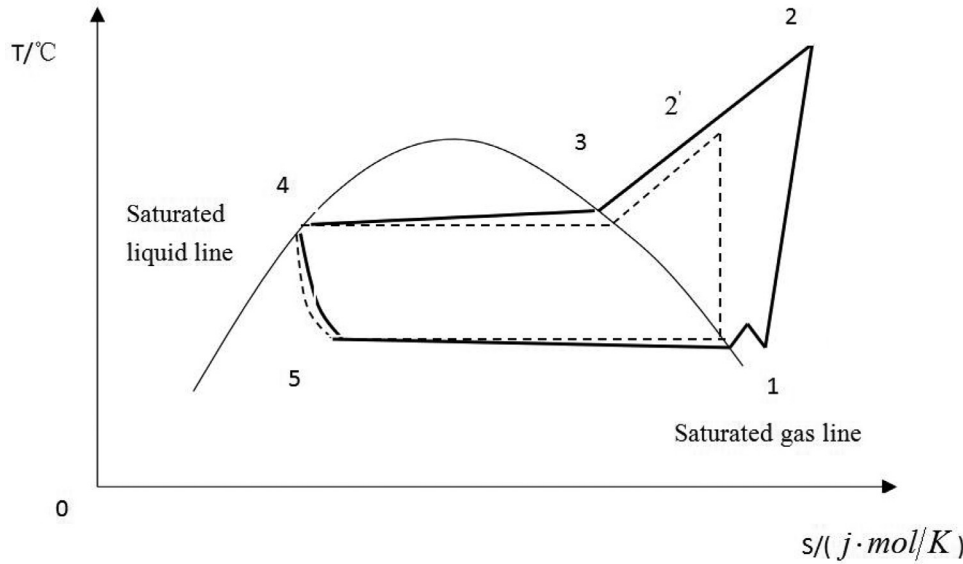


Fig. 2. The T-S diagram of the cooling source.

3.4. The mathematical model of the cooling source

3.4.1. The mathematical model of the compressor

According to Fig. 2, the mass flow of the refrigerant is \dot{m}_{ref} , it comes to the compressor at the state 1. And the outlet at state 2'. Due to the irreversible process of the compress, the actual outlet state is state 2. There are exergy loss and entropy generations. The exergy balance equation is as follows [22]:

$$\dot{e}_1 + \dot{W} = \dot{e}_2 + \dot{i}_{comp} \quad (15)$$

In the formula, \dot{e}_1 is hourly exergy input to the compressor; \dot{W} is the hourly work input by the compressor; \dot{e}_2 is hourly exergy output of the compressor; \dot{i}_{comp} is hourly exergy loss of the compressor.

The exergy input by the compressor is:

$$\dot{e}_{in,comp} = \dot{W} = \dot{m}_{ref}(\dot{H}_2 - \dot{H}_1) \quad (16)$$

In the formula, \dot{H}_2 is hourly enthalpy of state 2; \dot{H}_1 is hourly enthalpy of state 1.

The entropy generation of the irreversible process is:

$$\dot{s}_{gen,12} = \dot{s}_2 - \dot{s}_1 \quad (17)$$

In the formula, \dot{s}_2 is hourly entropy of state 2; \dot{s}_1 is hourly entropy of state 1.

Then the exergy loss of the compressor is:

$$\dot{I}_{comp} = \dot{e}_1 - \dot{e}_2 + \dot{w} = \dot{m}_{ref}T_0(\dot{s}_2 - \dot{s}_1) \quad (18)$$

In the ideal reversible process of the compress, the power consumption is:

$$\dot{W} = \dot{m}_{ref} \cdot (\dot{H}_{2'} - \dot{H}_1) \quad (19)$$

The parameter of the real outlet state 2 of the compressor can be defined by the formula:

$$\eta_{is,c} = \frac{\dot{H}_{2'} - \dot{H}_1}{\dot{H}_2 - \dot{H}_1} \quad (20)$$

In the formula, η is the compress efficiency, it is decentralized compressor, suppose it is 0.85. \dot{H}_2 is actual enthalpy and $\dot{H}_{2'}$ is ideal enthalpy.

$$\dot{H}_2 = \frac{\dot{H}_{2'} - \dot{H}_1}{\eta} + \dot{H}_1 \quad (21)$$

3.4.2. The mathematical model of the condenser

The heat of condensation is equal to the enthalpy drop from the state 2 to state 4, seen in Fig. 2.

$$\dot{Q}_{cond} = \dot{H}_2 - \dot{H}_4 \quad (22)$$

In the formula, \dot{H}_2 is hourly enthalpy at state 2, and \dot{H}_4 is hourly enthalpy at state 4. \dot{Q}_{cond} is hourly condensation heat exhaust to the environment.

According to the T-S diagram, the state of the 4 point can be determined.

$$\dot{I}_{cond} = \dot{m}_{ref} \cdot \dot{i}_{cond} \quad (23)$$

And:

$$\dot{i}_{cond} = \dot{m}_{ref} \cdot \left[(\dot{H}_2 - \dot{H}_4) - T_0 \cdot (\dot{s}_2 - \dot{s}_4) \right] \quad (24)$$

3.4.3. The mathematical model of the valve

As shown in Fig. 2, the throttling process line is 4~5. Based on the exergy balance equation and adiabatic throttling equation, the exergy loss of throttle valve is gotten:

$$\dot{I}_{exp} = T_0 \cdot \dot{m}_{ref}(\dot{s}_5 - \dot{s}_4) \quad (25)$$

3.4.4. The mathematical model of evaporator

In the evaporator, the circulating refrigerant absorbs heat from the low temperature heat source to transform into gaseous state and enter the compressor. For example, the process line 5~1 in Fig. 2. When the cooling capacity is utilized, the exergy loss is estimated from the exergy balance equation [23].

$$\begin{aligned} \dot{I}_{ev} = \dot{m}_{ref} \cdot \left[(\dot{h}_5 - \dot{h}_1) - T_0 \cdot (\dot{s}_5 - \dot{s}_1) \right] \\ + \dot{m}_{ev,w} \cdot \left[(\dot{h}_{evwo} - \dot{h}_{evwi}) - T_0 \cdot (\dot{s}_{evwo} - \dot{s}_{evwi}) \right] \end{aligned} \quad (26)$$

The formula $\dot{m}_{ev,w}$ is the flow of cold water, $\dot{h}_{evwi}, \dot{h}_{evwo}$ are the enthalpy of cold water for inlet and outlet, and $\dot{s}_{evwi}, \dot{s}_{evwo}$ are the entropy of cold water import and export.

3.5. The mathematical model of the exergy efficiency

The COP and exergy efficiency η is:

$$COP = \frac{\int_0^t \dot{q} \cdot dt}{\int_0^t \dot{W} \cdot dt} \quad (27)$$

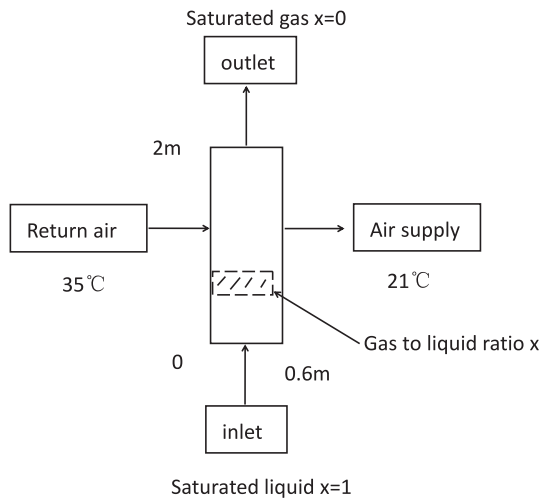


Fig. 3. The flowchart diagram of the evaporator terminal of the heat pipe.

$$\eta = \frac{\int_0^t \dot{e} \cdot dt}{\int_0^t \dot{e}_w \cdot dt} \quad (28)$$

In the formula: \dot{q} is the hourly heat transfer; \dot{W} is the hourly input work; t is the operate time; \dot{e} is hourly exergy transfer; \dot{e}_w is the hourly input exergy.

The actual climate parameters, such as temperature, are taken as a function of time. As an input parameter, the hourly temperature of the whole year is integrated in this period. The average temperature of the unit can be obtained by dividing the total amount by the time of the whole year. As shown in the formula:

$$\bar{T} = \frac{\int_0^t \dot{T} \cdot dt}{\tau} \quad (29)$$

In the formula: \bar{T} is the average temperature; \dot{T} is the hourly temperature; t is the operation time; τ is the time period.

4. The simulation model of unit type water cooled multi continuous heat pipe system

4.1. The simulation model of the evaporator of the heat pipe

According to formula 3, the simulation model of the evaporator of the heat pipe is established [24]. Seen in Fig. 3.

Similarly, a simulation model of heat transfer coefficient and heat transfer can be established.

4.2. The simulation model of the cdu

According to the mathematical model of heat exchanger, a simulation model is established. Seen in Fig. 4.

5. Experimental test

5.1. The purpose of the experiment

In the IDC room, the heat exhaust by the IT servers is vary with the high degree of the IT servers and the operation time, and the distance from the evaporation terminal of the heat pipe to the CDU is quite different. It is easy to cause uneven liquid distribution in pipe network, resulting in dry burning and other problems. Two of the evaporation terminal of the heat pipe in the MSHPS was tested. see in Fig. 1. And the heat pipe test platform can be seen in Fig. 5.

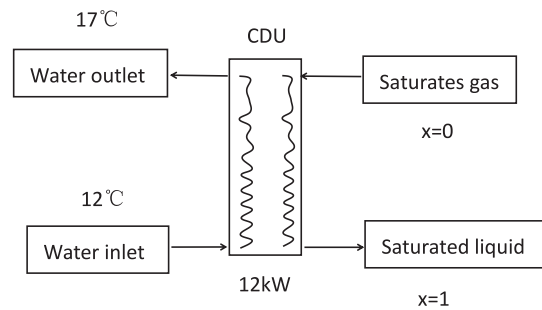


Fig. 4. The flowchart diagram of the CDU.

Table 3

The style of the experimental equipment.

Name	Model	Measurement range	Resolution	Remarks
Flowmeter	OMEGA	0.001–9.999 m/s	1%	Doppler flow meter
thermometer	NTC-3M10K	–20 °C - 150 °C	0.05 °C	
Pressure gage	SL1808T	–0.1–250MPa	grade0.4	

Table 4

The parameter setting.

Serial number	Parameter	Value
1	Inlet air temperature of back plate 1 (°C)	35
2	Inlet air temperature of backboard 2 (°C)	37.5
3	Total mass flow rate of refrigerant (kg / s)	0.0901
4	Flow of branch 1 (kg / s)	0.0371
5	Air volume of branch 1 (m ³ / s)	0.4152
6	Diameter of branch 1 (cm)	16
7	Inlet pressure of branch 1 (kPa)	885.7
8	outlet pressure of branch 1 (kPa)	887.8
9	Flow of branch 2 (kg / s)	0.0530
10	Air volume of branch 2 (m ³ / s)	0.5033
11	Diameter of branch 2 (cm)	16
12	Cold water inlet temperature (°C)	12
13	Cold water outlet temperature (°C)	17
14	Cold water flow (kg / s)	0.8124

5.2. Test of construction of system liquid separation test bench

Two back plates of heat pipe air conditioner are set, and the model is 6 kW. The structure is copper tube and aluminum fin structure. The inlet air temperature of one block is 35 °C and that of the other block is reduced from 40 °C to 30 °C. The wind speed is about 2.5 m/s. The accuracy of the calculation results is verified by measuring the flow and total flow of the branch pipe by the flow meter. Seen in Fig. 6.

5.3. The experimental equipment

The inlet air temperature of back plate 1# is about 35 °C and the outlet air temperature of back plate 1# is about 21 °C. The refrigerant is R22. The phase transition temperature of the designed refrigerant is about 19 °C. The corresponding pressure is about 885.7 kPa. The inlet air temperature of backboard 2# increased from 30 °C to 40 °C, and the outlet air temperature was about 21 °C. (Table 3)

5.4. Initial parameter setting

The initial calculation values are shown in Table 4: the inlet air temperature of backplane 1 # is 35 °C, and that of backplane 2 # is 37.5 °C.

Take the meteorological conditions of a place (such as Wuhan city) as an example as input [26].

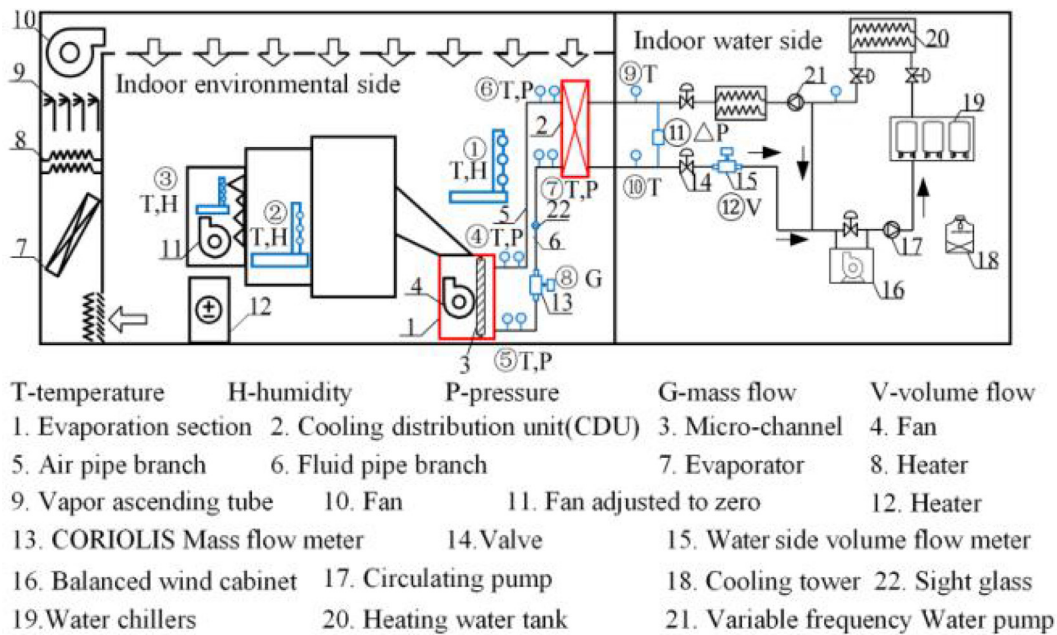


Fig. 5. Schematic diagram of backplane heat pipe test platform of enthalpy difference laboratory [25].

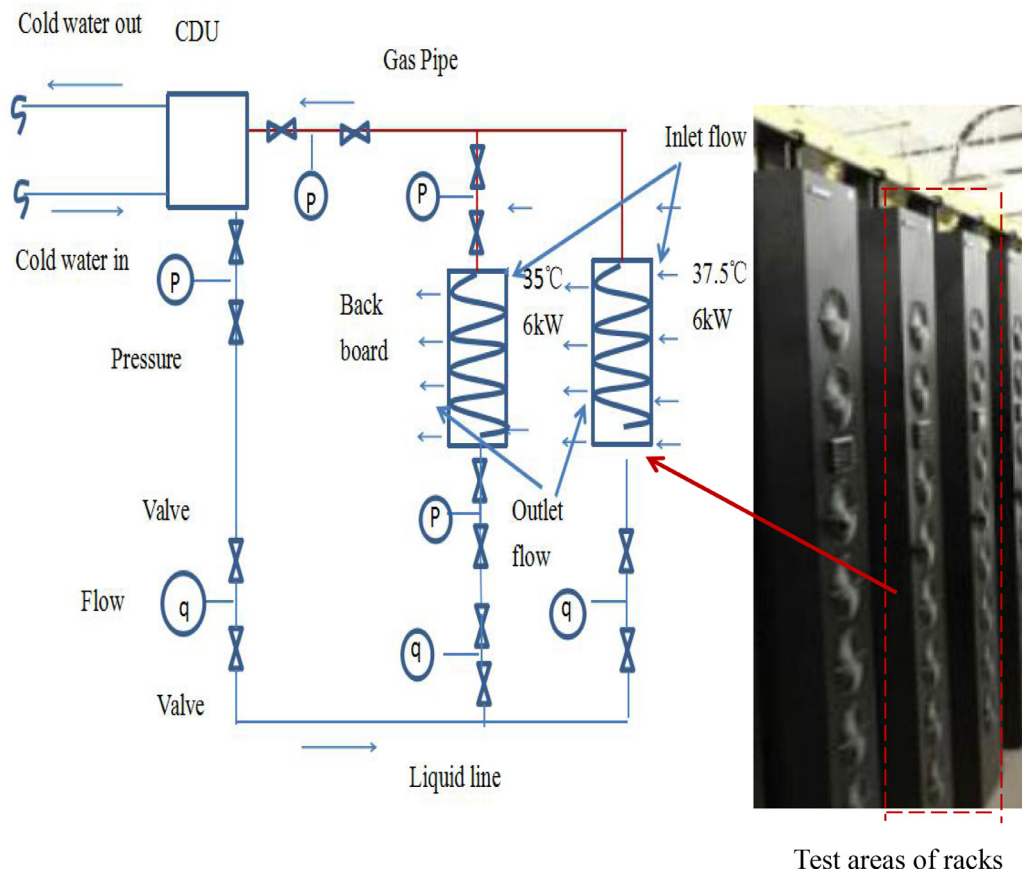


Fig. 6. The flow and pressure test diagram.

6. Results and discussions

It can be seen from the relationship between the liquid to gas ratio of the heat exchanger vary with the height and operation time of the heat exchanger. It shows that the liquid to gas ratio is lower than

0.72, the heat transfer efficiency reduce greatly. And the corresponding height is about 1.3 m. So when arranging the IT server, it is advisable to concentrate on the location below 1.3 m, seen in Fig. 7.

The calculation results show that heat transfer rate of the evaporation teminal of the heat pipe gradually slows down with operation time.

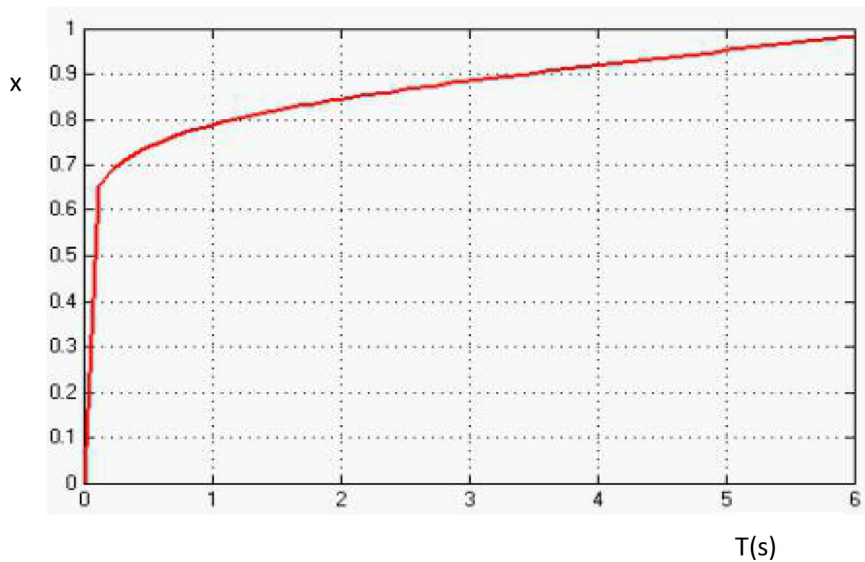


Fig. 7. The liquid to gas ratio (x) vs. the operating time in the evaporator.

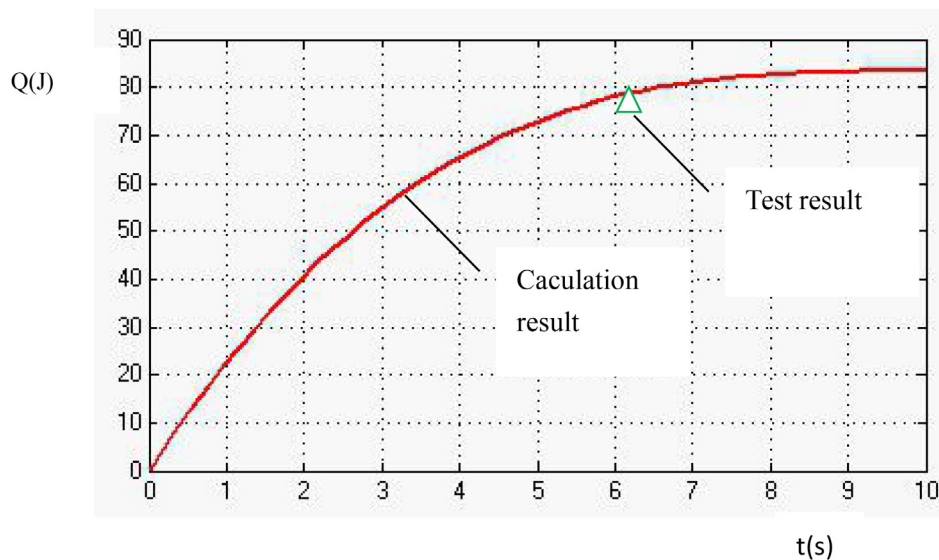


Fig. 8. The total heat transfer vs. the heat transfer time of the heat pipe exchanger.

Table 5

The error of the mass flow of the branch VS. the test cases.

Inlet air temperature of backboard 2# (°C)	Calculation result of branch 1# (kg/s)	Test data of branch 1# (kg/s)	Error(%)	Calculation result of branch 2# (kg/s)	Test data of branch 2# (kg/s)	Error(%)
30	0.059	0.058	1.7	0.032	0.03	6.7
32.5	0.055	0.051	7.8	0.038	0.031	23
35	0.051	0.052	1.9	0.046	0.041	12
37.5	0.048	0.039	23	0.056	0.059	5
40	0.043	0.04	7.5	0.068	0.071	4

The evaporation terminal of the heat pipe has a heat transfer of about 74 J after 6 s of heat transfer. Seen in Fig. 8.

The heat transfer efficiency of the CDU is calculated by changing the flow rate of cold water. As shown in the diagram, the heat transfer efficiency is equal to heat transfer divide the operation period. If the flow rate is smaller, the heat transfer period is short, but the total heat transferred in a period is few; if the flow rate is bigger, the total heat transferred in a period is large, but the heat transfer period is long, so the optimum flow rate of CDU is 0.82 kg/s, and the corresponding heat transfer efficiency is 0.81. Seen in Fig. 9.

The inlet air temperature of backboard 2# increases from 30 °C to 40 °C. According to the self balance of the system, when the inlet air temperature of backboard 1# is higher than backboard 2#, there are more refrigerant flow to the branch 1. Then, when the inlet air temperature of backboard 1# is smaller than backboard 2#, there are few refrigerant flow to the branch 1. And the flow calculation and test values of each branch are as follows. Seen in Fig. 10.

Test conditions: the inlet air temperature of backboard 1# is about 35 °C, The outlet air temperature is about 21 °C.

It can be seen from Fig 10, with increase of the inlet temperature of backboard 2# from 30 °C to 40 °C, the flow of branch 1 decrease

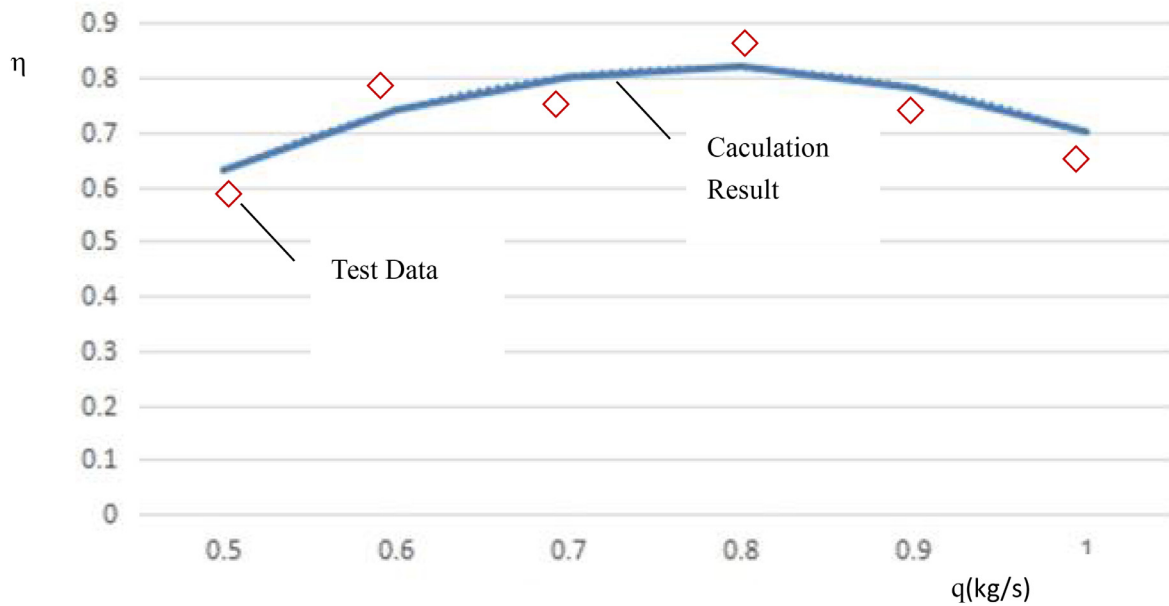


Fig. 9. The η of the system vs. the mass flow of the cooling water.

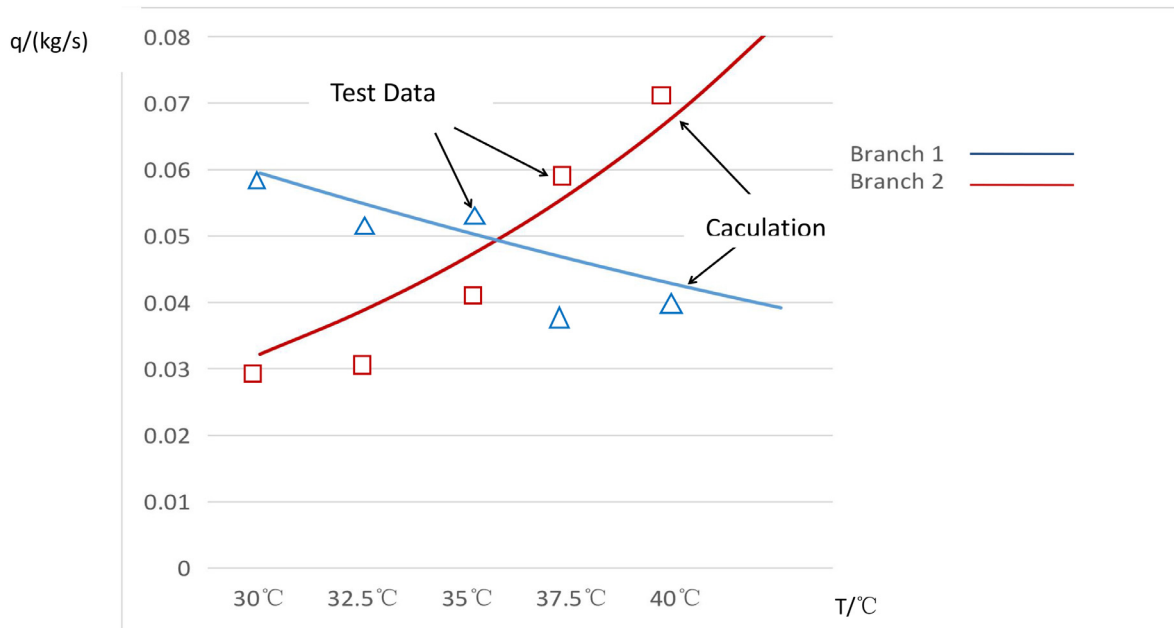


Fig. 10. The flow of the branch VS. the inlet temperature of backboard 2#.

Table 6
Temperature and RH conditions of five typical climatic regions in China.

City	Climate zone	Annual average temperature/°C	Annual average RH
Urumchi	Server cold	8.3	59%
Beijing	Cold	14.2	50%
Kunming	Mild	15.7	73%
Changsha	Hot summer and cold winter	17.1	83%
Guangzhou	Hot summer and warm winter	22.1	80%

from 0.06 to 0.042 kg/s, and the flow of branch 2 increase from 0.032 to 0.069 kg/s.

6.1. Error analysis

To verificate the accuracy of the calculation result of the simulation model and the test datas, the error analysis formula is employed:

$$\sigma = \frac{\text{calculation} \cdot \text{result} - \text{test} \cdot \text{data}}{\text{test} \cdot \text{data}} \times 100\% \quad (30)$$

From the table ,it can be seen that when the inlet temperature of backboard 2# at 37.5 °C, the error is the biggest, is about. And the average error of the mass flow of the branch is about 6.7%. (Table 5)

Test conditions: the inlet air temperature of backboard1# is about 35 °C, The outlet air temperature is about 21 °C.

The meteorological parameter of the five given cities is show in Table 6. And the free cooling time and complex mode (part time free cooling) time of a year can be seen from the typical city of Changsha.

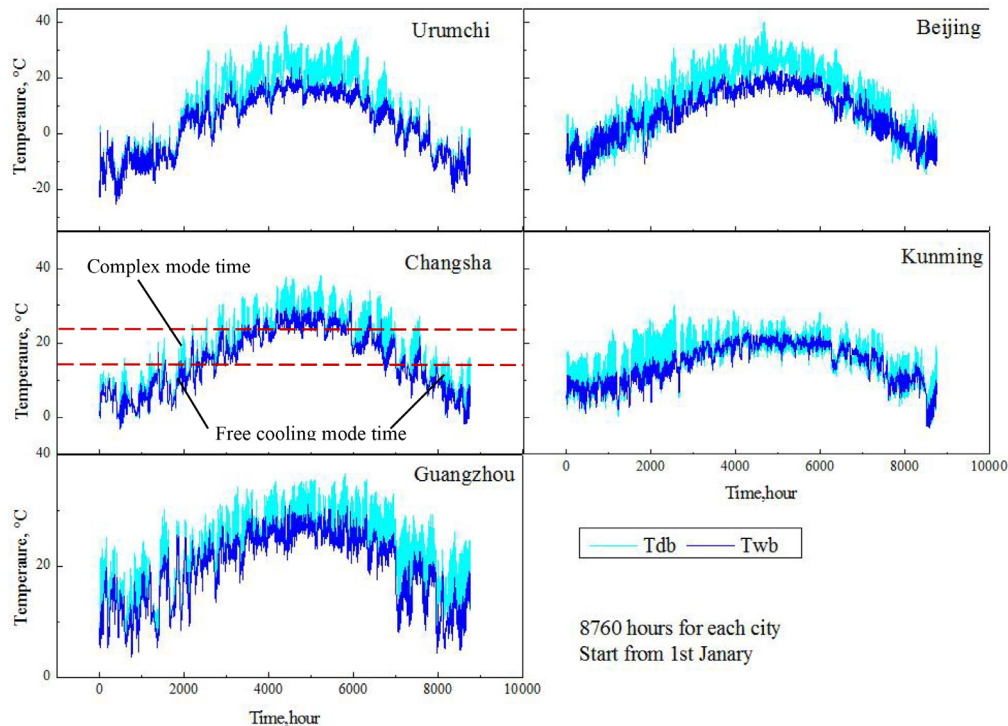


Fig. 11. The meteorological parameter of the five given cities and the free cooling time .

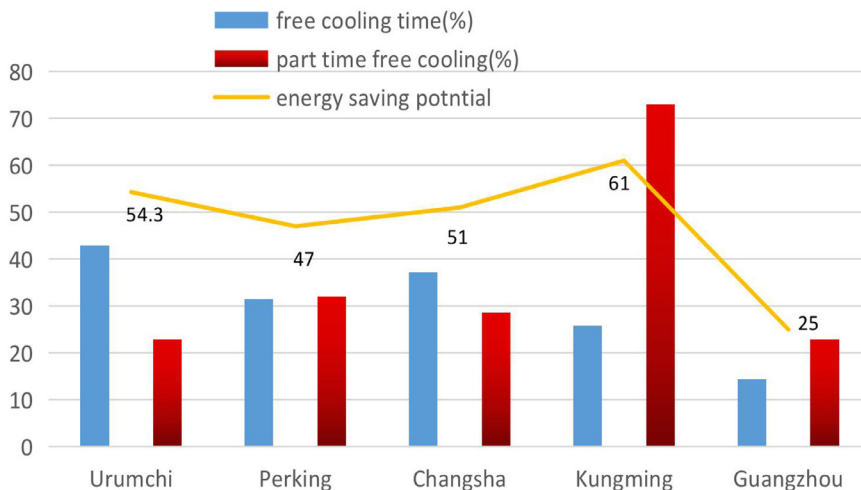


Fig. 12. The free cooling time,part time free cooling and energy saving potential of typical city in China.

If the T_{db} is lower than 14°C , it is the free cooling mode, if the T_{db} is lower than 24°C and bigger than 14°C , the system running complex mode (part time free cooling), and when the T_{db} is bigger than 24°C , the system running traditional mechanical refrigerate mode. Seen in Fig. 11.

Take the outdoor temperature of the major city of China as the input parameter, the free cooling time, part time free cooling and the energy saving potential in five typical climatic regions of China is seen in Fig. 12.

7. Conclusions

- (1) In this paper, a time integration model for heat transfer in heat exchangers is established based on finite time thermodynamic analysis. The model can reflect the actual heat transfer process

of heat exchanger. The model can be used to optimize the charging capacity of heat exchangers. And the model can reflect the relationship between heat transfer and heat exchanger height. Provide judgment and reference for the layout of IT equipment.

- (2) The hourly simulation model of CDU is simple and the simulation error is small. Compared with classical thermodynamic analysis, it can reflect the actual operation of the system. The simulation precision is high. Moreover, the model can provide reference for the design and optimization of CDU parameters.
- (3) Compared with the traditional air conditioning system, the flow rate of working fluid in the unit water-cooled multi connected heat pipe system is much lower than that in the traditional refrigeration system, it is about 10–20% of the traditional refrigeration system. Which results in the failure of the empirical formula of "one driving more" in the refrigeration system. The existing cal-

culuation of flow rate and thermal resistance are independent engineering projects, and there is no unified conclusion, so it can not be widely applied. In this paper, the liquid separation model is established according to the network node flow method. By using M language of MATLAB software, the program for solving the network node pressure and flow rate of the unit water-cooled multi connected heat pipe system is compiled. The adaptive performance of the system under different loads is simulated. The test results show that the calculation method meets the requirements of engineering accuracy, and can be used as a reference for the design of refrigeration requirements under different load conditions.

- (4) The model provides a new method for the simulation of thermal system.

Declaration of Competing Interest

All authors of the manuscript have no conflict of interests to declare.

References

- [1] V. Ricardo, A. Hossein, L. Iolanda, et al., The role of artificial intelligence in achieving the sustainable development goals., *Nat. Commun.* 11 (1) (2020) 233.
- [2] M.A.M Hassan, Investigation of performance of heat pipe as heat exchanger using alternative refrigerants, *Int. J. Energy Eng.* 139 (1) (2013) 18–24.
- [3] Chang Yue, Quan Zhang, Zhiqiang Zhai, et al., Numerical investigation on thermal characteristics and flow distribution of a parallel micro-channel separate heat pipe in data center, *Inter J. Ref.* (98) (2019) 150–160.
- [4] Si Kai. Zou, Quan. Zhang, Yue Bin. Yu, et al., Field study on the self-adaptive capacity of multi-split heat pipe system (MSHPS) under non-uniform conditions in data center, *Appl. Therm Eng.* (160) (2019) 11–19.
- [5] Li Ling, et al., Simulation of a micro channel separate heat pipe (MCSHP) under low heat flux and low mass flux, *Appl. Therm. Eng.* 119 (5) (2017) 25–33.
- [6] Liping Zeng, Xing Liu, Quan Zhang, et al., Research on heat transfer performance of micro-channel backplane heat pipe air conditioning system in data center, *Appl. Sci.* (10) (2020) 583–598.
- [7] Sikai Zou, Quan Zhang, Li Ling, et al., Experimental investigation on the thermal performance of a water-cooled loop thermosyphon system under fan failure conditions, *Inter. J. Ref.* (2020) In Press.
- [8] Yanghua Cai, Zongtao Li, Jingmei Zhai, et al., Experimental investigation on a novel multi-branch heat pipe for multi-heat source electronics channel heat exchangers, *Int. J. Heat Mass Transf.* (104) (2017) 467–477.
- [9] Feihu Chen, Shuguang Liao, Simulation Research on heat pipe air conditioning system in data center based on thermodynamic simulation software, *Refriger. Energy* (2) (2016) 28–34 (In Chinese).
- [10] Tao Ding, et al., Experiment research on influence factors of the separated heat pipe system, especially the filling ratio and Freon types, *Appl. Therm. Eng.* 118 (25) (2017) 357–364.
- [11] Li Ling, Quan Zhang, Liping Zeng, Performance and energy efficiency analysis of data center cooling plant by using lake water source, in: 10th International Symposium on Heating, Ventilation and Air Conditioning, ISHVAC, 2017.
- [12] L. Cecchinato, M. Corradi, S. Minetto, Energy performance of supermarket refrigeration and air conditioning integrated systems working with natural refrigerants, *Appl Therm Eng* (48) (2012) 378–391.
- [13] Sung-Taek Jeon, Jin-Pyo. Cho, An experimental study on the performance of the separate type heat pipe in accordance with the refrigerant charge, *J. Korea Acad.-Industrial Cooper. Soc.* 16 (3) (2015) 1600–1604.
- [14] Hao Tian, Zhiguang He, Zhen Li, A combined cooling solution for high heat density data centers using multi-stage heat pipe loops, *Energy Build.* (94) (2015) 177–188.
- [15] Zongwei Han, Yanqing Zhang, Xin Meng, et al., Simulation study on the operating characteristics of the heat pipe for combined evaporative cooling of computer room air-conditioning system, *Energy* (98) (2016) 15–25.
- [16] Ali Habibi Khalaj, Saman K. Halgamuge, A Review on efficient thermal management of air-and liquid-cooled data centers: from chip to the cooling system, *Appl Energy* (205) (2017) 1165–1188.
- [17] Penglei Zhang, Baolong Wang, Wei Wu, et al., Heat recovery from Internet data centers for space heating based on an integrated air conditioner with thermosyphon, *Renew. Energ.* (80) (2015) 396–406.
- [18] Zhenying Wang, Xiaotong Zhang, Zhen Li, et al., Analysis on energy efficiency of an integrated heat pipe system in data centers, *Appl. Therm. Eng.* 90 (5) (2015) 937–944.
- [19] Chao Dang Li, Jia Qian, Yi Lu, Investigation on thermal design of a rack with the pulsating heat pipe for cooling CPUs, *Appl. Therm. Eng.* 110 (5) (2017) 390–398.
- [20] Shi Rongrong, Flow Boiling Heat Transfer in Microchannels, Nanjing University of Aeronautics and Astronautics, 2015 (In Chinese).
- [21] L.Y. Zhang, Y.Y. Liu, Experimental investigation and economic analysis of gravity heat pipe exchanger applied in communication base station, *Appl. Energ.* 194 (15) (2017) 499–507.
- [22] Lingen Chen, Fengrui Sun, Chih Wu, Optimal allocation of heat-exchanger area for refrigeration and air-conditioning plants, *Appl. Energ.* 77 (3) (2004) 339–354.
- [23] Marija S. Todorovica, Jeong Tai Kimb, Data centre's energy efficiency optimization and greening—case study methodology and R&D needs, *Energy Build.* (85) (2014) 564–578.
- [24] Mustafa AliErsöz, Abdullah Yıldız, Thermoeconomic analysis of thermosyphon heat pipes, *Renew Energy* (85) (2016) 880–889.
- [25] Li Ling, Quan Zhang, et al., Experimental investigation on the thermal performance of water cooled multi-split heat pipe system (MSHPS) for space cooling in modular data centers, *Appl. Therm. Eng.* 107 (25) (2016) 591–601.
- [26] Xingxing Zhang, Comparative study of a novel liquid-vapour separator incorporated gravitational loop heat pipe against the conventional gravitational straight and loop heat pipes – Part II: experimental testing and simulation model validation, *Energy Convers. Manage.* 93 (15) (2015) 228–238.

Numerical Investigation of Double Corrugated Steel Plate Shear Walls

Rakesh Kumar Panda, *Department of Civil Engineering, Aryan Institute of Engineering & Technology, Bhubaneswar, rakeshpanda116@gmail.com*

Jitendra Narayan Biswal, *Department of Mechanical Engineering, Aryan Institute of Engineering & Technology, Bhubaneswar, jnarayan679@gmail.com*

Sidhanta Behera, *Department of Civil Engineering, Raajdhani Engineering College, Bhubaneswar, sidhantabehera29@outlook.com*

Subhasis Sarkar, *Department of Mechanical Engineering, NM Institute of Engineering & Technology, Bhubaneswar, subhasissarkar14@yahoo.co.in*

Abstract: Corrugated steel plate shear walls have recently been demonstrated to be a reliable lateral force resisting method for building constructions. In comparison to flat plates, corrugated plates have better out-of-plane stiffness and improved buckling stability, resulting in improved hysteretic behaviour. However, due to cold-form process limitations, the thickness of the corrugated plates may be limited. The cyclic performance of double corrugated steel plate shear walls is investigated in this research. Parametric investigations were conducted on a one-story single-bay specimen that was constructed and simulated. On the cyclic performance of double corrugated steel plate shear walls, the parametric study looked at the orientation of corrugated plates (horizontal or vertical), disconnection of infill plates from columns, disconnection of infill plates from each other, infill plate thickness, and infill plate aspect ratio. The findings of this study suggest that proper selection of the aforementioned parameters can result in cyclic performance that is desirable. Finally, a suggestion is made for determining the initial stiffness and ultimate strength of double corrugated steel plate shear walls.
Keywords: Steel plate shear wall; Corrugated plate; Double infill plate; Cyclic behavior; Numerical simulation.

1. Introduction

Steel plate shear walls (SPSWs) have been widely used as a lateral force resisting system (LFRS) in building design and retrofit. SPSWs are classified into two types, stiffened and unstiffened. The stiffened types have higher stiffness and strength and energy dissipation. However, in the stiffened SPSWs the construction is significantly costly due to thin plates welding [1]. Unstiffened SPSWs have low buckling strength and allow shear buckling and development of diagonal tension field under lateral load. The post-buckling diagonal tension strips induce large axial and flexural demands on the frame. If the frame is capacity designed for expected yield strength of infill plates, as is required by AISC provisions [2], the required column sizes can be considerable. On the other hand, in retrofit situations large demands induced from the infill plates yielding would likely require significant reinforcement of the existing columns. For reducing column demand, researchers have proposed variety of methods such as perforating the infill plate to reduce SPSW stiffness and strength [3], using low yield point steel for infill plates [4] or utilizing light gauge plate for infill plates [5]. Berman and Bruneau [5] conducted tests on three light-gauge flat and corrugated SPSWs. The corrugated panel was placed diagonally with an inclination angle of 45 degrees to the horizontal line. The results showed that corrugated specimen experienced rapid loss in strength and infill plate fractures occurred at the location of repeated local buckling.

Thin flat SPSWs experience severe pinching in their hysteresis loops due to diagonal tension field effects. To enhance the buckling load and hysteresis behavior of flat SPSWs, corrugated SPSWs were also proposed by Emami et al. [6]. They carried out laboratory tests to compare the cyclic performance of corrugated steel plate shear walls (CSPSWs) and a flat steel plate shear wall (FSPSW). The corrugated plates were laid both horizontal and vertical. It was revealed that CSPSWs show significantly less pinching in their hysteresis loops than the FSPSW due to higher out of plane stiffness and buckling strength of corrugated plates with respect to flat plates. Emami and Mofid [7] conducted numerical study on CSPSWs and confirmed the effectiveness of corrugated plates in enhancing SPSWs behavior. Farzampour et al. [8] in a numerical study compared monotonic behavior of SPSW and CSPSW with openings. Bahrebar et al. [9] performed numerical study on the cyclic behavior of the CSPSW with a square opening. Cao and Huang [10] carried out experimental and numerical study on two CSPSWs and showed that by properly designing the geometry of corrugated infill plates, the CSPSWs could avoid elastic buckling. Tong et al. [11] investigated the elastic buckling of double corrugated plate shear wall theoretically and numerically via finite element analysis. Dou et al. [12] studied the elastic shear buckling of infill panels in sinusoidally CSPSWs. Farzampour et al. [13] proposed design procedures for CSPSWs with reduced beam section. Bahrebar et al. [14] investigated the cyclic performance of perforated steel plate shear wall with curved corrugated webs. Fang et al. [15] carried out experimental study on the hysteretic behavior of semi-rigid frame with a

corrugated plate. Bahrebar et al. [16] studied the response of low yield point steel plate shear wall with curved corrugated web plates and reduced beam sections.

The growth of SPSW structures in high-rise construction worldwide requires larger range of thicknesses for infill panels. However, the available thickness for single corrugated plates may be limited due to cold-forming process restrictions. A double corrugated SPSWs (DCSPSW) consists of two similar corrugated steel plates placed symmetrically and bolted together at contact points with uniform spacing (Figure 1). In this study, the cyclic performance of DCSPSWs is evaluated. To this end, a one-story single-bay specimen was modelled and analysed using nonlinear material and geometry options available in ABAQUS [17] software package. A parametric study was performed on the model by varying its geometry and corrugated plate properties. The parametric study considered the orientation of corrugated plates (horizontal or vertical), the effect of disconnecting the plates from the columns, the effect of disconnecting the plates from each other, corrugated plate thickness and aspect ratio. In the end, recommendations for calculating the initial stiffness and ultimate strength of DCSPSWs are given.

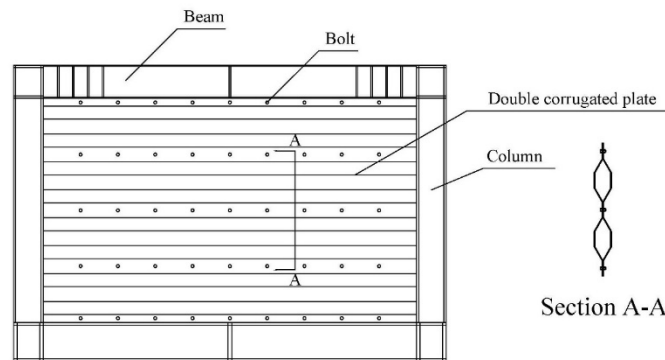


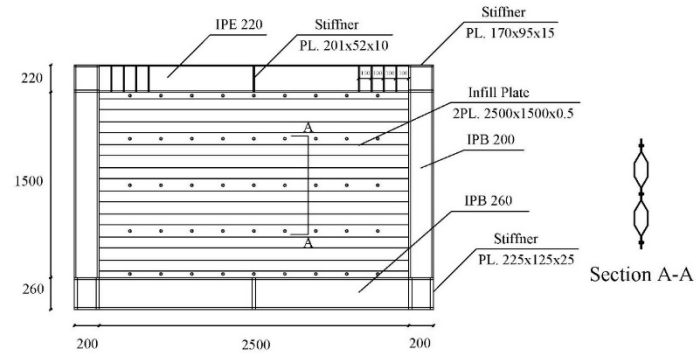
Figure 1. Double corrugated steel plate shear wall (DCSPSW)

2. Finite element modeling

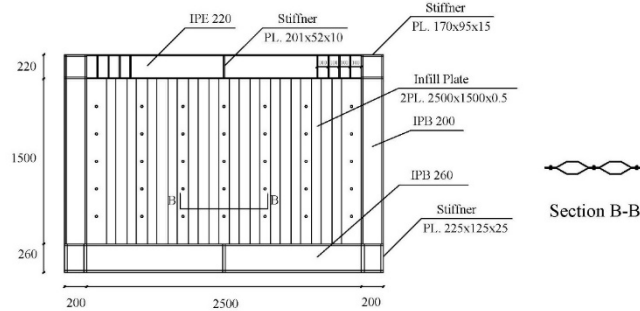
One-story single-bay specimen with moment-resisting beam to column connections was preliminary designed according to the procedures specified in reference [1]. Specimens' dimensions and component sizes are illustrated in Figure 2. In horizontal and vertical DCSPSW specimens, corrugation fold lines are parallel to the beams and columns, respectively. The height and length of specimens are measured as 1.74 m and 2.7 m, center to center of members, respectively. The model represents half-scale conventional residential building framing.

The models were developed in the finite element package ABAQUS [17]. Both material and geometrical nonlinearities were considered in the models. The fish plates connecting the infill panel to the beams and columns, were not modelled in the finite element simulation. This approximation seems to have negligible effects on the analysis results [18]. Boundary frame components, i.e. beams, columns and stiffeners and double corrugated infill panels were modelled using S4R element, a four-node doubly curved shell element. This element has six degree of freedom per node with reduced integration and finite membrane strain. Mesh size for boundary frame members is 50 mm and for infill plate is 25 mm. Since the beam-to-column connections are rigid, shell elements at intersecting parts were directly connected. Bolts were not simulated directly. However, to model the effect of bolts, infill plates at the contact surfaces are directly connected (Figure 3). The double infill plates are connected to the boundary elements using "Tie" constraint command. The material for infill plate and boundary frame components were ST12 and ST37 steels according to DIN standard [19], respectively. Mechanical properties of ST12 and ST37 steel were adopted from coupon tests done by Hosseinzadeh et al. [20] and Jahanpour et al. [21], respectively and are shown in Table 1. In order to get cyclic deteriorations in the steel material strength and stiffness, "ductile damage" using stress triaxiality dependent fracture initiation criterion and fracture evolution law in the form of strain softening was accommodated in material modelling [22].

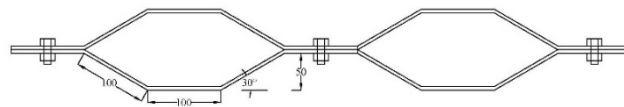
To prevent the out-of-plane displacement of the specimen, as provided by lateral supports in typical test setups, the nodes at the perimeter of the top beam–column connections panel and at the center of the top beam were restrained from translation in out-of-plane direction. The bottom flange of the bottom beam was fixed in the model similar to the boundary conditions of Emami et al. [6]. Typical finite element models for both horizontal and vertical DCSPSW specimens are shown in Figure 4. It was reported that in single corrugated SPSWs initial imperfection has no meaningful effect on the finite element results [7]. However, in this study, initial imperfection as out of plane deformation of 1 mm according to model eigenvalue buckling analysis was applied to the model. This was achieved by using "imperfection" command to modify the nodes coordinates.



(a) Horizontal DCSPSW



(b) Vertical DCSPSW



(c) Geometry of corrugated plates

Figure 2. DCSPSW specimens dimensions and member sizes (mm)

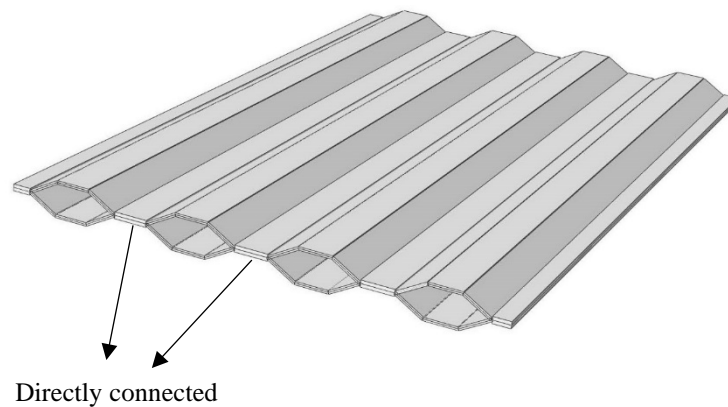
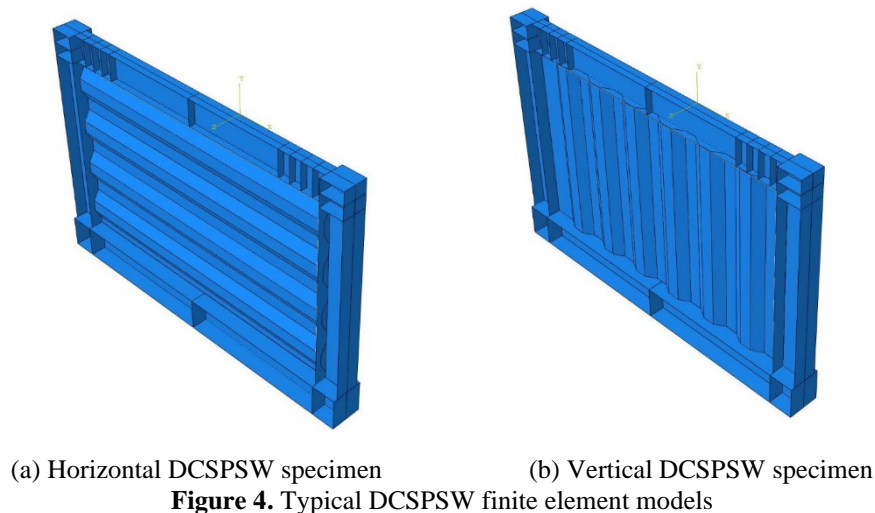


Figure 3. Finite element model of DCSPSW infill plates

Table 1. Material properties used in models

Element	Young's modulus E (GPa)	Yield stress F_y (MPa)	Ultimate stress F_u (MPa)
Plate (ST12)	200	262	360
Frame (ST37)	202	280	390



As is practical in typical SPSW experiments [6,23], the effect of vertical load was neglected. The models were loaded horizontally at the top beam level using displacement control procedure according to the history shown in Figure 5. The loading protocol was created with combining the ATC-24 [24] and the AISC [2] requirements for cyclic loading as used in previous studies [23,25]. To develop the loading cycle amplitudes, specimen yield parameters are required. To this end, pushover analysis was carried out on the finite element model and yield displacement and force values were estimated.

Two displacement amplitudes of one third and two third of the estimated yield displacement were selected for elastic cycles. As yield drift was estimated to be 0.3%, these amplitudes correspond to a drift of 0.1 and 0.2%, respectively. ATC-24 [24] recommends that number of cycles with peak displacement less than yield displacement should be at least six. Thus, three cycles at each of these drift amplitudes were performed. Three cycles were performed at the estimated yield displacement according to ATC 24 [24] loading protocol. After that, peak displacements were increased by a ductility increment of one until achieving a ductility of three. Three cycles at each amplitude were applied. After this step, the number of cycles at each peak displacement was reduced from three to two. Peak displacements were increased by a ductility increment of one until reaching an estimated ductility of seven. Estimated ductility of seven coincided with 2.0% drift. After this point, peak displacements were increased by drift increments of 0.5% until reaching drift of 4.0%, and increments of 1.0% until reaching drift of 6.0%. Figure 5 shows the resulting loading history.

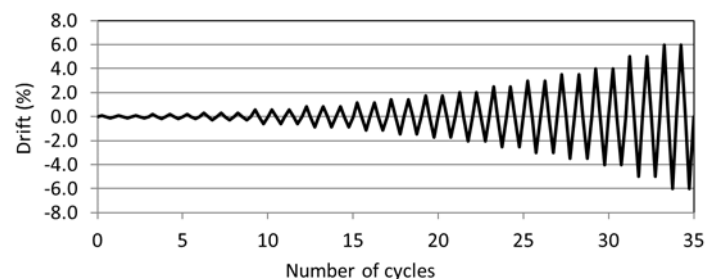


Figure 5. Cyclic loading protocol

3. Validation

In order to verify the accuracy of the finite element model, two sets of well-established experimental tests were considered for calibration. The first set is a flat SPSW tested by Vian et al. [25], and the other set is flat and single horizontal/vertical corrugated SPSWs tested by Emami et al. [6]. Hysteresis curves as well as model overall behaviour and failure modes under cyclic loading have been compared with those obtained from the experiments. Hysteresis curve of flat SPSW tested by Vian et al. and numerical results are shown in Figure 6. The experimental and numerical results of models tested by Emami et al. are illustrated in Figure 7 and tabulated in Table 2. Good agreement between the numerical and test results indicates the validity of the finite element modeling and its assumptions.

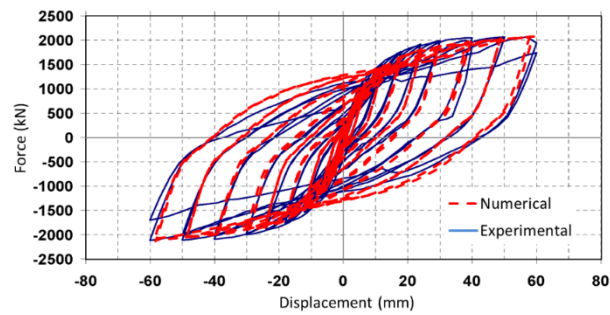


Figure 6. Comparison of experimental and analytical hysteresis curve for SPSW tested by Vian et al. [25]

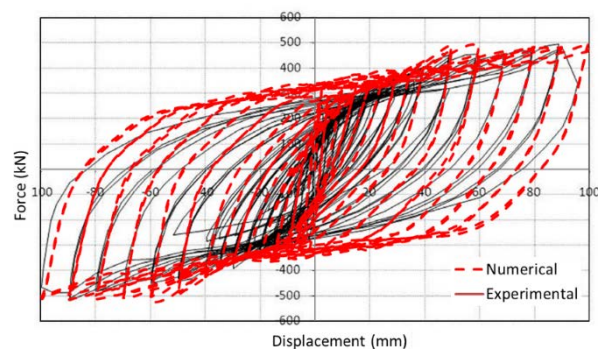
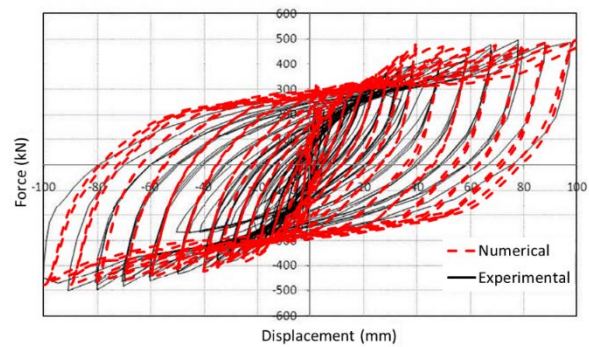
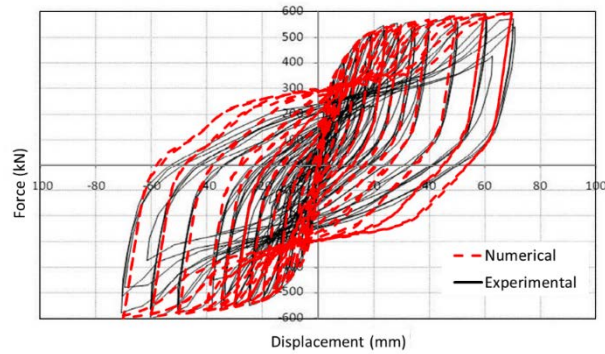


Figure 7. Comparison of experimental and analytical hysteresis curve for SPSWs tested by Emami et al. [6]

Table 2. Comparison of experimental and analytical results for initial stiffness and ultimate strength

	Initial stiffness (MN/m)			Ultimate strength (kN)		
	Experimental	Numerical	Exp/Num	Experimental	Numerical	Exp/Num
F-SPSW	108	110.8	0.98	597	599.6	1.00
H-CSPSW	130	133.1	0.98	502	492.7	1.02
V-CSPSW	125	131.3	0.95	498	524.5	0.95

4. Parametric study

To study the performance of doubly corrugated SPSWs, parametric studies were carried out on specimens whose details are illustrated in Figure 2. Parametric study includes the effect of corrugated plates orientation (horizontal or vertical), whether corrugated plates are connected to the columns or not, whether corrugated plates are connected together or not, corrugated plate thickness (t) and DCSPSW aspect ratio (Ar). The four different light gauge plate thicknesses and four different aspect ratios (length divided by height of the plate) considered are indicated in Table 3.

Table 3. DCSPSW parameters variation

Corrugated plates orientation	Infill plate to columns connection	Corrugated plate to plate connection	corrugated plate thickness, t (mm)	DCSPSW aspect ratio, Ar
H (horizontal) & V (vertical)	Yes, No	Yes, No	0.5, 0.6, 0.7, 0.8	1, 1.67, 2.33, 3

4.1 Effect of corrugated plate orientation

Figure 8 presents the hysteresis curves for horizontal and vertical DCSPSWs and bare frame. Thickness of infill plate is 0.5 mm and aspect ratio is 1.67 and infill plates are connected to each other and fully restrained by beams and columns. According to ATC recommendation [26] ultimate displacement capacity of specimens should be limited to deformation associated with 80% of the ultimate strength on the descending branch of the modified backbone curve. Here, 20 % strength loss occurs at the drift of 3%. So hysteresis curves are reported up to 3% drift. The initial stiffness, ultimate strength and energy dissipation capacity of specimens are tabulated in Table 4. It is clear that DCSPSWs have much better performance in comparison to bare frame due to contributions of infill plates. Also note that, the horizontal and vertical DCSPSWs have comparable stiffness, strength, and energy dissipation capacity.

Figure 9 illustrates the maximum in-plane principal stress contour in horizontal and vertical DCSPSWs at 3% drift. In DCSPSWs like single corrugated SPSWs, diagonal tension strips develop to resist lateral load. In addition, like single corrugated SPSWs the inclination angle of the tension field measured relative to the horizontal axis in horizontal DCSPSW specimen is less than that of vertical DCSPSW. Thus in H-DCSPSW, the columns and beams at the boundary play a role in forming tension field strips. On the contrary, in V-DCSPSW, as inclination angle of the tension strips is higher, development of diagonal tension field strips relies mostly on beams and less on columns.

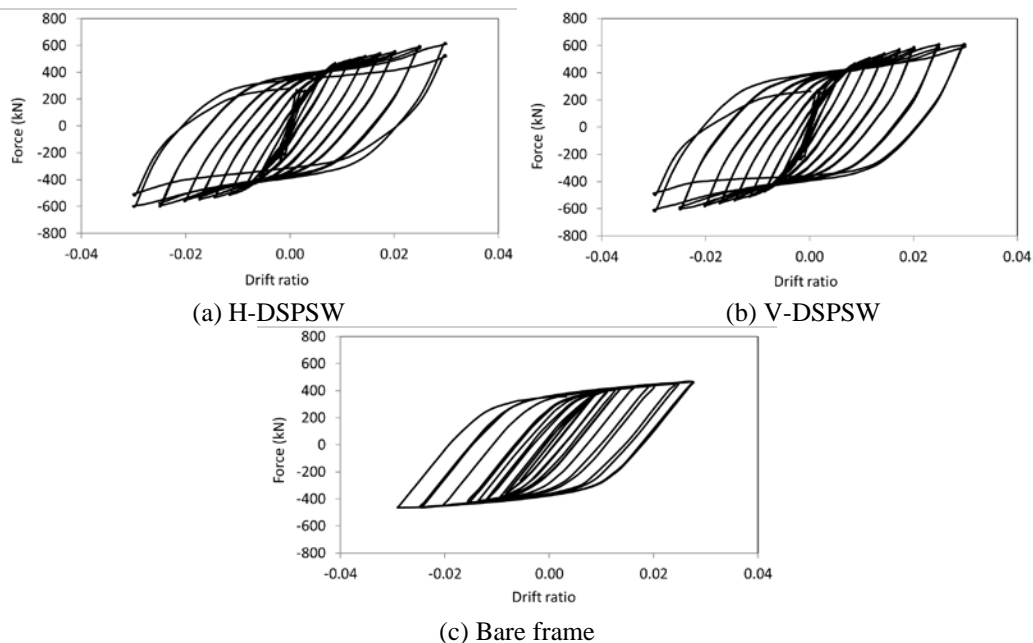


Figure 8. Hysteresis curves of DCSPSWs with different configurations and bare frame

Table 4. Performance parameters of specimens

Parameter	H-DCSPSW	V-DCSPSW	Bare Frame
Initial stiffness (MN/m)	145.6	145.3	27.7
Ultimate strength (kN)	619.9	620.7	465.3
Energy dissipation (kN-m)	379.2	395.8	288.4

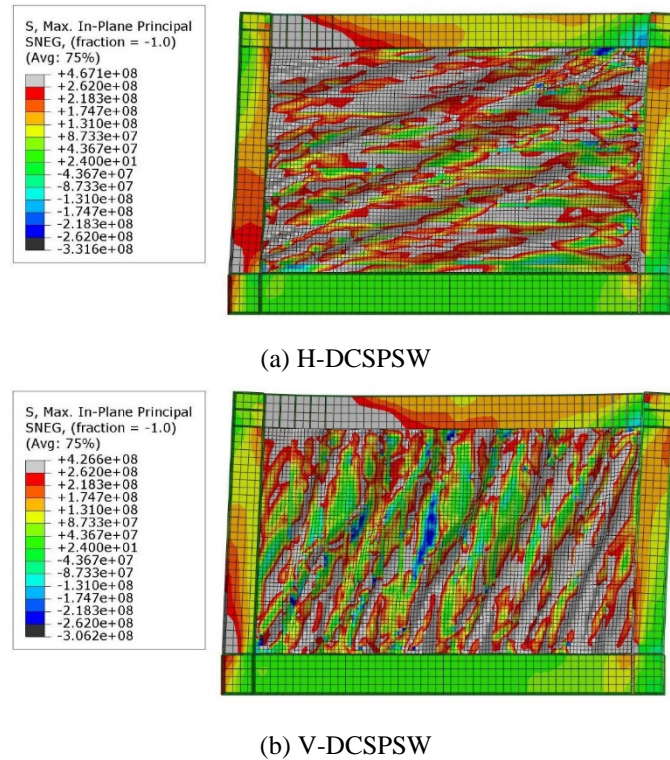


Figure 9. Maximum in-plane principal stress contours in DCSPSW (N/m²)

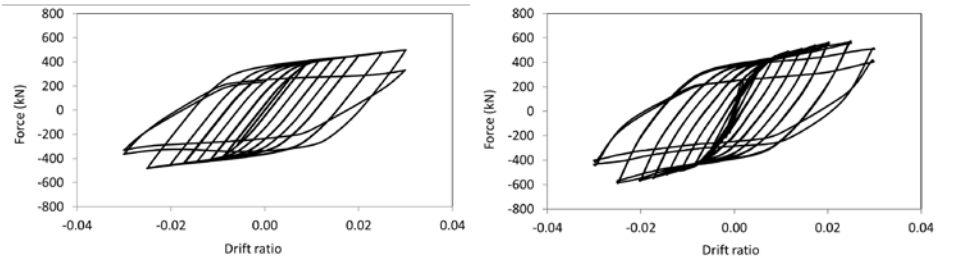
4.2 Effect of infill plate to column connections

The diagonal tension strips impose high axial and flexural demands on the columns which may lead to premature failure of columns. For reducing column demands in SPSWs, several methods have been suggested by researchers including releasing the infill plate from columns and connecting it only to the beams [27,28]. In addition, connecting the corrugated infill plate specially the light gauge one to the surrounding frame members proved to be difficult due to thickness and geometry of the plate [5]. This could considerably increase the construction time. In beam-only-connected SPSWs, infill panel is only connected to the frame beams and connections between infill panel and columns are omitted.

The effects of infill plate connections to columns on the hysteretic performance of DCSPSW are investigated in this section. To make beam-only-connected DCSPSW in ABAQUS, it is just enough to remove the tie constraints between the columns and corrugated plates. The performances of DCSPSWs with both horizontal and vertical corrugation orientation with $t=0.5$ mm and $A_r=1.67$ were evaluated. Infill plates were connected to each other. The hysteresis curves of beam-only-connected horizontal and vertical DCSPSWs are illustrated in Figure 10. The initial stiffness, ultimate strength and energy dissipation capacity of these specimens are presented in Table 5. By comparing Table 4 and Table 5, it can be seen that detaching columns from the infill plates reduces column demands at the expense of reduction in initial stiffness, ultimate strength and energy dissipation of DCSPSWs. In the case of horizontal DCSPSW, releasing columns from the infill plates decreased the initial stiffness from 145.6 MN/m in the fully connected specimen to 28.3 MN/m, showing 81% reduction. It reduced the ultimate strength and energy dissipation from 619.9 to 497.0 kN and 379.2 to 308.5 kN-m showing 20% and 19% reductions, respectively. However, in the case of vertical DCSPSW releasing columns from the infill plates decreased the initial stiffness from 145.3 MN/m in the fully connected specimen to 113.3 MN/m showing only 22% reduction. It reduced the ultimate strength and energy dissipation from 620.7 to 587.5 kN and 395.8 to 356.6 kN-m showing 5% and 10% reductions, respectively. It can be seen that the decrease in responses in beam-only-connected vertical DCSPSW is less than the decrease in responses in beam-only-connected horizontal DCSPSW and thus, the former has a better performance.

Figure 11 illustrates the maximum in-plane principal stress contour in beam-only-connected H-DCSPSW and V-DCSPSW at 3% drift. In the previous section, it was shown that in H-DCSPSW, columns and beams play a role in forming diagonal tension field strips. Thus, by comparing Figure 9 (a) with Figure 11 (a) it can be seen that releasing columns from the infill plates in H-DCSPSW eliminates vertical boundary condition and thus eliminates most of the active tension field strips and just one strip from bottom left corner to upper right corner remains in beam-only-connected H-DCSPSW. Eliminating tension field strips corresponds to a decrease in infill plates' contributions and causes substantial decrease in initial stiffness, ultimate strength and energy dissipation. On the

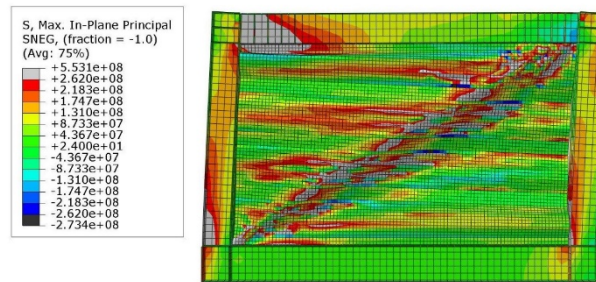
contrary, in V-DCSPSW, formation of tension field strips relies more on horizontal boundary conditions than vertical boundary conditions. Comparing Figure 9 (b) with Figure 11 (b) shows that releasing columns from the infill plates in V-DCSPSW eliminates just a few tension field strips and major part of infill plates' contributions remain. Therefore, beam-only-connected V-DCSPSW experiences less reduction in initial stiffness, ultimate strength and energy dissipation in comparison with beam-only-connected H-DCSPSW.



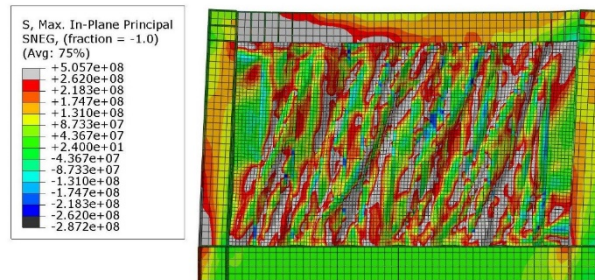
(a) Beam-only-connected H-DCSPSW (b) Beam-only-connected V-DCSPSW
Figure 10. Hysteresis curves of DCSPSWs with beam-only-connected infill plates

Table 5. Performance parameters for beam only connected specimens

Parameter	H-DCSPSW	V-DCSPSW
Initial stiffness (MN/m)	28.3	113.3
Ultimate strength (kN)	497.0	587.5
Energy dissipation (kN-m)	308.5	356.6



(a) Beam-only-connected H-DCSPSW



(b) Beam-only-connected V-DCSPSW

Figure 11. Maximum in-plane principal stress contours in beam only connected DCSPSW (N/m²)

4.3 Effect of plate to plate connections in DCSPSWs

Figure 12 presents the hysteresis curves for horizontal and vertical DCSPSWs when the infill plates are detached from each other. In other words, bolts are omitted and corrugated plates are placed simply alongside each other with no connections. Thickness of infill plates is 0.5 mm and aspect ratio is 1.67 and infill plates are connected fully to the beams and columns. The initial stiffness, ultimate strength and energy dissipation capacity of DCSPSWs with separate infill plates are presented in Table 6. It can be seen that horizontal and vertical DCSPSWs with separate infill plates have relatively similar cyclic performance. In addition, comparing Table 4 and Table 6 reveals the effect of plate to plate connections on the response of DCSPSWs. In the case of H-DCSPSW, detaching plates from each other decreased the initial stiffness, ultimate strength and energy dissipation from 145.6 MN/m, 619.9 kN and 379.2 kN-m to 144.9 MN/m, 606.9 kN and 371.3 kN-m showing 0.5%, 2% and 2% reductions,

respectively. In the case of V-DCSPSW detaching plates from each other decreased the initial stiffness, ultimate strength and energy dissipation from 145.3 MN/m, 620.7 kN and 395.8 kN-m to 142.3 MN/m, 610.4 kN and 363.9 kN-m showing 2%, 2% and 8% reductions, respectively.

It can be seen that detaching plates from each other reduces the responses in DCSPSWs. This reduction is attributed to the fact that when DCSPSW infill plates are not connected to each other the out of plane stiffness of the section decreases and this causes a lower performance. However, this reduction is relatively small and DCSPSWs with detached infill plates have acceptable cyclic performance.

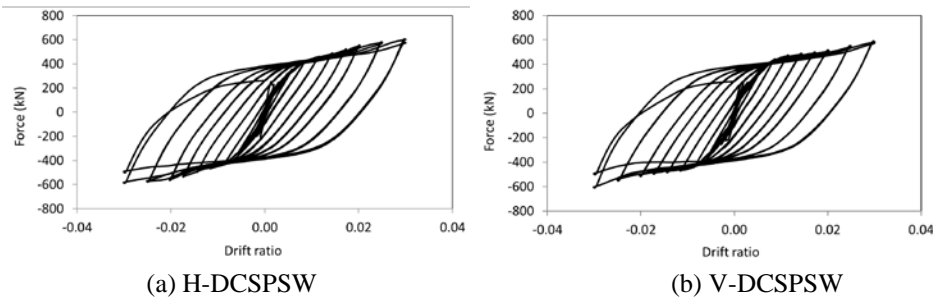


Figure 12. Hysteresis curves of DCSPSWs with detached infill plates

Table 6. Performance parameters for DCSPSWs with detached infill plates		
Parameter	HDSPSW	VDSPSW
Initial stiffness (MN/m)	144.9	142.3
Ultimate strength (kN)	606.9	610.4
Energy dissipation (kN-m)	371.3	363.9

4.4 Effect of thickness

The effects of infill plate thickness on the cyclic behavior of DCSPSWs are investigated in this section. Performances of DCSPSWs with both horizontal and vertical orientations with $t = 0.5, 0.6, 0.7$, and 0.8 mm were evaluated. Infill plates are connected fully to the beams and columns and also are connected to each other. Aspect ratio is 1.67. The cyclic behavior of horizontal and vertical DCSPSWs are illustrated in Figures 13 and 14, respectively. From these figures it can be seen that for both horizontal and vertical DCSPSWs increasing the infill plate thickness improves the cyclic behavior. However, it should be noted that this increase can also lead to larger demands on boundary frame members and this must be considered in the design.

The response of H-DCSPSW and V-DCSPSW as a function of infill plate thickness is given in Figures 15 (a) through (c). Initial stiffness, ultimate strength and energy dissipation increase proportionally with infill plate thickness for both. For H-DCSPSW increasing the infill plate thickness from 0.5 mm to 0.8 mm result in 43%, 11% and 12% increase in the initial stiffness, ultimate strength and energy dissipation, respectively.

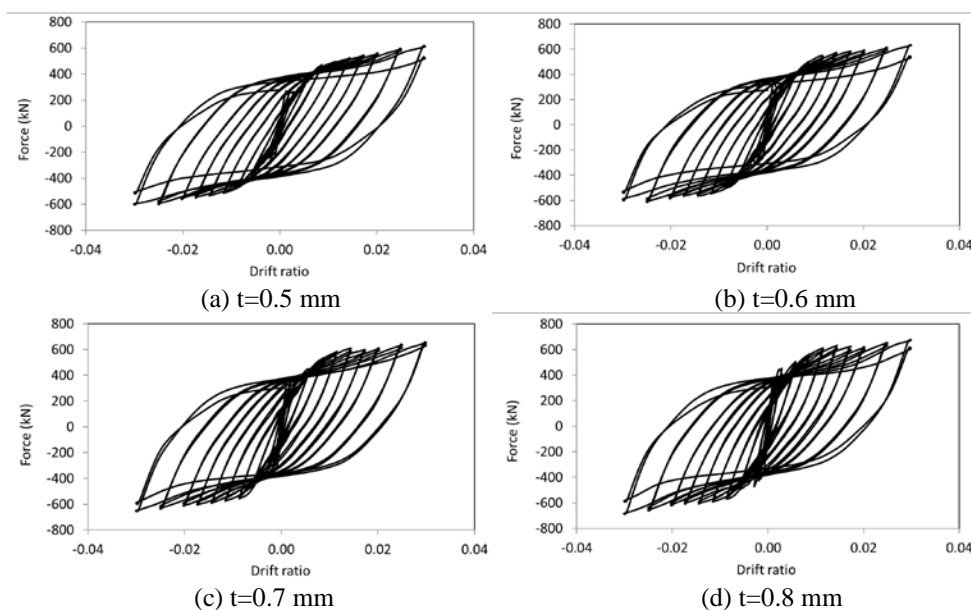


Figure 13. Hysteresis curves of horizontal DCSPSW with different plate thicknesses

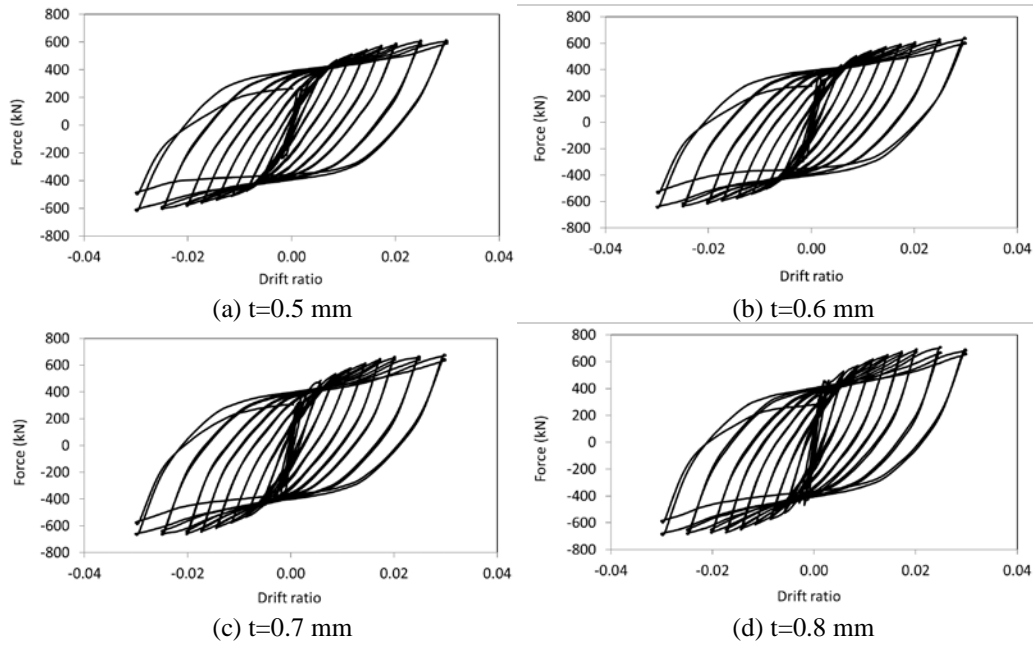


Figure 14. Hysteresis curves of vertical DCSPSW with different plate thicknesses

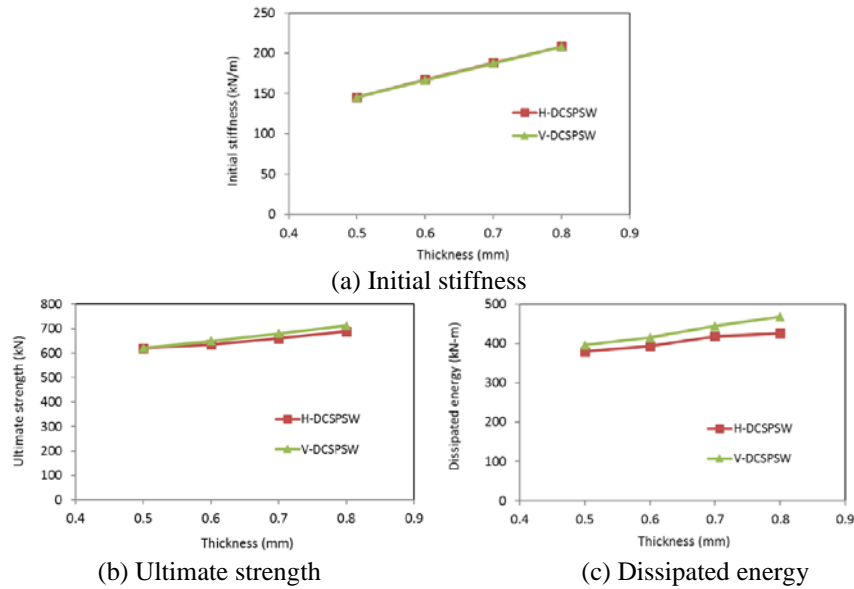


Figure 15. The response of H-DCSPSW and V-DCSPSW as a function of infill plate thickness

4.5 Effect of panel aspect ratio

The effects of panel aspect ratio (A_r) on the cyclic performance of DCSPSWs are investigated in this section. To study the different panel aspect ratios, the panel height was kept constant and equal to 1500 mm and length of the panel was varied. Panel aspect ratios are summarized in Table 7 and illustrated in Figure 16. The hysteresis curves of the horizontal DCSPSWs with $t=0.5$ mm are shown in Figure 17. Infill plates are connected fully to the beams and columns and are connected to each other. From Figure 17, it is found that increasing the panel aspect ratio from 1.00 to 3.00 can be effective in enhancing the cyclic performance of the DCSPSWs. In fact, increasing of the panel aspect ratio increases the number of tension field strips forming in the panel and this results in greater initial stiffness, ultimate strength and dissipated energy.

Table 7. Panel aspect ratios

H, Height of panel (mm)	1500	1500	1500	1500
L, Length of panel (mm)	1500	2500	3500	4500
A_r , panel aspect ratio	1.00	1.67	2.33	3.00

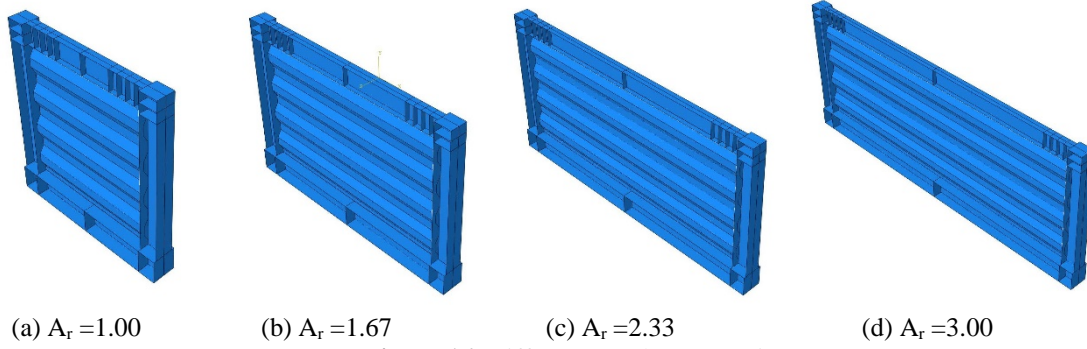


Figure 16. Different panel aspect ratios

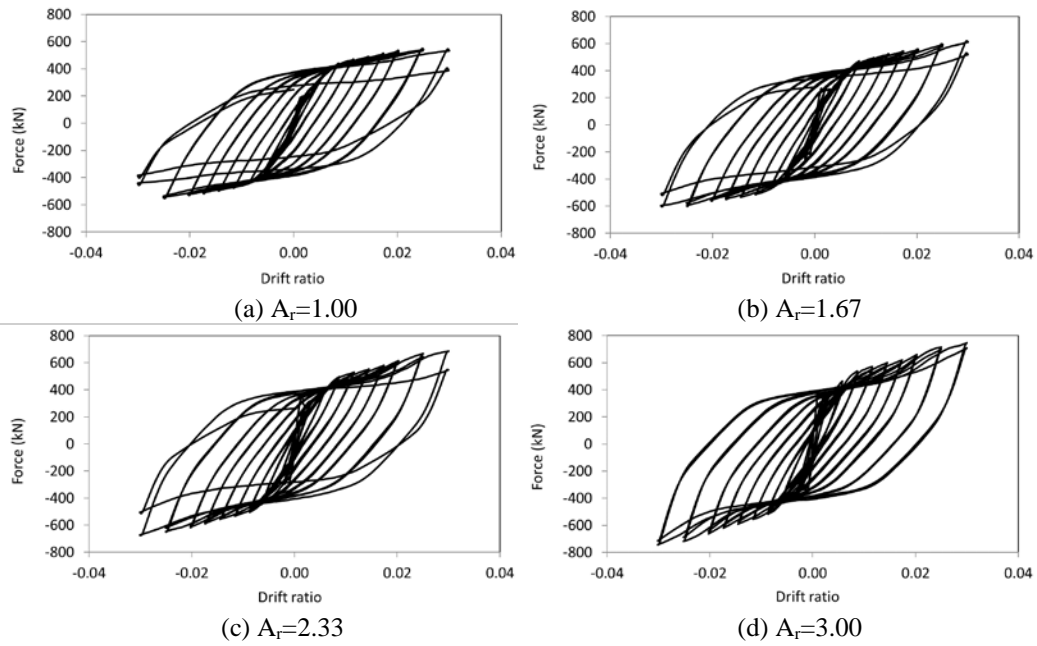


Figure 17. Hysteresis curves for beam-only-connected horizontal DCSPSW with varying panel aspect ratios

The responses of horizontal DCSPSWs as a function of panel aspect ratio are tabulated in Table 8. It can be seen that, initial stiffness, ultimate strength and energy dissipation increase with infill panel aspect ratio. Increasing the panel aspect ratio from 1.0 to 3.0 increase the initial stiffness, ultimate strength and energy dissipation from 100.2 MN/m, 553.7 kN and 357.3 kN-m to 235.3 MN/m, 753.6 kN and 412.4 kN-m showing 135%, 36% and 15% increase, respectively. So it is better to use DCSPSWs in wider bays of a building.

Table 8. Performance parameters of horizontal DCSPSWs as a function of panel aspect ratio

Ar	Initial stiffness (MN/m)	Ultimate strength (kN)	Energy dissipation (kN-m)
1.00	100.2	553.7	357.3
1.67	145.6	619.9	379.2
2.33	190.5	687.1	390.4
3.00	235.3	753.6	412.4

5. Initial stiffness and ultimate strength of DCSPSWs

Ultimate shear strength of DCSPSWs can be estimated via Equation (1):

$$F_{su} = F_{fu} + F_{pt} \quad (1)$$

where F_{su} is the ultimate shear strength of the steel plate shear wall, F_{fu} is strength of bare frame and F_{pt} is strength of plate. F_{fu} is given by Equation (2):

$$F_{fu} = 4M_p/h_s \quad (2)$$

where M_p is the smallest of the plastic moment capacity of the beam and columns and h_s is height of the specimen. F_{pt} is given by Equation (3) [13]:

$$F_{pt} = Lt(\tau_{cr.in}^e + 0.5\sigma_{ty} \sin 2\theta) \quad (3)$$

in which L and t are length and thickness of the infill plate, respectively. $\tau_{cr.in}^e$ is the plate interactive shear buckling stress and σ_{ty} is the yield stress of tension field calculated via Von-Mises criterion. $\tau_{cr.in}^e$ is obtained as follows [13,29]:

$$\left(\frac{1}{\tau_{cr.in}^e}\right)^2 = \left(\frac{1}{\tau_{cr.L}^e}\right)^2 + \left(\frac{1}{\tau_{cr.G}^e}\right)^2 + \left(\frac{1}{\tau_y}\right)^2 \quad (4)$$

in which τ_y is yielding shear stress, $\tau_{cr.L}^e$ and $\tau_{cr.G}^e$ are local and global shear buckling stresses which can be calculated from Equations (5) and (6):

$$\tau_{cr.L}^e = \left[5.34 + 4\left(\frac{a}{h}\right)^2\right] \frac{\pi^2 E}{12(1-\vartheta^2)} \left(\frac{t}{a}\right)^2 \quad (5)$$

$$\tau_{cr.G}^e = \frac{36\varphi E}{[12(1-\vartheta^2)]^{0.25}} \left[\left(\frac{d}{t}\right)^2 + 1\right]^{0.75} \left(\frac{t}{h}\right)^2 \quad (6)$$

E is Young's modulus of elasticity and ϑ is Poisson ratio; h is panel height; φ is boundary condition factor varying from 1.0 to 1.9 and assumed to be 1.0 due to simple support condition [13]. γ is a factor which accounts for corrugation geometry and obtained using Equation (7):

$$\gamma = \frac{a+b}{a+c} \quad (7)$$

a , b , c and d are parameters of corrugated panel geometry which are illustrated in Figure 18. σ_{ty} is the yield tension field stress calculated using Equation (8) [13]:

$$\sigma_{ty}^2 + (3\tau_{cr.in}^e \sin 2\theta)\sigma_{ty} + (3\tau_{cr.in}^e{}^2 - \sigma_y^2) = 0 \quad (8)$$

where θ is tension field inclination angle measured relative to the horizontal axis and assumed to be 30 and 60 degree for horizontal and vertical specimens [6]. σ_y is yield stress of steel plate.

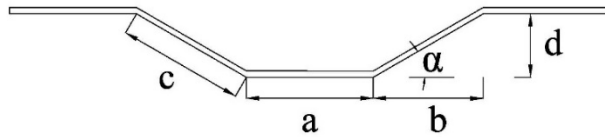


Figure 18. Parameters of corrugated panel geometry

To estimate the equivalent thickness of DCSPSWs, a single panel corrugated SPSW with the same infill plate shape and twice the thickness was modeled and their initial stiffness and ultimate strength were calculated (Figure 19). The boundary elements (beams and columns) were kept the same. Initial stiffness and ultimate strength of DCSPSW with each plate thickness of t were compared with those of single corrugated SPSW with infill plate thickness of $2t$. Thus, initial stiffness ratio was defined as the ratio of initial stiffness of double panel SPSW with each plate thickness of t with respect to that of single panel SPSW with infill plate thickness of $2t$. Ultimate strength ratio was defined in a similar way.

Figure 20 presents the initial stiffness and ultimate strength ratio as a function of t for both horizontal and vertical corrugated SPSWs. Panel aspect ratio is 1.67. It can be seen that the initial stiffness ratio is a bit larger than one for considered thicknesses showing that initial stiffness of double corrugated SPSW is a bit larger than initial stiffness of single corrugated SPSW with infill plate thickness of $2t$. This can be attributed to the fact that

double corrugated SPSW has larger out of plane stiffness in comparison to single corrugated SPSW with thickness of $2t$. Ultimate strength ratio is approximately equal to one which means that ultimate strength of double panel SPSW is approximately equal to ultimate strength of single panel SPSW with infill plate thickness of $2t$.

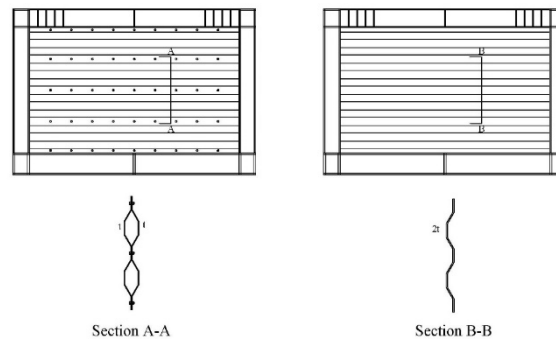


Figure 19. Comparison of double corrugated SPSW with plate thicknesses of t with single corrugated SPSW with infill plate thickness of $2t$

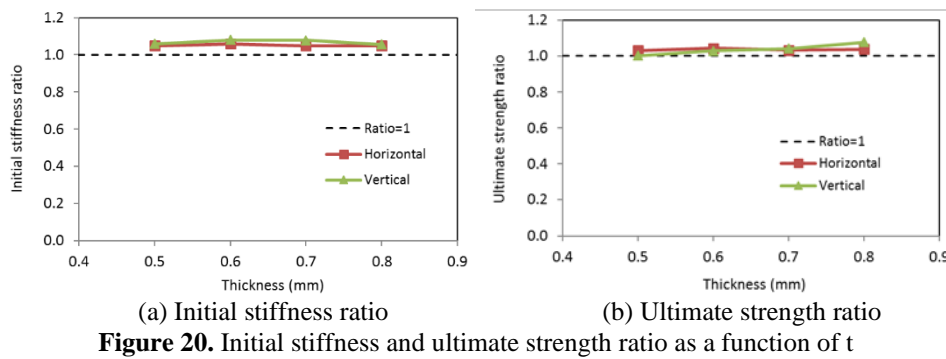


Figure 20. Initial stiffness and ultimate strength ratio as a function of t

Initial stiffness and ultimate strength ratio as a function of panel aspect ratio (A_r) for horizontal corrugated SPSWs are tabulated in Table 9. Each infill plate thickness in double panel SPSWs is 0.5 mm and infill plate thickness in single panel SPSWs is 1.0 mm. It can be seen that the initial stiffness and ultimate strength of DCSPSW is greater than those of single corrugated SPSW. However, the difference is less than 6% and 3% for initial stiffness and ultimate strength ratio, respectively. Thus, it can be concluded that for different thicknesses and aspect ratios using an equivalent thickness of $2t$ in Equations (3) to (8) for DCSPSW is valid and conservative.

To elaborate, ultimate shear strength of horizontal and vertical DCSPSWs with each infill plate thickness of 0.5 mm and panel aspect ratio of 1.67 were estimated through analytical method using Equations (1) to (8) and compared with finite element (FE) results (Table 10). Equivalent thickness of the infill plate was assumed to be 1.0 mm. Table 10 indicates that analytical equations can predict the ultimate strength of DCSPSWs with less than 4% error.

Table 9. Initial stiffness and ultimate strength ratio as a function of panel aspect ratio

A_r	DCSPSW (each infill plate thickness = t)		Single corrugated SPSW (infill plate thickness = $2t$)		ratios	
	Initial stiffness (MN/m)	Ultimate strength (kN)	Initial stiffness (MN/m)	Ultimate strength (kN)	Initial stiffness ratio	Ultimate strength ratio
1.00	100.2	553.7	95.4	537.6	1.05	1.03
1.67	145.6	619.9	137.4	601.9	1.06	1.03
2.33	190.5	687.1	181.4	673.6	1.05	1.02
3.00	235.3	753.6	224.1	731.7	1.05	1.03

Table 10. Comparison of ultimate strength calculated with analytical method and FE analysis

Specimen	Strength by analytical method (kN)	Strength by FE analysis (kN)	Error (%)
Horizontal	642.2	619.9	3.5
Vertical	642.2	620.7	3.4

6. Conclusions

Cyclic performance of double corrugated steel plate shear walls (DCSPSWs) was investigated in this study. Several finite element models were developed and analysed for parametric studies. Infill plate orientation, connection of infill plate to columns, connection of infill plates together, infill plate thickness and panel aspect ratio were considered as the main parameters in this performance evaluation. Responses of interest are force-deformation relationship, initial stiffness, ultimate strength and energy dissipation capacity. The following conclusions can be drawn based on this study:

- 1) Horizontal and vertical DCSPSWs fully restrained by beams and columns, have comparable stiffness, strength and energy dissipation capacity.
- 2) Releasing columns from infill plates reduces column demands at the expense of reduction in seismic responses of DCSPSWs. However, decrease in responses of beam-only-connected V-DCSPSWs is meaningfully less than the decrease in responses of beam-only-connected H-DCSPSWs and thus beam-only-connected V-DCSPSWs have a better performance.
- 3) Detaching corrugated plates from each other in DCSPSWs cause negligible reduction in responses in comparison with bolted plates. In other words, DCSPSWs with detached infill plates have acceptable cyclic performance.
- 4) By increasing the corrugated plate thickness, initial stiffness, ultimate strength and energy dissipation increase proportionally for both H-DCSPSW and V-DCSPSW.
- 5) Increasing panel aspect ratio can be effective in enhancing the cyclic performance of the DCSPSWs. In other words, it is better to use DCSPSWs in wider bays of a building.
- 6) The initial stiffness and ultimate strength of DCSPSWs can be estimated by using an equivalent thickness of $2t$ in the given equations.
- 7) Analytical equations can predict the ultimate strength of DCSPSWs with less than 4% error.

7. References

- [1] Sabelli R, Bruneau M. Design guide 20: steel plate shear walls. AISC, Chicago, IL. 2007.
- [2] AISC. Seismic provisions for structural steel buildings. American Institute of Steel Construction. ANSI/AISC 341-16, Chicago, IL. 2016.
- [3] Purba R, Bruneau M. Finite-element investigation and design recommendations for perforated steel plate shear walls. *Journal of Structural Engineering*. 2009;135(11):1367-1376.
- [4] Zirakian T, Zhang J. Structural performance of unstiffened low yield point steel plate shear walls. *Journal of Constructional Steel Research*. 2015;112:40-53.
- [5] Berman J, Bruneau M. Experimental investigation of light-gauge steel plate shear walls. *Journal of Structural Engineering*. 2005;131(2):259-267.
- [6] Emami F, Mofid M, Vafai A. Experimental study on cyclic behavior of trapezoidally corrugated steel shear walls. *Engineering Structures*. 2013;48(6):750-762.
- [7] Emami F, Mofid M. On the hysteresis behavior of trapezoidally corrugated steel shear walls. *The Structural Design of Tall and Special Buildings*. 2014;23(2):94-104.
- [8] Farzampour A, Laman JA. Behavior prediction of corrugated steel plate shear walls with openings. *Journal of Constructional Steel Research*. 2015;114:258-268.
- [9] Bahrebar M, Zaman Kabir M, Zirakian T, Hajsadeghi M, Lim J. Structural performance assessment of trapezoidally corrugated and centrally-perforated steel plate shear walls. *Journal of Constructional Steel Research*. 2016;122:584-594.
- [10] Cao Q, Huang J. Experimental study and numerical simulation of corrugated steel plate shear walls subjected to cyclic loads. *Thin-Walled Structures*. 2018;127:306-317.
- [11] Tong JZ, Guo YL, Zuo JQ. Elastic buckling and load-resistant behaviors of double-corrugated-plate shear walls under pure in-plane shear loads. *Thin-Walled Structures*. 2018;130:593-612.
- [12] Dou C, Pi Y, Gao W. Shear resistance and post-buckling behavior of corrugated panels in steel plate shear walls. *Thin-Walled Structures*. 2018;131:816-826.
- [13] Farzampour A, Mansouri I, Lee C, Sim H, Hu JW. Analysis and design recommendations for corrugated steel plate shear walls with a reduced beam section. *Thin-Walled Structures*. 2018;132:658-666.
- [14] Bahrebar M, Lim JBP, Clifton GC, Zirakian T, Shahmohammadi A, Hajsadeghi M. Perforated steel plate shear walls with curved corrugated webs under cyclic loading. *Structures*. 2020;24:600-609.
- [15] Fang J, Bao W, Ren F, Guan T, Xue G, Jiang J. Experimental study of hysteretic behavior of semi-rigid frame with a corrugated plate. *Journal of Construction Steel Research*. 2020;174:106289.

- [16] Bahrebar M, Lim JBP, Clifton GC, Zirakian T, Shahmohammadi A, Hajsadeghi M. Response assessment and prediction of low yield point steel plate shear wall with curved corrugated web plates and reduced beam sections. *Structures*. 2020;28:1729-1745.
- [17] ABAQUS 6.14.3. ABAQUS 6.14.3 Documentation. Hibbitt, Karlson, Sorenson, Inc. 2015.
- [18] Driver RG, Kulak GL, Kennedy DJL, Elwi AE. Seismic behavior of steel plate shear walls. *Structural Engineering Report No. 215*. Department of Civil Engineering, University of Alberta. Edmonton, Alberta, Canada. 1997.
- [19] DIN 1623. 1629 International standard of germany. 1983.
- [20] Hosseinzadeh L, Emami F, Mofid M. Experimental investigation on the behavior of corrugated steel shear wall subjected to the different angle of trapezoidal plate. *The Structural Design of Tall and Special Buildings*. 2017;26 (17):1-17.
- [21] Jahanpour A, Jönsson J, Moharrami H. Seismic behavior of semi-supported steel shear walls. *Journal of Construction Steel Research*. 2012;74:118-133.
- [22] Yu HL, Jeong DY. Application of stress triaxiality dependent fracture criterion in the finite element analysis of unnotched charpy specimens. *Theoretical and Applied Fracture Mechanics*. 2010;54 (1):54-62.
- [23] Vian D, Bruneau M, Tsai K, Lin Y. Special perforated steel plate shear walls with reduced beam section anchor beams. I: Experimental investigation. *Journal of Structural Engineering*. 2009;135(3):211-220.
- [24] ATC. Guidelines for cyclic seismic testing of components of steel structures. Applied Technology Council. Report No. 24. Redwood City. Ca. 1992.
- [25] Vian D, Bruneau M, Purba R. Special perforated steel plate shear walls with reduced beam section anchor beams. II: Analysis and design recommendations. *Journal of Structural Engineering*. 2009;135(3):221-228.
- [26] ATC. Modeling and acceptance criteria for seismic design and analysis of tall buildings. Applied Technology Council. Report No. 72. Redwood City. Ca. 2010.
- [27] Choi I, Park H. Steel plate shear walls with various infill plate designs. *Journal of Structural Engineering*. 2009;135(7):785-796.
- [28] Guo L, Rong Q, Ma X, Zhang S. Behavior of steel plate shear wall connected to frame beams only. *International Journal of Steel Structures*. 2011;11(4):467-479.
- [29] Yi J, Gil H, Youm K, Lee H. Interactive shear buckling corrugated steel webs. *Engineering Structures*. 2008;30(6):1659-1666.

Analysis for Sustainable Concrete Structure Reinforced by Embedded Parts

Harish Chand Giri, *Department of Mechanical Engineering, Aryan Institute of Engineering & Technology, Bhubaneswar, harishchand4@gmail.com*

Anjan Kumar M. U., *Department of Civil Engineering, NM Institute of Engineering & Technology, Bhubaneswar, anjankumar28@yahoo.co.in*

Monalika Mohanty, *Department of Civil Engineering, Raajdhani Engineering College, Bhubaneswar, monalika_m256@gmail.com*

Kankan Mandal, *Department of Civil Engineering, Capital Engineering College, Bhubaneswar, kankanmandal2@outlook.com*

ABSTRACT

Plate embedded parts and grooved embedded parts reinforced concrete structures were explored in this study. To ensure long-term functionality, two types of plate embedded parts and three types of grooved embedded parts were coated. Later, bending experiments were used to determine the ultimate failure capacity, which were then compared to the theoretically calculated results. Furthermore, three grooved embedded components were simulated using ABAQUS to compare the findings with the results of the experimental investigation, which were in close agreement with the theoretically estimated and finite element analysis results. The failure modes of the implanted specimens under the five operating conditions were all concrete vertebral failure, according to the results. The ultimate bearing capacity of plate-type embedded components was found to be higher than that of grooved embedded parts. Furthermore, these five types of embedded parts have not yet reached their maximum flexural and shear capacity.

1. Introduction

As the construction industry develops rapidly, the mechanical properties of the concrete have attached more attention [1, 2]. Consequently, the reinforced concrete (RC) structures have been widely used in constructions with the advantages of high sustainability, excellent mechanical strength, and considerable deformability resistance [3, 4]. However, the ordinary RC structures cannot meet the increasing demand of engineering specifically for the formworks in structure nodes [5–7]. This phenomenon points to the need for novel RC structures for filling

structure nodes' formworks and producing high-quality constructions [8].

The application of sustainable embedded parts in steel-concrete composite structure joints has been used extensively as a promising material [9]. The embedded parts' structure comprising Halfen channel embedded parts and plate embedded parts are raising attention and can be the feasible solutions towards current drawbacks [10]. The embedded parts' structures do not depend on the secondary construction of the ground in constructions with the advantages of the convenient assembly procedure, low cost, and labor [11]. Stout et al. [12] patented a method for making

cast-in-place concrete structures to reveal integrally bounded confines in the structure. Stout et al. [13] also explored a void-creating device to be embedded in a concrete structure, aiming at defining a labyrinth of passageways with the concrete structure, which revealed the passage procedure for service parts through the interior parts within the concrete.

At present, drawing, shearing, and seismic resistance are major concerns for embedded parts worldwide. In engineering application, the slot embedded parts, bearing the bending force and shear force in most cases as the joint of the steel-concrete structure [14]. However, few studies have been conducted on the bending-shear test performance of slot embedded parts. Moreover, despite the embedded parts being widely used, there are few standard designs for slot embedded parts.

In this study, a novel coating treatment was conducted upon three kinds of HALFEN channel embedded parts and two kinds of plate embedded parts to reveal the sustainable function. The bending-shear experiments were carried out with different specifications to analyze the ultimate bearing capacity and failure modes. Under the actual test conditions, the theoretical calculation and finite element analysis using ABAQUS were carried out on the flexural and shear test to determine the reliability of the HALFEN channel embedded parts in the practical application. The study can be regarded as a guideline in this research area.

2. Experimental Study

2.1. Experimental Design. 15 specimens for two types of embedded parts were analyzed comprising A-1, A-2, B-1, B-2, and B-3. The A group was the structure reinforced by embedded plate and the B group means the grooved embedded parts corresponded to three different types of grooved embedded parts. Each batch contains three samples and the loading configurations are constant. Specifically, A-1 and A-2 were each reinforced by a 150 mm × 150 mm × 10 mm and a 150 mm × 150 mm × 20 mm anchor plate separately. Meanwhile, the embedded plate was welded by 4 steel bar anchor legs (200 mm in length and 20 mm in diameter) and the anchor legs were also welded to an I-beam (150 mm) with different distances towards edges (10 mm for A-1 and 20 mm for A-2). For the B group, the specimen was reinforced by HALFEN groove (40 mm width and 22 mm height for B-1, 50 mm width and 30 mm height for B-2, and 52 mm width and 34 mm height for B-3). The groove was weld by 4 anchor legs with a length of 100 mm (overall length of 300 mm). The anchor legs were linked with 5 T bolts on the other side.

The concrete specimen sizes were 450 mm × 450 mm × 450 mm (A group) and 600 mm × 400 mm × 300 mm (B group). The design strength of all specimens was C30 and the embedded parts were Q345-type galvanized steel. The surface of the anchor plate was even with the concrete, embedding all anchor legs. The bending or shearing loads were applied to the I beam or T bolt, and the loading eccentricity was 40 mm from the anchor plate plane. The specimen parameters were demonstrated in Table 1.

2.2. Sustainable Treatment. All designed embedded parts experienced coating treatment to guarantee sufficient sustainability in-service lifespan. A self-developed Zn-Al-Mg-RE alloy on a small scale is utilized coating, as shown in Figure 1. This is because the alloy not only exhibits outstanding corrosion resistance but also fills the microcracks in the coating which enhances the mechanical performance. First, pure Zn strip at the content of 99.9% is sprayed onto the surface of embedded parts as a base by a high-velocity spraying gun (HAS-02) cooperated by a CDM system (AS3000) at 200 μm thickness. Later, the Zn-Al-Mg alloys are coated upon the surface of the embedded part with a thickness of 400 μm. The spraying current stands at 140 A, and spraying voltage employs 30 V. The spraying distance keeps at 250 mm and the air pressure is 0.65 MPa.

2.3. Loading Parameters. The 500t servo compression-testing machine is utilized to load the test specimens. Meanwhile, a self-control device is set on the upside of the specimen to prevent the sliding effect on the workbench. The structure diagram of the entire loading system and self-control device are, respectively, shown in Figure 2.

As for the loading procedure, the servo machine first utilized a 0.2 kN/s preload rate till the 10% yield load followed by a recovering process. After the inspection of the loading device and instrument, the servo machine applied uniaxial load at a rate of 0.4 kN/s with 50 mm eccentricity until failure. The loading value, as well as the strain data, was collected automatically by the servo machine and the static strain tester. Especially, both the circumscribed I-beam of plate-type and the circumscribed T-type bolt of slot-type built-in fitting obtained 4 anchor legs using 8 wires to connect with the static strain tester during loading. The loading procedure of plate-type built-in fitting and slot-type built-in fitting separately are illustrated in Figure 3.

3. Test Results

3.1. Mechanical Properties. The experimental results are shown in Figure 4. The average failure load of A-1 was 378.73 kN and was 78 kN higher than that of A-2 (299.93 kN). The mean loading capacities for the B batch were 89.76 kN for the B-1 sample, 125.34 kN for the B-2 sample, and 105.63 kN for the B-3 sample.

3.2. Failure Mode. The failure modes and surface cracks for all five embedded specimens are denoted in Figure 5.

All the specimens were damaged by the concrete vertebral body with considerable cracks. For the embedded structures, the concrete around the groove began to crack slightly and then gradually expanded. After a specific threshold (98 kN for B-1 and 92 kN for B-2), the cracks on the original extend rapidly and terminally came into failure. Major cracks in the vertical direction on both sides of the middle groove steel were found, the bottom joint was protruded around the T-bolt and the upper part was pulled out due to the exerted force on the edge.

TABLE 1: Specimen parameters for A and B groups.

Group	Built-in type	Anchor number and size	Sample size (mm)	Circumscribed device
A-1	Plate-type	4 * 100 * 20	450 × 450 × 450	No. 14 I-beam
A-2	Plate-type	4 * 100 * 20	450 × 450 × 450	No. 14 I-beam
B-1	Slot-type	4 * 100 * 20	600 × 400 × 300	5 T-type bolts
B-2	Slot-type	4 * 100 * 20	600 × 400 × 300	5 T-type bolts
B-3	Slot-type	4 * 100 * 20	600 × 400 × 300	5 T-type bolts

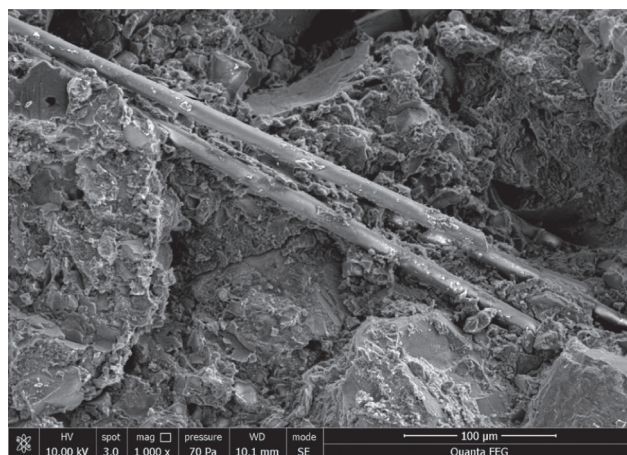


FIGURE 1: Microscale set up of Zn-Al-Mg-RE coating.

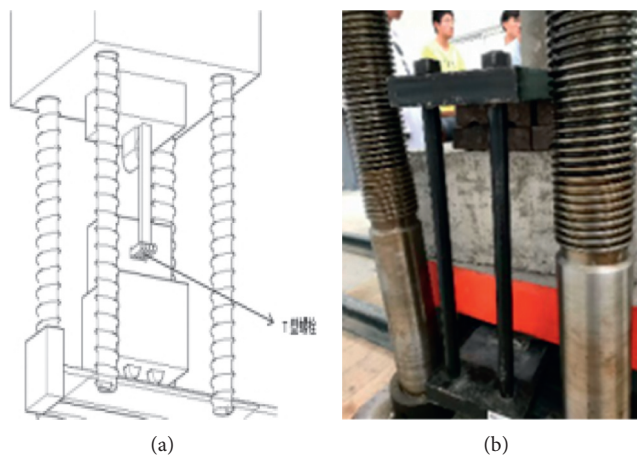


FIGURE 2: (a) Servo testing machine structure diagram. (b) Self-control experiment device.

4. Theoretical Calculations

The bearing capacity of a section of embedded components is calculated according to CEN/TS 1992-4-3:2009 [15].

4.1. Design Calculation and Analysis of Plate Embedded Parts.

As for the damage characteristics, when the force moment e/z is less than 0.3, the embedded parts are first crushed by concrete with general shear-bearing embedded parts. When the force moment e/z is more than 0.6, the embedded parts are all damaged by the pulled anchor leg. Otherwise, the

embedded part failure is caused by the compound effect of crushed concrete or the pulled anchor leg. In this study, the eccentricity is 40 mm, and the vertical distance Z between the anchor legs is 130 mm. Therefore, the moment equals 0.3 and the theoretical damage characteristic ought to be a crushing effect to form vertebral body damage, which is consistent with the actual damage characteristics.

According to the experimental study and theoretical analysis of uniformly arranged bending-shear embedded parts with straight anchor legs, the strength of bending-shear embedded parts can be calculated according to the following equation [16, 17]:

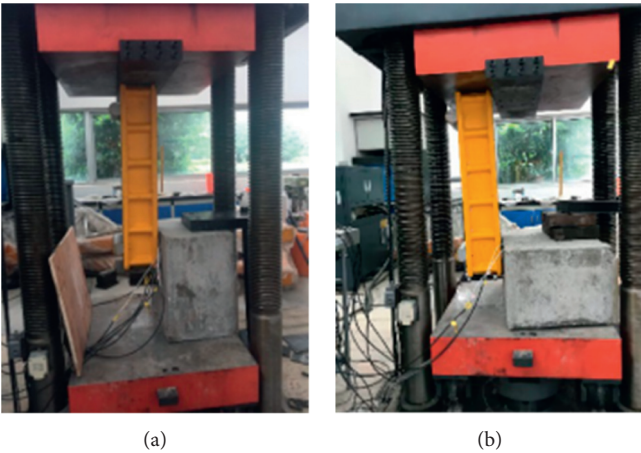


FIGURE 3: The built-in fitting for (a) plate-type and (b) slot-type.

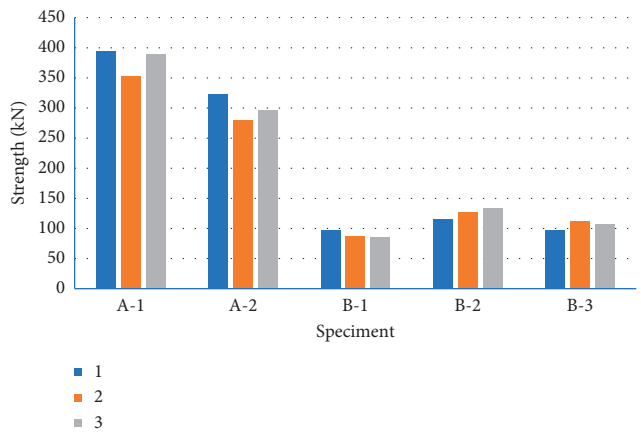


FIGURE 4: Experimental results of plate and groove embedded parts.

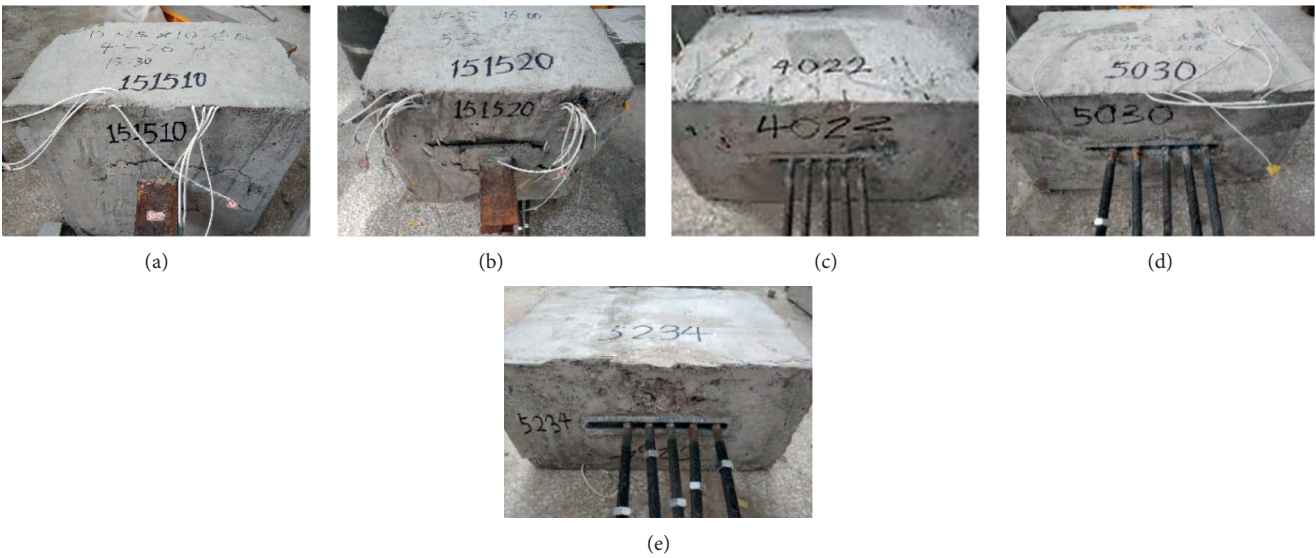


FIGURE 5: Specimen failure form for (a) A-1, (b) A-2, (c) B-1, (d) B-2, and (e) B-3.

$$\frac{V}{V_{u0}} + \frac{0.3M}{Mu0} = 1, \quad (1)$$

where $V/V_{u0} \geq 0.7$, or $(e/z) \leq 0.57 (\alpha_a \alpha_b / \alpha_v)$.

According to the reliability analysis of embedded parts, the shear strength of embedded parts can be calculated according to equation (2) and the bending strength of embedded parts can be calculated according to equations (3) to (5):

$$v_{u0} = \alpha_v \alpha_r f_y A_s, \quad (2)$$

$$M_{u0} = 0.4 \alpha_a \alpha_b \alpha_r f_y A_s z, \quad (3)$$

$$\alpha_v = (4 - 0.08d) \sqrt{\frac{f_c}{f_y}} \leq 0.7, \quad (4)$$

$$\alpha_a = \frac{l'_a}{l_a}, \quad (5)$$

where α_v symbols the shear strength coefficient of anchor legs, f_c is the design value of concrete compressive strength, f_y equals the design value of tensile strength of embedded anchor legs, d is the diameter of steel bars, α_r means the influence coefficient of the number of anchor legs, A_s is the section area for all anchor legs, α_a symbols the reduction coefficient of anchor length, α_b is the reduction factor of bending deformation of anchor plate which generally equals 1, l'_a is the actual length of the anchor leg (200), and l_a means the anchorage length (600) of tensile anchor legs is usually selected and calculated according to Table 2.

By combining the listed formulas, equation (6) is obtained shown as follows:

$$\frac{V}{\alpha_v \alpha_r f_y A_s} + \frac{M}{1.3 \alpha_a \alpha_b \alpha_r f_y A_s z} = 1. \quad (6)$$

As the embedded parts met the structural requirements and the anchor plate can be considered as nonbending deformation, α_b thus equals 1. The embedded parts are equipped with two rows of anchor legs, and α_r is taken as 1. The design value of compressive strength of concrete specimens is 14.3 N/mm², and the design value of tensile strength of embedded anchor legs is 310 N/mm².

As a result, $\alpha_a = 1/3$ and the shear strength coefficient of anchor legs α_v is 0.52. The theoretical calculation solution V is 148 kN, which is far lower than the experimental results of A-1 and A-2, meeting the safety considerations.

4.2. Practical Calculation and Analysis of Groove Embedded Parts. The embedded depth of the anchor leg was shallow, which is less than 150 mm. The failure form of the groove embedded structure was usually concrete cone failure, and the experimental results verified this assumption. According to CEN/TS 1992-4-3:2009 [15], the formula of a failure bearing capacity of the concrete cone is described as [18, 19]

$$N_{Rk,c} = N_{Rk,c}^0 \times \alpha_{s,N} \times \alpha_{e,N} \times \alpha_{c,N} \times \varphi_{re,N} \times \varphi_{ucr,N}, \quad (7)$$

TABLE 2: The formula for calculating anchorage length.

Type of reinforcement	Strength grade of concrete			
	C15 (d)	C20 (d)	C25 (d)	≥C30
Crescent rebar	50	40	35	30d

where $N_{Rk,c}$ is the failure capacity of the concrete cone when a single anchor leg of groove-type embedded part is applied, $\alpha_{s,N}$, $\alpha_{e,N}$, and $\alpha_{c,N}$ are the adjacent anchor correction coefficient, boundary effect correction coefficient, and corner effect correction coefficient, respectively, and $\varphi_{ucr,N}$ is the cracking correction coefficient of concrete, and when noncracking concrete equals to 1.4, $\varphi_{re,N}$ is the shadow of bearing capacity considering the peeling of surface concrete. The formula for calculating the response coefficient is expressed in equation (8). $N_{Rk,c}^0$ means the standard value of bearing capacity of concrete cone failure reinforced by single anchor legs of groove embedded parts under tension which is calculated as equation (9):

$$\phi_{re,N} = 0.5 + \frac{h_{ef}}{200} \leq 1, \quad (8)$$

$$N_{Rk,c}^0 = 8.5 \times \alpha_{ch} \times \sqrt{f_{ck,cube}} \times h_{ef}^{1.5}, \quad (9)$$

where α_{ch} is the correction factor of channel steel to concrete cone less than 1, $f_{ck,cube}$ is the standard value of compressive strength of concrete cube (N/mm²), and h_{ef} is the length of anchor leg of groove embedded parts.

According to the listed formulas, h_{ef} is 100 mm, and $\varphi_{re,N}$ is thus calculated as 1. When the specimen is C30, $f_{ck,cube}$ take 34.9 N/mm² and α_{ch} was chosen as 1; then, $N_{Rk,c}^0$ is calculated as 50.2 kN. The adjacent anchor repair coefficient, boundary effect repair coefficient, and corner effect repair coefficient $\alpha_{s,N}$, $\alpha_{e,N}$, and $\alpha_{c,N}$, are 1, 1.1, and 1.2, respectively, according to the actual situation. The concrete is noncracking concrete, and $\varphi_{ucr,N}$ is 1.4. As a result, $N_{Rk,c}$ is calculated as 102.1 kN, which is in close agreement with the experimental values.

5. Finite Element Simulation Analysis of Groove Embedded Parts Test

5.1. Establishment of the Finite Element Model for Slot Embedded Parts

5.1.1. Selection of Materials. The groove embedded components (B-1, B-2, and B-3) were simulated in finite element analysis consisting of steel plate, groove embedded parts, and concrete structure. The T-type bolt is simplified as a steel plate in modeling as its main function was to transmit force to embedded parts. The steel Poisson's ratio was 0.274, and the elastic modulus was 2.06×10^3 MPa.

There were three constitutive models of concrete which are provided in ABAQUS including the brittle cracking model, dispersive cracking model, and damage-plasticity model [20, 21]. The plastic damage model of concrete is adopted in this paper because it was able to simulate the mechanical behavior of concrete under

monotonous, reciprocating, and dynamic loads under low hydrostatic pressure and has good convergence. As for the uniaxial constitutive relationship of concrete, it was based on the damage-plasticity mode and consisted of the elastic section, strengthening section, and softening section. Poisson's ratio took 0.167 in the elastic section. The inelastic strain and damage constitutive relationship are demonstrated in equations (10) and (11) [22, 23]:

$$\varepsilon_{c,in} = \frac{\varepsilon - \sigma}{E_0}, \quad (10)$$

$$\sigma = (1 - d)D_0: (\varepsilon - \varepsilon^{pl}) = D: (\varepsilon - \varepsilon^{pl}), \quad (11)$$

where E_0 means the initial modulus of elasticity, D_0 is the initial elastic stiffness, D symbols the degraded elastic stiffness, and d is the damaging factor variable within the domain of 0 and 1.

The uniaxial tension constitutive relation defined the peak stress f_t as $0.35f_{cu}^{0.55}$ and the softening section when the strain exceeds the ultimate strain ε_{cu} . Meanwhile, the ultimate tensile strain and the corresponding residual stress in the tension-softening section of concrete have a great influence on the convergence of the calculation. The residual stress is thus defined as $0.13f_t$. Other related parameters are selected according to the measured values. The plastic nonlinear model is difficult to converge in the calculation. Considering that plastic deformation hardly occurs in the noncontact parts (concrete and embedded part), this area post minor impact towards test results. Therefore, the noncontact region is set as linear elastic material, and the contact part between concrete and embedded parts is defined as plastic material.

5.1.2. Interaction and Boundary Conditions. The binding constraints were established at the contact areas between the steel plate and the embedded parts. To facilitate the loading, a reference point was set on the upper surface of the steel plate followed by a kinematic coupling procedure. To coincide with the test results, some surface-to-surface contact pairs were set. Specifically, the steel plate with larger stiffness was set as the main surface and the concrete part was set as the slave surface. Moreover, the finite slip formula was utilized to define the finite element contact because the relative displacement between the embedded parts and the concrete may be arbitrary. The tangential and normal behaviors were mainly considered in the contact properties and the Coulomb friction was adopted in the friction model and the friction coefficient was 0.4.

The model was placed on the loading table of the press with a clamp on the opposite side of the embedded part. The load was applied smoothly on the bolt to transfer the force to the embedded part. According to the experimental setting, three degrees-of-freedom constraints were applied to the concrete bottom and the displacement constraints were utilized for the steel plate.

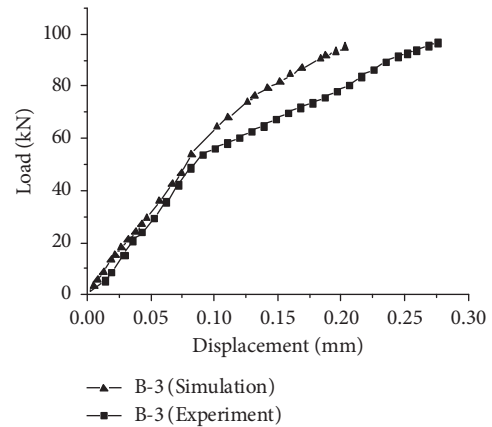


FIGURE 6: Comparison diagram of displacement load curve of B-3.

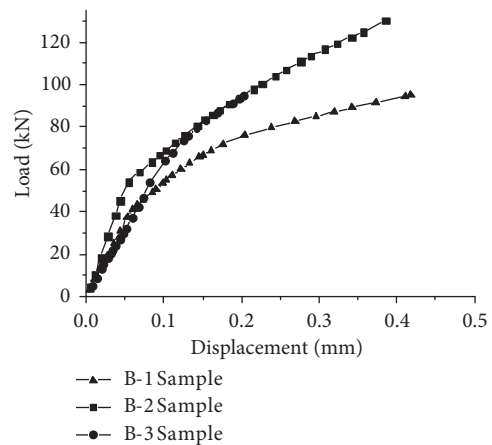


FIGURE 7: Simulated displacement load curve of three specimens.

5.1.3. Mesh Generation. In this paper, the 8-node hexahedron reduction integral entity element C3D8R was used in the plastic nonlinearity analysis. The embedded component was in 8 mm mesh size and the concrete unit was 30 mm; the contact interface unit was in 7 mm.

5.2. Finite Element Analysis Results. Figure 6 is the comparison of displacement load curve measured in the experiment and simulated by the finite element method. The experimental results of the embedded parts were in close agreement with the finite element analysis results. The displacement load-curve comparison obtained by finite element simulation is shown in Figure 7. It can be seen that the groove embedded parts have obvious elastic and plastic stages and are verified with the mechanical bearing capacity in the experiments.

Figure 8 demonstrates the concrete stress cloud diagram for the simulated B group specimens. The stress distribution on the upper surface in the finite element analysis was consistent with the damaged area of the concrete vertebral surface in experiments. When the embedded parts were subjected to bending and shearing force, the T-bolt would be pulled on the upper side, and we exert relatively large

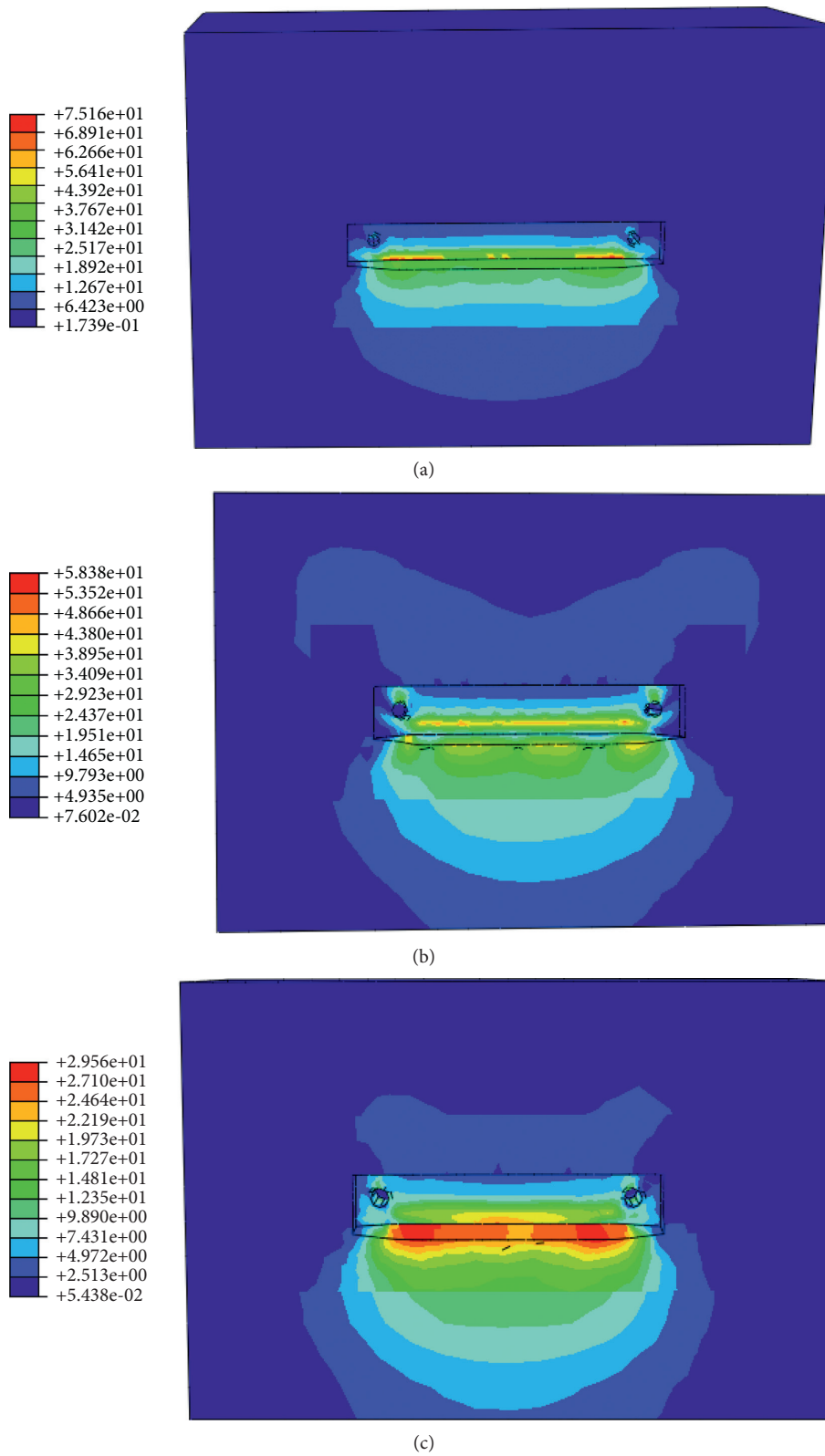


FIGURE 8: Concrete stress cloud diagram. (a) B-1, (b) B-2, and (c) B-3 (unit: MPa).

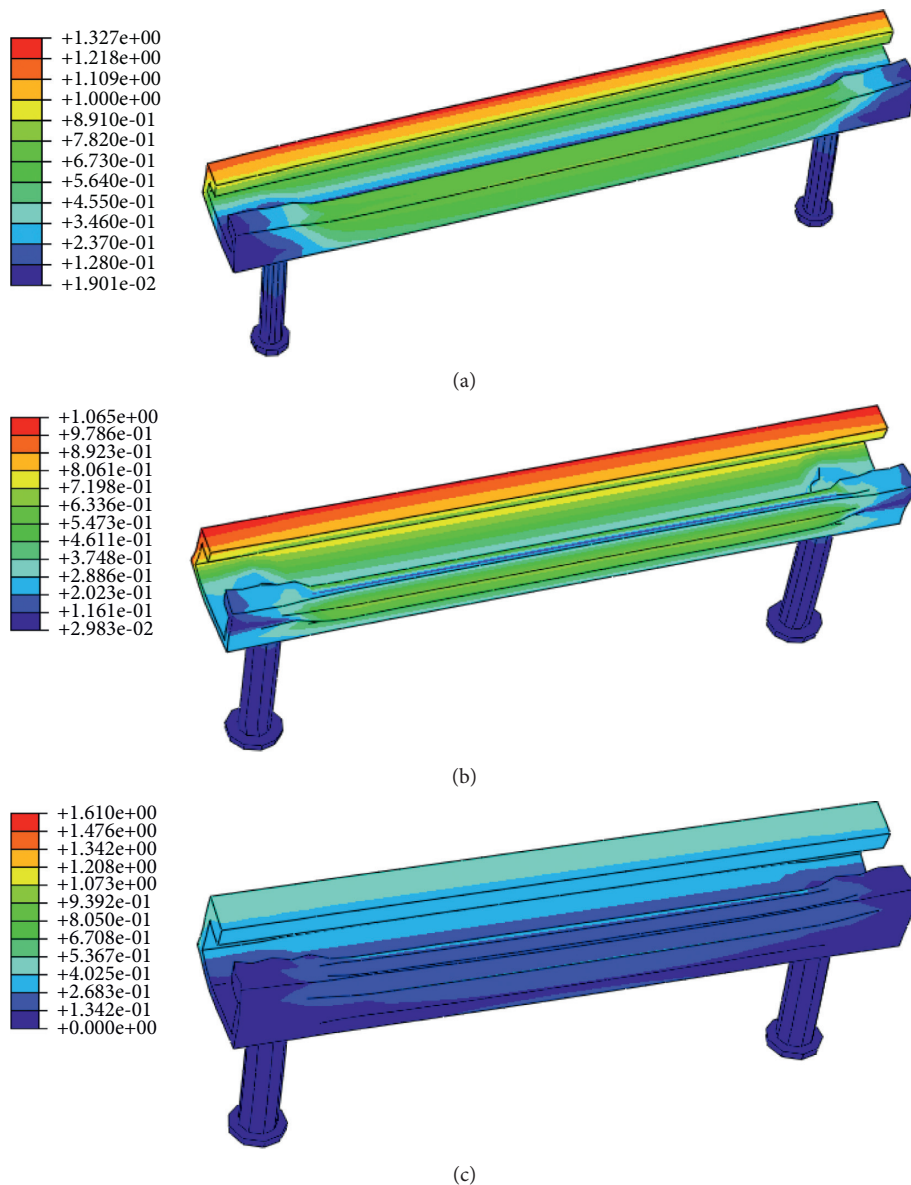


FIGURE 9: The embedded parts deformation diagram for (a) B-1, (b) B-2, and (c) B-3 (unit: mm).

compressive pressure on the lower side of the channel. When the displacement occurred upon T-bolt, the anchor leg in concrete would be pulled out slowly. Thereby, the punching effect upon the interaction between the anchor leg end and the concrete would increase. According to the stress cloud diagrams, the obvious stress concentration phenomenon was found at the interfaces for all three specimens, which was in agreement with the vertebral destruction caused by concrete in the mechanical experiments.

Figure 9 shows the deformation diagrams for the groove embedded parts' reinforced concretes. The displacement load-curve comparison figure obtained by finite element simulation is shown in Figure 10. From the listed figures, the maximum stresses for the simulated samples occurred at the bolt-channel steel interface and the anchor leg end. For the B-1 sample, the maximum stress reached 272.8 MPa and was mainly at the

connection between T-type bolts and groove steel. The groove-type embedded part was still in an elastic state, while the maximum stress of concrete stood at 75.16 MPa at the end of the anchor leg, exceeding the compressive ultimate limit. The B-2 sample obtains the maximum stress of 268 MPa also at the connection surface between T-type bolts and groove steel. Meanwhile, the groove-type embedded parts have not fully kept the plastic state, but the concrete's maximum stress (58.38 MPa) has already reached the compressive limit at the end of anchor legs. For the B-3 specimen, the HALFEN groove's peak stress was simulated as 281.8 MPa at the connection part between channel steel and T-type bolts. Simultaneously, both the embedded parts and the concrete component did not exceed the plastic level threshold. The works can lay the foundation for future artificial intelligence optimization works.

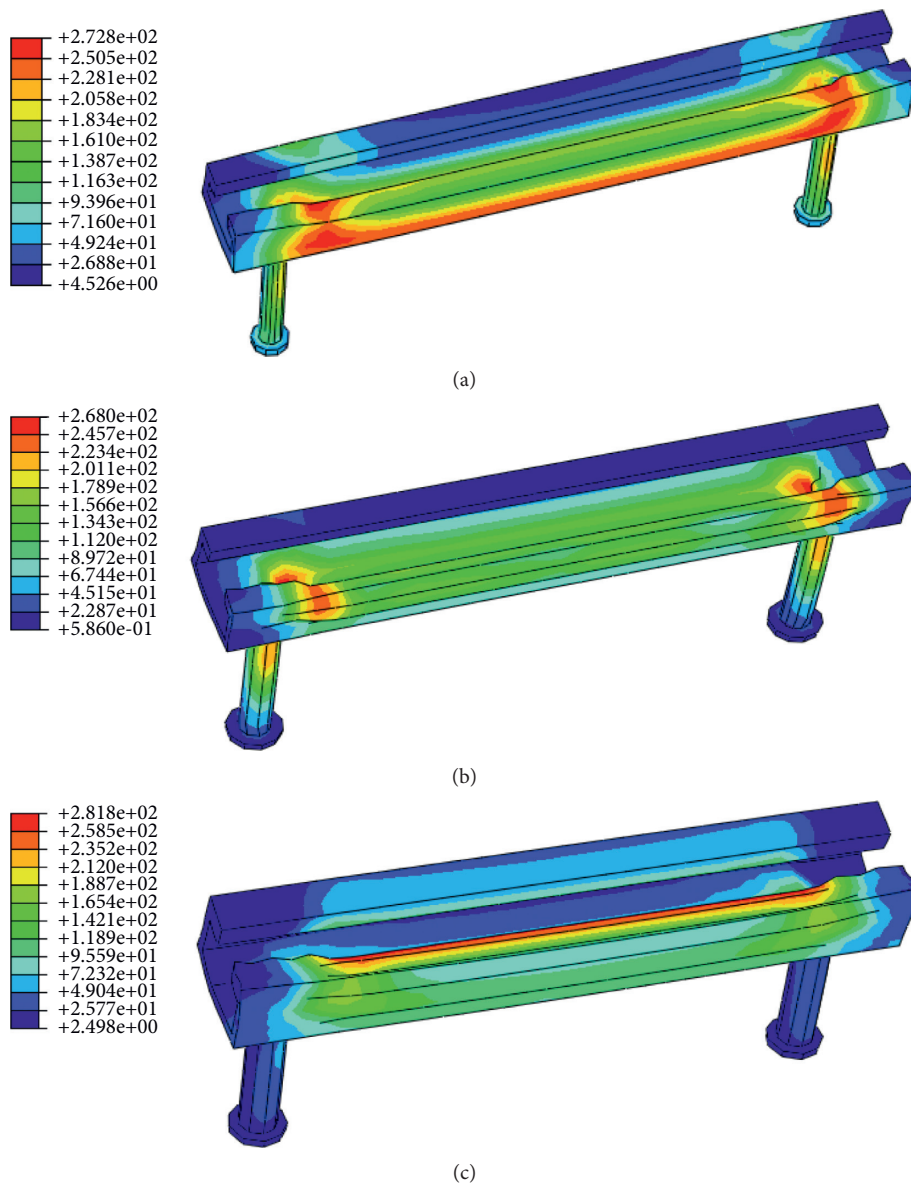


FIGURE 10: The embedded stress diagram for (a) B-1, (b) B-2, and (c) B-3 (unit: MPa).

6. Conclusion

The purpose of the study was to investigate the reliability of sustainable plate embedded parts and grooved embedded parts' reinforced concrete structures. The main conclusions of the study can be summarized as follows:

- (1) The self-developed Zn-Al-Mg-RE coating enhances the sustainability performance of the embedded parts, which benefits the whole concrete structure of a longer service life span. The plate embedded parts supplied higher bearing capacity and the HALFEN groove with 50 mm width and 30 mm height was the most suitable category in reinforcing works.
- (2) The theoretical calculation of failure bearing capacity for both plate embedded parts and grooved embedded parts reinforced concrete structures was consistent with the experimental results. The failure modes for embedded parts' reinforced concrete structures were the destruction of concrete vertebrae with obvious cracks.
- (3) Based on the finite element analysis of three groove embedded specimens, the concrete at the end of the anchor leg had an obvious stress concentration phenomenon, which was consistent with the phenomenon of vertebral body destruction caused by concrete in the experiment. The finite element simulations were in according to the experimental results and theoretical calculation results.

References

- [1] S. O. Hong and C. J. Aldrete, "Simple method for upgrading an existing reinforced-concrete structure," *Practice Periodical on Structural Design and Construction*, vol. 1, no. 1, pp. 47–50, 1996.
- [2] K. M. A. Hossain, M. Lachemi, M. Sammour, and M. Sonebi, "Influence of polyvinyl alcohol, steel, and hybrid fibers on fresh and rheological properties of self-consolidating concrete," *Journal of Materials in Civil Engineering*, vol. 24, no. 9, pp. 1211–1220, 2012.
- [3] D. Hu and K. Ma, "A study on reliability of reinforced concrete structure," *Journal of Building Structures*, vol. 14, 1987.
- [4] R. Pucinotti, "Reinforced concrete structure: non destructive in situ strength assessment of concrete," *Construction and Building Materials*, vol. 75, no. 75, pp. 331–341, 2015.
- [5] L. Hu, Y. Wang, P. Feng, H. Wang, and H. Qiang, "Debonding development in cracked steel plates strengthened by CFRP laminates under fatigue loading: experimental and boundary element method analysis," *Thin-Walled Structures*, vol. 166, Article ID 108038, 2021.
- [6] L. Hu and P. Feng, "Prestressed CFRP-reinforced steel columns under axial and eccentric compression," *Composite Structures*, vol. 268, Article ID 113940, 2021.
- [7] L. Hu, P. Feng, and X.-L. Zhao, "Fatigue design of CFRP strengthened steel members," *Thin-Walled Structures*, vol. 119, pp. 482–498, 2017.
- [8] F. Aslani and S. Nejadi, "Bond behavior of reinforcement in conventional and self-compacting concrete," *Advances in Structural Engineering*, vol. 15, no. 12, pp. 2033–2051, 2012.
- [9] L. Gerola, "Connecting horizontal panels and vertical panels in prefabricated buildings," Google Patents, 1972.
- [10] L. L. Hu, X. L. Zhao, and P. Feng, "Fatigue behavior of cracked high-strength steel plates strengthened by CFRP sheets," *Journal of Composites for Construction*, vol. 20, no. 6, Article ID 04016043, 2016.
- [11] R. Böllinghaus, "Transport anchor for embedding in prefabricated reinforced concrete parts," Google Patents, 2002.
- [12] R. K. Stout, "Method for making cast-in-place concrete structures," Google Patents, 1975.
- [13] R. K. Stout, "Void creating device to be embedded in a concrete structure," Google Patents, 1975.
- [14] B. Zoubek, M. Fischinger, and T. Isakovic, "Estimation of the cyclic capacity of beam-to-column dowel connections in precast industrial buildings," *Bulletin of Earthquake Engineering*, vol. 13, no. 7, pp. 1–24, 2014.
- [15] D. Standards, *Design of Fastenings for Use in Concrete - Part 4-3: Anchor Channels*, 1992.
- [16] X. Liu, M. A. Bradford, and A. Ataei, "Flexural performance of innovative sustainable composite steel-concrete beams," *Engineering Structures*, vol. 130, pp. 282–296, 2017.
- [17] P. K. Sarker, "Bond strength of reinforcing steel embedded in fly ash-based geopolymer concrete," *Materials and Structures*, vol. 44, no. 5, pp. 1021–1030, 2011.
- [18] P. Valeri, M. F. Ruiz, and A. Muttoni, "Modelling of textile reinforced concrete in bending and shear with elastic-cracked stress fields," *Engineering Structures*, vol. 215, Article ID 110664, 2020.
- [19] B. Han, Y. Wang, S. Dong et al., "Smart concretes and structures: a review," *Journal of Intelligent Material Systems and Structures*, vol. 26, no. 11, pp. 1303–1345, 2015.
- [20] K. Hibbitt, Sorensen. *ABAQUS/Standard User Subroutines Reference Manual*, Sorensen, Inc, Chicago, IL, USA, 2002.
- [21] A. Jawdhari and I. Harik, "Finite element analysis of RC beams strengthened in flexure with CFRP rod panels," *Construction and Building Materials*, vol. 163, pp. 751–766, 2018.
- [22] W. Demin and H. Fukang, "Investigation for plastic damage constitutive models of the concrete material," *Procedia engineering*, vol. 210, pp. 71–78, 2017.
- [23] T. Supaviriyakit, P. Pornpongsaroj, and A. Pimanmas, "Finite element analysis of FRP-strengthened RC beams," *Songklanakarin Journal of Science and Technology*, vol. 26, no. 4, pp. 497–507, 2004.

A thorough examination of the impact of biodiesel's physical and chemical qualities on combustion parameters, engine performance, and emissions.

Sarat Kumar Mishra, *Department of Mechanical Engineering, Aryan Institute of Engineering & Technology, Bhubaneswar, skmishra784@gmail.com*

Sidharth Pradhan, *Department of Mechanical Engineering, Capital Engineering College, Bhubaneswar, sidharthpradhan265@gmail.com*

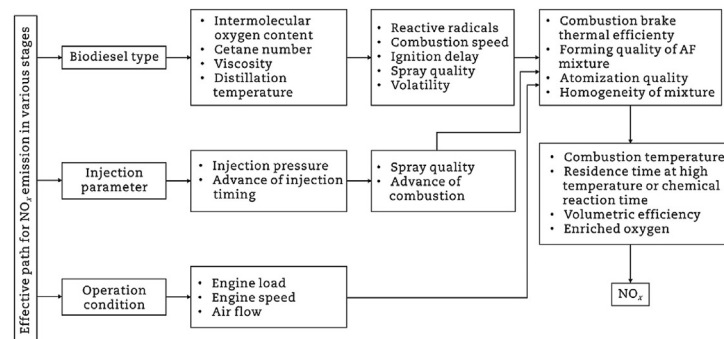
Rajaram Sahu, *Department of Mechanical Engineering, Raajdhani Engineering College, Bhubaneswar, rajaramsahu65@gmail.com*

Shakyasingha Sahoo, *Department of Mechanical Engineering, NM Institute of Engineering & Technology, Bhubaneswar, shakyasinghasahoo@gmail.com*

HIGHLIGHTS

- Biodiesel is the most promising alternative fuel in CI engines.
- The primary source of the third-generation biofuel is the algae.
- Ignition delayed due to the occurrence of the physical and chemical processes.
- Summarized physicochemical properties of different biodiesels from first to third generation.

GRAPHICAL ABSTRACT



ARTICLE INFO

ABSTRACT

Energy is a fundamental prerequisite for global progress. The ever-increasing need for energy resources, combined with the rapid depletion of fossil fuels, has researchers concerned about the need to focus on alternative energy sources that can quickly replace the lack of fossil fuels.

Keywords:

Biodiesel

Physicochemical

Combustion

Ignition

Emission

Biodiesel is considered as one of the promising alternative renewable energy fuels that may be found in a variety of forms in virtually every country. This research examines the future of biodiesel, focusing on the various fuel attributes (physicochemical) of 100 biodiesels from the first, second, and third generations, as well as the evaluation of CI engine characteristics. The ASTM standards have been found to be compatible with the fuel qualities of first-, second-, and third-generation biodiesel. From a production standpoint, the possibility of multiple generations of biodiesel feedstocks was examined in this research. This article also looked at several biodiesel feedstock sources, biodiesel conversion technology, and second-generation biodiesel performance and emission characteristics, among other things. The majority of research found that biodiesel made from plant feedstock is more expensive than diesel. As a result, non-edible sources will be given higher weight. However, the engine characteristics are shown promising behavior with biodiesel and a slight increase in NOX is also reported on using various biodiesel.

1. Introduction

1.1. Present energy scenario

The rapid increase in energy consumption is due to the regular rise in automobiles' industrial and population growth and economic development. Fig. 1 shows the current energy scenario and the projection of energy consumption until 2035. Oil fuel is the dominant provider empowering the global economy. It is almost sure that diesel will acquire approximately 60% of the energy growth accounting for almost 80% of total energy supply in 2035 (Chhabra et al., 2021). The energy scenario is predicted to continue adding in the upcoming years (Yusri et al., 2018). Fig. 2 shows the prediction of per capita renewable water birthplaces availability ($\text{m}^3/\text{person}/\text{year}$) in the world. Further, future

utilization of activity in ceases of vigorous agricultural going-on to no small extent in the world by 70% (renewable water harvesting) and 30% only for high-income countries (Hajjari et al., 2017).

The above stats show that the world will be facing enormous problems for fulfilling the demand for energy resources for society, industries and other sectors in upcoming years. This increasing demand for energy has forced various researchers in the world to work for alternative sources of energy to meet the demand (Kumar Shukla et al., 2020; Palash et al., 2015). The burning of fossil fuels also produces harmful emissions polluting the environment. The transport sector is recognized as the most energy-consuming sector. To meet the increased demand for energy and reduce CO_2 emission, the world needs to have more effective and sustainable energy sources. Thus, the use of new clean-

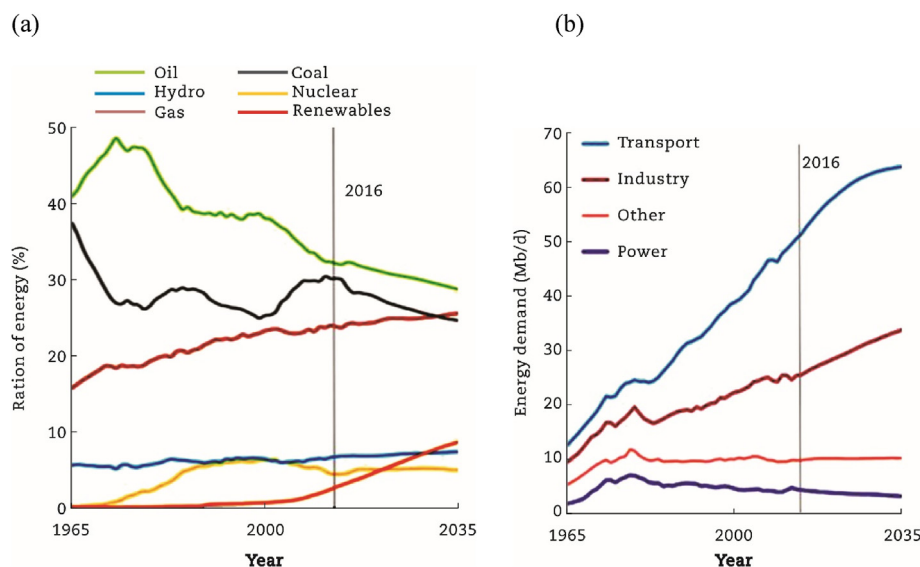


Fig. 1 – Scenario of energy consumption. (a) Shares of primary energy. (b) Liquids of demand by sector (Yusri et al., 2018).

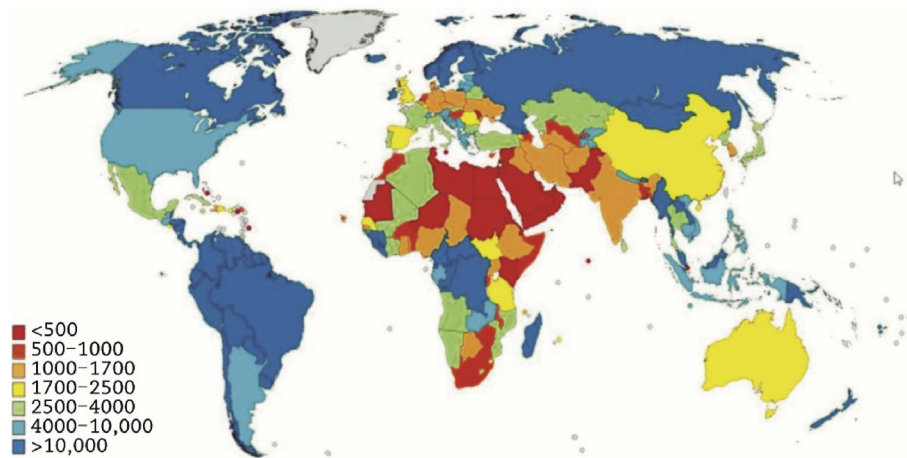


Fig. 2 – Renewable water birthplaces in the world (Hajjari et al., 2017).

burning and eco-friendly renewable energy fuels for CI engine as a replacement for petroleum fuel nowadays is a worldwide consideration (Jasrotia et al., 2019; Krishnamoorthi and Malayalamurthi, 2017). Biodiesel has been found as the most promising alternative fuel in CI engines by many researchers (Agarwal et al., 2015, 2016).

In this review paper, authors discussed the potential of various generations of biodiesel feedstocks from production perspectives. This paper also examined many aspects of these feedstocks which include different biodiesel feedstock sources, biodiesel conversion technology, and second-generation biodiesel performance and emission characteristics. The authors summarized the performance, combustion and emission characteristics of CI engine of hundreds different biodiesels from first, second and third generation of biofuels and compare them with conventional diesel fuel. The review also studies the fatty acid profiles of various biodiesels along with their engine characteristics upon using the surrogate fuels. The review also comprises of production, properties, potential estimation and economics of using biodiesel in compression ignition engines.

2. Biodiesel feedstocks

The characteristics of the diesel engine depend upon the different properties of fuel such as a viscosity of fuel, cloud point, flash point, heating value, fuel density, cetane number, pour point etc. (Bamgboye and Hansen, 2008; Dwivedi et al., 2016; Verma et al., 2019, 2020). The fuel properties should also meet the standard limits assigned by the ASTM, ISO, EN and many more, out of these ASTM is mostly used to compare the fuel properties before its being utilized as a fuel for the CI engine (Arbab et al., 2013). The overall engine performance is superior to the properties of fuel values within the acceptable range of standard limits. There is an improvement in the fuel properties when it is blended with two or more fuels and many researchers have used this combination as a substitute fuel for CI engine (Alptekin and Canakci, 2008; Kim and Lee, 2010). In this section, the properties that are widely used to check the fuel properties

in the CI engine are discussed. The study also evaluates the properties of biodiesel blend with diesel fuel at different blend ratios to improve the fuel quality for CI engine. Therefore, many researchers around the world are studying the quality of biodiesel and its blends concerning blend properties, blending of fuel and storage time (Alptekin and Canakci, 2009; Benjumea et al., 2011). Table 1 shows the different generation's biofuels and their feedstocks.

2.1. Different generations of feedstocks

Biofuels are categorized into three different generations depends upon their feedstock. In this section, a brief discussion on different generations of biodiesel and their feedstocks based on their suitability to use an alternative of fossil fuel has been introduced.

2.1.1. First-generation biodiesel

The first-generation biodiesel is derived directly from food crops, sugarcane, vegetable oil, etc. Crops such as sugar and wheat are widely used as a feedstock for the production of ethanol, while edible oilseeds have been used by many researchers for the production of biodiesel. Some biodiesel from the first generation has its benefits for reducing the greenhouse effect and CO₂ emission, while on the other side, some biodiesel produces an adverse effect. The major problem faced by the first-generation biodiesel is "fuel vs. food" security. Mostly, biodiesel is produced from food crops, and the rise in demand for biofuels has led to increasing the volume of crops that are being diverted from the food market, which results in an increase in food price globally over the last couple of years.

2.1.2. Second-generation biodiesel

Second-generation biofuels have been produced to overcome some limitations with first-generation biofuels. The second-generation biofuel is mostly derived from the non-edible seeds, organic waste, wood, waste food crops, etc., to eliminate some problems with the use of first-generation biodiesel. These are seen as a potential replacement for conventional edible food crops because they do not compete with food crops and do not need land clearing. Several researches

Table 1 – Generations of biofuels and their feedstocks (Altikriti et al., 2015; Fadhil et al., 2016b; Rajak and Verma, 2018a; Rajak et al., 2018).

Generation	Feedstock	Example
First-generation feedstock	Vegetable oil, corn sugar, edible oil seeds, animal fats, food crops, etc.	Palm, soybean, rapeseed, peanut, sunflower oil, coconut seed oil, linseed, castor, groundnut, corn oil, safflower oil, rice bran oil, camphor oil, etc.
Second-generation feedstock	Non-edible oil seeds, forest residues, sugarcane bagasse, etc.	Jatropha curcas, Karanja, mahua, cotton seed neem, annona methyl ester, aphanamixis polystachyn methyl ester, canola, calophyllum inophyllum methyl ester, sea mango, etc.
Third-generation feedstock	Algae, waste oil, waste animal fats	Microalgae oil, bael oil, waste cooking oil, waste frying oil, grease oil, fish oil, etc.

(Altikriti et al., 2015; Can et al., 2017; Fadhil et al., 2018; Ogunkunle and Ahmed, 2019) examined and discussed many aspects of second-generation biodiesel feedstocks. These factors include different biodiesel feedstock sources, biodiesel conversion technology, and second-generation biodiesel performance and emission characteristics.

2.1.3. Third-generation biodiesel

The third-generation biofuel is based on the improvement in the production of biomass. The primary source of the third-generation biofuel is the algae, and it takes many advantages to the specially engineered energy crop. The advantage of using the algae is due to its high energy efficiency, low-cost, and it is a renewable energy feedstock. It is also predicted that the potency of the algae is to generate more and more energy per acre than the conventional food crop. It is unsuitable for food production because algae can grow on land and water, therefore it reduces strain because already there is a depletion of water sources.

2.2. Biodiesel production from oils

Most researchers have focused on the transesterification technique for the production of biodiesel from various sources such as vegetable oil, fats, edible and non-edible seed to reduce the molecular weight of raw oil and viscosity (Puhan et al., 2009; Zareh et al., 2017). In the transesterification process, oil reacts with the alcohol in the presence of strong catalysts resulting in alkyl ester (biodiesel) and a by-product known as glycerol (Fadhil and Ahmed, 2016; Fadhil et al., 2018). The presence of a catalyst is necessary for the production of biodiesel so as to fasten reaction rate and also increase in ester yield. The most commonly used alcohols are ethanol and methanol, whereas as a catalyst, potassium hydroxide (KOH) and sodium hydroxide (NaOH) was used (Fadhil and Saeed, 2016). Table 2 shows the properties of various feedstock used for biodiesel.

3. Diesel engine characteristics

3.1. Combustion characteristics

In order to evaluate the combustion characteristics in a compression ignition engine fueled with biodiesel blends, several researchers chosen the various important parameters such as cylinder pressure, ignition delay, heat release rate the premixed combustion duration, and the fraction of heat release in premixed combustion phase (Chen et al., 2019, 2020; Lodi et al., 2020; Zhang et al., 2020). Start of combustion represented by the point where the heat release rate is zero. The difference between the injection timing and the start of combustion is called the ignition delay. The effect of these parameters are discussed in the preceding section.

3.1.1. Cylinder pressure

Cylinder pressure is the amount of pressure generated inside the combustion chamber on burning the fuel. The combustion process for diesel fuel begins later because of the longer ignition delay compared to biodiesel fuel and its blends. Qi et al. (2017)

Table 2 – Properties of various feedstock biodiesel.

Sr. No.	Biodiesel	CV (MJ/kg)	V (cSt at 40 °C)	MF	MW (kg/kmol)	Density (kg/m ³)	CN	FP (°C)	FPT (°C)	CP (°C)	PP (°C)	Percent of C (%)	Percent of H (%)	Percent of O (%)	Ref.
1	Annona methyl ester	41.100	4.2000	–	–	880.2000	52.00	76.0	92.0	–	–	–	–	10.80	Ramalingam et al. (2016); Senthil and Silambarasan (2015)
2	Aphanamixis polystachyn methyl ester	39.960	4.7177	–	–	873.5000 at 40 °C and 893.0000 at 15 °C	44.00	188.5	–	8.00	8.00	–	–	–	Senthil and Silambarasan (2015)
3	Aegle marmelos oil	36.300	24.3000	C ₁₈ H ₃₆ O ₂	–	896.0000	51.70	–	298.0	–	–5.00	–	–	–	Krishnamoorthi and Malayalamurthi (2017)
4	Butanol	33.630	2.2200	C ₄ H ₉ OH	74.12	794.0000–810.0000	25.00	35.0–37.0	–	–	–	64.86	13.50	21.00	Nabi et al. (2017); Şahin and Aksu (2015); Zheng et al. (2015)
5	Canola biodiesel	39.000	4.4000	C ₁₉ H ₃₅ O ₂	295.50	884.4000	54.30	177.6	–	–8.00	–	–	–	–	Ozsezen et al. (2009)
6	Calophyllum inophyllum methyl ester	38.900	5.7600	–	–	872.0000	58.70	179.0	198.0	13.20	4.00	0.03	–	–	Kshirsagar and Anand (2017); Ramesh Babu et al. (2017)
7	Ethanol	26.800	1.4000	C ₂ H ₅ OH	46.07	785.0000 at 20 °C	5.00	13.0	–	<–26.00	–	52.20	13.00	34.80	Herreros et al. (2015); Labeckas et al. (2014); Morsy (2015)
8	Waste fish oil	41.000	4.1420	–	–	870.0000 –880.0000 at 15 °C	51.50	164.0–173.0	125.0	–	–	82.06	8.64	9.30	Fadhill and Ahmed (2016); Ghareghani et al. (2017); Gnanasekaran et al. (2016)
9	Cotton seed oil	39.500	35.7000	C ₁₈ H ₃₂ O ₂	–	929.0000 at 15 °C	45.00	230.0	228.0	–	–	77.39	11.90	11.10	Daho et al. (2013); Srihari et al. (2017); Singh et al. (2018a, b)
10	Soybean methyl ester	39.700	4.7000	C _{18.74} H _{34.43} O ₂	–	880.0000 at 20 °C	51.00	69.0	–	–2.00	–7.00	–	–	–	Gonca and Dobrucali (2016); Rajak and Verma (2018a, b); Senthil Kumar et al. (2015)
11	Coconut methyl ester	37.800	27.6400	CH ₃ (CH ₂) ₈ –COOH	217.00	0.9089	60.00	391.0	–	279.00	264.00	–	–	–	Singh et al. (2018a, b); Zareh et al. (2017)
12	Hexanol biofuel	39.100	3.4120	C ₆ H ₁₃ OH	102.18	821.8000	23.00	59.0	–	–	–	–	–	15.70	De Pours et al. (2017)
13	Honge oil	36.100	5.6000	–	–	890.0000	42.00	163.0	–	–2.00	1.00	–	–	–	Khandal et al. (2017)
14	Jatropha oil methyl esters	39.500	4.1200	C ₁₂ –C ₂₂	–	–	48.13	165.0	–	–4.00	–6.00	–	–	12.25	Dubey and Gupta (2017); Singh et al. (2018a, b)
15	Waste cooking oil	38.200	5.8700	C _{6.41} H _{12.21} O _{0.68}	–	844.0000	53.00	130.0	132.0	–	–	80.21	12.60	7.30	Asokan et al. (2019); Lapuerta et al. (2005)

16	Corn oil	38.400	4.5000	$C_{17.89}H_{32.8}O_2$	—	880.0000	52.50	165.0	—	—3.00	—5.10	76.70	11.52	10.9	Singh et al. (2018a, b); Shehata et al. (2015)
17	Jojoba oil	42.760	25.4800	—	—	833.0000	52.50	292.0	—	—	6.00	81.80	5.20	—	Huzayyin et al. (2004); Saleh and Selim (2017)
18	Karanja methyl ester	37.300	27.8400	—	—	913.0000	39.00	205.0	209.0	13.20	6.40	—	—	—	Bajpai et al. (2009)
19	Pine oil	42.800	1.3000	$C_{10}H_{16}+$ $C_{10}H_{18}O$	140.00	875.1000	11.00	52.0	—	—12.00	—12.00	—	—	—	Vallinayagam et al. (2014a, b)
20	Kerosene biodiesel	41.780	1.1500	$C_{12}H_{26}$	170.33	797.0000	41.40	40.0	—	—78.00	—	84.61	15.39	—	Patil and Thipse (2015); Roy et al. (2014)
21	Rapeseed methyl ester	37.600	4.5000	$C_{19}H_{35.2}O_2$	—	920.9000	37.60	280.0	—	—4.00	—31.70	—	—	10.90	Senthil Kumar et al. (2015)
22	Palm oil	38.840	4.4000	$C_{18.07}H_{34.93}O_2$	284.17	870.0000	56.50	70.6	—	10.00	—	—	—	—	Bora and Saha (2015); Ozsezen et al. (2009)
23	Pongamia oil methyl ester	39.140	5.5000	$C_{17.63}H_{32.94}O_2$	—	890.0000	55.40	175.0	—	—	4.00	—	—	—	Bora and Saha (2015)
24	Neem methyl ester	41.000	4.6300	$C_{35}H_{44}O_{16}$	720.00	871.0000	53.50	222.0	210.0	—4.00	8.00	—	—	11.00	Dhamodaran et al. (2017); Sharma et al. (2009)
25	Rice bran oil	39.540	3.2400— 4.9800	$C_{18.05}H_{34.5}O_2$	—	880.0000	56.30	152.0	159.0	3.00	—1.00	—	—	11.25	Bora and Saha (2015); Chhabra et al. (2017); Dhamodaran et al. (2017)
26	Linseed methyl ester	39.750	4.2000	—	—	921.0000	48.00	161.0	—	—	—18.00	78.14	9.98	11.72	Puhan et al. (2009)
27	Cynara methyl ester	—	4.8000	$C_{18.7}H_{34.68}O_2$	292.64	887.0000	59.00	—	—	—	—	—	—	10.93	Lapueta et al. (2005)
28	Mahua methyl ester	36.000	24.5800	—	—	920.0000	57.00	232.0	—	15.00	10.00	77.90	12.80	9.30	Acharya et al. (2017)
29	Kapok methyl ester	39.400	4.2000	—	—	875.0000 at 40 °C	51.00	148.0	—	4.00	—4.40	—	—	—	Senthil Kumar et al. (2015)
30	Turkey rendering fat biodiesel	40.680	4.4900	—	—	885.8000 at 15 °C	52.40	178.1	—	—	4.00	—	—	—	Emiroğlu et al. (2018)
31	Sand apple ethyl ester	—	3.9000	—	—	899.0000	54.30	165.5	—	4.78	1.05	—	—	—	Ogunkunle and Ahmed (2019)
32	Sunflower methyl ester	—	4.1300	$C_{18.9}H_{34.8}O_2$	294.58	885.4000	56.40	—	—	—	—	—	—	10.86	Lapueta et al. (2005)
33	n-pentanol	34.650	2.8900	$C_5H_{11}-OH$	88.15	814.8000 at 15 °C	20.00	49.0	—	—	—	68.13	13.61	18.15	Dhanasekaran et al. (2017)
34	Terminalia oil	39.220	5.1700	—	—	882.8000	53.00	90.0	—	—	6.00	—	—	—	Chakraborty et al. (2009); Kakati and Gogoi (2016)
35	Bitter almond oil	—	26.1200	—	—	0.9224 at 15.6 °C	—	185.0	—	—4.00	—7.00	—	—	—	Fadhil et al. (2016a, 2017)
36	Bitter almond oil	—	26.1200	—	—	0.9224 at 15.6 °C	—	185.0	—	—4.00	—7.00	—	—	—	Fadhil et al. (2016a)

(continued on next page)

Table 2 – (continued)

Sr. No.	Biodiesel	CV (MJ/kg)	V (cSt at 40 °C)	MF	MW (kg/kmol)	Density (kg/m ³)	CN	FP (°C)	FPT (°C)	CP (°C)	PP (°C)	Percent of C (%)	Percent of H (%)	Percent of O (%)	Ref.
37	Beauty leaf	–	4.5000	–	–	0.8900	56.50	145.6	–	12.55	–2.76	–	–	–	Hassan et al. (2015)
38	Cashew nut shell oil	35.800	55.3000	C ₂₂ H ₃₀ O ₃	–	0.9581 at 15 °C	33.00	234.0	–	–	–	–	–	–	Kasiraman et al. (2012)
39	Camphor oil	38.200	1.9000	C ₁₀ H ₁₆ O	–	0.8952 at 15 °C	5.00	50.0	–	–	–	–	–	–	Kasiraman et al. (2012)
40	Orange oil	39.000	3.5200	C ₁₀ H ₁₆	–	0.8169 at 15 °C	47.00	74.0	–	–	–	–	–	–	Kasiraman et al. (2016)
41	Camelina sativa oil	38.200	28.9400	–	–	925.4000 at 15 °C	–	>220.0	–	–	–	–	–	–	Kruczynski (2013)
42	Castor oil methyl ester	38.300	10.8000	–	–	918.0000 at 15 °C	78.00	186.0	–	–	–27.00	–	–	–	Ozcanli et al. (2017)
43	Mustard oil	39.857	5.7700	–	–	880.0000 at 15 °C	50.00	158.0	–	–	–12.00	–	–	–	Uyumaz (2018)
44	Waste tire pyrolysis oil	42.830	3.2000–3.3500	–	–	935.0000 at 15 °C	28.00	43.0	50.0	–	–	86.92	10.46	–	Mani and Nagarajan (2009)
45	Waste plastic oil	44.340	2.5200	–	–	837.5000 at 15 °C	51.00	42.0	45.0	2.00	–	–	–	–	Mani and Nagarajan (2009)
46	Koroch seed oil	40.510	26.0600	–	–	931.0000 at 15 °C	55.00	95.0	–	4.00	3.00	–	–	–	Kakati and Gogoi (2016)
47	Kutkura fruit seed oil	38.169	28.9200	–	–	922.5000 at 15 °C	45.84	–	–	5.00	–2.00	–	–	–	Kakati and Gogoi (2016)
48	Coconut oil	39.920	4.0200	–	–	856.0000	56.70	145.5	–	4.00	3.00	73.20	12.50	14.30	How et al. (2018a)
49	Waste frying oil methyl ester	39.550	4.3180	–	–	888.0000 at 15 °C	52.00	156.0	–	3.00	–2.50	–	–	–	Utlü and Koçak (2008)
50	Terebinth oil	39.100	4.4800	–	–	920.0000 at 15 °C	46.00	228.0	–	–	–	–	–	–	Ilklic et al. (2015)
51	Cymbopogon flexuosus biofuel	37.000	4.6000	–	–	905.0000	–	55.0	–	–	–	–	–	–	Dhinesh et al. (2017)
52	Hazelnut methyl ester	40.000	3.9100–4.5400	–	–	861.9000	52.20	168.0	–	–11.00	–	75.70	11.60	11.90	Efe et al. (2018)
53	Algae oil methyl esters	37.060	4.7300	–	–	883.6000	–	179.0	–	–	–	–	–	–	Makareviciene et al. (2014)
54	Tallow methyl ester	39.858	5.0700	C ₅₃ H ₁₀₂ O ₆	–	877.0000 at 17 °C	58.80	30.0	–	–	0	76.77	12.80	11.47	Öner and Altun (2009)
55	Bisethoxy methyl furan	30.800	5.9900	C ₁₀ H ₁₆ O ₃	184.23	1011.7000 at 15 °C	–	59.5	–	–	–	–	–	–	De Jong et al. (2012)
56	Amani seed oil	39.400	5.8400	–	–	898.2000	53.80	145.0	155.0	10.00	2.00	–	–	–	Kakati et al. (2017)
57	Thész boros-király biodiesel	34.810	6.4300	–	–	905.0000 at 15 °C	50.80	221.0	–	–	–	–	–	13.92	Szabados and Bereczky (2018)
58	Bauhinia variegata oil	39.900	4.6000	–	–	875.0000 at 15 °C	–	181.0	–	4.00	3.00	–	–	–	Yatish et al. (2018)
59	Pithecellobium dulce seed oil	39.510	3.5400	–	–	870.0000	68.00	158.0	165.0	6.00	–8.00	76.78	13.17	9.414	Chandra Sekhar et al. (2018)
60	Rubber seed oil	36.500–41.070	5.8100–5.9600	–	–	860.0000–881.0000 at 40 °C	37.00–49.00	130.0–140.0	–	–	–	–	–	–	Geo et al. (2017)

(continued on next page)

Table 2 – (continued)

Sr. No.	Biodiesel	CV (MJ/kg)	V (cSt at 40 °C)	MF (kg/kmol)	MW (kg/kmol)	Density (kg/m ³)	CN	FP (°C)	FPT (°C)	CP (°C)	PP (°C)	Percent of C (%)	Percent of H (%)	Percent of O (%)	Ref.
86	Polanga	41.390	3.9900–5.3400	–	–	869.0000	57.30	140.0	–	13.20	4.20	–	–	–	Sahoo and Das (2009)
87	Tobacco seed oil methyl ester	38.430–39.810	3.5000–4.2300	–	–	860.0000–888.5000 at 40 °C	49.00–51.60	152.0–165.4	–	–	–	–	–	–	Usta et al. (2011)
88	Waste tire pyrolysis	42.080	2.7100	–	–	887.2000 at 15 °C	44.00	39.0	–	–	–	85.49	10.48	2.74	Ayoob and Fadhil (2020); Wang et al. (2016)
89	Black soldier fly larvae	–	5.2000	–	–	872.0000	50.00	121.0	–	–	–	–	–	–	Nguyen et al. (2017)
90	Ceibapentandra oil	43.600	3.2200	–	–	883.5000	47.00	36.0	–	–	–	–	–	–	Tamilselvan et al. (2018)
91	Ethyl ester of fish oil	40.050	4.7400	–	–	885.0000	52.60	114.0	125.0	–	–	–	–	–	Sakthivel et al. (2014)
92	Crude rice bran oil methyl ester	38.850	4.0300	–	–	–	–	169.0	–	–	–	–	–	–	Saravanan et al. (2013)
93	Spent coffee ground	–	4.6100	–	–	878.0000	–	–	–	12.50	–	–	–	–	Tuntiwiwattanapun and Tongcumpou (2018)
94	Chicken feather biodiesel	–	3.9000	–	–	810.0000	50.00	120.0	–	2.00	–	–	–	–	Purandaradas et al. (2018)
95	Rooster feather biodiesel	–	4.3000	–	–	870.0000	55.00	126.0	–	3.00	–	–	–	–	Purandaradas et al. (2018)
96	Shea olein	46.200	4.4200	–	–	877.0000	–	131.0	–	–	–	–	–	–	Mutyalu et al. (2018)
97	Kaner seed oil	42.400	4.2000	–	–	870.0000	–	175.0	186.0	–	–	–	–	–	Yadav et al. (2017)
98	Cleome viscosa methyl ester	39.200	5.4100	–	–	896.0000	–	178.0	–	–	–	–	–	–	Perumal and Ilankumaran (2018)
99	Poultry litter oil methyl ester	29.000	5.4800	–	–	737.0000	61.00	154.0	178.0	–	–	–	–	–	Ramesh et al. (2018)
100	Simarouba oil methyl ester	38.500	4.6800	–	–	865.0000	56.00	165.0	172.0	–	14.20	0.10	–	–	Mishra et al. (2018)

experimentally investigated soybean biodiesel and its blends (30%, 50%, and 80%) at variable load conditions in a single-cylinder 4-stroke CI engine. Combustion of biodiesel and its blends produced higher peak pressure at lower engine loads, while at higher load conditions there was no significant change. The cylinder pressure for biodiesel fuel and diesel was found to be 8.12 and 8.11 MPa at 90% load condition, respectively.

3.1.2. Heat release rate

Heat release rate plays a crucial role in the analysis of combustion in CI engine. The model used to calculate the HRR was based on the theories and different laws of thermodynamics. The higher viscosity and low volatility of the rapeseed seed oil biodiesel and its various blends will affect improper fuel atomization and reduces the heat release rate (Atabani et al., 2012). This is because of the high viscosity and lower calorific value of the JME, and on the other side, turpentine biodiesel has CV higher and the low viscosity, and this makes the lake of JBD (Dubey and Gupta, 2018).

3.1.3. Ignition delay

The ignition delay in the CI engine is described by the time interval between the fuel injection timing and the start of combustion. Ignition delayed due to the physical processes (such as atomization, evaporation and mixing of fuel with air) and chemical processes such as pre-combustion reactions. These processes are mainly influenced by fuel characteristics, operating variables and engine design. Ignition delay plays a crucial role in the combustion and emission characteristics of the CI engine fueled with diesel and biodiesel blends.

Dhamodaran et al. (2017) investigated three different biodiesels, namely rice bran, neem and cotton seeds oil as an alternative fuel in CI engine under various loading conditions. They found that RBME indicates low ignition delay because of higher cetane value RBME biodiesel (Kaisan et al., 2017). Ignition delay was higher with diesel fuel, while on the other side, lower ignition duration is found with RBME. Ignition delay for other tested fuel reduced with increasing the load, due to the confinement of heat generating in the previous cycle, dilution of exhaust gas temperature and temperature at the combustion chamber wall. Another possible reason for this reduction in ignition temperature at higher load conditions is higher in-cylinder temperature, which increases the fuel vaporization rate, leading to a decrease in ignition delay.

Several researchers proposed empirical relations to estimate the ignition delay period based on fuel compositions and injection conditions. Wolfer presents the most used empirical link for ignition delay (Westlund, 2009).

$$\tau = AP^n \exp\left(\frac{E_a}{R_u T}\right) \quad (1)$$

where A and n are constants, E_a is the fuel's activation energy, P and T are the mean pressure and temperature of the combustor's compressed air, R_u is the universal gas constant.

Another empirical relation to evaluating the ignition delay is proposed by the Saravanan et al. (2014), which is also applicable to the diesel and biodiesel fuel blends, given below in Eq. (2).

$$\tau = \exp(-(0.0187CN + 8.551))P_i^{0.7352} \exp\left(\frac{4626.44}{T_L}\right) \quad (2)$$

where P_i is the pressure at the start of the injection, T_L is the load condition temperature and CN is the cetane number.

3.1.4. Combustion duration

Behçet et al. (2014) investigated fish oil biodiesel and its blends with diesel fuel in different proportions in a CI engine under variable loading conditions with constant engine speed. The author observed that the combustion duration process increases with an increasing load for all blends of biodiesel because, at higher loading condition, more fuel is injected into the combustion chamber. Blends of biodiesel and neat biodiesel indicated lower combustion duration for all engine operating conditions. The presence of higher oxygen percentage in the biodiesel reduces combustion duration and improves burning at a faster rate (Candeia et al., 2009; Lin and Lin, 2007; Wu et al., 2009).

3.2. Performance characteristics

3.2.1. Brake thermal efficiency

Savariraj et al. (2011) investigated mahua biodiesel and its blends (B25, B50, B75, B100) under different load conditions. They found that the brake thermal efficiency (BTE) for all load conditions is lower for biodiesel and blends. However, increasing biodiesel percentage in diesel reduces BTE compared to diesel due to the higher density, higher viscosity and low calorific value of the mahua oil biodiesel and its blends (Vijay Kumar et al., 2018).

3.2.2. Brake specific fuel consumption

Baiju et al. (2009) investigated the diesel engine characteristics by using Karanja oil methyl and ethyl esters (KOME and KOEE) as a fuel with different blends and regular diesel fuel and at other load conditions. With an increase in engine load, a reduction in BSFC was reported for all tested fuels. B20 KOME blend indicated lower fuel consumption at full load conditions. Therefore, this decrement in the diesel-biodiesel blend is may be due to the engine takes more fuel to obtain the same output power because of its low calorific value than diesel fuel.

3.2.3. Exhaust gas temperature

Sakthivel et al. (2014) used fish oil biodiesel with its blends in different proportion such as (20%, 40%, 60%, 80%, and 100%) in a single cylinder, with a constant engine speed of 1500 rpm under different loading conditions. EGT for blend B20 (270.4 °C) was found close to diesel fuel (269.2 °C). The mean EGT was about 2.4%, 2.1%, 1.1% and 3.3% for blend B40, B60, B80 and B100 respectively, higher than diesel fuel. The increase in EGT for biodiesel fuel is because higher oxygen percentage improves the combustion process. The low volatility and higher viscosity of biodiesel fuel lead to slow-burning of the fuel and causes an increase in temperature (Behçet et al., 2014). Generally, the fuel having a lower cetane number increases the ignition delay and more accumulate the fuel-air mixing, which also effects on the faster heat release rate at the start of the combustion process, and results in higher temperature (Singh et al., 2018a, b).

3.2.4. Engine torque

How et al. (2018b) investigated calophyllum inophyllum biodiesel as a fuel in medium-duty, four cylinders, four strokes, diesel turbocharged, CI engine at different engine speeds (1500, 2000, 2500, 3000, 3500, 4000 rpm) and torque conditions. The results showed maximum torque at 2000 rpm for all the tested fuels. Higher biodiesel blends reported a reduction in engine torque over the entire testing speed range for all fuels. The reduction was accepted, and also many researchers aligned the same (Habibullah et al., 2014; Liaquat et al., 2013). The reason for this decrement is because of biodiesel fuel having higher viscosity and lower calorific than diesel. Besides, this blend with a higher percentage of biodiesel fuel reduces the engine torque.

3.2.5. Brake power

Brake power is the amount of power generated at the output shaft by the engine. Zareh et al. (2017) studied the performance and emission characteristics using three different biodiesel namely castor oil biodiesel (CAB), coconut oil biodiesel (COB) and waste cooking oil biodiesel (WCB). The results showed that the biodiesel properties such as viscosity, lower and higher heating value influenced the brake power of the CI engine. This reduction of power is due to the biodiesel and its blends having low heating value than diesel (Vieira da Silva et al., 2017).

3.3. Emission characteristics

3.3.1. Smoke emission

Gnanasekaran et al. (2016) investigated the effects of the ethyl ester of fish oil (EEFO) and its blends with different injection timing (21°, 24° and 27° before top dead center) on a direct injection characteristic. Results reported higher average smoke emission by 7% for diesel and 3%–4% for biodiesel blend with 21° compared to 24° before the top dead center. Higher smoke emission for biodiesel compared to diesel fuel was measured due to reduced volatility, higher viscosity and improper fuel and air mixing.

3.3.2. Particulate matter (PM) emission

Nabi et al. (2017) investigated the PM emission on multi-cylinder, high-pressure common rail, and turbocharged engine fueled with regular diesel and diesel-butanol blends. The B10, B20 and B30 blends by volume basis at 10%, 20% and 30% n-butanol respectively with diesel fuel at CR17.5 with different engine load. The PM emissions decreased with n-butanol and maximum reduction of 70% with biodiesel at B6 blend due to associated with the absence of aromatics, sulfur and fuel oxygen in the blends. Herreros et al. (2015) obtained the engine characteristics fuelled by ethanol-diesel blends. The PM emission associated with the soot is a solid carbonaceous and soluble organic material that is adsorbed/condensed hydrocarbons onto the soot particles' surface. The PM emission decreases with higher loads and also affected by exhaust gas recirculation.

3.3.3. Carbon dioxide (CO₂) emission

Ramalingam et al. (2016) investigated annona biodiesel fuel additive using 1, 4-dioxane. The CO₂ emission reduced with additive A20, A20DO5 (A20 with 5 mL 1, 4-dioxane) and A20DO10 (A20 with 10 mL 1, 4-dioxane) as compared to diesel fuel due to higher percentage oxygen and CO₂ emission higher with higher engine load. Palash et al. (2015) investigated aphanamixis polystachya methyl ester with diesel on a DI engine. The blend APME10 found to be higher by 6.21% than diesel due to higher oxygen present within the APME10 and obtained complete combustion than diesel.

3.3.4. Carbon monoxide (CO) emission

Vallinayagam et al. (2014a, b) evaluated the effects of neat pine biodiesel and diesel on direct injection engine characteristics. The experiment was conducted at different inlet air temperatures and constant injection timing with constant engine speed. Authors studied CO emission with different air inlet temperature. They reported lower emission for pine biofuel at 40 °C air inlet temperature higher engine load. Meanwhile, the air inlet temperature of 60 °C shows a reduction by 13.2% lower than diesel fuel at

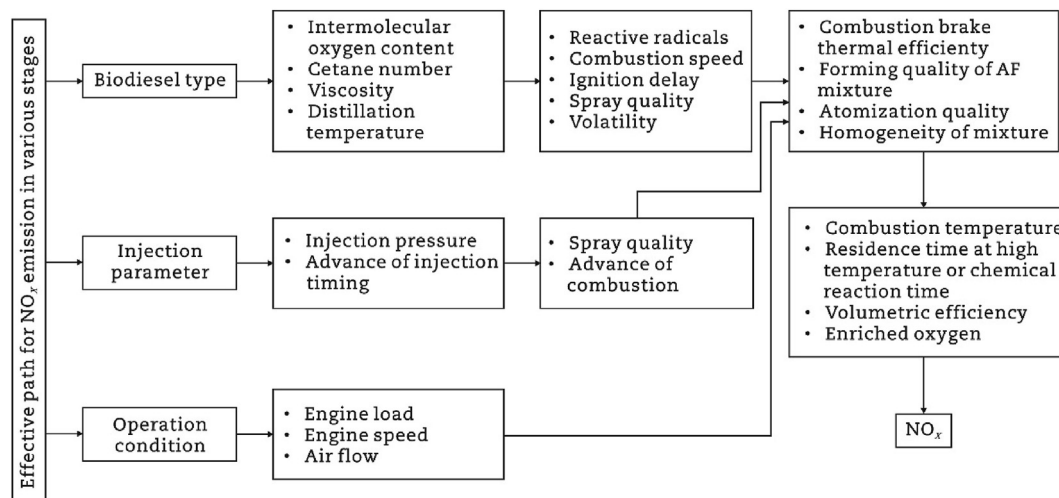


Fig. 3 – Effective parameters and path of NO_x emission during combustion.

Table 3 – Results for different biodiesels on different operating conditions.

Sr. No.	Year	Biodiesel	Fuel blend	Operating condition	Performance	Combustion	Emission	Reference
1	2015	Aphanamixis polystachyn methyl ester	AMPE5, AMPE10	Different engine speed at full load condition	↓: Brake Power ↑: BSFC	–	↓: CO, NO	Palash et al. (2015)
2	2017	Aegle marmelos oil (bael oil)	B20, B30, B40	Varying compression ratio and different engine load	↑: BTE ↓: BSFC	–	↓: CO, HO, NO _x , smoke	Krishnamoorthi and Malayalamurthi (2017)
3	2014	Annona methyl ester	A20, A40, A60, A80, A100	Constant speed and different engine load	↑: BTE	–	↓: CO, HO, smoke ↑: NO _x	Senthil and Silambarasan (2015)
4	2015	n-butanol	nB2, nB4, nB6	Different engine speed and load	↑: BSFC, BTE	↑: cylinder pressure, HRR	↓: CO ₂ , HC, NO _x ↑: smoke	Şahin and Aksu (2015)
5	2015	Butanol	nB100	Constant speed and IMEP	↑: BTE	↑: maximum rate of pressure rises ↓: cylinder pressure, HRR	↓: NO _x , soot	Zheng et al. (2015)
6	2017	Canola biodiesel	5, 10, 15, 20	Constant engine speed with different loading condition	↑: BSFC, BTE	↑: cylinder pressure, HRR	↓: CO, HC, smoke ↑: NO _x , CO ₂	Can et al. (2017)
7	2017	Calophyllum inophyllum methyl ester	CIME10, CIME15, CIME20, CIME25	Different injection timing, injection pressure, and loading conditions	↑: BSFC, BTE	↑: cylinder pressure ↓: HRR	↓: UBHC, CO, SOOT, O ₂ ↑: CO ₂ , NO	Kshirsagar and Anand (2017)
8	2015	Ethanol	25, 50, 75, 100	Different engine speed	↑: BSFC, BTE ↓: EGT	–	↓: NO ↑: CO, HC	Morsy (2015)
9	2017	Waste fish oil	B25, B50, B75, B100	Constant engine speed and different engine load	↑: BTE	↑: cylinder pressure ↓: HRR	↓: CO, UHC ↑: NO _x , CO ₂	Ghareghani et al. (2017)
10	2013	Cotton seed oil	CSO20, CSO40, CSO60, CSO80, CSO100	Different engine load with constant engine speed	↑: BSFC ↓: BTE	↓: HRR	↑: CO ↓: NO _x , CO ₂	Daho et al. (2013)
11	2017	Coconut methyl ester	COB5, COB10, COB20, COB30	Different engine load and engine speed	↑: BSFC, BTE	–	↓: PM, CO, CO ₂ ↑: NO _x	Zareh et al. (2017)
12	2017	Honge oil		Different EGR, fuel injection pressure and injection timing with constant speed and compression ratio	↑: BTE	↑: peak cylinder pressure, HRR ↓: ignition delay, combustion duration	↓: HC, CO, smoke ↑: NO _x	Khandal et al. (2017)
13	2017	Jatropha oil methyl esters	BT50, BT70, and BT90	Constant speed with different engine load	↓: BTE	–	↓: NO _x , CO, HC, smoke ↑: CO ₂	Dubey and Gupta (2017)
14	2004	Jojoba oil	20, 40, 60 and 100	Different engine speed	↑: BTE ↓: BSFC	–	↓: soot ↑: NO _x	Huzayyin et al. (2004)
15	2009	Karanja methyl ester	5, 10, 15 and 20	Different engine load	↑: BTE ↓: BSFC, EGT	–	↓: NO _x , smoke	Bajpai et al. (2009)
16	2014	Pine oil	B100	Different engine load	↓: BSFC	↑: cylinder pressure	↓: HC, CO, smoke ↑: NO _x	Vallinayagam et al. (2014b)
17	2014	Kerosene biodiesel	5, 10, 20, 50, 100	Different engine load	↑: BSFC	–	↓: CO, HC, NO _x ↑: CO, UHC	Roy et al. (2014)
18	2017	Neem methyl ester	100	Different engine load and constant engine speed	↑: EGT ↓: BTE	↑: HRR ↓: cylinder pressure	↓: NO _x , smoke	Dhamodaran et al. (2017)
19	2009	Neem biodiesel	20	Different brake power	↑: BTE ↓: BSFC	–	↓: NO _x , HC, CO, smoke	Sharma et al. (2009)

(continued on next page)

Table 3 – (continued)

Sr. No.	Year	Biodiesel	Fuel blend	Operating condition	Performance	Combustion	Emission	Reference
20	2009	Linseed methyl ester	100	Different injection pressure	↓: BTE	↑: cylinder pressure ↓: ignition delay, combustion duration	↓: CO, HC, CO ₂ ↑: NO _x	Puhan et al. (2009)
21	2015	kapok methyl ester	20, 40, 60, 80, 100	Different engine load and constant engine speed	↑: BSFC, EGT ↓: BTE	–	↓: CO, HC, NO _x	Senthil Kumar et al. (2015)
22	2018	Turkey rendering fat biodiesel	TRFB10, TRFB20, TRFB50	Different engine load and constant engine speed	↑: BSFC ↓: BTE	↑: cylinder peak pressure, HRR	↓: smoke ↑: NO _x	Emiroğlu et al. (2018)
23	2017	Calophyllum inophyllum methyl ester	butylated hydroxytoluene, ethanol	constant engine speed	↑: BSFC, BTE	–	–	Ashok et al. (2017)
24	2013	Camelina sativa oil	100	Different engine speed	↓: BTE	–	↑: NO _x , HC, CO, smoke	Kruczyński (2013)
25	2018	Mustard oil	M10, M20, M30	constant speed with various load condition	↑: BSFC ↓: indicated thermal efficiency	↓: cylinder pressure	↓: CO, smoke, ↑: NO _x	Uyumaz (2018)
26	2016	Koroch seed oil	10, 20	Different engine load	↑: BTE, indicated thermal efficiency ↓: BTE	–	↓: smoke	Kakati and Gogoi (2016)
27	2017	Hazelnut methyl ester	20, 50, 100	Different engine speed	–	–	–	Efe et al. (2018)
28	2018	Bauhinia variegata oil	10, 20, 30, 40, 100	Different engine load	↓: BTE	–	↓: HC, CO ↑: NO _x	Yatish et al. (2018)
29	2016	Pistacia lentiscus	BD5, BD30, BD50, BD100	Constant engine speed with different engine load	↑: BSFC, BTE	–	↓: HC, CO, PM ↑: NO _x	Khiari et al. (2016)
30	2015	Aphanamixis polystachya methyl ester	APME5, APME10	Variable engine speed	↓: torque, brake power ↑: BSFC	–	↓: CO, HC ↑: CO ₂ , NO	Palash et al. (2015); Wu et al. (2013)
31	2017	Soya soap stock-based acid oil biodiesel	100	Different engine speed	↓: indicated thermal efficiency, BTE	↑: cylinder peak pressure, cylinder temperature, injection duration, combustion duration ↓: heat release rate	↓: UHC, CO, smoke ↑: NO _x	Tripathi and Subramanian (2017)
32	2014	Eucalyptus biodiesel	100	Constant speed with various load condition	↑: BSFC	–	↓: UHC, CO, CO ₂ ↑: NO _x	Tarabet et al. (2014)
33	2014	Animal fat biodiesel	A10, A20, A25, A30, A40 and A50	Constant speed with various load condition	↑: SFC, BTE	–	↑: NO _x ↓: particle number	Barrios et al. (2014)
34	2017	Salvia macrosiphon oil	5, 10, 15 and 20	Different engine speed	↑: BTE ↓: SFC	–	↓: CO, HC ↑: CO ₂ , NO _x	Hoseini et al. (2017)
35	2017	Groton methyl ester	CM20	Constant speed with various load condition	↑: BSFC, EGT ↓: BTE	↓: ignition delay, combustion duration, peak heat release rate	↓: CO, HC ↑: NO _x	Ruhul et al. (2017)
36	2009	Paradise oil methyl ester	20, 30, 40, 50	Different engine loading condition	↑: BTE	–	↓: CO, HC, CO ↑: NO _x	Devan and Mahalakshmi (2009)
37	2011	Tobacco seed oil methyl ester	–	–	NA	–	–	Usta et al. (2011)

(continued on next page)

Table 3 – (continued)

Sr. No.	Year	Biodiesel	Fuel blend	Operating condition	Performance	Combustion	Emission	Reference
60	2017	Castor oil methyl ester	CME20	Different engine speed	↑: power, torque ↓: BSFC	–	↓: CO ↑: NO _x	Ozcanli et al. (2017)
61	2009	Waste plastic oil	100	Different injection timing and engine load	↑: BTE	↓: cylinder pressure	↓: CO, UHC, NO _x	Mani and Nagarajan (2009)
62	2018	Coconut oil biodiesel	B20, B50	Different SOI and with constant engine speed	NA	–	↓: NO _x , smoke	How et al. (2018a)
63	2008	Waste frying oil methyl ester	100	Different engine speed	↓: BTE	–	↓: CO, NO _x ↑: smoke	Utlü and Koçak (2008)
64	2014	Terebinth oil	B10, B50	Different engine speed	↑: BSFC, ↓: power	–	↓: CO, HC, CO ₂ ↑: NO _x	Ilkiliç et al. (2015)
65	2016	Gymbopogon flexuosus biofuel	C20, C100	constant speed with various load condition	↑: BTE	↑: cylinder peak pressure, HRR	↓: NO _x , HC, CO, smoke	Dhinesh et al. (2017)
66	2014	Algae oil methyl esters (AME)	AME20	Different engine load	↑: BTE	–	↓: HC, smoke	Makareviciene et al. (2014)
67	2009	Tallow methyl ester	B5, B20, B50, B100	Different engine speed	↑: BSFC ↓: BTE	–	↓: CO, NO _x , SO ₂ , smoke	Öner and Altun (2009)
68	2009	Thész-Boros-Király	100	Different engine speed, load, and torque	NA	↑: ignition delay, HRR	↓: HC ↑: NO _x	Öner and Altun (2009)
69	2018	Pithecellobium dulce seed oil	20, 40, 60, 80	Constant speed with various load condition	↑: BSFC, ↓: BTE, EGT	↓: cylinder pressure, HRR	↓: CO ₂ , smoke ↓: CO, HC, NO _x	Chandra Sekhar et al. (2018)
70	2017	Rubber seed oil	25, 50, 75, 100	Constant speed with various load condition	↑: BTE	↑: peak pressure, maximum rate of pressure rises, HRR, ignition delay ↓: combustion duration	↓: smoke ↑: HC, NO _x , CO	Geo et al. (2017)
71	2015	Honne oil methyl ester	20, 40, 60, 80, 100	Difference compression ratio and engine load with constant engine speed	↑: BSFC ↓: BTE	–	↓: CO, HC, smoke ↑: NO _x	Channapattana et al. (2015)
72	2017	Microalgae chlorella protothecoides	MCP20, MCP50, B100	Different engine speed	↓: brake power torque, exhaust gas temperature ↑: BSFC, BTE	–	↓: CO, CO ₂ , NO _x ↑: O ₂	Al-lwayzy and Yusaf (2017)
73	2015	Mango seed biodiesel	20, 100	Different engine load and ppm	↑: BSFC, BTE ↓: BTE	–	↓: NO _x ↑: CO, smoke, HC	Velmurugan and Sathiyagnanam (2016)
74	2017	Tung oil	DT30E20, DT30E30	Different engine speed	↑: BSFC, BTE	↑: peak pressure, maximum rate of pressure rises, HRR ↑: cylinder pressure ↓: ignition delay	↓: smoke, CO, HC ↑: NO _x	Qi et al. (2017)
75	2013	Wood pyrolysis oil	5, 10, 15	Different engine load	↑: BTE	–	↓: NO, smoke	Prakash et al. (2013)
76	2014	Geiba pentandra biodiesel	10, 20, 30, 50	Different engine speed	↓: BSFC	–	↓: CO ₂ , CO, smoke ↑: NO _x	Ong et al. (2014)
77	2011	Safflower oil	B5, B20, B50	Different engine speed	↑: BSFC	–	↓: PM, smoke ↑: NO _x , HC	Ilkiliç et al. (2011)
78	2017	Tea seed oil biodiesel	B10, B20	Different engine speed	↑: BSFC	–	↓: CO ↑: CO ₂ , NO _x	Serin and Yıldızhan (2018)

79	2010	Chinese pistache biodiesel	100	Constant speed with various load condition	↑: SFC	–	↓: CO, HC, NO _x , smoke	Huang et al. (2010)
80	2014	Peanut methyl ester	100	Different engine speed	–	–	↓: CO ↑: NO _x	Tosun et al. (2014)
81	2014	Carbon black	10	Different injection pressure and load	↑: BTE ↓: EGT	–	↓: HC, CO, NO _x , smoke, NO	Tosun et al. (2014)
82	2016	Moringa methyl ester	20	Different engine speed	↑: BSFC ↓: BP	–	↓: CO, HC, NO	Rashed et al. (2016)
83	2009	Polanga	20, 50, 100	Different engine loading condition	NA	↑: peak cylinder pressure ↓: ignition delay	–	Sahoo and Das (2009)
84	2018	Spent coffee ground	NA	NA	NA	–	–	Tuntiwiwattanapun and Tongcumpou (2018)
85	2016	Shea olein biodiesel	10, 20, 100	Constant load and different injection pressure	↑: BSFC, BTE ↓: EGT	–	↓: CO, HC ↑: NO _x	Mutyalu et al. (2018)
86	2018	Cleome viscosa methyl ester	20, 40, 60, 80, 100	Different engine load	↑: EGT ↓: BSFC, BTE	–	↓: HC, CO, CO ₂ ↑: NO _x	Perumal and Ilankumaran (2018)
87	2018	Poultry litter oil methyl	20	Different engine load condition	↑: BTE	↓: cylinder pressure, HRR	↓: UHC, CO, NO _x	Ramesh et al. (2018)
88	2016	Cymbopogon flexuosus biofuel	10, 20, 30, 40, 100	constant speed with various load condition	↑: BSFC ↓: BTE	↓: cylinder pressure, HRR	↓: HC, CO, smoke ↑: CO ₂ , NO _x	Dhinesh et al. (2016)
89	2011	Mahua biodiesel	25, 50, 75, 100	Different engine load and constant engine speed	↑: BSFC ↓: BTE	–	↓: HC ↑: NO, CO, smoke	Savariraj et al. (2011)
90	2017	Waste cooking oil	B20, B30, B40, B100	Different engine load condition	↑: BSFC ↓: BTE	↑: HRR ↓: cylinder pressure	↓: CO ↑: NO _x	Senthur Prabu et al. (2017)
Note: "↑" means increase, "↓" means decrease, "–" means no change, "NA" means not available.								

100% load due to higher in-cylinder temperature and the essential occurrence of oxygen within pine oil.

3.3.5. Unburnt hydrocarbon (UHC) emission

[Saleh and Selim \(2017\)](#) performed an experimental investigation on characteristics of a diesel engine using diesel fuel, jojoba methyl ester-diesel-ethanol ternary fuel blends (B5, B10, B15, B20, and B25) with variable engine load and constant engine. The single-cylinder direct-injection engine used in this investigation. The investigated result of UHC emission shows that it increased with a higher engine load. This happens due to the rich fuel-air mixture in the combustion chamber and increasing fuel consumption. This shows a reduction in UHC emission for the JME blend of B10 by 39% at 520 kPa and B5 by 27% lower compared to diesel fuel due to more oxygen content. They conclude that UHC emission highest lower recorded at B10 blend compared to diesel fuel.

3.3.6. Oxides of nitrogen (NO_x) emission

In the exhaust of CI engine, NO_x formation occurred due to the thermal NO_x procedure, which is affected by the burned mixture temperature, the confined air/fuel ratio and the dwell time at higher temperatures in the engine cylinder. [Chen et al. \(2018c\)](#) provides a detail discussion on the NO_x emission of biodiesel. Authors reported that fuel injection parameters such as injection timings and injection pressure perform an important role in combustion temperature and NO_x emissions.

[Ruhul et al. \(2017\)](#) investigated the effects of millettia pinnata and croton megalocarpus biodiesel on a DI CI engine characteristics with variable engine load and engine speed. The result of NO_x emission evaluated the used of chain reaction based on zeldovich mechanism. The NO_x emission obtained higher with engine speed and higher for blends biodiesel (MP20, CM20, MP15CM5, MP10CM10 and MP5CM15) compared to diesel fuel due to a higher percentage of oxygen contents and higher combustion temperature within the premixed and diffusion combustion phase. Numerous studies ([Chen et al., 2018a](#); [Dwivedi et al., 2019](#); [Geng et al., 2020](#)) have been established the increasing trend of NO_x emission by using biodiesel. But some studies ([Guo et al., 2019](#); [Nair et al., 2017](#); [Pereira et al., 2007](#)) also shown the reduction in NO_x due to the addition of biodiesel. [Nair et al. \(2017\)](#) and [Pereira et al. \(2007\)](#) reported less NO_x emission by using neem biodiesel and soybean biodiesel, respectively, than diesel. At low load, [Chen et al. \(2018b\)](#) reported that the NO_x emission of biodiesel is less than that of diesel for the engine operating under lower or medium speeds due to weak air swirl movement and poor in-cylinder heat condition.

NO_x emission of biodiesel is a significantly important issue, and it depends upon various parameters such as biodiesel type, engine technology and structure, operation conditions, combustion temperature and injection parameters ([Dwivedi et al., 2018](#); [Verma et al., 2020](#); [Zare et al., 2018, 2020](#)). Effective parameters and path of NO_x emission is shown in [Fig. 3](#). The engine characteristics for various biodiesel fuel blends are reported by researchers are shown in [Table 3](#).

4. Conclusions

First, second and third-generation biodiesel and their blends have different properties that influence diesel engine characteristics such as BTE, BSFC, EGT, smoke emission, NO_x emission, brake power, etc. Therefore, the selection of different generation feedstock is necessary and generally depends upon the domestic birthplaces of the region. The variation with different generation biodiesel feedstocks and its blends properties will impact the overall performance, combustion and emission characteristics of the CI engine. There are numerous previous studies that have been reviewed in this study which can be concluded based on previously studied.

- First-, second- and third-generation biodiesel and their blends feedstocks will impact energy and percentage of oxygen, cetane number, the heating value of fuel, density, and viscosity.
- The calorific value of the fuel is an important attribute to produce engine power. It was observed that different generation biodiesel blends reduce the engine power because of lower calorific values of fuel (MJ/kg) than diesel fuel. For some biodiesel, the calorific value of the fuel is higher such as 42.76, 45.76, 43.60, 46.20, 42.83, and 42.80 MJ/kg for jojoba, eucalyptus, ceibapentandra oil, shea olein, waste tire pyrolysis oil, and pine oil and lower calorific value are found for 26.80, 29.00, 35.10, 34.65 and 30.80 MJ/kg for ethanol, poultry litter oil methyl ester, corn oil, n-pentanol and bisethoxy methyl furan as compared to diesel fuel (42.50 MJ/kg), respectively.
- The combustion quality should be improved to meet the higher engine thermal efficiency; therefore, the maximum amount of fuel energy produced by the fuel is transferred to the engine. Therefore, oxygen is the crucial property for biodiesel that will improve the combustion process and efficiency of the engine. Besides this, preventing heat losses produces during the combustion process and ignition delay is lower due to the higher cetane value of the fuel, and it also improves the air/fuel rate and indicates a better combustion process.
- PM emission is a composite combination of carbon, sulfur, nitrogen and other compounds produced. In numerous previous studies presented that biodiesel-diesel blends (B20) reduce PM emissions by 22% compared to regular diesel fuel, which is occurred due to a higher percentage of oxygen that helps to improve combustion and spray characteristics.
- Unburnt hydrocarbon (UHC) emission indicated the level of inclusiveness for one combustion progression as it measures the total of unburned hydrocarbon. According to many studies, diesel-biodiesel blends reduce the UHC by about 15% for blend B20. Because of the higher cetane value of the blend, it causes a shorter ignition delay period and improves the efficiency of the engine.
- Percentage of oxygen content within the fuel leads to increase NO_x emission, as the presence of oxygen percentage of the biodiesel will form complete combustion of the fuel and it also increases the combustion temperature inside

the combustion chamber. Diesel-biodiesel has shown lower NO_x emissions up to 10% due to the presence of a higher percentage of oxygen for blend B20 compared to diesel fuel.

- Diesel-biodiesel blends (B20) show a reduction in CO emissions by 18% compared to regular diesel fuel. It is noticed that the oxygen percentage in biodiesel plays an essential role in sustaining the oxidation process during the exhaust stroke. The CO emission gets affected by energy contents and latent heat of vaporization of the fuel.

Thus, based on the review, it can be concluded that first-, second- and third-generation biodiesel-diesel blends slightly affected CI engine performance and showed a reduction in destructive exhaust gas emissions fueled with diesel-biodiesel blends of first-, second- and third-generation than with diesel fuel.

Conflict of interest

The authors do not have any conflict of interest with other entities or researchers.

Nomenclature

ANN	Artificial neural network
APME	Aphanamixis polystachya methyl ester
AC	Air cooling
bTDC	Before top dead center
BTE	Brake thermal efficiency
BHT	Butylated hydroxytoluene
BSFC	Brake specific fuel consumption
BME	Butanol-methyl ester
BP	Brake power
CA	Crank angle
CO ₂	Carbon dioxide
CO	Carbon monoxide
CI	Compression ignition
CN	Cetane number
C	Carbon
CFB	Cymbopogon flexuosus biodiesel
CR	Compression ratio
CAB	Castor oil biodiesel
COB	Coconut oil biodiesel
CIME	Calophyllum inophyllum methyl ester
CM	Croton megalocarpus
CP	Cloud point
CV	Calorific value
EGT	Exhaust gas temperature
EGR	Exhaust gas recirculation
EME	Ethanol methyl ester

EEFO	Ethyl ester of fish oil
FT	Fuel type
FP	Flash point
FPT	Fire point
HC	Hydrocarbon
H	Hydrogen
HRR	Heat release rate
HEX	Hexanol
IC	Internal cooling
IP	Injection pressure
JME	Jatropha methyl ester
KV	Kinetic viscosity
MFB	Mass fraction burned
MME	Methanol-methyl ester
MP	Millettia pinnata
MF	Molecular formula
MW	Molecular weight
NO _x	Nitrogen oxide
NG	Natural gas
NH	Nozzle hole
ND	Nozzle diameter
O ₂	Oxygen
PM	Particulate matter
PME	Peanut methyl ester
PP	Pour point
RC	Radiator cooling
RBME	Rice brain methyl ester
SOI	Start of injection
SO _x	Sulfur oxide
TDC	Top dead center
UHC	Unburned hydrocarbon
WPO	Wood pyrolysis oil
WCB	Waste cooking oil biodiesel
WC	Water cooling

REFERENCES

- Acharya, N., Nanda, P., Panda, S., et al., 2017. Analysis of properties and estimation of optimum blending ratio of blended mahua biodiesel. *Engineering Science and Technology, an International Journal* 20 (2), 511–517.
- Agarwal, A.K., Dhar, A., Gupta, J.G., et al., 2015. Effect of fuel injection pressure and injection timing of Karanja biodiesel blends on fuel spray, engine performance, emissions and combustion characteristics. *Energy Conversion and Management* 91, 302–314.
- Agarwal, A.K., Shrivastava, A., Prasad, R.K., 2016. Evaluation of toxic potential of particulates emitted from jatropha biodiesel fuelled engine. *Renewable Energy* 99, 564–572.
- Al-lwayzy, S.H., Yusaf, T., 2017. Diesel engine performance and exhaust gas emissions using microalgae chlorella protothecoides biodiesel. *Renewable Energy* 101, 690–701.
- Alptekin, E., Canakci, M., 2009. Characterization of the key fuel properties of methyl ester-diesel fuel blends. *Fuel* 88 (1), 75–80.
- Alptekin, E., Canakci, M., 2008. Determination of the density and the viscosities of biodiesel-diesel fuel blends. *Renewable Energy* 33 (12), 2623–2630.
- Altikriti, E.T., Fadhil, A.B., Dheyab, M.M., 2015. Two-step base catalyzed transesterification of chicken fat: optimization of

- parameters. *Energy Sources, Part A: Recovery, Utilization, and Environmental Effects* 37 (17), 1861–1866.
- Arbab, M.I., Masjuki, H.H., Varman, M., et al., 2013. Fuel properties, engine performance and emission characteristic of common biodiesels as a renewable and sustainable source of fuel. *Renewable and Sustainable Energy Reviews* 22, 133–147.
- Ashok, B., Nanthagopal, K., Jeevanantham, A.K., et al., 2017. An assessment of calophyllum inophyllum biodiesel fuelled diesel engine characteristics using novel antioxidant additives. *Energy Conversion and Management* 148, 935–943.
- Asokan, M.A., Senthur Prabu, S., Bade, P.K.K., et al., 2019. Performance, combustion and emission characteristics of julfiflora biodiesel fuelled DI diesel engine. *Energy* 173, 883–892.
- Atabani, A.E., Silitonga, A.S., Badruddin, I.A., et al., 2012. A comprehensive review on biodiesel as an alternative energy resource and its characteristics. *Renewable and Sustainable Energy Reviews* 16 (4), 2070–2093.
- Ayoo, A.K., Fadhil, A.B., 2020. Valorization of waste tires in the synthesis of an effective carbon based catalyst for biodiesel production from a mixture of non-edible oils. *Fuel* 264, 116754.
- Baiju, B., Naik, M.K., Das, L.M., 2009. A comparative evaluation of compression ignition engine characteristics using methyl and ethyl esters of Karanja oil. *Renewable Energy* 34 (6), 1616–1621.
- Bajpai, S., Sahoo, P.K., Das, L.M., 2009. Feasibility of blending karanja vegetable oil in petro-diesel and utilization in a direct injection diesel engine. *Fuel* 88 (4), 705–711.
- Bamgboye, A.I., Hansen, A.C., 2008. Prediction of cetane number of biodiesel fuel from the fatty acid methyl ester (FAME) composition. *International Agrophysics* 22 (1), 21–29.
- Banapurmath, N.R., Tewari, P.G., Hosmath, R.S., 2008. Performance and emission characteristics of a DI compression ignition engine operated on honge, jatropha and sesame oil methyl esters. *Renewable Energy* 33 (9), 1982–1988.
- Barrios, C.C., Domínguez-Sáez, A., Martín, C., et al., 2014. Effects of animal fat based biodiesel on a TDI diesel engine performance, combustion characteristics and particle number and size distribution emissions. *Fuel* 117, 618–628.
- Behçet, R., Yumrutaş, R., Oktay, H., 2014. Effects of fuels produced from fish and cooking oils on performance and emissions of a diesel engine. *Energy* 71, 645–655.
- Benjumea, P., Agudelo, J.R., Agudelo, A.F., 2011. Effect of the degree of unsaturation of biodiesel fuels on engine performance, combustion characteristics, and emissions. *Energy and Fuels* 25, 77–85.
- Bora, B.J., Saha, U.K., 2015. Comparative assessment of a biogas run dual fuel diesel engine with rice bran oil methyl ester, pongamia oil methyl ester and palm oil methyl ester as pilot fuels. *Renewable Energy* 81, 490–498.
- Can, Ö., Öztürk, E., Yücesu, H.S., 2017. Combustion and exhaust emissions of canola biodiesel blends in a single cylinder DI diesel engine. *Renewable Energy* 109, 73–82.
- Candeia, R.A., Silva, M.C.D., Carvalho Filho, J.R., et al., 2009. Influence of soybean biodiesel content on basic properties of biodiesel-diesel blends. *Fuel* 88 (4), 738–743.
- Chakraborty, M., Baruah, D.C., Konwer, D., 2009. Investigation of terminalia (terminalia belerica Roxb.) seed oil as prospective biodiesel source for north-east India. *Fuel Processing Technology* 90 (12), 1435–1441.
- Chandra Sekhar, S., Karuppasamy, K., Vedaraman, N., et al., 2018. Biodiesel production process optimization from Pithecellobium dulce seed oil: performance, combustion, and emission analysis on compression ignition engine fuelled with diesel/biodiesel blends. *Energy Conversion and Management* 161, 141–154.
- Channapattana, S.V., Kantharaj, C., Shinde, V.S., et al., 2015. Emissions and performance evaluation of di ci-vcr engine fuelled with honne oil methyl ester/diesel blends. *Energy Procedia* 74, 281–288.
- Chen, H., Ding, M., Li, Y., et al., 2020. Feedstocks, environmental effects and development suggestions for biodiesel in China. *Journal of Traffic and Transportation Engineering (English Edition)* 7 (6), 791–807.
- Chen, H., He, J., Zhong, X., 2019. Engine combustion and emission fuelled with natural gas: a review. *Journal of the Energy Institute* 92, 1123–1136.
- Chen, Y., Ma, J., Han, B., et al., 2018a. Emissions of automobiles fueled with alternative fuels based on engine technology: a review. *Journal of Traffic and Transportation Engineering (English Edition)* 5 (4), 318–334.
- Chen, H., Xie, B., Ma, J., et al., 2018b. NO_x emission of biodiesel compared to diesel: higher or lower? *Applied Thermal Engineering* 137, 584–593.
- Chen, H., Xie, B., Ma, J., et al., 2018c. NO_x emission of biodiesel compared to diesel: higher or lower? *Applied Thermal Engineering* 137, 584–593.
- Chhabra, M., Dwivedi, G., Baredar, P., et al., 2021. Production & optimization of biodiesel from rubber oil using BBD technique. *Materialstoday: Proceedings* 38 (1), 69–73.
- Chhabra, M., Sharma, A., Dwivedi, G., 2017. Performance evaluation of diesel engine using rice bran biodiesel. *Egyptian Journal of Petroleum* 26 (2), 511–518.
- Daho, T., Vaitilingom, G., Ouiming, S.K., et al., 2013. Influence of engine load and fuel droplet size on performance of a CI engine fueled with cottonseed oil and its blends with diesel fuel. *Applied Energy* 111, 1046–1053.
- De Jong, E., Vijlbrief, T., Hijkoop, R., et al., 2012. Promising results with YXY diesel components in an ESC test cycle using a PACCAR diesel engine. *Biomass and Bioenergy* 36, 151–159.
- De Pours, M.V., Sathiyagnanam, A.P., Rana, D., et al., 2017. 1-hexanol as a sustainable biofuel in DI diesel engines and its effect on combustion and emissions under the influence of injection timing and exhaust gas recirculation (EGR). *Applied Thermal Engineering* 113, 1505–1513.
- Devan, P.K., Mahalakshmi, N.V., 2009. A study of the performance, emission and combustion characteristics of a compression ignition engine using methyl ester of paradise oil-eucalyptus oil blends. *Applied Energy* 86 (5), 675–680.
- Dhamodaran, G., Krishnan, R., Pochareddy, Y.K., et al., 2017. A comparative study of combustion, emission, and performance characteristics of rice-, bran-, neem-, and cottonseed-oil biodiesels with varying degree of unsaturation. *Fuel* 187, 296–305.
- Dhanasekaran, R., Krishnamoorthy, V., Rana, D., et al., 2017. A sustainable and eco-friendly fueling approach for direct-injection diesel engines using restaurant yellow grease and n-pentanol in blends with diesel fuel. *Fuel* 193, 419–431.
- Dhinesh, B., Isaac JoshuaRamesh Lalvani, J., Parthasarathy, M., et al., 2016. An assessment on performance, emission and combustion characteristics of single cylinder diesel engine powered by cymbopogon flexuosus biofuel. *Energy Conversion and Management* 117, 466–474.
- Dhinesh, B., Niruban Bharathi, R., Isaac JoshuaRamesh Lalvani, J., et al., 2017. An experimental analysis on the influence of fuel borne additives on the single cylinder diesel engine powered by cymbopogon flexuosus biofuel. *Journal of the Energy Institute* 90 (4), 634–645.
- Dubey, P., Gupta, R., 2018. Influences of dual bio-fuel (jatropha biodiesel and turpentine oil) on single cylinder variable compression ratio diesel engine. *Renewable Energy* 115, 1294–1302.
- Dubey, P., Gupta, R., 2017. Effects of dual bio-fuel (jatropha biodiesel and turpentine oil) on a single cylinder naturally aspirated diesel engine without EGR. *Applied Thermal Engineering* 115, 1137–1147.
- Dwivedi, G., Pillai, S., Shukla, A.K., 2019. Study of performance and emissions of engines fueled by biofuels and its blends.

- In: Agarwal, A., Gautam, A., Sharma, N., et al. (Eds.), *Methanol and the Alternate Fuel Economy*. Springer, Singapore, pp. 77–106.
- Dwivedi, G., Sharma, M.P., Verma, P., et al., 2018. Engine performance using waste cooking biodiesel and its blends with kerosene and ethanol. *Materialstoday: Proceedings* 5, 22955–22962.
- Dwivedi, G., Verma, P., Sharma, M., 2016. Impact of oil and biodiesel on engine operation in cold climatic condition. *Journal of Materials and Environmental Science* 7, 4540–4555.
- Efe, Ş., Ceviz, M.A., Temur, H., 2018. Comparative engine characteristics of biodiesels from hazelnut, corn, soybean, canola and sunflower oils on DI diesel engine. *Renewable Energy* 119, 142–151.
- Emiroğlu, A.O., Keskin, A., Şen, M., 2018. Experimental investigation of the effects of Turkey rendering fat biodiesel on combustion, performance and exhaust emissions of a diesel engine. *Fuel* 216, 266–273.
- Fadhil, A.B., Ahmed, A.I., 2016. Ethanolysis of fish oil via optimized protocol and purification by dry washing of crude ethyl esters. *Journal of the Taiwan Institute of Chemical Engineers* 58, 71–83.
- Fadhil, A.B., Ahmed, A.I., Salih, H.A., 2017. Production of liquid fuels and activated carbons from fish waste. *Fuel* 187, 435–445.
- Fadhil, A.B., Aziz, A.M., Altamer, M.H., 2018. Optimization of methyl esters production from non-edible oils using activated carbon supported potassium hydroxide as a solid base catalyst. *Arab Journal of Basic and Applied Sciences* 25, 56–65.
- Fadhil, A.B., Aziz, A.M., Altamer, M.H., 2016a. Potassium acetate supported on activated carbon for transesterification of new non-edible oil, bitter almond oil. *Fuel* 170, 130–140.
- Fadhil, A.B., Saeed, L.I., 2016. Sulfonated tea waste: a low-cost adsorbent for purification of biodiesel. *International Journal of Green Energy* 13, 110–118.
- Fadhil, A.B., Saeed, I.K., Saeed, L.I., et al., 2016b. Co-solvent ethanolysis of chicken waste: optimization of parameters and characterization of biodiesel. *Energy Sources, Part A: Recovery, Utilization, and Environmental Effects* 38, 2883–2890.
- Geng, L., Wang, Y., Wang, J., et al., 2020. Numerical simulation of the influence of fuel temperature and injection parameters on biodiesel spray characteristics. *Energy Science & Engineering* 8, 312–326.
- Geo, V.E., Sonthalia, A., Nagarajan, G., et al., 2017. Studies on performance, combustion and emission of a single cylinder diesel engine fuelled with rubber seed oil and its biodiesel along with ethanol as injected fuel. *Fuel* 209, 733–741.
- Gharehghani, A., Mirsalim, M., Hosseini, R., 2017. Effects of waste fish oil biodiesel on diesel engine combustion characteristics and emission. *Renewable Energy* 101, 930–936.
- Giannelos, P.N., Sxizas, S., Lois, E., et al., 2005. Physical, chemical and fuel related properties of tomato seed oil for evaluating its direct use in diesel engines. *Industrial Crops and Products* 22 (3), 193–199.
- Gnanasekaran, S., Saravanan, N., Ilangkumaran, M., 2016. Influence of injection timing on performance, emission and combustion characteristics of a DI diesel engine running on fish oil biodiesel. *Energy* 116, 1218–1229.
- Gonca, G., Dobrucali, E., 2016. Theoretical and experimental study on the performance of a diesel engine fueled with diesel-biodiesel blends. *Renewable Energy* 93, 658–666.
- Guo, Y., Stevanovic, S., Verma, P., et al., 2019. An experimental study of the role of biodiesel on the performance of diesel particulate filters. *Fuel* 247, 67–76.
- Habibullah, M., Masjuki, H.H., Kalam, M.A., et al., 2014. Biodiesel production and performance evaluation of coconut, palm and their combined blend with diesel in a single-cylinder diesel engine. *Energy Conversion and Management* 87, 250–257.
- Hajjari, M., Tabatabaei, M., Aghbashlo, M., et al., 2017. A review on the prospects of sustainable biodiesel production: a global scenario with an emphasis on waste-oil biodiesel utilization. *Renewable and Sustainable Energy Reviews* 72, 445–464.
- Hassan, N.M.S., Rasul, M.G., Harch, C.A., 2015. Modelling and experimental investigation of engine performance and emissions fuelled with biodiesel produced from Australian beauty leaf tree. *Fuel* 150, 625–635.
- Herreros, J.M., Schroer, K., Sukjit, E., et al., 2015. Extending the environmental benefits of ethanol-diesel blends through DGE incorporation. *Applied Energy* 146, 335–343.
- Hoseini, S.S., Najafi, G., Ghobadian, B., et al., 2017. Effects of biodiesel fuel obtained from *Salvia macrosiphon* oil (ultrasonic-assisted) on performance and emissions of diesel engine. *Energy* 131, 289–296.
- How, H.G., Masjuki, H.H., Kalam, M.A., et al., 2018a. Influence of injection timing and split injection strategies on performance, emissions, and combustion characteristics of diesel engine fueled with biodiesel blended fuels. *Fuel* 213, 106–114.
- How, H.G., Masjuki, H.H., Kalam, M.A., et al., 2018b. Effect of *Calophyllum Inophyllum* biodiesel-diesel blends on combustion, performance, exhaust particulate matter and gaseous emissions in a multi-cylinder diesel engine. *Fuel* 227, 154–164.
- Huang, J., Wang, Y., Qin, J., et al., 2010. Comparative study of performance and emissions of a diesel engine using Chinese pistache and *jatropha* biodiesel. *Fuel Processing Technology* 91 (11), 1761–1767.
- Huzaayin, A.S., Bawady, A.H., Rady, M.A., et al., 2004. Experimental evaluation of diesel engine performance and emission using blends of jojoba oil and diesel fuel. *Energy Conversion and Management* 45 (13–14), 2093–2112.
- Ilkiliç, C., Aydın, S., Behcet, R., et al., 2011. Biodiesel from safflower oil and its application in a diesel engine. *Fuel Processing Technology* 92 (3), 356–362.
- Ilkiliç, C., Çilin, E., Aydın, H., 2015. Terebinth oil for biodiesel production and its diesel engine application. *Journal of the Energy Institute* 88 (3), 292–303.
- Jasrotia, A., Shukla, A.K., Kumar, N., 2019. Impact of nanoparticles on the performance and emissions of diesel engine using mahua biodiesel. In: *International Conference in Mechanical and Energy Technology*, Greater Noida, 2019.
- Kaisan, M.U., Anafi, F.O., Nuskowski, J., et al., 2017. Exhaust emissions of biodiesel binary and multi-blends from cotton, *jatropha* and neem oil from stationary multi cylinder CI engine. *Transportation Research Part D: Transport and Environment* 53, 403–414.
- Kakati, J., Gogoi, T.K., 2016. Biodiesel production from *kutkura* (*meyna spinosa* Roxb. Ex.) fruit seed oil: its characterization and engine performance evaluation with 10% and 20% blends. *Energy Conversion and Management* 121, 152–161.
- Kakati, J., Gogoi, T.K., Pakshirajan, K., 2017. Production of biodiesel from amari (*amoor wallichii* king) tree seeds using optimum process parameters and its characterization. *Energy Conversion and Management* 135, 281–290.
- Kasiraman, G., Edwin Geo, V., Nagalingam, B., 2016. Assessment of cashew nut shell oil as an alternate fuel for CI (compression ignition) engines. *Energy* 101, 402–410.
- Kasiraman, G., Nagalingam, B., Balakrishnan, M., 2012. Performance, emission and combustion improvements in a direct injection diesel engine using cashew nut shell oil as fuel with camphor oil blending. *Energy* 47 (1), 116–124.
- Khandal, S.V., Banapurmath, N.R., Gaitonde, V.N., 2017. Effect of exhaust gas recirculation, fuel injection pressure and

OUR PROJECTS



Electrical



Electronics &
Telecommunication



Electrical & Electronics



Mechanical



CIVIL



CSE/IT



Production



Applied Electronics



For more details scan the QR code Above



Plot no-N1/52, Street opposite
to Hanuman Temple Near
CRPF Gate,
CRPF
Square, Bhubaneswar, Odisha



+91-7205005344



services@oltrongroup.com

**Oltron
Group**